Universitat Autònoma de Barcelona

Procedència i patró de dispersió de sediments en conques d'avantpaís: Avantatges d'un enfoc multimètode i aplicació al cas de la conca sudpirinenca de Jaca

Xavier Coll Carrillo

Procedència i patró de dispersió de sediments en conques d'avantpaís:

Avantatges d'un enfoc multimètode i aplicació al cas de la conca sudpirinenca de Jaca

Xavier Coll Carrillo

Tesi Doctoral
2022

Universitat Autònoma de Barcelona

Facultat de Ciències
Departament de Geologia

Departament de Geologia, Facultat de Ciències

Universitat Autònoma de Barcelona

Procedència i patró de dispersió de sediments en conques d'avantpaís:

Avantatges d'un enfoc multimètode i aplicació al cas de la conca sudpirinenca de Jaca

Memòria presentada per Xavier Coll Carrillo per optar al títol de Doctor en Geologia

Març, 2022

La tesi doctoral ha estat dirigida per:

Dr. David Manuel Gómez Gras, Departament de Geologia de la Universitat Autònoma de Barcelona

Dr. Antonio Teixell Cácharo, Departament de Geologia de la Universitat Autònoma de Barcelona

Dra. Marta Roigé Taribó, Departament de Geologia de la Universitat Autònoma de Barcelona

Dr. David Manuel Gómez Gras Dr. Antonio Teixell Cácharo Dra. Marta Roigé Taribó

Xavier Coll Carrillo

Foto de la portada: Ventall al·luvial del Luna

A la meva família i amics

“El cosmos es todo lo que es, todo lo que fue y todo lo que será. Nuestras más ligeras contemplaciones del cosmos nos hacen estremecer: Sentimos como un cosquilleo nos llena los nervios, una voz muda, una ligera sensación como de un recuerdo lejano o como si cayéramos desde gran altura. Sabemos que nos aproximamos al más grande de los misterios”

Carl Sagan

“Somos el medio para que el cosmos se conozca a sí mismo.”

Carl Sagan

Aquesta tesi ha estat realitzada en el marc del Programa de Doctorat en Geologia, codirigida pel Dr. David Manuel Gómez Gras, el Dr. Antonio Teixell Cácharo, la Dra. Marta Roigé Taribó, i tutoritzada pel Dr. David Manuel Gómez Gras.

La realització d'aquesta tesi doctoral ha estat possible gràcies al finançament proporcionat per:

- Concurs per a la contractació de personal investigador en formació i personal investigador postdoctoral per al curs 2016-2017 (PIF, Universitat Autònoma de Barcelona).

- Ajuts destinats a universitats, centres de recerca i fundacions hospitalàries per contractar personal investigador novell per a l'any 2017 (FI, Agència de Gestió d'Ajuts Universitaris i de Recerca, 2017 FI_B 00376).

- Ayudas para la formación de profesorado universitario 2016 (FPU, Ministerio de Educación Cultura y Deporte, FPU16/00219).

- Ministerio de Economía y Competitividad, projecte "From rifting to mountain building in inversion orogens: tectonic, sedimentary and geomorphologic records" (CGL2014-54180-P).

- Ministerio de Ciencia, Inovación y Universidades , projecte "Registro de la extensión y la contracción en cadenas de montañas y cuencas periféricas: una aproximación tectónica, sedimentaria y de geofluidos"(GC2018-093903-B-C21).

- Jackson School of Geosciences (University of Texas at Austin).

ÍNDEX

Abstract/Resum

ABSTRACT

Foreland basins record the erosional and exhumational history of source areas, providing valuable information to decipher the chronology of deformation and orogenic growth. Sedimentary provenance analysis becomes key to unravel the links between tectonics and sedimentation, the evolution of the drainage network, and sediment dispersal patterns from a source to sink approach.

This thesis presents a multimethod provenance analysis of the sedimentary systems of the Jaca basin, comprising heavy minerals, U-Pb geochronology and (U-Th)/He thermochronology of detrital zircons, and the integration of these with petrographic analysis. This combined methodology is applied to the last deposits of the turbidite sedimentation stage (Lutetian), to the deltaic systems developed during the continentalization of the basin, and to the terrestrial systems that constitute the last stages of sedimentation (Priabonian-Miocene) in the basin.

In the eastern Jaca basin, the multimethod approach has revealed that during the last turbidite systems (the Rapitán channel), the metamorphic Paleozoic of the northern Axial Zone was locally exposed in the west-central Pyrenees. During the Priabonian, whereas the northern part of the Belsué-Atarés deltaic system was fed from source areas located to the north-east of the Jaca basin, the southern part was sourced from the eastern Pyrennes. Later, two distinct axially-fed systems individualized during the sedimentation of the Campodarbe Fm. The first system, which fed the easternmost sector of the Jaca basin, was sourced from the central Pyrenees, highly influenced by the diapiric structures outcropping in this area. The second system, developed in the western sector, was sourced from the eastern Pyrenees. This differentiation is only revealed through heavy mineral analysis. On the other hand, sedimentation in the westernmost Jaca basin was not influenced by the east-sourced axially-fed systems. Instead, it was sourced from the Basque massifs (western Pyrenees) and the Urbasa-Andía ranges (Basque-Cantabrian Pyrenees) from the Bartonian to the Miocene.

This thesis evidences that the integration of several provenance proxies stands as the only way to resolve ambiguous signatures in foreland basins influenced by sediment recycling, or where different source areas have the capability to produce the same provenance signatures depending on the marker considered.

RESUM

Les conques d'avantpaís registren la història erosiva i de l'exhumació de les seves àrees font, aportant informació indispensable per desxifrar la cronologia de la deformació i el creixement orogènic. Els estudis de procedència sedimentària esdevenen una eina indispensable per desxifrar les relacions entre la tectònica-sedimentació, l'evolució de les xarxes de drenatge, i els patrons de dispersió de sediments amb una concepció paleogeogràfica completa *source to sink.*

En aquesta tesi es presenta un estudi multimètode de la procedència dels sistemes sedimentaris de la conca de Jaca, basat en l'anàlisi de minerals pesants, l'anàlisi geocronològic d'U-Pb i termocronologic d'(U-Th)/He en zircons detrítics, i l'anàlisi i integració de dades de petrografia. Aquesta metodologia s'aplica en els dipòsits que constitueixen els últims estadis de sedimentació turbíditica (Lutecià), els sistemes deltaics que es desenvolupen durant la continentalització de de la conca, i els sistemes terrestres que representen els últims estadis de sedimentació (Priabonià-Miocè).

Aquest enfoc multimètode ha revelat en la conca de Jaca oriental que, durant els últims sistemes turbidítics (canal de Rapitán), el basament metamòrfic del Paleozoic inferior de la Zona Axial septentrional aflorava localment en el Pirineu centre-occidental durant el Bartonià. Durant el Priabonià, el sistema deltaic de Belsué-Atarés era alimentat, en la seva part nord, per àrees font ubicades al nord est de la conca de Jaca, i en la part sud per àrees fot al Pirineu oriental. Posteriorment, s'individualitzen dos sistemes de drenatge axial durant la sedimentació fluvial de la Fm. Campodarbe. El primer sistema alimenta el sector més oriental de la conca de Jaca, amb l'àrea font ubicada al Pirineu central, amb forta influència de les estructures diapíriques aflorants en aquella zona. El segon sistema, s'imposa en la part més occidental i es nodreix del Pirineu oriental. Aquesta diferenciació no s'observa sinó amb l'anàlisi dels minerals pesants. Per altra banda, la sedimentació en la conca de Jaca occidental no és influenciada pels drenatges axials procedents de l'est, sinó que es nodreix de l'erosió dels massissos bascs (Pirineu occidental) i la Sierra d'Urbasa-Andía del Pirineu basc-cantàbric des de el Bartonià fins al Miocè.

aquesta tesi evidencia que la integració de diferents tècniques d'anàlisi de la procedència és l'única manera de resoldre senyals ambigües en conques d'avantpaís dominades per processos de reciclatge sedimentari, i on les àrees font insuficientment diferenciades tenen l'habilitat de produir les mateixes senyals de procedència depenent del marcador considerat.

Capítol 1

Introducció

1.1. Anàlisi de procedència sedimentaria

El registre sedimentari pot preservar signatures d'events geològics en les àrees font i de possibles canvis soferts durant el seu transport i posterior dipòsit. En aquest sentit, la filosofia source to sink (figura 1.1) estudia tots els segments d'un sistema sedimentari (sediment routing systems, des de l'àrea font fins a la conca deposicional, incloent les àrees de transferència de sediment que connecten ambdós extrems (Castelltort & Van Den Driessche, 2003; Allen, 2009; Allen & Allen, 2013).

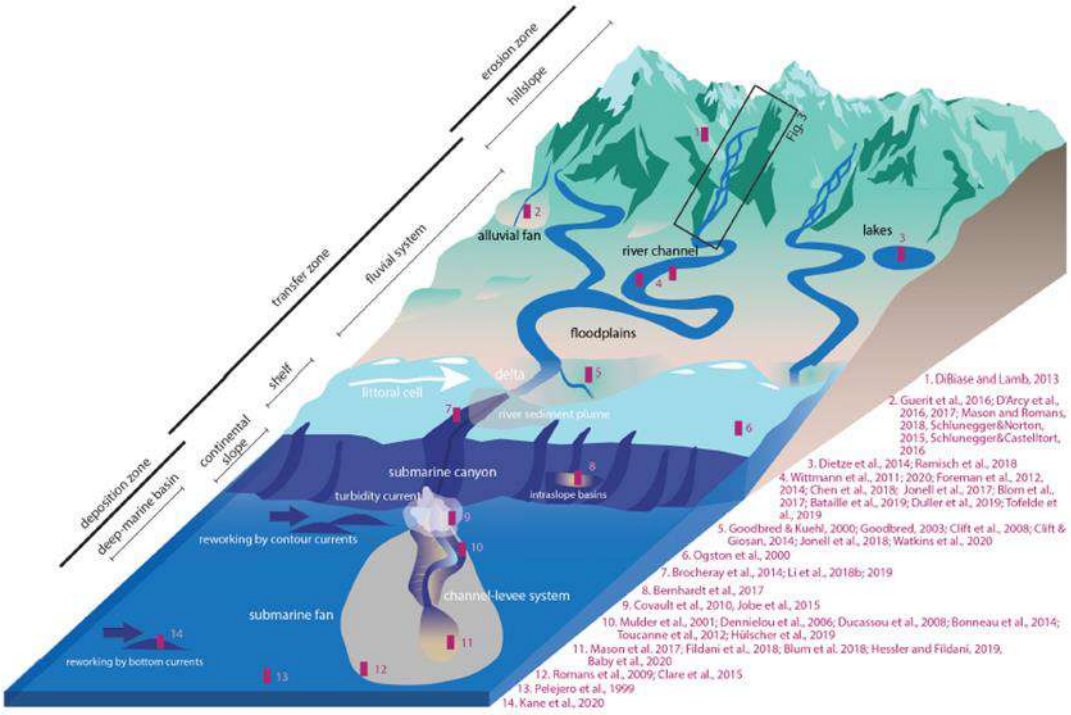

Figura 1.1. *Model conceptual d'un perfil source to sink (extret de Tofelde et al., 2021).*

Dins d'aquesta filosofia s'engloben diferents tipologies d'estudis, els quals contemplen els diferents paràmetres que influeixen en la generació de sediment, la propagació de senyals climàtiques i tectòniques, o la predicció de volums de sediment que es remobilitzen al llarg d'un sediment routing System (Paola et al., 1992; Caracciolo, 2020) . De particular interès són els estudis d'anàlisi de procedència sedimentària (Haughton, 1991) els quals van començar a ser emprats fa més de cent anys i comprenen diferents disciplines de la geologia, com són la petrologia, la mineralogia, la geocronologia, la termocronologia, o la geoquímica. Aquests estudis permeten testejar models tectònics de creixement d'oròdens, cartografiar sistemes deposicionals, predir la qualitat de reservoris detrítics, o definir relacions àrea font-conca de sedimentació. El resultat final que s'aconsegueix amb la realització d'aquests estudis permet obtindre informació inestimable en relació a la paleogeografia,

els patrons de dispersió de sediment de les xarxes de drenatge o la localització d'àrees sotmeses a subsidència o aixecament (Dickinson, 1970).

Els primers treballs de procedència de sediments intentaven relacionar la composició dels grans, les àrees font, i el context climàtic en qüestió. Posteriorment, amb l'aparició de la tectònica de plaques, es va començar també a intentar relacionar la composició dels sediments amb el context geotectònic. Dickinson & Suczek (1979) i Dickinson (1985) van evidenciar aquesta relació, la qual va permetre entendre la influència que exerceixen el clima, la tectònica, el relleu, el transport i la litologia de les àrees font en les composicions dels sediments que se'n deriven (figura 1.2). En les últimes dècades, els avenços tecnològics han permès incorporar l'ús d'isòtops estables, anàlisis geoquímics, elements traça (Haughton et al., 1991), i diverses tècniques de datacions geocronològiques i termocronològiques (Davis i Lin, 2003). No obstant, com és lògic, totes aquestes tècniques es troben subjectes a limitacions intrínseques degudes a una gran varietat de processos i/o característiques, que en alguns casos poden arribar a ser molt importants. Per exemple, en contextos en els que intervenen múltiples àrees font susceptibles de generar senyals de procedència similars o indiferenciables, o en contexts en que la influència que tenen els processos de reciclatge de sediments sobre la propagació d'aquestes senyals és subestimada o directament no considerada.

Els estudis de procedència es caracteritzen per una forta component deductiva que obliga a la necessitat d'obtenir la major informació possible. En aquest sentit, la integració de diferents mètodes de procedència es imprescindible per a comprendre la informació que es deriva de cada tècnica analítica i assolir una visió completa del cas d'estudi (Nie et al., 2012). En aquest sentit, l'anàlisi de minerals pesants, el qual representa l'eina principal emprada en aquesta tesi, pot aportar informació sobre minerals diagnòstics presents en àrees font molt concretes. D'entre les tècniques basades en els minerals pesants més emprades en els últims anys destaquen la geocronologia de zircons detrítics, la qual indica l'edat de cristal·lització dels grans, i la termocronologia de zircons detrítics que aporta informació de l'exhumació d'una àrea font. No obstant, s'ha de tenir present que, normalment, els minerals pesants representen com a molt un 1% del percentatge de grans en roques detrítiques, i d'entre ells, els zircons es troben encara en percentatges més baixos. Per tant, és important tenir en compte que els estudis de procedència basats en aquest tipus de minerals poden no ser suficientment acurats. En canvi, altres eines més clàssiques, com ara l'anàlisi petrogràfic en làmina prima o l'estudi de les poblacions de còdols en conglomerats, permeten caracteritzar el contingut total de la roca i obtenir així un anàlisi més complet d'aquesta. Així doncs, en funció de les característiques de les

diferents tècniques, és important valorar la integració d'aquestes per tal d'obtenir la màxima informació possible i evitar conclusions errònies o poc resolutives.

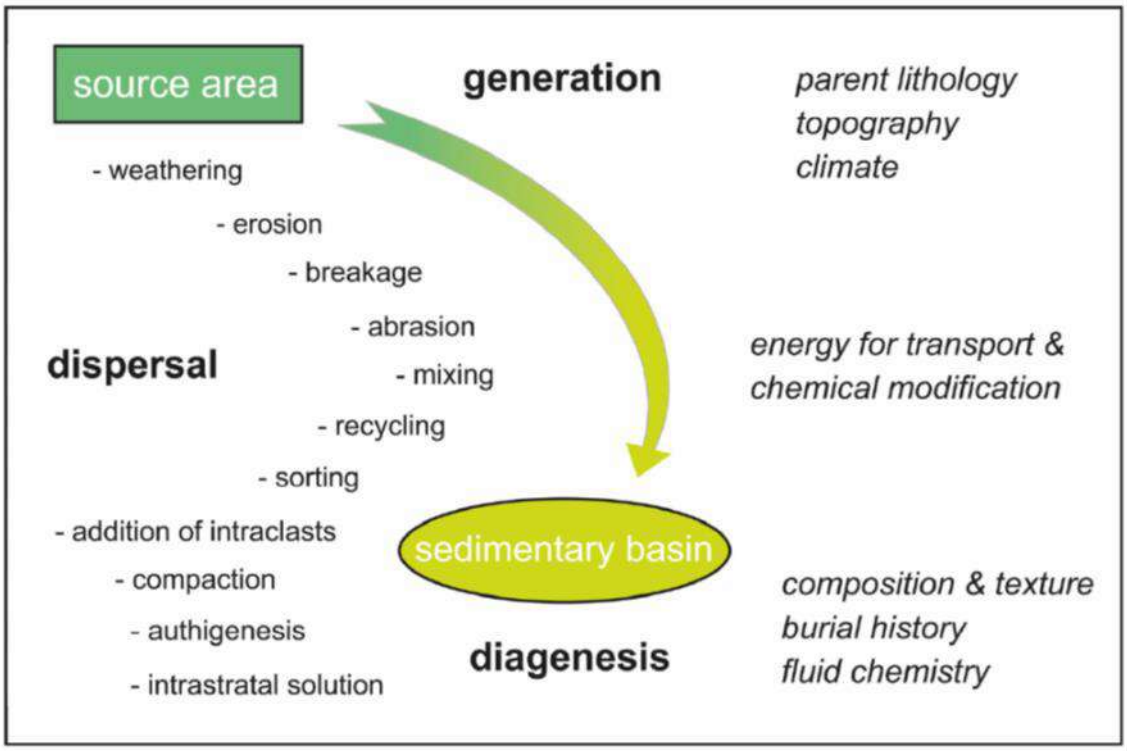

Figura 1.2. *Principals estadis en l'evolució d'un sediment (en negreta), els processos que poden modificar la composició d'aquest des de l'àrea font a la conca de sedimentació, i els processos al que és sotmès aquest sediment (en cursiva). (extret de Weltje i von Eynatten, 2004).*

Per últim, cal remarcar que els estudis de procedència no només requereixen la integració de diverses tècniques analítiques, sinó que la complementació amb el coneixement de la geologia regional, i altres disciplines com ara la tectònica o l'estratigrafia seqüencial, és clau per obtenir una major resolució en l'anàlisi de conques.

1.2. La conca Sudpirinenca

L'excel·lent registre sedimentari de la conca Sudpirinenca la converteix en una conca d'avantpaís de referència per a estudis tectònics, sedimentològics, i de procedència arreu del món (p.e. Mutti 1985; Mutti et al. 1985; Remacha and Fernández 2003; Remacha et al. 2005; Caja et al. 2010; Fontana et al. 1989; Gupta and Pickering 2008; Labaume et al. 1985, 2016; Labaume and Teixell 2018; Roigé et al. 2016, 2017; Boya 2018; Garcés et al. 2020). Els sectors oriental i centre-occidental de la conca

concentren la major part d'aquests treballs (sub-conques de Tremp-Graus i Ainsa) mentre que el sector més occidental, conegut com a sub-conca de Jaca, és relativament, menys conegut. No obstant, el registre sedimentari Lutecià superior-Miocè de la conca de Jaca constitueix exemple extraordinari per a estudiar les relacions tectònica-sedimentació i el reciclatge sedimentari durant la seva continentalització i la competència entre les àrees font actives i els patrons de dispersió de sediments.

1.2.1. Marc geològic

El cinturó de plecs i encavalcaments dels Pirineus va créixer diacrònicament, des del Cretaci tardà fins al Miocè, com a resultat de la col·lisió obliqua entre les plaques Ibérica i Europea (Vergés et al., 2002; Puigdefàbregas et al., 1992; Mouthereau et al., 2014; Teixell et al., 2018). La subducció de l'escorça inferior de la placa Ibèrica sota la placa Europea, va donar lloc a la inversió de les conques mesozoiques prèvies, desenvolupades durant el rifting Cretaci, i a l'apilament del basament, resultant en un prisma orogènic de doble vergència.

El cor del cinturó, conegut com la Zona Axial, està constituït per un seguit de làmines encavalcants de basament paleozoic. Al nord, la Zona Nordpirinenca, representa un seguit de conques mesozoiques (figura 1.3), delimitada per la conca de rerepaís d'Aquitània (Lagabrielle et al., 2010). Al sud de la Zona Axial (Zona Sudpirinenca), la deformació va ser acumulada per un ventall d'encavalcaments (Labaume & Seguret, 1985; Cámara & Klimowitz, 1985; Muñoz et al., 2018), que en el Pirineu centre-occidental, està constituït per quatre làmines encavalcants principals: Lakora-Eaux-Chaudes, Gavarnie, Broto i Guarga. Aquestes làmines involucren al basament paleozoic, una successió preorogènica mesozoica, i la conca d'avantpaís Sudpirinenca (Cretaci superior-Miocè inferior), la qual ha motivat un gran nombre d'estudis enfocats a reconstruir la paleogeografia de la conca durant aquest període de temps (Nijman i Nio, 1975; Mutti et al., 1972; Valloni et al., 1984; Nagtegaal i Weerd, 1985; Mutti, 1985; Fontana et al., 1989; Puigdefàbregas et al., 1992; Dreyer et al., 1999; Vincent, 2001; Gupta i Pickering, 2008; Caja et al., 2010; Whitchurch et al., 2011; Gómez-Gras et al., 2016; Roigé et al., 2016: Roigé et al., 2017; Thomson et al., 2017; Thompson et al., 2019; Odlum et al 2019). La conca Sudpirinenca es va formar inicialment com una conca estreta d'orientació est-oest, en connexió amb l'oceà l'Atlàntic fins a finals de l'Eocè (Costa et al., 2010). Aquesta conca era alimentada per un sistema de drenatge axial paral·lel a l'orògen, que progressivament, va ser substituït per un seguit de sistemes de drenatge transversal que es van imposar com a conseqüència de la creació de noves àrees font en el Pirineu central, el qual va experimentar una exhumació intensa durant el

Paleogen (Puigdefàbregas et al., 1992; Fitzgerald et al., 1999; Metcalf et al., 2009). Durant l'Eocè, els ambients fluvio-deltaics es concertaven en les sub-conques d'Àger i Tremp-Graus (zona oriental de la conca Sudpirinenca), canalitzant sediments cap a als ambients de talús i marins profunds de les sub-conques d'Aínsa i Jaca. Aquesta successió d'ambients marins profunds es coneix com a les turbidites del Grup Hecho, les quals es nodrien del Pirineu oriental i central, amb contribucions del massís de l'Ebre (Roigé et al., 2016; Thompson et al., 2017).

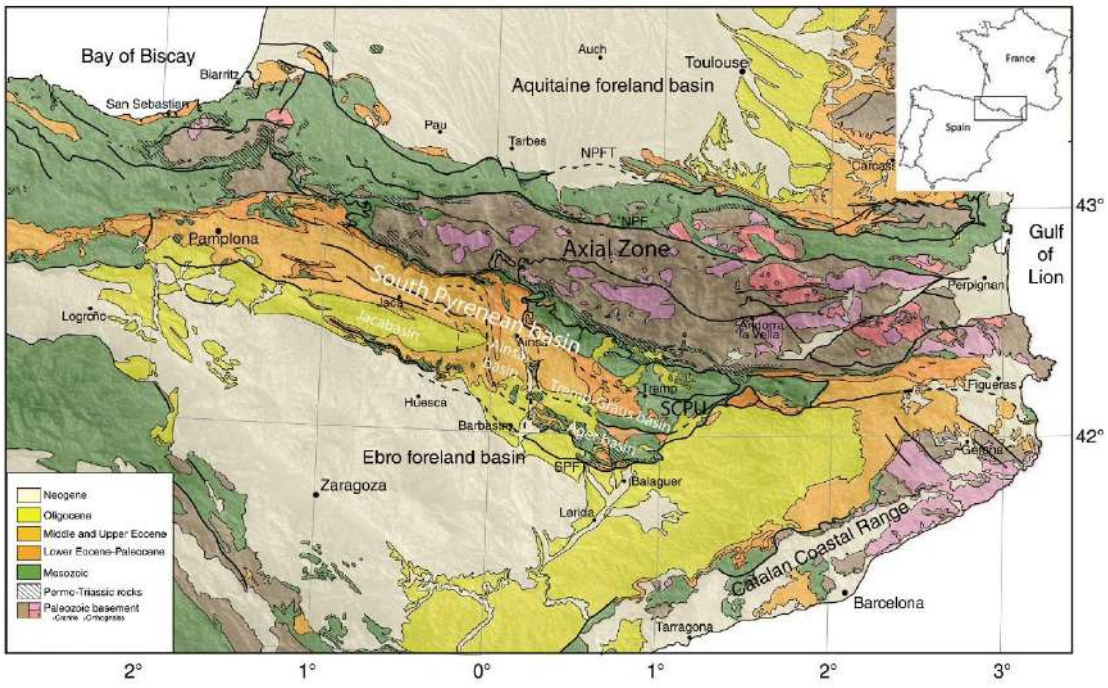

Figura 1.3. *Mapa geològic dels Pirineus, mostrant les conques d'Àger, Tremp-Graus, Ainsa i Jaca (extret de Mouthereau et al. 2014).*

La present tesi s'emmarca en la conca de Jaca, on la sedimentació turbidítica eocena és substituïda progressivament per ambients continentals a finals de l'Eocè i Oligocè, constituïnt els últims estadis de rebliment de la conca (Mutti et al., 1972; Puigdefàbregas, 1975). Durant el Lutecià, els sistemes turbidítics del Grup Hecho superior (Banastón i Jaca) eren alimentats per àrees font ubicades a l'est (Roigé et al., 2016), i puntualment, pel producte de les inestabilitats en les plataformes carbonàtiques del marge sud de la conca (calcàries de Boltaña i Guara) (Soler-Sampere i Puigdefàbregas, 1970; Labaume et al., 1985; Puigdefàbregas i Souquet, 1986; Barnolas i Teixell, 1994), les quals van donar lloc a megaturbidites carbonàtiques. Durant el Bartonià, la sedimentació dels últims estadis turbidítics (el canal turbidític de Rapitán a la part oriental i el canal turbidític d'Ezkaba a la part occidental), registren els primers aports procedents del nord de la conca (Payros et al., 1999; Roigé et al., 2016).

Durant el Bartonià-Priabonià, la sedimentació marina profunda és substituïda progressivament pels ambients deltaics i fluvials constituïts per les Formacions Gres de Sabiñanigo, Ardanatz, Belsué-Atarés, Liédena i Campodarbe (Hehuwat, 1970; Puigdefàbregas, 1975; Boya, 2018). Aquests sistemes registren una competència entre els sistemes axials derivats de l'est i els sistemes transversals derivats del nord, imposant-se els últims progressivament d'est a oest i de sud a nord (Roigé et al., 2017, Roigé 2018). Durant el Chatià-Aquitanià, la Formació Bernués representa la completa instauració dels sistemes transversals procedents del nord i la conca deixa de rebre aports dels sistemes axials procedents de l'est. La connexió amb l'est és interrompuda degut a la incorporació de la pròpia conca a l'orògen, la qual esdevé aixecada per l'encavalcament de Guarga, el qual dona lloc a les Serres Exteriors. És en aquest moment en que la conca de Jaca passa a ser erosionada, concentrant-se la sedimentació a la conca de l'Ebre.

1.2.2. Antecedents

Els treballs paleogeogràfics i de procedència referents als Pirineus focalitzen en l'evolució dels sistemes sedimentaris de la conca Sudpirinenca durant el Paleogen. Aquests estudis s'han centrat majoritàriament en les conques *piggy-back* d'Àger i Tremp-Graus, i la seva relació amb la sedimentació turbidítica a les conques d'Aínsa i Jaca durant els primers estadis d'exhumació de la part central del Pirineu. Únicament els treballs de Roigé et al. (2016, 2017, 2019) estudien en profunditat la procedència dels últims estadis turbidítics de la conca de Jaca oriental (Lutecià-Bartonià) i dels posteriors sistemes fluvio-al·luvials (Priabonià-Miocè). En la conca de Jaca occidental, l'únic treball de procedència existent (Payros, 1997) es centra en l'evolució paleogeografica que experimenta la conca des del Tanetià fins al Bartonià inferior.

1.2.2.1 La conca turbidítica eocena

Els estudis de Fontana et al. (1989) a les conques d'Aínsa i Jaca, Caja et al. (2010) a la conca de d'Aínsa (Fig. 1.4), i Roigé et al. (2016) van caracteritzar la composició i procedència dels dipòsits turbidítics del Grup Hecho superior de la conca de Jaca. Fontana et al. (1989) van definir tres petrofàcies, que emfatitzaven la coexistència de grans intraconcals i extraconcals en una mateixa mostra detrítica, en gran part carbonàtics, i que va definir com a gresos híbrids. Aquestes petrofàcies són litoarenites, gresos híbrids i calclitites. En base a aquestes petrofacies, estableixen que la sedimentació turbidítica rebia aports d'àrees font ubicades a l'est de la conca, constituïdes pel

basament paleozoic cristal·lí i metamòrfic de la Zona Axial, i de roques carbonàtiques incorporades en les làmines encavalcants de la Zona Sudpirinenca Central.

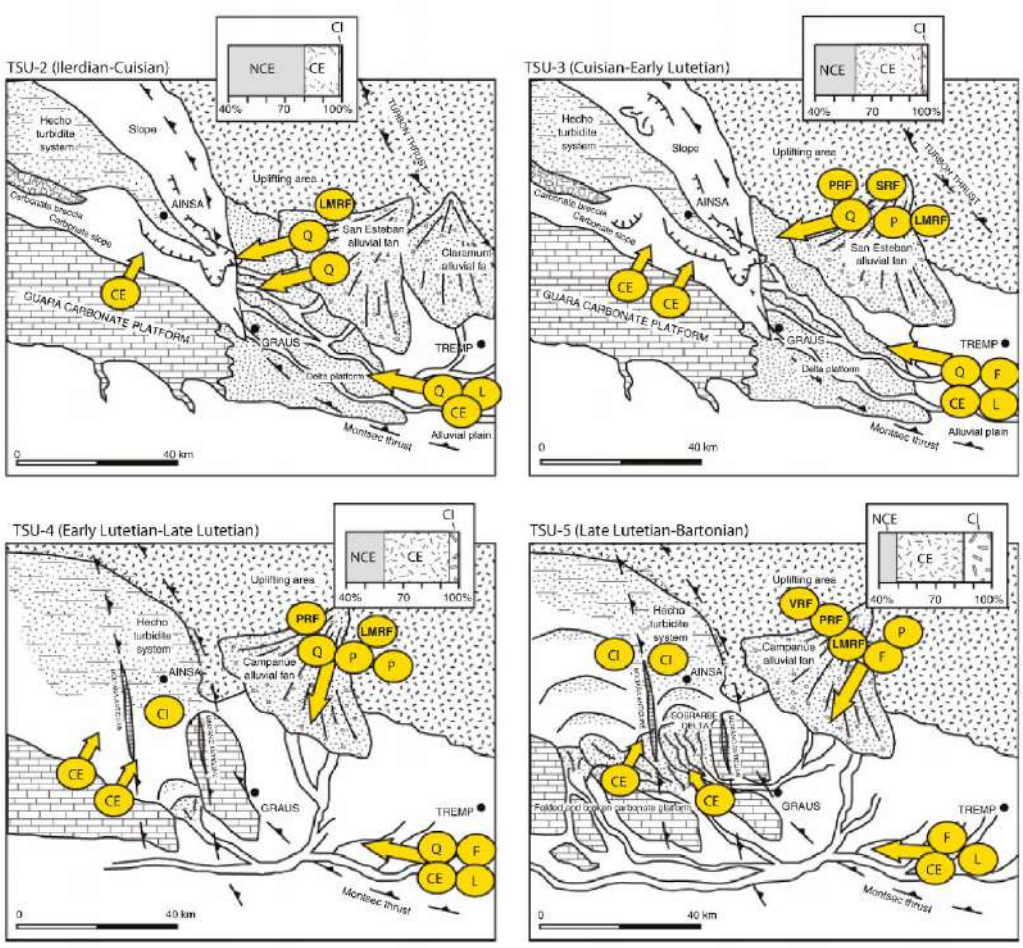

Figura 1.4. *Mapa paleogeogràfic extret de Caja et al. (2010) mostrant la paleogeografia i l'evolució de les àrees font per cada Unitat Tectono-Sedimentaria durant la sedimentació del Grup Hecho a la conca d'Aínsa. NCE, grans extraconcals no carbonàtics; CE, grans carbonàtics extraconcals, CI, grans carbonàtics intraconcals; Q, quars; F, feldspat potàssic; P, plagioclasi; L, litics; LMRF, fragments metamòrfics de baix grau; PRF, fragments plutònics; SRF, fragments sedimentaris.*

En aquest sentit, Roigé et al. (2016) i Roigé (2018) van caracteritzar la composició petrològica i la geocronologia de zircons detrítics de les turbidites del Grup Hecho superior de la conca de Jaca. Aquests treballs van determinar que els sistemes turbidítics de Banastón i Jaca inferior eren alimentats per àrees font ubicades a l'est, en el Pirineu Central, les quals subministraven abundants grans carbonàtics i plutònics, mentre que els últims estadis de sedimentació turbidítica registren l'aixecament de noves àrees font ubicades al nord de la conca en relació amb l'activitat de l'encavalcament de Lakora-Eaux-Chaudes.

Payros, (1997) caracteritza l'evolució paleogeogràfica de la conca de Jaca oriental des del Tanetià superior fins al Bartonià inferior. Durant aquest període la sedimentació turbidítica en la zona era alimentada pels sistemes turbidítics equivalents de la conca de Jaca oriental. Al Bartonià inferior, l'últim estadi de sedimentació turbidítica en la zona (Formació Ezkaba) registra aports procedents del nord, que tindrien l'àrea font ubicada en els massissos bascs.

Els equivalents proximals de la sedimentació turbidítica són descrits per Caja et al. (2010), el qual estableix les contribucions litològiques de cada àrea font per a cada sistema turbidític de la conca d'Aínsa (Fig. 1.4). Durant l'Ilerdià-Cuisià, els sistemes turbidític es caracteritzen per una composició més quarsítica derivada de l'erosió de materials Paleozoics intensament meteoritzats. Per contra, durant el Cuisià-Lutecià, s'incrementen els feldspats i fragments de roca, fet que relacionen amb l'aixecament progressiu de la Zona Axial i de les unitats encavalcants de la Zona Central Sudpirinenca. Les reconstruccions paleogeogràfiques indiquen la presència d'una àrea font situada al nord de la conca d'Aínsa, en la Zona Axial dels Pirineus, i l'existència de contribucions dels sistemes deltaics i fluvials de les conques d'Àger i Tremp. L'àrea font d'aquests sistemes ha motivat diversos estudis com els de Whitchurch et al. (2011) o Thomson et al. (2017). Mentre que Witchurch et al. (2011) considera només àrees font ubicades al Pirineu oriental i central, Caja et al. (2010) i Thompson et al. (2017) consideren també aports del massís de l'Ebre ubicats en la Serralada Costero-Catalana (figura 1.5), els quals han estat detalladament caracteritzats en estadis previs (Formació Tremp) per Gómez-Gras et al. (2017).

1.2.2.2. La conca molàssica fini-eocena i oligocena

La sedimentació turbidítica a la conca Sudpirinenca, es reemplaçada de forma diacrònica durant el Lutecià-Bartonia, seguint la direcció general de progradació dels sistemes sedimentaris, d'est a oest. Durant aquest període, el creixement de diverses estructures com l'anticlinal de Boltaña va condicionar en gran mesura la progradació dels sistemes fluvials i al·luvials de la conca d'Aínsa cap a la conca de Jaca. En aquest sentit Vinyoles et al. (2021) estableixen les relacions tectònica-sedimentació d'ambdues conques, i les taxes de sedimentació d'aquestes, fortament influenciades per la tectònica sincrònica (Fig. 1.6).

Roigé et al. (2017) i Roigé (2018) caracteritzen l'evolució dels sistemes sedimentaris de la conca de Jaca constituïts pels ambients transicionals de les Formacions Gres de Sabiñanigo i Belsué-Atarés, i fluvio-al·luvials de les Formacions Campodarbe i Bernués (Figura 1.7). Aquests autors defineixen

quatre petrofacies que registren l'evolució de les àrees font ubicades a l'est de la conca, en el Pirineu Central, i la progressiva instauració dels sistemes transversals procedents del nord, els quals fonamentalment registren el reciclatge de la conca turbidítica eocena amb contribucions de la Zona Nordpirinenca. Els sistemes equivalents en la conca d'Aínsa corresponen a les Formacions Escanilla i Graus, que es nodrien dels sistemes al·luvials del Sis i Gurp durant l'Eocè superior-Oligocè (Bentham et al., 1992; Dreyer et al., 1999; Vincent, 2001; Michael, 2013).

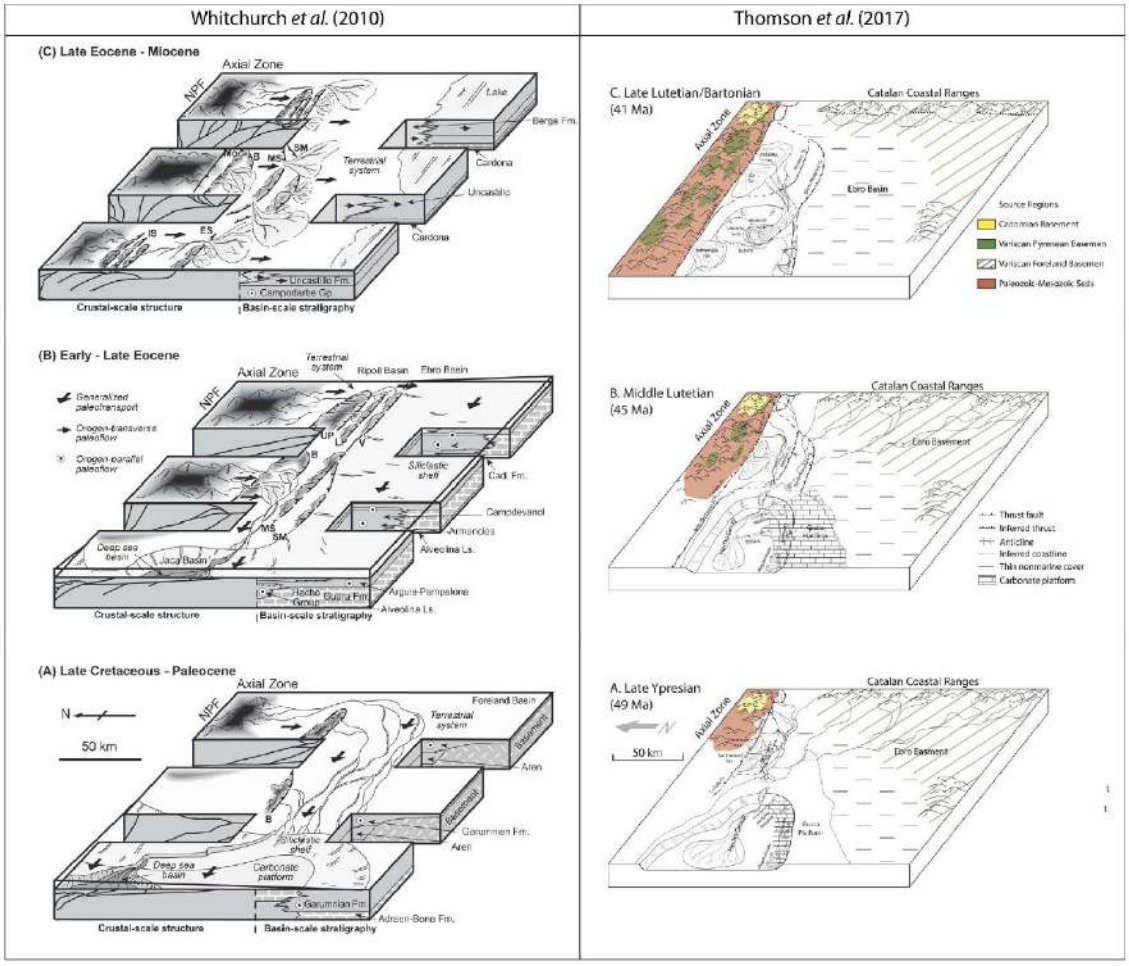

Figura 1.5. *A l'esquerra: reconstruccions paleogeogràfiques des del Cretaci fins al Miocè de Whitchurch et al. (2010). A la dreta: mapa paleogeogràfic extret de Thomson et al. (2017) mostrant la paleogeografia i l'evolució de les àrees font per la conca Sudpirinenca durant l'Eocè.*

En la conca de Jaca occidental els sistemes equivalents estarien constituïts per les Formacions Ardanatz, Líedena, Campodarbe i Bernués. Els pocs treballs que es centren en aquesta àrea són essencialment sedimentològics, i relacionen les Formacions Ardanatz i Liédena amb la progradació del delta de Belsué-Atarés a l'est de la conca (Astibia et al., 2005; 2014).

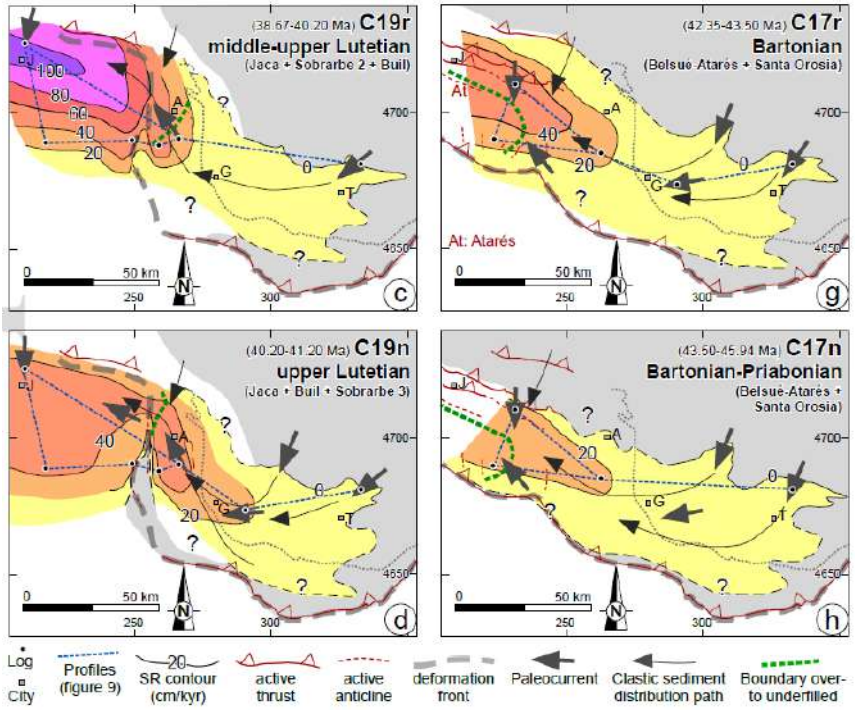

***Figura 1.6**. Reconstrucció paleogeogràfica proposada per Vinyoles et al. (2020), i referències contingudes, amb la potència de sediments acumulada estimada del Lutecià al Priabonià en les conques d'Ainsa i Jaca.*

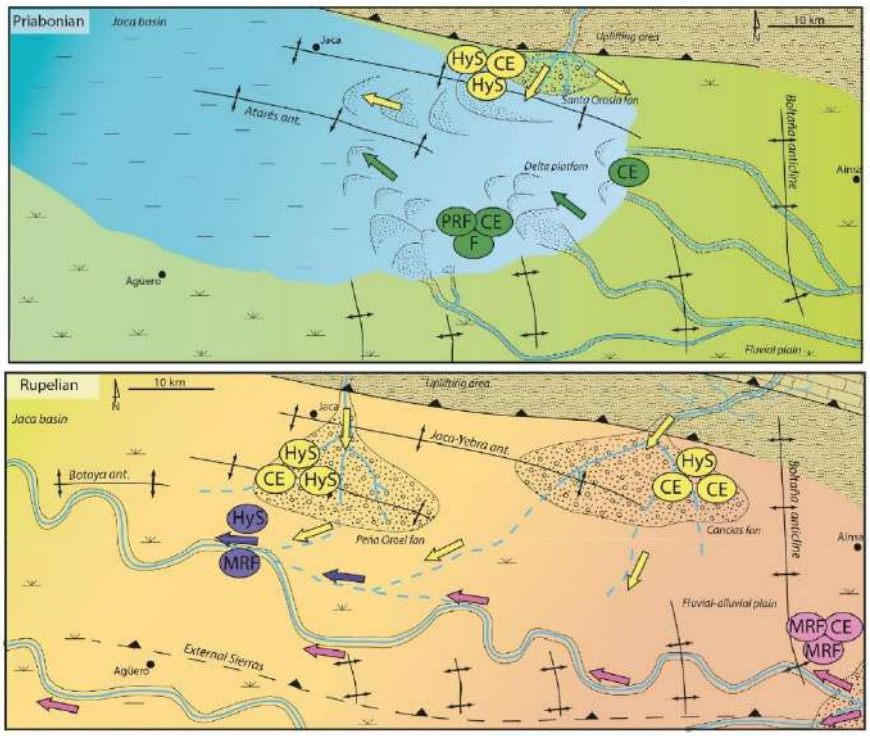

Figura 1.7. Reconstruccions paleogeogràfiques de la conca de Jaca oriental, mostrant l'evolució composicional dels sistemes axials durant el Priabonià-Rupelià, i la progressiva instauració dels sistemes transversals que registren el reciclatge de la conca turbidítica. CE, grans carbonàtics extraconcals; F, feldspat; MRF, fragments metamòrfics; PRF, fragments plutònics; HyS, fragments de gresos híbrids.

Capítol 2

Interès, objectius i estructura de la tesi

2.1 Interès i objectius del treball.

En un context amb múltiples àrees font que no presenten necessàriament litologies distintives, com és el cas dels Pirineus, les interpretacions sobre procedència poden ser ambigües o poc fonamentades si sobre tot aquestes es basen en un únic mètode d'anàlisi de procedència. Per aquest motiu en aquesta tesi es presenta un anàlisi de procedència basat en diversos mètodes com son la petrografia, els minerals pesants, i la geocronologia i termocronologia en zircons detrítics.

Els únics estudis de procedència realitzats en la conca de Jaca es centren en el sector occidental, caracteritzant la petrografia de la zona nord i sud, i les senyals de procedència d'U-Pb de la zona nord (Roigé et al., 2016; Roigé et al., 2017; Roigé, 2018). És per això que en aquesta tesi s'estudien els minerals pesants d'ambdues zones (fins ara no abordats), amb l'objectiu de millorar la resolució del marc paleogeogràfic existent. Tot i que aquest tipus d'anàlisis han sigut àmpliament utilitzats en altres oròsgens com els Alps o l'Himàlaia (Cerveny et al. 1989; Lihou & Mange-Rajetzky 1996; von Eynatten & Gaupp 1999; Garzanti et al., 2004, 2006, 2012, 2013; Uddin et al. 2007; Andò et al. 2014, 2019), en el marc dels Pirineus existeixen pocs estudis que es basin en aquesta tècnica (Ullastre & Masriera 1982; Hirst & Nichols 1986; Rubio et al. 1996; Yuste et al. 2006; Barsó 2007; Michael 2013), essent escassos els que intenten integrar les dades obtingudes amb altres mètodes com la petrografia, o en els que aquesta integració es poc resolutiva.

En quant a estudis de procedència basats en la geocronologia i/o termocronologia de zircons detrítics, en la conca de Jaca l'únic estudi d'U-Pb s'ha centrat en la zona nord (Roigé, 2018). Per aquest motiu en aquesta tesi es caracteritza la geocronologia i termocronologia de zircons detrítics en el marge sud de la conca oriental i en la conca de Jaca occidental. Els pocs treballs que apliquen aquestes tècniques en l'àmbit dels Pirineus, es centren en les conques d'Aínsa o Tremp-Graus, i a diferencia de Roigé (2018), sense tenir en compte les valuoses dades que aporta la petrologia a l'hora d'avaluar les senyals d'U-Pb (Whittchurch et al., 2011; Filledeau et al., 2012; Michael, 2013; Thompson et al., 2017).

Amb l'objectiu de millorar les interpretacions derivades de l'anàlisi multimètode, en aquesta tesi també s'han realitzat anàlisis complementaris en les conques d'Aínsa i de l'Ebre, les quals contenen sistemes sedimentaris estretament lligats, des del punt de vista genètic, amb la conca de Jaca.

L'objectiu general de la tesi, és analitzar la procedència dels sistemes sedimentaris de la conca de Jaca mitjançant un estudi multimètode, basat en la integració de diverses tècniques d'anàlisi de procedència com són la petrologia, l'anàlisi de minerals pesants, la geocronologia i la termocronologia de zircons detrítics.

Els objectius concrets d'aquesta tesi, lògicament estan encaminats a aconseguir dur a terme aquesta proposta multimètode, i són:

- Caracteritzar les associacions de minerals pesants de la zona nord i sud de la conca de Jaca oriental dels sistemes sedimentaris que representen els últims estadis de sedimentació turbidítica, i la seva evolució a ambients transicionals i continentals.

- Caracteritzar les senyals de procedència d'U-Pb en zircons detrítics dels sistemes sedimentaris del marge sud de la conca de Jaca oriental, de la conca de Jaca occidental i de la conca de l'Ebre

- Caracteritzar les senyals de procedència de ZHe en zircons detrítics del marge sud de la conca de Jaca oriental, de la conca de Jaca occidental i de la conca de l'Ebre.

- Integrar totes aquestes dades amb les dades existents de petrografia, d'U-Pb, i ZHe, així com amb noves dades de petrografia adquirides durant la realització d'aquesta tesi.

- Comparar totes les senyals de procedència adquirides en aquest treball amb les existents en les conques d'Aínsa i de l'Ebre, així com amb les de les àrees font.

- Refinar i/o augmentar la resolució del marc paleogeogràfic existent.

- Aprofundir sobre el reciclatge dels dipòsits turbidítics durant la sedimentació al·luvial, en especial en la propagació de les senyals d'U-Pb en zircons detrítics.

2.2. Estructura de la Tesi

Aquesta memòria de tesi doctoral es presenta com un treball en format de compendi de publicacions, en la qual els capítols centrals corresponen a articles ja publicats en revistes científiques SCI (capítols 4 i 5), o bé en preparació o enviats (capítol 6). El capítol 1 és introdueix el marc d'aquesta tesi, el present capítol 2 exposa l'interès del treball realitzat, els objectius i l'estructura de la tesi, i el capítol 3 descriu la metodologia emprada d'una forma general, donat que en cadascun dels capítols que mostren resultats, s'exposa de manera ben detallada i referenciada. El capítol 7 presenta una discussió integrada, que finalitza amb el capítol 8, exposant les conclusions més importants d'aquesta tesi.
La bibliografia dels capítols en format article està inclosa en aquests, mentre que per la resta de capítols s'ha agrupat en l'apartat referències. Els annexos contenen treballs realitzats durant els anys d'investigació relacionats amb aquesta tesi. L'annex 1 consisteix en un article publicat, al qual vaig contribuir. L'annex 2 consisteix en dues publicacions. L'Annex 3 incorpora els abstractes publicats, els pòsters, i les presentacions realitzades en congressos internacionals. L'annex 4, presenta totes les dades tabulades d'U-Pb obtingudes en zircons detrítics. Finalment, l'annex 5 presenta totes les dades tabulades de (U-Th)/He obtingudes en zircons detrítics.

Els capítols en format article han estat ordenats seguint la seqüència de rebliment de la conca de Jaca de nord a sud. El capítol 4 versa sobre la zona nord de la conca de Jaca oriental. En ell, es descriuen les associacions de minerals pesants de les últimes turbidites de la conca i la seva evolució als primers sistemes deltaics i al·luvials, i es relacionen amb les possibles àrees font. El capítol 5, versa sobre el marge sud de la conca de Jaca oriental. En ell, es descriuen les associacions de minerals pesants dels sistemes deltaics i fluvio-al·luvials de la conca de Jaca, així com també de les conques d'Aínsa i de l'Ebre per tal d'establir correlacions entre els diferents sistemes sedimentaris. En aquest capítol s'integren també les dades de petrografia de Roigé (2018). Per últim, el capítol 8, versa sobre les senyals de procedència de U-Pb i (U-Th)/He del marge sud de la conca de Jaca oriental, la conca de Jaca occidental, i la conca de l'Ebre. En aquest capítol es fa un esforç per integrar aquestes dades amb les quantitatives de petrografia de Roigé (2018) i dades qualitatives de la conca de Jaca occidental obtingudes durant aquesta tesi.

- Capítol 4: *Coll, X., Gómez-Gras, D., Roigé, M., Teixell, A., Boya, S., & Mestres, N. (2020). Heavy-mineral provenance signatures during the infill and uplift of a foreland basin: An*

example from the Jaca basin (southern Pyrenees, Spain). Journal of Sedimentary Research, 90(12), 1747-1769. https://doi.org/10.2110/jsr.2020.084.

- Capítol 5: *Coll, X., Roigé, M., Gómez-Gras, D., Teixell, A., Boya, S., & Mestres, N. (2022). Interplay of Multiple Sediment Routing Systems Revealed by Combined Sandstone Petrography and Heavy Mineral Analysis (HMA) in the South Pyrenean Foreland Basin. Minerals, 12(2), 262. https://doi.org/10.3390/min12020262.*

- Capítol 6: *Coll, X., Gómez-Gras, D., Roigé, M., Stockli, D., Teixell, A., & Boya, S.* DZ U-Pb and ZHe Provenance Signatures in the South Pyrenean Foreland basin: Interplay of Direct vs Recycled Sources During Pyrenean Orogenic Growth. En preparació.

A l'apartat d'annexos hi figuren dues col·laboracions en publicacions, una publicació més, quatre pòsters, i una presentació oral.

Annex 1

- Burrel, L.; Teixell, A.; Gómez-Gras, D.; Coll, X. (2021). Basement-involved thrusting, salt migration and intramontane conglom-1107 erates: a case from the Southern Pyrenees. Bull. Soc. Géol. Fr. 2021, 192, . https://doi.org/10.1051/bsgf/2021013.

Annex 2

- Coll, X., Gómez-Gras, D., Roigé, M., & Mestres, N. (2017). Heavy-mineral assemblages as a provenance indicator in the Jaca basin (Middle-Late Eocene, southern Pyrenees). Geogaceta, 61, 159-162.

- Gómez-Gras, D., Collado, R., Coll, X., & Roigé, M. (2017). Caracterización composicional de las areniscas del Cretácico Superior en las Sierras Marginales y Exteriores (cuenca surpirenaica): análisis mediante minerales pesados y petrografía óptica. Geogaceta, 61, 163-166.

Annex 3

- Coll, X., Gómez-Gras, D., Roigé, M. & Mestres, N. (2017). Heavy-mineral assemblages as a provenance indicator in the Jaca basin (Middle-Late Eocene, southern Pyrenees). SEPM Research Conference, Propagation of Environmental Signals within Source-to-Sink Stratigraphy, Tremp-Ainsa, Spain, 2017.

- Coll, X., Gómez-Gras, D., Roigé, M., Teixell, A. & Mestres, N. (2017). Heavy-mineral assemblages as a provenance indicator in the Jaca basin (Middle-Late Eocene, southern Pyrenees). 33rd IAS International Meeting of Sedimentology, Toulouse, France, 2017.

- Caldera, N., Teixell, A., Griera, A. Labaume, P., Coll, X. & Mestres, N. (2018). On the tectonic structures of the Eaux-Chaudes massif (western Pyrenees): a Helvetic nappe type in the Pyrenees? YOUSGET Young Researchers in Structural Geology and Tectonics, Montgenevre, France, 2018.

- Coll, X., Gómez-Gras, D., Roigé, M., Boya, S., Teixell, A. & Poyatos-Moré, M. (2019). Heavy-Mineral Provenance Signatures During the Evolution from Marine to Terrestrial Environaments in the Jaca Basin (Southern Pyrenees). 34th IAS International Meeting of Sedimentology, Roma, Italy, 2019.

- Coll, X., Gómez-Gras, D., Roigé, M., Boya, S., Teixell, A. & Poyatos-Moré, M. (2019). Interplay of Multiple Sediment Sources in an Overfilled Foreland Basin (Southern Pyrenees). 34th IAS International Meeting of Sedimentology, Roma: Italy, 2019.

Capítol 3

Metodologia

En aquesta tesi s'ha desenvolupat un anàlisi multimètode basat en la integració de diverses tècniques d'anàlisi de procedència com són la petrografia, l'anàlisi de minerals pesants, la geocronologia i la termocronologia de zircons detrítics.

En aquest apartat es descriuen les diferents tècniques emprades d'una forma general, donat que es tracten de forma molt més acurada en cadascun dels capítols següents realitzats en format article (capítols 4, 5 i 6).

3.1. Recerca bibliogràfica i plantejament del treball de camp

Els treballs d'estratigrafia, sedimentologia i procedència duts a terme en la conca Sudpirinenca han estat claus a l'hora de plantejar les zones i els sistemes a estudiar i mostrejar. La recerca bibliogràfica s'ha expandit fora de l'àmbit de la conca de Jaca, abastant diferents períodes de temps de tota la conca Sudpirinenca, així com també dels Pirineus, amb l'objectiu d'extreure el màxim d'informació en relació a la composició, l'evolució i la contribució de les àrees font, i de la configuració de les xarxes de drenatge de la conca.

L'anàlisi bibliogràfic ha revelat la existència de nombrosos estudis de procedència centrats en la part central-occidental de la conca Sudpirinenca (conques d'Àger, Tremp-Graus i Aínsa), fet que contrasta amb els pocs treballs duts a terme en la conca de Jaca. Tot i que els treballs existents es centren en la estratigrafia, la sedimentologia o la tectònica, han proporcionat dades essencials per al plantejament de la present tesi doctoral.

3.2. Treball de camp

El treball de camp ha consistit principalment en el mostreig dels gresos i en l'anàlisi petrològic dels clasts in situ (Fig. 3.1). La distribució de les seccions estratigràfiques a mostrejar s'ha realitzat en funció de la distribució i representativitat d'aquestes en la conca, i s'ha organitzat de forma que permeti caracteritzar els canvis composicionals de la conca.

La distribució areal de les mostres de gresos per a l'estudi petrogràfic s'ha establert en virtut a la representativitat dels sistemes analitzats, així com als possibles canvis detectats en les observacions al camp. Per a la presa de mostres de minerals pesants i zircons, s'han considerat els canvis

composicionals observats en làmina prima amb el microscopi petrogràfic, amb el fi d'optimitzar la resolució del mostreig.

Figura 3.1. *(A) Descripció de clasts en conglomerats. (B) Mostreig de gresos per a la identificació de petrogràfica i de minerals pesants. (C) Mostreig de matriu gresosa en conglomerats, i de clastos per a la identificació petrogràfica.*

La descripció de clasts de conglomerats s'ha realitzat insitu en aquells llocs on les condicions de l'aflorament ho permetia. També s'ha mostrejat la matriu gresosa dels conglomerats i alguns clastes per tal de relacionar els fragments de mida sorra amb les litologies observades en la mida rudita.

Una altra part imprescindible del treball de camp efectuat ha consistit en el mostreig de possibles àrees font amb l'objectiu d'identificar les litologies dels còdols presents en els dipòsits conglomeràtics. En aquest sentit s'han inclòs diverses localitats dels massissos bascs i de la vessant sud del Pirineu central de les que també s'ha realitzat una làmina prima per a l'estudi petrològic. Finalment també s'han mostrejat diferents sistemes detrítics dipositats en les sub-conques sudpirinenques adjacents, com les d'Àger, Tremp- Graus i Aínsa, com els ventalls del Sis i el Gurp per a establir possibles correlacions o bé per identificar les diferents àrees font actives en els diferents estadis de la conca.

3.3. Treball de Laboratori.

El treball de laboratori ha consistit en l'anàlisi petrogràfic dels gresos, la separació dels minerals pesants, l'anàlisi amb espectrometria Raman, i l'anàlisi geocronològic d'U-Pb i termocronològic (U-Th)/He en zircons detrítics.

L'anàlisi petrogràfic ha consistit en la descripció de làmines primes mitjançant el microscopi petrogràfic (Laboratori de làmines primes i Microscòpia de la Universitat Autònoma de Barcelona) basat en els criteris de Dickinson (1970); Zuffa (1980); Zuffa (1985) i Ingersoll et al. (1984), que ha servit per escollir les mostres més representatives per a realitzar els anàlisis de minerals pesants, U-Pb i (U-Th)/He, a més de per a comprendre la informació que es deriva d'aquestes tècniques i integrar-la amb la informació extreta de la petrologia. Les làmines primes de les mostres corresponents a les litologies directament mostrejades en l'àrea font també han estat descrites i comparades amb els fragments de roca observats en els afloraments conglomeratics i en el microscopi petrogràfic.

En total en aquesta tesi s'han obtingut un total de 400 mostres que han estat totes caracteritzades i classificades petrològicament, de les que s'han escollit 49 per a la identificació de minerals pesants, 25 per a l'anàlisi d'U-Pb, i 10 per a l'anàlisi (U-Th)/He. La separació dels minerals pesants, així com també dels zircons detrítics s'ha realitzat en el laboratori de Petrologia i Geoquímica de la Universitat Autònoma de Barcelona (Figura 3.2A). La identificació de minerals pesants s'ha realitzat mitjançant una primera observació amb el microscopi petrogràfic i posteriorment amb la espectrometria Raman a l'Institut de Ciència de Materials de Barcelona, ICMAB-CSIC sota la supervisió del Dr. Narcís Mestres (Figura 3.2B). Els anàlisis de d'U-Pb i (U-Th)/He s'han realitzat al UTChron de la Univeristy of Texas at Austin sota la supervisió del Dr. Daniel Stockli i el Dr. Rudra Chatterjee (Figura 3.2C). Els detalls de cada mètode es troben especificats en els capítols 4, 5 i 6.

Els procediments per a la separació mineral estan descrits en els capítols 4, 5, i 6, i es basen en la metodologia proposada per Mange i Maurer (1992) i Andó (2020). Els passos que es van seguir van consistir en la disgregació de les mostres, fins a aconseguir una mida sorra que es va tractar amb àcid acètic per a dissoldre el màxim de carbonats possibles. Posteriorment, es van sotmetre a una màquina d'ultrasons per a una millor disgregació dels grans i de envoltes argiloses, i les mostres es van tamisar per de seleccionar només les granulometries entre 32 i 500 μm. Finalment la fracció densa (>2,9 g/cm$^{3)}$ es va recuperar mitjançant el líquid dens politungstat de sodi amb el mètode de la centrífuga i la

congelació parcial amb nitrogen. La fracció pesant obtinguda es va incloure en resina i es va realitzar una làmina prima polida de cada mostra per tal de millorar el procés d'obtenció d'espectres Raman.

Figura 3.2. *(A) Separació de minerals pesants amb líquid dens al Laboratori de Petrologia i Geoquímica de la Universitat Autònoma de Barcelona. (B) Equip d'espectrometria Raman del Institut de Ciència dels Materials. (C) Equip d'anàlisi geocronòlogic LA-ICP-MS del laboratori UTChron a la University of Texas en Austin (Jackson School of Geosciences).*

Per al cas de separació de zircons la metodologia va ser la mateixa, però en aquest cas, no es va realitzat la dissolució de carbonats amb àcid acètic. La fracció <500 μm va ser sotmesa a una preconcentració de la fracció pesada amb una taula d'aigües Holman Wilfley abans de realitzar la separació amb el líquid dens, el qual va ser preparat preparat amb una densitat de 3.2 g/cm^3. Finalment, la fracció pesant recuperada es va sotmetre a un separador magnètic Frantz per aconseguir el concentrat final de zircons.

3.4. Treball de gabinet

El treball de gabinet ha consistit en la interpretació dels espectres Raman obtinguts i els anàlisis estadístics de les dades de de petrografia quantitativa, de minerals pesants, U-Pb i (U-Th)/He.

La identificació dels minerals pesants s'ha dut a terme comparant els espectres Raman obtinguts amb espectres de referència publicats (Wang et al. 2004; Kuebler et al. 2006; Andò & Garzanti 2014). Addicionalment, s'ha dut a terme la verificació dels minerals identificats amb el microscopi petrogràfic.

Les dades de petrografia quantitativa, de minerals pesants i de U-Pb i (U-Th)/He han sigut tractades estadísticament amb l'anàlisi de correspondència (Greenacre, 1984; Vermeesch 2018). Aquest mètode d'anàlisi estadístic multivariant permet visualitzar les similituds composicionals entre les diferents mostres d'una manera senzilla, en un gràfic que mostra una representació bidimensional en termes composicionals. En aquest sentit, l'anàlisi estadístic ha permès confirmar les quatre petrofacies descrites per Roigé (2018), caracteritzar cinc associacions de minerals pesants, tres senyals de procedencia d'U-Pb, i dues senyals de procedència d'(U-Th)/He.

Finalment, aquesta tesi culmina amb un intent preliminar d'aproximació predictiva de propagació de senyals d'U-Pb. Aquest intent de modelització no s'ha d'entendre com quelcom dogmàtic o inamovible, sinó com una eina de control més, la qual convida a l'investigador a reflexionar profundament les conclusions derivades d'aquest tipus d'estudis. També aquesta proposta preliminar pretén fer reflexionar dues vegades abans de formular resolucions generalistes que, molt probablement, no reflecteixen la complexitat real del cas d'estudi, i per tant, corrent un elevat risc d'esdevenir errònies o incompletes. Els detalls d'aquesta metodologia s'exposen en la discussió integrada de la tesi, en el capítol 7.3.

3.5. Síntesi de resultats i redacció d'articles

Finalment, la redacció d'aquesta memòria de tesi ha estat presentada en format de compendi de publicacions, on els capítols centrals corresponen a treballs publicats (capítols 4 i 5), o en preparació o enviats (capítol 6). Una gran part de la feina desenvolupada durant la consecució d'aquesta tesi doctoral ha consistit en la redacció, edició, i revisió d'aquests articles, en els quals s'han sintetitzat i integrat els resultats obtinguts en el decurs de la tesi.

Capítol 4

Heavy-mineral provenance signatures during the infill and uplift of a foreland basin: An example from the Jaca basin (southern Pyrenees, Spain)

El capítol 4 correspon a l'article publicat a la revista Journal of Sedimentary Research publicat l'any 2020.

X. Coll ha realitzat el tractament de les mostres (descrit en la metodologia) i ha realitzat el comptatge de totes les mostres i els anàlisis amb spectrometria Raman. Ha sintetitzat i realitzat l'anàlisi estadístic de totes les mostres, i ha confeccionat tots els diagrames composicionals de minerals pesants. També ha redactat la major part del text i ha realitzat la major part de les figures.

Coll, X., Gómez-Gras, D., Roigé, M., Teixell, A., Boya, S., & Mestres, N. (2020). Heavy-mineral provenance signatures during the infill and uplift of a foreland basin: An example from the Jaca basin (southern Pyrenees, Spain). Journal of Sedimentary Research, 90, 1747-1769. https://doi.org/10.2110/jsr.2020.084.

Journal of Sedimentary Research

Journal of Sedimentary Research, 2020, v. 90, 1747–1769
Research Article
DOI: 10.2110/jsr.2020.084

HEAVY-MINERAL PROVENANCE SIGNATURES DURING THE INFILL AND UPLIFT OF A FORELAND BASIN: AN EXAMPLE FROM THE JACA BASIN (SOUTHERN PYRENEES, SPAIN)

XAVIER COLL,[1] DAVID GÓMEZ-GRAS,[1] MARTA ROIGÉ,[1] ANTONIO TEIXELL,[1] SALVA BOYA,[1] AND NARCÍS MESTRES[2]

[1]*Departament de Geologia, Universitat Autònoma de Barcelona, 08193 Bellaterra, Spain*

[2]*Institut de Ciència de Materials de Barcelona, ICMAB, Consejo Superior de Investigaciones Científicas, CSIC, Campus de la UAB 08193 Bellaterra, Barcelona, Spain*

e-mail: Xavier.Coll@uab.cat

ABSTRACT: **In the Jaca foreland basin (southern Pyrenees), two main sediment routing systems merge from the late Eocene to the early Miocene, providing an excellent example of interaction of different source areas with distinct petrographic signatures. An axially drained fluvial system, with its source area located in the eastern Central Pyrenees, is progressively replaced by a transverse-drained system that leads to the recycling of the older turbiditic foredeep. Aiming to provide new insights into the source-area evolution of the Jaca foreland basin, we provide new data on heavy-mineral suites, from the turbiditic underfilled stage to the youngest alluvial-fan systems of the Jaca basin, and integrate the heavy-mineral signatures with available sandstone petrography. Our results show a dominance of the ultrastable Ap-Zrn-Tur-Rt assemblage through the entire basin evolution. However, a late alluvial sedimentation stage brings an increase in other more unstable heavy minerals, pointing to specific source areas belonging to the Axial and the North Pyrenean Zone and providing new insights into the response of the heavy-mineral suites to sediment recycling. Furthermore, we assess the degree of diagenetic overprint vs. provenance signals and infer that the loss of unstable heavy minerals due intrastratal dissolution is negligible at least in the Peña Oroel and San Juan de la Peña sections. Finally, we provide new evidence to the idea that during the late Eocene the water divide of the transverse drainage system was located in the North Pyrenean Zone, and areas constituted by the Paleozoic basement were exposed in the west-Central Pyrenees at that time. Our findings provide new insights into the heavy-mineral response in recycled foreland basins adjacent to fold-and-thrust belts.**

INTRODUCTION

The sedimentary infill of a foreland basin may record the interaction of distinct source areas, thus offering a good opportunity to study the interplay between them and to infer the evolution of the uplift and exhumation of mountain belts (e.g., Dickinson and Suczek 1979; Steidtmann and Schmitt 1988). Sediment provenance studies are important to understand the processes occurring in the hinterland of a sedimentary basin, helping to constrain the timing of geodynamic events, to unravel sediment pathways, and to correlate stratigraphic sequences (Graham et al. 1986; Haughton et al. 1991; Mange-Rajetzky 1995; Von Eynatten and Dunkl 2012; Garzanti et al. 2013a, 2013b; Kilhams et al. 2014; Caracciolo et al. 2016). In complex geodynamic settings, the integration of as many provenance tools as possible is essential to resolve ambiguous provenance signals when facing sediment routing in related basins (Dickinson 1988; Nie et al. 2012; Garzanti et al. 2013a; Garzanti 2016; Caracciolo et al. 2019; McKellar et al. 2020).

The use of heavy minerals to assess sediment provenance in source-to-sink studies has been proven to be a powerful tool in many basins and different settings (Morton et al. 1994, 2004; von Eynatten 1999; Mange et al. 2003; Garzanti and Andò 2007b; Garzanti et al. 2007, 2013a, 2014; Fossum et al. 2019). Different sources can be revealed in sediments with similar petrographic compositions through the study of the heavy-mineral suites (Mange-Rajetzky 1995). However, since ancient sandstones are usually affected by intrastratal dissolution (Morton and Hallsworth 1999, 2007; Andò et al. 2012), most studies tend to focus on modern sediments (Garzanti et al. 2003, 2013a, 2013b, 2014, 2018; Garzanti and Andò 2007a, 2007b). In addition, interpreting heavy-mineral suites without contrasting petrographic data may lead to misleading conclusions, especially when the degree of diagenetic overprint is enough to substantially modify the original detrital suite.

The Eocene–Miocene Jaca foreland basin of the Southern Pyrenees (Fig. 1) has been thoroughly studied regarding sedimentology, tectonics, and petrography (Mutti 1985; Mutti et al. 1985; Remacha and Fernández 2003; Remacha et al. 2005; Caja et al. 2010; Fontana et al. 1989; Gupta and Pickering 2008; Labaume et al. 1985, 2016a; Labaume and Teixell 2018; Roigé et al. 2016, 2017; Boya 2018; Garcés et al. 2020) as it is an outstanding example of a basin infill evolving in an active convergent tectonic setting. Different sediment routing systems merge in this basin, providing an example of interaction of different source areas with distinct petrographic signatures, recording several stages of exhumation of the Pyrenean belt (Puigdefàbregas 1975; Roigé et al. 2016, 2017). The well-constrained geological setting of the Jaca basin offers an excellent opportunity to test how heavy-mineral suites respond to changes in the sediment routing system, the sedimentary environment (from deep-marine to terrestrial), and the potential diagenetic overprint.

Despite the wide use of heavy minerals as provenance indicators in other orogens such as the Alps or the Himalayas (Cerveny et al. 1989; Lihou and Mange-Rajetzky 1996; von Eynatten and Gaupp 1999; Garzanti et al.

Published Online: December 2020
 1527-1404/20/090-1747

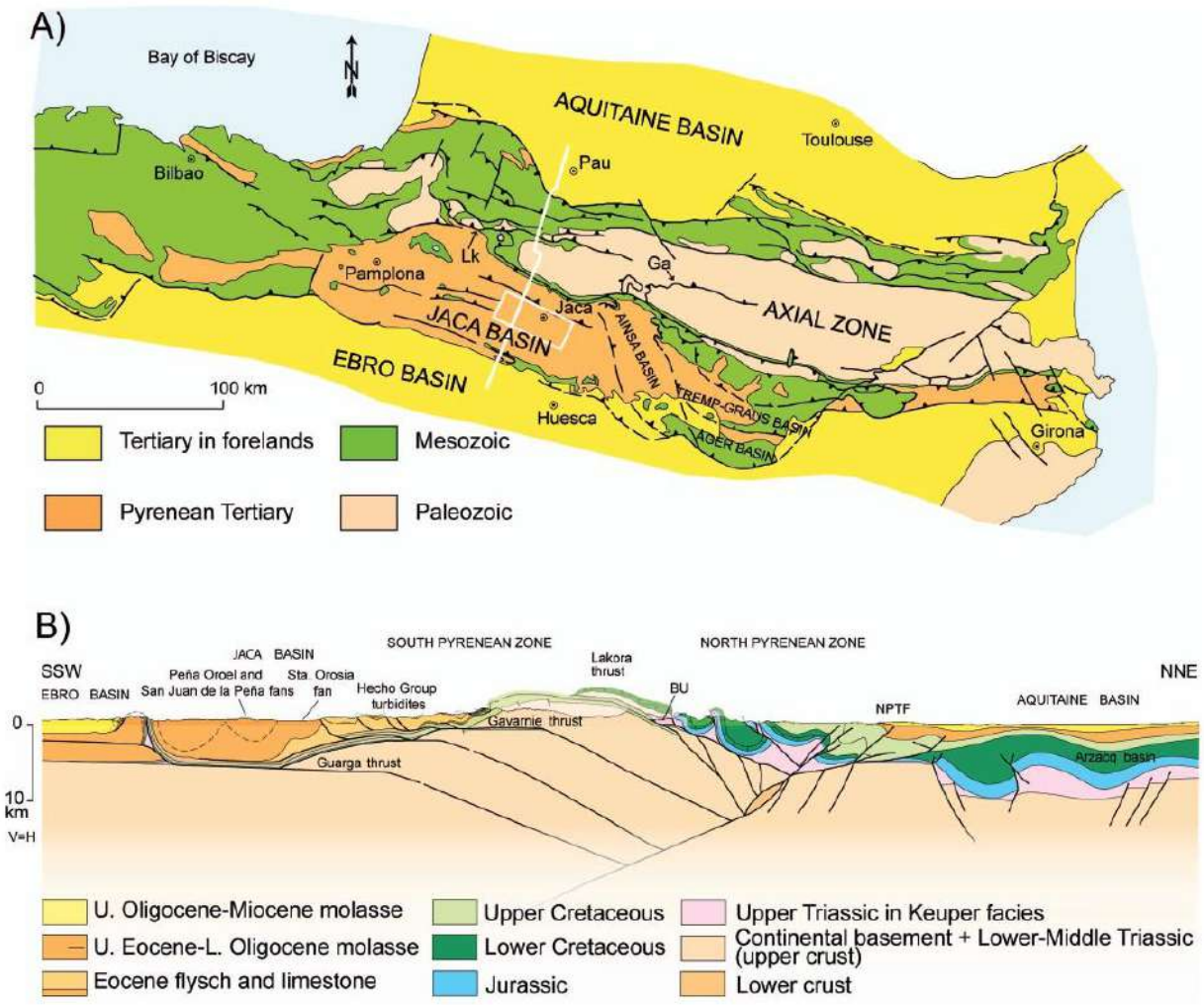

FIG. 1.—**A)** Simplified geological map of the Pyrenees (redrawn from Teixell 1996), showing the location of the study area (white frame). White line indicates cross-section in Part B. Lk, Lakora thrust; Ga, Gavarnie thrust. **B)** Crustal cross section of the west-central Pyrenees (simplified from Teixell et al. 2016), showing both the South Pyrenean Zone and the North Pyrenean Zone. NPFT, North-Pyrenean Frontal Thrust; BU, Bedous Triassic Unit.

2004, 2006, 2012, 2013a; Uddin et al. 2007; Andò et al. 2014, 2019), in the Pyrenees few or mainly old studies have used this approach to unravel sediment provenance in the South Pyrenean and the Ebro basin (Ullastre and Masriera 1982; Hirst and Nichols 1986; Rubio et al. 1996; Yuste et al. 2006; Barsó 2007; Michael 2013; Gómez-Gras et al. 2017). In the Ainsa–Jaca basin, only Valloni et al. (1984) and Coll et al. (2017) addressed the study of heavy minerals in the intensely studied Eocene turbidites of the Hecho Group (Mutti 1985), leading to strongly different results.

We provide new characterization of the heavy-mineral suites of the clastic systems of the northern Jaca basin, from the deep-marine sedimentation stage to the latest stage of its continentalization (late Lutetian–Miocene), in order to unravel provenance signatures and to gain understanding of the degree of diagenetic overprint throughout the study area. In addition, we aim to provide new insights into the sediment-routing responses to the creation of new drainage patterns during the uplift and topographic growth of the Pyrenees, through the integration of heavy-mineral analysis with available sandstone petrography data (Roigé et al. 2016, 2017).

GEOLOGICAL SETTING

Structural and Stratigraphic Framework

From the Late Cretaceous until the early Miocene, the collision between the Eurasian and Iberian plates originated the Pyrenean fold-and-thrust belt (Roure et al. 1989; Muñoz 1992; Teixell 1998; Vergés et al. 2002; Mouthereau et al. 2014). As the lower crust of the Iberian Plate was subducted under the European Plate, a doubly vergent orogenic prism developed diachronously from east to west in the upper crust, leading to the inversion of the former Mesozoic basin and the stacking of the basement. Inverted hyper-extensional Mesozoic basins constitute the North Pyrenean Zone (Lagabrielle et al 2010), bordered to the north by the Aquitanian basin (Fig. 1). Conversely, the Southern Pyrenees consists of a thrust fan

that is constituted by four main thrust sheets in the west-central Pyrenees (Teixell 1996; Labaume et al. 2016a). These are the Lakora–Eaux-Chaudes, Gavarnie, Broto, and Guarga thrust sheets, which involve the Paleozoic basement, a preorogenic Mesozoic succession, and the Cretaceous to early Miocene foreland basin. The late Santonian to early Miocene synorogenic sequence constitutes the detached South Pyrenean foreland basin (including the Jaca basin), separated by the autochthonous Ebro basin to the south by the thrust front of the External Sierras.

During the Eocene, the Ager and Tremp–Graus basins of the east-central Pyrenees concentrated the fluvio-deltaic environments, funnelling sediments to the west, to the slope and deep-marine Ainsa and Jaca basins, where a thick turbidite succession known as the Hecho Group was deposited in the Jaca basin (Nijman and Nio 1975; Mutti 1985; Puigdefàbregas et al. 1992; Caja et al. 2010; Garcés et al. 2020). The lower to middle Eocene deep-marine turbiditic sedimentation stage was axially fed from the east, with its source area located in the uplifting central Pyrenees and the Ebro Massif to the south (Caja et al. 2010; Roigé et al. 2016; Gómez-Gras et al. 2016). Nevertheless, a provenance shift occurred during the last turbidite-sedimentation stage (the Rapitán channel, Remacha et al. 1995), evidenced by a change in paleocurrents, facies, and sediment composition, that recorded the first north-derived sediments from newly emerged source areas (Roigé et al. 2016). In the Bartonian, the shallow marine and transitional environments replaced the deep-marine sedimentation, and the basin depocenter migrated to the south (Oms et al. 2003; Teixell 1996). The Larrés Marls and the Sabiñanigo sandstone formation are the first delta-slope and delta-front sediments recorded in the basin (Puigdefàbregas 1975; Boya 2018), followed by the Pamplona Marls (Mangin 1960) and the delta front of the Priabonian Belsué–Atarés sandstone formation.

The growth of fold structures in the Jaca basin (Puigdefàbregas 1975; Hogan 1993; Labaume et al. 2016a) controlled the westward progradation of these deposits. Finally, during the late Eocene–early Miocene, the molasse deposits of the Campodarbe Group represent the overfilled sedimentation stage of the basin (Puigdefàbregas 1975; Labaume et al. 1985; Oliva-Urcia et al. 2016; Roigé et al. 2019). The central part of the basin (Guarga syncline, Fig. 1B), where the Campodarbe Group reaches more than 3000 m in thickness, is characterized by the interplay of an east-derived fluvial system with a north-derived alluvial-fan system (Puigdefàbregas 1975; Montes and Colombo 1996; Roigé 2018). Four different north-derived alluvial fans can be identified in the Jaca basin: the Santa Orosia, Canciás, Peña Oroel, and San Juan de la Peña fans. The continentalization of the basin was diachronous, from east to west (Puigdefàbregas 1975; Dreyer et al. 1999), and ended at 36 Ma with the closure of the basin and the development of endorheic conditions (Ortí et al. 1986; Payros et al. 1999; Barnolas and Gil-Peña 2001; Costa et al. 2010).

Petrography and Provenance

Roigé (2018) defined the paleogeographic evolution of the Jaca basin drainages describing the interplay between axially fed sediments from the east with transversely fed sediments from the north in the Jaca basin. Four different petrofacies were identified and mapped based on the relative abundance of the most significant components such as hybrid sandstone rock fragments (which are those displaying intrabasinal and extrabasinal grains), feldspar and lithic grains, and carbonate extrabasinal particles.

The "hybrid-clast-dominated" petrofacies (HCD) is characterized by high percentages of hybrid sandstone and/or siltstone rock fragments together with limestone rock fragments, and a low abundance of metamorphic and sandstone rock fragments (Roigé et al. 2017). The "carbonate extrabasinal enriched" petrofacies (CEE) is dominated by carbonate extrabasinal components, subordinate hybrid sandstone rock fragments, and a very low siliciclastic content. In the "siliciclastic dominant" petrofacies (SD), carbonate grains and hybrid sandstone rock fragments are scarce, and shales, schists, and quartzites are the most representative particles, with sandstone and siltstone rock fragments, micas, and feldspar as subordinate grains. The "mixed lithic and carbonate" petrofacies (MLC) displays a high percentages of carbonate grains, hybrid sandstone rock fragments and lithic grains.

During the deposition of the Banastón turbidite system of the upper Hecho Group (Fig. 2), "carbonate extrabasinal enriched" sediment entered the basin sourced from the east (east-central Pyrenees). During the deposition of the overlying Jaca turbidite system, this eastern source evolved to a more siliciclastic composition (Roigé et al. 2017). The last turbidite sedimentation stage (the Rapitán channel) displays the first composition derived from northern sources (HCD petrofacies), evidenced by the increase in sandstone rock fragments. In the Bartonian–Priabonian, deltaic environments record the strong interplay between the axially fed "carbonate enriched" and "siliciclastic dominant" sediments with the first transverse alluvial fans characterized by the abundance of hybrid sandstone rock fragments that can be linked to the uplift and recycling of the former turbidite basin. The interplay between these two drainage patterns is further evidenced by the occurrence of the "mixed lithic and carbonate" petrofacies in the Peña Oroel and San Juan de la Peña areas, as well as the occurrence of the "hybrid-clast-dominated" petrofacies (Roigé et al. 2017) in the southern flank of the Yebra anticline during the sedimentation of the Belsué–Atarés delta. Finally, the upper parts of the Canciás and San Juan de la Peña fans also record a compositional evolution highlighted by the increase of lithic and carbonate grains.

Potential Sources of Heavy Minerals

The ability of source to produce a rich and varied heavy-mineral suite depends on the rock type (Mange and Maurer 1992; Garzanti and Andò 2007a, 2007b). Igneous and metamorphic rocks may contain various heavy minerals as the main constituents or accessory phases. By contrast, the heavy-mineral content of sedimentary rocks does not exceed 1% of the total volume. Usually, sandstones may be able to produce a recycled ultrastable suite, whereas carbonate rocks are usually devoid of heavy minerals or display very low content, mostly related to aeolian input or diluted suspended material from terrestrial sources.

Potential sources of heavy minerals during the late Eocene–Miocene in the Jaca basin can be: i) the Paleozoic basement occurring in the Axial or North Pyrenean Zone, ii) the preorogenic Mesozoic cover successions of the North and South Pyrenean Zone, and iii) the synorogenic assemblage of late Cretaceous–middle Eocene deposits. The Paleozoic basement is constituted by an assemblage of Cambro-Ordovician to Devonian metasedimentary units, followed by Carboniferous flysch deposits, which are in turn intruded by Variscan granitoids (Carboniferous–Permian) (Zwart and Sitter 1979; Zwart 1986; Debon et al. 1996 Guitard et al. 1996; Ribeiro et al. 2019). In general, the whole Paleozoic basement displays a very-low to low grade of metamorphism, though it increases to medium and high grade in large metamorphic domes that occur along the Guitar Axial Zone.

The Paleozoic basement of the Pyrenees is unconformably overlain by Permo-Triassic red beds or Cretaceous limestones. Shales, carbonates (Muschelkalk facies), evaporites (Keuper facies), and dolerites (ophites) complete the Triassic succession. The Jurassic and Cretaceous in the Southern Pyrenees are mainly represented by a thick carbonate and shale succession. Nonetheless, in the North Pyrenean Zone, (Fig. 1) a Jurassic–Lower Cretaceous carbonate succession is followed by a thick sequence of deep-water shales and turbidites (Albian to Maastrichtian) intruded by subvolcanic basaltic rocks (Souquet 1967; Azambre 1967). A Cretaceous HT-LP metamorphism appears restricted to a narrow east–west-trending belt (Internal Metamorphic Zone) in the North Pyrenean Zone, related to crustal thinning and mantle exhumation during rifting (Goldberg and

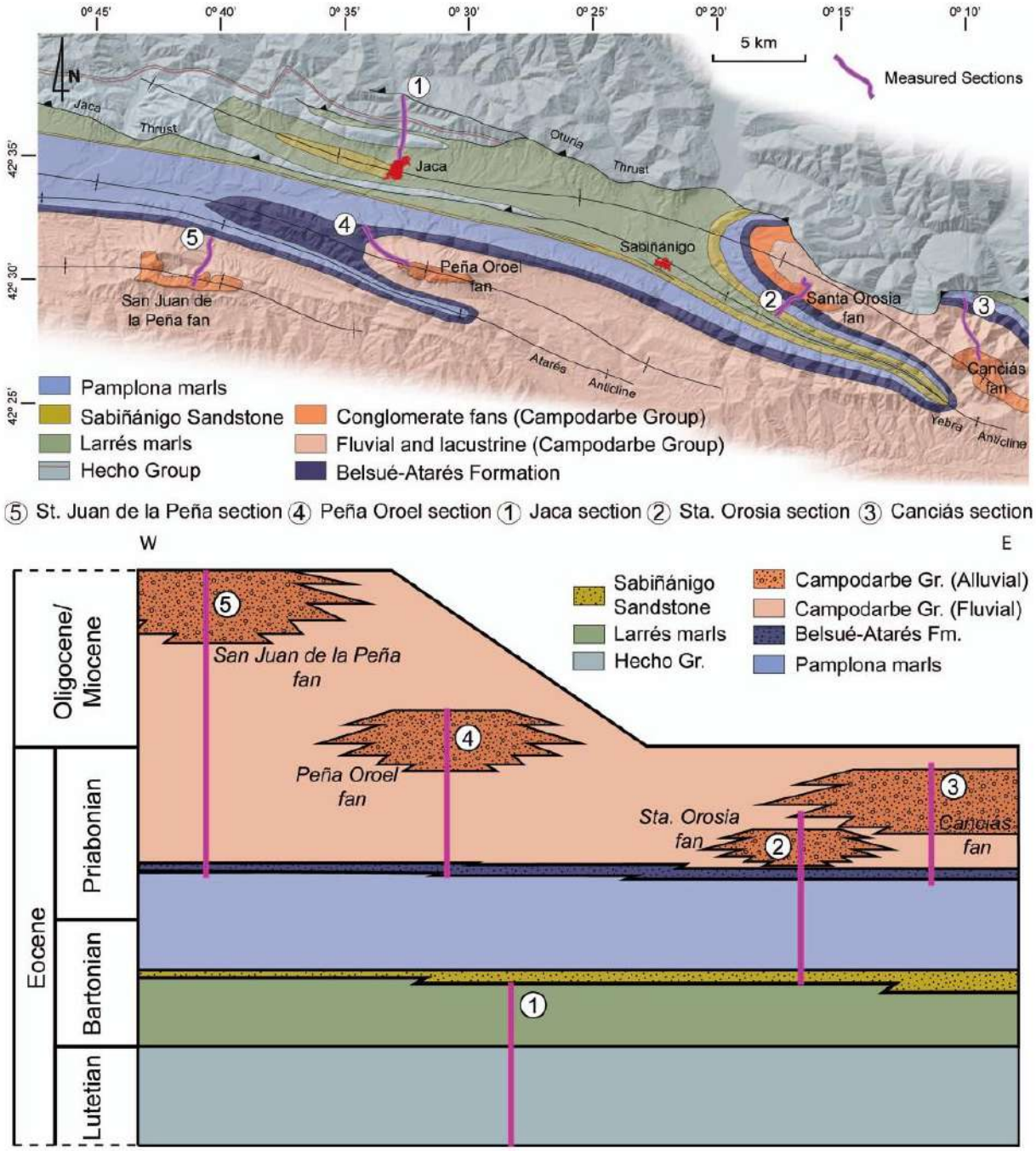

FIG. 2.—**A)** Geological map of the northern sector of the Jaca basin (modified from Roigé et al. 2017). Purple lines show the location of the stratigraphic sections represented in Figure 6. **B)** General stratigraphic cross-section sketch summarizing the relationships of the analyzed deposits (modified from Roigé et al. 2017). Stratigraphic ages are extracted from Labaume et al. (1985), Hogan and Burbank (1996), Oms et al. (2003), and Roigé et al (2019). Blue-purple bars indicate the position of the measured stratigraphic logs in this work.

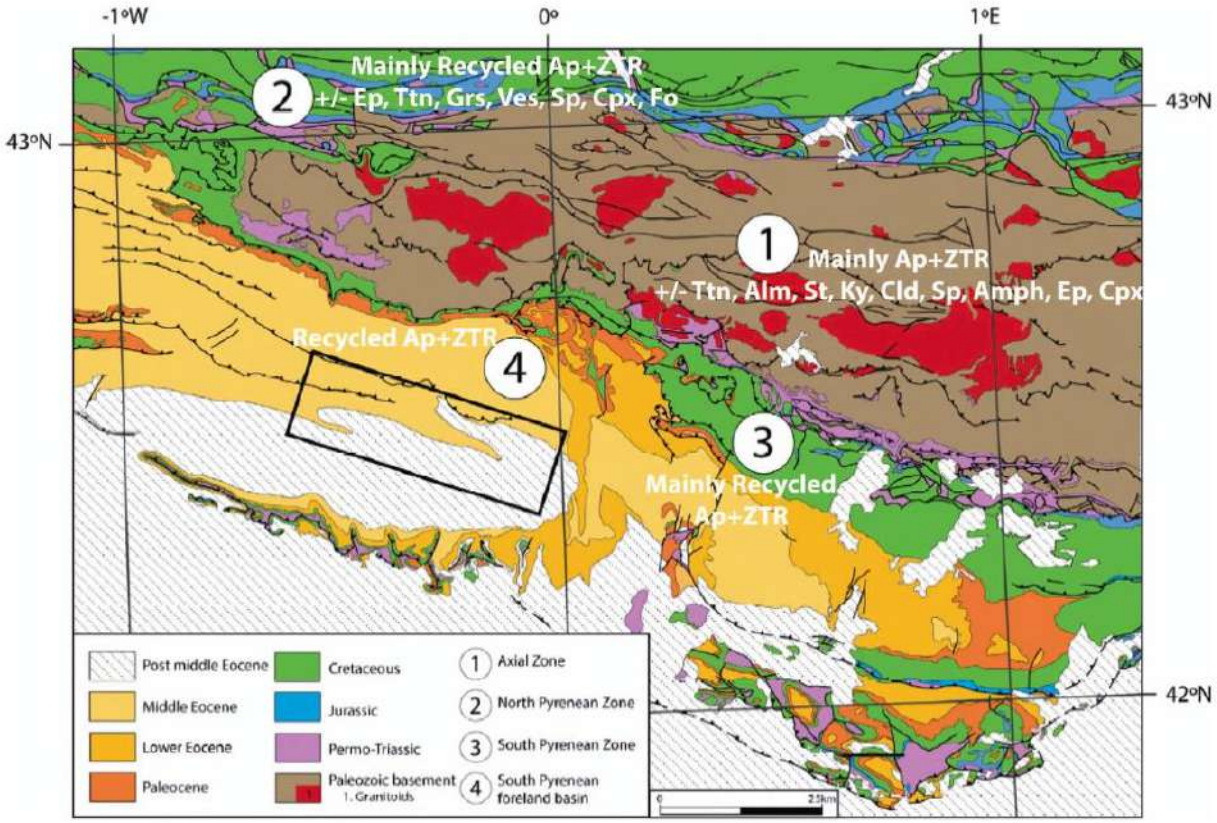

FIG. 3.—Geological map of the Pyrenees showing the potential sources of heavy minerals (modified from Roigé et al. 2017).

Leyreloup 1990; Clerc et al. 2015). Subsequent foreland-basin deposits are best preserved in the Southern Pyrenees Platform carbonates (limestone, dolostone, and sandstone deposits) developed in the distal basin margin from Cretaceous to Lutetian times whereas the basin trough was characterized by the Eocene clastic infill of the Àger, Tremp, Ainsa, and Jaca basins, which mainly consist of siliciclastic alluvial, deltaic, and turbidite deposits.

Zircon, tourmaline, rutile, and apatite grains occur in a wide variety of igneous, sedimentary, and metamorphic rocks of the Paleozoic basement, Mesozoic metamorphic rocks, and Mesozoic and Tertiary sedimentary cover (Fig. 3). Minerals such as chloritoid, almandine, staurolite, and kyanite are prone to be derived from Paleozoic metapelites (phyllites, schists, and granulites; Zwart and Sitter 1979; Zwart 1986; Guitard et al. 1996) but have not been reported in the Mesozoic metapelites of the Internal Metamorphic Zone. Almandine garnet might be also sourced from igneous rocks such as Permo-Carboniferous rhyolites, dacites, ignimbrites, and volcaniclastic sediments (Bixel 1987; Gilbert and Rogers 1989) or late Variscan muscovite granites (Harris 1974). By contrast, grossular garnet is usually associated with skarn deposits, thermally metamorphosed impure limestones and marbles occurring in the Axial and North Pyrenean zones. In addition, grossular has also been described in volcanic rocks such as the syenites of the North Pyrenean Zone (Azambre et al. 1989).

Clinopyroxene, olivine, spinel, epidote, and amphibole occur in various igneous rocks such as Triassic dolerites or Cretaceous basalts, picrites, teschenites, syenites, and lamprophyres of the North Pyrenean Zone (Azambre 1967; Azambre et al. 1987, 1989; Ternet et al. 1995; Lago et al. 2000). Clinopyroxene and amphibole are also common in basic igneous rocks (basalts and andesites) of the Stephano-Permian vulcanism (Bixel 1987). In addition, epidote, amphibole, clinopyroxene, titanite, and vesuvianite also occur in Paleozoic marbles and calcschists, skarn deposits, and hornfels related to Paleozoic granites, as well as in the metamorphic Mesozoic limestones of the North Pyrenean Zone (Ternet et al. 1995; Majesté-Menjoulàs et al. 1999). Spinel and olivine, as well as clinopyroxene and amphibole, are also present in regionally metamorphosed carbonate rocks that have achieved the amphibolite facies. Titanite is a common accessory mineral in many igneous and metamorphic rocks, and thus it can be found in Paleozoic granites, Triassic dolerites, metapelites, and impure calc-silicate rocks (Azambre 1967; Azambre et al. 1987; Zwart and Sitter 1979; Zwart 1986; Guitard et al. 1996; Ribeiro et al. 2019).

SAMPLING AND METHODS

A total of 24 samples of sandstone were collected from five sections (Jaca, Santa Orosia, Canciás, Peña Oroel, and San Juan de la Peña) for heavy-mineral analysis of the turbidite, deltaic, and fluvio-alluvial deposits of the Jaca basin. In cases where medium-grained sandstone was not available, fine to very coarse grain sizes were collected. In addition, samples from each depositional system were collected from similar facies in order to minimize hydraulic-sorting effects related to different processes within the same depositional environment (Andò et al. 2019). They were crushed and submitted to digestion with diluted 10% acetic acid for

carbonate removal and better desegregation of well cemented sands. The 32 to 500 μm window was recovered through wet sieving prior to heavy-mineral separation. The heavy fraction was separated by centrifuging in Na-polytungstate (2.90 g/cm^3) and recovered by partial freezing with liquid nitrogen (e.g., Mange and Maurer 1992; Andò 2020).

Polished thin sections (30 micrometers) of the heavy-mineral fraction were prepared for each sample, and mineral identification was done using Raman spectroscopy. The counting method used was the ribbon or area method (Galehouse 1971). A representative area of the thin section was selected, and all the minerals in that area up to 200 grains were identified. The obtained Raman spectra (Figs. 4, 5) were compared with reference spectra (Wang et al. 2004; Kuebler et al. 2006; Andò and Garzanti 2014) and verified under the optical microscope. Opaque, diagenetic, carbonate, and micaceous minerals were not considered for identification, and only the relative abundances of detrital heavy minerals are reported in this paper. Statistical treatment of the heavy-mineral counting data was done using the Provenance R-package (Vermeesch et al. 2016; Vermeesch 2018). In addition, heavy-mineral analysis was integrated with sandstone petrography data already published in Roigé (2018).

Since the data obtained by the area method are counts, correspondence analysis with the provenance R package (Vermeesch 2018) was used for the statistical treatment. This procedure may introduce some bias as point-counting was not the method used to acquire the data. However, in multi-dimensional datasets, this is a good way to visualize and interpret the results of counts.

RESULTS

The relative abundances of heavy minerals (Tab. 1) of the study samples are presented as percentage pie charts in their stratigraphic position (Fig. 6) for optimal visualization and integration with sandstone petrography (Roigé et al. 2016, 2017). Since all samples display more than 71.1% of the ultrastable association Ap-Zrn-Tur-Rt, the modal relative compositions of each system are presented as Ap (apatite), ZTR (zircon-tourmaline-rutile), and &tHM (other transparent heavy minerals).

The Hecho Group turbidites (91–100% ZTR+Ap) and the Sabiñanigo delta sandstones (96–97% ZTR+Ap) display the higher percentages of the ultrastable suite. Although this assemblage also dominates the alluvial-fan deposits, a clear difference can be observed between the heavy-mineral suites of the deep-marine and the terrestrial environments, since the latter often show higher relative abundances of other transparent heavy minerals (staurolite, garnet, kyanite, chloritoid, titanite, epidote, clinopyroxene, amphibole, vesuvianite, spinel, olivine, or sphalerite) and an increase of the ultrastable ZTR. Moreover, the turbidite deposits are dominated by euhedral, angular and subrounded grains (Ap-Zrn-Tur-Rt), whereas the alluvial-sedimentation stage records an increase in rounded to well-rounded grains.

Jaca Profile

This profile addresses the heavy-mineral suites of the Hecho Group turbidites. The Banastón turbidite system (CEE petrofacies) is dominated by zircon, tourmaline, and rutile (Ap_{41}-ZTR_{57}-$\&tHM_2$), whereas the Jaca turbidite system (Ap_{58}-ZTR_{37}-$\&tHM_5$) and the Rapitán channel (HCD petrofacies, Ap_{58}-ZTR_{33}-$\&tHM_9$) contain the highest relative abundances of apatite. Nonetheless, the lower part of the Jaca turbidite system is similar to the Banastón turbidite system regarding their heavy-mineral suites and sandstone composition. The highest apatite content (75.8%) is found in the upper part of the Jaca turbidite system (J9, SD petrofacies). In addition, the Rapitán channel records an increase in other transparent heavy minerals such as almandine, and the first appearance of grossular, clinopyroxene, sphalerite, and staurolite, whereas the former turbiditic systems area characterized by the presence of almandine and spinel and chloritoid.

Santa Orosia Profile

This profile starts with the deltaic deposits of the Sabiñanigo sandstone (Ap_{46}-ZTR_{51}-$\&tHM_3$), which display a suite similar to that of the Banastón turbidite system, though the relative abundance of apatite in the lower part (55.2%, CEE petrofacies) is much higher than in the upper part (37.1%, HCD petrofacies). Conversely, ZTR increases to the top, from 42% to 59%. As in the Banastón and Jaca turbidites, spinel and almandine are also present in the assemblage.

Upsection, the younger Belsué–Atarés deltaic sandstones (CEE petrofacies) display a different assemblage (Ap_{25}-ZTR_{57}-$\&tHM_{18}$) from the Sabiñanigo delta sandstone. As for the Sabiñanigo sandstone, apatite relative abundances are higher at the base (31.2%) than at the top (18.5%), and ZTR increases to the top, from 40% to 74%. However, a characteristic feature of this Formation is the relative abundance of &tHM ($Ttn_{2.9}$-$St_{1.3}$-$Alm_{1.3}$-$Cld_{0.3}$-$Ep_{0.3}$-$Fo_{0.3}$), which in the lower part achieves 29%. By contrast, the upper part displays titanite, staurolite, and almandine as well, but their relative abundances are much lower ($Ttn_{1.3}$-$St_{1.8}$-$Alm_{2.6}$) and there is no trace of epidote, forsterite, or chloritoid.

The overlying deposits of the late Eocene Santa Orosia fan (HCD petrofacies) are dominated by zircon, tourmaline, and rutile (Ap_{30}-ZTR_{53}-$OtHM_{17}$). However, there is a marked increase in other transparent heavy minerals (up to 24% in the middle part of the fan) compared to the former turbidite and delta systems. Titanite, almandine, and staurolite are common, though in low relative proportions ($Ttn_{5.1}$-$Alm_{4.4}$-$St_{4.4}$). A characteristic feature of the Santa Orosia alluvial fan is the presence of clinopyroxene (0.8%), though it disappears at the top.

Canciás Profile

Here, the Belsué–Atarés deltaic sandstones (Ap_{44}-ZTR_{54}-$OtHM_2$) display higher relative abundances of apatite and less of other transparent heavy minerals ($Alm_{1.4}$-$Grs_{0.5}$-$Ep_{0.5}$) compared to the Santa Orosia profile. The overlying Oligocene Canciás fan displays a different assemblage (Ap_{30}-ZTR_{70}-$\&tHM_{16}$), highlighted by the increase in other transparent heavy minerals. It is important to notice that this fan records three different compositions trough the "hybrid-clast-dominated," "mixed lithic and carbonate," and "carbonate enriched" petrofacies. In the lower part (C8, Ap_{29}-ZTR_{59}-$\&tHM_{13}$), the assemblage is similar to the one occurring at the top of the Santa Orosia fan (JY39, Ap_{31}-ZTR_{55}-$\&tHM_{14}$), with similar relative proportions of almandine, staurolite, titanite, and grossular (C8, $Alm_{3.9}$-$St_{4.4}$-Ttn_2-$Grs_{0.5}$; JY39, $Alm_{4.3}$-$St_{3.1}$-$Ttn_{3.5}$-$Grs_{1.2}$), and both corresponding to the "hybrid-clast-dominated" petrofacies. Up section, sample C13 (Ap_0-ZTR_{85}-$\&tHM_{14}$, MLC) is characterized by the scarcity of apatite (0.5%) and the high content of tourmaline (62.7%). In the "hybrid-clast-dominated" upper part of the fan (C17, Ap_{13}-ZTR_{66}-$\&tHM_{21}$) the heavy-mineral suite records an increase in the epidote relative abundance (14.2%) as well as apatite (13%), though its content is low compared to the lower part of the fan. Another interesting feature is that grossular dominates over almandine in the upper part of the Canciás fan, whereas in the lower turbiditic, deltaic, and alluvial deposits (Santa Orosia and lower Canciás fan) almandine is more abundant than grossular. Staurolite is also less common in the upper part (0.5%) of the Canciás fan than in its lower part (4.4%) or the Santa Orosia fan (4.4%).

Peña Oroel Profile

Here, the Belsué–Atarés Formation (Ap_{12}-ZTR_{66}-$\&tHM_{22}$) displays the highest relative abundance of other transparent heavy minerals in two different petrofacies (HCD petrofacies, Ap_{12}-ZTR_{61}-$OtHM_{27}$; MLC, Ap_{12}-ZTR_{71}-$\&tHM_{17}$). The most characteristic feature of these suites is the presence of clinopyroxene and vesuvianite, especially in the lower "hybrid-clast-dominated" part (Cpx, 12.6%; Ves, 2.3%). Both petrofacies show a similar heavy-mineral assemblage, though sample JJ6 (MLC petrofacies)

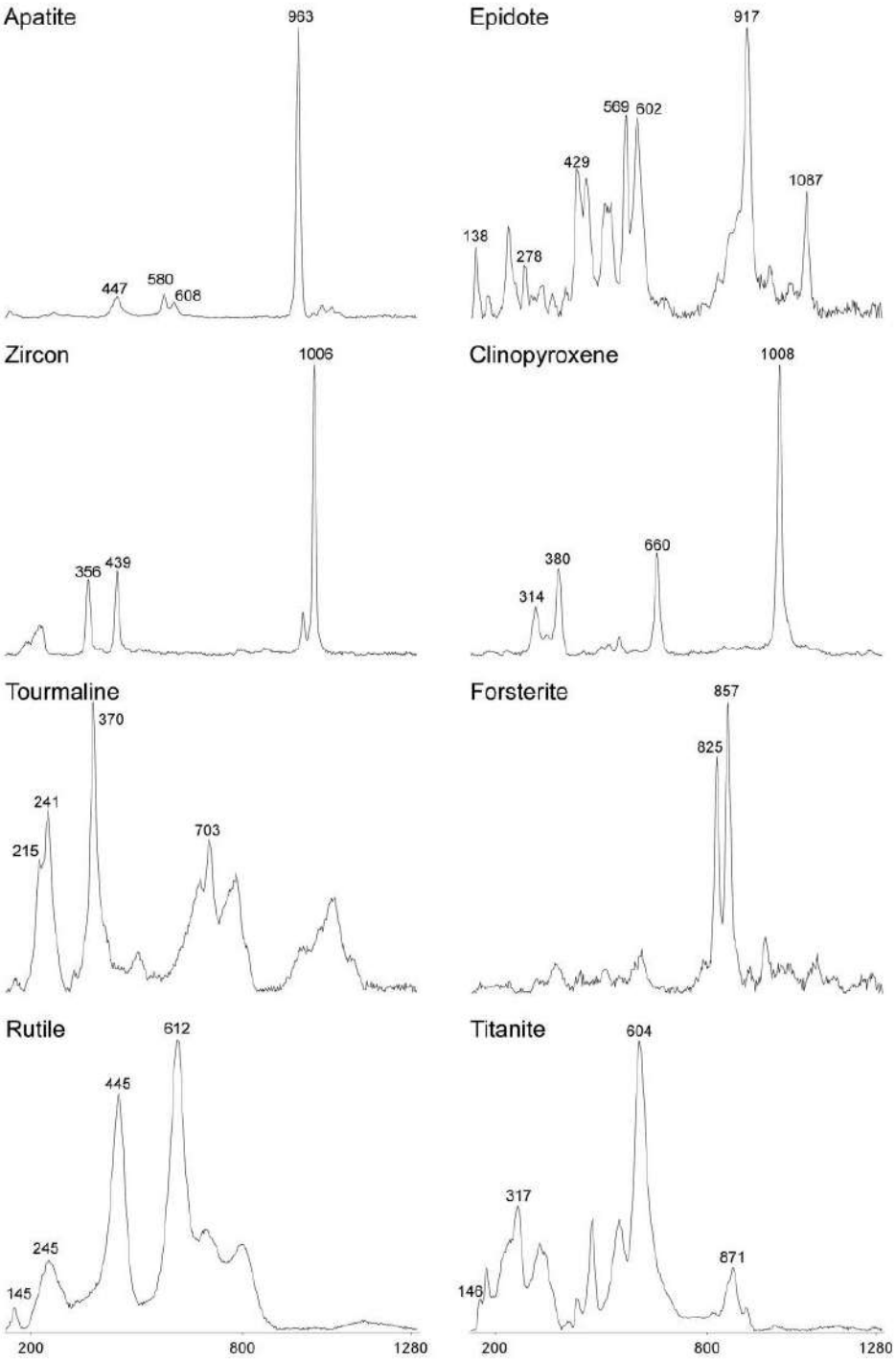

FIG. 4.—Representative Raman spectra of heavy minerals from the late Eocene–Miocene Jaca basin.

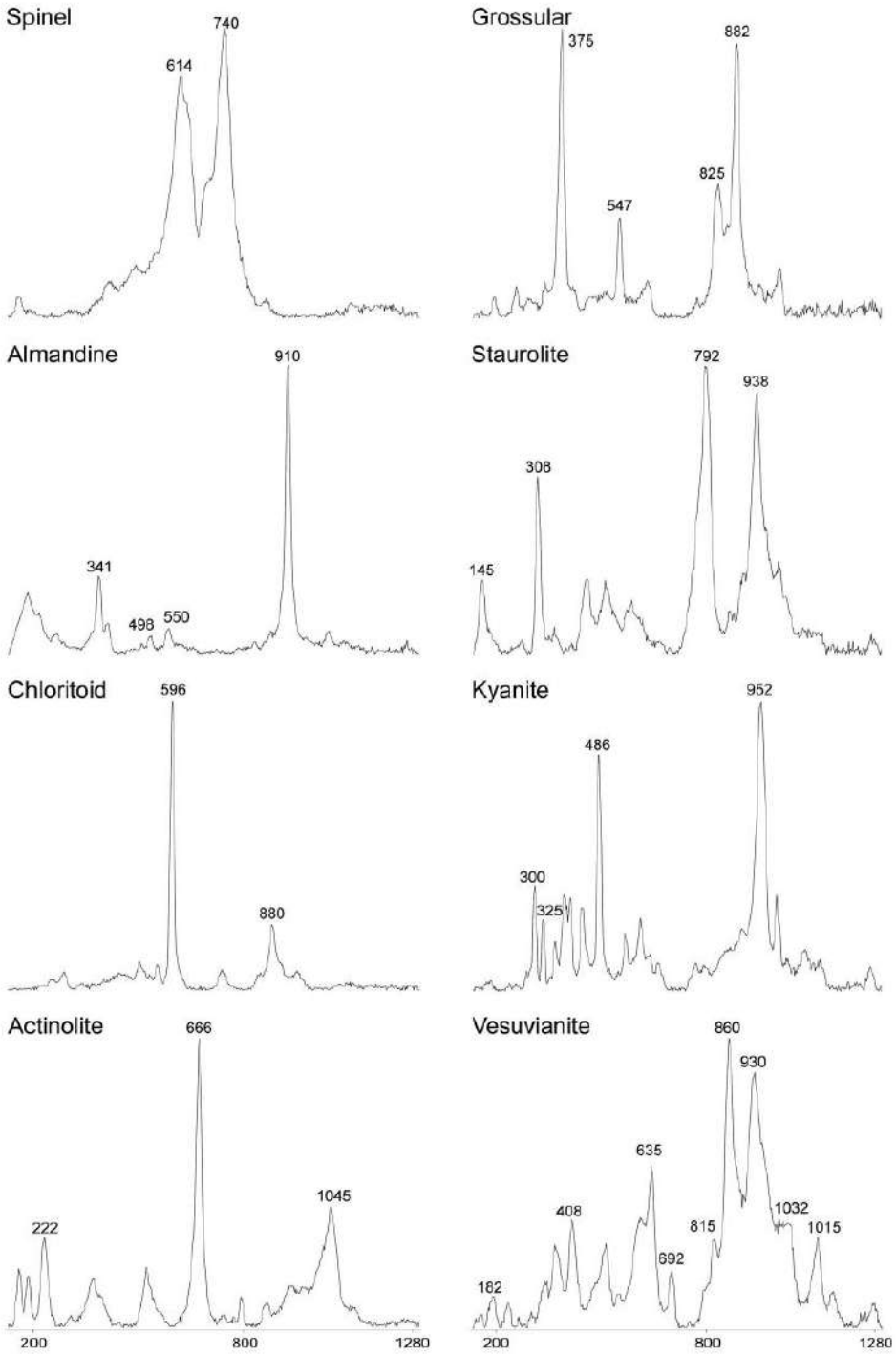

FIG. 5.—Representative Raman spectra of heavy minerals from the late Eocene–Miocene Jaca basin.

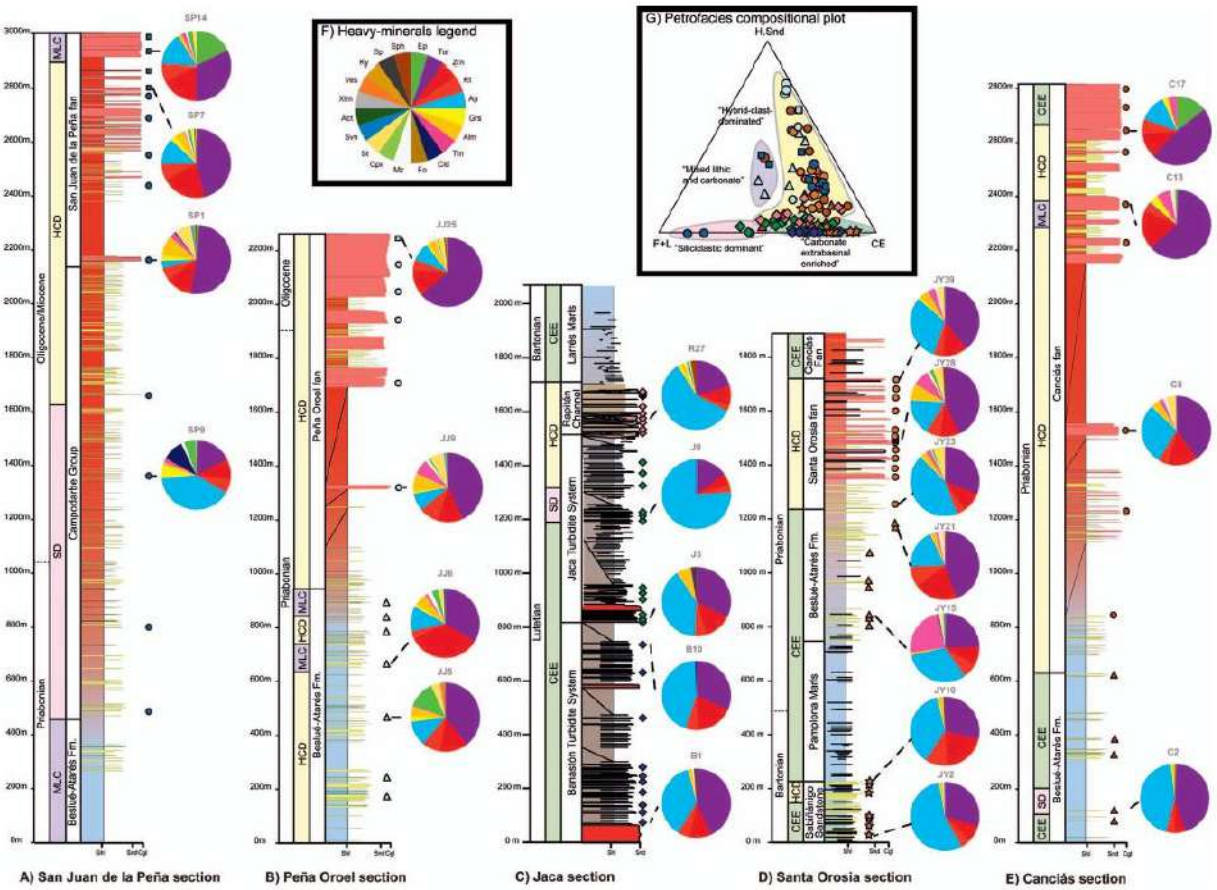

FIG. 6.—Heavy-mineral results for all the sections (see location in Fig. 2), with the stratigraphic log of each section. **A)** San Juan de la Peña section. **B)** Peña Oroel section. **C)** Jaca section. **D)** Santa Orosia section. **E)** Canciás section and position of the analyzed samples and the occurrence of petrofacies (modified from Roigé et al. 2017). Squares, dots, triangles, and rhombs correspond to petrographic samples studied in previous works (Roigé et al. 2016, 2017). **F)** Color legend used for heavy-mineral pie diagrams. **G)** Ternary diagram used for petrofacies discrimination (data from Roigé et al. 2018).

does not record the presence of vesuvianite, the clinopyroxene relative abundance is lower (3.1%), and zircon increases up to 34.4%.

The characteristic feature of the Peña Oroel fan is the predominance of the "hybrid-clast-dominated" petrofacies through the entire section. Similar to the Canciás profile, these alluvial deposits (Ap_8-ZTR_{72}-$\&tHM_{19}$) exhibit low relative abundances of apatite, high ZTR, and higher content of other transparent heavy minerals when compared to the Hecho turbidite deposits. As in the Santa Orosia fan, in the Peña Oroel alluvial deposits the most abundant garnet is almandine (6%), and staurolite is common (5%). The upper part of the fan records the occurrence of kyanite, actinolite, clinopyroxene, and vesuvianite.

San Juan de la Peña Profile

This profile starts with the fluvial deposits of the Campodarbe Formation. These sandstones are classified as "siliciclastic dominant" petrofacies and their heavy-mineral suite is dominated by apatite (Ap_{40}-ZTR_{33}-$\&tHM_{27}$). However, they show the highest relative abundance of other transparent heavy minerals ($Cld_{9.8}$-$Grs_{5.7}$-$Cpx_{5.2}$-$Ttn_{2.1}$-$Alm_{1.5}$-$Ep_{0.5}$), with chloritoid, grossular, and clinopyroxene being the most represented. Almandine, titanite, and epidote are also present.

By contrast, the overlying late Oligocene to Miocene San Juan de la Peña alluvial-fan system, where the dominant petrofacies is the "hybrid-clast-dominated," exhibits higher relative abundances of ZTR and minor apatite (Ap_{10}-ZTR_{67}-$\&tHM_{22}$). However, this fan records a compositional change in the upper part, where sandstones are classified as "mixed lithic and carbonate" petrofacies. Although epidote is also present in the lower parts of the fan (0.9%), the compositional change is accompanied by an increase of epidote relative abundance (up to 17.5%). Other heavy minerals present in the alluvial sediments are clinopyroxene, titanite, actinolite, almandine, grossular, staurolite, vesuvianite, and spinel.

Statistical Treatment

In the previous section, results were described in terms of the relative abundances of heavy minerals. However, such a display does not consider the statistical uncertainty of the counting data (Vermeesch 2018). The best way to solve this problem in multi-dimensional datasets is to visualize and interpret the results through correspondence analysis (Greenacre 1984). Therefore, a set of biplots are used to visualize the results of the statistical analysis. The first one (Fig. 7A) shows the correspondence analysis of the raw data. Although it does not explain the overall variance in a satisfactory

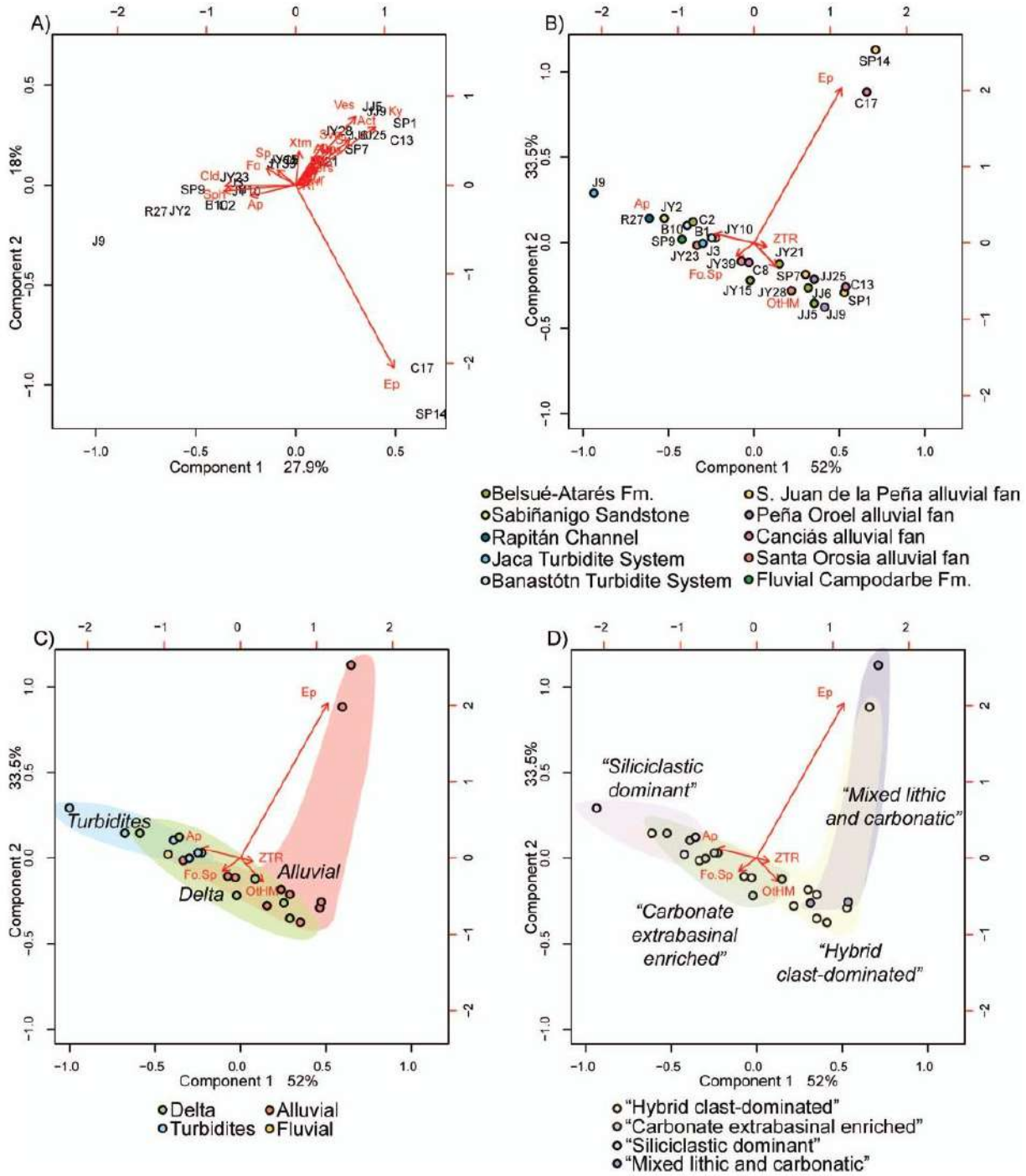

FIG. 7.—Correspondence analysis of the heavy-mineral compositions displayed as biplots. **A)** Biplot of raw data where Ep, epidote; Tur, Tourmaline; Zrn, zircón; Rt, rutile; Ap, apatite; Grs, grossular; Alm, Almandine; Ttn, titanite; Cld, chloritoid; Fo, forsterite; Mz, monazite; Cpx, clinopyroxene; St, staurolite; Svn, svanbergite; Act, actinolite; Xtm, xenotime; Ves, vesuvianite, Ky, kyanite; Sp, spinel; Sph, sphalerite. **B)** Biplot of data treated according to correlations shown by the raw data analysis. **C)** Biplot of heavy-mineral compositions of sedimentary environments. **D)** Biplot of heavy-mineral compositions of petrofacies. **E)** Biplot of heavy-mineral compositions of sedimentary units. In Parts B, C, D, and E: Ap, Ap+Cld+Sph; ZTR, Zrn+Tur+Rt; OtHM, Alm+Grs+Ttn+Ves+Cpx+Act+St+Ky+Xtm+Svn; Fo.Sp, Fo+Sp; Ep, Ep.

way, it clearly shows a correlation between some minerals. Apatite correlates with chloritoid and sphalerite; spinel with forsterite; zircon with tourmaline and rutile; finally, there is a correlation between the rest of the minerals.

Due to the scarcity of some minerals, zero values dominate the data (Table 1). This might be a problem when applying correspondence analysis because this method is very sensitive to the least abundant components (Vermeesch 2018). In order to avoid undesirable noise, minerals were grouped based on the correlations shown by the correspondence analysis of the raw data. A new analysis was performed (Fig. 7B), accounting for as much as 88.5% of the variance and maintaining the original structure of the biplot.

Figure 7C shows that samples from the turbidite systems cluster around apatite, indicating that they are compositionally similar and enriched in this mineral. Conversely, alluvial-fan deposits group around the OtHM and ZTR. Samples plot close to epidote in the upper parts of the Canciás and San Juan de la Peña fans (C17 and SP14, respectively), indicating a different composition when contrasting to the lower parts of the fans.

Deltaic deposits display the highest dispersion (Fig. 7C). While the heavy-mineral suites of the Sabiñánigo sandstone are similar to the former turbidites, the mineral assemblages of the Belsué–Atarés sandstone vary depending on the stratigraphic profile and the various petrofacies. The mineral suites of the Belsué–Atarés delta are enriched in apatite in the Canciás profile (C2), whereas the abundance of other transparent heavy minerals is higher in the Santa Orosia (JY15, JY21) and Peña Oroel (JJ5, JJ6) sections. The Belsué–Atarés Formation seems to be compositionally similar in the Santa Orosia (JY15, JY21) and Peña Oroel profiles (JJ5, JJ6), according to the correspondence analysis (Fig. 7B), though it is enriched in OtHM in the Peña Oroel profile.

Regarding the petrographic analysis of bulk sandstone, there is a correlation between the heavy-mineral assemblages and the petrofacies displayed by each sample (Roigé et al. 2017), though the "carbonate enriched" and the "hybrid-clast-dominated" petrofacies show some dispersion (Fig. 7D). The "carbonate enriched" and the "siliciclastic dominant" petrofacies are enriched in apatite, whereas the characteristic feature of the "hybrid-clast-dominated" and the "mixed lithic and carbonatic" petrofacies is their higher relative abundance of other transparent heavy minerals (OtHM) and ZTR.

DISCUSSION

Provenance vs. Diagenetic Overprint

Before attempting to extract any provenance interpretation based on detrital heavy-mineral assemblages of ancient rocks, one has to be aware of the overprinting processes, which can modify the original detrital signature (Morton and Hallsworth 1999; Garzanti et al. 2008, 2009, 2018; Garzanti and Andò 2019). Source-rock lithology exerts the main control on the composition of detrital heavy-mineral assemblages. However, weathering at the source area, physical sorting, and, particularly, dissolution during deep-burial diagenesis can modify the final absolute or relative abundances of heavy minerals found in a detrital rock. Many authors have faced the issue of intrastratal dissolution, a process that can greatly modify the detrital assemblages during deep-burial diagenesis (Morton 1984; Milliken 1990; Morton and Hallsworth 1999, 2007; Velbel 2007; Andò et al. 2012; Garzanti and Andò 2007a, 2019). Substantial loss of heavy minerals has been described in many basins of the world (Walderhaug and Porten 2007; Milliken and Mack 1990; Morton and Hallsworth 2007; Garzanti et al. 2018) with increasing burial depth, but a given mineral may dissolve or remain at different depths in different basins. Nevertheless, there is a consensus in the order of persistence of different heavy minerals with burial. Basically, dissolution depends on pore-fluid temperature and composition, the rate of pore-fluid movement, and geological time (Morton and Hallsworth 2007). The study of dissolution textures (Andò et al. 2012) combined with paleotemperature data and integration of sandstone petrography, can provide some insights about the possible loss of minerals due to deep-burial diagenesis.

In the Jaca basin, the main difference between the heavy-mineral suites of the turbidite and the alluvial sedimentation stages is the increase of unstable heavy minerals displayed by the terrestrial environments. This is a typical pattern when older and more deeply buried sandstones have gone through stronger diagenesis than younger and less deeply buried sediments. Since burial diagenesis may account for the ultrastable assemblage displayed by the turbidite and deltaic deposits, each section is analyzed separately in order to properly assess the degree of diagenetic overprint based on paleotemperature data and dissolution textures.

Jaca Profile.—In this profile, the ultrastable association of the Hecho Group turbidites might be the result of intrastratal dissolution due to burial depth. However, erosion of felsic acidic igneous rocks or ancient sandstones may produce a similar suite (Götze 1998). Based on the high content of terrigenous carbonate grains, feldspar, and plutonic rock fragments, Roigé et al. (2016) established that the Banastón and the lower Jaca turbidite systems were sourced mainly from the Mesozoic and Paleocene platform carbonates of the South-Central Pyrenean Unit and granitoids of the Paleozoic basement (east-central Pyrenees). As carbonate rocks are poor "heavy-mineral suppliers," it is more likely that the assemblage was derived mainly from the erosion of granitic sources, especially those grains that display a euhedral to angular character, which are more abundant in the Banastón and lower Jaca turbidite system. Conversely, the more rounded grains might be sourced from the recycling of the Paleocene or Cretaceous sandstone formations, which is in accordance with the occurrence of well-rounded quartz grains recorded by sandstone petrography (Roigé et al. 2017). In addition, the occurrence of siliciclastic sandstone rock fragments and detrital quartz grains with inherited overgrowths, together with early Variscan detrital zircon U-Pb dates (Roigé 2018), points to the Carboniferous flysch as another possible source for the more rounded heavy-mineral grains.

The observation of dissolution textures on grains provides important insights into the possible loss of minerals due to deep-burial diagenesis or weathering processes. Ultrastable minerals (Ap-Zrn-Tur-Rt), display unweathered or only initial corrosion features (Fig. 8). Almandine also shows no signs of corrosion, although in the lower part of the Jaca turbidite system some grains display advanced corrosion features (Fig. 8) pointing to a higher impact of diagenesis, probably more intense in the Banastón turbidite system.

By contrast, the occurrence of uncorroded clinopyroxene (1.3%) in the Rapitán channel just 700 m above the top of the Banastón turbidite system might indicate that dissolution processes were not too intense, at least in the Jaca turbidite system. Clinopyroxene is well known for its instability during deep burial, only more resistant than olivine (Morton 1984; Morton and Hallsworth 1999, 2007), therefore being a good proxy to assess diagenesis importance. These clinopyroxene grains, as well as almandine and grossular (Fig. 8), display an incipient degree of corrosion (Andò et al. 2012) (Fig. 8), pointing to a low impact of diagenesis on the heavy-mineral suites. Since no etched or skeletal clinopyroxene grains have been reported, we infer that dissolution processes due to intrastratal dissolution probably were not too intense. Therefore, we infer that if unstable minerals dominated the original assemblage of the Jaca turbidites, the 700 m depth difference between the Rapitán Channel and the lower Jaca turbidite system does not seem to be enough to completely erase more stable minerals such as epidote, titanite, kyanite, staurolite, or garnet from the sedimentary record since clinopyroxene is well known for its instability during deep burial, only more resistant than olivine (Morton 1984; Morton and Hallsworth 1999, 2007). Moreover, in the Norwegian continental shelf, ultrastable zircon, tourmaline, rutile, apatite, and spinel exceed depths of

TABLE 1.—*Results of the counting expressed as relative abundances of heavy minerals. Banastón TS, Banastón turbidite sytem; Jaca TS, Jaca turbidite system; Rap C, Rapitán Channel; Sabiñánigo, Sabiñánigo Sandstone; Belsué, Belsué–Atarés Fm.; Camp, Campodarbe Group; Sta. Orosia fan, Santa Orosia fan; Canciás fan, Canciás fan; Oroel fan, Peña Oroel fan; S. Juan de la Peña fan, San Juan de la Peña fan; CEE, "carbonate extrabasinal enriched" petrofacies; SD, "siliciclastic dominant" petrofacies; HCD, "hybrid-clast-dominated" petrofacies; MLC, "mixed lithic and carbonate" petrofacies; Petrofacies data from Roigé et al. (2018); Ep, epidote; Tur, tourmaline; Zrn, zircón; Rt, rutile; Ap, apatite; Grs, grossular; Alm, Almandine; Ttn, titanite; Cld, chloritoid; Fo, forsterite; Mz, monazite; Cpx, clinopyroxene; St, staurolite; Svn, svanbergite; Act, actinolite; Xtm, xenotime; Ves, vesuvianite; Ky, kyanite; Sp, spinel; Sph, sphalerite.*

	Jaca Section					Santa Orosia Section								Canciás Section			Peña Oroel Section				San Juan de la Peña Section			
	Banastón TS		Jaca TS		Rap C	Sabiñánigo		Belsué		Sta. Orosia fan			Belsué	Canciás fan			Belsué		Oroel fan		Camp	S. Juan de la Peña fan		
	CEE	**CEE**	**CEE**	**SD**	**HCD**	**CEE**	**HCD**	**CEE**	**CEE**	**HCD**	**HCD**	**HCD**	**SD**	**HCD**	**MLC**	**HCD**	**HCD**	**MLC**	**HCD**	**HCD**	**SD**	**HCD**	**HCD**	**MLC**
	B1	B10	J3	J9	R27	JY2	JY10	JY15	JY21	JY23	JY28	JY39	C2	C8	C13	C17	JJ5	JJ6	JJ9	JJ25	SP9	SP1	SP7	SP14
Ep	0.0	0.0	0.0	0.0	0.0	0.0	0.0	0.3	0.0	0.0	0.0	0.0	0.5	0.0	0.5	14.2	0.0	0.0	0.0	0.0	0.5	1.3	0.5	17.5
Tur	43.0	31.7	32.2	15.0	20.6	29.5	28.6	24.3	44.5	30.8	43.2	39.4	44.5	39.9	62.7	47.8	39.2	33.5	42.9	63.5	17.0	51.3	45.5	32.7
Zrn	10.1	17.3	12.8	5.8	9.0	7.6	20.5	9.0	20.3	9.6	8.9	11.0	5.3	13.8	18.1	11.7	13.1	34.4	11.9	12.5	9.3	12.4	21.2	17.5
Rt	5.8	5.9	5.7	3.4	3.0	4.8	10.3	6.6	9.7	3.8	6.8	4.7	3.8	4.9	4.4	6.9	8.6	3.6	9.1	5.0	6.7	6.0	7.7	8.1
Ap	37.2	44.6	39.8	75.8	58.4	55.2	37.1	31.2	18.5	43.3	16.9	31.1	44.0	28.6	0.5	12.6	11.7	11.6	8.3	8.5	40.2	3.4	12.2	15.2
Grs	0.0	0.0	0.0	0.0	1.3	0.0	0.4	0.0	0.0	0.4	0.0	1.2	0.5	0.5	3.4	2.0	2.7	1.3	0.8	1.0	5.7	2.6	2.7	0.0
Alm	1.9	0.0	6.6	0.0	2.1	1.9	2.2	1.3	2.6	2.9	8.1	4.3	1.4	3.9	1.0	0.8	4.5	5.8	8.7	4.0	1.5	9.4	4.5	1.9
Ttn	0.0	0.0	0.5	0.0	0.0	0.0	0.0	23.9	1.3	2.1	7.6	3.5	0.0	2.0	6.4	4.0	0.5	1.3	7.1	0.0	2.1	3.0	0.5	1.9
Cld	0.0	0.5	0.0	0.0	0.0	0.0	0.0	0.3	0.0	0.0	0.0	0.0	0.0	0.0	0.0	0.0	0.0	0.0	0.0	0.0	9.8	0.4	0.0	0.0
Fo	0.0	0.0	0.0	0.0	0.0	0.0	0.0	0.3	0.0	0.4	0.0	0.0	0.0	0.0	0.0	0.0	0.0	0.0	0.0	0.0	0.0	0.0	0.0	0.0
Mz	0.5	0.0	0.0	0.0	0.9	0.5	0.0	0.7	1.3	0.4	1.3	1.2	0.0	1.5	1.5	0.0	0.0	2.2	1.6	0.5	1.5	0.4	1.4	0.9
Cpx	0.0	0.0	0.0	0.0	1.3	0.0	0.0	0.0	0.0	0.8	1.7	0.0	0.0	0.0	0.0	0.0	12.6	3.1	0.8	0.5	5.2	0.0	1.4	2.4
St	0.0	0.0	0.0	0.0	0.4	0.0	0.0	1.3	1.8	5.4	4.7	3.1	0.0	4.4	1.0	0.0	4.1	2.2	6.7	3.0	0.0	7.3	1.8	1.9
Svn	0.0	0.0	0.0	0.0	0.4	0.5	0.0	0.7	0.0	0.0	0.0	0.4	0.0	0.0	0.5	0.0	0.5	0.4	0.8	0.0	0.0	1.3	0.0	0.0
Act	0.0	0.0	0.0	0.0	0.0	0.0	0.0	0.0	0.0	0.0	0.0	0.0	0.0	0.0	0.0	0.0	0.0	0.4	0.0	0.5	0.0	0.0	0.5	0.0
Xtm	0.5	0.0	0.0	0.0	0.0	0.0	0.4	0.0	0.0	0.0	0.0	0.0	0.0	0.5	0.0	0.0	0.5	0.0	0.8	0.0	0.5	0.0	0.0	0.0
Ves	0.0	0.0	0.0	0.0	0.0	0.0	0.0	0.0	0.0	0.0	0.0	0.0	0.0	0.0	0.0	0.0	2.3	0.0	0.0	0.5	0.0	0.0	0.5	0.0
Ky	0.0	0.0	0.0	0.0	0.0	0.0	0.0	0.0	0.0	0.0	0.0	0.0	0.0	0.0	0.0	0.0	0.0	0.0	0.0	0.5	0.0	0.9	0.0	0.0
Sp	0.5	0.0	2.4	0.0	0.0	0.0	0.4	0.0	0.0	0.0	0.0	0.0	0.0	0.0	0.0	0.0	0.0	0.0	0.4	0.0	0.0	0.4	0.0	0.0
Sph	0.5	0.0	0.0	0.0	2.6	0.0	0.0	0.0	0.0	0.0	0.8	0.0	0.0	0.0	0.0	0.0	0.0	0.0	0.0	0.0	0.0	0.0	0.0	0.0

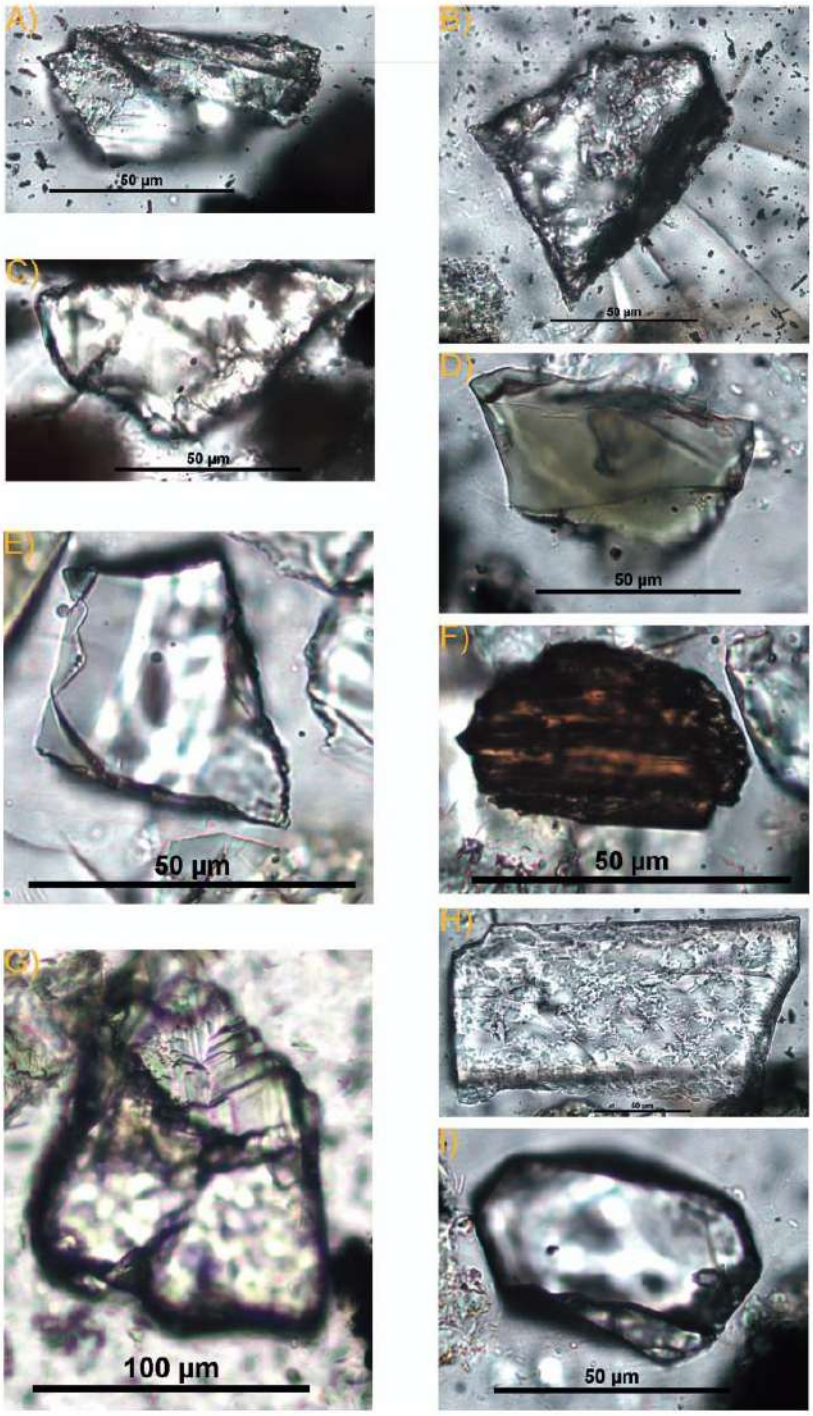

FIG. 8.—**A)** Clinopyroxene from the Rapitán channel displaying no signs of advanced corrosion features. **B)** Almandine from the Rapitán channel displaying no signs of corrosion. **C)** Staurolite from the Rapitán channel displaying no signs of corrosion. **D)** Tourmaline from the Banastón turbidite system displaying no signs of corrosion. **E)** Zircon from the Banastón turbidite system displaying no signs of corrosion. **F)** Rutile from the Banastón turbidite system displaying no signs of corrosion. **G)** Almandine from the lower Jaca turbidite system displaying advanced dissolution features. **H)** Apatite from the Rapitán channel displaying no signs of corrosion. **I)** Zircon from the Banastón turbidite system displaying no signs of corrosion.

5000 m and more than 200°C without dissolution features. Epidote is able to survive burial temperatures up to 95°C, whereas staurolite and garnet can survive up to 110°C and 175°C, respectively (Walderhaug and Porten 2007). Thermal modeling of the Jaca basin (Crognier 2016) and apatite fission-track data (Labaume et al. 2016a) revealed that maximum paleotemperatures for the upper Hecho Group turbidites remained below 90°C in the Jaca section (70°C according to vitrinite reflectance). Therefore, the absence of these minerals or at least the low abundance

of garnet and staurolite is most likely a provenance effect rather than a diagenetic feature, though loss of minerals due to intrastratal dissolution cannot be completely discarded as evidenced by some advanced corrosion features in almandine grains (Fig. 8). Nonetheless, the heavy-mineral assemblages of the Banastón and the Jaca turbidite systems are coherent with the erosion of granitic sources, ancient sandstones, and very low- to low-grade metamorphic terrains.

Santa Orosia Profile.—According to thermal modeling (Crognier 2016), the 90°C paleotemperature isotherm should be at approximately 2500 m below the top of the Santa Orosia fan. Therefore, maximum paleotemperatures for the Sabiñanigo and the Belsué–Atarés formations in the present-day outcrops would be 75°C and 50°C, respectively, according to sediment thickness. In fact, vitrinite-reflectance measurements in the northern flank of the Yebra anticline indicate a maximum paleotemperature of less than 60°C for the Sabiñanigo sandstone (Labaume et al 2016). Therefore, minerals such as epidote, staurolite, or garnet would have survived these temperatures, at least without advanced dissolution features. This is the case for garnet (almandine and grossular) and staurolite, in that the grains present in the Sabiñanigo sandstone show only unweathered or initially corroded surface textures (Fig. 9), thus suggesting that they were not significantly affected by intrastratal dissolution. Moreover, olivine grains (the most unstable mineral under burial diagenesis) in the Belsué–Atarés delta, as well as in the Santa Orosia alluvial fan, also show unweathered or initially corroded surface textures (Fig 9). Therefore, their relative abundance seems to be a provenance signal, as well as the high relative abundance of the ultrastable suite Ap-Zrn-Tur-Rt and the absence of epidote.

Upwards in the section, the lower part of the Belsué–Atarés Formation displays a sudden input of titanite and records the presence of almandine, staurolite, chloritoid, epidote, and forsterite (the latter known as the most unstable heavy mineral; Morton and Hallsworth 1999), whereas the upper part shows a strong decrease in titanite together with the absence of chloritoid, epidote, and forsterite (Table 1, Fig. 6). Here, the low abundance of unstable minerals seems to be a provenance feature of the Belsué–Atarés Formation, since burial temperatures should be lower than in the Sabiñanigo sandstone. These deltaic deposits are characterized by the "carbonate extrabasinal enriched" petrofacies, where detrital carbonates are the most abundant component (Roigé et al. 2017). Nevertheless, the siliciclastic population contains volcanic and metamorphic rock fragments (phyllites, schists, chloritoschists, and quartzites) that are probably linked to the occurrence of almandine, staurolite, chloritoid, titanite, and epidote. Almandine, staurolite, and chloritoid are prone to be sourced from phyllites and schists, whereas forsterite is more likely to be derived from basic igneous rocks, although it could be sourced from dolomitic marbles as well. Titanite and epidote could be linked to both types of rocks.

Anomalous high paleotemperatures were detected in the northern flank of the Canciás syncline, close to the Oturia thrust, related to fluid flow along the fault (Labaume et al. 2016). However, it is probable that maximum paleotemperatures achieved by the Santa Orosia fan were much lower in the southern flank of the Canciás syncline. Occurrence of fresh clinopyroxene in the lower part of the Santa Orosia fan may indicate that loss of unstable minerals in this area is not significant and supports the idea of low paleotemperatures in the southern part of the Santa Orosia fan.

The Santa Orosia alluvial-fan deposits are characterized by the "hybrid-clast-dominated" petrofacies, where recycled turbidite rock fragments are the most abundant component. Therefore, part of the Ap-Zrn-Tur-Rt assemblage is probably a consequence of the recycling of the older turbidite basin, in as much as the characteristic feature of the Hecho Group turbidites is a high content of Ap-Zrn-Tur-Rt. Even other minerals, such as garnet or staurolite, might be able to survive the recycling process and could be linked to the recycling of the former turbidite basin (Mange and Maurer 1992). However, the fact that staurolite has been reported only in the Rapitán channel (1%), and titanite is absent in all the turbidite systems but present in the Santa Orosia fan, suggests that additional metamorphic and/or igneous sources were the main suppliers of these minerals. Authigenic titanites have been described in the literature. However, since they display mainly angular to subrounded textures they have been interpreted as detrital, also excluding the possibility of recycled old authigenic titanite since no rounded to well-rounded titanites have been observed. Moreover, the occurrence of metamorphic and volcanic grains in the sand fraction of the alluvial-fan deposits supports the idea of staurolite and titanite being supplied from a direct source rather than a recycled origin and reinforces the idea that igneous and metamorphic sources also contributed to the Ap-Zrn-Tur-Rt suite.

Canciás Profile.—In the lower part of this profile, the Belsué–Atarés Formation records the presence of epidote and very low proportions of almandine and grossular (Table 1, Fig. 6). Paleotemperatures in the present-day outcrops of this profile remained below 90°C (Crognier 2016). Thus, the low proportion of garnet appears to be a provenance signal rather than a diagenetic overprint. This also seems to be the case for epidote, though it is less stable than garnet and its scarcity could be related to burial diagenesis. Nonetheless, the absence of titanite and staurolite, both more stable than epidote but less than garnet, do seem to mirror its absence in the source area.

In the upper part of the section, titanite, staurolite, almandine, grossular, and epidote are present in the Canciás fan deposits (Table 1, Fig. 6). As in the Santa Orosia fan, the presence of these minerals points to the erosion of new source areas consisting of metamorphic and igneous rocks. Almandine and staurolite are probably related to the erosion of the Paleozoic basement, whereas titanite could also be sourced from Triassic and Cretaceous igneous rocks. However, sandstone petrography does not record the occurrence of volcanic rock fragments in the lower and middle Canciás fan. By contrast, phyllites, schists, and quartzites do occur, and therefore the source of titanite is more likely to be metamorphic than igneous. Grossular could be derived from thermally metamorphosed limestones occurring in the Paleozoic basement, as well as in the North Pyrenean Mesozoic, or even from syenites occurring in the North Pyrenean Zone. Nonetheless, no evidence of these rock types is found in the sand fraction of the alluvial deposits. Epidote is probably linked to the erosion of basic igneous rocks, such as Triassic dolerites, that have undergone spilitization. Occurrence of volcanic clasts in the upper part of the fan clearly supports this origin (Roigé et al. 2017).

The middle Canciás fan records an extreme low relative abundance of apatite, which contrasts with the Santa Orosia alluvial fan and the lower part of the Canciás fan. Both fans record the recycling of the Hecho Group turbidites, where apatite is the most abundant mineral. However, whereas the younger Santa Orosia fan displays high abundances of apatite, this mineral is almost absent in the Canciás fan. Furthermore, apatite it is present in all samples, and its absence is not a characteristic feature of the mixed lithic and carbonate petrofacies, as evidenced by its occurrence in the Peña Oroel and San Juan de la Peña sections. Since some advanced dissolution textures displayed by apatite and tourmaline grains (Fig. 10) suggesting weathering processes, we infer that periods of acidic groundwater percolation (Morton and Hallsworth 1999) in the present-day outcrops, alluvial storage, or most likely weathering at the source area might account for its almost complete absence, since apatite is the most unstable mineral under weathering conditions (Morton and Hallsworth 1999).

According to paleotemperature distribution in the area (Crognier 2016), it is very unlikely that the upper part of the Canciás fan was deeply buried. Therefore, the sudden increase of the epidote relative abundance, just below the compositional change from the "hybrid-clast-dominated" to the "carbonate extrabasinal enriched" petrofacies, is probably related with this compositional change rather than to dissolution processes. Furthermore, it

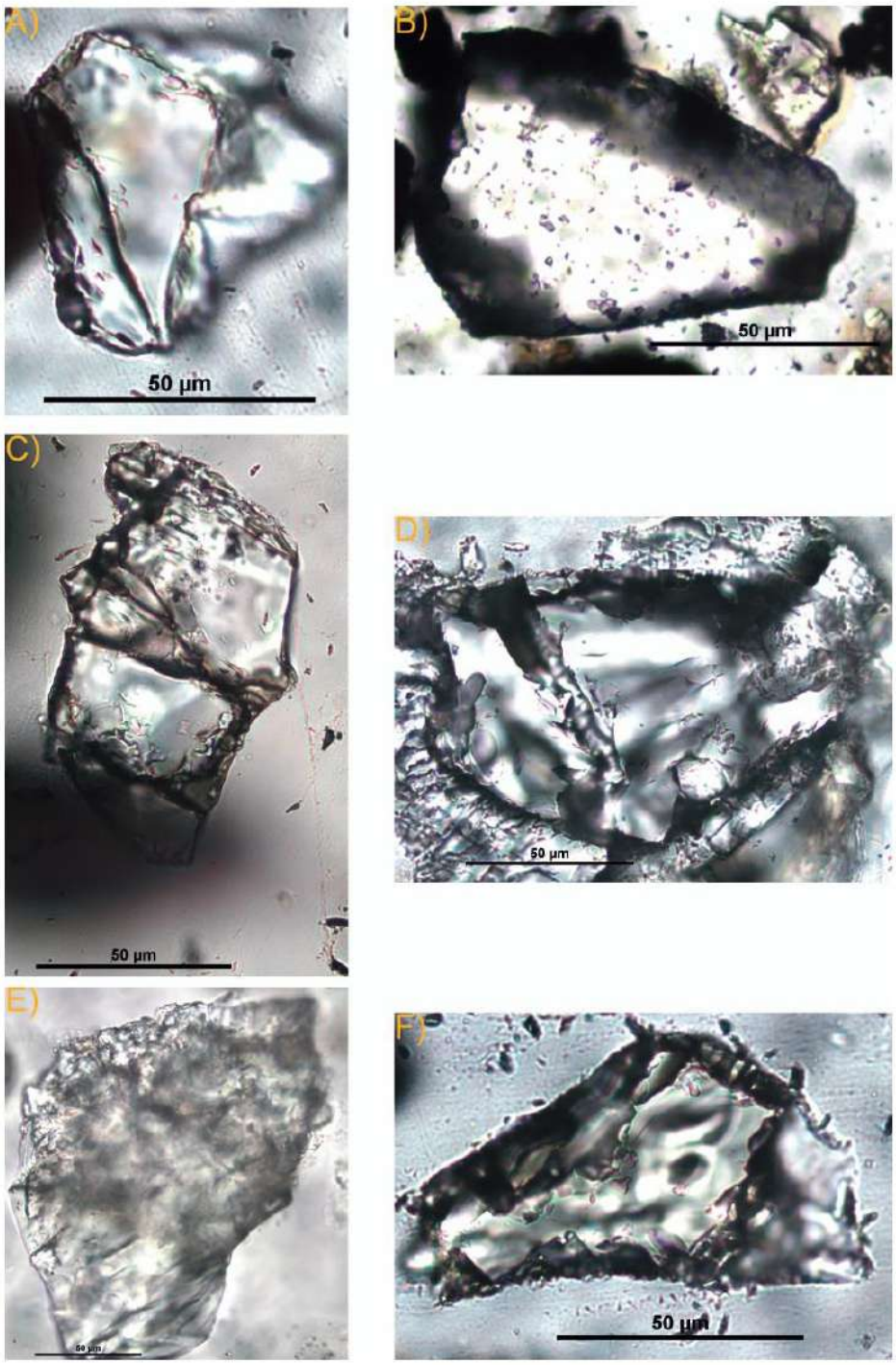

FIG. 9.—**A)** Olivine from the Belsué–Atarés delta displaying no signs of intense corrosion. **B)** Almadine from the Sabiñanigo Sandstone displaying no signs of corrosion. **C)** Olivine from the Santa Orosia alluvial fan displaying no signs of intense corrosion. **D)** Grossular from the Sabiánigo Sandstone displaying no signs of corrosion. **E)** Clinopyroxene from the Santa Orosia alluvial fan displaying slight corrosion. **F)** Staurolite from the Sabiñanigo Sandstone displaying no signs of corrosion.

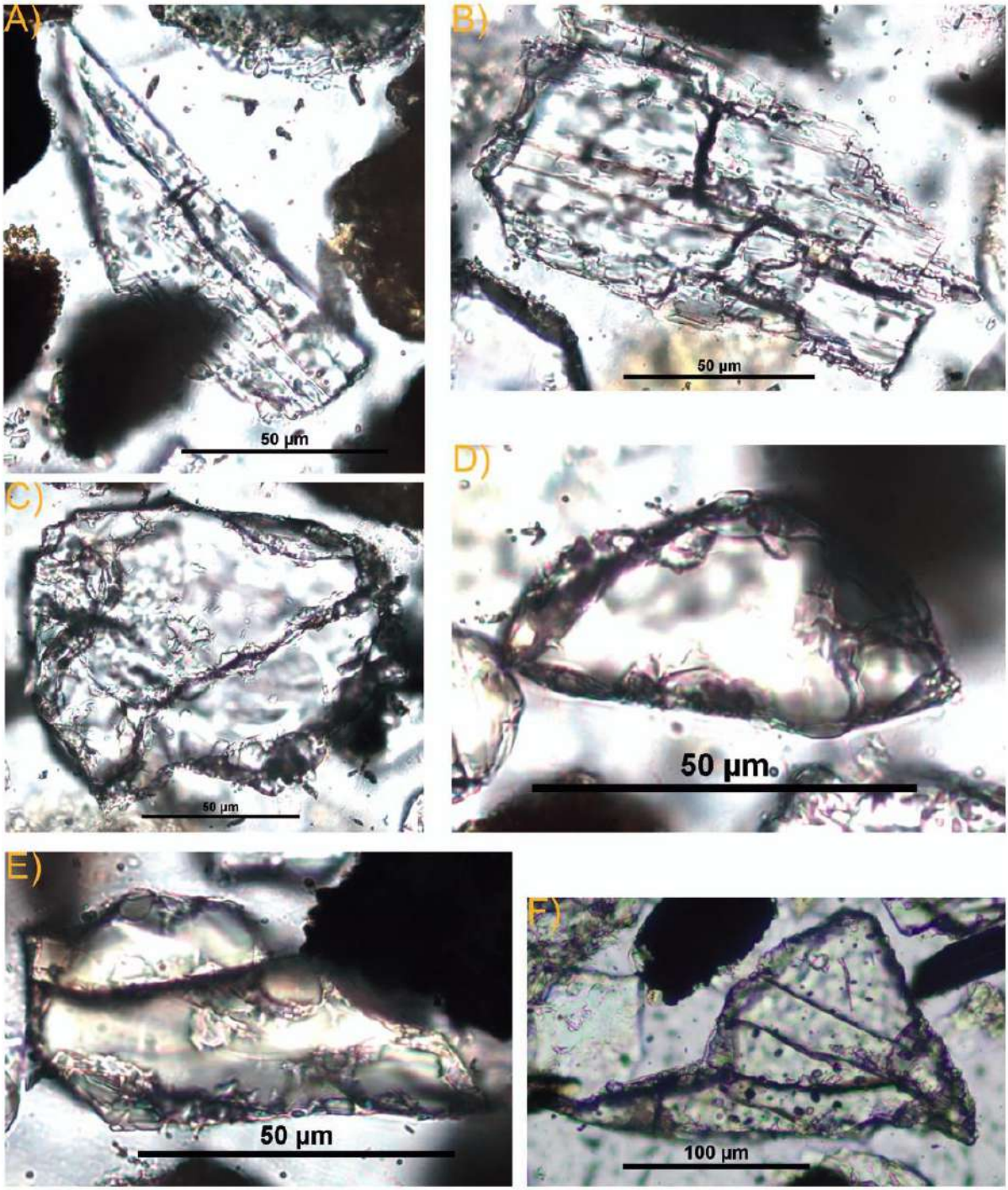

FIG. 10.—**A)** Tourmaline from the Canciás fan displaying slight to advanced degree of corrosion. **B)** Apatite from the Canciás fan displaying slight to advanced degree of corrosion.

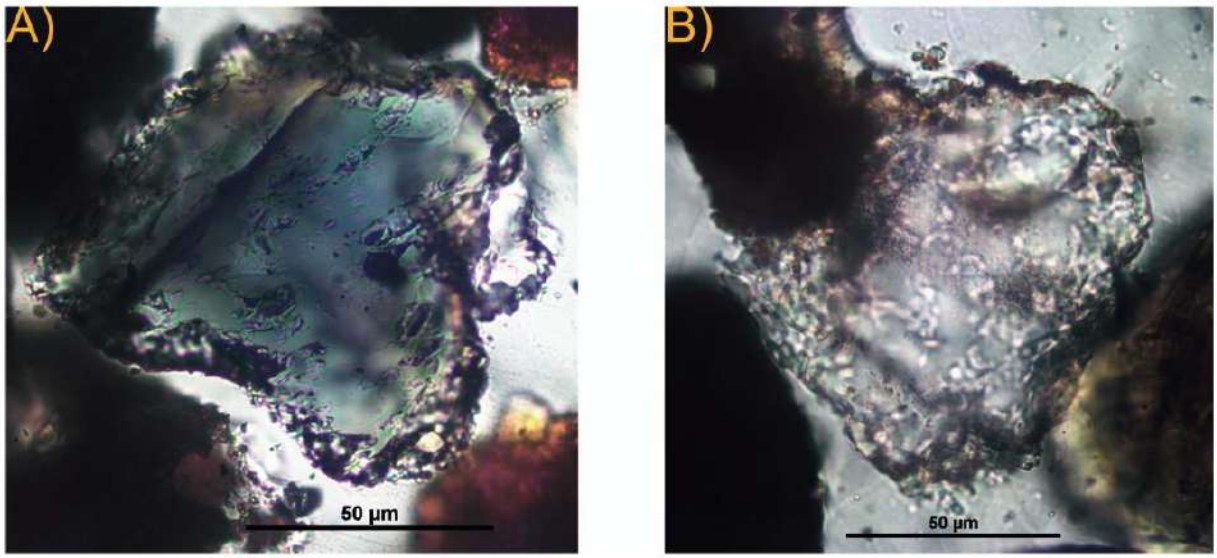

FIG. 11.—**A)** Clinopyroxene from the Belsué–Atarés delta displaying no signs of intense corrosion. **B)** Clinopyroxene from the Belsué–Atarés delta displaying slight degree of corrosion. **C)** Almandine from the Belsué–Atarés delta displaying no signs of intense corrosion. **D)** Grossular from the Belsué–Atarés delta displaying no signs of intense corrosion. **E)** Staurolite from the Belsué–Atarés delta displaying no signs of intense corrosion. **F)** Clinopyroxene from the fluvial Campodarbe Formation displaying no signs of intense corrosion.

implies that the lower part of the fan probably displays its detrital provenance signature.

Peña Oroel Profile.—In this area, the most characteristic feature of the Belsué–Atarés delta formation is the abundance of fresh clinopyroxene (12%, Fig. 6). Hence, we infer that the high abundance of this unstable mineral, the fact that no highly corroded or skeletal grains have been observed (Fig. 11A, B), and that staurolite, grossular, and almandine do not display corrosion features (Fig. 11C, D, E), indicates that burial diagenesis did not have a profound effect in this area. This is in accordance with paleotemperatures deduced from thermal modeling (Crognier 2016), revealing that the maximum temperature remained below 50°C.

Here, the Belsué–Atarés delta exhibits the north-derived "hybrid-clast-dominated" petrofacies, though to the top, a compositional change is observed due to the interaction with the east-derived "siliciclastic dominant" input. Due to this mixing, the upper deltaic deposits display the "mixed lithic and carbonate" petrofacies. However, samples from both petrofacies plot close (Fig. 7D), highlighting their compositional similarity regarding their heavy-mineral signature. The fact that the siliciclastic content of both petrofacies is probably the main source of heavy minerals might be the reason why the heavy-mineral provenance signatures of both petrofacies do not show significant differences. The presence of vesuvianite and grossular as well as clinopyroxene point to a source consisting of impure limestones that have gone through thermal metamorphism, though clinopyroxene could also be sourced from basic igneous rocks. Occurrence of paleovolcanic lithic rock fragments with lathwork texture made of plagioclase and altered augite in the Belsué–Atarés Formation (Roigé et al. 2017) points to an igneous origin for clinopyroxene. Therefore, vesuvianite and grossular most probably derive from the thermally metamorphosed Mesozoic limestone hosts of these volcanic rocks.

In the Peña Oroel alluvial fan, occurrence of almandine, staurolite, and even kyanite points to erosion of the Paleozoic metapelites, although they could have a recycled origin from Cretaceous sandstones as the Marboré Sandstone (Recio et al. 1987). The Ap-ZTR ultrastable suite could also be derived from the recycling of the turbidite basin, erosion of igneous and metamorphic sources, or Mesozoic and Paleocene sandstones.

San Juan de la Peña Profile.—In the San Juan de la Peña profile, the fluvial Campodarbe Formation also displays uncorroded (Fig. 11F) or slightly corroded (5.1%, Table 1, Fig. 6) clinopyroxene. From this data, we infer that although diagenesis could reduce the total original amount of heavy minerals present in the sediments, no extensive dissolution of heavy minerals seems to have occurred. If other unstable minerals such as Epidote (more unstable and common than clinopyroxene in the Pyrenean context) would have occurred in proportions similar to that of clinopyroxene, dissolution in this profile would have not been enough to completely erase Ep from the sedimentary record.

The statistical analysis (Fig. 7D) reflects three different heavy-mineral assemblages that coincide with the three different petrofacies. The "siliciclastic dominant" petrofacies displayed by the fluvial Campodarbe Formation is enriched in apatite. The "hybrid-clast-dominated" petrofacies is characterized by higher relative abundances of other transparent heavy minerals and ZTR. Finally, the characteristic feature of the "mixed lithic and carbonate" petrofacies is its high relative abundance of epidote (18%).

As for the former alluvial fans, the origin of the Ap-ZTR assemblage can be attributed to recycling of the turbidite basin, or from Paleozoic, Mesozoic, and Paleocene sandstone sources, or directly sourced from igneous and metamorphic rocks. The presence of staurolite, almandine, and chloritoid points unequivocally to metamorphic sources of the Paleozoic basement, whereas clinopyroxene, epidote, actinolite, titanite, vesuvianite, and grossular could be also sourced from Mesozoic subvolcanic rocks and their thermally metamorphosed hosts. Occurrence of volcanic rock fragments in the fluvial Campodarbe Formation is probably related to the presence of clinopyroxene, titanite, and epidote. Conversely, its high relative abundance of chloritoid, an abundant mineral in Carboniferous slates (Zwart 1986), must be linked to the high

abundance of metamorphic rock fragments sourced from the Paleozoic basement.

In the San Juan de la Peña fan staurolite, almandine, and even kyanite also point to metamorphic sources of the Paleozoic basement, whereas clinopyroxene, epidote, actinolite, and titanite are most likely to be derived from Triassic or Cretaceous igneous rocks, as evidenced by the presence of volcanic rock fragments in the sandy fraction. Vesuvianite and grossular reinforce this idea, since they would be derived from the thermally metamorphosed limestones that host the igneous rocks.

General Remarks.—According to our results, the Hecho Group turbidites display an ultrastable heavy-mineral suite. By contrast, the alluvial deposits show a more varied assemblage with highly unstable minerals such as clinopyroxene, indicating that intrastratal dissolution did not play a critical role. From the ultrastable suite displayed by the Hecho Group turbidites we cannot exclude a possible diagenetic overprint on their original detrital assemblages. Controversially, our results differ largely from Valloni et al. (1984) who reported a very unstable heavy-mineral suite, characterized by high abundance of augite and garnet but no apatite in the Jaca–Fiscal turbidites. However, our data show that apatite is a characteristic mineral of the upper Hecho Group turbidites, garnet relative abundance is very low, and clinopyroxene is absent in the Banastón and Jaca turbidite systems, being present only in the Rapitán channel (1.3%). Moreover, Valloni et al. (1984) reports the presence of glaucophane and riebeckite in these deep-marine deposits. However, these metamorphic minerals have never been described in the Pyrenees, most likely because they imply a degree of metamorphism (blueschist facies) that was never achieved during the Variscan or Pyrenean orogenic cycles (Zwart and Sitter 1979; Zwart 1986; Guitard et al. 1996; Ribeiro et al. 2019). Since heavy-mineral identification under the microscope in the Hecho Group turbidites could be an arduous task due to the degree of turbid minerals, our use of the more objective Raman spectroscopy technique for mineral identification might account for the differences between our results and those from Valloni et al. (1984).

Therefore, although the Hecho Group turbidites are the formation most affected by burial diagenesis, it seems that the effect of mineral dissolution is not enough to completely erase minerals such as epidote from the detrital record. Moreover, burial diagenesis is slight in the Belsué–Atarés delta (Peña Oroel profile) and the fluvial Campodarbe (San Juan de la Peña profile) formations, and probably plays a minor role in the Sabiñanigo and the Belsué–Atarés deltaic formations in the Santa Orosia profile (Figs. 2, 6), according to paleotemperature distribution and the occurrence of detrital unstable minerals such as olivine.

Although the overlying alluvial fans are also dominated by an ultrastable ZTR heavy-mineral suite, they display a more varied assemblage containing other minerals such as grossular, staurolite, titanite, epidote, and clinopyroxene. These heavy-mineral signatures are similar to the ones recorded by other Pyrenean alluvial fans. For instance, in the Sis fan (Tremp–Graus basin), the Eocene–Oligocene conglomerates (Vincent 2001; Beamud et al. 2003) that record the exhumation of the east-central Pyrenees also display a heavy-mineral suite dominated by ultrastable Ap-Zrn-Tur (Michael 2013). Other transparent heavy minerals are scarce, except for garnet (a common mineral) and epidote. The latter dominates the assemblages in the upper part of the Sis alluvial deposits. Even at the top of the fan, where metasedimentary clasts (phyllites and slates) represent more than the 35% of the clasts, zircon, tourmaline, and apatite are the second most common minerals and there is no trace of other metamorphic minerals such as staurolite, chloritoid, andalusite, sillimanite, or kyanite. This is in accordance with the typical heavy-mineral suites derived from a fold-and-thrust belt, where the sedimentary cover provides few and mainly recycled minerals and only the erosion of the low-medium to high metamorphic and igneous basement would supply minerals such as garnet, staurolite, chloritoid, titanite, clinopyroxene, epidote, or kyanite (Garzanti and Andò 2007b). However, erosion of very low- to low-grade metamorphic rocks and granites can also produce a Tur-Zrn-Rt-Ap dominated heavy-mineral assemblage. Hence, in the Jaca basin, we infer that the detrital heavy-mineral assemblages of all the alluvial fans were not modified in a significant way by intrastratal dissolution, and therefore they display their provenance signature. Moreover, the dominance of the ultrastable suite Ap-Tur-Zrn-Rt in this wedge-top basin seems to reflect the abundance of these minerals in their source rocks rather than a strong diagenetic feature.

The heavy-mineral signatures of the sedimentary infill of the Jaca basin record an increase in the relative abundance of the ultrastable ZTR and other unstable minerals together with a decrease in apatite relative abundance during the alluvial-fan sedimentation stage (Fig. 6; Table 1). This reflects the recycling process of the turbidite basin, since zircon, tourmaline, and rutile are the most resistant minerals to weathering and recycling processes (Mange and Maurer 1992; Garzanti and Andò 2007b; Garzanti et al. 2013a). Moreover, the increase of rounded and well-rounded ZTR grains, when compared to the former turbidite and deltaic deposits, evidences this processes, which is a typical pattern in foreland basins where sediment recycling is the main process controlling the composition of sediments. By contrast, apatite relative abundance is much lower when compared to the Hecho Group turbidites, probably reflecting paleoweathering prior to recycling. Nevertheless, careful investigation of apatite dissolution textures shows no evidence of intense weathering during alluvial-fan sedimentation. Finally, the occurrence of clinopyroxene, epidote, staurolite, grossular, or titanite, and euhedral to angular apatite, zircon, tourmaline, and rutile grains, also points to the contribution of new crystalline sources to the north of the basin. This feature points to the uplift and contribution of new source areas constituted by the Paleozoic basement and the Mesozoic as the source of the more unstable minerals at the same time that the former turbidite basin was being eroded.

Implications for Sediment-Routing Patterns

During the deposition of the Hecho Group turbidites, sediment input was sourced from the east, in the exhumed areas of the central Pyrenees. The increase of apatite through the Banastón and Jaca turbidite systems can be linked to the increase of siliciclastics recorded by sandstone petrography (Roigé et al. 2016), due to the enhanced exhumation in the Axial zone of the central Pyrenees. By contrast, the last turbidite system (Rapitán channel) records the first appearance of minerals such as clinopyroxene, grossular, staurolite, and sphalerite, highlighting a provenance shift related to the erosion of a new source area. This in accordance with a shift in paleocurrent directions, facies, and bulk petrography (Remacha et al. 2005; Roigé et al. 2016). This change has recently been related to the first north-derived sediments entering the basin due to the uplift caused by the Lakora–Eaux–Chaudes thrust system (Roigé et al. 2016; Labaume et al. 2016a). Therefore, we infer that the first occurrence of clinopyroxene, grossular, and staurolite point to new source areas directly to the north of the Jaca basin by this thrust system, which, although active since earlier times (Teixell 1996), did not reach a threshold topography to become a significant source area to the southern foredeep until latest Lutetian times. Clinopyroxene is most likely to be derived from Triassic subvolcanic rocks (ophites), as evidenced by the occurrence of detrital volcanic rock fragments in the Rapitán channel (Roigé et al. 2016), that crop out in the North Pyrenean Zone or close to the limit with the Axial Zone (i.e., the Bedous area). Grossular, instead, points to thermally metamorphosed impure limestones that can be sourced from Paleozoic or Mesozoic carbonate rocks that have been affected by thermal metamorphism. By contrast, staurolite points to medium- and high-grade metapelitic rocks (staurolite-bearing schists) that should be located in the Paleozoic basement of the Axial Zone or in the North Pyrenean Zone (i.e., Lesponne, Chiroulet, or Barousse massifs).

After the turbidite sedimentation stage, the Sabiñanigo and Belsué–Atarés deltaic sandstones show an interplay between east- and north-derived sources (Roigé et al. 2016, 2017). The different heavy-mineral provenance signatures of the Belsué–Atarés Formation in the Peña Oroel and the Yebra de Basa area do highlight this interplay of sources. In the Yebra de Basa area, the Belsué–Atarés Formation was sourced from the east during the first stages of sedimentation (northern limb of the Yebra de Basa anticline), as evidenced by its ZTR+Ap heavy-mineral suite and its high content of carbonate extrabasinal grains (Roigé 2016, 2017). However, when the delta progradation reached the southern limb of the Yebra de Basa anticline, its composition evolved to hybrid-clast dominated (northern sources, Roigé et al. 2017), evidencing a reorganization of the drainage network due to the activity of the Gavarnie thrust and the uplift and erosion of the former turbidite basin. This is further supported by apatite fission-track thermochronology data (Labaume et al. 2016a) that reveals that the onset of the exhumation of the turbidite basin took place during the Priabonian (35 Ma). To the west, in the Peña Oroel area, the Belsué–Atarés delta records a mixing of northern and eastern sources, highlighted by the occurrence of clinopyroxene, staurolite, titanite, grossular, actinolite, and the "hybrid-clast-dominated" and "mixed lithic and carbonate" petrofacies. The late Lutetian–Priabonian Escanilla Formation has been proposed as the proximal time equivalent of the Bartonian–Priabonian east-derived Belsué–Atarés delta. However, the heavy-mineral signatures of the Escanilla and the Belsué–Atarés delta formations do not match. The characteristic feature of the Escanilla Formation is its high content of epidote (> 50%, Michael 2013), which is almost non-existent in the east-derived Belsué–Atarés Formation (< 0.5%). Thus, according to heavy-mineral provenance signatures, the Escanilla Formation could not have fed the Belsué–Atarés delta in the northern area of the Jaca basin. During the deposition of the Belsué–Atarés Formation, the Oturia thrust and the Yebra de Basa anticline where active (Priabonian–Rupelian, Labaume et al. 2016a). This geotectonic setting would have produced local relief, depocenters, and a reorganization in the drainage network of the basin that would have yielded to the compartmentalization of the basin during the sedimentation of the Belsué–Atarés delta. Thus, the sediments fed from the fluvial Escanilla Formation (Ainsa basin) could not reach the northern part of the basin.

After the deposition of the Belsué–Atarés deltaic sediments, the Priabonian Santa Orosia fan marks the onset of the alluvial sedimentation stage in the basin. The ultrastable association displayed by these alluvial deposits can be linked to the recycling of the proximal, turbidite foreland basin, which was progressively incorporated in the southward-propagating thrust belt. Apatite fission-track thermochronology data and the inferred thermal modeling of the Hecho Group turbidites reveal that their exhumation took place during the Priabonian, related to the Gavarnie thrusting, and continued until the Miocene with the Guarga thrusting (Labaume et al. 2016a). This is further supported by the dominance of hybrid-sandstone rock fragments recorded by sandstone petrography that were interpreted as the result of the uplift of the former turbidite foredeep due to the activity of the Gavarnie thrust (Roigé et al. 2016, 2017; Labaume et al. 2016a). However, the presence of ultrastable idiomorphic grains (Ap, Zrn, Tur, Rt) together with more unstable minerals (St, Alm, Ttn, Cpx, Ep) points to additional metamorphic and/or igneous sources that can be linked to the occurrence of metamorphic rock fragments in the sand fraction.

Another important feature revealed by the heavy-mineral assemblages of the Santa Orosia alluvial fan, is its similarity with the Belsué–Atarés delta suites in the Peña Oroel area. This feature highlights that the Santa Orosia fan sourced the Belsué–Atarés delta in the latter area. Sedimentological data from Boya (2018) indicates that the Belsué–Atarés delta constitutes the distal equivalent deposits of the Santa Orosia fan in the northern flank of the Oroel syncline. Furthermore, sandstone petrography data from Roigé et al. (2017) reveals that these deposits share the same sediment composition, as both formations display the "hybrid-clast-dominated" petrofacies.

To the east of the basin, the younger Canciás alluvial fan shows heavy-mineral suites similar to those of the Santa Orosia fan. However, the upper part of the fan displays a sudden increase of epidote, probably linked a major erosion of Triassic dolerites (ophites) as evidenced by the occurrence of volcanic rock clasts (Roigé et al. 2017). Therefore, the new source area should be located somewhere where Triassic dolerites were cropping out, such as nearby the Coticlla thrust (north of Ainsa; Ríos et al. 1982). This is supported by sandstone petrography, since the increase of Paleogene and Mesozoic limestone grains recorded in the upper part of the fan point to the erosion of new source areas located in the Peña Montañesa or Coticlla thrusts (Roigé et al. 2017).

The interpretation of the heavy-mineral suite of the fluvial Campodarbe Formation in the San Juan de la Peña (western part of the study area) is challenging. The "siliciclastic dominant" petrofacies and main paleocurrent directions towards the west and northwest imply that these deposits were sourced from the east, somewhere in the south-central Pyrenees, and were transported through the alluvial and fluvial systems of the Ainsa basin (Puigdefàbregas 1975; Roigé et al. 2017; Boya 2018). According to similarities in sediment composition, the upper fluvial Escanilla Formation (Bentham et al. 1992) has been proposed as the proximal equivalent of the fluvial Campodarbe Formation at San Juan de la Peña (Roigé et al. 2017). However, the heavy-mineral signatures of the Escanilla and the Campodarbe formations in the San Juan de la Peña section do not match. The characteristic feature of the Escanilla Formation is its high relative abundance of epidote (> 50%; Michael 2013), which is almost non-existent in the east-derived fluvial Campodarbe Formation (0.5%). Even the Chattian–Aquitanian Graus Formation (overlying the Escanilla Formation in the Tremp–Graus basin; Reynolds 1987) displays a heavy-mineral suite dominated by epidote (> 50%; Coll et al. 2019); therefore neither of these formations could be a feeder of the Campodarbe fluvial system in this sector of the basin based on their heavy-mineral provenance signature. However, an important feature of the Campodarbe Formation is that it has different assemblages in the southern margin of the Jaca basin (Coll et al. 2019). For instance, in the southeastern part of the basin the Campodarbe Formation contains a high abundance of epidote, thus enabling the Escanilla Formation as a feeder. Conversely, to the west, epidote is absent, requiring a different source. Therefore, we propose that the similarity between the fluvial Campodarbe in the northern (San Juan de la Peña area) and the one recorded in southern part of the basin indicates that an additional routing system entered the basin from the southern margin (i.e., the Arguís area), giving evidence for the interplay between different routing systems during the sedimentation of the Campodarbe Formation. Further research is needed to fully understand the interplay of provenance signals recorded by this formation in the Jaca basin.

Finally, the youngest alluvial deposits in the basin are the Peña Oroel and San Juan de la Peña alluvial fans. Both have similar heavy-mineral suites, indicating very similar source areas. This fact is also revealed by sandstone petrography, since the "hybrid-clast-dominated" petrofacies is the characteristic feature of these deposits. However, the upper part of the San Juan de la Peña fan records an increase of the relative abundance of epidote, coinciding with a petrofacies change in its upper part, as in the Canciás fan. The presence of epidote at San Juan de la Peña, 50 km to the west of Canciás, is interpreted as derived from the erosion of Triassic dolerites that occur to the north of the basin, in the North Pyrenean Zone (Azambre et al. 1987), showing that the source area was large, extending to this area.

Another important fact can be inferred from the appearance of epidote in the Canciás and the San Juan de la Peña fans. In the older late Lutetian–Oligocene Sis alluvial fan of the northern part of the Tremp–Graus basin (Vincent 2001; Beamud et al. 2003), the first appreciable relative abundance of epidote (20%) appears in the Bartonian conglomerates

(Michael 2013). However, in the Jaca basin, epidote does not appear in the sedimentary record (15%) until the upper part of the younger Canciás fan (Priabonian) and more to the west it appears in the Miocene upper part of the San Juan de la Peña fan. Hence, the epidote occurrence in the South Pyrenean Basin is diachronous from east to west, and therefore we infer that it is related to the east–west propagation of the Pyrenean thrust deformation and main uplift.

The dominance of the "hybrid-clast-dominated" petrofacies in all the alluvial systems evidences the recycling process of the former turbidite basin. Since the ultrastable Zrn-Tur-Rt-Ap suite dominates both the Hecho Group turbidites and the alluvial systems, we infer that the main source of this assemblage is the recycling of the Hecho Group turbidites. This is supported by thermocronological data from Labaume et al. (2016a) that reveals that exhumation of the Hecho Group turbidites took place in the Jaca basin from the Priabonian due to the activity of the Gavarnie thrust. However, the presence of other minerals such as epidote, clinopyroxene, olivine, titanite, vesuvianite, amphibole, spinel, or sphalerite and idiomorphic zircon, tourmaline, rutile, and apatite in all the alluvial deposits lends support to continued emerging sources to the north of the basin consisting of Mesozoic and Paleozoic igneous and metamorphic terrains of the Axial or North Pyrenean zones. The occurrence of green subvolcanic ophite clasts and volcanic clasts with amygdaloid texture derived from the North Pyrenean Zone in all the alluvial fans (Roigé et al. 2017) most likely links these heavy-mineral suites to the erosion of the North Pyrenean Mesozoic thermally metamorphosed carbonate hosts and associated basic volcanic rocks and their related. Therefore, the source of these heavy minerals implies that the drainage divide of the paleodrainage system was farther to the north in the middle to late Eocene and migrated to the south since then (Roigé et al. 2017). This is further supported by geomorphological data from Babault et al. (2011) and Ortuño and Vilaplanas (2018). The latter authors deduced that the main drainage divide was located in the North Pyrenean Zone (35 km farther to the north than at the present day in the west-central Pyrenees) according to the distribution of remnants of low-relief topography.

Thermochronological data (Jolivet et al. 2007; Meresse 2010; Labaume et al. 2016b; Bosch et al. 2016) show that most of the western Axial Zone could not have acted as a source until at least the middle to late Eocene to Oligocene (AFT cooling ages of 20 to 35 My). Conversely, the North Pyrenean Zone experienced cooling since the early Paleogene (Vacherat et al. 2014; Bosch et al. 2016), thus supporting the North Pyrenean Zone as the main source of Mesozoic and Paleozoic grains. However, areas of the Axial Zone of the west-central Pyrenees such as the Lesponne massif, close to the limit with the North Pyrenean Zone, where staurolite- and almandine-bearing schists occur (Pouget 1989), could be exposed and thus act as a source area already during the late Eocene. Metamorphic rock fragments (schists, phyllites, chloritoschists lithic, and quartzites) reported by sandstone petrography in all fans point to a direct Variscan metapelite source for staurolite and almandine that could not be sourced from Mesozoic metacarbonates or igneous rocks. Thermochronological data from apatite fission-track dating (Morris et al. 1998; Jolivet et al. 2007), suggest that areas in the northeastern part of the western Axial Zone were undergoing exhumation at that time. Hence, the heavy-mineral provenance signature of the alluvial fans of the Jaca basin reinforce the idea that during the late Eocene the drainage divide of the transverse drainage system extended to the North Pyrenean Zone, and some local areas of the Axial Zone basement could have been providing sediment as well.

CONCLUSIONS

The heavy-mineral suites of the clastic systems of the northern Jaca basin are dominated by the ultrastable association apatite, zircon, tourmaline, and rutile. The relative abundance of these minerals is higher in the early foredeep turbidite deposits, whereas the characteristic feature of the subsequent alluvial-sedimentation stage is the higher relative abundance of other more unstable heavy minerals such as staurolite, almandine, clinopyroxene, grossular, vesuvianite, titanite, and epidote and an increase of the ultrastable zircon, tourmaline, and rutile assemblage. The heavy-mineral suites of the bulk of the Eocene Hecho Group turbidites can be related to eastern source areas located in the east-central Pyrenees (Axial Zone), shifting to north-derived in the uppermost (late Lutetian) part of the group (North Pyrenean sources). On the other hand, the subsequent alluvial assemblages of the Jaca basin are sourced mainly from the recycling of the earlier turbidite basin, although with contributions from the North Pyrenean deformed belt.

The diagenetic overprint experienced by the Hecho Group turbidites does not seem enough to completely erase minerals such as epidote, titanite, staurolite, or grossular from the sedimentary record or to account for the low abundance of almandine. Furthermore, it seems to be negligible or slight in the overlying deltaic, fluvial, and alluvial environments, at least in the Peña Oroel and San Juan de la Peña areas, where fresh clinopyroxene occurs at the base of both sections. Therefore, we conclude that the dominance of the ultrastable suite Ap-Tur-Zrn-Rt in the Jaca wedge-top basin reflects the abundance of these minerals in their source rocks rather than a strong diagenetic feature experienced by the sedimentary infill of the Jaca basin. Furthermore, the Jaca foreland basin is an example that sediment recycling increases the ZTR relative abundance in the sedimentary record, although additional crystalline sources were being eroded at the same time.

The occurrence of unstable minerals in all of the upper Eocene to Miocene alluvial fans implies the uplift and contribution of source areas consisting of the Paleozoic and Mesozoic metamorphic and igneous terrains as the source of the more unstable minerals, at the same time that the former turbidite basin was being eroded. The integration of heavy-mineral analysis with sandstone petrography allowed a better characterization of the source rocks and helped to point to probable specific source areas located in the North Pyrenean Zone or the northern Axial Zone of the Pyrenees as the Lesponne or Barousse crystalline massifs.

Our findings reinforce the idea that during the late Eocene the drainage divide of the transverse drainage system north of the Jaca basin extended to the North Pyrenean Zone, and to some local areas of the Axial Zone basement exposed in the west-central Pyrenees.

Our results also show that the heavy-mineral suites of the Belsué–Atarés and the fluvial Campodarbe formations, giving evidence for that stratigraphic correlations with the fluvial and alluvial systems of the Aínsa basin should be revisited, new sediment pathways should be considered, or further research is needed regarding the heavy-mineral provenance signature of both basins.

From our data, we infer that epidote is sourced mainly from Triassic dolerites (ophites) that have gone through spilitization. The epidote occurrence in the Jaca basin takes place first in the eastern segment, in the older alluvial deposits (Canciás fan, Oligocene), and later in the youngest San Juan de la Peña fan (Oligocene–Miocene) located in the westernmost part of the basin. Since this trend is also observed in the nearby Tremp–Graus basin, the epidote occurrence in the South Pyrenean basin is diachronic from east to west and therefore highlights the east–west propagation of Pyrenean deformation.

ACKNOWLEGMENTS

This paper is a contribution to the projects CGL2014-54180-P and PGC2018-093903-B-C21, financed by the Ministerio de Economía y Competitividad (MINECO) and Ministerio de Ciencia, Inovación y Universidades (MCIU) of Spain. X. Coll acknowledges support from the Ministerio de Cultura, Deporte y Educacción (MCDE) of Spain (FPU grant). We are very grateful to the reviewers Eric Lasseur and Sergio Andò, and to editor John

Southard, for providing constructive reviews that helped to improve the original paper.

REFERENCES

Andò, S., 2020, Gravimetric separation of heavy minerals in sediments and rocks: Minerals, v. 10, p. 273.

Andò, S., and Garzanti, E., 2014, Raman spectroscopy in heavy-mineral studies, *in* Scott, R., Smyth, H., Morton, A., and Richardson, N., eds., Sediment Provenance Studies, in Hydrocarbon Exploration and Production: Geological Society of London, Special Publication 386, p. 395–412.

Andò, S., Garzanti, E., Padoan, M., and Limonta, M., 2012, Corrosion of heavy minerals during weathering and diagenesis: a catalog for optical analysis: Sedimentary Geology, v. 280, p. 165–178.

Andò, S., Morton, A., and Garzanti, E., 2014, Metamorphic grade of source rocks revealed by chemical fingerprints of detrital amphibole and garnet, *in* Scott, R., Smyth, H., Morton, A., and Richardson, N., eds., Sediment Provenance Studies in Hydrocarbon Exploration and Production: Geological Society of London, Special Publication 386, p. 351–371.

Andò, S., Aharonovich, S., Hahn, A., George, S.C., Clift, P.D., and Garzanti, E., 2019, Integrating heavy-mineral, geochemical and biomarker analyses of Plio-Pleistocene sandy and silty turbidites: a novel approach for provenance studies (Indus Fan, IODP Expedition 355): Geological Magazine, v. 157, p. 1–10.

Azambre, B., 1967, Sur les roches intrusives sous-saturées du Crétacé des Pyrénées: Séances de l'Académie des Sciences, Comptes Rendus Hebdomadaires, v. 271, p. 641–643.

Azambre, B., Rossy, M., and Lago, M., 1987, Caracteristiques petrologiques des dolerites tholeiitiques d'age triasique (ophites) du domaine pyreneen: Bulletin de Minéralogie, v. 110, p. 379–396.

Azambre, B., Crouzel, F., Debroas, E.J., Soulé, J.C., and Ternet, Y., 1989, Notice Explicative de la Carte Géologique de la France, feuille Bagnères-de-Bigorre (1053): Bureau des Recherches Géologiques et Minières, Orléans, 1:50000.

Babault, J., van den Driessche, J., and Teixell, A., 2011, Retro- to pro-side migration of the main drainage divide in the Pyrenees: geologic and geomorphological evidence: European Geosciences Union, General Assembly, v. 13, p. 2011–12567.

Barnolas, A., and Gil-Peña, I., 2001, Ejemplos de relleno sedimentario multiepisódico en una cuenca de antepaís fragmentada: La Cuenca Surpirenaica: Boletín Geológico y Minero, v. 112, p. 17–38.

Barsó, D., 2007, Análisis de la procedencia de los conglomerados sinorogénicos de La Pobla de Segur (Lérida) y su relación con la evolución tectónica de los Pirineos centro meridionales durante el Eoceno medio-Oligoceno [Ph.D. Thesis]: Universitat de Barcelona, 209 p.

Beamud, E., Garcés, M., Cabrera, L., Muñoz, J.A., and Almar, Y., 2003, A new middle to late Eocene continental chronostratigraphy from NE Spain: Earth and Planetary Science Letters, v. 216, p. 501–514.

Bentham, P.A., Burbank, D.W., and Puigdefábregas, C., 1992, Temporal and spatial controls on the alluvial architecture of an axial drainage system: late Eocene Escanilla Formation, southern Pyrenean foreland basin, Spain: Basin Research, v. 4, p. 335–352.

Bixel, F., 1987, Le volcanisme stéphano-permien des Pyrénées. Pétrographie, minéralogie, géochimie: Cuadernos de Geología Ibérica, v. 11, p. 41–55.

Bosch, G.V., Teixell, A., Jolivet, M., Labaume, P., Stockli, D., Domènech, M., and Monié, P., 2016, Timing of Eocene–Miocene thrust activity in the Western Axial Zone and Chaînons Béarnais (west-central Pyrenees) revealed by multi-method thermochronology: Comptes Rendus Geoscience, v. 348, p. 246–256.

Bova, S., 2018, El sistema deltaico de la Arenisca de Sabiñánigo y la continentalización de la cuenca de Jaca [Ph.D. Thesis]: Universitat Autònoma de Barcelona, 231 p.

Caja, M.A., Marfil, R., Garcia, D., Remacha, E., Morad, S., Mansurbeg, H., Amorosi, A., Martínez-Calvo, C., and Lahoz-Beltrá, R., 2010, Provenance of siliciclastic and hybrid turbiditic arenites of the Eocene Hecho Group, Spanish Pyrenees: implications for the tectonic evolution of a foreland basin: Basin Research, v. 22, p. 157–180.

Caracciolo, L., Garzanti, E., von Eynatten, H., and Weltje, G.J., 2016, Sediment generation and provenance: processes and pathways: Sedimentary Geology, v. 336, p. 1–2.

Caracciolo, L., Andò, S., Vermeesch, P., Garzanti, E., McCabe, R., Barbarano, M., Paleari, C., Rittner, M., and Pearce, T., 2019, A multidisciplinary approach for the quantitative provenance analysis of siltstone: Mesozoic Mandawa Basin, southeastern Tanzania, *in* Bond, C.E., and Lebit, H.D., eds., Folding and Fracturing of Rocks: 50 Years of Research since the Seminal Text Book of J.G. Ramsay: Geological Society of London, Special Publication 484, p. 275–293.

Cerveny, P.F., Johnson, N.M., Tahirkheli, R.A.K., and Bonis, N.R., 1989, Tectonic and geomorphic implications of Siwalik Group heavy minerals, Potwar Plateau, Pakistan, *in* Malinconico, L.L., and Lillie, R.J., eds., Tectonics of the Western Himalayas: Geological Society of America, Special Papers 232, p. 129–136.

Clerc, C., Lahfid, A., Monié, P., Lagabrielle, Y., Chopin, C., Poujol, M., Boulvais, P., Ringenbach, J.C., Masini, E., and de St Blanquat, M., 2015, High-temperature metamorphism during extreme thinning of the continental crust: a reappraisal of the North Pyrenean passive paleomargin: Solid Earth, v. 6, p. 643–668.

Coll, X., Gómez-Gras, D., Roigé, M., and Mestres, N., 2017, Heavy-mineral assemblages as a provenance indicator in the Jaca basin (Middle–Late Eocene, southern Pyrenees): Geogaceta, v. 61 p. 159–162.

Coll, X., Gómez-Gras, D., Roigé, M., Bova, S., Teixell, A., and Poyatos-Moré, M., 2019, Interplay of multiple sediment sources in an overfilled foreland basin (Southern Pyrenees) [Abstract]: International Association of Sedimentologists, 34th International Meeting of Sedimentology, Abstracts, p. 872.

Costa, E., Garces, M., Lopez-Blanco, M., Beamud, E., Gomez-Paccard, M., and Larrasoaña, J.C., 2010, Closing and continentalization of the South Pyrenean foreland basin (NE Spain): magnetochronological constraints: Basin Research, v. 22, p. 904–917.

Crognier, N., 2016, Évolution thermique, circulation de fluides et fracturation associées à la structuration du bassin d'avant-pays sud-pyrénéen [Ph.D. Thesis]: l'Université de Pau et des Pays de l'Adour, Pau, France, 344 p.

Debon, F., Enrique, P., and Autran, A., 1996, Le plutonisme hercynien des Pyrénées, *in* Barnolas, A., and Chiron, J., eds., Synthèse géologique et géophysique des Pyrénées: Bureau de Recherches Géologiques et Minières-Instituto Tecnologico Geominero de España, p. 361–499.

Dickinson, W.R., 1988, Provenance and sediment dispersal in relation to paleotectonics and paleogeography of sedimentary basins, *in* Kleinspehn, K.L., and Paola, C., eds., New Perspectives in Basin Analysis: Berlin, Springer, p. 3–25.

Dickinson, W.R., and Suczek, C.A., 1979, Plate tectonics and sandstone compositions: American Association of Petroleum Geologists, Bulletin, v. 63, p. 2164–2182.

Dreyer, T., Corregidor, J., Arbues, P., and Puigdefabregas, C., 1999, Architecture of the tectonically influenced Sobrarbe deltaic complex in the Ainsa Basin, northern Spain: Sedimentary Geology, v. 127, p. 127–169.

Fontana, D., Zuffa, G.G., and Garzanti, E., 1989, The interaction of eustacy and tectonism from provenance studies of the Eocene Hecho Group Turbidite Complex (South-Central Pyrenees, Spain): Basin Research, v. 2, p. 223–237.

Fossum, K., Morton, A.C., Dypvik, H., and Hudson, W.E., 2019, Integrated heavy mineral study of Jurassic to Paleogene sandstones in the Mandawa Basin, Tanzania: sediment provenance and source-to-sink relations: Journal of African Earth Sciences, v. 150, p. 546–565.

Galehouse, J., 1971, Point counting, *in* Carver, R., ed., Procedures in Sedimentary Petrology: New York, Wiley, p. 385–407.

Garcés, M., López-Blanco, M., Valero, L., Beamud, E., Muñoz, J.A., Oliva-Urcia, B., Vinyoles, A., Arbués, P., Cabello, P., and Cabrera, L., 2020, Paleogeographic and sedimentary evolution of the south-Pyrenean foreland basin: Marine and Petroleum Geology, v. 113, no. 104105.

Garzanti, E., 2016, From static to dynamic provenance analysis: sedimentary petrology upgraded: Sedimentary Geology, v. 336, p. 3–13.

Garzanti, E., and Andò, S., 2007a, Heavy mineral concentration in modern sands: implications for provenance interpretation, *in* Mange, M.A., and Wright, D.T., eds., Heavy Minerals in Use: Amsterdam, Elsevier, Developments in Sedimentology 58, p. 517–545.

Garzanti, E., and Andò, S., 2007b, Plate tectonics and heavy mineral suites of modern sands, *in* Mange, M.A., and Wright, D.T., eds., Heavy Minerals in Use: Amsterdam, Elsevier, Developments in Sedimentology 58, p. 741–763.

Garzanti, E., and Andò, S., 2019, Heavy Minerals for Junior Woodchucks: Minerals, v. 8, p. 148–172.

Garzanti, E., Ando, S., Vezzoli, G., and Dell'era, D., 2003, From rifted margins to foreland basins: investigating provenance and sediment dispersal across desert Arabia (Oman, U.A.E.): Journal of Sedimentary Research, v. 73, p. 572–588.

Garzanti, E., Vezzoli, G., Lombardo, B., Andò, S., Mauri, E., Monguzzi, S., and Russo, M., 2004, Collision-Orogen provenance (western alps): detrital signatures and unroofing trends: The Journal of Geology, v. 112, p. 145–164.

Garzanti, E., Andò, S., and Vezzoli, G., 2006, The continental crust as a source of sand (Southern Alps cross section, Northern Italy): The Journal of Geology, v. 114, p. 533–554.

Garzanti, E., Doglioni, C., Vezzoli, G., and Andò, S., 2007, Orogenic belts and orogenic sediment provenance: The Journal of Geology, v. 115, p. 315–334.

Garzanti, E., Ando, S., and Vezzoli, G., 2008, Settling equivalence of detrital minerals and grain-size dependence of sediment composition: Earth and Planetary Science Letters, v. 273, p. 138–151.

Garzanti, E., Andò, S., and Vezzoli, G., 2009, Grain-size dependence of sediment composition and environmental bias in provenance studies: Earth and Planetary Science Letters, v. 277, p. 422–432.

Garzanti, E., Resentini, A., Vezzoli, G., Andò, S., Malusà, M., and Padoan, M., 2012, Forward compositional modelling of Alpine orogenic sediments: Sedimentary Geology, v. 280, p. 149–164.

Garzanti, E., Limonta, M., Resentini, A., Bandopadhyay, P.C., Najman, Y., Andò, S., and Vezzoli, G., 2013a, Sediment recycling at convergent plate margins (Indo-Burman Ranges and Andaman–Nicobar Ridge): Earth-Science Reviews, v. 123, p. 113–132.

Garzanti, E., Padoan, M., Andò, S., Resentini, A., Vezzoli, G., and Lustrino, M., 2013b, Weathering and relative durability of detrital minerals in equatorial climate: sand petrology and geochemistry in the East African Rift: The Journal of Geology, v. 121, p. 547–580.

Garzanti, E., Vermeesch, P., Padoan, M., Resentini, A., Vezzoli, G., and Andò, S., 2014, Provenance of passive-margin sand (Southern Africa): The Journal of Geology, v. 122, p. 17–42.

Garzanti, E., Andò, S., Limonta, M., Fielding, L., and Najman, Y., 2018, Diagenetic control on mineralogical suites in sand, silt, and mud (Cenozoic Nile Delta): implications for provenance reconstructions: Earth-Science Reviews, v. 185, p. 122–139.

Gilbert, J.S., and Rogers, N.W., 1989, The significance of garnet in the Permo-Carboniferous volcanic rocks of the Pyrenees: Geological Society of London, Journal, v. 146, p. 477–490.

Golberg, J.M., and Leyreloup, A.F., 1990, High temperature-low pressure Cretaceous metamorphism related to crustal thinning (Eastern North Pyrenean Zone, France): Contributions to Mineralogy and Petrology, v. 104, p. 19–207.

Gómez-Gras, D., Roigé, M., Fondevilla, V., Oms, O., Boya, S., and Remacha, E., 2016, Provenance constraints on the Tremp Formation paleogeography (southern Pyrenees): Ebro Massif vs Pyrenees sources: Cretaceous Research, v. 57, p. 414–427.

Gómez-Gras, D., Collado, R., Coll, X., and Roigé, M., 2017, Compositional characterization of the Upper Cretaceous sandstones in the Sierras Marginales y Exteriores (South-Pyrenean basin): heavy-mineral and sandstone petrography analysis: Geogaceta, v. 61, p. 163–166.

Götze, J., 1998, Geochemistry and provenance of the Altendorf feldspathic sandstone in the Middle Bunter of the Thuringian basin (Germany): Chemical Geology, v. 150, p. 43–61.

Graham, S.A., Tolson, R.B., DeCelles, P.G., Ingersoll, R.V., Bargar, E., Caldwell, M., Cavazza, W., Edwards, D.P., Follo, M.F., Handschy, J.F., Lemke, L., Moxon, I., Rice, R., Smith, G. A., and White, J., 1986, Provenance modelling as a technique for analysing source terrane evolution and controls on foreland sedimentation, *in* Allen, P.A., and Homewood, P.N., eds., Foreland Basins: International Association of Sedimentologists, Special Publication 8, p. 425–436.

Greenacre, M., 1984, Theory and applications of correspondence analysis: London, Academic Press, 364 p.

Guitard, G., Vielzeuf, D., and Martinez, F., 1996, Métamorphisme hercynien, *in* Barnolas, A., and Chiron, J., eds., synthèse géologique et géophysique des Pyrénées: Bureau de Recherches Géologiques et Minières-Instituto Tecnologico Geominero de España, p. 501–584.

Gupta, K.D., and Pickering, K.T., 2008, Petrography and temporal changes in petrofacies of deep-marine Ainsa–Jaca basin sandstone systems, Early and Middle Eocene, Spanish Pyrenees: Sedimentology, v. 55, p. 1083–1114.

Harris, N.B.W., 1974, The petrology and petrogenesis of some muscovite granite sills from the Barousse Massif, Central Pyrenees: Contributions to Mineralogy and Petrology, v. 45, p. 215–230.

Haughton, P.D.W., Todd, S.P., and Morton, A.C., 1991, Sedimentary provenance studies, *in* Haughton, P.D.W., Todd, S.P., and Morton, A.C., eds., Developments in Sedimentary Provenance Studies: Geological Society of London, Special Publication 57, p. 1–11.

Hirst, J.P.P., and Nichols, G.J., 1986, Thrust tectonic controls on Miocene alluvial distribution patterns, southern Pyrenees, *in* Allen, P.A., and Homewood, P., eds., Foreland Basins: International Association of Sedimentologists, Special Publication 8, p. 247–258.

Hogan, P., 1993, Geochronologic, Tectonic and Stratigraphic Evolution of the Southwest Pyrenean Foreland Basin, Northern Spain [Ph.D. Thesis]: University of Southern California, Los Angeles, 208 p.

Hogan, P.J., and Burbank, D.W., 1996, Evolution of the Jaca piggyback basin and emergence of the external sierra, Southern Pyrenees, *in* Friend, P., and Dabrio, C., eds., Tertiary Basins of Spain: Cambridge, Cambridge University Press, p. 153–160.

Jolivet, M., Labaume, P., Monié, P., Brunel, M., Arnaud, N., and Campani, M., 2007, Thermochronology constraints for the propagation sequence of the south Pyrenean basement thrust system (France–Spain): Tectonics, v. 26, no. TC5007.

Kilhams, B., Morton, A., Borella, R., Wilkins, A., and Hurst, A., 2014, Understanding the provenance and reservoir quality of the Sele Formation sandstones of the UK Central Graben utilizing detrital garnet suites, *in* Scott, R.A., Smyth, H.R., Morton, A.C., and Richardson, N., eds., Sediment Provenance Studies in Hydrocarbon Exploration and Production: Geological Society of London, Special Publication 386, p. 129–142.

Kuebler, K.E., Jolliff, B.L., Wang, A., and Haskin, L.A. 2006, Extracting olivine (Fo–Fa) compositions from Raman spectral peak positions: Geochimica et Cosmochimica Acta, v. 70, p. 6201–6222.

Labaume, P., and Teixell, A., 2018, 3D structure of subsurface thrusts in the eastern Jaca Basin, southern Pyrenees: Geologica Acta, v. 16, p. 477–498.

Labaume, P., Séguret, M., and Seyve, C., 1985, Evolution of a turbiditic foreland basin and analogy with an accretionary prism: example of the Eocene South-Pyrenean Basin: Tectonics, v. 4, p. 661–685.

Labaume, P., Meresse, F., Jolivet, M., Teixell, A., and Lahfid, A., 2016a, Tectonothermal history of an exhumed thrust-sheet-top basin: an example from the south Pyrenean thrust belt: Tectonics, v. 35, p. 1280–1313.

Labaume, P., Meresse, F., Jolivet, M., and Teixell, A., 2016b, Exhumation sequence of the basement thrust units in the west-central Pyrenees: constraints from apatite fission track analysis: Geogaceta, v. 60, p. 11–14.

Lagabrielle, Y., Laraume, P., and de Saint Blanquat, M., 2010, Mantle exhumation, crustal denudation, and gravity tectonics during Cretaceous rifting in the Pyrenean realm (SW Europe): insights from the geological setting of the lherzolite bodies: Tectonics, v. 29, no. TC4012.

Lago, M., Galé, C., Arranz, E., Vaquer, R., Gil, A., and Pocoví, A., 2000, Triassic tholeiitic dolerites (ophite) of the El Grado diapir: Estudios Geológicos, v. 56, p. 3–8.

Lihou, J.C., and Mange-Rajetzky, M.A., 1996, Provenance of the Sardona Flysch, eastern Swiss Alps: example of high-resolution heavy mineral analysis applied to an ultrastable assemblage: Sedimentary Geology, v. 105, p. 141–157.

Majesté-Menjoulas, C., Debon, F., and Barrère, P., 1999, Notice Explicative de la Carte Géologique de la France, feuille Gavarnie (1082): Bureau des Recherches Géologiques et Minières, Orléans, 1:50000.

Mange, M.A., and Maurer, H.F.W., 1992, Heavy Minerals in Colour: London, Chapman and Hall, 147 p.

Mange, M.A., Dewey, J.F., and Wright, D.T., 2003, Heavy minerals solve structural and stratigraphic problems in Ordovician strata of the western Irish Caledonides: Geological Magazine, v. 140, p. 25–30.

Mange-Rajetzky, M.A., 1995, Subdivision and correlation of monotonous sandstone sequences using high-resolution heavy mineral analysis, a case study: the Triassic of the Central Graben, *in* Dunay, R.E., and Hailwood, E.A., eds., Non-biostratigraphical Methods of Dating and Correlation: Geological Society of London, Special Publication 89, p. 23–30.

Mangen, J., 1960, Le Nummulitique Sud-Pyrénéen à l'ouest de l'Aragón: Pirineos v. 51–58, p. 77–111.

McKellar, Z., Hartley, A.J., Morton, A.C., and Feei, D., 2020, A multidisciplinary approach to sediment provenance analysis of the late Silurian–Devonian Lower Old Red Sandstone succession, northern Midland Valley Basin, Scotland: Geological Society of London, Journal, v. 177, p. 297–314.

Meresse, F., 2010, Dynamique d'un prisme orogénique intracontinental: évolution thermochronologique (traces de fission sur apatite) et tectonique de la Zone Axiale et des piémonts des Pyrénées centrooccidentales [Ph.D. Thesis]: Université de Montpellier 2, Montpellier, France, 280 p.

Michael, N., 2013, Functioning of an Ancient Routing System, the Escanilla Formation, South Central Pyrenees [Ph.D. Thesis]: Imperial College of London, London, 284 p.

Milliken, K.L., 2007, Provenance and diagenesis of heavy minerals, Cenozoic units of the northwestern Gulf of Mexico sedimentary basin, *in* Mange, M.A., and Wright, D.T., eds., Heavy Minerals in Use: Amsterdam, Elsevier, Developments in Sedimentology 58, p. 247–261.

Milliken, K.L., and Mack, L.E., 1990, Subsurface dissolution of heavy minerals, Frio Formation sandstones of the ancestral Rio Grande Province, South Texas: Sedimentary Geology, v. 68, p. 187–199.

Montes, M., and Colombo, F., 1996, Análisis secuencial y correlación de los abanicos aluviales de Peña Oroel y la Sierra de Cancias (Eoceno superior, Cuenca Surpirenaica Central): Geogaceta, v. 20, p. 76–79.

Morris, R.G., Sinclair, H.D., and Yelland, A.J., 1998, Exhumation of the Pyrenean orogen: implications for sediment discharge: Basin Research, v. 10, p. 69–85.

Morton, A.C., 1984, Stability of detrital heavy minerals in Tertiary sandstones from the North Sea Basin: Clay Minerals, v. 19, p. 287–308.

Morton, A.C., and Hallsworth, C., 1999, Processes controlling the composition of heavy mineral assemblages in sandstones: Sedimentary Geology, v. 124, p. 3–29.

Morton, A.C., and Hallsworth, C., 2007, Stability of detrital heavy minerals during burial diagenesis, *in* Mange, M.A., and Wright, D.T., eds., Heavy Minerals in Use: Amsterdam, Elsevier, Developments in Sedimentology 58, p. 215–245.

Morton, A.C., Hallsworth, C., and Chalton, B., 2004, Garnet compositions in Scottish and Norwegian basement terrains: a framework for interpretation of North Sea sandstone provenance: Marine and Petroleum Geology, v. 21, p. 393–410.

Morton, A.C., Humphreys, B., and Dharmayanti, D.A., 1994, Palaeogeographic implications of the heavy mineral distribution in Miocene sandstones of the North Sumatra Basin: Journal of Southeast Asian Earth Sciences, v. 10, p. 177–190.

Mouthereau, F., Filleaudeau, P.Y., Vacherat, A., Pik, R., Lacombe, O., Fellin, M.G., Castelltort, S., Christophoul, F., and Masini, E., 2014, Placing limits to shortening evolution in the Pyrenees: role of margin architecture and implications for the Iberia–Europe convergence: Tectonics, v. 33, p. 2283–2314.

Muñoz, J.A., 1992, Evolution of a continental collision belt: ECORS-Pyrenees crustal balanced cross-section, *in* McClay K.R., ed., Thrust Tectonics: London, Chapman and Hall, p. 235–246.

Mutti, E., 1985, Turbidite systems and their relations to depositional sequences, *in* Zuffa, G.G., ed., Provenance of Arenites: Dordrecht, Springer, p. 65–93.

Mutti, E., Remacha, E., Rosell, J., Valloni, R., and Zamorano, M., 1985, Stratigraphy and facies characteristics of the Eocene Hecho group turbidite systems, South-Central Pyrenees: International Association of Sedimentologists, 6th European regional meeting, Lleida, Field Trip 12 Guidebook, p. 519–576.

Nie, J., Horton, B.K., Saylor, J.E., Mora, A., Mange, M., Garzione, C.N., Basu, A., Moreno, C.J., Caballero, V., and Parra, M., 2012, Integrated provenance analysis of a convergent retroarc foreland system: U–Pb ages, heavy minerals, Nd isotopes, and sandstone compositions of the Middle Magdalena Valley basin, northern Andes, Colombia: Earth-Science Reviews, v. 110, p. 111–126.

Nijman, W., and Nio, S., 1975, The Eocene Montañana Delta (Tremp–Graus Basin, provinces of Lérida and Huesca, Southern Pyrenees, N Spain), Field Trip B Guidebook (The Sedimentary Evolution of the Paleogene South Pyrenean Basin): International Association of Sedimentologists, XI International Sedimentological Congress, Excursion Guidebook, p. 1–20.

Oliva-Urcia, B., Beamud, E., Garcés, M., Arenas, C., Soto, R., Pueyo, E.L., and Pardo, G., 2016, New magnetostratigraphic dating of the Palaeogene syntectonic sediments of the west-central Pyrenees: tectonostratigraphic implications, *in* Pueyo, E.L., Cifelli, F.,

Sussman, A.J., and Oliva-Urcia, B., eds., Palaeomagnetism in Fold and Thrust Belts: New Perspectives: Geological Society of London, Special Publication 425, p. 107–128.

Oms, O., Dinarès-Turell, J., and Remacha, E., 2003, Magnetic stratigraphy from deep clastic turbidites: an example from the Eocene Hecho group (southern Pyrenees): Studia Geophysica et Geodactica, v. 47, p. 275–288.

Orti, F., Salvany, J.M., Rosell, L., Pueyo, J.J., and Inglès, M., 1986, Evaporitas antiguas (Navarra) y actuales (Los Manegros) de la Cuenca del Ebro, *in* Anadón, P., and Cabrera, L., eds., Guia de Las Excursiones Del XI Congreso Español de Sedimentologia: Generalitat de Catalunya, Comissió Interdepartamental de Recerca i Innovació Tecnològica, Barcelona, p. 21–21.

Ortuño, M., and Viaplana-Muzas, M., 2018, Active fault control in the distribution of elevated low relief topography in the Central-Western Pyrenees: Geologica Acta, v. 16, p. 499–518.

Payros, A., Pujalte, V., and Orue-Etxebarria, X., 1999, The South Pyrenean Eocene carbonate megabreccias revisited: new interpretation based on evidence from the Pamplona Basin: Sedimentary Geology, v. 125, p. 165–194.

Puiget, P., 1989, Évolution géodynamique hercynienne des Pyrénées centrales. Contraintes structurales métamorphiques, magmatiques et sédimentologiques [Ph.D. Thesis]: Université Toulouse III Paul Sabatier, Toulouse, France.

Puigdefábregas, C., 1975, La sedimentación molásica en la cuenca de Jaca: Pirineos, v. 104, p. 1–188.

Puigdefábregas, C., Muñoz, J.A., and Vergés, J., 1992, Thrusting and foreland basin evolution in the southern Pyrenees, *in* McClay K.R., ed., Thrust Tectonics: London, Chapman and Hall, p. 247–254.

Recio, J.M., Torres-Girón, M.L., and Garcia-Ruiz, J.M., 1987, Genetical and physicochemical aspects of the silty deposits of Monte Perdido Massif: Pirineos, v. 160, p. 95–103.

Remacha, E., and Fernández, L.P., 2003, High-resolution correlation patterns in the turbidite systems of the Hecho Group (South-Central Pyrenees, Spain), *in* Mutti, E., Steffens, G.S., Pirmez, C., Orlando, M., and Roberts, D., eds., Turbidites: Models and Problems: Marine and Petroleum Geology, v. 20, p. 711–726.

Remacha, E., Oms, O., and Coello, J., 1995, The Rapitán turbidite channel and its related eastern levee–overbank deposits, Eocene Hecho group, south-central Pyrenees, Spain, *in* Pickering, K., Hiscott, R., Kenyon, N., Ricci Lucchi, F., and Smith, R., eds., Atlas of Deep-Water Environments: Architectural Style in Turbidite Systems: London, Chapman and Hall, p. 145–149.

Remacha, E., Fernandez, L.P., and Maestro, E., 2005, The transition between sheet-like lobe and basin-plain turbidites in the Hecho Basin (South-Central Pyrenees, Spain): Journal of Sedimentary Research, v. 75, p. 798–819.

Reynolds, A.D., 1987, Tectonically controlled alluvial sedimentation in the South Pyrenean foreland basin [Ph.D. Thesis]: University of Liverpool, 309 p.

Ribeiro, M.L., Reche, J., López-Carmona, A., and Quesada, C., 2019, Variscan metamorphism, *in* Quesada, C., and Oliveira, J.T., eds., The Geology of Iberia: A Geodynamic Approach: Regional Geology Reviews, Springer, p. 473–498.

Ríos Aragüés, L.M., Lanaja del Busto, J.M., Ríos Mitchell, J.M., and Marín Blanco, F.J., 1982, Mapa Geológico de España, hoja no. 179 (Bielsa), Instituto Geológico y Minero de España Madrid, 1:50,000.

Roigé, M., 2018, Procedència i evolució dels sistemes sedimentaris de la conca de Jaca (conca d'avantpais Sudpirinenca): interacció entre diverses àrees font en un context tectònic actiu [Ph.D. Thesis]: Universitat Autònoma de Barcelona, 312 p.

Roigé, M., Gómez-Gras, D., Remacha, E., Daza, R., and Boya, S., 2016, Tectonic control on sediment sources in the Jaca basin (Middle and Upper Eocene of the South-Central Pyrenees): Comptes Rendus Geoscience, v. 348, p. 236–245.

Roigé, M., Gómez-Gras, D., Remacha, E., Boya, S., Viaplana-Muzas, M., and Teixell, A., 2017, Recycling an uplifted early foreland basin fill: an example from the Jaca basin (Southern Pyrenees, Spain): Sedimentary Geology, v. 360, p. 1–21.

Roigé, M., Gómez-Gras, D., Stockli, D.F., Teixell, A., Boya, S., and Remacha, E., 2019, Detrital zircon U–Pb insights into the timing and provenance of the South Pyrenean Jaca basin: Geological Society of London, Journal, v. 176, p. 1182–1190.

Roure, F., Choukroune, P., Berastegui, X., Muñoz, J.A., Villien, A., Matheron, P., Bareyt, M., Seguret, M., Camara, P., and Deramond, J., 1989, Ecors deep seismic data and balanced cross sections: geometric constraints on the evolution of the Pyrenees: Tectonics, v. 8, p. 41–50.

Rubio, V., Vigil, R., García, R., and González, J.A., 1996, Caracterización mineralógica de sedimentos arenosos en la cuenca del río Ara (Huesca): Cuaternario y Geomorfología, v. 10, p. 33–44.

Souquet, P., 1967, Le Crétacé Supérieur Sud-Pyrénées en Catalogne, Aragon et Navarra [Ph.D. Thesis]: Université de Toulouse, Toulouse, France, 529 p.

Steidtmann, J.R., and Schmitt, J.G., 1988, Provenance and dispersal of tectogenic sediments in thin-skinned, thrusted terrains, *in* Kleinspehn, K.L., and Paola, C., eds., New Perspectives in Basin Analysis: New York, Springer-Verlag, p. 353–366.

Teixell, A., 1996, The Ansó transect of the southern Pyrenees: basement and cover thrust geometries: Geological Society of London, Journal, v. 153, p. 301–310.

Teixell, A., 1998, Crustal structure and orogenic material budget in the west central Pyrenees: Tectonics, v. 17, p. 395–406.

Teixell, A., Labaume, P., and Lagabrielle, Y., 2016, The crustal evolution of the west-central Pyrenees revisited: inferences from a new kinematic scenario: Comptes Rendus Geoscience, v. 348, p. 257–267.

Ternet, Y., Barrere, P., and Debroas, E.J., 1995, Notice Explicative de la Carte Géologique de la France, feuille Campan (1071): Bureau des Recherches Géologiques et Minières, Orléans, 1:50,000.

Uddin, A., Kumar, P., Sarma, J.N., and Akhter, S.H., 2007, Heavy mineral constraints on the provenance of Cenozoic sediments from the foreland basins of Assam and Bangladesh: erosional history of the eastern Himalayas and the Indo-Burman Ranges, *in* Mange, M.A., and Wright, D.T., eds., Heavy Minerals in Use: Amsterdam, Elsevier, Developments in Sedimentology 58, p. 823–847.

Ullastre, J., and Masriera, A., 1982, Hipótesis y problemas acerca del origen de las Asociaciones de minerales pesados del Senoniense del Pirineo Catalán: Cuadernos de Geología Ibérica, v. 8, p. 949–964.

Vacherat, A., Mouthereau, F., Pik, R., Bernet, M., Gautheron, C., Masini, E., Pourhiet, L.L., Tibari, B., and Lahfid, A., 2014, Thermal imprint of rift-related processes in orogens as recorded in the Pyrenees: Earth and Planetary Science Letters, v. 408, p. 296–306.

Valloni, R., Marchi, M., and Mutti, E., 1984, Studio conoscitivo della moda detritica delle torbiditi eoceniche del Gruppo di Echo (Spagna): Giornale di Geologia, v. 46, p. 45–56.

Velbel, M.A., 2007, Surface textures and dissolution processes of heavy minerals in the sedimentary cycle: examples from pyroxenes and amphiboles, *in* Mange, M.A., and Wright, D.T., eds., Heavy Minerals in Use: Amsterdam, Elsevier, Developments in Sedimentology 58, p. 113–150.

Vergés, J., Fernández, M., and Martínez, A., 2002, The Pyrenean orogen: pre-, syn-, and post-collisional evolution: Journal of the Virtual Explorer, v. 08, p. 55–74.

Vermeesch, P., 2018, Statistical models for point-counting data: Earth and Planetary Science Letters, v. 501, p. 112–118.

Vermeesch, P., Resentini, A., and Garzanti, E., 2016, An R package for statistical provenance analysis: Sedimentary Geology, v. 336, p. 14–25.

Vincent, S.J., 2001, The Sis paleovalley a record of proximal fluvial sedimentation and drainage basin development in response to Pyrenean mountain building: Sedimentology, v. 48, p. 1235–1276.

von Eynatten, H., and Dunkl, I., 2012, Assessing the sediment factory: the role of single grain analysis: Earth Science Reviews, v. 115, p. 97–120.

von Eynatten, H., and Gaupp, R., 1999, Provenance of Cretaceous synorogenic sandstones in the Eastern Alps: constraints from framework petrography, heavy mineral analysis and mineral chemistry: Sedimentary Geology, v. 124, p. 81–111.

Walderhaug, O., and Porten, K.W., 2007, Stability of detrital heavy minerals on the Norwegian Continental Shelf as a function of depth and temperature: Journal of Sedimentary Research, v. 77, p. 992–1002.

Wang, A., Kuebler, K.E., Jolliff, B.L., and Haskin, L.A., 2004, Raman spectroscopy of Fe-Ti-Cr-oxides, case study: Martian meteorite EETA79001: American Mineralogist, v. 89, p. 665–680.

Yuste, A., Bauluz, B., and Luzón, A., 2006, Asociaciones características de minerales pesados en las areniscas del borde septentrional de la cuenca del Ebro (zona central): Macla: Sociedad Española de Mineralogía, Revista, v. 6, p. 501–504.

Zwart, H.J., 1986, The Variscan geology of the Pyrenees: Tectonophysics, v. 129, p. 9–27.

Zwart, H.J., and Sitter, L.D., 1979, The geology of the Central Pyrenees: Leidse Geologische Mededelingen, v. 50, p. 1–74.

Received 19 May 2020; accepted 7 November 2020.

Capítol 5

Interplay of Multiple Sediment Routing Systems Revealed by Combined Sandstone Petrography and Heavy Mineral Analysis (HMA) in the South Pyrenean Foreland Basin

El capítol 5 correspon a l'article publicat a la revista Minerals publicat l'any 2022.

X. Coll ha realitzat el tractament de les mostres (descrit en la metodologia) i ha realitzat el comptatge de totes les mostres i els anàlisis amb spectrometria Raman. Ha sintetitzat i realitzat l'anàlisi estadístic de totes les mostres, i ha confeccionat tots els diagrames composicionals. També ha redactat la major part del text i ha realitzat la major part de les figures.

Coll, X., Roigé, M., Gómez-Gras, D., Teixell, A., Boya, S., & Mestres, N. (2022). Interplay of Multiple Sediment Routing Systems Revealed by Combined Sandstone Petrography and Heavy Mineral Analysis (HMA) in the South Pyrenean Foreland Basin. Minerals, 12(2), 262. https://doi.org/10.3390/min12020262.

minerals

MDPI

Article

Interplay of Multiple Sediment Routing Systems Revealed by Combined Sandstone Petrography and Heavy Mineral Analysis (HMA) in the South Pyrenean Foreland Basin

Xavier Coll [1], Marta Roigé [1], David Gómez-Gras [1,*], Antonio Teixell [1], Salvador Boya [1] and Narcís Mestres [2]

[1] Departament de Geologia, Universitat Autònoma de Barcelona, 08193 Bellaterra, Spain; xavier.coll.c@gmail.com (X.C.); roige.marta@gmail.com (M.R.); antonio.teixell@uab.cat (A.T.); salvaboya@gmail.com (S.B.)

[2] Institut de Ciència de Materials de Barcelona, ICMAB-CSIC, Campus de la UAB, 08193 Bellaterra, Spain; narcis@icmab.es

* Correspondence: david.gomez@uab.cat

Abstract: Combined sandstone petrography and heavy mineral analysis allow to decipher different sediment routing systems that could not be resolved by one method alone in the South Pyrenean foreland basin. We apply this approach to deltaic and alluvial deposits of the southern part of the Jaca basin, and in the time equivalent systems of the nearby Ainsa and Ebro basins, in order to unravel the evolution of source areas and the fluvial drainage from the Eocene to the Miocene. Our study allows the identification of four petrofacies and five heavy-mineral suites, which evidence the interplay of distinct routing systems, controlled by the emergence of tectonic structures. Two distinct axially-fed systems from the east coexisted in the fluvial Campodarbe Formation of the southern Jaca basin that were progressively replaced from east to west by transverse-fed systems sourced from northern source areas. In the late stages of evolution, the Ebro autochthonous basin and the Jaca piggy-back basin received detritus from source areas directly north of the basin from the Axial Zone and from the Basque Pyrenees. Coupling sandstone petrography with heavy mineral provenance analysis allows challenging the existing model of the South Pyrenean sediment dispersal, highlighting the relevance of this approach in source-to-sink studies.

Keywords: provenance; sandstone petrography; heavy minerals; sediment routing systems; Jaca basin; South Pyrenean foreland; Pyrenees

check for updates

Citation: Coll, X.; Roigé, M.; Gómez-Gras, D.; Teixell, A.; Boya, S.; Mestres, N. Interplay of Multiple Sediment Routing Systems Revealed by Combined Sandstone Petrography and Heavy Mineral Analysis (HMA) in the South Pyrenean Foreland Basin. *Minerals* **2022**, *12*, 262. https://doi.org/10.3390/min12020262

Academic Editor: Davide Lenaz

Received: 18 January 2022
Accepted: 15 February 2022
Published: 18 February 2022

1. Introduction

The sedimentary record of a foreland basin offers the opportunity to study the interplay between distinct source areas, allowing to infer the uplift and exhumation history of mountain belts [1–3]. Sediment provenance analysis is a useful tool to understand the processes occurring in the hinterland of a sedimentary basin and enables to constrain the timing of geodynamic events, as well as to unravel sediment pathways and correlate stratigraphic sequences [4–10]. This arduous task requires combining as many provenance indicators as possible in order to achieve the highest resolution for identifying and characterizing the sediment routing systems in the related basins [8,11–15]. Sandstone petrography and heavy mineral analysis are widespread techniques in sedimentary provenance studies [5,8,16–22]. Since each of these methods can record different provenance signals, the integration of both is crucial to fully characterize and understand the functioning of sediment routing systems.

The deltaic to fluvial–alluvial sedimentary record of the South Pyrenean foreland basin (SPB) records stages of strong exhumation of the Pyrenean mountain belt. From mid Eocene to early Miocene times, these sediments were deposited in thrust-sheet-top basins featuring a wide range of lithologies from diverse sources [23–31]. In the western sector of the South Pyrenean foreland, the growing of the External Sierras thrust system from late

Eocene times (Figure 1) caused the compartmentalization of the Jaca thrust-sheet-top basin to the north and the autochthonous Ebro basin to the south [23,32–34].

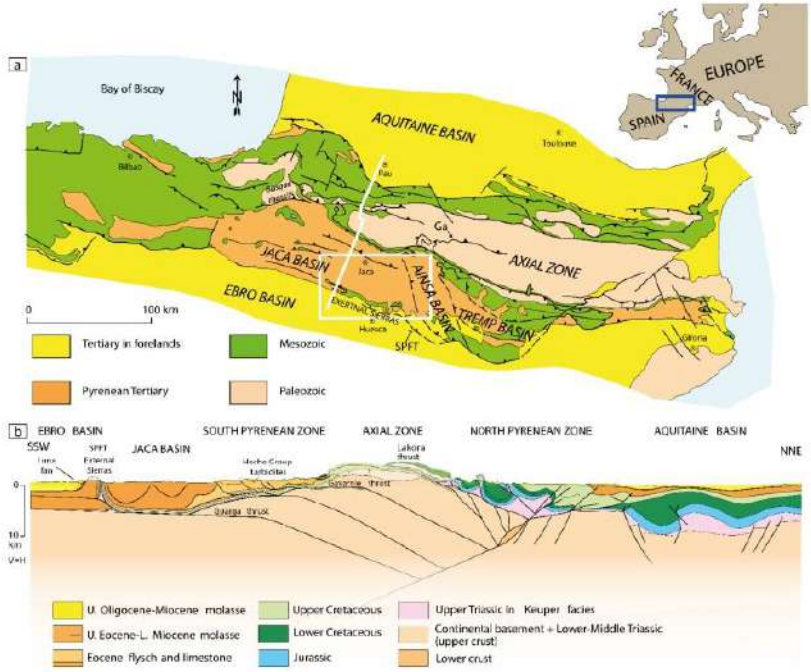

Figure 1. (**a**) Simplified geological map of the Pyrenees (redrawn from Teixell et al. [35]), showing the location of the study area (white frame). White line indicates cross-section in Figure 1b. White box corresponds to study area. Ga: Gavarnie thrust, SPTF: South Pyrenean Frontal Thrust. (**b**) Crustal cross-section of the west-central Pyrenees (simplified from Teixell et al. [36]), showing both the South Pyrenean Zone and the North Pyrenean Zone.

Previous provenance studies focused in the northern sector of the Jaca basin [29,30,37–39] or in the eastern Ainsa and Tremp-Graus basins (Figure 1) [28,31,40–43], Nevertheless, the sediment provenance (i.e., sandstone petrography, heavy minerals) of the southern part of the Jaca basin remain unknown.

The use of heavy mineral analysis as an effective provenance tool to unravel sediment sources or sediment pathways has been widely demonstrated in the Alps or the Himalayas, mainly on modern sediments [8,16,44–51]. However, few studies characterized the heavy mineral provenance signatures of the South Pyrenean and Ebro basins [28,39,40,52–58] and none have focused on the southern margin of the Jaca basin. In addition, the works integrating their results with a solid compositional framework based on sandstone petrography detrital modes are scarce. This contrasts with the amount of fruitful works that characterized the stratigraphy, sedimentology, magnetostratigraphy, paleontology, and tectonic structure of this area [23,24,59–79]. These provide a solid stratigraphic framework to characterize the sediment of source areas and the related routing systems, crucial to track the overarching evolution of the foreland basin in relation to the tectonic development of the Pyrenean orogenic belt.

In this work, we aim to unravel the compositional nature of the transitional to alluvial environments of the southern part of the Jaca basin through a provenance study that integrates sandstone petrography and heavy mineral analysis, constraining the interplay between the different active source areas that supplied the axial and the transverse systems. The time-equivalent deposits in the Ainsa basin (Escanilla Formation) are also analyzed

in order to test the connectivity between both basins. The Ebro basin deposits that occur south of the External Sierras thrust front are also investigated to compare their sediment provenance with those of the Jaca thrust-sheet-top basin, providing new insights into the last stages of the terrestrial sedimentation.

This work highlights the importance of coupling sandstone petrography and heavy mineral analysis in order to constrain sediment provenance and sediment dispersal patterns, with applications to collisional orogens where different source areas can produce similar compositional signatures. Our results demonstrate that a provenance framework based on a single technique can lead to biased conclusions and can overlook important details of the sediment routing into a clastic basin.

2. Geological Setting

2.1. Structural and Stratigraphic Framework

The Pyrenean fold-and-thrust belt grew diachronously, from late Cretaceous to Miocene, as a result of the oblique character of the collision between the Iberian and European plates [80–83]. The subduction of the lower crust of the Iberian plate under the European plate led to the inversion of the former Mesozoic rift basins and the stacking of the basement, resulting in an upper-crustal doubly-vergent orogenic prism. The core of the belt (known as the Axial Zone) is made of basement-involved stacked thrust sheets flanked to the north by a series of inverted hyper-extensional Mesozoic basins (the North Pyrenean Zone (Figure 1) [84]). The tertiary foreland deposits that occur further north constitute the Aquitanian basin. By contrast, the deformation in the southern Pyrenees was accommodated by a thrust imbricate fan [85–87], which in the west central Pyrenees comprise four main thrust sheets (Lakora-Eaux-Chaudes, Gavarnie, Broto, and Guarga). These thrust sheets involve the Paleozoic basement, a preorogenic Mesozoic succession, and the late Cretaceous to early Miocene foreland basin. In the Jaca area, the proximal basin was detached constituting a wedge-top basin, bordered to the south by the thrust front of the External Sierras (Figure 1b). South of the thrust front, the autochthonous Ebro basin exposes a young sedimentary record of the final stages of the Pyrenean exhumation.

Variscan low grade metamorphic rocks and granitoids comprise the major part of the Paleozoic basement (the core of the Pyrenean belt), which are, in turn, unconformably overlain by Permo–Triassic red beds or Cretaceous limestones. The preorogenic Mesozoic succession starts with the Triassic Keuper facies, which are involved in thrust sheet propagation, acting as an evaporite detachment level during extension and contraction, and salt diapirism processes that played a critical role in the formation of Mesozoic minibasins and the exhumation of the Paleozoic basement in the central Pyrenees [88,89]. The rest of the succession is made up of a thick Jurassic–Cretaceous carbonate and sandstone-shale successions.

The South Pyrenean basin contains synorogenic deposits of late Santonian to early Miocene age. During the Eocene, fluvio-deltaic sedimentary environments were concentrated in the Àger and Tremp-Graus basins (eastern sector of the South Pyrenean basin), funneling sediments to the west, to the slope, and deep-marine sedimentation environments of the Ainsa and Jaca basins [24,27,29,90,91]. This deep-marine succession (known as the Hecho Group turbidites [91]) developed during an underfilled foreland basin stage, which with the growth of the orogen, was progressively replaced, from east to west, by deltaic and alluvial deposits leading to an overfilled foreland basin stage (mid to late Eocene [23,25]).

The deep-marine deposits were replaced by the deltaic and fluvial Sobrarbe (Lutetian–Bartonian) and Escanilla (Bartonian–Priabonian) Formations in the Ainsa basin [92]. These systems, which have their source area located in the central Pyrenees and received sediments from the Sis and Gurp-Pobla paleovalleys, prograde westward into the Jaca basin [24,28]. The youngest deposits preserved in the Ainsa basin are the Graus Formation conglomerates (Chattian–Aquitanian), unconformably overlying the Escanilla Formation [93]. In the Jaca basin, the time equivalent deposits to the Escanilla and Sobrarbe are the Sabiñanigo Sandstone (Bartonian) and Belsué-Atarés (Bartonian–Priabonian) delta formations, the fluvial

Campodarbe formation (Bartonian–Oligocene), and the Bernués formation (Oligocene–Miocene), which record the evolution from transitional to fully terrestrial environments. This transition is diachronic and ends with the onset of the endorheic basin stage at 36 Ma, when terrestrial environments spread throughout the entire basin [66,71,94,95].

The Belsué-Atarés delta prograded from east to west at the same time that obliquely-trending folds started to grow in the southern margin of the Jaca basin [23,75,96]. These produced marked thickness variations and a strong diachrony of the sedimentary record. In the north-western part of the Jaca basin, a subordinated delta system occurs instead of the Belsué-Atarés delta (the Martés sandstone [23]). These deltaic environments were progressively substituted by the fluvial to alluvial Campodarbe and Bernués Formations spanning until the lower Miocene [23,76,97].

The Campodarbe Formation [60] is a fluvial to alluvial succession, where at least two main sediment routings can be identified [23]. In the northern margin, an east-derived axial fluvial system, entering the basin trough the south-eastern margin, interacts with a north-derived transverse alluvial fan system, mainly controlled by the activity of the Gavarnie thrust, and mostly derived from the recycling of a former lower to middle Eocene turbidite basin [23,29,30,97]. By contrast, the sedimentation in the southern edge was dominated by axially-fed fluvial systems that have its proximal time equivalents in the nearby Ainsa basin (Figure 1) (Escanilla Formation) and was strongly controlled by the growth of tectonic structures [23,24,32,63,65,67,75,98]. The last stages of the basin infill are marked by the Bernués Formation (Chattian–Aquitanian [23,97,99]), a complex of alluvial fan deposits sourced from the existing reliefs to the north of the basin.

As the orogenic deformation progressed to the south, the External Sierras thrust front [35,59,74,85] became strongly emergent (Oligocene–Miocene) and split the Campodarbe Formation in the Jaca basin to the north from the Ebro basin to the south. In the Ebro basin, the top of the Campodarbe Formation has been dated at 24.5 Ma (Chattian) [74,77], whereas the fluvial/alluvial deposits of the overlying Uncastillo Formation have been dated as Chattian–Aquitanian. The activity of the Guarga thrust sheet triggered the formation of this north-derived Luna alluvial fan system, which is sourced from the recycling of the Jaca basin and the existing reliefs of the Axial Zone farther to the north [23,100,101].

2.2. Source Rock Lithologies

The potential source areas for the Jaca basin during the late Eocene–Miocene are: (i) the Paleozoic basement of the Axial and North Pyrenean Zones, (ii) the preorogenic Mesozoic cover succession, and (iii) the earlier synorogenic assemblage of the upper Cretaceous to middle Eocene deposits (Figure 2).

The Paleozoic basement is constituted by Variscan granitoids that intrude an assemblage of Cambro–Ordovician (and locally Neoproterozoic) to Devonian metasedimentary units, which are, in turn, overlain by flysch deposits of Carboniferous (Culm facies). In the Eastern Pyrenees, the Cambro–Ordovician metasedimentary units dominate the present-day outcrops, intruded by the Ordovician orthogneisses and Variscan granitoids [102–106]. In this area, scarce Neoproterozoic outcrops are also present, mainly constituted by schists, limestones, dolomites, and migmatites. By contrast, in the central Pyrenees, the metasedimentary Devonian terrains (mainly limestones) coexist with the Cambro–Ordovician metasiliciclastic rocks. This metasedimentary succession is also intruded by Variscan granitoids, but Ordovician Orthogneiss do not occur in this area. In the western Axial Zone, Devonian and Carboniferous rocks are dominant with Cambro–Ordovician terrains almost non-existent. In general, the entire Paleozoic basement displays a very-low to low grade metamorphism, though it can reach the medium and high grade in the metamorphic domes that occur along the Axial Zone, mainly involving the Precambrian and Cambro–Ordovician terrains.

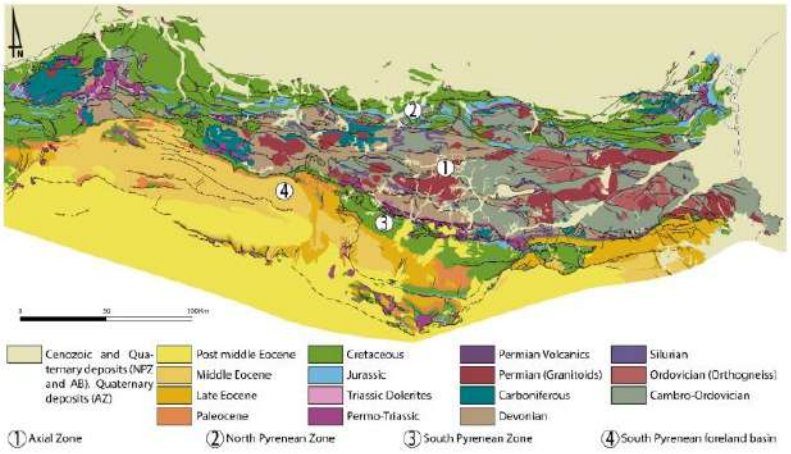

Figure 2. Geological map of the central Pyrenees (modified from a synthesis by Rodríguez-Fernández et al. [107]) showing the potential source rock terrains for the late Eocene–Oligocene systems of the Jaca basin. Dark frame represents the location of the study area. AB: Aquitanian basin; NPZ: North Pyrenean Zone; AZ: Axial Zone.

The Paleozoic basement of the Axial Zone is unconformably overlain by Permo–Triassic red beds or Jurassic–Cretaceous carbonates. Shales, carbonates (Muschelkalk facies), evaporites (Keuper facies), and dolerites (ophites) follow the lower Triassic sandstone. In the North Pyrenean Zone, Jurassic-lower Cretaceous carbonate deposits are followed by a thick shale and turbidite sequence (Albian to Maastrichtian) intruded by subvolcanic basaltic rocks [108,109]. Contrary to what occurs in the South Pyrenean Zone, Paleozoic basement (locally Neoproterozoic) outcrops also occur, mainly concentrated in the east-central and western Pyrenees. In addition, a restricted narrow east-west-trending belt (the Internal Metamorphic Zone) displays a HT-LP metamorphism related to crustal thinning and mantle exhumation during the Cretaceous rifting [110,111], mainly affecting the Jurassic and Cretaceous succession. In contrast, in the South Pyrenean Zone, the Jurassic, the Cretaceous, and part of the early foreland-basins deposits consist of platform limestones, dolostones, and sandstones. These deposits developed in the distal margin of the marine foreland basin from late Cretaceous to Lutetian times, whereas the basin trough was characterized by clastic deposits.

2.3. *Heavy Minerals and Source Rock Lithologies*

The heavy-mineral content of a sedimentary rock usually does not exceed 1% of the total volume. Source rock type and fertility are the primary controls on the heavy mineral content that a source can provide [19,112,113]. Igneous and medium to high grade metamorphic rocks can contain various heavy minerals as their main constituents or accessory phases, whereas siliciclastic sedimentary rocks mainly produce recycled ultrastable minerals. By contrast, marine carbonate rocks are usually devoid of heavy minerals, although they may produce a few recycled minerals, originally incorporated by aeolian input or by diluted suspended material from terrestrial sources.

In the Pyrenees, zircon, tourmaline, rutile, and apatite grains occur in a wide variety of igneous, sedimentary, and metamorphic rocks of the Paleozoic basement, Mesozoic metamorphic rocks, and Mesozoic and Tertiary sedimentary cover (Figure 2). Paleozoic metapelites such as phyllites, schists, and granulites might contain chloritoid, almandine, staurolite, and kyanite [102,103,105]. However, these minerals have never been reported in the Mesozoic metapelites of the North Pyrenean Zone. Permo–Carboniferous igneous rocks described in the Pyrenees (Carboniferous rhyolites, dacites, ignimbrites, volcaniclastic

sediments [114,115] or late Variscan muscovite granites [116]) can also be a source of almandine garnet. By contrast, grossular garnet is usually associated with skarn deposits, thermally metamorphosed impure limestones, and marbles occurring in the Axial and North Pyrenean Zones, although volcanic rocks of the North Pyrenean Zone (syenites) may contain grossular as well [117]. Clinopyroxene, olivine, spinel, and epidote have been described in various igneous rocks such as Triassic dolerites or Cretaceous basalts, picrites, teschenites, syenites, and lamprophyres of the North Pyrenean Zone [117–120]. Clinopyroxene also occurs commonly in basaltic and andesitic rocks of the Stephano-Permian vulcanism [114]. In addition, epidote, titanite, and clinopyroxene can be found in Paleozoic marbles and calcschists, skarn deposits, and hornfels related to Paleozoic granites, as well as in the metamorphic Mesozoic limestones of the North Pyrenean Zone [119,121]. In regionally metamorphosed carbonate rocks of the amphibolite facies, spinel, olivine, clinopyroxene, and amphibole have been reported. Titanite, a common accessory mineral of many igneous and metamorphic rocks, can be found in Paleozoic granitic sources, Triassic dolerites, metapelites, and impure calc-silicate rocks [102,103,105,106,109,118].

3. Sampling and Analytical Methods

The deltaic to fluvial/alluvial environments of the Belsué-Atarés, Campodarbe, and Bernués Formations were sampled along 6 stratigraphic sections of the southern part of the Jaca basin (San Felices, Rodellar-Bibán, Monrepós, Gállego, Salinas, and Martés sections) (Figure 3). In addition, a section in the Ebro basin (Luesia section, covering the Campodarbe and Uncastillo Formations) and another one in the Ainsa basin (Ainsa section, including the Sobrarbe and Escanilla Formations) were also sampled to compare the compositional features with the time-equivalent deposits of the Jaca basin.

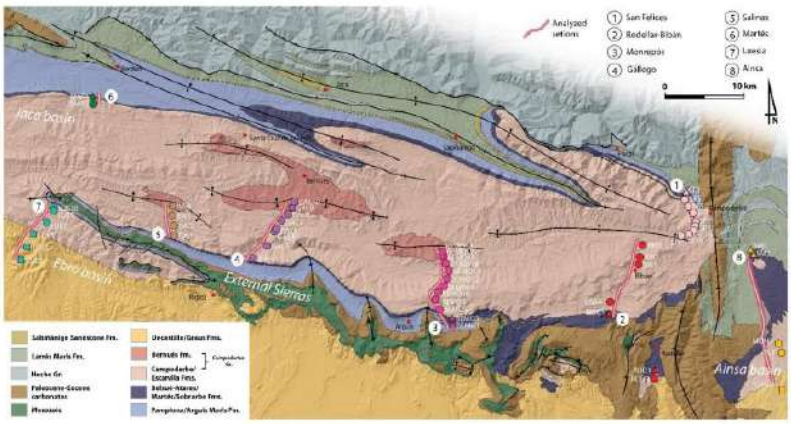

Figure 3. Geological map of the of the Jaca basin (modified from Puigdefàbregas [23]). Yellow-purple lines show the location of the analyzed sections. Numbers refer to each section: (1) San Felices section, (2) Rodellar-Bibán section, (3) Monrepós section, (4) Gállego section, (5) Salinas section, (6) Martés section, (7) Luesia section, and (8) Ainsa section. Numbers and symbols refer to each of the analyzed samples for sandstone petrography analyses.

Ninety-four sandstone and conglomerate samples were collected in the field for petrography and heavy mineral analysis. The number and spacing of petrography samples were established according to the representativeness of each analyzed sedimentary system within the stratigraphic sections. Fifty-three samples were chosen for quantification of the detrital modes through point-counting analysis under the polarizing microscope. After establishing a provenance framework based on sandstone petrography, twenty-five samples were selected for heavy mineral analysis.

3.1. Sandstone Petrography

The petrographic study was carried on thin sections stained with Na-cobaltinitrite for suitable identification of feldspar [122]. In order to distinguish carbonate compositions such as dolomite, ankerite or calcite, Alizarine red-S staining was applied. The Gazzi–Dickinson point counting method [1,123–125] was used to calculate the detrital modes, counting three to five hundred points for each thin section [126]. The points were classified as framework grains, diagenetic minerals, matrix, and porosity. Framework grains were labeled according to Zuffa [125] as noncarbonate extrabasinal (NCE), noncarbonate intrabasinal (NCI), carbonate extrabasinal (CE), and carbonate intrabasinal (CI). For metamorphic rock fragments, the classification of Garzanti and Vezzoli [127] was applied, while volcanic grains were classified according to Margsaglia and Ingersoll [128] and Critelli and Ingersoll [129]. The results were plotted and classified into first to fourth order ternary diagrams following Zuffa [125].

3.2. Heavy Minerals

Medium grained sandstone samples were targeted for sampling in order to avoid hydraulic-sorting effects that might bias the analytical results [130–133]. Fine to very coarse grain sizes were collected only in cases where medium grained sandstone was not available. In addition, samples from each depositional system were collected from similar facies in order to minimize hydraulic-sorting effects related to different processes within the same depositional environment.

Samples were crushed with a Retsch Disc Mill DM 200 prior to acid digestion with diluted 10% acetic acid for carbonate removal and avoiding apatite dissolution [112]. Struers Metason 200 ultrasound machine was used during 5 min in order help desegregation of well cemented sands and clay coatings. The 32 to 500 micrometer window was obtained through wet sieving, in order to avoid the clay to fine silt fraction but to analyze an acceptable grain-size window that does not produce a potential bias due to hydraulic-sorting effects [130–132]. The recovery of the dense fraction (2.90 g/cm^3) was performed by the centrifuging method, using the nontoxic dense liquid Na-polytungstate and partial freezing with liquid nitrogen [112,133]. 30 µm polished thin sections of the heavy-mineral fraction were prepared for each sample.

We used Raman spectroscopy for the identification of mineral grains [134,135]. A representative area of each thin section was selected and at least 200 non-diagenetic transparent heavy minerals were analyzed (opaque, carbonate, and micaceous minerals were not considered for identification) [112,136,137]. Therefore, only relative abundances of heavy minerals are reported in this paper. Raman scattering experiments were performed at room temperature in the backscattering geometry using a T64000 Horiba Jobin Yvon micro-Raman spectrometer equipped with high sensitivity liquid Nitrogen cooled CCD (charge-coupled device) as the detector. Samples were mounted on the XY stage of a BX40 Olympus microscope. The 488 nm laser line was used for the measurements. The incident laser beam was focused to a 2 µm spot on the samples using a 50-microscope objective. Laser power was kept below 0.4 mW to avoid laser-induced heating. Spectrometer resolution was 2 cm^{-1}. The obtained spectra (Figures S1 and S2) were compared with reference spectra [135,138,139] and mineral identification was verified under the optical microscope.

3.3. Statistical Treatment

In this work, we apply correspondence analysis [140] as an exploratory compositional data analysis tool to assess similarities between samples. The results are displayed as biplots in order to facilitate the visualization and interpretation of the results.

Statistical treatment of the point-counting data (petrographic and heavy mineral data) was performed using the Provenance R-package [141,142], which allowed the distinction between different petrofacies and heavy-mineral suites. Since the heavy-mineral data were acquired using the area method, the statistical bias might be greater; however, we believe it is not significant for the purpose of this work.

4. Results

4.1. Sandstone Petrography

4.1.1. Grain Types

Framework grains are here described in order to establish their most probable provenance. Non-framework grains are authigenic minerals, related to cementation and replacing processes in most of the cases where calcite is the main cement typology. All percentages here described are referred over total framework grains.

Noncarbonate Extrabasinal Grains (NCE)

Quartz is a widely represented type of grain. Its contents range from 7.3 to 51.9%. Several types of quartz have been distinguished: monocrystalline, polycrystalline, and quartz contained in a rock fragment. Characteristic quartz with evaporitic inclusions (anhydrite and halite) occurs in proportions of 0.4–2.6%.

Feldspar grain contents are (Figure S3) up to 12.4% of abundance, classified as orthoclase (<6.5%), microcline (<4.5%), and plagioclase (<5.5%). K-feldspar usually appears non-altered, whereas plagioclase usually shows some degree of alteration.

Lithic grains (Figure S3) dominate the framework components in many samples. They consist of metamorphic, plutonic, volcanic, and noncarbonate sedimentary rock fragments. Metamorphic rock fragments are the most abundant type of grain in most of the samples (up to 46.1%). Metamorphic grains include very low to low grade (metapelites and phyllites), medium grade (mica schists, schists, and chloritic schists), and high grade (quartzite). Plutonic grains (granitoid rock fragments) are very scarce (<1.7%) and recognized in very few samples. Volcanic grains represent up to 3.6% in some samples. Three textures of paleovolcanic lithics have been identified: (i) lathwork texture made of plagioclase and altered augite crystals, (ii) microlithic texture made of plagioclase microlites, and in lower proportion, (iii) vitric texture. Noncarbonate sedimentary rock fragments (3.4–53.6%) are sandstone, hybrid sandstone (Figure S3), siltstone, hybrid siltstone, and silicified rock fragments. Silicified rock fragments have been also subdivided into radiolarite rock fragments and silicified limestones.

Noncarbonate Intrabasinal Grains (NCI)

Noncarbonate intrabasinal grains are scarce (<5.3%), appearing always as glauconite or argillaceous rip-up clasts.

Carbonate Extrabasinal Grains (CE)

Carbonate extrabasinal grains occur with a wide variety of textures, reaching proportions up to 64.6%. Distinction has been made into (i) bioclastic and sparitic limestones, (ii) dolostones, and (iii) dolomitic and dolomitized limestones. Most common components contained in these rock fragments are bioclasts as foraminifera (nummulitids, discocyclinids, miliolids, alveolinids), red algae, or bivalves. Dolostone fragments (<6.7%) have been recognized as dolomicrite, polycrystalline sparitic fragments and single-grain dolomite.

Carbonate Intrabasinal Grains (CI)

Carbonate intrabasinal grains are rare (<4%) and appear as micritic intraclasts and caliche concretions, or as bioclasts (red algae, bivalves, and benthic foraminifera such as Nummulites).

4.1.2. Modal Sandstone Composition

Sandstone detrital modes are classified in three ternary diagrams (Figure S4), in order to visualize the compositional trends and the potential shifts of the source areas. A first-order diagram is used to classify the analyzed samples according to Zuffa 1980 [143]. The results show that the analyzed samples correspond to lithic arenites and calclithites. A second-order classification diagram following Dickinson et al. [144] shows an increase in

lithic fragments from the deltaic to the alluvial environments. Finally, a third-order diagram shows the dominance of metamorphic and sedimentary over volcanic lithic grains.

4.1.3. Petrofacies

We use a ternary plot in order to discriminate among the petrofacies defined by Roigé et al. [30] for the northern Jaca basin. The plot (Figure 4a) compares the relative abundance of hybrid sandstone rock fragments (Hy.Sst), feldspar and lithic rock fragments, excluding hybrid sandstone rock fragments (F+L) and carbonate extrabasinal grains (CE). The discrimination between the relative abundance of these types of grains allows to define four petrofacies that reflect the interplay of different source areas and the evolution of the basin.

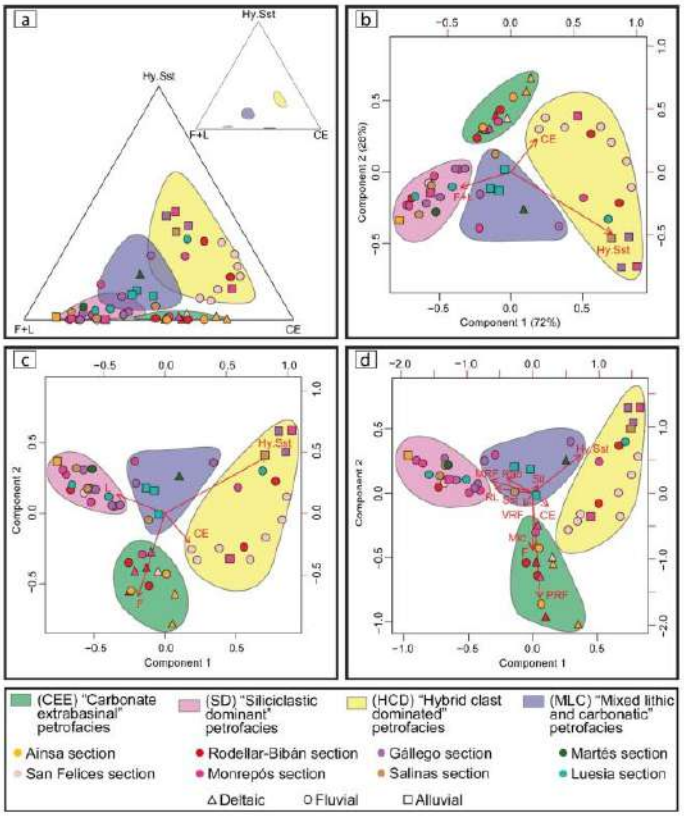

Figure 4. Compositional plots for all the analyzed samples. Feldspar (F), metamorphic r.f. (MRF), plutonic r.f. (PRF), volcanic r.f. (VRF), hybrid sandstone r.f. (Hy.Sst), siliciclastic sandstone (Sst), micas (Mic), silicified r.f. (Sil), radiolarite r.f. (Rad), Fe-Oxide replacement r.f. (RL), and carbonate extrabasinal grains (CE). (**a**) Compositional plot discriminates the four main groups of petrofacies described for all the analyzed samples showing the confidence region (90%) of the entire population of each petrofacies, while the small ternary diagram on the right side shows the mean confidence regions (90%) for each petrofacies. (**b**) Biplot showing the statistical significance of the four petrofacies model (100% of the variance is explained). (**c**) Biplot displaying the results of a correspondence analysis where F and L have been considered as two different variables in order to illustrate the compositional variations of feldspar (F) and lithics (L). (**d**) Biplot showing the compositions of samples and petrofacies considering a wide range of grains.

Correspondence analysis is here used in order to assess the statistical significance of the defined petrofacies. The results (Figure 4b) indicate that the four petrofacies model accounts for a hundred percent of the variance. Moreover, additional biplots differentiating F from L (Figure 4c) or showing the relative abundance of more types of grains (Figure 4d) are used for further description and visualization of samples' composition.

Carbonate Extrabasinal Enriched Petrofacies (CEE)

In this petrofacies (Figures 5A and S5a), carbonate extrabasinal grains are the most dominant rock fragment (48.5–75.3%). Lime mudstone and wackestone rock fragments of Mesozoic age are the most represented, including wackestone rock fragments containing *phitonellid* tests (Turonian limestones from the southern Pyrenees), while grainstone, packstone, and dolostone rock fragments are also present. This petrofacies also displays significant enrichment in microcline, orthoclase, plagioclase, plutonic rock fragments, and mica (Figure 4c,d), but it lacks hybrid sandstone rock fragments (<2.6%).

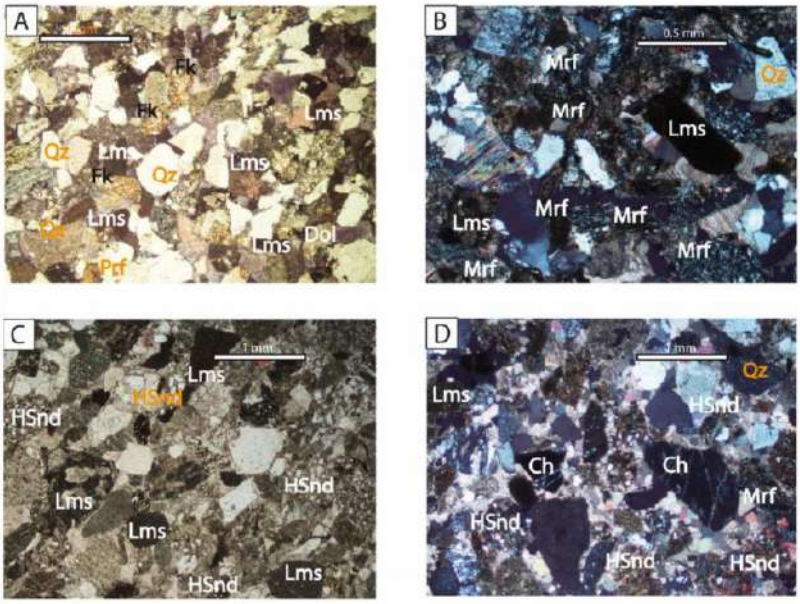

Figure 5. Optical photomicrographs of the described petrofacies. (**A**) General view of "carbonate extrabasinal enriched" petrofacies, with abundant micritic and bioclastic limestone (Lms) fragments and quartz (Qz), K-feldpar (Fk), plutonic rock fragments (Prf), and dolomite grains (Dol) (XPL). Sample ROD1, Belsué-Atarés Formation. (**B**) "Siliciclastic dominant" petrofacies characterized by the highest contents of quartz (Q), metamorphic rock fragments (Mrf), and limestone grains (Lms) and by the absence of hybrid sandstone rock fragments (XPL). Sample GAL4, Campodarbe Formation. (**C**) General view of "hybrid clast-dominated" petrofacies showing the large amount of hybrid sandstone rock fragments (HSnd) and limestone rock fragments (Lms) (PPL). (**D**) Appearance of "mixed lithic and carbonatic" petrofacies, showing the coexistence of hybrid sandstone rock fragments (HSnd) with abundant carbonatic (Lms) and siliciclastic grains radiolarite (Ch), quartz (Qz), and metamorphic grains (Mrf) (XPL).

In the interstratified conglomerate layers, the most common clast types are Mesozoic grey micritic limestones and dolostones. Epidote-bearing dolerites (Triassic ophites) are also present. Subordinate clasts are siliciclastic red sandstone (Permotriassic) and white quartz pebbles, green quartzite (Paleozoic), and black quartz clasts (Carboniferous radiolarites).

The CEE petrofacies occurs in the oldest analyzed sedimentary systems of the basin (the Sobrarbe and Escanilla Formations in the Ainsa basin, the Belsué-Atarés Formation and the basal Campodarbe Formation in the Jaca basin; Figure 6).

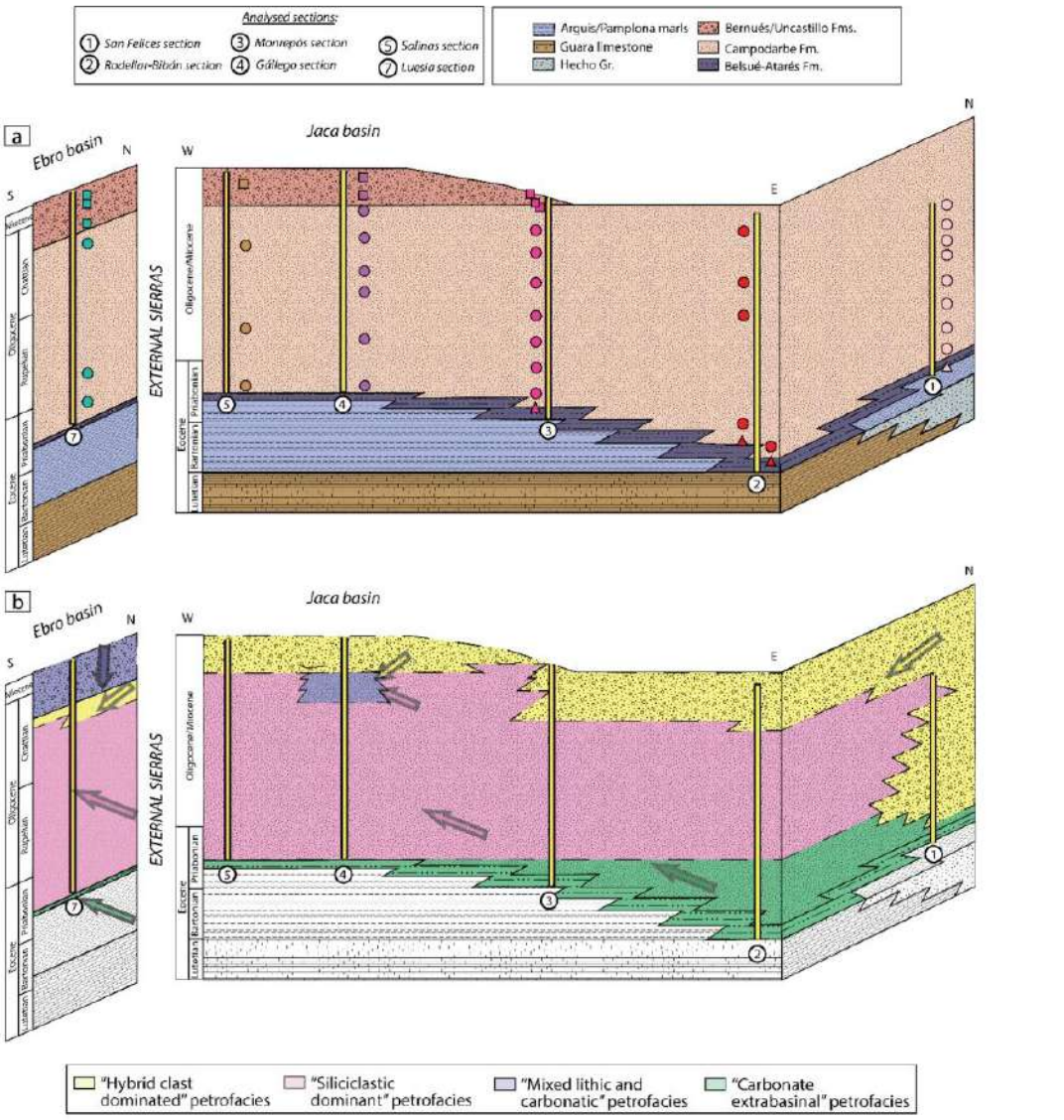

Figure 6. (**a**) General stratigraphic cross-section sketch with symbols representing the relative position of the analyzed samples presented in Figure 3, used here to understand the petrofacies scheme below. (**b**) Colored stratigraphic cross-section sketch in order to illustrate the distribution of the petrofacies laterally and through time. Yellow color corresponds to "hybrid clast-dominated" petrofacies, green color to "carbonate extrabasinal enriched" petrofacies, blue color to "mixed lithic and carbonatic" petrofacies, and pink color to "siliciclastic dominant" petrofacies. Colored arrows are used to facilitate reading of the provenance information. Dashed lines represent the boundaries between petrofacies.

The Sobrarbe Formation (samples SM1 and SM3 in Figure 3) displays the highest relative content of carbonate grains (mudstone, packstone, and grainstone rock fragments; Figure 4a), together with subordinate granite, schist, and feldspar grains. Up section, the overlying Escanilla Formation (samples MO1 and OL1) displays the same compositional features, with a slight increase in lithic fragments (Figure 4c).

In the Jaca basin, this petrofacies is observed in the Belsué-Atarés Formation in the San Felices, Rodellar-Bibán, and Monrepós sections, displaying a composition very close to that described in the Escanilla Formation in the Ainsa basin (Figure 4). In the Rodellar-Bibán section (samples ROD1 and ROD3), the petrofacies contains the highest abundance of feldspar grains (reaching up to 18.5% of framework grains).

Siliciclastic Dominant Petrofacies (SD)

Siliciclastic components are the most dominant grain type (Figures 5B and S5b,c), and the abundance of carbonate grains is always under 37%. Hybrid sandstone rock fragments are present in this petrofacies but are scarce (>5.5%). An enrichment of MRF is always observed (Figure 4d), together with significant amounts of radiolarite rock fragments and quartz-rich sandstone/siltstone rock fragments. Subordinate sandstone/siltstone rock fragments usually contain mica and opaques (RL).

In the conglomerate beds, the dominant clast types are siliciclastic red sandstone and microconglomerate pebbles (deriving from the Buntsandstein facies), together with low grade metamorphic clasts (slates and schists; Paleozoic), epidote-bearing dolerites (Triassic ophites), granitoids (Variscan), white quartz, green quartzites (Paleozoic), and black quartz clasts (Carboniferous radiolarites). Grey micritic limestones and dolostones (Mesozoic) and Devonian limestones are also present. Hybrid sandstone clasts are scarce.

In the Ainsa basin, siliciclastic dominant petrofacies are represented in the upper part of the Escanilla Formation (sample GRAD1; Figure 6), where metamorphic rock fragments such as metasiltstone, slate, and phyllite are overwhelming (Figure 4d).

In the Jaca basin, the Campodarbe and Bernués Formations display similar content to that of the upper part of the Escanilla Formation in the Ainsa basin. In the Rodellar and San Felices sections, this SD petrofacies is scarce. By contrast, to the west, the SD petrofacies dominates most of the Campodarbe Formation (Bibán, Monrepós, Gállego, Martés, Salinas, and Luesia sections; Figure 6). Only one sample of the Bernués Formation in the Monrepós section displays this petrofacies (BEMO-18).

Hybrid Clast-Dominated Petrofacies (HCD)

Limestone rock fragments are the most represented component in most of the samples of this petrofacies (>30.6%; Figure 4). However, the distinctive feature of this petrofacies (Figures 5C and S5d) is the high content (>8.4%) of hybrid sandstone/siltstone rock fragments (rock fragments that contain both extrabasinal and intrabasinal carbonate components in similar proportions) when compared to the other petrofacies. Silicic components such as metamorphic and siliciclastic sandstone rock fragments display a low abundance (<9.7 and <12.3%, respectively; Figure 4c,d).

In the conglomerate layers of this petrofacies, hybrid sandstone rock fragments (mainly derived from the recycling Eocene Hecho turbidites) and grey micritic limestones and dolostones (Mesozoic and lower Tertiary) dominate over the lithologies described in the "siliciclastic dominant" petrofacies (Permotriassic pebbles, low grade metamorphics, granitoids, white quartz, green quartzite, and radiolarites). Triassic dolerites have also been observed in the eastern sector of the basin. In the Bernués Formation (Gállego and Salinas section), clasts of metamorphic breccia (Ibarrondoa breccia; upper Cretaceous, North Pyrenean Zone) have been identified.

The HCD petrofacies dominates the Campodarbe deposits in the San Felices section (Figure 6), whereas in the south-west part of the basin, only the upper parts of this Formation (Rodellar-Bibán and Monrepós sections) record this petrofacies. The overlying Bernués Formation maintain these compositional features (Figures 4 and 6).

Mixed Lithic and Carbonatic Petrofacies (MLC)

This petrofacies (Figure 4a) is characterized by 20.9–45.9% carbonate grains (Figures 5D and S5e,f), including wackestone rock fragments containing *philonellid* tests (Turonian limestones from the southern Pyrenees). It also contains, as noncarbonate grains, up to 27.5% hybrid sandstone rock fragments and high proportions of lithic grains (20.9–45.9%; excluding hybrid sandstone rock fragments) such as metamorphic r.f., radiolarite r.f., siliciclastic sandstone, and volcanic lithic grains, as well as K-feldspar.

This petrofacies is observed in a limited number of samples (Figures 4 and 6) and shows two different sub-groups that can be identified in function of the lithic fragment types (Figure S6). In the Campodarbe Formation, it appears toward the top in the Monrepós section and extends to lower stratigraphic levels in the Gállego and Salinas sections (samples BEMO14, GAL7, GAL8, BAI3). It shows a significant enrichment in metamorphic rock fragments (MRF) and Fe-Oxide replacement r.f. (RL) (Figure S6). In contrast, in the transitional Martés deposits (sample MAR1) and in the alluvial Uncastillo Formation (samples LUE2, LUE3 and LUE5), lithic grains are enriched in silicified r.f. (Sil), radiolarite r.f (Rad), and volcanic r.f. (VRF).

The conglomerate layers of the Campodarbe Formation in the Gállego and Salinas sections display hybrid sandstone clasts (mainly Hecho Group turbidites; Eocene), low grade metamorphic clasts (slates and schists; Paleozoic), Permotriassic red sandstones, Devonian limestones, and grey micritic limestones and dolostones (Mesozoic). In the Monrepós area, epidote-bearing dolerites (Triassic ophites) are also present. In the Luesia section, the conglomerate pebbles are mainly dominated by hybrid sandstones and alveolina limestones. However, granitoids, diorites, basic volcanic rocks (Permian), siliciclastic red sandstone and microconglomerate (Buntsandstein facies), white quartz, green quartzite, and radiolarite are also common.

4.2. Heavy Minerals

Seventeen different transparent heavy minerals were successfully identified with the aid of Raman spectroscopy. Apatite (Ap), zircon (Zrn), tourmaline (Tur), rutile (Rt), epidote (Ep), titanite (Ttn), grossular (Grs), almandine (Alm), and staurolite (St) are the most abundant, whereas other transparent heavy minerals such as monazite (Mz), xenotime (Xtm), clinopyroxene (Cpx), spinel (Sp), sphalerite (Sph), chloritoid (Cld), andalusite (And), and kyanite (Ky) are scarce.

4.2.1. Heavy-Mineral Suites

We use correspondence analysis in order to explore similarities between the heavy-mineral content of samples and to define distinct heavy-mineral assemblages. Based on the results of the correspondence analysis (Figure 7), and the clear differences observed in the relative abundance of the heavy minerals (Figure S7), five different heavy-mineral suites can be labeled, based on the relative enrichment in Ap, ZTR (Zrn+Tur+Rt), Ep, St, Ttn, Grs, Alm, and other transparent heavy minerals (OtHM). The correspondence analysis (Figure 7a) provides evidence of the occurrence of an Ep+St+Ttn suite ("Ep dominated" suite), an Ap+ZTR suite ("Ap+ZTR dominated" suite), and a Grt+OtHM suite. However, this last mineral assemblage can be subdivided into a "Grs enriched" suite, an "Ep+St+Grs enriched" suite, and a "Ttn (+Grs +/−Ep) enriched" suite (Figure 7c), based on Grs, Ep, Ttn, St, and OtHM content.

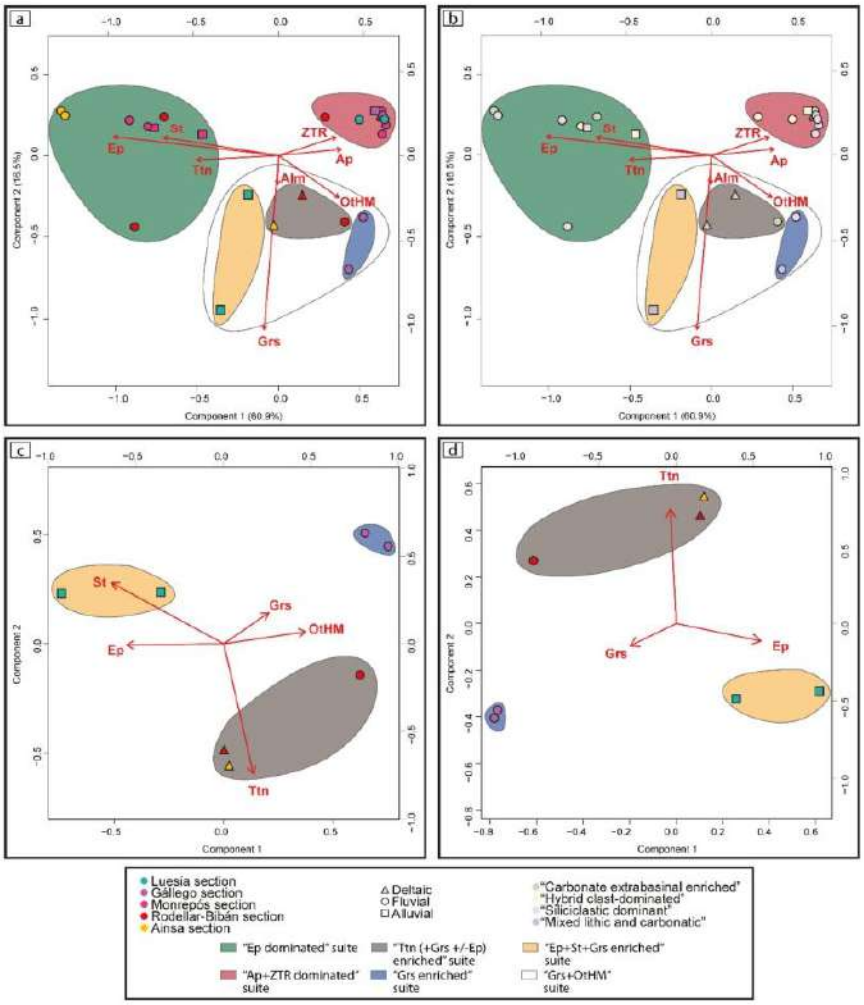

Figure 7. Heavy-mineral compositional plots. (**a**) Biplot displaying the results of correspondence analysis applied to all analyzed samples and considering all encountered minerals. OtHM include scarce minerals (Mz, Xtm, Cpx, Sp, Sph, Cld, And, and Ky). Colored symbols indicate sample's section. (**b**) Biplot displaying the results of correspondence analysis applied to all analyzed samples. Colored symbols indicate the petrofacies. (**c**) Biplot displaying the results of correspondence analysis applied to samples belonging to the Grs+OtHM enriched heavy-mineral suite only considering Grs, Ttn, Ep, St, and OtHM. (**d**) Biplot displaying the results of correspondence analysis applied to samples belonging to the Grs+OtHM enriched heavy-mineral suite only considering Grs, Ttn, and Ep.

"Grs (+Ttn +/−Ep) Enriched" Suite

This is the oldest mineral suite recorded in the study area, and it is dominated by ZTR (26.7–49.1%) and Ap (22.1–23.8%). However, it shows an important enrichment in Grs (12.1–16.0%), Ttn (5.6–13.8%), and Ep (0.0–12.0%) (Figure S7). The most characteristic feature of this assemblage is its Ttn content (Figure 7c,d). This suite occurs in the oldest deposits of the Ainsa and Jaca basins (the Sobrarbe delta, the Belsué-Atarés delta, and the lower fluvial Campodarbe Formation; Figures 7c and 8a) and is restricted to the easternmost sector of the study area.

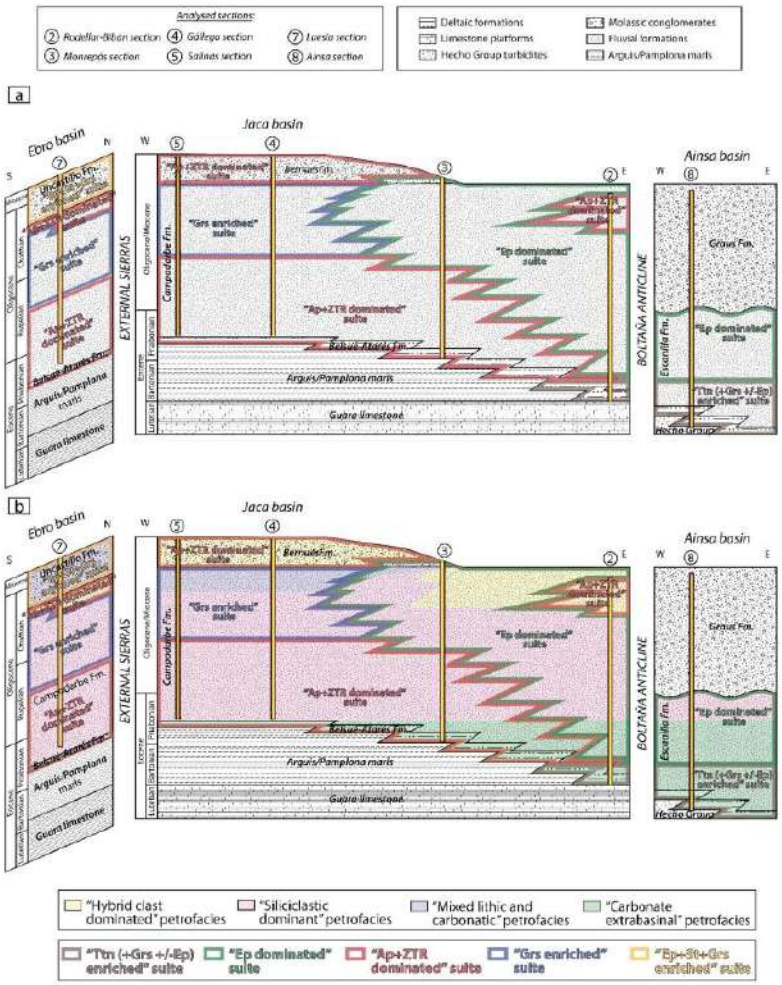

Figure 8. **(a)** Colored stratigraphic cross-section in order to illustrate the distribution of the heavy-mineral suites laterally and through time. (b) Colored stratigraphic cross-section in order to illustrate the distribution of the petrofacies and heavy-mineral suites laterally and through time.

"Ap+ZTR Dominated" Suite

The distinctive feature of this suite is the dominance of Ap and ZTR. Together, they represent more than 87.7% of the mineral spectra, reaching up to 98.1% in the middle Campodarbe Formation in the Monrepós section (BEMO-8). Although OtHM (such as Cld, Mz, Xtm, or Sp) are scarce, this suite shows an enrichment in this component. The suite occurs in the Belsué-Atarés deltaic formation in the Nocito area (west of the Rodellar section) and dominates the lower and middle Campodarbe Formation in the Monrepós and Gállego sections, as well as the Bernués Formation in the Gállego area (Figure 8a). In the Ebro basin, it is present along the whole sedimentary record of the Campodarbe Formation. By contrast, in the Ainsa basin, this assemblage is not represented.

"Ep Dominated" Suite

The main feature of this assemblage is the overwhelming presence of Ep, always higher than 40.5%, and reaching up to 77.4% in the lower Escanilla Fm in the Ainsa basin

(Figure 8a). This suite is found only in the eastern sector of the study area (Ainsa and eastern Jaca basin), dominating the fluvial Escanilla and Campodarbe Formations, but interestingly, it does not extend to the equivalent units of the western part of the Jaca basin (Gállego and Salinas sections). Its first appearance in the analyzed sections occurs in the upper Bartonian in the Ainsa and Bibán sections, whereas at Monrepós, it is not recorded until the Oligocene (upper Campodarbe).

"Grs Enriched" Suite

Although this suite is mainly dominated by Ap and ZTR (70.5–79.5%; Figures S7 and 7c,d), its remarkable feature is that it displays an enrichment in Grs (14.5–23.3%), Ep is absent, and Ttn scarce (0.5%). It occurs in the middle-upper Campodarbe deposits of the Gállego, Salinas, and Luesia sections (Figure 8a).

"Ep+St+Grs Enriched" Suite

This suite displays a Grs content (13.7–30.8%) similar to that of the Grs enriched suite (Figure S7), but it is always accompanied by remarkable proportions of Ep (24.0–27.6%; more than the Grs+Ttn+/−Ep enriched suite; Figure 7d) and St (Figure 7c); Ttn is scarce (1.5–1.9%). Ap+ZTR contents (33.9–53.9%) are much lower than in the Grs enriched and the Ap+ZTR dominated suites. The suite is only recorded in the Ebro basin, in the alluvial deposits of the Luesia fan (top of the Luesia section).

5. Discussion

5.1. Considerations about the Heavy-Mineral Detrital Signatures

The original detrital heavy-mineral suites derived from a source rock might be altered through a series of processes. Among them, dissolution during deep burial diagenesis is the most critical in old sedimentary rocks [130–132,145–147]. Therefore, it is important to assess the possible diagenetic overprint prior to extract potentially biased conclusions about the provenance and connectivity of the studied deposits. In the Jaca basin, the sharp appearance of epidote in the record, the low paleotemperatures experienced by the studied sedimentary rocks (<50 °C) [32,148], and the absence of advanced dissolution features in the more unstable minerals [149], such as epidote or titanite, point to a very low impact of diagenesis on the detrital heavy-mineral suites. Therefore, we can infer that heavy-mineral data are reflecting provenance features instead of burial-related overprint.

5.2. Provenance Implications and Evolution of Source Areas

Sandstone detrital modes and heavy minerals in the Jaca basin indicate more than a single source area, evidencing the interplay between fluvial–alluvial systems of diverse provenance from Eocene to Miocene times. The four petrofacies and the five heavy-mineral suites established in this study allow a better discrimination of these source areas, as well as the identification of different sediment routings and their evolution through time. These inferences are here discussed in terms of provenance and connectivity, based on an integrated approach that encompasses the petrofacies and the heavy-mineral suites.

The Belsué-Atarés Formation represents the first deltaic unit registered in the southern border of the Jaca basin (Figure 8). "Carbonate extrabasinal enriched" petrofacies is distinctive on this formation. The petrographic signatures are characterized by a dominance of carbonate grains, with subordinate plutonic rock fragments. Together with paleocurrents and facies architecture [23,59], these petrographic signatures support a provenance from the east, in the central Pyrenees. This source area would have included the Paleozoic basement of the Axial Zone, which provided significant amounts of plutonic components, together with Mesozoic and Paleocene limestones, which mainly delivered a wide range of carbonate grains. The compositional similarity ("carbonate extrabasinal enriched" petrofacies with "Ttn+Grs(+/−Ep) enriched" suite) between the Sobrarbe (Ainsa) and Belsué-Atarés (Jaca) Formations implies that they were connected during Lutetian–Bartonian times (Figure 8b).

During the Bartonian, this source continued supplying sediment to the Ainsa basin, feeding the fluvial Escanilla Formation, and transferring sediment to the Campodarbe and Belsué-Atarés Formations in the eastern part of the Jaca basin. From the middle Bartonian onwards, the Escanilla Formation displays the "Ep dominated" suite, which can be traced to the Jaca basin in its easternmost part (Figure 8). The main characteristic of this assemblage is the overwhelming content of epidote, pointing to a source with abundant Triassic dolerites [39,118]. Compositional similarity between the Campodarbe Formation and the Escanilla Formation (both formations display CEE petrofacies and Ep dominated suite) implies connectivity between the two fluvial units.

However, it is remarkable that, during the Bartonian, west of the Rodellar-Bibán section, the Campodarbe Formation displays the other distinct heavy-mineral suite, the "Ap+ZTR dominated". Idiomorphic Ap and ZTR in this suite can be linked to granitic sources [39], whereas the more rounded Ap and ZTR grains can be attributed to the recycling of the siliciclastic Mesozoic (i.e., Vallcarga Fm. [150]) and Paleocene sedimentary cover (i.e., Tremp Fm. [43]), but the lack of epidote is evidence of the lack of Triassic dolerites in the source area. The occurrence of the two different heavy-mineral suites in different outcrops of the Campodarbe Formation with the same petrofacies points to the contribution by two distinct fluvial systems following different routings, one feeding the eastern part of the basin, sourced from the central Pyrenees (where abundant Triassic dolerites occur), and the other feeding the western part, sourced from the eastern Pyrenees.

During the Priabonian, paleocurrent directions and facies architecture continue indicating an eastern provenance for the Campodarbe Formation, but a change of the petrofacies typology (from CEE to SD) is evidence of a shift in the source area, marked by an increase in metamorphic rock fragments. This shift indicates a persisting input from the Paleozoic basement but highlights a major change in the sourcing lithologies within the Axial Zone. Nonetheless, the new petrofacies (SD) still displays the two former heavy-mineral suites ("Ep dominated" and "Ap+ZTR dominated"; Figure 8b). The "Ep dominated" suite is evidence of the continued presence of Triassic dolerites in the source area, whereas the "Ap+ZTR dominated" suite points to the lack of these rocks. The dominance of Ap and ZTR in the heavy mineral provenance signal, together with the abundance of metamorphic rock fragments and siliciclastic sandstone, can be related to sources with a very low to low degree of metamorphism, as well as to the recycling of Carboniferous and Permo–Triassic siliciclastic sandstones [39].

The change from the CEE to the SD petrofacies is also identified in the upper part of the Escanilla Formation, in the Ainsa basin (Ainsa section), as well as in the Campodarbe Formation, in the Jaca basin (Rodellar-Bibán and Monrepós sections; Figure 6). Therefore, these sections record the evolution of the central and eastern Pyrenean sources, from a plutonic dominated toward a metamorphic dominated source area, that could be linked to a reorganization of the drainage area in the Axial Zone caused by uplift or thrust emplacement in the source area [30,151–153]. However, the compositional difference recorded by the heavy-mineral detrital signatures highlights the persistence of the two different axially-fed east-sourced systems from late Bartonian (Figure 8).

Moreover, during the Priabonian, the northeastern part of the basin (San Felices section) records the onset of north-sourced sediments, evidenced by the substitution of the "carbonate extrabasinal enriched" for the "hybrid clast-dominated" petrofacies. By contrast, the advent of north-sourced sediments to the southern margin of the Jaca basin (transverse-fed system) (Figure 6) takes place during the Oligocene as shown by the substitution of the "siliciclastic dominant" petrofacies (associated with the eastern provenance of the axially-fed systems) by the "hybrid clast-dominated" petrofacies (transverse system).

As in the former described petrofacies, the "hybrid clast-dominated" petrofacies displays two distinct heavy-mineral suites. The "Ap+ZTR dominated" suite can be attributed to the recycling of the Eocene turbidite basin [39] (north of the Jaca basin). By contrast, the "Ep dominated suite" is evidence of the strong eastern contribution and the mixing of the axial and transverse systems in the eastern part of the basin. This mixing is also

evidenced by the occurrence of the "mixed lithic and carbonatic" petrofacies at the top of the Monrepós section, resulting from the interplay of the "hybrid clast-dominated" petrofacies with the "siliciclastic dominant" petrofacies.

In the western part of the basin (Gállego and Salinas sections), the mixing between the axial and transverse systems is also registered by the "mixed lithic and carbonatic petrofacies, which displays a "Grs enriched" suite (Figure 8), evidencing the interplay between the "siliciclastic dominant Grs enriched" axial system and the "hybrid clast-dominated Ap+ZTR dominated" transverse system.

Therefore, in the Jaca basin, the different heavy mineral provenance signatures recorded in the eastern and western areas allow to characterize two axially-fed, east-sourced fluvial systems that coexisted during the sedimentation of the Campodarbe Fm, which is at variance with the classical sedimentological model of a unique fluvial system transferring sediments from east to west [23]. The fluvial Campodarbe Fm displays coarser grain-sizes in the eastern part of the basin and finer grain sizes to the west. This shift was interpreted as a facies change of the same fluvial course, with its proximal facies located to the east and the distal to the west. Nevertheless, the different heavy mineral provenance signatures reveal that, in fact, this facies change corresponds to two different fluvial networks with different source areas instead of to proximal-distal parts of a unique fluvial system. The easternmost fluvial system ("Ep dominated") could correspond to the Bibán fluvial facies of Puigdefàbregas [23], which laterally passes northwest to the fluvio–lacustrine facies of Santa Cruz-Bailo. Meanwhile, the westernmost fluvial system ("Ap+ZTR dominated") would correspond to the Monrepós-Anzánigo fluvial facies, laterally passing to the west to the fluvio–lacustrine facies of Javier-Pintano-Villalangua.

Much more to the west, in the Luesia section, the lower Campodarbe Formation does not show significant variations with its equivalents located in the Jaca basin. At the upper part, it records the irruption of the transverse-fed system characterized by the "hybrid clast dominated" petrofacies and the "Ap+ZTR dominated" suite (Figure 8b). To the top, an abrupt provenance change is recorded by the Oligo–Miocene alluvial deposits of the Luna fan (Uncastillo Formation, in the Ebro basin), evidenced by the occurrence of the "mixed lithic and carbonatic" petrofacies and the "Ep+St+Grs enriched" suite, only recorded in these alluvial deposits (Figure 8b). This provenance signature contrasts with its time equivalent Bernués Formation, which characterizes the north-derived alluvial sedimentation more to the east (Gállego and Salinas sections). Although some components are common, the relatively high content of siliciclastic sandstone, radiolarite, and volcanic rock fragments allow to infer a distinctive source area for the conglomerates of the Luna fan, which is also highlighted by the enrichment of epidote, titanite, and grossular in the heavy-mineral detrital signatures.

It follows that the abundant siliciclastic content of the Luna fan cannot be derived from the same source areas of the hybrid sandstone and carbonate-rich San Juan de la Peña and Peña Oroel fans (Bernués formation), located straight north of the Luesia area [30]. Hence, we propose that the source area of the Luna fan was located in the western Pyrenees, in the Paleozoic Basque massifs (Figure 1), which account for this distinctive petrologic signature. The work by Hirst and Nichols [53] also pointed to this western source, based on heavy mineral data from the Luna fan. All these are in agreement with thermochronological data from the Axial Zone of the western Pyrenees, which show older exhumation ages than the Axial Zone of the west-central Pyrenees [154–156].

The interpretation of the "mixed lithic and carbonate" petrofacies recorded in the Martés sandstone in the northwestern part of the Jaca basin is more challenging. The siliciclastic content of this unit is very close to the composition described in the Luna alluvial fan, which could indicate the same source area for both, located to the northwest, in the western Pyrenees. This interpretation would discard an eastern source area from the central Pyrenees, as assumed before, according to the low content on metamorphic rock fragments. Nonetheless, this interpretation is not in accordance with north-west paleocurrent directions reported for the Martés sandstone by Puigdefàbregas [23], which imply a north-west

directed paleoflow, probably derived from eastern source areas according to late Eocene basin paleogeography.

5.3. Functioning of the Sediment Routing Systems

During late Lutetian to Bartonian times (Figure 9a), deltaic sedimentation in the southern Jaca basin was mainly derived from eastern source areas. These sources were the Paleozoic basement and the Mesozoic and Paleogene sedimentary cover of the growing central Pyrenees. The Paleozoic source rocks contributed by delivering plutonic components trough a unique fluvial system for the first stage of deltaic sedimentation (late Lutetian to Bartonian). However, from the late Bartonian onwards, heavy-mineral detrital signatures reveal that two distinct axially-fed fluvial systems from the central-east Pyrenees were delivering sediment to the basin; one dominated by epidote and the other dominated by ultrastable apatite, zircon, tourmaline, and rutile (Ap+ZTR). The first one fed the easternmost sector of the Jaca basin through the Escanilla sediment routing system [28]. The other extended its influence to the westernmost area and must have entered the basin following a more meridional sediment routing through the Priabonian Salinar and/or the Rupelian lower Peraltilla Formations of the autochthonous foreland basin [157], which are characterized by absent or scarce epidote (Figure 9b). The axially-fed system enriched in epidote is sourced from the central Pyrenees, from the same source areas as the Sis and Gurp alluvial fan conglomerates, where Triassic dolerite rock fragments (bearing abundant epidote) are frequent (northern part of the Central South Pyrenean Unit), with abundant Keuper diapiric occurrences [158–160]. However, the Ap+ZTR dominant system must be sourced from a farther, more eastern sector of the southern Pyrenees, where Triassic dolerites of the Keuper facies are less abundant or absent (Pedraforca-Port del Comte area and present-day Segre Valley, Eastern Pyrenees).

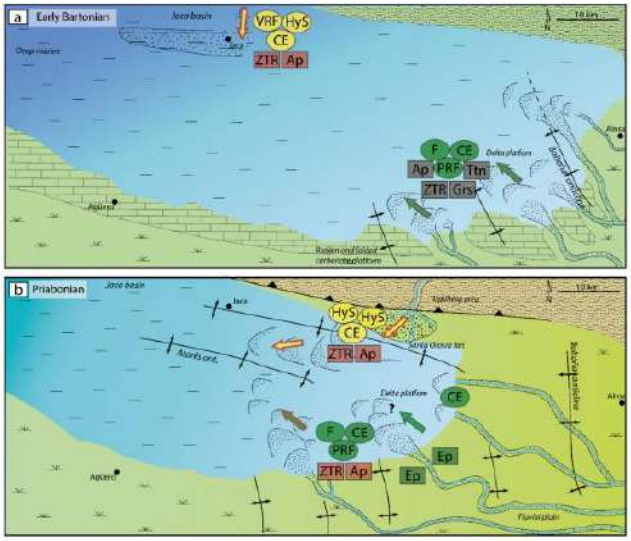

Figure 9. Paleogeographic scheme of the Jaca basin during Bartonian–Priabonian times. (**a**) Early Bartonian. (**b**) Priabonian. Circles and squares highlight distinct components. PRF: plutonic rock fragments, F: feldspar grains, CE: carbonate extrabasinal grains, HyS: hybrid sandstone rock fragments, VRF: volcanic rock fragments, Ap: apatite, ZTR: ZTR, Ep: epidote, Grs: grossular, Ttn: titanite. Circle colors correspond to petrofacies described in Figure 4. Square colors correspond to heavy-mineral suites described in Figure 7. Arrows indicate petrofacies (fill) and heavy-mineral suite (stroke). Reconstruction of the maps based on Puigdefàbregas, Bentham et al., Hogan, Montes, Caja et al., Huyghe et al., Roigé et al., Boya, Coll et al. [23,24,27,29,30,39,63,67,72,76,97].

Both differentiated fluvial systems persisted but evolved to a more dominant metamorphic composition that persisted from middle Priabonian until at least Chattian–Aquitanian times (Figure 10a), as demonstrated by the compositional features of the upper Campodarbe Formation.

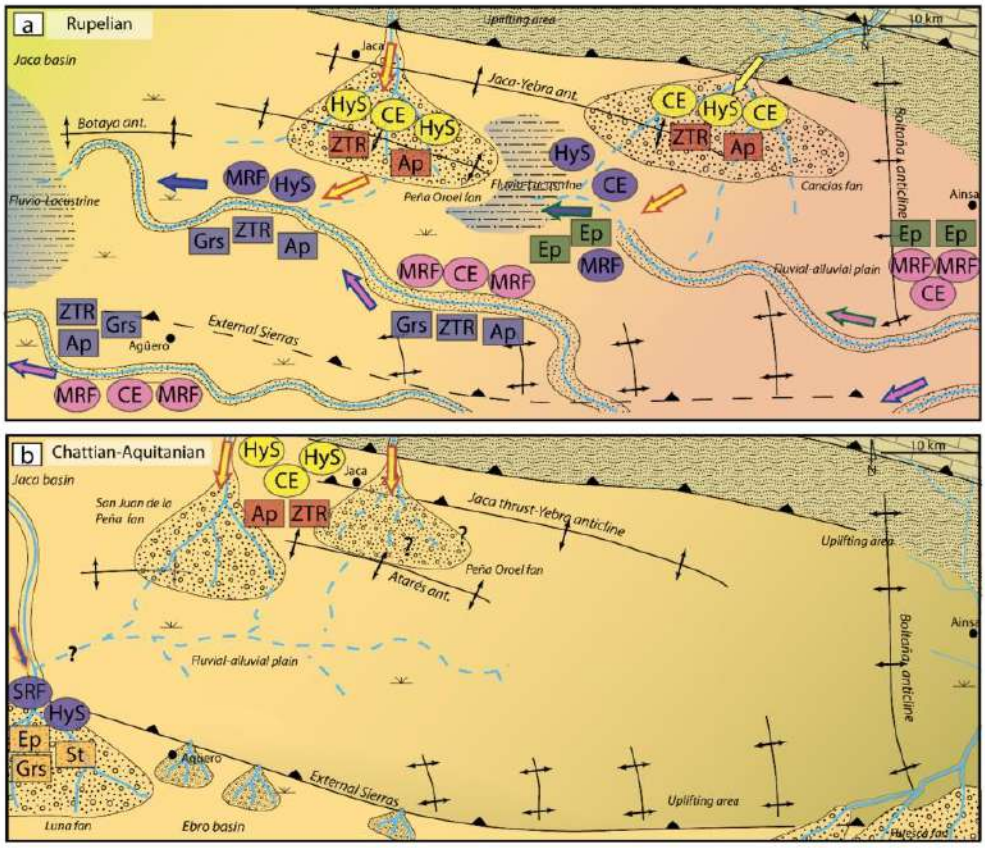

Figure 10. Paleogeographic scheme of the Jaca and Ebro basins during Rupelian–Aquitanian times. (**a**) Rupelian. (**b**) Chattian–Aquitanian. Circles and squares highlight distinct components. MRF: metamorphic rock fragments, SRF: sedimentary rock fragments, CE: carbonate extrabasinal grains, HyS: hybrid sandstone rock fragments, Ap: apatite, ZTR: ZTR, Ep: epidote, Grs: grossular, Ttn: titanite, St: staurolite. Circle colors correspond to petrofacies described in Figure 4. Square colors correspond to heavy-mineral suites described in Figure 7. Arrows indicate petrofacies (fill) and heavy-mineral suite (stroke). Reconstruction of the maps based on Hirst and Nichols, Puigdefábregas, Friend et al., Arenas, Nichols and Hirst, Jones, Roigé et al., Boya, Coll et al. [23,29,30,39,53,76,97,99,161–163].

Moreover, during this time, northern sources, mainly composed by the Eocene Group turbidites, were uplifted in the northern Jaca basin by the activity of the Gavarnie thrust. These source areas led to progressive mixing and finally caused the replacement of the two distinct axial-fed fluvial systems by transverse north-derived alluvial systems, producing a westward and southward displacement of the axial fluvial network.

The later stages of the Jaca basin (Figure 10b) were determined by the activity of the Guarga thrust that produced the uplift of the basin margins (External Sierras) preventing the axial fluvial network to enter the basin. The Chattian to Aquitanian period was mainly characterized by two north-derived systems from different source areas. For the Bernués

Formation (Jaca basin), the source area was situated immediately to the north of the basin, composed by the Hecho Group turbidites and the North Pyrenean Zone [30], although in the eastern sector the influence of the east-derived systems persisted in the first stages of the sedimentation. In contrast, the source area for the Uncastillo Formation (Ebro basin) was located in the western Pyrenees, composed by the Paleozoic basement Basque massifs and the earlier foreland deposits (Hecho Group and Campodarbe Formations).

6. Conclusions

The combination of new sandstone petrography and heavy-mineral data allowed to constrain the interplay of diverse sediment routing systems in the transitional to terrestrial environments of the Jaca thrust-sheet-top basin and the Ebro autochthonous basin during Lutetian to Miocene times. Additional data of the equivalent sedimentary systems of the Ainsa basin more to the east allowed for a better characterization of the evolution of eastern source areas.

Deltaic sedimentation in the southern Jaca basin (Bartonian–Priabonian) was mainly derived from eastern source areas, located in the central Pyrenees, in which the Paleozoic basement contributed by delivering dominant plutonic components.

During Priabonian times, the Campodarbe Formation records a change in the source area that yielded to the evolution of a Paleozoic source richer in metamorphic rocks, a signature that persisted until at least Oligo–Miocene times. However, heavy-mineral detrital signatures evidence that two distinct major fluvial systems coexisted, one sourced from the central Pyrenees and the other from the eastern Pyrenees, delivering sediment to different parts of the basin. This differentiation (Figure 11) could not have been made without the aid of the heavy mineral analysis.

On the other hand, north-derived transverse fluvial systems eventually replaced the axial systems, progressing from east to west. In the Chattian to Aquitanian record, two main north-derived systems can be distinguished in the Jaca and Ebro basins. Whereas in the Jaca basin, the Bernués Formation came from source areas comprising the North Pyrenean Zone and, more importantly, the uplifted Eocene foreland basin, the coetaneous Uncastillo Formation of the Ebro basin was sourced from the western Pyrenees, comprising the Paleozoic Basque massifs and also by previous foreland deposits.

This work highlights how the integration of sandstone petrography and heavy mineral analysis provides a higher resolution to characterize the evolution of sediment routing systems from a "source-to-sink" approach. Our study provides evidence that the coupling of these techniques is a much more powerful tool that can resolve aspects of the routing systems that could not be disentangled by one method alone. Although, nowadays, the integration of sandstone petrography and heavy mineral analysis is considered as time-consuming and rarely used, this work argues that it is the best approach to fully characterize source-to-sink relationships in a clastic sedimentary basin.

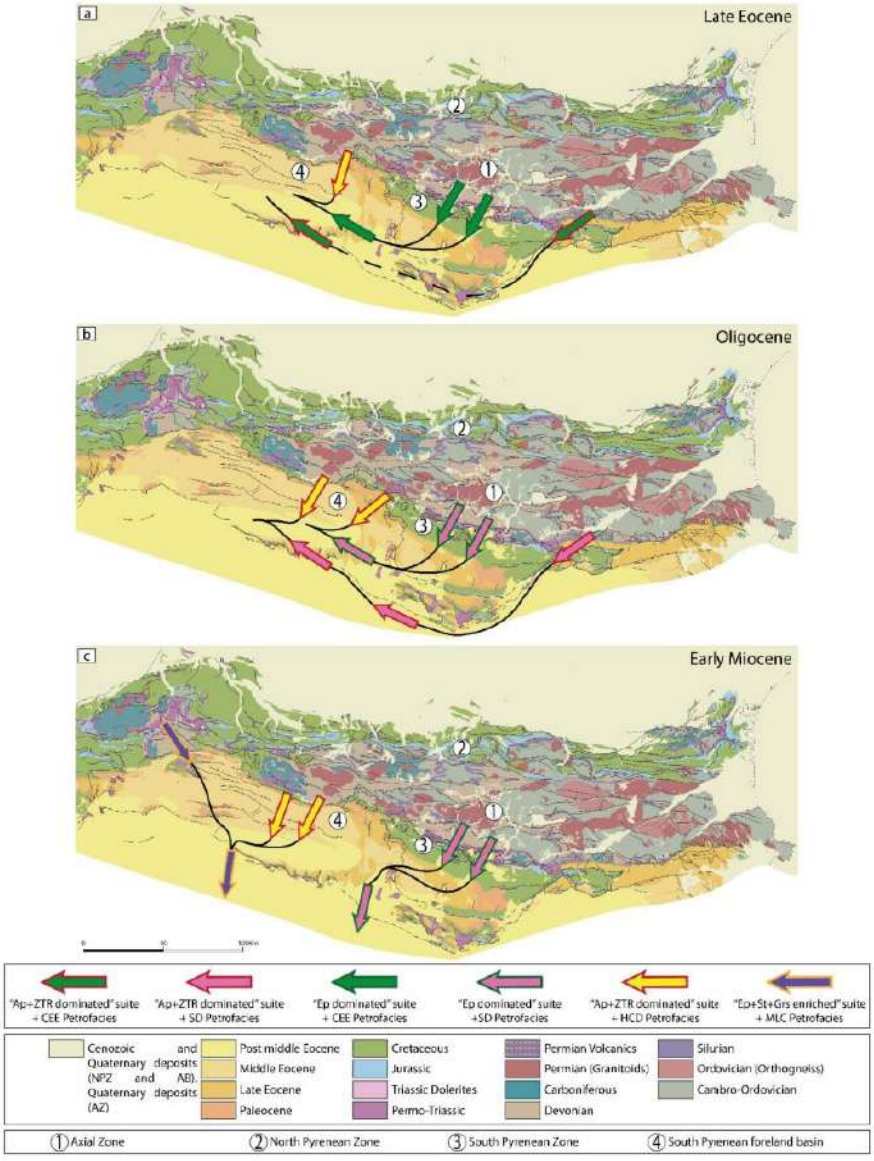

Figure 11. Summary of source areas and sediment routings in the South Pyrenean Basin from late Eocene to early Miocene displayed in a present-day map, not restored. Coarse arrows indicate composition of source areas (stroke color: heavy-mineral suite, fill: petrofacies). Thin arrows indicate sediment routing approximately. **(a)** Late Eocene routing systems. Two different axially-fed east sourced systems (one more meridional) coexist with a transverse-fed north sourced system supplying the Jaca basin. **(b)** Oligocene routing systems. Two different axially-fed east sourced systems (one more meridional) coexist with two transverse-fed north sourced systems supplying the Jaca basin. **(c)** Early Miocene routing systems. Two different transverse-fed north sourced systems supply sediment to the Ebro basin in the western area, whereas in the eastern part, two transverse-fed north sourced systems supply the Huesca fan.

Supplementary Materials: The following information is available online at https://www.mdpi.com/article/10.3390/min12020262/s1, Figure S1: Representative Raman spectra of heavy minerals from the late Eocene–Miocene Jaca basin, Figure S2: Optical photomicrographs of distinct extrabasinal grains, Figure S3: Compositional plots for all the analyzed samples, Figure S4: Images of the appearance of each of the described petrofacies in the conglomerate-sized deposits, Figure S5: Biplot of the two sub-groups of the MLC petrofacies, Figure S6: Heavy-mineral percentage pie charts for all the analyzed samples in a general stratigraphic cross-section sketch, Figure S7. Heavy-mineral percentage pie charts for all the analyzed samples in a general stratigraphic cross-section sketch. Table S1: Sandstone compositional data (point counting analyses), Table S2: Heavy-mineral compositional data (point counting analyses), Sample coordinates: Geographic coordinates of the studied samples.

Author Contributions: Conceptualization, D.G.-G., M.R., X.C., S.B., and A.T.; methodology, D.G.-G., M.R., X.C., and N.M.; formal analysis, X.C., and M.R.; investigation, X.C., M.R., D.G.-G., and S.B.; data curation, X.C., M.R., D.G.-G., and S.B.; writing—original draft preparation, X.C., and M.R.; writing—review and editing, X.C., M.R., D.G.-G., A.T., S.B., and N.M.; visualization, X.C, M.R., and D.G.-G.; supervision, D.G.-G., M.R., and A.T.; project administration and funding acquisition, A.T. All authors have read and agreed to the published version of the manuscript.

Funding: This research was funded by the projects CGL2014-54180-P and PGC2018-093903-B-C21, financed by the Ministerio de Economia y Competitividad (MINECO) and Ministerio de Ciencia, Inovación y Universidades (MCIU) of Spain. X. Coll acknowledges support from the Ministerio de Cultura, Deporte y Educacción (MECD) of Spain (FPU16/00219).

Institutional Review Board Statement: Not applicable.

Informed Consent Statement: Not applicable.

Data Availability Statement: The data presented in this study are available in the Supplementary Materials here.

Acknowledgments: We are very grateful to the anonymous reviewers for providing constructive reviews that helped to improve the original paper.

Conflicts of Interest: The authors declare no conflict of interest. The funders had no role in the design of the study; in the collection, analyses, or interpretation of data; in the writing of the manuscript; or in the decision to publish the results.

References

1. Dickinson, W.R. Interpreting detrital modes of graywacke and arkose. *J. Sediment. Res.* **1970**, *40*, 695–707.
2. Dickinson, W.R.; Suczek, C.A. Plate tectonics and sandstone compositions. *Am. Assoc. Pet. Geol. Bull.* **1979**, *63*, 2164–2182.
3. Steidtmann, J.R.; Schmitt, J.G. Provenance and dispersal of tectogenic sediments in thin-skinned, thrusted terrains. In *New Perspectives in Basin Analysis. Frontiers in Sedimentary Geology*, 1st ed.; Kleinspehn, K.L., Paola, C., Eds.; Springer: New York, NY, USA, 1988; pp. 353–366.
4. Graham, S.A.; Tolson, R.B.; DeCelles, P.G.; Ingersoll, R.V.; Bargar, E.; Caldwell, M.; Cavazza, W.; Edwards, D.P.; Follo, M.F.; Handschy, J.F.; et al. Provenance modelling as a technique for analysing source terrane evolution and controls on foreland sedimentation. *Basins* **1986**, *8*, 425–436.
5. Haughton, P.D.W.; Todd, S.P.; Morton, A.C. Sedimentary provenance studies. *Geol. Soc. Lond. Spec. Publ.* **1991**, *57*, 1–11. [CrossRef]
6. Mange-Rajetzky, M.A. Subdivision and correlation of monotonous sandstone sequences using high-resolution heavy mineral analysis, a case study: The Triassic of the Central Graben. *Geol. Soc. Lond. Spec. Publ.* **1995**, *89*, 23–30. [CrossRef]
7. Von Eynatten, H.; Dunkl, I. Assessing the sediment factory: The role of single grain analysis. *Earth Sci. Rev.* **2012**, *115*, 97–120. [CrossRef]
8. Garzanti, E.; Limonta, M.; Resentini, A.; Bandopadhyay, P.C.; Najman, Y.; Andò, S.; Vezzoli, G. Sediment recycling at convergent plate margins (Indo-Burman ranges and Andaman–Nicobar Ridge). *Earth Sci. Rev.* **2013**, *123*, 113–132. [CrossRef]
9. Kilhams, B.; Morton, A.; Borella, R.; Wilkins, A.; Hurst, A. Understanding the provenance and reservoir quality of the Sele Formation sandstones of the UK Central Graben utilizing detrital garnet suites. *Geol. Soc. Lond. Spec. Publ.* **2014**, *386*, 129–142. [CrossRef]
10. Caracciolo, L.; Garzanti, E.; Von Eynatten, H.; Weltje, G.J. Sediment generation and provenance: Processes and pathways. *Sediment. Geol.* **2016**, *336*, 1–2. [CrossRef]

11. Dickinson, W.R. Provenance and sediment dispersal in relation to paleotectonics and paleogeography of sedimentary basins. In *New Perspectives in Basin Analysis. Frontiers in Sedimentary Geology*, 1st ed.; Kleinspehn, K.L., Paola, C., Eds.; Springer: New York, NY, USA, 1988; pp. 3–25.
12. Nie, J.; Horton, B.K.; Saylor, J.E.; Mora, A.; Mange, M.; Garzione, C.N.; Basu, A.; Moreno, C.J.; Caballero, V.; Parra, M. Integrated provenance analysis of a convergent retroarc foreland system: U–Pb ages, heavy minerals, Nd isotopes, and sandstone compositions of the Middle Magdalena Valley basin, northern Andes, Colombia. *Earth Sci. Rev.* **2012**, *110*, 111–126. [CrossRef]
13. Garzanti, E. From static to dynamic provenance analysis—Sedimentary petrology upgraded. *Sediment. Geol.* **2016**, *336*, 3–13. [CrossRef]
14. Caracciolo, L.; Andò, S.; Vermeesch, P.; Garzanti, E.; McCabe, R.; Barbarano, M.; Paleari, C.; Rittner, M.; Pearce, T.T. A multidisciplinary approach for the quantitative provenance analysis of siltstone: Mesozoic Mandawa Basin, southeastern Tanzania. *Geol. Soc. Lond. Spec. Publ.* **2020**, *484*, 275–293. [CrossRef]
15. McKellar, Z.; Hartley, A.J.; Morton, A.C.; Frei, D.A. multidisciplinary approach to sediment provenance analysis of the late Silurian–Devonian Lower Old Red Sandstone succession, northern Midland Valley Basin, Scotland. *J. Geol. Soc. Lond.* **2020**, *177*, 297–314. [CrossRef]
16. Von Eynatten, H.; Gaupp, R. Provenance of Cretaceous synorogenic sandstones in the Eastern Alps: Constraints from framework petrography, heavy mineral analysis and mineral chemistry. *Sediment. Geol.* **1999**, *124*, 81–111. [CrossRef]
17. Morton, A.; Hallsworth, C.; Chalton, B. Garnet compositions in Scottish and Norwegian basement terrains: A framework for interpretation of North Sea sandstone provenance. *Mar. Pet. Geol.* **2004**, *21*, 393–410. [CrossRef]
18. Mange, M.A.; Dewey, J.F.; Wright, D.T. Heavy minerals solve structural and stratigraphic problems in Ordovician strata of the western Irish Caledonides. *Geol. Mag.* **2003**, *140*, 25–30. [CrossRef]
19. Garzanti, E.; Andò, S. Plate tectonics and heavy mineral suites of modern sands. *Dev. Sedimentol.* **2007**, *58*, 741–763.
20. Garzanti, E.; Doglioni, C.; Vezzoli, G.; Ando, S. Orogenic belts and orogenic sediment provenance. *J. Geol.* **2007**, *115*, 315–334. [CrossRef]
21. Garzanti, E.; Vermeesch, P.; Padoan, M.; Resentini, A.; Vezzoli, G.; Andò, S. Provenance of passive-margin sand (Southern Africa). *J. Geol.* **2014**, *122*, 17–42. [CrossRef]
22. Fossum, K.; Morton, A.C.; Dypvik, H.; Hudson, W.E. Integrated heavy mineral study of Jurassic to Paleogene sandstones in the Mandawa Basin, Tanzania: Sediment provenance and source-to-sink relations. *J. Afr. Earth. Sci.* **2019**, *150*, 546–565. [CrossRef]
23. Puigdefábregas, C. *La sedimentación molásica en la cuenca de Jaca*; Número Extraordinario de Revista Pirineos; Instituto de Estudios Pirenaicos: Jaca, Spain, 1975; Volume 104, pp. 1–188.
24. Bentham, P.A.; Burbank, D.W.; Puigdefabregas, C. Temporal and spatial controls on the alluvial architecture of an axial drainage system: Late Eocene Escanilla Formation, southern Pyrenean foreland basin, Spain. *Basin Res.* **1992**, *4*, 335–352. [CrossRef]
25. Dreyer, T.; Corregidor, J.; Arbues, P.; Puigdefabregas, C. Architecture of the tectonically influenced Sobrarbe deltaic complex in the Ainsa Basin, northern Spain. *Sediment. Geol.* **1999**, *127*, 127–169. [CrossRef]
26. Vincent, S.J. The Sis palaeovalley: A record of proximal fluvial sedimentation and drainage basin development in response to Pyrenean mountain building. *Sedimentology* **2001**, *48*, 1235–1276. [CrossRef]
27. Caja, M.A.; Marfil, R.; Garcia, D.; Remacha, E.; Morad, S.; Mansurbeg, H.; Amorosi, A.; Martínez-Calvo, C.; Lahoz-Beltrá, R. Provenance of siliciclastic and hybrid turbiditic arenites of the Eocene Hecho Group, Spanish Pyrenees: Implications for the tectonic evolution of a foreland basin. *Basin Res.* **2010**, *22*, 157–180. [CrossRef]
28. Michael, N. Functioning of an Ancient Routing System, the Escanilla Formation, South Central Pyrenees. Ph.D. Thesis, Imperial College London, London, UK, 2013.
29. Roigé, M.; Gómez-Gras, D.; Remacha, E.; Daza, R.; Boya, S. Tectonic control on sediment sources in the Jaca basin (Middle and Upper Eocene of the South-Central Pyrenees). *C. R. Geosci.* **2016**, *348*, 236–245. [CrossRef]
30. Roigé, M.; Gómez-Gras, D.; Remacha, E.; Boya, S.; Viaplana-Muzas, M.; Teixell, A. Recycling an uplifted early foreland basin fill: An example from the Jaca basin (Southern Pyrenees, Spain). *Sediment. Geol.* **2017**, *360*, 1–21. [CrossRef]
31. Thomson, K.D.; Stockli, D.F.; Clark, J.D.; Puigdefàbregas, C.; Fildani, A. Detrital zircon (U-Th)/(He-Pb) double-dating constraints on provenance and foreland basin evolution of the Ainsa Basin, south-central Pyrenees, Spain. *Tectonics* **2017**, *36*, 1352–1375. [CrossRef]
32. Labaume, P.; Meresse, F.; Jolivet, M.; Teixell, A.; Lahfid, A. Tectonothermal history of an exhumed thrust-sheet-top basin: An example from the south Pyrenean thrust belt. *Tectonics* **2016**, *35*, 1280–1313. [CrossRef]
33. Pocoví, A.; Millán, H.; Navarro, J.J.; Martínez, M.B. Rasgos estructurales de la Sierra de Salinas y zona de los Mallos (Sierras Exteriores, Prepirineo, provincias de Huesca y Zaragoza). *Geogaceta* **1990**, *8*, 36–39.
34. Teixell Cácharo, A.; García-Sansegundo, J. Estructura del sector central de la Cuenca de Jaca (Pirineos meridionales). *Rev. Soc. Geol. Esp.* **1995**, *8*, 215–228.
35. Teixell, A. The Ansó transect of the southern Pyrenees: Basement and cover thrust geometries. *J. Geol. Soc.* **1996**, *153*, 301–310. [CrossRef]
36. Teixell, A.; Labaume, P.; Lagabrielle, Y. The crustal evolution of the west-central Pyrenees revisited: Inferences from a new kinematic scenario. *C. R. Geosci.* **2016**, *348*, 257–267. [CrossRef]
37. Fontana, D.; Zuffa, G.G.; Garzanti, E. The interaction of eustacy and tectonism from provenance studies of the Eocene Hecho Group Turbidite Complex (South-Central Pyrenees, Spain). *Basin Res.* **1989**, *2*, 223–237. [CrossRef]

38. Gupta, K.D.; Pickering, K.T. Petrography and temporal changes in petrofacies of deep-marine Ainsa–Jaca basin sandstone systems, Early and Middle Eocene, Spanish Pyrenees. *Sedimentology* **2008**, *55*, 1083–1114. [CrossRef]
39. Coll, X.; Gómez-Gras, D.; Roigé, M.; Teixell, A.; Boya, S.; Mestres, N. Heavy-mineral provenance signatures during the infill and uplift of a foreland basin: An example from the Jaca basin (southern Pyrenees, Spain). *J. Sediment. Res.* **2020**, *90*, 1747–1769. [CrossRef]
40. Ullastre, J.; Masriera, A. Hipótesis y problemas acerca del origen de las asociaciones de minerales pesados del Senoniense del Pirineo Catalán. *J. Iber. Geol.* **1982**, *8*, 949–964.
41. Whitchurch, A.L.; Carter, A.; Sinclair, H.D.; Duller, R.A.; Whittaker, A.C.; Allen, P.A. Sediment routing system evolution within a diachronously uplifting orogen: Insights from detrital zircon thermochronological analyses from the South-Central Pyrenees. *Am. J. Sci.* **2011**, *311*, 442–482. [CrossRef]
42. Filleaudeau, P.Y.; Mouthereau, F.; Pik, R. Thermo-tectonic evolution of the south-central Pyrenees from rifting to orogeny: Insights from detrital zircon U/Pb and (U-Th)/He thermochronometry. *Basin Res.* **2012**, *24*, 401–417. [CrossRef]
43. Gómez-Gras, D.; Roigé, M.; Fondevilla, V.; Oms, O.; Boya, S.; Remacha, E. Provenance constraints on the Tremp Formation paleogeography (southern Pyrenees): Ebro Massif vs Pyrenees sources. *Cretac. Res.* **2016**, *57*, 414–427. [CrossRef]
44. Cerveny, P.F.; Johnson, N.M. Tectonic and geomorphic implications of Siwalik Group. *Geol. Soc. Am. Spec. Pap.* **1989**, *232*, 129–136.
45. Lihou, J.C.; Mange-Rajetzky, M.A. Provenance of the Sardona Flysch, eastern Swiss Alps: Example of high-resolution heavy mineral analysis applied to an ultrastable assemblage. *Sediment. Geol.* **1996**, *105*, 141–157. [CrossRef]
46. Garzanti, E.; Vezzoli, G.; Lombardo, B.; Ando, S.; Mauri, E.; Monguzzi, S.; Russo, M. Collision-orogen provenance (western Alps): Detrital signatures and unroofing trends. *J. Geol.* **2004**, *112*, 145–164. [CrossRef]
47. Garzanti, E.; Ando, S.; Vezzoli, G. The continental crust as a source of sand (southern Alps cross section, northern Italy). *J. Geol.* **2006**, *114*, 533–554. [CrossRef]
48. Garzanti, E.; Resentini, A.; Vezzoli, G.; Andò, S.; Malusà, M.; Padoan, M. Forward compositional modelling of Alpine orogenic sediments. *Sediment. Geol.* **2012**, *280*, 149–164. [CrossRef]
49. Uddin, A.; Kumar, P.; Sarma, J.N.; Akhter, S.H. Heavy mineral constraints on the provenance of Cenozoic sediments from the foreland basins of Assam and Bangladesh: Erosional history of the eastern Himalayas and the Indo-Burman Ranges. *Dev. Sedimentol.* **2007**, *58*, 823–847.
50. Andò, S.; Morton, A.; Garzanti, E. Metamorphic grade of source rocks revealed by chemical fingerprints of detrital amphibole and garnet. *Geol. Soc. Lond. Spec. Publ.* **2014**, *386*, 351–371. [CrossRef]
51. Andò, S.; Aharonovich, S.; Hahn, A.; George, S.C.; Clift, P.D.; Garzanti, E. Integrating heavy-mineral, geochemical and biomarker analyses of Plio-Pleistocene sandy and silty turbidites: A novel approach for provenance studies (Indus Fan, IODP Expedition 355). *Geol. Mag.* **2020**, *157*, 929–938. [CrossRef]
52. Valloni, R.; Marchi, M.; Mutti, E. Studio conoscitivo della moda detritica delle torbiditi eoceniche del Gruppo di Echo (Spagna). *Gior. Geol.* **1984**, *46*, 45–56.
53. Hirst, J.P.P.; Nichols, G.J. Thrust tectonic controls on Miocene alluvial distribution patterns, southern Pyrenees. *Basins* **1986**, *8*, 247–258.
54. Rubio, V.; Vigil, R.; García, R.; González, J.A. Caracterización mineralógica de sedimentos arenosos en la cuenca del río Ara (Huesca). *Cuatern. Geomorfol.* **1996**, *10*, 33–44.
55. Yuste, A.; Bauluz, B.; Luzón, A. Asociaciones características de minerales pesados en las areniscas del borde septentrional de la cuenca del ebro (zona central). *Rev. Soc. Esp. Mineral.* **2006**, *6*, 501–504.
56. Barsó, D. Análisis de la procedencia de los conglomerados sinorogénicos de la pobla de segur (Lérida) y su relación con la evolución tectónica de los pirineos centro-meridionales durante el eoceno medio-oligoceno. Ph.D. Thesis, Universitat de Barcelona, Barcelona, Spain, 2007.
57. Coll, X.; Gómez-Gras, D.; Roigé, M.; Mestres, N. Heavy-mineral assemblages as a provenance indicator in the Jaca basin (Middle-Late Eocene, southern Pyrenees). *Geogaceta* **2017**, *61*, 159–162.
58. Gómez-Gras, D.; Collado, R.; Coll, X.; Roigé, M. Caracterización composicional de las areniscas del Cretácico Superior en las Sierras Marginales y Exteriores (cuenca surpirenaica): Análisis mediante minerales pesados y petrografía óptica. *Geogaceta* **2017**, *61*, 163–166.
59. Soler-Sampere, M.; Puigdefàbregas, C. Líneas generales de la geología del Alto Aragón Occidental. *Pirineos* **1970**, *96*, 5–20.
60. Mutti, E.; Luterbacher, H.; Ferrer, J.; Rosell, J. Schema stratigrafico e lineamenti di facies del Paleogeno Marino della zona centrale sudpirenaica tra Tremp (Catalogna) e Pamplona (Navarra). *Mem. Soc. Geol. Ital.* **1972**, *1972 11*, 391–416.
61. Canudo, J.I. Los foraminíferos planctonicos del Paleoceno-Eocene del Prepirineo oscense en el sector de Arguis. Ph.D. Thesis, Universidad de Zaragoza, Zaragoza, Spain, 1990.
62. Lafont, F. Influences relatives de la subsidence et de l'eustatisme sur la localisation et la géométrie des réservoirs d'un système deltaïque. Exemple de l'Eocène du bassin de Jaca, Pyrénées espagnoles. Ph.D. Thesis, Université Rennes 1, Rennes, France, 1994.
63. Hogan, P.J. Geochronologic, Tectonic, and Stratigraphic Evolution of the Southwest Pyrenean Foreland basin, Northern Spain. Ph.D. Thesis, University of Southern California, Los Angeles, CA, USA, 1993.
64. Millán-Garrido, H.; Pocoví, A.; Casas, A.M. La transversal de Gavarnie-Guara. Estructura y edad de los mantos de Gavarnie, Guara-Gèdre y Guarga (Pirineo centro-occidental). *Geogaceta* **2006**, *40*, 73–90.

65. Hogan, P.J.; Burbank, D.W. Evolution of the Jaca piggyback basin and emergence of the External Sierra, southern Pyrenees. In *Tertiary Basins of Spain*, 1st ed.; Friend, P., Dabrio, C., Eds.; Cambridge University Press: Cambridge, UK, 1996; pp. 153–160.
66. Barnolas, A.; Gil-Peña, I. Ejemplos de relleno sedimentario multiepisódico en una cuenca de antepaís fragmentada: La Cuenca Surpirenaica. *Bol. Inst. Geol. Min. Esp.* **2001**, *112*, 17–38.
67. Montes, M. Estratigrafía del Eoceno-Oligoceno de la Cuenca de jaca (Sinclinorio de Guarga). Ph.D. Thesis, Universitat de Barcelona, Barcelona, Spain, 2002.
68. Pueyo, E.L.; Millán, H.; Pocovı, A. Rotation velocity of a thrust: A paleomagnetic study in the External Sierras (Southern Pyrenees). *Sediment. Geol.* **2002**, *146*, 191–208. [CrossRef]
69. Castelltort, S.; Guillocheau, F.; Robin, C.; Rouby, D.; Nalpas, T.; Lafont, F.; Eschard, R. Fold control on the stratigraphic record: A quantified sequence stratigraphic study of the Pico del Aguila anticline in the south-western Pyrenees (Spain). *Basin Res.* **2003**, *15*, 527–551.
70. Castelltort, S.; Pochat, S.; Van den Driessche, J. How reliable are growth strata in interpreting short-term (10 s to 100 s ka) growth structures kinematics? *C. R. Geosci.* **2004**, *336*, 151–158. [CrossRef]
71. Costa, E.; Garces, M.; López-Blanco, M.; Beamud, E.; Gómez-Paccard, M.; Larrasoaña, J.C. Closing and continentalization of the South Pyrenean foreland basin (NE Spain): Magnetochronological constraints. *Basin Res.* **2010**, *22*, 904–917. [CrossRef]
72. Huyghe, D.; Castelltort, S.; Mouthereau, F.; Serra-Kiel, J.; Filleaudeau, P.Y.; Emmanuel, L.; Berthier, B.; Renard, M. Large scale facies change in the middle Eocene South-Pyrenean foreland basin: The role of tectonics and prelude to Cenozoic ice-ages. *Sediment. Geol.* **2012**, *253*, 25–46. [CrossRef]
73. Rodríguez-Pintó, A.; Pueyo, E.L.; Serra-Kiel, J.; Samsó, J.M.; Barnolas, A.; Pocoví, A. Lutetian magnetostratigraphic calibration of larger foraminifera zonation (SBZ) in the Southern Pyrenees: The Isuela section. *Palaeogeogr. Palaeoclimatol. Palaeoecol.* **2012**, *333*, 107–120. [CrossRef]
74. Oliva-Urcia, B.; Beamud, E.; Garcés, M.; Arenas, C.; Soto, R.; Pueyo, E.L.; Pardo, G. New magnetostratigraphic dating of the Palaeogene syntectonic sediments of the west-central Pyrenees: Tectonostratigraphic implications. *Geol. Soc. Lond. Spec. Publ.* **2016**, *425*, 107–128. [CrossRef]
75. Labaume, P.; Teixell, A. 3D structure of subsurface thrusts in the eastern Jaca Basin, southern Pyrenees. *Geol. Acta* **2018**, *16*, 477–498.
76. Boya Duocastella, S. El Sistema deltaico de la Arenisca de Sabiñánigo y la continentalización de la cuenca de Jaca. Ph.D. Thesis, Universitat Autònoma de Barcelona, Barcelona, Spain, 2018.
77. Oliva-Urcia, B.; Beamud, E.; Arenas, C.; Pueyo, E.L.; Garcés, M.; Soto, R.; Valero, L.; Pérez-Rivarés, F.J. Dating the northern deposits of the Ebro foreland basin; implications for the kinematics of the SW Pyrenean front. *Tectonophysics* **2019**, *765*, 11–34. [CrossRef]
78. Garces, M.; Lopez-Blanco, M.; Valero, L.; Beamud, E.; Muñoz, J.A.; Oliva-Urcia, B.; Vinyoles, A.; Arbues, P.; Cabello, P.; Cabrera, L. Paleogeographic and sedimentary evolution of the South Pyrenean foreland basin. *Mar. Pet. Geol.* **2020**, *113*, 104105:1–104105:20. [CrossRef]
79. Vinyoles, A.; López-Blanco, M.; Garcés, M.; Arbués, P.; Valero, L.; Beamud, E.; Oliva-Urcia, B.; Cabello, P. 10 Myr evolution of sedimentation rates in a deep marine to non-marine foreland basin system: Tectonic and sedimentary controls (Eocene, Tremp–Jaca Basin, Southern Pyrenees, NE Spain). *Basin Res.* **2021**, *33*, 447–477. [CrossRef]
80. Puigdefàbregas, C.; Muñoz, J.A.; Vergés, J. Thrusting and foreland basin evolution in the southern Pyrenees. In *Thrust Tectonics*; McClay, K.R., Ed.; Springer: Berlin/Heidelberg, Germany, 1992; pp. 353–366.
81. Teixell, A.; Labaume, P.; Ayarza, P.; Espurt, N.; de Saint Blanquat, M.; Lagabrielle, Y. Crustal structure and evolution of the Pyrenean-Cantabrian belt: A review and new interpretations from recent concepts and data. *Tectonophysics* **2018**, *724*, 146–170. [CrossRef]
82. Vergés, J.; Fernàndez, M.; Martìnez, A. The Pyrenean orogen: Pre-, syn-, and post-collisional evolution. *J. Virtual Explor.* **2002**, *8*, 55–74. [CrossRef]
83. Mouthereau, F.; Filleaudeau, P.Y.; Vacherat, A.; Pik, R.; Lacombe, O.; Fellin, M.G.; Castelltort, S.; Christophoul, F.; Masini, E. Placing limits to shortening evolution in the Pyrenees: Role of margin architecture and implications for the Iberia/Europe convergence. *Tectonics* **2014**, *33*, 2283–2314. [CrossRef]
84. Lagabrielle, Y.; Labaume, P.; de Saint Blanquat, M. Mantle exhumation, crustal denudation, and gravity tectonics during Cretaceous rifting in the Pyrenean realm (SW Europe): Insights from the geological setting of the lherzolite bodies. *Tectonics* **2010**, *29*, TC4012:1–TC4012:26. [CrossRef]
85. Labaume, P.; Séguret, M.; Seyve, C. Evolution of a turbiditic foreland basin and analogy with an accretionary prism: Example of the Eocene south-Pyrenean basin. *Tectonics* **1985**, *4*, 661–685. [CrossRef]
86. Cámara, P.; Klimowitz, J. Interpretación geodinámica de la vertiente centro-occidental surpirenaica (Cuencas de Jaca-Tremp). *Estud. Geol.* **1985**, *41*, 391–404. [CrossRef]
87. Muñoz, J.A.; Mencos, J.; Roca, E.; Carrera, N.; Gratacós, O.; Ferrer, O.; Fernández, O. The structure of the South-Central-Pyrenean fold and thrust belt as constrained by subsurface data. *Geol. Acta* **2018**, *16*, 439–460.
88. Saura, E.; Ardèvol i Oró, L.; Teixell, A.; Vergés, J. Rising and falling diapirs, shifting depocenters, and flap overturning in the Cretaceous Sopeira and Sant Gervàs subbasins (Ribagorça Basin, southern Pyrenees). *Tectonics* **2016**, *35*, 638–662. [CrossRef]
89. Burrel, L.; Teixell, A.; Gómez-Gras, D.; Coll, X. Basement-involved thrusting, salt migration and intramontane conglomerates: A case from the Southern Pyrenees. *Bull. Soc. Géol. Fr.* **2021**, *192*, 24. [CrossRef]

90. Nijman, W.; Nio, S.-D. The Eocene Montañana Delta (Tremp-Graus Basin, provinces of Lérida and Huesca, Southern Pyrenees, N Spain). In *Sedimentary Evolution of the Paleogene South Pyrenean Basin, Proceedings of the IAS 9th International Sedimentological Congress, Nice, France, 1 January–30 November 1974*; Rosell., J., Puigdefàbregas, C., Eds.; Vakgroep Sedimentologie, Rijksuniveriteit Leiden-Utrecht: Utrecht, The Netherlands, 1975.
91. Mutti, E. Turbidite systems and their relations to depositional sequences. In *Provenance of Arenites*, 1st ed.; Zuffa, G.G., Ed.; Springer: Dordrecht, The Netherlands, 1985; pp. 65–93.
92. Mochales, T.; Barnolas, A.; Pueyo, E.L.; Serra-Kiel, J.; Casas, A.M.; Samsó, J.M.; Ramajo, J.; Sanjuán, J. Chronostratigraphy of the Boltaña anticline and the Ainsa Basin (southern Pyrenees). *Geol. Soc. Am. Bull.* **2012**, *124*, 1229–1250. [CrossRef]
93. Reynolds, A.D. Tectonically Controlled Fluvial Sedimentation in the South Pyrenean Foreland Basin. Ph.D. Thesis, University of Liverpool, Liverpool, UK, 1987.
94. Ortí, F.; Salvany, J.M.; Rosell, L.; Pueyo, J.J.; Inglés, M. Evaporitas antiguas (Navarra) y actuales (Los Manegros) de la Cuenca del Ebro. In *Guía de las Excursiones, Proceedings of the XI Congreso Español de sedimentología, Barcelona, Spain, 15–18 September 1986*; Anadón., P., Cabrera, L., Eds.; Universitat de Barcelona: Barcelona, Spain, 1986.
95. Payros, A.; Pujalte, V.; Orue-Etxebarria, X. The South Pyrenean Eocene carbonate megabreccias revisited: New interpretation based on evidence from the Pamplona Basin. *Sediment. Geol.* **1999**, *125*, 165–194. [CrossRef]
96. Millán, H.; Aurell, M.; Meléndez, A. Synchronous detachment folds and coeval sedimentation in the Prepyrenean External Sierras (Spain): A case study for a tectonic origin of sequences and systems tracts. *Sedimentology* **1994**, *41*, 1001–1024. [CrossRef]
97. Roigé, M.; Gómez-Gras, D.; Stockli, D.F.; Teixell, A.; Boya, S.; Remacha, E. Detrital zircon U–Pb insights into the timing and provenance of the South Pyrenean Jaca basin. *J. Geol. Soc.* **2019**, *176*, 1182–1190. [CrossRef]
98. Jolley, E.J. Thrust Tectonics and Alluvial Architecture of the Jaca Basin, Southern Pyrenees. Ph.D. Thesis, University of Wales, Cardiff, Wales, 1988.
99. Arenas, C. Sedimentología y paleogeografía del Terciario del margen pirenaico y sector central de la Cuenca del Ebro (zona aragonesa occidental). Ph.D. Thesis, Universidad de Zaragoza, Zaragoza, Spain, 1993.
100. Friend, P.F.; Hirst, J.P.P.; Hogan, P.J.; Jolley, E.J.; McElroy, R.; Nichols, G.J.; Rodríguez, J. *Pyrenean tectonic control of Oligo-Miocene river systems, Huesca, Aragón, Spain, In Excursion Guidebook No. 4, Proceedings of the 4th International Conference on Fluvial Sedimentology, Sitges, Spain, 2–4 October 1989*; Marzo, M., Puigdefàbregas, C., Eds.; Servei Geològic de Catalunya: Barcelona, Spain, 1989.
101. Arenas, C.; Millán, H.; Pardo, G.; Pocoví, A. Ebro Basin continental sedimentation associated with late compressional Pyrenean tectonics (north-eastern Iberia): Controls on basin margin fans and fluvial systems. *Basin Res.* **2001**, *13*, 65–89. [CrossRef]
102. Zwart, H.J.; De Sitter, L.U. The geology of the Central Pyrenees. *Leidse Geol. Meded.* **1979**, *50*, 1–74.
103. Zwart, H.J. The Variscan geology of the Pyrenees. *Tectonophysics* **1986**, *129*, 9–27. [CrossRef]
104. Debon, F.; Enrique, P.; Autran, A.; Barnolas, A.; Chiron, J.C. Le plutonisme hercynien des Pyrénées. In *Synthèse Géologique et Géophysique des Pyrénées*; Barnolas, A., Chiron, J.C., Eds.; Bureau de Recherches Géologiques et Minières-Instituto Tecnologico Geominero de España: Orléans, France; Madrid, Spain, 1996; Volume 1, pp. 361–499.
105. Guitard, G.; Vielzeuf, D.; Martinez, F. Métamorphisme hercynien. In *Synthèse Géologique Et Géophysique Des Pyrénées*; Barnolas, A., Chiron, J.C., Eds.; Bureau de Recherches Géologiques et Minières-Instituto Tecnologico Geominero de España: Orléans, France; Madrid, Spain, 1996; Volume 1, pp. 501–584.
106. Ribeiro, M.L.; Reche, J.; López-Carmona, A.; Quesada, C. Variscan metamorphism. In *The Geology of Iberia: A Geodynamic Approach*; Quesada, C., Oliveira, J.T., Eds.; Springer Nature: Cham, Switzerland, 2019; Volume 3, pp. 473–498.
107. Rodríguez-Fernández, L.R.; López-Olmedo, F.; Oliveira, J.T.; Medialdea, T.; Terrinha, P.; Matas, J.; Martín-Serrano, A.; Martín-Parra, L.M.; Rubio, F.; Marín, C.; et al. *Mapa Geológico de la Península Ibérica, Baleares y Canarias a escala 1:1.000.000*; IGME: Madrid, Spain, 2015.
108. Souquet, P. Le Crétacé supérieur sudpyrénéen en Catalogne, Aragon et Navarre. Ph.D. Thesis, Université de Toulouse, Toulouse, France, 1967.
109. Azambre, B. Sur les roches intrusives sous-saturées du Crétacé des Pyrénées. *C. R. Hebd. Séances Acad. Sci.* **1967**, *271*, 641–643.
110. Golberg, J.M.; Leyreloup, A.F. High temperature-low pressure Cretaceous metamorphism related to crustal thinning (Eastern North Pyrenean Zone, France). *Contrib. Mineral. Petrol.* **1990**, *104*, 194–207. [CrossRef]
111. Clerc, C.; Lahfid, A.; Monié, P.; Lagabrielle, Y.; Chopin, C.; Poujol, M.; Boulvais, P.; Ringenbach, J.C.; Masini, E.; de St Blanquat, M. High-temperature metamorphism during extreme thinning of the continental crust: A reappraisal of the North Pyrenean passive paleomargin. *Solid Earth* **2015**, *6*, 643–668. [CrossRef]
112. Mange, M.A.; Maurer, H.F.W. *Heavy Minerals in Colour*; Chapman and Hall: London, UK, 1992; 147p.
113. Garzanti, E.; Andò, S. Heavy mineral concentration in modern sands: Implications for provenance interpretation. *Dev. Sedimentol.* **2007**, *58*, 517–545.
114. Bixel, F. Le volcanisme stéphano-permien des Pyrénées. Pétrographie, minéralogie, géochimie. *J. Iber. Geol.* **1987**, *11*, 41–55.
115. Gilbert, J.S.; Rogers, N.W. The significance of garnet in the Permo-Carboniferous volcanic rocks of the Pyrenees. *J. Geol. Soc.* **1989**, *146*, 477–490. [CrossRef]
116. Harris, N.B.W. The petrology and petrogenesis of some muscovite granite sills from the Barousse Massif, Central Pyrenees. *Contrib. Mineral. Petrol.* **1974**, *45*, 215–230. [CrossRef]

117. Azambre, B.; Crouzel, F.; Debroas, E.J.; Soulé, J.C.; Ternet, Y. *Notice Explicative. Carte géologique de la France au 1: 50000. Feuille Bagnères-de-Bigorre (1053)*; BRGM: Orléans, France, 1989; 79p.
118. Azambre, B.; Rossy, M.; Lago, M. Caracteristiques petrologiques des dolerites tholeiitiques d'age triasique (ophites) du domaine pyreneen. *Bull. Soc. Minéral.* **1987**, *110*, 379–396. [CrossRef]
119. Ternet, Y.; Barrere, P.; Debroas, E.J. *Notice Explicative de la Carte géologique de la France (1/50000), feuille Campan (1071)*; BRGM: Orléans, France, 1995; 117p.
120. Lago, M.; Galé, C.; Arranz, E.; Vaquer, R.; Gil, A.; Pocovi, A. Triassic tholeiitic dolerites (ophite) of the El Grado diapir. *Estud. Geol.* **2000**, *56*, 3–8.
121. Majesté-Menjoulás, C.; Debon, F.; Barrère, P. *Notice Explicative de la Carte Géologique de la France (1/50000), Feuille Gavarnie (1082)*; BRGM: Orléans, France, 1999; 158p.
122. Chayes, F. The finer-grained calcalkaline granites of New England. *J. Geol.* **1952**, *60*, 207–254. [CrossRef]
123. Gazzi, P. Le Arenarie del Flysch Sopracretaceo dell'Appennino Modenese: Correlazioni con il Flysch di Monghidoro. *Mineral. Petrogr. Acta* **1966**, *12*, 69–97.
124. Ingersoll, R.V.; Bullard, T.F.; Ford, R.L.; Grimm, J.P.; Pickle, J.D.; Sares, S.W. The Effect of Grain Size on Detrital Modes: A Test of the Gazzi-Dickinson Point-Counting Method. *J. Sediment. Res.* **1984**, *54*, 103–116.
125. Zuffa, G.G. Optical analyses of arenites: Influence of methodology on compositional results. In *Provenance of Arenites*; Zuffa, G.G., Ed.; NATO-ASI Series; Springer: Dordrecht, The Netherlands, 1985; Volume 148, pp. 21–29.
126. Dryden, A.L., Jr. Accuracy in percentage representation of heavy mineral frequencies. *Proc. Natl. Acad. Sci. USA* **1931**, *17*, 233–238. [CrossRef]
127. Garzanti, E.; Vezzoli, G. A classification of metamorphic grains in sands based on their composition and grade. *J. Sediment. Res.* **2003**, *73*, 830–837. [CrossRef]
128. Marsaglia, K.M.; Ingersoll, R.V. Compositional trends in arc-related, deep-marine sand and sandstone: A reassessment of magmatic-arc provenance. *Geol. Soc. Am. Bull.* **1992**, *104*, 1637–1649. [CrossRef]
129. Critelli, S.; Ingersoll, R.V. Interpretation of neovolcanic versus palaeovolcanic sand grains: An example from Miocene deep-marine sandstone of the Topanga Group (Southern California). *Sedimentology* **1995**, *42*, 783–804. [CrossRef]
130. Garzanti, E.; Andò, S.; Vezzoli, G. Settling equivalence of detrital minerals and grain-size dependence of sediment composition. *Earth Planet. Sci. Lett.* **2008**, *273*, 138–151. [CrossRef]
131. Garzanti, E.; Andò, S.; Vezzoli, G. Grain-size dependence of sediment composition and environmental bias in provenance studies. *Earth Planet. Sci. Lett.* **2009**, *277*, 422–432. [CrossRef]
132. Garzanti, E.; Andò, S. Heavy minerals for junior woodchucks. *Minerals* **2019**, *9*, 148. [CrossRef]
133. Andò, S. Gravimetric Separation of Heavy Minerals in Sediments and Rocks. *Minerals* **2020**, *10*, 273. [CrossRef]
134. Nasdala, L.; Smith, D.C.; Kaindl, R.; Ziemann, M. Raman spectroscopy: Analytical perspectives in mineralogical research. In *Spectroscopic Methods in Mineralogy*; Beran, A., Libowitzky, E., Eds.; Eötvös University Press: Budapest, Hungary, 2004; pp. 281–343.
135. Andò, S.; Garzanti, E. Raman spectroscopy in heavy-mineral studies. *Geol. Soc. Lond. Spec. Publ.* **2014**, *386*, 395–412. [CrossRef]
136. Galehouse, J.S. Point counting. In *Procedures in Sedimentary Petrology*; Carver, R.E., Ed.; Wiley: New York, NY, USA, 1971; pp. 385–407.
137. Mange, M.A.; Wright, D.T. *Heavy Minerals in Use*; Elsevier: Amsterdam, The Netherlands, 2007; 1283p.
138. Wang, A.; Kuebler, K.E.; Jolliff, B.L.; Haskin, L.A. Raman spectroscopy of Fe-Ti-Cr-oxides, case study: Martian meteorite EETA79001. *Am. Mineral.* **2004**, *89*, 665–680. [CrossRef]
139. Kuebler, K.E.; Jolliff, B.L.; Wang, A.; Haskin, L.A. Extracting olivine (Fo–Fa) compositions from Raman spectral peak positions. *Geochim. Cosmochim. Acta* **2006**, *70*, 6201–6222. [CrossRef]
140. Greenacre, M.J. *Theory and Applications of Correspondence Analysis*; London Academic Press: London, UK, 1984; 364p.
141. Vermeesch, P.; Resentini, A.; Garzanti, E. An R package for statistical provenance analysis. *Sediment. Geol.* **2016**, *336*, 14–25. [CrossRef]
142. Vermeesch, P. Statistical models for point-counting data. *Earth Planet. Sci. Lett.* **2018**, *501*, 112–118. [CrossRef]
143. Zuffa, G.G. Hybrid arenites; their composition and classification. *J. Sediment. Petrol.* **1980**, *50*, 21–29.
144. Dickinson, W.R.; Beard, L.S.; Brakenridge, G.R.; Erjavec, J.L.; Ferguson, R.C.; Inman, K.F.; Knepp, R.A.; Lindberg, F.A.; Ryberg, P.T. Provenance of North American Phanerozoic sandstones in relation to tectonic setting. *Geol. Soc. Am. Bull.* **1983**, *94*, 222–235. [CrossRef]
145. Morton, A.C.; Hallsworth, C.R. Processes controlling the composition of heavy mineral assemblages in sandstones. *Sediment. Geol.* **1999**, *124*, 3–29. [CrossRef]
146. Walderhaug, O.; Porten, K.W. Stability of detrital heavy minerals on the Norwegian continental shelf as a function of depth and temperature. *J. Sediment. Res.* **2007**, *77*, 992–1002. [CrossRef]
147. Garzanti, E.; Andò, S.; Limonta, M.; Fielding, L.; Najman, Y. Diagenetic control on mineralogical suites in sand, silt, and mud (Cenozoic Nile Delta): Implications for provenance reconstructions. *Earth Sci. Rev.* **2018**, *185*, 122–139. [CrossRef]
148. Crognier, N. Evolution thermique, circulation de fluide et fracturation associées à la structuration du bassin d'avant-pays sud-pyrénéen. Ph.D. Thesis, Université de Pau et des Pays de l'Adour, Pau, France, 2016.
149. Andò, S.; Garzanti, E.; Padoan, M.; Limonta, M. Corrosion of heavy minerals during weathering and diagenesis: A catalog for optical analysis. *Sediment. Geol.* **2012**, *280*, 165–178. [CrossRef]

150. Simó, A.; Puigdefrábregas, C.; Gili, E. Transition from shelf to basin on an active slope, Upper Cretaceous, Tremp area, southern Pyrenees. In Proceedings of the 6th European Regional Meeting of Sedimentology Excursion Guidebook, Lleida, Spain, 15–17 April 1985; Mila, M.D., Rosell, J., Eds.; Institut d'Estudis Ilerdencs: Lleida, Spain, 1985; pp. 63–108.
151. Babault, J.; Van Den Driessche, J.; Teixell, A. Longitudinal to transverse drainage network evolution in the High Atlas (Morocco): The role of tectonics. *Tectonics* **2012**, *31*, TC4020. [CrossRef]
152. Viaplana-Muzas, M.; Babault, J.; Dominguez, S.; Van Den Driessche, J.; Legrand, X. Drainage network evolution and patterns of sedimentation in an experimental wedge. *Tectonophysics* **2015**, *664*, 109–124. [CrossRef]
153. Viaplana-Muzas, M.; Babault, J.; Dominguez, S.; Van Den Driessche, J.; Legrand, X. Modelling of drainage dynamics influence on sediment routing system in a fold-and-thrust belt. *Basin Res.* **2019**, *31*, 290–310. [CrossRef]
154. Vacherat, A.; Mouthereau, F.; Pik, R.; Bellahsen, N.; Gautheron, C.; Bernet, M.; Daudet, M.; Balansa, J.; Tibari, B.; Pinna Jamme, R. Rift-to-collision transition recorded by tectonothermal evolution of the northern Pyrenees. *Tectonics* **2016**, *35*, 907–933. [CrossRef]
155. Bosch, G.V.; Teixell, A.; Jolivet, M.; Labaume, P.; Stockli, D.; Domènech, M.; Monié, P. Timing of Eocene–Miocene thrust activity in the Western Axial Zone and Chaînons Béarnais (west-central Pyrenees) revealed by multi-method thermochronology. *C. R. Geosci.* **2016**, *348*, 246–256. [CrossRef]
156. Hart, N.R.; Stockli, D.F.; Lavier, L.L.; Hayman, N.W. Thermal evolution of a hyperextended rift basin, Mauléon Basin, western Pyrenees. *Tectonics* **2017**, *36*, 1103–1128. [CrossRef]
157. Senz, J.G.; Zamorano, M. Evolución tectónica y sedimentaria durante el Priaboniense superior-Mioceno inferior, en el frente de cabalgamiento de las Sierras Marginales occidentales. *Acta Geol. Hisp.* **1992**, *27*, 195–209.
158. Cámara, P.; Flinch, J.F. The southern Pyrenees: A salt-based fold-and-thrust belt. In *Permo-Triassic Salt Provinces of Europe, North Africa and the Atlantic Margins*, 1st ed.; Soto, J.I., Flinch, J.F., Tari, G., Eds.; Elsevier: Amsterdam, The Netherlands, 2017; pp. 395–415.
159. Burrel, L.; Teixell, A. Contractional salt tectonics and role of pre-existing diapiric structures in the Southern Pyrenean foreland fold–thrust belt (Montsec and Serres Marginals). *J. Geol. Soc.* **2021**, *178*, jgs2020-085. [CrossRef]
160. Hudec, M.R.; Dooley, T.P.; Burrel, L.; Teixell, A.; Fernandez, N. An alternative model for the role of salt depositional configuration and preexisting salt structures in the evolution of the Southern Pyrenees, Spain. *J. Struct. Geol.* **2021**, *146*, 104325. [CrossRef]
161. Friend, P.F.; Hirst, J.P.P.; Nichols, G.J. Sandstone-body structure and river processes in the Ebro Basin of Aragon, Spain. *J. Iber. Geol.* **1986**, *10*, 9–30.
162. Nichols, G.J.; Hirst, J.P. Alluvial fans and fluvial distributary systems, Oligo-Miocene, northern Spain; contrasting processes and products. *J. Sediment. Res.* **1998**, *68*, 879–889. [CrossRef]
163. Jones, S.J. Tectonic controls on drainage evolution and development of terminal alluvial fans, southern Pyrenees, Spain. *Terra Nova* **2004**, *16*, 121–127. [CrossRef]

minerals

MDPI

Supplementary Materials: Interplay of Multiple Sediment Routing Systems Revealed by Combined Sandstone Petrography and Heavy Mineral Analysis (HMA) in the South Pyrenean Foreland Basin

Xavier Coll, Marta Roigé, David Gómez-Gras*, Antonio Teixell, Salvador Boya and Narcís Mestres

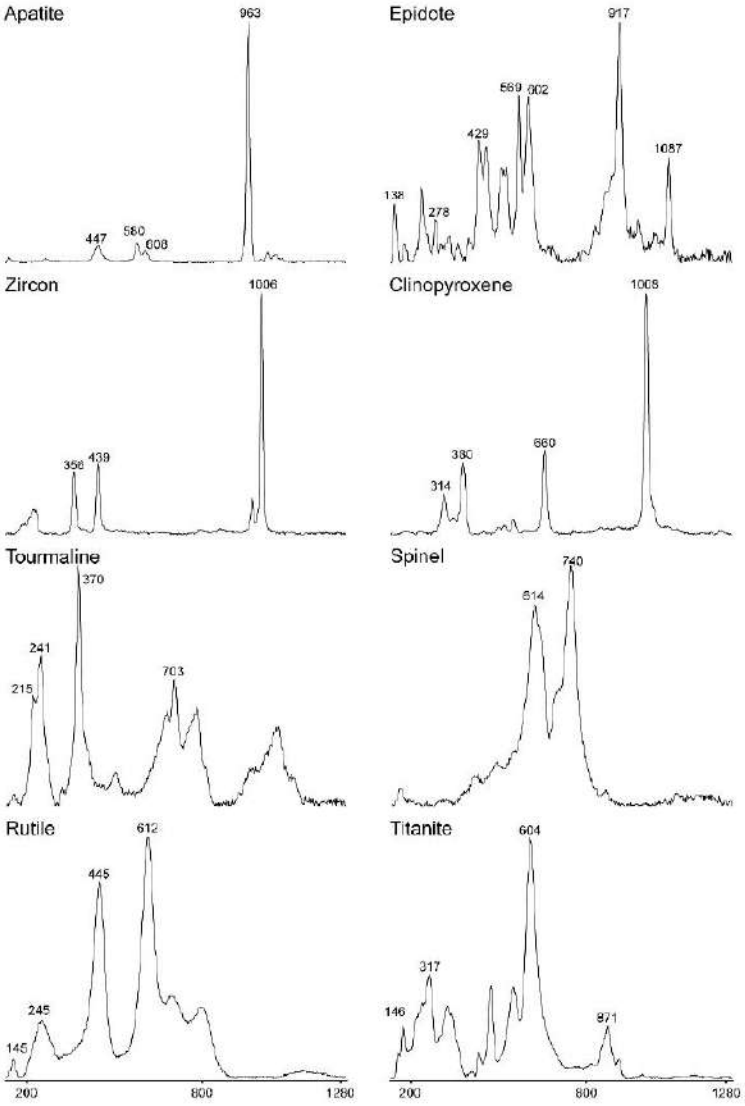

Figure S1. Representative Raman spectra of heavy minerals from the late Eocene–Miocene Jaca basin (1).

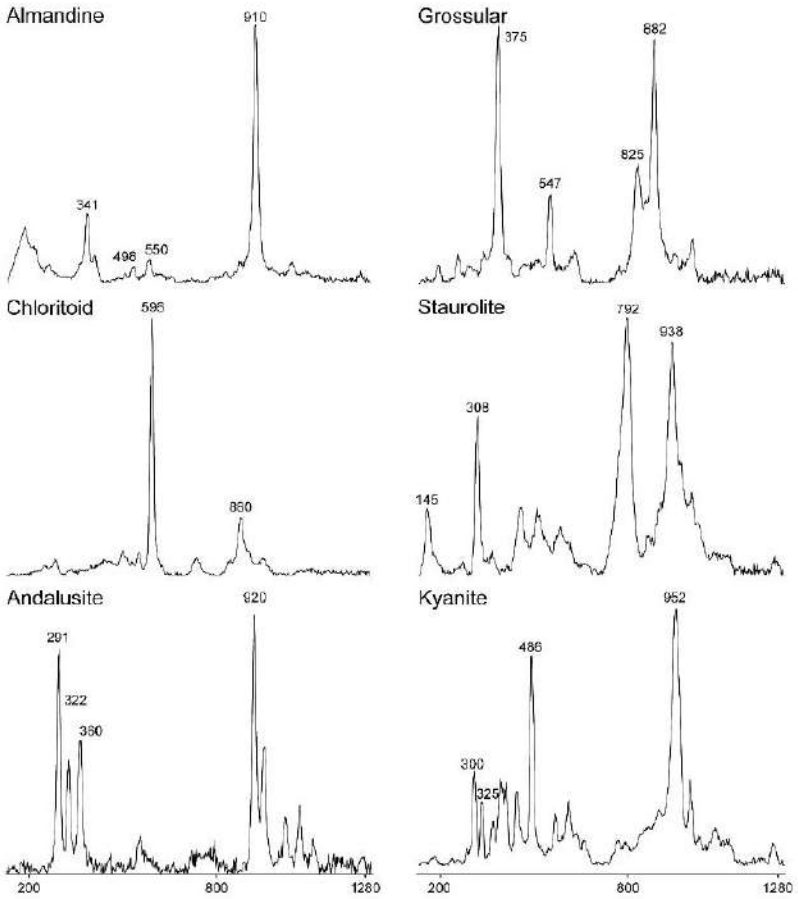

Figure S2. Representative Raman spectra of heavy minerals from the late Eocene–Miocene Jaca basin (2).

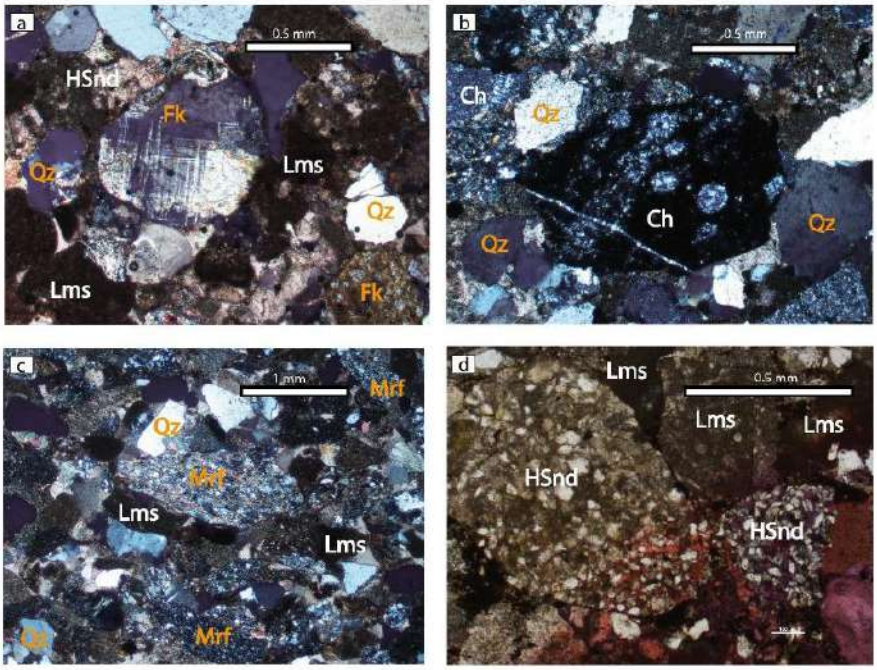

Figure S3. Optical photomicrographs of distinct extrabasinal grains.

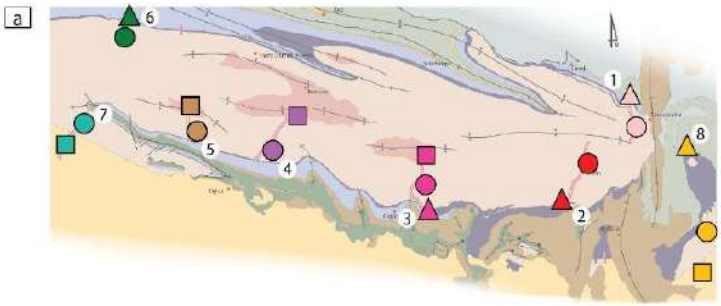

7. Luesia 6. Martés 5. Salinas 4. Gállego 3. Monrepós 2. Rodellar-Bibán 1. San Felices 8. Ainsa

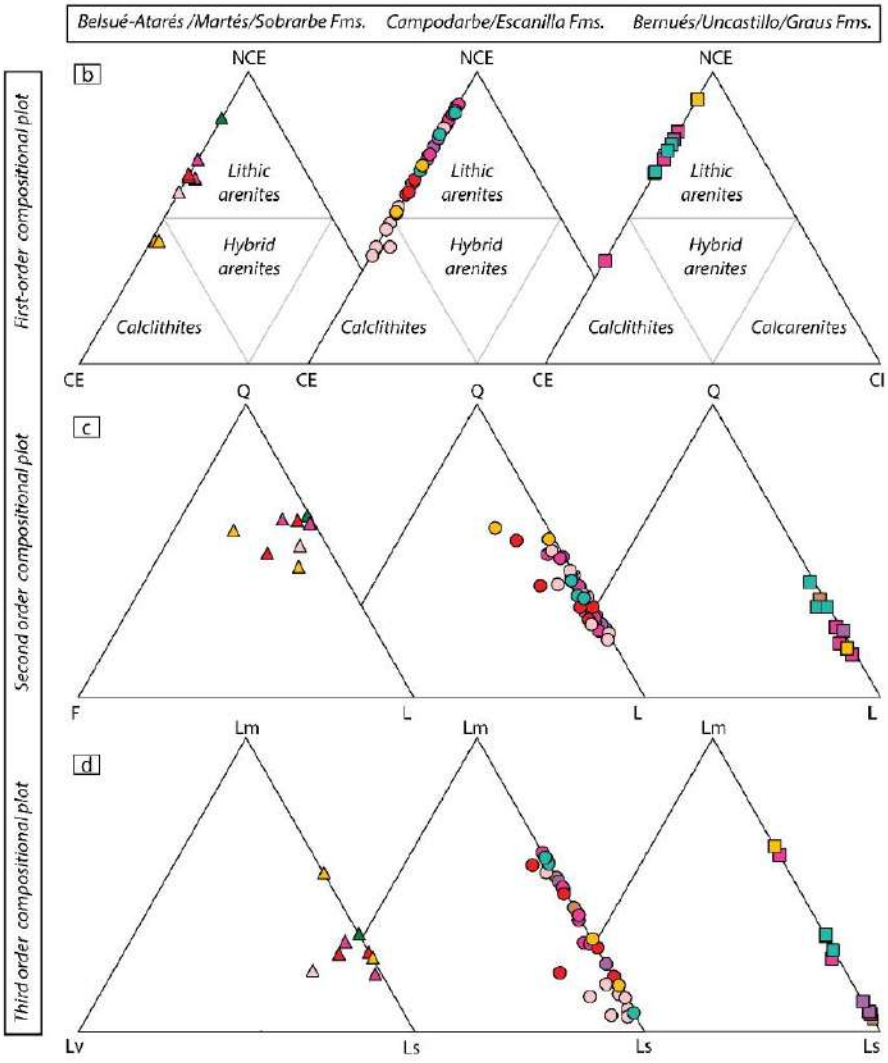

Figure S4. Compositional plots for all the analyzed samples.

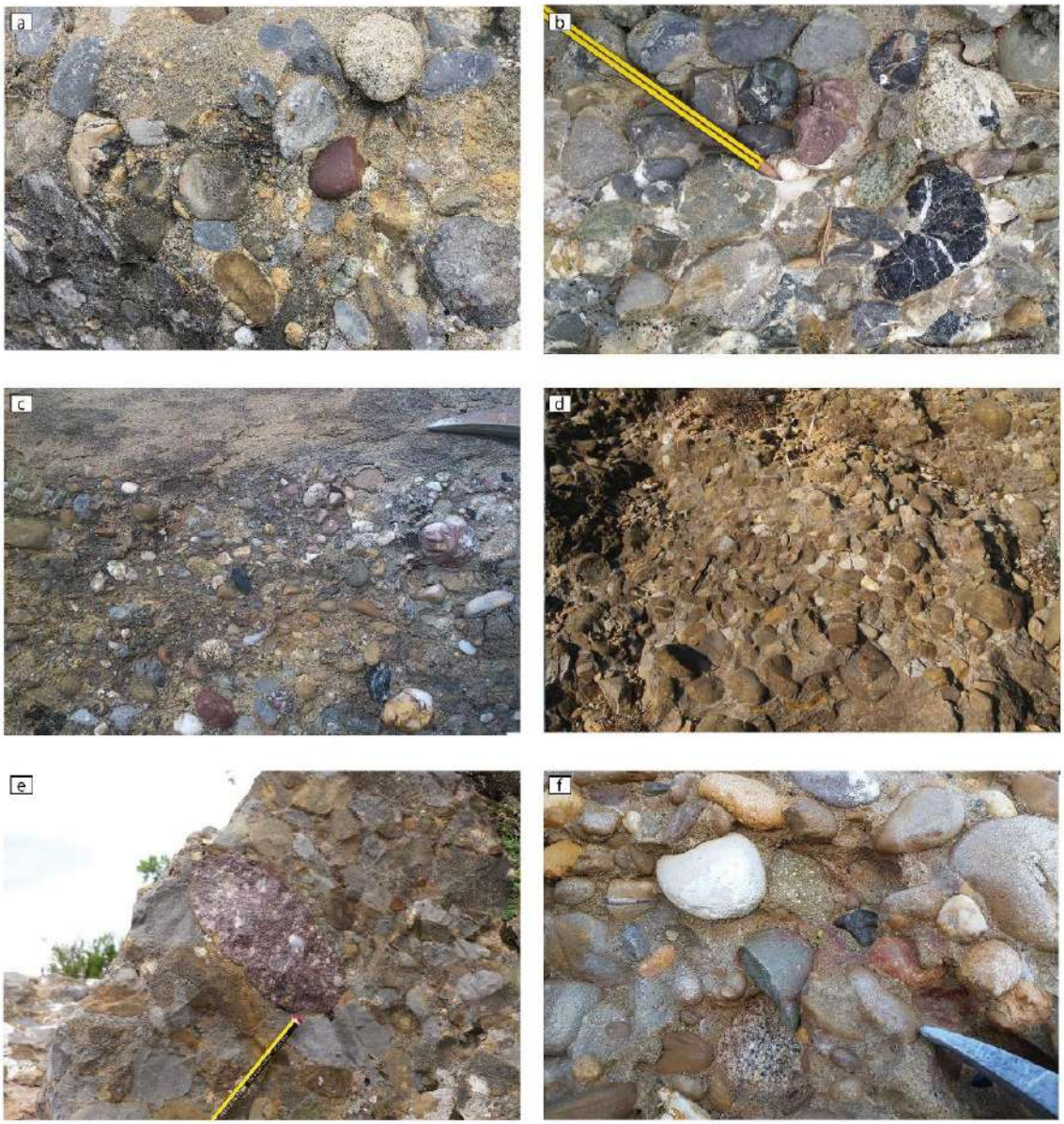

Figure S5. Images of the appearance of each of the described petrofacies in the conglomerate-sized deposits.

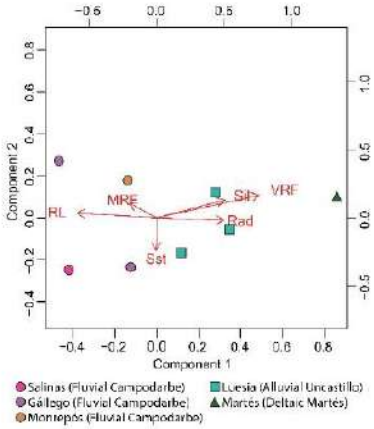

Figure S6. Biplot of the two sub-groups of the MLC petrofacies.

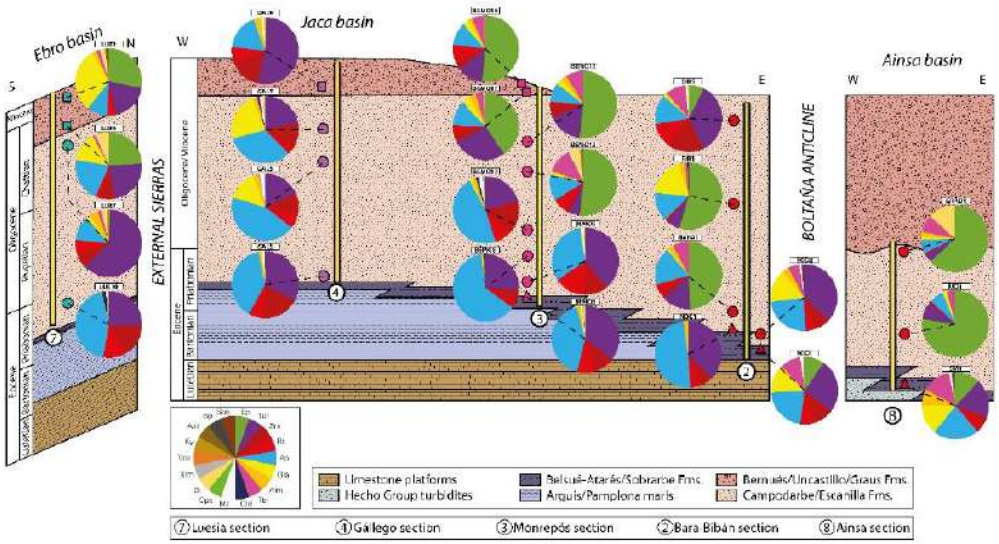

Figure S7. Heavy-mineral percentage pie charts for all the analyzed samples in a general stratigraphic cross-section sketch.

Table S1. Sandstone compositional data (point counting analyses).

	SFE2	SFE3	SFE5	SFE7	SFE11	SFE13	SFE16	SFE18	SFE19	ROD1	ROD3	NOC1	BARA1	BIB1	BIB2	BIB5	BEMO1	BEMO3	BEMO5	BEMO8	BEMO10	BEMO11	BEMO12	BEMO13	BEMO14	BEMO16	BEMO17	BEMO18
Total siliciclastic extrabasinal	134	86	121	101	117	85	108	186	86	151	139	151	146	162	87	120	156	150	150	194	184	165	214	142	162	67	145	183
Total detrital quartz	69	33	52	22	40	21	54	65	17	74	53	91	78	50	23	37	96	89	73	92	70	50	55	38	37	18	21	34
Monocrystalline non-undulose quartz	37	19	35	16	28	10	38	38	15	35	38	54	54	26	11	34	71	49	53	44	39	22	23	20	13	11	11	9
Monocrystalline undulose quartz	1	0	1	1	0	0	2	1	0	8	1	3	7	2	0	0	3	2	0	1	0	1	0	0	0	0	0	0
Quartz with inherited syntaxial cement	1	0	0	0	0	0	0	0	0	0	1	0	0	0	0	0	0	1	0	0	0	0	0	0	0	0	0	0
Quartz polycristalline with 2-3 subgrains	7	2	2	4	2	2	5	10	0	8	3	7	6	1	0	1	2	3	4	8	8	4	2	3	0	0	0	2
Quartz polycristalline with >3 subgrains	14	7	6	0	7	1	3	2	1	8	3	19	5	6	4	2	12	14	6	20	7	6	10	8	1	4	4	9
Quartz keuper	6	0	1	1	0	1	0	0	0	3	3	0	3	1	1	0	2	3	1	2	1	1	3	0	1	0	0	3
Quartz in plutonic r.f.	1	1	0	0	0	0	0	0	0	10	0	0	1	1	0	0	2	3	0	1	0	0	0	0	0	0	0	0
Quartz in metamorphic r.f.	0	0	0	0	0	0	0	0	0	0	0	0	0	0	0	0	0	0	0	0	0	0	0	0	0	0	0	0
Quartz in sandstone r.f.	2	4	5	0	3	7	6	14	1	2	4	8	2	13	7	0	4	14	9	16	15	16	17	5	21	1	2	11
Quartz in hybrid sandstone r.f.	0	0	2	0	0	0	0	0	0	0	0	0	0	0	0	0	0	0	0	0	0	0	0	2	1	0	4	0
Cc replacement on quartz	0	0	0	0	0	0	0	0	0	0	0	0	0	0	0	0	0	0	0	0	0	0	0	0	0	0	0	0
Total detrital feldspar	11	6	1	0	0	3	3	2	1	29	17	7	17	6	3	0	14	2	7	3	1	2	4	2	4	1	2	5
Detrital K-feld	3	1	1	0	0	3	3	2	1	14	9	3	6	5	3	0	6	0	5	1	0	1	4	2	4	1	1	5
K-feld in plutonic r.f.	0	0	0	0	0	0	0	0	0	1	3	0	1	0	0	0	0	0	0	0	0	0	0	0	0	0	0	0
Detrital plagioclase	5	2	0	0	0	0	0	0	0	8	4	4	10	1	0	0	4	1	2	1	0	1	0	0	0	0	1	0
Plagioclase in plutonic r.f.	0	0	0	0	0	0	0	0	0	1	0	0	0	0	0	0	0	0	0	0	0	0	0	0	0	0	0	0
Detrital Microcline	3	3	0	0	0	0	0	0	0	5	1	0	0	0	0	0	4	1	0	1	1	0	0	0	0	0	0	0
Microcline in plutonic r.f	0	0	0	0	0	0	0	0	0	0	0	0	0	0	0	0	0	0	0	0	0	0	0	0	0	0	0	0
Illite replacement on feldpar	0	0	0	0	0	0	0	0	0	0	0	0	0	0	0	0	0	0	0	0	0	0	0	0	0	0	0	0
Illite replacement feldspar on plut. R.f.	0	0	0	0	0	0	0	0	0	0	0	0	0	0	0	0	0	0	0	0	0	0	0	0	0	0	0	0
Cc replacement on K-feld	0	0	0	0	0	0	0	0	0	0	0	0	0	0	0	0	0	0	0	0	0	0	0	0	0	0	0	0
Total fine lithics	54	47	68	79	77	61	51	119	68	48	60	53	51	106	61	83	48	59	70	99	113	113	155	102	121	50	122	144
Phyllites	2	0	7	0	1	3	3	41	0	1	7	7	12	20	5	6	3	1	13	10	23	18	47	2	9	4	2	21
Schists	7	0	3	0	1	4	4	19	6	2	4	5	3	20	8	8	8	4	4	22	32	27	41	9	22	5	4	45
Chloritochists lithic	0	0	0	0	0	0	0	0	0	0	0	1	0	0	0	0	0	0	0	0	0	0	0	0	0	0	0	0
Quartzite	3	3	2	6	2	1	0	13	2	6	3	3	13	14	6	1	2	8	5	9	6	5	14	5	11	3	1	19
Plutonic r.f.	0	0	0	0	0	0	0	1	0	4	0	2	2	0	0	0	0	0	0	0	0	0	0	0	0	0	0	0
Cc replacement on plut. r.f.	0	0	0	0	0	0	0	0	0	0	0	0	0	0	0	0	0	0	0	0	0	0	0	0	0	0	0	0
Volcanic r.f.	0	0	1	0	1	6	0	0	0	0	0	0	2	0	1	2	1	0	0	1	0	0	2	0	0	0	0	2
Volcanic chert	0	0	0	0	0	0	0	0	0	0	0	0	0	0	0	0	0	0	0	0	0	0	0	0	0	0	0	0
Vitric volcanic lithic	0	0	0	0	0	0	0	0	0	0	0	0	0	0	0	0	0	0	0	0	0	0	0	0	0	0	0	0
Volcanic lithic with microlitic	3	0	0	0	0	0	0	0	0	0	0	0	0	0	0	0	0	0	0	2	0	1	0	0	0	0	0	2
Volcanic lithic with lathwork texture	0	0	0	0	0	0	2	0	0	7	8	0	0	0	0	0	1	3	2	2	0	0	0	4	1	0	2	3
sandstone r.f.	4	1	0	1	1	4	3	7	1	6	2	7	3	8	0	1	2	2	1	1	2	3	7	4	10	0	2	0
Hybrid sandstone r.f.	0	8	1	22	23	6	3	0	10	0	0	0	0	0	15	9	0	0	0	0	0	0	0	4	5	5	15	2
Siltstone r.f.	16	1	6	3	4	11	16	31	10	15	30	17	11	25	5	5	17	21	22	18	22	32	18	11	28	7	19	24
Hybrid Siltstone r.f.	4	26	25	40	36	9	10	0	39	0	1	0	0	0	21	47	1	2	2	0	0	5	1	48	19	18	71	2
Chlorite	0	0	0	0	0	0	0	0	0	0	0	0	0	0	0	0	4	0	0	0	0	0	0	0	0	1	0	1
Chert	4	0	0	0	0	0	0	0	0	4	4	1	1	3	0	0	5	5	5	2	1	1	2	3	3	2	2	5
Muscovite	2	0	0	0	0	0	1	0	0	0	1	2	1	1	0	0	1	0	0	0	0	0	0	1	0	0	0	0
Biotite	0	0	2	0	0	0	0	0	0	0	0	1	0	0	0	0	0	0	0	1	1	0	0	0	0	0	0	0
Heavy minerals	0	0	0	0	0	0	0	0	0	0	0	0	0	0	0	0	0	0	1	0	1	0	0	1	0	0	0	0
Silicified r.f.	6	8	5	5	7	16	1	2	0	0	1	5	3	2	0	3	3	5	13	9	5	4	0	6	0	1	4	1
Cc replacement silificied r.f.	0	0	0	0	0	0	0	0	0	0	0	0	0	0	0	0	0	0	0	0	0	0	0	0	0	0	0	0
Fe-oxid replacement r.f.	2	0	16	2	0	0	5	1	0	0	6	1	0	9	0	1	0	0	0	9	12	11	9	1	12	4	0	11
Silificied limestone	0	0	0	0	0	0	0	0	0	0	0	0	0	0	0	0	0	0	0	0	0	0	0	0	0	0	0	0
Radiolarite r.f.	0	0	0	0	1	1	3	4	0	1	2	1	0	4	0	0	0	8	2	13	8	6	14	3	1	0	0	6
Alterite	1	0	0	0	0	0	0	0	0	2	0	0	0	0	0	0	0	0	0	0	0	0	0	0	0	0	0	0
Total carbonate extrabasinal	93	129	130	141	101	99	101	45	145	82	81	84	106	28	132	83	68	80	87	44	23	65	33	88	33	122	61	48
Monocrystalline sparitic limestone	0	1	2	3	2	0	2	1	0	4	6	2	13	3	1	0	10	7	1	1	1	2	0	4	0	3	3	1
Polycrystalline sparitic r.f.	7	3	3	1	2	1	7	3	7	14	3	17	16	1	2	3	5	6	14	5	2	2	5	0	0	2	0	7
Dolomitized polycrystalline r.f.	0	0	0	0	0	0	0	0	1		3		0	0	0	0	0	1	0	0	0	0	0	0	0	0	0	0
Biomicritic	7	0	10	7	7	15	2	5	10	1	10	2	5	0	5	8	10	6	1	0	0	0	2	0	0	0	0	2
Biosparitic	0	0	0	0	0	1	0	0	1	0	0	1	0	0	0	1	0	0	1	0	0	0	0	0	0	2	0	0
Dolomicrite r.f	0	0	0	0	0	0	0	0	0	1	1	1	1	0	0	0	0	0	2	0	0	0	1	0	0	0	0	0
Dolomite monocrystalline	0	0	0	0	0	0	3	0	0	0	2	4	8	0	0	0	4	1	4	0	0	1	2	0	0	0	0	0
Dolostone r.f. (sacaroidea)	1	0	0	0	0	0	14	2	0	5	6	8	8	0	3	0	0	7	6	4	0	1	3	0	0	0	0	3
Bioclastic grainstone r.f.	18	12	21	26	6	4	4	4	14	6	5	1	1	0	9	2	1	8	0	4	1	2	0	4	15	18	3	2
Dolomitized bioclastic grainstone r.f.	0	0	0	0	0	0	0	0	0	0	0	0	0	0	0	0	0	0	0	0	0	0	0	0	0	0	0	0
Bioclastic Packes-Wackes r.f.	18	67	82	61	60	48	25	13	61	18	23	11	11	3	51	31	8	9	17	10	3	25	11	53	18	60	32	17
Dolomitized bioclastic Packes-Wackes r.f.	0	0	0	0	0	0	0	0	0	0	0	0	0	1	0	0	0	0	0	0	0	0	0	0	0	0	0	0
Biomicritic mudstone r.f.	42	27	29	22	21	30	43	17	48	33	22	37	43	20	61	38	30	35	41	20	16	32	9	27	0	37	21	16
Dolomitized biomicritic mudstone	0	0	0	0	3	0	0	0	0	0	0	0	0	0	0	0	0	0	0	0	0	0	0	0	0	0	0	0
Extrabasinal bioclasts	0	19	3	21	0	0	1	0	3	0	0	0	0	0	0	0	0	0	0	0	0	0	0	0	0	0	2	0
Total carbonate intrabasinal	0	0	0	10	0	0	0	0	1	0	0	0	0	0	0	0	0	6	0	0	0	0	0	0	0	0	1	0
Reworked calcrete clasts	0	0	0	10	0	0	0	0	1	0	0	0	0	0	0	0	0	0	0	0	0	0	0	0	0	0	1	0
Bioclasts	0	0	0	0	0	0	0	0	0	0	0	0	0	0	0	0	0	6	0	0	0	0	0	0	0	0	0	0
Total non-carbonate intrabasinal	0	0	0	0	0	0	0	0	0	0	0	0	0	0	0	0	0	0	0	0	0	0	0	0	0	0	0	0
Total matrix	0	0	7	0	0	0	0	0	0	0	0	0	0	0	0	0	3	0	0	0	0	0	0	0	0	0	0	0
Diagenetics minerals	87	130	77	84	100	136	115	96	92	83	108	83	74	145	104	97	103	80	70	81	106	106	59	85	115	144	127	89
Total porosity	0	0	0	0	0	0	0	0	0	0	0	0	0	0	0	0	0	0	2	0	0	0	0	0	0	0	0	5
TOTAL POINTS	314	345	328	343	318	320	324	327	324	316	328	318	326	335	323	300	332	316	309	319	313	336	306	315	310	333	334	325

Table S1. Sandstone compositional data (point counting analyses)

	GAL2	GAL3	GAL4	GAL5	GAL7	GAL8	GAL9	GAL10	BAI1	BAI2	BAI3	BAI4	MART1	MART2	LUE10	LUE9	LUE7	LUE5	LUE3	LUE2	SM1	SM3	MO1	OL1	GRAD1
Total siliciclastic extrabasinal	151	173	188	187	166	157	142	181	175	204	157	162	225	189	207	185	154	137	162	191	83	107	151	115	175
Total detrital quartz	42	83	55	43	41	65	32	56	65	55	65	51	139	70	82	64	52	42	64	59	37	61	87	62	29
Monocrystalline non-undulose quartz	26	48	31	17	29	45	18	37	53	30	45	42	63	42	52	47	42	28	47	37	21	45	68	47	21
Monocrystalline undulose quartz	0	0	1	0	0	0	0	0	0	0	3	0	5	0	3	1	2	0	2	0	2	6	1	3	0
Quartz with inherited syntaxial cement	0	0	0	0	0	0	0	0	0	0	0	0	0	0	0	0	0	1	0	0	1	0	0	0	0
Quartz polycristalline with 2-3 subgrains	1	3	1	3	1	0	1	3	2	1	1	1	25	4	3	4	2	1	1	4	1	4	8	2	4
Quartz polycristalline with >3 subgrains	8	9	9	3	2	7	3	4	2	15	3	3	22	9	10	5	6	3	5	11	3	3	8	6	0
Quartz keuper	1	4	1	0	3	5	1	0	1	0	2	0	0	0	2	0	0	0	1	2	4	2	1	1	0
Quartz in plutonic r.f.	0	0	0	0	1	0	0	1	0	0	0	0	6	0	0	0	0	1	0	0	2	1	0	0	0
Quartz in metamorphic r.f.	0	0	0	0	0	0	0	0	0	0	0	0	18	0	0	0	0	0	0	0	0	0	0	0	0
Quartz in sandstone r.f.	6	19	12	0	5	8	9	8	7	9	11	5	0	15	12	7	0	8	7	5	3	0	1	3	4
Quartz in hybrid sandstone r.f.	0	0	0	20	0	0	0	3	0	0	0	0	0	0	0	0	0	0	1	0	0	0	0	0	0
Cc replacement on quartz	0	0	0	0	0	0	0	0	0	0	0	0	0	0	0	0	0	0	0	0	0	0	0	0	0
Total detrital feldspar	1	1	6	0	1	2	0	3	1	4	1	2	2	2	4	5	2	5	2	1	10	27	24	2	3
Detrital K-feld	0	1	3	0	1	2	0	3	0	3	0	2	0	0	1	2	2	0	2	1	8	7	10	0	2
K-feld in plutonic r.f.	0	0	0	0	0	0	0	0	0	0	0	0	0	0	0	0	0	1	0	0	0	0	0	0	0
Detrital plagioclase	1	0	3	0	0	0	0	0	1	1	1	0	2	2	2	3	0	4	0	0	1	14	4	1	0
Plagioclase in plutonic r.f.	0	0	0	0	0	0	0	0	0	0	0	0	0	0	0	0	0	0	0	0	0	0	0	0	0
Detrital Microcline	0	0	0	0	0	0	0	0	0	0	0	0	0	0	1	0	0	0	0	0	1	5	10	1	1
Microcline in plutonic r.f	0	0	0	0	0	0	0	0	0	0	0	0	0	0	0	0	0	0	0	0	0	1	0	0	0
Illite replacement on feldpar	0	0	0	0	0	0	0	0	0	0	0	0	0	0	0	0	0	0	0	0	0	0	0	0	0
Illite replacement feldspar on plut. R.f.	0	0	0	0	0	0	0	0	0	0	0	0	0	0	0	0	0	0	0	0	0	0	0	0	0
Cc replacement on K-feld	0	0	0	0	0	0	0	0	0	0	0	0	0	0	0	0	0	0	0	0	0	0	0	0	0
Total fine lithics	108	89	127	144	124	90	110	122	109	145	91	99	84	117	121	116	100	90	96	131	36	19	40	51	143
Phyllites	20	20	24	43	25	4	1	1	16	13	15	1	1	20	24	23	2	1	6	8	6	0	3	0	40
Schists	39	28	33	34	39	11	4	5	42	48	17	0	6	29	42	36	1	17	15	18	8	3	5	3	45
Chloritochists lithic	0	0	0	0	0	0	0	0	1	0	0	0	0	0	1	0	0	0	0	0	0	0	0	0	0
Quartzite	6	4	8	13	7	7	3	7	8	14	9	3	4	3	8	12	3	7	9	17	6	0	2	5	4
Plutonic r.f.	0	0	0	0	0	0	0	0	0	0	0	0	0	0	0	0	0	0	0	0	0	3	0	0	0
Cc replacement on plut. r.f.	0	0	0	0	0	0	0	0	0	0	0	0	0	0	0	0	0	0	0	0	0	0	0	0	0
Volcanic r.f.	0	0	0	0	0	0	0	0	0	0	0	0	0	0	0	0	0	0	0	0	0	0	0	0	0
Volcanic chert	0	0	0	0	0	0	0	0	0	1	0	0	0	0	0	0	0	1	0	0	0	0	0	0	0
Vitric volcanic lithic	0	0	0	0	0	0	0	0	0	0	0	0	0	0	0	0	0	0	0	0	0	0	0	0	0
Volcanic lithic with microlitic	0	0	4	0	0	0	0	0	0	0	0	0	3	0	0	0	0	0	0	0	0	0	0	0	0
Volcanic lithic with lathwork texture	1	2	0	3	1	0	1	1	0	3	1	0	2	1	1	3	0	4	1	0	1	1	0	0	1
sandstone r.f.	0	2	2	0	0	0	4	1	2	2	1	0	0	2	3	4	1	12	4	7	1	1	0	1	7
Hybrid sandstone r.f.	2	1	2	0	8	3	12	21	0	1	2	9	7	0	0	4	0	4	0	1	0	0	0	0	2
Siltstone r.f.	11	22	23	28	17	21	6	15	19	33	15	11	14	30	23	17	14	10	14	29	11	7	11	14	29
Hybrid Siltstone r.f.	4	2	5	5	10	35	63	59	1	5	8	52	18	8	0	4	62	13	19	21	2	0	0	0	0
Chlorite	1	1	0	0	0	0	0	0	0	0	0	0	0	0	0	0	0	0	0	0	0	0	1	0	0
Chert	2	3	0	3	4	2	0	2	0	7	4	1	9	0	0	0	4	3	7	5	0	0	4	0	1
Muscovite	0	0	0	1	0	0	1	0	1	0	0	0	0	0	0	0	0	0	0	0	1	3	3	2	0
Biotite	0	0	0	0	0	0	0	0	0	0	0	0	0	0	0	0	0	0	0	0	0	0	1	0	0
Heavy minerals	0	0	0	0	0	0	0	0	0	0	0	0	0	2	0	0	0	0	0	0	0	0	0	1	4
Silicified r.f.	7	0	4	4	0	4	8	8	4	7	7	20	10	2	6	4	13	7	11	6	0	0	4	4	0
Cc replacement silificied r.f.	0	0	0	6	0	0	0	0	0	0	0	0	0	0	0	0	0	0	0	0	0	0	0	0	0
Fe-oxid replacement r.f.	13	0	17	0	10	2	0	1	15	8	7	1	0	20	12	6	0	1	1	2	0	0	6	21	8
Silificied limestone	0	0	0	0	0	0	0	0	0	0	0	0	0	0	0	0	0	0	0	0	0	0	0	0	0
Radiolarite r.f.	2	4	5	4	3	1	7	1	0	3	5	1	10	0	1	3	0	10	8	17	0	1	0	0	2
Alterite	0	0	0	0	0	0	0	0	0	0	0	0	0	0	0	0	0	0	0	0	0	0	0	0	0
Total carbonate extrabasinal	64	50	43	37	57	46	76	55	40	28	78	61	43	28	33	51	78	71	54	70	111	140	72	105	18
Monocrystalline sparitic limestone	1	2	1	0	4	1	1	0	2	0	1	0	0	0	3	2	1	0	0	1	0	10	1	2	0
Polycrystalline sparitic r.f.	0	2	0	1	4	0	1	0	1	0	0	0	0	2	1	0	0	0	2	1	0	15	0	3	0
Dolomitized polycrystalline r.f.	0	0	0	0	0	0	0	0	0	0	0	0	0	0	0	0	0	0	0	0	0	2	0	0	0
Biomicritic	0	0	0	0	0	0	0	0	0	0	0	0	0	0	1	0	0	0	0	0	20	0	11	0	0
Biosparitic	0	0	0	0	0	0	0	0	0	0	0	0	0	0	0	2	0	0	2	1	0	0	0	0	0
Dolomicrite r.f	0	0	0	0	0	0	0	0	0	0	0	0	0	0	0	0	0	0	0	0	0	0	0	3	0
Dolomite monocrystalline	1	0	0	0	0	0	0	0	0	0	0	0	0	0	0	0	0	0	0	0	4	0	1	8	0
Dolostone r.f. (sacaroidea)	2	0	0	1	0	0	0	0	0	0	0	0	0	0	0	2	0	0	0	2	0	9	1	3	0
Bioclastic grainstone r.f.	2	6	13	5	5	0	4	1	0	3	11	0	0	2	1	7	2	20	1	1	3	4	1	8	0
Dolomitized bioclastic grainstone r.f.	0	0	0	0	0	0	0	0	0	0	0	0	0	0	0	0	0	0	0	0	0	0	0	0	0
Bioclastic Packes-Wackes r.f.	26	9	16	9	17	25	40	45	7	18	43	33	29	11	2	11	26	34	23	34	35	49	17	24	5
Dolomitized bioclastic Packes-Wackes r.f.	0	0	0	0	0	0	0	0	0	0	0	0	0	0	0	0	0	0	0	0	0	0	0	0	0
Biomicritic mudstone r.f.	32	31	13	21	26	16	23	9	28	6	23	18	14	13	25	27	44	13	24	26	49	51	40	54	13
Dolomitized biomicritic mudstone	0	0	0	0	0	0	0	0	0	0	0	0	0	0	0	0	0	0	0	0	0	0	0	0	0
Extrabasinal bioclasts	0	0	0	0	1	4	7	0	2	1	0	10	0	0	0	0	3	4	2	4	0	0	0	0	0
Total carbonate intrabasinal	0	0	0	0	0	0	0	0	0	0	0	0	0	0	1	0	0	0	0	0	2	5	0	0	0
Reworked calcrete clasts	0	0	0	0	0	0	0	0	0	0	0	0	0	0	0	0	0	0	0	0	0	0	0	0	0
Bioclasts	0	0	0	0	0	0	0	0	0	0	0	0	0	0	1	0	0	0	0	0	2	5	0	0	0
Total non-carbonate intrabasinal	0	0	0	0	0	0	0	0	0	0	0	0	0	0	0	12	0	0	0	0	0	14	0	0	0
Total matrix	0	0	0	0	0	0	0	0	0	0	0	0	0	0	0	0	0	0	0	7	0	0	0	0	0
Diagenetics minerals	105	99	77	93	103	111	105	68	101	64	69	112	66	104	77	76	89	108	102	78	123	76	100	98	139
Total porosity	0	0	0	0	0	0	0	0	0	0	0	0	0	0	0	0	0	0	0	0	0	0	0	0	0
TOTAL POINTS	320	322	308	317	326	314	323	304	316	316	304	325	334	321	318	324	321	316	318	346	319	342	323	318	332

Coordinates of all analyzed samples		
SAMPLE	**LONGITUD (°)**	**LATITUD (°)**
SF2	-0,018591	42,443120
SF3	-0,018408	42,439545
SF5	-0,019158	42,433337
SF7	-0,016588	42,427703
SFF11	-0,008588	42,412665
SF13	-0,010117	42,401625
SF16	-0,023500	42,404270
SF18	-0,031054	42,399049
SF19	-0,031521	42,398309
ROD1	-0,069426	42,263344
ROD2	-0,069854	42,250591
ROD3	-0,071918	42,250009
NOC1	-0,257966	42,307087
BARA1	-0,134526	42,328047
BIB1	-0,096665	42,375599
BIB2	-0,097333	42,377110
BIB5	-0,089202	42,395417
BEMO1	-0,362595	42,308801
BEMO3	-0,374380	42,316461
BEMO5	-0,398677	42,327743
BEMO8	-0,404566	42,335712
BEMO10	-0,393164	42,339824
BEMO11	-0,393989	42,347487
BEMO12	-0,381139	42,360232
BEMO13	-0,382663	42,367505
BEMO14	-0,387023	42,376454
BEMO16	-0,384576	42,383626
BEMO17	-0,391734	42,393261
BEMO18	-0,392359	42,395807
GAL2	-0,677216	42,387679
GAL3	-0,650748	42,406417
GAL4	-0,640698	42,419734
GAL5	-0,638352	42,422737
GAL7	-0,627324	42,428003
GAL8	-0,620982	42,438063
GAL9	-0,614691	42,444841
GAL10	-0,595807	42,471654
BAI1	-0,786450	42,415467
BAI2	-0,795190	42,433117
BAI3	-0,794264	42,444900
BAI4	-0,793457	42,458830
MAR1	-0,893066	42,566938
MAR2	-0,892234	42,564698
LUE10	-0,971590	42,456351
LUE9	-0,970459	42,448904
LUE7	-0,986307	42,437526
LUE5	-1,001983	42,425902
LUE3	-1,012528	42,409528
LUE2	-1,029362	42,394131
SM1	0,077514	42,371359
SM2	0,077303	42,371386
MO1	0,126053	42,276964
OL1	0,124928	42,274410
GRAD1	0,223083	42,174838

Capítol 6

DZ U-Pb and ZHe Provenance Signatures in the South Pyrenean Foreland basin: Interplay of Direct vs Recycled Sources During Pyrenean Orogenic Growth

El capítol 6 correspon a un article en preparació.

X. Coll ha mostrejat totes les seccions i ha realitzat el tractament de les mostres (descrit en la metodologia). També va realitzar tots els anàlisis d'U-Pb en zircons detrítics al laboratori UTChron de la University of Texas at Austin. A part, també ha redactat la major part del text i ha realitzat la major part de les figures.

DZ U-Pb and ZHe Provenance Signatures in the South Pyrenean Foreland basin: Interplay of Direct vs Recycled Sources During Pyrenean Orogenic Growth.

DZ U-Pb and ZHe Provenance Signatures in the South Pyrenean Foreland basin: Interplay of Direct vs Recycled Sources During Pyrenean Orogenic Growth.

Xavier Coll1,*; David Gómez-Gras1; Marta Roigé1; Daniel Stockli2; Antonio Teixell1; Salvador Boya1.

Coll et al. in preparation

1Department de Geologia, Universitat Autònoma de Barcelona, 08193 Bellaterra, Spain

2The University of Texas at Austin, Department of Geological Sciences, Austin, TX 78712, USA

(*) Corresponding author

ABSTRACT

The Eocene to Miocene clastic wedge of the South Pyrenean foreland basin is a reference model to investigate the progressive evolution of sediment provenance, and source-to-sink dynamics. We present new detrital zircon (DZ) U-Pb and (U-Th)/He (ZHe) data from the Jaca basin and the Ebro basin, providing insights into the evolution of the foreland basin sedimentary systems that record a major tectonic and drainage reorganization. Three distinc DZ U-Pb signatures have been identified: (i) Variscan dominated; (ii) mixed Cadomian-Variscan; (iii) Cadomian dominated; and two DZ ZHe signatures (i) Pyrenean dominated; (ii) non-Pyrenean dominated. Coupling DZ U-Pb, ZHe, and petrographic data allows to clearly discriminate among distinctive Pyrenean sources as well as to understand how DZ signatures are propagated in a source-to-sink system conditioned. Our results indicate that whereas the eastern Jaca basin was fed from eastern source areas located in the central and eastern Pyrenees, the western Jaca basin was fed from the Basque massifs and the Urbassa-Andía Sierra (western and Basque-Cantabrian Pyrenees.

1. INTRODUCTION

Sedimentary Provenance Analysis is the key to decipher source-to-sink processes and the links between tectonics and sedimentation, particularly in foreland basins related to collision orogens (e.g. Dickinson, 1970; Dickinson & Suzeck, 1979; Steidman & Schimt, 1988; Garzatnti et al., 2004; Garzanti et al., 2007; Allen 2017). Foreland basins record the erosional and exhumational history of their source areas, providing valuable insights into the chronology of the deformation and unroofing

of the related orogen as well as the basin paleogeography (e.g. Fosdick et al., 2015; Labaume et al., 2016; Koshnaw et al., 2018; Thompson et al., 2017; Thompson et al., 2019; Odlum et al., 2019).
Detrital zircon (DZ) U-Pb and (U-Th)/He double-dating allows to obtain crystallization and exhumation age constraints of the source areas feeding the basin. Since zircon is one of the most ubiquitous heavy minerals in crustal rocks, being highly resistant to weathering and diagenetic processes, DZ signatures have become a powerful and widely-applied provenance tool worldwide in the last decades (Hart et al., 2016; Thompson et al., 2017; Hart et al., 2017; Thompson et al., 2019; Odlum 2019; Pujols & Stockli, 2021; Laskari et al., 2022a,b.) However, the resolution of this kind of studies might be limited due to multiple source areas with similar or monotonous DZ age distributions, and recycling and/or cannibalization of older siliciclastic sedimentary rocks that might bias the reconstruction of the source area (Dickinson 2009; Garzanti et al., 2013). Although extensive literature deals with the U-Pb signatures of direct sources, the role of sediment recycling in the propagation of DZ signatures is poorly constrained (Roigé 2018). Therefore, as it happens with any other provenance study method (i.e. sandstone petrography or heavy mineral analysis), it is crucial to integrate as many provenance tools as possible in order to record the true complexity of the case study and obtain the highest resolution (Thompson et al., 2019; Coll et al., 2022).

Due to its extraordinary well-preserved sedimentary record, the South Pyrenean basin is a reference model for foreland basin worldwide. The Late Lutetian to Miocene evolution of its western part -known as the Jaca basin)- provides an excellent natural laboratory to study sediment recycling during its continentalization as well as the interplay between active source areas and sediment routings (Michael 2013; Thompson et al., 2017; Roigé et al., 2016; Roigé et al., 2017; Coll et al., 2020; Coll et al., 2022). The well-known Hecho Group turbidites were deposited in an axially-oriented turbiditic through fed from the Southern Pyrenees during the Eocene. However, the activity of the Gavarnie and Guarga thrusts uplifted these deposits and promoted their erosion during Priabonian to Miocene times, which were redeposited in the fluvio-alluvial deposits (Campodarbe and Bernués Formations) of the northern and southern Jaca basin (Puigdefàbregas 1975; Teixell & García-Sansegundo., 1995; Labaume et al., 2016; Roigé et al 2016; Roigé et al., 2017; Coll et al., 2022).

The paleogeography of the basin has been well stablished from various works that have studied its stratigraphy, sedimentology and tectonics (e.g., Soler-Sampere and Puigdefàbregas, 1970; Puigdefàbregas, 1975; Mutti, 1985; Barnolas and Teixell, 1994; Payros et al., 1999; Oms et al., 2003; Remacha et al., 2005; Labaume et al., 2016; Oliva-Urcia et al., 2019; Vinyoles et al., 2021), as well as

provenance studies that focused into its clastic infill (Fontana et al., 1989; Gupta & Pickering, 2008; Caja et al., 2010; Whitchurch et al., 2011; Filleaudeau et al., 2012; Michael, 2013; Roigé et al., 2016; Roigé et al., 2017; Gómez-Gras et al., 2017; Thomson et al., 2017; Coll et al., 2020; Coll et al., 2022). All this research allowed to constrain the occurrence of distinct axially-fed east sourced systems (mainly supplying Paleozoic basement rocks and Mesozoic carbonates from the central and eastern Pyrenees) that were progressively replaced by diverse transverse-fed north sourced systems (mainly Mesozoic sedimentary rocks and recycling the middle-upper Eocene siliciclastic rocks from the southern flank of the west-central Pyrenees).

In the eastern Jaca basin, the provenance of the northern and southern margin are well constrained from sandstone petrography and heavy mineral analysis (Roigé et., 2016; Roigé et al., 2017; Coll et al., 2020; Coll et al., 2022). Nonetheless, provenance studies using DZ signatures are only focused in the northern margin (Roigé 2018). By contrast, in the western Jaca basin, the provenance of the late Eocene-Miocene siliciclastic systems is poorly constrained (Puigdefàbregas, 1975; Payros et al., 1997; Astibia et al., 2005), and no quantitative data exists regarding sandstone detrital modes, heavy minerals, and DZ U-Pb or ZHe provenance signatures.

Our study aims to investigate the impact of the major reconfiguration of the catchment areas by applying DZ U-Pb and (U-Th)/He analysis in the southern margin and western area of the Jaca basin as well as in the Ebro basin. We (a) characterize the DZ U-Pb signatures recorded by the deltas, fluvial and alluvial fan systems of the eastern and western Jaca basin, as well as of the Ebro basin, (b) characterize the zircon (U-Th)/He provenance signatures in order to constrain the exhumational history of the source areas, (c) compare these results with the more proximal, time equivalents of the nearby Ainsa and Tremp-Graus Basins (Whitchurch et al., 2011; Filleaudeau et al., 2012; Michael, 2013; Thomson et al., 2017), (d) contribute to the knowledge of the propagation and interplay of DZ signatures during recycling processes, and (e) highlight the importance of integrating these techniques with published petrographic data from the northern and southern margin of the Jaca basin (Roigé et al., 2016, 2017; Coll et al., 2022), and new petrographic data from the western Jaca basin in order to constrain sediment provenance and sediment dispersal patterns, with applications to collision orogens where different source areas can produce similar compositional signatures.

In the last decades, a great number of provenance studies are solely based on U-Pb-He, disregarding additional provenance constraints from sandstone petrography (e.g. Whitchurch; 2011; Filledeau et al.,

2012; Vachearat., 2017). Such methodology is not able to provide enough resolution, particularly when recycling of clastic formations of different ages with similar signatures play an important role. Nonetheless, the integration of DZ data with sandstone petrography allows a much better discrimination of the nature of source areas and the evolution their catchment areas (Nie et al., 2012; Roigé 2018; Thompson et al., 2019;).

Our results evidence that a provenance framework based on a single-method approach cannot unequivocally resolve the nature of the source areas and sediment routing systems, leading to biased interpretations or undesired low resolution. Therefore, we propose that coupling provenance indicators such as heavy mineral analysis, U-Pb geochronology, and U-Th-He thermocrhonology with sandstone petrography is the most powerful approach to unravel sediment provenance and tectono-sedimentary links in foreland basins.

2. GEOLOGICAL SETTING

2.1. Geological and stratigraphic framework

The Jaca basin constitutes the western area of the south Pyrenean foreland basin (Figure 1). From the Late Cretaceous to early Miocene, the Eurasian and Iberian plate collision led to the formation of the Pyrenean fold-and-thrust belt, which grew diachronously as a result of the oblique character of the collision (Puigdefàbregas et al., 1992; Teixell et al., 2018; Vergés et al., 2002; Mouthereau et al., 2014). The core of the belt (known as the Axial Zone) is made of basement-involved stacked thrust sheets, flanked to the north by the North Pyrenean Zone (where the pre-collisional rift architecture is still preserved; Lagabrielle et al., 2010; Figure 1). The Cenozoic sedimentary deposits that occur further north constitute the retro-wedge foreland basin (Aquitanian basin). In the South Pyrenean Zone, the deformation was accommodated by a thrust imbricate fan (Cámara & Klimowitz, 1985; Labaume et al., 1985; Teixell, 1996; Labaume et al., 2016; Muñoz et al., 2018), which in the-west central Pyrenees is constituted by four main thrust sheets (Lakora-Eaux-Chaudes, Gavarnie, Broto and Guarga; Figure 1b). These thrust sheets involve the Paleozoic basement, a pre-orogenic Paleozoic and Mesozoic sedimentary cover, and a late Cretaceous to early Miocene foreland basin, which is bordered to the south by the External Sierras thrust front and the youngest sedimentary record of the final stages of the Pyrenean exhumation (the Ebro basin).

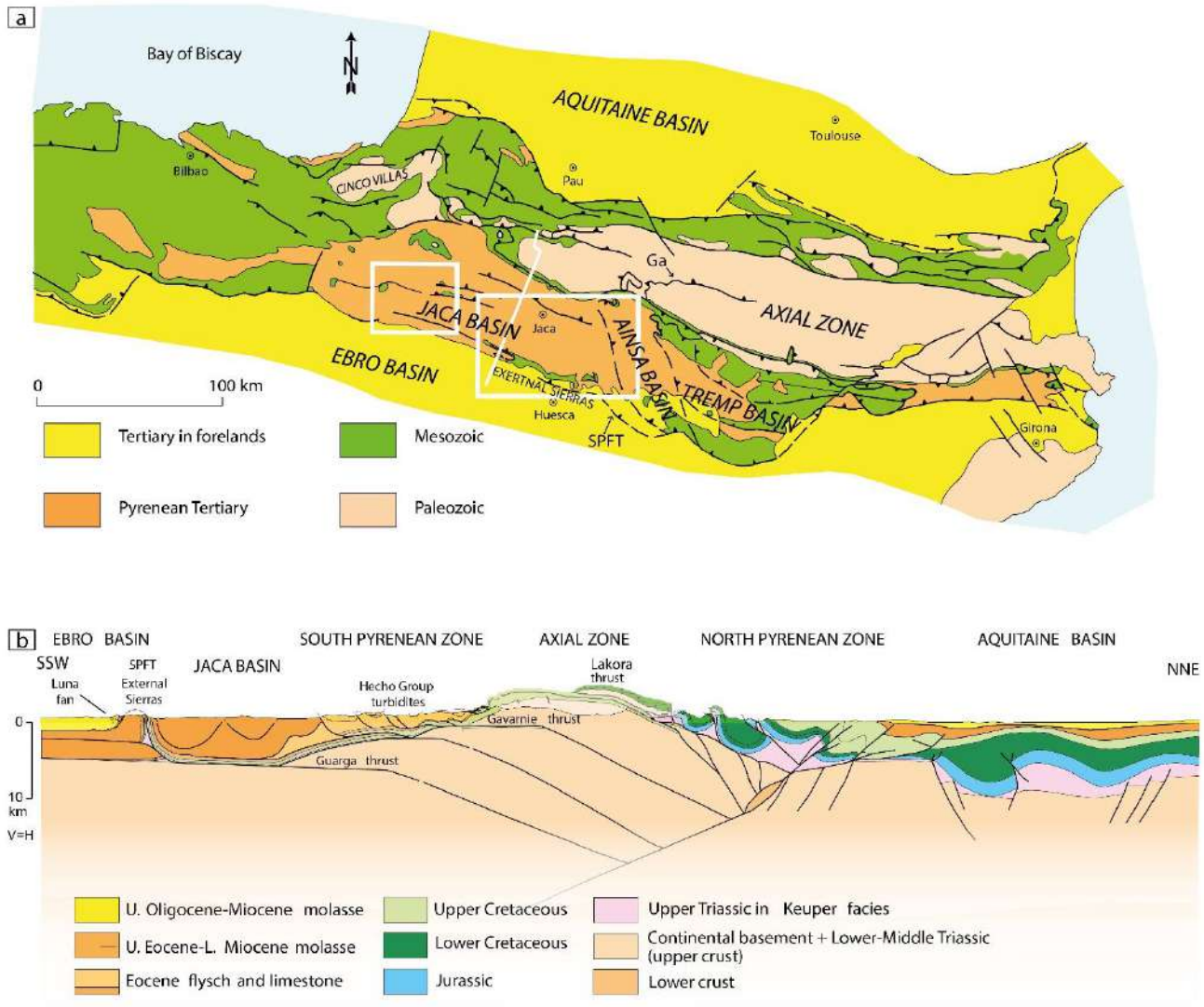

Figure 1. *(a) Simplified geological map of the Pyrenees (redrawn from Teixell et al. 1996), showing the location of the study area (white frame). White line indicates cross-section in Figure 1b. White box corresponds to Figure 3 map area. Ga: Gavarnie thrust, SPTF: South Pyrenean Frontal Thrust; (b) Crustal cross-section of the west-central Pyrenees (simplified from Teixell et al. 2016), showing both the South Pyrenean Zone and the North Pyrenean Zone.*

The core of the Pyrenean belt is constituted by Paleozoic basement, mainly Variscan low-grade metamorphic rocks and granitoids that are unconformably overlain by Permo-Triassic red beds or Cretaceous limestones. The preorogenic Mesozoic succession includes the Triassic Keuper facies, which are involved in thrust sheet propagation, acting as an evaporite detachment level during extension and contraction, and salt diapirism processes that played a critical role in the formation of Mesozoic mini-basins and the exhumation of the Paleozoic basement in the central Pyrenees (Saura et al., 2016; Burrel & Teixell, 2021; Burrel et al., 2021; Hudec et al., 2021). The rest of the succession is made up of a thick Jurassic-Cretaceous carbonate and sandstone-shale successions. The South Pyrenean foreland basin is an assemblage of synorogenic rocks, related to the late Santonian-early

Miocene shortening, that recorded a major drainage reorganization in the mid-late Eocene. The progression of the fold-and-thrust belt deformation triggered a shift from a predominantly axial drainage network to a series of transverse systems sourced from the orogenic belt to the north (Whitchurch et al., 2011).

2.1.1 The eastern Jaca basin.

Fluvio-deltaic sedimentary environments developed in the Àger and Tremp-Graus basins (eastern sector of the South Pyrenean basin) during the Eocene, funneling sediments to the west, were the slope and deep-marine sedimentation environments of the Ainsa and Jaca basins (the Hecho Group turbidites) were developing during the underfilled foreland basin stage (Nijman & Nio, 1975; Mutti, 1985; Bentham et al., 1992; Caja et al., 2010). With the growth of the orogen, these environments were progressively replaced from east to west, during mid to late Eocene (Puigdefàbregas, 1975; Dreyer et al., 1999), by deltaic deposits, and by fluvio-alluvial environments during Oligocene-Miocene times (Campodarbe and Bernués Formations).

The Pamplona marls Fm. (Figures 2,3) constitutes the prodelta deposits of the Belsué-Atarés Fm (Puigdefabregas, 1975). During the Bartonian-Priabonian, the Belsué-Atarés delta prograded from east to west sourced from the central and eastern Pyrenees (Roigé et al., 2017; Coll et al., 2021). In the Northwestern part of the basin, the Belsué-Atarés Fm. passes to the Martés and Güendulain Formations (Puigdefàbregas, 1975). All these deltaic environments were progressively substituted by the fluvial to alluvial Campodarbe and Bernués Formations (Bartonian-Miocene; Puigdefàbregas, 1975; Boya, 2018; Roigé et al., 2019), which marked the endorheic basin stage and the onset of continental sedimentation throughout the entire basin at 36 Ma (Barnolas & Gil-Peña., 2001; Costa et al., 2010; Ortí et al., 1986; Payrós et al., 2000).

The Campodarbe Formation (Mutti et al., 1972) is a fluvial to alluvial succession, where at least two main sediment routings can be identified (Puigdefàbregas, 1975). In the northern margin, an east-derived axial fluvial system, entering the Jaca basin through the southeastern margin, interacts with a north-derived transverse alluvial fan system, mainly controlled by the activity of the Gavarnie thrust, and mostly derived from the recycling of a former lower to middle Eocene turbidite basin (Puigdefàbregas, 1975; Roigé et al., 2016; Roigé et al., 2017; Coll et al., 2020). By contrast, the sedimentation in the southern edge was dominated by two axially-fed fluvial systems sourced from the

Central and Eastern Pyrenees (Coll et al., 2022), and strongly controlled by growing tectonic structures of the External Sierras (Puigdefabregas, 1975; Jolley, 1988; Hogan, 1993; Hogan & Burbank., 1996 Labaume et al., 2016; Labaume & Teixell., 2018). The last stages of the basin infill are marked by the Bernués Formation (Chattian-Aquitanian; Puigdefàbregas, 1975; Arenas, 1993; Roigé et al., 2019), a complex of alluvial fan deposits sourced from the north of the basin.

As the orogenic deformation progressed to the south, the External Sierras thrust front (Soler-Sampere & Puigdefàbregas, 1970; Labaume et al., 1985; Teixell, 1996; Oliva-Urcia et al., 2016;) became strongly emergent (Oligocene-Miocene) and split the Campodarbe Formation in the Jaca basin to the north from the Ebro basin to the south. The activity of the Guarga thrust sheet triggered the formation of the north-derived Luna alluvial fan system, sourced from recycling of the Jaca basin and the Internal Sierras and the Axial Zone farther to the north, and the Basque massifs to the northwest (Puigdefàbregas, 1975; Arenas et al., 2001; Coll et al., 2022).

2.1.2. The western Jaca basin

In this area, time-equivalent deposits of the eastern Jaca basin comprise a stratigraphic succession constituted, from base to top, by: the Ezkaba Sandstone Fm., the Pamplona Marls Fm., the Ardanatz Fm., the Illundain marls Fm., the Yesa turbidites, the Guendulain Fm., and the Campodarbe and Bernués Fms. (Figures 2, 3).

The Bartonian Ezkaba Sandstone Fm. (western time-equivalent deposits of the deltaic Sabiñánigo Fm; Puigdefàbregas 1975; Pyaros et al., 1997) is a channel levee turbidite system developed at the base of the Bartonian-Priabonian Pamplona Marls Formation (Mangin, 1960; Astibia et al., 2005) in the northwestern sector of the basin, and it is sourced from the Basque massifs (Payros et al. 1997). The Pamplona Marls Fm., the Ardanatz Fm. (Bartonian) and the Bartonian-Priabonian Ilundain Marls Fm correspond to prodelta, delta front, and restricted platform environments that were related to the progradation of the Belsué-Atarés delta in the eastern Jaca basin (Puigdefàbregas, 1975; Astibia et al., 2005; Astibia et al., 2014).

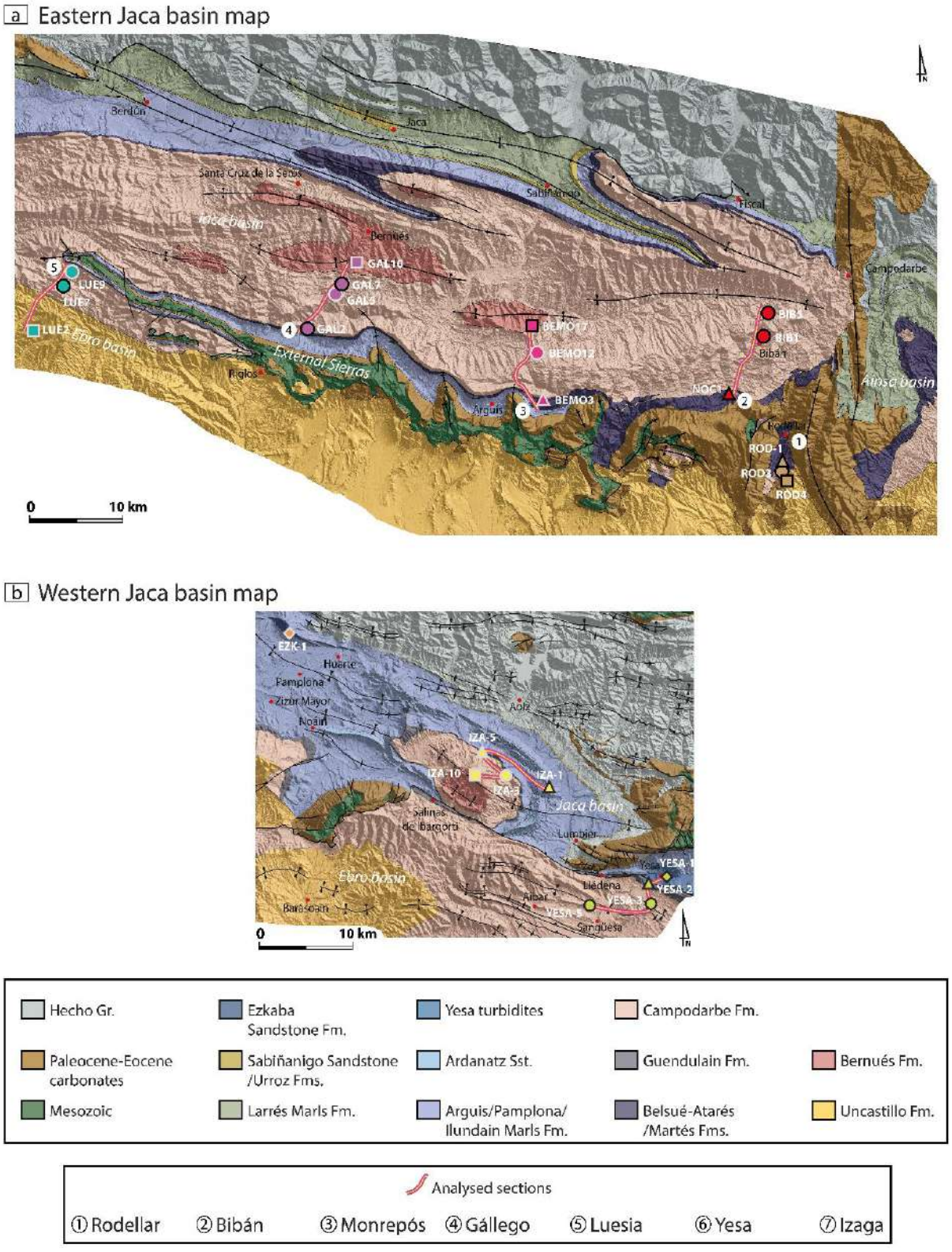

Figure 2. *Geological map of the of the Jaca basin (modified from Puigdefàbregas 1975). (a) Eastern Jaca bain. (b) Western Jaca basin. Yellow-purple lines show the location of the analyzed sections. Numbers refer to each section: (1) Rodellar section; (2) Bibán section; (3) Monrepós section, (4) Gállego section, (5) Luesia section, (6) Yesa section, and (7) Izaga section. Numbers and symbols refer to each of the analyzed samples for sandstone petrography analyses. Black stroke indicates U-Pb analysis and white stroke doble dated samples.*

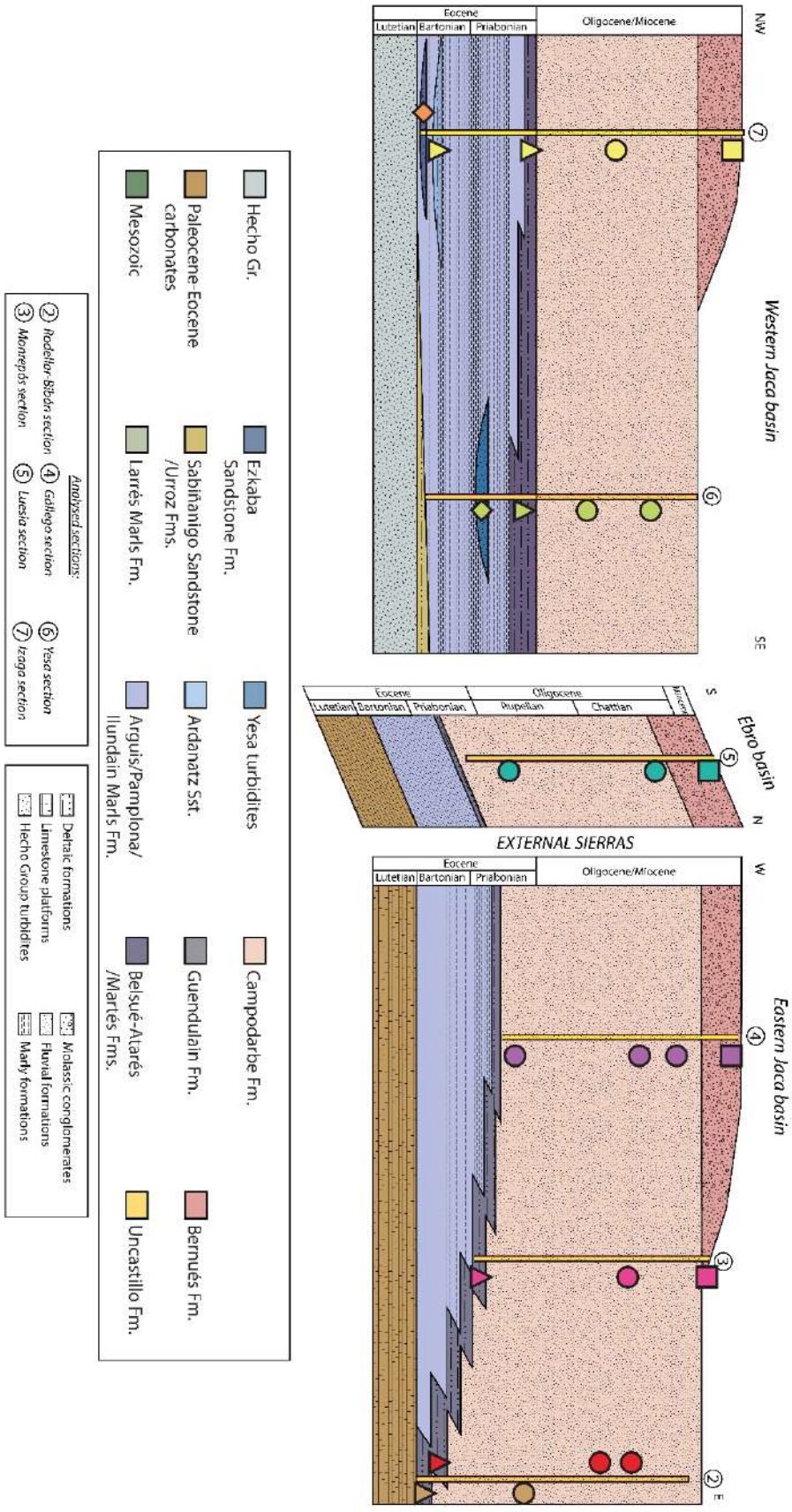

Figure 3. *General stratigraphic cross-section sketch with symbols representing the relative position of the analyzed samples.*

The Ardanatz Fm. (Bartonian) is a set of flood-influenced delta-front sandstone lobes interbedded at the base of the Ilundain Marls Fm. (Astibia et al., 2005). The general distribution of facies (shallow-water environments to the west and turbiditic channels to the east) suggests no link with the Belsué-Atarés delta. To the east, another formation has been related with the progradation of the Belsué-Atarés delta, the Yesa turbidites (Priabonian), which occur at the top of the Pamplona marls (Puigdefàbregas, 1975).

The Priabonian Güendulain Fm. (Payros et al. 2000) constitute a series of coastal deposits divided in three distinct members: the lower evaporite, the middle sabkha marl, and the upper Liédena Sandstone Fm. The latter, constitute a wave-dominated delta containing the last deposits with marine influence in the Jaca basin.

The overlying Campodarbe and Bernués Fms. represent the development of fully terrestrial environments (fluvio-lacustrine and alluvial) throughout the whole basin. In the Izaga syncline area, the Campodarbe Fm. is constituted by lacustrine environments (Zabalza facies ss; Puigdefàbregas; 1975) until the irruption of the Izaga alluvial fan, sourced from northern areas comprising Paleocene-Eocene sedimentary rocks (Puigdefàbregas, 1975).

2.2. U-Pb characterization of potential source areas

In order to comprehend the DZ U-Pb from the Jaca basin, it is necessary to review the age signatures of the different possible sources. These can be the different tectonic domains of the central and western Pyrenees, which include Paleozoic metasedimentary and igneous basement of the Axial Zone, the preorogenic Mesozoic sedimentary cover successions, and the early synorogenic Late Cretaceous to Middle Eocene deposits.

The metasedimentary succession of the Axial Zone (Cambrian-Ordovician-Devonian-Silurian) display DZ U-Pb signatures dominated by >700 Ma age modes, with an important Cadomian component (520-700Ma), and subsidiary 420-520 Ma (Hart et al., 2016; Margalef., 2016). Orthogneissic rocks of the crystalline core of the Pyrenees mainly display lower Ordovician ages (Dennele et al., 2016). Carboniferous strata contain dominant recycled Cambro-Devonian DZ signatures and syndepositional volcanic zircons of 325-360 Ma (Martínez et al., 2015; Hart et al., 2016). Igneous rocks of the Paleozoic basement are mainly constituted by Variscan granitoids with ages ranging from 280-315

Ma. Permo-Triassic clastic deposits display dominant Cadomian (520-700Ma) and >700 Ma age components, with scarce Variscan ages (Hart et al., 2016). Permian and upper Triassic volcanic and subvolcanic rocks in the region are not expected to contribute zircon grains due to its mafic character, although some grains could be detected. Cretaceous sedimentary rocks display different DZ U-Pb signatures depending on the location and the stratigraphic level. Scarce data show Variscan dominated ages can be found in the clastic lower and upper Cretaceous deposits from the Central and eastern Pyrenees (Filledeau et al., 2012; Thompson et al., 2016; Odlum et al., 2016;) and North Mauleón basin (NPZ; Hart et al., 2016), whereas Cadomian-dominated occur in the lower Cretaceous of the Mendibelza area, the upper Cretaceous of the North Mauleón basin (Hart et al., 2016), and the upper Cretaceous Aren Formation (Central Pyrenees; Whitchurch et al., 2011) as well as in the Adraén Fm. in the Baga area (Odlum et al., 2019). Moreover, Paleocene-Eocene Deposits of the south-central Pyrenean basin (Ainsa, Tremp, and Àger basins; Fig. 1) show variable DZ distributions, which reflect the provenance evolution experienced by these sedimentary systems, alternating dominant Cadomian and Cambro-Devonian ages with Variscan components trough time (Whitchurch et al., 2011; Filleaudeau et al., 2012; Thomson et al., 2017; Odlum et al., 2019; Thomson et al., 2019). Finally, Oligo-Miocene calc-alkaline magmatism reported from the Mediterranean basin related to the opening of the Valencia through could supply some Cenozoic zircons trough ash clouds (Marti et al. 1992; Sabat et al. 1995; Roigé et al. 2019).

In addition to the different age modes displayed by the different rocks, their zircon fertility also has an impact on the DZ populations of the studied deposits (Moecher and Samson, 2006; Dickinson, 2008; Malusà et al., 2016). A qualitative approach (Thomson et al. 2016) infers the highest zircon fertility for the Variscan granitoids, whereas in the fine-grained Cambro-Ordovician metasedimentary formations moderate fertility is expected (Hart et al., 2016). By contrast, Triassic sandstones (dominantly arkosic) might display a high zircon fertility as they were sourced from the crystalline basement. Cretaceous to Paleocene formations (mainly carbonates), are expected to have a very low to scarce zircon fertility, although siliciclastic sandstones might display moderate to high fertility.

In addition, we assume that the Eocene clastic formations (including the Hecho Group turbidites) have a moderate zircon fertility, depending on their abundance of carbonate (low fertility) vs siliciclastic (high fertility) grains. Moreover, turbidite layers sourced from acid igneous rocks will produce a higher zircon fertility than those sourced from metasedimentary basement rocks, and zircons produced by

fine-grained metasedimentary (Neoproterozoic dominated) are expected to be smaller than those delivered from plutonic (Variscan dominated).

2.3. (U-Th)/He (ZHe) characterization of potential source areas

Pyrenean ZHe ages (<85 Ma) record Pyrenean shortening and exhumation during plate collision (Iberia-Eurasia) and are restricted to the thermally reset Paleozoic igneous-metamorphic basement (Axial Zone and North Pyrenean Zone) exhumed during the Pyrenean Orogeny (Whitchurch et al., 2011; Filleaudeau et al., 2012; Thomson et al., 2017). Cretaceous rifting ZHe ages (85-155 Ma) are related to rifting-hyperextension and HT-LP metamorphism along the Iberian-Eurasia plate boundary. These ages can be found in the syn-rift sedimentary units of the Pedraforca thrust sheet and the inverted Organyà basin (Odlum et al., 2019) as well as in the North Pyrenean Zone late Cretaceous sedimentary cover, where the pre-collisional rift architecture is still preserved (Bosch et al., 2016)Liasic ZHe ages (180-201 Ma) can be attributed to widespread ophitic magmatism and the magmatic episode associated with the central Atlantic Magmatic Province (Marzoli et al., 1999; Mothereau et al., 2014). Permo-Triassic and Variscan ZHe ages can be attributed to non-reseted zircon grains originally sourced from the Ebro massif to the Cretaceous-Eocene South Pyrenean foreland basin.

3. METHODOLOGY

Twenty-five sandstone samples (2-4 Kg) from seven different profiles were collected in the field. In order to avoid hydraulic-sorting effects that might bias the analytical results, medium-grained sandstones were targeted, avoiding locally reworked deposits (Malusà et al., 2016; Garzanti et al., 2008; Garzanti et al., 2009; Garzanti et al., 2019; Andò, 2020). In addition, samples from each depositional system were collected from similar facies in order to minimize hydraulic-sorting effects related to different processes within the same depositional environment.

Following standard heavy mineral separation methods, samples were crushed with a Retsch Disc Mill DM 200 and submitted to Struers Metason 200 ultrasound machine (5 minutes) to help desegregation of well cemented sands and clay coatings. The <500µm window was obtained through dry sieving with a digital electromagnetic sieve shaker BA-200. The recovery of the heavy fraction was done in two steps, using a Holman-Wilfley laboratory shaker table, and by the centrifuging method (using nontoxic dense liquid Na-polytungstate; 3.10g/cm3) and partial freezing with liquid nitrogen (Andò,

2020). Finally, zircons were obtained using a Frantz isodynamic magnetic separation. Mineral separation was performed at the Thin Section Lab of the Department of Geology of the Universitat Autònoma de Barcelona.

Data from published sandstone petrography (Roigé et al. 2016; Roigé et al. 2017; Coll et al 2022), heavy minerals (Coll et al 2020; Coll et al 2022); and DZ U/Pb (Roigé, 2018) were integrated with the new U-Pb and (U-Th)/He DZ provenance dataset to refine provenance interpretations and to address and quantify the role of sediment recycling and cannibalization of older foreland basin strata within the deforming fold and thrust belt.

3.1 Zircon U-Pb Geochronology

Zircons grains were mounted onto double-sided adhesive plastic pucks and left unpolished for depth-profile analysis (Campbell et al., 2005; Hart et al., 2017). For each sample, at least 120 zircons were selected randomly and analyzed using the laser ablation-inductively coupled plasma-mass spectrometry (LA-ICP-MS) U-Pb geochronology, in order to obtain a statistically robust and representative provenance dataset (Vermeesch, 2004). U-Pb analysis was performed using a PhotonMachine Analyte G.2 excimer laser with a HeLex 238 sample cell and a Thermo Scientific Element2 ICP-MS. GJ1 was used as a primary standard (Jackson et al., 2004), and Plesovice (Sláma et al., 2008) were used as secondary standard, in order to obtain a data quality control. A 30 µm laser spot ablated 15 µm deep pits on the flat prism plane of the zircon grains. Data were reduced using VizualAgeTM data reduction scheme for the IoliteTM on Igor ProTM software (Paton et al., 2011). During data reduction individual analysis were deleted if the grains were not zircon or there was evidence of errors in analysis. 206Pb/238U ages are used for grains younger than 850 Ma, while 207Pb/206Pb ages are used for grains older than 850 Ma. Individual zircon ages were excluded if there was a 206Pb/238U 2σ error greater than 10%, or 206Pb/238U and 207Pb/235U discordance greater than 10% for grains younger than 850 Ma or 206Pb/238U age and 206Pb/207Pb discordance greater than 20% for grains older than 850 Ma. All the ages are presented with two sigma absolute errors.

3.2. Zircon (U-Th)/He Thermochronology

After U/Pb DZ signatures characterization, 10 samples were selected for (U-Th)/He DZ Analysis. Six to nineteen concordant single age zircons free of uranium zonation (per sample) were targeted for

double dating analysis, based on of U-Pb age components relative abundance and the criteria for (U-Th)/He analysis (Farley, 2002; Saylor et al., 2012; Hart, 2015; Hart et al., 2017). Grains were individually packed into platinum (Pt) foil packets and were heated and degassed under ultra-high vacuum. Total He concentration was measured on a quadrupole mass spectrometer. Completely degassed grains were removed from Pt packets and dissolved with a combination of Hf and HNO3. Dissolved grains were analyzed on a Thermo Scientific Element2 ICP-MS for absolute U, Th, and Sm concentrations (Wolfe & Stockli, 2010). Fish Canyon Tuff zircons were run with unknown grains to monitor data quality (Reiners, 2005). 8% standard error was applied to all measurements. Partially/fractured or completely broken grains during unpacking from Pt packets, as well as grains containing fluid inclusions, were excluded from the analysis. Incomplete dissolved grains were also excluded. All U-Pb and He analyses were conducted at the UTChron Laboratory at the University of Texas at Austin.

3.3. Statistical Analysis

We apply multi-dimensional scaling (MDS) and correspondence analysis (CA) as exploratory compositional data analysis tools to assess similarities/dissimilarities between samples (Vermeesch, 2013; 2018). Results are displayed as biplots in order to facilitate the visualization and results interpretation. Statistical treatment was done using the Provenance R-package (Vermeesch, 2016; 2018), and allowed the distinction between distinctive U-Pb and (U-Th)/He components signatures.

4. RESULTS AND DISCUSSION

4.1. DZ U-Pb geochronological signatures

DZ U-Pb age populations (Table S1) are grouped into twelve U-Pb age components: Cenozoic (0-66 Ma), Late Mesozoic (66-180 Ma), Permo-Triassic (180-280 Ma), Late Variscan (280-310 Ma); Early Variscan (310-370 Ma), Cambro-Devonian (370-520 Ma), Cadomian (520-700 Ma), Neoproterozoic (700-900 Ma), Kibaran (900-1200 Ma), Mesoproterozoic (1200-1500 Ma), Paleoproterozoic (1500-2200 Ma), and Archean (2200-4600 Ma). DZ U-Pb ages are plotted as kernel density estimators (KDE) and histograms, and as percentages of the 12 U-Pb components (Table 1; Figures 4,5).

Sample	Fm.	n	Cenozoic	Late Mesozoic	Permo-Triassic	Late Variscan	Early Variscan	Cambro-Devonian	Cadomian	Neo-proterozoic	Kibaran	Meso-proterozoic	Paleo-proterozoic	Archean
			0-66 Ma	66-180 Ma	180-280 Ma	280-310 Ma	310-370 Ma	370-520 Ma	520-700 Ma	700-900 Ma	900-1200 Ma	1200-1500 Ma	1500-2200 Ma	2200-4600 Ma
RD1	Belsué-Atarés Fm.	126	0,0	0,0	3,2	21,4	29,4	7,9	21,4	4,0	4,8	1,6	2,4	4,0
RD3	Campodarbe Fm.	118	0,0	0,0	0,0	24,6	28,0	12,7	13,6	3,4	6,8	0,8	5,9	4,2
RD4	Graus Fm.	129	0,0	0,0	0,0	6,2	16,3	17,8	26,4	8,5	7,8	0,8	8,5	7,8
NC1	Belsué-Atarés Fm.	131	0,0	0,0	0,8	7,6	19,8	15,3	26,7	8,4	10,7	0,8	4,6	5,3
BB1	Campodarbe Fm.	125	0,0	0,0	0,8	11,2	20,0	15,2	24,8	3,2	9,6	2,4	8,0	4,8
BB5	Campodarbe Fm.	126	0,0	0,0	1,6	4,0	4,0	16,7	38,9	5,6	11,9	1,6	6,3	9,5
BM3	Belsué-Atarés Fm.	87	0,0	0,0	0,0	8,0	17,2	17,2	39,1	3,4	3,4	1,1	5,7	4,6
BM12	Campodarbe Fm.	121	0,0	0,0	1,7	9,1	22,3	14,0	27,3	8,3	7,4	0,8	5,0	4,1
BM17	Bernués Fm.	127	0,0	0,0	2,4	5,5	5,5	14,2	29,9	9,4	11,8	0,0	11,8	9,4
GL2	Campodarbe Fm.	130	0,0	0,0	1,5	7,7	13,1	14,6	34,6	6,2	8,5	0,0	6,9	6,9
GL5	Campodarbe Fm.	139	0,0	0,0	1,4	11,5	21,6	16,5	23,0	5,0	7,2	0,0	8,6	5,0
GL7	Campodarbe Fm.	129	0,0	0,0	0,8	8,5	14,7	14,0	31,8	10,1	7,8	0,0	5,4	7,0
GL10	Bernués Fm.	146	0,7	0,0	0,0	10,3	4,8	15,8	37,0	9,6	6,8	0,0	8,2	6,8
LU9	Campodarbe Fm.	127	0,0	0,0	0,0	13,4	18,9	11,8	22,0	7,1	13,4	0,0	9,4	3,9
LU7	Campodarbe Fm.	125	0,0	0,0	0,0	8,0	6,4	16,8	36,8	5,6	11,2	0,0	8,0	7,2
LU2	Uncastillo Fm.	134	0,0	0,0	1,5	11,2	14,2	14,2	27,6	7,5	14,2	1,5	5,2	3,0
YS1	Yesa turbidites	116	0,0	0,0	1,7	6,9	2,6	12,9	41,4	6,0	5,2	0,9	13,8	8,6
YS2	Liédena Sst.	130	0,0	0,0	1,5	5,4	7,7	18,5	33,8	9,2	6,9	3,8	7,7	5,4
YS3	Campodarbe Fm.	128	0,0	0,0	0,8	8,6	9,4	13,3	34,4	7,8	13,3	1,6	6,3	4,7
YS5	Campodarbe Fm.	130	0,0	0,0	0,8	7,7	3,8	15,4	41,5	5,4	11,5	0,8	9,2	3,8
EK2	Ezkaba Fm.	139	0,0	0,0	1,4	2,2	6,5	17,3	33,1	7,2	15,1	0,7	9,4	7,2
IZ1	Gongolaz Sst.	128	0,0	0,0	0,8	4,7	3,9	11,7	43,8	7,8	10,2	0,8	10,9	5,5
IZ5	Liédena Sst.	140	0,0	0,0	0,0	7,1	14,3	15,7	36,4	5,0	5,7	1,4	8,6	5,7
IZ3	Campodarbe Fm.	145	0,0	0,0	0,7	5,5	2,8	13,1	41,4	9,0	11,7	2,1	9,7	4,1
IZ10	Bernués Fm.	146	0,0	0,0	0,7	7,5	6,2	9,6	32,9	4,8	15,8	2,1	15,1	5,5

Table 1. *Detrital zircon U-Pb results summarized in component percentages.*

In the eastern Jaca basin, the Belsué-Atarés delta and Campodarbe Fm. cropping out in the External Sierras constitute the lowermost analyzed deposits. It displays more than 50% of Variscan age components (Table 1; Figure 2,4). Upsection and to the west, the fluvial Campodarbe Fm. records an important Variscan age component, but Cambro-Devonian and Cadomian U-Pb age components increase. By contrast, the uppermost parts of the Campodarbe Fm., as well as the Bernués Fm., are characterized by minor Variscan age U-Pb components with a dominance of Cambro-Devonian and Cadomian components (>50%). In the Luesia section (Ebro basin), the Campodarbe Fm. show the same evolution of the DZ-U-Pb signatures upsection. By contrast, the youngest analyzed deposits (Uncastillo Fm.; Ebro basin) display and important Variscan age component.

In the western Jaca basin (Figure 5), the entire succession from the Ezkaba Fm. to the Bernués Fm. is dominated by Cadomian and Cambro-Devonian age components, similar to the youngest deposits in the eastern Jaca basin. Therefore, the evolution of the DZ U-Pb signatures in the eastern Jaca basin is not observed in the western sector of the basin.

MDS and CA (Figures 6) allows to classify the analyzed samples into three distinct DZ U-Pb age signatures based on age populations (Figures 6a,b) and age components (Figures 6c,d): (i) Variscan dominated, characterized by more than 50% of Variscan age components (Early Variscan + Late Variscan), (ii) mixed Cadomian-Variscan, characterized by an important Variscan age component, but with higher abundances of Cadomian and Cambro-Devonian age components, and finally, (iii)

Cadomian dominated, characterized by the dominance of Cadomian and Cambro-Devonian age components (>50%) and the lowest abundance of Variscan age components.

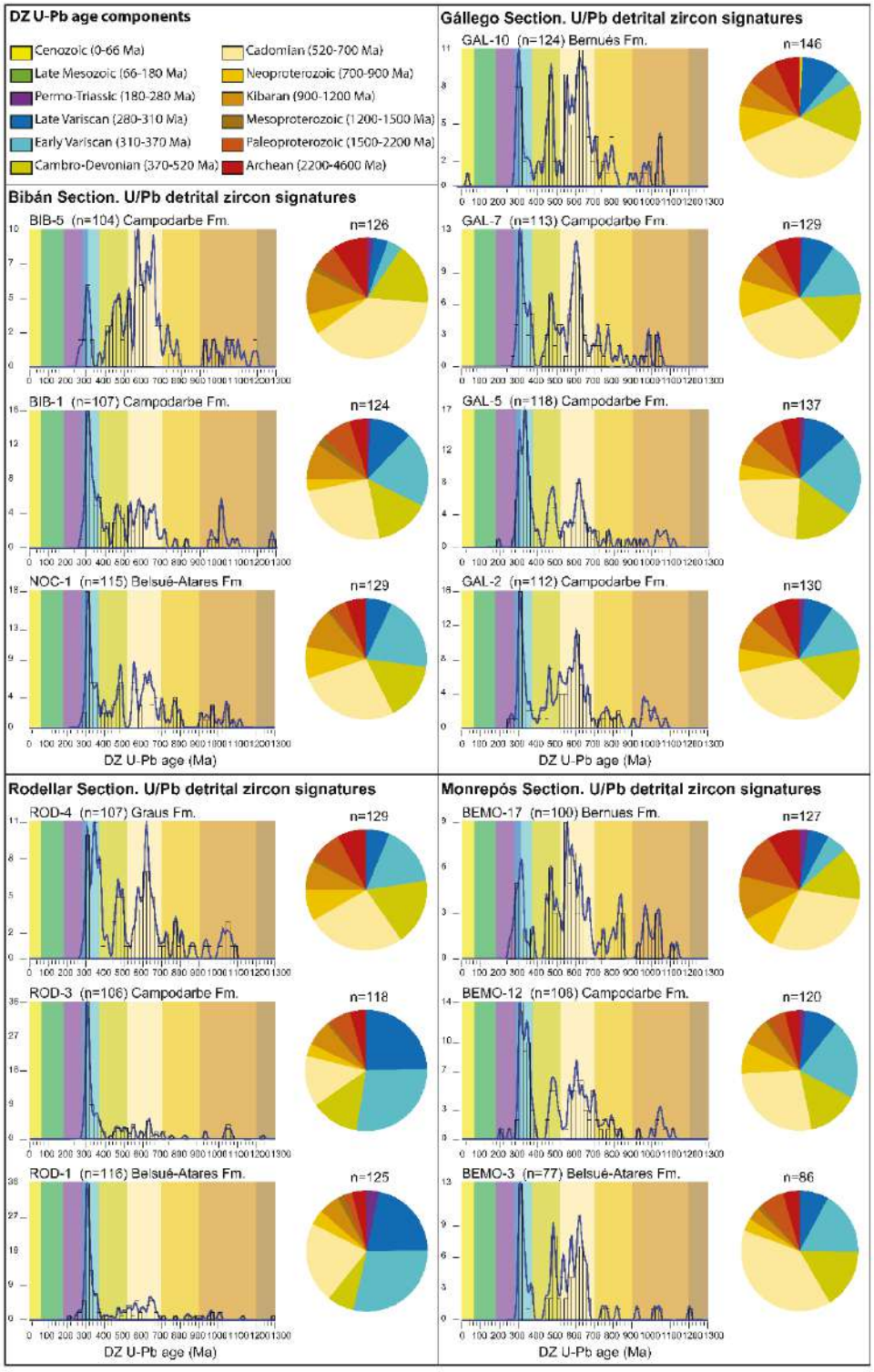

Figure 4. *DZ U-Pb results for the eastern Jaca basin. DZ U-Pb results are represented as Kernel density estimators (Nonadaptative, bandwidth of 8 Ma), histogram diagrams from 0 to 1300 Ma. (bin width of 20 Ma.), and pie percentage charts.*

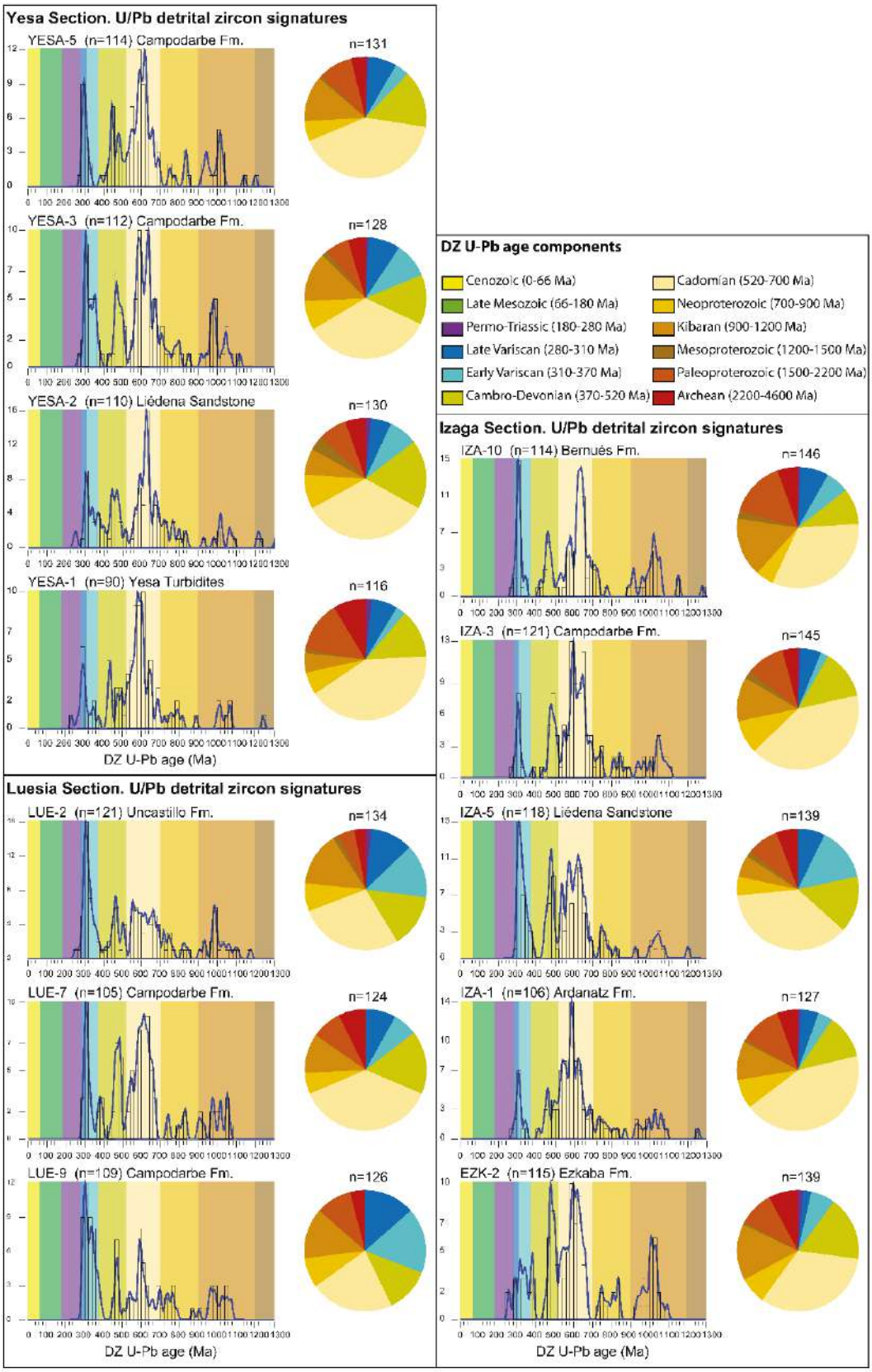

Figure 5. *DZ U-Pb results for the western Jaca basin and Ebro basin. DZ U-Pb results are represented as Kernel density estimators (Nonadaptative, bandwidth of 8 Ma), histogram diagrams from 0 to 1300 Ma. (bin width of 20 Ma.), and pie percentage charts.*

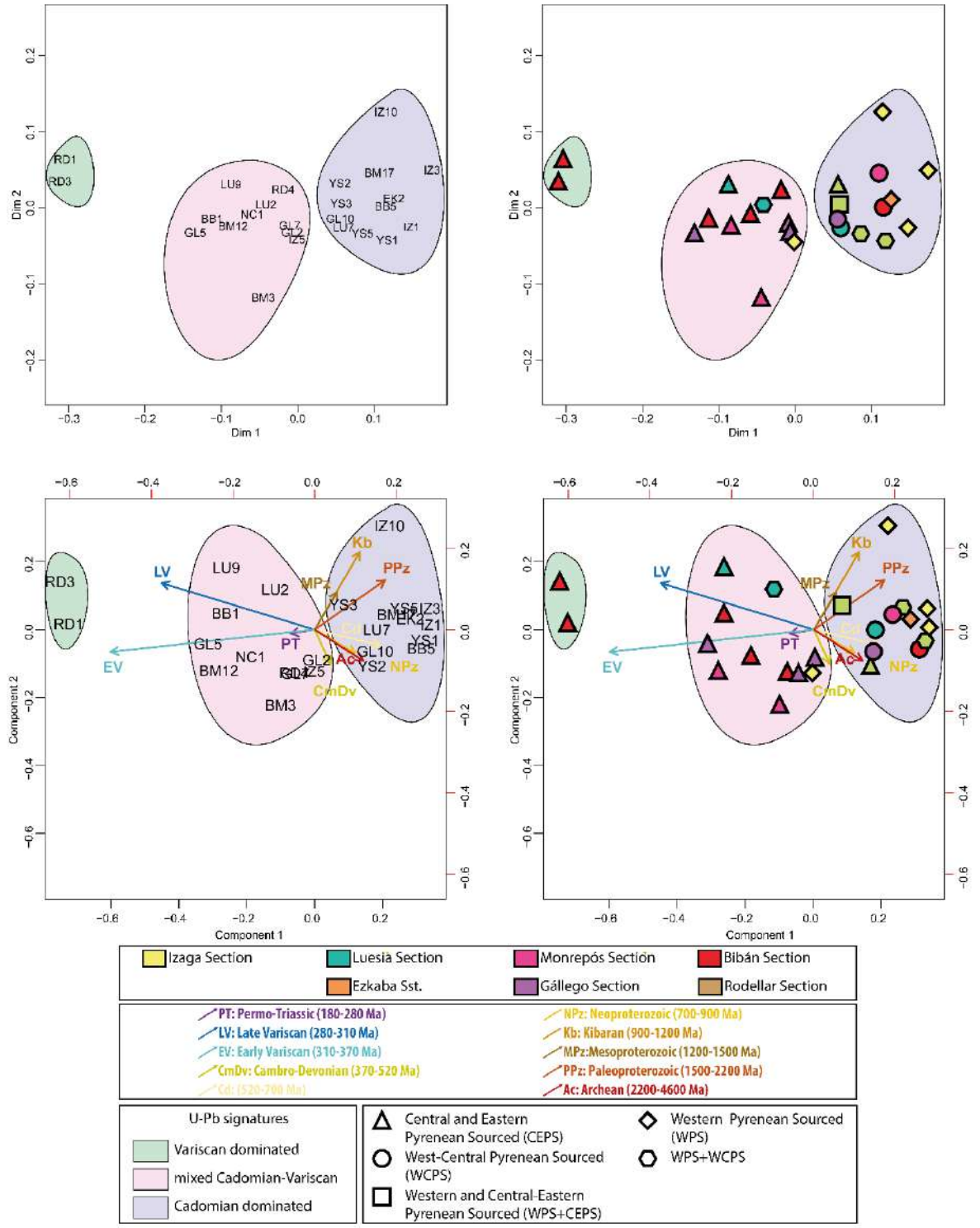

Figure 6. *(a,b) MDS of U-Pb ages (c,d) CA of U-Pb age components. Central Eastern Pyrenean sourced; WPS: Western Pyrenean Sourced (Basque massifs or Basque massifs+Urbassa-Andía Sierra or Urbassa-Andia Sierra); WCPS: West Central Pyrenean Sourced (Eocene Turbidite basin+Internal Sierras+North Pyrenean Zone or Eocene Turbidite basin+Internal Sierras+North Pyrenean Zone+Jaca thrust sheet top basin); WPS+WCPS: Pyrenean Sourced Western Pyrenean Sourced (Basque massifs or Basque massifs+Urbassa-Andía Sierra or Urbassa-Andia Sierra) + West Central Pyrenean Sourced (Eocene Turbidite basin+Internal Sierras+North Pyrenean Zone or Eocene Turbidite basin+Internal Sierras+North Pyrenean Zone+Jaca thrust sheet top basin).*

4.2. DZ (U-Th)/He thermochronological signatures

DZ (U-Th)/He age populations (Table S2) are grouped into five (U-Th)/He events age: Pyrenean Orogeny (20-85 Ma), Cretaceous rifting (85-155 Ma), Liasic Cooling (180-201 Ma), Permo-Triassic Rifting (201-280 Ma), and Variscan Orogeny (280-390 Ma). Results are displayed as detrital zircon U-Pb-He double dating plots, and percentages of the 5 (U-Th)/He events age (Table 2; Figure 7).

Sample	Fm.	Section	n	Pyrenean Orogeny (20-85 Ma)	Cretaceous Rifting (85-155 Ma)	Liasic Cooling (175-201 Ma)	Permo-Triassic Rifting (201-295 Ma)	Variscan Orogeny (>295 Ma)
BM3	Belsué-Atarés Fm	Monrepós	17	76,5	11,8	0,0	11,8	0,0
BM12	Campodarbe Fm.	Monrepós	16	100,0	0,0	0,0	0,0	0,0
GL5	Campodarbe Fm.	Gállego	19	78,9	15,8	0,0	5,3	0,0
GL10	Bernués Fm.	Gállego	13	76,9	7,7	0,0	15,4	0,0
LU9	Campodarbe Fm.	Luesia	13	92,3	7,7	0,0	0,0	0,0
LU2	Uncastillo Fm.	Luesia	14	78,6	0,0	0,0	14,3	7,1
EK2	Ezkaba Fm.	Izaga	8	0,0	25,0	12,5	62,5	0,0
IZ5	Liédena Sst.	Izaga	8	12,5	12,5	12,5	50,0	12,5
IZ3	Campodarbe Fm.	Izaga	8	0,0	12,5	25,0	37,5	25,0
IZ10	Bernués Fm.	Izaga	6	16,7	33,3	16,7	33,3	0,0

Table 2. *Detrital zircon (U-Th)/He results summarized in component percentages.*

MDS and CA (Figure 8) allow to identify two distinct DZ ZHe signatures based on ZHe age populations (Figures 8a,b) and components (Figures 8c,d): (i) Pyrenean Orogeny ZHe ages dominated, characterized by more than 75% of ZHe Pyrenean ages, and (ii) Non-Pyrenean Orogeny ZHe dominated signatures, characterized by 0-15% of ZHe Pyrenean ages, major Permo-Triassic, and subsidiary Cretaceous rifting, Liasic cooling and Variscan orogeny ages.

The clastic infill of the eastern Jaca basin (Belsué-Atarés delta, Campodarbe, Campodarbe and Bernués Formations) and samples from the Ebro basin (Campodarbe and Uncastillo Formations) display Pyrenean dominated ZHe signatures. By contrast, non-Pyrenean dominated ZHe signatures characterize the Bartonian to Miocene sedimentary record of the western Jaca basin.

5. DISCUSSION

5.1. DZ U-Pb age components signatures

5.1.1 The eastern Jaca basin

A high abundance of Variscan age components are displayed int the Belsué-Atarés delta and the fluvial Campodarbe Fm. of the southeasternmost edge of the eastern Jaca basin (Rodellar section; Figure 6;

carbonate enriched petrofacies of Roigé et al. (2017) and Coll et al. (2022) with abundant K-feldspar and plutonic rock fragments). This Variscan dominated DZ suite can be attributed to the high contribution of Variscan granitoids and also Cretaceous sedimentary rocks containing Variscan enriched age signatures (Hart et al., 2016; Filledeau et al., 2012), both sourced from the Central and Eastern Pyrenees trough east-sourced axial systems (Coll et al., 2022). Upsection and to the west (Bibán, Monrepós and Gállego; Figure 6; siliciclastic dominant petrofacies of Coll et al., 2022 with abundant metamorphic rock fragments and Carboniferous to Permo-Triassic sedimentary), the decrease in Variscan age components and the increase of Cambro-Devonian and Cadomian age components can be linked to the drainage area reorganization that produced a shift from a plutonic dominated towards a metamorphic dominated source area (Michael 2013; Coll et al., 2022). Hence, we infer that the increase of the metamorphic sources together with the decrease of granite sources produced the shift from Variscan dominated to Mixed Cadomian-Variscan DZ U-Pb signatures. This can be linked with the Cambro-Devonian metasedimentary succession from the Pyrenees, characterized by an important Cadomian age component (Hart et al., 2016; Margalef et al., 2016), and with the Carboniferous and Triassic sedimentary rocks dominated by Cadomian and scarce Variscan age components (Hart et al., 2016; Martínez et al., 2016). The same trends both in DZ U-Pb age components (Michael, 2013; Thompson et al., 2017) and petrofacies (Coll et al., 2022) is also observed in the time-equivalent Escanilla Fm. (Ainsa basin), evidencing that this sediment routing system (Michael, 2013) fed the eastern Jaca basin during late Eocene-Oligocene times (Coll et al., 2022).

Upsection, the uppermost Campodarbe and Bernués Fms. are characterized by Cadomian dominated U-Pb age signatures (Figure 6) that can be linked to the onset of north-derived transverse systems (Puigdefpabregas 1975; Hybrid clast dominated petrofacies of Coll et al., 2022 characterized by abundant hybrid sandstone rock fragments). The source area of this systems are mainly the Eocene turbidites of the Hecho Group, and also the Mesozoic and Paleozoic rocks from the North Pyrenean Zone.

The DZ U-Pb signature of the Hecho Group turbidites changes through the different turbiditic systems (Roigé, 2018). While the Banastón and lower Jaca turbidite systems are characterized by abundant Variscan U-Pb age components (Variscan dominated and mixed Cadomian-Variscan signatures), the middle-upper Jaca turbidite systems show Cadomian dominated signatures. Hence, we infer that the north-derived transverse systems of the Jaca basin essentially recycled the middle-upper Jaca turbidite systems which display Cadomian dominated signatures. Moreover, the North Pyrenean source area of

these alluvial systems of is constituted by upper Cretaceous rocks from the NPZ (limestones and calcarenites), scarce Paleozoic metasediments, and Carboniferous to Triassic siliciclastic sandstones (Roigé et al., 2017), all of them characterized by Cadomian dominated U-Pb signatures (Hart et al., 2016).

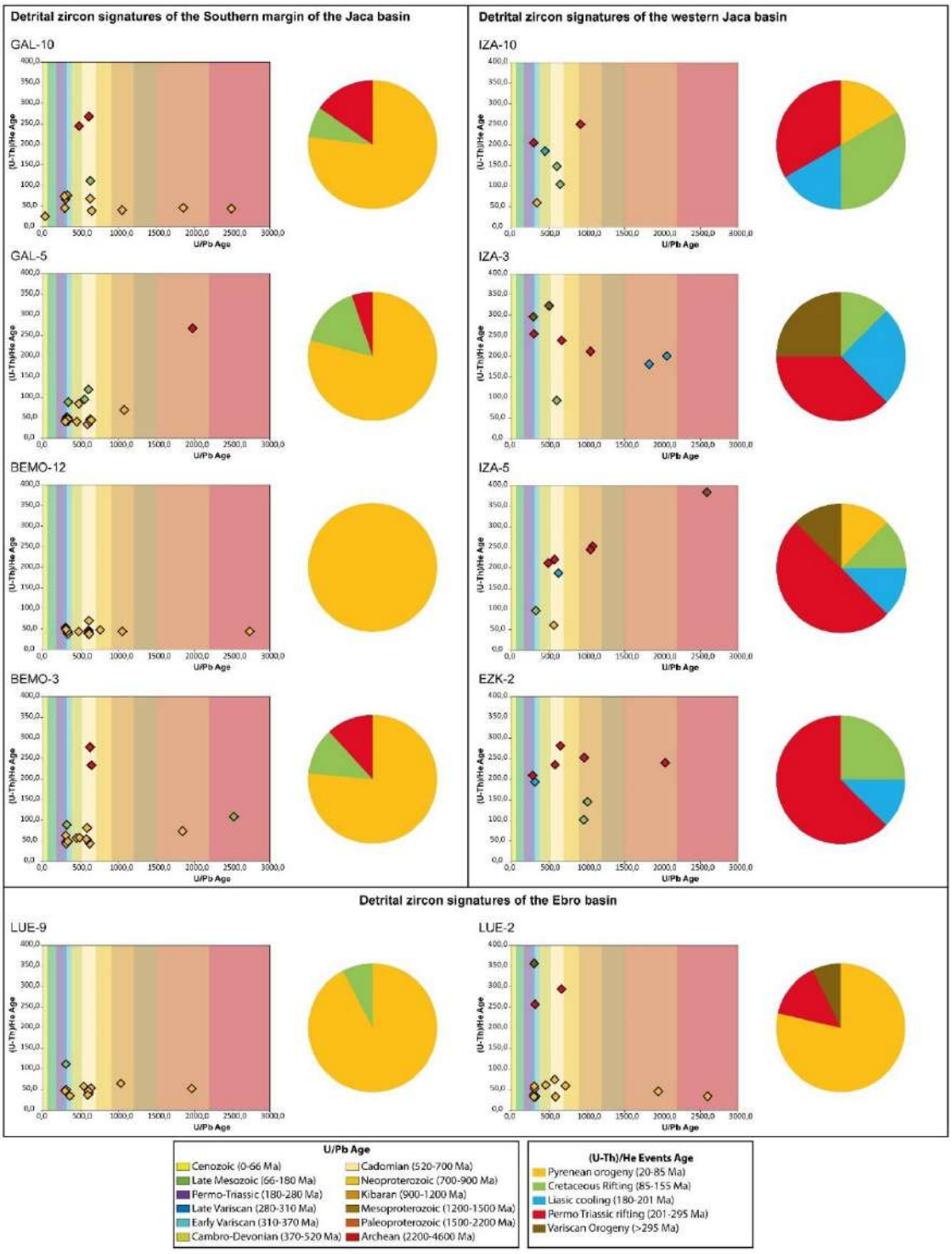

Figure 7. *(U-Th)/He results of the analysed samples represented as scatterplot of (U-Th)/He age versus U-Pb age for double-dated grains.*

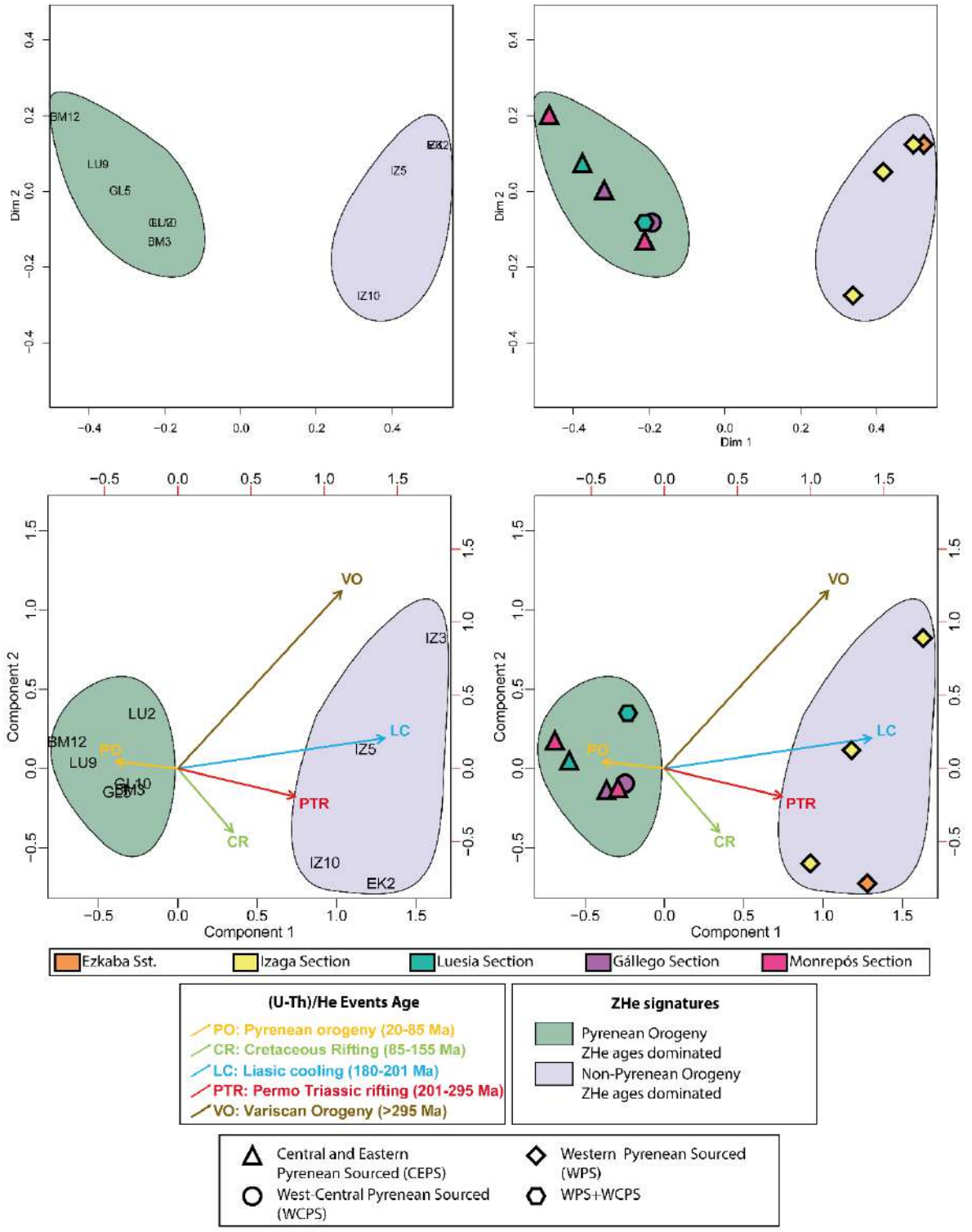

Figure 8. *(a,b) MDS of (U-Th)/He ages (c,d) CA of (U-Th)/He age components. Central Eastern Pyrenean sourced; WPS: Western Pyrenean Sourced (Basque massifs or Basque massifs+Urbassa-Andía Sierra or Urbassa-Andia Sierra); WCPS: West Central Pyrenean Sourced (Eocene Turbidite basin+Internal Sierras+North Pyrenean Zone or Eocene Turbidite basin+Internal Sierras+North Pyrenean Zone+Jaca thrust sheet top basin); WPS+WCPS: Pyrenean Sourced Western Pyrenean Sourced (Basque massifs or Basque massifs+Urbassa-Andía Sierra or Urbassa-Andia Sierra) + West Central Pyrenean Sourced (Eocene Turbidite basin+Internal Sierras+North Pyrenean Zone or Eocene Turbidite basin+Internal Sierras+North Pyrenean Zone+Jaca thrust sheet top basin).*

5.1.2 The western Jaca basin

In the western Jaca basin (Figure 2,3), all the sedimentary clastic systems display monotonous U-Pb Cadomian dominated signatures (Figure 6), similar to the north-sourced transverse-feed systems of the eastern Jaca basin, except for the Liédena sandstone in the Izaga area, which show Mixed Variscan-Cadomian signatures.

Petrographic data from the Izaga profile reveals that the Ezkaba sandstone (Bartonian), the Ardanatz (Bartonian) and the Liédena sandstone (Priabonian)Fms display a similar sandstone composition, characterized by abundant K-feldspar and fresh plagioclase, intrabasinal bioclasts, and carbonate rock fragments (evidenced by the presence of Turonian wackestone rock fragments containing phitonellid tests). Some metamorphic and siliciclastic sandstone rock fragments, and scarce plutonic grains, are also observed. This petrographic assemblage points to a source area constituted by Late Cretaceous sedimentary cover and Paleozoic siliciclastic sandstones and metasediments. The abundance of feldspars must be related to recycling of Carboniferous sedimentary cover (Culm facies) extensively outcropping in the Basque massifs, This is in accordance with Payros (1997), who inferred a siliciclastic source area located to the north, in the Paleozoic Basque massifs for the Ezkaba sandstone. The Ezkaba, Ardanatz, and Liédena Fomations show DZ U-Pb Cadomian dominated signatures, which can be related to recycling of Carboniferous (dominated by Cadomian ages), Ordovician-Devonian metasedimentary (Cambro-Devonian and Proterozoic U-Pb ages), and Upper Cretaceous sedimentary cover (Cadomian dominated and mixed Variscan-Cadoiman signatures), located in the NPZ (Hart et al., 2016).

Upsection, in the Campodarbe Fm. (Priabonian to Chatian) (Figures 3,5,6) the same DZ U-Pb signatures and abundance of K-feldspar and plagioclase persist. Nevertheless, an important provenance change is evidenced by calcarenite rock fragments, silicified grains (some of them with idiomorphic dolomite crystals), and carbonate rock fragments, which can be related to the erosion of the sedimentary succession cropping out in the Urbassa-Andía Sierra (Payros, 1997; Tariño, 2006). Therefore, in the Oligocene, the Urbassa-Andía Sierra started to deliver sediments to the Izaga area.

Finally, in the upper Izaga alluvial fan deposits, no contributions from the Basque massif are recorded (absence of feldspar and metamorphic grains) and the Urbassa-Andía Sierra remained as the only source. Therefore, since no U-Pb data exists in this source area, and no shift is observed in the U-Pb signatures, Mesozoic, Paleocene and Eocene sources of this area should be characterized by Cadomian dominated U-Pb signatures.

The Yesa profile also displays monotonous DZ U-Pb age signatures throughout the whole section (Figures 3,5,6). Nonetheless, the Yesa turbidites shows a sandstone petrography suite with Mesozoic carbonate rock fragments (upper Cretaceous mudstone-wackestone rock fragments containing phitonellid tests), K-feldspar, fresh plagioclase, and subsidiary metamorphic rock fragments, which highlight contributions from the Basque massifs and the surrounding Mesozoic sedimentary cover. By contrast, Tertiary carbonate rock fragments, bioclasts and hybrid sandstone rock fragments (Upper Hecho Group turbidites) point to sources located in the hanging wall of the Leyre thrust (NE).

Upsection, in the Yesa profile, the Liédena sandstone (Cadomian dominated U-Pb signatures) shows a provenance change. In contrast to the Izaga area, the Liédena sandstone shows abundant metamorphic rock fragments, Permo-Triassic siliciclastic sandstone and siltstone rock fragments, crystalline carbonates, and scarce K-feldspar. The similarity with the east-sourced Campodarbe Fm. (Coll et al., 2022), and NW directed paleocurrents (Puigdefàbregas, 1975) evidence an eastern source for this area. However, east-sourced systems in the eastern Jaca basin display Mixed Cadomian-Variscan U-Pb signatures. Hence, we infer that the contribution of Permo-Triassic and metamorphic rock fragments could be linked to the Cadomian dominated signatures of the Liédena Fm. (east-sourced in this area).

The overlying Campodarbe Fm. shows an interplay between contributions from the Basque massifs (K-feldspar, fresh plagioclase, and silicified rock fragments) and Eastern Pyrenean sources (abundant metamorphic rock fragments, Permo-Triassic sandstones and siltstones, and crystalline limestones). DZ U-Pb signatures still show Cadomian dominated signatures resulting from higher contributions from the Basque massifs and minor supply from eastern sources. By contrast, although the top of the Campodarbe Fm. still shows the same Cadomian dominated signatures, there is no influence from eastern sources, as evidenced by the lack of metamorphic rock fragments and Triassic sandstones, and records contributions from the Basque massifs and the recycling of the Eocene turbidite basin located to the north.

In the Ebro Basin (Luesia section, Figures 2,3,5) the Campodarbe Fm. shows the same DZ U-Pb trends as in the eastern Jaca basin (a shift from Variscan enriched to Variscan impoverished signatures) which corresponds to the change from east-source axially-fed systems to north-sourced transverse-fed systems (Coll et al., 2022). However, the overlying Miocene Luna fan system shows a Mixed Cadomian-Variscan DZ signature. The source area has been identified in the Basque massifs Paleozoic

basement and the earlier foreland deposits (Hecho Group and Campodarbe Formations; Hirst & Nichols, 1986; Coll et al., 2022). The Mixed Cadomian-Variscan U-Pb signatures of the Luna fan (Figure 6), could be related to the recycling of the mixed Cadomian-Variscan Campodarbe and Variscan dominated Upper Hecho Group turbidites, as evidenced by sandstone petrography detrital modes (Coll et al., 2022).

5.2. DZ ZHe signatures

In the eastern Jaca basin (Monrepós and Gállego sections), the Belsué-Atarés delta and the Campodarbe Formations display ZHe Pyrenean dominated signatures, containing subsidiary Permo-Tiassic and Cretaceous rifting age components (Figures 7,8). However, the Campodarbe Fm. in the Monrepós section only shows Pyrenean age components.

These distinct signatures must be related to the occurrence of two different eastern-sourced axially-fed systems evidenced by distinctive heavy-mineral provenance signatures (Coll et al., 2022). The Campodarbe Fm. in the eastern part of the Jaca basin (Monrepós section) was fed by the fluvial Escanilla Fm. (Ainsa basin), which is devoid of ZHe Permo-Triassic age components (Thompson et al., 2017), and both constituted one of the axially-fed systems sourced from the central-Pyrenees. The other axially-fed system fed the Belsué-Atarés delta, and the western fluvial Campodarbe Fm., sourced from the eastern Pyrenees Coll et al., 2022), where Cretaceous rifting and Permo-Triassic age components are contained in the late Cretaceous-Garumnian Formations (Odlum et al., 2019). Moreover, Pyrenean ZHe ages encountered in the eastern-Pyrenean sourced system are older than in the central-Pyrenean sourced system (Table S2). Therefore, ZHe provenance signatures reinforce the idea of two different sediment routing system, sourced from the Central and Eastern Pyrenees (Coll et al., 2022).

The youngest analyzed deposits in the Jaca basin, the north sourced Bernués Fm., show ZHe Pyrenean dominated signatures (Figure. 8), with subsidiary Cretaceous rifting and Permo-Triassic age components that could be related to Cretaceous sedimentary rocks occurring in the North Pyrenean Zone, which mainly contain these DZ ZHe age signatures (i.e. Maastrichtian; Bosch et al., 2016).

In the western Jaca basin (Izaga area), ZHe signatures are markedly different to the ones encountered in the eastern Jaca basin. The analysed samples show ZHe Non-Pyrenean dominated ages (mainly

Permo-Triassic; Figures 7,8), pointing to the Basque massifs and Urbassa-Andía Sierra sources, which is in accordance with petrographic data and DZ U-Pb signatures. In the southern edge of the Basque massifs (Alduides massif), the Ordovician-Devonian Paleozoic basement shows ZHe signatures dominated by Cretaceous rifting ages with Liasic and Permo-Triassic age components (Hart et al., 2017). Therefore, the uppermost part of the present-day eroded Paleozoic basement (mainly Carboniferous) must have sourced unreseted zircon grains displaying older than Pyrenean ZHe signatures.

Finally, the Uncastillo Fm. in the Ebro basin (Luesia section; Figure 2) displays Pyrenean dominated ZHe ages (Figures 7,8) with subordinate Permo-Triassic and Variscan ZHe components. Since this alluvial fan records the erosion of the Hecho Group turbidites, the Jaca thrust sheet top basin, and the Basque massifs (Hirst & Nichols, 1986; Coll et al., 2022), ZHe Pyrenean ages must be linked to recycling of reseted zircon grains derived from the earlier foreland deposits (Hecho Group and Campodarbe Formations), whereas Permo-Triassic and Variscan age components must be linked to the Paleozoic and Mesozoic sedimentary cover occurring in the Basque massifs and NPZ.

5.3. Insights into the propagation of DZ provenance signatures

The main controlling factors influencing the DZ signatures in clastic successions are source rock distribution ages, source rock fertility, and relative contribution of each lithology to the analyzed grain-size window (sand-sized). U-Pb signatures of potential sources and zircon fertility should be obtained from detailed analysis of each lithology in the source areas, and the relative contribution of source areas can only be inferred from detailed sandstone petrography. In our work, source rock distribution ages and zircon fertility have been thoroughly described in section 2.2, and detailed sandstone petrography from Coll et al. (2022) have been used to assess the relative contribution of each lithology.

In the Southern margin of the Jaca basin, sedimentary systems with a high granitic components (Belsué-Atarés, Rodellar section, carbonate extrabasinal enriched petrofacies) display U-Pb Variscan dominated signatures, which do not change in the overlying systems (Campodarbe Fm. siliciclastic dominant petrofacies) influenced by a metamorphic source area with a scarce granitic component. To the west, the Beslué-Atarés Fm., in Monrepós section (carbonate extrabasinal enriched petrofacies wit an evident granitic component) is characterized by U-Pb mixed Cadomian-Variscan signatures, wich do not change in the overlying systems (Campodarbe Fm., siliciclastic dominant Fm., displaying a

scarce or absent granitic component). In both situations, the fact that no correlation exist between the abundance of granitic and Variscan components imply a non-granitic lithology in the source area which is able to provide enough Variscan zircons to offset the persistence of the U-Pb signatures. Therefore, we infer Cretaceous sedimentary cover as an important contributor of Variscan zircons, which can be characterized by U-Pb Variscan dominated signatures (Filledeau et al., 2012; Odlum et al., 2019). The contribution of this source is evidenced by carbonate rock fragments observed in both petrofacies, and highlights that the recycling of cretaceous sedimentary cover can contribute to the propagation of non-granitic derived Variscan components. This evidence that a provenance analysis solely based in U-Pb without considering the role of recycling into the propagation of U-Pb signatures might lead to misinterpretations regarding the nature of the source areas in foreland basins.

The recycling of the of the Hecho Group turbidites of the Jaca basin, characterized by Variscan dominated (Banastón and lower Jaca turbidite systems) to Cadomian dominated (middle-upper Jaca turbidite systems) signatures (Roigé 2018) should propagate, at least, mixed Cadomian-Variscan signatures due to their high abundance in the sand fraction (Coll et al., 2022). However, the observed DZ U-Pb signatures are Cadomian dominated. Even if inferring a low zircon fertility for this source (although moderate-high fertility is more expected), their high contribution in front of Paleozoic metasedimentary and siliciclastic sandstone sources would be enough to produce mixed Cadomian-Variscan signatures. Even if assuming that the second most represented source, the Cretaceous sedimentary cover, delivers Cadomian dominated signatures (Hart et al., 2016), its lower fertility would not be enough to mask Variscan enriched signatures. Therefore, DZ U-Pb highlights Cadomian dominated signatures derived from major recycling of the turbidite basin is linked to main contributions from the middle-upper Jaca turbidite systems.

Conversely, in the western Jaca basin, monotonous DZ U-Pb Cadomian dominated signatures are displayed in all the analyzed deposits. This contrasts with the several compositional changes recorded by sandstone petrography in these deposits. Therefore, we can infer that DZ U-Pb failed to discriminate between the different source areas. However, U-Pb provenance signatures highlight the recylcling of the Carboniferous sedimentary cover. K-feldspar, plagioclase and, subsidiary plutonic rock fragments might indicate a granitic source that could be related to Ordovician gneisses or Variscan granitoids from the Paleozoic basement of the Basque massifs. However, in such case, high contribution from these crystalline sources together with high zircon fertility would strongly increase Cambro-Devonian (gneiss) or Variscan age signatures (Granites). Nevertheless, since Variscan or Cambro-Devonian

dominated signatures are not observed, DZ U-Pb highlight recycling of detrital Carboniferous zircons instead of a direct granitic/gneissic source. Late Variscan ages would be derived from Cretaceous and Paleocene-Eocene sediments also present in the source areas. Moreover, DZ U-Pb in the western Jaca basin highlight the role of recycled vs direct sources.

Finally, in the Ebro basin, provenance constraints from sandstone petrography allow a better understanding of DZ U-Pb signatures propagation. The Miocene Luna alluvial fan system is sourced from the Basque massifs and the recycling of the Hecho Group turbidites and Campodarbe Fm. (Hirst and Nichols, 1986; Arenas, 1993, Coll et al., 2022). In this case, the Mixed Cadomian-Variscan signatures must respond to contributions from the Campodarbe Fm., as well as to higher contributions from the Upper Hecho group turbidites (Banastón and lower Jaca turbidite systems). The onset of sedimentation in the Ebro basin, probably favored major incision on these formations in the hinterland, increasing contributions from theseand leading to increase these signatures in the Luna alluvial fan.

Summarizing, in the western Jaca basin provenance analysis solely based on DZ-U-Pb have failed to highlight the interplay between Western Pyrenean, Eastern Pyrenean, and West-Central Pyrenean sources (Figure 6), as well as recycled vs first cycle sources. In the Pyrenees, DZ U-Pb signatures stand as a good proxy to distinguish between Variscan granites, Ordovician gneiss, Cambro-Devonian metasedimentary, and Carboniferous to Permo-Triassic sources due to their well-known provenance signatures. However, when Cretaceous, Paleocene and Eocene contributions are underestimated, unravel provenance unequivocally may become unrealistic,. Although integration with DZ ZHe signatures can aid to reduce the ambiguity of provenance signals, a good control of the source area lithology contribution based on sandstone detrital modes is necessary to fully understand how DZ signatures are propagated and to avoid biased provenance conclusions. So, DZ signatures highly increase their power as a reliable provenance indicator when coupled with petrographic data. Therefore, studies comprising sandstone petrography, U-Pb, and ZHe provenance signatures stand as the most powerful tool to obtain the highest resolution in sedimentary provenance analysis and, single-method approaches must be avoided.

5.4. Synthesis of the South Pyrenean Sediment Routing Systems

5.4.1. Eastern Jaca basin

During late Lutetian to Bartonian times, deltaic sedimentation in the southern Jaca basin was mainly derived from eastern source areas through a unique fluvial system developed during the first stage of deltaic sedimentation (Coll et al., 2022). These sources were the Paleozoic basement (mostly Variscan granitoids) and the Mesozoic and Paleogene sedimentary cover of the growing central Pyrenees.

From early Priabonian onwards, two distinct axially-fed fluvial systems from the central and eastern Pyrenees respectively, one dominated by ep and ZHe Pyrenean signatures and the other characterized by the absence of epidote and ZHe Pyrenean signatures with subsidiary Cretaceous rifting and Permo-Triassic ages, were delivering sediment to the basin (Coll et al., 2022). Both systems were sourced from Variscan granitoids, together with Mesozoic sedimentary cover and evolved, during the Priabonian, to a more dominant metamorphic composition during the Priabonian and persisted until Chattian times (Coll et al., 2022).

The youngest deposits of the Jaca basin (uppermost Campodarbe and Bernués Fms.), record the recycling of the uppermost sedimentary systems of the former Eocene turbidite basin with contributions from the North Pyrenean Zone (Puigdefàbregas 1975; Roigé et al., 2017; Coll et al., 2022).

5.4.2. Western Jaca basin

In the Bartonian, the Ezkaba channel levee records the first input of north derived systems sourced from the Basque massifs (Payros et al., 1997), mainly from Carboniferous deposits (Culm facies) with contributions from Cretaceous sedimentary cover. The overlying Ardanatz delta continues evidencing the Basque massifs as an active source, which extended its influence to the west during the sedimentation of the Priabonian Yesa turbidites. However, during the last stages of the Priabonian sedimentation (Liédena sandstone), a strong interplay between Western and Eastern Pyrenean, as well as west-central Pyrenean sources occurred in the limit between the eastern and western Jaca basin.

During the development of the Ruppelian middle Campodarbe Fm., whereas eastern and western Pyrenean sources influenced the sedimentation in the Yesa area, the Izaga area, started to receive contributions from the Urbassa-Andía Sierra. In the Chattian-Aquitanian, whereas the Yesa area was fed from the west, west-central, central-eastern Pyrenean sources, Urbassa-Andia sources imposed in the Izaga area and contributions from the Basque massif stopped in this part of the basin.

5.4.3. The Ebro Basin

During Priabonian-Rupelian, the lower Campodarbe Fm. was fed from the same source areas as the time-equivalent deposits in the present-day Gállego Valley (eastern Jaca basin). North-sourced systems, fed from time-equivalent deposits in the Jaca basin reach the Ebro basin during Chattian. Finally, the Aquitanian Luna alluvial fan systems was sourced from the erosion of the Eocene turbidite basin, the Jaca thrust sheet top basin, and the Basque massifs.

6. CONCLUSIONS

The integration of the three distinct DZ U-Pb signatures (Variscan dominated, mixed Cadomian-Variscan, and Cadomian dominated) and two ZHe signatures (Pyrenean dominated, and non-Pyrenean dominated) defined in this work, with sandstone petrography, allowed to characterize diferent routing systems with distinct source areas.

The different DZ U-Pb and ZHe signatures, indicates that eastern and western Jaca basin have different source areas with distinct provenance signatures. Whereas the eastern Jaca basin was sourced from the central and eastern Pyrenees, and recorded the evolution of this source areas until the onset of north-derived systems recycling the former Eocene turbidite basin, the western Jaca basin was mainly sourced by the Basque massifs and the Urbassa-Andia Sierra (Western Pyrenees).

Our work demonstrates that the western sources extended its influence to the Yesa area through the Ardanatz, Yesa turbidites and Campodarbe Formations, which is contrary to previous interpretations that linked these systems to the progradation of the Belsué-Atarés delta system (Puigdefàbregas 1975; Astibia et al., 2005). Moreover, our data highlights the interplay between western, west-central, and central-east Pyrenean sources in the Yesa area during the sedimentation of the Fluvial Campodarbe

Formation, which is also contrary to the classical view of an east-sourced fluvial system that extended its influence to the western Jaca basin.

Coupling U-Pb-He provenance signatures with sandstone petrography allowed understanding the propagation of DZ signatures and the influence of direct vs recycled sources, a goal that could not be achieved by solely looking at DZ signatures. In the other hand, complementing petrographic data with DZ signatures allowed to highlight contributions from specific sources such as the uppermost Hecho group turbidites and the Carboniferous cover of the Basque massifs.

Our work highlights the power of coupling sandstone petrography with DZ signatures in order to constrain sediment sources and avoid biased provenance interpretations in foreland basins fed from recycling orogens.

7. REFERENCES

Allen, P. A. (2017). Sediment routing systems: The fate of sediment from source to sink. Cambridge University Press.

Andò, S. (2020). Gravimetric separation of heavy minerals in sediments and rocks. Minerals, 10(3), 273.

Arenas, C. (1993). Sedimentología y paleogeografía del Terciario del margen pirenaico y sector central de la Cuenca del Ebro (zona aragonesa occidental) (Doctoral dissertation, Universidad de Zaragoza).

Arenas, C., Millán, H., Pardo, G., & Pocoví, A. (2001). Ebro Basin continental sedimentation associated with late compressional Pyrenean tectonics (north-eastern Iberia): controls on basin margin fans and fluvial systems. Basin Research, 13(1), 65-89.

Astibia, H., Elorza, J., Pisera, A., Alvarez-Pérez, G., Payros, A., & Ortiz, S. (2014). Sponges and corals from the Middle Eocene (Bartonian) marly formations of the Pamplona Basin (Navarre, Western Pyrenees): taphonomy, taxonomy, and paleoenvironments. Facies, 60(1), 91-110.

Astibia, H., Payros, A., Suberbiola, X. P., Elorza, J., Berreteaga, A., Etxebarria, N., Badiola, A., & Tosquella, J. (2005). Sedimentology and taphonomy of sirenian remains from the Middle Eocene of the Pamplona Basin (Navarre, western Pyrenees). Facies, 50(3), 463-475.

Barnolas, A., & Gil-Peña, I. (2001). Ejemplos de relleno sedimentario multiepisódico en una cuenca de antepaís fragmentada: La Cuenca Surpirenaica. Boletín Geológico y Minero, 112(3), 17-38.

Barnolas, A., & Teixell, A. (1994). Platform sedimentation and collapse in a carbonate-dominated margin of a foreland basin (Jaca basin, Eocene, southern Pyrenees). Geology, 22(12), 1107-1110.

Bentham, P. A., Burbank, D. W., & Puigdefabregas, C. A. I. (1992). Temporal and spatial controls on the alluvial architecture of an axial drainage system: late Eocene Escanilla Formation, southern Pyrenean foreland basin, Spain. Basin Research, 4(3-4), 335-352.

Bosch, G. V., Teixell, A., Jolivet, M., Labaume, P., Stockli, D., Domenech, M., & Monie, P. (2016). Timing of Eocene–Miocene thrust activity in the Western Axial Zone and Chaınons Be arnais (west-central Pyrenees) revealed by multi-method thermochronology.

Boya, S. (2018). El sistema deltaico de la Arenisca de Sabiñánigo y la continentalización de la cuenca de Jaca (Doctoral dissertation, Universitat Autònoma de Barcelona).

Burrel, L., & Teixell, A. (2021). Contractional salt tectonics and role of pre-existing diapiric structures in the Southern Pyrenean foreland fold–thrust belt (Montsec and Serres Marginals). Journal of the Geological Society, 178(4).

Burrel, L., Teixell, A., Gómez-Gras, D., & Coll, X. (2021). Basement-involved thrusting, salt migration and intramontane conglomerates: a case from the Southern Pyrenees. BSGF-Earth Sciences Bulletin, 192(1), 24.

Caja, M. A., Marfil, R., Garcia, D., Remacha, E., Morad, S., Mansurbeg, H., ... & Lahoz-Beltrá, R. (2010). Provenance of siliciclastic and hybrid turbiditic arenites of the Eocene Hecho Group, Spanish Pyrenees: implications for the tectonic evolution of a foreland basin. Basin Research, 22(2), 157-180.

Cámara, P., & Klimowitz, J. (1985). Interpretación geodinámica de la vertiente centro-occidental surpirenaica (Cuencas de Jaca-Tremp). Estudios geológicos, 41(5-6), 391-404.

Campbell, I. H., Reiners, P. W., Allen, C. M., Nicolescu, S., & Upadhyay, R. (2005). He–Pb double dating of detrital zircons from the Ganges and Indus Rivers: Implication for quantifying sediment recycling and provenance studies. Earth and Planetary Science Letters, 237(3-4), 402-432.

Coll, X., Gómez-Gras, D., Roigé, M., Teixell, A., Boya, S., & Mestres, N. (2020). Heavy-mineral provenance signatures during the infill and uplift of a foreland basin: An example from the Jaca basin (southern Pyrenees, Spain). Journal of Sedimentary Research, 90(12), 1747-1769.

Coll, X., Roigé, M., Gómez-Gras, D., Teixell, A., Boya, S., & Mestres, N. (2022). Interplay of Multiple Sediment Routing Systems Revealed by Combined Sandstone Petrography and Heavy Mineral Analysis (HMA) in the South Pyrenean Foreland Basin. Minerals, 12(2), 262.

Costa, E., Garces, M., López-Blanco, M., Beamud, E., Gómez-Paccard, M., & Larrasoaña, J. C. (2010). Closing and continentalization of the South Pyrenean foreland basin (NE Spain): magnetochronological constraints. Basin Research, 22(6), 904-917.

Denele, Y., Barbey, P., Deloule, E., Pelleter, E., Olivier, P., & Gleizes, G. (2009). Middle Ordovician U-Pb age of the Aston and Hospitalet orthogneissic laccoliths: their role in the Variscan evolution of the Pyrenees. Bulletin de la Société géologique de France, 180(3), 209-216.

Dickinson, W. R. (1970). Interpreting detrital modes of graywacke and arkose. Journal of Sedimentary Research, 40(2), 695-707.

Dickinson, W. R. (2008). Impact of differential zircon fertility of granitoid basement rocks in North America on age populations of detrital zircons and implications for granite petrogenesis. Earth and Planetary Science Letters, 275(1-2), 80-92.

Dickinson, W. R., & Gehrels, G. E. (2009). Use of U–Pb ages of detrital zircons to infer maximum depositional ages of strata: a test against a Colorado Plateau Mesozoic database. Earth and Planetary Science Letters, 288(1-2), 115-125.

Dickinson, W. R., & Suczek, C. A. (1979). Plate tectonics and sandstone compositions. Aapg Bulletin, 63(12), 2164-2182.

Dreyer, T., Corregidor, J., Arbues, P., & Puigdefabregas, C. (1999). Architecture of the tectonically influenced Sobrarbe deltaic complex in the Ainsa Basin, northern Spain. Sedimentary Geology, 127(3-4), 127-169.

Farley, K. A. (2002). (U-Th)/He dating: Techniques, calibrations, and applications. Reviews in Mineralogy and Geochemistry, 47(1), 819-844.

Filleaudeau, P. Y., Mouthereau, F., & Pik, R. (2012). Thermo-tectonic evolution of the south-central Pyrenees from rifting to orogeny: Insights from detrital zircon U/Pb and (U-Th)/He thermochronometry. Basin Research, 24(4), 401-417.

Fontana, D., Zuffa, G. G., & Garzanti, E. The interaction of eustacy and tectonism from provenance studies of the Eocene Hecho Group Turbidite Complex (South-Central Pyrenees, Spain). Basin Research, 2(4), 223-237.

Fosdick, J. C., Grove, M., Graham, S. A., Hourigan, J. K., Lovera, O., & Romans, B. W. (2015). Detrital thermochronologic record of burial heating and sediment recycling in the Magallanes foreland basin, Patagonian Andes. Basin Research, 27(4), 546-572.

Garzanti, E., & Andò, S. (2019). Heavy minerals for junior woodchucks. Minerals, 9(3), 148.

Garzanti, E., Andò, S., & Vezzoli, G. (2008). Settling equivalence of detrital minerals and grain-size dependence of sediment composition. Earth and Planetary Science Letters, 273(1-2), 138-151.

Garzanti, E., Andò, S., & Vezzoli, G. (2009). Grain-size dependence of sediment composition and environmental bias in provenance studies. Earth and Planetary Science Letters, 277(3-4), 422-432.

Garzanti, E., Doglioni, C., Vezzoli, G., & Ando, S. (2007). Orogenic belts and orogenic sediment provenance. The Journal of Geology, 115(3), 315-334.

Garzanti, E., Limonta, M., Resentini, A., Bandopadhyay, P. C., Najman, Y., Andò, S., & Vezzoli, G. (2013). Sediment recycling at convergent plate margins (Indo-Burman ranges and Andaman–Nicobar Ridge). Earth-Science Reviews, 123, 113-132.

Garzanti, E., Vezzoli, G., Lombardo, B., Ando, S., Mauri, E., Monguzzi, S., & Russo, M. (2004). Collision-orogen provenance (western Alps): Detrital signatures and unroofing trends. The Journal of Geology, 112(2), 145-164.

Gómez-Gras, D., Roigé, M., Fondevilla, V., Oms, O., Boya, S., & Remacha, E. (2016). Provenance constraints on the Tremp Formation paleogeography (southern Pyrenees): Ebro Massif vs Pyrenees sources. Cretaceous Research, 57, 414-427.

Gupta, K. D., & Pickering, K. T. (2008). Petrography and temporal changes in petrofacies of deep-marine Ainsa–Jaca basin sandstone systems, Early and Middle Eocene, Spanish Pyrenees. Sedimentology, 55(4), 1083-1114.

Hart, N. R. (2015). Temporal constraints on progressive rifting of a hyper-extended continental margin using bedrock and detrital zircon (U-Th)/(Pb-He) dating, Mauléon Basin, western Pyrenees ((Doctoral dissertation, University of Texas at Austin).

Hart, N. R., Stockli, D. F., & Hayman, N. W. (2016). Provenance evolution during progressive rifting and hyperextension using bedrock and detrital zircon U-Pb geochronology, Mauléon Basin, western Pyrenees. Geosphere, 12(4), 1166-1186.

Hart, N. R., Stockli, D. F., Lavier, L. L., & Hayman, N. W. (2017). Thermal evolution of a hyperextended rift basin, Mauléon Basin, western Pyrenees. Tectonics, 36(6), 1103-1128.

Hirst, J. P. P., & Nichols, G. J. (1986). Thrust tectonic controls on Miocene alluvial distribution patterns, southern Pyrenees. Foreland basins, 247-258.

Hogan, P. J. (1993). Geochronologic, tectonic and stratigraphic evolution of the Southwest Pyrenean foreland basin, northern Spain (Doctoral dissertation, University of southern California).

Hogan, P. J., & Burbank, D. W. (1996). Evolution of the Jaca piggyback basin and emergence of the External Sierra, southern Pyrenees. In Tertiary Basins of Spain. Cambridge University Press.

Hudec, M. R., Dooley, T. P., Burrel, L., Teixell, A., & Fernandez, N. (2021). An alternative model for the role of salt depositional configuration and preexisting salt structures in the evolution of the Southern Pyrenees, Spain. Journal of Structural Geology, 146, 104325.

Jackson, S. E., Pearson, N. J., Griffin, W. L., & Belousova, E. A. (2004). The application of laser ablation-inductively coupled plasma-mass spectrometry to in situ U–Pb zircon geochronology. Chemical geology, 211(1-2), 47-69.

Jolley, E. J. (1987). Thrust tectonics and alluvial architecture of the Jaca Basin, Southern Pyrenees (Doctoral dissertation, University College).

Koshnaw, R. I., Stockli, D. F., & Schlunegger, F. (2019). Timing of the Arabia-Eurasia continental collision—Evidence from detrital zircon U-Pb geochronology of the Red Bed Series strata of the northwest Zagros hinterland, Kurdistan region of Iraq. Geology, 47(1), 47-50.

Labaume, P., Meresse, F., Jolivet, M., Teixell, A., & Lahfid, A. (2016). Tectonothermal history of an exhumed thrust-sheet-top basin: An example from the south Pyrenean thrust belt. Tectonics, 35(5), 1280-1313.

Labaume, P., Séguret, M., & Seyve, C. (1985). Evolution of a turbiditic foreland basin and analogy with an accretionary prism: Example of the Eocene south-Pyrenean basin. Tectonics, 4(7), 661-685.

Labaume, P., & Teixell, A. (2018). 3D structure of subsurface thrusts in the eastern Jaca Basin, southern Pyrenees. Geologica Acta, 477-498.

Lagabrielle, Y., Labaume, P., & de Saint Blanquat, M. (2010). Mantle exhumation, crustal denudation, and gravity tectonics during Cretaceous rifting in the Pyrenean realm (SW Europe): Insights from the geological setting of the lherzolite bodies. Tectonics, 29(4).

Laskari, S., Soukis, K., Lozios, S., Stockli, D. F., Poulaki, E. M., & Stouraiti, C. (2021). Provenance Analysis and Structural Study of the Cycladic Blueschist Unit Rocks from Iraklia Island: From the Paleozoic Basement Unroofing to the Cenozoic Exhumation.

Laskari, S., Soukis, K., Stockli, D. F., Lozios, S., & Zambetakis-Lekkas, A. (2022). Reconstructing the southern Pelagonian domain in the Aegean Sea: Insights from U-Pb detrital zircon analysis, lithostratigraphic and structural study, and zircon (U-Th)/He thermochronology on Amorgos Island (SE Cyclades, Greece). Gondwana Research.

Malusà, M. G., Resentini, A., & Garzanti, E. (2016). Hydraulic sorting and mineral fertility bias in detrital geochronology. Gondwana Research, 31, 1-19.

Mangin, J. P. (1958). Le Nummulitique Sud-Pyreneen alouest de lAeagon. Rev. Ins. de Estudios Pirenaicos, 51, 58.

Margalef, A., Castiñeiras, P., Casas, J.M., Navidad, M., Liesa, M., Linnemann, U., Hofmann, M., & Gärtner, A. (2016). Detrital zircons from the Ordovician rocks of the Pyrenees: Geochronological constraints and provenance. Tectonophysics, 681, 124-134.

Martí, J., Mitjavila, J., Roca, E., & Aparicio, A. (1992). Cenozoic magmatism of the valencia trough (western mediterranean): Relationship between structural evolution and volcanism∗. Tectonophysics, 203(1-4), 145-165.

Martínez, F. J., Reche, J., & Iriondo, A. (2008). U–Pb Shrimp-RG zircon ages of Variscan igneous rocks from the Guilleries massif (NE Iberia pre-Mesozoic basement). Geological implications. Comptes Rendus Geoscience, 340(4), 223-232.

Marzoli, A., Renne, P. R., Piccirillo, E. M., Ernesto, M., Bellieni, G., & Min, A. D. (1999). Extensive 200-million-year-old continental flood basalts of the Central Atlantic Magmatic Province. Science, 284(5414), 616-618.

Michael, N. (2013). Functioning of an ancient routing system, the Escanilla Formation, South Central Pyrenees (Doctoral dissertation, Imperial College London).

Moecher, D. P., & Samson, S. D. (2006). Differential zircon fertility of source terranes and natural bias in the detrital zircon record: Implications for sedimentary provenance analysis. Earth and Planetary Science Letters, 247(3-4), 252-266.

Mouthereau, F., Filleaudeau, P. Y., Vacherat, A., Pik, R., Lacombe, O., Fellin, M.G., Castelltort, S., Christophoul, F., & Masini, E. (2014). Placing limits to shortening evolution in the Pyrenees: Role of margin architecture and implications for the Iberia/Europe convergence. Tectonics, 33(12), 2283-2314.

Muñoz, J. A., Mencos, J., Roca, E., Carrera, N., Gratacós, O., Ferrer, O., & Fernández, Ò. (2018). The structure of the South-Central-Pyrenean fold and thrust belt as constrained by subsurface data. Geologica Acta, 439-460.

Mutti, E. (1985). Turbidite systems and their relations to depositional sequences. In Provenance of arenites (pp. 65-93). Springer, Dordrecht.

Mutti, E., Luterbacher, H., Ferrer, J., & Rosell, J. (1972). Schema stratigrafico e lineamenti di facies del Paleogeno Marino della zona centrale sudpirenaica tra Tremp (Catalogna) e Pamplona (Navarra). Mem. Soc. Geol. Ital. 11, 391–416.

Nijman, W., & Nio, S. D. (1976). The Eocene Montañana Delta: Tremp-Graus Basin, Provinces of Lérida and Huesca, Southern Pyrenee, N. Spain. Vakgroep Sedimentologie, Rijksuniveriteit Leiden-Utrecht.

Odlum, M. L., Stockli, D. F., Capaldi, T. N., Thomson, K. D., Clark, J., Puigdefàbregas, C., & Fildani, A. (2019). Tectonic and sediment provenance evolution of the South Eastern Pyrenean foreland basins during rift margin inversion and orogenic uplift. Tectonophysics, 765, 226-248.

Oliva-Urcia, B., Beamud, E., Arenas, C., Pueyo, E. L., Garcés, M., Soto, R., Valero, L., & Pérez-Rivarés, F. J. (2019). Dating the northern deposits of the Ebro foreland basin; implications for the kinematics of the SW Pyrenean front. Tectonophysics, 765, 11-34.

Oliva-Urcia, B., Beamud, E., Garcés, M., Arenas, C., Soto, R., Pueyo, E. L., & Pardo, G. (2016). New magnetostratigraphic dating of the Palaeogene syntectonic sediments of the west-central Pyrenees: tectonostratigraphic implications. Geological Society, London, Special Publications, 425(1), 107-128.

Oms, O., Dinarès-Turell, J., & Remacha, E. (2003). Magnetic stratigraphy from deep clastic turbidites: an example from the Eocene Hecho group (southern Pyrenees). Studia Geophysica et Geodaetica, 47(2), 275-288.

Ortí, F., Salvany, J. M., Rosell, L., Pueyo, J. J., & Inglés, M. (1986). Evaporitas antiguas (Navarra) y actuales (Los Manegros) de la Cuenca del Ebro. In XI Congreso espa~ nol de sedimentologia: guia de las excursiones, Barcelona, 15 a 18 de septiembre de 1986 (pp. 2-1).

Paton, C., Hellstrom, J., Paul, B., Woodhead, J., & Hergt, J. (2011). Iolite: Freeware for the visualisation and processing of mass spectrometric data. Journal of Analytical Atomic Spectrometry, 26(12), 2508-2518.

Payros, A., Astibia, H., Cearreta, A., Pereda-Suberbiola, X., Murelaga, X., & Badiola, A. (2000). The Upper Eocene South Pyrenean Coastal deposits (Liedena sandstone, navarre): Sedimentary facies, benthic formanifera and avian ichnology. Facies, 42(1), 107-131.

Payros, A., Pujalte, V., Orue-Etxebarria, X., & Baceta, J. I. (1997). A Bartonian channel-levee turbiditic system in the Pamplona Basin: Tectonic and paleogeographic implications. Geogaceta, 22, 145-148.

Payros, A., Pujalte, V., & Orue-Etxebarria, X. (1999). The South Pyrenean Eocene carbonate megabreccias revisited: new interpretation based on evidence from the Pamplona Basin. Sedimentary Geology, 125(3-4), 165-194.

Puigdefábregas, C. (1975). La sedimentación molásica en la cuenca de Jaca.

Puigdefàbregas, C., Muñoz, J. A., & Vergés, J. (1992). Thrusting and foreland basin evolution in the southern Pyrenees. In Thrust tectonics (pp. 247-254). Springer, Dordrecht.

Pujols, E. J., & Stockli, D. F. (2021). Zircon (U-Th)/(He-Pb) double-dating constraints on the interplay between thrust deformation and foreland basin architecture, Sevier foreland basin, Utah. Geosphere, 17(6), 1890-1913.

Reiners, P. W. (2005). Zircon (U-Th)/He thermochronometry. Reviews in Mineralogy and Geochemistry, 58(1), 151-179.

Remacha, E., Fernández, L. P., & Maestro, E. (2005). The transition between sheet-like lobe and basin-plain turbidites in the Hecho Basin (South-Central Pyrenees, Spain). Journal of Sedimentary Research, 75(5), 798-819.

Roigé M. (2018). Procedència i evolució dels sistemes sedimentaris de la conca de Jaca (conca d'avantpaís Sudpirinenca): Interacció entre diverses àrees font en un context tectònic actiu (Doctoral dissertation, Universitat Autònoma de Barcelona).

Roigé, M., Gómez-Gras, D., Remacha, E., Boya, S., Viaplana-Muzas, M., & Teixell, A. (2017). Recycling an uplifted early foreland basin fill: An example from the Jaca basin (Southern Pyrenees, Spain). Sedimentary Geology, 360, 1-21.

Roigé, M., Gómez-Gras, D., Remacha, E., Daza, R., & Boya, S. (2016). Tectonic control on sediment sources in the Jaca basin (Middle and Upper Eocene of the South-Central Pyrenees). Comptes Rendus Geoscience, 348(3-4), 236-245.

Roigé, M., Gómez-Gras, D., Stockli, D. F., Teixell, A., Boya, S., & Remacha, E. (2019). Detrital zircon U–Pb insights into the timing and provenance of the South Pyrenean Jaca basin. Journal of the Geological Society, 176(6), 1182-1190.

Sabat, F., Roca, E., Muñoz, J. A., Verges, J., Santanach, P., Masana, E., Sans, M., Estevez, A., & Santiesteban, C. (1995). Role of extension and compression in the evolution of the eastern margin of Iberia: the ESCI-Valencia Trough seismic profile. Revista de la Sociedad Geológica de España, 8(4), 431-448.

Saura, E., Ardèvol i Oró, L., Teixell, A., & Vergés, J. (2016). Rising and falling diapirs, shifting depocenters, and flap overturning in the Cretaceous Sopeira and Sant Gervàs subbasins (Ribagorça Basin, southern Pyrenees). Tectonics, 35(3), 638-662.

Sláma, J., Košler, J., Condon, D. J., Crowley, J. L., Gerdes, A., Hanchar, J. M., Horstwood, M. S., Morris, G. A., Nasdala, L., Norberg, N., & Schaltegger, U., (2008). Plešovice zircon—a new natural reference material for U–Pb and Hf isotopic microanalysis. Chemical Geology, 249(1-2), 1-35.

Soler-Sampere, M., & Puigdefàbregas, C. (1970). Líneas generales de la geología del Alto Aragón Occidental.

Steidtmann, J. R., & Schmitt, J. G. (1988). Provenance and dispersal of tectogenic sediments in thin-skinned, thrusted terrains. In New perspectives in basin analysis (pp. 353-366). Springer, New York, NY.

Tarriño, A. (2006). El sílex en la cuenca vasco cantábrica y pirineo navarro: caracterización y su aprovechamiento en la prehistoria (Doctoral dissertation, Universidad del País Vasco-Euskal Herriko Unibertsitatea).

Teixell, A. (1996). The Ansó transect of the southern Pyrenees: basement and cover thrust geometries. Journal of the Geological Society, 153(2), 301-310.

Teixell, A., & García-Sansegundo, J. (1995). Estructura del sector central de la Cuenca de Jaca (Pirineos meridionales). Rev. Soc. Geol. España, 8, 207-220.

Teixell, A., Labaume, P., Ayarza, P., Espurt, N., de Saint Blanquat, M., & Lagabrielle, Y. (2018). Crustal structure and evolution of the Pyrenean-Cantabrian belt: A review and new interpretations from recent concepts and data. Tectonophysics, 724, 146-170.

Teixell, A., Labaume, P., & Lagabrielle, Y. (2016). The crustal evolution of the west-central Pyrenees revisited: Inferences from a new kinematic scenario. Comptes Rendus Geoscience, 348(3-4), 257-267.

Thomson, K. D., Stockli, D. F., Clark, J. D., Puigdefàbregas, C., & Fildani, A. (2017). Detrital zircon (U-Th)/(He-Pb) double-dating constraints on provenance and foreland basin evolution of the Ainsa Basin, south-central Pyrenees, Spain. Tectonics, 36(7), 1352-1375.

Thomson, K. D., Stockli, D. F., Odlum, M. L., Tolentino, P., Puigdefàbregas, C., Clark, J., & Fildani, A. (2020). Sediment provenance and routing evolution in the Late Cretaceous–Eocene Ager Basin, south-central Pyrenees, Spain. Basin Research, 32(3), 485-504.

Vacherat, A., Mouthereau, F., Pik, R., Huyghe, D., Paquette, J.L., Christophoul, F., Loget, N. & Tibari, B. (2017). Rift-to-collision sediment routing in the Pyrenees: A synthesis from sedimentological, geochronological and kinematic constraints. Earth-Science Reviews, 172, 43-74.

Vergés, J., Fernàndez, M., & Martìnez, A. (2002). The Pyrenean orogen: pre-, syn-, and post-collisional evolution. Journal of the Virtual Explorer, 8, 55-74.

Vermeesch, P. (2004). How many grains are needed for a provenance study?. Earth and Planetary Science Letters, 224(3-4), 441-451.

Vermeesch, P. (2013). Multi-sample comparison of detrital age distributions. Chemical Geology, 341, 140-146.

Vermeesch, P., Resentini, A., & Garzanti, E. (2016). An R package for statistical provenance analysis. Sedimentary Geology, 336, 14-25.

Vermeesch, P. (2018). Statistical models for point-counting data. Earth and Planetary Science Letters, 501, 112-118.

Vinyoles, A., López-Blanco, M., Garcés, M., Arbués, P., Valero, L., Beamud, E., ... & Cabello, P. (2021). 10 Myr evolution of sedimentation rates in a deep marine to non-marine foreland basin system:

Tectonic and sedimentary controls (Eocene, Tremp–Jaca Basin, Southern Pyrenees, NE Spain). Basin Research, 33(1), 447-477.

Whitchurch, A. L., Carter, A., Sinclair, H. D., Duller, R. A., Whittaker, A. C., & Allen, P. A. (2011). Sediment routing system evolution within a diachronously uplifting orogen: Insights from detrital zircon thermochronological analyses from the South-Central Pyrenees. American Journal of Science, 311(5), 442-482.

Wolfe, M. R., & Stockli, D. F. (2010). Zircon (U–Th)/He thermochronometry in the KTB drill hole, Germany, and its implications for bulk He diffusion kinetics in zircon. Earth and Planetary Science Letters, 295(1-2), 69-82.

Capítol 7

Discussió integrada: Anàlisi de procedència multimètode i evolució dels sistemes sedimentaris de la conca de Jaca

7.1. Anàlisi de procedència multimètode

En els anteriors capítols s'han exposat els resultats referents a l'anàlisi de procedència dels sistemes sedimentaris de la conca de Jaca. Tal i com s'ha exposat en els capítols anteriors, els anàlisis petrològics i estadístics han permès caracteritzar el contingut en minerals pesants del sistemes del marge nord de la conca de Jaca (figura 1, 2), definir cinc associacions minerals en el marge sud (figura 3, 4), tres senyals característiques de U-Pb en zircons detrítics (figura 5, 6), i dues senyals característiques de ZHe en zircons detrítics (5, 7). En aquest capítol es procedeix a discutir aquestes dades per tal d'integrar-les en referència als objectius plantejats en el capítol 2.

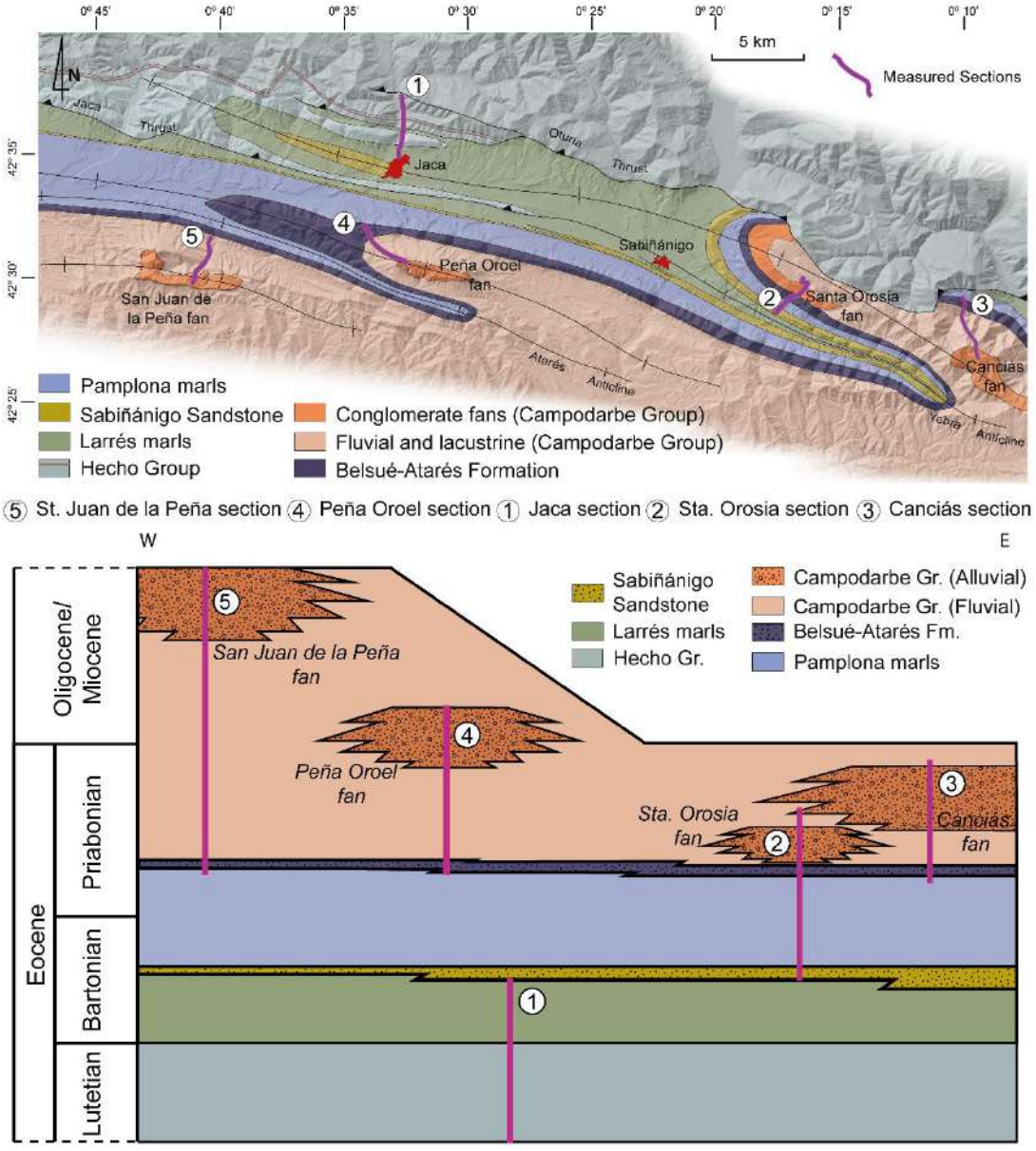

Figura 7.1. *Mapa geològic del marge nord de la conca de Jaca i esquema estratigràfic resumint les relacions entre els les unitats deposicionals analitzades (modificat de Roigé et al., 2017).*

Els estudis de procedència es caracteritzen per una forta component deductiva que té com a objectiu caracteritzar la litologia de les àrees font, la seva ubicació geogràfica, la seva evolució, i la connexió amb la conca deposicional a través dels *sediment routing systems*. En aquest sentit, en els capítols anteriors he descrit la informació que s'obté dels diferents mètodes d'anàlisi de procedència (petrografia, anàlisis de minerals pesants, U-Pb i ZHe en zircons detrítics) i he assenyalat com una discussió integrada d'aquests mètodes diversos és l´única manera d'interpretar correctament la informació que se'n deriva. En la part nord de la conca de Jaca, la integració de les dades de minerals pesants obtingudes en aquesta tesi i de les dades de petrografia i U-Pb en zircons detrítics de Roigé et al. (2016, 2017, 2018) ha permès augmentar la resolució del marc paleogeogràfic concebut. Aquesta integració m'ha permès relacionar la associació ultraestable (Ap-Zrn-Tur-Rt) amb el drenatge d'àrees font cristal·lines (fonamentalment granítiques) i formacions sedimentàries mesozoiques de la Zona Sudpirinenca i la Zona Axial, més a l'est de la conca de Jaca. La abundància d'aquests minerals pesants en roques plutòniques àcides (Mange & Maurer, 1992; Götze,1998), la seva resistència durant els processos de reciclatge (Hubert, 1962; Mange & Maurer, 1992; Garzanti et al., 2007; Garzanti et al., 2013), la absència de roques metamòrfiques de grau mig-alt en l'àrea font de la Zona Axial (que no subministrà minerals característics tals com l'epidota, els granats, l'estaurolita o els aluminosilicats), juntament amb un grau de diagènesi insuficient per a esborrar l'associació mineral mencionada del registre sedimentari (Walderhaug & Porten, 2007; Crognier, 2016; Labaume et al., 2016), suporten aquesta interpretació. Els grans idiomòrfics estarien relacionats amb les roques cristal·lines (granits), mentre que els més arrodonits derivarien del reciclatge de la cobertora sedimentària.

Durant la sedimentació de l`últim sistema turbidític de Jaca (el canal de Rapitán), l'aparició de minerals com la grossulària, l'almandí o l'estaurolita indiquen l'aixecament de noves àrees font al nord de la conca, en relació amb l'encavalcament de Lakora/Eaux-Chaudes (Roigé et al., 2016). Aquests minerals em permeten assenyalar àrees font específiques com la Zona Nordpirinenca i els massissos metamòrfics de Lesponne, Chiroulet o Barousse (Zona Axial), on s'han descrit calcàries mesozoiques amb grossulària (relacionades amb el metamorfisme del Cretaci) i metapelites varisques de mitjà-alt grau que contenen estaurolita i almandí (Pouget 1989). Les dades de termocronologia existents al nord de la conca de Jaca indiquen que, tot i que la Zona Axial directament al nord no va poder actuar com a àrea font fins al Eocè superior-Oligocè (Jolivet et al. 2007; Meresse 2010; Labaume et al. 2016b; Bosch et al. 2016), la Zona Nordpirinenca sí que va experimentar una exhumació des del Paleògen inferior (Vacherat et al. 2014; Bosch et al. 2016). Àrees de la Zona Axial septentrional limítrofes amb la Zona Nordpirinenca, com el massís de Lesponne, podrien haver estat ja exposades des del Eocè

mig-superior. La presència de fragments de roca metamòrfics (Roigé et al., 2016; 2017) apunten a una àrea font varisca metapelítica com a font d'almandí i estaurolita. La presència d'aquests minerals metamòrfics tant en els últims sistemes turbidítics com en els posteriors sistemes al·luvials transversals (Priabonià-Miocè), evidencien que la divisòria d'aigües s'estenia fins a la Zona Nordpirinenca (Babault et al., 2011; Roigé et al., 2017; Ortuño & Viaplana, 2018) i que, localment, àrees del Paleozoic de la Zona Axial septentrional ja estaven exposades.

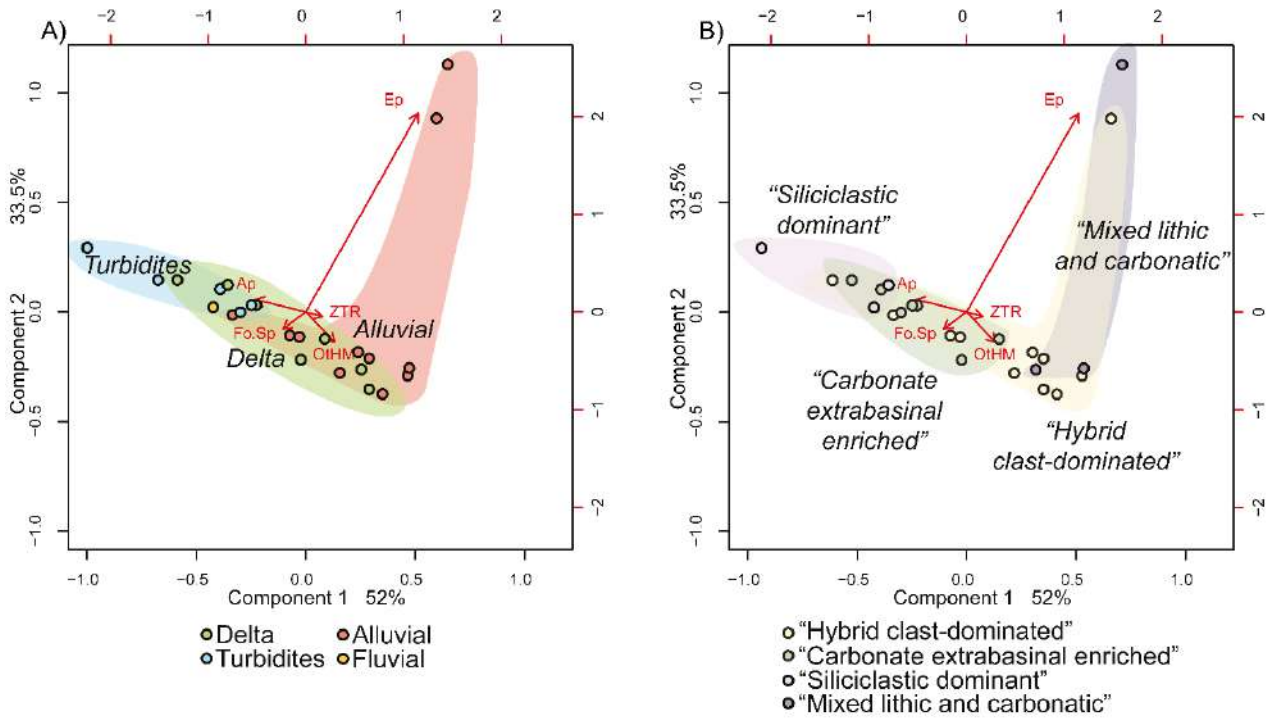

Figura 7. 2. *Resultats de l'anàlisi de correspondència e minerals pesants del marge nord de la conca de Jaca. (A) mostres etiquetades segons ambient deposicional. (B) mostres etiquetades segons petrofacies. Ep:epidota; ZTR: zircó+turmalina+rutil; Fo.Sp: fosterita+espinela; OtHM: altres minerals pesants.*

La integració de les petrofacies, els minerals pesants i les senyals d'U-Pb en zircons detrítics observades en el sistema deltaic de Belsué-Atarés revela una complexitat dels *sediment routing systems* difícil de resoldre. La formació Escanilla inferior de la conca d'Aínsa i la formació deltaica de Belsué-Atarés mostren la mateixa petrofacies *carbonate extrabasinal enriched* (Roigé, 2018). No obstant, les senyals d'U-Pb de la Formació Belsué-Atarés en el perfil de Santa Orosia (Roigé, 2018) són *mixed Cadomian-Variscan*, mentre que les senyals d'U-Pb de la Fm. Escanilla inferior (Michael 2013; Thompson 2017) son *Variscan dominated*. La formació Escanilla superior es caracteritza per les mateixes senyals d'U-Pb *mixed Cadomian-Variscan* que la formació Belsué-Atarés (Michael 2013; Roigé 2018). Per contra, la formació Escanilla presenta una associació de minerals pesants dominada

per l'epidota, mentre que aquest mineral és absent en els dipòsits deltaics de Belsué-Atarés. La possible dissolució d'aquest mineral degut a processos diagenètics ha estat descartada en base a les baixes paleotemperatures deduïdes per Crognier (2016) i a la presència de clinopiroxè (mineral més susceptible a la diagènesis que l'epidota) en els dipòsits suprajacents del ventall al·luvial de Santa Orosia. Per tant, puc deduir que el *sediment routing system* d'Escanilla, tot i ser equivalent temporal del delta de Belsué-Atarés, no alimentava aquests dipòsits en el marge nord-est de la conca de Jaca.

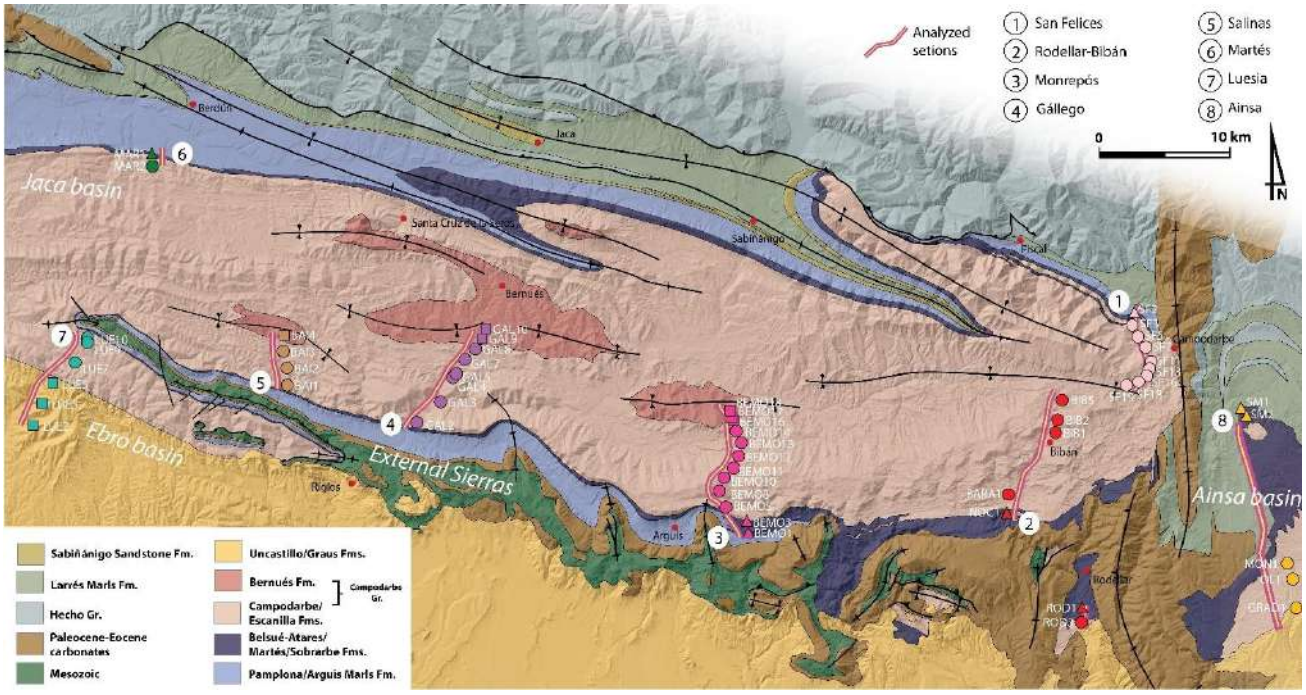

Figura 7. 3. *Mapa geològic de la conca de Jaca (modificat de Puigdefàbregas, 1975), amb la localització de les mostres de petrografia de Roigé (2018) i de minerals pesants (Coll et al., 2022).*

Cap a l'oest (Perfil de Peña Oroel), les tres senyals de procedència indiquen que el sistema al·luvial de Santa Orosia alimentava el delta de Belsué-Atarés en aquesta àrea. Les similituds entre ambdós sistemes: petrofacies rica en fragments de gresos híbrids (Roigé, 2018), senyals d'U-Pb que aquí classifico com *Cadomian dominated* (Roigé, 2018), i associacions de minerals pesants amb presència de clinopiroxè, estaurolita i grossulària (Coll et al., 2020) així ho evidencien.

En el marge sud de la conca de Jaca, els dipòsits deltaics de Belsué-Atarés es caracteritzen per una associació de minerals pesants amb absència d'epidota, juntament amb senyals d'U-Pb *mixed Cadomian-Variscan*. Per tant, l'Escanilla *sediment routing system (ric en epidota)* tampoc influenciava la sedimentació deltaica en el marge sud de la conca. A més, les senyals diferents d'U-Pb de la Formació Belsué-Atarés de la zona de Santa Orosia al nord (*Cadomian dominated*) i de les zones de

Bara-Bibán i Monrepós al sud (*mixed Cadomian-Variscan*) demostren que existeixen dos àrees font diferents, com explicaré més endavant, tot i caracteritzar-se per la mateixa petrofacies.

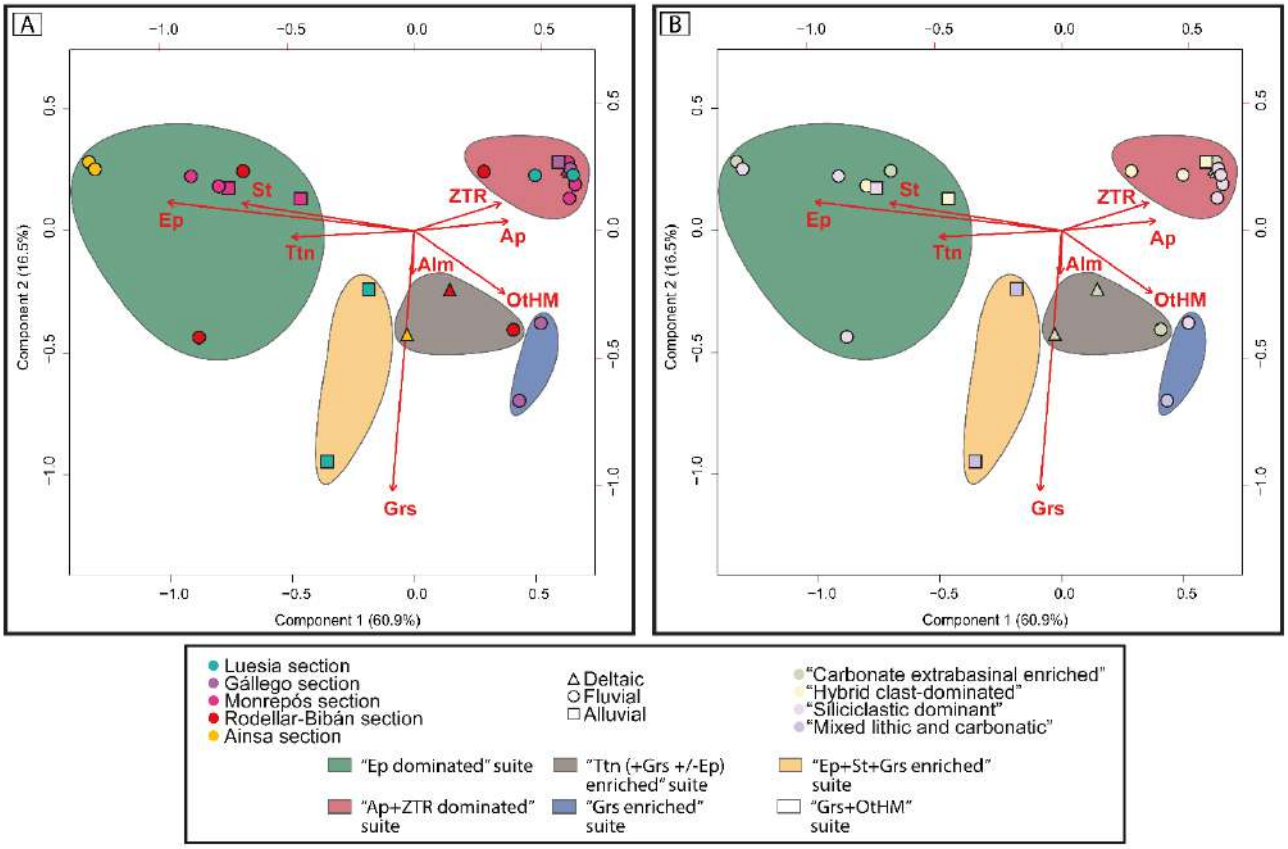

Figura 7.4. *Associacions de minerals pesants del marge sud de la conca de Jaca definides a partir de l'anàlisi de correspondència. (A) El color de les motres indica la secció i la forma el ambient sedimentàri. (B) El color de les motres indica la petrofacies i la forma el ambient sedimentàri. Ep:epidota; ZTR: zircó+turmalina+rutil; Alm: almandí; Grs: grossulària; Tt: titanita; St: estaurolita; OtHM: altres minerals pesants.*

En aquest treball he posat de manifest que les associacions de minerals pesants descrites (Coll et al., 2020), que caracteritzen el sistema fluvial axial (Fm. Campodarbe) previ a l'establiment dels sistemes al·luvials transversals, evidencien una complexitat no registrada ni per la petrografia sedimentària (Roigé et al., 2017) ni per les senyals de procedència d'U-Pb en zircons detrítics (Roigé, 2018). Roigé et al. (2017) relaciona la petrofacies siliciclàstica, que caracteritza l'àrea de San Juan de la Peña, i els paleocorrents dominants cap al W-NW, amb una àrea font ubicada al Pirineu central, la qual alimentava la conca de Jaca a través dels sistemes fluvio-al·luvials de la conca d'Aínsa (Fm. Escanilla). Per contra, l'anàlisi de minerals pesants revela que el sistema fluvial axial de San Juan de la Peña (Fm. Campodarbe) no presenta epidota, un marcador clau de correlació amb la Fm. Escanilla, la qual en mostra continguts superiors al 50% des de la base (Michael, 2013). La possible pèrdua d'aquest

marcador degut a processos diagenètics en la Fm. Campodarbe ha estat també descartada en base al contingut notable de clinopiroxè, mineral altament inestable en front de processos post-deposicionals (Morton & Hallsworth., 1999, 2007). Així doncs, les dades de minerals pesants indiquen que la sedimentació en el marge nord de la conca de Jaca tampoc estava influenciada per el *routing system* de la Fm. Escanilla, contràriament al que succeeix al marge sud, tal i com descriuré més endavant.

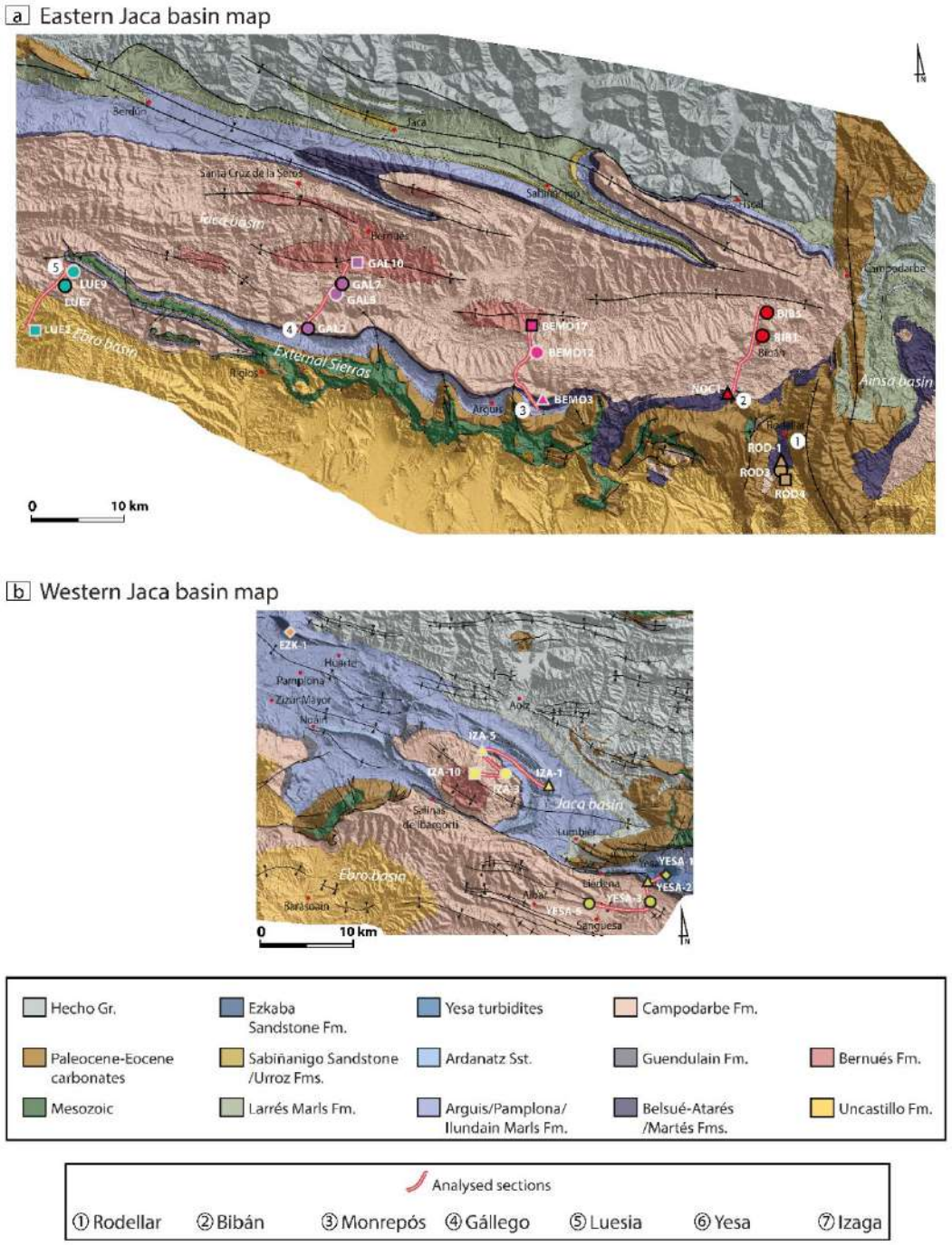

Figura 7.5. *Mapa geològic de la conca de Jaca (modificat de Puigdefàbregas, 1975) amb la localització de les mostres. (A) conca de Jaca oriental. (B) Conca de Jaca occidental.*

La utilització de diferents mètodes d'anàlisi de procedència portada a terme en aquest treball ha evidenciat severes contradiccions sedimentològiques pel que fa a la transferència de sediment entre diferents formacions coetànies com la Belsué-Atarés i l'Escanilla. No obstant, la consideració integrada dels mètodes d'anàlisi de procedència utilitzats en aquesta tesi, com son la petrografia, els minerals pesants, la geocronologia i termocronologia en zircons detrítics, ha permès relacionar la transmissió de sediments entre diferents formacions.

D'aquesta manera, en el marge sud de la conca de Jaca, la integració dels quatre mètodes ha permès definir la existència de dos sistemes fluvials axials coetanis, ambdós procedents de l'est i amb una mateixa petrofacies i senyal d'U-Pb, però amb associacions de minerals pesants diferents i senyals de ZHe en zircons detrítics també diferents. L'estudi petrològic de Roigé (2018) mostra que la Fm. Campodarbe evoluciona d'una àrea font Paleozoica, dominantment granítica, activa durant el Bartonià-Priabonià (petrofacies *carbonate extrabasinal enriched*), cap a una àrea font dominantment metamòrfica (petrofacies *siliciclastic dominant*), que roman activa des del Priabonià fins que es substituïda per els sistemes transversals que drenen les àrees font situades al nord de la conca (petrofacies *hybrid clast-dominated*). Aquesta evolució és fàcilment observable amb la petrografia però no és registrada per cap de les altres senyals de procedència.

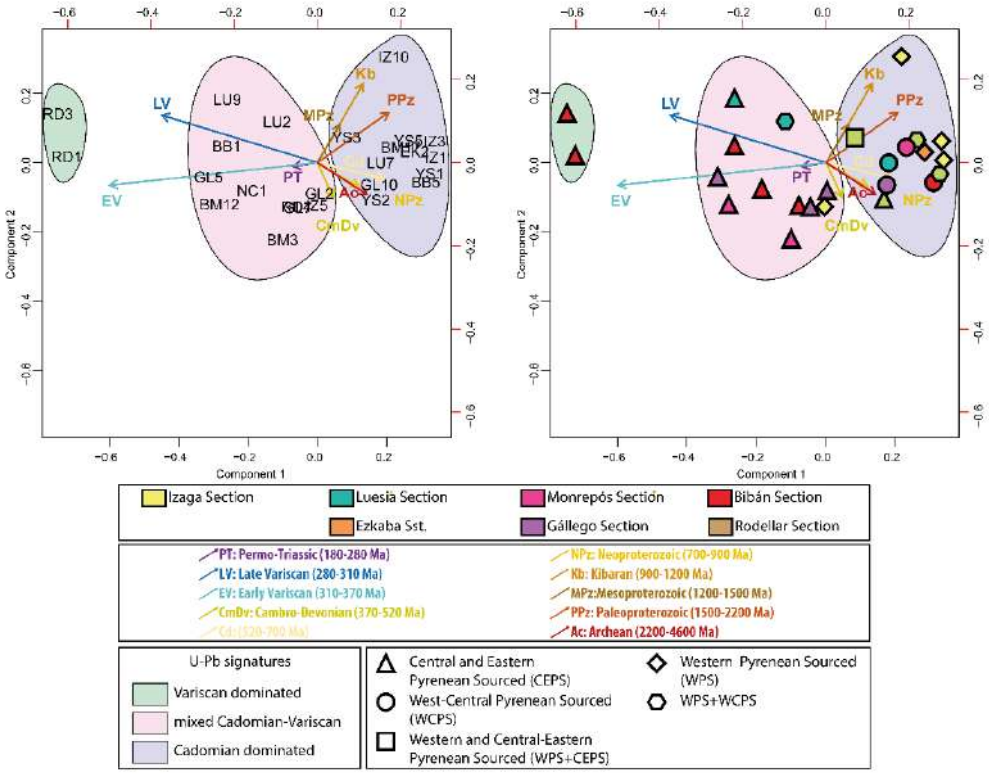

Figura 7.6. *Senyals característiques d'U-Pb de la conca de Jaca.*

Això no obstant, l'estudi dels minerals pesants i de la termocronologia dels zircons detrítics és el que permet definir els dos sistemes axials, clarament diferenciats i amb àrees font diferents. El primer sistema té l'àrea font ubicada al Pirineu central, on afloraven diapirs del Keuper incloent dolerites triàsiques (ofites) amb abundància d'epidota (zona nord de la Unitat Sudpirinenca Central), i per tant es caracteritza per ser ric en epidota i mostrar senyals de ZHe únicament pirinenques. Aquest sistema, alimenta el sector més oriental de la conca de Jaca transferint sediments de la Fm. Escanilla. El segon sistema tindria l'àrea font en el Pirineu oriental, en la zona del Pedraforca-Port del Compte, i al nord de la mateixa, en l'actual vall del Segre, on les dolerites triàsiques i les fàcies Keuper són escasses o absents, i està caracteritzat per l'absència d'epidota, i una barreja de senyals ZHe pirinenques, cretàciques i permotriàsiques. Aquest sistema si que s'estén cap a la part més occidental de la conca de Jaca (àrees del Gállego i San Juan de la Peña), seguint un *routing system* més meridional, transferint sediments de la Fm. Salinar (Priabonià) i/o la Fm. Peraltilla inferior (Rupelià) del autòcton de la conca de l'Ebre.

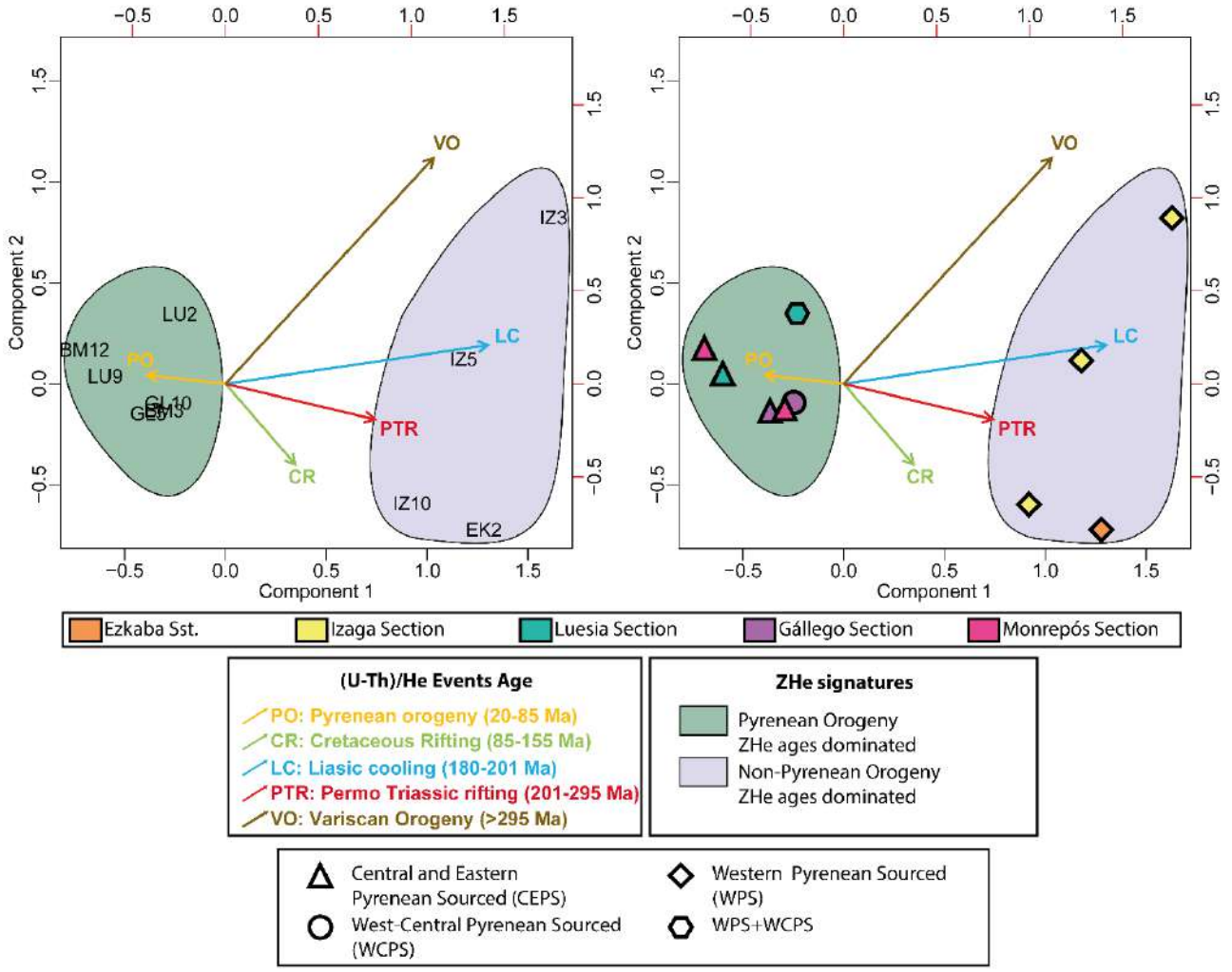

Figura 7.7. *Senyals ZHe característiques de la conca de Jaca.*

Amb tot, puc concloure que els minerals pesants i la termocronologia han estat més sensibles en la identificació d'àrees font diferents, que en caracteritzar evolucions d'una mateixa àrea font durant el temps de sedimentació d'una formació. Aquest fet es habitual i degut, de manera general, al cost dels anàlisis de geocronologia i termocronologia , que condiciona que aquest tipus d'estudis de procedència es basin en poques mostres, generalment molt separades en el temps i l'espai. Quan els sistemes transversals procedents del nord (petrofacies *hybrid clast-dominated*) s'estenen i acaben imposant-se en el marge sud, els minerals pesants i l'U-Pb en zircons detrítics també registren el canvi.

7.2. La importància del reciclatge vs els aports directes en les dades de procedència de la conca de Jaca

La integració de l'estudi de procedència en zircons detrítics amb les dades de petrografia, permet entendre la propagació de les senyals d'U-Pb, en un context en el que diferents àrees font tenen la capacitat de generar senyals similars. A més, cal assenyalar que infravalorar el paper del reciclatge de les diferents formacions sedimentàries dóna lloc a interpretacions no realistes únicament esmenables mitjançant un estudi petrogràfic detallat.

En el marge sud de la conca de Jaca, els sistemes amb una forta component granítica (Belsué-Atarés, secció de Rodellar, petrofacies *carbonate extrabasinal enriched*) contenen senyals d'U-Pb *Variscan dominated*, mantenint-se aquesta senyal en els sistemes suprajacents (Fm. Campodarbe, petrofacies *siliciclastic dominant*) fortament influenciats per una àrea font metamòrfica i amb una component granítica escassa. Cap a l'oest, la formació Belsué-Atarés en la secció de Monrepós (petrofacies *carbonate extrabasinal enriched*, amb una component granítica notable*)* es caracteritza per una senyal d'U-Pb *mixed Cadomian-Variscan*, mantenint-se aquesta senyal en els sistemes suprajacents (Fm. Campodarbe, petrofacies *siliciclastic dominant*, amb una component granítica escassa o absent). En ambdós casos, el fet que no existeixi una correlació entre l'abundància de components granítics i la de components U-Pb variscs, implica que hi ha alguna litologia no granítica en l'àrea font que és capaç de proporcionar zircons variscs suficients per compensar la constància d'aquesta senyal. Interpreto que aquesta contribució correspon a la cobertora cretàcica, que pot contenir senyals varisques importants (Filledeau, 2012; Odlum et al., 2019), i és evidenciada pel notable contingut en fragments carbonàtics observats en ambdues petrofacies. Això indicaria que el reciclatge de formacions sedimentàries cretàciques pot contribuir a la propagació de components varíscs no derivats d'un aport granític directe. Aquest fet evidencia que un anàlisi de procedència basat únicament en U-Pb, que no consideri

el rol del reciclatge en la propagació de les senyals, pot induir a interpretacions errònies respecte a la naturalesa de l'àrea font en conques d'avantpaís.

El reciclatge de la conca turbidítica eocena és un bon exemple de com la petrologia ens permet entendre la propagació de les senyals d'U-Pb. Roigé (2018) va estudiar la geocronologia d'U-Pb de les turbidites de la part alta del Grup d'Hecho, les quals es caracteritzen per senyals *Variscan dominated* en la part inferior (sistemes turbidítics de Banastón i Jaca inferior) mentre que en la part superior (sistemes turbidítics de Jaca mig i superior) mostren senyals *Cadomian dominated*. Donat que els posteriors sistemes al·luvials transversals derivats del nord mostren una senyal *Cadomian dominated*, es pot inferir que el que s'està reciclant majoritàriament en aquests dipòsits son els sistemes turbidítics de Jaca mig i superior.

La importància d'integrar els anàlisis de U-Pb i ZHe amb dades petrogràfiques es torna a evidenciar en l'estudi de la part occidental de la conca de Jaca. Mentre que els sistemes axials de la part oriental es caracteritzen per senyals U-Pb *mixed Cadomian-Variscan* i senyals de ZHe *Pyrenean dominated*, la conca de Jaca occidental, per contra, es caracteritza per senyals d'U-Pb *Cadomian dominated*, i senyals ZHe *non-Pyrenean dominated*. Això evidencia que els sistemes axials de la conca de Jaca oriental no s'estenien fins a la zona occidental, que es nodria d'àrees font diferents. No obstant, com en la zona occidental la senyal d'U-Pb no varia al llarg del registre sedimentari Bartonià-Miocè, torna a ser la petrologia qui aporta informació sobre l'evolució de les àrees font en aquet sector de la conca. Les dades de petrografia revelen que en l'àrea d'Izaga les formacions Ezkaba, Ardanatz i Liédena (Bartonià-Priabonià) es nodrien de l'erosió dels massissos bascs i la cobertora mesozoica (Pirineu occidental), com indica l'abundància de feldspat potàssic i plagiòclasi fresca i la presència de fragments de calcàries amb tintínids (Turonià). Aquesta interpretació està d'acord amb Payros (1997), que va senyalar els massissos bascs com a àrea font de la formació Ezkaba en funció del seu contingut siliciclàstic i paleocorrents cap al Sud. Durant la sedimentació de la Fm. Campodarbe (Oligocè), la presència de fragments de gresos calcarenítics, grans silicificats (alguns d'ells amb cristalls de dolomita idiomòrfica), i carbonats derivats del Paleocè-Eocè, indiquen que la xarxa de drenatge s'estén cap a la Serra d'Urbasa-Andía, on afloren aquestes formacions (Payros, 1997; Tariño, 2006). Finalment, el sistema al·luvial d'Izaga (Fm. Bernués; Chatià-Aquitanià) s'alimenta únicament de la Serra d'Urbasa-Andía. L'absència de feldspats, fragments de roca plutònics, metamòrfics i de gresos siliciclàstics senyala que els massissos bascs han deixat de contribuir, mentre que la dominància de

còdols de calcarenites, calcàries mesozoiques i paleocenes, així com de còdols amb silicificacions, indica això.

Més a l'est, en el perfil de Yesa, el registre sedimentari mostra la interacció de les àrees font del Pirineu oriental, central i occidental (massissos bascs), esdevenint una veritable àrea de confluència de sistemes axials i transversals. Les turbidites de Yesa (Priabonià) es nodreixen de l'erosió de les turbidites del Grup d'Hecho i de les plataformes eocenes (fragments de gresos híbrids, fragments de carbonats terciaris, bioclasts), amb influència dels massissos bascs (feldspat potàssic, plagiòclasi fresca, fragments de carbonats mesozoics). Per contra, la Fm. Liédena és alimentada pels sistemes axials de procedència est, evidenciat per l'abundància de fragments de roca metamòrfics, de gresos i lutites permotriàsiques, feldspat potàssic escàs, i absència de plagiòclasi, característica dels sistemes axials de la petrofacies dominantment siliciclàstica (Roigé, 2018). Finalment, la Fm. Campodarbe registra aports alhora dels massissos bascs i del Pirineu oriental durant el Rupelià, i dels Massissos Bascs i la conca turbidítica eocena durant el Chatià.

En aquest context, la integració de la petrografia amb les dades d'U-Pb es absolutament necessària per comprendre la monotonia de les senyals geocronològiques registrades. La presència de feldspat potàssic, plagiòclasi fresca i fragments plutònics en els sediments derivats dels massissos bascs podria derivar o bé de l'erosió de granits variscs, o de gneissos ordovicians, o bé dels gresos del Carbonífer en fàcies Culm, que també són rics en aquests components. En el cas dels granits, es propagaria una forta senyal varisca d'U-Pb, mentre en el cas dels gneissos ordovicians, transmetrien una forta senyal d'U-Pb cambro-devoniana (Dennele et al., 2016), i més tenint en compte a l'elevada fertilitat en zircons en ambdues roques. Contràriament, la senyal que deriva de l'erosió dels massissos bascs és *Cadomian dominated*, que és la intrínseca del Carbonífer (Hart et al., 2016, Martínez et al., 2016). Per tant, les senyals de procedència d'U-Pb, indiquen la contribució del Carbonífer com a font dels feldspats, i ressalten la importància del reciclatge en front dels aports directes.

Finalment, la integració de les dades de petrografia, minerals pesants i U-Pb indica contribucions dels massissos bascs durant la sedimentació del sistema al·luvial de Luna (Miocè, conca de l'Ebre). La associació de minerals pesants enriquida en epidota, grossulària i estaurolita i les senyals d'U-Pb enriquides en varisc, diferents de les dels ventalls al·luvials de San Juan de la Peña i Peña Oroel (Roigé 2018), indiquen una àrea font diferent de la d'aquests. L'enriquiment en senyals varisques seria degut al reciclatge dels dipòsits sinorogènics previs (Fm. Campodarbe i turbidites del Grup d'Hecho).

En resum, en aquesta tesi es fa palesa la necessitat d'integrar diferents mètodes d'anàlisi de procedència per tal de desxifrar senyals ambigües, que dificulten la caracterització de l'evolució de les àrees font en contextos on no existeixen àrees font litològicament molt diferenciades.

7.3. Sintesi paleogeogràfica de la conca de Jaca

En aquest estudi de procedència que s'ha dut a terme en la conca molàssica de Jaca, la integració de les dades de minerals pesants, de geocronologia d'U-Pb i termocronologia d'(U-Th)/He en zircons detrítics, i la seva combinació amb dades de petrografia, ha permès definir els patrons de dispersió de sediments i les àrees font durant l'Eocè mig-Miocè.

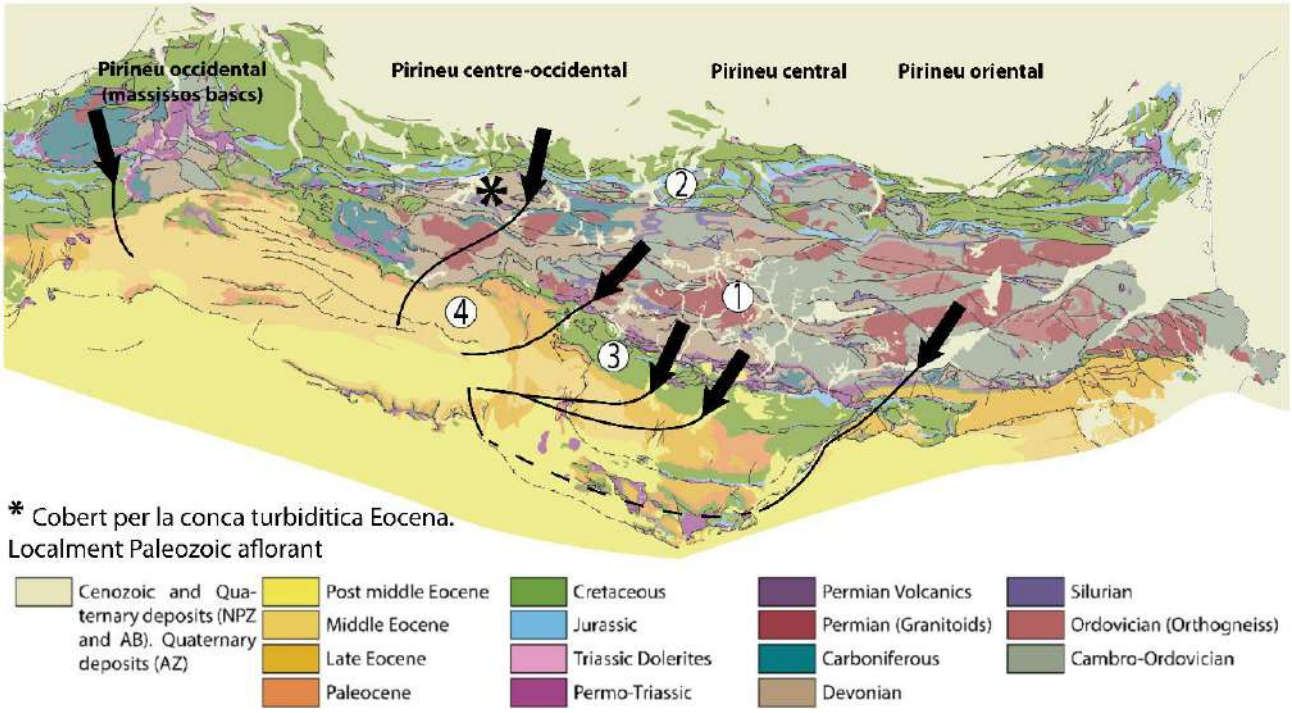

Figura 8.1. *Routing Systems durant el Bartonià baix (Formacions Ezkaba, canal turbidític del Rapitán, Belsué-Atarés oriental). 1: Zona Axial; 2: Zona Nordpirinenca; 3: Zona Sudpirinenca; 4: Conca Sudpirinenca.*

Les principals conclusions en relació a les rutes de dispersió de sediments en les diferents parts de la conca de Jaca són:

1) Conca de Jaca oriental:

- Durant el Lutecià mig, les associacions de minerals pesants, combinades amb la petrografia i les senyals d'U-Pb (Roigé et al., 2017; Roigé, 2018) confirmen que la sedimentació turbidítica

(Grup d'Hecho) era alimentada per un sistema de drenatge axial, procedent d'àrees font mesozoiques i paleozoiques situades a l'est de la conca, en la Zona Sudpirinenca i la Zona Axial.

- A l'inici del Bartonià, en els últims dipòsits turbidítics l'associació de minerals pesants (canal de Rapitán) registra l'erosió del basament metamòrfic del Paleozoic inferior de la Zona Axial septentrional, localment aflorant en el Pirineu centre-occidental, i de la Zona Nordpirinenca immediatament adjacent, en relació amb l'activitat dels encavalcaments de Lakora/Eaux-Chaudes i equivalents.

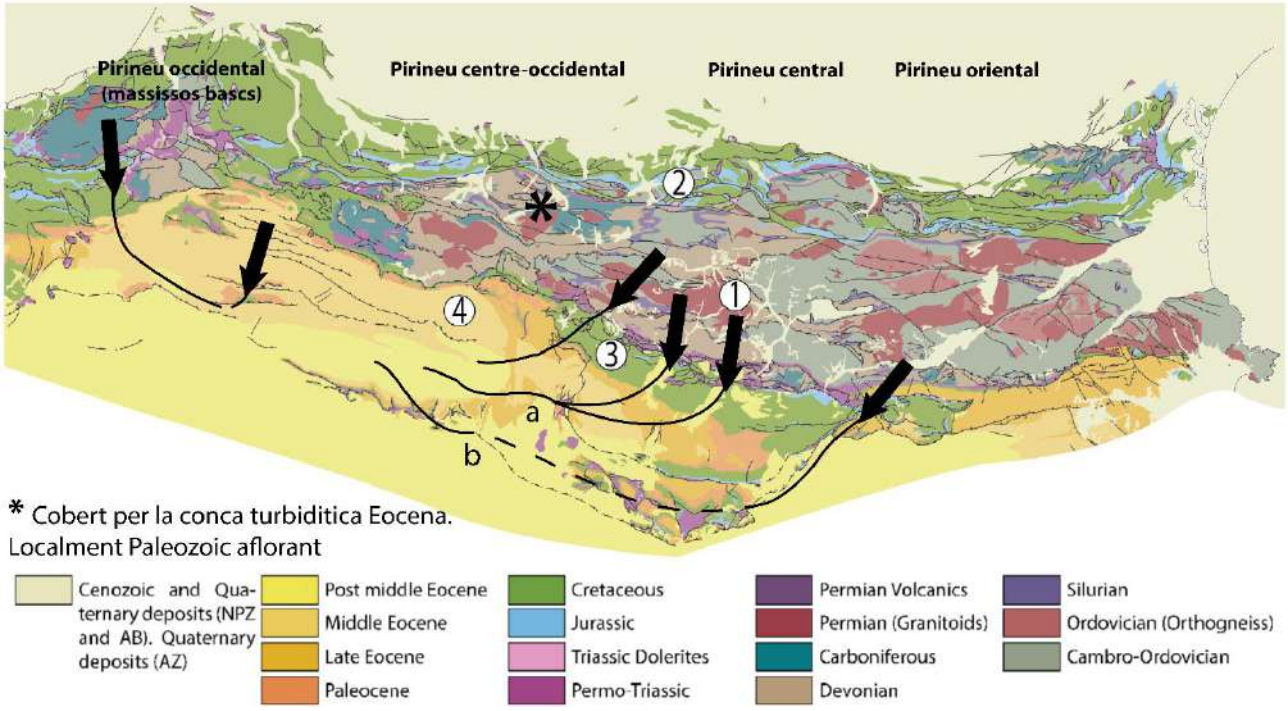

Figura 8.2. *Routing Systems durant el Priabonià (Formacions Liédena, turbidites de Yesa, Belsué-Atarés, i Campodarbe amb epidota -a- i sense epidota -b-). 1: Zona Axial; 2: Zona Nordpirinenca; 3: Zona Sudpirinenca; 4: Conca Sudpirinenca.*

- Els dipòsits deltaics de la formació Belsué-Atarés (Bartonià-Priabonià) són alimentats en el marge nord pel *fan delta* de Santa Orosia (sistema de drenatge transversal) i al sud pels sistemes fluvials axials persistents de la Formació Campodarbe (Bartonià-Chattià). En aquest darrer conjunt de drenatge axial, en funció dels minerals pesants s'individualitzen dos sistemes fluvials diferents, indiferenciables per altres mètodes. El primer sistema alimenta el sector més oriental de la conca de Jaca a través de la Fm. Escanilla, amb l'àrea font ubicada al Pirineu central (amb abundant epidota derivada dels diapirs triàssics). El segon sistema, estén la seva influencia cap a la part més occidental, seguint un *routing system* més meridional, a través de

la Fm. Salinar (Priabonià) i/o la Fm. Peraltilla inferior (Rupelià) del autòcton de la conca de l'Ebre, amb l'àrea font en el Pirineu oriental, en la zona del Pedraforca-Port del Compte i al nord de la mateixa, en l'actual vall del Segre (amb epidota absent).

- Els últims dipòsits de la conca de Jaca (Formació Campodarbe superior i Bernués), registren majoritàriament el reciclatge dels últims sistemes turbidítics de la conca eocena (unitats de Jaca mig-superior), amb contribucions de la Zona Nordpirinenca i localment de la Zona Axial del Pirineu centre-occidental.

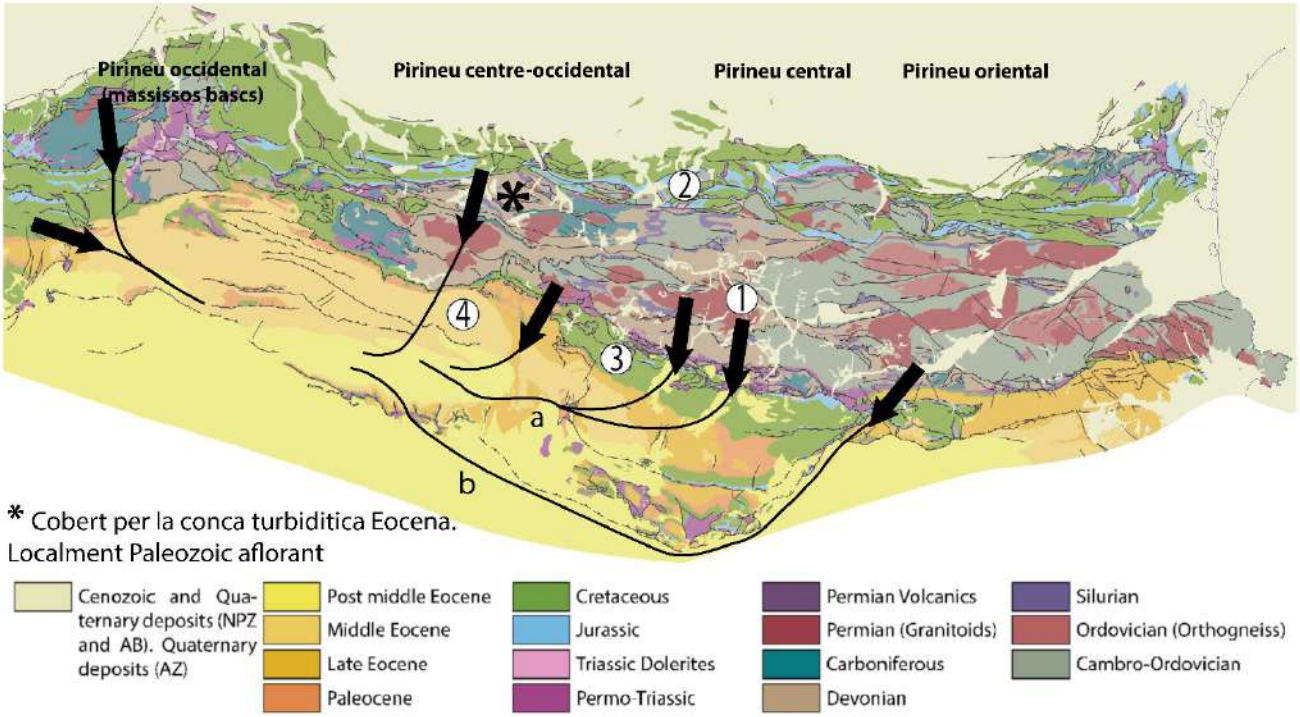

Figura 8.3. *Routing Systems durant el Rupelià (Formacions Campodarbe occidental i oriental -a- amb epidota i -b- sense epidota). 1: Zona Axial; 2: Zona Nordpirinenca; 3: Zona Sudpirinenca; 4: Conca Sudpirinenca.*

2) Conca de Jaca Occidental:

- En el Bartonià, el sistema turbidític d'Ezkaba constitueix el primer sistema alimentat per àrees font al nord, ubicades en els massissos bascs, i constituïdes per sediments carbonífers i contribucions la cobertora sedimentaria cretàcica.

- La sedimentació de la Formació Ardanatz continua governada per les àrees que alimentaven la Formació Ezkaba.

- Durant el Priabonià, les turbidites de Yesa mostren una competència entre les àrees font del Pirineu occidental (massissos bascs) i les del Pirineu centre-occidental (conca turbidítica eocena).

- Durant els últims estadis de sedimentació del Priabonià, la Formació Liédena registra una competència entre les àrees font del Pirineu occidental i el Pirineu oriental.

- La competència entre les àrees font del Pirineu occidental i oriental persisteix durant els primers estadis de la Formació Campodarbe (Rupelià) en el límit entre la Conca de Jaca occidental i oriental (àrea de Yesa). Per contra, en la part més occidental (Izaga), la Sierra d'Urbasa-Andía comença a actuar com a àrea font juntament amb els massissos bascs.

- Finalment, durant el Chatià-Aquitanià, en l'àrea de Yesa, la formació Campodarbe (Chatià) rep aports dels massissos bascs i del reciclatge de la conca turbidítica eocena, mentre que el sistema al·luvial d'Izaga (Aquitanià) es nodreix només de l'erosió de la Sierra d'Urbasa-Andía.

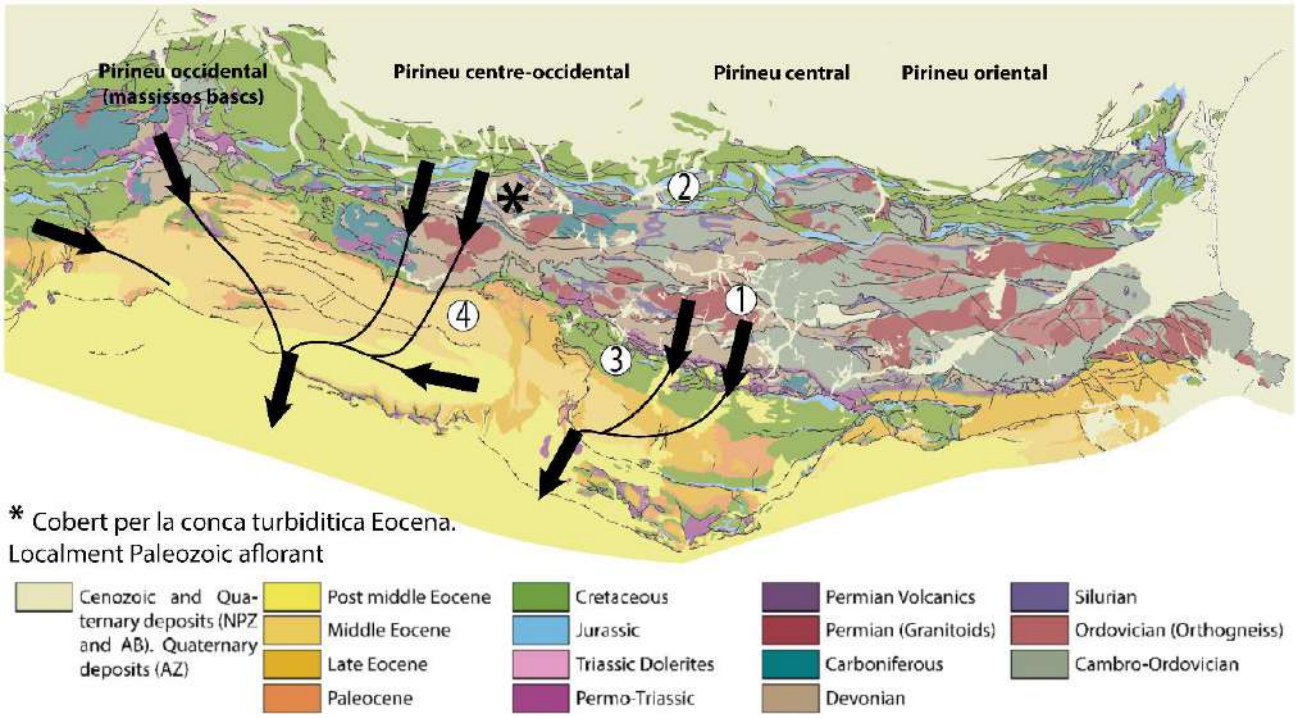

Figura 8.4. *Routing Systems durant Chatià-Aquitanià (ventalls de Luna i Huesca). 1: Zona Axial; 2: Zona Nordpirinenca; 3: Zona Sudpirinenca; 4: Conca Sudpirinenca.*

3) Conca de l'Ebre:

- Durant el Priabonià-Rupelià, els sistemes axials de la Formació Campodarbe s'alimenta de les mateixes àrees font que els dipòsits equivalents en l'àrea del riu Gállego, ubicades en el Pirineu oriental. Posterioment, els sistemes al·luvials transversals procedents del nord (Pirineu centre-occidental i conca turbidítica eocena) s'imposen en la conca de l'Ebre durant el Chatià.

- Per últim, en l'Aquitanià, el ventall al·luvial del Luna registra l'erosió dels dipòsits previs de la conca d'avantpaís (turbidites del Grup d'Hecho i Formació Campodarbe) i dels massissos bascs.

7.4. Intent preliminar d'aproximació predictiva de propagació de senyals d'U-Pb

En aquesta tesi s'ha fet evident que disposar d'un anàlisi petrogràfic quantitatiu i detallat permet assolir una comprensió profunda de la informació que es deriva d'altres indicadors de procedència com ara els minerals pesants, o la geocronologia i termocronologia de zircons detrítics. De particular interès es la propagació de senyals d'U-Pb, mètode àmpliament utilitzat en diferents estudis arreu del món en contextos geològics diversos, però que no solen integrar dades petrogràfiques.

El treball de (Roigé 2018) va posar de manifest que, contràriament a lo esperable, els ventalls al·luvials que es nodrien fonamentalment del reciclatge de les turbidites del Grup d'Hecho superior, es caracteritzen per una senyal *Cadomian dominated (*Roigé et al., 2018*)*. No obstant, en aquesta tesi s'ha interpretat com al resultat de l'erosió dels sistemes turbidítics de Jaca mig i superior, gràcies a la metodologia que es descriu a continuació.

A partir de la contribució de les diferents litologies a la fracció sorra (obtinguda a partir de comptatges en làmina prima), es pot inferir la contribució de formacions específiques (i.e. granits variscs, formacions metamòrfiques cambro-devonianes...), caracteritzades per senyals d'U-Pb específiques (Whitchurch et al., 2011; Filledeau et al., 2012; Martínez et al., 2015; Dennele et al., 2016; Hart et al., 2016; Margalef et al., 2016; Thompson et al., 2016, 2020; Odlum et al., 2019), Si a més, es considera també la fertilitat de zircons d'aquestes litologies, basat en l'aproximació qualitativa de Thompson et al. (2017), es pot fer una modelització que permet predir les senyals d'U-Pb.

En l'exemple que es descriu a continuació, s'agafa de referència la mostra GAL-10, la qual pertany a la petrofacies *hybrid clast-dominated* i és indicativa del reciclatge de les turbidites del Grup d'Hecho (Roigé, 2018). A partir de les dades quantitatives dels diferents tipus de grans (Roigé, 2018) es pot determinar la contribució de cada litologia (formació) expressada en percentatge respecte al total del comptatge i normalitzada en base als grans considerats (% de contribució).

- Els feldspats i fragments plutònics es poden relacionar amb els granits variscs, caracteritzats per una senyal d'U-Pb completament varisca. S'otorga coeficient de fertilitat màxim (1). Contribució 2,21%.

- Els fragments de roca metamòrfics es poden relacionar amb les formacions Cambro-Devonianes, caracteritzades per una forta component cadomiana i l'absència d'edats varisques. S'otorga coeficient de fertilitat moderat (0,75). Contribució 7,18%.

- Els fragments de roques sedimentaries siliciclàstiques es poder relacionar amb aports del Carbonífer, Permià i Triàssic, caracteritzades per una forta senyal cadomiana i una escassa component varisca. S'otorga coeficient de fertilitat moderat-alt (0,85). Contribució 14,36%.

- Els grans carbonatics extraconcals es poden relacionar amb la cobertora cretàcica, la qual pot mostrar des de senyals *Variscan dominated* a senyals *Cadomian dominated*. S'otorga coeficient de fertilitat baix (0,25). Contribució 30,39%.

- Els fragments de gresos híbrids, es poden relacionen amb l'erosió de les turbidites del Grup d'Hecho. S'otorga coeficient de fertilitat (0,65). Contribució 45,86 %.

Amb l'objectiu de valorar la capacitat de les contribucions cretàciques d'emmascarar la forta component varisca que derivaria de l'erosió de les turbidites del Grup d'Hecho superior, s'ha assumit una senyal *Cadomian dominated* per al Cretaci, mentre que per a les turbidites del Grup d'Hecho s'han considerat 3 hipòtesis:

- 1ª hipòtesi: Erosió de tots els sistemes turbiditícs superiors del Grup d'Hecho en conjunt. S'assumeix que es caracteritzen per una senyal *mixed Cadomian-Variscan*.

- 2ª hipòtesi: Erosió dels sistemes turbiditics de Banastón i Jaca inferior. S'assumeix que es caracteritzen per una senyal *Variscan dominated*.

- 3ª hipòtesi: Erosió dels sistemes turbiditícs de Jaca mig-superior. S'assumeix que es caracteritzen per senyal *Cadomian dominated*.

Els percentatges dels diferents components d'U-Pb de cada grup litològic (gresos híbrids, fragments carbonàtics extraconcals, fragments metamòrfics, fragments de gresos siliciclàstics, feldspats, fragments plutònics) es multiplica per la seva contribució a la fracció sorra (el tant per cent normalitzat en base als grans considerats), i per un coeficient de fertilitat associat a cada litologia (CF). D'aquesta manera, s'obté la contribució real de les senyals d'U-Pb ponderada d'acord amb la fertilitat de les litologies i la seva contribució. Finalment es sumen els aports ponderats de cada grup litològic a cada component d'U-Pb i el resultat es normalitza sobre 100 per a obtenir la predicció.
El model 1 (figura 7.8), mostra que l'erosió de totes les turbidites superiors del Grup d'Hecho, propagaria una senyal *mixed Cadomian-Variscan*.

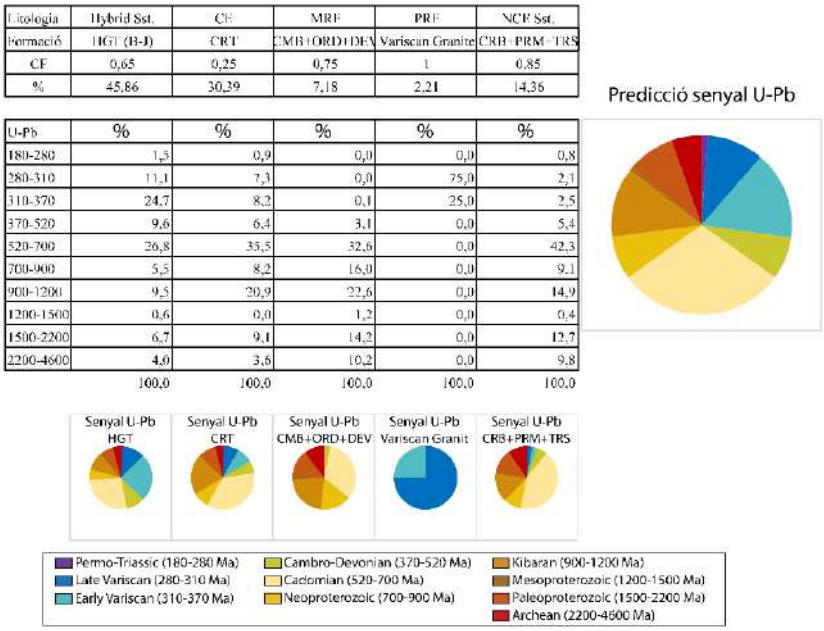

Figura 7.8. *Model 1. HGT (B-J): sistemes turbidítics de Banastón i Jaca; CRT: Cretaci; CMB: Cambrià; ORD: Ordovicià; DEV: Devonià, PRF: fragments plutònics; Fk: Feldspat potàssic; CRB: Carbonífer; PRM: Permià; TRS: Triàsic; CF: coeficient de fertilitat.*

El model 2 (figura 7.9), mostra que l'erosió dels sistemes de Banastón i Jaca inferior, propagaria també una senyal *mixed Cadomian-Variscan,* més rica en la component varísca.

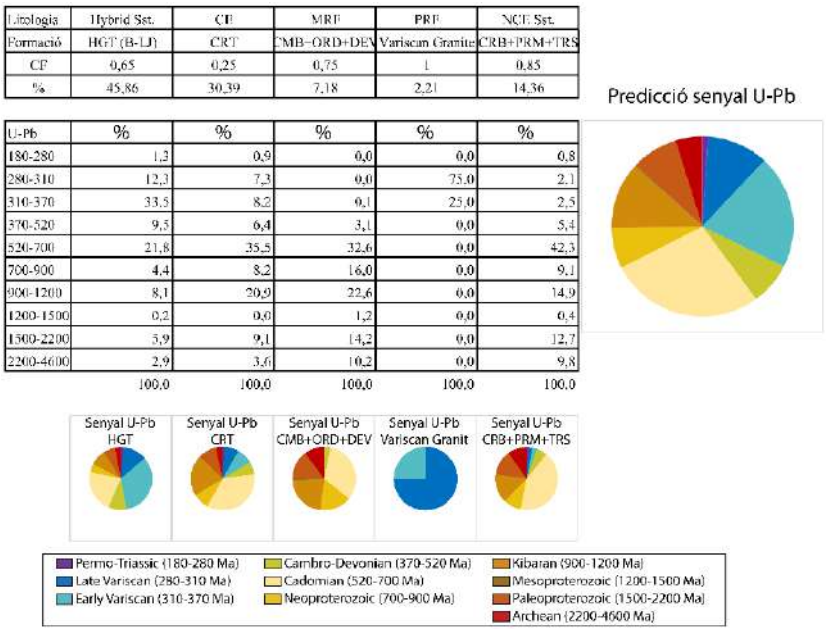

Figura 7.9. *Model 2. HGT (B-LJ): sistemes turbidítics de Banastón i Jaca inferior; CRT: Cretaci; CMB: Cambrià; ORD: Ordovicià; DEV: Devonià, PRF: fragments plutònics; Fk: Feldspat potàssic; CRB: Carbonífer; PRM: Permià; TRS: Triàsic; CF: coeficient de fertilitat.*

El model 3 (figura 7.10), mostra que l'erosió dels sistemes de Jaca mig-superior, propagaria una senayal *Cadomian dominated*.

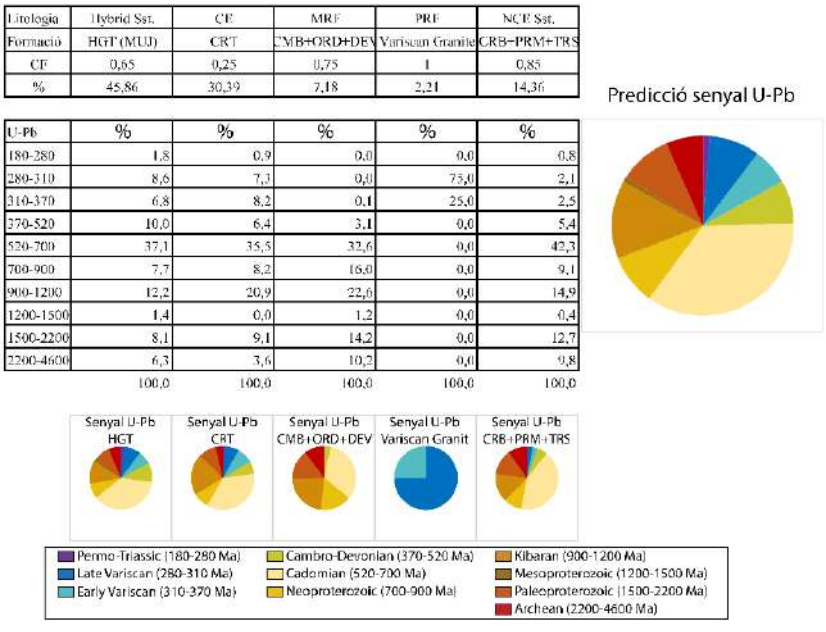

Figura 7.10. *Model 3. HGT (MUJ): sistemes turbidítics de Jaca mig i superior; CRT: Cretaci; CMB: Cambrià; ORD: Ordovicià; DEV: Devonià, PRF: fragments plutònics; Fk: Feldspat potàssic; CRB: Carbonífer; PRM: Permià; TRS: Triàsic; CF: coeficient de fertilitat.*

Si es comparen les 3 prediccions i les senyals d'U-Pb mesurades en la mostra GAL-10, s'observa que la única hipòtesi que transmet una senyal *Cadomian dominated* és la del model 3, en la que s'ha considerat només l'erosió dels sistemes turbídits de Jaca mig i superior (caracteritzats per la senyal d'U-Pb *Cadomian dominated*). Puc deduir doncs que, integrant dades quantitatives de petrografia i components d'U-Pb, fonamentalment només s'erosionaven els sistemes turbídits de Jaca mig i superior.

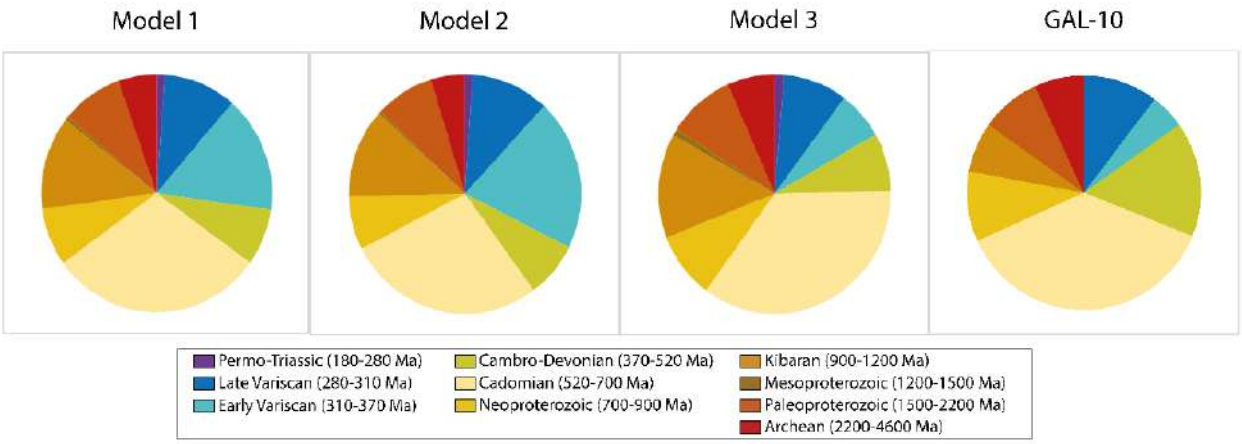

Figura 7.11. *Comparació entre la predicció dels 3 models i els resultats d'U-Pb en la mostra GAL-10*

Aquesta modelització il·lustra la necessitat d'unir la petrografia amb les senyals de procedència d'U-Pb per avaluar més detalladament el rol del reciclatge i dels aports directes, així com la importància de conèixer les senyals d'U-Pb que es puguin derivar de l'àrea font, sigui aquesta cristal·lina o sedimentària.

Capítol 8

Conclusions

La integració de diverses tècniques d'estudi de procedència sedimentària, com són l'anàlisi petrològic, l'anàlisi de minerals pesants, i l'estudi geocronològic d'U-Pb i termocronològic d'(U-Th)/He en zircons detrítics, juntament amb les observacions pròpies del treball de camp, han permès definir les característiques composicionals i l'evolució de les àrees font i patrons de dispersió dels sistemes sedimentaris de la conca de Jaca des de l'Eocè mig fins al Miocè inferior. Aquesta tesi proposa la integració d'aquests diferents mètodes com la via més idònia per realitzar apropiadament un anàlisi de procedència sedimentària.

El cas de la conca de Jaca, ha demostrat que enfoc multimètode d'aquest tipus esdevé indispensable quan es tracta de desxifrar senyals de procedència ambigües que dificulten la caracterització de l'evolució de les àrees font. Aquesta problemàtica és particularment palesa a la conca d'avantpaís Sudpirinenca, on les litologies susceptibles de constituir àrea font són molt similars en tot el domini Pirinenc, i on els processos de reciclatge són importants. Aquest estudi ha mostrat que les interpretacions que només es basen en un sol mètode presenten un risc elevat d'esdevenir incompletes, conduint a reconstruccions paleogeogràfiques poc acurades o directament errònies.

The integration of several sediment provenance methods, such as petrologic analysis, heavy mineral suites, and detrital zircon U-Pb geochronology and (U-Th)/He thermochronology, together with field observations, allows to define the compositional features and the evolution of source areas and routing systems of the middle Eocene-Miocene deposits of the Jaca basin. This thesis proposes the integration of these methods as the most appropriate way to properly perform sediment provenance analysis.

The Jaca basin case-study has shown that a mulimethod approach of this kind becomes necessary in order to decipher ambiguous provenance signatures, which difficult the characterization of the evolution of source areas. This issue is particularly conspicuous in the South Pyrenean foreland basin, where the lithologies that are prone to constitute source areas are very similar in all the Pyrenean realm, and where sediment recycling processes play an important role. This study has revealed that interpretations solely based on a single method have a high risk of becoming incomplete, leading to non-accurate or misleading paleogeographic reconstructions.

Referències

Allen, P. A. (2009). *Earth surface processes*. John Wiley & Sons.

Allen, P. A., & Allen, J. R. (2013). *Basin analysis: Principles and application to petroleum play assessment*. John Wiley & Sons.

Andò, S. (2020). Gravimetric separation of heavy minerals in sediments and rocks. Minerals, 10(3), 273.

Andò, S., Aharonovich, S., Hahn, A., George, S. C., Clift, P. D., & Garzanti, E. (2020). Integrating heavy-mineral, geochemical and biomarker analyses of Plio-Pleistocene sandy and silty turbidites: a novel approach for provenance studies (Indus Fan, IODP Expedition 355). *Geological Magazine*, 157(6), 929-938.

Andò, S., & Garzanti, E. (2014). Raman spectroscopy in heavy-mineral studies. *Geological Society, London, Special Publications*, 386(1), 395-412.

Andò, S., Morton, A., & Garzanti, E. (2014). Metamorphic grade of source rocks revealed by chemical fingerprints of detrital amphibole and garnet. *Geological Society, London, Special Publications*, 386(1), 351-371.

Astibia, H., Elorza, J., Pisera, A., Alvarez-Pérez, G., Payros, A., & Ortiz, S. (2014). Sponges and corals from the Middle Eocene (Bartonian) marly formations of the Pamplona Basin (Navarre, Western Pyrenees): taphonomy, taxonomy, and paleoenvironments. *Facies*, 60(1), 91-110.

Astibia, H., Payros, A., Suberbiola, X. P., Elorza, J., Berreteaga, A., Etxebarria, N., Badiola, A., & Tosquella, J. (2005). Sedimentology and taphonomy of sirenian remains from the Middle Eocene of the Pamplona Basin (Navarre, western Pyrenees). *Facies*, 50(3), 463-475.

Babault, J., van den Driessche, J., & Teixell, A. (2011, April). Retro-to pro-side migration of the main drainage divide in the Pyrenees: geologic and geomorphological evidence. In *European Gosciences Union General Assembly 2011* (Vol. 13, pp. EGU2011-12567).

Barsó, D. (2007). *Análisis de la procedencia de los conglomerados sinorogénicos de la pobla de segur (lérida) y su relación con la evolución¿ tectónica de los pirineos centro-meridionales durante el eoceno medio-oligoceno* (Doctoral dissertation, Universitat de Barcelona).

Bentham, P. A., Burbank, D. W., & Puigdefabregas, C. A. I. (1992). Temporal and spatial controls on the alluvial architecture of an axial drainage system: late Eocene Escanilla Formation, southern Pyrenean foreland basin, Spain. *Basin Research*, 4(3-4), 335-352.

Barnolas, A., & Teixell, A. (1994). Platform sedimentation and collapse in a carbonate-dominated margin of a foreland basin (Jaca basin, Eocene, southern Pyrenees). *Geology*, 22(12), 1107-1110.

Bosch, G. V., Teixell, A., Jolivet, M., Labaume, P., Stockli, D., Domènech, M., & Monié, P. (2016). Timing of Eocene–Miocene thrust activity in the Western Axial Zone and Chaînons Béarnais (west-central Pyrenees) revealed by multi-method thermochronology. *Comptes Rendus Geoscience*, 348(3-4), 246-256.

Boya, S. (2018). *El sistema deltaico de la Arenisca de Sabiñánigo y la continentalización de la cuenca de Jaca* (Doctoral dissertation, Universitat Autònoma de Barcelona).

Caja, M. A., Marfil, R., Garcia, D., Remacha, E., Morad, S., Mansurbeg, H., Amorosi, A., Martínez-Calvo, C. & Lahoz-Beltrá, R. (2010). Provenance of siliciclastic and hybrid turbiditic arenites of the Eocene Hecho Group, Spanish Pyrenees: implications for the tectonic evolution of a foreland basin. *Basin Research*, 22(2), 157-180.

Cámara, P., & Klimowitz, J. (1985). Interpretación geodinámica de la vertiente centro-occidental surpirenaica (Cuencas de Jaca-Tremp). *Estudios geológicos*, 41(5-6), 391-404.

Caracciolo, L. (2020). Sediment generation and sediment routing systems from a quantitative provenance analysis perspective: Review, application and future development. *Earth-Science Reviews*, 209, 103226.

Castelltort, S., & Van Den Driessche, J. (2003). How plausible are high-frequency sediment supply-driven cycles in the stratigraphic record?. *Sedimentary geology*, 157(1-2), 3-13.

Cerveny, P. F., & Johnson, N. M. (1989). Tectonic and geomorphic implications of Siwalik Group. *Tectonics of the Western Himalayas*, 232, 129.

Costa, E., Garces, M., López-Blanco, M., Beamud, E., Gómez-Paccard, M., & Larrasoaña, J. C. (2010). Closing and continentalization of the South Pyrenean foreland basin (NE Spain): magnetochronological constraints. *Basin Research*, 22(6), 904-917.

Crognier, N. (2016). *Evolution thermique, circulation de fluide et fracturation associées à la structuration du bassin d'avant-pays sud-pyrénéen* (Doctoral dissertation, Pau).

Davis, D. W., & Lin, S. (2003). Unraveling the geologic history of the Hemlo Archean gold deposit, Superior Province, Canada: A U-Pb geochronological study. *Economic Geology*, 98(1), 51-67.

Denele, Y., Barbey, P., Deloule, E., Pelleter, E., Olivier, P., & Gleizes, G. (2009). Middle Ordovician U-Pb age of the Aston and Hospitalet orthogneissic laccoliths: their role in the Variscan evolution of the Pyrenees. *Bulletin de la Société géologique de France*, 180(3), 209-216.

Dickinson, W. R. (1970). Interpreting detrital modes of graywacke and arkose. *Journal of Sedimentary Research*, 40(2), 695-707.

Dickinson, W. R. (1985). Interpreting provenance relations from detrital modes of sandstones. In *Provenance of arenites* (pp. 333-361). Springer, Dordrecht.

Dickinson, W. R., & Suczek, C. A. (1979). Plate tectonics and sandstone compositions. *Aapg Bulletin*, 63(12), 2164-2182.

Dreyer, T., Corregidor, J., Arbues, P., & Puigdefabregas, C. (1999). Architecture of the tectonically influenced Sobrarbe deltaic complex in the Ainsa Basin, northern Spain. *Sedimentary Geology*, 127(3-4), 127-169.

Filleaudeau, P. Y., Mouthereau, F., & Pik, R. (2012). Thermo-tectonic evolution of the south-central Pyrenees from rifting to orogeny: Insights from detrital zircon U/Pb and (U-Th)/He thermochronometry. *Basin Research*, 24(4), 401-417.

Fitzgerald, P. G., Muñoz, J. A., Coney, P. J., & Baldwin, S. L. (1999). Asymmetric exhumation across the Pyrenean orogen: implications for the tectonic evolution of a collisional orogen. *Earth and Planetary Science Letters*, 173(3), 157-170.

Fontana, D., Zuffa, G. G., & Garzanti, E. (1989). The interaction of eustacy and tectonism from provenance studies of the Eocene Hecho Group Turbidite Complex (South-Central Pyrenees, Spain). *Basin Research*, 2(4), 223-237.

Garcés, M., Lopez-Blanco, M., Valero, L., Beamud, E., Muñoz, J. A., Oliva-Urcia, B., Vinyoles, A., Arbues, P., Cabello, P. & Cabrera, L. (2020). Paleogeographic and sedimentary evolution of the South Pyrenean foreland basin. *Marine and Petroleum Geology*, 113, 104105.

Garzanti, E., Ando, S., & Vezzoli, G. (2006). The continental crust as a source of sand (Southern Alps cross section, northern Italy). *The Journal of Geology*, 114(5), 533-554.

Garzanti, E., Doglioni, C., Vezzoli, G., & Ando, S. (2007). Orogenic belts and orogenic sediment provenance. *The Journal of Geology*, 115(3), 315-334.

Garzanti, E., Limonta, M., Resentini, A., Bandopadhyay, P. C., Najman, Y., Andò, S., & Vezzoli, G. (2013). Sediment recycling at convergent plate margins (Indo-Burman ranges and Andaman–Nicobar Ridge). *Earth-Science Reviews*, 123, 113-132.

Garzanti, E., Padoan, M., Andò, S., Resentini, A., Vezzoli, G., & Lustrino, M. (2013). Weathering and relative durability of detrital minerals in equatorial climate: sand petrology and geochemistry in the East African Rift. *The Journal of Geology*, 121(6), 547-580.

Garzanti, E., Resentini, A., Vezzoli, G., Andò, S., Malusà, M., & Padoan, M. (2012). Forward compositional modelling of Alpine orogenic sediments. *Sedimentary Geology*, 280, 149-164.

Garzanti, E., Vezzoli, G., Lombardo, B., Ando, S., Mauri, E., Monguzzi, S., & Russo, M. (2004). Collision-orogen provenance (western Alps): Detrital signatures and unroofing trends. *The Journal of Geology*, 112(2), 145-164.

Gómez-Gras, D., Roigé, M., Fondevilla, V., Oms, O., Boya, S., & Remacha, E. (2016). Provenance constraints on the Tremp Formation paleogeography (southern Pyrenees): Ebro Massif vs Pyrenees sources. *Cretaceous Research*, 57, 414-427.

Greenacre, M. J. (1984). *Theory and applications of correspondence analysis*. London, Academic Press.

Götze, J. (1998). Geochemistry and provenance of the Altendorf feldspathic sandstone in the Middle Bunter of the Thuringian basin (Germany). *Chemical geology*, 150(1-2), 43-61.

Gupta, K. D., & Pickering, K. T. (2008). Petrography and temporal changes in petrofacies of deep-marine Ainsa–Jaca basin sandstone systems, Early and Middle Eocene, Spanish Pyrenees. *Sedimentology*, 55(4), 1083-1114.

Hart, N. R., Stockli, D. F., & Hayman, N. W. (2016). Provenance evolution during progressive rifting and hyperextension using bedrock and detrital zircon U-Pb geochronology, Mauléon Basin, western Pyrenees. *Geosphere*, 12(4), 1166-1186.

Haughton, P. D. W., Todd, S. P., & Morton, A. C. (1991). Sedimentary provenance studies. *Geological Society, London, Special Publications*, 57(1), 1-11.

Hehuwat, F. H. A. (1970). *The Transition from Marine to Continental Sedimentation in the Eocene of the Guarga Synclinorium, Huesca Province, Spain* (Doctoral dissertation, Verlag nicht ermittelbar).

Hirst, J. P. P., & Nichols, G. J. (1986). Thrust tectonic controls on Miocene alluvial distribution patterns, southern Pyrenees. *Foreland basins*, 247-258.

Hubert, J. F. (1962). A zircon-tourmaline-rutile maturity index and the interdependence of the composition of heavy mineral assemblages with the gross composition and texture of sandstones. Journal of Sedimentary Research, 32(3), 440-450.

Ingersoll, R. V., Bullard, T. F., Ford, R. L., Grimm, J. P., Pickle, J. D. & Sares, S. W. (1984). The effect of grain size on detrital modes: a test of the Gazzi-Dickinson point-counting method. *Journal of Sedimentary Research*, 54(1), 103-116.

Jolivet, M., Labaume, P., Monié, P., Brunel, M., Arnaud, N., & Campani, M. (2007). Thermochronology constraints for the propagation sequence of the south Pyrenean basement thrust system (France-Spain). *Tectonics*, 26(5).

Kuebler, K. E., Jolliff, B. L., Wang, A., & Haskin, L. A. (2006). Extracting olivine (Fo–Fa) compositions from Raman spectral peak positions. *Geochimica et Cosmochimica Acta*, 70(24), 6201-6222.

Labaume, P., & Teixell, A. (2018). 3D structure of subsurface thrusts in the eastern Jaca Basin, southern Pyrenees. *Geologica Acta*, 477-498.

Labaume, P., Séguret, M., & Seyve, C. (1985). Evolution of a turbiditic foreland basin and analogy with an accretionary prism: Example of the Eocene south-Pyrenean basin. *Tectonics*, 4(7), 661-685.

Labaume, P., Meresse, F., Jolivet, M., Teixell, A., & Lahfid, A. (2016). Tectonothermal history of an exhumed thrust-sheet-top basin: An example from the south Pyrenean thrust belt. *Tectonics*, 35(5), 1280-1313.

Lagabrielle, Y., Labaume, P., & de Saint Blanquat, M. (2010). Mantle exhumation, crustal denudation, and gravity tectonics during Cretaceous rifting in the Pyrenean realm (SW Europe): Insights from the geological setting of the lherzolite bodies. *Tectonics*, 29(4).

Lihou, J. C., & Mange-Rajetzky, M. A. (1996). Provenance of the Sardona Flysch, eastern Swiss Alps: example of high-resolution heavy mineral analysis applied to an ultrastable assemblage. *Sedimentary Geology*, 105(3-4), 141-157.

Margalef, A., Castiñeiras, P., Casas, J.M., Navidad, M., Liesa, M., Linnemann, U., Hofmann, M., & Gärtner, A. (2016). Detrital zircons from the Ordovician rocks of the Pyrenees: Geochronological constraints and provenance. *Tectonophysics*, 681, 124-134.

Mange, M. A., & Maurer, H. (2012). *Heavy minerals in colour*. London, Chapman and Hall.

Martínez, F. J., Dietsch, C., Aleinikoff, J., Cirés, J., Arboleya, M. L., Reche, J., & Gómez-Gras, D. (2016). Provenance, age, and tectonic evolution of Variscan flysch, southeastern France and northeastern Spain, based on zircon geochronology. *Bulletin*, 128(5-6), 842-859.

Meresse, F. (2010). *Dynamique d'un prisme orogénique intracontinental: évolution thermochronologique (traces de fission sur apatite) et tectonique de la Zone Axiale et des piémonts des Pyrénées centro-occidentales* (Doctoral dissertation, Université de Montpellier 2).

Metcalf, J. R., Fitzgerald, P. G., Baldwin, S. L., & Muñoz, J. A. (2009). Thermochronology of a convergent orogen: Constraints on the timing of thrust faulting and subsequent exhumation of the Maladeta Pluton in the Central Pyrenean Axial Zone. *Earth and Planetary Science Letters*, 287(3-4), 488-503.

Michael, N. (2013). *Functioning of an ancient routing system, the Escanilla Formation, South Central Pyrenees* (Doctoral dissertation, Imperial College London).

Morton, A. C., & Hallsworth, C. R. (1999). Processes controlling the composition of heavy mineral assemblages in sandstones. *Sedimentary geology*, 124(1-4), 3-29.

Morton, A. C., & Hallsworth, C. (2007). Stability of detrital heavy minerals during burial diagenesis. *Developments in Sedimentology*, 58, 215-245.

Mouthereau, F., Filleaudeau, P. Y., Vacherat, A., Pik, R., Lacombe, O., Fellin, M. G., Castelltort, S., Christophoul, F. & Masini, E. (2014). Placing limits to shortening evolution in the Pyrenees: Role of margin architecture and implications for the Iberia/Europe convergence. *Tectonics*, 33(12), 2283-2314.

Muñoz, J. A., Mencos, J., Roca, E., Carrera, N., Gratacós, O., Ferrer, O., & Fernández, Ò. (2018). The structure of the South-Central-Pyrenean fold and thrust belt as constrained by subsurface data. *Geologica Acta*, 439-460.

Mutti, E. (1985). *Turbidite systems and their relations to depositional sequences. In Provenance of arenites* (pp. 65-93). Springer, Dordrecht.

Mutti, E., Luterbacher, H., Ferrer, J., & Rosell, J., 1972. Schema stratigrafico e lineamenti di facies del Paleogeno Marino della zona centrale sudpirenaica tra Tremp (Catalogna) e Pamplona (Navarra): *Memorie della Società Geologica Italiana*, 11, p. 391–416.

Nagtegaal, P. C., & Weerd, T. (1985). Provenance of Cambro-Ordovician to Oligocene sandstones in the Southern Pyrénées, Spain. *Geologie en mijnbouw*, 64(1), 25-40.

Nie, J., Horton, B. K., Saylor, J. E., Mora, A., Mange, M., Garzione, C. N., Basu, A., Moreno, C. J., Caballero, V. & Parra, M. (2012). Integrated provenance analysis of a convergent retroarc foreland system: U–Pb ages, heavy minerals, Nd isotopes, and sandstone compositions of the Middle Magdalena Valley basin, northern Andes, Colombia. *Earth-Science Reviews*, 110(1-4), 111-126.

Nijman, W., & Nio, S. D. (1976). *The Eocene Montañana Delta: Tremp-Graus Basin, Provinces of Lérida and Huesca, Southern Pyrenee, N. Spain*. Vakgroep Sedimentologie, Rijksuniveriteit Leiden-Utrecht.

Odlum, M. L., Stockli, D. F., Capaldi, T. N., Thomson, K. D., Clark, J., Puigdefàbregas, C., & Fildani, A. (2019). Tectonic and sediment provenance evolution of the South Eastern Pyrenean foreland basins during rift margin inversion and orogenic uplift. *Tectonophysics*, 765, 226-248.

Ortuño Candela, M., & Vilaplana, M. (2018). Active fault control in the distribution of Elevated Low Relief Topography in the Central-Western Pyrenees. *Geologica Acta, 2018*, 16(4), 499-518.

Paola, C., Heller, P. L., & Angevine, C. L. (1992). The large-scale dynamics of grain-size variation in alluvial basins, 1: Theory. *Basin research*, 4(2), 73-90.

Payros, A. (1997). *El Eoceno de la cuenca de Pamplona: estratigrafía, facies y evolución paleogeográfica*. PhD Thesis, Univ. del País Vasco, Bilbao.

Payros, A., Pujalte, V., Orue-Etxebarria, X., & Baceta, J. I. (1997). A Bartonian channel-levee turbiditic system in the Pamplona Basin: Tectonic and paleogeographic implications. *Geogaceta*, 22, 145-148.

Pouget, P. (1989). *Evolution geodynamique hercynienne des pyrenees centrales: contraintes structurales, metamorphiques, magmatiques et sedimentologiques* (Doctoral dissertation, Toulouse 3).

Puigdefábregas, C. (1975). La sedimentación molásica en la cuenca de Jaca. *Pirineos*, 104.

Puigdefàbregas, C., Muñoz, J. A., & Vergés, J. (1992). *Thrusting and foreland basin evolution in the southern Pyrenees*. In Thrust tectonics (pp. 247-254). Springer, Dordrecht.

Puigdefàbregas, C., & Souquet, P. (1986). Tecto-sedimentary cycles and depositional sequences of the Mesozoic and Tertiary from the Pyrenees. *Tectonophysics*, 129(1-4), 173-203.

Remacha, E., & Fernández, L. P. (2003). High-resolution correlation patterns in the turbidite systems of the Hecho Group (South-Central Pyrenees, Spain). *Marine and Petroleum Geology*, 20(6-8), 711-726.

Remacha, E., Fernández, L. P., & Maestro, E. (2005). The transition between sheet-like lobe and basin-plain turbidites in the Hecho Basin (South-Central Pyrenees, Spain). *Journal of Sedimentary Research*, 75(5), 798-819.

Roigé, M. (2018). *Procedència i evolució dels sistemes sedimentaris de la conca de Jaca (conca d'avantpaís Sudpirinenca): Interacció entre diverses àrees font en un context tectònic actiu* (Doctoral dissertation, Universitat Autònoma de Barcelona).

Roigé, M., Gómez-Gras, D., Remacha, E., Boya, S., Viaplana-Muzas, M., & Teixell, A. (2017). Recycling an uplifted early foreland basin fill: An example from the Jaca basin (Southern Pyrenees, Spain). *Sedimentary Geology*, 360, 1-21.

Roigé, M., Gómez-Gras, D., Remacha, E., Daza, R., & Boya, S. (2016). Tectonic control on sediment sources in the Jaca basin (Middle and Upper Eocene of the South-Central Pyrenees). *Comptes Rendus Geoscience*, 348(3-4), 236-245.

Roigé, M., Gómez-Gras, D., Stockli, D. F., Teixell, A., Boya, S., & Remacha, E. (2019). Detrital zircon U–Pb insights into the timing and provenance of the South Pyrenean Jaca basin. Journal of the Geological Society, 176(6), 1182-1190.

Rubio, V., Vigil, R., García, R., & González, J. A. (1996). Caracterización mineralógica de sedimentos arenosos en la cuenca del río Ara (Huesca). *Cuaternario y Geomorfología*, 33-44.

Soler-Sampere, M., & Puigdefàbregas, C. (1970). Líneas generales de la geología del Alto Aragón Occidental. *Pirineos*.

Tarriño, A. (2006). *El sílex en la cuenca vasco cantábrica y pirineo navarro: caracterización y su aprovechamiento en la prehistoria* (Doctoral dissertation, Universidad del País Vasco-Euskal Herriko Unibertsitatea).

Teixell, A., Labaume, P., Ayarza, P., Espurt, N., de Saint Blanquat, M., & Lagabrielle, Y. (2018). Crustal structure and evolution of the Pyrenean-Cantabrian belt: A review and new interpretations from recent concepts and data. *Tectonophysics*, 724, 146-170.

Thomson, K. D., Stockli, D. F., Clark, J. D., Puigdefàbregas, C., & Fildani, A. (2017). Detrital zircon (U-Th)/(He-Pb) double-dating constraints on provenance and foreland basin evolution of the Ainsa Basin, south-central Pyrenees, Spain. *Tectonics*, 36(7), 1352-1375.

Thomson, K. D., Stockli, D. F., Odlum, M. L., Tolentino, P., Puigdefàbregas, C., Clark, J., & Fildani, A. (2020). Sediment provenance and routing evolution in the Late Cretaceous–Eocene Ager Basin, south-central Pyrenees, Spain. *Basin Research*, 32(3), 485-504.

Tofelde, S., Bernhardt, A., Guerit, L., & Romans, B. W. (2021). Times associated with source-to-sink propagation of environmental signals during landscape transience. *Frontiers in Earth Science*, 9, 227.

Uddin, A., Kumar, P., Sarma, J. N., & Akhter, S. H. (2007). Heavy mineral constraints on the provenance of Cenozoic sediments from the foreland basins of Assam and Bangladesh: erosional history of the eastern Himalayas and the Indo-Burman Ranges. *Developments in Sedimentology*, 58, 823-847.

Ullastre, J. U. A. N., Masriera, A., & de Geología Ibérica, C. (1982). Hipótesis y problemas acerca del origen de las asociaciones de minerales pesados del Senoniense del Pirineo Catalán. *Cuadernos de Geología Ibérica*, 8, 949-964.

Vacherat, A., Mouthereau, F., Pik, R., Huyghe, D., Paquette, J.L., Christophoul, F., Loget, N. & Tibari, B. (2017). Rift-to-collision sediment routing in the Pyrenees: A synthesis from sedimentological, geochronological and kinematic constraints. *Earth-Science Reviews*, 172, 43-74.

Valloni, R., Marchi, M., & Mutti, E. (1984). Studio conoscitivo della moda detritica delle torbiditi eoceniche del Gruppo di Echo (Spagna). *Giornale di Geologia*, 46(1), 45-56.

Vergés, J., Fernàndez, M., & Martìnez, A. (2002). The Pyrenean orogen: pre-, syn-, and post-collisional evolution. *Journal of the Virtual Explorer*, 8, 55-74.

Vermeesch, P. (2018). Statistical models for point-counting data. *Earth and Planetary Science Letters*, 501, 112-118.

Vincent, S. J. (2001). The Sis palaeovalley: a record of proximal fluvial sedimentation and drainage basin development in response to Pyrenean mountain building. *Sedimentology*, 48(6), 1235-1276.

Vinyoles, A., López-Blanco, M., Garcés, M., Arbués, P., Valero, L., Beamud, E., Oliva-Urcia, B., & Cabello, P. (2021). 10 Myr evolution of sedimentation rates in a deep marine to non-marine foreland basin system: Tectonic and sedimentary controls (Eocene, Tremp–Jaca Basin, Southern Pyrenees, NE Spain). Basin Research, 33(1), 447-477.

von Eynatten, H., & Gaupp, R. (1999). Provenance of Cretaceous synorogenic sandstones in the Eastern Alps: constraints from framework petrography, heavy mineral analysis and mineral chemistry. *Sedimentary Geology*, 124(1-4), 81-111.

Walderhaug, O., & Porten, K. W. (2007). Stability of detrital heavy minerals on the Norwegian continental shelf as a function of depth and temperature. *Journal of Sedimentary Research*, 77(12), 992-1002.

Wang, A., Kuebler, K. E., Jolliff, B. L., & Haskin, L. A. (2004). Raman spectroscopy of Fe-Ti-Cr-oxides, case study: Martian meteorite EETA79001. *American Mineralogist*, 89(5-6), 665-680.

Weltje, G. J., & von Eynatten, H. (2004). Quantitative provenance analysis of sediments: review and outlook. *Sedimentary Geology*, 171(1-4), 1-11.

Whitchurch, A. L., Carter, A., Sinclair, H. D., Duller, R. A., Whittaker, A. C., & Allen, P. A. (2011). Sediment routing system evolution within a diachronously uplifting orogen: Insights from detrital zircon thermochronological analyses from the South-Central Pyrenees. *American Journal of Science*, 311(5), 442-482.

Zuffa, G. G. (1980). Hybrid arenites; their composition and classification. *Journal of Sedimentary Research*, 50(1), 21-29.

Agraïments

El 2003 vaig venir cap a la universitat, amb tan sols 17 anys, i sincerament, no se ben bé a que vaig venir a fer... suposo que tenia ganes de veure món i viure experiències noves. En aquell moment, per mi la geologia era poc més que un documental de *National Geographic*, però tot i així, em sentia captivat per aquelles indrets i explicacions, per la passió que mostrava aquella gent pel nostre planeta, i tot i que no tenia moltes ganes d'estudiar, tenia clar que volia saber més sobre aquesta disciplina tant fascinant.

19 anys més tard (si, 19, he passat més anys de la meva vida com a estudiant universitari que com a altra cosa. Quan ho penso...) per fi he arribat al final d'aquest camí. Crec que els meus pares i el meu germà encara no s'ho creuen... Podria haver enfocat la meva vida d'una altra manera, podria haver fet mil coses diferents, però la veritat, no em penedeixo en absolut d'haver arribat fins aquí, encara que m'hagi costat el meu temps... Al final, estic plenament satisfet de l'experiència viscuda i el poc coneixement que he aconseguit aprendre i retenir.

Sempre m'ha agradat anar a la muntanya, però durant els últims anys, he vist com la meva visió del paisatge canviava, com tot el que observava cobrava un sentit més profund. Quan hi porto els amics em miren amb cara de "*i ara que li passa amb aquest? S'ha fotut un got de vi més? Però si només és una pedra de color verd*", i assenteixen amb el cap quan intento transmetre'ls alguna cosa del que he après al llarg de tots aquests anys. Per sort sembla que si que els transmeto alguna cosa, doncs al final sempre em diuen "*buenu, i a la pròxima a on anem*?"

Tot això és gràcies als meus directors de tesi David, Marta i Toni, als qui vull mostrar el meu agraïment en primer lloc. La seva passió per la geologia, per la ciència ben feta, i les ganes de passar-ho bé mentre fem tot això ha calat dins meu. No aconseguiré mai trobar paraules suficients per expressar aquesta gratitud, i si ho aconseguís, probablement la explicació sonaria enrevessada i l'hauríem d'editar per a fer-la comprensible. Vull remarcar que en tots aquest anys, tret d'alguns moments de discussió científica acalorada basada a vegades en obsessions meves, sempre he tingut les vostres portes obertes per a qualsevol cosa. Mai hi ha hagut una mala mirada, una bronca, un menyspreu, res dolent. Crec que es important remarca-ho perquè no tothom té aquesta sort, i estic agraït que per sobre de tot, sou persones.

Però anem a vere David... encara recordo quan em vas trucar l'últim any de carrera per aplicar a una beca per desenvolupar un protocol de separació mineral a la UAB. Vaig acceptar content, però en l'instant que vaig penjar em vaig "acollonir". Minerals pesants? Què és això? No eren metalls pesants? Però si amb prou feines ser reconèixer un feldspat... Com m'ho faré per fer un TFG sobre això? Gràcies per pensar en mi i per haver-me acompanyat tots aquests anys, per tota la confiança i per creure en mi

inclòs després de perdre la llibreta de camp a Sos del Rey Católico en el primer dia de camp. Els teus ànims i reconeixents, sense que te'ls hagi demanat mai, la veritat és que han sigut molt importants per arribar fins aquí. Tot i que has sigut el meu director, el meu cap, mai he tingut aquesta sensació... sempre t'he vist com un amic. Gràcies.

A tu Marta, la patrona, gràcies per tota l'ajuda i simpatia. Deus haver acabat fins als... de les meves preguntes insistents basades en les meves obsessions geològiques. Però ha sigut un plaer treballar amb tu, i també amb l'Alís aquests últims mesos. Gràcies també per obrir-me les portes de casa teva i per tots els bons moments. Lamento que aquells conglomerats fossin tant avorrits, només amb turbidites, sense quarsites de colors, ni Bunts, res exòtic... i jo obsessionat amb la epidota. Has sigut un exemple a seguir per mi.

A tu Toni també gràcies per tot el suport i ajuda. És un gust treballar amb un pou de coneixement del Pirineu com tu, i veure la passió que poses en la teva feina. La veritat és que sembla que parlem penso: ara em preguntarà algo i s'adonarà que en el fons no se res... Per alguna raó geològica imposes aquest respecte, però per sobre de tot ets una gran persona amb la que dona gust treballar e intentar absorbir una mica del teu coneixement. Gràcies.

Vull agrair també a tots els membres del departament de Geologia, que m'han acompanyat i m'han fet sentir més que còmoda durant tot aquest temps. En especial a les secres per la simpatia i rapidesa amb el que he gestionat sempre qualsevol mal de cap. També als Laborans, Lluís, Marc i Pepi, que em vau obrir les portes de laboratori per entrar i m'heu fet sentir com a casa cada vegada que anava per allà. Gràcies també per la vostra inestimable feina.

Menció molt especial al Narcís Mestres. Ara mateix son les 0:30 del dia en que diposito la tesi i estic segur que encara et preguntes si tot això portarà algun lloc. Al final sembla que si que ho hem aconseguit. Amb tu m'ho he passat molt bé, millor que amb el Raman, al qual també li he agafat una petita estima i tot. Sort en vam tenir del Tomaso aquell cop que vaig descalibrar el Raman i ell, l'espectrometre, es negava a tornar a funcionar perquè segurament ja estava cansat de veurem per allà, amb aquelles jornades de 9 a 7. El dia que vas marxar a casa i et vas oblidar de mi també vaig riure bastant. Gràcies per tot Narcís.

I would like to extent my gratitude to Danny Stockli, Lisa, Rudra, Dani (the mexican), Dani (the texan) for the good times in Austin despite the covid thinig... I am specially grateful to Rudra, for all the suport.

Hablando de Texas, Gracias Nacho por alquilar-me tu apartamento en Austin.

A tots els predocs presents i als que ho éreu quan jo vaig començar, i que m'heu acompanyat durant aquesta etapa (Dr. Ruiz, Dra. Burrel, Guillem, Norbert, Gerard, Sabí, Carla, Maria, Anna, Gisela). Em pregunto qui serà el següent i si ja està notant la pressió jeje. També gràcies als que heu tornat al Departament, Isac i Miquel, gràcies pel vostre suport i ànims.

Gràcies especials a tu Salva també que has sigut com un psedodirector. I pensar que vam entrar a la uni al mateix any... El teu suport també ha sigut clau en aquesta etapa de la meva vida. Però et diré que segueixo sent fan dels agressive colors.

A tots els meus amics, que m'han donat suport durant aquest temps Marc, Camila i Mireia. Gràcies especials als amics de tota la vida que vaig oblidar durant tots aquests anys. Gràcies per rebrem com si no hagués marxat mai i acompanyar-me en l'etapa final del doctorat covid-free, Ian Patrick, Rul Romeu, Pepe la Rosa, Arenow, i als nous que he fet al reconectar amb vosaltres, Jú (la de los ciclos), Evelyn Patrick, Arantza, la Lí, Carles, el Monestir del Tallat, i a la resta que sempre estem fent un vichy pel celler.

Com he dit al principi, se que encara no us ho creieu, però gracies papas i Marc també pel suport i ànims rebuts tots aquests anys. Sempre que us he necessitat heu estat allà incondicionalment. Aprofito aquestes línies per dir-vos que us estimo. A tu Pedronks també, per ensenyar-me que és Pink Floyd fa tants i tants anys. Segurament alguna idea clau d'aquesta tesi ha nascut amb algun tema inspirador de Pink Floyd de fons. Al yayo també, que sempre deia que iva a tener suerte...

... i sembla que tenia raó. Això del covid ha sigut... per tothom... però en el fons, a mi, m'ha portat cap a tu Claudia, així que sembla que si que tenia raó el meu avi. Tu has viscut més d'aprop que ningú la meva recta final (covid, un peu torçat, la grip, l'estrès, un got trencat, bloqueig a l'hora d'escriure, un plat trencat...), gràcies per tot el suport incondicional i per haver volgut compartir tot això amb mi. Ara que sembla que poso punt i final a aquesta etapa, el que si que tinc clar, és que el que faci d'ara en endavant ho vull fer al teu costat, i de la Bagui també.

Annex 1

Basement-involved thrusting, salt migration and intramontane conglomerates: a case from the Southern Pyrenees

En l’annex 1 s’incorpora l’article publicat a la revista BSGF-Earth Science Bulletin publicat l’any 2021 com a part d’un volum especial *Orogen lifecycle: learnings and perspectives from Pyrenees, Western Mediterranean and anàlogues*.

X. Coll ha col·laborat en les campanyes de camp, la discussió dels resultats i la edició del text.

Burrel, L.; Teixell, A.; Gómez-Gras, D.; Coll, X. (2021). Basement-involved thrusting, salt migration and intramontane conglom-1107 erates: a case from the Southern Pyrenees. Bull. Soc. Géol. Fr. 2021, 192, . https://doi.org/10.1051/bsgf/2021013.

BSGF - Earth Sciences Bulletin 2021, 192, 24
© L. Burrel *et al.*, Published by EDP Sciences 2021
https://doi.org/10.1051/bsgf/2021013

Special Issue Orogen lifecycle: learnings and perspectives from Pyrenees, Western Mediterranean and analogues ed. O. Lacombe, S. Tavani, A. Teixell, D. Pedreira and S. Calassou (Guest editors)

Available online at:
www.bsgf.fr

OPEN ACCESS

Basement-involved thrusting, salt migration and intramontane conglomerates: a case from the Southern Pyrenees

Laura Burrel*, Antonio Teixell, David Gómez-Gras and Xavier Coll

Departament de Geologia, Universitat Autònoma de Barcelona, Bellaterra 08193, Spain

Received: 11 June 2020 / Accepted: 25 March 2021 / Publishing online: 22 April 2021

Abstract – The northern margin of the Organyà basin (Southern Pyrenees) has a complex structure in which syn-rift Lower Cretaceous carbonates flank a wide Keuper evaporite province, featuring the leading edges of the basement-involved thrust sheets of the Pyrenean antiformal stack. Recent studies show that Keuper diapirs and salt walls grew during the Cretaceous extensional episode, conditioning the development of differentiated depocenters and minibasins. The role of salt tectonics during the Pyrenean orogeny has not been addressed in previous structural studies, but present-day cross-sections indicate a Keuper evaporite-bearing vertical thickness of up to 3000 m in the Senterada-Gerri de la Sal area. We infer that salt migration was a determinant mechanism in triggering a gentle northward tilting of the Organyà basin during the Eocene-Oligocene, recorded in the La Pobla de Segur and Gurp syn-tectonic conglomerates in a large north-directed onlap, opposite to the main sedimentary influx direction. Contemporaneously, we interpret that salt migration, promoted by conglomerate differential loading, enabled the sinking and rotation of the unrooted Nogueres thrust units (*têtes plongeantes*). We use new and published structural data for the Lower Cretaceous margin of the Organyà basin, combined with structural and clast provenance data from the Cenozoic alluvial fan conglomerates of La Pobla and Gurp, to understand the Lutetian to late Oligocene evolution of the northern margin of the Central South-Pyrenean Unit. The tectono-sedimentary evolution of this area and the salt evacuation patterns are closely related to the exhumation history of the stacked Paleozoic thrust sheets of the Pyrenean hinterland to the north. In this study, we correlate the movements over a mobile substratum and the paleogeographic changes of conglomeratic basins at the toe of an exhuming orogenic interior.

Keywords: Salt tectonics / Antiformal stack / Basement thrusting / Alluvial fans / Differential loading / Routing systems / Pyrenees

Résumé – Chevauchements de socle, migration du sel et conglomérats intramontagneux : un cas des Pyrénées méridionales. La marge nord du bassin d'Organyà (Pyrénées méridionales) présente une structure complexe dans laquelle les carbonates du Crétacé inférieur, syn-rift, flanquent un vaste domaine d'évaporites du Keuper, en interaction avec la partie frontale des nappes chevauchantes de l'empilement axial pyrénéen (têtes plongeantes des Nogueres). Des observations récentes montrent que des diapirs de Keuper se sont développés pendant l'épisode d'extension crétacée, conditionnant le développement de dépocentres et de minibassins différenciés. Le rôle de la tectonique salifère pendant l'orogenèse pyrénéenne n'a pas été abordé dans ce secteur dans les études structurales précédentes, mais les coupes transversales actuelles indiquent une épaisseur verticale de Keuper à évaporites allant jusqu'à 3000 m dans la région de Senterada-Gerri de la Sal. Nous en déduisons que la migration du sel a été un mécanisme déterminant dans le déclenchement d'un léger basculement vers le nord du bassin d'Organyà pendant l'Éocène-Oligocène, enregistré dans les conglomérats syn-tectoniques de La Pobla de Segur et de Gurp par un onlap régional dirigé vers le nord, à l'opposé de la direction principale du flux sédimentaire. Simultanément, la migration du sel, favorisée par la charge différentielle des conglomérats, a permis l'enfoncement et la rotation des têtes plongeantes des Nogueres, séparées de leur racine par l'érosion. Nous utilisons des données structurales nouvelles et publiées sur la marge du Crétacé inférieur du bassin d'Organyà, combinées aux données structurales et de provenance des clastes des conglomérats alluviaux du Cénozoïque de La Pobla et de Gurp, pour comprendre l'évolution du Lutétien à l'Oligocène tardif de la marge nord de l'Unité Sud-Pyrénéenne

*Corresponding author: lauraburrel@gmail.com

Centrale. L'évolution tectono-sédimentaire de cette zone et les modèles d'évacuation du sel sont liés à l'histoire de l'exhumation des nappes chevauchantes de matériel paléozoïque empilées au nord dans la Zone Axiale pyrénéenne. Dans cette étude, nous corrélons les mouvements sur un substrat mobile avec les changements paléogéographiques des bassins conglomératiques au pied d'un intérieur orogénique en exhumation.

Mots clés : Tectonique salifère / Chevauchements de socle / Éventail alluvial / Charge différentielle / Systèmes de routage sédimentaire / Conglomérats / Pyrénées

1 Introduction

In basins that evolve on top of thick evaporite detachment levels, differential loading of prograding sedimentary systems triggers salt mobilization towards areas with a smaller overburden load and an associated depocentre migration (Ge *et al.*, 1997). In salt-bearing foreland basins, load-induced halokinetic movements in addition to the compressional forces from the orogeny can play an important role in shaping the architecture of alluvial fans. Nevertheless, due to the imprint of compressional structures such as thrusts and fault-related folds, the contribution of halokinesis in syn-orogenic sedimentation on fold-and-thrust belts has been often disregarded.

The intramontane alluvial fans of the Central South-Pyrenean Unit (CSPU) are late Lutetian to late Oligocene in age and crop out in three main areas known from East to West as the La Pobla de Segur, Gurp, and Sis conglomeratic basins (Rosell and Riba, 1966; Mey, 1968; Séguret, 1969; Garrido-Mejías and Ríos, 1972; Mellere, 1993; Vincent, 2001) (Fig. 1). Additionally, to the north of the La Pobla and Gurp basins, the Senterada conglomeratic basin is an E-W depression that comprises three smaller isolated outcrop areas, on top of the Paleozoic and Triassic of the Nogueres thrust sheet. From south to north, the alluvial fans progressively retrograde, displacing the apical areas to the north, shifting sedimentation from the Organyà basin northern margin towards the unrooted leading edge of the Axial Zone antiformal stack (the Nogueres *têtes plongéantes*; Séguret, 1972) and a Keuper evaporite province in between, which we call the Senterada salt province (Fig. 2). The evolution of the catchment areas and geometry of these alluvial systems (Figs. 2 and 3) has been strongly influenced by the joint effects of the Axial Zone uplift, horizontal shortening and salt evacuation. With the intervention of such diverse factors, the geological history registered within the Middle Eocene to Oligocene intramontane conglomerates in the South-Pyrenean thrust belt puts forward an interesting case study.

The starting point of this study involved revisiting the work by Rosell and Riba (1966) and Garrido-Mejías and Ríos (1972), who noted an unusual dip and apparent downlap to the north in the lower alluvial systems of the La Pobla basin (Fig. 4A). This observation contrasted with the major northward provenance of the fans, and the authors attributed the downlap to the synsedimentary tilting of the conglomeratic basin towards the north, progressively shifting the basin depocentre in that direction. In this study, we return to this idea in the light of the more recently developed salt tectonics concepts, invoking load-induced salt migration as the main factor inducing the north-directed tilting and associated depocentre migration.

Salt tectonics may quickly modify the connection between catchment areas, sedimentary routing systems and depocentres. In the framework of a growing orogen, sudden local changes in provenance often indicate smaller-scale tectonic activity related to salt expulsion, but can often be overprinted by basement thrusting and related growth structures. Originally interbedded with Triassic Keuper evaporites, the uninterrupted presence of ophite clasts within the intramontane conglomerate of the Southern Pyrenees indicates the continuous erosion of Keuper exposures. This provides an excellent marker to track salt-related movements from the mid Lutetian to the Oligocene, where exposed diapirs and salt walls can be interpreted as part of the source area. Focusing on the geometry and provenance indicators of the Gurp, La Pobla and Senterada basins, we present new palaeogeographic maps and cross-sections, illustrating the evolution of the conglomeratic basins in relation to the uplifting antiformal stack and the migration of the Keuper evaporites.

2 Geological setting and previous studies

The Alpine thrust structure of the Axial Zone of the Pyrenees has been extensively studied (Séguret, 1972; Williams and Fischer, 1984; Roure *et al.*, 1989; Muñoz, 1992; Vergés, 1993; Beaumont *et al.*, 2000; Mouthereau *et al.*, 2014; Muñoz *et al.*, 2018; Teixell *et al.*, 2018; García-Senz *et al.*, 2019; Calvet *et al.*, 2020), defined as an antiformal stack of Paleozoic basement-involved, south-directed thrust sheets. The frontal part of the antiformal stack, detached by erosion from its root to the north, consists of foreland-dipping thrusts and related downward-facing folds referred to as the Nogueres *têtes plongeantes* (Séguret, 1972). Recent numerical modelling studies have explored the role of the Triassic evaporites in crustal-scale orogenic inversion, which are key in enabling gliding, stacking and rotation of the duplex thrusts (Grool *et al.*, 2019; Jourdon *et al.*, 2020). In the South-Central Pyrenees, the Nogueres thrust sheet consists internally of a set of minor imbricates of Silurian and Devonian metasedimentary rocks with Permo-Triassic deposits unconformably on top (Mey, 1968; Séguret, 1972; Zwart, 1979; Muñoz, 1992; Saura and Teixell, 2006). These subunits are interleaved with Triassic shales and evaporites of the Keuper facies (Fig. 2). The Variscan structure of the Nogueres units, preceding the Pyrenean Orogeny, and the Permo-Triassic basin configuration has been documented in several works (Mey, 1968; Zwart, 1979; Muñoz, 1992; Saura, 2004; Saura and Teixell, 2006; Lloret *et al.*, 2018). Under the Nogueres thrust sheet, the Orri thrust sheet, bearing the igneous and metamorphic complexes of the Axial Zone (Muñoz, 1992), crops out to the north (Fig. 1).

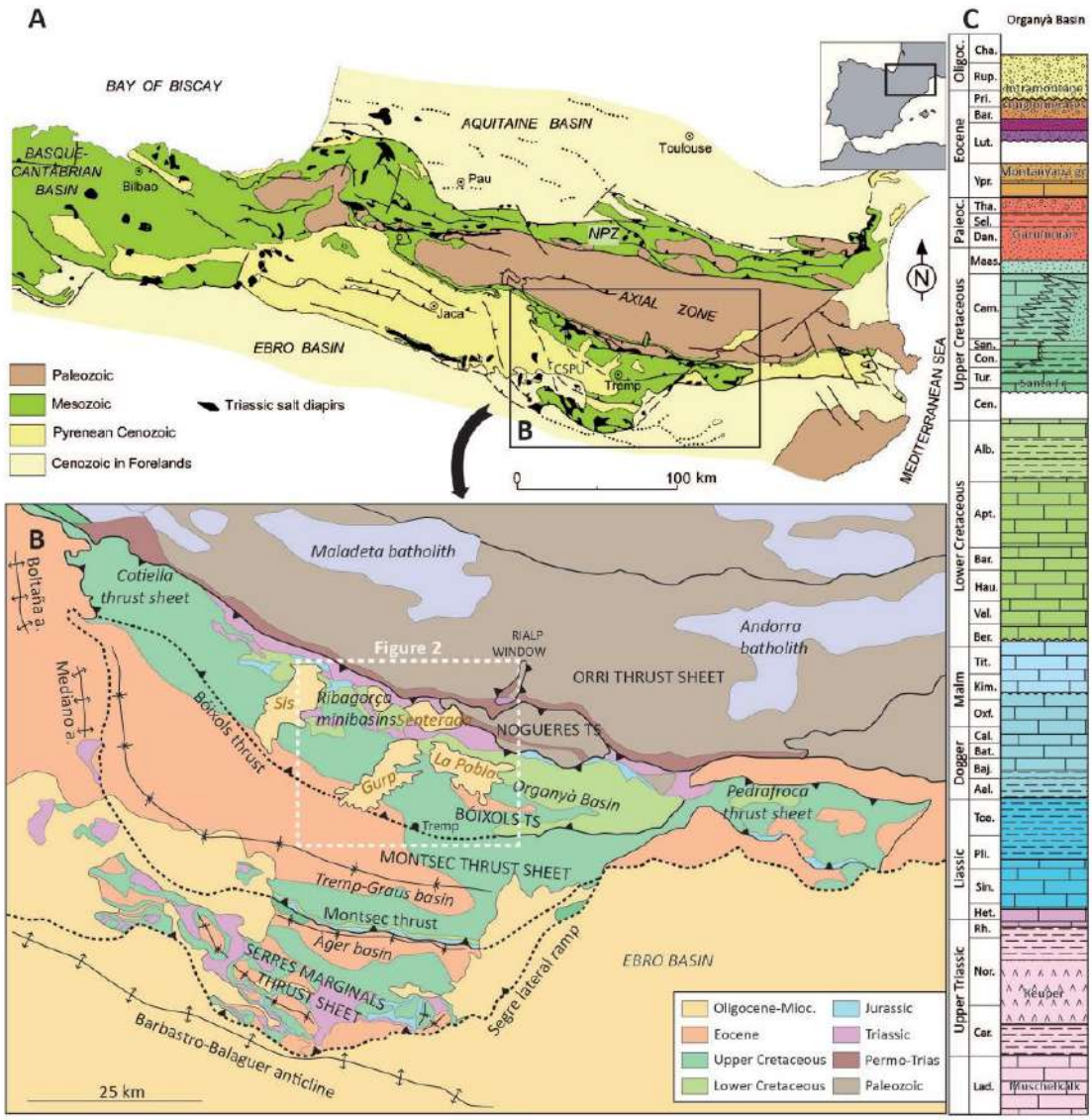

Fig. 1. A. Geologic sketch map of the Pyrenean orogen. B. Geological map of the South-Central Pyrenean unit indicating the location of the study area (Fig. 2). C. Stratigraphic column of the Organyà and Tremp-Graus basins.

According to thermochronological data (apatite and zircon fission tracks: AFT, ZFT) by Fitzgerald *et al.* (1999) and Metcalf *et al.* (2009), a first stage of heating around 70–50 My in the Orri thrust sheet can be attributed to burial by the upper thrust sheets as the Nogueres (Fig. 3). Oldest cooling ages of the Lacourt massif of the North Pyrenean zone (the root zone to the Nogueres zone according to Teixell *et al.*, 2018) at 70 (ZFT) and 55 My (AFT) (Yelland, 1991; Fitzgerald *et al.*, 1999) could be consistent with this. From 50 to 30 My, the uplift of the Orri thrust sheet accelerates the amplitude growth of the Axial Zone antiformal stack, rapidly exhuming and cooling the granite massifs contained in the sheet (Ribérot, Maladeta, Marimanya, etc.). Rapid cooling continued in the massifs of the North Pyrenean Zone (Sinclair *et al.*, 2005; Vacherat *et al.*, 2016). Finally, the emplacement of the lowermost Rialp thrust sheet, at around 30 My, marks a stage of slower cooling and exhumation

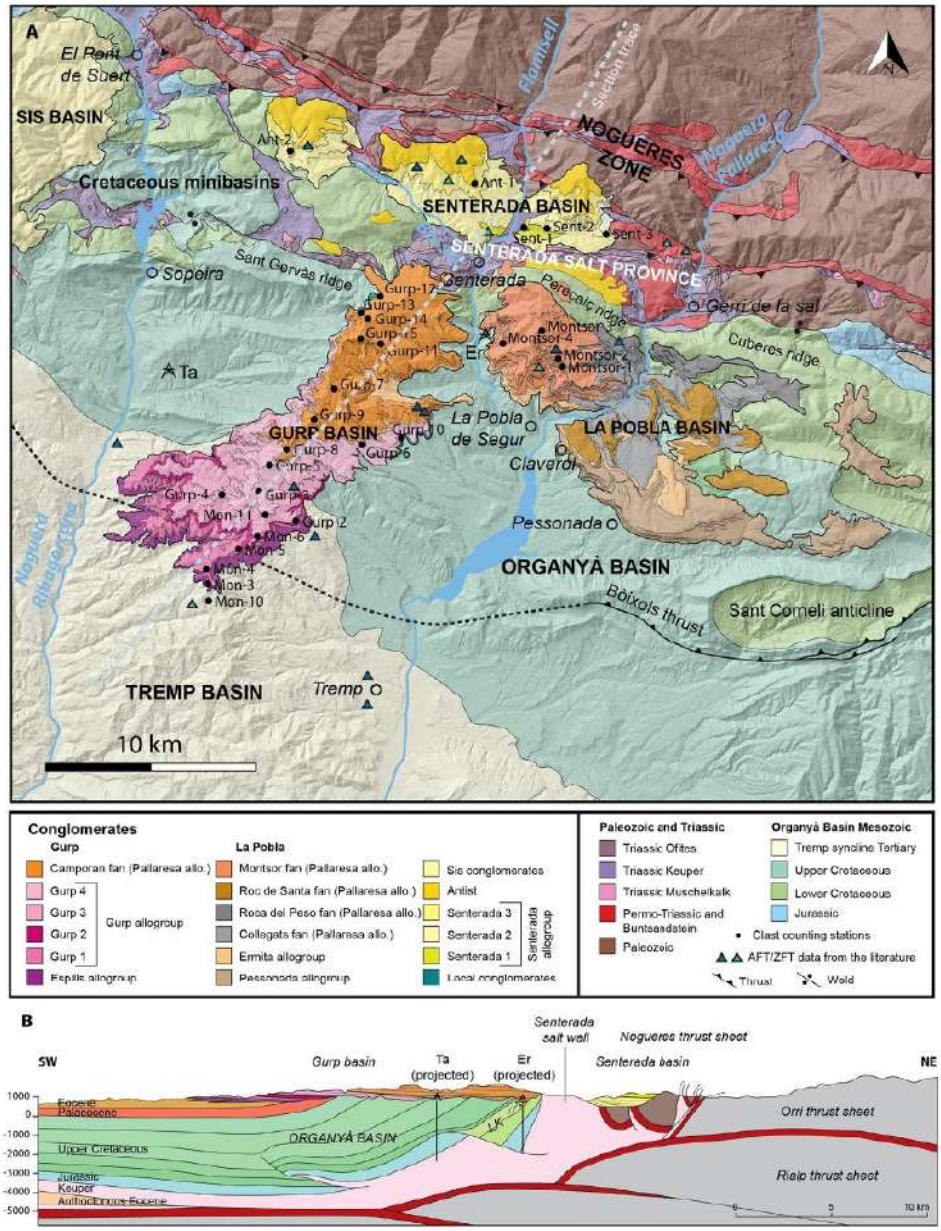

Fig. 2. A. Detailed geological map of the study area showing the location of the clast counting stations. Ta: Tamúrcia well; Er: Erinyà well. The limits of the conglomerate fans are modified from the ICGC 1:25000 maps of Tremp and Espills for the Gurp basin, and from Saura (2004) and Barsó (2007) for the La Pobla and Senterada Basins. The Organyà Basin and the Nogueres Zone have been drawn from the ICGC 1:50000 map of the Pallars Jussà. The AFT/ZFT sample locations refer to the papers by Beamud *et al.*, 2011, Whitchurch *et al.*, 2011, Fillon *et al.*, 2013, and Michael (2013). B. Schematic cross-section along the Gurp basin transect. LK, lower Cretaceous. The Organyà basin structure is modified from the sections in Mencos *et al.* (2015) and Muñoz *et al.* (2018), the Nogueres shallow structure is from Saura and Teixell (2006), and the deep structure of the antiformal stack is modified from Muñoz *et al.* (2018).

up to the present day (Gibson, 2004; Sinclair *et al.*, 2005; Metcalf *et al.*, 2009; Whitchurch *et al.*, 2011; Calvet *et al.*, 2020).

The Axial Zone antiformal stack is flanked to the south by the thin-skinned South-Pyrenean fold-and-thrust belt, constituted by Mesozoic and Paleogene rocks detached from the basement by the Triassic Keuper, which is also a source layer for diapirism (see a review in Cámara and Flinch, 2017). The eastern part of the thrust belt in the central Pyrenees was referred to as the Central South-Pyrenean Unit (CSPU; Séguret, 1972) (Fig. 1), a name we retain for convenience in the description. The Keuper outcrops extensively between the Nogueres thrust slices and the CSPU, forming what we call the Senterada salt province. Over the mid-Triassic Muschelkalk carbonates, the Keuper facies of the Senterada salt province is composed of four different formations (Salvany and Bastida, 2004): (a) the Adons mudstones and carbonates; (b) the Boix gypsum formation, consisting of red and versicolor gypsum; (c) the Senterada gypsum formation, cropping out in the Pont de Suert and Senterada areas; and finally (d) the Avellanes mudstones and carbonates formation. Due to the weathering conditions, halite is not found in the outcrops. However, most wells that cut across the Keuper in the SCPU, including Erinyà and Tamúrcia wells in the study area (Fig. 2), indicate thick halite successions (Lanaja *et al.*, 1987). Moreover, the salty water springs in Gerri de la Sal confirm that halite is an important component of the Keuper facies under the surface.

The evaporite depositional thickness within the Keuper facies in the Senterada province is hard to estimate, due to intense deformation. The Erinyà and Tamúrcia wells (Fig. 2) stopped after drilling 46 m and 29 m into the Keuper halite and mudstone, so the basal depth of the evaporite unit is unknown. The presence of abundant Muschelkalk carbonate lenses within the deformed Keuper facies suggest that Middle Muschelkalk evaporites, not clearly identified at the surface but reported in wells in the Iberian and Ebro basins (Bartrina and Hernández, 1990; Jurado, 1990; Ortí *et al.*, 2017), could have acted as the basal level of the source layer for fault detachment and diapirism.

Halokinetic deformation has been reported along the northern margin of the CSPU in the Cotiella thrust sheet (McClay *et al.*, 2004; Lopez-Mir *et al.*, 2014) and the Ribagorça basin (Saura *et al.*, 2016; García-Senz and Muñoz, 2019a) (Fig. 1) during the Pyrenean Mesozoic rifting stage. To the southeast of these halokinetic depocenters, the lower Cretaceous Organyà basin was a synformal basin filled with a thick carbonate succession (Berástegui *et al.*, 1990; Caus *et al.*, 1990; García-Senz, 2002). The Jurassic and lower Cretaceous succession of the northern limb of the Organyà syncline is shown in these works with constant thickness by the isopach data. It terminates sharply against a south-dipping discontinuity interpreted as an Eocene backthrust (the Morreres backthrust) that uplifts the basin above the Senterada Keuper province (Berástegui *et al.*, 1990; Muñoz, 1992; García-Senz, 2002). In this study, we revise this concept.

The Organyà basin is limited to the south by the Bóixols thrust, the oldest of the South-Pyrenean piggy-back succession, emplaced during the late Santonian as a reactivation of an extensional fault system (Berástegui *et al.*, 1990; Vergés and Muñoz, 1990). Peybernès (1976), Berástegui *et al.* (1990) and García-Senz (2002) report a progressive onlap of the Lower Cretaceous carbonates against the Jurassic pre-rift strata in the Bóixols hanging-wall and interpret it as a roll-over anticline against a listric fault, inspired by the geometries observed in physical models by Ellis and McClay (1988). To the south of the Bóixols thrust, the central part of the CSPU is the broad, flat-bottomed syncline known as the Tremp-Graus basin, filled by the synorogenic sediments from the upper Santonian to the Eocene, and limited to the south by the Montsec thrust (Fig. 1).

Mid Eocene and Oligocene alluvial conglomerate inliers of the South-Pyrenean thrust belt were sedimented unconformably above deformed Mesozoic and Tertiary rocks of the SCPU (Fig. 1) (Rosell and Riba, 1966). The major basal unconformity at the base of these intramontane conglomerates, and an apparent downlap to the north of the conglomerate beds against it (Fig. 4A), has been reported since the early Pyrenean studies. During the first half of the 20th century, the fossil-bearing levels of Sossís in the lower part of the succession were dated as Bartonian (Bataller, 1943; Crusafont *et al.*, 1956). Rosell and Riba (1966) published the first complete stratigraphic description, and mapped the La Pobla basin. Their study also included clast compositional identification, differentiating alluvial fan units with predominant Paleozoic or Mesozoic provenance, and the downlap against the basal unconformity is interpreted as produced by the tilting of the basin, pointing towards a progressive development of the basal unconformity, rather than a post-depositional tilting. Robles and Ardévol (1984) studied the relationships between the alluvial fans and the Sossís and Claverol lacustrine intercalation, differentiating climatic cycles within the stratigraphic succession that were correlated with the progradation and retrogradation of the fans, and produced a series of palaeogeographic maps. The carbonate and marly members of the lacustrine units, often interbedded with coal beds, are very rich in vertebrate and invertebrate fossil content indicating a Bartonian age (*i.e.* compilation of paleontological data in López-Martínez *et al.*, 1998 and Beamud *et al.*, 2003).

Studies by Mellere and Marzo (1992) and Mellere (1993) proposed a new stratigraphic framework for the La Pobla de Segur conglomerates, which was based on mappable unconformity surfaces and clast compositional changes. Five allogroups were defined: Pessonada, Ermita, Pallaresa, Senterada, and Antist. The apparent downlap of the conglomerate beds against the basal unconformity was attributed to the reactivation of the Bóixols thrust or deeper structures. Magnetostratigraphic dating of the La Pobla conglomerates (Beamud *et al.*, 2003, 2011) was anchored in the lacustrine fossil localities, and covered an age span of around 18 My. These data, combined with AFT data in granitic clasts (Beamud *et al.*, 2011), in detrital samples of the CSPU (Whitchurch *et al.*, 2011; Fillon and van der Beek, 2012; Fillon *et al.*, 2013) and thermal modelling (Beamud *et al.*, 2011; Whitchurch *et al.*, 2011) led to a refined chronostratigraphic framework for the La Pobla and Sis conglomerates, which range from the late Lutetian to the late Oligocene. Provenance studies in the La Pobla conglomerates by Barsó (2007) and Barsó and Ramos (2007), focused on clast counting and heavy minerals identification. The observed provenance changes were correlated with exhumation data in the Axial zone antiformal stack (Gibson, 2004; Beamud *et al.*, 2011). These studies explain the disconnection of the La Pobla and Senterada basins as a result of the Morreres backthrust emergence.

Contrary to what happens in the La Pobla basin, there are no extensive stratigraphic studies nor a solid chronostratigraphic framework for the Gurp conglomerates. The southern part of the Serra de Gurp is mapped in the ICGC 1:25000 maps of Tremp and Espills (Muñoz *et al.*, 2009; Samsó *et al.*, 2010), outlining the sedimentological and compositional characteristics of the main conglomerate units. The Gurp basin succession starts with the Espills allogroup, which is followed by the Gurp allogroup and the Ermita and Pallaresa allogrups, the latter two equivalents to the La Pobla basin. Michael (2013) correlated the Gurp conglomerates with the Escanilla fluvial system of the Ainsa basin based on clast counting, and also provided sparse detrital AFT data. In this study, we will use the unit divisions proposed by Mellere and Marzo (1992) for the La Pobla and Senterada basins and the ICGC maps for the Gurp basin.

3 Methods

Field campaigns were carried out to obtain additional structural data of the northern Organyà Basin flanking with the Senterada salt province. Structural data has also been gathered within the conglomeratic basins to constrain their geometry, with special focus in the less studied Gurp basin. The deep structure of the Organyà basin adopted in this work for cross-section construction is modified from the sections in Mencos *et al.* (2015) and Muñoz *et al.* (2018), the Nogueres Zone shallow structure is from Saura (2004) and the deep structure of the basement thrust system stack is modified from Muñoz *et al.* (2018).

Quantification of the main clast lithologies in the conglomerate units was performed in the outcrop locations indicated in Figure 2. We have analyzed a total of 18 clast-counting stations, 11 of which are located in the Gurp basin, 4 in the La Pobla basin, and 3 in the Senterada basin. In the La Pobla and Senterada basins fewer stations were required given that clast counting had been previously performed by Barsó (2007). The method used was that by Howard (1993), which consists in counting subsets of 100 clasts each to obtain lithology percentages. The repetition of four clast-countings, which are closely spaced in each station, was not possible in some localities due to the limited outcrop space and conditions. In cases where in-situ identification of clasts was difficult, their lithology was determined by thin-section observations under microscope.

To simplify the clast counting results, we have grouped the 42 identified lithologies (Appendix 1) into 8 provenance groups:

- Tertiary limestones and sandstones: Alveolina limestones, and deltaic and fluvial Eocene sandstones from the Tremp basin;
- Mesozoic carbonates: Dogger black dolomites and breccias, orbitolina-bearing limestones, rudist bearing limestones, sparitic limestones, black shales, and bioclastic limestones from the Cretaceous of the CSPU;
- Micritic limestone: Grey coloured limestone clasts with no visible fossil content. Likely to belong to the Triassic Muschelkalk, the Jurassic, or the lower Cretaceous.
- Triassic dolerites (ophites), originally interbedded with the Keuper evaporites and mudstones;
- Permo-Triassic clasts: Permian red sandstones and breccias, Buntsandstein quartz conglomerates and quartz pebbles, Buntsandstein white sandstones, caliche nodules, and pumite fragments. They were likely sourced from the Nogueres area (the thrust sheet and its relative autochthon);
- Carboniferous: Microconglomerate and sandstone typical of the Culm facies, sourced from the Nogueres thrust sheet;
- Silurian and Devonian: Silurian black slates, ochre Devonian limestones and calcareous slates, and crinoid or goniatites bearing Devonian limestones (Griotte facies), sourced from the upper subunits of the Nogueres thrust sheet;
- Paleozoic granites;
- Paleozoic metamorphic rocks: marbles (occasionally with pyrite and andalusite crystals), slates, gneiss, deformed quartz and quartzites.

4 Tectonostratigraphy of the La Pobla, Gurp and Senterada conglomeratic basins

4.1 The substratum of the northern margin of the Organyà basin

This study addresses the role that salt tectonics played in the Eocene and Oligocene evolution of the northern half of the Organyà basin. However, to fully understand the role of pre-compressional salt behavior, we made new field observations of the Mesozoic strata, the detailed architecture of which goes beyond the scope of this paper. The Lower Cretaceous stratigraphy and structure of the Noguera Pallaresa and Flamisell transects is extensively documented by García-Senz, (2002). The northern margin of the Organyà basin was represented as a salt wall in the chronostratigraphic chart in García-Senz and Muñoz (2019b, Fig. 5.8).

We observed that the Aptian and Albian carbonate and marl strata in the Flamisell river valley (Fig. 2) describe a progressive unconformity from dips of 60–80 degrees overturned adjacent to the Senterada Keuper province to right way-up dips of 40–50 degrees further south (Fig. 4C), consistent with synsedimentary diapiric rise at Senterada. In the Noguera Pallaresa river valley, the Peracalç overturned syncline (Fig. 2) has a complex faulted structure (García-Senz, 2002), which has challenged the identification of growth patterns in this area. The Albian Lluçà marls (Fig. 1C) in the Flamisell valley contain interbedded lenses of Keuper evaporites (Fig. 2B). These bodies were reported as high-angle extensional fault welds (García-Senz and Muñoz, 2019b), although regarding their interbedded position within the succession and the proximity with the Senterada salt province they could also be the remnants of a salt sheet extruded from the Senterada diapir during the rifting stage. Towards the east, in the Cuberes ridge (Fig. 2A) the diapiric contact between the Keuper province and the Mesozoic overburden cuts across older carbonates of the Upper Jurassic, Neocomian and Barremian (García-Senz, 2002). Dips change from 65°N overturned in the Noguera Pallaresa valley to 50°S in the eastern part of the study area (Fig. 2A), where Keuper evaporites have been completely squeezed out and the Jurassic strata are directly in contact with the Paleozoic of the Nogueres thrust sheet (Fig. 2A). In the

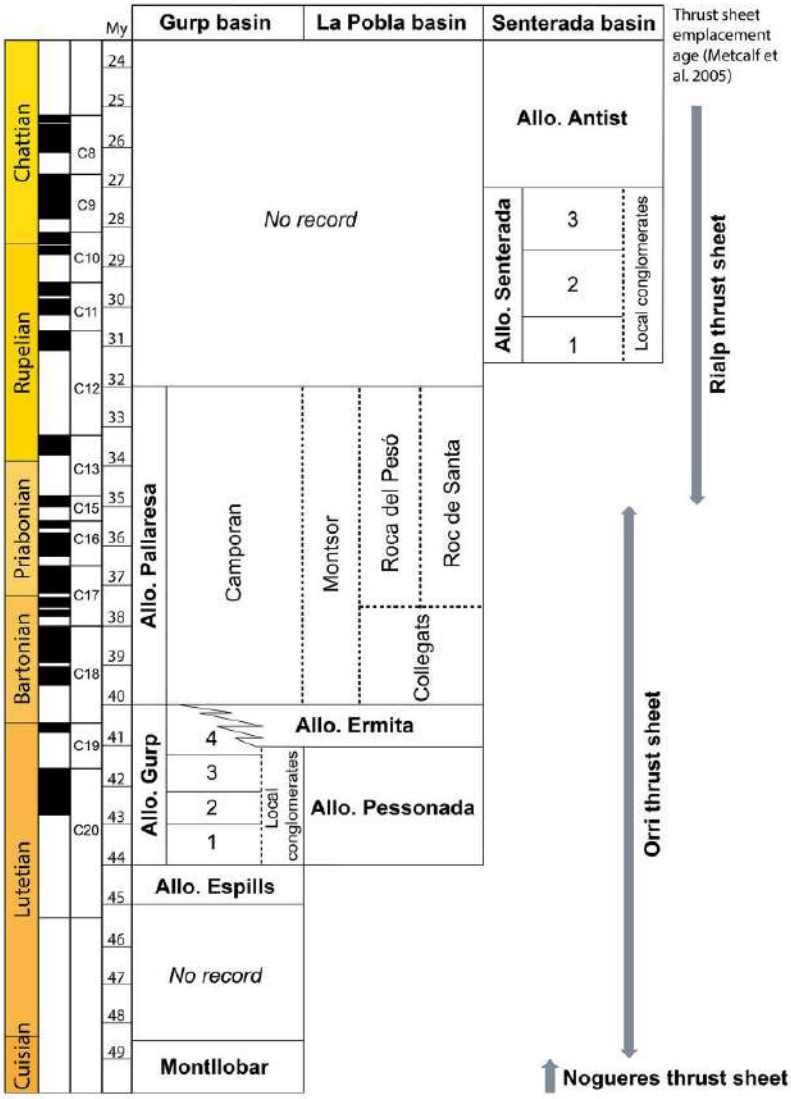

Fig. 3. Tectonostratigraphic framework for the syn-orogenic conglomerate units used in this study. Modifications from previous works are explained in the text. The ages of the allogroups are constrained by magnetostratigraphy (Beamud *et al.*, 2003) but the ages of the different fans within the allogroups are estimated from their stratigraphic relationships. The age of emplacement of the basement thrust sheets is taken from Metcalf *et al.* (2009).

light of these observations and the work by previous authors indicating syn-rift diapir rise in the northern margin of the Organyà basin (Saura *et al.*, 2016; García-Senz and Muñoz, 2019b), we interpret the contact between the Mesozoic carbonates at the basin edge and the Keuper province primarily as a diapiric contact (Fig. 2B). Although some fault reactivation during the Pyrenean contraction may not be discarded, we do not find evidence supporting its interpretation as a major backthrust (*i.e.* the Morreres backthrust; Muñoz, 1992, Mellere, 1993). Further research will be required to understand the numerous faults identified the northern margin of the Organyà basin in contact with the Keuper (García-Senz, 2002). In Section 6, we put forward a case for salt tectonic activity during the Cretaceous rifting and the Cenozoic orogeny in the area.

In the following sections, we focus on observations for the syn-orogenic evolution of the Paleogene intramontane conglomeratic basins. In view of the variability of the alluvial

systems through space and time, we describe them unit by unit using the allogroup classification proposed by Mellere and Marzo (1992) for the La Pobla basin, but incorporating some modifications in the stratigraphy (Fig. 3).

4.2 The Espills allogroup (Middle Lutetian)

The Espills allogroup (Muñoz *et al.*, 2009) is the first unit above the basal unconformity in the Gurp basin. In the southern area, the Espills conglomerates are deposited in a low angle unconformity with the Cuisian Montanyana group of the Tremp-Graus basin (Fig. 1C). The Espills strata dip about 10 degrees N and the underlying Cuisian layers are close to horizontal.

The maximum vertical thickness of the allogroup is 110 m (Samsó *et al.*, 2010). To the north, the Espills conglomerates onlap and pinch out against the Alveolina limestone ridge of the Tremp-Graus basin (Fig. 2A). Paleocurrent directions in the Espills allogroup are SSW directed and the clast composition is mainly Paleozoic, with a significant number of metamorphic clasts and granites (Fig. 5B), indicating a northern provenance. Within the Espills allogroup there are also clasts with provenance from the Mesozoic and Tertiary cover, as well as Triassic dolerites (ophites). Although no studies have conclusively dated the Espills allogroup yet, based on the correlation with the units above, this allogroup has been assigned to the Middle Lutetian (Beamud *et al.*, 2003; Samsó *et al.*, 2010), older than the Pessonada Allogroup of the La Pobla basin.

4.3 The Gurp allogroup (Upper Lutetian)

The Gurp allogroup (Samsó *et al.*, 2010) was deposited unconformably above the Espills allogroup. The ICGC cartography divided this allogroup in four units: Gurp-1, 2, 3 and 4, based on mappable photohorizons, with a total thickness of about 500 m.

The Gurp conglomerates also register the tilting to the north, with dips of 10 to 20 degrees towards the N and NE. The northern extent of the allogroup is limited by the Upper Cretaceous limestone and sandstone ridges of the Tremp-Graus basin, where the Gurp allogroup units onlap and pinch out. The paleocurrents in the Gurp units are SSW directed (Samsó *et al.*, 2010), recording a northern provenance mainly constituted by Devonian limestones and calcareous slate clasts (calcshists), metamorphic rocks and scarce granites. There is also an important fraction of Triassic ophitic dolerites and Lower and Upper Cretaceous clasts (Fig. 5C and D).

4.4 The Pessonada allogroup (Upper Lutetian)

The Pessonada allogroup (Robles and Ardévol, 1984; Mellere and Marzo, 1992), named after the conglomerate ridge east of La Pobla de Segur, is the first and southernmost in the La Pobla basin. It has a thickness of about 1000 m (Mellere, 1993) and lays directly on the basal unconformity, flat or tilted to the north in this part of the La Pobla basin (Fig. 3A). There are smaller-scale angular intraformational unconformities related to minor thrusts (Mellere and Marzo, 1992). The Pessonada conglomerates dip 30 to 40 degrees N, in apparent downlap against the basal unconformity.

The Pessonada allogrup is the proximal and middle part of a locally sourced alluvial fan. Paleocurrent directions are mostly SSW directed (Mellere, 1993). However, cobble imbrications suggest that some small fans were sourced from the E and S. The conglomerates are clast-supported and their composition is almost exclusively Mesozoic micritic grey limestones, probably Cretaceous in age, as well as minor Upper Cretaceous sandstone (Mellere, 1993; Rosell *et al.*, 1994a, 1994b). Magnetostratigraphic data places the base of the Pessonada allogroup in the upper Lutetian at 44 My (Beamud *et al.*, 2003, 2011) (Fig. 3).

4.5 The Ermita allogroup (Uppermost Lutetian to Bartonian)

The Ermita allogroup (Robles and Ardévol, 1984; Mellere and Marzo, 1992) is a fan-delta system which progrades into lacustrine environments to the south, and reaches a total thickness of 200–250 m (Mellere, 1993). The Ermita conglomerates overlie the Pesonada allogrup in the south of the La Pobla basin, while to the north they sit on top of the flat basal unconformity (Fig. 4A).

As is the case in the Pessonada allogroup, the clast composition of the Ermita conglomerates is local Mesozoic limestone and paleocurrents are also SSW directed. The Ermita allogroup also crops out in the eastern sector of the Gurp basin, overlying the Gurp allogroup, with a vertical thickness no greater than 100 m.

Based on mammal fossil chronostratigraphy and magneto-stratigraphy, the Ermita allogroup sedimentation happened near the Lutetian-Bartonian boundary, at ~41–40 My (Beamud *et al.*, 2011) (Fig. 3).

4.6 The Pallaresa allogroup (Bartonian to Rupelian)

The Pallaresa allogroup (Mellere and Marzo, 1992) comprises five interfingering alluvial fan systems, with different composition and provenance: Collegats, Roc de Santa, Roca del Pesó and Montsor in the La Pobla Basin, and Camporan fan in the Gurp basin.

The lower ones lie unconformably over the Gurp and Ermita allogroups (Fig. 4A and B). Towards the north of the Gurp and La Pobla basins, the Pallaresa allogroup conglomerates lie directly above the basal unconformity over the Mesozoic. In this area, the basal unconformity transitions from being flat-lying in its lowest point in the Noguera Pallaresa valley, to become irregular and climbing up the uplifted carbonate ridges of the northern margin of the Organyà basin (Fig. 4B and C). The conglomerates of the La Pobla basin cut across the ridges of Peracalç and Cuberes, the most likely entering points of the alluvial systems into the basin. Dips in the La Pobla basin for the Pallaresa allogroup are around 10 to 30 degrees towards the N and NW. In contrast, the conglomerate beds of the allogroup in the Gurp basin are tilted to the E (dips of 15 to 25 degrees NE). This eastward component is likely depositional, since the conglomerates truncate the Sant Gervàs cretaceous ridge and progressively onlap to the north (Figs. 2 and 4C). The erosional incision at

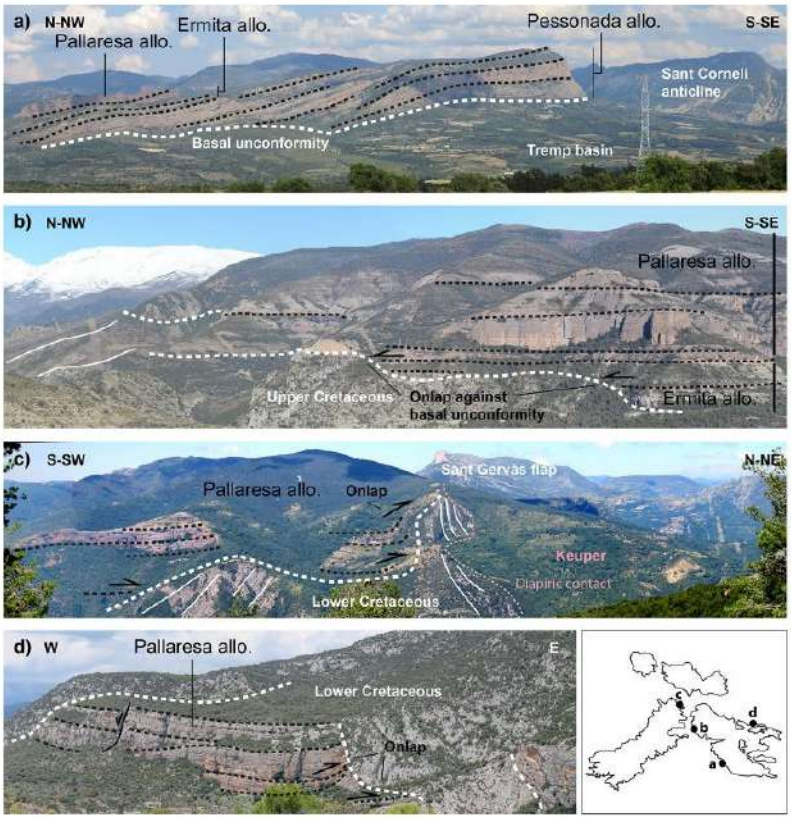

Fig. 4. A. Flat basal unconformity and north-directed downlap of the conglomerates in the Serra de Pessonada. Field of view is 5 km B. Ermita and Pallaresa allogroups onlapping against the irregular basal unconformity in the Flamisell valley (Serra de Montsor). The horizontal dip of the beds is apparent due to the orientation of the photo. Tilting of the beds ranges from 20°N at the bottom of the Pallaresa allogroup to nearly horizontal at the top. Field of view is 6 km. C. Onlap of the Pallaresa allogroup conglomerates (Camporan system) against the Lower Cretaceous ridge in the northern Gurp basin. Field of view is 4 km. D. Pallaresa allogroup conglomerates (Roca del Pesó system) infilling Lower Cretaceous palaeoreliefs in the NE margin of the Organyà basin. Field of view is 2 km.

Sant Gervàs indicates a possible entry point of the conglomerate sediments into the basin.

The Pallaresa allogroup in the La Pobla basin transitions gradually from the Ermita allogroup. The Collegats system maintains a very local source area and small size (2 km^2 extension and 200 m thick). In the Congost de Collegats in the Noguera Pallaresa river valley, conglomerates onlap over a folded paleorelief in the Mesozoic carbonates (Reille, 1971). During the orogeny the onlap geometries were deformed by flexural slip, producing fault-propagation growth folds in the conglomerate beds (García-Senz, 2002, Fig. 3.27). Between the Noguera Pallaresa and Flamisell valleys, the Collegats system interfingers with the Montsor fan system (Rosell and Riba, 1966; Robles and Ardévol, 1984), around 800 m thick (Beamud *et al.*, 2003) and active during the entire sedimentation of the Pallaresa allogroup. Montsor fans covered larger areas (more than 50 km^2) (Mellere, 1993). In the south, the Montsor layers sit on top of the basal Collegats system, dipping between 8 and 27 degrees to the N. In the Flamisell river valley, the Montsor conglomerates directly onlap the basal unconformity over the Lower Cretaceous palaeoreliefs (Fig. 4B). On top of the Collegats system in the SE of the La Pobla Basin, the Roc de Santa system dip around 20 degrees to the NE and show W-directed palaeocurrents. The Roca del Pesó system infill the Lower Cretaceous palaeorreliefs in the northern La Pobla Basin (Fig. 4D). The irregularities in the basal unconformity cause a variety of dips, but the regional dip to the north is still predominant.

Barsó (2007) loosely assigned the Pallaresa allogroup of the Gurp basin to the Montsor alluvial fan system. However, our new clast counting results (Fig. 6) show very different clast composition between the stations in the Montsor fan in the La Pobla basin, and the fan in the Gurp basin. The most remarkable difference is the presence of Carboniferous Culm

clasts in Montsor fan (Figs. 5D and 6) and their total absence in the Gurp basin (Camporan area), which indicate two time-equivalent fans but with different catchment areas. Hence the Gurp and La Pobla upper Pallaresa allogroup conglomerates belong to different fans, even if time-equivalent. We have named the newly identified fan at Gurp the Camporan fan, after the name of the highest peak in the Serra de Gurp (Figs. 2 and 3).

The Pallaresa allogroup fans were active from the Lutetian-Bartonian boundary to the late Priabonian, about 34 My ago (Beamud *et al.*, 2011). Previous studies (Mellere and Marzo, 1992; Mellere, 1993; Beamud *et al.*, 2003; Barsó, 2007) considered the upper part of the Serra de Montsor succession as belonging to the Oligocene Senterada and Antist allogroups (Fig. 3). In the following sections, we discuss the reasons to keep the conglomerates of the upper part of the Serra de Montsor within the Pallaresa allogroup.

4.7 The Senterada allogroup (Rupelian to Chattian)

The Senterada allogroup (Mellere and Marzo, 1992) has been reported as cropping out in the upper part of the Serra de Montsor in the La Pobla basin, as well as in the Senterada basin to the north, which is a narrow E-W sedimentary depression disconnected form the Pobla basin to the south (Fig. 2A).

The Senterada basin section is around 400 m thick (Beamud *et al.*, 2011), and in the present day it is considerably lower in the topography than the upper levels of the La Pobla and Gurp basins. Progressive unconformities within the Senterada allogroup (Saura, 2004) open to the north and onlap against the margin of the Faiada Lower Cretaceous minibasin of the Ribagorçana valley (Saura *et al.*, 2016). The lower units have variable dip directions as the beds are infilling an irregular topography, usually sitting directly above the Keuper evaporites and ophites (Fig. 2). The clasts in this basal unit are heterometric and angular, indicating limited transport, and Permo-Triassic and Devonian lithologies reflect the composition of the nearby Nogueres thrust sheet. Saura (2004), named these deposits Sarroca group, after the locality to the NW of Senterada.

The Senterada allogroup conglomerates are here divided into three different units. The lower one is characterized by dominant Permo-Triassic clasts (Fig. 5G), the second is predominantly made up of Devonian and Carboniferous clasts, and the third without a clear lithologic predominance. The third unit of Senterada is usually matrix-supported and heavily weathered, so the poor outcrop conditions challenge a systematic clast composition analysis. The matrix in the Senterada conglomerates is composed of fine-grained material with reddish coloration, characteristic of the Buntsandstein sandstones and lutites. It is worth noting that, within the Senterada basin conglomerates, the Mesozoic carbonate clasts are almost non-existent.

The age of the Senterada allogroup, determined by palaeomagnetism in the Senterada basin profile, was determined as Rupelian to early Chattian, 33 to 27 My (Beamud *et al.*, 2011). The magnetostratigraphic profiles by Beamud *et al.* (2011) in the Pallaresa allogroup were sampled across a continuous section from the base of the allogroup to halfway up the Montsor mountain. The sampling was resumed in the base of the Senterada basin in the Flamisell valley, assumed to be time-equivalent to the upper part of Serra de Montsor, attributed to Senterada and Antist allogroups. As a consequence of the sampling interruption, the data show a hiatus of 3 My (34–31 My) between the last sample in the Montsor mountain and the first sample in the Senterada basin. However, the stratigraphic succession at Serra de Montsor ridge appears fairly continuous, with no major unconformities or identifiable paraconformities. We have not observed any significant change in the clast composition between the lower Montsor fan and the conglomerates in the upper part of the ridge. For this reason, we assign the upper part of the Montsor mountain to the Pallaresa allogroup (Figs. 2 and 3), and not to the Senterada and Antist allogroups as defined in the separate Senterada basin, which, in contrast, do present a different composition from Montsor fan (Fig. 6).

Another important reason to consider the upper part of the Serra de Montsor ridge as not equivalent to the Senterada basin conglomerates is the present-day difference in topographic elevation between the two. While the base of the unsampled upper section of the Montsor mountain is around 1330 m high, the base of the conglomerates in the Senterada basin succession is around 800 m high in the Flamisell and Bòssia river valleys (Fig. 2). To sediment on top of the Montsor ridge, the north-derived Senterada alluvial systems would have had to climb up a topographic difference of more than 500 m. This appears to be an unlikely scenario, taking into account the height of the Lower Cretaceous ridges and the fact that the source area of the Senterada conglomerates is very local. We consider that a potential sinking of the Senterada basin, or an uplift of La Pobla basin due to a late-Oligocene to Miocene backthrust reactivation after the deposition of the Senterada and Antist conglomerates would not account for the compositional differences between the upper Montsor ridge and the Senterada basin.

Instead, we interpret that the small scale of the alluvial fans (with very local provenance and matrix support) and the significant height of the Lower Cretaceous ridges prevented the Senterada conglomerates to overspill into the upper parts of the La Pobla basin. We favour the idea that Senterada conglomerates had a very local catchment area within the nearby Nogueres thrust sheet (hence the mainly Permo-Triassic and Devonian composition, Figs. 5G and 6).

4.8 The Antist allogroup (Chattian)

The Antist allogroup, 300 m thick (Mellere and Marzo, 1992), has been reported to crop out in the Senterada basin and in the upper part of the Serra de Montsor in the La Pobla basin. As the upper Senterada unit, the Antist conglomerates are very coarse, matrix-supported and poorly cemented, so the outcrop conditions are an impediment to a systematic composition analysis. The Antist alluvial fan is very proximal and contains a clast composition characteristic of the Nogueres thrust sheet, predominantly Devonian limestones and Permo-Triassic red clasts. Triassic ophites, green quartzites, and marbles are common clasts as well. To the west there are local areas with abundant granite clasts (Fig. 5h). The presence of Carboniferous Culm sandstones has also been reported for the eastern area. The Antist allogroup is not deformed or tilted, so it has

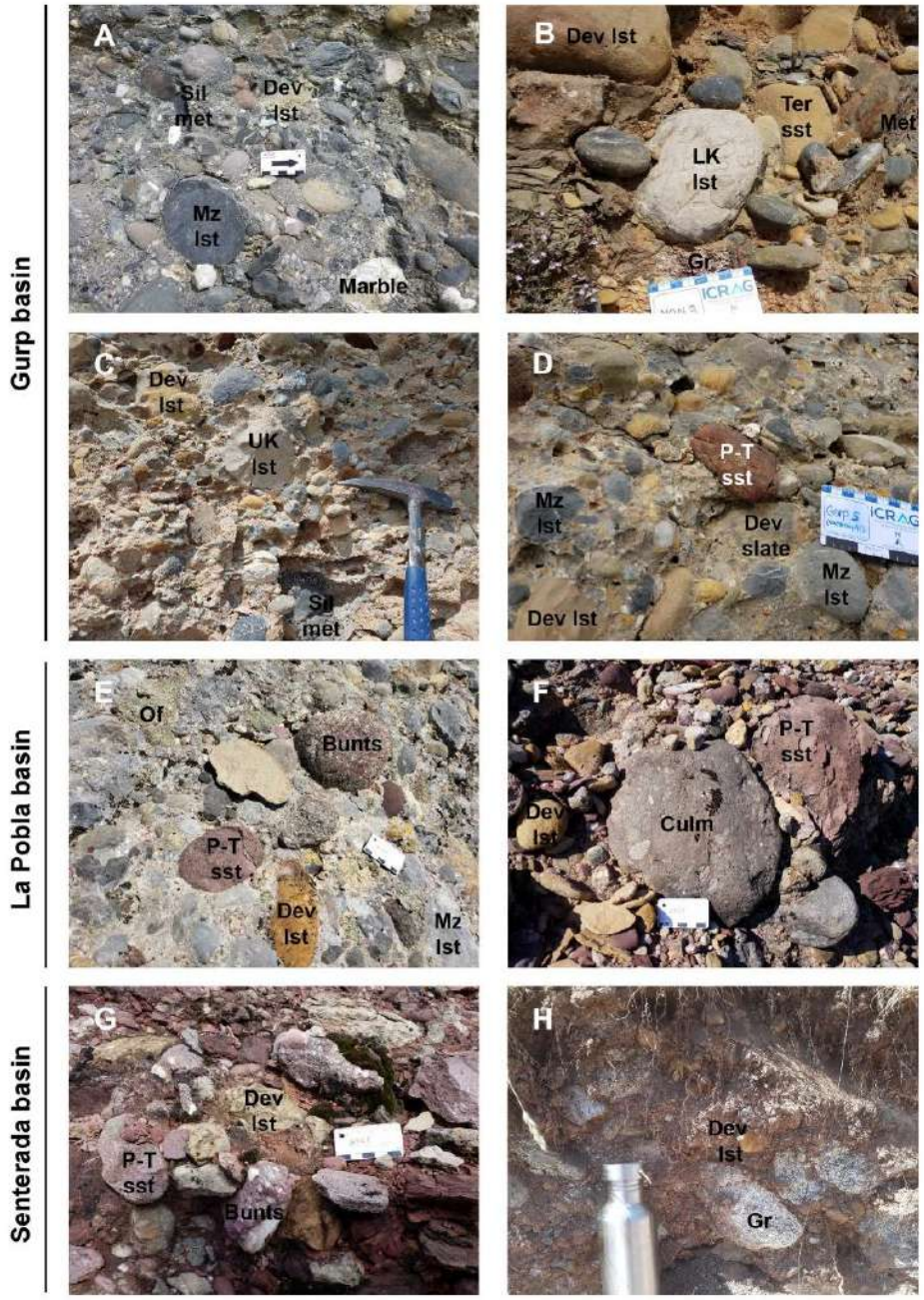

Fig. 5. Images of clast-counting stations, illustrating different clast lithologies (locations in Fig. 2A). A. Mon-10, Montllobar conglomerates. B. Mon-3, Espills allogroup. C. Mon-5. Gurp allogroup, unit 1. D. Gurp-5. Gurp allogroup, unit 4. E. Montsor-1, Pallaresa allogroup, Montsor fan. F. Montsor-3, Pallaresa allogroup, Montsor fan. G. Sent-1, Senterada allogroup, unit 1. H. Ant-2, Antist allogroup. Dev lst: Devonian limestone; Mz lst: Mesozoic limestone, Gr: Granit; P-T sst: Permo-Triassic sandstone; Bunts: Buntsandstein conglomerate; Culm: Culm conglomerate and sandstone; Of: Ophite; Sil met: Silurian metamorphic schist; Dev sch: Devonian schist; UK lst: Upper cretaceous limestone; LK: Lower cretaceous limestone; Met: Metamorphic rock fragment; Ter sst: Tertiary sandstone.

been stated that the Antist conglomerates register the end of the Pyrenean deformation in this area (Mellere and Marzo, 1992; Beamud *et al.*, 2003).

The age of the Antist system has been determined as Chattian, 27–24 My (Fig. 3), and it is time-equivalent to the Sis Collegats alluvial system in the Sis valley (not to be mistaken with the Pallaresa allogroup Collegats system) and the Graus fluvial sediments of the Tremp-Graus basin (Beamud *et al.*, 2011).

5 Clast-counting lithology results

A profile through the Gurp basin records significant changes in provenance from base to top. The Montllobar conglomerates (Fig. 5A), from the underlying Montanyana group, which forms the upper part of the filling of the Tremp-Graus syncline (Nijman and Nio, 1975), are mostly sourced from Mesozoic and Tertiary carbonates from the surrounding palaeoreliefs (69%). However, the proportion of Paleozoic clasts is around 31%, indicating a clear northern provenance already in the late Ypresian (Fig. 6).

In the Lutetian Espills unit (Mon-3 station) (Fig. 5B) over 50% of the clasts derive from Paleozoic rocks: Silurian black slates (10.9%) and Devonian brown limestones (14.6%) and calcareous slates (29.3%) with occasional granite (1.2%) and gneiss (1.2%) pebbles. Post-Paleozoic lithologies are in a lesser proportion: Tertiary calcarenites (12.2%), Alveolina limestone (4.9%), Micritic grey limestone (19.5%), Orbitolina limestone (5.3%) and rudist limestone (1.2%). It is also worth noting that 4.9% of the clasts are Triassic ophites, despite this being a weak lithology that quickly weathers during transport. This proportion is similar to that of the lower sections of the overlying Gurp allogroup (Fig. 5C).

Several counting stations were analysed in the Gurp allogroup (Figs. 2, 5c, 5d and 6): the allogroup is mainly constituted by clasts of grey micritic limestones (42.7% Gurp-1; 21.4% Gurp-2; 30.3% and 27.2% Gurp-3; and 15.3% and 28.9% Gurp-4), Devonian limestones (18.6% Gurp-1; 8.3% Gurp-2, 11.2% and 18.5% Gurp-3; 24.7% and 11.1% Gurp-4) and Devonian calcareous slates (13.3% Gurp-1, 36.9% Gurp-2, 29.2% and 19.8% Gurp-3, 12.9% and 7.8% Gurp-4). Triassic ophites (2.7% Gurp-1; 9.5% Gurp-2, 9% and 13.6% Gurp-3; 14.1% and 6.7% Gurp-4) are also well represented. Minor proportions of Axial Zone metamorphic pebbles (8% Gurp-1, 1.2% Gurp-2, 1.1% and 12.3% Gurp-3, 5.9% and 7.7% Gurp-4) and granites (around 1% in Gurp-2, Gurp-3 and Gurp-4) have also been found.

It should be noted that the Permo-Triassic clasts are absent in the Espills, Gurp-1, Gurp-2, Gurp-3 units and in the lower and middle part Gurp-4 unit (Fig. 5D). These begin to appear at the top of Gurp-4 unit (3.3%%) and are common throughout the Camporan unit (Pallaresa allogroup) at the top of the Gurp basin (17.5–34.2%). These Permo-Triassic clasts mainly derive of detrital red beds. White to green colored ignimbrite clasts are also occasionally found.

The Ermita allogroup in the Serra de Gurp section (Gurp-6 station) is predominantly composed of 82.1% Mesozoic cover (42.4% grey micritic limestones, 38.8% Mesozoic carbonates, and 1.1% ophites). Tertiary sandstone and limestone clasts (15.6%) are also present. Additionally, there is an occasional appearance of Devonian limestones (2.2%) (Fig. 6), very similar to the proportions reported by Mellere and Marzo, (1992) and Barsó (2007) for the La Pobla basin. However, the finding of epidote detrital grains in the Ermita allogrup of the La Pobla basin may indicate that the catchment area went through of Triassic ophites.

The transit from the Gurp to the Pallaresa allogroup, where the Ermita group is absent (Gurp-8 station), is marked by an increasing proportion of Permo-Triassic clasts (17.5%). Silurian black slates (1%), Devonian calcareous slates (4.1%) and Devonian ochre limestones (19.6%) clasts are still present in a significant proportion (24.6%). The Mesozoic lithologies (grey micritic limestones 43.3%, Orbitolina bearing limestones (5.2%), undifferentiated Mesozoic carbonates (6.3%), ophites (3.1%) represent more than half of the clasts throughout the Pallaresa allogroup in the Gurp basin. To the top of the Pallaresa Allogrup (Gurp-9 station) in the Gurp basin (Camporan fan), the presence of Mesozoic lithologies decreases (47.1%) and Permo-Triassic (34.2%) clasts increase with a minor contribution of Devonian limestone (11.8%) and Axial Zone clasts (1.2%).

Clast-counting data in the Montsor system of the Pallaresa allogroup of the La Pobla basin (Figs. 2, 5E, F and 6), in contrast, provides significantly different results. The Mesozoic clasts content is much lower than in the Gurp basin, ranging from 20% to just 6% in the upper part. The proportion between Permo-Triassic clasts on the one hand, and Silurian and Devonian on the other, varies throughout the unit. At the base (Montsor-4 station), the proportion of Permo-Triassic pebbles is 55.9% while for Silurian and Devonian clasts it is 18.3% and for grey Mesozoic limestones it is 7.5%. An important observation is the presence of Carboniferous Culm sandstones and microconglomerates (Fig. 5F) in a proportion of 16.1%, even though this lithology is completely absent in the Gurp basin succession. The Montsor-1 clast-counting station (Fig. 5E) is located in a bed with unique clast proportions, to such an extent that the layer has a distinct colour in the outcrop and it can be distinguished in aerial images, so much that the bed was specifically mapped in the 1:50000 geological map Tremp chart (Rosell *et al.*, 1994a, 1994b). This is due to a comparatively high proportion of Mesozoic carbonates (45%), some of them light-coloured, and green ophites (25%) together with a significant presence of granites and leucogranites (10.9%). This is the highest proportion of ophites reported in the entire conglomerate succession. Permo-Triassic (7.9%), Devonian limestones (5.9%) and Culm clasts (2%) are also represented.

In the following stations in Serra de Montsor succession (Montsor-2 and Montsor-3 stations) (Fig. 5F) the Permo-Triassic clasts increase significantly towards the top (21.8% Montsor-2; 55.9% Montsor-3) together with Silurian and Devonian clasts (35.4% Montsor-2; 24.4% Montsor-3). The proportion of Culm clasts increases and then decreases to the top (19.8% Montsor-2; 6.1% Montsor-3). Mesozoic carbonates (19.8% Montsor-2; 6.1% Montsor-3) decrease from base to top. There are no clasts of green ophites and the weathered granites, frequent in the white layer appear in very minor proportions in the upper part of the succession (2.1% Montsor-2, 1% Montsor-3).

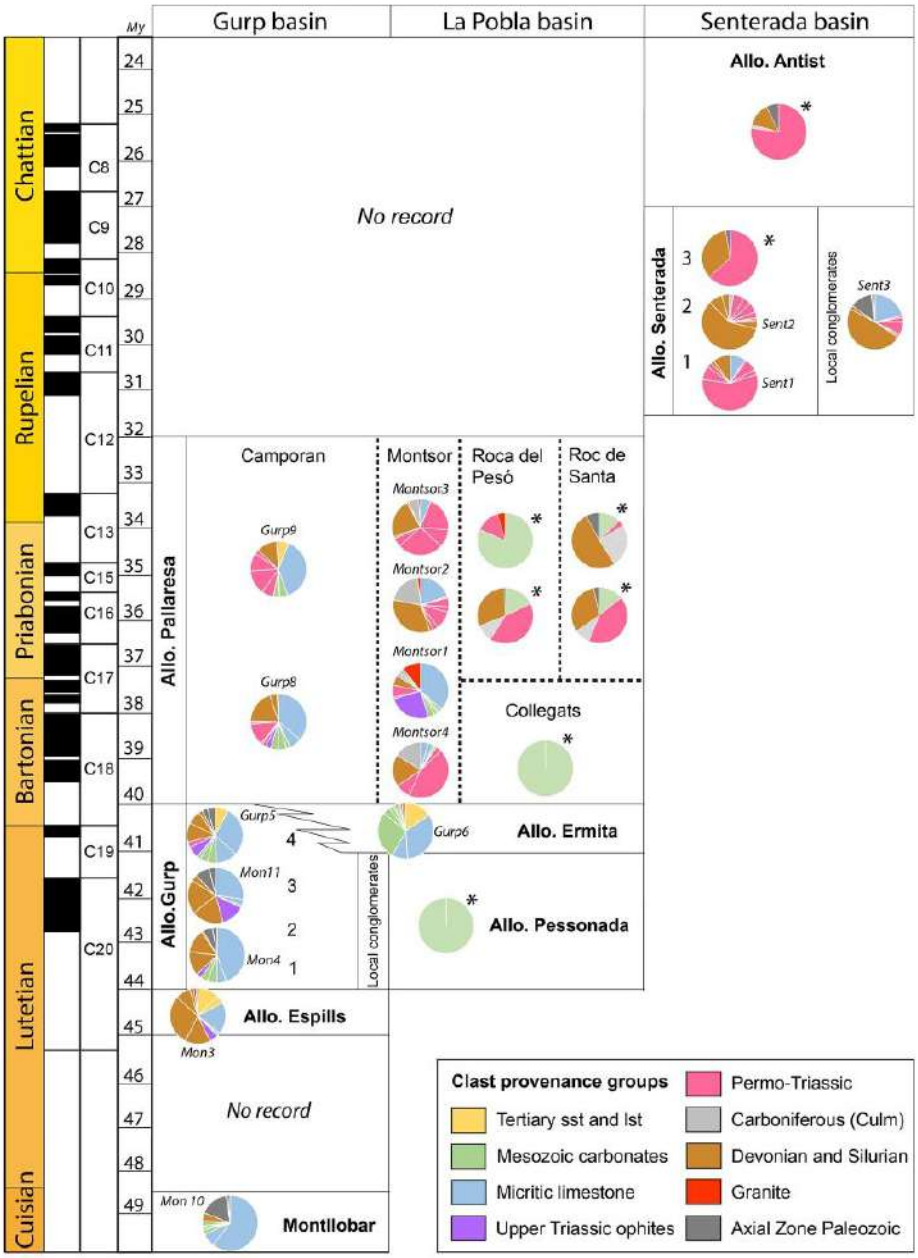

Fig. 6. Pie charts documenting the clast lithology percentages in the counting stations. Location of samples in Figure 2. The charts marked with * are from Barsó (2007).

The results of the Senterada basin reveal a very different clast composition between the Senterada 1 unit (Sent-1 station; Figs. 5G and 6), with predominantly cobbles of Permo-Triassic lithologies (78%) in a fine-grained matrix of red sand, and the Senterada 2 unit (Sent-2 station; Fig. 6), mostly composed of Devonian clasts (76.4%, with brown crinoidal limestone and pink Goniatites-bearing limestone of Griotte facies). In this latter unit, the Permo-Triassic conglomerates and sandstones

are in 21.3%, whereas Mesozoic limestones are represented in a very minor proportion (2.2%). The upper Senterada 3 unit has very poor outcrop conditions, due to the high proportion of matrix content, so we were unable to set a clast counting station in any of the areas surveyed. It has been reported as having a clast proportion of approximately half Devonian limestones and half Permo-Triassic clasts (Barsó, 2007). The poor outcrop conditions have also prevented systematic clast-counting in the Antist allogroup. Field observations have shown that clast composition within the Antist allogroup varies in different outcrops. In certain there is a predominance of granite clasts (Fig. 5h), while in other areas the predominance is pebbles of Buntsandstein conglomerates and sandstones and Devonian limestone clasts (Barsó, 2007). Axial Zone well-rounded metamorphic clasts as green quartzites with folded quartz veins, marbles, dark-metasandstones, slates and quartz pebbles are lithologies widely represented.

6 Evolution of alluvial fan catchment areas

The middle Lutetian Espills allogroup at the base of the Serra de Gurp succession has no time-equivalent in the La Pobla basin. It is composed of 50% of Paleozoic clasts, mostly originated in Devonian and Silurian lithologies of the Nogueres thrust sheet but with the occasional appearance of granite and gneiss pebbles. The upper Lutetian Pessonada allogroup fans in the La Pobla basin are entirely composed of Cretaceous carbonate clasts, while the equivalent Gurp allogroup fans in the Gurp basin have around 40–60% of clast composition from the Nogueres Devonian and Silurian, metamorphic clasts and Triassic ophites (Fig. 6).

Based on the counting results and the geometrical observations in Section 3, we interpret the Pessonada allogroup as a small system of local alluvial fans sourced from Cretaceous carbonates to the north over the Senterada salt province (now eroded), equivalent to the northern Ribagorça diapir and minibasin province (*i.e.* Saura *et al.*, 2016), and from the northern margin of the Organyà basin (Fig. 7A). To the southern part of the Organyà basin, the Pessonada alluvial fans likely onlapped the relief of the Sant Corneli anticline, which could have also provided carbonate clasts in smaller-scale flows. In contrast, the catchments of the Gurp fans (Espills and Gurp allogroups) were much larger, extending throughout a larger area in the hinterland (Fig. 7A). Although an important contribution was from the Cretaceous reliefs immediately to the north, the catchment area extended up to the exposed salt province, supplying the Triassic ophitic dolerites, as well as further north into the Nogueres thrust sheets supplying Devonian and Silurian clasts. The absence of Permo-Triassic clasts in the Espills and lower Gurp allogroups suggests that the Paleozoic clasts where sourced from an area where Cretaceous carbonates were directly overlying the Silurian and Devonian (Fig. 7A). The omission of the Permo-Triassic succession is most probably caused by a northern termination of the Permo-Triassic basins in the Nogueres thrust sheet (as inferred in the Nogueres reconstruction by Teixell *et al.*, 2018, and similarly to what happens in parts of Axial Zone today). However, the precise position of the northern limit of the Permo-Triassic basins and the extent of the Mesozoic cover during the Late Lutetian are unknown.

The granite and gneiss pebbles were sourced by more distant areas. The most likely source are the Lower Paleozoic gneiss massifs and Variscan plutons like those of Castillon, Trois Seigneurs and Lacourt, located in the North Pyrenean zone (the root of the Nogueres thrust sheet following the tectonic reconstruction by Teixell *et al.*, 2018). These massifs have AFT and ZFT cooling ages from the Late Cretaceous to the early Oligocene (Sinclair *et al.*, 2005; Whitchurch *et al.*, 2011), therefore it is possible that they were exposed at the surface by the late Lutetian, the age of sedimentation of the first alluvial fan of the Gurp basin. This is further supported by AFT ages of 75–55 Ma in clasts of the upper Gurp and Pallaresa allogroups in the Gurp basin (Michael, 2013) and geomorphological criteria that place the mid Eocene watershed past the North-Pyrenean Zone (Ortuño and Viaplana-Muzas, 2018). It is worth noting that the crystalline massifs of the present-day Axial Zone yielded younger fission-track cooling ages (centered on 45–30 My in the above referred works), with which they are unlikely sources for the Lutetian conglomerates.

Regarding clast composition, the Bartonian-Priabonian Pallaresa allogroup systems can be separated into two groups: on one hand local fans (Collegats system) predominantly sourced from adjacent reliefs formed by Mesozoic carbonates, and on the other, more extensive fans with larger catchment areas predominantly sourced from the Nogueres thrust sheet Siluro-Devonian, Carboniferous and Permo-Triassic rocks (Camporan, Montsor, Roca del Pesó and Roc de Santa systems) (Figs. 6 and 7B). The abundance of Buntsandstein and Permian clasts in all the Nogueres-sourced fans indicates that the leading edge of the thrust sheet, containing the Permo-Triassic lithologies, was cropping out during the Bartonian.

The almost complete absence of gneiss and other Lower Paleozoic lithologies within the Pallaresa allogroup fans we interpret it reflects the progressive southward displacement of the Pyrenean water divide: during the Lutetian the North-Pyrenean massifs were part of the drainage area (Roigé *et al.*, 2017; Ortuño and Viaplana-Muzas, 2018), while in the Bartonian and Priabonian a local southward migration of the divide localized the drainage area in the southern Nogueres thrust sheet domain (Fig. 7A and B). The few granite pebbles found within the Pallaresa allogroup could have been sourced from minor intrusions within the Nogueres thrust sheet, now eroded (Beamud *et al.*, 2011).

The southern extent of the eastern fans in the La Pobla basin was probably still limited by the Sant Corneli anticline, while the Camporan and Montsor fans infilled the Lower Cretaceous reliefs to the north and then expanded freely to the south, stacking flat above the Pessonada, Ermita, and Gurp allogroups (Figs. 4A and B and 7B). The proximity between the present-day outcrops of the Camporan and Montsor systems, together with the reported dip measurements, suggests that the two could have interfingered in the area of the present-day Flamisell river valley (Fig. 2A).

As explained in Section 3, we consider the Oligocene conglomerates of the Senterada and Antist groups as restricted to the Senterada basin. These conglomerate systems were trapped and confined in an E-W oriented synformal minibasin, sitting directly above the Keuper, and finally overlapping onto the Paleozoic to the north and the Sant Gervàs and Peracalç ridges to the south (Fig. 7C). The clast composition within the Senterada units, with predominant Buntsandstein and

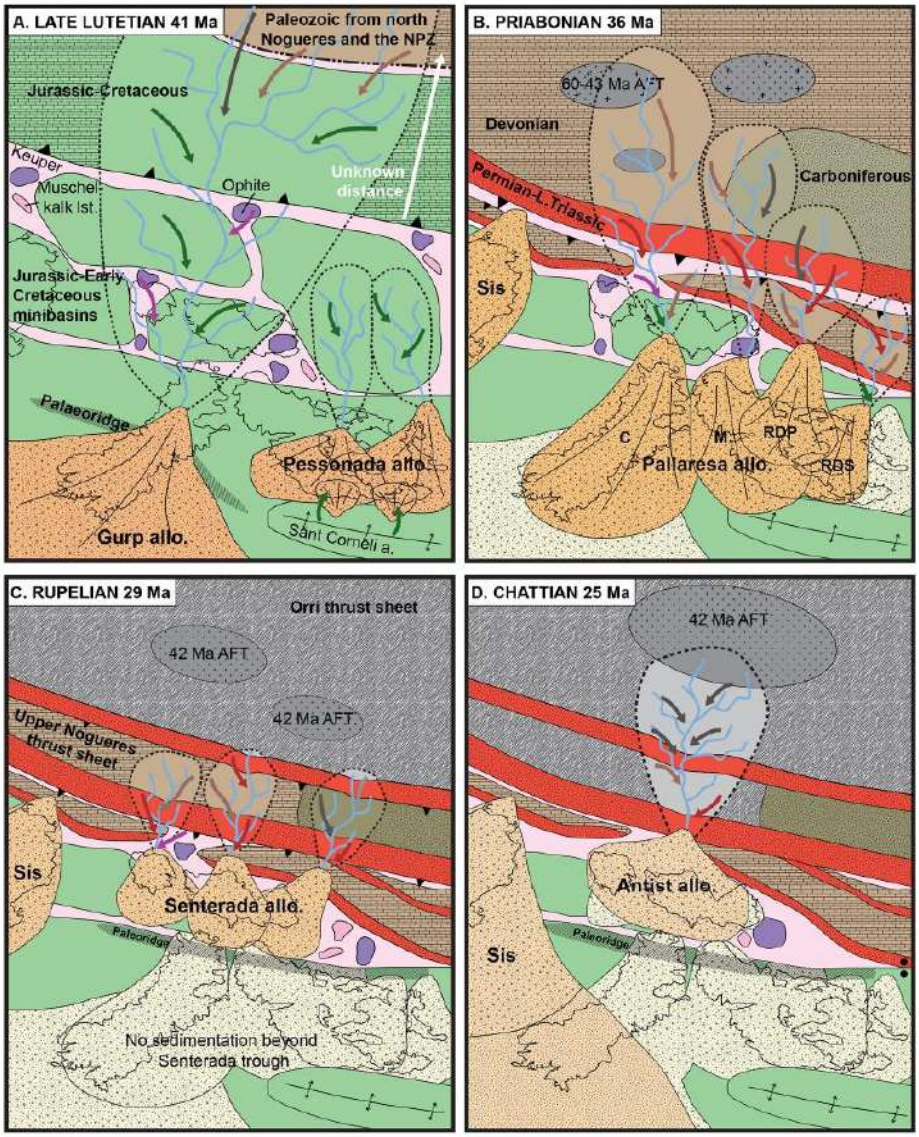

Fig. 7. Palaeogeographical reconstruction showing the evolution of the intramontane alluvial fans and their catchment areas from Late Lutetian to Late Oligocene. AFT data from Beamud *et al.*, 2011. C: Camporan fan; M: Montsor fan; RDS: Roc de Santa fan; RDP: Roca del Pesó fan.

Siluro-Devonian limestones and slates (Fig. 6) reflects the composition of the nearby Nogueres thrust subunits. There is very little contribution of granites or high-grade metamorphics from areas further north, indicating that the fans had small catchment areas (Fig. 7C). In the Antist allogroup, however, the presence of Lower Paleozoic metamorphics and granite pebbles indicates that the late Oligocene the catchment areas expanded, draining also from the plutons of the Orri thrust sheet at the core of the antiformal stack (Fig. 7D) that was progressively unroofed during the late Eocene and Oligocene, as indicated by thermochronology (Metcalf *et al.*, 2009).

7 Role of salt tectonics and basement thrusting in the evolution of the synorogenic conglomeratic basins

For most of the Early Cretaceous rifting stage the Senterada Keuper province was already a complex salt wall system, probably exposed or close to the surface (García-Senz *et al.*, 2019). The differential load of syn-rift sediments in the Organyà basin likely mobilized salt withdrawal from under the basin towards the salt walls, contributing to the rising and tilting of the northern basin margin and forming the progressive unconformity observed in Cretaceous sediments. The northern boundary of the Organyà basin observed today is primarily the diapiric contact with the Senterada salt province.

Salt wall rise was reactivated by the early Pyrenean shortening, by squeezing between the Organyà basin and the Nogueres thrust sheet emplaced onto the Keuper. The uninterrupted contribution of Triassic ophite clasts in the Gurp and La Pobla conglomerates (Fig. 6) indicates that diapirs of the Senterada salt province were exposed at the surface throughout the entire evolution of the conglomeratic basins. This is between the mid Lutetian and the late Rupelian-Chattian (and possibly since the Early Eocene as witnessed by the Triassic clasts in the upper Montanyana group Montllobar conglomerates, Fig. 6). The content of ophite clasts in the conglomerates begins much earlier than the appearance of Triassic Bundtsandstein clasts from the Nogueres zone at around 40 My, and for this reason we discard the Keuper interleaved between the Nogueres thrust slices as the primary ophite contributor to the conglomerate basins. The continuous exposure of the salt walls during conglomeratic sedimentation had a major effect in enabling uninterrupted load-induced salt withdrawal and associated basin tilting, that would not have happened if the salt province was covered and salt had nowhere to extrude.

On the basis of the structural and provenance data presented above, we propose new palaeogeographic and cross-section reconstructions (Figs. 7 and 8) of four stages in the evolution of the intramontane conglomeratic basins of Gurp, La Pobla, and Senterada between the mid Eocene to the Oligocene.

As explained in the previous section, the Gurp and La Pobla basins were separate depocentres in the interior of a low-relief, South-Pyrenean thrust belt during the mid and late Lutetian (Fig. 7A). Differential loading caused by the conglomerate weight triggered low-amplitude salt evacuation of the evaporites under the Organyà basin towards the Senterada salt walls (Fig. 8A). However, the Mesozoic carbonate succession of the Organyà basin edge is much thicker compared to the synorogenic conglomerates (Fig. 2B). For this reason, load-induced movements produce only a moderate tilting of the basin margin, reflected in the apparent north-directed downlap of the La Pobla and Gurp conglomerates against the basal unconformity and the long-lived progressive unconformity within the conglomerate beds (Fig. 4A). The resulting geometry is very similar to the classic illustrations by Trusheim (1960) (Fig. 7) on the development of a salt stock.

In the latest Lutetian, stacking under the Nogueres thrust sheet begun: the Orri thrust sheet was in the early stages of emplacement (Muñoz, 1992; Sinclair *et al.*, 2005; Metcalf *et al.*, 2009). The Nogueres thrust sheet was under further exhumation but not yet eroded enough to disconnect the downward facing leading edge from the root zone to the north. The Orri thrust sheet granites (*e.g.* Maladeta, Fig. 2A) have late Lutetian and younger AFT cooling ages, indicating that they were still covered by a great thickness of rock (Fig. 8A).

From the Bartonian onwards, the Orri thrust sheet uplift caused complete erosion the Nogueres thrust sheet Mesozoic cover to the east of the Flamisell river (Fig. 8B). This exposed the Permo-Triassic rocks of the Nogueres leading edge, which became the main source area for the Pallaresa allogroup fans in the Gurp and La Pobla basins (Fig. 7B). The fact that the La Pobla fans are enriched in Carboniferous clasts, while this lithology is absent in the Gurp basin, suggests that the Gurp and La Pobla systems were different fans with distinct catchment areas, but likely interfingered in a shared alluvial plain (Fig. 7B). The differential loading of the conglomerates and the retrogradation of the systems kept pumping salt towards the Senterada salt province, continuing the northward tilting of the conglomeratic basins (Fig. 8B).

Detrital AFT data from the upper Gurp and Pallaresa allogroups of the Gurp basin yield cooling ages between 75 and 55 My (Michael, 2013), reflecting the timing of the Nogueres sheet emplacement. The absence of younger detrital AFT ages from the Orri sheet is consistent with the evidence gathered from clast composition, indicating that the Nogueres thrust sheet was the main contributor to the upper fans in the Gurp basin (Beamud *et al.*, 2011).

By the start of the Oligocene, with the emplacement of the lower basement thrust sheets (Rialp and others, Muñoz *et al.*, 2018), the leading edge of the Nogueres thrust sheet was erosionally detached from its root (Fig. 8C). Sinking into the Keuper salt may partly account for the strong rotation and complete overturning of the Triassic layers of the Nogueres "*têtes plongéantes*". The immersion of the overturned thrust leading edge into the Senterada salt province, together with regional shortening, further mobilized of the underlying Keuper evaporites towards the salt diapirs. In a positive feedback loop, the loading of the conglomerates on top of the Triassic and the detached Paleozoic sheets accelerated their gravitational sinking in the salt (Fig. 8C). This caused the development of an E-W orientated sedimentary depression along the Senterada evaporite province (a "minibasin"). The locally sourced conglomerates were confined to this depression (Senterada basin), too low to be able to climb up the Cretaceous ridges to the south and overspill onto the La Pobla basin (Fig. 7C). Due to salt evacuation to the south, the Senterada basin depocentre progressively displaced to the north, and sediments onlapped the Paleozoic and Triassic outcrops (Fig. 8C).

The flat-lying, late Oligocene Antist allogroup had a wider catchment area, including Axial Zone granites and metamorphic clasts from the then exhumed Orri thrust sheet. Sedimentation of the lower members of the Antist allogroup was still confined to the Senterada trough (Fig. 7D), as attested by the position of the present day outcrops. It cannot be discarded that sedimentation of the Antist group could overspill the Senterada basin and cover the older conglomerates of the Gurp and La Pobla basin towards the south. This was suggested by Fillon *et al.* (2013) on the basis of

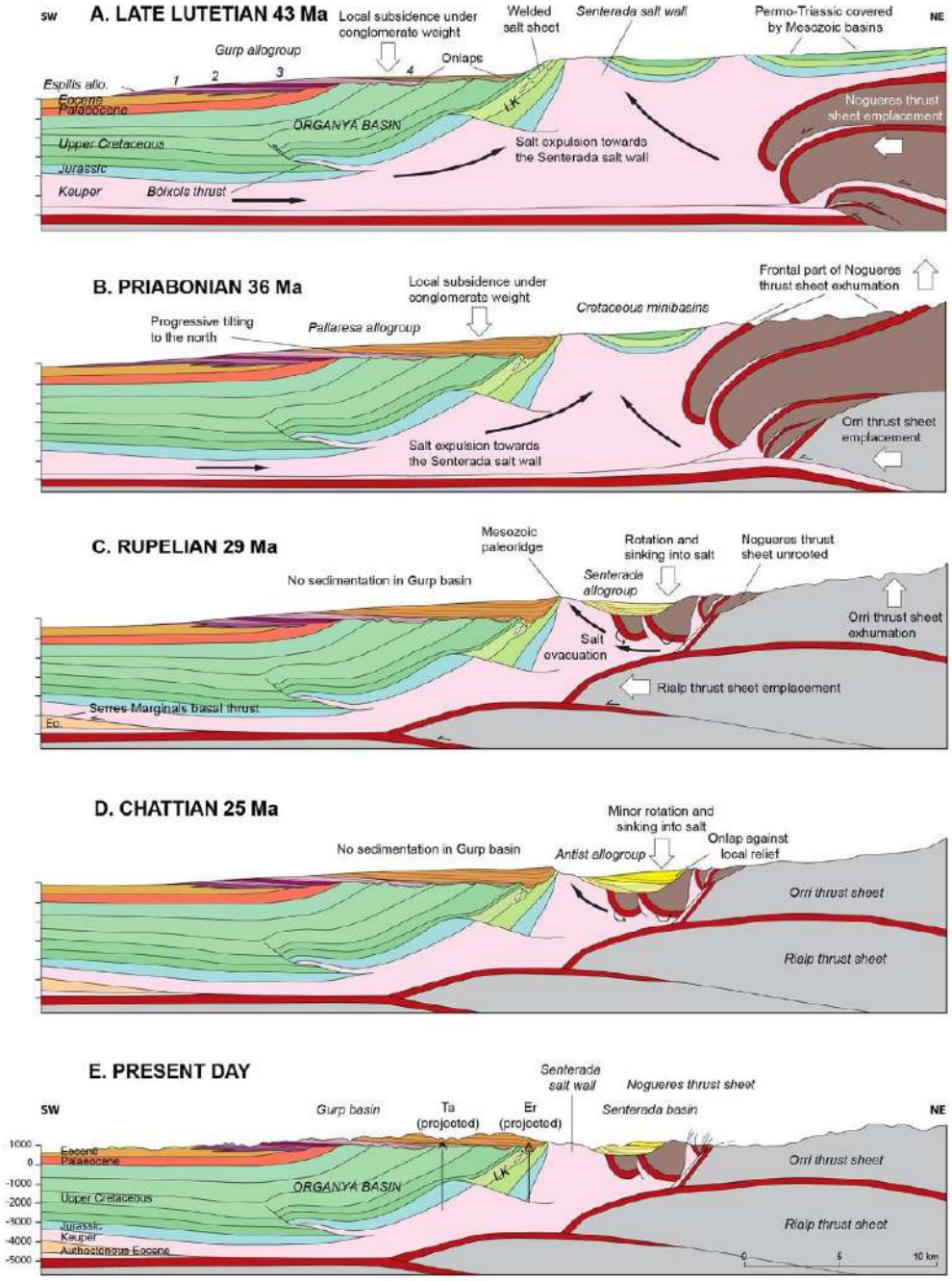

Fig. 8. Restored cross-sections of the sequential evolution (Late Lutetian to present day) of the northern margin of the Organyà basin and the adjacent salt province as a response of the growth of the Axial Zone antiformal stack and the differential loading by synorogenic alluvial sediments. Er: Erinyà well; Ta: Tamúrcia well.

thermochronology-derived burial data, although such upper conglomerate succession, if present, has been removed by erosion.

The sedimentation of the Antist conglomerates during the Chattian is contemporary to the Rialp thrust sheet emplacement. As interpreted by Teixell and Muñoz (2000) and Muñoz *et al.* (2018), the leading edge of the Rialp thrust sheet has significant displacement below the Senterada basin and even the northern edge of the Organyà basin (Fig. 8D). However, the basement thrusting did not translate in deformation of the Mesozoic cover or the Eocene-Oligocene conglomerates, which crop out flat and undeformed. A possible explanation for this is that the thick Keuper accumulations within the Senterada salt province promoted the complete decoupling between the basement and the cover above. In this case, shortening was accommodated by the expulsion of great volumes of salt through the exposed Senterada salt walls and the pumping of salt towards the foreland. A second interpretation is that the conglomerates and the Mesozoic cover do not register thrust uplift during the Rupelian because the Rialp thrust sheet did not reach that far south as interpreted. With this solution, the thick volumes of Keuper would not have extruded, and present day Senterada salt province would still have preserved several kms of vertical evaporite thickness underneath. In the restorations in Figure 8 we have followed the first approach, relying on the displacement attributed to Rialp thrust sheet by the authors cited above. We would like to emphasize again the large initial volumes of Keuper involved in either of the two interpretations.

8 Conclusions

In this study we present a reinterpretation of the evolution of the intramontane conglomeratic basins in the northern part of the Southern Pyrenees based on new field observations, clast counting and revisiting previous structural interpretations taking into account the recent advances in salt tectonics. The results are illustrated in new palaeogeographic maps and a representative cross-section sequentially restored at four stages from the late Lutetian to the late Oligocene of the La Pobla, Gurp and Senterada conglomeratic basins and their drainage areas. The maps and the restored cross-section highlight the role of the interplay between hinterland basement thrusting and Keuper salt migration in conditioning the dimensions and shape of the intramontane alluvial fan systems.

Diapirism is identified in the northern margin of the Organyà Mesozoic basin since the Early Cretaceous rifting times: thinning stratigraphy towards the Senterada salt province, progressive unconformities and interbedded Keuper lenses within the Lower Cretaceous carbonates and shales are strong evidence for salt movements in this epoch, as has been recently documented in this and other areas of the Southern Pyrenees by different authors. Consequently, we reinterpret the Morreres backthrust structure as a diapiric contact between the northern margin of the Organyà basin and the Senterada salt wall province.

During the Pyrenean contraction, the Senterada salt walls were exposed in the surface at least from the upper Ypresian to the Oligocene, as evidenced by the widespread presence of Triassic ophite clasts in all the conglomerate units. Alluvial fans sourced in the reliefs of the growing antiformal stack of the Axial Zone rapidly deposited the gravel load over a mobile salt-bearing substratum at its toe. From Lutetian times onwards, the differential load of the alluvial systems of the La Pobla and Gurp basins contributed to generate accommodation space and caused a moderate and progressive northward tilting of the northern Organyà basin margin, enabled by the expulsion of salt through the exposed Senterada salt province. This is reflected in the north-directed onlap of the Pessonada and Gurp conglomerates against the basal unconformity, opposite to the main sediment influx direction.

During the late Lutetian, the La Pobla basin was receiving only local sediment influx from the Mesozoic carbonates of the extensional minibasins (like those preserved today in the northern Ribagorçana valley) and northern Organyà basin margin. At the same time, the alluvial fans of Espills and Gurp allogroups drained from a much more extensive area; we propose that the North Pyrenean zone metamorphic and granite massifs sourced the gneiss, marble and granite pebbles, while the Siluro-Devonian limestones and slates were supplied by the Nogueres thrust sheet, not yet unrooted by erosion. By the Priabonian, the emplacement of the Orri thrust sheet had already uplifted the Nogueres thrust sheet and the topographic uplift of the antiformal stack initiated the migration of the watershed divide to the south. This is reflected in the increasing proportion of proximal lithologies derived from the Nogueres Zone in the Pallaresa allogroup fans, such as Permo-Triassic lithologies of the frontal part of the Nogueres sheet and Carboniferous Culm sandstone pebbles. The alluvial fans progressively retrograded to the north, infilling the palaeoreliefs of the northern Organyà basin. In any case, the total subsidence and Eocene-Oligocene strata rotation was moderate due to the thick Mesozoic succession existing between the fan conglomerates and the Keuper salt. The erosional unrooting of the Nogueres thrust sheet during the Oligocene enabled the sinking and rotation of the detached leading edge into the evaporites of the Senterada salt province, partly explaining their strong overturning. Subsidence was enhanced by the sedimentation of the Senterada and Antist conglomerates on top, which due to load-induced salt withdrawal kept trapped into the Senterada sedimentary depression, defined by the width of the salt province.

The study of the northern margin of the South-Pyrenean Central Unit revisits important observations regarding intramontane conglomerate geometries. With the addition of new structural and compositional data, and making use of salt tectonics concepts developed in the last decades we propose a new interpretation of the structural evolution of this complex area of the Southern Pyrenees. This study presents a good example of how halokinesis, induced by differential sedimentary loading, can interact with compressional structures and their erosion, having a strong effect in basin geometry and shaping of alluvial routing systems.

Acknowledgements. This work is part of projects CGL2014-54180-P and PGC2018-093903-B-C21 of the Spanish MINECO and MICIU. Discussion in the frame of the OROGEN project community is acknowledged. We also thank Frank Peel for comments and suggestions, and Guillem Piris and Norbert Caldera for assistance in field campaigns and the reviews by Jesús García-Senz and Hugh Sinclair, which helped to improve the original manuscript.

References

Barsó D. 2007. Análisis de la procedencia de los conglomerados sinorogénicos de La Pobla de Segur (Lérida) y su relación con la evolución tectónica de los Pirineos centro-meridionales durante el Eoceno medio-Oligoceno. Tesis de la Universitat de Barcelona.

Barsó D, Ramos E. 2007. Procedencia de los conglomerados sinorogénicos de La Pobla de. *Geogaceta* 41: 19–22.

Bartrina T, Hernández E. 1990. Las unidades evaporíticas del Triásico del subsuelo del Maestrazgo. In: Formaciones Evaporíticas de La Cuenca Del Ebro y Cadenas Periféricas y de La Zona de Levante. Nuevas Aportaciones y Guía de Superficie. Universitat de Barcelona, pp. 34–38.

Bataller JR. 1943. El Anoplotherium commune CUV. del Eocénico de Sossís. *Las Ciencias* 8.

Beamud E, Garcés M, Cabrera L, Muñoz JA, Almar Y. 2003. A new middle to late Eocene continental chronostratigraphy from NE Spain. *Earth and Planetary Science Letters* 216: 501–514. https://doi.org/10.1016/S0012-821X(03)00539-9.

Beamud E, Muñoz JA, Fitzgerald PG, Baldwin SL, Garcés M, Cabrera L, *et al.* 2011. Magnetostratigraphy and detrital apatite fission track thermochronology in syntectonic conglomerates: constraints on the exhumation of the South-Central Pyrenees. *Basin Research* 23: 309–331. https://doi.org/10.1111/j.1365-2117.2010.00492.x.

Beaumont C, Muñoz JA, Hamilton J, Fullsack P. 2000. Factors controlling the Alpine evolution of the central Pyrenees inferred from a comparison of observations and geodynamical models. *Journal of Geophysical Research* 105: 8121–8145. https://doi.org/10.1029/1999JB900390.

Berástegui X, García-Senz J, Losantos M. 1990. Tecto-sedimentary evolution of the Organyà extensional basin (central south Pyrenean unit, Spain) during the Lower Cretaceous. *Bulletin de la Societé Géologique de la France* 8: 251–264.

Calvet M, Gunnell Y, Laumonier B. 2020. Denudation history and palaeogeography of the Pyrenees and their peripheral basins: an 84-million-year geomorphological perspective. *Earth-Science Reviews*, in press. https://doi.org/10.1016/j.earscirev.2020.103436.

Cámara P, Flinch JF. 2017. The Southern Pyrenees: A Salt-Based Fold-and-Thrust Belt. *Permo-Triassic Salt Provinces of Europe, North Africa and the Atlantic Margins*: 395–415. https://doi.org/10.1016/B978-0-12-809417-4.00019-7.

Caus E, Rod D, Sire A. 1990. Stratigraphy of the Lower Cretaceous (Berriasian-Barremian) sediments in the Organyà Basin, Pyrenees, Spain. *Cretaceous Research* 11: 313–320.

Crusafont M, Vilalta J, Truyols J. 1956. Caracerización del Eoceno continental en la cuenca de Tremp y edad de la orogénesis pirenaica. *IIe Congr. Int. Etud. Pyr. Toulouse* 2: 29–53.

Ellis PG, McClay KR. 1988. Listric extensional fault systems – results of analogue model experiments. *Basin Research* 1: 55–70. https://doi.org/10.1111/j.1365-2117.1988.tb00005.x.

Fillon C, Gautheron C, van der Beek P. 2013. Oligocene–Miocene burial and exhumation of the Southern Pyrenean foreland quantified by low-temperature thermochronology. *Journal of the Geological Society* 170: 67–77. https://doi.org/10.1144/jgs2012-051.

Fillon C, van der Beek P. 2012. Post-orogenic evolution of the southern Pyrenees: Constraints from inverse thermo-kinematic modelling of low-temperature thermochronology data. *Basin Research* 24: 418–436. https://doi.org/10.1111/j.1365-2117.2011.00533.x.

Fitzgerald PG, Muñoz JA, Coney PJ, Baldwin SL. 1999. Asymmetric exhumation across the Pyrenean orogen: Implications for the tectonic evolution of a collisional orogen. *Earth and Planetary Science Letters* 173: 157–170. https://doi.org/10.1016/S0012-821X(99)00225-3.

García-Senz J. 2002. Cuencas extensivas del Cretácico Inferior en los Pirineos centrales, formación y subsecuente inversión. Phd thesis, Universitat de Barcelona.

García-Senz J, Muñoz JA. 2019a. The Late Albian to Middle Cenomanian Aulet and Las Aras Basins, in: Martín-Chivelet J, *et al.* Late Cretaceous Post-Rift to Convergence in Iberia. In: Quesada C, Oliveira J, eds. The Geology of Iberia: A Geodynamic Approach. Regional Geology Reviews. Springer International Publishing, pp. 320–324.

García-Senz J, Muñoz JA. 2019b. South Central Pyrenees: The Organyà Rift Basin, in: Martín-Chivelet J, *et al.* The Late Jurassic–Early Cretaceous Rifting. In: Quesada C, Oliveira J, eds. The Geology of Iberia: A Geodynamic Approach. Regional Geology Reviews. Springer International Publishing, pp. 169–249. https://doi.org/10.1007/978-3-030-11295-0_5.

García-Senz J, Pedrera A, Ayala C, Ruiz-Constán A, Robador A, Luis, *et al.* 2019. Inversion of the north Iberian hyperextended margin: the role of exhumed mantle indentation during continental collision. In: Hammerstein JA, Di Cuia R, Cottam MA, Zamora G, Butler RWH, eds. Fold and Thrust Belts: Structural Style, Evolution and Exploration. *Geological Society of London, Special Publications* 490. https://doi.org/10.1144/SP490-2019-112.

Garrido-Mejías A, Ríos LM. 1972. Síntesis geológica del Secundario y Terciario entre los ríos Cinca y Segre (Pirineo Central de la vertiente sur pirenaica, provincias de Huesca y Lérida. *Boletín Geológico y Minero* 83: 1–47.

Ge H, Jackson MPA, Vendeville BC. 1997. Kinematics and Dynamics of Salt Tectonics Driven by Progradation. *AAPG Bulletin* 81: 398–423. https://doi.org/10.1306/522B4361-1727-11D7-8645000102C1865D.

Gibson M. 2004. The localisation of erosional denudation during the growth and decay of the Pyrenean Orogen. PhD thesis. University of Edinburgh.

Grool AR, Huismans RS, Ford M. 2019. Salt décollement and rift inheritance controls on crustal deformation in orogens. *Terra Nova* 31: 562–568. https://doi.org/10.1111/ter.12428.

Howard L. 1993. The statistics of counting clasts in rudites: a review, with examples from the upper Palaeogene of southern California, USA. *Sedimentology* 40: 157–174. https://doi.org/10.1111/j.1365-3091.1993.tb01759.x.

Jourdon A, Mouthereau F, Le Pourhiet L, Callot J. 2020. Topographic and Tectonic Evolution of Mountain Belts Controlled by Salt Thickness and Rift Architecture. *Tectonics* 39. https://doi.org/10.1029/2019TC005903.

Jurado M. 1990. El Triásico y el Liásico basal evaporíticos del subsuelo de la cuenca del Ebro, in: Formaciones Evaporíticas de La Cuenca Del Ebro y Cadenas Periféricas, y de La Zona de Levante. ENRESA-GPPG, Universidad de Barcelona, pp. 21–28.

Lanaja J, Querol M, Navarro A. 1987. Contribución de la exploración petrolífera al conocimiento de la geología de España.

Lloret J, Ronchi A, López-Gómez J, Gretter N, De la Horra R, Barrenechea JF, *et al.* 2018. Syn-tectonic sedimentary evolution of the continental late Palaeozoic-early Mesozoic Erill Castell-Estac Basin and its significance in the development of the central Pyrenees Basin. *Sedimentary Geology* 374: 134–157. https://doi.org/10.1016/j.sedgeo.2018.07.014.

López-Martínez N, Civis J, Casanovas ML, Daams R. 1998. Geología y Paleontología del Eoceno de la Pobla de Segur (Lleida). Edicions i Publicacions de la Universitat de Lleida.

Lopez-Mir B, Muñoz JA, García Senz J. 2014. Restoration of basins driven by extension and salt tectonics: Example from the Cotiella Basin in the central Pyrenees. *Journal of Structural Geology* 69: 147–162. https://doi.org/10.1016/j.jsg.2014.09.022.

McClay K, Muñoz JA, García-Senz J. 2004. Extensional salt tectonics in a contractional orogen: A newly identified tectonic event in the Spanish Pyrenees. *Geology* 32: 737–740. https://doi.org/10.1130/G20565.1.

Mellere D. 1993. Thrust-Generated, Back-Fill Stacking of Alluvial Fan Sequences, South-Central Pyrenees, Spain (La Pobla De Segur Conglomerates). *Special publications International Association of Sedimentology* 20: 259–276. https://doi.org/10.1002/9781444304053.ch14.

Mellere D, Marzo M. 1992. Los depósitos aluviales sintectónicos de la Pobla de Segur: alogrupos y su significado tectonoestratigráfico. *Acta Geol Hispánica Volum homenatge a Oriol Riba* 27: 145–159.

Mencos J, Carrera N, Muñoz JA. 2015. Influence of rift basin geometry on the subsequent postrift sedimentation and basin inversion: The Organyà Basin and the Bóixols thrust sheet (south central Pyrenees). pp. 1452–1474. https://doi.org/10.1002/2014TC003692.Received.

Metcalf JR, Fitzgerald PG, Baldwin SL, Muñoz JA. 2009. Thermochronology of a convergent orogen: Constraints on the timing of thrust faulting and subsequent exhumation of the Maladeta Pluton in the Central Pyrenean Axial Zone. *Earth and Planetary Science Letters* 287: 488–503. https://doi.org/10.1016/j.epsl.2009.08.036.

Mey PHW. 1968. Geology of the Upper Ribagorzana valleys, Central Pyrenees, Spain. Leidse Geol. Mededelingen 41: 229–292.

Michael NA. 2013. The Functioning of Sediment Routing Systems Using a Mass Balance Approach: Example from the Eocene of the. https://doi.org/10.1086/673176.

Mouthereau F, Filleaudeau PY, Vacherat A, Pik R, Lacombe O, Fellin MG, *et al.* 2014. Placing limits to shortening evolution in the Pyrenees: Role of margin architecture and implications for the Iberia/Europe convergence. *Tectonics* 33: 2283–2314. https://doi.org/10.1002/2014TC003663.

Muñoz JA. 1992. Evolution of a continental collision belt: ECORS-Pyrenees crustal balanced cross-section. In: Thrust Tectonics. Dordrecht: Springer, pp. 235–246. https://doi.org/10.1007/978-94-011-3066-0_21.

Muñoz JA, Carrera N, Mencos J, Beamud E, Perea H, Arbués P, *et al.* 2009. 252-1-1 sheet, Tremp, 1:25000 geological map.

Muñoz JA, Mencos J, Roca E, Carrera N, Gratacós O, Ferrer O, *et al.* 2018. The structure of the South-Central-Pyrenean fold and thrust belt as constrained by subsurface data. *Geologica Acta* 16: 439–460. https://doi.org/10.1344/GeologicaActa2018.16.4.7.

Nijman W, Nio SD. 1975. The Eocene Montañana delta. In: Rosell J, Puigdefabregas C, eds. Sedimentary Evolution of the Paleogene South Pyrenean Basin. IAS 9th International Congress, Nice.

Ortí F, Pérez-López A, Salvany JM. 2017. Triassic evaporites of Iberia: Sedimentological and palaeogeographical implications for the western Neotethys evolution during the Middle Triassic – Earliest Jurassic. *Palaeogeography, Palaeoclimatology, Palaeoecology* 471: 157–180. https://doi.org/10.1016/j.palaeo.2017.01.025.

Ortuño M, Viaplana-Muzas M. 2018. Active fault control in the distribution of elevated low relief topography in the Central-Western Pyrenees. *Geologica Acta* 16: 499–518. https://doi.org/10.1344/GeologicaActa2018.16.4.10.

Peybernès B. 1976. Le Jurassique et le Crétacé inférieur des Pyrénées franco-espagnoles entre la Garonne et la Méditerranée. PhD thesis. Université Toulouse 3 (Paul Sabatier).

Reille JL. 1971. Les relations entre tectonogenése et sedimentation sur la vessant sud des Pyrenées Centrales. PhD thesis. Université de Montpellier.

Robles S, Ardévol L. 1984.Evolución paleogeográfica y sedimentológica de la cuenca palustre de Sossís (Eoceno superior, Prepirineo de Lérida): ejemplo de la influencia de su actividad de abanicos aluviales en el desarrollo de una cuenca lacustre asociada. *Publicaciones del departamento de estratigrafía de la UAB. Tomo homenaje a Luis Sánchez de la Torre* 20: 223–267.

Roigé M, Gómez-Gras D, Remacha E, Boya S, Viaplana-Muzas M, Teixell A. 2017. Recycling an uplifted early foreland basin fill: An example from the Jaca basin (Southern Pyrenees, Spain). *Sedimentary Geology* 360: 1–21. https://doi.org/10.1016/j.sedgeo.2017.08.007.

Rosell J, Gómez-Gras D, Luterbacher H, Llompart C. 1994a. Memoria del mapa geológico de la hoja n°252/33-11 (Tremp). 1:50.000 Segunda Serie (MAGNA). Primera edición. IGME.

Rosell J, Gómez-Gras D, Luterbacher H, Llompart C, Gabaldón V. 1994b. Mapa geológico de la hoja n°252 (Tremp), in: 1:50.000 Segunda Serie (MAGNA). Primera Edición. IGME.

Rosell J, Riba O. 1966. Nota sobre la disposición sedimentaria de los conglomerados de la Pobla de Segur (Província de Lérida). Zaragoza: Instituto de Estudios Pirenaicos, pp. 1–16.

Roure F, Choukroune P, Berástegui X, Muñoz JA, Villien A, Matheron P, *et al.* 1989. Ecors deep seismic data and balanced cross sections: Geometric constraints on the evolution of the Pyrenees. *Tectonics* 8: 41–50. https://doi.org/10.1029/TC008i001p00041.

Salvany JM, Bastida J. 2004. Análisis litoestratigráfico del keuper surpirenaico central. *Revista de la Sociedad Geológica de España* 17: 3–26.

Samsó JM, Cuevas JL, Mercadé L, Arbués P, Barberà X, Corregidor J, *et al.* 2010. 251-2-2 sheet, Espills, 1:25000 geological map.

Saura E. 2004. Anàlisi estructural de la zona de les Nogueres Pirineus Centrals. Tesi de la Universitat Autònoma de Barcelona.

Saura E, Ardèvol L, Teixell A, Vergés J. 2016. Rising and falling diapirs, shifting depocenters, and flap overturning in the Cretaceous Sopeira and Sant Gervàs subbasins (Ribagorça Basin, southern Pyrenees). *Tectonics* 35: 638–662. https://doi.org/10.1002/2015TC004001.

Saura E, Teixell A. 2006. Inversion of small basins: effects on structural variations at the leading edge of the Axial Zone antiformal stack (Southern Pyrenees, Spain). *Journal of Structural Geology* 28: 1909–1920. https://doi.org/10.1016/j.jsg.2006.06.005.

Séguret M. 1972. Étude tectonique des nappeset séries décollées de la partie centrale du vessant sud des Pyrénées. Caractère synsédimentaire, rôle de la compresion et de la gravité. PhD thesis. Univ. de Montpellier.

Séguret M. 1969. Carte géologique des têtes plongeantes des Nogueras : versant sud des Pyrénées centrales.

Sinclair HD, Gibson M, Naylor M, Morris RG. 2005. Asymmetric growth of the Pyrenees revealed through measurement and modeling of orogenic fluxes. *American Journal of Science* 305: 369–406. https://doi.org/10.2475/ajs.305.5.369.

Teixell A, Labaume P, Ayarza P, Espurt N, de Saint Blanquat M, Lagabrielle Y. 2018. Crustal structure and evolution of the Pyrenean-Cantabrian belt: A review and new interpretations from recent concepts and data. *Tectonophysics* 724–725: 146–170. https://doi.org/10.1016/j.tecto.2018.01.009.

Teixell A, Muñoz JA. 2000. Evolución tectono-sedimentaria Pirineo meridional durante el terciario: Una síntesis basada en la transversal del río Noguera Ribagorçana. *Revista de la Sociedad Geológica de España* 13: 251–264.

Trusheim F. 1960. Mechanism of salt migration in Northern Germany. *AAPG Bulletin* 44: 1519–1540.

Vacherat A, Mouthereau F, Pik R, Bellahsen N, Gautheron C, Bernet M, *et al.* 2016. Rift-to-collision transition recorded by tectono-thermal evolution of the northern Pyrenees Rift-to-collision transition recorded by tectonothermal evolution of the northern Pyrenees. *Tectonics* 35: 907–933. https://doi.org/10.1002/2015TC004016.

Vergés J. 1993. Estudi geològic del vessant sud del Pirineu oriental i central. Evolució cinemàtica en 3D. PhD thesis. Universitat de Barcelona.

Vergés J, Muñoz JA. 1990. Thrust sequences in the southern central Pyrenees. *Bulletin de la Societé Geologique de la France* 8: 265–271.

Vincent SJ. 2001. The Sis palaeovalley: a record of proximal fluvial sedimentation and drainage basin development in response to Pyrenean mountain building. *Sedimentology* 48: 1235–1276.

Whitchurch AL, Carter A, Sinclair HD, Duller RA, Whittaker AC, Allen PA. 2011. Sediment routing system evolution within a diachronously uplifting orogen: Insights from detrital zircon thermochronological analyses from the South-Central pyrenees. *American Journal of Science* 311: 442–482. https://doi.org/10.2475/05.2011.03.

Williams GD, Fischer MW. 1984. A balanced section across the Pyrenean Orogenic Belt. *Tectonics* 3: 773–780. https://doi.org/10.1029/TC003i007p00773.

Yelland AJ. 1991. Thermo-tectonics of the Pyrenees and Provence from fission track studies. PhD thesis from Birkbeck College. University of London.

Zwart HJ. 1979. The Geology of the Central Pyrenees. *Leidse Geologische Mededelingen* 1–74.

Appendix 1

Sample Unit	Mon10 Montlobar	Mon3 Espills	Mon4 Garp1	Mon6 Base Garp3	Mon11 Top Garp3	Garp2 Garp2	Garp3 Garp4	Garp5 Top Garp4	Garp6 Emita	Garp8 Campcan1	Garp9 Campcan1	Sen1 Santesdal	Sen2 Santesdal2	Sen13 Santesdal2	Mont01 Mont ophite b	Montsor2 Montsor middl	Montsor3 Montsor top	Montsor4 Montsor base
Ochre sandstone	0	0	0	0	0	0	0	0	7.8	15.6	0	5.9	0	0	0	0	0	0
Ochre calcarenite	0	12.2	0	0	0	0	0	0	0	0	0	0	0	0	0	0	0	0
Alveoline limestone	0	4.9	0	0	0	0	0	0	0	0	0	0	0	0	0	0	0	0
Micritic limestones	57.1	18.3	42.7	30.3	27.2	21.4	15.3	28.9	33.3	36.1	36.8	9	2.2	21.5	36.6	19.8	6.1	4.3
Grey limestone with white veins	7.1	1.2	5.3	1.1	3.7	0	0	13.2	8.9	7.2	4.7	0	0	0	0	0	0	3.2
Ochre bioclastic limestone	0	0	0	0	0	0	0	0	0	0	1.2	0	0	0	0	0	0	0
Bioclastic limestone	2.4	0	4	0	1.2	2.4	3.5	0	27.8	2.1	0	0	0	0	0	0	0	1.1
Orbitolina limestone	0	0	5.3	1.1	0	2.4	1.7	5.6	0	5.2	2.4	0	0	0	0	1	0	0
White limestone	0	0	0	0	0	0	0	0	4.4	0	0	0	0	0	0	0	0	0
Sparitic white limestone	0	0	0	0	0	0	0	0	2.2	0	0	0	0	0	0	0	0	0
Rudist limestone	1.2	1.2	4	0	0	6	1.7	4.4	1.1	4.1	0	0	0	0	0	0	0	0
Jurassic Breccia	0	0	0	0	0	0	0	2.2	0	0	0	0	0	0	2	0	0	1.1
Marl	1.2	0	0	0	0	0	0	0	2.2	0	0	0	0	0	0	0	0	0
Intraformational mudstone	0	0	0	0	0	0	0	0	1.1	0	0	0	0	0	0	0	0	0
Black colomite	0	0	0	0	0	0	0	0	0	0	0	0	0	0	4	0	0	0
Ophite	0	4.9	2.7	9	13.6	9.5	14.1	6.7	1.1	2.1	0	1	0	0	24.8	0	0	0
Buntsenstein conglomerate	0	0	0	0	0	0	0	0	0	2.1	7.1	7	6.7	1.1	1	5.2	20.4	3.2
Quartz	0	0	0	0	0	0	0	0	0	1	0	3	4.5	2.2	0	3.1	10.2	0
Permo-Triassic red sandstone	0	0	0	0	0	0	0	3.3	0	12.4	14.1	57	5.6	2.5	0.5	30.4	26.5	44.1
Buntsenstein white sandstone	0	0	0	0	0	0	0	0	0	1	10.6	8	3.4	1.1	0	3.1	5.3	8.6
Pumice	0	0	0	0	0	0	0	0	0	0	0	0	1.1	0	0	0	0	0
Permo-Triassic breccia	0	0	0	0	0	0	0	0	0	1	2.4	0	0	0	0	0	0	0
Permo-Triassic Calche	0	0	0	0	0	0	0	0	0	0	0	4	0	0	0	0	0	0
Grisite limestone	0	0	0	0	0	0	0	0	0	0	0	0	1.1	1.1	0	2.1	1	0
Red limestone	0	0	0	0	0	0	0	0	2.2	0	0	0	0	0	0	0	0	0
Urgonian-Devonian limestone	0	0	0	0	0	0	0	0	0	0	0	2	4.5	0	0	0	0	0
Devonian limestone	6	14.6	13.3	11.2	16.5	8.3	24.7	11.1	0	19.6	11.8	10	58.4	46.4	5.5	33.3	22.4	18.3
Ochre limestone	2.4	0	0	0	0	0	0	0	0	0	0	0	0	0	0	0	0	0
Devonian limestone with chimneys	0	0	0	0	0	0	0	0	0	0	0	0	0	7.5	2.7	0	0	0
Calcarous slate, calcschist	4.8	29.3	13.3	29.2	19.8	36.9	12.9	7.8	0	4.1	0	0	4.5	12.9	0	0	1	0
Culm sandstone	0	0	0	0	0	0	0	0	0	0	0	0	0	0	2	19.8	6.1	16.1
Carboniferous slate	0	0	0	0	0	0	0	0	0	0	0	0	0	0	2	0	0	0
Black lutite shale	0	8.5	1	10.1	3.7	8.3	20	2.2	0	1	0	0	0	0	0	0	0	0
Black shale with andalusite	0	2.4	0	5.6	0	2.4	0	0	0	0	0	0	0	0	0	0	0	0
limestone with andalusite	0	0	5.3	0	8.6	0	2.4	3.3	0	0	1.2	0	0	0	0	0	0	0
Marble	0	0	0	1.1	0	0	0	0	0	0	0	0	0	0	1	0	0	0
Marble limestone	15.5	0	2.7	0	3.7	1.2	3.5	4.4	0	0	0	0	0	0	0	0	0	0
Black limestone with pyrite	1.2	0	0	0	0	0	0	0	0	0	0	0	0	0	0	0	0	0
Foliated quartz	1.2	0	0	0	0	0	0	0	0	0	0	0	0	0	0	0	0	0
Gneiss	0	3.2	0	0	0	0	0	0	0	0	0	0	0	0	0	0	0	0
Cambro-ordovician Schist	0	0	0	0	0	0	0	0	0	0	0	0	0	0	1.1	0	0	0
Quartzite	0	0	0	0	0	0	0	0	0	0	0	0	0	0	1.1	0	0	0
Granite	0	1.2	0	0	1.2	0	1.2	0	0	0	0	0	0	0	0	2.1	1	0
Total	100	100	100	100	100	100	100	100	100	100	100	100	100	100	100	100	100	100

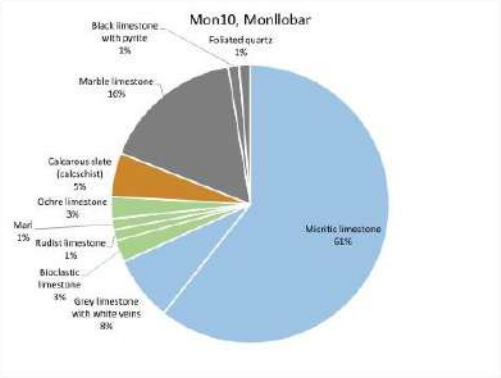
Mon10, Monllobar
Black limestone with pyrite 1%
Foliated quartz 1%
Marble limestone 16%
Calcareous slate (calcschist) 5%
Ochre limestone 3%
Marl 1%
Rudist limestone 1%
Bioclastic limestone 3%
Grey limestone with white veins 8%
Micritic limestone 61%

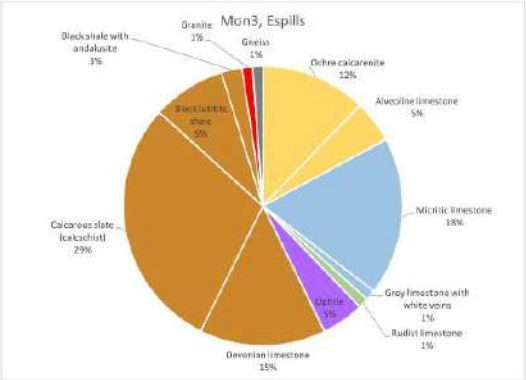
Mon3, Espills
Granite 1%
Gneiss 1%
Black shale with andalusite 3%
Ochre calcarenite 12%
Alveoline limestone 5%
Black lutitic shale 5%
Micritic limestone 18%
Calcareous slate (calcschist) 29%
Gray limestone with white veins 1%
Ophite 5%
Rudist limestone 1%
Devonian limestone 15%

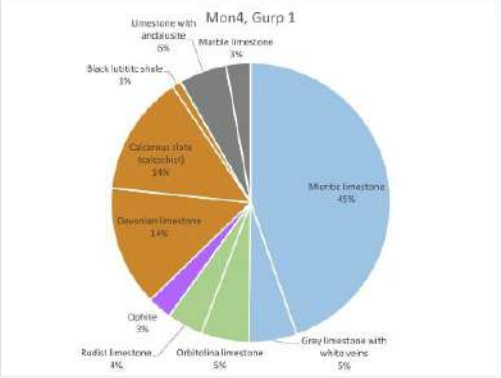
Mon4, Gurp 1
Limestone with andalusite 6%
Marble limestone 3%
Black lutitic shale 3%
Calcareous slate (calcschist) 14%
Micritic limestone 45%
Devonian limestone 14%
Ophite 3%
Rudist limestone 4%
Orbitolina limestone 5%
Gray limestone with white veins 5%

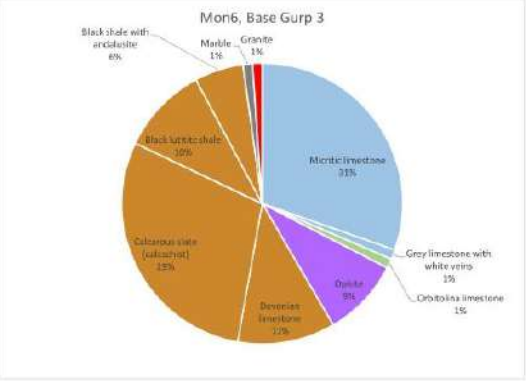
Mon6, Base Gurp 3
Black shale with andalusite 6%
Marble 1%
Granite 1%
Black lutitic shale 10%
Micritic limestone 31%
Calcareous slate (calcschist) 15%
Gray limestone with white veins 1%
Ophite 9%
Orbitolina limestone 1%
Devonian limestone 22%

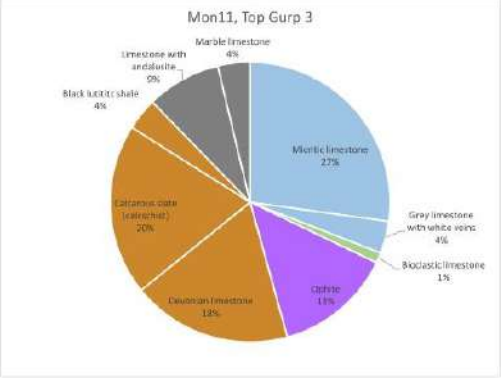
Mon11, Top Gurp 3
Marble limestone 4%
Limestone with andalusite 9%
Black lutitic shale 4%
Micritic limestone 27%
Calcareous slate (calcschist) 20%
Gray limestone with white veins 4%
Bioclastic limestone 1%
Ophite 18%
Devonian limestone 18%

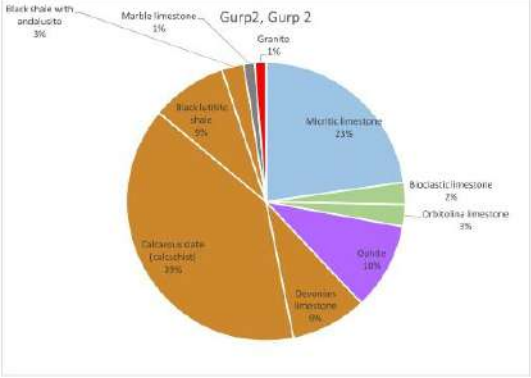
Gurp2, Gurp 2
Black shale with andalusite 3%
Marble limestone 1%
Granite 1%
Black lutitic shale 9%
Micritic limestone 23%
Bioclastic limestone 2%
Orbitolina limestone 3%
Calcareous slate (calcschist) 23%
Ophite 18%
Devonian limestone 6%

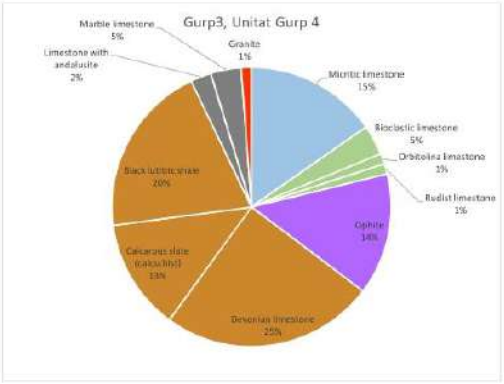
Gurp3, Unitat Gurp 4
Marble limestone 5%
Granite 1%
Limestone with andalusite 2%
Micritic limestone 15%
Bioclastic limestone 5%
Orbitolina limestone 1%
Rudist limestone 1%
Ophite 14%
Devonian limestone 25%
Calcareous slate (calcschist) 13%
Black lutitic shale 20%

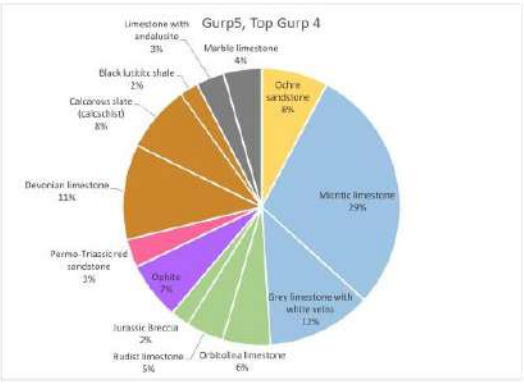
Gurp5, Top Gurp 4
Limestone with andalusite 3%
Marble limestone 4%
Black lutitic shale 2%
Calcareous slate (calcschist) 8%
Ochre sandstone 8%
Devonian limestone 11%
Micritic limestone 29%
Permo-Triassic red sandstone 3%
Ophite 7%
Grey limestone with white veins 12%
Jurassic breccia 2%
Rudist limestone 5%
Orbitolina limestone 6%

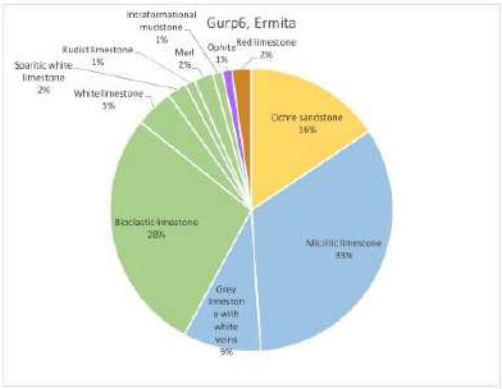
Gurp6, Ermita
Intraformational mudstone 1%
Rudist limestone 1%
Marl 2%
Ophite 1%
Red limestone 2%
Sparitic white limestone 2%
White limestone 5%
Ochre sandstone 16%
Micritic limestone 33%
Bioclastic limestone 28%
Grey limestone with white veins 9%

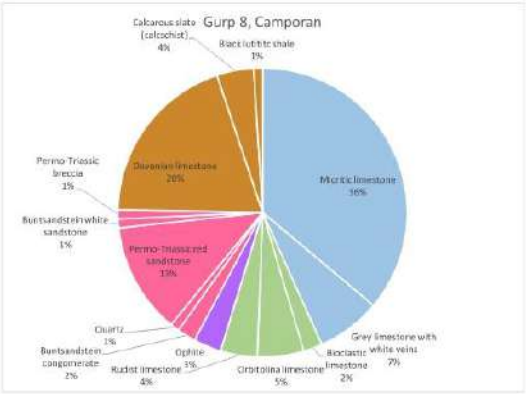
Gurp 8, Camporan
Calcareous slate (calcschist) 4%
Black lutitic shale 3%
Permo-Triassic breccia 1%
Devonian limestone 20%
Micritic limestone 36%
Buntsandstein white sandstone 1%
Permo-Triassic red sandstone 13%
Quartz 1%
Buntsandstein conglomerate 2%
Ophite 1%
Rudist limestone 4%
Orbitolina limestone 5%
Bioclastic limestone 2%
Grey limestone with white veins 7%

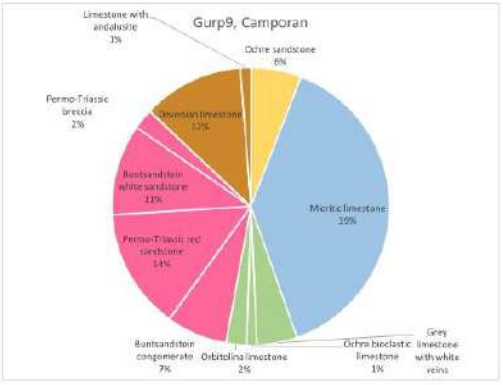
Gurp9, Camporan
Limestone with andalusite 1%
Ochre sandstone 6%
Permo-Triassic breccia 2%
Devonian limestone 12%
Buntsandstein white sandstone 11%
Micritic limestone 39%
Permo-Triassic red sandstone 14%
Buntsandstein conglomerate 7%
Orbitolina limestone 2%
Ochre bioclastic limestone 1%
Grey limestone with white veins

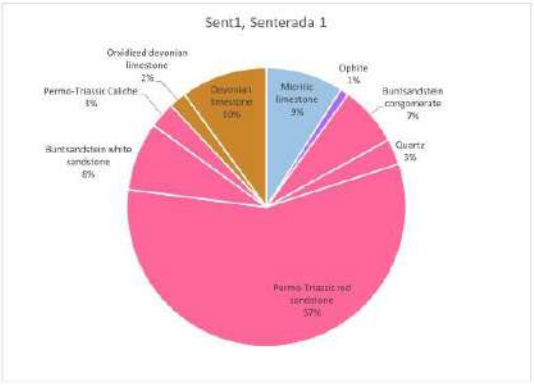
Sent1, Senterada 1
Oriédicel devonian limestone 2%
Permo-Triassic Caliche 3%
Devonian limestone 10%
Micritic limestone 9%
Ophite 1%
Buntsandstein conglomerate 7%
Quartz 3%
Buntsandstein white sandstone 8%
Permo-Triassic red sandstone 57%

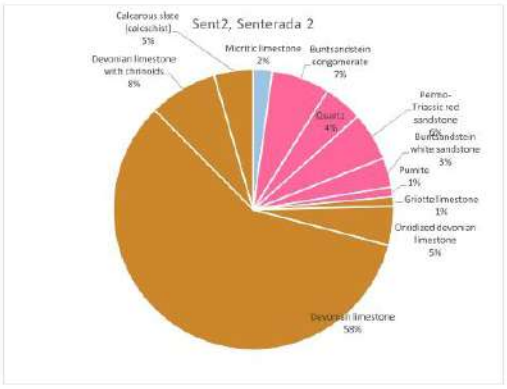

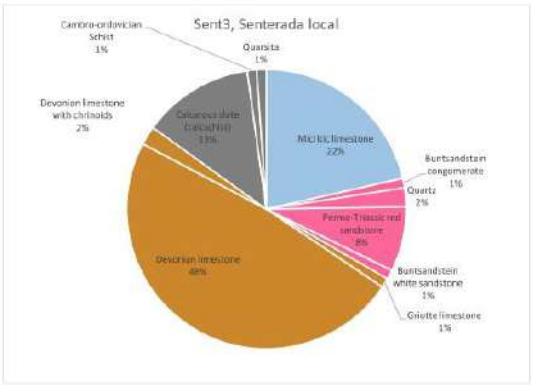

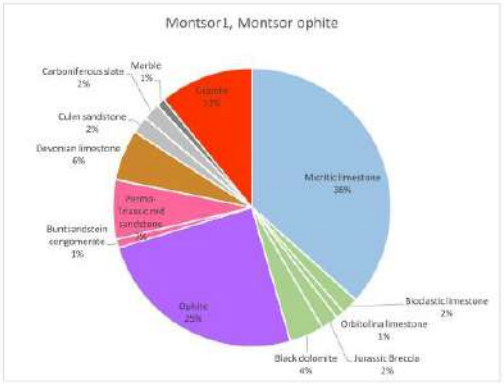

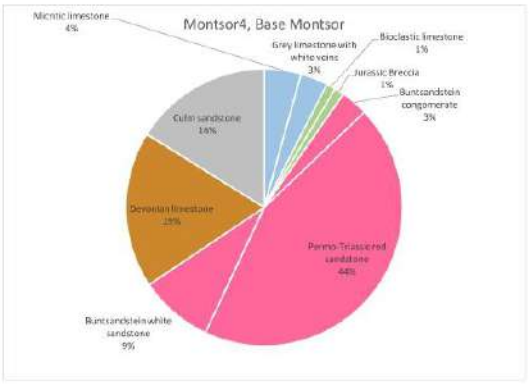

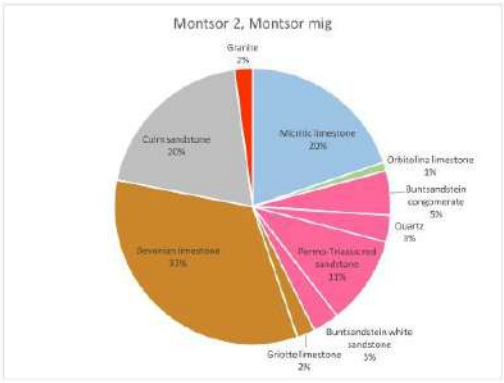

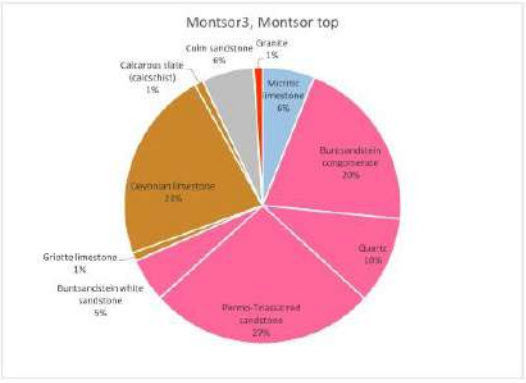

Cite this article as: Burrel L, Teixell A, Gómez-Gras D, Coll X. 2021. Basement-involved thrusting, salt migration and intramontane conglomerates: a case from the Southern Pyrenees, *BSGF - Earth Sciences Bulletin* 192: 24.

Annex 2

Altres Publicacions

En l’annex 2 s’incorporen els articles publicats en el número 61 de la Revista semestral de Ciencias de la Tierra GEOGACETA.

X. Coll ha col·laborat en les campanyes de camp, la discussió dels resultats, la redacció i edició del text, i la elaboració i edició de figures.

1.- Coll, X., Gómez-Gras, D., Roigé, M., & Mestres, N. (2017). Heavy-mineral assemblages as a provenance indicator in the Jaca basin (Middle-Late Eocene, southern Pyrenees). Geogaceta, 61, 159-162.

2.- Gómez-Gras, D., Collado, R., Coll, X., & Roigé, M. (2017). Caracterización composicional de las areniscas del Cretácico Superior en las Sierras Marginales y Exteriores (cuenca surpirenaica): análisis mediante minerales pesados y petrografía óptica. Geogaceta, 61, 163-166.

GEOGACETA, 61, 2017

Heavy-mineral assemblages as a provenance indicator in the Jaca basin (Middle-Late Eocene, southern Pyrenees)

Asociaciones de Minerales pesados como indicadores de procedencia en la cuenca de Jaca (Eoceno Medio-Tardío, sector central surpirenaico)

Xavier Coll[1], David Gómez-Gras[1], Marta Roigé[1] Narcís Mestres[2]

[1] Departament de Geologia, Facultat de Ciències, Universitat Autònoma de Barcelona, 08193 Bellaterra (Barcelona), España. xcc021285@gmail.com, david.gomez@uab.cat, roige.marta@gmail.com

[2] Institut de Ciència de Materials de Barcelona ICMAB, Consejo Superior de Investigaciones Científicas CSIC, Campus UAB, 08193 Bellaterra, Catalonia, Spain. narcis.mestres@icmab.es

ABSTRACT

The Jaca sequence records a major paleogeographic change in the south-central-pyrenean basin, recorded by the replacement of the deep-marine Hecho Group turbidites (Upper Lutetian) by deltaic and alluvials (Bartonian-Priabonian). This work studies the heavy-mineral assemblages of the Eocene clastic systems in the northern Jaca basin, applying optical analysis and Raman spectroscopy. All the clastic systems display impoverished heavy-mineral suites, mainly constituted by titanium oxides, apatite, zircon and tourmaline. Other heavy minerals, as staurolite, weathered pyrite, goethite and hematite, are found in the alluvial systems. Our results show a major heavy-mineral content shift along the transition from turbidites to shallow-water and continental deposits. The turbiditic systems display high content of apatite sourced from the Axial Zone in the eastern Pyrenees, whereas the alluvial systems are characterized by a heavy-mineral suite containing goethite and staurolite. The shift is here interpreted as related to the onset of the Gavarnie thrust, which resulted in the uplift and recycling of the turbidites as well as the exhumation of Paleozoic basement, located to the north of the Jaca basin.

Key-words: *Pyrenees, Jaca basin, heavy minerals, provenance.*

RESUMEN

La secuencia de Jaca registra un cambio paleogeográfico importante en la cuenca surpirenaica central, registrado por la sedimentación marina, representada por las turbiditas del Grupo de Hecho (Luteciense), por ambientes deltaicos y aluviales (Bartoniense-Priaboniense). Este trabajo estudia las asociaciones de minerales pesados de los sistemas clásticos eocenos de la parte norte de la cuenca de Jaca, mediante el análisis petrográfico y la espectrometría Raman. Todos los sistemas muestran asociaciones empobrecidas, constituidas básicamente por óxidos de titanio, apatito, zircón y turmalina. En los sistemas aluviales, en cambio, se identifican otros minerales, como estaurolita, pirita alterada, goethita y hematites. Los resultados muestran un cambio importante en las asociaciones de minerales pesados en la transición desde los depósitos turbidíticos hasta los someros y continentales. Los sistemas turbidíticos muestran elevadas proporciones de apatito, con un área fuente en la Zona Axial de los Pirineos Orientales, mientras que los sistemas aluviales se caracterizan por un contenido elevado en goethita y por la presencia de estaurolita. Se interpreta que el cambio se relacionaría con el inicio del emplazamiento del cabalgamiento de Gavarnie, que provocó el levantamiento de las turbiditas y la exhumación del basamento paleozoico al norte de la cuenca de Jaca.

Palabras clave: *Pirineos, cuenca de Jaca, minerales pesados, procedencia.*

Geogaceta, 61 (2017), 159-162
ISSN (versión impresa): 0213-683X
ISSN (Internet): 2173-6545

Recepción: 14 de julio de 2016
Revisión: 3 de noviembre de 2016
Aceptación: 25 de noviembre 2016

Introduction

The Jaca sequence (Remacha *et al.*, 1987) records a main paleogeographic change from the deep-marine sedimentation stage, recorded by the Upper Hecho Group turbidites (Upper Lutetian), to the generalization of terrestrial sedimentation in the Priabonian.

Although provenance constraints for these systems have been based on paleocurrents (Puigdefàbregas, 1975; Oms, 1994; Oms and Remacha, 1992; Remacha and Fernández, 2003, Remacha and Picart, 1991) and sandstone petrography (Daza, 2010; Roigé *et al.*, 2013, 2016), their heavy-mineral content remains unknown.

Because of precise conditions of formation, many heavy minerals, provide diagnostic information for provenance interpretation, as well as for tectonic setting, that other studies or provenance tools cannot provide (Mange-Ratgetzky and Murer, 1991; Morton and Hallsworth, 1999).

This paper explores the use of heavy-mineral assemblages as provenance indicators for the clastic systems of the northern Jaca basin. Heavy minerals have been studied by means of optical petrography and Raman spectroscopy.

Geological setting

The study area is located in the Tertiary Jaca Basin (South-Central Pyrenees; Labaume *et al.*, 1985; Canudo y Molina, 1988; Hogan and Burbank, 1996). The studied systems (Figs. 1 and 2) are the Banastón and Jaca turbidite systems, the Sabiñánigo and

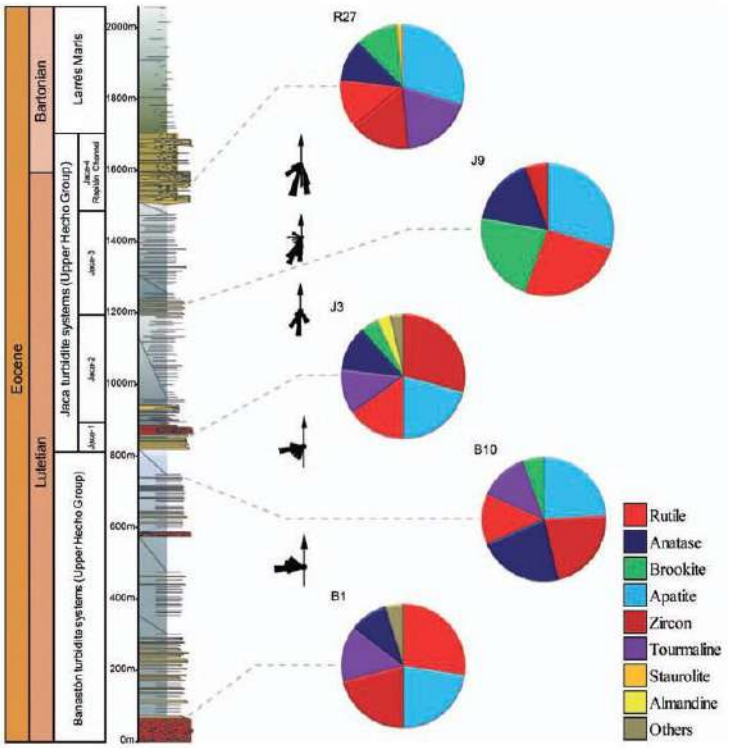

Fig. 1.- Pie charts showing the heavy-mineral assemblages of the turbidite systems. The stratigraphic log is from Roigé *et al.* (2016), where the sample locations can be observed; palaeocurrent data are from Oms, 1994; Oms and Remacha, 1992; Remacha and Fernández, 2003, Remacha and Picart, 1991).

Fig. 1.- Gráficos circulares mostrando las asociaciones de minerales pesados de los sistemas turbidíticos con indicación de la posición de las muestras analizadas. Columna estratigráfica tomada de Roigé et al. *(2016), trabajo en el que se puede apreciar la localización de las muestras; las direcciones de paleocorrientes proceden de Oms, 1994; Oms and Remacha, 1992; Remacha and Fernández, 2003, Remacha and Picart, 1991).*

Atarés delta systems, the Santa Orosia alluvial system and the Canciás alluvial fan.

The Banastón and Jaca turbidite systems belong to the Upper Hecho Group (Remacha and Fernández, 2003). The Banastón system in the study area is constituted by distal turbidites (sandstones and shales) with three interleaved carbonate megaturbidites. Sediments were fed from the east (Remacha *et al.*, 2005), from a source area located in the emerged eastern Pyrenees (Puigdefàbregas *et al.*, 1992; Teixell 1998; Caja *et al.*, 2010).

The Jaca turbidite systems form four composite depositional sequences (CDS 1-4 from Remacha and Picart, 1991). The lower composite depositional sequences (Jaca-1, Jaca-2, Jaca-3) show a composition similar to that of the Banastón systems. By contrast, Jaca-4 (represented by the Rapitán channel-levee complex) displays an increase of sandstone and subvolcanic rock fragments (Roigé *et al.*, 2016). This compositional variation suggests a change of source area related to the Lakora thrust emplacement, which would have created a new source area to the North. The Rapitán channel-levee complex is genetically related to the overlying Sabiñánigo delta, with the turbidites being transitionally replaced by the Sabiñánigo prodeltaic marls (Larrés marls).

The Sabiñánigo Sandstone constitutes a delta system, which prograded towards the SW (Puigdefàbregas, 1975) and comprises prodeltaic and shelfal deposits. Paleocurrent directions suggest sediment input coming from the E and NE, although an additional SE input cannot be precluded (Remacha *et al.*, 1987). This system was fed by two different source areas, located to the north and east, respectively (Roigé *et al.*, 2016). The presence of carbonate extrabasinal clasts and detrital monocrystalline dolomite grains is interpreted to reflect a source area constituted by Mesozoic rocks of the South-Central Pyrenean Unit (Roigé *et al.*, 2013, 2016). The existence of hybrid sandstone clasts is attributed to an early erosion of the turbidite basin (Roigé *et al.*, 2013, 2016).

The Sabiñánigo sandstone is transitionally overlain by the Pamplona marls, which would represent outer shelf deposits and also form the prodelta of the next delta system, the Atarés delta system (Oms and Remacha, 1992).

The Atarés delta systems (Fig. 2) is mostly made of flood-dominated delta front deposits fed from the east (Puidefàbregas, 1975; Oms and Remacha, 1992, Roigé *et al.*, 2016). The Sabiñánigo and Atarés sandstones display the same composition, having the former higher proportions of plutonic and subvolcanic rock fragments (Roigé *et al.*, 2016).

The Santa Orosia fan is characterized by thick conglomeratic beds interlayered with red shales. The source area of this fan is interpreted lie to the N and NE, suggested by a higher proportion of recycled sandstones from the Hecho Group (Roigé *et al.*, 2016). Therefore, a change in the source area occurred between the Sabiñánigo and Atarés delta systems and the Santa Orosia fan, which suggests a major paleogeographic change, which would be related to the onset of the Gavarnie thrust.

The upper Priabonian Santa Orosia alluvial fan marks the beginning of generalized terrestrial sedimentation in the Jaca basin. The continentalization of the basin took place by the diachronic irruption from east to west of the Canciás, Peña Oroel and San Juan de la Peña fans (Late Eocene-Oligocene).

Methodology

Sandstones and conglomerates samples were collected in the Jaca and Yebra de Basa areas. They were crushed, sieved and submitted to vibrating water separation table and to acid digestion with diluted 10% acetic acid (CH_3COOH) prior to heavy mineral separation.

Gravity settling process was done using the none-toxic liquid sodium polytungstate [$Na_6(H2W_{12}O_{40})$]. The recovered heavy minerals of each sample were mounted on slides.

Mineral identification (up to 200 grains per slide) was done under the polarising microscope, whereas opaque, turbid and dubious grains were identified using Raman spectroscopy. This inelastic light-scattering technique is based on the vibrational properties of solids, liquids and gases and the resulting Raman spectra depend on structure and composition. Acquired spectra were compared with reference spectra from several databases and published papers (www.rruff.info; Andó y Garzanti, 2014).

Diagenetic, carbonate and micaceous minerals were eliminated because they do not provide valuable information in provenance analysis.

Results and discussion

Turbidite and deltaic systems are characterized by the highest contents of apatite (Figs. 1 and 2), being higher than 20% in all samples, together with high contents of titanium oxides. Conversely, alluvial systems (Fig. 2) show a very low apatite content (<8%), excepting the Canciás alluvial fan (22,9%, JY36).

Apatite is commonly an accessory mineral of igneous rocks, most often related to granites. It is a stable mineral under deep burial conditions, so it may have a multicycle origin (Mange-Ratjetzky and Murer, 1991). According to paleocurrents by Remacha and Fernández (2003) and sediment composition (Roigé *et al.*, 2016), the Banastón and Jaca turbiditic systems have an eastern source area. High amounts of feldspar and plutonic rock fragments indicate exhumation of Paleozoic granitoids from the Axial Zone in the eastern Pyrenees (Roigé *et al.*, 2016), which are interpreted as the most likely source for apatite in the present study. Paleocurrents from Remacha y Picard (1991) and the presence of high amounts of carbonate extrabasinal fragments and detrital monocrystalline dolomite grains indicate an eastern origin for these systems (Roigé *et al.*, 2016), which also supports an eastern provenance for apatite. Evidence suggests that apatite is supplied directly from an eastern source area, however its presence in some of the north-sourced deposits (Canciás fan i.e.) must be related to the recycling of the Hecho Group turbidites.

Alluvial systems (Fig. 2), are characterized by very high contents of goethite plus hematite (mainly goethite, up to >60%), which are not present in the former systems. Alluvial fans are also characterized by the lowest contents of apatite (<8%) except for the Canciás alluvial system, where apatite content is higher than 20%. Another characteristic feature of all these systems is the presence of staurolite, which is absent in the former systems but the The Rapitán channel-levee complex (R27) and the lower Sabiñánigo Sandstone (JY2).

The Banastón and Jaca turbidite systems, the Rapitán complex included, display a high content of pyrite grains often related to calcite. Roigé *et al.* (2016) reported the occurrence of foraminifera that are commonly pyritized mainly in the Banastón and Jaca turbidites. Pyritization is a process that occurs in the water-sediment interface where both aerobic and anaerobic bacteria are found. Therefore, a diagenetic origin is deduced for the pyrite of the turbidite and deltaic systems.

Conversely, this diagenetic origin cannot be invoked for pyrite in alluvial fans. The abundance of pyrite in the alluvial systems is low if compared to the turbidite and deltaic systems. On the contrary, these alluvial systems display a high content of hematite and goethite, which display the opposite pattern of abundance. Pyrite oxidation leads to formation of hematite and goethite, therefore, both are interpreted to be derived from pyrite grains and pyrite-bearing bioclasts recycled from turbidite and deltaic deposits, being a clear signal of sediment recycling and a northern provenance.

Staurolite is almost exclusively a product of medium-grade metamorphism. It forms in mica schists derived from argillaceous sediments (Mange-Ratjetzky and Murer 1991) and constitutes a diagnostic mineral of the

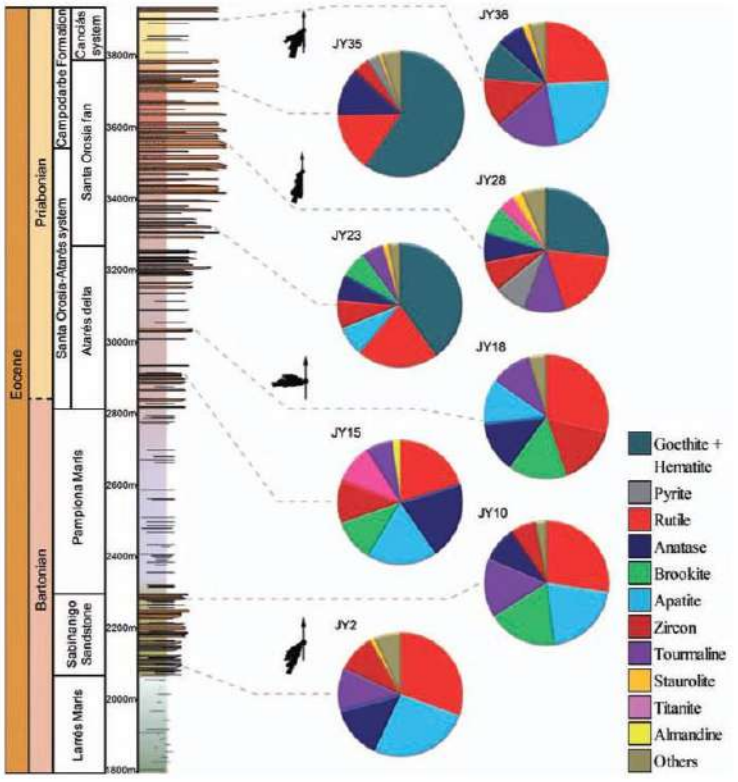

Fig. 2.- Pie charts showing the heavy-mineral assemblages of the deltaic and alluvial systems. The stratigraphic log is from Roigé *et al.* (2016), where the sample locations can be observed; palaeocurrent data are from Oms, 1994; Oms and Remacha, 1992; Remacha and Fernández, 2003, Remacha and Picart, 1991).

Fig. 2.- Gráficos circulares mostrando las asociaciones de minerales pesados de los sistemas turbidíticos con indicación de la posición de las muestras analizadas. Columna estratigráfica tomada de Roigé et al. *(2016), trabajo en el que se puede apreciar la localización de las muestras; las direcciones de paleocorrientes proceden de Oms, 1994; Oms and Remacha, 1992; Remacha and Fernández, 2003, Remacha and Picart, 1991).*

amphibolite grade of metamorphism. Roigé *et al.* (2016) reported the occurrence of metamorphic rock fragments, mainly from schists, in the Santa Orosia and Canciás fans. Puigdefàbregas (1975) documented a northern input for the Santa Orosia and Canciás alluvial fans, based on paleocurrents and facies architecture. A northern provenance has also been suggested for the Santa Orosia fan according to its sandstone composition (Roigé *et al.*, 2013, 2016).

The Rapitán complex is the only turbidite, system that records a northern provenance, through a content increase of subvolcanic rocks and sandstone rock fragments, which points to a northern provenance related to the emplacement of the Eaux-Chaudes/Lakora thrust (Roigé *et al.*, 2013, 2016). Thus, the presence of staurolite only in systems fed from the north suggests a northern provenance for this mineral. Furthermore, schists of the amphibolite metamorphic facies occur at north, in the Gavarnie and Chiroulet massifs (Barnolas and Chiron, 1996). Therefore, in this work, the presence of staurolite is interpreted as a sensitive indicator of a northen provenance from newly exhumed source areas to the north of the Jaca basin.

Conclusions

Staurolite is an indicator of a northen input and points to a source area constituted by amphibolite facies of metamorphism occurring to the north of the Jaca basin.

Apatite is related to granitic rocks and indicates an eastern provenance related with the Axial Zone in the eastern Pyrenees, where granites were exhumed.

Goethite grains, resulting from pyrite weathering, are clear indicators of sediment recycling.

An eastern provenance for the turbiditic systems of Banastón and Jaca is indicated by their heavy-mineral suites rich in apatite, whereas the first occurrence of staurolite in the Rapitán complex indicates a change in source area. The emplacement of the Eaux-Chaudes/Lakora thrust, which took place at the northern margin of the foreland basin during Rapitán times led to the uplift of new source areas to the north and the exhumation of a Paleozoic basement.

The decrease in apatite content, the presence of staurolite and the high indexes of sediment recycling, evidenced by high contents of goethite, in the Santa Orosia and Canciás alluvial-fan systems indicate a northern provenance with minor input form granitic rocks. This compositional change is related to the onset of the Gavarnie thrust, which again uplifted an area to the north of the Jaca basin. The uplift allowed the erosion of the turbidites producing a heavy-mineral suite rich in recycled pyrite (goethite). Paleozoic basement was also exhumed in some areas and supplied staurolite to the foreland basin.

Acknowledgments

This paper is a contribution to the project CGL2014-54180-P, financed by the Ministerio de Economía y Competitividad of Spain. We are very grateful to the reviewers and to the editors for their helpful comments to improve the manuscript.

References

Andò, S. and Garzanti, E. (2014). Geological Society, London, Special Publications 386, 395-412.

Barnolas, A. and Chiron, J.C. (1996). *Synthèse Géologique et Géophysique des Pyrénées vol. 1: Introduction*. Géophysique. Cycle Hercynien. Ed. BRGM-IGTE.

Caja, M.A., Marfil, R., García, D., Remacha, E., Morad, S., Mansurbeg, H., Amorisi, A., Martínez-Calvo, C. and Lahoz-Beltrá, R. (2010). *Basin Research* 22, 157-180.

Canudo, J. I. and Molina, E. (1988). In: *II Congreso Geológico de España*. Comunicaciones 1, 273-276.

Daza, R. (2010). *Procedencia de las areniscas de los sistemas turbidíticos de la secuencia de Jaca (UTS 5, Grupo de Hecho): Comparación con los sistemas coetáneos de la cuenca de Aínsa*. Tesis de Máster, Univ. Autònoma de Barcelona.

Hogan, P.J. and Burbank, D. (1996). In: *Tertiary Basins of Spain* (P. Friend y C. Dabrio, Eds.). Cambridge University Press, Cambridge, 153-160.

Labaume, P., Seguret, M. and Seyve, C. (1985). *Tectonics* 4, 661-685.

Mange-Rajetzky, M.A. and Murer, H. F.W. (1991). *Heavy minerals in Colour*. Chapman & Hall, London, 147 p.

Morton, A. C. and Hallsworth, C. R. (1999). *Sedimentary Geology* 124, 3-29.

Oms, O. (1994). *Estratigrafía del fan-delta de Santa Orosia*. Tesis de Licenciatura, Univ. Autònoma de Barcelona.

Oms, O. and Remacha, E. (1992). *Geogaceta* 12, 73-74.

Puigdebàbregas, C. (1975). *La sedimentación molásica en la cuenca de Jaca*, Zaragoza, 188p.

Puigdefàbregas, C., Muñoz, J.A. and Vergés, J. (1992). In: *Thrust Tectonics* (McClay, K.R. Eds.). Chapman & Hall, London, 247-254.

Remacha, E. and Fernández, L.P. (2003). *Marine and Petroleum Geology* 20, 711-726.

Remacha, E. and Picart, J. (1991). In: *I Congreso Español del Terciario*. Libro Guía Excursión nº 8, 116 p.

Remacha, E., Arbués, P. and Carreras, M. (1987). *Boletín Geológico y Minero* 98, 40-48.

Remacha, E., Fernández, L.P. and Maestro, E. (2005). *Journal of Sedimentary Research* 75, 798-819.

Roigé, M., Gómez-Gras, D. and Remacha, E. (2013). *Geogaceta* 53, 93-96.

Roigé, M., Gómez-Gras, D., Remacha, E., Daza, R. and Boya, S. (2016). *Comptes Rendus Geoscience* 348, 236-245.

Teixell, A. (1998). *Tectonics* 17, 395-406.

Caracterización composicional de las areniscas del Cretácico Superior en las Sierras Marginales y Exteriores (cuenca surpirenaica): análisis mediante minerales pesados y petrografía óptica

Compositional characterization of the Upper Cretaceous sandstones in the Sierras Marginales y Exteriores (south-Pyrenean basin): Heavy-mineral and sandstone petrography analysis

David Gómez-Gras, Raül Collado, Xavier Coll y Marta Roigé

Departament de Geologia, Facultat de Ciències, Universitat Autònoma de Barcelona, 08193 Bellaterra (Barcelona), España.
david.gomez@uab.cat, raul1991_8@hotmail.com xcc021285@gmail.com, roige.marta@gmail.com

ABSTRACT

Heavy-mineral analysis allows constraining provenance of detrital materials as well as their diagenetic history and the energetic characteristics of depositional environment. This technique, coupled with sandstone petrography, is applied for the first time to the Upper Cretaceous materials of the south-central Pyrenean basin, in the Sierras Marginales and Sierras Exteriores. The present paper determines the heavy-mineral suites and the petrography of the Santonian and Maastrichtian materials during a key moment of the south-central Pyrenean basin evolution, in which the inversion of the previous extensional basins occurs together with the earliest record of the detrital sedimentation of the foreland basin. The impoverished heavy-mineral assemblages, together with the high compositional maturity displayed by the Upper Cretaceous sandstones of the south-central Pyrenean basin (quartzarenites and K-feldspar arkoses), suggest that these sediments where affected by an intense dissolution which have strongly modified their original signal. Such composition was modified due to weathering processes that occurred at the source area, to mechanical breakdown during transport and to diagenesis during burial accompanied by acid-water circulation.

Key-words: *Heavy-minerals, petrography, Raman spectroscopy, Upper Cretaceous, south-Pyrenean basin.*

RESUMEN

El análisis de minerales pesados es una técnica que permite precisar sobre la procedencia de los materiales detríticos, así como su historia diagenética y las características energéticas de su ambiente de sedimentación. Esta técnica, juntamente con un análisis petrográfico cuantitativo, se aplica por primera vez en los materiales del Cretácico Superior de la cuenca surpirenaica central, en las Sierras Marginales y Sierras Exteriores. El presente trabajo establece las asociaciones de minerales pesados y la petrografía de los materiales del Santoniense y Maastrichtiense en un momento clave de la evolución de la cuenca surpirenaica central, en el que se produce la inversión de cuencas previas, y el registro más temprano de la sedimentación detrítica de la cuenca de antepaís. Las asociaciones empobrecidas de minerales pesados, junto a la madurez composicional elevada que muestran dichas areniscas (cuarzoarenitas y arcosas con feldespato potásico), sugieren que estos sedimentos han estado sometidos a una intensa disolución que ha modificado profundamente su composición original. Dicha composición fue alterada por los procesos de meteorización acaecidos en el área fuente, por la abrasión mecánica durante el transporte y por la diagénesis durante el enterramiento acompañada de la circulación de aguas ácidas.

Palabras clave: *Minerales pesados, petrografía, espectrometría Raman, Cretácico Superior, cuenca surpirenaica.*

Geogaceta, 61 (2017), 163-166
ISSN (versión impresa): 0213-683X
ISSN (Internet): 2173-6545

Recepción: 26 de julio de 2016
Revisión: 3 de noviembre de 2016
Aceptación: 25 de noviembre 2016

Introducción

El análisis de minerales pesados es una técnica que permite precisar sobre la procedencia de los materiales detríticos, así como su historia diagenética y las características energéticas de su ambiente de deposición. Cuando este tipo de análisis se complementa entre otros con datos de petrografía del conjunto de la roca, geoquímica de isotopos o datos de termocronología, se puede obtener información muy completa del contexto geotectónico del área fuente que proporciona el detrito (Morton y Hallsworth, 1999). El análisis de minerales pesados con el microscopio petrográfico puede ser una tarea difícil, ya que frecuentemente estos minerales pueden aparecer alterados o abrasionados, dificultando así su identificación óptica. Es por este motivo que en este trabajo se ha incorporado el uso de la espectrometría Raman como herramienta de análisis de minerales pesados, la cual permite un resultado composicional preciso de la muestra analizada.

Esta técnica, juntamente con un análisis petrográfico cuantitativo se aplica por primera vez en los materiales del Cretácico Superior de la cuenca surpirenaica central y concretamente en su parte más meridional, las Sierras Marginales y Exteriores. En cuanto a la procedencia de estos materiales, existen pocos trabajos petrológicos que hagan referencia a ellos, limitándose fundamentalmente a los que estudian las facies Garumniense (Formación Tremp). Gómez-Gras *et al.* (2016) mediante petrografía óp-

tica establecen que para el sector más meridional de la Fm. Tremp, es el Macizo del Ebro el que actúa como área fuente. Ullastre y Masriera (1982) determinan una asociación de minerales pesados característica para estas facies, dejando varias opciones sobre la interpretación de su área fuente. Dentro de este contexto, en este trabajo se pretende establecer la asociación de minerales pesados y la petrografía de los materiales del Santoniense y Maastrichtiense en un momento clave de la evolución de la cuenca surpirenaica central, en el que se produce la inversión de las cuencas previas y el registro más temprano de la sedimentación detrítica de la cuenca de antepais

Contexto geológico

Los Pirineos incluyen un cinturón de pliegues y cabalgamientos formados durante el Cretácico Superior y el Mioceno medio, como resultado de la colisión entre las placas Ibérica y Euroasiática (Muñoz, 1992). Durante el primer estadio de la compresión Alpina se produjo la inversión de las fallas y cuencas extensionales mesozoicas, mientras que en un segundo estadio se generaliza la propagación de cabalgamientos y se produce la subducción de la corteza inferior de la placa Ibérica bajo la placa Euroasiática (Roure *et al.*, 1989; Teixell, 1998). El orógeno pirenaico se caracteriza por constituir un prisma asimétrico con dos principales cuencas de antepaís; la cuenca del Ebro al sur, y la cuenca de Aquitania al norte (Fig. 1).

En los Pirineos centrales, la inversión tectónica de las cuencas cretácicas resultó en el emplazamiento de la Unidad Surpirenaica Central (Séguret, 1972), la cual se encuentra limitada al norte por la Zona Axial y está integrada por tres láminas cabalgantes principales, de norte a sur; Bóixols, Montsec y Sierras Marginales (Cámara y Klimovitz, 1985). Los materiales detríticos objeto de este estudio son los correspondientes al Cretácico Superior del extremo más meridional de la cuenca surpirenaica central, concretamente los que afloran en las láminas de las Sierras Marginales y en las Sierras Exteriores (límite sur de la cuenca de Jaca).

En las Sierras Marginales se han analizado los materiales del Santoniense - Campaniense y Maastrichtiense, en los sectores de Camarasa y Canelles (Fig. 1). Los materiales del Santoniense-Campaniense en estos sectores están constituidos por areniscas y localmente microconglomerados cuarzosos, que presentan un aumento claro de potencia de sur a norte. Estos materiales han sido interpretados por Clapés (1997) como propios de ambientes fluviales, deltaicos y mareales, muy energéticos de tipo incised-valley system y sedimentados en momentos transgresivos. En el sector de Canelles se han analizado las areniscas maastrichtienses equivalentes a la Fm. Arén en la cuenca de Tremp, correspondientes a facies de transición con cierta influencia mareal. Adicionalmente se han analizado también los depósitos detríticos del Santoniense en las Sierras Exteriores, en el sector de la Sierra de Guara (Fig. 1), los cuales se caracterizan por constituir facies de conglomerados y areniscas ricas en cuarzo, asociados a ambientes de plataforma (Lobato y Meléndez, 1988).

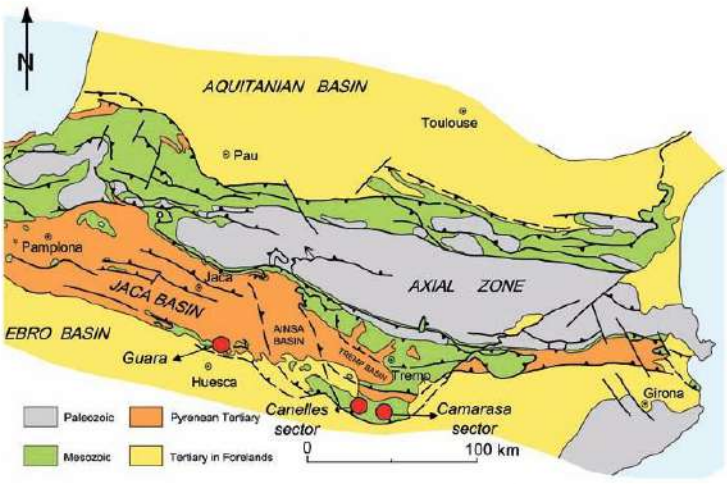

Fig. 1.- Mapa geológico simplificado de los Pirineos (modificado de Teixell, 1996) en el que se muestra la localización de las zonas de estudio (Gurara, Canelles y Camarasa). Ver figura en color en la web.

Fig. 1.- Simplified geological map of the Pyrenees (redrawn from Teixell, 1996), showing the location of the study area (Guara, Canelles and Camarasa). See Colour figure on the web.

Metodología

Se recogieron seis muestras de arenisca del Cretácico Superior que fueron trituradas, tamizadas y sometidas a un baño con ácido acético diluido al 10%, previamente al proceso de separación de minerales pesados.

El proceso de separación por gravedad se realizó utilizando politungstato de sodio (⊠=2.87 g/cm3) y la fracción pesante recuperada de cada muestra se montó en láminas delgadas.

La identificación de los minerales pesados (200 granos por lámina) se realizó, en primer lugar, mediante el microscopio petrográfico. Los granos opacos, túrbidos y de difícil identificación fueron analizados posteriormente mediante espectrometría Raman y los espectros resultantes se compararon con los de referencia presentes en las bases de datos (www.rruff.info, Downs 2006) y en la bibliografía (Andó y Garzanti, 2014).

Posteriormente se realizaron láminas delgadas de la fracción ligera y se efectuó un análisis modal cuantitativo con el microscopio petrográfico, realizando un contaje de trescientos puntos por lámina según el método de Gazzi-Dickinson (Gazzi, 1996; Dickinson, 1970). Las láminas fueron teñidas parcialmente utilizando alizarina red-s y potassium hexacyanoferrate, para los carbonatos, y recubiertas con resina Epofix con Bisphenol-A-Diglycidilether y Triethylenetetramine.

Resultados y discusión

Minerales pesados

Las muestras de minerales pesados presentan asociaciones empobrecidas (Fig. 2) y fundamentalmente constituidas por los minerales más estables (óxidos de titanio). Destaca el elevado contenido en goethita en las muestras del sector de Camarasa, la presencia de turmalina en las muestras de Canelles y la Sierra de Guara y la ausencia de granate en las muestras de Camarasa.

Los resultados obtenidos son característicos de asociaciones de minerales muy resistentes a la disolución por enterramiento y a la circulación de aguas ácidas (Morton y Hallsworth, 1999). Según estos autores, la variedad de minerales pesados presentes en los sedimentos depende de los procesos de meteorización en el área fuente, de la abrasión mecánica y los procesos de selección hidráulica durante el transporte y de la diagénesis durante el enterramiento.

En el Macizo del Ebro las rocas cristalinas fueron sometidas a una intensa meteorización debido a la larga exposición subaérea del Triásico al Cretácico (Gómez-Gras, 1993; Gómez-Gras y Ferrer, 1999; Gómez-Gras *et al.*, 2004; Parcerisa, Gómez-Gras y Martín-Martín, 2006). La fuerte meteorización a la que habría estado sometida el área fuente, habria generado la perdida de los minerales más inestables (los ferromagnesianos y las plagioclasas). Los procesos de abrasión mecánica durante el transporte también han debido jugar un papel importante en la pérdida de los minerales menos estables debido a que estos materiales fueron sedimentados en ambientes de elevada energía ligados a eventos transgresivos (Clapés, 1997).

La desaparición de los minerales pesados menos resistentes se puede asociar con la profundidad de enterramiento (Morton, 1984). En este sentido, la ausencia de anfibol, epidota, titanita, cianita y estaurolita sugiere un enterramiento mínimo de 2400 m para todas las muestras. La falta de granate en las muestras de Camarasa i Canelles 2 (base de la serie) quizás apunta a que han sufrido un enterramiento mayor (mínimo 3500 m).

Dichas profundidades de enterramiento son compatibles con las postuladas por Fillon *et al.* (2013) quienes, basándose en datos de termocronología, establecieron profundidades de entre 2,6 km a 3,2 km para los materiales del Cretácico Superior en la zona surpirenaica central.

La ausencia en todas las muestras de apatito, que es el mineral más estable en relación con el enterramiento, se interpreta como el resultado de la circulación de aguas ácidas durante la diagénesis, ya que éste es el más vulnerable bajo estas condiciones (Morton y Hallsworth, 1999).

Petrografía de las areniscas

Los granos siliciclásticos, constituidos por cuarzo (principalmente monocristalino), son el componente más abundante en todas las muestras (45,5%-70,1%). Entre ellos destaca la presencia de granos con abundantes inclusiones de minerales evaporíticos (4,65%). Los feldespatos potásicos presentan porcentajes menores (22,4%-30,5%) y son inexistentes en el sector de Guara.

Los fragmentos de roca metamórficos (esquistos, pizarras y cuarcitas) son poco abundantes (0,9%-6,9%) e inexistentes en Camarasa 2.

Los granos carbonaticos extracuencales únicamente presentan proporciones considerables en Guara y Canelles 1 (13,5%) y están representados por fragmentos de calizas esparíticas y biomicríticas.

Desde el punto de vista composicional, estas areniscas se clasifican como cuarzoarenitas y arcosas (Fig. 3). El contenido elevado en cuarzo y feldespato potásico (más resistentes a la meteorización y disolución) son indicativos de una madurez composicional elevada. Los feldespatos potásicos se atribuyen a rocas cristalinas paleozoicas como granitoides, ya que frecuentemente aparecen junto con el cuarzo formando fragmentos plutónicos, mientras que los granos de cuarzo con inclusiones evaporíticas (halita y anhidrita), se relacionan con la erosión de las facies Keuper (Marfil 1970), indicando un área fuente con presencia de cobertera mesozoica.

Los fragmentos de roca metamórficos son indicativos de un área fuente metamórfica de edad paleozoica. Por el contrario, el área fuente más probable para los granos carbonaticos se establece en las calizas que forman la cobertera mesozoica, donde los fragmentos de rocas micríticas y biomicríticas procederían de la erosión de formaciones del Triásico y Cretácico.

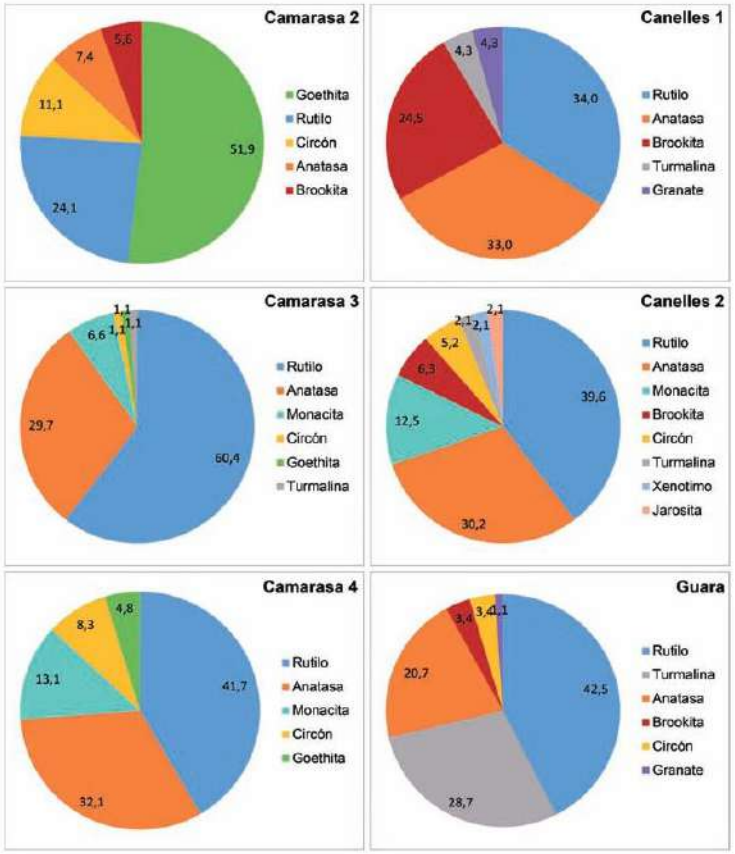

Fig. 2.- Asociaciones de minerales pesados para el Cretácico Superior de la cuenca surpirenaica central representadas en gráficos circulares con el porcentaje de abundancia de cada mineral. Ver figura en color en la web.

Fig. 2.- Heavy-mineral assemblages for the Upper Cretaceous of the south-central Pyrenean basin displayed as percentage pie charts showing the relative abundance of each mineral. See Colour figure on the web.

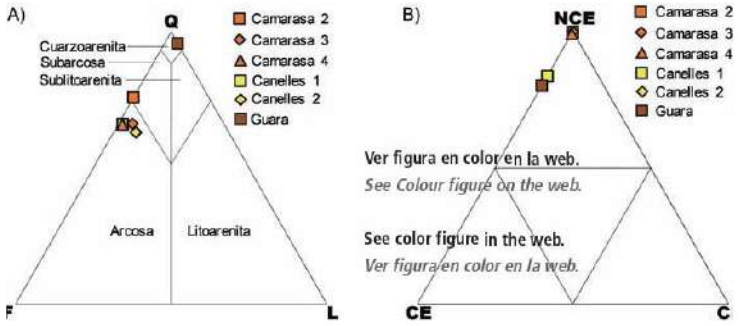

Fig. 3.- Proyección ternaria composicional de las areniscas del Cretácico Superior. A) Diagrama Q-F-L en el sentido Pettijohn *et al.* (1972) en donde los granos de cuarzo corresponden a la abreviatura Q, F corresponde a granos de feldespato y L a litoclastos. B) Diagrama NCE-CE-CI en el sentido de Zuffa (1980), donde granos no-carbonáticos extracuencales corresponden a la abreviatura NCE, CE corresponde a granos carbonáticos extracuencales y CI a granos carbonáticos intracuencales.

Fig. 3.- Compositional ternary plot for the Upper Cretacic sandstones A) Ternary plot Q-F-L, in the sense of Pettijohn et al. *(1972), where quartz grains are abridged as Q, feldspars as F and lithic grains as L; B) Ternary plot NCE-CE-CI, in the sense of Zuffa (1980), where non-carbonate extrabasinal grains are abridged as NCE, carbonate extrabasinal grains as CE and CI are carbonate intrabasinal grains.*

Según Gómez-Gras *et al.* (2016), el Macizo del Ebro actuó como área fuente principal durante el Cretácico para la mayor parte de los sedimentos depositados en la cuenca surpirenaica central. Las reconstrucciones paleogeográficas registran una zona expuesta inmediatamente al sur de esta cuenca, donde las rocas cristalinas fueron sometidas a una intensa meteorización desde el Triásico hasta el Cretácico.

Dichas interpretaciones son compatibles con los resultados obtenidos en el presente trabajo, en el que se postula un área fuente afectada por una intensa meteorización que daría como resultado sedimentos con una elevada madurez composicional (cuarzoarenitas y subarcosas).

Conclusiones

Las asociaciones de minerales pesados empobrecidas, junto a la madurez composicional elevada que muestran las areniscas del Cretácico Superior de la zona surpirenaica, sugieren que estos sedimentos han estado sometidos a una intensa disolución que ha modificado profundamente la composición de su procedencia original. Esta composición original fue modificada por los procesos de meteorización acaecidos en el área fuente, por la abrasión mecánica durante el transporte y por la diagénesis durante el enterramiento acompañada de la circulación de aguas ácidas. La acción conjunta de todos estos procesos condujo a la progresiva disolución de las especies minerales menos estables.

A partir de las asociaciones de minerales pesados encontrados se han deducido profundidades de enterramiento comprendidas entre 2400 m y 3500 m que son compatibles con las postuladas a partir de estudios de termocronología en los materiales del Cretácico Superior de la zona surpirenaica central.

Agradecimientos

Este trabajo es una contribución al CGL2014-54180-P, financiado por el Ministerio de Economía y Competitividad de España. Agradecemos a los revisores y editores sus comentarios para mejorar el texto.

Referencias

Andò, S. y Garzanti, E. (2014). *Geological Society, London, Special Publications* 386, 395-412.

Cámara, P. y Klimowitz, J. (1985). *Estudios Geológicos* 41, 391-404.

Clapés, C. (1997). *Els nivells de gresos Santonians de les Serres Marginals (Pre-Pirineu Central). Treball de recerca.* Tésis doctoral, Universitat Autònoma de Barcelona, 289p.

Dickinson, W. (1970). *Sedimentary Petrology* 40, 695-707.

Fillon, C., Gautheron, C. y van der Beek, P. (2013). *Journal of the Geological Society* 170, 67-77.

Gazzi, P. (1966). *Mineralogica et Petrographica Acta* 12, 69-97.

Gómez-Gras, D. (1993). *Boletín Geológico y Minero* 104, 115-161.

Gómez-Gras, D. y Ferrer, C. (1999). *Revista de la Sociedad Geológica de España* 12, 281-299.

Gómez-Gras, D., Núñez, J. A., Lacasa, G. y Parcerisa, D. (2004). En: *32nd International Geological Congress, Abstracts book* 2, p. 1099.

Gómez-Gras, D., Roigé, M., Fondevilla, V., Oms, O., Boya, S. y Remacha, E. (2016). *Cretaceous Research* 57, 414-427.

Lobato, A. y Meléndez, A. (1988). En: *II Congreso Geológico de España, Comunicaciones* 1, 99-102.

Marfil, R. (1970). *Estudios Geológicos* 2, 113-163.

Morton, A.C. (1984). *Clay Mineralogy* 19, 287–308.

Morton, A. C. y Hallsworth, C. R. (1999). *Sedimentary Geology* 124, 3-29.

Muñoz, J. A. (1992). En: *Thrust Tectonics* (McClay, K.R. Eds.). Chapman and Hall, New York, 235-246.

Parcerisa, D., Gómez-Gras, D., y Martín-Martín, J. D. (2006). *Geological Society of America Special Papers* 416, 105-117.

Pettijohn, F. J., Potter, P. E., y Siever, R. (1972). *Sand and Sandstone.* Springer, Berlin-Herdelberg-New York, 618p.

Roure, F., Choukroune, P., Berastegui, X., Muñoz, J. A., Villien, A., Matheron, P., Bareyt, M., Séguret, M., Camara, P. y Déramond, J. (1989). *Tectonics* 8, 41-50.

Seguret, M. (1972). *Etude tectonique du versant sud des Pyrenees centrales: nappes et series decolles, role du serrage et de gravity'Presses.* Univ. Sci. Tech. Languedoc.

Teixell, A. (1996). *Journal of the Geological Society of London* 153, 301-310.

Teixell, A. (1998). *Tectonics* 17, 395-406.

Ullastre, J. y Masriera, A. (1982). *Cuadernos de Geología Ibérica* 8, 949-964.

Zuffa, G. (1980). *Journal of Sedimentary Petrology* 50, 21-29.

Annex 3

Congressos Internacionals

En l'annex 3 s'incorporen els abstractes publicats, els pòsters, i les presentacions realitzades en congressos internacionals.

1.- Coll, X., Gómez-Gras, D., Roigé, M. & Mestres, N. (2017). Heavy-mineral assemblages as a provenance indicator in the Jaca basin (Middle-Late Eocene, southern Pyrenees). SEPM Research Conference, Propagation of Environmental Signals within Source-to-Sink Stratigraphy, Tremp-Ainsa, Spain, 2017.

2.- Coll, X., Gómez-Gras, D., Roigé, M., Teixell, A. & Mestres, N. (2017). Heavy-mineral assemblages as a provenance indicator in the Jaca basin (Middle-Late Eocene, southern Pyrenees). 33rd IAS International Meeting of Sedimentology, Toulouse, France, 2017.

3.- Caldera, N., Teixell, A., Griera, A. Labaume, P., Coll, X. & Mestres, N. (2018). On the tectonic structures of the Eaux-Chaudes massif (western Pyrenees): a Helvetic nappe type in the Pyrenees? YOUSGET Young Researchers in Structural Geology and Tectonics, Montgenevre, France, 2018.

4.- Coll, X., Gómez-Gras, D., Roigé, M., Boya, S., Teixell, A. & Poyatos-Moré, M. (2019). Heavy-Mineral Provenance Signatures During the Evolution from Marine to Terrestrial Environaments in the Jaca Basin (Southern Pyrenees). 34th IAS International Meeting of Sedimentology, Roma, Italy, 2019.

5.- Coll, X., Gómez-Gras, D., Roigé, M., Boya, S., Teixell, A. & Poyatos-Moré, M. (2019). Interplay of Multiple Sediment Sources in an Overfilled Foreland Basin (Southern Pyrenees). 34th IAS International Meeting of Sedimentology, Roma: Italy, 2019.

SEPM Research Conference
Propagation of Environmental Signals within Source-to-Sink Stratigraphy
June 5-9th, 2017 — Tremp & Ainsa, Spanish Pyrenees

Heavy-mineral assemblages as a provenance indicator in the Jaca basin (Middle-Late Eocene, southern Pyrenees)

Xavier Coll[1], David Gómez-Gras[1], Marta Roigé[1] & Narcís Mestres[2]

[1]Departament de Geologia de la Universitat Autònoma de Barcelona, Bellaterra (Catalunya), Spain.
[2] Institut de Ciència de Materials de Barcelona, Consejo Superior de Investigaciones Científicas, Bellaterra (Catalunya), Spain.

Heavy-mineral analysis (HMA) is one of the most sensitive and widely-used techniques in the determination of sandstone provenance. Heavy minerals provide diagnostic information for provenance interpretation, as well as for tectonic setting, that cannot be achieved by other means. The Jaca sequence records a main paleogeographic change from the deep-marine sedimentation stage, recorded by the Upper Hecho Group turbidites (Upper Lutetian), to the generalization of terrestrial sedimentation in the Bartonian-Priabonian. Our study focuses on the the clastic systems of the northern Jaca basin (Middle-Late Eocene, South-Central Pyrenees), which encompasses the Banastón and Jaca turbidite systems, the Sabiñánigo and Atarés delta systems, the Santa Orosia alluvial system and the Canciás alluvial fan.

Although provenance constraints for these systems have been based on paleocurrents, basin architecture and sandstone petrography, their heavy-mineral content remains unknown. We explore the use of heavy-mineral assemblages as provenance indicators, by means of optical petrography and Raman spectroscopy, combined with available petrological data, aiming to constrain changes in the source area along the basin's evolution. All the clastic systems display impoverished heavy-mineral suites, mainly constituted by titanium oxides, apatite, zircon and tourmaline.

Heavy-mineral assemblages in sediments depend on weathering, transport, hydraulic processes, diagenesis and mainly burial depth. All these processes act on heavy mineral grains, from its source area to its sedimentation, burial and re-exhumation, and can lead to an impoverished heavy-mineral association, where only the most resistant minerals such as zircon, tourmaline, apatite, rutile and other titanium oxides will remain. Most of the heavy mineral content derived from an orogen is usually dissolved during diagenesis and therefore erased from the sediment record depending on the burial depth. The most likely reason for the observed impoverishment in the turbidite suites is the burial depth acquired by these sediments, which would lead to the dissolution of less stable heavy minerals. Impoverishment of the heavy mineral suites in the alluvial systems may be due to the fact that their major input is derived from the recycling of the turbidites. However, some of the surviving grains can be linked to specific source areas and are diagnostic provenance indicators.

Heavy-mineral assemblages as a provenance indicator in the Jaca basin (Middle-Late Eocene, Southern Pyrenees)

Xavier Coll[1], David Gómez-Gras[1], Marta Roigé[1], Narcis Mestres[2]

[1]Department of Geology, Universitat Autònoma de Barcelona, Bellaterra, Spain (E-mail: xcc021285@gmail.com)

[2]Institut de Ciència de Materials de Barcelona ICMAB, CSIC, Bellaterra, Spain. (E-mail: narcis.mestres@icmab.es)

Introduction

The Eocene clastic systems of the Jaca foreland basin, record a main paleogeographic change, from the upper Lutetian deep-marine sedimentation stage (Upper Hecho Group turbidites) to the generalization of terrestrial environments in the Bartonian-Priabonian.

Despite all the research regarding tectono-stratigraphy, sedimentology, and petrography, the heavy-mineral content is not yet known.

Since diagnostic information of sediment provenance, dispersal patterns and tectonic setting is derived from heavy-mineral analysis (HMA), we explore the use of heavy-mineral suites as a provenance indicator in the Jaca basin.

Results are integrated within framework petrography from Roigé et al. (2016).

Geological setting

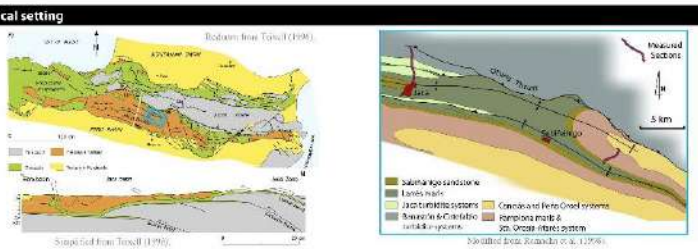

The Pyrenean fold-and-thrust belt consists of a lower duplex involving basement rocks from Paleozoic to Permotriasic (Axial Zone) and an upper cover imbricated thrust system of Mesozoic to Miocene sedimentary rocks (South Pyrenean Zone), with a synorogenic succession of clastic and carbonate rocks from Late Santonian to Early Miocene (South Pyrenean basin).

During Early and Middle Eocene times, fluvio-deltaic environments in the the South Pyrenean basin, where restricted to the east (Tremp-Graus and Ager basins), whereby coastal/slope and deep-marine spread through the west (Ainsa and Jaca basins).

Over the underfilled stage, turbidites dominated all over the deep-marine Jaca basin (Banastón and Jaca turbidite systems), bordered by active thrust sheets to the north (hinterland) and carbonate platforms to the south. The Bartonian-Priabonian overfilled stage brought the spreading of transitional (Sabiñanigo Sandstone) and continental settings (Santa Orosia-Atarés alluvial system) throughout the basin.

Methodology

27 sandstone and conglomerate samples from the TSU-4 (Banastón turbidite system) and TSU-5 (Jaca turbidite system, Sabiñanigo delta and Santa Orosia-Atarés alluvial system) were collected in the Jaca and Yebra de Basa area for HMA.

13 were crushed, sieved and submitted to a vibrating water separation table prior to acid digestion with acetic acid (10%).

Heavy-mineral gravity setting was performed using sodium polytungstate (2.87g/cm3).

Heavy grains were mounted on slides for mineral identification under polarizing microscope.

Up to 200 grains per slide where counted using the point-counting area method.

Raman spectroscopy was used to reduce uncertainties at identifying opaque, turbid and dubious grains.

Detrital grains were plotted into percentage pie charts in a stratigraphic log.

Results & Dicussion

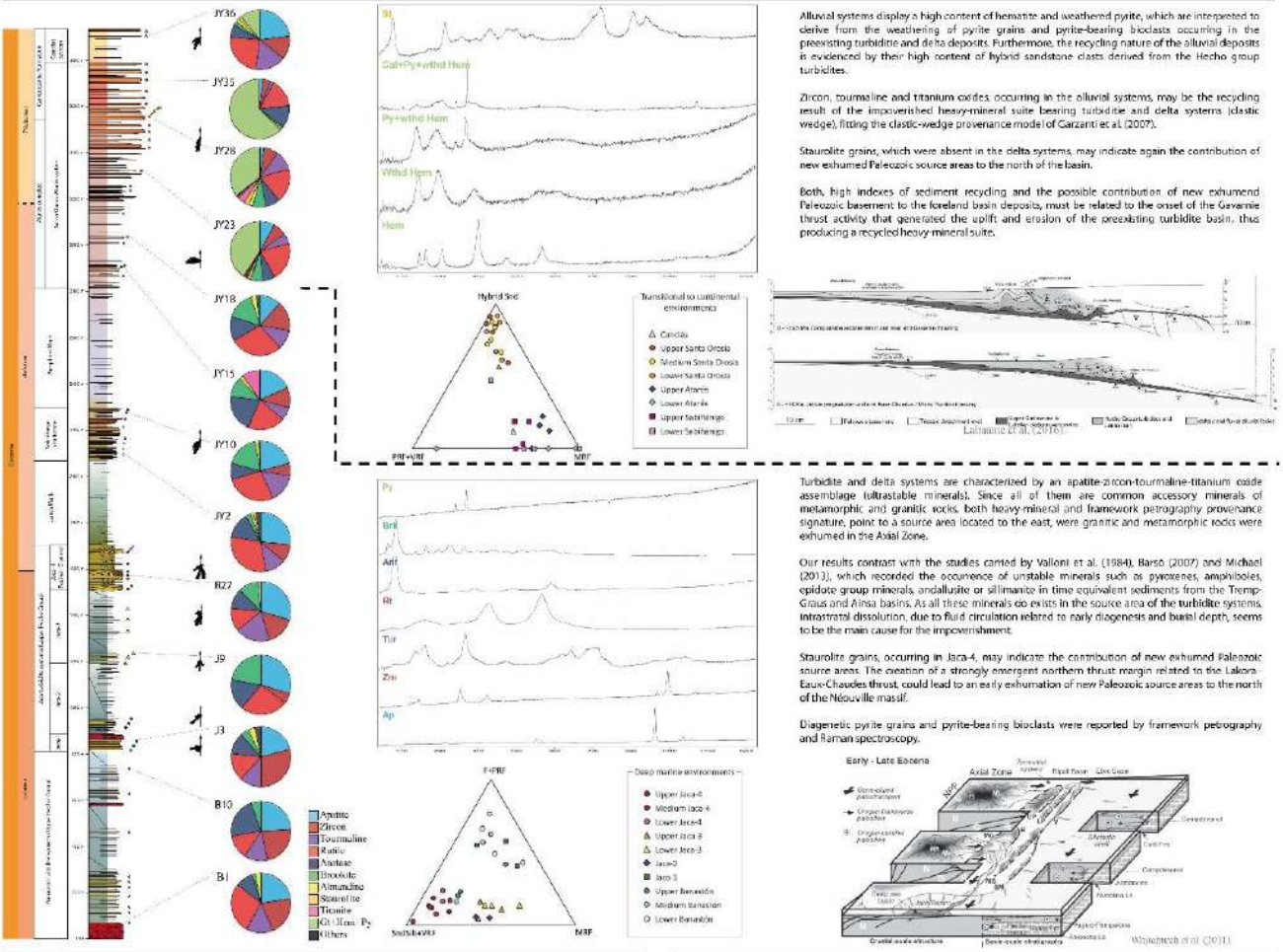

Alluvial systems display a high content of hematite and weathered pyrite, which are interpreted to derive from the weathering of pyrite grains and pyrite-bearing bioclasts occurring in the preexisting turbiditic and delta deposits. Furthermore, the recycling nature of the alluvial deposits is evidenced by their high content of hybrid sandstone clasts derived from the Hecho group turbidites.

Zircon, tourmaline and titanium oxides, occurring in the alluvial systems, may be the recycling result of the impoverished heavy-mineral suite bearing turbiditic and delta systems (clastic wedge), fitting the clastic-wedge provenance model of Garzanti et al. (2007).

Staurolite grains, which were absent in the delta systems, may indicate again the contribution of new exhumed Paleozoic source areas to the north of the basin.

Both, high indexes of sediment recycling and the possible contribution of new exhumed Paleozoic basement to the foreland basin deposits, must be related to the onset of the Gavarnie thrust activity that generated the uplift and erosion of the preexisting turbiditic basin, thus producing a recycled heavy-mineral suite.

Lahmine et al. (2016)

Turbidite and delta systems are characterized by an apatite-zircon-tourmaline-titanium oxide assemblage (ultrastable minerals). Since all of them are common accessory minerals of metamorphic and granitic rocks, both heavy-mineral and framework petrography provenance signature, point to a source area located to the east, were granitic and metamorphic rocks were exhumed in the Axial Zone.

Our results contrast with the studies carried by Valloni et al. (1984), Barsó (2007) and Michael (2013), which recorded the occurrence of unstable minerals such as pyroxenes, amphiboles, epidote group minerals, andalusite or sillimanite in time equivalent sediments from the Tremp-Graus and Ainsa basins. As all these minerals do exists in the source area of the turbidite systems, intrastratal dissolution, due to fluid circulation related to early diagenesis and burial depth, seems to be the main cause for the impoverishment.

Staurolite grains, occurring in Jaca-4, may indicate the contribution of new exhumed Paleozoic source areas. The creation of a strongly emergent northern thrust margin related to the Lakora-Eaux-Chaudes thrust, could lead to an early exhumation of new Paleozoic source areas to the north of the Nèouville massif.

Diagenetic pyrite grains and pyrite-bearing bioclasts were reported by framework petrography and Raman spectroscopy.

Conclusions

The clastic systems of the northern Jaca basin display impoverished heavy-mineral suites.

Intrastratal dissolution due to fluid circulation, related to diagenesis and burial depth, is the most likely explanation for the impoverishment, in the turbidite and delta systems, rather than a provenance effect.

Alluvial systems record a major heavy-mineral content shift related to the onset of the Gavarnie thrust activity. As a result, a recycled heavy-mineral suite is derived from the former turbidite and delta deposits.

Raman spectroscopy played a critical role identifying opaque grains, which provided important provenance information for the alluvial heavy-mineral assemblages.

Future Work

Since the complexity of the factors controlling the heavy-mineral assemblages in the South Pyrenean basin becomes evident, further research is needed in order to disentangle the interplay between source rock lithology, tectonics and diagenesis and how they may imprint or mask diagnostic provenance information in the resulting detrital suites. An integrated approach, coupling sandstone petrography, high-resolution heavy mineral analysis (HRHMA) and detrital zircon geochronology, must be fulfilled in order to avoid data misinterpretation. Raman spectroscopy stands as the best method to reduce ambiguity in heavy-mineral identification and to attempt HRHMA.

We are now working on sandstone petrography and HRHMA of the fluvial systems in the southern margin to attempt correlation with the alluvial systems to the north. Our ultimate goal is to implement this workflow at the western part of the Jaca-Pamplona basin, where the fluvial and alluvial deposits in the Izati Valley and the Izaga syncline (Aoiz area) are going to be studied.

Reneferences

HEAVY-MINERAL ASSEMBLAGES AS PROVENANCE INDICATORS IN THE JACA BASIN (MIDDLE-LATE EOCENE, SOUTHERN PYRENEES)

Xavier COLL[(1,@)], David GÓMEZ-GRAS[(1)], Marta ROIGE[(1)], Antonio TEIXELL[(1)], Narcís MESTRES[(2)]

[(1)] Departament de Geologia, Universitat Autònoma de Barcelona (Spain)
[(2)] Institut de Ciència de Materials de Barcelona (Spain)
[(@)] xcc021285@gmail.com

The South Pyrenean basin consists of a synorogenic succession of clastic and carbonate rocks from Late Santonian to Early Miocene age. During Early and Middle Eocene times, fluvio-deltaic environments were restricted to the east (Tremp-Graus and Ager basins), whereby coastal/slope and deep-marine settings spread through the west (Ainsa and Jaca basins). Over this underfilled stage, turbidites dominated in the deep-marine Jaca basin (Banastón and Jaca turbidite systems), bordered by active thrust sheets to the north (hinterland) and carbonate platforms to the south. The Bartonian-Priabonian overfilled stage brought the spreading of transitional (Sabiñanigo Sandstone) and continental settings (Santa Orosia-Atarés alluvial system) throughout the basin. Although provenance constraints for these systems have been based on paleocurrents, basin architecture and sandstone petrography, their heavy-mineral content is not yet known. Aiming to constrain changes in the source area during the basin's evolution, we explore the use of heavy-mineral suites as a provenance indicator in the Jaca foreland basin, by means of Raman spectroscopy coupled with sandstone petrography, and provide new data on the heavy-mineral content. Heavy-mineral analysis (HMA) is one of the most sensitive and widely-used techniques regarding sediment provenance analysis because it provides diagnostic information that cannot be obtained by means of other tools. However, most of the heavy mineral content derived from an orogen is usually dissolved during diagenesis and therefore erased from the sediment record during deep burial. Our results show that the heavy-mineral provenance signature in the northern Jaca basin is masked by intrastratal dissolution during burial diagenesis. Nevertheless, a major heavy-mineral content shift is recorded by opaque grains along the transition from turbidite and shallowwater to continental deposits. The use of Raman spectroscopy for identification of opaque grains, coupled with sandstone petrography, helped to disentangle the interplay between source rock lithology, tectonics and diagenesis of the detrital heavy-mineral suites of the South Pyrenean basin. This allowed to link the compositional change with the onset of the Gavarnie thrust activity, which lead to the uplift and erosion of the preexisting turbidite basin, thus producing a recycled heavy-mineral suite.

Heavy-mineral assemblages as a provenance indicator in the Jaca basin (Middle-Late Eocene, Southern Pyrenees)

Xavier Coll[1], David Gómez-Gras[1], Marta Roigé[1], Antonio Teixell[1] & Narcis Mestres[2]

[1]Department of Geology, Universitat Autònoma de Barcelona, Bellaterra, Spain (E-mail: xcc021285@gmail.com)

[2]Institut de Ciència de Materials de Barcelona ICMAB, CSIC, Bellaterra, Spain. (E-mail: narcis.mestres@icmab.es)

Introduction

The Eocene clastic systems of the Jaca foreland basin record a main paleogeographic change, from the upper Lutetian deep-marine sedimentation stage (Upper Hecho Group turbidites) to the generalization of terrestrial environments in the Bartonian-Priabonian.

Despite all the research regarding tectono-stratigraphy, sedimentology, and petrography, the heavy-mineral content is not yet known.

Since diagnostic information of sediment provenance, dispersal patterns and tectonic setting is derived from heavy-mineral analysis (HMA), we explore the use of heavy-mineral suites as a provenance indicator in the Jaca basin.

Results are integrated within framework petrography from Roigé et al. (2016).

Geological setting

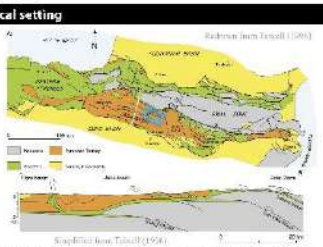

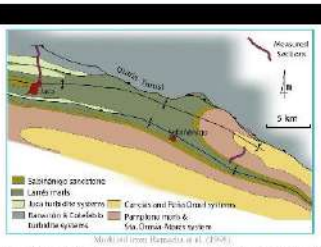

The Pyrenean fold-and-thrust belt consists of a lower duplex involving basement rocks from Paleozoic to Permotriasic (Axial Zone) and an upper cover imbricated thrust system of Mesozoic to Miocene sedimentary rocks (South Pyrenean Zone), with a synorogenic succession of clastic and carbonate rocks from Late Santonian to Early Miocene (South Pyrenean basin).

During Early and Middle Eocene times, fluvio-deltaic environments in the the South Pyrenean basin, where restricted to the east (Tremp-Graus and Ager basins), whereby coastal/slope and deep-marine spread through the west (Ainsa and Jaca basins).

Over the underfilled stage, turbidites dominated all over the deep-marine Jaca basin (Banastón and Jaca turbidite systems), bordered by active thrust sheets to the north (hinterland) and carbonate platforms to the south. The Bartonian-Priabonian overfilled stage brought the spreading of transitional (Sabiñanigo Sandstone) and continental settings (Santa Orosia-Atarés alluvial system) throughout the basin.

Methodology

27 sandstone and conglomerate samples from the TSU 4 (Banastón turbidite system) and TSU 5 (Jaca turbidite system, Sabiñanigo delta and Santa Orosia-Atarés alluvial system) were collected in the Jaca and Yebra de Basa area for HMA.

13 were crushed, sieved and submitted to a vibrating water separation table prior to acid digestion with acetic acid (10%).

Heavy-mineral gravity settling was performed using sodium polytungstate (2.87g/cm3).

Heavy grains were mounted on slides for mineral identification under polarizing microscope.

Up to 200 grains per slide where counted using the point-counting area method.

Raman spectroscopy was used to reduce uncertainties at identifying opaque, turbid and dubious grains.

Detrital grains were plotted into percentage pie charts in a stratigraphic log.

Results & Dicussion

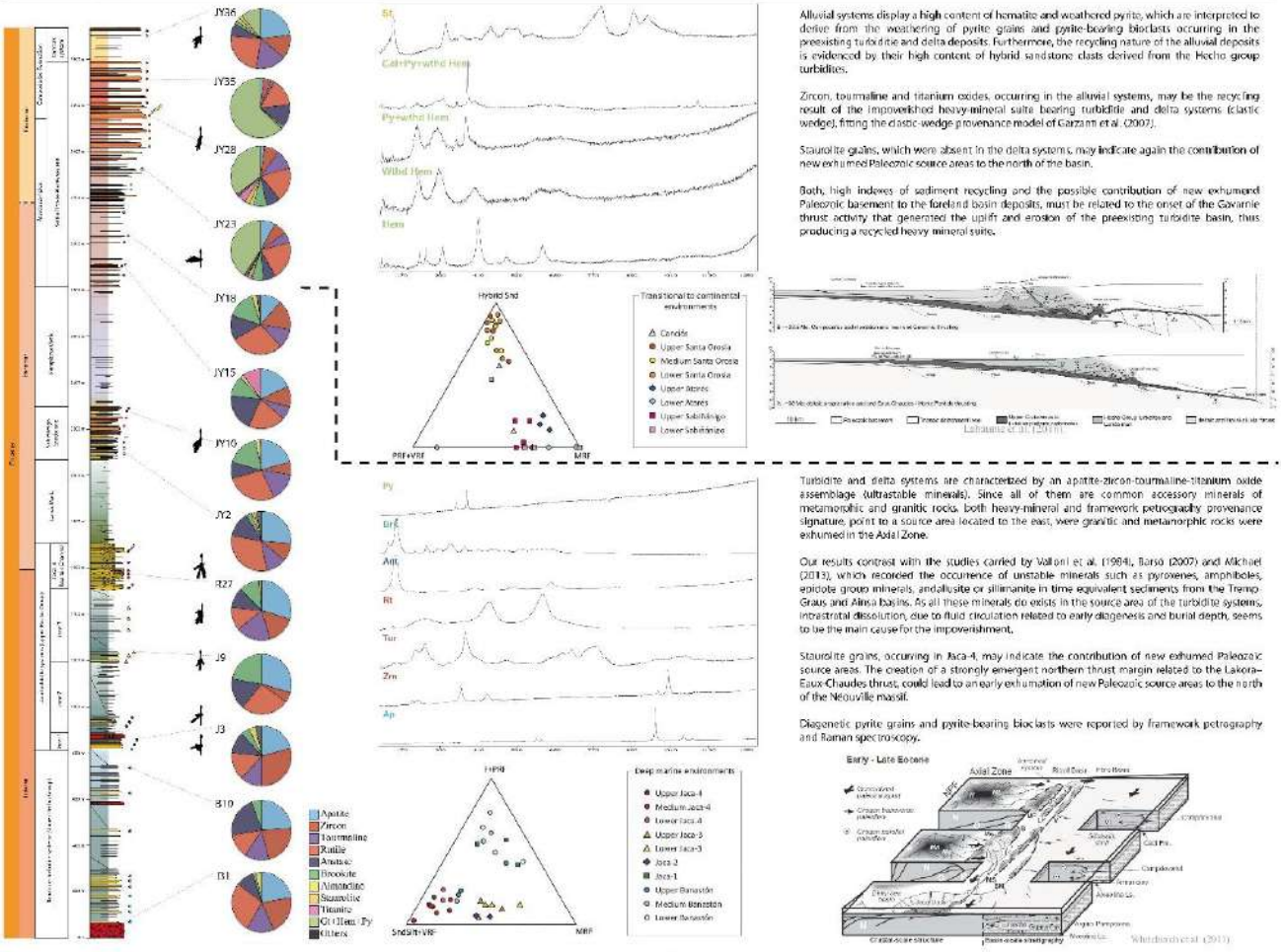

Alluvial systems display a high content of hematite and weathered pyrite, which are interpreted to derive from the weathering of pyrite grains and pyrite-bearing bioclasts occurring in the preexisting turbiditic and delta deposits. Furthermore, the recycling nature of the alluvial deposits is evidenced by their high content of hybrid sandstone clasts derived from the Hecho group turbidites.

Zircon, tourmaline and titanium oxides, occurring in the alluvial systems, may be the recycling result of the impoverished heavy-mineral suite bearing turbidite and delta systems (clastic wedge), fitting the clastic-wedge provenance model of Garzanti et al. (2007).

Staurolite grains, which were absent in the delta systems, may indicate again the contribution of new exhumed Paleozoic source areas to the north of the basin.

Both, high indexes of sediment recycling and the possible contribution of new exhumed Paleozoic basement to the foreland basin deposits, must be related to the onset of the Gavarnie thrust activity that generated the uplift and erosion of the preexisting turbidite basin, thus producing a recycled heavy mineral suite.

Turbidite and delta systems are characterized by an apatite-zircon-tourmaline-titanium oxide assemblage (ultrastable minerals). Since all of them are common accessory minerals of metamorphic and granitic rocks, both heavy-mineral and framework petrography provenance signature, point to a source area located to the east, were granitic and metamorphic rocks were exhumed in the Axial Zone.

Our results contrast with the studies carried by Vallori et al. (1984), Barsó (2007) and Michael (2013), which recorded the occurrence of unstable minerals such as pyroxenes, amphiboles, epidote group minerals, andalusite or sillimanite in time equivalent sediments from the Tremp-Graus and Ainsa basins. As all these minerals do exists in the source area of the turbidite systems, intrastratal dissolution, due to fluid circulation related to early diagenesis and burial depth, seems to be the main cause for the impoverishment.

Staurolite grains, occurring in Jaca-4, may indicate the contribution of new exhumed Paleozoic source areas. The creation of a strongly emergent northern thrust margin related to the Lakora–Eaux-Chaudes thrust, could lead to an early exhumation of new Paleozoic source areas to the north of the Nogueville massif.

Diagenetic pyrite grains and pyrite-bearing bioclasts were reported by framework petrography and Raman spectroscopy.

Conclusions

The clastic systems of the northern Jaca basin display impoverished heavy-mineral suites.

Intrastratal dissolution due to fluid circulation, related to diagenesis and burial depth, is the most likely explanation for the impoverishment in the turbidite and delta systems, rather than a provenance effect.

Alluvial systems record a major heavy-mineral content shift related to the onset of the Gavarnie thrust activity. As a result, a recycled heavy-mineral suite is derived from the former turbidite and delta deposits.

Raman spectroscopy played a critical role identifying opaque grains, which provided important provenance information for the alluvial heavy-mineral assemblages.

Future Work

Since the complexity of the factors controlling the heavy-mineral assemblages in the South Pyrenean basin becomes evident, further research is needed in order to disentangle the interplay between source rock lithology, tectonics and diagenesis and how they may imprint or mask diagnostic provenance information in the resulting detrital suites. An integrated approach, coupling sandstone petrography, high-resolution heavy mineral analysis (HRHMA) and detrital zircon geochronology, must be fulfilled in order to avoid data misinterpretation. Raman spectroscopy stands as the best method to reduce ambiguity in heavy-mineral identification and to attempt HRHMA.

We are now working on sandstone petrography and HRHMA of the fluvial systems in the southern margin to attempt correlation with the alluvial systems to the north. Our ultimate goal is to implement this workflow at the western part of the Jaca-Pamplona basin, where the fluvial and alluvial deposits in the Irati Valley and the Izaga syncline (Aoiz area) are going to be studied.

Reneferences

On the tectonic structures of the Eaux-Chaudes massif (western Pyrenees): a Helvetic nappe type in the Pyrenees?

Norbert Caldera 1); Antonio Teixell 1); Albert Griera 1); Pierre Labaume 2); Xavier Coll 1); Narcís Mestres 3)
1) Universitat Autònoma de Barcelona (UAB); 2) Université de Montpellier-CNRS; 3) Institut de Ciències dels Materials de Barcelona (ICMAB)

The Eaux-Chaudes massif is a complex south verging fold-and-thrust structure located in the western Axial Zone of the Pyrenees. The stratigraphic succession consist of Upper Cretaceous limestones lying unconformably directly on the Paleozoic basement. The structure has been interpreted as a duplex in Cretaceous rocks with a roof thrust carrying allochtonous Paleozoic rocks, called the Eaux-Chaudes thrust (Ternet, 1965).

Our initial work consisted on field analysis and mapping, structural data collection and sample collection followed by cross-section construction. Thin section analysis allowed us to quantify microstructural features and to estimate paleotemperatures by Raman Spectroscopy of Carbonaceous Material (RSCM).

Our preliminar results provide new elements to reassess the former interpretation: overturned bedding polarity and high-strain shearing have been identified within an allochtonous Upper Cretaceous unit, which overall forms a large basement-involved recumbent anticline with Paleozoic rocks in the core, much in the style of the Helvetic nappes of the Alps. Kinematic indicators as stretching lineation, angular relationships between schistosity and bedding, and S-C type structures evidence a south directed tectonic transport for the structure. As strain intensity increases in the overturned fold limb, recrystallization and shape-preferred orientation of calcite grains appears. The recrystallized matrix grain size ranges between 10 and 35 µm. Five samples have been analysed by RSCM and fitted them by Beyssac method (Beyssac, et al. 2002), which yielded paleotemperatures above 320°C (i.e. near lower greenschist facies) in upper Cretaceous rocks.

These results lead us to propose a new interpretation of the Pyrenean deformation conditions in the northern Axial Zone of the Pyrenees, characterized by high ductility with a subordinate role of thrust faulting.

Ternet, Y. Etude du synclinal complexe des Eaux-Chaudes (Basses-Pyrénées). PhD thesis, Univ. of Toulouse, 152 p.

Beyssac, O., Goffé, B., Chopin, C. & Rouzaud, J. N. Raman spectra of carbonaceous material in metasediments: new geothermometer. J. Metamorph. Geol. 20, 859-871 (2002).

Heavy-mineral provenance signatures during the evolution from marine to terrestrial environments in the Jaca basin (Southern Pyrenees)

Xavier Coll Carrillo (1), David Gómez-Gras (1), Marta Roige (1), Salvador Boya (1), Antonio Teixell (1), Miquel Poyatos-Moré (2)

(1) Universitat Autònoma de Barcelona, (2) University of Oslo

The South Pyrenean basin consists of a synorogenic succession of clastic and carbonate rocks from Late Santonian to Early Miocene age. During Early and Middle Eocene times, fluvio-deltaic environments were restricted to the east (Tremp-Graus and Ager basins), whereby coastal/slope and deep-marine settings spread through the west (Ainsa and Jaca basins). Over this underfilled stage, turbidites dominated in the deep-marine Jaca basin (Banastón and Jaca turbidite systems), bordered by active thrust sheets to the north (hinterland) and carbonate platforms to the south. The Bartonian-Priabonian overfilled stage brought the spreading of transitional (Belsué-Atarés Formation) and continental settings (Campodarbe Formation) throughout the basin. Although provenance constraints for these systems have been based on paleocurrents, basin architecture and sandstone petrography, their heavy-mineral content is not yet known. Aiming to constrain changes in the source area during the basin's evolution, we explore the use of heavy-mineral suites as a provenance indicator in the Jaca foreland basin, by means of Raman spectroscopy coupled with sandstone petrography, and provide new data on the heavy-mineral content. Heavy-mineral analysis (HMA) is one of the most sensitive and widely-used techniques regarding sediment provenance analysis because it provides diagnostic information that cannot be obtained by means of other tools. However, most of the heavy-mineral content derived from an orogen is usually dissolved during diagenesis and therefore erased from the sediment record during deep burial. Our results show that the heavy-mineral provenance signature in the northern Jaca basin is masked by intrastratal dissolution during burial diagenesis. In order to unravel the effects of diagenesis on heavy mineral suites from the Jaca basin, we provide new results from the nearby Ainsa and Ebro basins, where time equivalent systems occur. Nevertheless, a major heavy-mineral content shift is recorded by opaque grains along the transition from turbidite and shallow-water to continental deposits. The use of Raman spectroscopy for identification of opaque grains, coupled with sandstone petrography, helped to disentangle the interplay between source rock lithology, tectonics and diagenesis of the detrital heavy-mineral suites of the South Pyrenean basin.

Heavy-mineral provenance signatures during the evolution from marine to terrestrial environments in the Jaca basin (Southern Pyrenees)

Xavier Coll[1]*, David Gómez-Gras[1], Marta Roigé[1], Salvador Boya[1], Antonio Teixell[1], Miquel Pooyatos-Moré[2],

(*) Email: XavierColl@uab.cat
1- Provenance Research Group, Departament de Geologia, Universitat Autònoma de Barcelona, Spain
2- Provenance Research Group, Department of Geosciences, University of Oslo, Norway

INTRODUCTION AND GEOLOGICAL SETTING

Understanding the evolution of the sediment routing system of a basin provides important clues on the geotectonic evolution of the source area.

Coupling HMA with sandstone petrography can provide a higher resolution in provenance studies that may not be achieved if these techniques are used separately.

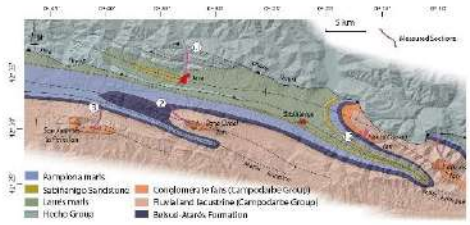

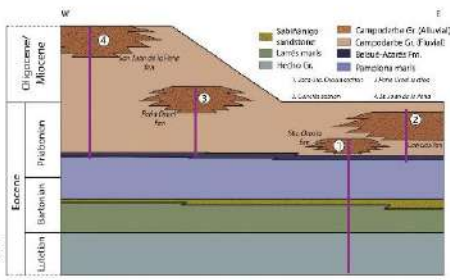

The Eocene to Miocene sedimentary infill of the Jaca Basin records a main paleogeographic change, from the deep-marine sedimentation stage (Upper Hecho Group turbidites) to the generalization of alluvial sedimentation in the Campodarbe and Bernués formations, leading to sediment recycling of earlier foreland basin deposits.

SAMPLES AND METHODS

A total of 24 sandstone samples were crushed and submitted to acid digestion with acetic acid (10%) for carbonate removal and better disgregation of grains.

After wet sieving (32-500 Mm), heavy minerals were separated with the dense liquid Na-polytungstate (2.90 g/cm3) following the centrifuge technique and the partial freezing method procedures of Mange & Maurer (1991).

The recovered heavy-mineral fraction was grain-counted by the area method (Galehouse, 1971) using Raman Spectroscopy and optical microscope.

HM results are integrated with available petrographic data (Roigé et al., 2017) in order to unravel the provenance signature of the heavy minerals.

HEAVY MINERAL AND SANDSTONE PETROGRAPHY RESULTS

The Banastón and Jaca turbidite systems, as well as the Rapitán Channel, display a HM suite mainly dominated by ultrastable Ap-Tur-Zrn-Rt. This is also the case for the Sabiñanigo Sandstone and the Belsué-Atarés Fm in the Santa Orosia and Canciás sections.

Although the alluvial fans still record the dominance of the ultrastable association Ap-Tur-Zrn-Rt, They display more varied HM suites including minerals such as St, Grt (Pyralspite and Ugrandite), Ves, Ttn, Ky, Cpx, Act and Ep.

Based on characteristic and significant compositional variations, four main petrofacies were identified.

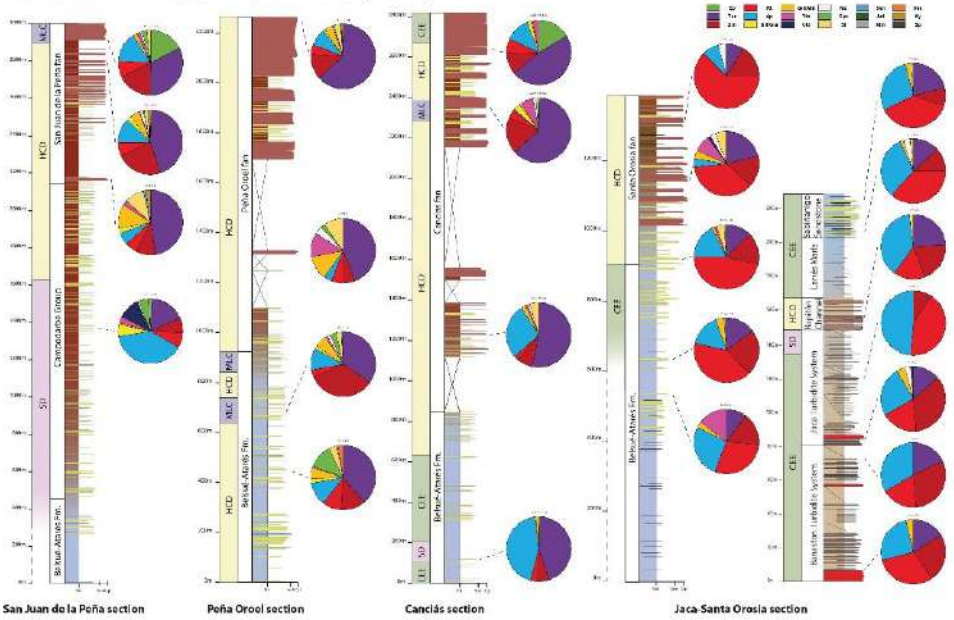

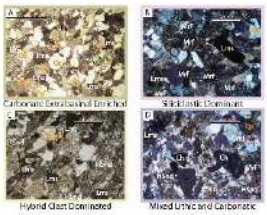

All alluvial fans record the Recycling of the former turbiditic basin due to the activity of the Gavarnie thrust.

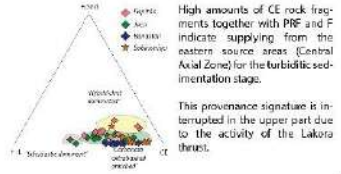

High amounts of CE rock fragments together with PRF and F indicate supplying from the eastern source areas (Central Axial Zone) for the turbiditic sedimentation stage.

This provenance signature is interrupted in the upper part due to the activity of the Lakora thrust.

COUPLING HM WITH SANDSTONE PETROGRAPHY

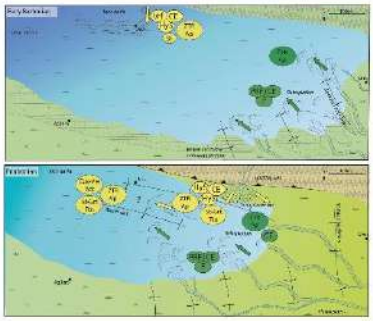

During the Turbiditic and Deltaic sedimentation stage PRF, CE and F ("CEE petrofacies") and an ultrastable HM suite (Ap-Zrn-Tur-Rt) are supplied to the basin from the Central Pyrenees trough a long axially drained system.

Nonetheless, the last turbiditic stage (Rapitán channel) records the first entrance of sediment coming from the north through an increase of HyS, Vrf and the occurrence of St (staurolite).

Source areas mainly conformed by "HM unfertile carbonate rocks", granitic sources, low-grade metamorphics and recycling of turbidite sandstones might be related with the widespread occurrence of the ultrastable HM assemblage. However, the loss of unstable minerals due to intrastratal dissolution cannot be dismissed.

With the onset of the north-derived alluvial sedimentation stage, the recycling of the former turbiditic basin becomes the dominant process ("HCD petrofacies") at the north of the basin, whereas in the southern part the east-derived axially drained systems prevail.

During the Priabonian, the HM provenance of the first alluvial fan (Sta. Orosia) is still dominated by the Ap-Zrn-Tur-Rt suite due to the recycling of the ultrastable HM suite bearing turbidites. Nonetheless, the Belsué-Atarés delta records the first occurrence of unstable minerals (Cpx, Ves, Act).

From Rupelian to Chattian-Aquitanian, new north-sourced alluvial fans (Canciás, Peña Oroel and St. Juan de la Peña) develop at the northern margin and the content of recycled turbidite fragments increase. Additionally, minerals such as Cld, Ep, Act, Cpx or Ky can be found in the HM record of the fluvial-alluvial systems.

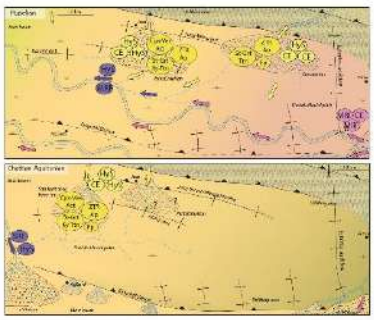

IMPLICATIONS FOR THE SEDIMENT ROUTING SYSTEM

Although recycling of the turbiditic basin is the main source during the alluvial sedimentation stage, metamorfic minerals such as St, Grt, Ky, Ves and Cld point to a direct source constituted by the Paleozoic basement (Axial Zone).

The occurrence of high proportions of Ep (20%) at the top of the Canciás and San Juan the la Peña fans coinciding with a petrofacies change (HCD to CEE and HCD to MLC respectively), points to a source area change during the last sedimentation stage of this fans.

According to petrofacies composition, the Belsué-Atarés in the Peña Oroel section might be sourced by the Sta. Orosia fan. However, the HM provenance signature implies an additional source.

In the San Juan de la Peña section, the source area of the thick fluvial succession of the Campodarbe Group could not be placed to the north. It must be located to the east, in the south-central Pyrenees, and funneled through the fluvial-alluvial systems of the Ainsa basin (i.e., upper Escanilla Formation). However, based on HM composition, it cannot be sourced by the Escanilla or Graus formations due to the absence of Epidote.

Cpx at the Base of St. Juan de la Peña and Peña Oroel sections discards significant diagenetic modifications in these part of the basin.

CONCLUSIONS

The use of HM coupled with sandstone petrography has provided new insights into the provenance of the Jaca basin infill that would have not been achieved if these techniques would have been used separately.

The ultrastable assemblage displayed by the turbiditic systems and the deltaic formations at the eastern margin might be its provenance signature although intrastatal dissolution cannot be discarded.

In the western part of the basin, significant diagenetic modifications can be dismissed due to the occurrence of Cpx at the base of the studied sections.

The alluvial sedimentation stage records the recycling of the former turbiditic basin. Moreover, the HM provenance signature points to an additional source area constituted by the Paleozoic basement in the Axial Zone.

REFERENCES

Roigé, M., Gómez Gras, D., Remacha, E., Boya, S., Viaplana-Muzas, M., & Teixell, A. (2017). Recycling an uplifted early foreland basin fill: An example from the Jaca basin (Southern Pyrenees, Spain). Sedimentary geology, 358, 1-21.

Roigé, M. (2018). Procediència i evolució dels sistemes sedimentaris de la conca de Jaca (conca d'avantpaís Sudpirinenca): Interacció entre diverses àrees fonts en un context tectònic actiu (PhD thesis). Universitat Autònoma de Barcelona (313 pp).

ACKNOWLEDGMENTS

This work is a contribution to the project CGL2014-54180-P, financed by the Ministerio de Economía y Competitividad of Spain. We are grateful to IAS for financial support.

Interplay of multiple sediment sources in the Jaca foreland basin (Southern Pyrenees)

Xavier Coll Carrillo (1), David Gómez-Gras (1), Marta Roige (1), Salvador Boya (1), Antonio Teixell (1), Miquel Poyatos-Moré (2)

(1) Universitat Autònoma de Barcelona, (2) University of Oslo

In the southern edge of the Jaca basin two main sediment routing systems merge, providing an excellent example of interaction of different source areas with distinct petrographic signatures, recording different stages of exhumation of the Pyrenean belt. We apply sandstone petrography coupled with heavy mineral analysis (HMA) in the deltaic to alluvial deposits of the southern part of the basin in order to decipher the evolution of source areas from Eocene to Miocene times. Our results allow identifying four petrofacies, which evidence the interplay of axially-fed sediments derived from the eastern sources (central Pyrenees) with transversely-fed sediments from the north (west-central Pyrenees), highly controlled by the emergence of tectonic structures. The axially-fed sediments display an important change in the source area that occurred during the Priabonian, and consisted on the shift from carbonate-rich source with plutonic rocks, by a siliciclastic-rich source area with overburden metamorphic lithic grains. The axially fed systems dominated the fluvial deposits of the Campodarbe Formation in the southern edge of the Jaca basin, which were progressively replaced from east to west by transverse-fed systems sourced from northern source areas. In the late stages of basin infill, the Ebro foreland basin and the Jaca thrust-sheet-top basin received north-derived detritus from two distinct source areas. While the Jaca basin continued recording a major recycling of former clastic deposits, the Ebro basin was characterized by additional contributions from Paleozoic sources from the western and central Pyrenees.Coupling of sandstone petrography and HMA allows to resolve ambiguous provenance signals, which hinder the characterization of the sediment routing evolution. Furthermore, distinct petrographic signatures constitute a valuable proxy to attempt stratigraphic correlation between systems, and mainly between partitioned basins as those forming the south Pyrenean foreland basin.

UAB
Universitat Autònoma de Barcelona

PROVENANCE
RESEARCH GROUP

INTERPLAY OF MULTIPLE SEDIMENT SOURCES IN AN OVERFILLED FORELAND BASIN (SOUTHERN PYRENEES)

Xavier Coll, David Gómez-Gras, Marta Roigé, Salvador Boya, Antonio Teixell, Miquel Poyatos-Moré

SEDIMENTARY PROVENANCE ANALYSIS

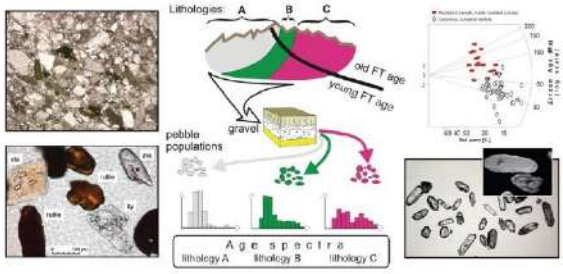

The composition of clastic sediments reflect the nature of source areas.

Different techniques are routinely applied.

Coupling various methods (i.e. sandstone petrography and HMA) provides a better resolution to unravel the provenance of arenites.

GEOLOGICAL SETTING The Jaca Basin

The Pyrenees

Fold and thrust belt.

The Jaca Basin

South Pyrenean foreland basin westernmost part.

Thrust sheet top basin.

Exceptional sedimentary record.

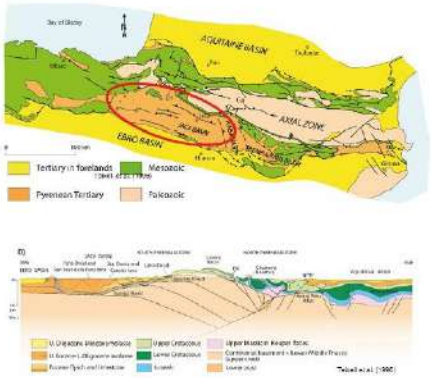

GEOLOGICAL SETTING The Jaca Basin

The turbiditic sedimentation stage ends at the same time that a reorganization of the drainage area occurs.

Thrust tectonics is responsible of the uplift of the former turbiditic basin and its recycling.

Ramacha et al. (2006)

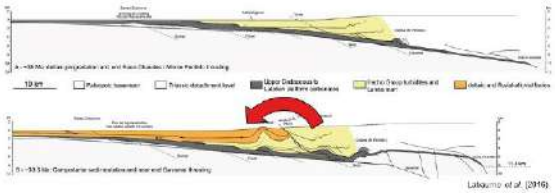

Labaume et al. (2016)

GEOLOGICAL SETTING The Jaca Basin

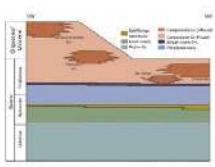

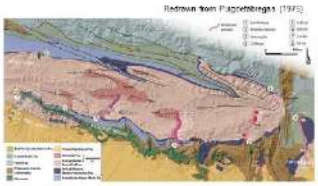

Redrawn from Puigdefàbregas (1975)

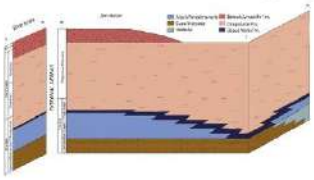

In the Bartonian, the deep marine sedimentation stage is replaced by transitional environments.

From east to west deltaic environments are replaced by fluvial and alluvial sedimentation.

METHODOLOGY

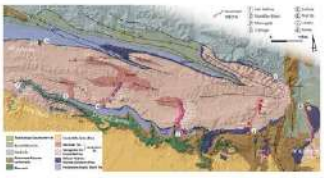

Sediment composition of deltaic to fluvial and alluvial systems was characterized using sandstone petrography.

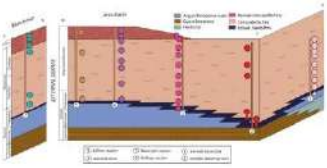

Additionally the HM suites of representative samples were identified using Raman spectroscopy.

RESULTS Sandstone Petrography

A fourth-order ternary diagram is used to discriminate among the petrofacies of the the northern Jaca basin (Roigé *et al.*, 2017).

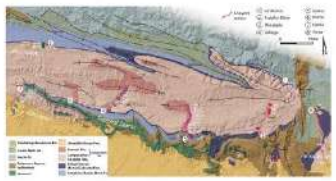

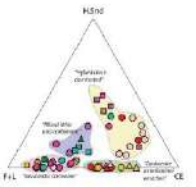

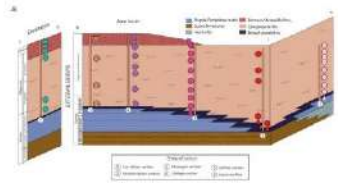

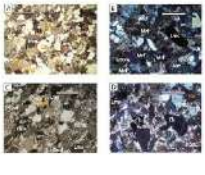

RESULTS Sandstone Petrography

A fourth-order ternary diagram is used to discriminate among the petrofacies of the the northern Jaca basin (Roigé *et al.*, 2017).

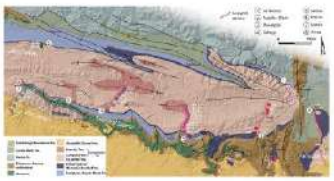

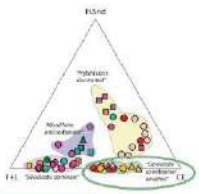

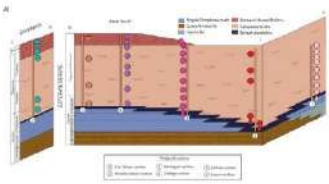

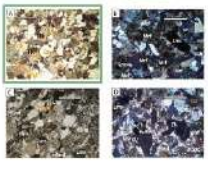

RESULTS Sandstone Petrography

A fourth-order ternary diagram is used to discriminate among the petrofacies of the the northern Jaca basin (Roigé *et al.*, 2017).

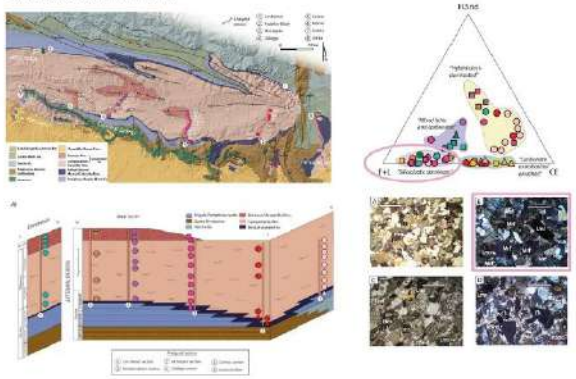

RESULTS Sandstone Petrography

A fourth-order ternary diagram is used to discriminate among the petrofacies of the the northern Jaca basin (Roigé *et al.*, 2017).

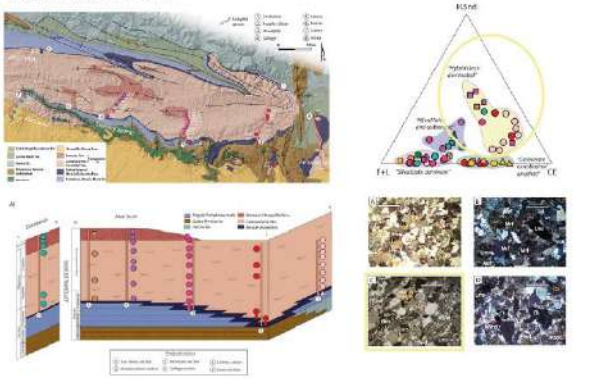

RESULTS Sandstone Petrography

A fourth-order ternary diagram is used to discriminate among the petrofacies of the the northern Jaca basin (Roigé *et al.*, 2017).

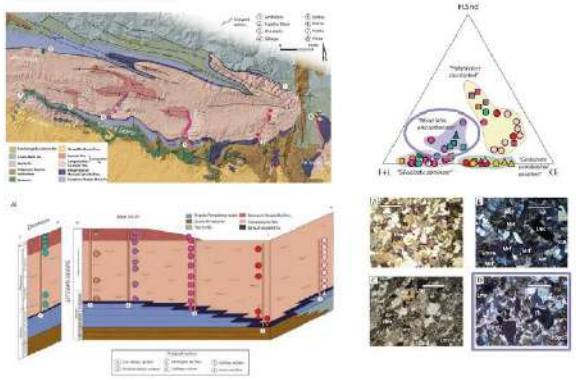

RESULTS Sandstone Petrography

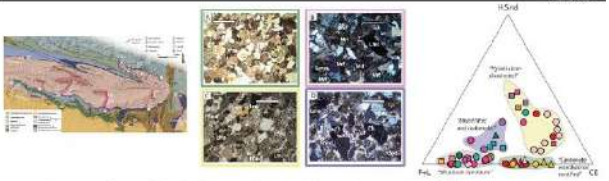

These petrofacies reflect the basin evolution and depict the interplay of different source areas.

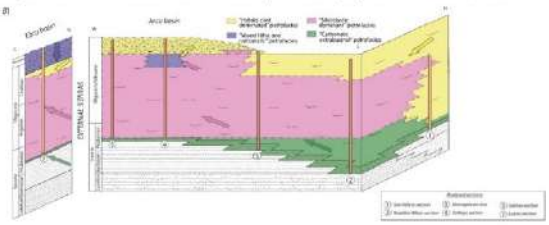

RESULTS Coupling Heavy Minerals with Sandstone Petrography

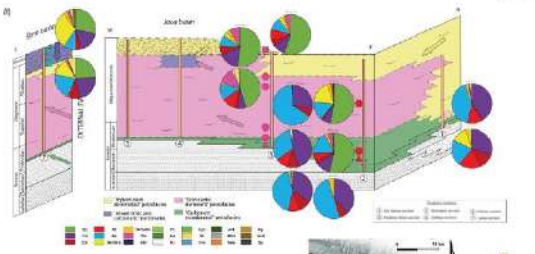

Three different HM suites were determined:

"ZTR+Ap dominant",

"Ep dominant",

"ZTR+Ap + Ep + Grt + St".

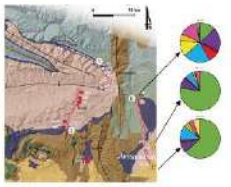

RESULTS Coupling Heavy Minerals with Sandstone Petrography

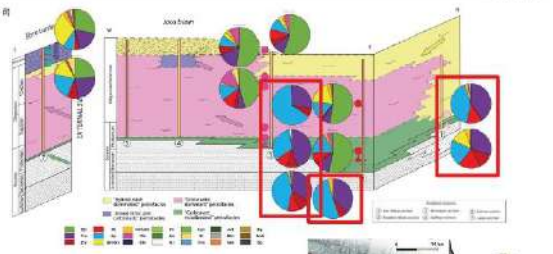

Three different HM suites were determined:

"ZTR+Ap dominant",

"Ep dominant",

"ZTR+Ap + Ep + Grt + St".

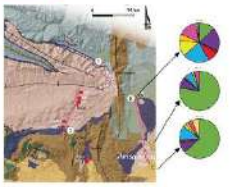

RESULTS Coupling Heavy Minerals with Sandstone Petrography

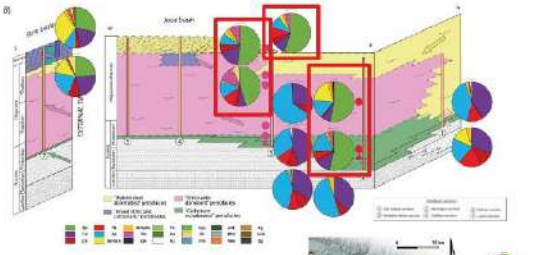

Three different HM suites were determined:

"ZTR+Ap dominant",

"Ep dominant",

"ZTR+Ap + Ep + Grt + St".

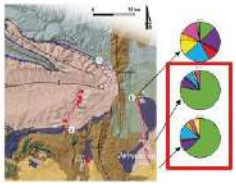

RESULTS Coupling Heavy Minerals with Sandstone Petrography

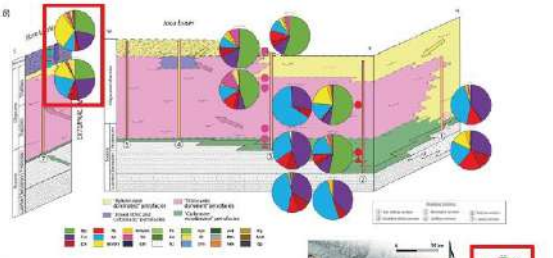

Three different HM suites were determined:

"ZTR+Ap dominant",

"Ep dominant",

"ZTR+Ap + Ep + Grt + St".

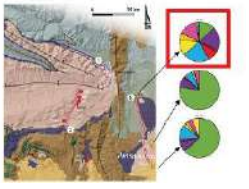

REGIONAL IMPLICATIONS

Deltaic sedimentation was mainly derived from eastern source areas.

Northern sources are mainly composed by the Hecho Group turbidites.

REGIONAL IMPLICATIONS

Transverse north-derived alluvial systems progressively replaced the axial-fed fluvial systems from east to west, and from north to south.

The uplift of the basin prevented the axial fluvial network from entering the basin.

North derived alluvial sedimentation coexisted in the Jaca and Ebro basins.

CONCLUSIONS

New **sandstone petrography** results allow to **constraint the interplay of diverse sediment routing systems** in the transitional to terrestrial environments of the **Jaca thrust-sheet-top basin**, and also from the **Ebro basin** during Lutetian to Miocene times.

Four petrofacies and **three HM suites** were defined **reflecting** the basin evolution and the **interplay of different source areas.**

Deltaic sedimentation in the southern Jaca basin (Bartonian-Priabonian) was **mainly derived from eastern source areas**, located in the **Central Pyrenees**, in which the **Paleozoic basement** contributed by delivering **dominant plutonic components** and a **"ZTR+Ap dominated"** HM assemblage.

During **Priabonian** times the **Paleozoic supply evolved to a metamorphic-rich source area** with an **"Ep Dominated"** HM signature that persisted until at least Oligo-Miocene times. **The main source of Ep** is the late Triasic dolerites (**ophites**).

Transverse **north-derived systems** progressively **replaced** the **axial-fed systems** producing a westward **displacement of the axial fluvial network,** increasing the content of hybrid ss. and ZTR+Ap in the sedimentary record.

From **Chattian to Aquitanian** times **two main north-derived systems coexisted** in the **Jaca** and **Ebro basins.**

Sandstone petrography coupled with HMA still is a powerful tool to attempt sedimentary provenance analysis.

PROVENANCE
RESEARCH GROUP

UAB
Universitat Autònoma de Barcelona

Annex 4

Resultats d'U-Pb en zircons detrítics

Sample Name:	[U]							207/235		206/238		207/206		Best age		Discordance	Rim/
Grain #	ppm	U/Th	207/235	2σ error	206/238	2σ error	RHO	Age Ma	2σ error	Age (Ma)	2σ error	Age (Ma)	2σ error	(Ma)	2σ error	%	Core
Rode-1b_1.FIN2	282,0	1,179	0,4270	0,01300	0,05710	0,0010	0,0459720	359,30	9,10	357,80	6,10	341,0	58,0	357,8	6,1	0,417	
Rode-1b_2.FIN2	92,1	1,437	1,6010	0,03800	0,16190	0,0032	0,4738200	967,00	15,00	967,00	18,00	952,0	47,0	952,0	47,0	1,576	
Rode-1b_3.FIN2	960,0	2,250	1,8330	0,04800	0,15550	0,0023	0,4861100	1056,00	17,00	932,00	13,00	1318,0	44,0	1318,0	44,0	29,287	Rim
Rode-1b_3.FIN2	132,7	0,739	4,5140	0,06100	0,29460	0,0029	0,4231800	1732,00	11,00	1664,00	14,00	1803,0	23,0	1803,0	23,0	7,709	Core
Rode-1b_4.FIN2	320,0	1,942	0,3760	0,01200	0,05202	0,0008	0,2713200	322,80	8,50	326,80	4,80	288,0	64,0	326,8	4,8	1,239	
Rode-1b_5.FIN2	226,0	0,690	0,7730	0,03700	0,09130	0,0014	0,2520600	571,00	12,00	563,30	8,50	588,0	54,0	563,3	8,5	1,349	
Rode-1b_8.FIN2	1048,0	1,519	0,8238	0,00920	0,09917	0,0010	0,5187000	609,70	5,10	609,40	5,70	597,0	25,0	609,4	5,7	0,049	
Rode-1b_9.FIN2	411,0	0,912	0,4133	0,00690	0,05577	0,0005	0,1181600	350,80	4,90	349,80	2,90	334,0	39,0	349,8	2,9	0,285	
Rode-1b_10.FIN2	1531,0	2,880	0,4110	0,02300	0,04550	0,0026	0,7737200	348,00	16,00	290,00	17,00	749,0	83,0	DISC	DISC	16,667	Rim
Rode-1b_10.FIN2	397,0	2,126	0,5630	0,01300	0,07310	0,0012	0,4983800	452,30	8,60	454,80	7,30	421,0	48,0	454,8	7,3	0,553	Core
Rode-1b_11.FIN2	245,7	2,520	0,7710	0,02100	0,08620	0,0016	0,3897000	581,00	12,00	532,80	9,50	749,0	49,0	532,8	9,5	8,296	
Rode-1b_12.FIN2	252,0	6,300	10,8600	0,28000	0,44560	0,0094	0,9087300	2502,00	24,00	2371,00	42,00	2606,0	18,0	2606,0	18,0	9,018	
Rode-1b_13.FIN2	636,9	4,920	0,8860	0,01300	0,10410	0,0011	0,3794000	643,40	7,10	638,10	6,40	653,0	29,0	638,1	6,4	0,824	
Rode-1b_14.FIN2	320,0	1,921	0,3633	0,00790	0,04990	0,0006	0,1203200	315,00	5,60	313,90	3,50	298,0	47,0	313,9	3,5	0,349	
Rode-1b_15.FIN2	285,8	1,345	0,3632	0,00880	0,04959	0,0006	0,1130800	313,80	6,50	312,00	3,60	315,0	52,0	312,0	3,6	0,574	
Rode-1b_16.FIN2	40,7	0,669	2,3850	0,08200	0,06710	0,0015	0,3885800	1231,00	24,00	418,60	9,00	3216,0	56,0	DISC	DISC	65,995	
Rode-1b_17.FIN2	212,0	2,310	1,4100	0,78000	0,08090	0,0073	0,0137280	770,00	240,00	501,00	44,00	1330,0	670,0	DISC	DISC	34,935	Rim
Rode-1b_17.FIN2	291,6	1,124	0,8319	0,01700	0,09660	0,0014	0,4275500	612,90	9,20	594,40	8,20	655,0	38,0	594,4	8,2	3,018	Core
Rode-1b_18.FIN2	784,0	1,871	0,3723	0,00660	0,04931	0,0006	0,1961900	320,90	4,90	310,20	3,90	374,0	37,0	310,2	3,9	3,334	
Rode-1b_19.FIN2	9390,0	18,600	0,2290	0,03300	0,02090	0,0013	0,3981800	209,00	27,00	133,60	8,40	1120,0	250,0	DISC	DISC	36,077	Rim
Rode-1b_19.FIN2	634,0	3,930	0,3866	0,00790	0,05287	0,0008	0,4480100	332,20	5,60	332,10	5,20	311,0	42,0	332,1	5,2	0,030	Core
Rode-1b_20.FIN2	218,0	1,730	1,2640	0,02300	0,13800	0,0019	0,4332000	828,00	10,00	833,00	11,00	798,0	35,0	833,0	11,0	0,604	
Rode-1b_21.FIN2	174,4	0,439	0,9290	0,02500	0,10770	0,0018	0,4664000	664,00	13,00	659,00	11,00	657,0	45,0	659,0	11,0	0,753	
Rode-1b_22.FIN2	972,0	47,400	0,7660	0,01000	0,09210	0,0011	0,1607500	577,10	5,70	568,00	6,30	592,0	25,0	568,0	6,3	1,577	
Rode-1b_23.FIN2	320,0	1,917	0,4012	0,00920	0,05065	0,0006	0,2555700	341,70	6,60	318,50	3,40	487,0	49,0	318,5	3,4	6,790	
Rode-1b_24.FIN2	382,0	5,220	0,5900	0,01000	0,07600	0,0009	0,3708000	469,80	6,70	472,10	5,40	440,0	38,0	472,1	5,4	0,490	
Rode-1b_25.FIN2	254,0	1,140	1,6740	0,02400	0,16880	0,0016	0,3238300	997,20	9,30	1005,40	8,80	966,0	28,0	966,0	28,0	4,079	
Rode-1b_26.FIN2	990,0	0,000	0,3900	0,02800	0,04960	0,0022	0,6460500	333,00	20,00	312,00	13,00	480,0	130,0	312,0	13,0	6,306	Rim
Rode-1b_26.FIN2	128,2	2,760	0,7340	0,02300	0,09030	0,0012	0,0806880	557,00	14,00	557,10	6,90	530,0	70,0	557,1	6,9	0,018	Core
Rode-1b_27.FIN2	185,0	1,135	0,6470	0,01500	0,08110	0,0013	0,2877600	505,40	8,90	502,60	8,00	501,0	53,0	502,6	8,0	0,554	
Rode-1b_28.FIN2	839,0	2,040	0,3974	0,00970	0,05280	0,0010	0,3706700	338,80	7,00	331,80	6,10	384,0	44,0	331,8	6,1	2,066	
Rode-1b_29.FIN2	364,0	1,960	0,3632	0,00890	0,04815	0,0006	0,1947200	313,80	6,60	303,10	3,40	371,0	55,0	303,1	3,4	3,410	
Rode-1b_30.FIN2	23,3	1,180	0,9510	0,05800	0,10850	0,0030	0,2377300	663,00	28,00	663,00	18,00	600,0	120,0	663,0	18,0	0,000	
Rode-1b_31.FIN2	128,0	0,789	0,8700	0,02700	0,10030	0,0019	0,0346180	632,00	14,00	616,00	11,00	657,0	54,0	616,0	11,0	2,532	
Rode-1b_32.FIN2	375,0	1,225	0,3464	0,00690	0,04815	0,0005	0,1915800	301,50	5,20	303,10	3,10	281,0	43,0	303,1	3,1	0,531	
Rode-1b_33.FIN2	2700,0	2,180	0,3540	0,01600	0,04460	0,0020	0,6217200	307,00	12,00	281,00	12,00	480,0	75,0	281,0	12,0	8,469	Rim
Rode-1b_33.FIN2	395,0	1,679	0,5580	0,03000	0,06870	0,0023	0,8178900	446,00	19,00	428,00	14,00	510,0	68,0	428,0	14,0	4,036	Core
Rode-1b_34.FIN2	744,0	2,217	0,3745	0,00820	0,05013	0,0008	0,5521500	322,30	6,10	315,20	4,90	367,0	41,0	315,2	4,9	2,203	
Rode-1b_35.FIN2	316,0	2,081	0,3550	0,00790	0,04900	0,0005	0,1330100	307,80	5,90	308,40	3,20	285,0	48,0	308,4	3,2	0,195	
Rode-1b_36.FIN2	607,0	0,432	0,7390	0,01100	0,08880	0,0011	0,4268700	561,30	6,40	548,50	6,40	617,0	31,0	548,5	6,4	2,280	
Rode-1b_37.FIN2	142,9	1,656	0,7180	0,01900	0,08740	0,0012	0,3565300	547,00	11,00	539,90	7,10	572,0	55,0	539,9	7,1	1,298	
Rode-1b_38.FIN2	2450,0	4,690	0,3310	0,01600	0,04200	0,0015	0,4385700	289,00	12,00	265,00	9,40	481,0	93,0	265,0	9,4	8,304	Rim
Rode-1b_38.FIN2	590,0	1,862	0,3766	0,00750	0,05115	0,0007	0,4837600	324,90	5,70	321,50	4,10	336,0	42,0	321,5	4,1	1,046	Core
Rode-1b_39.FIN2	304,0	2,089	0,3467	0,00780	0,04857	0,0005	0,2371100	301,60	5,90	305,70	3,20	282,0	54,0	305,7	3,2	1,359	
Rode-1b_40.FIN2	10,0	0,345	16,4100	0,52000	0,18490	0,0059	0,6663900	2890,00	30,00	1091,00	32,00	4615,0	42,0	DISC	DISC	76,360	
Rode-1b_41.FIN2	284,0	1,977	0,3914	0,00920	0,05052	0,0006	0,2673600	334,60	6,80	317,70	3,50	432,0	55,0	317,7	3,5	5,051	
Rode-1b_42.FIN2	519,0	2,355	0,3253	0,00820	0,04250	0,0009	0,5094100	285,30	6,20	268,20	5,50	428,0	49,0	268,2	5,5	5,994	

Sample Name:	[U]							207/235		206/238		207/206		Best age		Discordance	Rim/
Grain #	ppm	U/Th	207/235	2σ error	206/238	2σ error	RHO	Age Ma	2σ error	Age (Ma)	2σ error	Age (Ma)	2σ error	(Ma)	2σ error	%	Core
Rode-1b_43.FIN2	531,0	1,383	0,3442	0,00800	0,04766	0,0006	0,1807000	299,70	6,00	300,10	3,60	294,0	53,0	300,1	3,6	0,133	
Rode-1b_44.FIN2	472,0	25,000	0,4770	0,06000	0,05400	0,0022	0,0877270	391,00	36,00	339,00	13,00	660,0	220,0	339,0	13,0	13,299	Rim
Rode-1b_44.FIN2	183,0	1,356	1,8140	0,03400	0,17980	0,0028	0,6886400	1049,00	12,00	1066,00	15,00	1013,0	31,0	1013,0	31,0	5,232	Core
Rode-1b_45.FIN2	420,0	1,982	0,3471	0,00730	0,04911	0,0004	0,1747600	302,00	5,50	309,00	2,70	250,0	46,0	309,0	2,7	2,318	
Rode-1b_46.FIN2	70,4	1,680	1,0270	0,03500	0,11700	0,0037	0,4584200	718,00	18,00	712,00	21,00	741,0	75,0	712,0	21,0	0,836	
Rode-1b_47.FIN2	154,0	0,811	12,3300	0,12000	0,49770	0,0043	0,7262600	2628,50	9,00	2603,00	18,00	2654,0	11,0	2654,0	11,0	1,922	
Rode-1b_49.FIN2	705,0	1,920	0,8870	0,01200	0,10470	0,0010	0,3373900	644,10	6,60	641,80	5,80	657,0	29,0	641,8	5,8	0,357	
Rode-1b_50.FIN2	155,0	3,810	0,6080	0,03400	0,07600	0,0021	0,3390200	480,00	20,00	472,00	13,00	500,0	110,0	472,0	13,0	1,667	Rim
Rode-1b_50.FIN2	164,2	1,770	1,0570	0,04000	0,12110	0,0034	0,6984900	729,00	19,00	736,00	19,00	718,0	55,0	736,0	19,0	0,960	Core
Rode-1b_51.FIN2	599,3	4,800	0,8590	0,01500	0,09365	0,0008	0,3090400	629,00	8,10	577,10	4,90	826,0	33,0	577,1	4,9	8,251	
Rode-1b_52.FIN2	683,0	1,770	0,3631	0,00730	0,05006	0,0005	0,2998800	314,00	5,40	314,90	3,30	301,0	43,0	314,9	3,3	0,287	
Rode-1b_53.FIN2	392,0	2,095	0,4200	0,02200	0,04853	0,0007	0,1069500	347,00	13,00	305,40	4,30	596,0	82,0	305,4	4,3	11,988	
Rode-1b_54.FIN2	154,1	1,759	0,7050	0,03200	0,08440	0,0013	0,0724680	537,00	16,00	522,00	7,80	567,0	61,0	522,0	7,8	2,793	
Rode-1b_55.FIN2	290,0	1,830	8,2600	0,50000	0,30300	0,0170	0,9785900	2207,00	59,00	1690,00	86,00	2796,0	19,0	DISC	DISC	39,557	
Rode-1b_56.FIN2	248,0	1,599	0,3751	0,00900	0,05169	0,0007	0,0953080	322,60	6,60	324,80	4,20	310,0	53,0	324,8	4,2	0,682	
Rode-1b_57.FIN2	290,0	1,639	0,3531	0,00890	0,04819	0,0006	0,1494000	306,20	6,70	303,40	3,40	333,0	56,0	303,4	3,4	0,914	
Rode-1b_58.FIN2	205,4	0,564	0,8930	0,01800	0,10310	0,0019	0,0768800	646,00	9,70	632,00	11,00	696,0	46,0	632,0	11,0	2,167	
Rode-1b_59.FIN2	543,0	2,976	0,3537	0,00770	0,04805	0,0005	0,1710600	306,90	5,70	302,50	3,00	333,0	45,0	302,5	3,0	1,434	
Rode-1b_60.FIN2	146,0	1,034	0,4710	0,01900	0,05853	0,0009	0,0814440	385,00	10,00	366,60	5,30	485,0	70,0	366,6	5,3	4,779	
Rode-1b_61.FIN2	472,0	1,568	0,3559	0,00710	0,04896	0,0005	0,1523600	308,70	5,30	308,10	3,20	311,0	45,0	308,1	3,2	0,194	
Rode-1b_62.FIN2	375,0	3,550	0,3554	0,00770	0,04909	0,0006	0,2802300	308,10	5,70	308,90	3,70	306,0	45,0	308,9	3,7	0,260	
Rode-1b_63.FIN2	1640,0	0,552	0,7360	0,05400	0,07670	0,0052	0,3529500	556,00	31,00	476,00	31,00	860,0	160,0	476,0	31,0	14,388	Rim
Rode-1b_63.FIN2	669,0	0,879	0,9190	0,01600	0,10970	0,0017	0,7731600	660,80	8,70	670,60	9,80	641,0	25,0	670,6	9,8	1,483	Core
Rode-1b_64.FIN2	351,1	3,590	2,7200	0,08200	0,23410	0,0057	0,8928000	1326,00	23,00	1354,00	30,00	1292,0	28,0	1292,0	28,0	4,799	
Rode-1b_65.FIN2	134,0	2,390	13,7200	0,23000	0,54910	0,0093	0,7190100	2731,00	15,00	2829,00	36,00	2669,0	19,0	2669,0	19,0	5,995	
Rode-1b_66.FIN2	1460,0	3,290	0,2731	0,00720	0,03438	0,0008	0,7224300	244,60	5,70	217,80	5,00	514,0	39,0	217,8	5,0	10,957	
Rode-1b_67.FIN2	496,0	0,750	10,8400	0,22000	0,44190	0,0089	0,8367800	2503,00	19,00	2355,00	40,00	2639,0	18,0	2639,0	18,0	10,762	
Rode-1b_68.FIN2	397,0	2,323	0,3665	0,00820	0,05075	0,0006	0,2827100	316,40	6,10	319,10	3,70	302,0	46,0	319,1	3,7	0,853	
Rode-1b_69.FIN2	408,0	2,036	0,3523	0,00750	0,04824	0,0004	0,1825200	305,80	5,60	303,70	2,50	314,0	47,0	303,7	2,5	0,687	
Rode-1b_70.FIN2	1090,0	27,000	0,3620	0,01400	0,04720	0,0017	0,6222600	313,00	10,00	297,00	11,00	436,0	77,0	297,0	11,0	5,112	Rim
Rode-1b_70.FIN2	604,0	0,861	0,7540	0,01200	0,09070	0,0011	0,5694000	569,80	6,70	559,30	6,40	610,0	29,0	559,3	6,4	1,843	Core
Rode-1b_71.FIN2	678,0	0,868	0,4225	0,00710	0,05718	0,0005	0,3416200	357,40	5,00	358,40	3,00	352,0	35,0	358,4	3,0	0,280	
Rode-1b_72.FIN2	323,0	1,481	0,3577	0,00770	0,04914	0,0006	0,3273500	309,90	5,80	309,20	3,70	309,0	44,0	309,2	3,7	0,226	
Rode-1b_73.FIN2	1272,0	2,322	0,3776	0,00680	0,05211	0,0007	0,4872900	324,80	5,00	327,40	4,30	320,0	34,0	327,4	4,3	0,800	
Rode-1b_74.FIN2	173,8	0,888	1,4770	0,03100	0,14670	0,0023	0,6798100	918,00	13,00	882,00	13,00	1011,0	31,0	1011,0	31,0	12,760	
Rode-1b_75.FIN2	397,0	2,075	0,3622	0,00850	0,04996	0,0006	0,3781100	313,20	6,30	314,30	3,80	305,0	48,0	314,3	3,8	0,351	
Rode-1b_76.FIN2	609,0	1,242	0,7080	0,01400	0,07970	0,0017	0,3180200	542,20	8,20	494,00	10,00	755,0	41,0	494,0	10,0	8,890	
Rode-1b_77.FIN2	441,0	1,459	0,3699	0,00850	0,05118	0,0006	0,1619200	317,70	5,80	321,70	3,50	292,0	48,0	321,7	3,5	1,259	
Rode-1b_78.FIN2	260,0	6,020	1,1400	0,12000	0,08270	0,0079	0,0662400	766,00	55,00	511,00	47,00	1600,0	260,0	DISC	DISC	33,290	Rim
Rode-1b_78.FIN2	47,9	1,095	1,6070	0,05500	0,15950	0,0035	0,4823000	970,00	22,00	957,00	20,00	1002,0	62,0	1002,0	62,0	4,491	Core
Rode-1b_79.FIN2	528,0	2,210	11,3000	0,16000	0,45240	0,0062	0,8706600	2547,00	13,00	2407,00	28,00	2659,0	12,0	2659,0	12,0	9,477	
Rode-1b_80.FIN2	238,0	0,924	6,2600	0,13000	0,36700	0,0074	0,5693900	2007,00	19,00	2012,00	35,00	1997,0	32,0	1997,0	32,0	0,751	
Rode-1b_81.FIN2	837,0	1,803	0,3518	0,00690	0,04772	0,0006	0,3042900	305,60	5,20	300,50	3,40	332,0	40,0	300,5	3,4	1,669	
Rode-1b_82.FIN2	312,9	2,202	0,3501	0,00950	0,04828	0,0007	0,0653250	303,90	7,10	303,90	4,40	286,0	58,0	303,9	4,4	0,000	
Rode-1b_83.FIN2	293,3	0,950	0,4460	0,01400	0,05726	0,0009	0,0287250	373,60	9,40	358,90	5,70	446,0	63,0	358,9	5,7	3,935	
Rode-1b_84.FIN2	294,8	0,730	0,9240	0,01500	0,10620	0,0013	0,4396100	663,60	7,90	650,70	7,80	703,0	33,0	650,7	7,8	1,944	
Rode-1b_85.FIN2	493,0	3,560	0,4911	0,00850	0,06359	0,0007	0,3667500	406,50	5,80	397,30	4,40	460,0	36,0	397,3	4,4	2,263	

Sample Name:	[U]							207/235		206/238		207/206		Best age		Discordance	Rim/
Grain #	ppm	U/Th	207/235	2σ error	206/238	2σ error	RHO	Age Ma	2σ error	Age (Ma)	2σ error	Age (Ma)	2σ error	(Ma)	2σ error	%	Core
Rode-1b_86.FIN2	1560,0	82,000	0,9510	0,07900	0,10950	0,0060	0,6007000	675,00	40,00	670,00	35,00	680,0	120,0	670,0	35,0	0,741	Rim
Rode-1b_86.FIN2	275,0	0,742	1,6730	0,03600	0,16710	0,0023	0,7735200	996,00	13,00	996,00	13,00	1011,0	35,0	1011,0	35,0	1,484	Core
Rode-1b_87.FIN2	525,0	1,959	0,3645	0,00830	0,04935	0,0005	0,2684000	315,70	6,00	310,50	3,30	343,0	46,0	310,5	3,3	1,647	
Rode-1b_88.FIN2	730,0	2,030	0,3735	0,00830	0,05139	0,0008	0,3938100	321,60	6,10	323,00	4,60	319,0	45,0	323,0	4,6	0,435	
Rode-1b_89.FIN2	568,0	1,802	0,3390	0,04000	0,03980	0,0015	0,2798500	294,00	28,00	251,80	9,40	680,0	240,0	251,8	9,4	14,354	Rim
Rode-1b_89.FIN2	171,5	2,089	0,3390	0,01600	0,04689	0,0008	0,1012300	295,00	12,00	295,40	4,90	270,0	100,0	295,4	4,9	0,136	Core
Rode-1b_90.FIN2	195,0	0,500	0,8340	0,02300	0,09800	0,0013	0,3497300	613,00	12,00	602,50	7,60	625,0	52,0	602,5	7,6	1,713	
Rode-1b_91.FIN2	300,0	1,547	0,3481	0,00940	0,04739	0,0007	0,3314300	302,40	7,00	298,40	4,10	328,0	56,0	298,4	4,1	1,323	
Rode-1b_92.FIN2	734,0	9,400	1,5480	0,03300	0,15700	0,0026	0,7116900	947,00	13,00	940,00	15,00	964,0	29,0	964,0	29,0	2,490	
Rode-1b_93.FIN2	565,0	1,133	1,3320	0,02900	0,12810	0,0029	0,8003000	859,00	13,00	776,00	17,00	1078,0	29,0	776,0	17,0	9,662	
Rode-1b_94.FIN2	372,0	4,000	0,5440	0,01700	0,07050	0,0016	0,0395700	440,00	11,00	438,80	9,70	444,0	60,0	438,8	9,7	0,273	
Rode-1b_95.FIN2	316,0	1,546	0,3501	0,00980	0,04777	0,0006	0,1773100	302,40	6,80	300,80	3,80	301,0	56,0	300,8	3,8	0,529	
Rode-1b_96.FIN2	309,0	1,574	0,3402	0,00910	0,04637	0,0008	0,2016300	296,50	6,80	292,10	4,60	326,0	55,0	292,1	4,6	1,484	
Rode-1b_97.FIN2	3,6	0,340	0,8000	0,15000	0,02190	0,0030	0,0038544	497,00	80,00	139,00	19,00	900,0	2900,0	DISC	DISC	72,032	
Rode-1b_98.FIN2	353,0	5,380	0,9570	0,01500	0,11170	0,0013	0,3836800	680,40	7,80	682,40	7,30	674,0	34,0	682,4	7,3	0,294	
Rode-1b_99.FIN2	466,0	3,070	0,3746	0,00750	0,05260	0,0007	0,2021800	322,50	5,50	330,40	4,00	272,0	44,0	330,4	4,0	2,450	
Rode-1b_100.FIN2	255,0	1,653	0,3737	0,00990	0,05119	0,0006	0,2102500	321,40	7,30	321,80	3,80	310,0	55,0	321,8	3,8	0,124	
Rode-1b_101.FIN2	235,5	1,565	0,3525	0,00890	0,04848	0,0006	0,0708120	305,70	6,60	305,20	3,50	304,0	54,0	305,2	3,5	0,164	
Rode-1b_102.FIN2	1240,0	12,400	0,3110	0,05900	0,04100	0,0130	0,0024923	272,00	45,00	256,00	77,00	650,0	620,0	DISC	DISC	5,882	Rim
Rode-1b_102.FIN2	584,0	23,080	0,7460	0,01400	0,09080	0,0017	0,6541100	564,60	8,30	560,20	9,90	583,0	36,0	560,2	9,9	0,779	Core
Rode-1b_103.FIN2	422,0	2,460	0,3900	0,01600	0,04980	0,0018	0,3547800	330,00	11,00	313,00	11,00	481,0	68,0	313,0	11,0	5,152	
Rode-1b_104.FIN2	448,0	1,969	0,3749	0,00880	0,05119	0,0006	0,4395100	322,50	6,40	321,80	3,90	317,0	45,0	321,8	3,9	0,217	
Rode-1b_105.FIN2	631,0	7,000	0,4390	0,01800	0,05880	0,0018	0,2385300	372,00	14,00	368,00	11,00	390,0	100,0	368,0	11,0	1,075	Rim
Rode-1b_105.FIN2	92,6	2,140	1,0910	0,05300	0,12050	0,0036	0,4847400	744,00	26,00	733,00	21,00	767,0	89,0	733,0	21,0	1,478	Core
Rode-1b_106.FIN2	782,0	1,420	0,4313	0,00680	0,05700	0,0005	0,3057400	363,70	4,80	357,30	3,10	406,0	35,0	357,3	3,1	1,760	
Rode-1b_107.FIN2	356,0	2,480	0,3520	0,00760	0,04942	0,0006	0,2377100	305,60	5,70	310,90	3,40	268,0	46,0	310,9	3,4	1,734	
Rode-1b_108.FIN2	142,5	0,304	0,5140	0,01600	0,06665	0,0009	0,0858830	419,00	11,00	415,90	5,60	421,0	69,0	415,9	5,6	0,740	
Rode-1b_109.FIN2	183,0	1,260	0,4230	0,01400	0,05120	0,0010	0,0891780	357,00	10,00	321,90	6,30	581,0	81,0	321,9	6,3	9,832	
Rode-1b_110.FIN2	252,0	1,359	0,3550	0,01000	0,04927	0,0006	0,2643700	307,70	7,60	310,00	3,70	292,0	59,0	310,0	3,7	0,747	
Rode-1b_111.FIN2	196,7	1,189	1,5650	0,03200	0,14690	0,0026	0,4133200	953,00	12,00	883,00	15,00	1129,0	42,0	1129,0	42,0	21,789	
Rode-1b_112.FIN2	404,0	3,840	0,6390	0,01200	0,08230	0,0010	0,5120000	500,70	7,60	509,90	6,20	462,0	38,0	509,9	6,2	1,837	
Rode-1b_113.FIN2	283,7	1,120	0,3394	0,00840	0,04720	0,0005	0,1720600	296,00	6,20	297,30	2,80	280,0	48,0	297,3	2,8	0,439	
Rode-1b_114.FIN2	84,7	1,461	0,8170	0,03100	0,09650	0,0014	0,1028700	598,00	14,00	593,80	8,00	591,0	67,0	593,8	8,0	0,702	
Rode-1b_115.FIN2	47,2	0,675	2,5910	0,08700	0,06480	0,0014	0,2740300	1291,00	25,00	404,60	8,40	3405,0	54,0	DISC	DISC	68,660	
Rode-1b_116.FIN2	170,0	1,580	0,4270	0,01500	0,05490	0,0011	0,3326700	361,00	11,00	344,30	6,60	455,0	74,0	344,3	6,6	4,626	
Rode-1b_117.FIN2	300,0	1,558	1,3110	0,03100	0,14030	0,0027	0,4397600	847,00	13,00	846,00	15,00	833,0	50,0	846,0	15,0	0,118	
Rode-1b_118.FIN2	279,0	1,400	0,9640	0,06100	0,10770	0,0019	0,1860100	679,00	25,00	659,00	11,00	739,0	90,0	659,0	11,0	2,946	Rim
Rode-1b_118.FIN2	220,6	1,033	1,4200	0,04400	0,14760	0,0029	0,5138300	896,00	18,00	887,00	16,00	918,0	55,0	918,0	55,0	3,377	Core
Rode-1b_119.FIN2	229,0	0,997	0,6300	0,11000	0,03450	0,0044	0,0933670	476,00	61,00	218,00	27,00	1970,0	300,0	DISC	DISC	54,202	Rim
Rode-1b_119.FIN2	251,9	0,613	1,2860	0,05600	0,11290	0,0027	0,5687900	842,00	27,00	689,00	16,00	1268,0	62,0	DISC	DISC	18,171	Core
Rode-1b_120.FIN2	933,0	5,695	0,8788	0,00950	0,10389	0,0009	0,4922300	639,90	5,20	637,10	5,30	654,0	21,0	637,1	5,3	0,438	
Rode-1b_121.FIN2	328,6	1,691	0,3630	0,01000	0,04895	0,0007	0,1565400	313,30	7,70	308,00	4,30	342,0	57,0	308,0	4,3	1,692	
Rode-1b_122.FIN2	368,0	1,410	0,3880	0,01300	0,04950	0,0013	0,4471600	332,00	9,30	311,20	7,80	453,0	75,0	311,2	7,8	6,265	
Rode-1b_123.FIN2	127,0	2,231	0,6790	0,02300	0,08500	0,0012	0,2171200	523,00	14,00	526,00	6,90	503,0	72,0	526,0	6,9	0,574	
Rode-1b_124.FIN2	662,0	1,640	0,4067	0,00900	0,05468	0,0007	0,4966700	345,70	6,50	343,10	4,40	363,0	42,0	343,1	4,4	0,752	
Rode-1b_125.FIN2	198,0	0,954	0,8350	0,02000	0,10420	0,0018	0,5738300	616,00	12,00	639,00	10,00	532,0	45,0	639,0	10,0	3,734	
Rode-1b_126.FIN2	311,0	1,541	0,3553	0,00860	0,04901	0,0006	0,2058300	308,00	6,40	308,40	3,90	307,0	53,0	308,4	3,9	0,130	

Sample Name:	[U]							207/235		206/238		207/206		Best age		Discordance	Rim/
Grain #	ppm	U/Th	207/235	2σ error	206/238	2σ error	RHO	Age Ma	2σ error	Age (Ma)	2σ error	Age (Ma)	2σ error	(Ma)	2σ error	%	Core
Rode-1b_127.FIN2	891,0	1,169	0,8090	0,01500	0,09090	0,0015	0,7783200	600,40	8,60	561,90	8,60	761,0	25,0	561,9	8,6	6,412	
Rode-1b_128.FIN2	321,0	1,741	0,3553	0,00830	0,04850	0,0005	0,1051100	308,00	6,20	305,30	3,10	329,0	50,0	305,3	3,1	0,877	
Rode-1b_129.FIN2	344,0	2,740	5,1600	0,22000	0,32200	0,0130	0,1012300	1841,00	37,00	1795,00	63,00	1900,0	84,0	1900,0	84,0	5,526	Rim
Rode-1b_129.FIN2	289,0	0,895	9,3600	0,18000	0,43650	0,0084	0,8347200	2370,00	17,00	2332,00	38,00	2409,0	17,0	2409,0	17,0	3,196	Core
Rode-1b_130.FIN2	238,0	2,359	5,0200	0,12000	0,28910	0,0058	0,5718900	1816,00	20,00	1635,00	29,00	2047,0	28,0	2047,0	28,0	20,127	
Rode-1b_131.FIN2	254,0	2,340	1,4550	0,03300	0,15420	0,0026	0,7506000	910,00	13,00	924,00	15,00	880,0	30,0	880,0	30,0	5,000	
Rode-1b_132.FIN2	267,0	1,300	0,8660	0,02100	0,10600	0,0019	0,5639300	631,00	11,00	649,00	11,00	574,0	48,0	649,0	11,0	2,853	
Rode-1b_133.FIN2	235,0	2,006	0,3478	0,00970	0,04898	0,0005	0,0818710	302,00	7,30	308,20	3,20	257,0	60,0	308,2	3,2	2,053	
Rode-1b_134.FIN2	602,0	30,500	0,3945	0,00750	0,05287	0,0008	0,3650300	337,10	5,50	332,10	5,00	383,0	44,0	332,1	5,0	1,483	
Rode-1b_135.FIN2	26,6	0,755	5,8800	0,17000	0,08030	0,0018	0,3385500	1949,00	27,00	498,00	11,00	4316,0	45,0	DISC	DISC	74,448	
ROD-3_1.FIN2	392,0	2,951	0,3366	0,00630	0,04786	0,0005	0,2559100	294,10	4,80	301,30	2,90	234,0	40,0	301,3	2,9	2,448	
ROD-3_3.FIN2	156,0	3,040	0,4080	0,01100	0,05533	0,0008	0,2197900	346,40	7,60	347,10	4,90	342,0	58,0	347,1	4,9	0,202	
ROD-3_4.FIN2	486,0	1,543	0,4301	0,00780	0,05805	0,0009	0,5662500	362,70	5,50	363,70	5,20	351,0	34,0	363,7	5,2	0,276	
ROD-3_5.FIN2	503,0	2,690	0,8810	0,01500	0,10360	0,0015	0,7278700	641,50	8,20	635,00	8,60	664,0	26,0	635,0	8,6	1,013	
ROD-3_6.FIN2	251,0	1,622	1,5490	0,02200	0,16000	0,0020	0,6801100	950,00	8,70	956,00	11,00	932,0	23,0	932,0	23,0	2,575	
ROD-3_7.FIN2	570,0	1,250	0,3660	0,00880	0,04920	0,0011	0,5465200	316,10	6,50	309,40	6,60	361,0	49,0	309,4	6,6	2,120	
ROD-3_8.FIN2	582,0	27,500	5,1870	0,06500	0,32180	0,0034	0,6913700	1848,00	11,00	1798,00	17,00	1906,0	17,0	1906,0	17,0	5,666	
ROD-3_9.FIN2	699,0	2,360	0,4931	0,00790	0,06250	0,0007	0,6492000	406,50	5,40	390,70	4,10	486,0	27,0	390,7	4,1	3,887	
ROD-3_10.FIN2	47,7	1,047	0,5490	0,05400	0,05770	0,0028	0,0768480	441,00	36,00	362,00	17,00	850,0	220,0	DISC	DISC	17,914	Rim
ROD-3_10.FIN2	157,8	0,526	4,8760	0,09200	0,28640	0,0044	0,8164100	1796,00	16,00	1623,00	22,00	2000,0	20,0	2000,0	20,0	18,850	Core
ROD-3_11.FIN2	496,0	2,390	0,3631	0,00650	0,04999	0,0006	0,4643200	314,10	4,80	314,40	3,50	298,0	35,0	314,4	3,5	0,096	
ROD-3_12.FIN2	237,0	1,799	10,4200	0,18000	0,41810	0,0068	0,7698800	2468,00	16,00	2252,00	32,00	2659,0	18,0	2659,0	18,0	15,307	
ROD-3_13.FIN2	367,1	2,058	0,3688	0,00980	0,04990	0,0012	0,5366400	318,20	7,20	313,60	7,50	359,0	55,0	313,6	7,5	1,446	
ROD-3_14.FIN2	266,0	1,845	0,3429	0,00920	0,04792	0,0008	0,5579500	298,50	7,00	302,30	5,10	263,0	47,0	302,3	5,1	1,273	
ROD-3_16.FIN2	535,0	1,690	1,0100	0,01600	0,11510	0,0014	0,7513500	707,50	8,30	702,30	8,10	720,0	23,0	702,3	8,1	0,735	
ROD-3_17.FIN2	802,0	3,170	0,3331	0,00730	0,04513	0,0009	0,7694100	291,30	5,60	284,50	5,30	341,0	32,0	284,5	5,3	2,334	
ROD-3_18.FIN2	256,9	1,013	1,6970	0,02000	0,16400	0,0019	0,5578500	1008,30	8,00	979,00	10,00	1068,0	23,0	1068,0	23,0	8,333	
ROD-3_19.FIN2	487,0	1,468	4,4400	0,13000	0,27840	0,0074	0,8836000	1717,00	24,00	1582,00	37,00	1892,0	28,0	1892,0	28,0	16,385	
ROD-3_20.FIN2	533,0	3,550	0,3525	0,00570	0,04852	0,0005	0,4307300	306,30	4,30	305,40	2,70	302,0	35,0	305,4	2,7	0,294	
ROD-3_21.FIN2	186,8	1,731	0,3322	0,00870	0,04718	0,0008	0,5674100	291,30	6,80	297,10	4,80	257,0	50,0	297,1	4,8	1,991	
ROD-3_22.FIN2	501,0	1,584	0,7980	0,01100	0,09620	0,0012	0,6539800	595,70	6,50	591,80	7,20	598,0	26,0	591,8	7,2	0,655	
ROD-3_23.FIN2	552,0	3,340	0,3811	0,00780	0,05104	0,0007	0,6223100	328,00	5,60	320,80	4,50	375,0	37,0	320,8	4,5	2,195	
ROD-3_24.FIN2	310,0	1,600	10,7800	0,15000	0,47290	0,0061	0,8193600	2502,00	13,00	2494,00	27,00	2508,0	14,0	2508,0	14,0	0,558	
ROD-3_25.FIN2	205,0	1,847	0,3790	0,00900	0,05158	0,0007	0,4327400	325,40	6,60	324,20	4,30	318,0	47,0	324,2	4,3	0,369	
ROD-3_26.FIN2	436,0	2,404	0,3618	0,00730	0,05043	0,0005	0,3932700	313,00	5,40	317,20	3,30	279,0	41,0	317,2	3,3	1,342	
ROD-3_27.FIN2	181,3	1,254	0,5270	0,01800	0,05247	0,0008	0,0384880	427,00	12,00	329,60	4,90	967,0	77,0	DISC	DISC	22,810	
ROD-3_28.FIN2	480,0	16,000	0,8020	0,01700	0,08940	0,0013	0,5147200	597,10	9,30	551,70	7,60	763,0	39,0	551,7	7,6	7,603	
ROD-3_29.FIN2	1319,0	8,500	0,8800	0,01300	0,10370	0,0013	0,7424600	640,70	6,80	636,10	7,70	651,0	22,0	636,1	7,7	0,718	
ROD-3_30.FIN2	318,0	1,663	0,3625	0,00670	0,04933	0,0006	0,1890400	314,20	5,10	310,30	3,90	327,0	46,0	310,3	3,9	1,241	
ROD-3_31.FIN2	263,0	1,090	1,7250	0,02400	0,16760	0,0020	0,5597100	1016,30	9,00	999,00	11,00	1059,0	26,0	1059,0	26,0	5,666	
ROD-3_32.FIN2	149,7	1,975	0,6030	0,01600	0,07590	0,0013	0,6538300	479,00	9,50	471,10	8,00	513,0	45,0	471,1	8,0	1,649	
ROD-3_33.FIN2	677,0	3,090	0,4880	0,01400	0,05940	0,0015	0,7084700	404,00	10,00	371,90	8,90	593,0	48,0	371,9	8,9	7,946	
ROD-3_34.FIN2	22,0	3,320	1,1660	0,04700	0,12390	0,0023	0,1733000	778,00	22,00	753,00	13,00	814,0	88,0	753,0	13,0	3,213	
ROD-3_35.FIN2	660,0	3,400	0,3766	0,00580	0,04934	0,0006	0,4011400	324,20	4,30	310,40	3,80	418,0	35,0	310,4	3,8	4,257	
ROD-3_36.FIN2	223,0	2,016	0,3696	0,00930	0,04880	0,0005	0,2212400	318,50	6,90	307,10	3,30	385,0	54,0	307,1	3,3	3,579	
ROD-3_37.FIN2	135,0	0,951	0,3870	0,01300	0,05359	0,0008	0,2392900	330,60	9,20	337,00	4,80	271,0	65,0	337,0	4,8	1,936	

Sample Name:	[U]							207/235		206/238		207/206		Best age		Discordance	Rim/
Grain #	ppm	U/Th	207/235	2σ error	206/238	2σ error	RHO	Age Ma	2σ error	Age (Ma)	2σ error	Age (Ma)	2σ error	(Ma)	2σ error	%	Core
ROD-3_38.FIN2	173,0	2,130	0,4146	0,00940	0,05676	0,0010	0,3504000	352,20	6,90	355,80	5,80	318,0	50,0	355,8	5,8	1,022	
ROD-3_39.FIN2	211,7	1,872	7,5000	0,21000	0,34670	0,0082	0,7806300	2169,00	25,00	1918,00	40,00	2416,0	30,0	2416,0	30,0	20,613	
ROD-3_40.FIN2	276,0	3,030	0,3553	0,00690	0,04858	0,0007	0,3543200	308,80	5,00	305,80	4,20	315,0	43,0	305,8	4,2	0,972	
ROD-3_41.FIN2	611,0	6,090	0,6640	0,03500	0,08010	0,0033	0,5011400	516,00	22,00	497,00	20,00	600,0	110,0	497,0	20,0	3,682	Rim
ROD-3_41.FIN2	179,0	1,352	1,0920	0,02200	0,12470	0,0014	0,2963700	748,00	10,00	757,30	7,90	715,0	40,0	757,3	7,9	1,243	Core
ROD-3_42.FIN2	172,2	2,140	0,3585	0,00870	0,04907	0,0007	0,4691000	310,30	6,50	308,80	4,60	310,0	48,0	308,8	4,6	0,483	
ROD-3_43.FIN2	292,0	1,210	0,9800	0,01800	0,11070	0,0016	0,5376100	692,30	9,00	676,90	9,50	741,0	32,0	676,9	9,5	2,224	
ROD-3_44.FIN2	194,0	3,020	0,7970	0,01700	0,09570	0,0016	0,5535000	593,50	9,70	589,00	9,30	618,0	44,0	589,0	9,3	0,758	
ROD-3_45.FIN2	286,0	2,257	7,7900	0,22000	0,34600	0,0100	0,8161900	2203,00	25,00	1911,00	48,00	2489,0	29,0	2489,0	29,0	23,222	
ROD-3_46.FIN2	338,0	2,188	0,3511	0,00780	0,04875	0,0008	0,4492200	305,70	5,80	306,70	4,70	292,0	45,0	306,7	4,7	0,327	
ROD-3_47.FIN2	582,0	25,400	0,5810	0,02000	0,07280	0,0023	0,8881400	463,00	13,00	453,00	14,00	519,0	33,0	453,0	14,0	2,160	
ROD-3_48.FIN2	133,2	2,020	0,4180	0,01900	0,05033	0,0010	0,3908200	352,00	13,00	316,50	5,90	550,0	86,0	316,5	5,9	10,085	
ROD-3_49.FIN2	249,0	1,979	1,4690	0,03000	0,15090	0,0025	0,7129300	915,00	12,00	908,00	15,00	930,0	31,0	930,0	31,0	2,366	
ROD-3_50.FIN2	216,0	2,599	0,3594	0,00810	0,04942	0,0007	0,4826700	311,10	6,00	310,90	4,20	313,0	45,0	310,9	4,2	0,064	
ROD-3_51.FIN2	553,0	2,433	0,3522	0,00600	0,04752	0,0006	0,2826900	306,00	4,50	299,20	3,80	351,0	41,0	299,2	3,8	2,222	
ROD-3_52.FIN2	116,2	1,857	0,6920	0,01900	0,08150	0,0014	0,4794500	532,00	12,00	504,90	8,40	630,0	54,0	504,9	8,4	5,094	
ROD-3_53.FIN2	131,5	1,889	0,3780	0,01100	0,05039	0,0008	0,1911700	324,70	7,90	316,90	4,60	359,0	63,0	316,9	4,6	2,402	
ROD-3_54.FIN2	890,0	4,670	0,3566	0,00740	0,04845	0,0009	0,7025700	309,10	5,50	304,90	5,40	337,0	33,0	304,9	5,4	1,359	
ROD-3_55.FIN2	246,3	1,915	5,1130	0,08700	0,31430	0,0039	0,7965700	1835,00	15,00	1761,00	19,00	1931,0	18,0	1931,0	18,0	8,804	
ROD-3_56.FIN2	434,0	2,910	0,3574	0,00630	0,04825	0,0005	0,4084500	309,80	4,70	303,80	2,90	339,0	37,0	303,8	2,9	1,937	
ROD-3_57.FIN2	870,0	24,300	0,3420	0,01000	0,04690	0,0011	0,6005100	298,00	7,90	295,20	6,80	333,0	58,0	295,2	6,8	0,940	Rim
ROD-3_57.FIN2	157,7	0,618	0,7450	0,01700	0,08790	0,0013	0,2634800	564,20	9,60	543,30	7,70	637,0	51,0	543,3	7,7	3,704	Core
ROD-3_58.FIN2	389,0	2,210	0,4285	0,00750	0,05888	0,0007	0,4866100	361,60	5,30	368,80	4,40	323,0	36,0	368,8	4,4	1,991	
ROD-3_60.FIN2	376,0	1,278	0,4551	0,00820	0,05955	0,0007	0,4577100	380,20	5,70	372,80	4,30	412,0	36,0	372,8	4,3	1,946	
ROD-3_61.FIN2	250,0	2,712	0,3430	0,00790	0,04762	0,0007	0,2495900	298,80	6,00	299,80	4,30	287,0	46,0	299,8	4,3	0,335	
ROD-3_62.FIN2	499,0	1,917	0,3671	0,00760	0,05028	0,0006	0,4685000	318,40	5,60	316,20	3,80	331,0	39,0	316,2	3,8	0,691	
ROD-3_63.FIN2	331,0	1,730	0,7720	0,02100	0,09050	0,0023	0,7324200	579,00	12,00	558,00	13,00	674,0	40,0	558,0	13,0	3,627	Rim
ROD-3_63.FIN2	269,2	2,017	2,2220	0,06700	0,18150	0,0045	0,7549500	1185,00	21,00	1074,00	24,00	1391,0	38,0	1391,0	38,0	22,789	Core
ROD-3_65.FIN2	499,0	1,809	0,3456	0,00570	0,04785	0,0006	0,4824000	301,00	4,30	301,30	3,60	292,0	34,0	301,3	3,6	0,100	
ROD-3_66.FIN2	910,0	38,000	2,0250	0,09600	0,17990	0,0066	0,7001400	1122,00	32,00	1066,00	36,00	1237,0	66,0	1237,0	66,0	13,824	Rim
ROD-3_66.FIN2	191,8	0,874	6,3660	0,07200	0,36600	0,0038	0,6180600	2026,30	9,80	2010,00	18,00	2038,0	16,0	2038,0	16,0	1,374	Core
ROD-3_67.FIN2	83,8	1,148	1,7810	0,03300	0,17420	0,0021	0,4959000	1036,00	12,00	1035,00	11,00	1035,0	33,0	1035,0	33,0	0,000	
ROD-3_68.FIN2	523,0	10,300	0,8660	0,02800	0,10230	0,0026	0,7580600	632,00	15,00	628,00	15,00	653,0	46,0	628,0	15,0	0,633	Rim
ROD-3_68.FIN2	222,3	5,960	1,7720	0,05200	0,15090	0,0027	0,3830700	1033,00	19,00	906,00	15,00	1306,0	58,0	DISC	DISC	30,628	Core
ROD-3_69.FIN2	479,0	4,310	0,8810	0,01200	0,10310	0,0012	0,6567500	640,80	6,50	632,20	7,20	671,0	24,0	632,2	7,2	1,342	
ROD-3_70.FIN2	245,0	2,660	0,8420	0,02300	0,09980	0,0016	0,4716100	617,00	13,00	613,00	9,70	616,0	50,0	613,0	9,7	0,648	
ROD-3_71.FIN2	72,8	0,949	0,8550	0,02100	0,10220	0,0013	0,3112100	625,00	11,00	627,10	7,30	611,0	52,0	627,1	7,3	0,336	
ROD-3_72.FIN2	774,0	3,342	0,3518	0,00460	0,04875	0,0005	0,4790700	305,90	3,40	306,80	2,90	293,0	28,0	306,8	2,9	0,294	
ROD-3_73.FIN2	590,0	0,921	0,3808	0,00890	0,05241	0,0007	0,6185700	326,80	6,60	329,30	4,40	326,0	40,0	329,3	4,4	0,765	
ROD-3_74.FIN2	417,0	2,870	0,3445	0,00750	0,04680	0,0008	0,5726200	300,70	5,90	294,80	5,10	353,0	43,0	294,8	5,1	1,962	
ROD-3_75.FIN2	557,0	1,542	0,3637	0,00700	0,04950	0,0006	0,5135800	314,50	5,20	311,40	3,40	325,0	36,0	311,4	3,4	0,986	
ROD-3_76.FIN2	447,0	2,061	0,3447	0,00610	0,04828	0,0005	0,2865800	300,30	4,60	303,90	3,00	265,0	38,0	303,9	3,0	1,199	
ROD-3_77.FIN2	571,0	33,000	0,3740	0,03700	0,04970	0,0036	0,7646400	321,00	28,00	313,00	22,00	390,0	150,0	313,0	22,0	2,492	Rim
ROD-3_77.FIN2	141,5	1,577	1,2750	0,02100	0,13810	0,0016	0,2619900	833,60	9,20	833,90	9,00	825,0	36,0	833,9	9,0	0,036	Core
ROD-3_78.FIN2	261,0	2,414	0,3660	0,00930	0,04576	0,0008	0,2497600	316,00	6,90	288,40	5,00	509,0	90,0	288,4	5,0	8,734	
ROD-3_79.FIN2	480,0	2,685	0,3553	0,00690	0,05014	0,0007	0,4893400	308,30	5,20	315,40	4,00	260,0	40,0	315,4	4,0	2,303	
ROD-3_80.FIN2	310,0	2,189	0,5300	0,01500	0,06880	0,0017	0,4910700	431,10	9,90	429,00	10,00	459,0	64,0	429,0	10,0	0,487	Rim

Sample Name:	[U]							207/235		206/238		207/206		Best age		Discordance	Rim/
Grain #	ppm	U/Th	207/235	2σ error	206/238	2σ error	RHO	Age Ma	2σ error	Age (Ma)	2σ error	Age (Ma)	2σ error	(Ma)	2σ error	%	Core
ROD-3_80.FIN2	451,0	2,790	0,8080	0,01600	0,09600	0,0016	0,6036900	602,10	9,50	590,70	9,30	646,0	33,0	590,7	9,3	1,893	Core
ROD-3_81.FIN2	508,0	1,272	0,3579	0,00700	0,04935	0,0006	0,5431500	310,20	5,20	310,50	3,90	297,0	37,0	310,5	3,9	0,097	
ROD-3_82.FIN2	349,0	2,473	0,3414	0,00600	0,04840	0,0005	0,3093000	298,40	4,60	304,60	3,20	246,0	39,0	304,6	3,2	2,078	
ROD-3_83.FIN2	1290,0	3,038	0,4000	0,00570	0,05307	0,0007	0,7467400	341,40	4,10	333,30	4,50	392,0	22,0	333,3	4,5	2,373	
ROD-3_84.FIN2	127,3	1,680	4,5300	0,11000	0,28780	0,0067	0,8717000	1730,00	22,00	1628,00	34,00	1862,0	22,0	1862,0	22,0	12,567	
ROD-3_86.FIN2	48,1	2,770	1,6800	0,04200	0,16360	0,0026	0,6814300	997,00	16,00	976,00	14,00	1041,0	46,0	1041,0	46,0	6,244	
ROD-3_87.FIN2	414,0	2,488	0,6171	0,00880	0,07793	0,0007	0,4698900	487,40	5,50	483,70	4,10	501,0	29,0	483,7	4,1	0,759	
ROD-3_88.FIN2	826,0	3,270	0,3669	0,00530	0,05050	0,0006	0,6157500	317,00	4,00	317,60	3,50	309,0	28,0	317,6	3,5	0,189	
ROD-3_89.FIN2	356,0	1,249	0,4238	0,00810	0,05746	0,0007	0,4051600	358,10	5,80	360,10	4,10	336,0	40,0	360,1	4,1	0,559	
ROD-3_90.FIN2	123,9	1,030	1,7020	0,02600	0,16480	0,0019	0,5948700	1007,60	9,80	983,00	10,00	1057,0	27,0	1057,0	27,0	7,001	
ROD-3_92.FIN2	297,0	1,629	0,6440	0,01200	0,08100	0,0010	0,5681100	503,60	7,10	502,20	6,20	498,0	33,0	502,2	6,2	0,278	
ROD-3_93.FIN2	605,0	52,500	1,7210	0,02300	0,16900	0,0022	0,6568300	1018,60	8,60	1006,00	12,00	1040,0	22,0	1040,0	22,0	3,269	Rim
ROD-3_93.FIN2	104,8	2,130	2,8380	0,06400	0,23940	0,0045	0,4240100	1364,00	17,00	1383,00	23,00	1329,0	43,0	1329,0	43,0	4,063	Core
ROD-3_94.FIN2	565,0	7,200	0,5827	0,00820	0,07404	0,0007	0,3798900	466,50	5,40	460,40	4,40	490,0	31,0	460,4	4,4	1,308	
ROD-3_95.FIN2	370,0	1,895	1,2510	0,01800	0,13580	0,0015	0,4112600	823,00	8,30	820,80	8,30	812,0	27,0	820,8	8,3	0,267	
ROD-3_97.FIN2	0,3	0,020	910,0000	280,00000	8,50000	2,6000	0,9740000	6760,00	430,00	13700,00	2400,00	4960,0	100,0	DISC	DISC	176,210	
ROD-3_98.FIN2	128,0	3,700	10,6800	0,53000	0,47000	0,0180	0,9760000	2456,00	51,00	2462,00	82,00	2463,0	29,0	2463,0	29,0	0,041	
ROD-3_99.FIN2	405,0	1,900	0,3553	0,00700	0,04921	0,0005	0,2016500	308,20	5,20	309,60	3,00	289,0	43,0	309,6	3,0	0,454	
ROD-3_100.FIN2	212,0	1,394	0,3624	0,00830	0,04903	0,0006	0,3003900	313,30	6,20	308,50	3,50	338,0	50,0	308,5	3,5	1,532	
ROD-3_102.FIN2	250,0	1,726	0,3692	0,00730	0,04932	0,0006	0,2113600	318,60	5,40	310,30	3,40	367,0	46,0	310,3	3,4	2,605	
ROD-3_103.FIN2	70,7	2,632	0,3650	0,01100	0,05099	0,0007	0,0503710	315,50	8,40	320,60	4,60	273,0	68,0	320,6	4,6	1,616	
ROD-3_104.FIN2	434,0	0,573	0,9190	0,01200	0,10810	0,0010	0,5639900	661,20	6,30	661,60	6,10	652,0	24,0	661,6	6,1	0,060	
ROD-3_105.FIN2	383,0	6,450	0,8780	0,01100	0,10450	0,0013	0,6254600	639,40	6,20	640,70	7,80	639,0	23,0	640,7	7,8	0,203	
ROD-3_106.FIN2	231,0	10,460	0,7060	0,01100	0,08788	0,0009	0,5481800	541,30	6,80	542,90	5,50	526,0	30,0	542,9	5,5	0,296	
ROD-3_107.FIN2	312,0	1,102	6,0000	0,11000	0,34080	0,0061	0,9122700	1974,00	15,00	1889,00	30,00	2063,0	20,0	2063,0	20,0	8,434	
ROD-3_109.FIN2	366,7	1,326	0,4088	0,00610	0,05528	0,0005	0,2848000	348,20	4,50	346,80	3,30	349,0	35,0	346,8	3,3	0,402	
ROD-3_110.FIN2	463,0	11,400	0,5950	0,01100	0,07610	0,0013	0,6445000	473,80	6,90	472,60	7,50	478,0	38,0	472,6	7,5	0,253	
ROD-3_111.FIN2	175,0	2,116	0,3607	0,00890	0,04909	0,0005	0,0784940	311,90	6,60	308,90	2,90	316,0	53,0	308,9	2,9	0,962	
ROD-3_113.FIN2	489,0	2,530	0,3692	0,00830	0,05153	0,0007	0,4309400	318,30	6,10	323,90	4,30	278,0	45,0	323,9	4,3	1,759	
ROD-3_114.FIN2	709,0	4,520	0,4940	0,02400	0,06170	0,0020	0,6924200	407,00	16,00	386,00	12,00	499,0	56,0	386,0	12,0	5,160	Rim
ROD-3_114.FIN2	173,0	1,203	0,7480	0,01400	0,09240	0,0012	0,1357800	566,20	8,00	569,80	6,90	542,0	45,0	569,8	6,9	0,636	Core
ROD-3_115.FIN2	326,0	2,572	0,3534	0,00620	0,04873	0,0005	0,2700400	306,90	4,60	306,70	3,30	308,0	40,0	306,7	3,3	0,065	
ROD-3_117.FIN2	118,7	0,701	0,7610	0,01700	0,08930	0,0016	0,5477500	573,00	9,80	550,90	9,50	659,0	43,0	550,9	9,5	3,857	
ROD-3_118.FIN2	1400,0	5,500	0,3970	0,01500	0,05340	0,0013	0,7827300	339,90	11,00	335,50	8,10	355,0	52,0	335,5	8,1	1,032	Rim
ROD-3_118.FIN2	129,6	1,577	0,8800	0,02800	0,10660	0,0024	0,4801600	640,00	15,00	653,00	14,00	584,0	65,0	653,0	14,0	2,031	Core
ROD-3_119.FIN2	695,0	1,313	0,4052	0,00540	0,05506	0,0006	0,4668900	345,10	3,90	345,50	3,50	332,0	30,0	345,5	3,5	0,116	
ROD-3_120.FIN2	125,1	1,104	0,4170	0,01100	0,05705	0,0008	0,2930200	352,50	7,60	357,60	4,50	311,0	54,0	357,6	4,5	1,447	
ROD-3_121.FIN2	54,7	2,120	0,9480	0,04000	0,09140	0,0015	0,1805600	671,00	21,00	563,40	9,20	988,0	92,0	DISC	DISC	16,036	
ROD-3_122.FIN2	347,0	1,235	0,4146	0,00690	0,05646	0,0006	0,4449300	351,70	4,90	354,00	3,70	329,0	34,0	354,0	3,7	0,654	
ROD-3_123.FIN2	390,0	1,885	0,3467	0,00580	0,04807	0,0005	0,3116300	302,40	4,50	302,60	2,90	290,0	35,0	302,6	2,9	0,066	
ROD-3_125.FIN2	1320,0	2,572	0,3690	0,00410	0,05094	0,0005	0,5105900	318,80	3,10	320,30	2,80	306,0	23,0	320,3	2,8	0,471	
ROD-3_126.FIN2	373,0	2,300	0,3530	0,00900	0,04808	0,0007	0,5106700	306,20	6,70	302,70	4,20	319,0	47,0	302,7	4,2	1,143	
ROD-3_127.FIN2	785,0	1,262	0,7550	0,01300	0,08500	0,0016	0,8506100	570,00	7,60	525,50	9,50	748,0	23,0	525,5	9,5	7,807	
ROD-3_130.FIN2	218,0	5,350	0,6620	0,01200	0,08323	0,0009	0,4243300	515,10	7,10	515,30	5,50	507,0	35,0	515,3	5,5	0,039	
ROD-3_131.FIN2	864,0	7,550	4,0500	0,10000	0,26030	0,0044	0,7149800	1641,00	21,00	1491,00	23,00	1847,0	32,0	1847,0	32,0	19,274	Rim
ROD-3_131.FIN2	330,0	1,464	11,6900	0,34000	0,45500	0,0110	0,8987600	2575,00	27,00	2417,00	48,00	2679,0	22,0	2679,0	22,0	9,780	Core
ROD-3_132.FIN2	154,1	2,669	0,9890	0,01800	0,11560	0,0014	0,4269500	696,80	9,00	704,80	7,80	667,0	35,0	704,8	7,8	1,148	

Sample Name:	[U]							207/235		206/238		207/206		Best age		Discordance	Rim/
Grain #	ppm	U/Th	207/235	2σ error	206/238	2σ error	RHO	Age Ma	2σ error	Age (Ma)	2σ error	Age (Ma)	2σ error	(Ma)	2σ error	%	Core
ROD-3_133.FIN2	483,0	2,471	0,3514	0,00560	0,04799	0,0005	0,3318400	305,50	4,20	302,10	3,10	323,0	36,0	302,1	3,1	1,113	
ROD-3_134.FIN2	232,0	7,540	0,5710	0,01200	0,07360	0,0010	0,5041900	457,70	8,00	457,50	6,20	446,0	43,0	457,5	6,2	0,044	
ROD-3_135.FIN2	342,0	1,792	0,3422	0,00730	0,04755	0,0006	0,3744300	300,40	5,70	299,40	3,70	291,0	45,0	299,4	3,7	0,333	
ROD-4_1.FIN2	366,0	0,860	0,8490	0,01100	0,10047	0,0009	0,3918700	623,50	6,30	617,10	5,00	632,0	29,0	617,1	5,0	1,026	
ROD-4_2.FIN2	786,0	1,340	0,4403	0,00830	0,05687	0,0006	0,4342100	370,00	5,90	356,50	3,70	437,0	38,0	356,5	3,7	3,649	
ROD-4_3.FIN2	1247,0	1,640	0,4000	0,00480	0,05422	0,0005	0,5755600	341,40	3,50	340,40	2,80	331,0	23,0	340,4	2,8	0,293	
ROD-4_4.FIN2	556,0	2,444	0,6310	0,01200	0,07914	0,0009	0,4560100	496,30	7,40	490,90	5,30	503,0	38,0	490,9	5,3	1,088	
ROD-4_6.FIN2	382,0	3,020	0,5790	0,01200	0,07260	0,0011	0,3994700	463,60	7,90	451,60	6,40	511,0	45,0	451,6	6,4	2,588	Rim
ROD-4_6.FIN2	101,8	1,136	1,0930	0,03200	0,12180	0,0019	0,4172100	748,00	16,00	741,00	11,00	745,0	58,0	741,0	11,0	0,936	Core
ROD-4_7.FIN2	78,8	11,000	0,4350	0,03900	0,05880	0,0039	0,6072700	366,00	27,00	368,00	24,00	350,0	290,0	368,0	24,0	0,546	Rim
ROD-4_7.FIN2	250,8	1,016	5,1080	0,05200	0,31460	0,0034	0,6909700	1838,00	9,10	1763,00	17,00	1907,0	16,0	1907,0	16,0	7,551	Core
ROD-4_8.FIN2	532,0	2,290	0,7752	0,00980	0,09415	0,0009	0,5797500	582,20	5,60	580,00	5,40	581,0	22,0	580,0	5,4	0,378	
ROD-4_9.FIN2	568,0	1,108	0,4309	0,00870	0,05542	0,0005	0,3198600	363,40	6,10	347,70	3,20	444,0	43,0	347,7	3,2	4,320	
ROD-4_10.FIN2	459,1	3,830	0,3620	0,01200	0,04758	0,0009	0,4369300	313,70	9,10	299,70	5,80	408,0	70,0	299,7	5,8	4,463	Rim
ROD-4_10.FIN2	660,0	2,016	1,2610	0,02700	0,13370	0,0020	0,5123200	828,00	12,00	809,00	11,00	879,0	43,0	809,0	11,0	2,295	Core
ROD-4_11.FIN2	704,0	1,830	0,4237	0,00610	0,05631	0,0005	0,4986000	358,40	4,40	353,10	3,20	378,0	29,0	353,1	3,2	1,479	
ROD-4_12.FIN2	989,0	170,000	0,3949	0,00940	0,05297	0,0008	0,5476500	337,60	6,80	332,70	4,60	359,0	45,0	332,7	4,6	1,451	Rim
ROD-4_12.FIN2	507,0	3,480	0,6190	0,01500	0,07890	0,0011	0,6246900	488,70	9,30	489,70	6,70	463,0	46,0	489,7	6,7	0,205	Core
ROD-4_13.FIN2	383,0	4,700	0,5000	0,03300	0,06490	0,0012	0,3535600	411,00	22,00	405,10	7,60	450,0	140,0	405,1	7,6	1,436	Rim
ROD-4_13.FIN2	144,0	0,934	0,6670	0,01400	0,08124	0,0009	0,3050400	518,70	8,70	503,50	5,40	559,0	45,0	503,5	5,4	2,930	Core
ROD-4_14.FIN2	349,0	1,831	0,3467	0,00570	0,04767	0,0004	0,2853600	301,90	4,30	300,20	2,40	291,0	37,0	300,2	2,4	0,563	
ROD-4_15.FIN2	609,0	18,300	0,8430	0,02300	0,10060	0,0019	0,6805400	623,00	11,00	618,00	11,00	633,0	43,0	618,0	11,0	0,803	Rim
ROD-4_15.FIN2	160,3	1,032	1,5550	0,03000	0,15670	0,0025	0,5715600	952,00	12,00	938,00	14,00	967,0	35,0	967,0	35,0	2,999	Core
ROD-4_16.FIN2	81,0	1,618	0,8930	0,02300	0,10300	0,0012	0,2199700	645,00	12,00	631,70	7,10	668,0	51,0	631,7	7,1	2,062	
ROD-4_17.FIN2	390,0	1,637	0,6469	0,00930	0,07984	0,0007	0,4768300	506,00	5,80	495,10	4,40	531,0	29,0	495,1	4,4	2,154	
ROD-4_18.FIN2	237,0	2,094	0,5820	0,01000	0,07336	0,0008	0,1597800	465,20	6,70	456,30	4,60	491,0	41,0	456,3	4,6	1,913	
ROD-4_19.FIN2	701,0	1,298	1,1470	0,01800	0,11940	0,0017	0,6042400	775,30	8,40	726,70	9,70	897,0	29,0	726,7	9,7	6,269	
ROD-4_20.FIN2	139,0	1,691	9,9900	0,14000	0,45440	0,0050	0,6429500	2432,00	13,00	2414,00	22,00	2434,0	19,0	2434,0	19,0	0,822	
ROD-4_21.FIN2	576,0	3,325	0,6190	0,02100	0,07620	0,0017	0,3531700	488,00	13,00	473,00	10,00	553,0	77,0	473,0	10,0	3,074	Rim
ROD-4_21.FIN2	341,0	0,952	0,7700	0,01300	0,09380	0,0010	0,3111200	579,40	7,50	578,70	5,60	566,0	37,0	578,7	5,6	0,121	Core
ROD-4_22.FIN2	445,0	2,690	0,9140	0,06400	0,10890	0,0063	0,9705400	658,00	34,00	666,00	37,00	627,0	41,0	666,0	37,0	1,216	
ROD-4_23.FIN2	105,1	2,203	0,6760	0,02000	0,07598	0,0009	0,3957600	525,00	12,00	472,10	5,40	737,0	60,0	472,1	5,4	10,076	
ROD-4_24.FIN2	31,5	1,812	5,1700	0,13000	0,32090	0,0051	0,6827000	1844,00	21,00	1793,00	25,00	1889,0	34,0	1889,0	34,0	5,082	
ROD-4_25.FIN2	1580,0	68,500	0,4056	0,00740	0,05431	0,0009	0,3809900	345,50	5,40	340,90	5,30	369,0	43,0	340,9	5,3	1,331	Rim
ROD-4_25.FIN2	591,0	1,161	0,8950	0,01500	0,10480	0,0012	0,6324200	648,60	8,10	642,20	7,10	655,0	28,0	642,2	7,1	0,987	Core
ROD-4_26.FIN2	116,4	1,220	1,8750	0,02800	0,17810	0,0015	0,3239100	1070,60	9,90	1056,20	8,00	1089,0	31,0	1089,0	31,0	3,012	
ROD-4_27.FIN2	286,0	1,249	5,9600	0,10000	0,32110	0,0041	0,8601000	1969,00	15,00	1795,00	20,00	2148,0	22,0	2148,0	22,0	16,434	
ROD-4_28.FIN2	243,0	1,300	5,1590	0,07400	0,32270	0,0040	0,4837400	1845,00	12,00	1802,00	20,00	1880,0	23,0	1880,0	23,0	4,149	
ROD-4_29.FIN2	608,0	1,690	0,7650	0,01100	0,09208	0,0008	0,4044900	576,50	6,30	567,80	4,70	605,0	28,0	567,8	4,7	1,509	
ROD-4_30.FIN2	128,0	0,930	0,8610	0,02000	0,10200	0,0012	0,4968300	628,00	11,00	625,90	6,80	608,0	47,0	625,9	6,8	0,334	
ROD-4_31.FIN2	249,7	0,742	1,7390	0,02400	0,17070	0,0017	0,4770400	1022,00	9,10	1015,60	9,60	1022,0	25,0	1022,0	25,0	0,626	
ROD-4_32.FIN2	374,0	2,117	10,5600	0,14000	0,44820	0,0051	0,6337900	2484,00	12,00	2387,00	23,00	2566,0	16,0	2566,0	16,0	6,976	
ROD-4_33.FIN2	208,0	2,290	1,4510	0,02000	0,14920	0,0012	0,4320900	909,40	8,50	896,60	6,60	927,0	26,0	927,0	26,0	3,279	
ROD-4_34.FIN2	78,8	1,196	1,8490	0,02900	0,17870	0,0015	0,3238600	1061,00	10,00	1059,80	8,30	1048,0	30,0	1048,0	30,0	1,126	
ROD-4_35.FIN2	291,0	1,170	0,8930	0,02600	0,10640	0,0019	0,4892700	646,00	14,00	651,00	11,00	631,0	46,0	651,0	11,0	0,774	
ROD-4_36.FIN2	512,0	1,572	0,3640	0,00570	0,04910	0,0004	0,4258300	314,80	4,20	309,00	2,40	337,0	32,0	309,0	2,4	1,842	

Sample Name:	[U]							207/235		206/238		207/206		Best age		Discordance	Rim/
Grain #	ppm	U/Th	207/235	2σ error	206/238	2σ error	RHO	Age Ma	2σ error	Age (Ma)	2σ error	Age (Ma)	2σ error	(Ma)	2σ error	%	Core
ROD-4_38.FIN2	516,0	1,721	0,4320	0,00740	0,05534	0,0006	0,5407100	364,90	5,40	347,20	3,50	464,0	33,0	347,2	3,5	4,851	
ROD-4_39.FIN2	66,0	0,964	0,8220	0,02400	0,10120	0,0012	0,1083800	606,00	13,00	621,10	7,00	525,0	65,0	621,1	7,0	2,492	
ROD-4_40.FIN2	259,0	2,290	0,4402	0,00870	0,05952	0,0006	0,2747900	370,70	6,00	372,60	3,90	333,0	45,0	372,6	3,9	0,513	
ROD-4_41.FIN2	683,0	1,004	10,8300	0,18000	0,44650	0,0064	0,7766100	2507,00	15,00	2379,00	28,00	2619,0	15,0	2619,0	15,0	9,164	
ROD-4_42.FIN2	175,0	1,518	1,9180	0,02600	0,18470	0,0016	0,4828500	1086,30	9,00	1092,30	8,80	1069,0	25,0	1069,0	25,0	2,180	
ROD-4_44.FIN2	592,0	5,630	0,7830	0,01900	0,09610	0,0021	0,5158100	587,00	11,00	591,00	12,00	574,0	50,0	591,0	12,0	0,681	Rim
ROD-4_44.FIN2	149,5	2,613	1,0720	0,02400	0,12420	0,0012	0,3450800	738,00	12,00	754,40	7,10	680,0	44,0	754,4	7,1	2,222	Core
ROD-4_45.FIN2	3970,0	8,480	0,8490	0,02800	0,09330	0,0033	0,8431200	624,00	16,00	575,00	20,00	813,0	39,0	575,0	20,0	7,853	Rim
ROD-4_45.FIN2	358,0	4,380	1,1120	0,01700	0,12570	0,0014	0,4474000	759,30	8,30	763,40	7,90	743,0	30,0	763,4	7,9	0,540	Core
ROD-4_46.FIN2	1286,0	1,930	0,5970	0,01100	0,07370	0,0011	0,6211700	474,80	7,00	458,30	6,30	555,0	33,0	458,3	6,3	3,475	Rim
ROD-4_46.FIN2	398,0	1,125	0,8970	0,01500	0,10760	0,0014	0,4985900	649,80	8,00	658,70	8,40	611,0	33,0	658,7	8,4	1,370	Core
ROD-4_47.FIN2	1193,0	1,652	0,5966	0,00780	0,07557	0,0008	0,6446900	474,70	5,00	469,50	4,80	491,0	21,0	469,5	4,8	1,095	
ROD-4_49.FIN2	234,6	1,646	12,5700	0,10000	0,51070	0,0038	0,7252300	2646,90	7,80	2659,00	16,00	2636,5	9,8	2636,5	9,8	0,853	
ROD-4_50.FIN2	1370,0	8,020	0,5130	0,01800	0,06030	0,0020	0,3975600	420,00	12,00	377,00	12,00	675,0	79,0	377,0	12,0	10,238	Rim
ROD-4_50.FIN2	753,0	1,920	0,7450	0,01200	0,09070	0,0010	0,6583800	565,00	7,20	559,80	5,90	590,0	30,0	559,8	5,9	0,920	Core
ROD-4_51.FIN2	576,0	2,860	0,3616	0,00540	0,04912	0,0005	0,3583900	313,10	4,00	309,10	3,30	334,0	35,0	309,1	3,3	1,278	
ROD-4_52.FIN2	1580,0	17,600	0,3796	0,00480	0,05066	0,0005	0,2837500	327,00	3,70	318,50	2,90	386,0	32,0	318,5	2,9	2,599	
ROD-4_53.FIN2	683,0	1,216	0,4426	0,00630	0,05912	0,0006	0,5047900	371,70	4,40	370,30	3,60	392,0	30,0	370,3	3,6	0,377	
ROD-4_54.FIN2	1107,0	2,420	0,9880	0,01100	0,11200	0,0010	0,6082800	697,10	5,40	684,50	5,90	738,0	18,0	684,5	5,9	1,807	
ROD-4_55.FIN2	1327,0	6,240	0,7830	0,01100	0,08910	0,0012	0,6199100	586,70	6,40	550,20	6,90	736,0	24,0	550,2	6,9	6,221	
ROD-4_56.FIN2	2680,0	45,000	0,4131	0,00490	0,05540	0,0005	0,7079700	350,90	3,50	347,60	3,00	373,0	18,0	347,6	3,0	0,940	
ROD-4_57.FIN2	559,0	4,790	0,6440	0,01000	0,08181	0,0009	0,6451000	504,20	6,30	506,80	5,60	494,0	26,0	506,8	5,6	0,516	
ROD-4_59.FIN2	898,0	13,600	0,8550	0,00940	0,10081	0,0009	0,6637700	626,90	5,10	619,10	5,30	658,0	18,0	619,1	5,3	1,244	
ROD-4_60.FIN2	178,6	0,781	1,2190	0,01900	0,13320	0,0012	0,2962800	808,20	8,70	806,20	6,90	823,0	33,0	806,2	6,9	0,247	
ROD-4_61.FIN2	904,0	0,416	0,8679	0,00980	0,10096	0,0010	0,5810400	634,00	5,30	619,90	5,60	684,0	21,0	619,9	5,6	2,224	
ROD-4_62.FIN2	548,0	1,522	0,3615	0,00550	0,04947	0,0004	0,5531500	313,00	4,10	311,30	2,60	317,0	32,0	311,3	2,6	0,543	
ROD-4_63.FIN2	284,2	1,364	10,7900	0,11000	0,46200	0,0039	0,6761200	2503,80	9,20	2447,00	17,00	2555,0	13,0	2555,0	13,0	4,227	
ROD-4_64.FIN2	156,6	1,234	1,1430	0,02200	0,12700	0,0016	0,5719200	773,00	11,00	770,30	9,00	774,0	32,0	770,3	9,0	0,349	
ROD-4_65.FIN2	775,0	3,460	0,4029	0,00490	0,05430	0,0004	0,3111400	343,50	3,50	340,90	2,70	369,0	29,0	340,9	2,7	0,757	
ROD-4_66.FIN2	309,0	0,933	0,7956	0,00990	0,09684	0,0007	0,3368000	593,80	5,60	595,80	4,00	589,0	25,0	595,8	4,0	0,337	
ROD-4_67.FIN2	1700,0	1,060	0,4890	0,01300	0,05960	0,0016	0,7169500	404,10	8,80	373,00	10,00	600,0	45,0	373,0	10,0	7,696	Rim
ROD-4_67.FIN2	1450,0	0,780	0,6580	0,01300	0,07770	0,0014	0,7320700	512,90	8,20	482,00	8,10	654,0	30,0	482,0	8,1	6,025	Core
ROD-4_68.FIN2	80,0	9,500	0,4520	0,05300	0,04680	0,0020	0,3996300	376,00	37,00	295,00	13,00	800,0	240,0	DISC	DISC	21,543	Rim
ROD-4_68.FIN2	447,0	0,529	1,1730	0,01600	0,12930	0,0011	0,4403000	787,40	7,30	783,60	6,20	800,0	26,0	783,6	6,2	0,483	Core
ROD-4_69.FIN2	232,0	2,714	0,8140	0,02200	0,09850	0,0012	0,2391600	604,00	12,00	605,70	7,20	589,0	59,0	605,7	7,2	0,281	
ROD-4_70.FIN2	188,7	1,101	1,4000	0,03200	0,14950	0,0020	0,6506800	887,00	14,00	898,00	11,00	854,0	37,0	854,0	37,0	5,152	
ROD-4_71.FIN2	540,0	5,900	0,4910	0,03100	0,06650	0,0027	0,5301700	405,00	21,00	415,00	17,00	360,0	120,0	415,0	17,0	2,469	Rim
ROD-4_71.FIN2	377,0	0,595	0,8410	0,01500	0,09930	0,0013	0,6918800	618,70	8,20	610,40	7,80	648,0	28,0	610,4	7,8	1,342	Core
ROD-4_72.FIN2	602,0	34,100	0,5877	0,00900	0,07604	0,0008	0,3570500	469,10	5,70	472,40	4,50	461,0	32,0	472,4	4,5	0,703	
ROD-4_73.FIN2	586,0	1,678	0,4115	0,00720	0,05441	0,0006	0,5247000	349,50	5,20	341,50	3,50	400,0	33,0	341,5	3,5	2,289	
ROD-4_74.FIN2	218,0	1,178	0,9120	0,01300	0,10780	0,0008	0,2502300	658,20	7,10	659,90	4,70	653,0	32,0	659,9	4,7	0,258	
ROD-4_75.FIN2	357,0	1,610	5,9300	0,06700	0,35540	0,0034	0,5689600	1964,70	9,90	1960,00	16,00	1977,0	18,0	1977,0	18,0	0,860	
ROD-4_76.FIN2	279,0	0,854	0,8390	0,01200	0,09970	0,0008	0,3959700	617,70	6,70	612,60	4,90	646,0	29,0	612,6	4,9	0,826	
ROD-4_77.FIN2	168,0	3,120	1,0330	0,02600	0,11830	0,0017	0,2510100	719,00	13,00	720,90	9,60	718,0	54,0	720,9	9,6	0,264	Rim
ROD-4_77.FIN2	205,3	0,955	1,2910	0,02900	0,14220	0,0017	0,5435600	840,00	13,00	858,60	8,90	799,0	40,0	799,0	8,9	2,214	Core
ROD-4_78.FIN2	382,7	6,740	5,2960	0,08400	0,30830	0,0038	0,7367600	1867,00	14,00	1732,00	19,00	2024,0	19,0	2024,0	19,0	14,427	
ROD-4_79.FIN2	482,0	1,153	1,6720	0,01700	0,16560	0,0013	0,5836300	997,10	6,50	987,80	7,10	1024,0	17,0	1024,0	17,0	3,535	

Sample Name:	[U]							207/235		206/238		207/206		Best age		Discordance	Rim/
Grain #	ppm	U/Th	207/235	2σ error	206/238	2σ error	RHO	Age Ma	2σ error	Age (Ma)	2σ error	Age (Ma)	2σ error	(Ma)	2σ error	%	Core
ROD-4_80.FIN2	165,0	0,781	1,5850	0,02400	0,16390	0,0018	0,5523000	962,70	9,30	978,20	9,80	941,0	28,0	941,0	28,0	3,953	
ROD-4_81.FIN2	950,0	0,200	0,4980	0,02800	0,06210	0,0034	0,9184000	409,00	19,00	388,00	21,00	550,0	45,0	388,0	21,0	5,134	Rim
ROD-4_81.FIN2	59,2	2,980	0,9170	0,02600	0,10850	0,0014	0,2094600	660,00	14,00	663,80	7,90	632,0	63,0	663,8	7,9	0,576	Core
ROD-4_82.FIN2	250,0	0,768	11,5200	0,17000	0,47590	0,0054	0,7965800	2564,00	14,00	2509,00	23,00	2627,0	15,0	2627,0	15,0	4,492	
ROD-4_83.FIN2	164,6	0,417	5,9600	0,10000	0,35480	0,0052	0,6216200	1969,00	15,00	1957,00	24,00	1987,0	26,0	1987,0	26,0	1,510	
ROD-4_84.FIN2	120,3	1,580	1,8180	0,02400	0,17870	0,0015	0,3886800	1050,50	8,80	1059,50	8,30	1040,0	26,0	1040,0	26,0	1,875	
ROD-4_85.FIN2	198,3	0,996	5,3770	0,05100	0,33490	0,0025	0,5624700	1880,00	8,20	1862,00	12,00	1904,0	15,0	1904,0	15,0	2,206	
ROD-4_86.FIN2	419,0	0,734	0,8860	0,01100	0,10526	0,0009	0,4494300	643,70	6,00	645,10	5,10	645,0	25,0	645,1	5,1	0,217	
ROD-4_87.FIN2	288,0	1,877	2,9130	0,03800	0,24140	0,0020	0,6575000	1384,70	9,50	1393,00	11,00	1382,0	18,0	1382,0	18,0	0,796	
ROD-4_88.FIN2	294,0	1,529	0,3496	0,00720	0,04839	0,0005	0,3600700	303,90	5,40	304,60	3,00	299,0	42,0	304,6	3,0	0,230	
ROD-4_89.FIN2	296,0	2,294	0,3572	0,00720	0,04954	0,0005	0,0577840	309,50	5,40	311,70	2,90	296,0	47,0	311,7	2,9	0,711	
ROD-4_90.FIN2	517,0	1,365	0,7950	0,01100	0,09228	0,0010	0,6358000	594,50	6,70	568,90	5,60	696,0	26,0	568,9	5,6	4,306	
ROD-4_92.FIN2	334,0	1,438	0,9330	0,01100	0,10994	0,0010	0,4174800	668,70	5,90	672,30	5,60	667,0	24,0	672,3	5,6	0,538	
ROD-4_93.FIN2	115,8	0,760	5,3440	0,06400	0,33690	0,0025	0,5102700	1874,00	10,00	1871,00	12,00	1889,0	20,0	1889,0	20,0	0,953	
ROD-4_94.FIN2	271,0	0,553	0,8600	0,01500	0,09920	0,0011	0,2641500	629,30	8,40	609,50	6,20	708,0	38,0	609,5	6,2	3,146	
ROD-4_95.FIN2	161,0	1,512	4,9480	0,05700	0,33340	0,0033	0,7012600	1808,90	9,80	1854,00	16,00	1771,0	16,0	1771,0	16,0	4,687	
ROD-4_96.FIN2	67,7	0,292	0,8010	0,02800	0,09450	0,0013	0,2931200	594,00	15,00	581,90	7,50	637,0	74,0	581,9	7,5	2,037	
ROD-4_97.FIN2	259,2	1,166	0,3960	0,00850	0,05297	0,0005	0,1957500	338,80	6,30	332,70	3,10	373,0	46,0	332,7	3,1	1,800	
ROD-4_98.FIN2	215,7	2,570	0,3550	0,00730	0,04932	0,0005	0,0916430	307,90	5,50	310,30	2,90	296,0	48,0	310,3	2,9	0,779	
ROD-4_99.FIN2	683,0	1,010	1,8170	0,04400	0,17940	0,0029	0,5905300	1055,00	14,00	1063,00	16,00	1059,0	41,0	1059,0	41,0	0,378	Rim
ROD-4_99.FIN2	169,8	2,713	4,4450	0,09500	0,29100	0,0048	0,7280700	1719,00	18,00	1646,00	24,00	1821,0	26,0	1821,0	26,0	9,610	Core
ROD-4_100.FIN2	665,0	5,820	0,4208	0,00730	0,05643	0,0006	0,5537000	356,20	5,20	353,90	3,60	379,0	33,0	353,9	3,6	0,646	
ROD-4_101.FIN2	1092,0	9,400	0,8540	0,01900	0,10160	0,0021	0,7226300	627,00	10,00	624,00	12,00	661,0	34,0	624,0	12,0	0,478	Rim
ROD-4_101.FIN2	244,2	2,553	1,7340	0,02400	0,17180	0,0016	0,5216400	1020,20	9,00	1021,90	9,00	1024,0	24,0	1024,0	24,0	0,205	Core
ROD-4_102.FIN2	194,5	1,283	1,1330	0,01500	0,12840	0,0011	0,1808900	769,00	7,30	778,50	6,40	745,0	32,0	778,5	6,4	1,235	
ROD-4_103.FIN2	60,4	-5,000	0,8310	0,05300	0,10330	0,0025	0,3143900	621,00	35,00	634,00	14,00	570,0	150,0	634,0	14,0	2,093	Rim
ROD-4_103.FIN2	195,5	1,466	8,1580	0,09200	0,35390	0,0037	0,6989100	2240,10	9,90	1953,00	17,00	2540,0	15,0	2540,0	15,0	23,110	Core
ROD-4_104.FIN2	164,7	1,223	0,8150	0,01600	0,09701	0,0010	0,1187400	605,10	9,10	596,80	5,70	645,0	46,0	596,8	5,7	1,372	
ROD-4_105.FIN2	527,0	2,380	0,6190	0,01300	0,08010	0,0013	0,5978700	488,70	8,10	496,80	7,70	461,0	37,0	496,8	7,7	1,657	
ROD-4_106.FIN2	177,7	2,051	0,6190	0,01100	0,07853	0,0007	0,3305100	488,20	7,10	487,30	4,40	503,0	39,0	487,3	4,4	0,184	
ROD-4_107.FIN2	600,0	0,890	0,8590	0,01000	0,10359	0,0010	0,3668700	629,60	5,60	635,30	5,60	626,0	25,0	635,3	5,6	0,905	
ROD-4_108.FIN2	1360,0	2,430	0,3913	0,00570	0,05288	0,0007	0,6527600	335,00	4,20	332,10	4,20	373,0	27,0	332,1	4,2	0,866	
ROD-4_109.FIN2	467,0	3,690	1,0110	0,01400	0,11530	0,0011	0,6623000	708,10	7,30	703,20	6,30	737,0	23,0	703,2	6,3	0,692	
ROD-4_110.FIN2	296,0	1,517	0,5960	0,00970	0,07596	0,0007	0,2823500	474,90	6,30	471,90	4,30	495,0	37,0	471,9	4,3	0,632	
ROD-4_111.FIN2	180,1	3,190	5,5570	0,06300	0,33910	0,0030	0,5713800	1908,30	9,70	1882,00	14,00	1950,0	17,0	1950,0	17,0	3,487	
ROD-4_112.FIN2	326,0	41,800	0,4350	0,01700	0,05800	0,0010	0,4495300	366,00	12,00	363,30	6,20	412,0	77,0	363,3	6,2	0,738	Rim
ROD-4_112.FIN2	140,3	2,424	0,5420	0,01600	0,07090	0,0008	0,2556800	438,00	10,00	441,60	4,70	416,0	62,0	441,6	4,7	0,822	Core
ROD-4_113.FIN2	1790,0	4,300	0,3510	0,01100	0,04490	0,0013	0,5640500	305,50	8,20	283,00	8,10	502,0	62,0	283,0	8,1	7,365	Rim
ROD-4_113.FIN2	184,0	0,903	0,8310	0,01900	0,09870	0,0012	0,2482900	613,00	10,00	606,70	7,10	640,0	50,0	606,7	7,1	1,028	Core
ROD-4_114.FIN2	563,0	2,600	0,8860	0,01100	0,10680	0,0011	0,5613200	643,60	5,90	654,20	6,40	628,0	24,0	654,2	6,4	1,647	
ROD-4_115.FIN2	329,0	0,837	0,7690	0,01200	0,09320	0,0011	0,5314600	578,20	7,20	574,30	6,40	610,0	31,0	574,3	6,4	0,675	
ROD-4_116.FIN2	394,0	6,200	0,6117	0,00990	0,07934	0,0007	0,2625300	484,70	6,10	492,10	4,10	452,0	35,0	492,1	4,1	1,527	
ROD-4_117.FIN2	788,0	3,330	0,7220	0,01100	0,08900	0,0010	0,6804800	551,20	6,30	549,70	6,00	568,0	23,0	549,7	6,0	0,272	
ROD-4_118.FIN2	286,0	1,407	13,3500	0,16000	0,52560	0,0062	0,8093700	2702,00	11,00	2721,00	26,00	2693,0	14,0	2693,0	14,0	1,040	
ROD-4_119.FIN2	591,0	3,950	0,4392	0,00680	0,06004	0,0006	0,4849100	369,30	4,80	375,80	3,90	336,0	30,0	375,8	3,9	1,760	
ROD-4_120.FIN2	769,0	2,880	0,3489	0,00470	0,04822	0,0004	0,2603400	303,70	3,50	303,60	2,70	310,0	31,0	303,6	2,7	0,033	
ROD-4_121.FIN2	79,7	1,071	1,3710	0,02500	0,14580	0,0017	0,3411200	875,00	11,00	877,00	9,50	871,0	38,0	871,0	38,0	0,689	

Sample Name:	[U]							207/235		206/238		207/206		Best age		Discordance	Rim/
Grain #	ppm	U/Th	207/235	2σ error	206/238	2σ error	RHO	Age Ma	2σ error	Age (Ma)	2σ error	Age (Ma)	2σ error	(Ma)	2σ error	%	Core
ROD-4_122.FIN2	709,0	1,973	0,3732	0,00850	0,05098	0,0006	0,5262100	321,50	6,20	320,50	3,60	327,0	42,0	320,5	3,6	0,311	
ROD-4_123.FIN2	498,0	0,927	1,1320	0,01500	0,12650	0,0015	0,6833700	768,10	7,30	767,80	8,80	772,0	22,0	767,8	8,8	0,039	
ROD-4_124.FIN2	277,0	1,523	13,1400	0,15000	0,51250	0,0060	0,7380800	2688,00	11,00	2666,00	26,00	2708,0	14,0	2708,0	14,0	1,551	
ROD-4_125.FIN2	137,4	1,019	11,9300	0,11000	0,48780	0,0045	0,6299200	2597,20	8,70	2560,00	19,00	2630,0	13,0	2630,0	13,0	2,662	
ROD-4_126.FIN2	180,3	2,510	0,6870	0,01600	0,08490	0,0012	0,1772200	530,20	9,50	525,20	7,20	546,0	56,0	525,2	7,2	0,943	
ROD-4_127.FIN2	181,1	1,038	1,2110	0,01500	0,13330	0,0013	0,4844300	804,90	6,90	806,70	7,70	801,0	25,0	806,7	7,7	0,224	
ROD-4_128.FIN2	70,8	0,749	0,8790	0,02100	0,10120	0,0013	0,0929710	638,00	12,00	621,20	7,80	682,0	58,0	621,2	7,8	2,633	
ROD-4_129.FIN2	250,0	2,860	6,5930	0,08700	0,35760	0,0037	0,7709700	2057,00	12,00	1970,00	18,00	2149,0	15,0	2149,0	15,0	8,329	
ROD-4_130.FIN2	476,0	4,320	1,6550	0,01500	0,16480	0,0012	0,4758400	990,70	5,70	984,40	6,60	1004,0	18,0	1004,0	18,0	1,952	
ROD-4_131.FIN2	838,0	1,138	0,4281	0,00670	0,05553	0,0006	0,5118700	361,50	4,80	348,30	3,80	438,0	31,0	348,3	3,8	3,651	
ROD-4_132.FIN2	280,0	1,130	11,2800	0,14000	0,47740	0,0049	0,5589500	2544,00	11,00	2515,00	22,00	2565,0	18,0	2565,0	18,0	1,949	
ROD-4_133.FIN2	301,0	1,244	0,4653	0,00780	0,06060	0,0007	0,3019200	388,10	5,60	379,20	4,00	435,0	38,0	379,2	4,0	2,293	
ROD-4_134.FIN2	273,9	1,200	0,8840	0,01300	0,10500	0,0010	0,3072100	642,00	7,10	643,60	5,80	633,0	32,0	643,6	5,8	0,249	
ROD-4_135.FIN2	216,9	1,846	0,3495	0,00830	0,04919	0,0005	0,2290400	303,60	6,20	309,50	2,90	253,0	49,0	309,5	2,9	1,943	
NOC-1_1.FIN2	740,0	3,210	0,3580	0,00480	0,04899	0,0004	0,3827400	310,50	3,60	308,30	2,50	322,0	29,0	308,3	2,5	0,709	
NOC-1_2.FIN2	66,4	0,742	5,2430	0,07300	0,33100	0,0036	0,5330500	1858,00	12,00	1842,00	17,00	1876,0	23,0	1876,0	23,0	1,812	
NOC-1_3.FIN2	1085,0	0,763	0,7629	0,00730	0,09320	0,0010	0,6995500	576,10	4,40	574,40	5,70	588,0	21,0	574,4	5,7	0,295	
NOC-1_4.FIN2	191,9	0,924	12,5100	0,10000	0,49260	0,0039	0,5665600	2642,80	7,70	2581,00	17,00	2692,0	12,0	2692,0	12,0	4,123	
NOC-1_5.FIN2	208,3	4,510	6,7600	0,22000	0,36830	0,0067	0,6752000	2075,00	29,00	2020,00	32,00	2132,0	45,0	2132,0	45,0	5,253	Rim
NOC-1_5.FIN2	246,0	14,800	15,8000	0,25000	0,55260	0,0053	0,4769000	2866,00	14,00	2835,00	22,00	2882,0	24,0	2882,0	24,0	1,631	Core
NOC-1_6.FIN2	145,9	0,711	1,9740	0,02500	0,18580	0,0014	0,5230400	1105,50	8,60	1098,40	7,70	1116,0	24,0	1116,0	24,0	1,577	
NOC-1_7.FIN2	584,0	1,335	0,8600	0,01000	0,10066	0,0009	0,4667100	629,30	5,60	618,20	5,10	674,0	23,0	618,2	5,1	1,764	
NOC-1_8.FIN2	361,0	5,500	0,4309	0,00820	0,05717	0,0008	0,4157900	363,20	5,80	358,30	4,90	393,0	41,0	358,3	4,9	1,349	
NOC-1_9.FIN2	938,0	1,614	0,8065	0,00830	0,09775	0,0008	0,5359900	600,70	4,70	601,20	4,60	603,0	19,0	601,2	4,6	0,083	
NOC-1_10.FIN2	175,0	1,168	0,8570	0,01600	0,10270	0,0011	0,3585700	627,90	8,90	630,30	6,30	620,0	39,0	630,3	6,3	0,382	
NOC-1_11.FIN2	557,0	2,970	0,7090	0,01400	0,08830	0,0015	0,8107600	544,20	8,10	545,20	8,90	540,0	26,0	545,2	8,9	0,184	
NOC-1_12.FIN2	1540,0	78,000	0,3830	0,01800	0,05150	0,0026	0,3133600	329,00	13,00	324,00	16,00	390,0	130,0	324,0	16,0	1,520	Rim
NOC-1_12.FIN2	691,0	5,400	0,7840	0,01600	0,09220	0,0015	0,5384000	587,20	8,90	568,60	8,60	659,0	37,0	568,6	8,6	3,168	Core
NOC-1_13.FIN2	455,0	1,632	0,3579	0,00590	0,04996	0,0005	0,3553300	310,30	4,40	314,20	2,80	283,0	35,0	314,2	2,8	1,257	
NOC-1_14.FIN2	434,0	0,425	0,8570	0,01000	0,10330	0,0010	0,4645100	628,60	5,70	633,70	6,00	617,0	26,0	633,7	6,0	0,811	
NOC-1_15.FIN2	224,0	0,759	1,6190	0,02300	0,16710	0,0017	0,6081800	977,40	9,10	995,70	9,40	945,0	23,0	945,0	23,0	5,365	
NOC-1_16.FIN2	209,0	1,422	1,5940	0,02000	0,16250	0,0015	0,4982400	966,80	7,80	970,50	8,40	972,0	22,0	972,0	22,0	0,154	
NOC-1_17.FIN2	223,0	5,680	0,7180	0,01200	0,09006	0,0010	0,1452000	548,80	7,30	555,80	5,60	531,0	39,0	555,8	5,6	1,276	
NOC-1_18.FIN2	463,0	5,500	0,6450	0,02200	0,07940	0,0016	0,4091600	505,00	14,00	492,20	9,50	596,0	60,0	492,2	9,5	2,535	Rim
NOC-1_18.FIN2	210,0	3,038	2,5250	0,05700	0,17520	0,0031	0,6916700	1277,00	16,00	1041,00	17,00	1706,0	31,0	DISC	DISC	38,980	Core
NOC-1_19.FIN2	970,0	22,400	0,3748	0,00460	0,05154	0,0005	0,3973100	323,00	3,40	324,00	2,70	321,0	27,0	324,0	2,7	0,310	
NOC-1_20.FIN2	1348,0	4,240	0,3110	0,01300	0,03560	0,0014	0,9048700	274,10	9,90	225,70	8,70	724,0	39,0	DISC	DISC	17,658	Rim
NOC-1_20.FIN2	395,0	3,346	0,5400	0,01400	0,06416	0,0010	0,3545500	437,70	9,30	400,90	5,90	636,0	54,0	400,9	5,9	8,408	Core
NOC-1_21.FIN2	48,7	2,700	1,1490	0,02800	0,12930	0,0020	0,4212000	773,00	13,00	784,00	11,00	757,0	49,0	784,0	11,0	1,423	
NOC-1_22.FIN2	289,0	0,978	0,4387	0,00840	0,05836	0,0007	0,5360900	368,70	5,90	365,60	4,40	392,0	37,0	365,6	4,4	0,841	
NOC-1_23.FIN2	219,0	1,321	0,4587	0,00980	0,06250	0,0007	0,2525600	382,50	6,80	390,80	4,00	333,0	46,0	390,8	4,0	2,170	
NOC-1_24.FIN2	22,6	0,930	6,3200	0,17000	0,36480	0,0085	0,7135800	2012,00	24,00	2001,00	40,00	2033,0	33,0	2033,0	33,0	1,574	
NOC-1_25.FIN2	558,0	2,710	0,4158	0,00600	0,05660	0,0005	0,4743300	352,70	4,30	354,90	3,20	340,0	30,0	354,9	3,2	0,624	
NOC-1_28.FIN2	413,0	6,200	1,0150	0,01500	0,11540	0,0013	0,4077000	710,40	7,40	704,00	7,70	738,0	29,0	704,0	7,7	0,901	
NOC-1_29.FIN2	255,7	2,650	12,7200	0,36000	0,51400	0,0110	0,8970600	2645,00	27,00	2669,00	46,00	2641,0	21,0	2641,0	21,0	1,060	
NOC-1_30.FIN2	59,9	1,560	1,0130	0,02300	0,12070	0,0015	0,2885700	709,00	12,00	734,30	8,70	632,0	52,0	734,3	8,7	3,568	

Sample Name:	[U]							207/235		206/238		207/206		Best age		Discordance	Rim/
Grain #	ppm	U/Th	207/235	2σ error	206/238	2σ error	RHO	Age Ma	2σ error	Age (Ma)	2σ error	Age (Ma)	2σ error	(Ma)	2σ error	%	Core
NOC-1_31.FIN2	128,0	2,690	12,7400	0,65000	0,51700	0,0210	0,9650200	2612,00	51,00	2662,00	86,00	2597,0	32,0	2597,0	32,0	2,503	
NOC-1_32.FIN2	893,0	8,840	0,6237	0,00900	0,07883	0,0010	0,5801400	491,50	5,60	489,00	5,70	512,0	26,0	489,0	5,7	0,509	
NOC-1_33.FIN2	276,0	4,510	1,4850	0,02500	0,15470	0,0021	0,6149900	923,00	10,00	927,00	12,00	915,0	27,0	915,0	27,0	1,311	
NOC-1_34.FIN2	383,0	2,090	0,7524	0,00990	0,09175	0,0010	0,5331800	569,00	5,70	565,80	5,60	580,0	26,0	565,8	5,6	0,562	
NOC-1_35.FIN2	406,0	1,629	0,3544	0,00670	0,04923	0,0004	0,2593300	307,60	5,00	309,80	2,70	290,0	41,0	309,8	2,7	0,715	
NOC-1_36.FIN2	670,0	2,690	1,0030	0,01200	0,11570	0,0012	0,5128800	705,30	5,70	705,90	6,80	701,0	23,0	705,9	6,8	0,085	
NOC-1_37.FIN2	37,7	1,199	1,7490	0,04400	0,17350	0,0022	0,1926600	1026,00	17,00	1031,00	12,00	1003,0	54,0	1003,0	54,0	2,792	
NOC-1_38.FIN2	249,5	2,589	1,1080	0,01200	0,12530	0,0010	0,2991700	757,30	6,10	760,70	6,00	740,0	24,0	760,7	6,0	0,449	
NOC-1_39.FIN2	703,0	8,310	0,8840	0,01400	0,10430	0,0014	0,3872000	642,70	7,30	639,20	8,40	664,0	35,0	639,2	8,4	0,545	Rim
NOC-1_39.FIN2	181,2	1,053	1,1870	0,02500	0,13060	0,0014	0,2583300	793,00	12,00	791,00	8,20	789,0	45,0	791,0	8,2	0,252	Core
NOC-1_40.FIN2	335,0	1,945	0,3725	0,00760	0,05126	0,0007	0,5159300	320,90	5,60	322,20	4,10	303,0	39,0	322,2	4,1	0,405	
NOC-1_41.FIN2	692,0	4,440	0,8680	0,03100	0,10010	0,0025	0,6713800	633,00	17,00	615,00	15,00	700,0	57,0	615,0	15,0	2,844	
NOC-1_42.FIN2	216,7	3,390	0,6060	0,01100	0,07608	0,0008	0,2835900	480,00	6,90	472,60	4,60	501,0	40,0	472,6	4,6	1,542	
NOC-1_43.FIN2	744,0	2,510	0,5899	0,00630	0,07498	0,0006	0,5008100	470,50	4,00	466,00	3,50	492,0	21,0	466,0	3,5	0,956	
NOC-1_44.FIN2	633,0	1,802	0,5676	0,00660	0,07314	0,0007	0,3672200	456,10	4,30	455,00	4,20	455,0	27,0	455,0	4,2	0,241	
NOC-1_45.FIN2	2330,0	16,700	0,8600	0,03300	0,09930	0,0038	0,8117200	629,00	18,00	610,00	22,00	701,0	51,0	610,0	22,0	3,021	Rim
NOC-1_45.FIN2	265,9	1,127	1,6040	0,02400	0,15880	0,0012	0,5195400	970,70	9,10	949,90	6,50	1003,0	25,0	1003,0	25,0	5,294	Core
NOC-1_46.FIN2	356,0	1,522	0,7900	0,01000	0,09701	0,0008	0,4343700	590,80	5,70	596,80	4,90	560,0	26,0	596,8	4,9	1,016	
NOC-1_47.FIN2	401,0	2,183	0,3830	0,00630	0,05155	0,0005	0,2280400	328,80	4,60	324,00	3,10	349,0	38,0	324,0	3,1	1,460	
NOC-1_48.FIN2	1676,0	3,280	0,4221	0,00520	0,05473	0,0006	0,5863700	357,30	3,70	343,50	3,50	435,0	24,0	343,5	3,5	3,862	
NOC-1_49.FIN2	274,0	2,261	0,3478	0,00760	0,04813	0,0006	0,2466900	302,40	5,70	303,00	3,70	284,0	49,0	303,0	3,7	0,198	
NOC-1_50.FIN2	895,0	1,131	0,9070	0,01700	0,09980	0,0020	0,4914400	654,90	8,90	616,00	12,00	783,0	44,0	616,0	12,0	5,940	
NOC-1_51.FIN2	1082,0	77,400	0,4740	0,01300	0,06280	0,0013	0,5712600	393,30	8,70	392,60	7,70	387,0	52,0	392,6	7,7	0,178	Rim
NOC-1_51.FIN2	246,0	1,145	0,8450	0,01900	0,10010	0,0013	0,3004000	621,00	10,00	614,80	7,70	623,0	48,0	614,8	7,7	0,998	Core
NOC-1_52.FIN2	543,0	1,526	0,6136	0,00770	0,07701	0,0007	0,5459500	485,40	4,80	478,20	4,00	503,0	24,0	478,2	4,0	1,483	
NOC-1_53.FIN2	424,0	1,879	0,5680	0,01100	0,07180	0,0011	0,4850900	456,20	7,10	446,80	6,40	487,0	41,0	446,8	6,4	2,060	
NOC-1_54.FIN2	142,6	0,835	0,6030	0,01600	0,07690	0,0011	0,1512900	478,00	11,00	477,30	6,60	458,0	64,0	477,3	6,6	0,146	
NOC-1_55.FIN2	570,0	2,187	0,6860	0,02200	0,07335	0,0007	0,5343600	527,00	13,00	456,30	4,30	800,0	54,0	456,3	4,3	13,416	
NOC-1_56.FIN2	445,0	1,860	0,3862	0,00750	0,05019	0,0006	0,4985200	331,10	5,50	315,60	3,50	417,0	37,0	315,6	3,5	4,681	
NOC-1_57.FIN2	158,2	1,148	1,6170	0,02700	0,15830	0,0021	0,4627400	976,00	10,00	947,00	12,00	1032,0	31,0	1032,0	31,0	8,236	
NOC-1_58.FIN2	299,0	2,077	0,3653	0,00690	0,04926	0,0005	0,3304500	315,70	5,10	310,00	2,80	336,0	40,0	310,0	2,8	1,806	
NOC-1_59.FIN2	1006,0	27,000	0,8065	0,00860	0,09597	0,0008	0,4944400	600,10	4,90	590,70	4,60	622,0	21,0	590,7	4,6	1,566	
NOC-1_60.FIN2	306,0	1,509	1,6510	0,01900	0,16600	0,0015	0,5665600	990,00	7,10	990,00	8,20	975,0	20,0	975,0	20,0	1,538	
NOC-1_61.FIN2	430,0	1,798	0,3555	0,00610	0,04852	0,0004	0,2185800	309,00	4,70	305,40	2,40	318,0	39,0	305,4	2,4	1,165	
NOC-1_62.FIN2	553,0	4,040	0,5450	0,01000	0,06849	0,0008	0,5607300	441,50	6,70	427,00	4,90	502,0	35,0	427,0	4,9	3,284	
NOC-1_63.FIN2	95,8	1,665	1,1710	0,02600	0,12750	0,0015	0,2163900	785,00	12,00	773,20	8,40	797,0	48,0	773,2	8,4	1,503	
NOC-1_64.FIN2	1156,0	89,000	0,7700	0,02100	0,09110	0,0017	0,5256400	579,00	12,00	562,00	10,00	632,0	44,0	562,0	10,0	2,936	Rim
NOC-1_64.FIN2	125,1	0,652	5,2880	0,08300	0,33610	0,0045	0,6762500	1865,00	13,00	1867,00	22,00	1854,0	21,0	1854,0	21,0	0,701	Core
NOC-1_65.FIN2	412,0	0,735	1,1310	0,01500	0,12570	0,0012	0,6079100	768,20	7,10	763,20	6,80	771,0	22,0	763,2	6,8	0,651	
NOC-1_66.FIN2	114,9	1,155	12,6400	0,13000	0,50550	0,0048	0,7072400	2652,00	10,00	2637,00	21,00	2650,0	14,0	2650,0	14,0	0,491	
NOC-1_67.FIN2	451,9	2,373	0,4399	0,00610	0,05788	0,0005	0,3129300	369,90	4,30	362,70	2,90	396,0	30,0	362,7	2,9	1,946	
NOC-1_68.FIN2	219,0	1,910	0,3643	0,00780	0,04972	0,0005	0,0941820	314,80	5,80	312,80	3,00	310,0	49,0	312,8	3,0	0,635	
NOC-1_69.FIN2	381,0	1,690	0,8140	0,02100	0,09140	0,0020	0,4743600	604,00	12,00	564,00	12,00	749,0	50,0	564,0	12,0	6,623	
NOC-1_71.FIN2	538,0	1,290	0,8410	0,01200	0,10050	0,0010	0,5160400	619,50	6,60	617,20	6,10	618,0	27,0	617,2	6,1	0,371	
NOC-1_72.FIN2	423,0	1,158	0,4034	0,00660	0,05445	0,0005	0,4127300	343,70	4,80	341,80	3,10	342,0	35,0	341,8	3,1	0,553	
NOC-1_73.FIN2	108,5	1,559	0,8960	0,01700	0,10620	0,0011	0,2934900	649,40	9,50	650,20	6,70	642,0	42,0	650,2	6,7	0,123	
NOC-1_74.FIN2	314,0	1,899	0,3730	0,00780	0,05141	0,0005	0,3271800	321,30	5,80	323,10	3,10	293,0	44,0	323,1	3,1	0,560	

Sample Name:	[U]							207/235		206/238		207/206		Best age		Discordance	Rim/
Grain #	ppm	U/Th	207/235	2σ error	206/238	2σ error	RHO	Age Ma	2σ error	Age (Ma)	2σ error	Age (Ma)	2σ error	(Ma)	2σ error	%	Core
NOC-1_75.FIN2	298,0	6,480	0,7280	0,01200	0,08959	0,0009	0,4677000	554,50	6,80	553,10	5,00	550,0	31,0	553,1	5,0	0,252	
NOC-1_76.FIN2	607,0	10,760	0,6170	0,01000	0,07836	0,0009	0,5433500	487,50	6,50	486,30	5,40	490,0	32,0	486,3	5,4	0,246	Rim
NOC-1_76.FIN2	236,0	4,990	0,7820	0,01800	0,09750	0,0012	0,5553800	586,00	10,00	599,40	7,20	528,0	50,0	599,4	7,2	2,287	Core
NOC-1_77.FIN2	107,8	0,943	6,1300	0,07400	0,36220	0,0040	0,6080900	1994,00	11,00	1992,00	19,00	1988,0	21,0	1988,0	21,0	0,201	
NOC-1_78.FIN2	203,9	1,742	15,0200	0,16000	0,51880	0,0047	0,7184300	2815,00	10,00	2693,00	20,00	2900,0	12,0	2900,0	12,0	7,138	
NOC-1_79.FIN2	806,0	7,100	0,9460	0,05700	0,10800	0,0067	0,8209300	674,00	30,00	661,00	39,00	733,0	78,0	661,0	39,0	1,929	Rim
NOC-1_79.FIN2	236,0	1,310	1,5500	0,03300	0,15280	0,0018	0,2367400	951,00	13,00	916,70	9,90	1012,0	42,0	1012,0	42,0	9,417	Core
NOC-1_80.FIN2	239,0	1,474	0,3582	0,00860	0,04790	0,0005	0,1713000	310,10	6,40	301,60	3,00	357,0	53,0	301,6	3,0	2,741	
NOC-1_81.FIN2	1313,0	1,675	0,3380	0,00390	0,04674	0,0004	0,4171200	295,50	3,00	294,40	2,50	296,0	26,0	294,4	2,5	0,372	
NOC-1_82.FIN2	696,0	2,067	0,3585	0,00640	0,04928	0,0006	0,0694010	310,90	4,80	310,10	3,70	305,0	35,0	310,1	3,7	0,257	
NOC-1_83.FIN2	357,0	1,168	11,9800	0,10000	0,48990	0,0041	0,6859300	2602,10	8,20	2569,00	18,00	2623,0	11,0	2623,0	11,0	2,059	
NOC-1_84.FIN2	205,0	10,200	6,5800	0,22000	0,37360	0,0092	0,9369400	2039,00	31,00	2041,00	43,00	2046,0	23,0	2046,0	23,0	0,244	
NOC-1_86.FIN2	1730,0	14,300	0,3300	0,02400	0,04440	0,0020	0,9458400	288,00	19,00	280,00	12,00	413,0	56,0	280,0	12,0	2,778	Rim
NOC-1_86.FIN2	850,0	0,862	1,9760	0,05800	0,18050	0,0044	0,9099400	1105,00	20,00	1069,00	24,00	1169,0	24,0	1169,0	24,0	8,554	Core
NOC-1_87.FIN2	228,0	1,470	1,0010	0,03400	0,10810	0,0020	0,4947700	703,00	17,00	662,00	11,00	835,0	61,0	662,0	11,0	5,832	Rim
NOC-1_87.FIN2	72,7	0,612	1,5050	0,03800	0,15160	0,0024	0,1281800	930,00	15,00	909,00	14,00	977,0	54,0	977,0	54,0	6,960	Core
NOC-1_88.FIN2	488,0	2,180	0,3720	0,00640	0,05075	0,0006	0,4841400	320,70	4,70	319,10	3,40	316,0	35,0	319,1	3,4	0,499	
NOC-1_90.FIN2	355,0	3,240	0,9280	0,01300	0,11016	0,0009	0,4354600	665,90	6,90	673,60	5,20	632,0	28,0	673,6	5,2	1,156	
NOC-1_91.FIN2	394,0	1,857	0,3626	0,00670	0,04947	0,0005	0,3691800	313,70	5,00	311,20	3,20	320,0	39,0	311,2	3,2	0,797	
NOC-1_92.FIN2	484,0	3,540	0,8750	0,01300	0,10383	0,0010	0,4418200	637,50	6,80	636,70	5,70	627,0	28,0	636,7	5,7	0,125	
NOC-1_93.FIN2	809,0	2,140	0,9510	0,01100	0,16030	0,0018	0,7183000	678,10	5,80	958,00	10,00	907,0	18,0	907,0	18,0	5,623	
NOC-1_94.FIN2	376,2	4,880	0,7690	0,01700	0,08960	0,0015	0,4919100	578,60	9,80	552,90	8,80	672,0	45,0	552,9	8,8	4,442	
NOC-1_95.FIN2	1352,0	0,944	0,4162	0,00640	0,05431	0,0007	0,2969500	353,10	4,60	340,90	4,20	423,0	38,0	340,9	4,2	3,455	
NOC-1_96.FIN2	179,9	1,750	0,8780	0,01400	0,10525	0,0009	0,2374000	640,60	7,80	645,00	5,40	611,0	36,0	645,0	5,4	0,687	
NOC-1_97.FIN2	722,0	7,860	0,5220	0,01500	0,06790	0,0014	0,7956100	426,00	10,00	423,20	8,30	452,0	39,0	423,2	8,3	0,657	Rim
NOC-1_97.FIN2	111,9	1,420	0,8490	0,02700	0,10190	0,0018	0,5477300	622,00	15,00	625,00	11,00	588,0	58,0	625,0	11,0	0,482	Core
NOC-1_98.FIN2	663,0	6,360	1,5110	0,04000	0,15310	0,0031	0,8619300	937,00	15,00	918,00	17,00	964,0	32,0	964,0	32,0	4,772	
NOC-1_99.FIN2	84,3	1,122	1,8060	0,03000	0,17530	0,0017	0,2885100	1047,00	11,00	1041,20	9,50	1047,0	34,0	1047,0	34,0	0,554	
NOC-1_100.FIN2	131,0	0,650	1,5970	0,02600	0,16390	0,0015	0,4580900	968,00	10,00	978,50	8,10	934,0	31,0	934,0	31,0	4,764	
NOC-1_101.FIN2	937,0	1,603	1,2720	0,03400	0,12740	0,0026	0,6596800	832,00	15,00	773,00	15,00	1007,0	35,0	773,0	15,0	7,091	Rim
NOC-1_101.FIN2	579,0	0,948	1,9470	0,03400	0,17880	0,0026	0,8425100	1096,00	12,00	1060,00	14,00	1164,0	18,0	1164,0	18,0	8,935	Core
NOC-1_102.FIN2	17,0	0,712	1,2440	0,05600	0,13200	0,0029	0,2515900	808,00	26,00	801,00	17,00	788,0	96,0	801,0	17,0	0,866	
NOC-1_103.FIN2	314,3	1,619	2,7050	0,02900	0,22570	0,0017	0,5631500	1329,00	7,90	1311,80	9,10	1348,0	18,0	1348,0	18,0	2,685	
NOC-1_104.FIN2	264,0	2,103	0,6076	0,00910	0,07730	0,0008	0,3612500	481,40	5,80	479,90	5,00	472,0	33,0	479,9	5,0	0,312	
NOC-1_106.FIN2	264,6	1,595	0,8820	0,01700	0,10386	0,0010	0,3754600	641,20	9,00	636,90	5,70	650,0	39,0	636,9	5,7	0,671	
NOC-1_107.FIN2	443,0	2,431	4,0500	0,12000	0,23960	0,0052	0,6293300	1641,00	24,00	1384,00	27,00	1990,0	41,0	DISC	DISC	30,452	Rim
NOC-1_107.FIN2	263,0	3,950	9,8700	0,34000	0,43420	0,0096	0,9027700	2420,00	35,00	2322,00	43,00	2491,0	30,0	2491,0	30,0	6,784	Core
NOC-1_108.FIN2	163,8	1,925	0,3551	0,00940	0,04788	0,0006	0,2330700	307,60	7,00	301,50	3,40	334,0	56,0	301,5	3,4	1,983	
NOC-1_110.FIN2	716,0	14,620	6,7300	0,15000	0,35940	0,0049	0,8722200	2074,00	19,00	1979,00	23,00	2148,0	21,0	2148,0	21,0	7,868	
NOC-1_111.FIN2	610,0	1,874	0,3927	0,00520	0,05317	0,0004	0,4024200	336,00	3,80	333,90	2,50	340,0	28,0	333,9	2,5	0,625	
NOC-1_112.FIN2	354,0	3,860	1,0050	0,03000	0,11560	0,0024	0,6925600	705,00	15,00	705,00	14,00	698,0	46,0	705,0	14,0	0,000	
NOC-1_113.FIN2	164,3	1,093	0,4366	0,00940	0,05871	0,0006	0,2795600	367,00	6,60	367,70	3,70	342,0	46,0	367,7	3,7	0,191	
NOC-1_114.FIN2	84,3	0,730	0,7560	0,02600	0,07870	0,0017	0,4180800	567,00	15,00	488,00	10,00	854,0	68,0	488,0	10,0	13,933	
NOC-1_115.FIN2	392,6	15,000	0,9250	0,01400	0,10880	0,0014	0,3913500	664,40	7,50	665,80	7,90	653,0	33,0	665,8	7,9	0,211	Rim
NOC-1_115.FIN2	272,0	0,895	1,2770	0,03100	0,13730	0,0023	0,7206900	834,00	14,00	829,00	13,00	834,0	35,0	829,0	13,0	0,600	Core
NOC-1_116.FIN2	1352,0	2,240	0,3825	0,00660	0,05076	0,0009	0,7726700	329,80	5,10	319,10	5,50	394,0	25,0	319,1	5,5	3,244	
NOC-1_117.FIN2	131,0	19,300	0,8140	0,01700	0,09670	0,0015	0,3607800	603,00	9,20	595,00	8,60	626,0	43,0	595,0	8,6	1,327	

Sample Name:	[U]							207/235		206/238		207/206		Best age		Discordance	Rim/
Grain #	ppm	U/Th	207/235	2σ error	206/238	2σ error	RHO	Age Ma	2σ error	Age (Ma)	2σ error	Age (Ma)	2σ error	(Ma)	2σ error	%	Core
NOC-1_118.FIN2	182,0	2,684	0,3547	0,00840	0,04868	0,0006	0,1134900	308,30	6,50	306,40	3,40	301,0	54,0	306,4	3,4	0,616	
NOC-1_119.FIN2	60,0	1,983	1,8560	0,04000	0,17700	0,0022	0,2602000	1063,00	14,00	1050,00	12,00	1079,0	44,0	1079,0	44,0	2,688	
NOC-1_120.FIN2	142,0	1,463	1,8350	0,02400	0,17860	0,0016	0,2638100	1056,60	8,60	1058,90	8,60	1042,0	28,0	1042,0	28,0	1,622	
NOC-1_121.FIN2	59,3	1,068	0,7430	0,02000	0,09060	0,0012	0,1738200	562,00	12,00	559,20	7,00	544,0	62,0	559,2	7,0	0,498	
NOC-1_122.FIN2	457,0	2,190	0,3731	0,00700	0,05079	0,0006	0,4292900	321,50	5,20	319,30	3,50	323,0	38,0	319,3	3,5	0,684	
NOC-1_123.FIN2	265,0	1,783	0,4310	0,02000	0,05630	0,0014	0,3616900	362,00	13,00	353,10	8,30	407,0	86,0	353,1	8,3	2,459	Rim
NOC-1_123.FIN2	544,0	3,010	0,8490	0,02100	0,09730	0,0016	0,4891100	624,00	12,00	598,60	9,40	704,0	46,0	598,6	9,4	4,071	Core
NOC-1_124.FIN2	400,0	3,740	1,2120	0,01400	0,13190	0,0011	0,5532500	805,30	6,30	798,30	6,50	822,0	20,0	798,3	6,5	0,869	
NOC-1_125.FIN2	342,0	0,252	0,8340	0,01200	0,09983	0,0010	0,3987000	615,00	6,70	613,40	5,70	604,0	30,0	613,4	5,7	0,260	
NOC-1_126.FIN2	253,4	2,335	0,8980	0,01300	0,10708	0,0010	0,3970100	651,10	7,20	655,70	5,60	624,0	30,0	655,7	5,6	0,706	
NOC-1_127.FIN2	245,0	2,543	0,3591	0,00920	0,04959	0,0008	0,4706300	310,60	6,80	311,90	5,20	284,0	52,0	311,9	5,2	0,419	
NOC-1_128.FIN2	311,0	1,966	0,3778	0,00720	0,05079	0,0005	0,1790400	324,90	5,30	319,30	3,00	365,0	45,0	319,3	3,0	1,724	
NOC-1_129.FIN2	473,0	1,114	0,8800	0,01200	0,10437	0,0009	0,4022500	642,00	6,80	639,90	5,00	637,0	29,0	639,9	5,0	0,327	
NOC-1_130.FIN2	636,0	1,282	0,7790	0,02700	0,08910	0,0026	0,8043000	584,00	15,00	550,00	15,00	724,0	45,0	550,0	15,0	5,822	Rim
NOC-1_130.FIN2	265,8	1,763	1,1660	0,01900	0,12880	0,0014	0,5230500	783,50	8,90	780,80	7,90	781,0	29,0	780,8	7,9	0,345	Core
NOC-1_131.FIN2	435,0	1,862	0,7267	0,00900	0,09093	0,0009	0,3627700	554,20	5,30	560,90	5,10	524,0	29,0	560,9	5,1	1,209	
NOC-1_132.FIN2	321,0	3,800	0,6460	0,01300	0,07956	0,0010	0,6014900	505,10	7,70	493,40	5,70	549,0	34,0	493,4	5,7	2,316	
NOC-1_133.FIN2	213,0	1,580	1,8490	0,02200	0,18029	0,0017	0,3565900	1062,00	7,70	1067,80	9,40	1047,0	24,0	1047,0	24,0	1,987	
NOC-1_134.FIN2	1023,0	3,390	0,9910	0,01100	0,11390	0,0011	0,6196400	698,60	5,70	695,40	6,30	700,0	20,0	695,4	6,3	0,458	
NOC-1_135.FIN2	387,0	7,150	0,6075	0,00960	0,07830	0,0008	0,6989300	481,40	6,10	485,90	4,60	448,0	35,0	485,9	4,6	0,935	
NOC-1_136.FIN2	1610,0	7,600	0,4840	0,01900	0,06440	0,0011	0,5592800	400,00	13,00	402,10	6,60	542,0	36,0	402,1	6,6	0,525	
BIB-1_1.FIN2	306,0	2,114	0,3686	0,00670	0,05093	0,0006	0,3431800	318,20	5,00	320,20	3,40	297,0	40,0	320,2	3,4	0,629	
BIB-1_2.FIN2	363,0	1,495	0,4100	0,01600	0,04723	0,0008	0,4173400	348,00	11,00	297,50	4,70	712,0	76,0	297,5	4,7	14,511	
BIB-1_3.FIN2	204,5	1,549	0,7120	0,01100	0,09006	0,0008	0,2328500	545,10	6,50	555,80	4,90	510,0	36,0	555,8	4,9	1,963	
BIB-1_4.FIN2	274,6	2,325	0,7070	0,01100	0,08669	0,0009	0,2654800	543,60	6,80	535,90	5,60	578,0	38,0	535,9	5,6	1,416	
BIB-1_5.FIN2	55,0	1,350	3,1000	4,60000	0,08650	0,0048	0,1123200	605,00	67,00	534,00	28,00	1300,0	1100,0	534,0	28,0	11,736	Rim
BIB-1_5.FIN2	60,6	1,715	14,0500	0,57000	0,42500	0,0140	0,9310100	2737,00	39,00	2274,00	64,00	3119,0	26,0	3119,0	26,0	27,092	Core
BIB-1_6.FIN2	2190,0	28,100	0,3580	0,01400	0,04760	0,0018	0,4979700	311,00	10,00	300,00	11,00	432,0	87,0	300,0	11,0	3,537	Rim
BIB-1_6.FIN2	709,0	23,080	0,4268	0,00580	0,05766	0,0004	0,2054200	360,60	4,10	361,30	2,60	359,0	32,0	361,3	2,6	0,194	Core
BIB-1_7.FIN2	226,0	6,850	0,9130	0,01800	0,10970	0,0014	0,1133200	657,40	9,40	671,10	8,40	618,0	36,0	671,1	8,4	2,084	Rim
BIB-1_7.FIN2	278,0	1,830	1,1580	0,03800	0,12810	0,0027	0,8095300	779,00	18,00	777,00	15,00	783,0	40,0	777,0	15,0	0,257	Core
BIB-1_8.FIN2	221,2	1,036	0,4551	0,00960	0,06019	0,0007	0,3273100	380,00	6,60	376,70	4,30	404,0	45,0	376,7	4,3	0,868	
BIB-1_9.FIN2	2180,0	1,320	0,3780	0,01200	0,05030	0,0014	0,3535500	325,00	8,50	316,40	8,80	415,0	68,0	316,4	8,8	2,646	
BIB-1_11.FIN2	427,0	1,647	0,3645	0,00800	0,04819	0,0007	0,4189300	315,10	5,90	303,40	4,10	388,0	46,0	303,4	4,1	3,713	
BIB-1_12.FIN2	606,0	26,800	0,3190	0,01500	0,04380	0,0018	0,9044800	280,00	12,00	276,00	11,00	329,0	77,0	276,0	11,0	1,429	Rim
BIB-1_12.FIN2	162,0	2,050	1,0510	0,06400	0,12260	0,0038	0,6417100	727,00	32,00	745,00	22,00	640,0	110,0	745,0	22,0	2,476	Core
BIB-1_13.FIN2	337,2	1,701	0,3506	0,00610	0,04829	0,0005	0,2516800	304,80	4,50	304,00	3,00	296,0	40,0	304,0	3,0	0,262	
BIB-1_14.FIN2	252,0	2,396	8,6050	0,08200	0,42520	0,0037	0,5011700	2295,90	8,70	2284,00	17,00	2291,0	16,0	2291,0	16,0	0,306	
BIB-1_15.FIN2	189,2	1,317	0,8610	0,01500	0,10205	0,0009	0,2158700	629,20	8,00	626,30	5,20	619,0	39,0	626,3	5,2	0,461	
BIB-1_16.FIN2	652,0	3,350	0,6401	0,00840	0,08062	0,0009	0,4917800	502,60	5,10	499,70	5,20	489,0	27,0	499,7	5,2	0,577	
BIB-1_18.FIN2	1940,0	1,085	0,4399	0,00490	0,05785	0,0006	0,6059000	370,40	3,40	362,50	3,40	401,0	20,0	362,5	3,4	2,133	
BIB-1_19.FIN2	402,0	1,687	0,6985	0,00960	0,08630	0,0009	0,4048900	537,30	5,80	533,60	5,20	541,0	30,0	533,6	5,2	0,689	
BIB-1_20.FIN2	449,0	4,700	1,1660	0,03700	0,12680	0,0038	0,6640000	783,00	17,00	769,00	22,00	815,0	51,0	769,0	22,0	1,788	
BIB-1_21.FIN2	186,9	1,390	0,6130	0,01100	0,07780	0,0007	0,2413400	484,70	7,20	482,90	4,30	486,0	42,0	482,9	4,3	0,371	
BIB-1_22.FIN2	19,6	0,849	0,7450	0,03300	0,08650	0,0017	0,0218790	558,00	19,00	535,00	10,00	620,0	100,0	535,0	10,0	4,122	
BIB-1_23.FIN2	445,0	2,196	0,3748	0,00650	0,05030	0,0005	0,1625600	322,80	4,80	316,30	2,70	358,0	38,0	316,3	2,7	2,014	

Sample Name:	[U]							207/235		206/238		207/206		Best age		Discordance	Rim/
Grain #	ppm	U/Th	207/235	2σ error	206/238	2σ error	RHO	Age Ma	2σ error	Age (Ma)	2σ error	Age (Ma)	2σ error	(Ma)	2σ error	%	Core
BIB-1_24.FIN2	234,0	1,318	0,5930	0,01200	0,07470	0,0010	0,3320300	473,10	7,60	464,30	6,20	519,0	41,0	464,3	6,2	1,860	
BIB-1_25.FIN2	1490,0	36,500	0,6260	0,02700	0,07950	0,0030	0,7514100	493,00	17,00	493,00	18,00	520,0	63,0	493,0	18,0	0,000	Rim
BIB-1_25.FIN2	550,0	9,180	0,7180	0,01200	0,08920	0,0011	0,1742900	549,10	7,20	550,90	6,60	533,0	34,0	550,9	6,6	0,328	Core
BIB-1_27.FIN2	507,0	36,300	4,6810	0,05300	0,28560	0,0033	0,6407600	1762,90	9,50	1619,00	17,00	1943,0	17,0	1943,0	17,0	16,675	
BIB-1_28.FIN2	58,2	1,260	1,3930	0,03200	0,13700	0,0014	0,1891000	884,00	14,00	827,60	8,00	1024,0	48,0	827,6	8,0	6,380	
BIB-1_29.FIN2	518,0	1,020	5,6380	0,09800	0,29240	0,0052	0,9350200	1920,00	15,00	1652,00	25,00	2234,0	10,0	2234,0	10,0	26,052	
BIB-1_30.FIN2	217,0	6,500	0,4830	0,02300	0,06150	0,0018	0,5965700	399,00	16,00	385,00	11,00	482,0	83,0	385,0	11,0	3,509	Rim
BIB-1_30.FIN2	21,5	0,593	0,8080	0,05000	0,09300	0,0026	0,2010500	592,00	27,00	573,00	15,00	620,0	120,0	573,0	15,0	3,209	Core
BIB-1_32.FIN2	1558,0	6,600	0,6850	0,03500	0,07710	0,0034	0,8075400	528,00	22,00	479,00	21,00	767,0	67,0	479,0	21,0	9,280	Rim
BIB-1_32.FIN2	271,1	18,000	1,1780	0,01800	0,13040	0,0016	0,6318600	789,40	8,20	789,90	8,90	797,0	25,0	789,9	8,9	0,063	Core
BIB-1_33.FIN2	385,8	1,880	0,3567	0,00570	0,04920	0,0005	0,4224100	309,40	4,30	309,60	3,00	316,0	33,0	309,6	3,0	0,065	
BIB-1_34.FIN2	182,4	4,361	1,6070	0,02100	0,16340	0,0015	0,4098400	971,80	8,10	975,50	8,10	980,0	24,0	980,0	24,0	0,459	
BIB-1_35.FIN2	578,0	17,900	0,4910	0,01300	0,06530	0,0013	0,8575400	403,90	8,80	407,60	7,90	404,0	31,0	407,6	7,9	0,916	
BIB-1_36.FIN2	319,0	2,031	0,3715	0,00660	0,05131	0,0006	0,4567500	320,30	4,90	322,50	3,40	327,0	38,0	322,5	3,4	0,687	
BIB-1_37.FIN2	271,0	0,785	0,8860	0,01500	0,10720	0,0015	0,5657300	643,30	8,30	656,20	9,00	615,0	34,0	656,2	9,0	2,005	
BIB-1_38.FIN2	179,8	1,471	0,8690	0,01300	0,10410	0,0010	0,3390700	635,80	7,20	638,00	5,80	639,0	33,0	638,0	5,8	0,346	
BIB-1_39.FIN2	311,0	3,010	5,0810	0,08500	0,30640	0,0043	0,8889000	1831,00	15,00	1722,00	21,00	1973,0	13,0	1973,0	13,0	12,722	
BIB-1_41.FIN2	145,5	1,176	1,8040	0,02500	0,18020	0,0017	0,5060100	1046,60	9,30	1067,80	9,50	1015,0	24,0	1015,0	24,0	5,202	
BIB-1_42.FIN2	41,3	1,092	14,6300	0,21000	0,51340	0,0063	0,6689600	2789,00	14,00	2670,00	27,00	2878,0	21,0	2878,0	21,0	7,227	
BIB-1_43.FIN2	31,9	1,382	14,3600	0,28000	0,50540	0,0087	0,5911500	2767,00	18,00	2633,00	37,00	2861,0	25,0	2861,0	25,0	7,969	
BIB-1_44.FIN2	256,0	1,004	6,4190	0,08200	0,35790	0,0046	0,8044900	2033,00	12,00	1971,00	22,00	2082,0	17,0	2082,0	17,0	5,331	
BIB-1_45.FIN2	226,7	4,460	0,3312	0,00680	0,04636	0,0005	0,2804500	290,00	5,20	292,10	3,10	256,0	45,0	292,1	3,1	0,724	
BIB-1_46.FIN2	2430,0	3,640	0,3620	0,01500	0,04900	0,0030	0,6384200	313,00	11,00	309,00	18,00	368,0	86,0	309,0	18,0	1,278	Rim
BIB-1_46.FIN2	381,0	4,767	0,6367	0,00900	0,08160	0,0007	0,2063600	499,80	5,50	505,60	4,40	452,0	33,0	505,6	4,4	1,160	Core
BIB-1_47.FIN2	105,4	1,798	0,4400	0,01200	0,05801	0,0007	0,0127220	368,70	8,20	363,50	4,10	378,0	61,0	363,5	4,1	1,460	
BIB-1_48.FIN2	970,0	5,130	0,7960	0,02600	0,09500	0,0027	0,7089600	593,00	15,00	585,00	16,00	632,0	53,0	585,0	16,0	1,349	Rim
BIB-1_48.FIN2	235,0	0,972	1,6920	0,03000	0,16610	0,0019	0,5047400	1004,00	11,00	990,00	11,00	1027,0	32,0	1027,0	32,0	3,603	Core
BIB-1_49.FIN2	364,0	1,819	0,9720	0,01300	0,11320	0,0010	0,2076900	688,50	6,60	691,40	6,00	673,0	27,0	691,4	6,0	0,421	
BIB-1_50.FIN2	90,9	1,170	5,9470	0,09400	0,36260	0,0049	0,6862100	1968,00	14,00	1993,00	23,00	1942,0	19,0	1942,0	19,0	2,626	
BIB-1_51.FIN2	103,0	1,330	1,9220	0,03500	0,18560	0,0024	0,2601600	1089,00	12,00	1097,00	13,00	1071,0	36,0	1071,0	36,0	2,428	
BIB-1_52.FIN2	397,0	8,100	0,4945	0,00830	0,06412	0,0007	0,4828500	408,10	5,50	400,60	4,10	443,0	35,0	400,6	4,1	1,838	
BIB-1_53.FIN2	539,0	3,680	0,5865	0,00810	0,07454	0,0007	0,3960900	468,10	5,20	463,40	4,40	487,0	29,0	463,4	4,4	1,004	
BIB-1_54.FIN2	507,0	2,323	0,3574	0,00630	0,04874	0,0005	0,2449400	309,80	4,70	306,80	3,00	326,0	30,0	306,8	3,0	0,968	
BIB-1_55.FIN2	204,5	1,258	6,7420	0,05300	0,38180	0,0027	0,5155700	2077,30	7,00	2084,00	13,00	2067,0	13,0	2067,0	13,0	0,822	
BIB-1_56.FIN2	136,0	1,747	0,7790	0,01600	0,09712	0,0010	0,1340700	583,50	9,20	597,40	5,80	507,0	46,0	597,4	5,8	2,382	
BIB-1_57.FIN2	205,0	4,050	6,1580	0,05600	0,36190	0,0027	0,6196800	1997,40	7,90	1991,00	13,00	1994,0	13,0	1994,0	13,0	0,150	
BIB-1_58.FIN2	809,0	1,614	0,3942	0,00440	0,05336	0,0004	0,3689100	337,20	3,20	335,10	2,60	337,0	25,0	335,1	2,6	0,623	
BIB-1_59.FIN2	69,5	1,397	0,8790	0,02000	0,10320	0,0013	0,2488600	639,00	11,00	633,20	7,60	642,0	49,0	633,2	7,6	0,908	
BIB-1_60.FIN2	269,1	1,992	5,5140	0,07200	0,32410	0,0036	0,6374200	1902,00	11,00	1809,00	18,00	1993,0	20,0	1993,0	20,0	9,232	
BIB-1_61.FIN2	826,0	1,958	0,3975	0,00550	0,05323	0,0004	0,5320600	339,50	4,00	334,30	2,40	364,0	26,0	334,3	2,4	1,532	
BIB-1_62.FIN2	318,0	12,690	0,8420	0,01500	0,09890	0,0011	0,4299200	619,70	8,10	608,00	6,60	654,0	36,0	608,0	6,6	1,888	
BIB-1_63.FIN2	185,7	10,600	0,5840	0,01700	0,07305	0,0010	0,2300000	466,00	11,00	454,40	5,90	511,0	62,0	454,4	5,9	2,489	Rim
BIB-1_63.FIN2	62,6	1,442	1,1680	0,05200	0,12790	0,0029	0,2161900	782,00	25,00	775,00	17,00	785,0	99,0	775,0	17,0	0,895	Core
BIB-1_64.FIN2	665,0	0,390	0,5690	0,02400	0,06670	0,0023	0,6880800	457,00	15,00	416,00	14,00	687,0	64,0	416,0	14,0	8,972	Rim
BIB-1_64.FIN2	72,7	1,143	1,0380	0,03300	0,11950	0,0021	0,3409600	722,00	17,00	727,00	12,00	691,0	68,0	727,0	12,0	0,693	Core
BIB-1_65.FIN2	127,4	3,474	0,5940	0,01300	0,07636	0,0008	0,2253700	472,30	8,10	474,30	4,80	451,0	46,0	474,3	4,8	0,423	
BIB-1_66.FIN2	105,4	0,844	0,7630	0,02100	0,09340	0,0010	0,0670100	573,00	12,00	575,60	6,20	548,0	57,0	575,6	6,2	0,454	

Sample Name:	[U]							207/235		206/238		207/206		Best age		Discordance	Rim/
Grain #	ppm	U/Th	207/235	2σ error	206/238	2σ error	RHO	Age Ma	2σ error	Age (Ma)	2σ error	Age (Ma)	2σ error	(Ma)	2σ error	%	Core
BIB-1_67.FIN2	1468,0	134,000	0,4400	0,02700	0,05910	0,0025	0,6724000	369,00	19,00	370,00	15,00	347,0	69,0	370,0	15,0	0,271	Rim
BIB-1_67.FIN2	372,0	9,980	0,9640	0,01700	0,10170	0,0015	0,5121900	684,90	8,90	624,20	9,00	888,0	34,0	624,2	9,0	8,863	Core
BIB-1_68.FIN2	567,0	2,020	20,9400	0,24000	0,54970	0,0055	0,7315600	3134,00	11,00	2823,00	23,00	3340,0	12,0	3340,0	12,0	15,479	
BIB-1_71.FIN2	245,4	0,851	0,4139	0,00730	0,05514	0,0005	0,2529000	351,20	5,20	346,00	3,20	352,0	40,0	346,0	3,2	1,481	
BIB-1_73.FIN2	167,2	5,040	0,8820	0,01200	0,10310	0,0012	0,2309400	642,20	6,90	632,70	6,70	625,0	38,0	632,7	6,7	1,479	
BIB-1_74.FIN2	454,0	9,950	0,3520	0,01000	0,04750	0,0013	0,5839300	305,60	7,70	299,20	7,80	310,0	62,0	299,2	7,8	2,094	Rim
BIB-1_74.FIN2	179,0	4,480	0,6070	0,02100	0,07490	0,0017	0,6442200	480,00	13,00	466,00	10,00	516,0	57,0	466,0	10,0	2,917	Core
BIB-1_75.FIN2	1691,0	0,871	0,3452	0,00850	0,04443	0,0007	0,5464600	300,90	6,50	280,20	4,30	455,0	44,0	280,2	4,3	6,879	Rim
BIB-1_75.FIN2	870,0	1,515	0,4411	0,00680	0,05768	0,0007	0,2127200	370,80	4,80	361,50	3,90	401,0	38,0	361,5	3,9	2,508	Core
BIB-1_76.FIN2	566,5	2,368	5,6860	0,05800	0,31880	0,0026	0,7661400	1928,30	8,80	1784,00	13,00	2069,0	11,0	2069,0	11,0	13,775	
BIB-1_77.FIN2	431,0	0,753	0,3700	0,01000	0,04810	0,0010	0,6954300	318,50	7,50	302,70	6,00	418,0	41,0	302,7	6,0	4,961	
BIB-1_78.FIN2	288,0	2,940	1,8170	0,02900	0,17720	0,0019	0,4394800	1051,00	10,00	1051,00	11,00	1036,0	29,0	1036,0	29,0	1,448	Rim
BIB-1_78.FIN2	110,0	2,270	6,0800	0,12000	0,35550	0,0056	0,6808800	1985,00	17,00	1960,00	27,00	2007,0	29,0	2007,0	29,0	2,342	Core
BIB-1_79.FIN2	72,3	0,533	0,8340	0,02000	0,09880	0,0011	0,2202600	615,00	12,00	607,00	6,70	617,0	58,0	607,0	6,7	1,301	
BIB-1_80.FIN2	298,0	1,364	0,4636	0,00810	0,06077	0,0006	0,0716640	386,20	5,60	380,20	3,50	414,0	37,0	380,2	3,5	1,554	
BIB-1_81.FIN2	111,4	0,516	12,1300	0,15000	0,50040	0,0060	0,7787800	2615,00	11,00	2614,00	26,00	2608,0	14,0	2608,0	14,0	0,230	
BIB-1_82.FIN2	536,0	1,530	0,4284	0,00660	0,05763	0,0007	0,4743600	361,70	4,70	361,10	4,00	358,0	31,0	361,1	4,0	0,166	
BIB-1_83.FIN2	67,4	1,626	0,9390	0,02200	0,10820	0,0014	0,1747600	670,00	12,00	662,30	7,90	682,0	53,0	662,3	7,9	1,149	
BIB-1_84.FIN2	294,8	3,690	0,7590	0,01700	0,09220	0,0016	0,7787600	571,80	9,90	568,50	9,40	579,0	30,0	568,5	9,4	0,577	
BIB-1_85.FIN2	1483,0	1,651	0,9040	0,01800	0,10490	0,0022	0,5639400	653,60	9,70	643,00	13,00	698,0	26,0	643,0	13,0	1,622	
BIB-1_86.FIN2	80,7	2,192	0,7540	0,01900	0,09190	0,0012	0,2720800	568,00	11,00	566,80	7,20	554,0	55,0	566,8	7,2	0,211	
BIB-1_87.FIN2	306,0	1,866	0,5853	0,00940	0,07462	0,0007	0,1799300	467,20	6,00	463,90	4,20	473,0	40,0	463,9	4,2	0,706	
BIB-1_88.FIN2	365,0	4,680	0,7380	0,01500	0,08990	0,0012	0,6436200	559,90	8,60	554,80	7,20	567,0	34,0	554,8	7,2	0,911	
BIB-1_90.FIN2	63,3	0,433	0,8270	0,02200	0,09510	0,0013	0,2368400	611,00	12,00	585,40	7,50	688,0	58,0	585,4	7,5	4,190	
BIB-1_91.FIN2	207,0	0,363	1,5980	0,02500	0,15870	0,0016	0,4989800	968,00	10,00	949,50	8,90	1012,0	28,0	1012,0	28,0	6,176	
BIB-1_92.FIN2	274,0	3,243	1,7650	0,02300	0,17570	0,0019	0,6584800	1031,30	8,60	1043,00	10,00	1022,0	21,0	1022,0	21,0	2,055	
BIB-1_93.FIN2	524,0	7,450	0,5727	0,00930	0,07301	0,0009	0,6695400	459,30	6,00	454,20	5,10	487,0	31,0	454,2	5,1	1,110	
BIB-1_95.FIN2	854,0	0,744	0,9022	0,00820	0,10759	0,0008	0,5488900	653,10	4,50	658,70	4,50	645,0	18,0	658,7	4,5	0,857	
BIB-1_96.FIN2	184,9	0,998	0,8160	0,01700	0,09820	0,0010	0,2417000	604,60	9,40	603,60	5,90	607,0	45,0	603,6	5,9	0,165	
BIB-1_97.FIN2	126,5	1,014	0,6620	0,01400	0,08049	0,0008	0,0868610	515,40	8,10	499,00	4,80	582,0	50,0	499,0	4,8	3,182	
BIB-1_98.FIN2	682,0	0,600	1,6010	0,01700	0,15990	0,0015	0,5809600	969,70	6,70	956,00	8,40	1012,0	19,0	1012,0	19,0	5,534	
BIB-1_100.FIN2	1234,0	1,452	0,4089	0,00430	0,05527	0,0004	0,5369500	348,30	3,20	346,80	2,60	364,0	21,0	346,8	2,6	0,431	
BIB-1_101.FIN2	176,0	1,070	1,0120	0,01500	0,11700	0,0013	0,4944600	708,80	7,60	713,30	7,20	698,0	32,0	713,3	7,2	0,635	
BIB-1_102.FIN2	515,0	2,880	6,4900	0,13000	0,36580	0,0073	0,8675600	2044,00	18,00	2007,00	35,00	2079,0	18,0	2079,0	18,0	3,463	
BIB-1_103.FIN2	259,0	2,820	0,5540	0,01000	0,07153	0,0007	0,3524400	447,00	6,60	445,30	4,40	437,0	39,0	445,3	4,4	0,380	
BIB-1_104.FIN2	195,0	3,669	0,6400	0,01500	0,02316	0,0004	0,2680100	500,80	9,30	147,60	2,50	2788,0	42,0	DISC	DISC	70,527	
BIB-1_105.FIN2	290,0	2,010	0,3557	0,00670	0,04867	0,0004	0,0971590	308,50	5,00	306,30	2,70	305,0	44,0	306,3	2,7	0,713	
BIB-1_106.FIN2	715,0	2,023	0,3563	0,00480	0,04849	0,0004	0,4119900	309,20	3,60	305,20	2,50	322,0	28,0	305,2	2,5	1,294	
BIB-1_107.FIN2	188,9	0,996	0,4260	0,01200	0,05680	0,0014	0,4593200	359,20	8,40	355,60	8,20	374,0	60,0	355,6	8,2	1,002	
BIB-1_108.FIN2	397,0	1,990	0,3780	0,00730	0,04994	0,0007	0,4852000	325,00	5,40	314,60	4,10	389,0	40,0	314,6	4,1	3,200	
BIB-1_109.FIN2	347,0	1,476	0,7640	0,01500	0,09370	0,0010	0,5014300	574,70	8,60	577,10	5,90	560,0	37,0	577,1	5,9	0,418	
BIB-1_110.FIN2	656,0	4,120	0,7650	0,02400	0,08550	0,0023	0,5695800	576,00	14,00	529,00	14,00	787,0	56,0	529,0	14,0	8,160	Rim
BIB-1_110.FIN2	85,5	0,899	5,0600	0,11000	0,31670	0,0048	0,6458900	1827,00	18,00	1773,00	24,00	1884,0	29,0	1884,0	29,0	5,892	Core
BIB-1_111.FIN2	92,3	2,351	2,6290	0,03600	0,22790	0,0018	0,2263400	1308,00	10,00	1323,40	9,50	1276,0	28,0	1276,0	28,0	3,715	
BIB-1_112.FIN2	556,0	1,204	1,6140	0,01400	0,16060	0,0013	0,4771700	974,90	5,60	960,10	7,10	1013,0	18,0	1013,0	18,0	5,222	
BIB-1_113.FIN2	1159,0	1,594	0,4010	0,00450	0,05453	0,0005	0,5568200	342,10	3,30	342,30	3,00	350,0	21,0	342,3	3,0	0,058	
BIB-1_114.FIN2	92,2	0,318	5,2770	0,08800	0,32960	0,0041	0,6810100	1864,00	15,00	1836,00	20,00	1901,0	23,0	1901,0	23,0	3,419	

Sample Name:	[U]							207/235		206/238		207/206		Best age		Discordance	Rim/
Grain #	ppm	U/Th	207/235	2σ error	206/238	2σ error	RHO	Age Ma	2σ error	Age (Ma)	2σ error	Age (Ma)	2σ error	(Ma)	2σ error	%	Core
BIB-1_115.FIN2	961,0	1,572	0,3945	0,00500	0,05332	0,0005	0,5228900	337,40	3,60	334,80	3,20	355,0	27,0	334,8	3,2	0,771	
BIB-1_116.FIN2	287,0	1,740	0,7970	0,01400	0,09440	0,0012	0,3050300	594,20	7,60	581,30	6,90	656,0	39,0	581,3	6,9	2,171	
BIB-1_117.FIN2	2591,0	9,850	0,3770	0,00440	0,05057	0,0006	0,5945600	324,60	3,20	318,00	3,80	391,0	25,0	318,0	3,8	2,033	
BIB-1_118.FIN2	619,0	2,527	0,3680	0,00650	0,04989	0,0005	0,3322300	317,70	4,80	313,80	3,30	349,0	38,0	313,8	3,3	1,228	
BIB-1_119.FIN2	1200,0	10,400	0,3790	0,00620	0,05223	0,0008	0,6749600	326,50	4,70	328,10	5,00	326,0	25,0	328,1	5,0	0,490	
BIB-1_120.FIN2	659,0	1,014	0,8830	0,02700	0,09700	0,0015	0,6098000	639,00	14,00	596,70	8,80	811,0	40,0	596,7	8,8	6,620	
BIB-1_121.FIN2	112,0	1,230	0,9270	0,02400	0,10640	0,0014	0,3927800	665,00	12,00	651,60	8,20	704,0	51,0	651,6	8,2	2,015	
BIB-1_122.FIN2	616,0	1,640	1,4080	0,02400	0,14310	0,0025	0,7116800	892,00	10,00	862,00	14,00	962,0	25,0	962,0	25,0	10,395	
BIB-1_124.FIN2	295,5	1,180	2,2180	0,05300	0,19110	0,0044	0,4143100	1187,00	16,00	1126,00	24,00	1285,0	50,0	1285,0	50,0	12,374	
BIB-1_125.FIN2	2020,0	49,700	0,3930	0,01000	0,05460	0,0015	0,3532300	336,60	7,30	342,50	9,30	313,0	70,0	342,5	9,3	1,753	Rim
BIB-1_125.FIN2	959,0	2,302	0,6050	0,00740	0,07615	0,0008	0,5112600	480,10	4,70	473,00	4,90	495,0	26,0	473,0	4,9	1,479	Core
BIB-1_126.FIN2	794,0	3,228	0,3808	0,00590	0,05147	0,0005	0,4771200	327,30	4,30	323,50	3,10	332,0	31,0	323,5	3,1	1,161	
BIB-1_127.FIN2	344,0	1,705	0,3757	0,00670	0,05062	0,0006	0,1713000	323,40	4,90	318,30	3,70	343,0	39,0	318,3	3,7	1,577	
BIB-1_128.FIN2	94,9	0,573	1,6840	0,02800	0,16990	0,0016	0,1182400	1001,00	11,00	1011,50	8,90	956,0	33,0	956,0	33,0	5,805	
BIB-1_129.FIN2	138,4	1,534	1,7630	0,02600	0,17430	0,0016	0,4242800	1031,50	9,70	1035,40	8,80	1007,0	30,0	1007,0	30,0	2,820	
BIB-1_130.FIN2	316,0	1,920	1,8320	0,02800	0,17330	0,0018	0,5543300	1055,30	9,70	1029,70	9,80	1097,0	24,0	1097,0	24,0	6,135	
BIB-1_131.FIN2	317,0	1,349	0,6110	0,06500	0,06510	0,0054	0,0626400	482,00	40,00	406,00	32,00	870,0	150,0	DISC	DISC	15,768	Rim
BIB-1_131.FIN2	40,5	0,787	0,9180	0,03700	0,10890	0,0018	0,1486500	658,00	19,00	666,00	11,00	573,0	86,0	666,0	11,0	1,216	Core
BIB-1_132.FIN2	159,8	1,952	2,8710	0,03700	0,23940	0,0033	0,5908900	1374,00	10,00	1383,00	17,00	1364,0	25,0	1364,0	25,0	1,393	
BIB-1_133.FIN2	405,0	1,855	0,3512	0,00640	0,04738	0,0005	0,2910100	305,20	4,80	298,40	3,10	353,0	40,0	298,4	3,1	2,228	
BIB-1_134.FIN2	237,0	1,680	1,0130	0,01600	0,11690	0,0012	0,4733400	710,20	8,10	712,30	6,90	708,0	31,0	712,3	6,9	0,296	
BIB-1_135.FIN2	687,0	2,830	0,4290	0,01100	0,05163	0,0005	0,5619900	361,40	8,00	324,50	3,10	592,0	47,0	324,5	3,1	10,210	
BIB-1_136.FIN2	203,8	1,780	0,4355	0,00910	0,05890	0,0007	0,1276100	366,30	6,50	368,90	3,90	358,0	45,0	368,9	3,9	0,710	
BIB-1_137.FIN2	2010,0	45,000	0,3652	0,00720	0,05051	0,0009	0,7440000	315,80	5,30	317,60	5,60	320,0	31,0	317,6	5,6	0,570	
BIB-5_1.FIN2	574,0	1,070	0,8210	0,01200	0,10070	0,0012	0,7115100	608,90	7,10	618,50	7,30	577,0	27,0	618,5	7,3	1,577	
BIB-5_2.FIN2	239,0	0,783	6,6470	0,06700	0,38110	0,0039	0,6945500	2065,20	9,20	2080,00	18,00	2056,0	14,0	2056,0	14,0	1,167	
BIB-5_3.FIN2	517,0	5,100	0,9640	0,02500	0,11200	0,0027	0,6530000	684,00	13,00	684,00	16,00	692,0	45,0	684,0	16,0	0,000	
BIB-5_4.FIN2	154,9	1,039	1,9180	0,02800	0,18330	0,0021	0,4551100	1087,00	10,00	1085,00	11,00	1099,0	27,0	1099,0	27,0	1,274	
BIB-5_5.FIN2	355,0	1,658	0,5354	0,00930	0,06847	0,0009	0,5006400	434,70	6,10	426,80	5,50	481,0	35,0	426,8	5,5	1,817	
BIB-5_6.FIN2	2070,0	13,600	0,7340	0,03400	0,08140	0,0045	0,9070500	557,00	19,00	504,00	27,00	801,0	49,0	504,0	27,0	9,515	Rim
BIB-5_6.FIN2	195,0	1,626	1,3490	0,02700	0,13560	0,0019	0,5543500	865,00	11,00	820,00	11,00	995,0	35,0	820,0	11,0	5,202	Core
BIB-5_7.FIN2	339,0	0,590	0,8420	0,01100	0,09790	0,0011	0,4276300	619,40	6,10	602,20	6,40	686,0	29,0	602,2	6,4	2,777	
BIB-5_8.FIN2	1070,0	2,533	1,6510	0,01400	0,16540	0,0015	0,8410800	989,30	5,50	986,50	8,10	1002,0	13,0	1002,0	13,0	1,547	
BIB-5_9.FIN2	358,0	1,130	11,0200	0,15000	0,44290	0,0051	0,7804300	2523,00	13,00	2362,00	23,00	2657,0	14,0	2657,0	14,0	11,103	
BIB-5_10.FIN2	957,0	14,860	0,9080	0,01100	0,10720	0,0013	0,5958100	655,90	5,80	656,10	7,30	652,0	23,0	656,1	7,3	0,030	
BIB-5_11.FIN2	1060,0	8,500	5,1320	0,06400	0,32630	0,0043	0,9114000	1841,00	10,00	1819,00	21,00	1864,0	11,0	1864,0	11,0	2,414	
BIB-5_12.FIN2	445,0	5,640	0,5886	0,00880	0,07515	0,0008	0,5137700	469,40	5,60	467,10	4,60	479,0	31,0	467,1	4,6	0,490	
BIB-5_13.FIN2	463,0	5,450	0,6080	0,01000	0,07614	0,0009	0,6811600	481,70	6,40	472,90	5,60	523,0	32,0	472,9	5,6	1,827	
BIB-5_14.FIN2	334,0	1,830	8,3700	0,19000	0,35340	0,0073	0,9387400	2264,00	21,00	1947,00	35,00	2574,0	13,0	2574,0	13,0	24,359	
BIB-5_15.FIN2	314,5	0,866	12,3100	0,31000	0,48400	0,0110	0,9700600	2625,00	24,00	2545,00	47,00	2692,0	12,0	2692,0	12,0	5,461	
BIB-5_16.FIN2	55,0	0,545	1,7000	0,05300	0,16530	0,0023	0,3355200	1005,00	20,00	986,00	13,00	1040,0	59,0	1040,0	59,0	5,192	
BIB-5_17.FIN2	116,4	1,604	11,9600	0,28000	0,47600	0,0100	0,9241900	2591,00	23,00	2505,00	46,00	2671,0	15,0	2671,0	15,0	6,215	
BIB-5_18.FIN2	61,6	0,699	0,9700	0,03300	0,11100	0,0014	0,1103300	683,00	17,00	678,30	8,30	668,0	71,0	678,3	8,3	0,688	
BIB-5_19.FIN2	661,0	2,169	0,9550	0,01600	0,10480	0,0017	0,8254700	679,70	8,30	642,00	9,00	809,0	20,0	642,0	9,0	5,547	
BIB-5_20.FIN2	91,0	1,200	15,6000	0,43000	0,57100	0,0140	0,8752800	2848,00	27,00	2903,00	55,00	2817,0	30,0	2817,0	30,0	3,053	
BIB-5_21.FIN2	424,0	1,221	13,3900	0,34000	0,48100	0,0120	0,9604500	2700,00	28,00	2535,00	51,00	2840,0	13,0	2840,0	13,0	10,739	

Sample Name:	[U]							207/235		206/238		207/206		Best age		Discordance	Rim/
Grain #	ppm	U/Th	207/235	2σ error	206/238	2σ error	RHO	Age Ma	2σ error	Age (Ma)	2σ error	Age (Ma)	2σ error	(Ma)	2σ error	%	Core
BIB-5_22.FIN2	106,0	1,375	0,8720	0,02800	0,10290	0,0014	0,1749700	633,00	15,00	631,30	8,30	625,0	63,0	631,3	8,3	0,269	
BIB-5_23.FIN2	900,0	1,365	0,8440	0,01300	0,09630	0,0014	0,7092800	620,70	7,10	592,50	8,20	732,0	23,0	592,5	8,2	4,543	
BIB-5_24.FIN2	1171,0	1,560	1,1290	0,01900	0,12090	0,0015	0,6242600	766,60	8,90	735,80	8,90	861,0	27,0	735,8	8,9	4,018	
BIB-5_25.FIN2	166,0	1,123	0,7930	0,02300	0,09210	0,0014	0,2913600	591,00	13,00	567,70	8,60	674,0	60,0	567,7	8,6	3,942	
BIB-5_26.FIN2	134,4	1,682	3,7220	0,08400	0,22860	0,0042	0,8256900	1571,00	18,00	1326,00	22,00	1930,0	26,0	DISC	DISC	31,295	
BIB-5_27.FIN2	258,1	2,490	1,5130	0,02500	0,15580	0,0017	0,4506300	931,50	8,50	934,40	9,20	931,0	26,0	931,0	26,0	0,365	
BIB-5_28.FIN2	797,0	1,568	0,5449	0,00700	0,07033	0,0006	0,4316000	441,30	4,60	438,10	3,60	455,0	27,0	438,1	3,6	0,725	
BIB-5_29.FIN2	469,0	1,331	4,4560	0,05600	0,29960	0,0031	0,6866300	1723,00	11,00	1689,00	15,00	1765,0	18,0	1765,0	18,0	4,306	
BIB-5_30.FIN2	162,2	1,094	1,8910	0,03700	0,17910	0,0016	0,4348600	1075,00	13,00	1061,70	8,60	1105,0	35,0	1105,0	35,0	3,919	
BIB-5_31.FIN2	989,0	1,312	1,0930	0,01400	0,12010	0,0011	0,5920900	749,40	6,60	730,70	6,50	804,0	20,0	730,7	6,5	2,495	
BIB-5_32.FIN2	1940,0	2,050	0,5570	0,03400	0,05130	0,0035	0,9371100	448,00	21,00	322,00	21,00	1175,0	53,0	DISC	DISC	28,125	Rim
BIB-5_32.FIN2	557,0	4,850	1,1170	0,03500	0,11710	0,0031	0,8351600	761,00	17,00	714,00	18,00	897,0	48,0	714,0	18,0	6,176	Core
BIB-5_32.FIN2	259,0	5,150	1,5710	0,02500	0,15870	0,0018	0,4579900	958,00	9,90	949,00	10,00	983,0	29,0	983,0	29,0	3,459	Core
BIB-5_33.FIN2	761,0	82,000	0,8150	0,02200	0,09400	0,0021	0,6339000	606,00	13,00	579,00	13,00	717,0	44,0	579,0	13,0	4,455	Rim
BIB-5_33.FIN2	305,0	1,401	3,8700	0,04700	0,27640	0,0033	0,5741100	1606,60	9,80	1573,00	16,00	1652,0	21,0	1652,0	21,0	4,782	Core
BIB-5_34.FIN2	422,0	1,174	0,7170	0,01100	0,08570	0,0011	0,3609200	547,90	6,30	530,00	6,60	620,0	34,0	530,0	6,6	3,267	
BIB-5_35.FIN2	1143,0	12,000	0,7810	0,03100	0,09370	0,0026	0,8489600	585,00	18,00	577,00	15,00	635,0	43,0	577,0	15,0	1,368	Rim
BIB-5_35.FIN2	925,0	0,898	1,6100	0,01800	0,16170	0,0017	0,6210800	973,40	7,10	965,90	9,20	994,0	18,0	994,0	18,0	2,827	Core
BIB-5_36.FIN2	814,0	1,348	0,8220	0,01300	0,08970	0,0012	0,6350900	608,20	7,10	553,60	7,10	817,0	25,0	553,6	7,1	8,977	
BIB-5_37.FIN2	173,4	1,086	0,7740	0,01500	0,09160	0,0011	0,2743700	580,40	8,90	565,10	6,40	630,0	44,0	565,1	6,4	2,636	
BIB-5_38.FIN2	386,0	2,108	0,8360	0,01300	0,10086	0,0010	0,5977500	615,90	7,30	619,30	5,70	601,0	28,0	619,3	5,7	0,552	
BIB-5_39.FIN2	957,0	1,109	0,3054	0,00740	0,04160	0,0010	0,4763100	270,40	5,70	262,80	6,50	313,0	59,0	262,8	6,5	2,811	
BIB-5_40.FIN2	139,6	1,855	7,3540	0,09500	0,39340	0,0040	0,8583100	2153,00	12,00	2138,00	19,00	2167,0	16,0	2167,0	16,0	1,338	
BIB-5_41.FIN2	537,0	1,110	10,0000	0,16000	0,45210	0,0067	0,9148000	2431,00	15,00	2402,00	30,00	2457,0	12,0	2457,0	12,0	2,239	
BIB-5_42.FIN2	269,0	0,187	0,7720	0,05300	0,08540	0,0051	0,7771100	580,00	30,00	528,00	30,00	793,0	85,0	528,0	30,0	8,966	Rim
BIB-5_42.FIN2	143,9	0,423	1,0510	0,02000	0,11690	0,0015	0,3313600	728,00	10,00	712,20	8,60	781,0	41,0	712,2	8,6	2,170	Core
BIB-5_43.FIN2	644,0	1,091	1,6180	0,01900	0,14800	0,0016	0,6124700	977,00	7,50	889,30	8,90	1181,0	20,0	1181,0	20,0	24,699	
BIB-5_44.FIN2	411,4	2,780	1,1370	0,01800	0,12400	0,0018	0,5247500	770,20	8,50	753,00	10,00	816,0	32,0	753,0	10,0	2,233	
BIB-5_45.FIN2	596,0	1,178	0,7810	0,01100	0,09313	0,0009	0,4929800	585,40	6,00	573,90	5,50	635,0	26,0	573,9	5,5	1,964	
BIB-5_46.FIN2	314,7	0,926	1,5220	0,02900	0,15490	0,0021	0,7313400	937,00	12,00	928,00	11,00	961,0	26,0	961,0	26,0	3,434	
BIB-5_47.FIN2	124,4	1,042	1,6350	0,02800	0,16480	0,0016	0,1908300	982,00	11,00	983,40	9,00	974,0	31,0	974,0	31,0	0,965	
BIB-5_48.FIN2	865,0	7,300	0,6240	0,01700	0,07700	0,0019	0,7030600	491,00	11,00	478,00	11,00	575,0	47,0	478,0	11,0	2,648	
BIB-5_49.FIN2	64,6	0,632	0,8230	0,02300	0,09960	0,0018	0,1882900	607,00	13,00	612,00	10,00	585,0	64,0	612,0	10,0	0,824	
BIB-5_50.FIN2	730,0	1,297	1,6920	0,02100	0,16400	0,0017	0,5309900	1004,60	7,90	978,60	9,50	1065,0	22,0	1065,0	22,0	8,113	
BIB-5_51.FIN2	663,0	36,100	0,4550	0,01400	0,05960	0,0017	0,3213600	380,10	9,80	373,00	10,00	432,0	67,0	373,0	10,0	1,868	Rim
BIB-5_51.FIN2	369,8	4,410	0,5850	0,01000	0,07372	0,0010	0,3185100	468,40	6,30	458,40	5,80	515,0	39,0	458,4	5,8	2,135	Core
BIB-5_52.FIN2	516,0	1,237	0,6600	0,02100	0,06940	0,0015	0,6274400	514,00	13,00	432,50	9,00	884,0	54,0	DISC	DISC	15,856	Rim
BIB-5_52.FIN2	119,5	0,995	0,8890	0,02600	0,10500	0,0017	0,3011900	644,00	14,00	643,00	10,00	638,0	63,0	643,0	10,0	0,155	Core
BIB-5_53.FIN2	182,0	0,470	0,8320	0,01500	0,10090	0,0012	0,2112400	614,60	8,00	619,50	6,80	599,0	41,0	619,5	6,8	0,797	
BIB-5_54.FIN2	389,0	2,400	0,3730	0,00770	0,05109	0,0008	0,2391600	321,30	5,60	321,80	4,50	324,0	48,0	321,8	4,5	0,156	
BIB-5_55.FIN2	665,0	1,693	0,9820	0,01500	0,10490	0,0016	0,6544800	693,50	7,50	643,10	9,30	868,0	24,0	643,1	9,3	7,267	
BIB-5_56.FIN2	654,0	1,537	0,5799	0,00790	0,07339	0,0007	0,3021400	463,90	5,00	456,50	4,40	495,0	32,0	456,5	4,4	1,595	
BIB-5_57.FIN2	821,0	3,570	0,9440	0,01100	0,10630	0,0011	0,5999000	674,50	5,70	651,40	6,60	755,0	20,0	651,4	6,6	3,425	
BIB-5_58.FIN2	2560,0	3,566	0,3323	0,00610	0,03233	0,0006	0,5279800	291,10	4,70	205,10	3,80	1062,0	34,0	DISC	DISC	29,543	
BIB-5_59.FIN2	93,2	0,720	1,6420	0,03400	0,16110	0,0022	0,4277700	983,00	13,00	963,00	12,00	1040,0	40,0	1040,0	40,0	7,404	
BIB-5_60.FIN2	167,0	0,654	1,0670	0,02700	0,11980	0,0021	0,3230800	734,00	13,00	729,00	12,00	755,0	41,0	729,0	12,0	0,681	
BIB-5_61.FIN2	525,0	1,574	0,3669	0,00830	0,04774	0,0006	0,4551700	316,80	6,20	300,60	3,90	435,0	45,0	300,6	3,9	5,114	

Sample Name:	[U]							207/235		206/238		207/206		Best age		Discordance	Rim/
Grain #	ppm	U/Th	207/235	2σ error	206/238	2σ error	RHO	Age Ma	2σ error	Age (Ma)	2σ error	Age (Ma)	2σ error	(Ma)	2σ error	%	Core
BIB-5_62.FIN2	72,8	0,490	1,6670	0,04500	0,15050	0,0021	0,3229200	990,00	17,00	904,00	12,00	1199,0	52,0	1199,0	52,0	24,604	
BIB-5_63.FIN2	271,0	0,459	0,8030	0,01400	0,09577	0,0009	0,0098740	597,50	8,00	589,50	5,30	627,0	43,0	589,5	5,3	1,339	
BIB-5_64.FIN2	588,0	4,740	0,5969	0,00850	0,07529	0,0008	0,5551400	474,70	5,40	467,90	4,70	510,0	30,0	467,9	4,7	1,432	
BIB-5_65.FIN2	372,0	1,830	1,5230	0,03600	0,15310	0,0021	0,4985200	936,00	14,00	919,00	11,00	982,0	33,0	982,0	33,0	6,415	
BIB-5_66.FIN2	472,0	2,483	1,0710	0,02300	0,10750	0,0017	0,6599500	738,00	11,00	658,20	9,70	991,0	33,0	658,2	9,7	10,813	
BIB-5_67.FIN2	490,0	12,300	0,3600	0,02000	0,04950	0,0017	0,3729400	312,00	15,00	311,00	10,00	320,0	120,0	311,0	10,0	0,321	Rim
BIB-5_67.FIN2	440,0	9,070	0,5610	0,01000	0,07241	0,0009	0,4041300	451,80	6,50	450,60	5,30	460,0	39,0	450,6	5,3	0,266	Core
BIB-5_68.FIN2	65,6	1,292	1,5020	0,03200	0,15630	0,0021	0,3015000	928,00	13,00	936,00	12,00	923,0	45,0	923,0	45,0	1,408	
BIB-5_69.FIN2	428,0	1,590	12,7500	0,11000	0,49960	0,0042	0,7661500	2661,40	7,80	2613,00	17,00	2704,7	9,7	2704,7	9,7	3,390	
BIB-5_70.FIN2	346,2	1,197	6,0200	0,11000	0,34810	0,0055	0,9125300	1974,00	16,00	1924,00	26,00	2025,0	15,0	2025,0	15,0	4,988	
BIB-5_71.FIN2	1201,0	2,701	0,3729	0,00610	0,04781	0,0004	0,3763800	321,50	4,50	301,10	2,40	477,0	35,0	301,1	2,4	6,345	
BIB-5_72.FIN2	255,0	2,110	0,5660	0,01300	0,07165	0,0009	0,4274100	453,90	8,10	446,80	5,40	486,0	46,0	446,8	5,4	1,564	
BIB-5_73.FIN2	348,0	2,830	6,4200	0,17000	0,35530	0,0059	0,9130500	2025,00	23,00	1958,00	28,00	2101,0	23,0	2101,0	23,0	6,806	
BIB-5_74.FIN2	845,0	1,834	0,3611	0,00530	0,04842	0,0005	0,5012800	312,80	4,00	304,80	3,00	379,0	28,0	304,8	3,0	2,558	
BIB-5_75.FIN2	792,0	0,625	0,4086	0,00770	0,05113	0,0006	0,0461060	348,20	5,80	321,40	3,70	540,0	52,0	321,4	3,7	7,697	
BIB-5_76.FIN2	104,7	0,633	0,7860	0,02300	0,08460	0,0014	0,3264600	586,00	13,00	523,40	8,60	831,0	64,0	523,4	8,6	10,683	
BIB-5_77.FIN2	783,0	7,440	0,8760	0,01400	0,10270	0,0013	0,7446700	637,50	7,60	630,10	7,80	675,0	23,0	630,1	7,8	1,161	
BIB-5_78.FIN2	299,0	1,194	1,1960	0,01900	0,12800	0,0014	0,6192600	797,30	8,80	776,20	8,20	861,0	29,0	776,2	8,2	2,646	
BIB-5_79.FIN2	549,0	1,612	0,3589	0,00620	0,04941	0,0005	0,2980600	311,00	4,60	310,80	3,20	308,0	39,0	310,8	3,2	0,064	
BIB-5_80.FIN2	263,0	1,062	0,8520	0,01600	0,10220	0,0011	0,5076900	624,40	9,00	627,00	6,60	612,0	37,0	627,0	6,6	0,416	
BIB-5_81.FIN2	319,0	3,030	0,6170	0,01200	0,07820	0,0011	0,5006300	487,50	8,00	485,30	6,80	494,0	40,0	485,3	6,8	0,451	
BIB-5_82.FIN2	456,1	47,900	0,6710	0,01700	0,08280	0,0017	0,3633100	521,00	10,00	512,70	9,90	560,0	58,0	512,7	9,9	1,593	Rim
BIB-5_82.FIN2	168,7	1,400	0,8710	0,02100	0,10460	0,0013	0,3828500	635,00	11,00	641,40	7,30	607,0	48,0	641,4	7,3	1,008	Core
BIB-5_83.FIN2	443,0	0,982	11,8300	0,11000	0,46050	0,0045	0,8985800	2589,50	8,80	2441,00	20,00	2710,0	11,0	2710,0	11,0	9,926	
BIB-5_84.FIN2	137,0	1,335	14,5500	0,18000	0,54630	0,0059	0,8480700	2786,00	12,00	2808,00	25,00	2776,0	13,0	2776,0	13,0	1,153	
BIB-5_85.FIN2	369,3	1,201	1,1670	0,01700	0,12900	0,0013	0,4387400	784,10	7,80	782,00	7,70	788,0	28,0	782,0	7,7	0,268	
BIB-5_86.FIN2	137,8	1,027	13,2800	0,16000	0,51590	0,0058	0,7065700	2698,00	12,00	2680,00	25,00	2713,0	14,0	2713,0	14,0	1,216	
BIB-5_87.FIN2	599,0	1,679	0,8190	0,01600	0,09690	0,0015	0,3810400	606,50	9,20	596,20	8,90	644,0	37,0	596,2	8,9	1,698	
BIB-5_88.FIN2	430,0	2,085	0,9010	0,01600	0,10760	0,0011	0,5954600	651,00	8,30	658,80	6,70	630,0	29,0	658,8	6,7	1,198	
BIB-5_89.FIN2	4550,0	12,640	0,7310	0,02100	0,08520	0,0019	0,7572800	556,00	12,00	527,00	11,00	679,0	38,0	527,0	11,0	5,216	Rim
BIB-5_89.FIN2	2121,0	2,240	1,0990	0,01400	0,11510	0,0014	0,6758600	752,30	6,70	702,00	8,30	908,0	21,0	702,0	8,3	6,686	Core
BIB-5_90.FIN2	393,9	0,609	0,5335	0,00950	0,06715	0,0008	0,4570200	433,40	6,30	418,90	5,00	504,0	38,0	418,9	5,0	3,346	
BIB-5_91.FIN2	275,1	2,136	2,5550	0,02900	0,21600	0,0021	0,5554400	1287,70	8,50	1260,00	11,00	1329,0	21,0	1329,0	21,0	5,192	
BIB-5_92.FIN2	409,0	1,220	1,0400	0,01500	0,11300	0,0012	0,4370300	723,70	7,30	690,00	6,90	828,0	28,0	690,0	6,9	4,657	
BIB-5_93.FIN2	143,2	0,458	0,8000	0,02000	0,09440	0,0016	0,5038400	595,00	11,00	581,20	9,70	625,0	52,0	581,2	9,7	2,319	
BIB-5_94.FIN2	371,0	2,080	0,8330	0,01500	0,10060	0,0014	0,4960300	614,10	8,10	617,90	8,10	593,0	38,0	617,9	8,1	0,619	
BIB-5_95.FIN2	717,0	4,330	0,5764	0,00780	0,07265	0,0007	0,4923000	461,80	5,00	452,10	3,90	508,0	25,0	452,1	3,9	2,100	
BIB-5_96.FIN2	348,0	0,934	0,7780	0,01300	0,09450	0,0013	0,5702900	584,00	7,50	582,00	7,60	586,0	31,0	582,0	7,6	0,342	
BIB-5_97.FIN2	169,2	1,023	0,7580	0,01500	0,09160	0,0011	0,3376200	571,70	8,60	564,90	6,50	586,0	42,0	564,9	6,5	1,189	
BIB-5_98.FIN2	332,0	0,410	1,0260	0,02800	0,11210	0,0017	0,5621500	720,00	15,00	684,70	9,90	812,0	49,0	684,7	9,9	4,903	
BIB-5_99.FIN2	402,0	6,730	0,9340	0,01300	0,10816	0,0009	0,4080500	668,80	6,80	662,00	5,50	684,0	28,0	662,0	5,5	1,017	
BIB-5_100.FIN2	114,3	1,244	0,9100	0,02000	0,10580	0,0012	0,2115700	656,00	11,00	648,30	7,00	675,0	47,0	648,3	7,0	1,174	
BIB-5_101.FIN2	642,0	1,723	0,3682	0,00630	0,05039	0,0006	0,5136600	317,90	4,60	316,90	3,70	315,0	33,0	316,9	3,7	0,315	
BIB-5_102.FIN2	598,0	1,688	0,7920	0,01500	0,09270	0,0014	0,5971500	591,20	8,60	571,60	8,60	674,0	30,0	571,6	8,6	3,315	
BIB-5_103.FIN2	122,5	2,421	1,9830	0,03100	0,18530	0,0018	0,3683500	1108,00	11,00	1095,50	9,60	1132,0	31,0	1132,0	31,0	3,224	
BIB-5_104.FIN2	169,5	0,960	4,2800	0,16000	0,26860	0,0084	0,9385600	1675,00	31,00	1528,00	43,00	1875,0	25,0	1875,0	25,0	18,507	
BIB-5_105.FIN2	496,0	2,760	6,7640	0,08000	0,37130	0,0039	0,7775400	2080,00	10,00	2037,00	19,00	2116,0	13,0	2116,0	13,0	3,733	

Sample Name:	[U]							207/235		206/238		207/206		Best age		Discordance	Rim/
Grain #	ppm	U/Th	207/235	2σ error	206/238	2σ error	RHO	Age Ma	2σ error	Age (Ma)	2σ error	Age (Ma)	2σ error	(Ma)	2σ error	%	Core
BIB-5_106.FIN2	134,9	1,356	13,4300	0,31000	0,49100	0,0092	0,8646400	2711,00	21,00	2573,00	40,00	2818,0	18,0	2818,0	18,0	8,694	
BIB-5_107.FIN2	655,0	1,814	0,3442	0,00720	0,04632	0,0007	0,4948400	299,90	5,40	291,90	4,10	350,0	42,0	291,9	4,1	2,668	
BIB-5_108.FIN2	407,0	0,683	0,7950	0,01400	0,09280	0,0012	0,4050400	593,10	7,80	571,70	6,90	670,0	36,0	571,7	6,9	3,608	
BIB-5_109.FIN2	271,0	1,882	0,7660	0,01200	0,09212	0,0009	0,2575400	576,60	6,90	568,00	5,10	597,0	34,0	568,0	5,1	1,492	
BIB-5_110.FIN2	331,7	0,942	0,6940	0,01600	0,07650	0,0012	0,3532200	536,00	10,00	474,90	6,90	796,0	46,0	474,9	6,9	11,399	
BIB-5_111.FIN2	1650,0	14,700	0,9400	0,07300	0,10690	0,0073	0,9251500	670,00	39,00	654,00	43,00	729,0	61,0	654,0	43,0	2,388	Rim
BIB-5_111.FIN2	193,6	1,420	2,1230	0,03200	0,19260	0,0020	0,3283100	1155,00	10,00	1135,00	11,00	1178,0	28,0	1178,0	28,0	3,650	Core
BIB-5_112.FIN2	541,0	4,210	0,5630	0,01100	0,06490	0,0011	0,4158400	452,20	7,00	405,30	6,70	709,0	42,0	405,3	6,7	10,372	
BIB-5_113.FIN2	1265,0	3,570	0,7133	0,00910	0,08290	0,0010	0,6722300	546,10	5,40	513,00	6,20	686,0	21,0	513,0	6,2	6,061	
BIB-5_114.FIN2	498,0	0,460	0,8890	0,01100	0,10210	0,0010	0,5524500	645,00	5,70	626,60	6,00	708,0	22,0	626,6	6,0	2,853	
BIB-5_115.FIN2	1160,0	3,480	0,6060	0,02100	0,06050	0,0025	0,3615400	480,00	13,00	379,00	15,00	999,0	70,0	DISC	DISC	21,042	Rim
BIB-5_115.FIN2	337,0	1,884	0,7770	0,01600	0,09130	0,0010	0,7134300	582,90	9,30	563,10	5,90	650,0	42,0	563,1	5,9	3,397	Core
BIB-5_116.FIN2	653,0	3,700	0,5660	0,01500	0,06530	0,0017	0,4270300	454,80	9,40	408,00	10,00	691,0	59,0	408,0	10,0	10,290	
BIB-5_118.FIN2	843,0	1,198	1,4030	0,03200	0,12000	0,0035	0,8842700	887,00	13,00	730,00	20,00	1300,0	26,0	DISC	DISC	17,700	
BIB-5_119.FIN2	1400,0	2,635	1,0800	0,01700	0,10780	0,0015	0,8093400	742,70	8,20	660,00	8,70	1000,0	19,0	660,0	8,7	11,135	
BIB-5_120.FIN2	552,0	1,831	0,3430	0,00630	0,04663	0,0005	0,4550600	299,00	4,80	293,80	3,30	319,0	38,0	293,8	3,3	1,739	
BIB-5_121.FIN2	566,0	1,491	0,8320	0,01300	0,09850	0,0011	0,5954000	613,70	7,00	605,30	6,50	632,0	28,0	605,3	6,5	1,369	
BIB-5_122.FIN2	551,0	1,250	0,6460	0,01100	0,07915	0,0009	0,6755100	505,30	6,90	491,00	5,50	560,0	27,0	491,0	5,5	2,830	
BIB-5_123.FIN2	691,0	2,282	2,4560	0,04400	0,20050	0,0031	0,8838200	1257,00	13,00	1177,00	17,00	1398,0	19,0	1398,0	19,0	15,808	
BIB-5_124.FIN2	947,0	1,720	0,5847	0,00790	0,07060	0,0010	0,3739300	467,70	5,20	439,40	6,20	598,0	31,0	439,4	6,2	6,051	
BIB-5_125.FIN2	69,6	0,717	0,7960	0,02300	0,09700	0,0013	0,2946100	591,00	13,00	596,40	7,70	559,0	64,0	596,4	7,7	0,914	
BIB-5_126.FIN2	760,0	2,440	0,5950	0,00760	0,07309	0,0006	0,3256200	473,70	4,80	454,70	3,80	551,0	28,0	454,7	3,8	4,011	
BIB-5_127.FIN2	2350,0	8,170	0,3506	0,00450	0,04375	0,0007	0,5534800	304,90	3,40	275,90	4,60	532,0	31,0	275,9	4,6	9,511	
BIB-5_128.FIN2	406,0	1,077	1,6250	0,02400	0,15590	0,0018	0,6980200	978,40	9,20	933,50	9,90	1073,0	21,0	1073,0	21,0	13,001	
BIB-5_129.FIN2	298,1	5,690	0,9290	0,02200	0,10720	0,0019	0,7542300	665,00	12,00	656,00	11,00	694,0	33,0	656,0	11,0	1,353	
BIB-5_130.FIN2	424,0	1,257	0,6890	0,01000	0,08540	0,0010	0,5359800	531,80	6,10	528,00	6,00	538,0	29,0	528,0	6,0	0,715	
BIB-5_131.FIN2	659,3	0,914	2,5190	0,08700	0,18330	0,0058	0,9764300	1266,00	25,00	1082,00	32,00	1604,0	15,0	DISC	DISC	32,544	
BEMO-3_3.FIN2	247,2	0,568	0,6240	0,02000	0,07580	0,0010	0,3904500	491,00	13,00	471,10	6,00	575,0	66,0	471,1	6,0	4,053	
BEMO-3_7.FIN2	486,0	7,220	0,6070	0,01500	0,07749	0,0010	0,1235500	481,50	9,30	481,10	5,80	477,0	57,0	481,1	5,8	0,083	
BEMO-3_8.FIN2	248,6	0,963	1,1130	0,02400	0,12560	0,0015	0,1112000	759,00	11,00	762,40	8,80	744,0	46,0	762,4	8,8	0,448	
BEMO-3_9.FIN2	599,0	0,986	0,7760	0,01200	0,09210	0,0010	0,3229700	582,90	6,80	567,90	6,20	637,0	34,0	567,9	6,2	2,573	
BEMO-3_10.FIN2	750,0	0,922	0,4382	0,00550	0,05885	0,0004	0,2749600	368,70	3,90	368,60	2,70	364,0	28,0	368,6	2,7	0,027	
BEMO-3_11.FIN2	88,9	0,654	5,1010	0,06800	0,32690	0,0032	0,5053800	1835,00	11,00	1823,00	16,00	1844,0	20,0	1844,0	20,0	1,139	
BEMO-3_12.FIN2	618,0	1,460	0,3838	0,00530	0,05233	0,0005	0,2466800	329,60	3,80	328,80	2,80	332,0	33,0	328,8	2,8	0,243	
BEMO-3_13.FIN2	576,0	2,214	0,3706	0,00590	0,05020	0,0005	0,2379800	319,80	4,30	315,70	2,80	336,0	35,0	315,7	2,8	1,282	
BEMO-3_14.FIN2	648,0	1,374	0,3843	0,00540	0,05216	0,0004	0,1901600	329,90	4,00	327,80	2,60	338,0	33,0	327,8	2,6	0,637	
BEMO-3_16.FIN2	117,3	2,134	0,6350	0,01800	0,07960	0,0010	0,1885300	498,00	11,00	493,70	6,10	498,0	62,0	493,7	6,1	0,863	
BEMO-3_17.FIN2	147,2	1,491	0,9050	0,02300	0,10520	0,0011	0,2415100	652,00	12,00	644,50	6,40	671,0	53,0	644,5	6,4	1,150	
BEMO-3_18.FIN2	265,0	1,018	0,6230	0,01300	0,07821	0,0008	0,2554200	490,70	8,10	485,40	4,80	499,0	45,0	485,4	4,8	1,080	
BEMO-3_21.FIN2	84,4	0,730	0,9100	0,02300	0,10470	0,0013	0,2335900	656,00	12,00	641,50	7,80	694,0	53,0	641,5	7,8	2,210	
BEMO-3_22.FIN2	1253,0	5,390	0,7169	0,00920	0,08590	0,0011	0,3378100	548,60	5,40	531,50	6,30	614,0	32,0	531,5	6,3	3,117	
BEMO-3_23.FIN2	486,0	8,380	2,2830	0,04100	0,20610	0,0024	0,6440000	1206,00	13,00	1208,00	13,00	1203,0	29,0	1203,0	29,0	0,416	Rim
BEMO-3_23.FIN2	193,0	1,252	3,9520	0,07800	0,27020	0,0045	0,7045600	1623,00	16,00	1541,00	23,00	1722,0	24,0	1722,0	24,0	10,511	Core
BEMO-3_24.FIN2	174,2	8,140	0,6320	0,01900	0,08145	0,0010	0,1615500	495,00	12,00	504,70	5,70	441,0	62,0	504,7	5,7	1,960	
BEMO-3_25.FIN2	506,0	1,265	0,4118	0,00840	0,05400	0,0005	0,3586500	349,80	6,00	339,00	3,30	416,0	41,0	339,0	3,3	3,087	
BEMO-3_26.FIN2	401,0	0,976	0,4160	0,01300	0,05533	0,0008	0,2541300	353,10	9,30	347,10	5,20	378,0	69,0	347,1	5,2	1,699	Rim

Sample Name:	[U]							207/235		206/238		207/206		Best age		Discordance	Rim/
Grain #	ppm	U/Th	207/235	2σ error	206/238	2σ error	RHO	Age Ma	2σ error	Age (Ma)	2σ error	Age (Ma)	2σ error	(Ma)	2σ error	%	Core
BEMO-3_26.FIN2	141,0	1,384	0,4740	0,01700	0,06119	0,0009	0,2022900	393,00	12,00	382,80	5,60	448,0	79,0	382,8	5,6	2,595	Core
BEMO-3_28.FIN2	466,0	4,810	0,3518	0,00740	0,04835	0,0004	0,1320300	305,50	5,50	304,40	2,60	301,0	43,0	304,4	2,6	0,360	
BEMO-3_29.FIN2	318,0	4,500	0,6093	0,00960	0,07799	0,0007	0,2134600	482,40	6,10	484,10	4,20	462,0	36,0	484,1	4,2	0,352	
BEMO-3_31.FIN2	1987,0	22,120	0,9120	0,02300	0,10110	0,0017	0,5051200	658,00	12,00	620,90	9,90	784,0	42,0	620,9	9,9	5,638	Rim
BEMO-3_31.FIN2	357,0	1,500	10,7200	0,29000	0,46600	0,0082	0,8357800	2495,00	24,00	2465,00	36,00	2506,0	22,0	2506,0	22,0	1,636	Core
BEMO-3_36.FIN2	450,0	47,000	0,7640	0,04000	0,09230	0,0031	0,2454400	575,00	23,00	569,00	18,00	590,0	110,0	569,0	18,0	1,043	Rim
BEMO-3_36.FIN2	220,0	1,860	1,7630	0,02300	0,17320	0,0015	0,4367300	1030,70	8,50	1029,50	8,50	1030,0	25,0	1030,0	25,0	0,049	Core
BEMO-3_38.FIN2	151,0	2,035	0,8510	0,02100	0,10180	0,0011	0,2012100	626,00	11,00	624,60	6,60	612,0	52,0	624,6	6,6	0,224	
BEMO-3_39.FIN2	237,0	1,518	13,1940	0,09100	0,51550	0,0035	0,5214200	2692,80	6,50	2679,00	15,00	2702,0	11,0	2702,0	11,0	0,851	
BEMO-3_41.FIN2	76,8	1,411	0,9190	0,02500	0,10430	0,0013	0,0632710	659,00	13,00	639,20	7,70	715,0	61,0	639,2	7,7	3,005	
BEMO-3_42.FIN2	86,6	2,740	0,6510	0,02800	0,07260	0,0014	0,1146900	507,00	18,00	451,50	8,40	740,0	100,0	451,5	8,4	10,947	
BEMO-3_43.FIN2	84,8	1,074	0,8790	0,02400	0,10060	0,0012	0,2235200	642,00	13,00	617,70	7,20	710,0	60,0	617,7	7,2	3,785	
BEMO-3_44.FIN2	232,0	1,160	5,8930	0,05700	0,35170	0,0027	0,6184900	1958,90	8,40	1942,00	13,00	1977,0	15,0	1977,0	15,0	1,770	
BEMO-3_46.FIN2	284,0	1,617	0,8490	0,01300	0,09819	0,0008	0,4949500	623,30	7,30	603,70	4,90	696,0	30,0	603,7	4,9	3,145	
BEMO-3_47.FIN2	131,6	1,758	0,6260	0,01400	0,07778	0,0009	0,0293920	492,30	8,90	482,80	5,20	516,0	52,0	482,8	5,2	1,930	
BEMO-3_48.FIN2	405,0	11,300	0,6190	0,01700	0,07770	0,0011	0,1984700	488,00	11,00	482,60	6,80	502,0	64,0	482,6	6,8	1,107	Rim
BEMO-3_48.FIN2	226,3	2,235	0,7180	0,01700	0,08670	0,0011	0,2073800	549,00	10,00	536,20	6,30	592,0	53,0	536,2	6,3	2,332	Core
BEMO-3_54.FIN2	593,0	20,800	0,4520	0,03700	0,05750	0,0039	0,3857700	378,00	26,00	360,00	24,00	480,0	190,0	360,0	24,0	4,762	Rim
BEMO-3_54.FIN2	750,0	1,958	6,6740	0,05700	0,34430	0,0033	0,7386300	2068,60	7,60	1907,00	16,00	2230,0	12,0	2230,0	12,0	14,484	Core
BEMO-3_55.FIN2	144,2	0,862	1,8060	0,03700	0,17740	0,0022	0,4050700	1046,00	14,00	1052,00	12,00	1019,0	40,0	1019,0	40,0	3,238	
BEMO-3_56.FIN2	130,7	0,780	0,8520	0,01800	0,10210	0,0011	0,2716400	625,40	9,70	626,50	6,30	604,0	46,0	626,5	6,3	0,176	
BEMO-3_57.FIN2	159,7	1,622	0,7950	0,03000	0,09470	0,0011	0,0827680	585,00	11,00	583,10	6,40	568,0	51,0	583,1	6,4	0,325	
BEMO-3_58.FIN2	162,0	3,170	0,5700	0,01600	0,07093	0,0009	0,2079200	456,00	10,00	441,70	5,10	502,0	58,0	441,7	5,1	3,136	
BEMO-3_59.FIN2	286,0	1,425	0,7770	0,01500	0,09322	0,0008	0,0701390	582,50	8,50	574,50	5,00	594,0	41,0	574,5	5,0	1,373	
BEMO-3_60.FIN2	281,0	1,421	11,5900	0,17000	0,48360	0,0068	0,7738700	2569,00	14,00	2541,00	29,00	2588,0	16,0	2588,0	16,0	1,816	
BEMO-3_61.FIN2	1786,0	2,310	0,3783	0,00460	0,04967	0,0005	0,6324100	325,50	3,40	312,50	3,20	412,0	22,0	312,5	3,2	3,994	
BEMO-3_62.FIN2	157,0	1,763	0,7430	0,03700	0,08770	0,0023	0,1189500	562,00	21,00	542,00	13,00	630,0	120,0	542,0	13,0	3,559	
BEMO-3_63.FIN2	413,0	1,311	0,4465	0,00980	0,05908	0,0007	0,3642300	374,00	6,80	370,00	4,00	377,0	43,0	370,0	4,0	1,070	
BEMO-3_64.FIN2	500,0	2,602	0,8150	0,02200	0,09930	0,0019	0,5025000	604,00	12,00	610,00	11,00	569,0	51,0	610,0	11,0	0,993	
BEMO-3_65.FIN2	222,0	1,471	0,3520	0,01000	0,04788	0,0007	0,4852100	304,90	7,50	301,40	4,50	315,0	57,0	301,4	4,5	1,148	
BEMO-3_66.FIN2	113,7	1,657	0,3500	0,01200	0,04910	0,0007	0,0252670	303,20	8,70	308,90	4,50	246,0	71,0	308,9	4,5	1,880	
BEMO-3_67.FIN2	317,0	1,970	0,3588	0,00790	0,04901	0,0005	0,1642700	310,70	5,90	308,40	3,30	304,0	49,0	308,4	3,3	0,740	
BEMO-3_68.FIN2	208,9	0,840	0,9070	0,01400	0,10692	0,0010	0,3278500	654,60	7,50	654,70	5,70	649,0	32,0	654,7	5,7	0,015	
BEMO-3_69.FIN2	557,0	0,732	0,7730	0,01500	0,09500	0,0014	0,4495900	580,90	8,40	585,00	8,50	554,0	40,0	585,0	8,5	0,706	
BEMO-3_71.FIN2	126,9	1,182	0,3490	0,01200	0,04799	0,0006	0,0624300	302,80	8,80	302,10	3,50	295,0	71,0	302,1	3,5	0,231	
BEMO-3_74.FIN2	511,0	4,680	0,8730	0,01300	0,10235	0,0010	0,1744000	636,30	7,00	628,10	5,60	652,0	31,0	628,1	5,6	1,289	
BEMO-3_75.FIN2	1136,0	12,800	0,4130	0,02200	0,05300	0,0030	0,6101800	350,00	16,00	333,00	18,00	460,0	110,0	333,0	18,0	4,857	Rim
BEMO-3_75.FIN2	308,0	1,984	0,9120	0,02000	0,11000	0,0016	0,2431200	657,00	10,00	672,70	9,30	602,0	50,0	672,7	9,3	2,390	Core
BEMO-3_77.FIN2	1550,0	1,783	0,3927	0,00530	0,05262	0,0005	0,5546900	336,10	3,80	330,60	2,90	359,0	25,0	330,6	2,9	1,636	
BEMO-3_79.FIN2	486,0	2,480	0,6290	0,02000	0,08040	0,0019	0,6102700	495,00	12,00	498,00	11,00	472,0	57,0	498,0	11,0	0,606	
BEMO-3_82.FIN2	323,0	3,390	0,6490	0,01600	0,08320	0,0010	0,1561500	506,80	9,90	514,90	6,10	471,0	51,0	514,9	6,1	1,598	
BEMO-3_83.FIN2	916,0	1,930	11,0700	0,12000	0,48090	0,0062	0,8361600	2527,00	11,00	2530,00	27,00	2523,0	14,0	2523,0	14,0	0,277	
BEMO-3_84.FIN2	281,0	3,350	0,8500	0,03600	0,09790	0,0019	0,3976900	623,00	19,00	602,00	11,00	673,0	82,0	602,0	11,0	3,371	Rim
BEMO-3_84.FIN2	71,1	1,122	1,1550	0,04200	0,12330	0,0020	0,3061000	775,00	19,00	749,00	12,00	832,0	66,0	749,0	12,0	3,355	Core
BEMO-3_85.FIN2	77,5	1,049	4,0680	0,08300	0,28240	0,0035	0,2725800	1643,00	17,00	1603,00	18,00	1692,0	32,0	1692,0	32,0	5,260	
BEMO-3_86.FIN2	295,0	0,806	0,8880	0,01800	0,10760	0,0011	0,3255100	644,40	9,60	658,60	6,30	590,0	42,0	658,6	6,3	2,204	
BEMO-3_87.FIN2	40,4	0,559	1,6000	0,04400	0,16410	0,0021	0,0617770	967,00	18,00	979,00	12,00	925,0	65,0	925,0	65,0	5,838	

Sample Name:	[U]							207/235		206/238		207/206		Best age		Discordance	Rim/
Grain #	ppm	U/Th	207/235	2σ error	206/238	2σ error	RHO	Age Ma	2σ error	Age (Ma)	2σ error	Age (Ma)	2σ error	(Ma)	2σ error	%	Core
BEMO-3_88.FIN2	150,5	1,386	0,7050	0,01700	0,08640	0,0010	0,1617700	540,20	9,90	534,40	6,20	551,0	54,0	534,4	6,2	1,074	
BEMO-3_89.FIN2	1131,0	1,688	0,8740	0,01200	0,09982	0,0009	0,3979100	637,50	6,40	613,30	5,50	721,0	28,0	613,3	5,5	3,796	
BEMO-3_90.FIN2	388,1	0,842	1,0890	0,01500	0,12200	0,0010	0,3981500	749,30	7,50	741,90	5,80	769,0	30,0	741,9	5,8	0,988	
BEMO-3_91.FIN2	1498,0	2,940	0,3530	0,01200	0,04764	0,0009	0,3522300	306,40	9,10	300,00	5,40	351,0	74,0	300,0	5,4	2,089	
BEMO-3_93.FIN2	1853,0	6,970	0,3807	0,00600	0,05016	0,0008	0,2263400	327,40	4,40	315,40	4,60	419,0	45,0	315,4	4,6	3,665	
BEMO-3_94.FIN2	67,8	0,818	0,8100	0,02600	0,09470	0,0014	0,1370000	598,00	14,00	583,90	8,00	634,0	73,0	583,9	8,0	2,358	
BEMO-3_95.FIN2	1054,0	8,840	0,3674	0,00500	0,05051	0,0006	0,5271600	317,50	3,70	317,60	3,70	318,0	30,0	317,6	3,7	0,031	
BEMO-3_96.FIN2	106,3	0,796	8,9400	0,12000	0,44230	0,0048	0,2729800	2331,00	12,00	2360,00	21,00	2305,0	25,0	2305,0	25,0	2,386	
BEMO-3_98.FIN2	118,8	1,151	1,2830	0,03000	0,13570	0,0018	0,2186700	837,00	13,00	820,00	10,00	881,0	49,0	820,0	10,0	2,031	
BEMO-3_100.FIN2	319,7	1,266	5,9240	0,05900	0,34190	0,0030	0,5466400	1963,50	8,70	1895,00	14,00	2034,0	16,0	2034,0	16,0	6,834	
BEMO-3_101.FIN2	417,0	1,941	0,5960	0,01300	0,07476	0,0009	0,4243400	474,00	8,50	464,70	5,30	509,0	45,0	464,7	5,3	1,962	
BEMO-3_102.FIN2	457,0	2,050	1,7320	0,02600	0,17000	0,0019	0,5884300	1018,70	9,90	1012,00	10,00	1041,0	25,0	1041,0	25,0	2,786	
BEMO-3_103.FIN2	561,9	5,650	0,8600	0,01000	0,10135	0,0009	0,1959400	629,70	5,60	622,30	5,20	651,0	29,0	622,3	5,2	1,175	
BEMO-3_105.FIN2	377,0	9,520	0,8510	0,01200	0,10246	0,0009	0,3644700	624,30	6,50	628,70	5,40	599,0	31,0	628,7	5,4	0,705	
BEMO-3_107.FIN2	207,7	1,670	0,7950	0,04000	0,08960	0,0024	0,0592890	592,00	22,00	553,00	14,00	720,0	110,0	553,0	14,0	6,588	Rim
BEMO-3_107.FIN2	148,5	1,105	0,8690	0,01900	0,10140	0,0013	0,1352500	635,00	11,00	622,30	7,40	679,0	49,0	622,3	7,4	2,000	Core
BEMO-3_108.FIN2	606,0	10,890	0,3689	0,00810	0,05019	0,0007	0,4608900	319,80	6,40	315,70	4,30	338,0	46,0	315,7	4,3	1,282	
BEMO-3_109.FIN2	662,0	1,667	0,7618	0,00870	0,09365	0,0007	0,0415520	574,90	5,00	577,00	4,30	554,0	25,0	577,0	4,3	0,418	
BEMO-3_110.FIN2	431,0	8,810	0,9210	0,01300	0,10850	0,0012	0,3649500	661,90	7,00	664,00	6,80	649,0	31,0	664,0	6,8	0,317	
BEMO-3_111.FIN2	379,5	1,462	0,8220	0,01300	0,09914	0,0008	0,3347800	609,30	6,80	609,30	5,00	598,0	31,0	609,3	5,0	0,000	
BEMO-3_113.FIN2	399,0	93,000	0,4140	0,03300	0,05010	0,0010	0,1952400	351,00	23,00	315,30	6,20	560,0	160,0	315,3	6,2	10,171	Rim
BEMO-3_113.FIN2	65,6	1,863	1,0430	0,03300	0,11260	0,0017	0,0603700	722,00	16,00	688,00	10,00	814,0	69,0	688,0	10,0	4,709	Core
BEMO-3_114.FIN2	563,0	1,692	0,3448	0,00630	0,04783	0,0004	0,0495270	300,40	4,80	301,20	2,40	274,0	43,0	301,2	2,4	0,266	
BEMO-3_116.FIN2	87,8	3,081	0,9280	0,02600	0,10500	0,0014	0,0417000	663,00	14,00	643,70	7,90	708,0	61,0	643,7	7,9	2,911	
BEMO-3_117.FIN2	92,8	1,673	0,9180	0,02400	0,10810	0,0013	0,1703500	659,00	13,00	662,50	7,80	621,0	58,0	662,5	7,8	0,531	
BEMO-3_118.FIN2	160,0	1,487	0,7070	0,01900	0,08684	0,0010	0,2381600	540,00	11,00	536,70	5,80	528,0	57,0	536,7	5,8	0,611	
BEMO-3_123.FIN2	466,0	2,020	0,7790	0,01300	0,09460	0,0010	0,1282400	584,10	7,10	582,60	5,90	578,0	34,0	582,6	5,9	0,257	
BEMO-3_125.FIN2	280,0	2,460	0,7070	0,02400	0,08720	0,0015	0,0922580	541,00	14,00	538,60	8,90	537,0	80,0	538,6	8,9	0,444	
BEMO-3_126.FIN2	880,0	2,260	0,6180	0,01600	0,07740	0,0011	0,3026200	487,70	9,80	480,60	6,80	509,0	55,0	480,6	6,8	1,456	Rim
BEMO-3_126.FIN2	111,9	0,701	0,8300	0,03100	0,10030	0,0022	0,0715930	612,00	17,00	616,00	13,00	585,0	89,0	616,0	13,0	0,654	Core
BEMO-3_130.FIN2	256,0	0,588	5,8450	0,04700	0,35340	0,0026	0,5860200	1952,10	7,10	1951,00	12,00	1953,0	14,0	1953,0	14,0	0,102	
BEMO-12_1.FIN2	353,0	1,132	0,5928	0,00980	0,07628	0,0007	0,1784400	472,00	6,30	473,80	4,20	463,0	40,0	473,8	4,2	0,381	
BEMO-12_2.FIN2	216,1	0,774	1,7370	0,02600	0,16930	0,0014	0,6392900	1021,90	9,80	1008,20	7,70	1049,0	28,0	1049,0	28,0	3,889	
BEMO-12_3.FIN2	66,1	2,670	0,9550	0,02700	0,10850	0,0016	0,2000800	677,00	14,00	663,70	9,00	704,0	64,0	663,7	9,0	1,965	
BEMO-12_4.FIN2	962,0	28,700	0,9130	0,01600	0,10680	0,0014	0,4713200	658,20	8,70	654,10	8,00	673,0	35,0	654,1	8,0	0,623	Rim
BEMO-12_4.FIN2	460,0	0,547	4,3890	0,07000	0,28680	0,0030	0,6852900	1709,00	13,00	1625,00	15,00	1812,0	23,0	1812,0	23,0	10,320	Core
BEMO-12_5.FIN2	741,0	1,514	0,9980	0,01200	0,11364	0,0010	0,4300600	702,00	5,90	693,80	5,50	740,0	22,0	693,8	5,5	1,168	
BEMO-12_7.FIN2	80,0	1,489	0,7640	0,02500	0,09120	0,0014	0,1506000	573,00	15,00	562,50	8,00	611,0	77,0	562,5	8,0	1,832	
BEMO-12_8.FIN2	207,1	1,155	1,8020	0,02400	0,17350	0,0015	0,2862200	1044,90	8,70	1031,40	8,10	1078,0	26,0	1078,0	26,0	4,323	
BEMO-12_9.FIN2	619,0	0,694	0,3811	0,00620	0,05119	0,0005	0,2932900	327,50	4,60	321,80	2,80	362,0	36,0	321,8	2,8	1,740	
BEMO-12_10.FIN2	51,6	1,607	1,1390	0,03200	0,12460	0,0016	0,1499300	768,00	15,00	756,50	9,40	766,0	66,0	756,5	9,4	1,497	
BEMO-12_11.FIN2	3,0	-0,380	0,2070	0,07400	0,01150	0,0020	0,1276600	147,00	62,00	75,00	13,00	-6700,0	4100,0	DISC	DISC	48,980	
BEMO-12_12.FIN2	303,0	5,460	1,8610	0,02100	0,18040	0,0013	0,3867700	1066,50	7,30	1069,30	7,40	1059,0	22,0	1059,0	22,0	0,973	
BEMO-12_13.FIN2	413,0	2,234	0,7020	0,02200	0,08760	0,0018	0,4937800	540,00	13,00	541,00	11,00	546,0	55,0	541,0	11,0	0,185	Rim
BEMO-12_13.FIN2	103,3	1,323	0,8940	0,02200	0,10170	0,0013	0,2637700	647,00	12,00	624,20	7,70	709,0	54,0	624,2	7,7	3,524	Core
BEMO-12_14.FIN2	838,0	2,449	0,4066	0,00800	0,05520	0,0006	0,4845600	346,00	5,80	346,30	3,80	336,0	39,0	346,3	3,8	0,087	

Sample Name:	[U]							207/235		206/238		207/206		Best age		Discordance	Rim/
Grain #	ppm	U/Th	207/235	2σ error	206/238	2σ error	RHO	Age Ma	2σ error	Age (Ma)	2σ error	Age (Ma)	2σ error	(Ma)	2σ error	%	Core
BEMO-12_15.FIN2	765,0	2,080	5,3180	0,05500	0,34010	0,0033	0,6745800	1870,30	8,90	1886,00	16,00	1847,0	16,0	1847,0	16,0	2,112	
BEMO-12_16.FIN2	485,0	2,528	0,3616	0,00650	0,04911	0,0005	0,1886000	312,90	4,80	309,00	3,30	330,0	44,0	309,0	3,3	1,246	
BEMO-12_17.FIN2	318,0	1,287	0,3523	0,00840	0,04822	0,0005	0,2290700	305,70	6,30	303,50	2,80	310,0	53,0	303,5	2,8	0,720	
BEMO-12_18.FIN2	424,0	1,914	0,7550	0,01000	0,09182	0,0007	0,3682000	570,40	5,80	566,20	4,20	579,0	28,0	566,2	4,2	0,736	
BEMO-12_19.FIN2	70,3	2,220	1,1970	0,04400	0,12990	0,0021	0,2303300	797,00	20,00	787,00	12,00	802,0	76,0	787,0	12,0	1,255	
BEMO-12_20.FIN2	401,8	0,660	0,8900	0,01300	0,10386	0,0009	0,1872400	645,20	6,90	636,90	5,30	660,0	31,0	636,9	5,3	1,286	
BEMO-12_21.FIN2	164,2	0,942	10,2400	0,23000	0,40630	0,0074	0,8747600	2452,00	21,00	2196,00	34,00	2670,0	22,0	2670,0	22,0	17,753	
BEMO-12_22.FIN2	568,0	6,650	0,6070	0,01700	0,07520	0,0008	0,1504300	481,00	11,00	467,40	5,00	548,0	48,0	467,4	5,0	2,827	
BEMO-12_23.FIN2	678,0	7,010	0,6590	0,01400	0,08130	0,0011	0,4814100	513,20	8,50	503,80	6,60	562,0	41,0	503,8	6,6	1,832	
BEMO-12_24.FIN2	25,6	1,649	6,1800	0,14000	0,35290	0,0047	0,4042200	1994,00	20,00	1947,00	22,00	2035,0	39,0	2035,0	39,0	4,324	
BEMO-12_25.FIN2	175,6	2,420	0,5840	0,01400	0,07361	0,0008	0,0541600	465,90	9,10	457,80	4,70	484,0	57,0	457,8	4,7	1,739	
BEMO-12_26.FIN2	3780,0	0,418	0,3572	0,00760	0,04770	0,0010	0,7072700	310,00	5,70	300,40	6,30	379,0	38,0	300,4	6,3	3,097	Rim
BEMO-12_26.FIN2	304,0	0,903	0,8180	0,01500	0,09794	0,0010	0,2658700	605,80	8,10	602,20	5,60	604,0	39,0	602,2	5,6	0,594	Core
BEMO-12_27.FIN2	604,0	4,560	0,7850	0,00980	0,09450	0,0008	0,4170300	587,80	5,60	582,00	4,90	604,0	25,0	582,0	4,9	0,987	
BEMO-12_28.FIN2	183,0	1,246	0,7590	0,01400	0,09265	0,0009	0,1984900	573,10	8,20	571,10	5,40	567,0	42,0	571,1	5,4	0,349	
BEMO-12_29.FIN2	1104,0	32,100	0,3980	0,01000	0,05426	0,0009	0,3988500	339,70	7,60	340,60	5,70	326,0	55,0	340,6	5,7	0,265	Rim
BEMO-12_29.FIN2	81,0	0,884	6,0200	0,19000	0,33920	0,0076	0,4647700	1984,00	24,00	1882,00	37,00	2072,0	56,0	2072,0	56,0	9,170	Core
BEMO-12_30.FIN2	157,0	3,670	13,4300	0,15000	0,51650	0,0048	0,4910100	2708,00	11,00	2683,00	21,00	2731,0	17,0	2731,0	17,0	1,758	
BEMO-12_31.FIN2	54,8	0,448	11,7800	0,15000	0,46980	0,0054	0,4743300	2585,00	12,00	2481,00	24,00	2667,0	20,0	2667,0	20,0	6,974	
BEMO-12_32.FIN2	395,0	4,770	0,8120	0,01400	0,09686	0,0010	0,2279600	602,30	7,90	595,90	5,60	618,0	39,0	595,9	5,6	1,063	
BEMO-12_33.FIN2	199,0	15,300	0,9610	0,02400	0,10910	0,0014	0,2273700	681,00	13,00	667,30	8,00	712,0	54,0	667,3	8,0	2,012	
BEMO-12_34.FIN2	99,0	1,812	3,0010	0,04400	0,24120	0,0023	0,1297200	1406,00	11,00	1393,00	12,00	1438,0	29,0	1438,0	29,0	3,129	
BEMO-12_35.FIN2	414,1	1,384	0,6200	0,01100	0,07673	0,0007	0,3222900	488,80	6,60	476,50	4,40	544,0	36,0	476,5	4,4	2,516	
BEMO-12_36.FIN2	263,0	0,578	5,3090	0,05000	0,33300	0,0023	0,3584000	1869,10	8,00	1852,00	11,00	1890,0	17,0	1890,0	17,0	2,011	
BEMO-12_37.FIN2	227,0	1,654	0,7500	0,01600	0,09157	0,0009	0,1258400	566,40	9,20	564,70	5,00	564,0	47,0	564,7	5,0	0,300	
BEMO-12_38.FIN2	449,0	7,480	0,6160	0,01000	0,07884	0,0009	0,2814400	487,30	6,20	489,10	5,20	468,0	38,0	489,1	5,2	0,369	
BEMO-12_39.FIN2	28,0	-2,000	1,0100	0,13000	0,12210	0,0071	0,1944600	695,00	70,00	742,00	41,00	530,0	280,0	742,0	41,0	6,763	
BEMO-12_68.FIN2	167,0	10,130	1,7240	0,09200	0,10140	0,0014	0,9639800	657,90	8,40	601,40	7,10	908,0	25,0	601,4	7,1	8,588	
BEMO-12_39.FIN2	146,0	1,780	5,9720	0,08000	0,35560	0,0037	0,3782700	1970,00	12,00	1961,00	17,00	1983,0	22,0	1983,0	22,0	1,109	
BEMO-12_40.FIN2	1740,0	19,600	0,4240	0,01000	0,05620	0,0013	0,3635800	358,40	7,40	352,20	8,00	401,0	62,0	352,2	8,0	1,730	Rim
BEMO-12_40.FIN2	118,0	1,272	0,8710	0,02500	0,10240	0,0014	0,1142700	634,00	14,00	628,50	8,30	653,0	70,0	628,5	8,3	0,868	Core
BEMO-12_41.FIN2	304,0	2,000	0,3790	0,01000	0,05173	0,0007	0,1213500	326,90	7,20	325,10	4,10	335,0	62,0	325,1	4,1	0,551	
BEMO-12_42.FIN2	465,0	15,000	0,3540	0,01200	0,04719	0,0009	0,0982540	307,20	9,10	297,20	5,70	407,0	78,0	297,2	5,7	3,255	Rim
BEMO-12_42.FIN2	129,0	3,196	0,5960	0,02400	0,07260	0,0012	0,1879800	473,00	15,00	451,70	7,00	562,0	87,0	451,7	7,0	4,503	Core
BEMO-12_44.FIN2	408,8	3,777	1,1380	0,01300	0,12590	0,0010	0,4006700	771,10	6,20	764,20	5,80	794,0	22,0	764,2	5,8	0,895	
BEMO-12_45.FIN2	70,0	1,757	0,8720	0,02600	0,10400	0,0014	0,1924000	633,00	14,00	637,30	8,00	593,0	65,0	637,3	8,0	0,679	
BEMO-12_46.FIN2	299,0	1,321	0,3706	0,00890	0,05047	0,0006	0,2686700	319,30	6,60	317,40	3,60	318,0	52,0	317,4	3,6	0,595	
BEMO-12_47.FIN2	300,0	8,060	0,6260	0,02000	0,07582	0,0010	0,1797800	492,00	13,00	471,10	5,90	579,0	69,0	471,1	5,9	4,248	
BEMO-12_48.FIN2	289,0	1,594	0,3447	0,00740	0,04768	0,0006	0,0986970	301,10	5,80	300,20	3,50	310,0	52,0	300,2	3,5	0,299	
BEMO-12_49.FIN2	187,1	0,775	1,6740	0,02300	0,16680	0,0017	0,5090300	997,30	8,80	994,40	9,10	1000,0	30,0	1000,0	30,0	0,560	
BEMO-12_50.FIN2	8,8	-0,020	0,3710	0,06900	0,01070	0,0012	0,4106000	283,00	46,00	68,30	7,60	2200,0	2000,0	DISC	DISC	75,866	
BEMO-12_51.FIN2	15500,0	1,180	0,3180	0,02100	0,01080	0,0011	0,3731700	280,00	16,00	69,40	7,00	2940,0	150,0	DISC	DISC	75,214	Rim
BEMO-12_51.FIN2	486,0	1,683	0,3655	0,00950	0,04718	0,0006	0,2359800	315,60	7,10	297,20	3,50	431,0	57,0	297,2	3,5	5,830	Core
BEMO-12_53.FIN2	81,0	2,630	1,2270	0,03000	0,12970	0,0014	0,2006100	811,00	14,00	785,90	8,00	860,0	53,0	785,9	8,0	3,095	
BEMO-12_54.FIN2	49,1	1,339	0,6850	0,02200	0,08390	0,0013	0,1304300	527,00	13,00	519,10	7,90	527,0	72,0	519,1	7,9	1,499	
BEMO-12_55.FIN2	93,2	2,254	0,3710	0,01500	0,04978	0,0008	0,1346000	318,00	11,00	313,10	4,80	329,0	83,0	313,1	4,8	1,541	
BEMO-12_56.FIN2	1420,0	3,430	0,3697	0,00550	0,05150	0,0005	0,3780400	319,80	4,20	323,70	3,10	271,0	30,0	323,7	3,1	1,220	

Sample Name:	[U]							207/235		206/238		207/206		Best age		Discordance	Rim/
Grain #	ppm	U/Th	207/235	2σ error	206/238	2σ error	RHO	Age Ma	2σ error	Age (Ma)	2σ error	Age (Ma)	2σ error	(Ma)	2σ error	%	Core
BEMO-12_57.FIN2	458,0	2,220	1,3360	0,01600	0,14420	0,0014	0,5146300	860,50	6,90	867,90	8,10	835,0	23,0	835,0	8,1	0,860	
BEMO-12_58.FIN2	1320,0	3,107	0,3660	0,00630	0,04927	0,0005	0,2598000	316,30	4,70	310,00	2,80	346,0	38,0	310,0	2,8	1,992	
BEMO-12_59.FIN2	532,0	3,470	0,9820	0,01100	0,11393	0,0009	0,3862400	694,00	5,70	695,50	5,10	681,0	26,0	695,5	5,1	0,216	
BEMO-12_60.FIN2	203,9	0,616	1,6790	0,02100	0,16330	0,0015	0,3777200	999,30	8,00	975,10	8,30	1048,0	25,0	1048,0	25,0	6,956	
BEMO-12_61.FIN2	375,0	0,929	0,8910	0,02400	0,10650	0,0018	0,3069100	646,00	13,00	652,00	11,00	609,0	69,0	652,0	11,0	0,929	
BEMO-12_62.FIN2	460,0	1,241	0,4089	0,00860	0,05388	0,0005	0,1466800	347,40	6,20	338,30	3,20	400,0	49,0	338,3	3,2	2,619	
BEMO-12_63.FIN2	4090,0	0,982	0,2394	0,00500	0,03159	0,0004	0,3901700	217,90	4,10	200,50	2,50	400,0	44,0	200,5	2,5	7,985	
BEMO-12_64.FIN2	2860,0	11,800	0,9510	0,01700	0,11560	0,0017	0,5884800	677,80	8,90	705,10	9,70	581,0	32,0	705,1	9,7	4,028	
BEMO-12_65.FIN2	164,4	0,591	2,0110	0,03400	0,18960	0,0024	0,6272600	1117,00	11,00	1119,00	13,00	1114,0	30,0	1114,0	30,0	0,449	
BEMO-12_66.FIN2	247,0	2,840	0,6080	0,01200	0,07782	0,0008	0,3072600	481,60	7,30	483,10	4,60	459,0	41,0	483,1	4,6	0,311	
BEMO-12_67.FIN2	393,0	2,323	0,3497	0,00720	0,04765	0,0004	0,2449600	303,90	5,40	300,10	2,60	326,0	42,0	300,1	2,6	1,250	
BEMO-12_68.FIN2	410,0	1,560	0,9380	0,01500	0,11160	0,0012	0,3670800	671,10	7,70	681,90	7,00	628,0	34,0	681,9	7,0	1,609	
BEMO-12_70.FIN2	344,0	1,759	0,4287	0,00790	0,05854	0,0006	0,1459400	363,00	5,60	366,70	3,50	328,0	43,0	366,7	3,5	1,019	
BEMO-12_71.FIN2	219,3	0,653	1,0610	0,02600	0,11930	0,0019	0,4434300	733,00	13,00	727,00	11,00	743,0	49,0	727,0	11,0	0,819	
BEMO-12_73.FIN2	404,0	4,120	0,4020	0,01000	0,05337	0,0006	0,2970000	342,40	7,20	335,10	3,90	378,0	53,0	335,1	3,9	2,132	
BEMO-12_74.FIN2	887,0	4,130	0,5750	0,01100	0,07330	0,0011	0,3073600	461,10	7,20	456,00	6,40	483,0	45,0	456,0	6,4	1,106	
BEMO-12_75.FIN2	1250,0	0,876	0,4153	0,00510	0,05570	0,0005	0,3687000	352,40	3,60	349,70	3,00	371,0	26,0	349,7	3,0	0,766	
BEMO-12_76.FIN2	455,0	0,721	0,3895	0,00680	0,05268	0,0006	0,2352600	333,50	5,00	330,90	3,40	347,0	40,0	330,9	3,4	0,780	
BEMO-12_77.FIN2	135,2	1,196	1,7850	0,03200	0,17480	0,0016	0,1983300	1038,00	12,00	1038,20	8,90	1033,0	38,0	1033,0	38,0	0,503	
BEMO-12_78.FIN2	946,0	1,220	1,5290	0,01600	0,15800	0,0013	0,4855300	941,50	6,30	945,50	7,10	933,0	19,0	933,0	19,0	1,340	
BEMO-12_79.FIN2	475,0	4,200	0,6110	0,01200	0,07712	0,0008	0,2346800	483,70	7,20	478,90	4,90	502,0	42,0	478,9	4,9	0,992	Rim
BEMO-12_79.FIN2	880,0	1,599	0,8110	0,01800	0,09860	0,0021	0,5554200	602,40	9,90	606,00	13,00	590,0	45,0	606,0	13,0	0,598	Core
BEMO-12_80.FIN2	551,0	0,646	0,4129	0,00700	0,05497	0,0006	0,4287500	351,30	5,20	344,90	3,50	392,0	38,0	344,9	3,5	1,822	
BEMO-12_81.FIN2	97,9	1,161	0,8540	0,02100	0,10160	0,0013	0,1292100	624,00	11,00	623,60	7,40	610,0	54,0	623,6	7,4	0,064	
BEMO-12_82.FIN2	813,0	13,190	0,8430	0,01100	0,10170	0,0011	0,3925200	620,10	6,30	624,40	6,30	607,0	29,0	624,4	6,3	0,693	
BEMO-12_84.FIN2	428,0	3,222	0,9670	0,01800	0,11180	0,0013	0,3043400	685,80	9,40	682,90	7,60	694,0	39,0	682,9	7,6	0,423	
BEMO-12_85.FIN2	112,7	1,450	5,2730	0,07700	0,32540	0,0034	0,5782700	1862,00	12,00	1815,00	17,00	1917,0	21,0	1917,0	21,0	5,321	
BEMO-12_86.FIN2	3400,0	7,970	0,2884	0,00310	0,03930	0,0004	0,7555300	257,20	2,50	248,50	2,30	341,0	19,0	248,5	2,3	3,383	
BEMO-12_87.FIN2	824,0	1,921	8,2300	0,09500	0,41470	0,0046	0,8321300	2255,00	11,00	2235,00	21,00	2278,0	11,0	2278,0	11,0	1,888	
BEMO-12_88.FIN2	735,0	149,000	0,4101	0,00550	0,05567	0,0005	0,3653400	348,60	3,90	349,20	3,10	343,0	28,0	349,2	3,1	0,172	
BEMO-12_89.FIN2	273,0	1,517	0,9680	0,01600	0,11390	0,0011	0,3271800	686,40	8,50	696,50	6,60	648,0	36,0	696,5	6,6	1,471	
BEMO-12_91.FIN2	502,0	45,100	0,4480	0,01800	0,05739	0,0009	0,2693300	375,00	12,00	359,70	5,50	437,0	72,0	359,7	5,5	4,080	Rim
BEMO-12_91.FIN2	299,6	1,756	0,8780	0,02600	0,10500	0,0017	0,1444200	638,00	14,00	643,60	9,90	613,0	70,0	643,6	9,9	0,878	Core
BEMO-12_92.FIN2	273,0	0,829	0,7900	0,02300	0,09720	0,0011	0,1028400	590,00	13,00	597,60	6,50	576,0	58,0	597,6	6,5	1,288	
BEMO-12_93.FIN2	317,0	0,908	0,3910	0,01800	0,05270	0,0011	0,1826500	334,00	13,00	331,00	7,00	350,0	100,0	331,0	7,0	0,898	
BEMO-12_94.FIN2	524,0	2,042	0,3790	0,00680	0,05239	0,0005	0,2373700	325,80	5,00	329,10	3,20	298,0	42,0	329,1	3,2	1,013	
BEMO-12_96.FIN2	1630,0	10,430	0,4140	0,01100	0,05590	0,0011	0,4760800	351,40	8,10	350,40	7,00	354,0	58,0	350,4	7,0	0,285	Rim
BEMO-12_96.FIN2	100,9	2,282	2,8850	0,07000	0,18400	0,0032	0,2896400	1376,00	19,00	1088,00	17,00	1853,0	45,0	DISC	DISC	41,284	Core
BEMO-12_97.FIN2	760,0	5,570	0,6226	0,00950	0,07948	0,0008	0,3738500	491,00	5,90	493,00	4,90	472,0	34,0	493,0	4,9	0,407	
BEMO-12_101.FIN2	355,0	1,096	12,1370	0,09700	0,50230	0,0034	0,6406300	2615,00	7,40	2623,00	15,00	2607,0	11,0	2607,0	11,0	0,614	
BEMO-12_102.FIN2	227,6	1,045	1,2200	0,02000	0,13260	0,0012	0,4084700	808,80	9,00	802,40	6,90	820,0	32,0	802,4	6,9	0,791	
BEMO-12_103.FIN2	815,0	13,640	0,7750	0,01400	0,09490	0,0011	0,2825400	582,30	7,90	584,60	6,50	566,0	40,0	584,6	6,5	0,395	
BEMO-12_105.FIN2	192,0	1,333	0,7910	0,01500	0,09586	0,0009	0,2386200	590,60	8,70	590,00	5,10	584,0	43,0	590,0	5,1	0,102	
BEMO-12_106.FIN2	3640,0	18,010	0,8490	0,01300	0,10280	0,0012	0,3171200	623,90	7,30	630,70	7,10	595,0	35,0	630,7	7,1	1,090	
BEMO-12_107.FIN2	408,0	13,580	0,6110	0,01900	0,07920	0,0016	0,0032633	484,00	12,00	491,40	9,40	427,0	84,0	491,4	9,4	1,529	Rim
BEMO-12_107.FIN2	320,0	2,133	5,2620	0,07000	0,30960	0,0036	0,6405500	1861,00	11,00	1738,00	18,00	2000,0	19,0	2000,0	19,0	13,100	Core
BEMO-12_110.FIN2	765,0	2,145	0,6313	0,00710	0,08034	0,0008	0,3110000	496,60	4,40	498,10	4,50	493,0	26,0	498,1	4,5	0,302	

Sample Name:	[U]							207/235		206/238		207/206		Best age		Discordance	Rim/
Grain #	ppm	U/Th	207/235	2σ error	206/238	2σ error	RHO	Age Ma	2σ error	Age (Ma)	2σ error	Age (Ma)	2σ error	(Ma)	2σ error	%	Core
BEMO-12_111.FIN2	232,0	1,127	1,8460	0,02500	0,18110	0,0016	0,2548700	1060,60	8,80	1072,50	8,90	1037,0	30,0	1037,0	30,0	3,423	
BEMO-12_114.FIN2	226,0	0,911	0,6690	0,01200	0,08300	0,0008	0,4170300	520,10	7,50	513,90	4,80	533,0	37,0	513,9	4,8	1,192	
BEMO-12_115.FIN2	1668,0	6,490	0,7379	0,00690	0,09154	0,0006	0,4398300	560,90	4,00	564,60	3,70	537,0	20,0	564,6	3,7	0,660	
BEMO-12_116.FIN2	268,0	1,606	0,3507	0,00760	0,04828	0,0006	0,2231900	305,30	5,90	303,90	3,40	303,0	49,0	303,9	3,4	0,459	
BEMO-12_117.FIN2	54,8	6,040	0,1250	0,01100	0,01513	0,0005	0,2124800	118,00	10,00	96,80	3,20	430,0	180,0	DISC	DISC	17,966	
BEMO-12_118.FIN2	396,0	1,418	0,3979	0,00720	0,05409	0,0005	0,1679400	339,60	5,20	339,50	3,00	329,0	44,0	339,5	3,0	0,029	
BEMO-12_119.FIN2	450,0	1,133	0,4281	0,00850	0,05802	0,0006	0,1910400	361,10	6,10	363,60	3,60	337,0	45,0	363,6	3,6	0,692	
BEMO-12_120.FIN2	327,0	1,202	0,8770	0,01200	0,10341	0,0009	0,3130100	638,40	6,60	634,30	5,40	645,0	31,0	634,3	5,4	0,642	
BEMO-12_121.FIN2	151,1	0,877	0,8300	0,01800	0,09868	0,0010	0,2856900	611,80	9,80	606,50	5,70	611,0	46,0	606,5	5,7	0,866	
BEMO-12_123.FIN2	454,0	1,832	0,7950	0,01500	0,09810	0,0013	0,6148200	593,70	8,60	603,40	7,80	548,0	32,0	603,4	7,8	1,634	
BEMO-12_124.FIN2	821,0	3,400	0,4163	0,00600	0,05573	0,0006	0,4193600	353,00	4,30	349,50	3,70	371,0	32,0	349,5	3,7	0,992	
BEMO-12_125.FIN2	286,0	0,990	0,3976	0,00750	0,05433	0,0005	0,2744500	339,30	5,40	341,00	3,30	324,0	43,0	341,0	3,3	0,501	
BEMO-12_126.FIN2	189,0	2,763	0,3530	0,01300	0,04944	0,0007	0,1848200	306,40	9,50	311,10	4,50	264,0	76,0	311,1	4,5	1,534	
BEMO-12_127.FIN2	131,0	0,783	0,8550	0,02100	0,09900	0,0011	0,3168600	625,00	12,00	608,70	6,50	682,0	51,0	608,7	6,5	2,608	
BEMO-12_129.FIN2	397,0	1,786	0,4509	0,00770	0,06122	0,0005	0,3764900	378,00	5,50	383,00	3,20	340,0	36,0	383,0	3,2	1,323	
BEMO-12_130.FIN2	326,0	0,698	0,8210	0,02000	0,09880	0,0015	0,3322000	608,00	11,00	607,20	8,60	603,0	51,0	607,2	8,6	0,132	
BEMO-12_131.FIN2	294,0	1,733	0,3590	0,01000	0,05026	0,0007	0,0432540	310,50	7,70	316,10	4,20	266,0	64,0	316,1	4,2	1,804	
BEMO-12_132.FIN2	408,0	10,800	0,8220	0,01600	0,09930	0,0013	0,5041200	609,00	9,10	610,10	7,50	611,0	38,0	610,1	7,5	0,181	
BEMO-12_133.FIN2	803,0	1,636	6,3790	0,07400	0,37570	0,0049	0,5460500	2029,00	10,00	2056,00	23,00	2000,0	22,0	2000,0	22,0	2,800	Rim
BEMO-12_133.FIN2	816,5	1,366	14,5200	0,16000	0,55920	0,0062	0,5529300	2784,00	10,00	2862,00	26,00	2726,0	17,0	2726,0	17,0	4,989	Core
BEMO-12_134.FIN2	155,0	1,185	0,8080	0,01900	0,10660	0,0013	0,0883850	649,20	9,90	652,90	7,30	629,0	47,0	652,9	7,3	0,570	
BEMO-12_135.FIN2	2158,0	11,900	0,4550	0,02000	0,05990	0,0023	0,1426100	380,00	14,00	375,00	14,00	410,0	140,0	375,0	14,0	1,316	Rim
BEMO-12_135.FIN2	568,0	1,167	0,6570	0,01500	0,08280	0,0017	0,4835900	512,00	9,50	513,00	10,00	504,0	51,0	513,0	10,0	0,195	Core
BEMO-12_137.FIN2	357,0	1,790	0,3486	0,00760	0,04811	0,0007	0,2618200	303,00	5,70	302,80	4,40	294,0	50,0	302,8	4,4	0,066	
BEMO-12_138.FIN2	385,0	30,100	0,9940	0,01600	0,11570	0,0011	0,3749600	700,60	8,30	705,50	6,60	676,0	31,0	705,5	6,6	0,699	
BEMO-12_139.FIN2	551,0	1,874	0,3509	0,00630	0,04857	0,0005	0,2226900	305,00	4,70	305,70	3,30	292,0	39,0	305,7	3,3	0,230	
BEMO-12_140.FIN2	260,0	2,142	0,3595	0,00920	0,04971	0,0007	0,5298600	311,00	6,90	312,70	4,20	292,0	53,0	312,7	4,2	0,547	
BEMO-17_1.FIN2	217,4	4,750	0,6370	0,02200	0,08040	0,0012	0,2251500	506,00	16,00	498,40	7,10	540,0	82,0	498,4	7,1	1,502	
BEMO-17_2.FIN2	486,0	7,690	0,9520	0,01500	0,10810	0,0016	0,5945900	678,40	7,60	661,30	9,30	741,0	29,0	661,3	9,3	2,521	
BEMO-17_3.FIN2	514,0	1,448	0,3702	0,00730	0,05047	0,0005	0,4813500	319,40	5,30	317,40	2,90	342,0	41,0	317,4	2,9	0,626	
BEMO-17_4.FIN2	708,0	3,430	0,5713	0,00640	0,07207	0,0005	0,3520400	458,50	4,20	448,60	3,20	507,0	25,0	448,6	3,2	2,159	
BEMO-17_5.FIN2	235,0	1,470	0,8410	0,01500	0,09710	0,0011	0,2454300	620,20	8,30	597,40	6,30	686,0	41,0	597,4	6,3	3,676	
BEMO-17_7.FIN2	182,0	1,349	1,7060	0,02300	0,16900	0,0018	0,5478700	1009,40	8,70	1006,00	10,00	1005,0	25,0	1005,0	25,0	0,100	
BEMO-17_8.FIN2	128,0	2,270	0,5190	0,07900	0,04460	0,0044	0,6876900	432,00	57,00	281,00	27,00	1280,0	190,0	DISC	DISC	34,954	Rim
BEMO-17_8.FIN2	262,3	1,068	8,1500	0,29000	0,34100	0,0110	0,9703900	2241,00	32,00	1886,00	51,00	2590,0	15,0	2590,0	15,0	27,181	Core
BEMO-17_9.FIN2	195,0	1,092	0,8610	0,01400	0,10156	0,0009	0,4096600	629,80	7,40	623,40	5,40	636,0	31,0	623,4	5,4	1,016	
BEMO-17_10.FIN2	345,0	18,400	0,7490	0,04300	0,09440	0,0033	0,4464600	567,00	25,00	581,00	20,00	520,0	110,0	581,0	20,0	2,469	Rim
BEMO-17_10.FIN2	36,4	0,552	1,2740	0,04700	0,13380	0,0022	0,3207400	830,00	21,00	809,00	12,00	848,0	71,0	809,0	12,0	2,530	Core
BEMO-17_11.FIN2	690,0	7,300	0,8450	0,06200	0,09300	0,0045	0,8665100	620,00	34,00	573,00	27,00	771,0	83,0	573,0	27,0	7,581	Rim
BEMO-17_11.FIN2	467,0	0,975	1,7450	0,01900	0,17360	0,0017	0,5382800	1024,60	7,10	1031,70	9,20	1003,0	20,0	1003,0	20,0	2,861	Core
BEMO-17_12.FIN2	474,0	1,401	0,8869	0,00880	0,10494	0,0007	0,4993200	644,90	4,80	643,20	4,20	645,0	21,0	643,2	4,2	0,264	
BEMO-17_13.FIN2	102,9	1,346	0,7810	0,01800	0,09560	0,0010	0,2190100	586,00	11,00	588,80	6,00	564,0	52,0	588,8	6,0	0,478	
BEMO-17_14.FIN2	201,6	1,062	1,1010	0,02100	0,11790	0,0020	0,6718900	752,00	10,00	721,00	12,00	853,0	32,0	721,0	12,0	4,122	
BEMO-17_15.FIN2	390,0	0,673	5,3770	0,04800	0,33380	0,0027	0,5347300	1880,30	7,60	1856,00	13,00	1915,0	13,0	1915,0	13,0	3,081	
BEMO-17_16.FIN2	157,4	1,079	1,1890	0,02300	0,13160	0,0014	0,4638800	793,00	11,00	796,90	7,90	800,0	37,0	796,9	7,9	0,492	
BEMO-17_17.FIN2	177,0	0,635	0,6400	0,01100	0,08127	0,0008	0,3285300	501,70	6,60	503,60	4,70	503,0	38,0	503,6	4,7	0,379	

Sample Name:	[U]							207/235		206/238		207/206		Best age		Discordance	Rim/
Grain #	ppm	U/Th	207/235	2σ error	206/238	2σ error	RHO	Age Ma	2σ error	Age (Ma)	2σ error	Age (Ma)	2σ error	(Ma)	2σ error	%	Core
BEMO-17_18.FIN2	373,8	1,187	0,8390	0,01400	0,09700	0,0009	0,4209300	617,40	7,90	596,70	5,50	700,0	32,0	596,7	5,5	3,353	
BEMO-17_19.FIN2	137,4	1,128	5,9120	0,07400	0,35580	0,0045	0,7117000	1963,00	11,00	1962,00	21,00	1968,0	18,0	1968,0	18,0	0,305	
BEMO-17_20.FIN2	3750,0	1,397	0,8650	0,02300	0,08520	0,0023	0,6711300	632,00	12,00	527,00	14,00	1033,0	52,0	DISC	DISC	16,614	Rim
BEMO-17_20.FIN2	944,0	2,096	1,4490	0,01500	0,14700	0,0013	0,6449900	909,00	6,10	884,20	7,50	969,0	16,0	969,0	16,0	8,751	Core
BEMO-17_21.FIN2	88,7	1,179	0,7270	0,01700	0,08922	0,0009	0,1178600	553,00	10,00	551,50	5,70	544,0	54,0	551,5	5,7	0,271	
BEMO-17_22.FIN2	691,0	8,420	0,9453	0,00920	0,10945	0,0008	0,5209100	675,80	4,90	669,50	4,70	687,0	19,0	669,5	4,7	0,932	
BEMO-17_23.FIN2	225,3	1,202	1,2240	0,01500	0,13280	0,0012	0,2089100	810,70	7,00	803,50	6,70	831,0	30,0	803,5	6,7	0,888	
BEMO-17_24.FIN2	187,4	0,306	0,8100	0,01300	0,09675	0,0009	0,1433400	602,20	7,70	595,20	5,50	612,0	39,0	595,2	5,5	1,162	
BEMO-17_25.FIN2	111,8	1,156	5,3840	0,07300	0,33370	0,0036	0,5214900	1880,00	12,00	1856,00	17,00	1899,0	21,0	1899,0	21,0	2,264	
BEMO-17_26.FIN2	66,2	0,543	6,0600	0,10000	0,34950	0,0044	0,5997500	1982,00	14,00	1931,00	21,00	2018,0	23,0	2018,0	23,0	4,311	
BEMO-17_27.FIN2	585,0	0,883	0,7410	0,01000	0,08910	0,0012	0,6325700	563,90	5,60	551,20	6,80	605,0	29,0	551,2	6,8	2,252	
BEMO-17_28.FIN2	405,8	0,833	1,8090	0,04600	0,14380	0,0038	0,4985600	1050,00	18,00	866,00	22,00	1462,0	43,0	DISC	DISC	40,766	
BEMO-17_29.FIN2	289,5	1,067	1,9380	0,02500	0,17990	0,0019	0,6784800	1094,00	8,70	1066,00	10,00	1135,0	20,0	1135,0	20,0	6,079	
BEMO-17_30.FIN2	139,7	1,325	4,1300	0,11000	0,26220	0,0068	0,8582000	1658,00	21,00	1500,00	35,00	1861,0	31,0	1861,0	31,0	19,398	
BEMO-17_32.FIN2	50,7	1,493	0,7660	0,02400	0,09050	0,0013	0,0282960	575,00	14,00	558,60	7,60	608,0	73,0	558,6	7,6	2,852	
BEMO-17_33.FIN2	298,0	0,679	0,8580	0,01100	0,10313	0,0009	0,3823200	628,00	6,30	632,60	5,10	596,0	28,0	632,6	5,1	0,732	
BEMO-17_34.FIN2	139,9	2,273	0,3539	0,00960	0,04930	0,0006	0,0845770	306,70	7,20	310,20	3,40	277,0	60,0	310,2	3,4	1,141	
BEMO-17_35.FIN2	625,0	4,630	9,0000	0,21000	0,38670	0,0077	0,9264200	2330,00	21,00	2104,00	36,00	2529,0	14,0	2529,0	14,0	16,805	
BEMO-17_36.FIN2	852,0	1,549	3,3300	0,16000	0,21920	0,0094	0,9732900	1458,00	40,00	1270,00	50,00	1781,0	18,0	1781,0	18,0	28,692	
BEMO-17_37.FIN2	613,0	2,196	0,3448	0,00510	0,04703	0,0004	0,2746300	300,50	3,80	296,30	2,50	331,0	34,0	296,3	2,5	1,398	
BEMO-17_38.FIN2	58,7	1,240	0,7640	0,02200	0,09390	0,0014	0,1947400	575,00	13,00	578,30	8,30	556,0	72,0	578,3	8,3	0,574	
BEMO-17_39.FIN2	313,4	1,137	1,1680	0,02200	0,12890	0,0024	0,4809600	784,00	10,00	781,00	14,00	799,0	43,0	781,0	14,0	0,383	
BEMO-17_40.FIN2	708,0	0,701	0,6742	0,00880	0,07100	0,0010	0,7011500	522,80	5,30	442,00	6,20	898,0	22,0	DISC	DISC	15,455	
BEMO-17_41.FIN2	475,0	2,692	0,3706	0,00600	0,05127	0,0006	0,4035600	319,70	4,50	322,30	3,60	294,0	35,0	322,3	3,6	0,813	
BEMO-17_42.FIN2	447,0	5,730	0,5700	0,03200	0,07620	0,0044	0,5099500	456,00	21,00	473,00	27,00	390,0	110,0	473,0	27,0	3,728	Rim
BEMO-17_42.FIN2	570,0	2,992	1,0580	0,02300	0,11680	0,0020	0,7044300	732,00	12,00	712,00	11,00	784,0	34,0	712,0	11,0	2,732	Core
BEMO-17_43.FIN2	85,9	0,960	5,5480	0,06600	0,33370	0,0032	0,5755600	1906,00	10,00	1858,00	16,00	1949,0	17,0	1949,0	17,0	4,669	
BEMO-17_44.FIN2	159,7	1,840	4,4800	0,11000	0,25480	0,0054	0,8061700	1724,00	21,00	1462,00	28,00	2035,0	28,0	2035,0	28,0	28,157	
BEMO-17_45.FIN2	309,0	1,025	0,7220	0,02800	0,07900	0,0024	0,4410900	550,00	17,00	490,00	15,00	760,0	79,0	490,0	15,0	10,909	
BEMO-17_46.FIN2	75,8	4,230	0,7400	0,12000	0,06470	0,0060	0,2569000	560,00	67,00	404,00	36,00	1200,0	280,0	DISC	DISC	27,857	Rim
BEMO-17_46.FIN2	505,0	0,993	10,5800	0,17000	0,41090	0,0062	0,9182200	2488,00	14,00	2221,00	28,00	2661,0	12,0	2661,0	12,0	16,535	Core
BEMO-17_47.FIN2	835,0	5,700	1,5750	0,02300	0,14580	0,0022	0,7763200	958,80	9,40	878,00	12,00	1109,0	20,0	1109,0	20,0	20,830	
BEMO-17_48.FIN2	393,0	1,435	0,8680	0,01500	0,10170	0,0013	0,6167600	633,50	8,30	624,30	7,60	633,0	31,0	624,3	7,6	1,452	
BEMO-17_49.FIN2	573,0	5,780	0,5770	0,01000	0,07190	0,0011	0,6862100	461,50	6,70	447,30	6,40	497,0	29,0	447,3	6,4	3,077	
BEMO-17_50.FIN2	187,0	0,937	0,5150	0,01100	0,05986	0,0009	0,3827100	420,40	7,70	374,70	5,30	648,0	47,0	374,7	5,3	10,871	
BEMO-17_51.FIN2	41,5	1,129	0,8250	0,02800	0,09800	0,0016	0,2377100	609,00	15,00	602,60	9,20	609,0	71,0	602,6	9,2	1,051	
BEMO-17_52.FIN2	184,0	2,875	11,2900	0,17000	0,47210	0,0075	0,7133100	2543,00	15,00	2490,00	34,00	2581,0	21,0	2581,0	21,0	3,526	
BEMO-17_53.FIN2	1362,0	2,216	0,3281	0,00590	0,04506	0,0006	0,3443500	287,90	4,50	284,10	3,70	310,0	41,0	284,1	3,7	1,320	
BEMO-17_54.FIN2	840,0	7,110	0,6051	0,00720	0,07581	0,0008	0,4184800	480,10	4,60	471,00	4,70	524,0	26,0	471,0	4,7	1,895	
BEMO-17_55.FIN2	450,0	1,408	1,2650	0,02600	0,13710	0,0025	0,7606400	829,00	12,00	827,00	14,00	845,0	29,0	827,0	14,0	0,241	
BEMO-17_56.FIN2	368,0	9,270	0,8080	0,02500	0,08500	0,0024	0,6276600	599,00	14,00	526,00	14,00	890,0	52,0	526,0	14,0	12,187	
BEMO-17_57.FIN2	114,4	1,236	0,9290	0,01900	0,10660	0,0017	0,4007200	665,10	9,90	652,50	9,80	699,0	46,0	652,5	9,8	1,894	
BEMO-17_58.FIN2	924,0	11,100	1,4680	0,09800	0,15000	0,0110	0,4869800	915,00	41,00	900,00	61,00	990,0	150,0	900,0	150,0	9,091	Rim
BEMO-17_58.FIN2	52,4	1,067	6,8400	0,26000	0,37900	0,0110	0,8895800	2077,00	37,00	2065,00	54,00	2097,0	33,0	2097,0	33,0	1,526	Core
BEMO-17_59.FIN2	181,8	2,700	0,7170	0,02000	0,07570	0,0010	0,3817600	546,00	12,00	470,40	6,20	872,0	55,0	470,4	6,2	13,846	
BEMO-17_60.FIN2	708,0	3,660	0,7977	0,00800	0,09014	0,0008	0,5125900	595,10	4,50	556,30	4,80	751,0	20,0	556,3	4,8	6,520	
BEMO-17_61.FIN2	487,0	30,300	0,9250	0,02500	0,10970	0,0021	0,6449400	664,00	13,00	671,00	12,00	657,0	45,0	671,0	12,0	1,054	Rim

Sample Name:	[U]							207/235		206/238		207/206		Best age		Discordance	Rim/
Grain #	ppm	U/Th	207/235	2σ error	206/238	2σ error	RHO	Age Ma	2σ error	Age (Ma)	2σ error	Age (Ma)	2σ error	(Ma)	2σ error	%	Core
BEMO-17_61.FIN2	115,6	0,680	1,7640	0,03400	0,17750	0,0025	0,4040800	1031,00	13,00	1053,00	14,00	999,0	36,0	999,0	36,0	5,405	Core
BEMO-17_62.FIN2	864,0	2,321	0,3186	0,00670	0,03993	0,0005	0,6287400	280,50	5,10	252,40	3,30	521,0	37,0	252,4	3,3	10,018	
BEMO-17_63.FIN2	130,9	1,603	0,9210	0,01800	0,10960	0,0011	0,4630500	661,10	9,30	670,00	6,50	639,0	37,0	670,0	6,5	1,346	
BEMO-17_64.FIN2	223,0	2,160	1,7850	0,03100	0,17590	0,0027	0,7603800	1039,00	11,00	1044,00	15,00	1037,0	24,0	1037,0	24,0	0,675	
BEMO-17_65.FIN2	580,0	2,050	0,6880	0,01400	0,08380	0,0011	0,5081900	531,00	8,50	518,90	6,70	593,0	39,0	518,9	6,7	2,279	
BEMO-17_66.FIN2	372,0	2,985	5,2970	0,06000	0,33480	0,0033	0,7383100	1866,60	9,70	1861,00	16,00	1886,0	14,0	1886,0	14,0	1,326	
BEMO-17_67.FIN2	417,0	1,970	1,6030	0,03600	0,16200	0,0031	0,8800800	968,00	14,00	967,00	17,00	981,0	21,0	981,0	21,0	1,427	
BEMO-17_68.FIN2	195,0	1,442	0,7410	0,01300	0,09110	0,0010	0,3643100	561,80	7,60	561,90	5,70	562,0	39,0	561,9	5,7	0,018	
BEMO-17_69.FIN2	145,5	1,620	1,3020	0,01900	0,13980	0,0012	0,5024100	847,30	7,90	843,60	7,00	853,0	27,0	843,6	7,0	0,437	
BEMO-17_70.FIN2	371,0	6,620	1,8090	0,02000	0,17660	0,0015	0,5600400	1047,80	7,10	1047,90	8,50	1046,0	19,0	1046,0	19,0	0,182	
BEMO-17_71.FIN2	73,9	0,824	1,7810	0,02900	0,17540	0,0017	0,1546300	1036,00	11,00	1041,50	9,30	1024,0	36,0	1024,0	36,0	1,709	
BEMO-17_72.FIN2	55,3	2,890	1,4470	0,03900	0,14650	0,0020	0,2245400	906,00	16,00	881,00	11,00	953,0	54,0	953,0	54,0	7,555	
BEMO-17_73.FIN2	171,0	1,830	0,7500	0,01500	0,08955	0,0009	0,4153000	567,60	8,80	552,80	5,40	599,0	42,0	552,8	5,4	2,607	
BEMO-17_74.FIN2	217,0	1,950	0,5900	0,01000	0,07585	0,0008	0,2222900	470,90	6,70	471,20	5,00	457,0	42,0	471,2	5,0	0,064	
BEMO-17_75.FIN2	149,0	2,690	6,6300	0,13000	0,37390	0,0057	0,7380700	2059,00	18,00	2046,00	27,00	2075,0	23,0	2075,0	23,0	1,398	
BEMO-17_76.FIN2	292,0	0,986	0,8400	0,01100	0,10139	0,0009	0,2375100	618,50	6,00	622,50	5,10	606,0	30,0	622,5	5,1	0,647	
BEMO-17_77.FIN2	375,0	9,930	0,8630	0,01000	0,10328	0,0010	0,3565500	631,20	5,60	633,50	5,60	629,0	27,0	633,5	5,6	0,364	
BEMO-17_78.FIN2	330,0	1,589	1,5050	0,01600	0,15620	0,0011	0,4731800	931,70	6,60	935,80	6,00	931,0	20,0	931,0	20,0	0,516	
BEMO-17_79.FIN2	295,6	1,580	0,3442	0,00650	0,04725	0,0004	0,2403000	299,90	4,90	297,60	2,30	336,0	42,0	297,6	2,3	0,767	
BEMO-17_80.FIN2	256,6	1,167	0,5571	0,00930	0,07245	0,0007	0,3272800	448,90	6,00	450,90	4,10	450,0	34,0	450,9	4,1	0,446	
BEMO-17_81.FIN2	567,0	6,560	1,3670	0,02400	0,13960	0,0019	0,6825700	874,00	10,00	842,00	11,00	957,0	28,0	842,0	11,0	3,661	
BEMO-17_82.FIN2	1148,0	1,666	0,3460	0,00400	0,04651	0,0005	0,4987900	301,60	3,00	293,10	3,10	372,0	25,0	293,1	3,1	2,818	
BEMO-17_83.FIN2	182,6	0,714	5,2580	0,04700	0,32920	0,0026	0,5009500	1861,10	7,60	1834,00	13,00	1897,0	15,0	1897,0	15,0	3,321	
BEMO-17_84.FIN2	761,0	1,877	0,6250	0,02300	0,07140	0,0032	0,3843500	493,00	15,00	445,00	19,00	765,0	99,0	445,0	19,0	9,736	Rim
BEMO-17_84.FIN2	395,0	1,272	0,8980	0,01400	0,10700	0,0014	0,7266000	649,50	7,80	655,00	8,40	633,0	25,0	655,0	8,4	0,847	Core
BEMO-17_85.FIN2	489,0	2,255	1,6150	0,02700	0,15950	0,0025	0,8308300	974,00	11,00	953,00	14,00	1026,0	20,0	1026,0	20,0	7,115	
BEMO-17_86.FIN2	697,0	5,880	7,0800	0,13000	0,36530	0,0052	0,7860400	2118,00	16,00	2005,00	25,00	2240,0	20,0	2240,0	20,0	10,491	
BEMO-17_87.FIN2	426,0	1,184	9,0490	0,09500	0,42800	0,0034	0,8094400	2343,00	9,40	2296,00	15,00	2393,0	10,0	2393,0	10,0	4,053	
BEMO-17_88.FIN2	59,9	0,743	9,3900	0,18000	0,39120	0,0073	0,8492500	2371,00	18,00	2126,00	34,00	2605,0	17,0	2605,0	17,0	18,388	
BEMO-17_89.FIN2	479,0	1,521	4,8980	0,04500	0,31160	0,0031	0,7628400	1800,80	7,70	1748,00	15,00	1872,0	14,0	1872,0	14,0	6,624	
BEMO-17_90.FIN2	302,1	2,420	6,6100	0,10000	0,31340	0,0042	0,6874300	2059,00	13,00	1757,00	21,00	2388,0	20,0	2388,0	20,0	26,424	
BEMO-17_91.FIN2	248,7	2,630	6,4800	0,11000	0,35980	0,0058	0,7250900	2041,00	16,00	1980,00	28,00	2111,0	23,0	2111,0	23,0	6,206	
BEMO-17_92.FIN2	518,0	2,790	0,3595	0,00620	0,04883	0,0005	0,4026400	311,40	4,60	307,30	2,80	347,0	37,0	307,3	2,8	1,317	
BEMO-17_93.FIN2	1311,0	74,400	0,3630	0,01400	0,04900	0,0020	0,5934600	314,00	10,00	308,00	12,00	388,0	78,0	308,0	12,0	1,911	Rim
BEMO-17_93.FIN2	384,0	4,460	0,5640	0,01500	0,06960	0,0011	0,5060000	453,00	9,80	433,90	6,70	535,0	48,0	433,9	6,7	4,216	Core
BEMO-17_94.FIN2	132,4	1,696	6,9580	0,06900	0,38300	0,0035	0,6235800	2104,60	8,90	2090,00	16,00	2120,0	15,0	2120,0	15,0	1,415	
BEMO-17_96.FIN2	54,9	1,159	0,7270	0,02300	0,08810	0,0012	0,1418900	552,00	13,00	544,10	7,00	567,0	69,0	544,1	7,0	1,431	
BEMO-17_97.FIN2	497,0	5,420	10,1300	0,17000	0,42100	0,0053	0,8316700	2443,00	15,00	2264,00	24,00	2596,0	15,0	2596,0	15,0	12,789	
BEMO-17_98.FIN2	334,0	1,081	0,9720	0,01800	0,11250	0,0014	0,7931100	688,10	9,40	687,10	8,00	687,0	25,0	687,1	8,0	0,145	
BEMO-17_99.FIN2	126,6	2,230	0,8340	0,02300	0,09440	0,0016	0,4829800	616,00	13,00	581,30	9,50	728,0	55,0	581,3	9,5	5,633	
BEMO-17_100.FIN2	185,8	0,720	1,4550	0,02300	0,14710	0,0019	0,7665200	910,60	9,60	884,00	11,00	964,0	28,0	964,0	28,0	8,299	
BEMO-17_101.FIN2	169,1	1,578	2,5870	0,06200	0,18490	0,0038	0,8745600	1295,00	17,00	1093,00	21,00	1641,0	23,0	DISC	DISC	33,394	
BEMO-17_102.FIN2	61,1	0,773	10,5400	0,15000	0,45320	0,0063	0,6863400	2481,00	13,00	2408,00	28,00	2533,0	18,0	2533,0	18,0	4,935	
BEMO-17_103.FIN2	776,0	26,100	0,8890	0,01200	0,10020	0,0014	0,6628300	645,00	6,20	615,30	8,40	734,0	26,0	615,3	8,4	4,605	
BEMO-17_104.FIN2	987,0	1,860	0,6720	0,02300	0,08290	0,0027	0,6838500	524,00	12,00	513,00	16,00	554,0	57,0	513,0	16,0	2,099	
BEMO-17_105.FIN2	206,5	1,774	0,6440	0,01100	0,08021	0,0007	0,1939600	503,70	6,50	497,30	4,30	522,0	38,0	497,3	4,3	1,271	
BEMO-17_106.FIN2	255,2	0,898	0,7710	0,01100	0,09353	0,0007	0,3789900	579,60	6,20	576,30	4,30	580,0	29,0	576,3	4,3	0,569	

Sample Name:	[U]							207/235		206/238		207/206		Best age		Discordance	Rim/
Grain #	ppm	U/Th	207/235	2σ error	206/238	2σ error	RHO	Age Ma	2σ error	Age (Ma)	2σ error	Age (Ma)	2σ error	(Ma)	2σ error	%	Core
BEMO-17_107.FIN2	637,0	1,048	10,3800	0,21000	0,42920	0,0085	0,9607400	2463,00	19,00	2298,00	38,00	2607,1	9,3	2607,1	9,3	11,856	
BEMO-17_108.FIN2	761,0	2,343	0,3540	0,00540	0,04222	0,0006	0,5256700	307,50	4,10	266,50	3,70	626,0	33,0	266,5	3,7	13,333	
BEMO-17_109.FIN2	375,2	1,151	0,8390	0,01200	0,09850	0,0012	0,5454600	618,60	7,00	605,50	6,80	671,0	28,0	605,5	6,8	2,118	
BEMO-17_111.FIN2	362,3	2,540	0,3480	0,01200	0,04497	0,0008	0,2731800	302,90	9,00	283,50	4,80	471,0	80,0	283,5	4,8	6,405	
BEMO-17_112.FIN2	407,0	2,650	1,0740	0,01600	0,12200	0,0012	0,1121500	739,40	7,80	742,90	6,40	738,0	26,0	742,9	6,4	0,473	
BEMO-17_113.FIN2	123,8	0,610	0,8030	0,02300	0,09230	0,0011	0,3961000	596,00	13,00	569,20	6,60	694,0	56,0	569,2	6,6	4,497	
BEMO-17_114.FIN2	0,2	-0,490	94,0000	45,00000	0,73000	0,3100	0,9318600	4230,00	410,00	3200,00	940,00	5160,0	350,0	DISC	DISC	37,984	
BEMO-17_115.FIN2	290,0	10,760	0,6030	0,01300	0,07520	0,0014	0,4160600	478,70	8,20	467,00	8,40	523,0	45,0	467,0	8,4	2,444	
BEMO-17_116.FIN2	876,0	1,910	0,3417	0,00750	0,04401	0,0006	0,4444300	297,90	5,60	277,60	3,60	448,0	43,0	277,6	3,6	6,814	
BEMO-17_117.FIN2	446,0	8,330	0,6110	0,01600	0,07700	0,0018	0,6282200	483,00	10,00	478,00	11,00	506,0	50,0	478,0	11,0	1,035	
BEMO-17_118.FIN2	219,0	0,903	5,2500	0,12000	0,23670	0,0044	0,9221500	1854,00	21,00	1368,00	23,00	2457,0	16,0	DISC	DISC	44,322	
BEMO-17_119.FIN2	838,0	2,750	1,4180	0,01600	0,13810	0,0015	0,6950600	896,70	7,00	834,00	8,30	1046,0	18,0	834,0	8,3	6,992	
BEMO-17_120.FIN2	324,0	15,900	1,5560	0,02000	0,15680	0,0019	0,5973700	952,80	8,20	939,00	11,00	970,0	24,0	970,0	24,0	3,196	
BEMO-17_121.FIN2	45,5	1,673	5,5300	0,14000	0,32320	0,0072	0,8130100	1900,00	22,00	1802,00	36,00	2008,0	27,0	2008,0	27,0	10,259	
BEMO-17_122.FIN2	188,0	24,300	0,7380	0,01500	0,09040	0,0011	0,3913100	559,90	8,60	557,80	6,80	567,0	40,0	557,8	6,8	0,375	
BEMO-17_123.FIN2	276,0	2,075	0,3736	0,00800	0,05042	0,0005	0,2252600	321,70	5,90	317,10	2,80	347,0	48,0	317,1	2,8	1,430	
BEMO-17_124.FIN2	506,3	11,600	0,8780	0,01300	0,10200	0,0013	0,5443300	639,20	7,20	625,90	7,50	680,0	29,0	625,9	7,5	2,081	Rim
BEMO-17_124.FIN2	411,0	2,070	2,1300	0,12000	0,16840	0,0098	0,8449500	1157,90	41,00	1002,00	54,00	1451,0	61,0	DISC	DISC	30,944	Core
BEMO-17_125.FIN2	860,0	1,140	0,7133	0,00960	0,08836	0,0010	0,6246500	546,80	5,60	545,80	5,70	547,0	23,0	545,8	5,7	0,183	
BEMO-17_126.FIN2	601,0	8,380	0,4850	0,02800	0,06000	0,0024	0,4117900	401,00	19,00	376,00	15,00	520,0	130,0	376,0	15,0	6,234	Rim
BEMO-17_126.FIN2	426,0	7,240	0,6290	0,01100	0,07839	0,0008	0,1631200	494,40	6,70	486,50	4,90	504,0	40,0	486,5	4,9	1,508	Core
BEMO-17_127.FIN2	120,7	1,530	0,8120	0,02100	0,09060	0,0014	0,3026100	602,00	12,00	559,20	8,50	747,0	56,0	559,2	8,5	7,110	
BEMO-17_128.FIN2	219,0	0,771	1,7240	0,02000	0,16830	0,0015	0,4754000	1016,40	7,30	1002,70	8,30	1041,0	22,0	1041,0	22,0	3,679	
BEMO-17_129.FIN2	404,0	2,890	0,4065	0,00640	0,05569	0,0005	0,1772000	346,00	4,60	349,30	2,80	317,0	37,0	349,3	2,8	0,954	
BEMO-17_130.FIN2	858,0	3,180	1,1320	0,01100	0,12345	0,0009	0,6341000	768,40	5,10	750,30	5,20	816,0	16,0	750,3	5,2	2,356	
BEMO-17_131.FIN2	163,9	1,541	10,8300	0,19000	0,44490	0,0068	0,8218500	2509,00	15,00	2370,00	30,00	2615,0	15,0	2615,0	15,0	9,369	
BEMO-17_132.FIN2	117,5	1,050	1,4010	0,06300	0,13670	0,0056	0,6007300	886,00	27,00	825,00	32,00	1054,0	67,0	825,0	32,0	6,885	
BEMO-17_133.FIN2	160,0	0,739	0,7900	0,01500	0,09480	0,0010	0,4543200	590,90	8,60	583,80	5,90	609,0	37,0	583,8	5,9	1,202	
BEMO-17_134.FIN2	952,5	1,354	0,3868	0,00450	0,05248	0,0004	0,4796200	331,90	3,30	329,70	2,70	324,0	23,0	329,7	2,7	0,663	
BEMO-17_135.FIN2	149,0	1,636	1,3240	0,03300	0,13960	0,0025	0,7737400	854,00	15,00	844,00	14,00	865,0	33,0	844,0	14,0	1,171	
BEMO-17_136.FIN2	584,0	1,843	0,3690	0,00750	0,05036	0,0005	0,1746200	318,60	5,60	316,70	3,00	307,0	46,0	316,7	3,0	0,596	
GAL-10_1.FIN2	105,3	0,599	1,7550	0,02600	0,17170	0,0019	0,4171500	1028,70	9,80	1021,00	10,00	1038,0	30,0	1038,0	30,0	1,638	
GAL-10_2.FIN2	146,4	1,968	0,6130	0,01700	0,07620	0,0013	0,5040300	484,00	11,00	473,00	8,00	524,0	53,0	473,0	8,0	2,273	
GAL-10_3.FIN2	323,0	1,196	1,0930	0,01500	0,12120	0,0017	0,6555400	748,90	7,50	737,00	10,00	778,0	29,0	737,0	10,0	1,589	
GAL-10_4.FIN2	230,1	0,577	4,7870	0,09500	0,30700	0,0065	0,7229400	1781,00	17,00	1725,00	32,00	1847,0	27,0	1847,0	27,0	6,605	
GAL-10_5.FIN2	489,0	3,420	0,9000	0,01200	0,10520	0,0012	0,5404900	651,50	6,40	644,60	7,00	663,0	25,0	644,6	7,0	1,059	
GAL-10_6.FIN2	851,0	1,632	0,3373	0,00540	0,04632	0,0006	0,6675100	294,80	4,10	291,80	3,50	308,0	31,0	291,8	3,5	1,018	
GAL-10_7.FIN2	202,9	1,078	1,1440	0,02400	0,12040	0,0023	0,4938500	774,00	12,00	784,00	13,00	755,0	43,0	784,0	13,0	1,292	
GAL-10_8.FIN2	1032,0	5,300	0,5880	0,01100	0,06500	0,0011	0,7462000	468,80	7,20	405,60	6,60	775,0	28,0	405,6	6,6	13,481	
GAL-10_9.FIN2	710,0	5,660	0,5680	0,02600	0,07280	0,0031	0,5072500	456,00	17,00	453,00	19,00	469,0	93,0	453,0	19,0	0,658	Rim
GAL-10_9.FIN2	237,0	1,883	1,0030	0,02400	0,11310	0,0018	0,4671000	704,90	12,00	691,00	11,00	733,0	42,0	691,0	11,0	1,847	Core
GAL-10_10.FIN2	534,0	1,310	0,7640	0,01500	0,08780	0,0015	0,7383900	575,10	8,50	542,40	8,70	692,0	31,0	542,4	8,7	5,686	
GAL-10_11.FIN2	1500,0	2,300	0,4900	0,02000	0,05030	0,0026	0,4501900	404,00	13,00	316,00	16,00	950,0	100,0	DISC	DISC	21,782	Rim
GAL-10_11.FIN2	757,0	2,779	1,1660	0,01700	0,11580	0,0018	0,7419800	783,90	8,10	706,00	10,00	1006,0	22,0	706,0	10,0	9,937	Core
GAL-10_12.FIN2	375,8	0,928	0,6280	0,01200	0,07520	0,0011	0,5832900	494,10	7,60	467,20	6,70	609,0	34,0	467,2	6,7	5,444	
GAL-10_13.FIN2	917,0	4,940	0,3625	0,00670	0,04722	0,0008	0,5219500	313,70	4,90	297,40	4,60	437,0	39,0	297,4	4,6	5,196	

Sample Name:	[U]							207/235		206/238		207/206		Best age		Discordance	Rim/
Grain #	ppm	U/Th	207/235	2σ error	206/238	2σ error	RHO	Age Ma	2σ error	Age (Ma)	2σ error	Age (Ma)	2σ error	(Ma)	2σ error	%	Core
GAL-10_14.FIN2	448,0	0,630	0,8190	0,01400	0,09820	0,0015	0,6078700	606,50	7,90	603,70	9,10	622,0	34,0	603,7	9,1	0,462	
GAL-10_15.FIN2	400,0	4,890	0,9460	0,01600	0,11150	0,0016	0,7293000	675,70	8,80	681,40	9,00	660,0	26,0	681,4	9,0	0,844	
GAL-10_16.FIN2	623,0	2,860	0,8330	0,01300	0,09830	0,0016	0,6487500	614,20	7,10	603,90	9,10	649,0	28,0	603,9	9,1	1,677	
GAL-10_17.FIN2	197,0	2,660	0,7630	0,01300	0,09250	0,0016	0,7550200	574,70	7,70	571,30	9,80	596,0	32,0	571,3	9,8	0,592	
GAL-10_18.FIN2	218,0	1,800	0,6830	0,01300	0,08370	0,0012	0,5254300	527,60	7,50	518,10	7,30	560,0	32,0	518,1	7,3	1,801	
GAL-10_19.FIN2	291,0	1,351	12,4900	0,27000	0,49140	0,0095	0,8290300	2637,00	21,00	2574,00	41,00	2689,0	20,0	2689,0	20,0	4,277	
GAL-10_20.FIN2	405,0	0,723	1,8130	0,02800	0,17750	0,0025	0,5763000	1048,00	10,00	1053,00	14,00	1044,0	25,0	1044,0	25,0	0,862	
GAL-10_21.FIN2	100,4	2,106	0,8700	0,02100	0,10360	0,0017	0,4162700	634,00	11,00	635,10	9,80	620,0	48,0	635,1	9,8	0,174	
GAL-10_22.FIN2	127,3	1,040	11,4600	0,15000	0,46440	0,0066	0,7922700	2559,00	12,00	2457,00	29,00	2646,0	19,0	2646,0	19,0	7,143	
GAL-10_23.FIN2	580,0	3,270	0,7380	0,01100	0,08970	0,0013	0,7289200	560,50	6,50	553,90	7,50	626,0	24,0	553,9	7,5	1,178	
GAL-10_24.FIN2	429,0	3,613	0,3565	0,00610	0,04883	0,0007	0,5337500	309,20	4,60	307,30	4,10	326,0	34,0	307,3	4,1	0,614	
GAL-10_25.FIN2	101,6	1,518	1,2020	0,02400	0,13030	0,0017	0,3551400	801,00	12,00	789,10	9,80	829,0	39,0	789,1	9,8	1,486	
GAL-10_26.FIN2	184,7	1,327	0,7340	0,01100	0,09060	0,0010	0,2114000	558,50	6,20	559,20	6,00	560,0	35,0	559,2	6,0	0,125	
GAL-10_27.FIN2	256,7	0,661	8,9700	0,15000	0,37410	0,0066	0,8253600	2333,00	15,00	2048,00	31,00	2599,0	16,0	2599,0	16,0	21,200	
GAL-10_28.FIN2	751,0	1,965	0,5630	0,00700	0,07027	0,0008	0,6103000	453,10	4,50	437,70	4,70	541,0	23,0	437,7	4,7	3,399	
GAL-10_29.FIN2	450,0	13,800	0,5980	0,01000	0,07650	0,0013	0,4957900	475,30	6,60	475,20	7,50	494,0	39,0	475,2	7,5	0,021	
GAL-10_30.FIN2	365,0	10,700	1,0700	0,05100	0,10970	0,0020	0,4768400	738,00	25,00	671,00	12,00	959,0	93,0	671,0	12,0	9,079	Rim
GAL-10_30.FIN2	56,2	0,244	5,2580	0,08000	0,32230	0,0040	0,7277300	1860,00	13,00	1800,00	19,00	1939,0	22,0	1939,0	22,0	7,169	Core
GAL-10_31.FIN2	336,0	11,160	0,5710	0,01200	0,07350	0,0013	0,5818300	458,20	8,00	457,10	7,50	463,0	40,0	457,1	7,5	0,240	
GAL-10_32.FIN2	111,2	1,816	0,8600	0,01900	0,10200	0,0014	0,4795100	628,00	10,00	625,70	8,30	636,0	41,0	625,7	8,3	0,366	
GAL-10_33.FIN2	223,3	1,195	1,4300	0,02400	0,14920	0,0022	0,7371700	900,00	10,00	896,00	12,00	918,0	24,0	918,0	24,0	2,397	
GAL-10_34.FIN2	396,5	7,700	1,0490	0,02600	0,11650	0,0026	0,7769100	726,00	13,00	710,00	15,00	788,0	34,0	710,0	15,0	2,204	
GAL-10_35.FIN2	32,0	-7,000	0,7410	0,08400	0,09870	0,0070	0,3911400	574,00	61,00	606,00	41,00	470,0	240,0	606,0	41,0	5,575	Rim
GAL-10_35.FIN2	255,0	2,060	10,7800	0,14000	0,43700	0,0059	0,8194900	2502,00	13,00	2335,00	26,00	2650,0	14,0	2650,0	14,0	11,887	Core
GAL-10_36.FIN2	323,0	0,863	5,1540	0,06100	0,32350	0,0043	0,7187200	1844,00	10,00	1805,00	21,00	1899,0	16,0	1899,0	16,0	4,950	
GAL-10_37.FIN2	741,0	1,416	10,5100	0,14000	0,42150	0,0058	0,7568300	2479,00	12,00	2266,00	27,00	2666,0	15,0	2666,0	15,0	15,004	
GAL-10_38.FIN2	4050,0	1,770	0,5090	0,01800	0,02979	0,0010	0,5624000	417,00	12,00	189,20	6,20	1999,0	57,0	DISC	DISC	54,628	Rim
GAL-10_38.FIN2	457,0	1,718	0,4500	0,01100	0,05007	0,0010	0,4988300	376,90	7,70	314,90	6,00	776,0	48,0	DISC	DISC	16,450	Core
GAL-10_39.FIN2	308,0	1,876	1,2090	0,02700	0,13150	0,0032	0,4373900	804,00	12,00	796,00	18,00	816,0	57,0	796,0	18,0	0,995	
GAL-10_40.FIN2	390,0	1,260	5,1400	0,12000	0,29180	0,0067	0,9069600	1837,00	19,00	1647,00	33,00	2060,0	17,0	2060,0	17,0	20,049	
GAL-10_41.FIN2	17,4	0,819	0,5160	0,03400	0,01385	0,0006	0,0316760	416,00	23,00	88,60	3,50	3250,0	120,0	DISC	DISC	78,702	
GAL-10_42.FIN2	156,0	1,475	10,6600	0,24000	0,43990	0,0090	0,8629200	2491,00	21,00	2346,00	41,00	2608,0	20,0	2608,0	20,0	10,046	
GAL-10_43.FIN2	3160,0	13,100	0,5080	0,01100	0,05710	0,0013	0,8236400	416,70	7,50	357,80	8,20	755,0	28,0	357,8	8,2	14,135	Rim
GAL-10_43.FIN2	533,0	9,100	0,6380	0,01500	0,07800	0,0012	0,6742500	501,40	8,60	484,10	7,10	575,0	37,0	484,1	7,1	3,450	Core
GAL-10_44.FIN2	512,5	19,400	0,8770	0,01100	0,10260	0,0010	0,5700200	638,70	6,10	629,80	6,00	660,0	24,0	629,8	6,0	1,393	
GAL-10_45.FIN2	229,0	4,520	4,3200	0,21000	0,28500	0,0110	0,9623500	1683,00	41,00	1614,00	53,00	1781,0	30,0	1781,0	30,0	9,377	
GAL-10_46.FIN2	263,0	0,748	0,8590	0,01400	0,10300	0,0011	0,4182100	628,40	7,60	631,80	6,70	609,0	33,0	631,8	6,7	0,541	
GAL-10_47.FIN2	427,0	0,613	1,4430	0,03100	0,14440	0,0026	0,6990700	906,00	13,00	869,00	15,00	990,0	32,0	990,0	32,0	12,222	
GAL-10_48.FIN2	1034,0	1,870	0,3535	0,00680	0,04848	0,0009	0,6401300	308,40	5,50	305,10	5,50	331,0	38,0	305,1	5,5	1,070	
GAL-10_49.FIN2	202,9	1,163	1,7130	0,03500	0,16580	0,0029	0,5924900	1012,90	13,00	988,00	16,00	1044,0	34,0	1044,0	34,0	5,364	
GAL-10_50.FIN2	218,4	3,220	1,4790	0,03000	0,15500	0,0024	0,6582900	920,00	12,00	928,00	14,00	891,0	32,0	891,0	32,0	4,153	
GAL-10_51.FIN2	487,0	3,960	0,8570	0,01100	0,10100	0,0012	0,5946700	627,90	5,90	619,90	6,80	645,0	24,0	619,9	6,8	1,274	
GAL-10_52.FIN2	264,0	2,100	1,1250	0,01600	0,12410	0,0015	0,5923700	764,20	7,60	753,70	8,50	792,0	25,0	753,7	8,5	1,374	
GAL-10_53.FIN2	1025,0	1,907	1,5290	0,03200	0,14810	0,0030	0,8361600	940,00	13,00	890,00	17,00	1055,0	26,0	1055,0	26,0	15,640	
GAL-10_54.FIN2	634,0	0,610	0,7510	0,01100	0,08920	0,0014	0,6613100	568,40	6,10	550,70	8,10	638,0	29,0	550,7	8,1	3,114	
GAL-10_55.FIN2	709,0	0,877	0,0310	0,00150	0,00471	0,0001	0,0722450	31,00	1,40	30,29	0,53	89,0	91,0	30,3	0,5	2,290	
GAL-10_56.FIN2	616,0	9,920	0,8720	0,01400	0,10040	0,0015	0,6147800	636,00	7,40	616,50	8,50	696,0	29,0	616,5	8,5	3,066	

Sample Name:	[U]							207/235		206/238		207/206		Best age		Discordance	Rim/
Grain #	ppm	U/Th	207/235	2σ error	206/238	2σ error	RHO	Age Ma	2σ error	Age (Ma)	2σ error	Age (Ma)	2σ error	(Ma)	2σ error	%	Core
GAL-10_57.FIN2	83,1	1,212	6,1660	0,09200	0,35540	0,0057	0,6637400	1998,00	13,00	1959,00	27,00	2037,0	23,0	2037,0	23,0	3,829	
GAL-10_58.FIN2	159,0	1,055	0,8450	0,01500	0,10110	0,0013	0,4290200	621,70	8,80	620,40	7,70	622,0	38,0	620,4	7,7	0,209	
GAL-10_59.FIN2	328,0	2,101	0,3730	0,01000	0,05030	0,0011	0,3962400	321,60	7,60	316,50	6,50	367,0	63,0	316,5	6,5	1,586	
GAL-10_60.FIN2	279,3	1,783	0,3721	0,00740	0,04874	0,0006	0,3519700	320,60	5,50	306,80	3,40	413,0	44,0	306,8	3,4	4,304	
GAL-10_61.FIN2	657,0	0,476	10,4800	0,19000	0,45140	0,0086	0,4975700	2480,00	18,00	2399,00	38,00	2542,0	17,0	2542,0	17,0	5,625	
GAL-10_62.FIN2	272,0	1,105	0,8520	0,01200	0,10210	0,0012	0,5916700	625,60	6,70	626,40	7,00	630,0	29,0	626,4	7,0	0,128	
GAL-10_63.FIN2	314,9	5,790	1,4780	0,02100	0,15130	0,0021	0,7186200	920,30	8,50	909,00	11,00	959,0	21,0	959,0	21,0	5,214	
GAL-10_64.FIN2	245,2	0,711	0,8150	0,01300	0,09880	0,0011	0,5785200	604,40	7,30	607,00	6,40	593,0	28,0	607,0	6,4	0,430	
GAL-10_65.FIN2	215,1	1,091	0,8080	0,01300	0,09530	0,0012	0,5216500	600,40	7,30	586,90	7,30	646,0	32,0	586,9	7,3	2,249	
GAL-10_66.FIN2	208,8	1,079	5,6060	0,08100	0,32180	0,0054	0,8448100	1915,00	13,00	1797,00	27,00	2038,0	21,0	2038,0	21,0	11,825	
GAL-10_67.FIN2	173,6	2,488	0,6590	0,01300	0,08360	0,0011	0,6630700	512,70	8,10	517,70	6,80	485,0	38,0	517,7	6,8	0,975	
GAL-10_68.FIN2	551,0	2,720	0,6490	0,01600	0,07940	0,0018	0,7659600	506,30	9,70	492,00	11,00	570,0	41,0	492,0	11,0	2,824	
GAL-10_69.FIN2	514,0	2,970	0,3568	0,00820	0,04832	0,0006	0,5182900	309,50	6,10	304,20	3,80	354,0	44,0	304,2	3,8	1,712	
GAL-10_70.FIN2	614,0	2,615	0,3433	0,00520	0,04781	0,0005	0,5582800	299,40	3,90	301,10	2,80	290,0	29,0	301,1	2,8	0,568	
GAL-10_71.FIN2	87,5	16,900	0,9880	0,02400	0,11050	0,0020	0,5824100	695,00	12,00	675,00	11,00	753,0	43,0	675,0	11,0	2,878	
GAL-10_72.FIN2	594,0	1,655	0,8530	0,01300	0,10110	0,0013	0,6430200	625,70	6,90	621,00	7,60	640,0	25,0	621,0	7,6	0,751	
GAL-10_73.FIN2	566,0	2,350	1,5350	0,03000	0,15720	0,0028	0,7686700	944,00	12,00	940,00	16,00	966,0	25,0	966,0	25,0	2,692	
GAL-10_74.FIN2	441,0	5,200	0,8730	0,01300	0,10510	0,0014	0,6187400	636,10	7,20	644,10	8,00	605,0	22,0	644,1	8,0	1,258	
GAL-10_75.FIN2	393,0	1,993	0,3304	0,00720	0,04526	0,0007	0,4569100	290,80	5,50	285,30	4,00	331,0	45,0	285,3	4,0	1,891	
GAL-10_76.FIN2	296,9	12,400	0,9350	0,01400	0,10730	0,0010	0,5491900	671,00	7,50	656,70	5,90	711,0	28,0	656,7	5,9	2,131	
GAL-10_77.FIN2	304,9	1,960	0,6110	0,01300	0,07650	0,0014	0,4643300	483,60	8,20	474,90	8,10	518,0	46,0	474,9	8,1	1,799	
GAL-10_78.FIN2	319,0	5,510	0,6010	0,01200	0,07730	0,0011	0,6067700	477,40	7,40	480,00	6,70	452,0	36,0	480,0	6,7	0,545	
GAL-10_79.FIN2	411,0	2,443	2,9760	0,06000	0,19250	0,0034	0,8792800	1400,00	16,00	1134,00	18,00	1829,0	18,0	DISC	DISC	37,999	
GAL-10_80.FIN2	1687,0	6,620	0,7837	0,00810	0,09371	0,0010	0,7562100	587,80	4,50	577,30	5,80	624,0	15,0	577,3	5,8	1,786	
GAL-10_81.FIN2	280,3	5,930	0,7340	0,01700	0,08940	0,0019	0,6244700	557,00	10,00	551,00	11,00	581,0	40,0	551,0	11,0	1,077	
GAL-10_82.FIN2	473,0	1,970	0,5611	0,00860	0,07031	0,0010	0,3125500	452,40	5,80	437,90	5,80	510,0	38,0	437,9	5,8	3,205	
GAL-10_83.FIN2	1583,0	8,430	0,7410	0,01800	0,09070	0,0022	0,8745300	562,00	11,00	559,00	13,00	573,0	32,0	559,0	13,0	0,534	Rim
GAL-10_83.FIN2	208,0	4,500	1,3890	0,04200	0,14940	0,0041	0,9069100	880,00	19,00	897,00	23,00	844,0	32,0	844,0	23,0	1,932	Core
GAL-10_84.FIN2	488,0	1,343	1,1710	0,02900	0,11280	0,0027	0,7989300	786,00	13,00	689,00	15,00	1055,0	36,0	689,0	15,0	12,341	
GAL-10_85.FIN2	480,0	2,364	0,3401	0,00530	0,04600	0,0005	0,3582300	297,90	4,00	290,30	3,30	335,0	34,0	290,3	3,3	2,256	
GAL-10_86.FIN2	1340,0	4,900	0,4520	0,03000	0,05510	0,0029	0,5098600	378,00	21,00	346,00	18,00	580,0	130,0	346,0	18,0	8,466	Rim
GAL-10_86.FIN2	1636,0	9,300	1,0600	0,01600	0,11620	0,0017	0,7116500	733,00	7,70	708,50	9,70	798,0	23,0	708,5	9,7	3,342	Core
GAL-10_87.FIN2	40,0	0,688	1,7400	0,05600	0,17330	0,0036	0,3036700	1020,00	21,00	1029,00	20,00	985,0	69,0	985,0	69,0	4,467	
GAL-10_88.FIN2	262,0	1,374	0,6120	0,01500	0,07380	0,0011	0,6706200	483,30	9,30	458,90	6,40	579,0	44,0	458,9	6,4	5,049	
GAL-10_89.FIN2	367,0	4,830	0,8260	0,02300	0,09120	0,0024	0,4694400	611,00	13,00	563,00	14,00	783,0	72,0	563,0	14,0	7,856	Rim
GAL-10_89.FIN2	732,0	4,007	1,2900	0,03300	0,13140	0,0036	0,7619700	840,00	14,00	795,00	20,00	961,0	38,0	795,0	20,0	5,357	Core
GAL-10_90.FIN2	656,0	14,890	0,9150	0,01400	0,10660	0,0019	0,5357000	659,50	7,30	653,00	11,00	660,0	34,0	653,0	11,0	0,986	Rim
GAL-10_90.FIN2	303,1	1,222	1,4880	0,03800	0,15320	0,0028	0,7450600	924,00	16,00	918,00	16,00	934,0	36,0	934,0	36,0	1,713	Core
GAL-10_91.FIN2	215,0	3,150	1,1130	0,02100	0,12600	0,0019	0,6231800	758,00	10,00	765,00	11,00	729,0	32,0	765,0	11,0	0,923	
GAL-10_92.FIN2	663,0	2,146	1,7480	0,01700	0,17030	0,0014	0,4619200	1025,70	6,20	1013,30	7,80	1047,0	18,0	1047,0	18,0	3,219	
GAL-10_93.FIN2	353,3	9,250	11,8900	0,25000	0,41730	0,0094	0,9586200	2594,00	20,00	2247,00	43,00	2879,0	21,0	2879,0	21,0	21,952	
GAL-10_94.FIN2	251,6	0,809	0,8170	0,02100	0,09420	0,0017	0,7205700	608,00	12,00	579,80	9,80	699,0	42,0	579,8	9,8	4,638	
GAL-10_95.FIN2	756,0	7,810	0,9080	0,01100	0,10730	0,0013	0,6971500	655,20	5,80	656,70	7,30	649,0	22,0	656,7	7,3	0,229	
GAL-10_96.FIN2	1500,0	18,900	0,6133	0,00890	0,07658	0,0010	0,7059600	485,20	5,60	475,60	5,80	519,0	24,0	475,6	5,8	1,979	
GAL-10_97.FIN2	244,0	1,545	0,7740	0,01400	0,09500	0,0013	0,5773600	581,20	7,80	585,00	7,40	556,0	33,0	585,0	7,4	0,654	
GAL-10_98.FIN2	1135,0	2,210	0,7330	0,01200	0,09030	0,0015	0,6920800	557,70	7,00	556,90	8,70	565,0	29,0	556,9	8,7	0,143	
GAL-10_99.FIN2	607,0	2,560	0,9190	0,01300	0,10870	0,0013	0,6785100	661,00	6,70	664,90	7,60	640,0	23,0	664,9	7,6	0,590	

Sample Name:	[U]							207/235		206/238		207/206		Best age		Discordance	Rim/
Grain #	ppm	U/Th	207/235	2σ error	206/238	2σ error	RHO	Age Ma	2σ error	Age (Ma)	2σ error	Age (Ma)	2σ error	(Ma)	2σ error	%	Core
GAL-10_100.FIN2	293,0	3,650	13,8700	0,28000	0,52600	0,0100	0,9300600	2739,00	20,00	2736,00	47,00	2752,0	14,0	2752,0	14,0	0,581	
GAL-10_101.FIN2	10500,0	3,670	0,4020	0,01300	0,02750	0,0009	0,7035400	345,10	8,10	174,90	5,50	1734,0	47,0	DISC	DISC	49,319	Rim
GAL-10_101.FIN2	1096,0	2,189	0,3522	0,00870	0,04562	0,0006	0,3578300	305,80	6,50	287,50	3,60	436,0	47,0	287,5	3,6	5,984	Core
GAL-10_102.FIN2	411,0	5,800	0,4565	0,00930	0,05850	0,0011	0,6190000	381,00	6,50	366,20	6,70	465,0	36,0	366,2	6,7	3,885	
GAL-10_103.FIN2	118,3	0,700	0,8850	0,01600	0,10580	0,0012	0,0613080	642,40	8,60	648,00	7,30	616,0	40,0	648,0	7,3	0,872	
GAL-10_104.FIN2	214,0	5,360	0,5780	0,01200	0,07510	0,0011	0,3961000	461,80	7,50	467,00	6,60	440,0	43,0	467,0	6,6	1,126	
GAL-10_105.FIN2	316,7	6,400	0,9270	0,01700	0,10660	0,0019	0,6422200	664,70	9,10	652,00	11,00	721,0	35,0	652,0	11,0	1,911	
GAL-10_106.FIN2	331,0	1,872	1,0960	0,03000	0,12490	0,0027	0,4739900	750,00	14,00	759,00	15,00	733,0	49,0	759,0	15,0	1,200	
GAL-10_107.FIN2	64,8	1,037	4,1490	0,06800	0,28540	0,0037	0,6778400	1662,00	14,00	1617,00	19,00	1731,0	23,0	1731,0	23,0	6,586	
GAL-10_108.FIN2	4810,0	6,060	0,5110	0,02300	0,03220	0,0013	0,4641400	419,00	15,00	204,20	7,90	1893,0	76,0	DISC	DISC	51,265	Rim
GAL-10_108.FIN2	369,0	2,056	0,3918	0,00770	0,05203	0,0007	0,3677900	335,20	5,60	326,90	4,20	394,0	42,0	326,9	4,2	2,476	Core
GAL-10_109.FIN2	925,0	4,170	0,8560	0,02200	0,09020	0,0017	0,7967100	627,00	12,00	556,00	10,00	892,0	33,0	556,0	10,0	11,324	
GAL-10_110.FIN2	85,3	0,400	0,8110	0,02000	0,09850	0,0014	0,3941000	600,00	11,00	605,50	8,30	572,0	52,0	605,5	8,3	0,917	
GAL-10_111.FIN2	382,0	0,587	9,8000	0,26000	0,43500	0,0120	0,8636400	2412,00	24,00	2326,00	52,00	2490,0	25,0	2490,0	25,0	6,586	
GAL-10_112.FIN2	155,0	0,788	3,3000	0,21000	0,22300	0,0100	0,8093300	1476,00	48,00	1298,00	54,00	1762,0	68,0	1762,0	68,0	26,334	Rim
GAL-10_112.FIN2	453,0	1,438	12,9200	0,26000	0,47890	0,0089	0,8226200	2670,00	18,00	2527,00	41,00	2820,0	18,0	2820,0	18,0	10,390	Core
GAL-10_113.FIN2	1088,0	36,700	0,4930	0,04400	0,06300	0,0032	0,6799000	406,00	30,00	394,00	20,00	470,0	150,0	394,0	20,0	2,956	Rim
GAL-10_113.FIN2	213,0	1,433	1,8670	0,04600	0,17950	0,0039	0,7559400	1065,00	17,00	1063,00	21,00	1080,0	34,0	1080,0	34,0	1,574	Core
GAL-10_114.FIN2	980,0	116,000	0,8830	0,02400	0,10430	0,0023	0,7825200	641,00	13,00	639,00	13,00	656,0	32,0	639,0	13,0	0,312	Rim
GAL-10_114.FIN2	167,0	1,416	1,5870	0,05000	0,16400	0,0043	0,7222700	961,00	19,00	978,00	24,00	932,0	45,0	932,0	45,0	4,936	Core
GAL-10_115.FIN2	273,0	1,467	0,9190	0,01800	0,10700	0,0015	0,5759000	661,40	9,60	654,90	9,00	680,0	34,0	654,9	9,0	0,983	
GAL-10_116.FIN2	326,9	2,320	0,5687	0,00840	0,07338	0,0008	0,4555400	456,60	5,40	456,40	4,80	471,0	29,0	456,4	4,8	0,044	
GAL-10_117.FIN2	296,0	1,737	0,5495	0,00900	0,07149	0,0009	0,4133600	444,70	5,80	445,00	5,50	443,0	35,0	445,0	5,5	0,067	
GAL-10_118.FIN2	284,4	2,485	1,0560	0,02400	0,11500	0,0016	0,4722500	730,00	11,00	701,20	9,10	832,0	40,0	701,2	9,1	3,945	
GAL-10_119.FIN2	276,3	1,196	0,9040	0,01200	0,10720	0,0012	0,5569800	652,90	6,30	656,20	7,00	652,0	25,0	656,2	7,0	0,505	
GAL-10_120.FIN2	194,0	2,535	0,8460	0,01600	0,09960	0,0015	0,6138300	621,10	8,70	611,70	8,60	665,0	31,0	611,7	8,6	1,513	
GAL-10_121.FIN2	84,5	1,601	1,1930	0,02400	0,13190	0,0018	0,2906400	795,00	11,00	798,00	10,00	798,0	40,0	798,0	10,0	0,377	
GAL-10_122.FIN2	59,6	0,894	0,8590	0,02000	0,10420	0,0012	0,3891700	627,00	11,00	638,60	7,30	578,0	51,0	638,6	7,3	1,850	
GAL-10_123.FIN2	332,0	1,219	0,8340	0,01000	0,10035	0,0010	0,5856800	615,30	5,60	616,40	5,80	617,0	23,0	616,4	5,8	0,179	
GAL-10_124.FIN2	1215,0	2,246	0,3550	0,00520	0,04757	0,0006	0,6446500	308,30	3,90	299,60	3,70	373,0	26,0	299,6	3,7	2,822	
GAL-10_125.FIN2	191,4	0,685	0,5970	0,01200	0,07600	0,0011	0,4543200	474,70	7,40	471,80	6,50	487,0	41,0	471,8	6,5	0,611	
GAL-10_126.FIN2	164,0	3,090	1,0080	0,01800	0,11530	0,0014	0,5062500	706,10	9,20	703,20	7,90	715,0	35,0	703,2	7,9	0,411	
GAL-10_127.FIN2	646,0	19,600	0,8530	0,02000	0,10160	0,0020	0,7018100	625,00	11,00	624,00	11,00	633,0	35,0	624,0	11,0	0,160	
GAL-10_128.FIN2	242,5	0,846	0,8200	0,01500	0,09530	0,0013	0,5726000	606,60	8,40	586,40	7,60	684,0	33,0	586,4	7,6	3,330	
GAL-10_129.FIN2	879,0	2,330	0,3566	0,00450	0,04901	0,0005	0,6155800	309,80	3,30	308,40	3,10	314,0	24,0	308,4	3,1	0,452	
GAL-10_130.FIN2	599,0	1,820	0,5130	0,01100	0,06630	0,0011	0,7990900	420,40	7,10	413,40	6,40	462,0	28,0	413,4	6,4	1,665	
GAL-10_131.FIN2	75,3	1,143	5,2840	0,09900	0,33420	0,0055	0,6582800	1863,00	16,00	1857,00	27,00	1874,0	26,0	1874,0	26,0	0,907	
GAL-10_132.FIN2	443,0	1,155	0,3343	0,00500	0,04675	0,0005	0,4763900	292,60	3,80	294,50	2,80	275,0	33,0	294,5	2,8	0,649	
GAL-10_133.FIN2	526,0	1,979	0,3385	0,00580	0,04709	0,0007	0,5300000	295,70	4,40	297,10	4,30	286,0	36,0	297,1	4,3	0,473	
GAL-10_134.FIN2	159,2	0,888	3,4120	0,06900	0,25660	0,0051	0,7622200	1508,00	16,00	1471,00	26,00	1554,0	25,0	1554,0	25,0	5,341	
GAL-10_135.FIN2	102,4	0,934	5,9400	0,10000	0,35680	0,0055	0,7954700	1966,00	15,00	1966,00	26,00	1968,0	19,0	1968,0	19,0	0,102	
GAL-10_136.FIN2	565,0	2,268	12,1800	0,15000	0,48830	0,0063	0,7875800	2618,00	12,00	2562,00	27,00	2666,0	13,0	2666,0	13,0	3,901	
GAL-10_137.FIN2	757,0	3,250	0,3970	0,01100	0,05150	0,0011	0,6247300	338,60	8,10	323,60	7,00	440,0	50,0	323,6	7,0	4,430	
GAL-10_138.FIN2	216,0	7,200	0,7380	0,01400	0,08990	0,0010	0,4697300	560,20	8,10	555,00	6,10	586,0	37,0	555,0	6,1	0,928	
GAL-10_139.FIN2	472,0	2,040	0,6020	0,01700	0,07720	0,0018	0,7288400	478,00	11,00	479,00	11,00	474,0	41,0	479,0	11,0	0,209	
GAL-10_140.FIN2	213,0	4,200	0,7940	0,01500	0,09730	0,0012	0,2857200	593,90	8,90	599,30	7,30	570,0	43,0	599,3	7,3	0,909	
GAL-10_141.FIN2	592,0	8,200	5,1000	0,07700	0,32740	0,0057	0,5853700	1835,00	13,00	1825,00	28,00	1854,0	23,0	1854,0	23,0	1,564	

Sample Name:	[U]							207/235		206/238		207/206		Best age		Discordance	Rim/
Grain #	ppm	U/Th	207/235	2σ error	206/238	2σ error	RHO	Age Ma	2σ error	Age (Ma)	2σ error	Age (Ma)	2σ error	(Ma)	2σ error	%	Core
GAL-10_142.FIN2	108,5	1,172	0,8890	0,02100	0,10430	0,0017	0,3000400	644,00	11,00	639,20	9,80	652,0	49,0	639,2	9,8	0,745	
GAL-10_143.FIN2	885,0	2,120	0,3952	0,00610	0,05432	0,0005	0,5503000	337,80	4,40	340,90	3,20	311,0	29,0	340,9	3,2	0,918	
GAL-10_144.FIN2	241,0	0,625	0,9270	0,01600	0,10860	0,0014	0,4753700	665,80	8,40	664,50	8,20	666,0	35,0	664,5	8,2	0,195	
GAL-10_145.FIN2	569,0	1,810	0,7630	0,01100	0,09360	0,0011	0,6849600	575,20	6,20	578,40	6,70	574,0	23,0	578,4	6,7	0,556	
GAL-10_146.FIN2	168,5	3,164	0,8120	0,02000	0,09510	0,0014	0,6093000	602,00	11,00	585,40	8,40	651,0	44,0	585,4	8,4	2,757	
GAL-10_147.FIN2	437,0	2,189	0,3667	0,00750	0,04897	0,0007	0,4573400	317,30	5,70	308,10	4,50	365,0	42,0	308,1	4,5	2,899	
GAL-10_148.FIN2	392,9	4,210	0,6070	0,01100	0,07690	0,0013	0,6301600	481,70	7,30	477,30	7,70	491,0	33,0	477,3	7,7	0,913	
GAL-10_149.FIN2	320,0	3,376	1,3040	0,02400	0,13520	0,0018	0,6424200	846,00	10,00	817,00	10,00	913,0	28,0	817,0	10,0	3,428	
GAL-7_1.FIN2	316,0	3,195	0,3551	0,00640	0,04923	0,0005	0,2543600	308,10	4,80	309,80	2,90	281,0	39,0	309,8	2,9	0,552	
GAL-7_2.FIN2	277,0	2,660	0,8600	0,01200	0,10119	0,0009	0,4108800	630,10	6,60	621,30	5,20	658,0	29,0	621,3	5,2	1,397	
GAL-7_3.FIN2	503,0	1,377	1,2030	0,01800	0,13360	0,0014	0,5126300	803,10	7,80	808,10	8,00	783,0	27,0	808,1	8,0	0,623	
GAL-7_4.FIN2	90,4	1,182	1,2040	0,02900	0,12730	0,0023	0,2665500	801,00	13,00	772,00	13,00	873,0	55,0	772,0	13,0	3,620	
GAL-7_5.FIN2	425,0	1,528	1,0120	0,01300	0,11454	0,0010	0,1671600	709,30	6,40	699,00	5,50	739,0	29,0	699,0	5,5	1,452	
GAL-7_6.FIN2	350,0	2,960	0,5962	0,00980	0,07625	0,0006	0,3046900	474,10	6,20	473,70	3,70	464,0	35,0	473,7	3,7	0,084	
GAL-7_7.FIN2	73,8	2,500	1,1650	0,02500	0,12830	0,0016	0,0657000	783,00	11,00	779,00	9,10	784,0	50,0	779,0	9,1	0,511	
GAL-7_8.FIN2	589,0	1,673	0,3940	0,01100	0,04997	0,0006	0,3502000	336,50	7,80	314,30	3,80	491,0	59,0	314,3	3,8	6,597	
GAL-7_10.FIN2	172,6	1,492	0,3453	0,00910	0,04638	0,0005	0,2009800	301,10	7,10	292,20	3,30	352,0	59,0	292,2	3,3	2,956	
GAL-7_11.FIN2	146,3	1,167	0,3790	0,01300	0,05042	0,0007	0,2793600	325,30	9,20	317,10	4,30	378,0	71,0	317,1	4,3	2,521	
GAL-7_12.FIN2	1541,0	2,880	0,8148	0,00700	0,09778	0,0008	0,5299600	604,90	3,90	601,30	4,70	612,0	18,0	601,3	4,7	0,595	
GAL-7_13.FIN2	1000,0	0,891	0,3931	0,00500	0,05399	0,0005	0,3329300	336,40	3,60	339,00	2,90	312,0	29,0	339,0	2,9	0,773	
GAL-7_14.FIN2	118,6	1,147	1,0930	0,02400	0,12280	0,0013	0,0243240	748,00	11,00	746,30	7,40	740,0	47,0	746,3	7,4	0,227	
GAL-7_15.FIN2	465,0	1,199	1,6600	0,01800	0,16740	0,0015	0,5168900	992,70	7,00	997,70	8,40	979,0	21,0	979,0	21,0	1,910	
GAL-7_16.FIN2	479,0	7,330	0,9130	0,03300	0,10180	0,0016	0,3476400	658,00	18,00	624,70	9,20	768,0	71,0	624,7	9,2	5,061	Rim
GAL-7_16.FIN2	257,0	1,322	12,1400	0,25000	0,48700	0,0110	0,8873400	2613,00	20,00	2554,00	46,00	2650,0	19,0	2650,0	19,0	3,623	Core
GAL-7_17.FIN2	133,6	3,600	13,9300	0,18000	0,52280	0,0043	0,6061900	2742,00	12,00	2710,00	18,00	2765,0	17,0	2765,0	17,0	1,989	
GAL-7_18.FIN2	702,0	2,990	0,4410	0,01100	0,05815	0,0006	0,2060700	370,70	7,80	364,30	3,40	401,0	56,0	364,3	3,4	1,726	
GAL-7_19.FIN2	520,0	2,724	0,7116	0,00960	0,08725	0,0007	0,3864900	545,20	5,70	539,20	4,20	567,0	27,0	539,2	4,2	1,101	
GAL-7_20.FIN2	315,0	4,440	0,7780	0,01600	0,09382	0,0009	0,4385700	583,10	8,40	578,00	5,10	596,0	37,0	578,0	5,1	0,875	
GAL-7_21.FIN2	1188,0	1,498	0,7839	0,00670	0,09606	0,0008	0,4189400	587,40	3,80	591,20	4,40	571,0	20,0	591,2	4,4	0,647	
GAL-7_22.FIN2	171,0	2,370	1,7670	0,02300	0,17160	0,0016	0,3040000	1032,00	8,60	1020,90	8,70	1056,0	27,0	1056,0	27,0	3,324	
GAL-7_23.FIN2	516,0	6,530	3,4800	0,14000	0,22150	0,0089	0,9375400	1517,00	34,00	1288,00	47,00	1862,0	27,0	DISC		DISC	30,827	
GAL-7_24.FIN2	906,0	18,600	0,7060	0,01400	0,08850	0,0010	0,2458300	541,90	8,40	546,60	6,10	520,0	44,0	546,6	6,1	0,867	Rim
GAL-7_24.FIN2	876,0	0,791	1,3840	0,02200	0,14430	0,0020	0,4718200	881,70	9,50	869,00	11,00	912,0	31,0	912,0	31,0	4,715	Core
GAL-7_25.FIN2	539,0	5,580	0,8629	0,00890	0,10285	0,0007	0,2350600	631,30	4,90	631,10	3,90	632,0	23,0	631,1	3,9	0,032	
GAL-7_26.FIN2	600,0	1,404	0,7960	0,01200	0,09182	0,0010	0,4809000	594,10	6,60	566,20	5,70	701,0	31,0	566,2	5,7	4,696	
GAL-7_27.FIN2	496,7	1,638	1,0580	0,02100	0,11370	0,0013	0,0773590	732,00	10,00	694,30	7,30	846,0	44,0	694,3	7,3	5,150	
GAL-7_28.FIN2	353,0	0,955	0,8080	0,01000	0,09699	0,0009	0,2706400	601,30	5,60	596,70	5,20	608,0	31,0	596,7	5,2	0,765	
GAL-7_29.FIN2	442,0	67,000	0,3750	0,01000	0,05180	0,0007	0,1825800	322,90	7,50	325,50	4,50	301,0	62,0	325,5	4,5	0,805	Rim
GAL-7_29.FIN2	434,0	3,690	3,8200	0,10000	0,22590	0,0033	0,7377700	1594,00	22,00	1313,00	17,00	1989,0	36,0	DISC		DISC	33,987	Core
GAL-7_30.FIN2	332,2	3,900	0,7056	0,00980	0,08695	0,0008	0,3334500	542,30	6,00	537,40	4,60	564,0	31,0	537,4	4,6	0,904	
GAL-7_31.FIN2	151,3	0,649	0,7820	0,01800	0,09376	0,0010	0,2628600	585,00	10,00	577,60	5,80	598,0	49,0	577,6	5,8	1,265	
GAL-7_33.FIN2	364,0	1,595	0,6890	0,01100	0,08582	0,0007	0,2995500	531,40	6,40	530,70	4,00	531,0	33,0	530,7	4,0	0,132	
GAL-7_34.FIN2	1439,0	0,886	0,8067	0,00820	0,09842	0,0009	0,5412200	600,20	4,60	605,10	5,00	582,0	20,0	605,1	5,0	0,816	
GAL-7_35.FIN2	548,3	0,741	0,8080	0,01200	0,09803	0,0010	0,4286700	600,60	6,60	602,80	5,60	598,0	32,0	602,8	5,6	0,366	
GAL-7_36.FIN2	1569,0	12,340	0,3690	0,01200	0,04800	0,0011	0,7006200	318,60	8,90	302,10	7,00	443,0	54,0	302,1	7,0	5,179	
GAL-7_37.FIN2	543,0	3,032	15,2860	0,09900	0,53400	0,0040	0,4969500	2832,50	6,20	2760,00	17,00	2887,0	12,0	2887,0	12,0	4,399	

Sample Name:	[U]							207/235		206/238		207/206		Best age		Discordance	Rim/
Grain #	ppm	U/Th	207/235	2σ error	206/238	2σ error	RHO	Age Ma	2σ error	Age (Ma)	2σ error	Age (Ma)	2σ error	(Ma)	2σ error	%	Core
GAL-7_38.FIN2	995,0	1,681	0,4382	0,00620	0,05807	0,0006	0,2993300	368,70	4,30	363,80	3,30	404,0	32,0	363,8	3,3	1,329	
GAL-7_39.FIN2	314,0	1,600	0,9100	0,01400	0,10700	0,0010	0,2495400	657,20	7,50	655,20	5,90	665,0	35,0	655,2	5,9	0,304	
GAL-7_40.FIN2	321,0	1,696	0,5598	0,00910	0,07200	0,0007	0,3957100	450,70	5,90	448,10	3,90	461,0	37,0	448,1	3,9	0,577	
GAL-7_41.FIN2	215,3	1,236	0,8360	0,01500	0,09820	0,0011	0,1172400	617,20	8,80	603,80	6,20	665,0	45,0	603,8	6,2	2,171	
GAL-7_42.FIN2	434,0	1,065	0,6760	0,01200	0,08361	0,0009	0,6234000	524,00	7,30	517,60	5,40	555,0	34,0	517,6	5,4	1,221	
GAL-7_43.FIN2	387,0	1,191	0,3304	0,00620	0,04690	0,0005	0,0164400	289,50	4,80	295,50	3,20	257,0	46,0	295,5	3,2	2,073	
GAL-7_44.FIN2	703,0	14,900	0,8600	0,01000	0,10300	0,0008	0,3432100	629,80	5,40	631,90	4,80	631,0	24,0	631,9	4,8	0,333	
GAL-7_45.FIN2	391,0	1,398	1,6090	0,01800	0,16200	0,0015	0,7344900	972,90	7,20	967,60	8,30	992,0	22,0	992,0	22,0	2,460	
GAL-7_46.FIN2	175,8	12,660	5,6470	0,08400	0,34040	0,0040	0,7530000	1920,00	13,00	1890,00	19,00	1958,0	20,0	1958,0	20,0	3,473	
GAL-7_47.FIN2	730,0	0,487	0,8657	0,00990	0,10354	0,0008	0,2614300	633,40	5,60	635,10	4,70	633,0	27,0	635,1	4,7	0,268	
GAL-7_48.FIN2	328,0	1,993	1,3120	0,01900	0,14230	0,0014	0,4442200	849,70	8,10	857,40	7,60	835,0	27,0	835,0	7,6	0,906	
GAL-7_49.FIN2	230,0	1,097	0,7930	0,01300	0,09564	0,0009	0,1886700	591,90	7,50	588,70	5,30	604,0	38,0	588,7	5,3	0,541	
GAL-7_50.FIN2	257,4	0,865	0,8250	0,01400	0,09977	0,0009	0,4199900	610,10	7,80	613,00	5,00	605,0	35,0	613,0	5,0	0,475	
GAL-7_51.FIN2	1096,0	4,150	0,6622	0,00840	0,08458	0,0009	0,6032700	515,60	5,20	523,30	5,10	492,0	25,0	523,3	5,1	1,493	
GAL-7_52.FIN2	307,5	1,647	0,3541	0,00740	0,04898	0,0005	0,3178900	307,20	5,60	308,20	2,90	302,0	44,0	308,2	2,9	0,326	
GAL-7_53.FIN2	925,0	1,070	0,9200	0,01400	0,10443	0,0010	0,3791500	661,50	7,40	640,30	5,80	746,0	32,0	640,3	5,8	3,205	
GAL-7_54.FIN2	96,3	5,000	8,0100	0,34000	0,40410	0,0094	0,5208400	2228,00	39,00	2187,00	44,00	2272,0	64,0	2272,0	64,0	3,741	Rim
GAL-7_54.FIN2	232,2	3,270	15,5600	0,20000	0,50400	0,0052	0,5795100	2848,00	12,00	2633,00	21,00	3009,0	17,0	3009,0	17,0	12,496	Core
GAL-7_55.FIN2	142,5	0,882	0,4450	0,01200	0,06006	0,0007	0,3119200	374,50	8,80	376,00	4,10	359,0	56,0	376,0	4,1	0,401	
GAL-7_56.FIN2	124,6	0,846	0,7950	0,01700	0,09730	0,0010	0,1443400	592,50	9,60	598,60	6,00	562,0	49,0	598,6	6,0	1,030	
GAL-7_57.FIN2	385,0	27,000	0,3611	0,00780	0,04968	0,0005	0,0249110	312,40	5,80	312,50	2,80	314,0	51,0	312,5	2,8	0,032	
GAL-7_58.FIN2	691,0	0,701	12,7100	0,12000	0,53380	0,0045	0,7778600	2657,20	8,60	2759,00	19,00	2584,0	10,0	2584,0	10,0	6,772	
GAL-7_59.FIN2	940,0	2,993	0,6188	0,00690	0,07895	0,0006	0,3802100	488,70	4,40	489,80	3,60	479,0	23,0	489,8	3,6	0,225	
GAL-7_60.FIN2	1280,0	7,200	1,6090	0,03300	0,16220	0,0027	0,8136800	974,00	13,00	969,00	15,00	984,0	25,0	984,0	25,0	1,524	
GAL-7_61.FIN2	460,8	1,870	16,7100	0,19000	0,55570	0,0067	0,7403800	2918,00	11,00	2848,00	28,00	2968,0	14,0	2968,0	14,0	4,043	
GAL-7_62.FIN2	1303,0	2,520	0,4053	0,00500	0,05484	0,0004	0,2813900	345,30	3,60	344,20	2,70	355,0	28,0	344,2	2,7	0,319	
GAL-7_63.FIN2	787,0	16,000	0,4240	0,01400	0,05770	0,0012	0,5387000	358,90	9,80	361,40	7,40	341,0	63,0	361,4	7,4	0,697	Rim
GAL-7_63.FIN2	207,0	0,464	0,7770	0,01400	0,09500	0,0010	0,1757300	582,80	7,80	584,90	5,90	568,0	41,0	584,9	5,9	0,360	Core
GAL-7_64.FIN2	570,0	1,167	1,1350	0,02100	0,11810	0,0015	0,5739300	769,20	9,90	719,30	8,50	916,0	31,0	719,3	8,5	6,487	
GAL-7_65.FIN2	312,0	2,270	1,7530	0,02000	0,17210	0,0014	0,4582600	1027,40	7,30	1023,60	7,60	1034,0	20,0	1034,0	20,0	1,006	
GAL-7_66.FIN2	558,0	0,630	0,8550	0,01500	0,10100	0,0012	0,3600200	626,90	8,00	620,40	6,90	669,0	33,0	620,4	6,9	1,037	
GAL-7_67.FIN2	545,0	2,515	0,3501	0,00630	0,04856	0,0005	0,3471600	305,00	4,90	305,70	2,70	288,0	39,0	305,7	2,7	0,230	
GAL-7_68.FIN2	856,0	1,161	1,1490	0,01400	0,12790	0,0014	0,6498600	776,20	6,60	775,90	7,80	778,0	20,0	775,9	7,8	0,039	
GAL-7_69.FIN2	272,0	1,434	1,1030	0,02900	0,11880	0,0021	0,3279100	754,00	14,00	724,00	12,00	838,0	56,0	724,0	12,0	3,979	
GAL-7_70.FIN2	443,1	1,508	0,4181	0,00700	0,05608	0,0005	0,1010600	354,20	5,00	351,70	2,70	358,0	40,0	351,7	2,7	0,706	
GAL-7_71.FIN2	592,0	0,885	0,8156	0,00950	0,09711	0,0007	0,3373200	605,10	5,30	597,40	3,90	624,0	24,0	597,4	3,9	1,273	
GAL-7_72.FIN2	1182,0	12,070	0,7990	0,02400	0,09310	0,0018	0,4027300	596,00	13,00	574,00	11,00	675,0	59,0	574,0	11,0	3,691	Rim
GAL-7_72.FIN2	750,0	0,970	10,1400	0,33000	0,41300	0,0130	0,9605600	2442,00	30,00	2236,00	63,00	2620,0	16,0	2620,0	16,0	14,656	Core
GAL-7_74.FIN2	411,0	2,850	1,5310	0,01700	0,15920	0,0015	0,5006000	943,10	6,80	952,20	8,30	912,0	22,0	912,0	22,0	4,408	
GAL-7_75.FIN2	486,0	17,300	0,6480	0,01800	0,07723	0,0008	0,3871900	506,00	11,00	479,50	4,90	612,0	46,0	479,5	4,9	5,237	Rim
GAL-7_75.FIN2	147,1	2,505	0,9490	0,04300	0,10650	0,0023	0,3071200	676,00	22,00	653,00	14,00	737,0	94,0	653,0	14,0	3,402	Core
GAL-7_76.FIN2	190,8	1,784	8,3900	0,14000	0,37340	0,0053	0,6772800	2272,00	15,00	2044,00	25,00	2479,0	22,0	2479,0	22,0	17,547	
GAL-7_77.FIN2	879,0	4,420	12,1700	0,15000	0,49190	0,0049	0,8257100	2617,00	11,00	2577,00	21,00	2643,0	12,0	2643,0	12,0	2,497	
GAL-7_78.FIN2	1063,0	1,820	1,3900	0,02100	0,13920	0,0017	0,8805100	884,20	8,90	839,80	9,90	990,0	24,0	839,8	9,9	5,021	
GAL-7_79.FIN2	822,0	2,699	0,3487	0,00520	0,04800	0,0004	0,4323400	304,00	4,00	302,20	2,60	303,0	34,0	302,2	2,6	0,592	
GAL-7_80.FIN2	1350,0	0,762	0,8200	0,01300	0,10030	0,0010	0,5844200	607,20	7,30	616,30	6,10	565,0	30,0	616,3	6,1	1,499	
GAL-7_81.FIN2	324,3	1,923	0,6560	0,02100	0,08170	0,0016	0,0435510	512,00	13,00	506,10	9,80	546,0	95,0	506,1	9,8	1,152	

Sample Name:	[U]							207/235		206/238		207/206		Best age		Discordance	Rim/
Grain #	ppm	U/Th	207/235	2σ error	206/238	2σ error	RHO	Age Ma	2σ error	Age (Ma)	2σ error	Age (Ma)	2σ error	(Ma)	2σ error	%	Core
GAL-7_82.FIN2	1330,0	2,440	0,3805	0,00930	0,05010	0,0007	0,3427500	327,10	6,90	315,10	4,20	398,0	54,0	315,1	4,2	3,669	
GAL-7_83.FIN2	1130,0	1,473	0,3530	0,01100	0,04420	0,0013	0,6067800	306,70	7,90	279,00	7,80	512,0	59,0	279,0	7,8	9,032	Rim
GAL-7_83.FIN2	179,6	1,176	0,7000	0,02400	0,08180	0,0018	0,4759300	537,00	14,00	507,00	11,00	651,0	68,0	507,0	11,0	5,587	Core
GAL-7_85.FIN2	831,0	14,800	0,5560	0,00720	0,07121	0,0006	0,4971100	448,60	4,70	443,40	3,80	466,0	25,0	443,4	3,8	1,159	
GAL-7_86.FIN2	2262,0	1,383	0,8144	0,00610	0,09919	0,0007	0,4720100	604,70	3,40	609,60	4,00	576,0	16,0	609,6	4,0	0,810	
GAL-7_87.FIN2	449,0	1,925	6,2510	0,04700	0,36300	0,0027	0,5673900	2010,80	6,60	1996,00	13,00	2018,0	12,0	2018,0	12,0	1,090	
GAL-7_88.FIN2	912,0	1,093	0,5836	0,00680	0,07451	0,0006	0,5042700	467,00	4,20	463,20	3,50	466,0	26,0	463,2	3,5	0,814	
GAL-7_89.FIN2	403,0	4,450	0,7557	0,00990	0,09259	0,0008	0,4085300	570,90	5,70	570,70	4,60	556,0	30,0	570,7	4,6	0,035	
GAL-7_90.FIN2	735,0	4,090	0,9620	0,01400	0,11100	0,0013	0,0131940	684,10	7,30	678,30	7,40	690,0	32,0	678,3	7,4	0,848	
GAL-7_91.FIN2	28,7	3,820	0,4290	0,06300	0,04620	0,0040	0,2038600	358,00	45,00	291,00	24,00	780,0	370,0	DISC	DISC	18,715	Rim
GAL-7_91.FIN2	890,0	1,768	0,5911	0,00820	0,07546	0,0007	0,3503500	471,20	5,20	468,90	4,30	472,0	29,0	468,9	4,3	0,488	Core
GAL-7_92.FIN2	235,0	1,264	0,3996	0,00970	0,05379	0,0006	0,4060200	342,40	7,00	337,70	3,40	340,0	51,0	337,7	3,4	1,373	
GAL-7_93.FIN2	824,0	1,990	0,3586	0,00490	0,04845	0,0004	0,3477200	310,90	3,70	305,00	2,20	338,0	30,0	305,0	2,2	1,898	
GAL-7_94.FIN2	341,0	4,620	1,7400	0,02300	0,16930	0,0015	0,3024600	1022,20	8,50	1008,20	8,20	1037,0	27,0	1037,0	27,0	2,777	
GAL-7_95.FIN2	116,1	1,525	6,0830	0,06800	0,35650	0,0035	0,4690000	1987,70	9,50	1965,00	17,00	1998,0	21,0	1998,0	21,0	1,652	
GAL-7_96.FIN2	333,0	1,744	0,6222	0,00980	0,07808	0,0008	0,0667050	490,50	6,10	484,60	4,50	492,0	40,0	484,6	4,5	1,203	
GAL-7_97.FIN2	657,0	1,866	0,5959	0,00830	0,07560	0,0005	0,2475700	474,20	5,20	469,80	3,20	475,0	30,0	469,8	3,2	0,928	
GAL-7_98.FIN2	627,0	1,416	0,8390	0,01000	0,09942	0,0008	0,3324600	618,40	5,70	611,00	4,40	629,0	26,0	611,0	4,4	1,197	
GAL-7_99.FIN2	338,0	2,585	0,6495	0,00900	0,08098	0,0006	0,1611700	508,30	5,70	501,90	3,50	513,0	33,0	501,9	3,5	1,259	
GAL-7_100.FIN2	2590,0	0,846	0,3860	0,01700	0,05200	0,0019	0,4757800	331,00	13,00	327,00	12,00	341,0	96,0	327,0	12,0	1,208	
GAL-7_101.FIN2	354,2	4,320	0,5610	0,03200	0,06850	0,0021	0,3251800	452,00	21,00	427,00	13,00	560,0	130,0	427,0	13,0	5,531	Rim
GAL-7_101.FIN2	159,5	1,937	0,8050	0,02100	0,09680	0,0016	0,2145200	599,00	12,00	595,80	9,70	591,0	61,0	595,8	9,7	0,534	Core
GAL-7_102.FIN2	135,9	0,670	6,0440	0,09500	0,35960	0,0039	0,6755000	1980,00	14,00	1980,00	19,00	1970,0	21,0	1970,0	21,0	0,508	
GAL-7_103.FIN2	226,7	1,316	0,8460	0,02000	0,10020	0,0014	0,3688900	621,00	11,00	615,50	8,40	615,0	50,0	615,5	8,4	0,886	
GAL-7_104.FIN2	224,0	1,300	6,8460	0,07100	0,38790	0,0037	0,5826300	2091,30	9,00	2112,00	17,00	2061,0	16,0	2061,0	16,0	2,475	
GAL-7_105.FIN2	518,0	1,127	0,8370	0,01800	0,09450	0,0011	0,2155400	616,70	9,80	581,90	6,30	732,0	46,0	581,9	6,3	5,643	
GAL-7_106.FIN2	510,0	0,907	0,8260	0,01400	0,09572	0,0009	0,4601300	611,30	8,00	589,20	5,00	679,0	33,0	589,2	5,0	3,615	
GAL-7_107.FIN2	527,0	1,324	6,5410	0,04400	0,37570	0,0025	0,4179600	2050,80	5,90	2056,00	12,00	2041,0	13,0	2041,0	13,0	0,735	
GAL-7_108.FIN2	1380,0	2,789	0,3837	0,00610	0,04949	0,0004	0,6153000	329,40	4,40	311,40	2,40	449,0	30,0	311,4	2,4	5,464	
GAL-7_109.FIN2	618,0	1,761	0,7947	0,00960	0,09633	0,0008	0,2765900	593,40	5,40	592,80	4,90	584,0	27,0	592,8	4,9	0,101	
GAL-7_110.FIN2	90,1	1,068	1,1810	0,03300	0,12610	0,0017	0,6094100	788,00	16,00	765,50	9,50	871,0	51,0	765,5	9,5	2,855	
GAL-7_111.FIN2	1120,0	0,899	0,8460	0,01200	0,10150	0,0013	0,5130000	622,10	6,70	623,00	7,80	616,0	29,0	623,0	7,8	0,145	
GAL-7_112.FIN2	2120,0	3,510	0,3485	0,00330	0,04829	0,0004	0,3526600	303,50	2,50	304,00	2,20	295,0	22,0	304,0	2,2	0,165	
GAL-7_113.FIN2	427,5	1,516	1,4760	0,01900	0,15110	0,0014	0,6612300	919,70	7,70	907,30	7,70	949,0	20,0	949,0	20,0	4,394	
GAL-7_114.FIN2	270,0	1,480	3,8000	0,06800	0,24410	0,0033	0,6636100	1591,00	14,00	1407,00	17,00	1843,0	25,0	1843,0	25,0	23,657	
GAL-7_115.FIN2	794,0	2,920	1,0300	0,02900	0,11700	0,0027	0,8605200	717,00	15,00	717,00	13,00	726,0	39,0	717,0	13,0	0,000	Rim
GAL-7_115.FIN2	749,0	2,207	1,2350	0,01600	0,13660	0,0013	0,4732800	815,80	7,40	825,40	7,40	793,0	24,0	825,4	7,4	1,177	Core
GAL-7_116.FIN2	469,0	3,670	1,0340	0,01000	0,11899	0,0009	0,5914700	720,50	5,10	724,60	5,40	708,0	20,0	724,6	5,4	0,569	
GAL-7_118.FIN2	867,0	1,320	0,8510	0,01500	0,09870	0,0013	0,3404700	624,50	8,40	606,80	7,60	687,0	40,0	606,8	7,6	2,834	
GAL-7_119.FIN2	135,0	1,379	0,9030	0,02100	0,10710	0,0012	0,2683900	651,00	11,00	657,00	7,00	632,0	49,0	657,0	7,0	0,922	
GAL-7_120.FIN2	581,0	3,170	0,6410	0,01400	0,08120	0,0013	0,6146500	502,40	8,90	503,40	7,90	495,0	39,0	503,4	7,9	0,199	
GAL-7_121.FIN2	298,0	1,272	1,6180	0,02200	0,16220	0,0014	0,3978100	975,80	8,50	968,60	8,00	990,0	27,0	990,0	27,0	2,162	
GAL-7_122.FIN2	1101,0	4,285	15,4500	0,20000	0,54000	0,0140	0,4527900	2843,00	13,00	2780,00	59,00	2870,0	28,0	2870,0	28,0	3,136	
GAL-7_123.FIN2	243,1	0,767	1,6680	0,02100	0,16390	0,0015	0,5622400	995,70	8,10	978,30	8,00	1036,0	24,0	1036,0	24,0	5,569	
GAL-7_124.FIN2	751,0	1,141	0,4336	0,00560	0,05745	0,0004	0,1721900	365,40	4,00	360,10	2,70	392,0	31,0	360,1	2,7	1,450	
GAL-7_125.FIN2	689,0	0,383	6,5300	0,14000	0,27870	0,0054	0,8532400	2048,00	21,00	1583,00	28,00	2561,0	19,0	DISC	DISC	38,188	
GAL-7_126.FIN2	293,0	1,118	8,7600	0,12000	0,39480	0,0046	0,7118600	2312,00	12,00	2144,00	21,00	2458,0	17,0	2458,0	17,0	12,775	

Sample Name:	[U]							207/235		206/238		207/206		Best age		Discordance	Rim/
Grain #	ppm	U/Th	207/235	2σ error	206/238	2σ error	RHO	Age Ma	2σ error	Age (Ma)	2σ error	Age (Ma)	2σ error	(Ma)	2σ error	%	Core
GAL-7_127.FIN2	823,0	5,980	0,4261	0,00730	0,05694	0,0006	0,5046500	359,90	5,20	357,00	3,50	371,0	33,0	357,0	3,5	0,806	
GAL-7_128.FIN2	409,7	0,313	1,3570	0,02700	0,14420	0,0019	0,6080900	870,00	11,00	868,00	11,00	871,0	31,0	871,0	31,0	0,344	
GAL-7_129.FIN2	595,9	5,340	0,5950	0,01200	0,07660	0,0013	0,3173100	473,80	7,90	475,60	7,90	462,0	56,0	475,6	7,9	0,380	Rim
GAL-7_129.FIN2	96,7	0,994	1,5600	0,03400	0,15420	0,0022	0,0347970	953,00	14,00	926,00	13,00	1009,0	53,0	1009,0	53,0	8,226	Core
GAL-7_130.FIN2	550,0	2,301	0,3442	0,00580	0,04754	0,0004	0,2827100	300,00	4,40	299,40	2,40	297,0	37,0	299,4	2,4	0,200	
GAL-7_131.FIN2	436,0	2,650	0,6048	0,00880	0,07686	0,0007	0,3078900	480,40	5,40	477,30	4,20	483,0	32,0	477,3	4,2	0,645	
GAL-7_132.FIN2	1129,0	2,181	0,3442	0,00420	0,04724	0,0004	0,4097500	300,10	3,20	297,50	2,20	310,0	26,0	297,5	2,2	0,866	
GAL-7_133.FIN2	876,0	0,810	0,3811	0,00680	0,05208	0,0006	0,5271000	327,40	4,90	327,30	3,50	323,0	34,0	327,3	3,5	0,031	
GAL-7_134.FIN2	483,0	1,861	0,3711	0,00720	0,05074	0,0005	0,2613800	319,90	5,30	319,10	3,10	312,0	41,0	319,1	3,1	0,250	
GAL-7_135.FIN2	383,0	3,320	0,5614	0,00900	0,07379	0,0006	0,1198800	452,50	6,00	458,90	3,60	407,0	39,0	458,9	3,6	1,414	
GAL-7_136.FIN2	2000,0	1,652	0,4015	0,00710	0,05329	0,0006	0,6064100	342,50	5,20	334,70	3,80	391,0	32,0	334,7	3,8	2,277	
GAL-5_1.FIN2	111,0	0,806	0,8560	0,02000	0,10150	0,0013	0,3300700	626,00	11,00	623,30	7,60	616,0	50,0	623,3	7,6	0,431	
GAL-5_2.FIN2	222,3	2,438	0,5770	0,01100	0,07337	0,0008	0,4889500	461,70	7,00	456,40	4,80	475,0	37,0	456,4	4,8	1,148	
GAL-5_3.FIN2	659,0	15,450	0,6100	0,01000	0,07760	0,0011	0,2652000	483,30	6,60	481,90	6,50	482,0	42,0	481,9	6,5	0,290	
GAL-5_4.FIN2	302,0	1,652	4,9460	0,04800	0,29710	0,0030	0,5680200	1809,00	8,20	1676,00	15,00	1962,0	16,0	1962,0	16,0	14,577	
GAL-5_5.FIN2	313,0	4,330	0,7160	0,01200	0,08762	0,0009	0,2492800	547,70	7,10	541,40	5,20	567,0	36,0	541,4	5,2	1,150	
GAL-5_6.FIN2	920,0	1,044	1,6160	0,02600	0,15610	0,0022	0,5474500	976,00	10,00	935,00	12,00	1062,0	30,0	1062,0	30,0	11,959	
GAL-5_7.FIN2	150,0	1,415	0,4940	0,01200	0,06369	0,0009	0,2993500	406,50	8,10	398,00	5,20	431,0	56,0	398,0	5,2	2,091	
GAL-5_8.FIN2	661,0	6,010	0,6890	0,03100	0,08670	0,0042	0,5801000	531,00	19,00	536,00	25,00	510,0	100,0	536,0	25,0	0,942	Rim
GAL-5_8.FIN2	1173,0	2,500	0,9600	0,01700	0,10820	0,0018	0,5946900	682,50	8,90	662,00	10,00	745,0	32,0	662,0	10,0	3,004	Core
GAL-5_9.FIN2	1371,0	1,914	0,4122	0,00520	0,05434	0,0006	0,6058100	350,20	3,70	341,10	3,50	405,0	27,0	341,1	3,5	2,599	
GAL-5_10.FIN2	208,5	2,450	0,3249	0,00780	0,04389	0,0006	0,3235300	285,80	5,80	276,80	3,90	341,0	52,0	276,8	3,9	3,149	
GAL-5_11.FIN2	1000,0	3,600	0,3651	0,00530	0,04962	0,0005	0,2395100	315,80	4,00	312,20	3,10	345,0	37,0	312,2	3,1	1,140	
GAL-5_12.FIN2	146,4	1,180	5,6130	0,09500	0,33430	0,0059	0,7529800	1914,00	14,00	1857,00	28,00	1979,0	21,0	1979,0	21,0	6,165	
GAL-5_13.FIN2	206,3	1,342	5,6450	0,09300	0,33180	0,0046	0,7542400	1921,00	15,00	1846,00	22,00	2007,0	20,0	2007,0	20,0	8,022	
GAL-5_14.FIN2	349,0	1,699	0,4127	0,00790	0,05547	0,0007	0,4669400	350,20	5,60	347,90	4,10	357,0	39,0	347,9	4,1	0,657	
GAL-5_15.FIN2	175,0	1,080	0,8430	0,01700	0,10170	0,0011	0,0538800	619,30	9,00	624,30	6,70	595,0	45,0	624,3	6,7	0,807	
GAL-5_16.FIN2	206,1	2,209	0,3407	0,00880	0,04672	0,0008	0,4135200	296,80	6,60	294,30	4,60	322,0	53,0	294,3	4,6	0,842	
GAL-5_18.FIN2	318,0	0,847	0,3720	0,00690	0,05114	0,0005	0,4085200	321,30	5,20	321,50	3,20	309,0	39,0	321,5	3,2	0,062	
GAL-5_19.FIN2	381,0	0,980	11,5100	0,15000	0,47510	0,0064	0,7979000	2562,00	14,00	2504,00	28,00	2609,0	16,0	2609,0	16,0	4,025	
GAL-5_20.FIN2	280,3	65,000	0,4290	0,02300	0,05800	0,0020	0,0733430	362,00	16,00	364,00	12,00	330,0	120,0	364,0	12,0	0,552	Rim
GAL-5_20.FIN2	201,1	1,110	0,8480	0,01700	0,10017	0,0010	0,3652300	622,50	9,10	615,30	5,70	646,0	40,0	615,3	5,7	1,157	Core
GAL-5_21.FIN2	250,0	0,848	0,7380	0,01900	0,08930	0,0015	0,4013800	560,00	11,00	551,40	8,80	592,0	53,0	551,4	8,8	1,536	
GAL-5_22.FIN2	304,0	2,580	0,6830	0,01200	0,08546	0,0009	0,3887300	527,60	7,00	528,60	5,30	520,0	36,0	528,6	5,3	0,190	
GAL-5_24.FIN2	258,0	1,550	0,4026	0,00830	0,05349	0,0006	0,3736900	342,90	6,00	335,90	3,80	392,0	44,0	335,9	3,8	2,041	
GAL-5_25.FIN2	40,0	0,989	1,5450	0,04600	0,15410	0,0029	0,3666100	942,00	18,00	923,00	16,00	972,0	64,0	972,0	64,0	5,041	
GAL-5_26.FIN2	763,0	19,700	0,4110	0,01300	0,05450	0,0016	0,5087600	349,10	9,50	342,00	10,00	403,0	68,0	342,0	10,0	2,034	Rim
GAL-5_26.FIN2	21,9	0,764	0,8230	0,07900	0,09950	0,0038	0,1062800	602,00	43,00	611,00	22,00	530,0	200,0	611,0	22,0	1,495	Core
GAL-5_27.FIN2	656,0	19,800	0,4136	0,00910	0,05249	0,0010	0,3834000	351,00	6,50	329,70	5,90	509,0	52,0	329,7	5,9	6,068	
GAL-5_28.FIN2	169,4	1,349	0,8400	0,01700	0,10030	0,0014	0,0461310	617,70	9,20	615,70	8,40	616,0	46,0	615,7	8,4	0,324	
GAL-5_29.FIN2	401,0	1,603	0,3400	0,01800	0,04510	0,0018	0,4414500	296,00	14,00	284,00	11,00	390,0	110,0	284,0	11,0	4,054	
GAL-5_30.FIN2	127,9	0,785	5,1200	0,09800	0,32340	0,0059	0,8293200	1834,00	17,00	1804,00	29,00	1879,0	23,0	1879,0	23,0	3,991	
GAL-5_31.FIN2	115,6	1,118	5,9910	0,06700	0,35690	0,0033	0,6646000	1972,80	9,60	1967,00	16,00	1990,0	17,0	1990,0	17,0	1,156	
GAL-5_32.FIN2	1193,0	23,800	0,4478	0,00670	0,05940	0,0007	0,4142700	375,50	4,70	372,00	4,00	403,0	33,0	372,0	4,0	0,932	
GAL-5_33.FIN2	99,1	0,932	0,9110	0,02100	0,10430	0,0012	0,4656900	655,00	11,00	639,20	7,00	695,0	51,0	639,2	7,0	2,412	
GAL-5_34.FIN2	221,0	1,191	0,7210	0,03500	0,08950	0,0025	0,4100300	550,00	21,00	552,00	15,00	534,0	98,0	552,0	15,0	0,364	

Sample Name:	[U]							207/235		206/238		207/206		Best age		Discordance	Rim/
Grain #	ppm	U/Th	207/235	2σ error	206/238	2σ error	RHO	Age Ma	2σ error	Age (Ma)	2σ error	Age (Ma)	2σ error	(Ma)	2σ error	%	Core
GAL-5_35.FIN2	477,0	9,400	0,5290	0,03500	0,06470	0,0031	0,5641100	430,00	23,00	404,00	19,00	570,0	120,0	404,0	19,0	6,047	Rim
GAL-5_35.FIN2	73,1	1,158	0,7550	0,02200	0,09090	0,0012	0,0849810	570,00	13,00	560,80	7,20	599,0	69,0	560,8	7,2	1,614	Core
GAL-5_36.FIN2	308,0	2,620	0,6420	0,01900	0,07560	0,0014	0,0143580	503,00	12,00	469,90	8,70	651,0	66,0	469,9	8,7	6,581	
GAL-5_37.FIN2	271,0	2,440	0,9760	0,03100	0,11000	0,0018	0,3305200	691,00	16,00	673,00	11,00	747,0	66,0	673,0	11,0	2,605	Rim
GAL-5_37.FIN2	340,0	2,510	6,7120	0,07900	0,36870	0,0049	0,5819200	2074,00	10,00	2023,00	23,00	2131,0	18,0	2131,0	18,0	5,068	Core
GAL-5_38.FIN2	177,6	1,999	0,9580	0,01700	0,10960	0,0012	0,1980700	682,10	9,00	670,10	6,80	715,0	38,0	670,1	6,8	1,759	
GAL-5_39.FIN2	330,0	2,538	0,3601	0,00800	0,04914	0,0006	0,1540000	311,90	6,00	309,20	3,60	315,0	53,0	309,2	3,6	0,866	
GAL-5_40.FIN2	134,5	2,150	0,6210	0,01900	0,07830	0,0012	0,2026300	489,00	12,00	486,10	6,90	487,0	67,0	486,1	6,9	0,593	
GAL-5_41.FIN2	1380,0	1,105	0,3880	0,01000	0,05140	0,0011	0,4939700	332,30	7,50	323,00	6,60	392,0	50,0	323,0	6,6	2,799	
GAL-5_42.FIN2	181,7	0,836	5,3900	0,13000	0,33920	0,0076	0,8226300	1880,00	22,00	1881,00	37,00	1867,0	29,0	1867,0	29,0	0,750	
GAL-5_43.FIN2	224,0	0,656	0,8260	0,01600	0,09780	0,0013	0,4720000	609,80	8,90	601,30	7,80	635,0	35,0	601,3	7,8	1,394	
GAL-5_44.FIN2	239,0	1,226	11,6300	0,16000	0,46710	0,0055	0,7449900	2572,00	13,00	2473,00	24,00	2650,0	16,0	2650,0	16,0	6,679	
GAL-5_46.FIN2	650,0	46,200	0,4020	0,01400	0,05270	0,0012	0,4887000	342,80	9,70	331,20	7,60	397,0	71,0	331,2	7,6	3,384	Rim
GAL-5_46.FIN2	384,0	4,980	5,0400	0,12000	0,30330	0,0064	0,8410000	1826,00	20,00	1706,00	32,00	1966,0	24,0	1966,0	24,0	13,225	Core
GAL-5_47.FIN2	231,0	5,820	0,6170	0,03800	0,07710	0,0018	0,5101800	499,00	34,00	479,00	11,00	570,0	150,0	479,0	11,0	4,008	Rim
GAL-5_47.FIN2	381,5	1,318	1,1780	0,03000	0,12590	0,0018	0,2459200	789,00	14,00	764,00	10,00	849,0	51,0	764,0	10,0	3,169	Core
GAL-5_48.FIN2	456,0	2,159	0,5660	0,01200	0,07300	0,0010	0,4059500	454,60	7,90	454,00	6,20	457,0	47,0	454,0	6,2	0,132	
GAL-5_49.FIN2	2060,0	2,357	0,4047	0,00460	0,05402	0,0005	0,3188600	344,90	3,30	339,10	3,10	372,0	28,0	339,1	3,1	1,682	
GAL-5_50.FIN2	564,0	3,480	1,4340	0,02400	0,15100	0,0019	0,7625700	901,00	10,00	906,00	11,00	876,0	22,0	876,0	22,0	3,425	
GAL-5_51.FIN2	292,0	0,498	1,7380	0,02500	0,16880	0,0017	0,5457800	1021,10	9,30	1005,50	9,40	1049,0	27,0	1049,0	27,0	4,147	
GAL-5_52.FIN2	714,0	4,220	0,3914	0,00880	0,05290	0,0011	0,5571400	334,60	6,40	332,00	6,50	350,0	43,0	332,0	6,5	0,777	
GAL-5_53.FIN2	656,0	1,530	1,6410	0,01800	0,16140	0,0015	0,6006900	985,40	6,80	964,60	8,10	1030,0	19,0	1030,0	19,0	6,350	
GAL-5_54.FIN2	273,7	1,519	0,7780	0,02000	0,09250	0,0014	0,1690700	583,00	11,00	570,50	8,20	625,0	55,0	570,5	8,2	2,144	
GAL-5_55.FIN2	28,0	1,764	1,4830	0,07900	0,14970	0,0046	0,3127000	916,00	32,00	899,00	26,00	940,0	100,0	940,0	100,0	4,362	
GAL-5_56.FIN2	435,0	10,090	0,5790	0,01100	0,07421	0,0009	0,3636000	463,50	6,80	461,40	5,60	475,0	42,0	461,4	5,6	0,453	
GAL-5_57.FIN2	99,4	7,130	0,8910	0,02600	0,10170	0,0012	0,0831770	640,00	11,00	624,10	7,10	672,0	50,0	624,1	7,1	2,484	
GAL-5_58.FIN2	1607,0	5,670	0,3486	0,00750	0,04842	0,0008	0,5119700	303,50	5,60	304,80	4,80	278,0	46,0	304,8	4,8	0,428	
GAL-5_59.FIN2	379,0	2,816	0,4387	0,00810	0,05927	0,0007	0,2891800	368,70	5,70	371,10	4,10	357,0	41,0	371,1	4,1	0,651	
GAL-5_60.FIN2	373,0	1,638	0,8420	0,01400	0,10070	0,0010	0,1792300	619,30	7,90	618,40	6,00	625,0	37,0	618,4	6,0	0,145	
GAL-5_61.FIN2	75,0	1,578	1,7100	0,04600	0,16670	0,0031	0,7022900	1007,00	18,00	993,00	17,00	1082,0	44,0	1082,0	44,0	8,226	
GAL-5_62.FIN2	886,0	75,000	0,4430	0,02700	0,05620	0,0042	0,5770400	372,00	19,00	352,00	26,00	500,0	140,0	352,0	26,0	5,376	Rim
GAL-5_62.FIN2	41,4	2,430	6,1300	0,13000	0,35290	0,0074	0,6036000	1991,00	20,00	1946,00	35,00	2048,0	33,0	2048,0	33,0	4,980	Core
GAL-5_63.FIN2	300,0	2,620	0,7840	0,01600	0,09570	0,0013	0,4910700	585,90	9,20	588,90	7,80	562,0	41,0	588,9	7,8	0,512	
GAL-5_64.FIN2	86,2	2,161	6,3800	0,17000	0,36450	0,0082	0,8302700	2024,00	24,00	2001,00	39,00	2051,0	26,0	2051,0	26,0	2,438	
GAL-5_65.FIN2	910,0	1,811	0,3587	0,00770	0,04869	0,0008	0,3489300	310,70	5,70	306,40	4,80	352,0	46,0	306,4	4,8	1,384	
GAL-5_66.FIN2	164,4	1,671	0,9070	0,01800	0,10650	0,0015	0,4618400	653,70	9,30	651,90	8,60	665,0	37,0	651,9	8,6	0,275	
GAL-5_67.FIN2	804,0	1,916	0,3558	0,00500	0,04864	0,0004	0,3914500	308,80	3,70	306,10	2,60	329,0	31,0	306,1	2,6	0,874	
GAL-5_68.FIN2	235,5	1,328	5,7200	0,14000	0,32910	0,0072	0,8861600	1927,00	22,00	1831,00	35,00	2038,0	20,0	2038,0	20,0	10,157	
GAL-5_69.FIN2	313,0	1,448	0,8320	0,01500	0,09670	0,0012	0,5708700	615,60	8,40	595,00	7,10	689,0	34,0	595,0	7,1	3,346	
GAL-5_70.FIN2	171,0	2,025	0,3690	0,01200	0,04883	0,0007	0,2559200	317,80	8,50	307,30	4,60	406,0	70,0	307,3	4,6	3,304	
GAL-5_71.FIN2	940,0	121,000	0,9850	0,02800	0,11480	0,0027	0,8053800	696,00	14,00	700,00	16,00	698,0	43,0	700,0	16,0	0,575	Rim
GAL-5_71.FIN2	357,0	2,760	1,4860	0,02000	0,15300	0,0015	0,3488400	924,90	7,80	917,70	8,20	932,0	27,0	932,0	27,0	1,534	Core
GAL-5_72.FIN2	720,0	2,367	0,3995	0,00510	0,05342	0,0005	0,1262700	341,00	3,70	335,40	3,20	374,0	34,0	335,4	3,2	1,642	
GAL-5_73.FIN2	795,0	2,090	0,3748	0,00590	0,05153	0,0006	0,3065200	322,90	4,30	323,90	3,40	320,0	39,0	323,9	3,4	0,310	
GAL-5_74.FIN2	1897,0	5,270	0,6933	0,00840	0,07733	0,0008	0,6035400	534,30	5,00	480,70	4,80	764,0	21,0	480,7	4,8	10,032	
GAL-5_75.FIN2	985,0	6,220	0,9370	0,03300	0,10350	0,0022	0,6655700	670,00	17,00	635,00	13,00	783,0	58,0	635,0	13,0	5,224	Rim
GAL-5_75.FIN2	337,0	0,667	4,2050	0,09900	0,27580	0,0050	0,7650700	1673,00	20,00	1570,00	25,00	1800,0	28,0	1800,0	28,0	12,778	Core

Sample Name:	[U]							207/235		206/238		207/206		Best age		Discordance	Rim/
Grain #	ppm	U/Th	207/235	2σ error	206/238	2σ error	RHO	Age Ma	2σ error	Age (Ma)	2σ error	Age (Ma)	2σ error	(Ma)	2σ error	%	Core
GAL-5_76.FIN2	498,0	150,000	0,3441	0,00930	0,04690	0,0010	0,2596600	299,90	7,00	295,30	6,20	326,0	64,0	295,3	6,2	1,534	Rim
GAL-5_76.FIN2	905,0	1,472	0,7490	0,02400	0,09580	0,0029	0,7253400	566,00	14,00	590,00	17,00	469,0	49,0	590,0	17,0	4,240	Core
GAL-5_77.FIN2	442,0	1,896	0,3831	0,00780	0,05308	0,0006	0,3695100	328,70	5,70	333,40	3,90	284,0	42,0	333,4	3,9	1,430	
GAL-5_78.FIN2	1650,0	13,490	0,8350	0,01100	0,09885	0,0008	0,4004200	615,60	5,80	607,60	4,80	640,0	25,0	607,6	4,8	1,300	
GAL-5_79.FIN2	466,0	1,234	0,3557	0,00720	0,04791	0,0006	0,3239100	308,50	5,40	301,60	3,50	356,0	45,0	301,6	3,5	2,237	
GAL-5_80.FIN2	259,0	1,830	0,5820	0,01100	0,07404	0,0007	0,2372100	464,70	6,80	460,40	4,10	469,0	41,0	460,4	4,1	0,925	
GAL-5_81.FIN2	210,0	2,300	0,4380	0,01100	0,05676	0,0008	0,3353800	367,80	7,60	355,80	5,10	432,0	54,0	355,8	5,1	3,263	
GAL-5_82.FIN2	311,4	1,651	0,4242	0,00690	0,05621	0,0006	0,2532100	358,60	4,90	352,50	3,50	394,0	39,0	352,5	3,5	1,701	
GAL-5_83.FIN2	168,0	0,665	0,8800	0,01800	0,10300	0,0015	0,3144400	640,00	10,00	632,00	9,00	649,0	47,0	632,0	9,0	1,250	
GAL-5_84.FIN2	22,2	1,407	6,9800	0,17000	0,38270	0,0056	0,2521100	2103,00	22,00	2087,00	26,00	2106,0	45,0	2106,0	45,0	0,902	
GAL-5_85.FIN2	288,8	1,590	0,8200	0,01300	0,09920	0,0011	0,4372800	607,50	7,40	609,50	6,30	595,0	34,0	609,5	6,3	0,329	
GAL-5_86.FIN2	91,1	1,078	9,3000	0,13000	0,42430	0,0052	0,6007200	2365,00	13,00	2278,00	24,00	2436,0	20,0	2436,0	20,0	6,486	
GAL-5_87.FIN2	539,0	1,841	0,3557	0,00920	0,04793	0,0009	0,3537300	308,40	6,90	301,70	5,50	344,0	53,0	301,7	5,5	2,173	
GAL-5_88.FIN2	167,0	3,062	0,6280	0,01800	0,07890	0,0011	0,2793500	493,00	11,00	489,30	6,60	503,0	63,0	489,3	6,6	0,751	
GAL-5_89.FIN2	5990,0	6,560	0,2370	0,01300	0,03070	0,0011	0,7480400	215,00	10,00	194,90	6,90	427,0	74,0	194,9	6,9	9,349	Rim
GAL-5_89.FIN2	1780,0	1,740	0,3286	0,00890	0,04225	0,0008	0,5777600	288,30	6,80	266,70	4,90	452,0	49,0	266,7	4,9	7,492	Core
GAL-5_90.FIN2	231,6	1,433	0,3448	0,00850	0,04662	0,0007	0,3720500	301,00	6,60	293,70	4,20	326,0	52,0	293,7	4,2	2,425	
GAL-5_91.FIN2	480,0	2,740	9,9150	0,09100	0,45050	0,0051	0,5878200	2426,30	8,50	2397,00	22,00	2441,0	15,0	2441,0	15,0	1,803	
GAL-5_92.FIN2	995,0	4,140	0,3810	0,01000	0,05310	0,0010	0,2818300	327,10	7,40	333,60	6,40	254,0	56,0	333,6	6,4	1,987	
GAL-5_93.FIN2	129,3	4,950	1,8730	0,03100	0,17960	0,0023	0,3687100	1071,00	11,00	1064,00	12,00	1074,0	35,0	1074,0	35,0	0,931	
GAL-5_94.FIN2	214,0	1,130	1,9130	0,06900	0,17920	0,0069	0,5421700	1083,00	24,00	1061,00	38,00	1118,0	70,0	1118,0	70,0	5,098	Rim
GAL-5_94.FIN2	38,6	1,500	4,0500	0,16000	0,20410	0,0058	0,3903400	1641,00	33,00	1197,00	31,00	2256,0	70,0	DISC	DISC	46,941	Core
GAL-5_95.FIN2	505,0	1,131	0,3979	0,00700	0,05313	0,0007	0,1755300	339,70	5,00	333,70	4,00	365,0	36,0	333,7	4,0	1,766	
GAL-5_96.FIN2	245,0	4,360	0,6120	0,01200	0,07620	0,0008	0,4026400	483,90	7,50	473,30	5,00	510,0	40,0	473,3	5,0	2,191	
GAL-5_97.FIN2	162,2	3,370	0,9000	0,02300	0,10570	0,0016	0,4406100	650,00	12,00	647,60	9,20	634,0	50,0	647,6	9,2	0,369	
GAL-5_98.FIN2	520,0	4,239	0,6180	0,01100	0,07840	0,0011	0,4515500	489,10	7,00	486,60	6,40	482,0	37,0	486,6	6,4	0,511	
GAL-5_99.FIN2	239,0	1,421	0,8320	0,01500	0,09880	0,0010	0,1079300	614,70	7,90	607,50	5,80	621,0	40,0	607,5	5,8	1,171	
GAL-5_100.FIN2	1040,0	1,795	0,3900	0,00830	0,05247	0,0008	0,5117700	334,20	6,00	329,60	5,00	349,0	43,0	329,6	5,0	1,376	
GAL-5_101.FIN2	214,0	1,838	1,4300	0,02500	0,14780	0,0023	0,6570400	900,00	11,00	888,00	13,00	908,0	30,0	908,0	30,0	2,203	
GAL-5_102.FIN2	869,0	1,080	0,3770	0,01200	0,05150	0,0012	0,2635300	324,50	8,60	323,60	7,50	304,0	70,0	323,6	7,5	0,277	
GAL-5_103.FIN2	770,0	4,550	0,3860	0,01900	0,04790	0,0021	0,6269900	331,00	14,00	302,00	13,00	529,0	87,0	302,0	13,0	8,761	Rim
GAL-5_103.FIN2	288,2	0,946	0,7880	0,01100	0,09580	0,0010	0,2446100	590,50	6,50	589,40	5,90	583,0	35,0	589,4	5,9	0,186	Core
GAL-5_104.FIN2	275,0	1,001	0,5780	0,01200	0,07450	0,0010	0,3858800	462,30	7,90	462,90	6,00	437,0	44,0	462,9	6,0	0,130	
GAL-5_105.FIN2	262,0	2,469	0,3469	0,00750	0,04781	0,0004	0,2541600	301,80	5,60	301,00	2,70	291,0	46,0	301,0	2,7	0,265	
GAL-5_106.FIN2	228,0	7,730	0,5680	0,01700	0,07160	0,0012	0,0546870	455,00	11,00	445,70	7,40	484,0	74,0	445,7	7,4	2,044	
GAL-5_107.FIN2	136,5	1,274	0,9050	0,01600	0,10520	0,0011	0,0574340	653,00	8,50	644,80	6,30	663,0	43,0	644,8	6,3	1,256	
GAL-5_108.FIN2	253,0	4,280	12,2300	0,19000	0,49500	0,0080	0,5772400	2621,00	14,00	2594,00	36,00	2642,0	23,0	2642,0	23,0	1,817	
GAL-5_109.FIN2	736,0	2,572	0,4669	0,00840	0,06179	0,0009	0,3425100	388,70	5,80	386,50	5,60	391,0	42,0	386,5	5,6	0,566	
GAL-5_110.FIN2	1240,0	167,000	0,4110	0,02100	0,05580	0,0019	0,5208900	349,00	15,00	350,00	12,00	331,0	97,0	350,0	12,0	0,287	Rim
GAL-5_110.FIN2	62,1	5,020	1,9610	0,07200	0,15460	0,0029	0,6346900	1101,00	23,00	926,00	16,00	1450,0	53,0	DISC	DISC	36,138	Core
GAL-5_111.FIN2	976,0	19,400	3,4260	0,02900	0,24220	0,0020	0,5427200	1509,70	6,60	1398,00	10,00	1665,0	15,0	1665,0	15,0	16,036	
GAL-5_112.FIN2	131,4	1,468	1,0910	0,02200	0,12280	0,0017	0,4691200	748,00	11,00	746,00	10,00	748,0	39,0	746,0	10,0	0,267	
GAL-5_113.FIN2	524,0	2,199	0,7750	0,01400	0,09262	0,0009	0,0133720	581,80	7,80	571,00	5,30	614,0	34,0	571,0	5,3	1,856	
GAL-5_114.FIN2	1380,0	2,630	0,3640	0,00520	0,04875	0,0005	0,3740600	315,40	4,00	306,80	2,90	366,0	32,0	306,8	2,9	2,727	
GAL-5_115.FIN2	775,0	3,528	1,2390	0,01400	0,13640	0,0012	0,5750300	818,40	6,10	824,30	6,90	794,0	20,0	824,3	6,9	0,721	
GAL-5_116.FIN2	369,0	1,990	1,6880	0,02800	0,16610	0,0024	0,4448600	1002,00	10,00	990,00	13,00	1028,0	32,0	1028,0	32,0	3,696	
GAL-5_117.FIN2	69,6	2,059	17,9500	0,28000	0,58100	0,0100	0,3205900	2983,00	15,00	2949,00	42,00	3006,0	27,0	3006,0	27,0	1,896	

Sample Name:	[U]							207/235		206/238		207/206		Best age		Discordance	Rim/
Grain #	ppm	U/Th	207/235	2σ error	206/238	2σ error	RHO	Age Ma	2σ error	Age (Ma)	2σ error	Age (Ma)	2σ error	(Ma)	2σ error	%	Core
GAL-5_118.FIN2	225,0	3,960	0,9950	0,03100	0,11510	0,0019	0,4301500	700,00	16,00	702,00	11,00	680,0	59,0	702,0	11,0	0,286	
GAL-5_119.FIN2	592,0	1,192	0,3894	0,00670	0,05118	0,0005	0,1089000	333,70	4,90	321,80	2,80	405,0	41,0	321,8	2,8	3,566	
GAL-5_120.FIN2	117,8	1,178	1,1800	0,03100	0,12780	0,0017	0,1924500	789,00	14,00	775,10	9,50	810,0	58,0	775,1	9,5	1,762	
GAL-5_121.FIN2	1080,0	2,481	0,3985	0,00690	0,05323	0,0005	0,3368600	340,20	5,00	334,30	3,30	368,0	39,0	334,3	3,3	1,734	
GAL-5_122.FIN2	263,0	4,410	0,6320	0,01700	0,08190	0,0011	0,0317740	496,00	10,00	507,20	6,40	429,0	59,0	507,2	6,4	2,258	
GAL-5_123.FIN2	931,0	75,700	0,6070	0,01200	0,07620	0,0011	0,4511100	481,50	7,60	473,20	6,60	514,0	41,0	473,2	6,6	1,724	
GAL-5_124.FIN2	133,8	3,799	0,7510	0,01800	0,09300	0,0011	0,1738300	567,00	10,00	572,90	6,20	523,0	53,0	572,9	6,2	1,041	
GAL-5_125.FIN2	234,0	0,893	0,5220	0,04600	0,05920	0,0044	0,2319300	425,00	30,00	370,00	27,00	860,0	330,0	370,0	27,0	12,941	Rim
GAL-5_125.FIN2	76,2	0,666	0,8380	0,02900	0,09790	0,0018	0,0994770	615,00	16,00	602,00	11,00	639,0	79,0	602,0	11,0	2,114	Core
GAL-5_126.FIN2	127,0	0,639	0,8140	0,02200	0,09670	0,0012	0,1050200	602,00	12,00	594,90	7,00	602,0	59,0	594,9	7,0	1,179	
GAL-5_127.FIN2	1638,0	26,780	0,6377	0,00710	0,08065	0,0008	0,4888000	500,60	4,40	500,00	4,80	493,0	24,0	500,0	4,8	0,120	
GAL-5_128.FIN2	385,0	1,640	0,4200	0,01100	0,05508	0,0007	0,0399250	353,30	6,30	345,60	4,00	381,0	44,0	345,6	4,0	2,179	
GAL-5_129.FIN2	1087,0	2,890	0,3423	0,00500	0,04677	0,0005	0,3260500	298,70	3,80	294,70	3,10	318,0	35,0	294,7	3,1	1,339	
GAL-5_130.FIN2	155,5	0,857	0,9180	0,02500	0,10070	0,0013	0,0340970	660,00	13,00	618,50	7,90	787,0	63,0	618,5	7,9	6,288	
GAL-5_131.FIN2	897,0	46,400	1,1800	0,10000	0,12810	0,0068	0,7930700	785,00	45,00	776,00	39,00	800,0	100,0	776,0	39,0	1,146	Rim
GAL-5_131.FIN2	289,9	1,580	10,9400	0,17000	0,46580	0,0061	0,7377400	2515,00	14,00	2464,00	27,00	2558,0	16,0	2558,0	16,0	3,675	Core
GAL-5_132.FIN2	799,0	0,921	0,3847	0,00570	0,05224	0,0005	0,3218900	330,20	4,20	328,20	3,00	330,0	33,0	328,2	3,0	0,606	
GAL-5_133.FIN2	32,9	0,236	10,2400	0,19000	0,44300	0,0067	0,6248600	2452,00	17,00	2362,00	30,00	2525,0	24,0	2525,0	24,0	6,455	
GAL-5_134.FIN2	116,3	1,047	5,3800	0,06300	0,34100	0,0036	0,5076200	1880,00	10,00	1891,00	17,00	1863,0	20,0	1863,0	20,0	1,503	
GAL-5_135.FIN2	248,0	2,380	0,9880	0,06000	0,11200	0,0028	0,4404700	696,00	30,00	684,00	16,00	780,0	140,0	684,0	16,0	1,724	Rim
GAL-5_135.FIN2	42,3	1,930	1,6970	0,06400	0,17040	0,0034	0,2925700	1003,00	24,00	1014,00	19,00	959,0	78,0	959,0	78,0	5,735	Core
GAL-5_136.FIN2	423,0	3,250	0,3618	0,00680	0,04995	0,0007	0,2023800	313,10	5,10	314,20	4,10	306,0	44,0	314,2	4,1	0,351	
GAL-5_137.FIN2	308,0	1,531	5,9720	0,05800	0,35560	0,0033	0,5703800	1970,40	8,50	1960,00	16,00	1977,0	16,0	1977,0	16,0	0,860	
GAL-5_138.FIN2	667,0	2,550	0,4062	0,00830	0,05478	0,0007	0,4861100	345,50	6,00	343,70	4,30	345,0	40,0	343,7	4,3	0,521	
GAL-5_139.FIN2	495,0	1,472	0,8410	0,01400	0,09970	0,0011	0,6343200	618,50	7,50	612,60	6,20	628,0	27,0	612,6	6,2	0,954	
GAL-5_140.FIN2	203,0	1,986	0,3470	0,01000	0,04711	0,0007	0,3821600	301,40	7,80	297,30	4,00	311,0	57,0	297,3	4,0	1,360	
GAL-2_1.FIN2	162,8	0,856	0,6730	0,01500	0,08489	0,0010	0,2966900	522,20	9,30	525,10	5,60	487,0	48,0	525,1	5,6	0,555	
GAL-2_2.FIN2	1460,0	2,600	0,6670	0,01900	0,07440	0,0022	0,7589200	518,00	12,00	463,00	13,00	772,0	42,0	463,0	13,0	10,618	Rim
GAL-2_2.FIN2	480,0	0,701	1,6830	0,03100	0,16470	0,0028	0,6363700	1001,90	12,00	983,00	15,00	1030,0	32,0	1030,0	32,0	4,563	Core
GAL-2_3.FIN2	589,0	6,710	0,6420	0,01700	0,07970	0,0017	0,8534300	502,00	11,00	494,00	10,00	526,0	33,0	494,0	10,0	1,594	
GAL-2_4.FIN2	326,0	1,874	0,9410	0,01200	0,10871	0,0010	0,3312800	672,40	6,20	665,20	5,50	681,0	27,0	665,2	5,5	1,071	
GAL-2_5.FIN2	940,0	1,357	0,3111	0,00870	0,04080	0,0010	0,7729300	275,00	6,80	257,40	6,20	408,0	39,0	257,4	6,2	6,400	
GAL-2_6.FIN2	493,0	2,520	0,3340	0,00670	0,04674	0,0006	0,4463700	292,10	5,10	294,50	3,50	252,0	40,0	294,5	3,5	0,822	
GAL-2_7.FIN2	397,0	2,610	0,9660	0,01300	0,11000	0,0012	0,4299000	685,50	6,80	672,50	6,90	716,0	29,0	672,5	6,9	1,896	
GAL-2_8.FIN2	315,0	1,357	5,2850	0,05100	0,33190	0,0026	0,7056500	1866,30	8,00	1849,00	12,00	1871,0	13,0	1871,0	13,0	1,176	
GAL-2_9.FIN2	233,9	1,411	0,6050	0,01200	0,07655	0,0008	0,4474100	479,10	7,80	475,40	4,60	471,0	39,0	475,4	4,6	0,772	
GAL-2_10.FIN2	1074,0	1,483	0,3945	0,00470	0,05227	0,0005	0,5774700	337,90	3,50	328,40	3,00	379,0	23,0	328,4	3,0	2,811	
GAL-2_11.FIN2	240,0	6,360	0,8120	0,01700	0,09810	0,0011	0,1821000	602,30	9,60	603,00	6,60	585,0	45,0	603,0	6,6	0,116	
GAL-2_12.FIN2	51,1	1,497	1,0080	0,03000	0,11460	0,0017	0,2187800	705,00	16,00	698,90	9,60	687,0	66,0	698,9	9,6	0,865	
GAL-2_13.FIN2	1010,0	4,250	0,7120	0,04700	0,07440	0,0031	0,6676700	545,00	28,00	463,00	18,00	890,0	100,0	DISC	DISC	15,046	Rim
GAL-2_13.FIN2	204,5	1,121	1,5140	0,03200	0,15120	0,0031	0,4907500	935,00	13,00	907,00	17,00	989,0	44,0	989,0	44,0	8,291	Core
GAL-2_14.FIN2	220,0	2,320	8,7700	0,15000	0,39500	0,0060	0,6329100	2310,00	15,00	2144,00	27,00	2458,0	20,0	2458,0	20,0	12,775	
GAL-2_15.FIN2	295,9	1,329	1,3540	0,02600	0,13890	0,0019	0,5476500	868,00	11,00	838,00	11,00	925,0	34,0	838,0	11,0	3,456	
GAL-2_16.FIN2	715,0	5,500	0,7490	0,01400	0,09110	0,0011	0,6005500	568,20	8,20	562,00	6,70	576,0	32,0	562,0	6,7	1,091	Rim
GAL-2_16.FIN2	196,6	1,946	8,0400	0,70000	0,34400	0,0240	0,9859500	2200,00	83,00	1890,00	120,00	2513,0	39,0	2513,0	39,0	24,791	Core
GAL-2_17.FIN2	457,0	1,396	0,3597	0,00660	0,04939	0,0004	0,2366400	311,50	4,90	310,80	2,60	294,0	40,0	310,8	2,6	0,225	

Sample Name:	[U]							207/235		206/238		207/206		Best age		Discordance	Rim/
Grain #	ppm	U/Th	207/235	2σ error	206/238	2σ error	RHO	Age Ma	2σ error	Age (Ma)	2σ error	Age (Ma)	2σ error	(Ma)	2σ error	%	Core
GAL-2_18.FIN2	641,0	1,476	0,3645	0,00670	0,04781	0,0006	0,5060800	315,10	5,00	301,00	3,40	395,0	34,0	301,0	3,4	4,475	
GAL-2_19.FIN2	154,2	0,899	1,4120	0,02300	0,14610	0,0016	0,3228600	892,40	9,80	878,80	9,20	907,0	34,0	907,0	34,0	3,109	
GAL-2_20.FIN2	388,0	0,683	11,1800	0,19000	0,45280	0,0072	0,8149500	2534,00	16,00	2405,00	32,00	2639,0	15,0	2639,0	15,0	8,867	
GAL-2_21.FIN2	1210,0	11,500	0,7700	0,05500	0,08300	0,0043	0,7904400	577,00	31,00	514,00	26,00	880,0	110,0	514,0	26,0	10,919	Rim
GAL-2_21.FIN2	153,0	2,550	4,0560	0,08700	0,27890	0,0046	0,6485100	1646,00	18,00	1585,00	23,00	1717,0	31,0	1717,0	31,0	7,688	Core
GAL-2_22.FIN2	173,6	1,983	0,5730	0,01400	0,07458	0,0010	0,3553300	458,40	9,10	463,60	5,80	418,0	52,0	463,6	5,8	1,134	
GAL-2_23.FIN2	120,9	0,303	5,9810	0,05600	0,35290	0,0032	0,4978000	1971,80	8,20	1949,00	15,00	1992,0	16,0	1992,0	16,0	2,159	
GAL-2_24.FIN2	242,0	0,959	4,4400	0,16000	0,28520	0,0086	0,9602600	1710,00	31,00	1614,00	44,00	1830,0	20,0	1830,0	20,0	11,803	
GAL-2_25.FIN2	802,0	4,970	0,5286	0,00950	0,06654	0,0010	0,7352000	430,10	6,20	415,10	5,90	511,0	27,0	415,1	5,9	3,488	
GAL-2_26.FIN2	266,2	0,829	7,9230	0,08300	0,33510	0,0038	0,6908200	2220,90	9,50	1862,00	18,00	2566,0	14,0	2566,0	14,0	27,436	
GAL-2_27.FIN2	704,0	4,430	0,4230	0,01400	0,05440	0,0010	0,7838600	356,00	9,90	341,30	6,30	438,0	46,0	341,3	6,3	4,129	
GAL-2_28.FIN2	427,0	4,550	0,6970	0,01700	0,08650	0,0016	0,7773700	536,00	10,00	534,50	9,40	541,0	32,0	534,5	9,4	0,280	
GAL-2_29.FIN2	551,0	1,755	0,3558	0,00700	0,04875	0,0006	0,4291200	309,30	5,10	306,80	3,60	313,0	42,0	306,8	3,6	0,808	
GAL-2_30.FIN2	779,0	38,900	0,8240	0,02700	0,09850	0,0029	0,6343300	609,00	15,00	605,00	17,00	649,0	59,0	605,0	17,0	0,657	Rim
GAL-2_30.FIN2	109,1	1,112	1,5630	0,04200	0,15630	0,0020	0,0499270	953,00	17,00	936,00	11,00	983,0	60,0	983,0	60,0	4,781	Core
GAL-2_31.FIN2	160,0	16,200	0,9430	0,02300	0,10880	0,0015	0,4204800	672,00	12,00	665,60	8,80	689,0	48,0	665,6	8,8	0,952	
GAL-2_32.FIN2	102,1	1,606	1,5570	0,03300	0,15770	0,0017	0,4398900	950,00	13,00	944,60	9,50	962,0	39,0	962,0	39,0	1,809	
GAL-2_33.FIN2	321,0	2,300	1,1960	0,02100	0,12910	0,0011	0,2423100	798,70	9,60	782,80	6,30	838,0	34,0	782,8	6,3	1,991	
GAL-2_34.FIN2	585,0	9,050	0,9160	0,01000	0,10739	0,0010	0,4900800	660,60	5,50	657,50	5,70	676,0	23,0	657,5	5,7	0,469	
GAL-2_35.FIN2	240,0	21,700	0,8930	0,04600	0,09950	0,0050	0,2865200	646,00	25,00	611,00	29,00	780,0	130,0	611,0	29,0	5,418	Rim
GAL-2_35.FIN2	86,8	2,910	1,3500	0,05000	0,15070	0,0029	0,5250700	868,00	23,00	904,00	16,00	773,0	70,0	773,0	16,0	4,147	Core
GAL-2_36.FIN2	433,0	1,323	11,2000	0,11000	0,46640	0,0042	0,8311400	2538,80	9,30	2467,00	19,00	2601,5	9,8	2601,5	9,8	5,170	
GAL-2_37.FIN2	125,5	1,149	0,8590	0,01800	0,10088	0,0009	0,1464500	627,00	10,00	619,50	5,20	647,0	47,0	619,5	5,2	1,196	
GAL-2_38.FIN2	388,0	1,366	0,7620	0,01200	0,09201	0,0010	0,3492300	574,30	6,90	567,30	5,70	602,0	34,0	567,3	5,7	1,219	
GAL-2_39.FIN2	189,0	8,100	0,7280	0,02800	0,08740	0,0027	0,6551900	553,00	16,00	540,00	16,00	629,0	66,0	540,0	16,0	2,351	Rim
GAL-2_39.FIN2	665,0	1,526	1,5830	0,02500	0,15620	0,0022	0,6919300	962,60	9,60	936,00	13,00	1026,0	23,0	1026,0	23,0	8,772	Core
GAL-2_40.FIN2	397,7	2,850	0,9240	0,02600	0,10400	0,0029	0,6419700	663,00	14,00	638,00	17,00	761,0	51,0	638,0	17,0	3,771	
GAL-2_41.FIN2	720,0	4,700	0,6990	0,02600	0,08260	0,0027	0,6728800	538,00	16,00	511,00	16,00	648,0	56,0	511,0	16,0	5,019	Rim
GAL-2_41.FIN2	434,0	0,826	1,7450	0,02100	0,17060	0,0019	0,6230900	1024,30	7,90	1015,00	10,00	1050,0	20,0	1050,0	20,0	3,333	Core
GAL-2_42.FIN2	427,0	1,298	0,3650	0,00720	0,05022	0,0006	0,3155900	315,50	5,30	315,80	3,50	309,0	43,0	315,8	3,5	0,095	
GAL-2_43.FIN2	368,0	0,855	1,7840	0,02100	0,17170	0,0015	0,5592900	1038,60	7,70	1021,20	8,40	1078,0	20,0	1078,0	20,0	5,269	
GAL-2_44.FIN2	593,0	1,688	0,7727	0,00950	0,09463	0,0009	0,4402400	581,60	5,60	582,80	5,40	579,0	25,0	582,8	5,4	0,206	
GAL-2_45.FIN2	82,8	0,931	0,6580	0,02400	0,08350	0,0011	0,1377000	511,00	15,00	516,90	6,30	457,0	86,0	516,9	6,3	1,155	
GAL-2_46.FIN2	241,0	23,000	0,7690	0,03700	0,09210	0,0019	0,4702600	576,00	21,00	568,00	11,00	584,0	88,0	568,0	11,0	1,389	Rim
GAL-2_46.FIN2	455,0	5,980	7,5200	0,15000	0,34640	0,0049	0,7574200	2174,00	18,00	1917,00	23,00	2420,0	23,0	2420,0	23,0	20,785	Core
GAL-2_47.FIN2	549,0	3,148	1,6550	0,01600	0,16390	0,0015	0,5000700	990,80	6,30	978,20	8,60	1018,0	19,0	1018,0	19,0	3,910	
GAL-2_48.FIN2	580,0	1,508	0,3460	0,00570	0,04799	0,0005	0,3215100	301,40	4,30	302,20	3,00	282,0	35,0	302,2	3,0	0,265	
GAL-2_49.FIN2	467,0	1,436	0,7950	0,01200	0,09640	0,0010	0,4748300	594,00	6,70	593,20	5,80	588,0	29,0	593,2	5,8	0,135	
GAL-2_50.FIN2	498,0	1,197	0,5792	0,00820	0,07467	0,0007	0,4170300	464,10	5,20	464,20	4,40	456,0	31,0	464,2	4,4	0,022	
GAL-2_51.FIN2	156,6	0,786	11,8500	0,11000	0,48200	0,0038	0,6374700	2590,90	8,60	2535,00	17,00	2630,0	12,0	2630,0	12,0	3,612	
GAL-2_52.FIN2	446,0	6,830	0,6650	0,01300	0,08330	0,0011	0,6695600	516,30	7,70	515,80	6,30	513,0	31,0	515,8	6,3	0,097	
GAL-2_53.FIN2	544,0	1,058	6,8500	0,42000	0,29000	0,0140	0,9865700	2048,00	53,00	1630,00	70,00	2527,0	26,0	DISC	DISC	35,497	
GAL-2_54.FIN2	454,0	1,470	4,1340	0,07600	0,28760	0,0046	0,8118200	1659,00	15,00	1629,00	23,00	1693,0	19,0	1693,0	19,0	3,780	
GAL-2_55.FIN2	231,0	1,420	1,3260	0,02700	0,13310	0,0019	0,6258800	855,00	12,00	805,00	11,00	980,0	29,0	805,0	11,0	5,848	
GAL-2_56.FIN2	219,0	0,829	0,8820	0,02500	0,09700	0,0015	0,5296600	638,00	13,00	596,50	8,70	774,0	52,0	596,5	8,7	6,505	
GAL-2_57.FIN2	276,8	0,566	0,8820	0,01400	0,10413	0,0009	0,3954900	640,70	7,80	638,50	5,20	635,0	33,0	638,5	5,2	0,343	
GAL-2_58.FIN2	147,7	2,054	0,7740	0,01800	0,09330	0,0011	0,3680700	580,00	10,00	574,80	6,50	582,0	47,0	574,8	6,5	0,897	

Sample Name:	[U]							207/235		206/238		207/206		Best age		Discordance	Rim/
Grain #	ppm	U/Th	207/235	2σ error	206/238	2σ error	RHO	Age Ma	2σ error	Age (Ma)	2σ error	Age (Ma)	2σ error	(Ma)	2σ error	%	Core
GAL-2_59.FIN2	289,0	2,680	5,9700	0,10000	0,35110	0,0060	0,8059500	1970,00	15,00	1939,00	29,00	2003,0	23,0	2003,0	23,0	3,195	
GAL-2_60.FIN2	288,1	1,080	0,6800	0,01100	0,08448	0,0009	0,3036000	526,30	6,80	522,80	5,20	530,0	38,0	522,8	5,2	0,665	
GAL-2_61.FIN2	548,0	1,663	0,7290	0,01100	0,08924	0,0008	0,3030900	555,50	6,20	551,00	4,60	564,0	33,0	551,0	4,6	0,810	
GAL-2_62.FIN2	788,0	0,799	0,8320	0,01200	0,09870	0,0011	0,7107000	613,90	6,60	606,50	6,60	638,0	22,0	606,5	6,6	1,205	
GAL-2_63.FIN2	508,0	1,851	5,9800	0,13000	0,28710	0,0046	0,9253700	1967,00	18,00	1626,00	23,00	2346,0	14,0	DISC	DISC	30,691	
GAL-2_64.FIN2	777,0	6,390	0,5460	0,01800	0,06980	0,0020	0,7129600	441,00	12,00	435,00	12,00	475,0	53,0	435,0	12,0	1,361	Rim
GAL-2_64.FIN2	127,8	1,429	0,8560	0,02600	0,10040	0,0015	0,3675400	625,00	14,00	616,80	9,00	634,0	62,0	616,8	9,0	1,312	Core
GAL-2_65.FIN2	323,0	8,500	0,5540	0,01800	0,06760	0,0015	0,7235300	445,00	12,00	421,20	8,80	533,0	49,0	421,2	8,8	5,348	
GAL-2_66.FIN2	390,0	1,088	0,4315	0,00760	0,05830	0,0006	0,2895700	363,70	5,30	365,30	3,60	337,0	39,0	365,3	3,6	0,440	
GAL-2_67.FIN2	272,2	1,288	0,7740	0,01200	0,09400	0,0010	0,4217300	580,90	7,10	579,00	5,80	578,0	32,0	579,0	5,8	0,327	
GAL-2_68.FIN2	364,0	0,771	0,8160	0,01100	0,09807	0,0010	0,4446300	604,90	6,40	603,00	5,80	599,0	28,0	603,0	5,8	0,314	
GAL-2_69.FIN2	283,9	0,866	0,3919	0,00910	0,05191	0,0007	0,4010700	335,80	6,40	326,20	4,30	391,0	48,0	326,2	4,3	2,859	
GAL-2_70.FIN2	771,0	2,551	0,3571	0,00590	0,04881	0,0004	0,2321000	309,70	4,40	307,20	2,40	316,0	37,0	307,2	2,4	0,807	
GAL-2_71.FIN2	580,0	58,000	0,3870	0,01200	0,05250	0,0012	0,4411600	331,30	8,50	329,80	7,10	334,0	62,0	329,8	7,1	0,453	
GAL-2_72.FIN2	261,0	0,563	0,9330	0,01400	0,10968	0,0010	0,4493000	668,30	7,40	670,80	5,70	651,0	30,0	670,8	5,7	0,374	
GAL-2_73.FIN2	561,0	2,483	0,8050	0,01000	0,09540	0,0010	0,3263700	598,70	5,90	587,40	6,10	630,0	30,0	587,4	6,1	1,887	
GAL-2_74.FIN2	385,6	1,312	0,4396	0,00770	0,05746	0,0006	0,3826600	369,40	5,40	360,10	3,50	401,0	37,0	360,1	3,5	2,518	
GAL-2_75.FIN2	279,1	6,120	0,6470	0,01100	0,08052	0,0007	0,1755600	505,80	6,90	499,20	4,40	512,0	41,0	499,2	4,4	1,305	
GAL-2_76.FIN2	135,3	1,324	11,5300	0,11000	0,47260	0,0045	0,6722500	2566,70	9,30	2496,00	20,00	2615,0	13,0	2615,0	13,0	4,551	
GAL-2_77.FIN2	403,8	1,492	1,2690	0,02100	0,13640	0,0017	0,5997900	830,70	9,20	823,90	9,80	834,0	28,0	823,9	9,8	0,819	
GAL-2_78.FIN2	1081,0	1,177	0,3633	0,00640	0,04882	0,0008	0,7400100	314,20	4,80	307,20	4,70	355,0	27,0	307,2	4,7	2,228	
GAL-2_79.FIN2	722,0	20,800	0,8760	0,03100	0,10450	0,0014	0,6452700	638,00	17,00	640,80	8,10	643,0	56,0	640,8	8,1	0,439	Rim
GAL-2_79.FIN2	251,7	0,820	1,5610	0,02500	0,15920	0,0016	0,5139200	955,00	10,00	952,00	9,10	949,0	28,0	949,0	28,0	0,316	Core
GAL-2_80.FIN2	188,4	2,106	1,7200	0,02600	0,16870	0,0014	0,3883200	1014,40	9,90	1004,90	8,00	1015,0	30,0	1015,0	30,0	0,995	
GAL-2_81.FIN2	143,0	1,570	1,5910	0,02900	0,16100	0,0021	0,3012200	964,00	11,00	962,00	12,00	959,0	40,0	959,0	40,0	0,313	
GAL-2_82.FIN2	269,0	0,766	0,7800	0,01600	0,09430	0,0013	0,3569200	585,00	9,50	580,60	7,60	601,0	40,0	580,6	7,6	0,752	
GAL-2_83.FIN2	390,5	0,903	0,8550	0,01200	0,10060	0,0010	0,3093800	626,80	6,40	618,10	5,90	640,0	30,0	618,1	5,9	1,388	
GAL-2_84.FIN2	691,0	2,390	0,3920	0,02500	0,04870	0,0019	0,3769000	335,00	18,00	306,00	12,00	510,0	130,0	306,0	12,0	8,657	Rim
GAL-2_84.FIN2	606,0	4,290	0,5279	0,00890	0,06660	0,0008	0,3513400	429,90	5,90	415,60	4,60	492,0	35,0	415,6	4,6	3,326	Core
GAL-2_85.FIN2	73,9	2,400	10,3700	0,29000	0,44180	0,0097	0,8456700	2463,00	25,00	2359,00	42,00	2534,0	27,0	2534,0	27,0	6,906	
GAL-2_86.FIN2	183,5	1,005	0,5840	0,01300	0,07402	0,0009	0,2725000	465,70	8,60	460,30	5,50	465,0	50,0	460,3	5,5	1,160	
GAL-2_87.FIN2	1246,0	4,720	0,3608	0,00480	0,04944	0,0004	0,5409200	312,60	3,50	311,00	2,40	309,0	25,0	311,0	2,4	0,512	
GAL-2_88.FIN2	403,0	25,000	0,7610	0,03300	0,09170	0,0027	0,4095800	574,00	19,00	566,00	16,00	592,0	91,0	566,0	16,0	1,394	Rim
GAL-2_88.FIN2	431,0	17,000	4,2510	0,06600	0,26860	0,0035	0,7594900	1682,00	13,00	1533,00	18,00	1861,0	19,0	1861,0	19,0	17,625	Core
GAL-2_89.FIN2	265,3	21,500	4,5170	0,06000	0,28740	0,0032	0,7786900	1732,00	11,00	1628,00	16,00	1851,0	15,0	1851,0	15,0	12,048	
GAL-2_90.FIN2	302,0	15,560	5,8500	0,15000	0,28740	0,0059	0,8868800	1945,00	22,00	1626,00	29,00	2301,0	20,0	2301,0	20,0	29,335	
GAL-2_91.FIN2	96,0	3,500	0,3180	0,02400	0,04280	0,0014	0,2467400	278,00	19,00	270,00	8,50	320,0	150,0	270,0	8,5	2,878	Rim
GAL-2_91.FIN2	143,9	1,732	0,5320	0,01600	0,06700	0,0010	0,1043500	432,00	10,00	417,70	6,10	483,0	72,0	417,7	6,1	3,310	Core
GAL-2_92.FIN2	461,0	4,890	0,8740	0,01500	0,10340	0,0014	0,5310200	636,60	8,00	633,80	8,10	632,0	33,0	633,8	8,1	0,440	
GAL-2_93.FIN2	1198,0	1,335	0,5022	0,00750	0,06194	0,0007	0,6037800	412,70	5,10	387,40	4,30	545,0	27,0	387,4	4,3	6,130	
GAL-2_94.FIN2	259,0	1,994	1,0680	0,02000	0,12090	0,0014	0,5985800	736,10	9,80	735,70	8,20	734,0	33,0	735,7	8,2	0,054	
GAL-2_95.FIN2	2431,0	1,118	0,3747	0,00500	0,05055	0,0006	0,8143100	322,90	3,70	317,80	3,90	361,0	18,0	317,8	3,9	1,579	
GAL-2_96.FIN2	222,0	0,997	10,5200	0,43000	0,43800	0,0160	0,9811400	2455,00	42,00	2325,00	74,00	2586,0	15,0	2586,0	15,0	10,093	
GAL-2_97.FIN2	322,0	1,298	1,5820	0,02300	0,15890	0,0016	0,4225600	961,50	8,90	950,70	8,60	979,0	29,0	979,0	29,0	2,891	
GAL-2_98.FIN2	143,6	1,017	0,8310	0,01600	0,09970	0,0010	0,2070200	612,70	8,60	612,50	5,90	603,0	43,0	612,5	5,9	0,033	
GAL-2_99.FIN2	335,0	2,048	0,7030	0,01400	0,08789	0,0009	0,3093000	541,60	8,70	543,00	5,60	529,0	43,0	543,0	5,6	0,258	
GAL-2_100.FIN2	714,0	2,398	0,3501	0,00600	0,04834	0,0005	0,3712600	304,40	4,50	304,30	3,10	300,0	36,0	304,3	3,1	0,033	

Sample Name:	[U]							207/235		206/238		207/206		Best age		Discordance	Rim/
Grain #	ppm	U/Th	207/235	2σ error	206/238	2σ error	RHO	Age Ma	2σ error	Age (Ma)	2σ error	Age (Ma)	2σ error	(Ma)	2σ error	%	Core
GAL-2_101.FIN2	423,0	1,050	0,3972	0,00910	0,05290	0,0006	0,2913600	338,80	6,60	332,30	3,50	394,0	49,0	332,3	3,5	1,919	
GAL-2_102.FIN2	293,0	1,111	0,8780	0,01700	0,10441	0,0010	0,3254700	638,60	9,10	640,80	5,90	622,0	39,0	640,8	5,9	0,345	
GAL-2_103.FIN2	326,0	6,100	1,0660	0,04400	0,12300	0,0036	0,6220800	736,00	22,00	748,00	21,00	707,0	69,0	748,0	21,0	1,630	Rim
GAL-2_103.FIN2	345,0	0,780	1,6150	0,01900	0,16320	0,0013	0,4260500	975,00	7,20	974,60	7,20	975,0	21,0	975,0	21,0	0,041	Core
GAL-2_104.FIN2	306,2	3,250	0,6180	0,01000	0,07861	0,0008	0,2500000	487,60	6,40	487,80	4,80	475,0	38,0	487,8	4,8	0,041	
GAL-2_105.FIN2	465,0	1,404	0,3614	0,00970	0,04810	0,0007	0,3043100	312,40	7,00	302,80	4,30	380,0	55,0	302,8	4,3	3,073	
GAL-2_106.FIN2	295,0	1,737	0,3640	0,00830	0,04953	0,0006	0,1508600	314,50	6,20	311,60	3,30	339,0	49,0	311,6	3,3	0,922	
GAL-2_107.FIN2	363,0	1,130	0,5750	0,01100	0,07502	0,0008	0,3915700	461,00	7,20	466,30	4,50	423,0	40,0	466,3	4,5	1,150	
GAL-2_108.FIN2	1209,0	27,300	0,4250	0,02300	0,05640	0,0027	0,7951200	359,00	16,00	354,00	16,00	396,0	73,0	354,0	16,0	1,393	Rim
GAL-2_108.FIN2	238,7	1,273	0,7560	0,01800	0,09170	0,0010	0,4472000	573,00	10,00	565,50	5,70	580,0	47,0	565,5	5,7	1,309	Core
GAL-2_109.FIN2	1238,0	1,961	0,9022	0,00980	0,10314	0,0010	0,5929200	652,40	5,20	632,70	5,70	718,0	19,0	632,7	5,7	3,020	
GAL-2_110.FIN2	81,4	0,991	4,3090	0,08500	0,28260	0,0044	0,6211500	1691,00	16,00	1604,00	22,00	1804,0	28,0	1804,0	28,0	11,086	
GAL-2_111.FIN2	578,0	17,900	0,8350	0,02600	0,09750	0,0016	0,6311200	615,00	15,00	599,70	9,40	688,0	47,0	599,7	9,4	2,488	Rim
GAL-2_111.FIN2	511,4	9,640	3,0910	0,05700	0,20650	0,0035	0,6289400	1429,00	14,00	1210,00	18,00	1758,0	30,0	DISC	DISC	31,172	Core
GAL-2_112.FIN2	774,0	10,870	0,7330	0,01200	0,09080	0,0011	0,5423100	558,50	7,10	560,30	6,80	541,0	33,0	560,3	6,8	0,322	
GAL-2_113.FIN2	255,0	5,770	0,6970	0,02100	0,08560	0,0014	0,5213700	534,00	12,00	529,50	8,10	532,0	50,0	529,5	8,1	0,843	
GAL-2_114.FIN2	537,0	1,550	0,5636	0,00950	0,07420	0,0008	0,5558100	453,30	6,20	461,40	4,50	402,0	35,0	461,4	4,5	1,787	
GAL-2_115.FIN2	328,0	0,584	1,1570	0,01500	0,12650	0,0012	0,2150400	781,50	7,60	767,70	6,90	815,0	31,0	767,7	6,9	1,766	
GAL-2_116.FIN2	1005,0	2,610	0,3737	0,00580	0,05026	0,0005	0,4947900	322,00	4,30	316,10	3,10	357,0	31,0	316,1	3,1	1,832	
GAL-2_117.FIN2	1251,0	4,140	0,3947	0,00560	0,05368	0,0005	0,3011200	337,50	4,10	337,00	2,90	332,0	32,0	337,0	2,9	0,148	
GAL-2_118.FIN2	460,0	1,913	4,8120	0,07800	0,30800	0,0050	0,8446000	1783,00	14,00	1732,00	24,00	1845,0	17,0	1845,0	17,0	6,125	
GAL-2_119.FIN2	440,0	21,200	0,5470	0,03800	0,07080	0,0033	0,6227300	441,00	25,00	441,00	20,00	440,0	120,0	441,0	20,0	0,000	Rim
GAL-2_119.FIN2	99,8	0,727	0,7730	0,02400	0,09460	0,0017	0,1562300	579,00	14,00	582,50	9,90	557,0	66,0	582,5	9,9	0,604	Core
GAL-2_120.FIN2	588,0	0,454	1,5400	0,01900	0,15530	0,0016	0,5815700	945,50	7,40	930,60	9,00	980,0	22,0	980,0	22,0	5,041	
GAL-2_121.FIN2	927,0	12,300	0,8880	0,05100	0,09870	0,0041	0,7675400	643,00	28,00	606,00	24,00	774,0	81,0	606,0	24,0	5,754	Rim
GAL-2_121.FIN2	317,0	2,078	3,1640	0,04300	0,24560	0,0028	0,6245500	1447,00	11,00	1415,00	15,00	1491,0	21,0	1491,0	21,0	5,097	Core
GAL-2_122.FIN2	49,5	0,645	1,1420	0,05700	0,12580	0,0025	0,2385400	767,00	27,00	763,00	14,00	740,0	100,0	763,0	14,0	0,522	
GAL-2_123.FIN2	677,0	1,548	0,3451	0,00620	0,04795	0,0006	0,4045800	300,60	4,70	301,90	3,40	285,0	38,0	301,9	3,4	0,432	
GAL-2_124.FIN2	204,0	0,717	1,6770	0,03000	0,16440	0,0024	0,6271100	998,00	11,00	981,00	13,00	1034,0	31,0	1034,0	31,0	5,126	
GAL-2_125.FIN2	656,0	4,040	0,7230	0,02100	0,08870	0,0020	0,8262600	550,00	12,00	548,00	12,00	555,0	35,0	548,0	12,0	0,364	
GAL-2_126.FIN2	732,0	0,748	0,8630	0,01200	0,09860	0,0010	0,2041900	631,20	6,40	606,20	5,90	718,0	32,0	606,2	5,9	3,961	
GAL-2_127.FIN2	293,1	2,246	0,8380	0,01400	0,10090	0,0011	0,5361600	616,80	7,80	619,40	6,70	608,0	31,0	619,4	6,7	0,422	
GAL-2_128.FIN2	511,0	1,910	0,3620	0,01800	0,04940	0,0011	0,1022500	313,00	13,00	310,90	6,50	330,0	110,0	310,9	6,5	0,671	Rim
GAL-2_128.FIN2	69,2	0,880	5,6700	0,14000	0,33990	0,0053	0,3760200	1924,00	20,00	1885,00	26,00	1964,0	42,0	1964,0	42,0	4,022	Core
GAL-2_129.FIN2	844,0	0,853	0,3829	0,00570	0,05193	0,0006	0,4946900	328,80	4,20	326,30	3,80	338,0	31,0	326,3	3,8	0,760	
GAL-2_130.FIN2	263,0	1,473	1,5720	0,02200	0,16050	0,0016	0,3382200	959,00	8,90	959,40	9,10	963,0	30,0	963,0	30,0	0,374	
GAL-2_131.FIN2	122,4	0,840	5,9560	0,08200	0,34420	0,0033	0,6161700	1969,00	12,00	1906,00	16,00	2029,0	20,0	2029,0	20,0	6,062	
GAL-2_132.FIN2	1170,0	16,800	0,8710	0,02700	0,10220	0,0025	0,8166400	635,00	15,00	627,00	15,00	667,0	43,0	627,0	15,0	1,260	Rim
GAL-2_132.FIN2	135,5	0,958	1,4980	0,03600	0,15680	0,0020	0,1816100	928,00	15,00	939,00	11,00	888,0	54,0	888,0	54,0	5,743	Core
LUE-9_1.FIN2	104,3	0,934	0,7280	0,02000	0,08750	0,0010	0,2333400	553,00	12,00	540,60	6,10	609,0	61,0	540,6	6,1	2,242	
LUE-9_2.FIN2	347,0	0,970	1,7740	0,01800	0,17300	0,0012	0,2100300	1036,10	6,60	1028,40	6,50	1052,0	21,0	1052,0	21,0	2,243	
LUE-9_3.FIN2	784,0	2,580	9,3300	0,22000	0,45010	0,0076	0,8933100	2364,00	23,00	2392,00	34,00	2352,0	20,0	2352,0	20,0	1,701	
LUE-9_4.FIN2	335,0	2,630	0,8470	0,01100	0,10023	0,0009	0,4149700	622,40	5,80	615,70	5,00	653,0	25,0	615,7	5,0	1,076	
LUE-9_5.FIN2	328,0	1,710	0,3433	0,00750	0,04707	0,0005	0,0219310	299,90	5,50	296,50	2,80	323,0	48,0	296,5	2,8	1,134	
LUE-9_6.FIN2	457,0	2,200	0,8010	0,02500	0,09620	0,0020	0,2720200	597,00	14,00	592,00	12,00	617,0	70,0	592,0	12,0	0,838	Rim
LUE-9_6.FIN2	335,0	2,531	5,5240	0,09200	0,33110	0,0048	0,7959200	1903,00	14,00	1847,00	22,00	1964,0	21,0	1964,0	21,0	5,957	Core

Sample Name:	[U]							207/235		206/238		207/206		Best age		Discordance	Rim/
Grain #	ppm	U/Th	207/235	2σ error	206/238	2σ error	RHO	Age Ma	2σ error	Age (Ma)	2σ error	Age (Ma)	2σ error	(Ma)	2σ error	%	Core
LUE-9_7.FIN2	212,4	1,748	7,1710	0,08400	0,38930	0,0059	0,2367700	2133,00	10,00	2119,00	27,00	2134,0	32,0	2134,0	32,0	0,703	
LUE-9_8.FIN2	32,0	0,622	5,7300	0,13000	0,34240	0,0054	0,4252900	1932,00	20,00	1897,00	26,00	1966,0	40,0	1966,0	40,0	3,510	
LUE-9_9.FIN2	85,5	1,561	0,9150	0,02200	0,10620	0,0011	0,1668200	657,00	12,00	650,30	6,20	657,0	53,0	650,3	6,2	1,020	
LUE-9_10.FIN2	202,6	0,620	1,6000	0,05700	0,15850	0,0049	0,3226800	977,00	22,00	948,00	27,00	1018,0	82,0	1018,0	82,0	6,876	
LUE-9_11.FIN2	261,0	0,983	1,0940	0,02400	0,12060	0,0018	0,2197600	749,00	12,00	734,00	10,00	786,0	50,0	734,0	10,0	2,003	
LUE-9_12.FIN2	535,0	2,746	0,3800	0,00710	0,05042	0,0006	0,5576000	326,60	5,10	317,10	3,80	375,0	33,0	317,1	3,8	2,909	
LUE-9_13.FIN2	69,6	0,833	0,8000	0,03200	0,09640	0,0017	0,4420050	594,00	18,00	593,00	10,00	563,0	92,0	593,0	10,0	0,168	
LUE-9_14.FIN2	574,0	3,220	0,5640	0,01100	0,07220	0,0012	0,6434800	453,50	7,20	449,10	7,40	462,0	38,0	449,1	7,4	0,970	
LUE-9_15.FIN2	171,0	2,160	0,5810	0,01200	0,07344	0,0007	0,1407700	464,10	7,60	456,80	4,40	472,0	45,0	456,8	4,4	1,573	
LUE-9_16.FIN2	252,0	1,909	0,3511	0,00740	0,04742	0,0005	0,1337500	305,00	5,60	298,70	2,90	331,0	48,0	298,7	2,9	2,066	
LUE-9_17.FIN2	1810,0	156,000	0,4126	0,00940	0,05557	0,0009	0,4783400	350,60	6,70	348,60	5,40	350,0	47,0	348,6	5,4	0,570	Rim
LUE-9_17.FIN2	385,0	3,360	0,8640	0,02400	0,09820	0,0019	0,3815800	632,00	13,00	604,00	11,00	716,0	58,0	604,0	11,0	4,430	Core
LUE-9_19.FIN2	339,0	1,756	0,3462	0,00690	0,04643	0,0005	0,3632900	301,40	5,10	292,50	2,90	353,0	41,0	292,5	2,9	2,953	
LUE-9_20.FIN2	1650,0	119,700	0,4234	0,00580	0,05676	0,0006	0,4037900	358,30	4,10	355,90	3,60	355,0	30,0	355,9	3,6	0,670	
LUE-9_21.FIN2	53,2	1,173	6,6350	0,08100	0,36900	0,0035	0,2925000	2065,00	11,00	2024,00	16,00	2088,0	24,0	2088,0	24,0	3,065	
LUE-9_23.FIN2	389,6	1,630	0,3548	0,00750	0,04848	0,0005	0,3421400	308,00	5,70	305,20	3,20	307,0	45,0	305,2	3,2	0,909	
LUE-9_24.FIN2	150,4	1,835	1,7080	0,03600	0,16680	0,0023	0,4222100	1010,00	13,00	994,00	13,00	1030,0	39,0	1030,0	39,0	3,495	
LUE-9_25.FIN2	1064,0	2,472	0,3351	0,00450	0,04652	0,0005	0,4121500	293,20	3,40	293,10	2,70	278,0	29,0	293,1	2,7	0,034	
LUE-9_26.FIN2	894,0	1,897	0,8054	0,00820	0,09761	0,0008	0,5060500	599,60	4,60	600,30	4,80	593,0	22,0	600,3	4,8	0,117	
LUE-9_27.FIN2	740,0	3,250	0,3956	0,00800	0,05383	0,0007	0,2087300	338,10	5,80	338,00	4,50	325,0	46,0	338,0	4,5	0,030	
LUE-9_28.FIN2	1650,0	32,300	0,7950	0,02900	0,09680	0,0044	0,8555900	593,00	17,00	596,00	26,00	582,0	71,0	596,0	26,0	0,506	Rim
LUE-9_28.FIN2	502,6	1,453	1,5660	0,02500	0,15900	0,0019	0,4433700	956,30	9,70	951,00	10,00	958,0	30,0	958,0	30,0	0,731	Core
LUE-9_29.FIN2	186,7	1,264	0,4460	0,01300	0,05916	0,0007	0,3011700	375,70	8,60	370,50	4,10	369,0	64,0	370,5	4,1	1,384	
LUE-9_30.FIN2	75,5	1,126	5,7710	0,07200	0,34970	0,0035	0,4049700	1941,00	11,00	1933,00	17,00	1943,0	22,0	1943,0	22,0	0,515	
LUE-9_31.FIN2	96,3	1,691	0,9100	0,02000	0,10760	0,0011	0,2042200	655,00	11,00	658,60	6,40	620,0	49,0	658,6	6,4	0,550	
LUE-9_32.FIN2	198,0	2,644	1,8740	0,02200	0,18160	0,0015	0,3246200	1072,00	7,80	1075,50	8,30	1059,0	24,0	1059,0	24,0	1,558	
LUE-9_33.FIN2	257,0	1,182	11,9310	0,08800	0,49560	0,0038	0,6054700	2598,90	7,10	2594,00	16,00	2598,0	12,0	2598,0	12,0	0,154	
LUE-9_34.FIN2	616,0	7,430	0,5860	0,01800	0,07600	0,0020	0,6565500	468,00	11,00	472,00	12,00	447,0	55,0	472,0	12,0	0,855	Rim
LUE-9_34.FIN2	92,6	1,356	6,4300	0,11000	0,34240	0,0048	0,5482700	2035,00	15,00	1898,00	23,00	2174,0	25,0	2174,0	25,0	12,695	Core
LUE-9_36.FIN2	424,0	6,730	0,6059	0,00970	0,07652	0,0009	0,1719500	480,30	6,10	475,30	5,20	495,0	33,0	475,3	5,2	1,041	
LUE-9_37.FIN2	245,9	2,412	1,1820	0,01600	0,13020	0,0012	0,2276800	791,30	7,40	788,70	6,60	803,0	29,0	788,7	6,6	0,329	
LUE-9_38.FIN2	364,0	2,120	0,3641	0,00710	0,04927	0,0005	0,0401060	314,70	5,30	310,00	2,90	348,0	47,0	310,0	2,9	1,493	
LUE-9_39.FIN2	585,0	1,783	0,3484	0,00680	0,04804	0,0004	0,1568900	303,00	5,10	302,50	2,70	299,0	43,0	302,5	2,7	0,165	
LUE-9_40.FIN2	576,6	1,802	0,3419	0,00580	0,04552	0,0004	0,4308300	298,30	4,40	286,90	2,40	380,0	35,0	286,9	2,4	3,822	
LUE-9_41.FIN2	236,1	6,100	14,5000	0,15000	0,52360	0,0058	0,4174200	2782,60	9,60	2713,00	25,00	2833,0	18,0	2833,0	18,0	4,236	
LUE-9_42.FIN2	190,0	1,320	0,7960	0,07800	0,09760	0,0083	0,4096600	593,00	43,00	600,00	48,00	570,0	210,0	600,0	48,0	1,180	Rim
LUE-9_42.FIN2	402,1	6,040	12,1000	0,22000	0,45950	0,0064	0,5997400	2611,00	17,00	2437,00	28,00	2750,0	25,0	2750,0	25,0	11,382	Core
LUE-9_43.FIN2	220,0	1,448	5,2340	0,06000	0,33330	0,0031	0,7349400	1857,70	9,70	1854,00	15,00	1866,0	17,0	1866,0	17,0	0,643	
LUE-9_44.FIN2	707,0	59,000	0,3980	0,01100	0,05490	0,0011	0,1295500	339,80	8,10	344,80	6,80	305,0	71,0	344,8	6,8	1,471	Rim
LUE-9_44.FIN2	29,2	0,399	0,9510	0,04400	0,11050	0,0022	0,0906160	673,00	23,00	675,00	13,00	640,0	99,0	675,0	13,0	0,297	Core
LUE-9_45.FIN2	642,0	1,723	0,4138	0,00630	0,05529	0,0006	0,6056400	351,20	4,50	346,90	3,50	379,0	30,0	346,9	3,5	1,224	
LUE-9_46.FIN2	312,0	1,760	0,3574	0,00700	0,04762	0,0006	0,3219100	309,80	5,20	299,80	3,50	383,0	43,0	299,8	3,5	3,228	
LUE-9_47.FIN2	344,0	1,786	0,7030	0,01100	0,08700	0,0009	0,2833500	540,60	6,60	537,70	5,20	552,0	32,0	537,7	5,2	0,536	
LUE-9_48.FIN2	3320,0	12,160	0,9560	0,01400	0,11490	0,0015	0,9152200	680,90	7,40	701,20	8,60	615,0	22,0	701,2	8,6	2,981	Rim
LUE-9_48.FIN2	215,6	0,970	1,6980	0,04500	0,17100	0,0035	0,6387100	1006,00	17,00	1017,00	19,00	962,0	48,0	962,0	48,0	5,717	Core
LUE-9_49.FIN2	619,1	0,969	0,4260	0,00750	0,05699	0,0006	0,1992200	360,00	5,30	357,20	3,30	377,0	40,0	357,2	3,3	0,778	
LUE-9_50.FIN2	137,0	2,232	1,4050	0,02500	0,14700	0,0016	0,2675600	890,00	11,00	883,70	9,30	905,0	37,0	905,0	37,0	2,354	

Sample Name:	[U]							207/235		206/238		207/206		Best age		Discordance	Rim/
Grain #	ppm	U/Th	207/235	2σ error	206/238	2σ error	RHO	Age Ma	2σ error	Age (Ma)	2σ error	Age (Ma)	2σ error	(Ma)	2σ error	%	Core
LUE-9_51.FIN2	617,0	2,810	0,4240	0,00980	0,05674	0,0009	0,5112400	358,50	7,00	355,70	5,60	371,0	45,0	355,7	5,6	0,781	
LUE-9_52.FIN2	395,0	1,392	1,5400	0,01700	0,15530	0,0014	0,5551600	945,70	6,60	930,50	7,60	990,0	19,0	990,0	19,0	6,010	
LUE-9_53.FIN2	429,0	0,910	0,7875	0,00970	0,09547	0,0009	0,3936800	589,20	5,50	587,70	5,00	599,0	25,0	587,7	5,0	0,255	
LUE-9_54.FIN2	343,7	3,723	6,4300	0,11000	0,36880	0,0037	0,6718200	2034,00	14,00	2023,00	17,00	2045,0	21,0	2045,0	21,0	1,076	
LUE-9_55.FIN2	690,0	2,579	0,3623	0,00590	0,04985	0,0004	0,2349000	313,60	4,40	313,60	2,10	312,0	37,0	313,6	2,1	0,000	
LUE-9_56.FIN2	317,0	1,546	0,3561	0,00700	0,04842	0,0005	0,0814540	308,80	5,20	304,80	2,90	320,0	47,0	304,8	2,9	1,295	
LUE-9_57.FIN2	430,0	8,500	0,4001	0,00700	0,05278	0,0005	0,0154100	341,90	4,90	331,60	3,00	398,0	43,0	331,6	3,0	3,013	
LUE-9_58.FIN2	156,5	1,576	0,8630	0,01800	0,10180	0,0012	0,1698900	629,90	9,90	624,70	6,70	636,0	44,0	624,7	6,7	0,826	
LUE-9_59.FIN2	188,5	0,472	0,8340	0,01400	0,09556	0,0009	0,1454000	614,50	7,50	588,20	5,20	703,0	38,0	588,2	5,2	4,280	
LUE-9_60.FIN2	409,0	1,091	1,0590	0,01800	0,11940	0,0011	0,3004600	732,40	8,80	726,80	6,20	750,0	37,0	726,8	6,2	0,765	
LUE-9_61.FIN2	1287,0	133,000	0,4059	0,00430	0,05466	0,0004	0,4213400	345,80	3,10	343,00	2,40	357,0	24,0	343,0	2,4	0,810	
LUE-9_62.FIN2	446,0	5,490	0,5883	0,00850	0,07550	0,0006	0,1133200	469,20	5,50	469,20	3,70	466,0	35,0	469,2	3,7	0,000	
LUE-9_63.FIN2	480,0	5,580	0,6000	0,00860	0,07644	0,0007	0,4324000	476,70	5,50	475,40	4,60	492,0	31,0	475,4	4,6	0,273	
LUE-9_64.FIN2	352,0	9,490	0,8110	0,01200	0,09710	0,0011	0,4233300	602,40	6,60	597,10	6,40	626,0	31,0	597,1	6,4	0,880	
LUE-9_65.FIN2	600,0	2,118	0,3542	0,00540	0,04884	0,0004	0,2588100	307,60	4,00	307,40	2,60	317,0	37,0	307,4	2,6	0,065	
LUE-9_66.FIN2	755,0	44,900	0,6520	0,03000	0,08190	0,0036	0,6069000	508,00	18,00	507,00	21,00	542,0	92,0	507,0	21,0	0,197	
LUE-9_67.FIN2	701,0	2,148	1,4330	0,01900	0,14570	0,0021	0,5500500	904,40	8,60	876,00	12,00	983,0	26,0	983,0	26,0	10,885	
LUE-9_68.FIN2	1679,0	2,750	0,3701	0,00720	0,04948	0,0006	0,4505500	319,50	5,40	311,30	3,90	381,0	40,0	311,3	3,9	2,567	
LUE-9_69.FIN2	108,4	0,836	1,8240	0,03600	0,17640	0,0028	0,2806600	1052,00	13,00	1046,00	16,00	1075,0	36,0	1075,0	36,0	2,698	
LUE-9_70.FIN2	582,0	1,379	1,1420	0,01600	0,12680	0,0015	0,4036600	772,50	7,60	769,50	8,40	785,0	29,0	769,5	8,4	0,388	
LUE-9_71.FIN2	636,0	2,540	0,4450	0,04800	0,04840	0,0042	0,5555300	373,00	33,00	304,00	26,00	830,0	180,0	DISC	DISC	18,499	Rim
LUE-9_71.FIN2	953,0	2,011	0,7650	0,01300	0,08860	0,0012	0,5195100	576,30	7,60	546,90	7,30	696,0	33,0	546,9	7,3	5,102	Core
LUE-9_72.FIN2	260,0	0,914	1,5140	0,01900	0,15400	0,0015	0,3947800	936,00	7,50	923,30	8,60	968,0	28,0	968,0	28,0	4,618	
LUE-9_73.FIN2	1148,0	39,400	0,7700	0,04500	0,09470	0,0056	0,7534700	577,00	26,00	583,00	33,00	569,0	92,0	583,0	33,0	1,040	Rim
LUE-9_73.FIN2	216,0	1,693	1,6880	0,02700	0,16820	0,0022	0,7249600	1002,00	10,00	1002,00	12,00	1010,0	27,0	1010,0	27,0	0,792	Core
LUE-9_74.FIN2	337,0	2,537	0,3645	0,00760	0,04945	0,0005	0,1622800	315,10	5,70	311,10	2,70	328,0	48,0	311,1	2,7	1,269	
LUE-9_75.FIN2	150,7	0,525	6,1740	0,06500	0,36350	0,0030	0,4557200	1999,20	9,20	1998,00	14,00	2003,0	17,0	2003,0	17,0	0,250	
LUE-9_76.FIN2	2074,0	1,905	1,5210	0,02600	0,15500	0,0024	0,6673500	939,00	10,00	929,00	13,00	963,0	27,0	963,0	27,0	3,531	Rim
LUE-9_76.FIN2	83,9	0,305	4,7100	0,22000	0,30910	0,0046	0,3239100	1766,00	39,00	1736,00	23,00	1800,0	80,0	1800,0	80,0	3,556	Core
LUE-9_77.FIN2	398,0	2,480	0,3583	0,00750	0,04875	0,0006	0,3114800	310,40	5,60	306,80	3,90	335,0	46,0	306,8	3,9	1,160	
LUE-9_78.FIN2	1002,0	2,640	1,2420	0,04000	0,12560	0,0048	0,6554100	819,00	18,00	762,00	28,00	985,0	62,0	762,0	28,0	6,960	Rim
LUE-9_78.FIN2	674,0	1,149	1,6670	0,02000	0,16870	0,0020	0,4822100	995,40	7,40	1005,00	11,00	980,0	24,0	980,0	24,0	2,551	Core
LUE-9_79.FIN2	370,0	51,400	0,4740	0,01200	0,06250	0,0011	0,6140700	392,60	8,10	390,90	6,60	415,0	38,0	390,9	6,6	0,433	
LUE-9_80.FIN2	377,0	1,543	0,3426	0,00620	0,04689	0,0004	0,1005900	298,70	4,70	295,40	2,50	314,0	41,0	295,4	2,5	1,105	
LUE-9_81.FIN2	1234,0	67,700	0,3869	0,00850	0,05220	0,0012	0,0785030	332,00	6,20	327,70	7,10	334,0	59,0	327,7	7,1	1,295	
LUE-9_82.FIN2	192,0	2,710	10,7800	0,19000	0,46970	0,0072	0,5590400	2503,00	17,00	2482,00	32,00	2520,0	27,0	2520,0	27,0	1,508	
LUE-9_83.FIN2	2205,0	20,500	3,7030	0,07300	0,25810	0,0080	0,5821400	1572,00	16,00	1480,00	41,00	1698,0	46,0	1698,0	46,0	12,839	
LUE-9_84.FIN2	399,0	1,845	0,3785	0,00800	0,05208	0,0006	0,1010300	325,30	5,90	327,30	3,90	314,0	46,0	327,3	3,9	0,615	
LUE-9_85.FIN2	394,0	3,000	0,4449	0,00940	0,05883	0,0007	0,3205900	373,00	6,60	368,40	4,30	392,0	45,0	368,4	4,3	1,233	
LUE-9_86.FIN2	701,0	3,000	0,6002	0,00880	0,07585	0,0010	0,3191100	476,80	5,60	471,20	5,80	487,0	34,0	471,2	5,8	1,174	
LUE-9_87.FIN2	130,4	1,166	0,6160	0,01700	0,07720	0,0011	0,2090500	486,00	10,00	479,10	6,40	495,0	61,0	479,1	6,4	1,420	
LUE-9_88.FIN2	352,0	1,628	1,5160	0,02400	0,15410	0,0026	0,4694900	936,00	9,60	924,00	15,00	957,0	35,0	957,0	35,0	3,448	
LUE-9_89.FIN2	571,0	73,000	0,4030	0,00950	0,05423	0,0009	0,4371000	343,20	6,90	340,40	5,20	370,0	53,0	340,4	5,2	0,816	
LUE-9_90.FIN2	223,0	1,320	0,6840	0,01300	0,08515	0,0008	0,3071000	528,80	7,70	527,30	4,90	516,0	40,0	527,3	4,9	0,284	
LUE-9_91.FIN2	836,0	2,422	0,3440	0,01100	0,04650	0,0010	0,4197700	300,00	8,40	292,80	6,40	339,0	66,0	292,8	6,4	2,400	
LUE-9_92.FIN2	276,0	4,650	5,5200	0,06700	0,33080	0,0036	0,7341300	1902,00	10,00	1841,00	17,00	1958,0	18,0	1958,0	18,0	5,975	
LUE-9_93.FIN2	44,5	1,138	0,8020	0,03300	0,09570	0,0019	0,0178160	594,00	19,00	589,00	11,00	573,0	97,0	589,0	11,0	0,842	

Sample Name:	[U]							207/235		206/238		207/206		Best age		Discordance	Rim/
Grain #	ppm	U/Th	207/235	2σ error	206/238	2σ error	RHO	Age Ma	2σ error	Age (Ma)	2σ error	Age (Ma)	2σ error	(Ma)	2σ error	%	Core
LUE-9_94.FIN2	303,0	0,992	0,4072	0,00800	0,05373	0,0005	0,2432500	346,20	5,80	337,30	3,20	390,0	45,0	337,3	3,2	2,571	
LUE-9_95.FIN2	759,0	0,723	0,3816	0,00540	0,05123	0,0005	0,5238000	327,90	4,00	322,10	3,30	359,0	30,0	322,1	3,3	1,769	
LUE-9_96.FIN2	638,0	12,790	0,5910	0,01500	0,07532	0,0010	0,2592200	470,80	9,60	468,10	5,70	454,0	57,0	468,1	5,7	0,573	Rim
LUE-9_96.FIN2	98,0	2,500	0,9220	0,03300	0,10900	0,0026	0,2257900	661,00	18,00	667,00	15,00	612,0	86,0	667,0	15,0	0,908	Core
LUE-9_97.FIN2	454,0	2,770	0,3577	0,00710	0,04927	0,0005	0,0163760	310,00	5,20	310,00	3,20	273,0	44,0	310,0	3,2	0,000	
LUE-9_98.FIN2	110,8	1,465	1,6430	0,02700	0,16350	0,0018	0,1744400	985,00	10,00	976,00	10,00	988,0	38,0	988,0	38,0	1,215	
LUE-9_99.FIN2	30,2	-6,800	0,4070	0,04100	0,05340	0,0016	0,4396800	339,00	29,00	335,00	10,00	280,0	180,0	335,0	10,0	1,180	
LUE-9_100.FIN2	275,0	0,828	0,7500	0,01200	0,09171	0,0008	0,0874250	567,20	7,00	565,60	5,00	545,0	39,0	565,6	5,0	0,282	
LUE-9_101.FIN2	568,0	0,927	0,3879	0,00630	0,05230	0,0004	0,4454900	332,40	4,60	328,60	2,70	337,0	34,0	328,6	2,7	1,143	
LUE-9_102.FIN2	180,8	0,521	0,7470	0,02200	0,09090	0,0015	0,1529100	565,00	13,00	560,60	9,00	558,0	69,0	560,6	9,0	0,779	
LUE-9_104.FIN2	288,0	1,822	1,7350	0,03200	0,16600	0,0028	0,7355300	1021,00	12,00	989,00	15,00	1074,0	33,0	1074,0	33,0	7,914	
LUE-9_105.FIN2	200,0	0,805	0,8500	0,01600	0,10105	0,0009	0,2232700	623,50	8,70	620,50	5,30	623,0	41,0	620,5	5,3	0,481	
LUE-9_107.FIN2	398,0	0,706	0,8270	0,01400	0,09870	0,0012	0,5582800	610,70	7,80	606,40	7,10	614,0	31,0	606,4	7,1	0,704	
LUE-9_108.FIN2	36,9	-1,600	0,4820	0,05100	0,01116	0,0005	0,3138300	375,00	28,00	71,50	3,10	3280,0	150,0	DISC	DISC	80,933	
LUE-9_109.FIN2	139,0	17,000	0,9670	0,03300	0,11230	0,0031	0,1782000	685,00	17,00	686,00	18,00	671,0	64,0	686,0	18,0	0,146	Rim
LUE-9_109.FIN2	179,1	21,600	1,3890	0,02700	0,14660	0,0019	0,6234400	883,00	11,00	882,00	10,00	875,0	31,0	875,0	31,0	0,800	Core
LUE-9_110.FIN2	298,0	0,930	0,8660	0,02000	0,10330	0,0013	0,4524800	631,00	11,00	633,70	7,60	619,0	45,0	633,7	7,6	0,428	
LUE-9_111.FIN2	770,0	1,227	1,7250	0,01500	0,17170	0,0012	0,5049900	1017,20	5,60	1021,10	6,50	1003,0	16,0	1003,0	16,0	1,805	
LUE-9_112.FIN2	212,3	2,520	1,0990	0,01700	0,12260	0,0013	0,2333100	751,70	8,00	745,40	7,70	766,0	32,0	745,4	7,7	0,838	
LUE-9_113.FIN2	328,0	2,183	1,1260	0,01600	0,12650	0,0012	0,5930900	764,80	7,60	767,50	6,80	761,0	27,0	767,5	6,8	0,353	
LUE-9_114.FIN2	941,0	-230,000	0,4034	0,00750	0,05395	0,0005	0,4513900	343,60	5,30	338,70	3,20	367,0	35,0	338,7	3,2	1,426	
LUE-9_115.FIN2	1039,0	9,960	0,4510	0,01200	0,05930	0,0021	0,0493770	377,90	8,30	371,00	13,00	425,0	91,0	371,0	13,0	1,826	Rim
LUE-9_115.FIN2	142,5	0,491	0,8780	0,02800	0,10070	0,0014	0,3260900	637,00	15,00	618,60	8,00	693,0	61,0	618,6	8,0	2,889	Core
LUE-9_116.FIN2	127,8	2,734	1,0380	0,02500	0,11470	0,0012	0,1093300	720,00	12,00	699,90	7,10	773,0	49,0	699,9	7,1	2,792	
LUE-9_117.FIN2	490,0	1,008	1,5250	0,02500	0,15040	0,0017	0,3384300	940,00	10,00	903,30	9,40	1030,0	34,0	1030,0	34,0	12,301	
LUE-9_118.FIN2	177,0	1,071	1,6410	0,03000	0,16570	0,0023	0,4116900	984,00	12,00	988,00	13,00	971,0	38,0	971,0	38,0	1,751	
LUE-9_119.FIN2	163,9	1,995	0,9410	0,01800	0,10880	0,0012	0,3411100	672,10	9,20	666,60	6,90	689,0	39,0	666,6	6,9	0,818	
LUE-9_120.FIN2	634,0	7,270	7,4010	0,07800	0,35340	0,0038	0,8516000	2160,20	9,60	1950,00	18,00	2371,0	17,0	2371,0	17,0	17,756	
LUE-9_121.FIN2	465,0	2,775	0,3478	0,00570	0,04801	0,0005	0,2108600	302,70	4,30	302,20	2,80	309,0	38,0	302,2	2,8	0,165	
LUE-9_122.FIN2	2010,0	48,000	0,9390	0,08200	0,09300	0,0120	0,6014500	671,00	44,00	574,00	71,00	1030,0	220,0	DISC	DISC	14,456	Rim
LUE-9_122.FIN2	331,2	2,641	1,5240	0,02000	0,16220	0,0017	0,3662700	939,00	8,10	969,00	9,40	873,0	28,0	873,0	28,0	10,997	Core
LUE-9_123.FIN2	251,2	1,324	1,7320	0,02700	0,17010	0,0021	0,6125400	1019,00	10,00	1012,00	12,00	1045,0	29,0	1045,0	29,0	3,158	
LUE-9_124.FIN2	254,6	1,400	5,6330	0,05500	0,34730	0,0029	0,7203600	1919,90	8,50	1921,00	14,00	1927,0	15,0	1927,0	15,0	0,311	
LUE-9_125.FIN2	762,0	65,000	0,9840	0,03000	0,11450	0,0040	0,7766800	695,00	15,00	699,00	23,00	665,0	54,0	699,0	23,0	0,576	Rim
LUE-9_125.FIN2	269,0	3,410	1,2870	0,02400	0,13880	0,0016	0,4103900	841,00	12,00	837,70	9,20	856,0	33,0	837,7	9,2	0,392	Core
LUE-9_126.FIN2	955,0	20,500	0,4440	0,02100	0,05940	0,0030	0,7047500	372,00	15,00	372,00	18,00	416,0	86,0	372,0	18,0	0,000	Rim
LUE-9_126.FIN2	159,0	0,551	0,7740	0,02700	0,09370	0,0017	0,2679300	579,00	15,00	577,30	9,80	582,0	70,0	577,3	9,8	0,294	Core
LUE-9_127.FIN2	172,0	2,450	5,7700	0,14000	0,35040	0,0085	0,8347400	1942,00	20,00	1934,00	40,00	1945,0	27,0	1945,0	27,0	0,566	
LUE-9_128.FIN2	872,0	1,324	0,8327	0,00970	0,09992	0,0009	0,6766500	614,60	5,40	613,80	5,20	612,0	21,0	613,8	5,2	0,130	
LUE-9_129.FIN2	465,0	6,700	0,4670	0,01200	0,06097	0,0010	0,2053000	388,70	8,20	381,40	5,80	427,0	60,0	381,4	5,8	1,878	
LUE-9_130.FIN2	212,0	1,208	6,0580	0,09900	0,36110	0,0050	0,8400900	1980,00	15,00	1986,00	24,00	1975,0	20,0	1975,0	20,0	0,557	
LUE-9_131.FIN2	396,0	1,821	0,3422	0,00650	0,04728	0,0005	0,1799500	298,40	4,90	297,80	2,80	289,0	44,0	297,8	2,8	0,201	
LUE-9_132.FIN2	402,0	1,148	1,0720	0,01400	0,12190	0,0012	0,5821600	739,00	6,90	741,50	6,80	734,0	24,0	741,5	6,8	0,338	
LUE-9_133.FIN2	2350,0	2,730	0,4100	0,02500	0,05560	0,0035	0,6385800	349,00	18,00	349,00	21,00	350,0	100,0	0,0	0,0	0,000	Rim
LUE-9_133.FIN2	456,0	1,750	0,6100	0,01100	0,07796	0,0007	0,5409700	483,10	6,60	483,90	4,40	465,0	38,0	0,0	0,0	0,000	Core
LUE-7_1.FIN2	666,0	2,435	0,3543	0,00670	0,04789	0,0004	0,1678500	307,50	5,00	301,50	2,70	340,0	43,0	301,5	2,7	1,951	

Sample Name:	[U]							207/235		206/238		207/206		Best age		Discordance	Rim/
Grain #	ppm	U/Th	207/235	2σ error	206/238	2σ error	RHO	Age Ma	2σ error	Age (Ma)	2σ error	Age (Ma)	2σ error	(Ma)	2σ error	%	Core
LUE-7_2.FIN2	289,3	1,671	0,7560	0,01400	0,09270	0,0011	0,4386400	571,80	7,90	571,40	6,60	551,0	39,0	571,4	6,6	0,070	
LUE-7_3.FIN2	662,0	1,908	0,3482	0,00580	0,04811	0,0005	0,4087400	303,00	4,30	302,90	3,00	284,0	36,0	302,9	3,0	0,033	
LUE-7_4.FIN2	461,0	2,351	0,3552	0,00710	0,04894	0,0004	0,2154600	308,80	5,50	308,00	2,70	298,0	44,0	308,0	2,7	0,259	
LUE-7_5.FIN2	261,0	2,680	0,6020	0,01200	0,07398	0,0008	0,2741600	478,60	7,90	460,10	4,60	551,0	44,0	460,1	4,6	3,865	
LUE-7_6.FIN2	332,0	1,111	0,3421	0,00790	0,04677	0,0005	0,2343600	298,10	6,00	294,70	3,10	315,0	50,0	294,7	3,1	1,141	
LUE-7_7.FIN2	444,0	2,550	0,8160	0,05300	0,09590	0,0048	0,8197100	604,00	30,00	590,00	28,00	653,0	86,0	590,0	28,0	2,318	Rim
LUE-7_7.FIN2	189,4	1,274	1,1570	0,02200	0,12840	0,0015	0,3460900	779,00	10,00	778,80	8,30	766,0	39,0	778,8	8,3	0,026	Core
LUE-7_9.FIN2	54,9	1,085	1,8160	0,04700	0,17530	0,0024	0,3155400	1050,00	17,00	1041,00	13,00	1051,0	52,0	1051,0	52,0	0,951	
LUE-7_10.FIN2	81,9	0,514	1,6880	0,03800	0,16830	0,0022	0,3126000	1004,00	15,00	1002,00	12,00	985,0	49,0	985,0	49,0	1,726	
LUE-7_11.FIN2	320,0	0,873	0,9080	0,02500	0,10400	0,0017	0,1996800	656,00	14,00	638,00	10,00	734,0	60,0	638,0	10,0	2,744	
LUE-7_12.FIN2	197,4	1,359	0,7870	0,01600	0,09452	0,0010	0,2179700	588,00	9,20	582,10	5,80	592,0	45,0	582,1	5,8	1,003	
LUE-7_13.FIN2	122,0	1,073	0,8550	0,02200	0,10040	0,0016	0,4534000	624,00	12,00	616,30	9,30	638,0	56,0	616,3	9,3	1,234	
LUE-7_14.FIN2	96,3	0,878	0,9620	0,02400	0,10960	0,0015	0,1268400	682,00	12,00	670,40	8,60	708,0	59,0	670,4	8,6	1,701	
LUE-7_15.FIN2	64,9	0,830	0,8590	0,03700	0,10130	0,0022	0,2500300	629,00	19,00	621,00	13,00	648,0	95,0	621,0	13,0	1,272	
LUE-7_16.FIN2	341,3	1,918	0,7560	0,01200	0,09230	0,0009	0,3251300	570,70	6,80	569,00	5,40	564,0	33,0	569,0	5,4	0,298	
LUE-7_17.FIN2	327,9	6,060	0,6180	0,01100	0,07664	0,0008	0,4681600	487,90	6,80	476,00	5,00	535,0	35,0	476,0	5,0	2,439	
LUE-7_18.FIN2	334,0	25,000	0,6560	0,03200	0,07900	0,0021	0,6074000	510,00	20,00	490,00	13,00	595,0	83,0	490,0	13,0	3,922	Rim
LUE-7_18.FIN2	137,6	0,765	0,8460	0,02200	0,10450	0,0016	0,2553700	622,00	13,00	640,30	9,50	542,0	60,0	640,3	9,5	2,942	Core
LUE-7_19.FIN2	1179,0	10,460	0,6750	0,01000	0,08380	0,0012	0,5435700	523,70	6,20	518,50	7,20	549,0	30,0	518,5	7,2	0,993	
LUE-7_20.FIN2	484,0	3,050	0,8800	0,01900	0,10060	0,0014	0,4404300	639,00	10,00	617,80	8,50	720,0	37,0	617,8	8,5	3,318	
LUE-7_21.FIN2	80,6	0,867	1,6780	0,03700	0,16530	0,0021	0,2786500	998,00	14,00	987,00	12,00	1015,0	45,0	1015,0	45,0	2,759	
LUE-7_22.FIN2	1350,0	39,900	0,5182	0,00840	0,06188	0,0006	0,1712300	423,50	5,60	387,00	3,80	624,0	39,0	387,0	3,8	8,619	
LUE-7_23.FIN2	1290,0	2,330	0,4100	0,02500	0,04580	0,0018	0,3957300	348,00	18,00	289,00	11,00	730,0	170,0	DISC	DISC	16,954	
LUE-7_24.FIN2	136,0	3,460	1,2560	0,02500	0,13730	0,0015	0,2880000	824,00	11,00	829,40	8,60	801,0	41,0	829,4	8,6	0,655	
LUE-7_25.FIN2	254,0	3,340	4,9780	0,07300	0,30050	0,0035	0,7691000	1813,00	12,00	1693,00	18,00	1955,0	18,0	1955,0	18,0	13,402	
LUE-7_26.FIN2	292,0	1,432	0,3253	0,00870	0,04587	0,0006	0,3054200	285,10	6,60	289,10	3,60	263,0	53,0	289,1	3,6	1,403	
LUE-7_27.FIN2	28,7	3,600	0,7190	0,03300	0,07820	0,0017	0,0092191	548,00	20,00	485,00	10,00	770,0	100,0	485,0	10,0	11,496	
LUE-7_28.FIN2	66,4	1,082	0,8900	0,02600	0,10690	0,0015	0,0414420	644,00	14,00	654,70	8,80	582,0	68,0	654,7	8,8	1,661	
LUE-7_29.FIN2	149,0	1,558	0,9430	0,02400	0,10810	0,0015	0,2188300	673,00	12,00	662,50	9,00	691,0	55,0	662,5	9,0	1,560	
LUE-7_30.FIN2	216,0	0,932	0,8110	0,01700	0,09670	0,0010	0,1057400	602,40	9,80	595,10	6,10	618,0	47,0	595,1	6,1	1,212	
LUE-7_31.FIN2	222,0	1,347	0,8820	0,02400	0,10690	0,0015	0,3751300	641,00	13,00	654,70	8,60	581,0	54,0	654,7	8,6	2,137	
LUE-7_32.FIN2	140,0	2,525	0,9090	0,03000	0,09990	0,0019	0,4102900	654,00	16,00	613,00	11,00	801,0	62,0	613,0	11,0	6,269	Rim
LUE-7_32.FIN2	50,3	2,740	1,0960	0,04300	0,12310	0,0027	0,0623610	748,00	21,00	748,00	15,00	732,0	93,0	748,0	15,0	0,000	Core
LUE-7_33.FIN2	829,0	0,941	0,7650	0,01100	0,08580	0,0010	0,6824200	575,90	6,40	530,50	6,20	757,0	23,0	530,5	6,2	7,883	
LUE-7_34.FIN2	688,0	0,917	0,4216	0,00960	0,05243	0,0007	0,1852400	357,90	7,10	329,40	4,00	537,0	54,0	329,4	4,0	7,963	
LUE-7_35.FIN2	122,1	9,900	14,9000	0,32000	0,54380	0,0080	0,6851000	2805,00	20,00	2798,00	33,00	2814,0	24,0	2814,0	24,0	0,569	
LUE-7_36.FIN2	473,0	1,530	2,6440	0,09700	0,18780	0,0052	0,9311200	1299,00	27,00	1107,00	28,00	1649,0	27,0	DISC	DISC	32,868	
LUE-7_37.FIN2	186,2	1,600	0,7970	0,02000	0,09670	0,0018	0,3024100	593,00	11,00	595,00	10,00	572,0	55,0	595,0	10,0	0,337	
LUE-7_38.FIN2	104,0	0,759	0,8360	0,02700	0,09910	0,0019	0,2733600	615,00	15,00	609,00	11,00	619,0	70,0	609,0	11,0	0,976	
LUE-7_39.FIN2	160,0	1,870	0,5870	0,05800	0,04490	0,0033	0,7223200	467,00	37,00	283,00	20,00	1500,0	130,0	DISC	DISC	39,400	Rim
LUE-7_39.FIN2	198,6	2,364	0,5940	0,01700	0,07550	0,0011	0,1616200	472,00	11,00	469,10	6,50	477,0	71,0	469,1	6,5	0,614	Core
LUE-7_40.FIN2	121,0	3,530	0,4490	0,01800	0,06100	0,0012	0,2090500	376,00	14,00	381,80	7,30	321,0	87,0	381,8	7,3	1,543	
LUE-7_41.FIN2	155,1	0,415	0,8680	0,01800	0,10380	0,0011	0,2165300	632,70	9,90	636,80	6,30	618,0	45,0	636,8	6,3	0,648	
LUE-7_42.FIN2	883,0	1,389	0,9590	0,01800	0,09130	0,0014	0,5869800	681,50	9,60	562,80	8,20	1093,0	30,0	DISC	DISC	17,417	
LUE-7_43.FIN2	726,0	6,870	0,7720	0,01600	0,08810	0,0015	0,1629400	580,60	9,20	544,40	8,70	730,0	53,0	544,4	8,7	6,235	Rim
LUE-7_43.FIN2	100,3	1,444	0,9460	0,02500	0,10330	0,0017	0,2560500	676,00	13,00	633,30	9,90	808,0	60,0	633,3	9,9	6,317	Core
LUE-7_44.FIN2	483,0	0,983	0,5680	0,01100	0,07299	0,0008	0,4067400	456,10	6,80	454,10	4,50	459,0	39,0	454,1	4,5	0,439	

Sample Name:	[U]							207/235		206/238		207/206		Best age		Discordance	Rim/
Grain #	ppm	U/Th	207/235	2σ error	206/238	2σ error	RHO	Age Ma	2σ error	Age (Ma)	2σ error	Age (Ma)	2σ error	(Ma)	2σ error	%	Core
LUE-7_45.FIN2	306,0	0,891	0,8670	0,01500	0,10010	0,0010	0,3211000	632,60	8,00	614,90	5,90	674,0	36,0	614,9	5,9	2,798	
LUE-7_46.FIN2	123,0	1,299	1,3590	0,04400	0,14120	0,0032	0,6713400	867,00	19,00	850,00	18,00	912,0	47,0	912,0	47,0	6,798	
LUE-7_47.FIN2	104,1	-12,600	0,3860	0,01400	0,05443	0,0009	0,1367600	331,00	10,00	341,60	5,80	253,0	75,0	341,6	5,8	3,202	
LUE-7_48.FIN2	339,0	25,000	0,7100	0,01200	0,08766	0,0009	0,3990300	543,90	7,20	541,60	5,60	553,0	36,0	541,6	5,6	0,423	
LUE-7_49.FIN2	291,5	1,740	0,8100	0,01800	0,09780	0,0014	0,3788000	601,00	10,00	601,50	8,20	601,0	46,0	601,5	8,2	0,083	
LUE-7_50.FIN2	123,6	0,657	0,8370	0,02200	0,09370	0,0015	0,3902100	615,90	12,00	577,10	9,00	753,0	53,0	577,1	9,0	6,163	
LUE-7_51.FIN2	301,0	1,440	8,8500	0,16000	0,41160	0,0052	0,7922700	2317,00	16,00	2220,00	24,00	2412,0	20,0	2412,0	20,0	7,960	
LUE-7_52.FIN2	1581,0	7,700	0,3554	0,00740	0,04819	0,0007	0,5978800	308,50	5,50	303,40	4,50	365,0	39,0	303,4	4,5	1,653	
LUE-7_53.FIN2	343,0	27,700	0,6160	0,01200	0,07783	0,0008	0,4670300	487,60	7,90	483,10	4,80	490,0	47,0	483,1	4,8	0,923	
LUE-7_54.FIN2	120,2	0,368	11,4200	0,13000	0,47060	0,0048	0,7817600	2556,00	11,00	2485,00	21,00	2615,0	16,0	2615,0	16,0	4,971	
LUE-7_55.FIN2	187,0	0,764	0,8180	0,01600	0,09820	0,0011	0,1996400	605,30	9,20	603,80	6,70	608,0	47,0	603,8	6,7	0,248	
LUE-7_56.FIN2	86,2	0,964	1,7190	0,04200	0,16750	0,0020	0,2812600	1013,00	15,00	998,00	11,00	1053,0	48,0	1053,0	48,0	5,223	
LUE-7_57.FIN2	185,0	1,000	5,7500	0,12000	0,33910	0,0062	0,9290400	1933,00	19,00	1880,00	30,00	1995,0	21,0	1995,0	21,0	5,764	
LUE-7_58.FIN2	611,0	0,628	0,8240	0,01200	0,09873	0,0009	0,5398600	609,40	6,70	606,90	5,20	619,0	27,0	606,9	5,2	0,410	
LUE-7_59.FIN2	427,0	1,486	0,3693	0,00960	0,04904	0,0005	0,5062100	318,20	7,10	308,60	3,20	412,0	56,0	308,6	3,2	3,017	
LUE-7_60.FIN2	407,0	4,720	1,6780	0,02100	0,16710	0,0015	0,5882000	998,90	8,00	995,70	8,30	1014,0	22,0	1014,0	22,0	1,805	
LUE-7_61.FIN2	798,0	22,700	0,3640	0,00530	0,05000	0,0005	0,2132500	315,40	4,10	314,50	3,10	328,0	34,0	314,5	3,1	0,285	
LUE-7_62.FIN2	141,4	2,620	0,9510	0,03200	0,10740	0,0019	0,3202700	677,00	17,00	658,00	11,00	719,0	83,0	658,0	11,0	2,806	
LUE-7_63.FIN2	226,0	1,350	4,0460	0,06400	0,28610	0,0028	0,6011500	1644,00	13,00	1621,00	14,00	1679,0	24,0	1679,0	24,0	3,454	
LUE-7_64.FIN2	412,0	3,040	0,5760	0,03200	0,07010	0,0037	0,6248300	461,00	21,00	437,00	23,00	600,0	100,0	437,0	23,0	5,206	Rim
LUE-7_64.FIN2	381,2	1,139	0,8260	0,01800	0,09770	0,0016	0,6429700	610,10	9,80	600,60	9,30	646,0	37,0	600,6	9,3	1,557	Core
LUE-7_65.FIN2	109,2	0,870	1,8660	0,03600	0,18010	0,0022	0,3373400	1066,90	13,00	1067,00	12,00	1064,0	36,0	1064,0	36,0	0,282	
LUE-7_66.FIN2	114,1	1,057	4,1220	0,07300	0,27750	0,0035	0,6033200	1655,00	14,00	1578,00	17,00	1762,0	28,0	1762,0	28,0	10,443	
LUE-7_67.FIN2	190,0	3,890	0,4710	0,03400	0,06000	0,0025	0,3624400	390,00	24,00	376,00	15,00	470,0	150,0	376,0	15,0	3,590	Rim
LUE-7_67.FIN2	62,7	1,530	0,7180	0,03600	0,09020	0,0021	0,3874100	545,00	22,00	556,00	12,00	480,0	100,0	556,0	12,0	2,018	Core
LUE-7_68.FIN2	298,0	0,995	1,8110	0,02400	0,17880	0,0018	0,5746400	1047,90	8,80	1060,30	9,90	1021,0	27,0	1021,0	27,0	3,849	
LUE-7_69.FIN2	241,1	2,740	0,6040	0,01300	0,07830	0,0012	0,3681800	478,80	8,20	486,00	7,20	425,0	47,0	486,0	7,2	1,504	
LUE-7_70.FIN2	282,0	7,870	0,6070	0,01500	0,07690	0,0011	0,3354900	481,10	9,60	477,60	6,40	493,0	51,0	477,6	6,4	0,727	
LUE-7_71.FIN2	65,5	0,638	1,5830	0,03700	0,15910	0,0021	0,2535100	961,00	15,00	951,00	12,00	971,0	48,0	971,0	48,0	2,060	
LUE-7_72.FIN2	784,0	69,600	0,3995	0,00640	0,05195	0,0005	0,1005600	340,90	4,60	326,40	2,80	434,0	39,0	326,4	2,8	4,253	
LUE-7_73.FIN2	47,2	0,982	1,0990	0,04100	0,12110	0,0023	0,2858000	749,00	20,00	736,00	13,00	764,0	79,0	736,0	13,0	1,736	
LUE-7_74.FIN2	309,0	16,500	3,8300	0,11000	0,27410	0,0044	0,7267000	1593,00	22,00	1561,00	22,00	1640,0	35,0	1640,0	35,0	4,817	
LUE-7_75.FIN2	453,0	2,010	0,3600	0,01800	0,04870	0,0013	0,5084300	312,00	13,00	306,30	8,30	353,0	97,0	306,3	8,3	1,827	
LUE-7_76.FIN2	7,5	0,665	1,5800	0,12000	0,14820	0,0060	0,2997400	920,00	49,00	888,00	34,00	970,0	160,0	970,0	160,0	8,454	
LUE-7_77.FIN2	504,5	5,970	0,8870	0,01300	0,10290	0,0011	0,4087100	643,90	6,90	631,30	6,40	691,0	30,0	631,3	6,4	1,957	
LUE-7_78.FIN2	363,0	1,905	0,7620	0,01200	0,09560	0,0010	0,4023800	574,40	7,20	588,60	6,20	521,0	36,0	588,6	6,2	2,472	
LUE-7_79.FIN2	253,7	4,192	0,8880	0,01600	0,10600	0,0010	0,1980000	645,10	8,30	649,20	6,00	617,0	40,0	649,2	6,0	0,636	
LUE-7_80.FIN2	222,7	6,550	0,7060	0,01500	0,08820	0,0011	0,3659500	541,10	8,60	544,80	6,40	521,0	43,0	544,8	6,4	0,684	
LUE-7_81.FIN2	70,6	0,755	0,8960	0,03000	0,10240	0,0015	0,0295990	645,00	16,00	628,50	8,60	681,0	73,0	628,5	8,6	2,558	
LUE-7_82.FIN2	252,0	1,298	0,8810	0,01700	0,10300	0,0012	0,3263400	641,00	9,70	631,50	7,20	683,0	45,0	631,5	7,2	1,482	
LUE-7_83.FIN2	442,0	0,751	0,8280	0,01200	0,09910	0,0010	0,3636000	611,50	6,50	609,10	6,10	626,0	31,0	609,1	6,1	0,392	
LUE-7_84.FIN2	193,3	1,950	0,4330	0,01100	0,05882	0,0007	0,0804840	364,30	7,80	368,40	4,10	336,0	57,0	368,4	4,1	1,125	
LUE-7_85.FIN2	308,0	7,400	6,9400	0,15000	0,39200	0,0074	0,7442700	2099,00	19,00	2129,00	34,00	2083,0	25,0	2083,0	25,0	2,208	
LUE-7_86.FIN2	255,0	1,690	0,8980	0,01500	0,10590	0,0010	0,5934200	649,30	8,00	648,80	6,10	658,0	34,0	648,8	6,1	0,077	
LUE-7_87.FIN2	77,8	2,390	1,5290	0,03600	0,15030	0,0017	0,3033300	938,00	14,00	952,70	9,60	900,0	48,0	900,0	48,0	5,856	
LUE-7_88.FIN2	796,0	8,860	1,4720	0,06300	0,13130	0,0068	0,0566770	918,00	26,00	795,00	39,00	1240,0	120,0	795,0	39,0	13,399	Rim
LUE-7_88.FIN2	148,0	2,870	1,8570	0,03900	0,18430	0,0022	0,2951200	1063,00	14,00	1090,00	12,00	1023,0	39,0	1023,0	39,0	6,549	Core

Sample Name:	[U]							207/235		206/238		207/206		Best age		Discordance	Rim/
Grain #	ppm	U/Th	207/235	2σ error	206/238	2σ error	RHO	Age Ma	2σ error	Age (Ma)	2σ error	Age (Ma)	2σ error	(Ma)	2σ error	%	Core
LUE-7_89.FIN2	599,0	31,700	1,7510	0,07400	0,12080	0,0059	0,5243700	1024,00	27,00	734,00	34,00	1707,0	88,0	DISC	DISC	28,320	
LUE-7_90.FIN2	356,0	0,940	3,6050	0,09400	0,22150	0,0061	0,8932000	1542,00	21,00	1287,00	32,00	1934,0	21,0	DISC	DISC	33,454	
LUE-7_91.FIN2	953,0	36,500	0,9390	0,01500	0,10980	0,0014	0,4374000	671,50	7,60	671,50	7,90	681,0	32,0	671,5	7,9	0,000	
LUE-7_92.FIN2	466,0	0,596	8,4400	0,24000	0,36600	0,0094	0,9625500	2267,00	26,00	2005,00	44,00	2532,0	13,0	2532,0	13,0	20,814	
LUE-7_93.FIN2	304,7	5,280	1,5320	0,02400	0,15550	0,0018	0,6375200	941,80	9,50	932,00	10,00	980,0	25,0	980,0	25,0	4,898	
LUE-7_94.FIN2	258,0	1,704	1,2650	0,01900	0,13810	0,0017	0,3705200	828,70	8,50	833,60	9,40	830,0	30,0	833,6	9,4	0,591	
LUE-7_95.FIN2	173,4	1,235	12,1000	0,33000	0,48900	0,0100	0,9184100	2601,00	25,00	2559,00	44,00	2645,0	18,0	2645,0	18,0	3,251	
LUE-7_96.FIN2	170,0	2,800	0,6140	0,01500	0,07890	0,0010	0,1868100	485,80	9,10	489,20	6,00	472,0	56,0	489,2	6,0	0,700	
LUE-7_97.FIN2	72,1	0,661	5,8400	0,20000	0,34290	0,0093	0,8515600	1937,00	31,00	1895,00	45,00	1992,0	30,0	1992,0	30,0	4,869	
LUE-7_98.FIN2	271,0	0,966	5,6300	0,12000	0,32470	0,0064	0,8499700	1914,00	20,00	1810,00	31,00	2040,0	25,0	2040,0	25,0	11,275	
LUE-7_99.FIN2	280,8	4,620	0,6170	0,01300	0,07500	0,0012	0,4078900	487,80	8,00	466,30	7,00	579,0	45,0	466,3	7,0	4,408	
LUE-7_100.FIN2	69,1	1,930	0,7440	0,02500	0,09180	0,0016	0,2811200	561,00	15,00	567,40	9,80	512,0	71,0	567,4	9,8	1,141	
LUE-7_101.FIN2	457,0	1,253	0,3583	0,00660	0,04954	0,0005	0,4539600	311,10	5,00	311,70	3,30	298,0	37,0	311,7	3,3	0,193	
LUE-7_102.FIN2	492,0	12,450	0,7150	0,01400	0,08540	0,0012	0,3246000	546,70	8,50	528,50	6,90	627,0	45,0	528,5	6,9	3,329	
LUE-7_103.FIN2	581,0	1,800	0,3558	0,00660	0,04963	0,0004	0,3357800	308,60	4,90	312,20	2,70	274,0	38,0	312,2	2,7	1,167	
LUE-7_104.FIN2	2560,0	1,382	0,4540	0,03600	0,02470	0,0017	0,7297900	379,00	25,00	157,00	11,00	2139,0	88,0	DISC	DISC	58,575	Rim
LUE-7_104.FIN2	494,0	1,211	0,4000	0,01400	0,05119	0,0007	0,3753500	342,00	10,00	321,80	4,10	441,0	67,0	321,8	4,1	5,906	Core
LUE-7_105.FIN2	199,0	1,308	0,8490	0,01800	0,10110	0,0010	0,4666300	623,50	9,90	620,90	6,00	615,0	42,0	620,9	6,0	0,417	
LUE-7_106.FIN2	172,5	0,728	1,2970	0,02300	0,13510	0,0015	0,1601300	843,70	9,80	817,00	8,60	901,0	40,0	817,0	8,6	3,165	
LUE-7_107.FIN2	113,1	3,250	13,6600	0,22000	0,51730	0,0075	0,7889600	2724,00	15,00	2689,00	33,00	2749,0	16,0	2749,0	16,0	2,183	
LUE-7_108.FIN2	401,0	2,070	0,9430	0,01500	0,10400	0,0014	0,3821200	674,10	8,10	637,60	8,40	794,0	36,0	637,6	8,4	5,415	
LUE-7_109.FIN2	639,0	1,941	0,8170	0,01200	0,09710	0,0011	0,5179700	605,60	6,40	597,50	6,40	624,0	28,0	597,5	6,4	1,338	
LUE-7_110.FIN2	71,2	1,083	5,2970	0,07200	0,33900	0,0034	0,3928700	1866,00	12,00	1881,00	17,00	1841,0	24,0	1841,0	24,0	2,173	
LUE-7_111.FIN2	133,3	1,990	0,7250	0,01700	0,09020	0,0011	0,3421600	552,00	10,00	556,60	6,80	517,0	50,0	556,6	6,8	0,833	
LUE-7_112.FIN2	121,0	1,606	14,7300	0,22000	0,51600	0,0057	0,6754500	2794,00	14,00	2681,00	25,00	2867,0	19,0	2867,0	19,0	6,488	
LUE-7_113.FIN2	628,0	1,090	13,4400	0,19000	0,50920	0,0038	0,6683200	2710,60	7,00	2653,00	16,00	2747,3	9,6	2747,3	9,6	3,432	
LUE-7_114.FIN2	208,5	0,868	1,1000	0,01800	0,12220	0,0012	0,3858000	752,00	8,70	743,00	6,70	769,0	36,0	743,0	6,7	1,197	
LUE-7_115.FIN2	386,0	9,830	0,8840	0,02200	0,10320	0,0016	0,1613400	642,00	12,00	632,90	9,30	665,0	58,0	632,9	9,3	1,417	Rim
LUE-7_115.FIN2	169,0	2,291	1,1520	0,03700	0,12470	0,0020	0,4392700	775,00	17,00	758,00	11,00	812,0	59,0	758,0	11,0	2,194	Core
LUE-7_116.FIN2	118,4	4,170	0,6120	0,01600	0,07810	0,0012	0,3843800	483,00	10,00	484,60	7,40	470,0	57,0	484,6	7,4	0,331	
LUE-7_117.FIN2	510,0	2,182	0,7560	0,01200	0,08900	0,0010	0,4940100	570,70	7,10	549,80	6,20	647,0	32,0	549,8	6,2	3,662	
LUE-7_118.FIN2	115,7	10,500	0,5050	0,01500	0,06321	0,0008	0,0407130	415,00	10,00	395,10	5,00	494,0	69,0	395,1	5,0	4,795	
LUE-7_119.FIN2	990,0	8,300	0,5390	0,02700	0,04420	0,0010	0,5799200	439,00	19,00	278,80	6,40	1354,0	77,0	DISC	DISC	36,492	
LUE-7_120.FIN2	272,0	1,000	0,7790	0,01400	0,09490	0,0011	0,2719600	584,60	8,30	584,10	6,30	569,0	42,0	584,1	6,3	0,086	
LUE-7_121.FIN2	404,0	0,622	4,9500	0,15000	0,25570	0,0069	0,9266000	1798,00	27,00	1464,00	36,00	2220,0	20,0	DISC	DISC	34,054	
LUE-7_122.FIN2	188,0	2,210	5,8840	0,06000	0,35710	0,0032	0,5654800	1959,70	8,50	1968,00	15,00	1947,0	15,0	1947,0	15,0	1,079	
LUE-7_123.FIN2	219,5	1,060	1,7240	0,02900	0,16750	0,0018	0,6557500	1018,90	10,00	997,90	9,70	1050,0	30,0	1050,0	30,0	4,962	
LUE-7_124.FIN2	143,6	0,900	0,8180	0,02200	0,09530	0,0016	0,4067500	604,00	12,00	586,30	9,50	652,0	52,0	586,3	9,5	2,930	
LUE-7_125.FIN2	309,7	4,550	0,5650	0,01100	0,07370	0,0008	0,3942200	453,90	7,30	458,40	4,70	410,0	41,0	458,4	4,7	0,991	
LUE-7_126.FIN2	153,3	0,825	1,5980	0,02500	0,16360	0,0016	0,3440500	967,00	10,00	976,70	8,90	929,0	31,0	929,0	31,0	5,135	
LUE-7_127.FIN2	734,0	2,475	0,3456	0,00650	0,04716	0,0006	0,3626500	301,50	5,00	297,00	3,50	318,0	41,0	297,0	3,5	1,493	
LUE-7_128.FIN2	243,5	1,625	0,3494	0,00890	0,04866	0,0006	0,1986100	303,50	6,70	306,30	3,80	262,0	56,0	306,3	3,8	0,923	
LUE-7_129.FIN2	212,7	1,795	0,7760	0,01500	0,09388	0,0009	0,1039800	583,90	8,60	578,40	5,30	577,0	46,0	578,4	5,3	0,942	
LUE-7_130.FIN2	760,0	1,822	0,5840	0,01300	0,07400	0,0013	0,5565100	466,40	8,50	460,20	7,90	490,0	46,0	460,2	7,9	1,329	Rim
LUE-7_130.FIN2	293,0	2,775	6,2500	0,11000	0,28200	0,0049	0,7762900	2013,00	17,00	1601,00	24,00	2457,0	21,0	DISC	DISC	34,839	Core
LUE-7_131.FIN2	297,0	5,780	13,3700	0,11000	0,50990	0,0043	0,6653100	2704,90	8,00	2655,00	18,00	2739,0	12,0	2739,0	12,0	3,067	
LUE-7_132.FIN2	252,0	4,320	0,5880	0,01400	0,07520	0,0012	0,2244800	469,90	9,30	467,50	7,40	477,0	59,0	467,5	7,4	0,511	

Sample Name:	[U]							207/235		206/238		207/206		Best age		Discordance	Rim/
Grain #	ppm	U/Th	207/235	2σ error	206/238	2σ error	RHO	Age Ma	2σ error	Age (Ma)	2σ error	Age (Ma)	2σ error	(Ma)	2σ error	%	Core
LUE-2_1.FIN2	300,0	2,840	0,5556	0,00870	0,07060	0,0006	0,2067200	448,00	5,70	439,70	3,70	470,0	36,0	439,7	3,7	1,853	
LUE-2_2.FIN2	113,5	7,390	0,6390	0,01900	0,08260	0,0011	0,1524600	500,00	12,00	511,80	6,80	431,0	70,0	511,8	6,8	2,360	
LUE-2_3.FIN2	460,7	7,060	0,7680	0,01100	0,09360	0,0010	0,2889800	578,30	6,40	576,90	6,20	570,0	33,0	576,9	6,2	0,242	
LUE-2_4.FIN2	314,0	27,200	0,6420	0,01800	0,08080	0,0014	0,6293600	504,00	11,00	500,80	8,50	511,0	50,0	500,8	8,5	0,635	
LUE-2_5.FIN2	473,0	0,884	0,8024	0,00920	0,09649	0,0008	0,4264600	597,70	5,10	593,70	4,90	597,0	24,0	593,7	4,9	0,669	
LUE-2_6.FIN2	397,0	6,270	0,6420	0,01000	0,08110	0,0008	0,3507300	503,00	6,20	502,60	4,50	491,0	35,0	502,6	4,5	0,080	
LUE-2_7.FIN2	206,0	2,390	0,7350	0,01600	0,08947	0,0010	0,2201400	559,10	9,40	552,30	5,60	575,0	47,0	552,3	5,6	1,216	
LUE-2_8.FIN2	350,0	1,581	1,3820	0,01900	0,14150	0,0013	0,4504000	881,60	7,80	853,10	7,60	933,0	26,0	933,0	26,0	8,564	
LUE-2_9.FIN2	57,1	1,029	6,1800	0,16000	0,35400	0,0077	0,4956500	1999,00	24,00	1953,00	37,00	2034,0	45,0	2034,0	45,0	3,982	
LUE-2_10.FIN2	226,0	0,651	0,7770	0,01600	0,09360	0,0010	0,1969900	584,30	8,90	576,60	6,10	587,0	47,0	576,6	6,1	1,318	
LUE-2_11.FIN2	603,0	1,953	0,7408	0,00960	0,08979	0,0007	0,3776800	562,30	5,60	554,20	4,10	571,0	26,0	554,2	4,1	1,441	
LUE-2_12.FIN2	136,3	1,339	1,5270	0,02500	0,15220	0,0018	0,3230200	939,50	9,80	913,00	10,00	988,0	33,0	988,0	33,0	7,591	
LUE-2_13.FIN2	503,0	2,307	0,3689	0,00710	0,04939	0,0005	0,0603140	318,30	5,30	310,80	2,80	350,0	46,0	310,8	2,8	2,356	
LUE-2_14.FIN2	202,0	1,920	0,9960	0,02300	0,11370	0,0015	0,2786100	701,00	11,00	694,30	8,50	694,0	44,0	694,3	8,5	0,956	
LUE-2_18.FIN2	128,8	7,530	1,5000	0,12000	0,09675	0,0009	0,7178000	757,00	29,00	595,10	5,20	1090,0	75,0	DISC	DISC	21,387	
LUE-2_15.FIN2	340,0	3,210	0,6620	0,01200	0,08171	0,0009	0,2871100	514,90	7,20	506,30	5,20	525,0	40,0	506,3	5,2	1,670	
LUE-2_16.FIN2	204,4	1,406	0,9770	0,01800	0,11300	0,0013	0,2559400	692,20	9,60	690,00	7,50	674,0	42,0	690,0	7,5	0,318	
LUE-2_17.FIN2	127,0	3,540	0,8500	0,02000	0,10130	0,0013	0,2274200	622,00	11,00	622,10	7,70	594,0	54,0	622,1	7,7	0,016	
LUE-2_18.FIN2	135,4	0,775	0,7370	0,01700	0,09170	0,0010	0,1459300	560,60	9,50	565,40	5,90	503,0	54,0	565,4	5,9	0,856	
LUE-2_19.FIN2	740,0	2,791	0,8493	0,00990	0,09853	0,0009	0,4593000	623,60	5,50	605,70	5,50	669,0	26,0	605,7	5,5	2,870	
LUE-2_21.FIN2	1351,0	28,600	0,4190	0,01300	0,05620	0,0013	0,7873300	354,90	9,20	352,50	7,90	368,0	64,0	352,5	7,9	0,676	Rim
LUE-2_21.FIN2	256,2	0,485	4,6730	0,07900	0,28400	0,0038	0,7626400	1761,00	14,00	1611,00	19,00	1930,0	24,0	1930,0	24,0	16,528	Core
LUE-2_22.FIN2	546,0	1,009	1,6020	0,02000	0,16080	0,0015	0,4614000	969,90	7,60	961,20	8,50	972,0	24,0	972,0	24,0	1,111	
LUE-2_23.FIN2	661,0	21,300	0,3715	0,00990	0,05063	0,0010	0,0520130	320,50	7,40	318,40	5,80	320,0	71,0	318,4	5,8	0,655	
LUE-2_24.FIN2	1306,0	2,109	0,4094	0,00420	0,05513	0,0004	0,3357800	348,70	3,10	345,90	2,70	350,0	24,0	345,9	2,7	0,803	
LUE-2_25.FIN2	219,0	0,829	1,5630	0,02600	0,15560	0,0016	0,3789100	957,00	11,00	932,40	8,90	999,0	33,0	999,0	33,0	6,667	
LUE-2_26.FIN2	734,0	93,000	0,3600	0,01400	0,04800	0,0010	0,4272700	312,00	11,00	302,40	6,20	373,0	81,0	302,0	6,2	3,205	Rim
LUE-2_26.FIN2	132,9	1,727	0,7050	0,02600	0,08270	0,0017	0,1995600	540,00	16,00	512,20	9,90	634,0	84,0	512,2	9,9	5,148	Core
LUE-2_27.FIN2	674,0	1,826	0,3856	0,00560	0,05195	0,0006	0,4448100	331,40	4,20	326,40	3,50	357,0	32,0	326,4	3,5	1,509	
LUE-2_28.FIN2	109,6	0,857	6,3550	0,08900	0,36740	0,0049	0,5829900	2023,00	12,00	2015,00	23,00	2029,0	23,0	2029,0	23,0	0,690	
LUE-2_29.FIN2	620,0	2,003	0,3448	0,00490	0,04823	0,0005	0,2010600	300,60	3,70	303,60	3,00	265,0	35,0	303,6	3,0	0,998	
LUE-2_30.FIN2	440,0	1,651	7,1890	0,05800	0,39380	0,0031	0,6082500	2134,40	7,20	2140,00	14,00	2120,0	13,0	2120,0	13,0	0,943	
LUE-2_31.FIN2	775,0	3,530	0,3979	0,00610	0,05346	0,0006	0,5408400	339,80	4,40	335,70	3,40	355,0	34,0	335,7	3,4	1,207	
LUE-2_32.FIN2	489,0	6,340	0,6072	0,00860	0,07585	0,0010	0,4222800	481,20	5,40	471,20	5,70	535,0	33,0	471,2	5,7	2,078	
LUE-2_33.FIN2	289,0	2,065	0,3576	0,00860	0,04897	0,0005	0,3509600	308,40	5,90	308,10	3,00	304,0	45,0	308,1	3,0	0,097	
LUE-2_34.FIN2	815,0	2,394	0,3396	0,00830	0,04589	0,0010	0,4900200	296,40	6,30	289,20	5,80	344,0	47,0	289,2	5,8	2,429	
LUE-2_35.FIN2	372,0	3,753	0,3544	0,00690	0,04855	0,0005	0,2391500	307,50	5,20	305,60	2,90	308,0	43,0	305,6	2,9	0,618	
LUE-2_36.FIN2	1270,0	54,000	0,9780	0,03100	0,11250	0,0029	0,6671600	692,00	16,00	687,00	17,00	708,0	50,0	687,0	17,0	0,723	Rim
LUE-2_36.FIN2	209,3	2,880	1,0720	0,01700	0,12140	0,0010	0,1945300	738,60	8,30	738,50	6,00	724,0	34,0	738,5	6,0	0,014	Core
LUE-2_37.FIN2	99,3	1,276	0,8980	0,02100	0,10440	0,0012	0,0769110	648,00	11,00	641,00	6,90	658,0	55,0	641,0	6,9	1,080	
LUE-2_38.FIN2	257,7	2,600	2,6110	0,05300	0,21710	0,0033	0,5577400	1302,00	15,00	1266,00	18,00	1371,0	38,0	1371,0	38,0	7,659	
LUE-2_40.FIN2	427,0	18,000	0,4590	0,01700	0,06090	0,0020	0,4844700	383,00	12,00	381,00	12,00	391,0	80,0	381,0	12,0	0,522	Rim
LUE-2_40.FIN2	429,0	3,169	0,6070	0,01000	0,07588	0,0008	0,2690700	480,80	6,40	471,50	4,70	524,0	36,0	471,5	4,7	1,934	Core
LUE-2_41.FIN2	534,0	3,330	0,3479	0,00540	0,04772	0,0004	0,2263300	302,80	4,10	300,50	2,40	312,0	36,0	300,5	2,4	0,760	
LUE-2_42.FIN2	250,8	1,432	0,3569	0,00850	0,04909	0,0005	0,3157900	309,20	6,30	308,90	3,10	302,0	48,0	308,9	3,1	0,097	
LUE-2_43.FIN2	261,0	4,260	0,5330	0,01100	0,06757	0,0009	0,4266600	432,60	7,30	421,40	5,10	482,0	45,0	421,4	5,1	2,589	

Sample Name:	[U]							207/235		206/238		207/206		Best age		Discordance	Rim/
Grain #	ppm	U/Th	207/235	2σ error	206/238	2σ error	RHO	Age Ma	2σ error	Age (Ma)	2σ error	Age (Ma)	2σ error	(Ma)	2σ error	%	Core
LUE-2_44.FIN2	34,6	-1,000	0,7400	0,04400	0,08890	0,0022	0,2924600	555,00	26,00	549,00	13,00	540,0	110,0	549,0	13,0	1,081	Rim
LUE-2_44.FIN2	160,0	3,950	1,8060	0,04900	0,17740	0,0046	0,4661600	1046,00	18,00	1052,00	25,00	1032,0	57,0	1032,0	57,0	1,938	Core
LUE-2_46.FIN2	1940,0	17,400	0,8580	0,02900	0,10280	0,0024	0,6177600	628,00	16,00	637,00	18,00	602,0	61,0	637,0	18,0	1,433	Rim
LUE-2_46.FIN2	60,5	2,536	1,0520	0,03300	0,11490	0,0016	0,1110900	731,00	16,00	700,70	9,10	809,0	66,0	700,7	9,1	4,145	Core
LUE-2_47.FIN2	82,0	2,544	1,4970	0,03900	0,15640	0,0023	0,4117900	925,00	16,00	936,00	13,00	908,0	52,0	908,0	52,0	3,084	
LUE-2_48.FIN2	616,4	1,702	0,9140	0,01000	0,10945	0,0009	0,3042700	658,40	5,40	669,40	5,40	622,0	25,0	669,4	5,4	1,671	
LUE-2_49.FIN2	664,0	2,061	0,3852	0,00710	0,05092	0,0007	0,5055900	330,30	5,20	320,10	4,30	394,0	38,0	320,1	4,3	3,088	
LUE-2_50.FIN2	683,0	2,544	0,3737	0,00570	0,05187	0,0005	0,3351900	322,10	4,20	326,00	2,80	300,0	32,0	326,0	2,8	1,211	
LUE-2_52.FIN2	345,0	1,843	0,6020	0,01000	0,07591	0,0008	0,5055600	477,70	6,40	471,60	4,70	518,0	38,0	471,6	4,7	1,277	
LUE-2_53.FIN2	155,3	3,110	1,1360	0,02600	0,12660	0,0027	0,5870500	768,00	12,00	768,00	15,00	765,0	46,0	768,0	15,0	0,000	
LUE-2_54.FIN2	897,0	1,676	0,3412	0,00750	0,04714	0,0008	0,5977300	297,50	5,70	296,90	5,10	305,0	39,0	296,9	5,1	0,202	
LUE-2_55.FIN2	424,0	9,700	5,9200	0,05800	0,35990	0,0033	0,6655100	1962,80	8,50	1981,00	16,00	1946,0	14,0	1946,0	14,0	1,799	
LUE-2_56.FIN2	970,0	21,600	0,4940	0,01100	0,06500	0,0016	0,5731500	407,70	7,60	405,60	9,70	440,0	52,0	405,6	9,7	0,515	Rim
LUE-2_56.FIN2	430,0	3,580	0,6110	0,02100	0,07700	0,0013	0,1636400	484,00	13,00	477,90	7,80	504,0	76,0	477,9	7,8	1,260	Core
LUE-2_57.FIN2	116,2	0,781	1,1140	0,06000	0,12390	0,0041	0,2946200	758,00	29,00	753,00	24,00	760,0	120,0	753,0	24,0	0,660	
LUE-2_58.FIN2	373,0	7,310	1,6570	0,02000	0,16660	0,0017	0,4162000	992,00	7,80	993,00	9,30	989,0	24,0	989,0	24,0	0,404	
LUE-2_59.FIN2	673,0	1,802	1,2700	0,01400	0,13710	0,0015	0,5952700	831,60	6,20	827,80	8,30	845,0	20,0	827,8	8,3	0,457	
LUE-2_60.FIN2	312,0	1,246	1,6160	0,02100	0,16330	0,0015	0,5075900	975,60	8,10	976,30	8,20	977,0	24,0	977,0	24,0	0,072	
LUE-2_61.FIN2	1461,0	3,290	0,5604	0,00690	0,07196	0,0007	0,4825900	451,50	4,50	448,60	4,10	467,0	25,0	448,6	4,1	0,642	
LUE-2_62.FIN2	233,4	0,719	4,8440	0,05900	0,31150	0,0041	0,6750700	1792,00	11,00	1747,00	20,00	1849,0	21,0	1849,0	21,0	5,516	
LUE-2_63.FIN2	216,0	0,685	0,8070	0,01500	0,09870	0,0011	0,3798600	599,30	8,40	606,80	6,30	562,0	40,0	606,8	6,3	1,251	
LUE-2_65.FIN2	564,0	6,380	0,5810	0,01100	0,07392	0,0009	0,5204500	464,50	7,30	459,60	5,40	495,0	38,0	459,6	5,4	1,055	
LUE-2_66.FIN2	711,0	1,310	0,3950	0,01100	0,05300	0,0010	0,3146100	337,50	8,30	332,80	6,20	352,0	65,0	332,8	6,2	1,393	
LUE-2_67.FIN2	1134,0	0,911	0,3860	0,01200	0,05173	0,0009	0,2849100	330,90	8,70	325,10	5,70	368,0	69,0	325,1	5,7	1,753	
LUE-2_68.FIN2	246,9	2,642	1,0720	0,01500	0,12230	0,0012	0,4706800	738,70	7,60	743,70	6,60	721,0	29,0	743,7	6,6	0,677	
LUE-2_69.FIN2	253,0	1,011	1,6810	0,02400	0,16920	0,0015	0,3598400	1001,10	9,50	1007,30	8,40	982,0	29,0	982,0	29,0	2,576	
LUE-2_70.FIN2	192,0	1,212	1,7060	0,02600	0,16850	0,0018	0,4902400	1009,20	9,80	1005,00	10,00	1010,0	31,0	1010,0	31,0	0,495	
LUE-2_71.FIN2	398,0	1,525	0,3590	0,01500	0,04800	0,0010	0,0873180	311,00	11,00	302,20	6,10	360,0	100,0	302,2	6,1	2,830	
LUE-2_72.FIN2	167,0	0,756	1,2240	0,03100	0,13530	0,0021	0,1570900	813,00	13,00	818,00	12,00	772,0	62,0	818,0	12,0	0,615	
LUE-2_73.FIN2	8410,0	2,167	0,3110	0,00600	0,04307	0,0009	0,5364000	274,90	4,70	271,80	5,40	299,0	47,0	271,8	5,4	1,128	
LUE-2_74.FIN2	184,5	1,823	1,9070	0,02500	0,18180	0,0016	0,1531900	1082,60	8,70	1076,40	8,60	1092,0	29,0	1092,0	29,0	1,429	
LUE-2_75.FIN2	335,0	2,270	0,9190	0,01600	0,10870	0,0013	0,2754200	661,30	8,60	664,80	7,80	636,0	43,0	664,8	7,8	0,529	
LUE-2_76.FIN2	1260,0	4,300	0,5789	0,00810	0,07447	0,0009	0,6773000	463,20	5,20	462,90	5,50	454,0	26,0	462,9	5,5	0,065	
LUE-2_77.FIN2	278,0	2,283	0,3364	0,00850	0,04746	0,0005	0,0493080	293,70	6,40	298,90	3,20	239,0	55,0	298,9	3,2	1,771	
LUE-2_78.FIN2	28,5	0,444	0,8060	0,03900	0,09310	0,0019	0,1515700	592,00	21,00	574,00	11,00	620,0	100,0	574,0	11,0	3,041	
LUE-2_79.FIN2	145,7	1,505	2,2090	0,05500	0,20130	0,0040	0,5401600	1182,00	18,00	1182,00	21,00	1176,0	44,0	1176,0	44,0	0,510	
LUE-2_80.FIN2	296,0	4,320	1,0690	0,03000	0,12190	0,0035	0,5461200	737,00	15,00	741,00	20,00	739,0	65,0	741,0	20,0	0,543	
LUE-2_81.FIN2	206,4	0,773	1,7320	0,03200	0,17000	0,0020	0,4730800	1019,90	12,00	1012,00	11,00	1027,0	34,0	1027,0	34,0	1,461	
LUE-2_82.FIN2	834,0	8,800	0,8510	0,06100	0,10200	0,0120	0,7927200	624,00	34,00	626,00	67,00	630,0	140,0	DISC	DISC	0,321	Rim
LUE-2_82.FIN2	55,0	0,100	4,4600	0,69000	0,30400	0,0240	0,4077900	1710,00	120,00	1710,00	120,00	1690,0	260,0	1690,0	260,0	1,183	Core
LUE-2_83.FIN2	176,0	3,280	0,9350	0,01800	0,10820	0,0010	0,2183100	669,70	9,70	662,30	5,80	680,0	43,0	662,3	5,8	1,105	
LUE-2_84.FIN2	389,0	2,530	0,9250	0,01200	0,10920	0,0010	0,4086000	664,20	6,50	668,10	5,80	648,0	27,0	668,1	5,8	0,587	
LUE-2_85.FIN2	531,0	1,343	0,9060	0,01100	0,10664	0,0010	0,3949600	654,00	6,10	653,10	5,70	655,0	28,0	653,1	5,7	0,138	
LUE-2_86.FIN2	357,0	1,029	0,4291	0,00840	0,05858	0,0005	0,3216900	361,90	6,00	367,00	3,10	317,0	41,0	367,0	3,1	1,409	
LUE-2_87.FIN2	311,3	1,785	0,8390	0,01200	0,10129	0,0010	0,4174200	617,60	6,80	621,80	5,60	607,0	28,0	621,8	5,6	0,680	
LUE-2_88.FIN2	158,9	6,030	0,5860	0,01600	0,07410	0,0011	0,4243800	467,00	10,00	460,90	6,60	478,0	55,0	460,9	6,6	1,306	
LUE-2_89.FIN2	460,0	1,340	0,7570	0,02500	0,09080	0,0029	0,6656600	571,00	14,00	560,00	17,00	627,0	70,0	560,0	17,0	1,926	

Sample Name:	[U]							207/235		206/238		207/206		Best age		Discordance	Rim/
Grain #	ppm	U/Th	207/235	2σ error	206/238	2σ error	RHO	Age Ma	2σ error	Age (Ma)	2σ error	Age (Ma)	2σ error	(Ma)	2σ error	%	Core
LUE-2_90.FIN2	198,0	2,730	13,8500	0,19000	0,52820	0,0064	0,7919700	2739,00	12,00	2732,00	27,00	2741,0	15,0	2741,0	15,0	0,328	
LUE-2_91.FIN2	429,0	1,601	0,3934	0,00730	0,05305	0,0005	0,4472600	336,30	5,30	333,20	3,20	346,0	41,0	333,2	3,2	0,922	
LUE-2_92.FIN2	144,4	1,157	9,5900	0,11000	0,44870	0,0047	0,6900300	2395,00	11,00	2388,00	21,00	2401,0	15,0	2401,0	15,0	0,541	
LUE-2_93.FIN2	238,0	0,982	1,4550	0,02700	0,14640	0,0016	0,4901300	910,00	11,00	880,40	9,10	987,0	35,0	987,0	35,0	10,800	
LUE-2_94.FIN2	506,0	1,723	0,3570	0,00600	0,04889	0,0004	0,1702500	309,60	4,50	307,70	2,70	328,0	40,0	307,7	2,7	0,614	
LUE-2_95.FIN2	240,8	1,174	0,7940	0,01300	0,09542	0,0008	0,4086700	592,10	7,60	587,50	5,00	603,0	36,0	587,5	5,0	0,777	
LUE-2_96.FIN2	209,5	1,187	0,8490	0,01400	0,10170	0,0011	0,3057300	624,10	8,00	624,00	6,20	614,0	38,0	624,0	6,2	0,016	
LUE-2_97.FIN2	1204,0	2,290	1,0120	0,01100	0,11770	0,0012	0,5614300	709,30	5,60	717,10	6,90	685,0	21,0	717,1	6,9	1,100	
LUE-2_98.FIN2	345,0	3,777	4,4740	0,03700	0,30830	0,0025	0,6031000	1726,30	6,60	1732,00	12,00	1711,0	14,0	1711,0	14,0	1,227	
LUE-2_99.FIN2	1078,0	1,428	0,5633	0,00840	0,07160	0,0010	0,5206200	453,20	5,50	445,90	6,30	492,0	27,0	445,9	6,3	1,611	
LUE-2_100.FIN2	185,0	0,927	1,9060	0,02700	0,17990	0,0020	0,4144900	1082,00	9,50	1066,00	11,00	1109,0	27,0	1109,0	27,0	3,877	
LUE-2_101.FIN2	332,0	0,391	11,3100	0,12000	0,46990	0,0047	0,7672700	2548,00	10,00	2482,00	20,00	2598,0	14,0	2598,0	14,0	4,465	
LUE-2_103.FIN2	60,7	0,937	1,6760	0,03800	0,16780	0,0023	0,4427200	996,00	14,00	1000,00	13,00	989,0	45,0	989,0	45,0	1,112	
LUE-2_104.FIN2	416,0	0,954	0,7650	0,01000	0,09416	0,0008	0,2838300	576,20	6,00	580,00	5,00	562,0	30,0	580,0	5,0	0,659	
LUE-2_105.FIN2	894,0	6,750	0,9650	0,04100	0,11170	0,0040	0,7196800	685,00	22,00	682,00	23,00	698,0	67,0	682,0	23,0	0,438	Rim
LUE-2_105.FIN2	88,1	1,212	1,8240	0,04300	0,17810	0,0032	0,1321500	1052,00	15,00	1056,00	18,00	1043,0	51,0	1043,0	51,0	1,246	Core
LUE-2_106.FIN2	392,0	1,780	0,3489	0,00690	0,04811	0,0005	0,2150300	303,40	5,20	302,90	3,30	304,0	45,0	302,9	3,3	0,165	
LUE-2_107.FIN2	573,0	1,755	0,3278	0,00550	0,04600	0,0005	0,3764900	287,60	4,20	289,90	3,00	262,0	36,0	289,9	3,0	0,800	
LUE-2_108.FIN2	394,5	7,350	0,8660	0,02700	0,10110	0,0023	0,7690600	633,00	15,00	621,00	13,00	672,0	59,0	621,0	13,0	1,896	Rim
LUE-2_108.FIN2	170,0	1,226	1,2840	0,05000	0,13790	0,0027	0,4174700	837,00	22,00	833,00	15,00	829,0	74,0	833,0	15,0	0,478	Core
LUE-2_109.FIN2	504,0	1,907	0,3701	0,00610	0,04932	0,0005	0,4016000	319,40	4,50	310,30	3,00	389,0	35,0	310,3	3,0	2,849	
LUE-2_110.FIN2	5860,0	2,420	0,2830	0,01900	0,03980	0,0033	0,7396700	253,00	15,00	252,00	21,00	280,0	130,0	252,0	21,0	0,395	Rim
LUE-2_110.FIN2	677,0	0,963	0,3693	0,00580	0,04977	0,0008	0,2627700	320,10	4,60	313,10	4,60	371,0	43,0	313,1	4,6	2,187	Core
LUE-2_111.FIN2	572,0	1,590	0,3736	0,00590	0,05087	0,0004	0,6000400	322,00	4,40	319,80	2,70	338,0	36,0	319,8	2,7	0,683	
LUE-2_112.FIN2	1084,0	8,700	0,8980	0,01100	0,10525	0,0009	0,6565600	650,00	6,20	645,00	5,20	686,0	22,0	645,0	5,2	0,769	
LUE-2_113.FIN2	38,9	2,720	0,8880	0,06200	0,10590	0,0030	0,1413600	639,00	34,00	648,00	17,00	580,0	150,0	648,0	17,0	1,408	
LUE-2_114.FIN2	286,0	1,586	0,7290	0,01500	0,09120	0,0010	0,4623300	556,60	8,50	562,40	5,90	542,0	43,0	562,4	5,9	1,042	
LUE-2_115.FIN2	189,0	1,585	0,7220	0,01600	0,08859	0,0009	0,1969300	551,60	9,50	547,10	5,40	560,0	49,0	547,1	5,4	0,816	
LUE-2_116.FIN2	454,0	2,701	0,3641	0,00680	0,04956	0,0005	0,2953000	315,40	5,00	311,80	3,00	338,0	38,0	311,8	3,0	1,141	
LUE-2_117.FIN2	283,0	0,766	1,0410	0,01800	0,11820	0,0012	0,2787200	723,20	9,00	719,80	7,00	740,0	37,0	719,8	7,0	0,470	
LUE-2_118.FIN2	766,6	5,724	0,3738	0,00660	0,05059	0,0004	0,4290700	322,10	4,90	318,10	2,50	362,0	37,0	318,1	2,5	1,242	
LUE-2_119.FIN2	442,0	1,057	0,7200	0,02200	0,08910	0,0021	0,3645200	550,00	13,00	550,00	12,00	559,0	66,0	550,0	12,0	0,000	
LUE-2_120.FIN2	438,0	1,370	1,6900	0,03000	0,16430	0,0027	0,4791900	1004,00	11,00	980,00	15,00	1067,0	35,0	1067,0	35,0	8,154	
LUE-2_121.FIN2	332,0	0,924	12,0600	0,16000	0,49780	0,0059	0,9112200	2606,00	13,00	2603,00	25,00	2611,0	14,0	2611,0	14,0	0,306	
LUE-2_122.FIN2	850,0	23,000	0,8160	0,02300	0,09920	0,0015	0,2828800	606,00	13,00	609,90	8,80	597,0	62,0	609,9	8,8	0,644	Rim
LUE-2_122.FIN2	192,0	0,962	5,0800	0,11000	0,32820	0,0058	0,8141100	1830,00	18,00	1829,00	29,00	1837,0	21,0	1837,0	21,0	0,435	Core
LUE-2_123.FIN2	1361,0	180,000	0,9120	0,01200	0,10790	0,0011	0,5098300	657,70	6,30	660,60	6,60	658,0	26,0	660,6	6,6	0,441	
LUE-2_124.FIN2	376,0	33,600	1,0370	0,02600	0,11830	0,0019	0,5048700	721,00	13,00	720,00	11,00	727,0	46,0	720,0	11,0	0,139	
LUE-2_125.FIN2	171,5	1,332	0,4310	0,01100	0,05852	0,0007	0,1259600	362,70	7,60	366,50	4,50	338,0	57,0	366,5	4,5	1,048	
LUE-2_126.FIN2	249,2	1,598	0,7950	0,01300	0,09680	0,0011	0,3525100	593,00	7,30	595,40	6,20	587,0	36,0	595,4	6,2	0,405	
LUE-2_127.FIN2	716,7	2,190	0,5828	0,00960	0,07392	0,0008	0,2422000	466,30	6,30	459,70	4,60	503,0	38,0	459,7	4,6	1,415	
LUE-2_128.FIN2	280,0	4,360	0,5830	0,01100	0,07515	0,0009	0,1944400	465,50	6,80	467,00	5,20	459,0	43,0	467,0	5,2	0,322	
LUE-2_129.FIN2	202,0	0,626	1,7990	0,02600	0,17620	0,0021	0,3419800	1043,40	9,40	1046,00	11,00	1056,0	31,0	1056,0	31,0	0,947	
LUE-2_130.FIN2	230,0	6,100	0,6120	0,01200	0,07940	0,0008	0,2306300	484,70	7,40	492,50	4,90	444,0	43,0	492,5	4,9	1,609	
LUE-2_131.FIN2	216,9	1,854	0,3560	0,01300	0,04777	0,0009	0,2314200	308,20	9,60	300,80	5,70	359,0	80,0	300,8	5,7	2,401	
LUE-2_132.FIN2	81,5	2,105	2,7090	0,04000	0,22790	0,0023	0,0601300	1329,00	11,00	1323,00	12,00	1351,0	33,0	1351,0	33,0	2,073	
LUE-2_133.FIN2	383,0	2,008	0,8070	0,02800	0,09670	0,0019	0,5551200	599,00	16,00	595,00	11,00	614,0	67,0	595,0	11,0	0,668	

Sample Name:	[U]							207/235		206/238		207/206		Best age		Discordance	Rim/
Grain #	ppm	U/Th	207/235	2σ error	206/238	2σ error	RHO	Age Ma	2σ error	Age (Ma)	2σ error	Age (Ma)	2σ error	(Ma)	2σ error	%	Core
LUE-2_134.FIN2	118,0	3,360	1,2930	0,02500	0,14010	0,0014	0,2867300	842,00	11,00	844,90	7,80	850,0	39,0	844,9	7,8	0,344	
LUE-2_135.FIN2	199,0	1,318	1,4730	0,03000	0,15150	0,0021	0,6353600	917,00	12,00	909,00	12,00	936,0	32,0	936,0	32,0	2,885	
LUE-2_136.FIN2	409,0	10,220	0,5920	0,03700	0,07590	0,0029	0,0562990	472,00	23,00	472,00	17,00	480,0	170,0	472,0	17,0	0,000	Rim
LUE-2_136.FIN2	92,2	1,859	0,7340	0,01900	0,09060	0,0010	0,1686500	557,00	11,00	559,10	6,10	551,0	60,0	559,1	6,1	0,377	Core
LUE-2_137.FIN2	212,7	1,231	1,7080	0,02600	0,16700	0,0016	0,6496500	1009,70	9,70	995,20	9,00	1038,0	30,0	1038,0	30,0	4,123	
LUE-2_138.FIN2	839,0	11,000	0,4660	0,04300	0,05690	0,0022	0,8040900	388,00	30,00	357,00	13,00	580,0	140,0	357,0	13,0	7,990	Rim
LUE-2_138.FIN2	1254,0	2,769	5,6560	0,09200	0,33440	0,0053	0,7580000	1924,00	14,00	1859,00	26,00	1997,0	20,0	1997,0	20,0	6,910	Core
LUE-2_139.FIN2	413,0	17,800	0,3360	0,01300	0,04690	0,0011	0,0992630	293,60	9,80	295,40	6,90	283,0	92,0	295,4	6,9	0,613	Rim
LUE-2_139.FIN2	177,1	1,698	0,8450	0,02800	0,09730	0,0014	0,2278900	620,00	15,00	598,40	8,00	691,0	68,0	598,4	8,0	3,484	Core
LUE-2_140.FIN2	716,0	1,583	0,4107	0,00700	0,05454	0,0006	0,3552800	349,00	5,10	342,30	3,50	391,0	39,0	342,3	3,5	1,920	
YESA-1_1.FIN2	886,0	70,000	0,8270	0,04800	0,09770	0,0031	0,5189200	610,00	26,00	601,00	18,00	630,0	100,0	601,0	18,0	1,475	Rim
YESA-1_1.FIN2	217,9	2,480	1,0780	0,01700	0,12190	0,0013	0,4644900	741,50	8,30	741,20	7,70	739,0	30,0	741,2	7,7	0,040	Core
YESA-1_2.FIN2	190,0	1,590	1,2260	0,01700	0,13160	0,0012	0,2961200	811,60	7,50	796,90	6,60	848,0	29,0	796,9	6,6	1,811	
YESA-1_3.FIN2	204,0	2,820	0,6340	0,01200	0,07711	0,0007	0,3284000	498,40	7,90	478,80	4,20	575,0	44,0	478,8	4,2	3,933	
YESA-1_4.FIN2	920,0	21,900	0,4340	0,02400	0,05600	0,0025	0,6633300	366,00	17,00	351,00	16,00	449,0	99,0	351,0	16,0	4,098	Rim
YESA-1_4.FIN2	341,0	1,457	0,7760	0,01100	0,09357	0,0009	0,4380900	583,60	6,30	576,50	5,40	603,0	28,0	576,5	5,4	1,217	Core
YESA-1_5.FIN2	449,0	124,000	0,3420	0,01000	0,04719	0,0008	0,4993400	298,50	7,70	297,20	5,00	303,0	58,0	297,2	5,0	0,436	
YESA-1_6.FIN2	960,0	2,106	0,4000	0,01400	0,04290	0,0011	0,5063100	342,00	10,00	270,50	7,00	854,0	61,0	DISC	DISC	20,906	
YESA-1_7.FIN2	534,0	1,920	0,7210	0,00990	0,08560	0,0008	0,5778600	550,70	5,80	529,40	4,50	641,0	25,0	529,4	4,5	3,868	
YESA-1_8.FIN2	1370,0	1,910	1,1090	0,06300	0,10650	0,0029	0,2345900	755,00	28,00	652,00	17,00	1068,0	93,0	652,0	17,0	13,642	Rim
YESA-1_8.FIN2	497,0	1,032	1,4990	0,04600	0,12190	0,0015	0,2954700	927,00	18,00	741,40	8,80	1389,0	54,0	DISC	DISC	20,022	Core
YESA-1_9.FIN2	192,9	1,696	0,7940	0,01700	0,09350	0,0012	0,2353600	592,40	9,50	576,20	7,30	648,0	47,0	576,2	7,3	2,735	
YESA-1_10.FIN2	454,0	1,350	0,6890	0,01800	0,07600	0,0022	0,5433100	535,00	12,00	472,00	13,00	806,0	59,0	472,0	13,0	11,776	Rim
YESA-1_10.FIN2	570,0	0,810	0,8280	0,01100	0,09800	0,0011	0,4712800	611,80	5,80	602,70	6,40	649,0	27,0	602,7	6,4	1,487	Core
YESA-1_11.FIN2	880,0	1,126	0,3812	0,00480	0,05176	0,0005	0,6129000	327,70	3,50	325,30	3,00	340,0	23,0	325,3	3,0	0,732	
YESA-1_12.FIN2	142,0	1,650	0,7790	0,01300	0,09342	0,0010	0,2302200	584,10	7,60	575,60	5,70	612,0	39,0	575,6	5,7	1,455	
YESA-1_14.FIN2	723,0	1,691	0,7117	0,00830	0,08495	0,0006	0,4476800	545,30	4,90	525,50	3,80	628,0	23,0	525,5	3,8	3,631	
YESA-1_15.FIN2	626,0	2,170	0,5060	0,02500	0,06000	0,0028	0,6087600	415,00	17,00	376,00	17,00	640,0	100,0	376,0	17,0	9,398	Rim
YESA-1_15.FIN2	137,8	1,530	0,8560	0,01700	0,10040	0,0012	0,2186900	627,80	9,60	616,80	7,30	650,0	45,0	616,8	7,3	1,752	Core
YESA-1_16.FIN2	1651,0	12,300	0,3630	0,01400	0,04602	0,0006	0,7642400	314,00	10,00	290,00	4,00	481,0	62,0	290,0	4,0	7,643	Rim
YESA-1_16.FIN2	864,0	0,614	0,9530	0,01900	0,07200	0,0011	0,6274400	679,20	9,90	448,30	6,40	1540,0	33,0	DISC	DISC	33,996	Core
YESA-1_17.FIN2	61,6	2,030	14,0800	0,14000	0,52830	0,0044	0,5319800	2753,40	9,40	2733,00	19,00	2768,0	14,0	2768,0	14,0	1,264	
YESA-1_18.FIN2	468,0	2,680	0,8500	0,01000	0,10003	0,0009	0,4565000	625,00	5,70	614,50	5,30	657,0	25,0	614,5	5,3	1,680	
YESA-1_19.FIN2	316,0	1,262	1,6620	0,01800	0,16400	0,0014	0,4684600	993,20	7,00	978,70	8,00	1015,0	21,0	1015,0	21,0	3,576	
YESA-1_20.FIN2	423,0	1,230	0,9720	0,01400	0,11220	0,0011	0,6070100	688,30	7,00	685,10	6,40	703,0	24,0	685,1	6,4	0,465	
YESA-1_21.FIN2	317,0	1,269	7,3150	0,09000	0,31940	0,0039	0,8365200	2149,00	11,00	1786,00	19,00	2518,0	14,0	2518,0	14,0	29,071	
YESA-1_22.FIN2	162,0	0,994	0,8670	0,01700	0,09990	0,0012	0,4997200	633,90	9,30	613,70	6,90	708,0	38,0	613,7	6,9	3,187	
YESA-1_23.FIN2	333,7	1,592	0,6870	0,01200	0,08330	0,0012	0,5975900	532,70	6,90	515,80	7,00	600,0	32,0	515,8	7,0	3,173	
YESA-1_24.FIN2	346,0	1,910	1,7830	0,01900	0,17250	0,0016	0,5482200	1040,10	6,80	1025,40	8,70	1071,0	19,0	1071,0	19,0	4,258	
YESA-1_25.FIN2	143,1	0,965	1,0900	0,02400	0,11900	0,0018	0,6425800	747,00	12,00	724,00	10,00	817,0	35,0	724,0	10,0	3,079	
YESA-1_26.FIN2	1164,0	1,192	0,6130	0,01400	0,06550	0,0016	0,8633800	484,20	8,80	408,70	9,60	862,0	24,0	DISC	DISC	15,593	
YESA-1_27.FIN2	601,0	0,960	0,8310	0,01100	0,09410	0,0010	0,3225300	613,60	6,30	579,70	6,10	739,0	31,0	579,7	6,1	5,525	
YESA-1_28.FIN2	1260,0	18,600	0,6510	0,01600	0,07000	0,0012	0,3631100	508,70	9,90	436,40	7,00	846,0	49,0	436,4	7,0	14,213	
YESA-1_29.FIN2	136,5	0,546	1,6020	0,02600	0,15630	0,0013	0,6346800	969,00	10,00	936,20	7,50	1047,0	30,0	1047,0	30,0	10,583	
YESA-1_30.FIN2	210,6	1,078	1,4470	0,04100	0,13550	0,0022	0,3425400	908,00	17,00	819,00	13,00	1130,0	56,0	819,0	13,0	9,802	
YESA-1_31.FIN2	134,3	0,555	0,7450	0,01600	0,08907	0,0009	0,2842100	563,70	9,40	550,00	5,20	609,0	45,0	550,0	5,2	2,430	

Sample Name:	[U]							207/235		206/238		207/206		Best age		Discordance	Rim/
Grain #	ppm	U/Th	207/235	2σ error	206/238	2σ error	RHO	Age Ma	2σ error	Age (Ma)	2σ error	Age (Ma)	2σ error	(Ma)	2σ error	%	Core
YESA-1_32.FIN2	413,0	1,353	14,4400	0,20000	0,53800	0,0076	0,9279200	2779,00	13,00	2778,00	31,00	2782,4	8,9	2782,4	8,9	0,158	
YESA-1_33.FIN2	2140,0	2,770	0,6860	0,03200	0,05700	0,0033	0,8868900	529,00	19,00	357,00	20,00	1371,0	65,0	DISC	DISC	32,514	Rim
YESA-1_33.FIN2	456,0	1,129	0,8550	0,01200	0,09946	0,0009	0,5804100	626,80	6,50	611,20	5,20	680,0	25,0	611,2	5,2	2,489	Core
YESA-1_35.FIN2	380,1	0,779	0,7260	0,01300	0,08541	0,0009	0,3092400	553,50	7,40	528,30	5,30	664,0	36,0	528,3	5,3	4,553	
YESA-1_36.FIN2	161,1	0,796	0,8750	0,01900	0,09840	0,0010	0,3376100	636,00	10,00	605,10	6,20	769,0	45,0	605,1	6,2	4,858	
YESA-1_37.FIN2	681,0	1,203	0,9532	0,00950	0,10752	0,0009	0,5421100	679,30	5,00	658,20	5,00	762,0	19,0	658,2	5,0	3,106	
YESA-1_38.FIN2	588,0	0,677	0,8410	0,01400	0,09470	0,0009	0,5441300	619,40	7,30	583,20	5,50	759,0	28,0	583,2	5,5	5,844	
YESA-1_39.FIN2	732,0	1,417	0,7600	0,02000	0,08850	0,0019	0,7906800	574,00	11,00	547,00	12,00	687,0	43,0	547,0	12,0	4,704	
YESA-1_40.FIN2	2020,0	10,100	0,4670	0,03400	0,03940	0,0022	0,9710300	388,00	24,00	249,00	14,00	1321,0	81,0	DISC	DISC	35,825	Rim
YESA-1_40.FIN2	746,0	2,146	3,0300	0,09500	0,16360	0,0045	0,9605100	1408,00	25,00	976,00	25,00	2150,0	16,0	DISC	DISC	54,605	Core
YESA-1_41.FIN2	826,0	2,068	0,4746	0,00930	0,04353	0,0006	0,0589420	393,60	6,30	274,70	3,60	1163,0	45,0	DISC	DISC	30,208	
YESA-1_42.FIN2	380,0	2,331	0,7390	0,02200	0,08030	0,0022	0,8162000	561,00	13,00	497,00	13,00	835,0	53,0	497,0	13,0	11,408	
YESA-1_43.FIN2	243,7	1,715	4,3340	0,04400	0,29250	0,0024	0,6024700	1698,60	8,40	1653,00	12,00	1765,0	16,0	1765,0	16,0	6,346	
YESA-1_44.FIN2	558,0	1,273	0,3842	0,00640	0,04728	0,0004	0,5323400	329,70	4,70	297,80	2,60	557,0	35,0	297,8	2,6	9,675	
YESA-1_45.FIN2	480,0	3,730	0,7220	0,01100	0,08885	0,0009	0,5115400	550,80	6,30	548,60	5,40	564,0	27,0	548,6	5,4	0,399	
YESA-1_46.FIN2	594,0	10,680	0,5528	0,00810	0,06921	0,0007	0,5041400	446,30	5,30	431,30	4,20	525,0	29,0	431,3	4,2	3,361	
YESA-1_47.FIN2	236,9	1,830	0,9000	0,03700	0,09920	0,0029	0,0361600	651,00	20,00	609,00	17,00	830,0	120,0	609,0	17,0	6,452	
YESA-1_48.FIN2	243,7	1,250	3,7780	0,04200	0,26790	0,0027	0,6729900	1586,70	8,90	1530,00	14,00	1666,0	16,0	1666,0	16,0	8,163	
YESA-1_49.FIN2	409,0	0,966	0,5473	0,00750	0,07090	0,0006	0,2768000	442,80	4,90	441,50	3,60	454,0	29,0	441,5	3,6	0,294	
YESA-1_50.FIN2	283,1	0,855	4,6000	0,12000	0,29540	0,0069	0,9146700	1743,00	23,00	1666,00	35,00	1847,0	21,0	1847,0	21,0	9,800	
YESA-1_51.FIN2	186,0	2,140	0,7660	0,01300	0,09193	0,0009	0,4205200	576,30	7,50	566,90	5,30	621,0	32,0	566,9	5,3	1,631	
YESA-1_52.FIN2	1578,0	3,070	0,3500	0,01300	0,03800	0,0011	0,6179300	304,50	9,80	240,70	7,00	828,0	56,0	DISC	DISC	20,952	Rim
YESA-1_52.FIN2	560,4	1,490	0,8290	0,01200	0,09600	0,0011	0,5918200	612,60	6,70	590,60	6,60	701,0	26,0	590,6	6,6	3,591	Core
YESA-1_54.FIN2	484,0	1,440	0,8640	0,01900	0,09520	0,0018	0,2787500	632,00	10,00	586,00	10,00	792,0	46,0	586,0	10,0	7,278	
YESA-1_55.FIN2	443,4	1,940	0,7120	0,02600	0,06036	0,0007	0,0422300	542,00	15,00	377,80	4,30	1296,0	71,0	DISC	DISC	30,295	
YESA-1_56.FIN2	756,0	1,860	0,3383	0,00500	0,04533	0,0004	0,3214700	295,60	3,80	285,80	2,20	373,0	32,0	285,8	2,2	3,315	
YESA-1_57.FIN2	685,0	2,410	9,4400	0,29000	0,39400	0,0100	0,9725900	2365,00	30,00	2133,00	47,00	2591,0	15,0	2591,0	15,0	17,677	
YESA-1_58.FIN2	662,0	11,600	10,6400	0,19000	0,40780	0,0070	0,6734800	2491,00	17,00	2204,00	32,00	2738,0	25,0	2738,0	25,0	19,503	Rim
YESA-1_58.FIN2	259,6	16,600	13,4400	0,15000	0,50220	0,0045	0,7695600	2712,00	10,00	2623,00	19,00	2781,0	12,0	2781,0	12,0	5,681	Core
YESA-1_59.FIN2	326,0	0,676	0,8210	0,01200	0,09577	0,0010	0,5653800	607,70	6,90	589,50	5,70	675,0	27,0	589,5	5,7	2,995	
YESA-1_60.FIN2	222,0	1,298	0,8370	0,01300	0,09810	0,0011	0,5339300	617,10	7,50	603,20	6,60	668,0	31,0	603,2	6,6	2,252	
YESA-1_61.FIN2	269,1	13,400	0,8430	0,01100	0,09817	0,0008	0,2331400	620,40	5,90	603,60	4,80	680,0	29,0	603,6	4,8	2,708	
YESA-1_62.FIN2	235,1	1,672	1,3950	0,01700	0,14700	0,0010	0,2440400	885,70	7,30	884,10	5,80	891,0	27,0	891,0	27,0	0,774	
YESA-1_63.FIN2	204,0	1,084	0,6980	0,02100	0,07280	0,0017	0,4153300	537,00	12,00	453,00	10,00	912,0	63,0	DISC	DISC	15,642	
YESA-1_64.FIN2	318,4	62,000	5,1650	0,06400	0,30850	0,0037	0,8463000	1845,00	11,00	1732,00	18,00	1983,0	12,0	1983,0	12,0	12,658	
YESA-1_65.FIN2	258,0	0,306	0,7580	0,01300	0,09204	0,0009	0,2608400	573,50	7,70	567,50	5,00	597,0	39,0	567,5	5,0	1,046	
YESA-1_66.FIN2	405,0	2,550	0,9430	0,01100	0,10648	0,0008	0,3626000	673,80	5,70	652,20	4,40	751,0	24,0	652,2	4,4	3,206	
YESA-1_67.FIN2	782,0	2,586	6,7230	0,09600	0,38410	0,0056	0,9037200	2073,00	13,00	2093,00	26,00	2058,0	10,0	2058,0	10,0	1,701	
YESA-1_68.FIN2	155,0	0,497	1,6610	0,02400	0,16430	0,0015	0,3882900	993,30	9,40	980,30	8,40	1023,0	28,0	1023,0	28,0	4,174	
YESA-1_69.FIN2	572,0	5,910	0,9400	0,01900	0,10600	0,0018	0,6604800	672,50	9,80	649,00	11,00	762,0	43,0	649,0	11,0	3,494	Rim
YESA-1_69.FIN2	138,3	1,796	1,1000	0,02400	0,12090	0,0016	0,4466500	753,00	12,00	735,70	9,00	799,0	42,0	735,7	9,0	2,297	Core
YESA-1_70.FIN2	593,0	5,250	5,1720	0,08800	0,29260	0,0050	0,9029500	1844,00	14,00	1652,00	25,00	2075,0	13,0	2075,0	13,0	20,386	
YESA-1_71.FIN2	175,0	0,853	0,3690	0,01100	0,04514	0,0006	0,1064600	318,00	7,90	284,60	3,40	563,0	67,0	284,6	3,4	10,503	
YESA-1_73.FIN2	577,0	2,470	4,0540	0,05500	0,27070	0,0036	0,8870000	1643,00	11,00	1543,00	18,00	1776,0	12,0	1776,0	12,0	13,119	
YESA-1_74.FIN2	196,7	2,078	0,6380	0,01200	0,06947	0,0008	0,3423400	500,00	7,50	432,90	4,70	811,0	39,0	432,9	4,7	13,420	
YESA-1_75.FIN2	143,5	1,333	5,3290	0,07400	0,33630	0,0037	0,7511000	1873,00	12,00	1868,00	18,00	1881,0	17,0	1881,0	17,0	0,691	
YESA-1_76.FIN2	298,0	0,858	4,0820	0,05400	0,26600	0,0026	0,8486300	1649,00	11,00	1520,00	13,00	1821,0	15,0	1821,0	15,0	16,529	

Sample Name:	[U]							207/235		206/238		207/206		Best age		Discordance	Rim/
Grain #	ppm	U/Th	207/235	2σ error	206/238	2σ error	RHO	Age Ma	2σ error	Age (Ma)	2σ error	Age (Ma)	2σ error	(Ma)	2σ error	%	Core
YESA-1_77.FIN2	1015,0	6,230	1,5300	0,08700	0,12330	0,0032	0,3877000	940,00	35,00	750,00	19,00	1410,0	100,0	DISC	DISC	20,213	Rim
YESA-1_77.FIN2	361,4	2,621	2,3480	0,03500	0,20740	0,0025	0,8304500	1226,00	11,00	1215,00	13,00	1245,0	22,0	1245,0	22,0	2,410	Core
YESA-1_78.FIN2	101,4	0,611	0,8250	0,02700	0,09500	0,0012	0,4556800	609,00	15,00	585,20	7,00	682,0	68,0	585,2	7,0	3,908	
YESA-1_79.FIN2	971,0	2,720	0,9230	0,05100	0,07570	0,0021	0,4414600	660,00	26,00	470,00	13,00	1360,0	91,0	DISC	DISC	28,788	Rim
YESA-1_79.FIN2	802,0	0,905	1,3380	0,02200	0,12970	0,0019	0,5521600	861,50	9,70	786,00	11,00	1058,0	25,0	786,0	11,0	8,764	Core
YESA-1_80.FIN2	110,5	3,960	0,8850	0,02500	0,10420	0,0015	0,0761940	642,00	14,00	638,70	8,60	646,0	68,0	638,7	8,6	0,514	
YESA-1_81.FIN2	355,0	2,096	3,4000	0,04100	0,25000	0,0028	0,8098400	1503,00	9,50	1438,00	14,00	1598,0	15,0	1598,0	15,0	10,013	
YESA-1_82.FIN2	1830,0	57,000	0,4720	0,03100	0,05110	0,0019	0,7521500	392,00	21,00	321,00	12,00	820,0	91,0	DISC	DISC	18,112	Rim
YESA-1_82.FIN2	548,0	9,630	0,6042	0,00720	0,07680	0,0007	0,3551000	479,50	4,50	476,90	3,90	485,0	26,0	476,9	3,9	0,542	Core
YESA-1_83.FIN2	655,0	6,860	1,1560	0,04800	0,11240	0,0045	0,8267300	779,00	23,00	686,00	26,00	1051,0	46,0	686,0	26,0	11,938	Rim
YESA-1_83.FIN2	247,0	2,920	1,4810	0,02300	0,15030	0,0020	0,3127800	921,40	9,40	902,00	11,00	964,0	25,0	964,0	25,0	6,432	Core
YESA-1_84.FIN2	194,0	2,451	0,8700	0,01800	0,10420	0,0012	0,3956500	635,10	9,50	638,90	6,90	601,0	44,0	638,9	6,9	0,598	
YESA-1_85.FIN2	443,0	1,454	0,8790	0,01400	0,10230	0,0014	0,7623800	639,40	7,80	627,80	8,00	678,0	24,0	627,8	8,0	1,814	
YESA-1_86.FIN2	367,0	12,940	0,8050	0,01200	0,09080	0,0014	0,6239100	599,60	7,00	559,80	8,20	753,0	27,0	559,8	8,2	6,638	
YESA-1_87.FIN2	990,0	9,700	0,3751	0,00700	0,04884	0,0006	0,4075400	323,20	5,20	307,40	3,70	437,0	42,0	307,4	3,7	4,889	
YESA-1_88.FIN2	616,0	3,120	0,4196	0,00720	0,05468	0,0006	0,4230700	355,40	5,10	343,20	3,60	430,0	33,0	343,2	3,6	3,433	
YESA-1_89.FIN2	51,4	1,207	1,1940	0,03600	0,12360	0,0015	0,1707600	793,00	17,00	751,00	8,80	901,0	64,0	751,0	8,8	5,296	
YESA-1_91.FIN2	236,1	3,440	0,6510	0,04200	0,08040	0,0031	0,6607700	515,00	29,00	499,00	18,00	560,0	130,0	499,0	18,0	3,107	Rim
YESA-1_91.FIN2	191,5	1,629	3,9500	0,11000	0,27070	0,0063	0,8968200	1619,00	22,00	1542,00	32,00	1719,0	22,0	1719,0	22,0	10,297	Core
YESA-1_92.FIN2	758,0	0,706	0,7560	0,01000	0,09165	0,0008	0,3798700	571,40	6,10	565,20	4,90	589,0	29,0	565,2	4,9	1,085	
YESA-1_93.FIN2	259,0	2,450	0,3457	0,00790	0,04598	0,0005	0,1841700	300,90	6,00	289,80	3,00	368,0	52,0	289,8	3,0	3,689	
YESA-1_94.FIN2	251,9	1,429	0,4800	0,01400	0,05113	0,0007	0,3001200	399,10	8,90	321,40	4,40	862,0	55,0	DISC	DISC	19,469	
YESA-1_95.FIN2	329,0	2,211	0,9060	0,03100	0,09410	0,0011	0,5589900	655,00	16,00	579,60	6,30	909,0	56,0	579,6	6,3	11,511	
YESA-1_96.FIN2	535,0	1,683	0,8356	0,00870	0,09752	0,0006	0,1936500	616,30	4,80	599,80	3,40	674,0	24,0	599,8	3,4	2,677	
YESA-1_97.FIN2	119,6	0,853	0,9150	0,01900	0,09660	0,0012	0,1142700	658,00	10,00	594,20	7,10	880,0	46,0	594,2	7,1	9,696	
YESA-1_98.FIN2	760,0	10,670	4,9290	0,07400	0,29460	0,0045	0,9010400	1805,00	13,00	1663,00	22,00	1972,0	12,0	1972,0	12,0	15,669	
YESA-1_99.FIN2	421,0	2,440	2,8480	0,03400	0,18420	0,0017	0,7138400	1367,20	8,80	1089,80	9,30	1826,0	15,0	DISC	DISC	40,318	
YESA-1_100.FIN2	201,6	1,450	6,4310	0,05700	0,35170	0,0025	0,5800800	2035,40	7,70	1942,00	12,00	2130,0	13,0	2130,0	13,0	8,826	
YESA-1_101.FIN2	240,6	0,597	9,7600	0,15000	0,40670	0,0056	0,9037700	2414,00	14,00	2198,00	26,00	2599,0	11,0	2599,0	11,0	15,429	
YESA-1_102.FIN2	47,5	1,421	6,4200	0,14000	0,35470	0,0075	0,5608600	2031,00	20,00	1955,00	36,00	2109,0	36,0	2109,0	36,0	7,302	
YESA-1_103.FIN2	346,5	1,346	9,8150	0,08200	0,43290	0,0032	0,6555800	2416,60	7,70	2318,00	14,00	2499,0	11,0	2499,0	11,0	7,243	
YESA-1_104.FIN2	435,0	4,380	0,6000	0,02900	0,07000	0,0019	0,3197600	476,00	19,00	436,00	12,00	665,0	96,0	436,0	12,0	8,403	Rim
YESA-1_104.FIN2	510,0	1,370	0,9240	0,02100	0,09970	0,0017	0,8304300	663,00	11,00	612,00	10,00	836,0	27,0	612,0	10,0	7,692	Core
YESA-1_105.FIN2	253,0	0,865	0,7990	0,02400	0,08700	0,0012	0,0670040	595,00	14,00	537,90	6,90	810,0	70,0	537,9	6,9	9,597	
YESA-1_106.FIN2	486,0	8,310	0,3810	0,00710	0,04831	0,0004	0,2244800	327,30	5,30	304,10	2,70	483,0	42,0	304,1	2,7	7,088	
YESA-1_108.FIN2	286,7	1,324	9,7900	0,11000	0,39140	0,0042	0,8768200	2413,70	9,90	2128,00	20,00	2666,9	9,3	2666,9	9,3	20,207	
YESA-1_109.FIN2	159,0	1,255	0,8770	0,01600	0,10440	0,0012	0,3327700	638,20	8,70	640,20	7,20	623,0	41,0	640,2	7,2	0,313	
YESA-1_110.FIN2	485,0	3,148	11,3400	0,15000	0,44890	0,0063	0,8608600	2549,00	13,00	2389,00	28,00	2688,0	11,0	2688,0	11,0	11,124	
YESA-1_111.FIN2	794,0	47,400	0,5520	0,03200	0,06760	0,0035	0,3982600	446,00	21,00	422,00	21,00	570,0	150,0	422,0	21,0	5,381	Rim
YESA-1_111.FIN2	320,2	1,956	3,2810	0,03300	0,25380	0,0023	0,6450200	1475,60	7,70	1458,00	12,00	1501,0	15,0	1501,0	15,0	2,865	Core
YESA-1_112.FIN2	311,0	1,063	1,6990	0,02200	0,16400	0,0016	0,5709100	1008,60	8,70	978,80	8,80	1068,0	22,0	1068,0	22,0	8,352	
YESA-1_113.FIN2	71,5	0,915	1,0240	0,02800	0,11410	0,0015	0,3614200	712,00	14,00	696,50	8,40	738,0	54,0	696,5	8,4	2,177	
YESA-1_114.FIN2	891,0	17,100	0,8310	0,01300	0,09410	0,0011	0,7082300	613,50	7,00	579,60	6,50	744,0	23,0	579,6	6,5	5,526	
YESA-1_115.FIN2	1163,0	0,965	0,7141	0,00870	0,08036	0,0010	0,4344700	547,00	5,10	498,20	5,70	772,0	29,0	498,2	5,7	8,921	
YESA-1_116.FIN2	773,0	2,484	0,8040	0,01400	0,09306	0,0008	0,5083700	598,30	7,80	573,60	4,70	698,0	31,0	573,6	4,7	4,128	
YESA-1_117.FIN2	728,0	2,950	0,4400	0,02200	0,04720	0,0021	0,6732400	369,00	16,00	297,00	13,00	854,0	82,0	DISC	DISC	19,512	Rim
YESA-1_117.FIN2	505,0	1,782	0,5840	0,01100	0,07092	0,0009	0,2039700	466,70	7,00	441,70	5,40	596,0	44,0	441,7	5,4	5,357	Core

Sample Name:	[U]							207/235		206/238		207/206		Best age		Discordance	Rim/
Grain #	ppm	U/Th	207/235	2σ error	206/238	2σ error	RHO	Age Ma	2σ error	Age (Ma)	2σ error	Age (Ma)	2σ error	(Ma)	2σ error	%	Core
YESA-1_118.FIN2	178,0	1,216	10,1300	0,20000	0,42000	0,0061	0,8631900	2444,00	18,00	2259,00	28,00	2615,0	17,0	2615,0	17,0	13,614	
YESA-1_119.FIN2	387,0	4,300	0,8240	0,01400	0,09650	0,0010	0,5679800	609,20	7,80	593,80	5,90	673,0	31,0	593,8	5,9	2,528	
YESA-1_120.FIN2	196,0	2,377	0,7340	0,01300	0,08964	0,0008	0,3761100	557,60	7,50	553,30	4,90	581,0	37,0	553,3	4,9	0,771	
YESA-1_121.FIN2	290,0	1,060	1,5040	0,01900	0,15120	0,0011	0,6064600	930,80	7,60	907,40	6,40	1004,0	23,0	1004,0	23,0	9,622	
YESA-1_122.FIN2	559,0	2,212	1,1640	0,01900	0,12620	0,0012	0,4268500	782,80	8,70	766,00	7,10	842,0	29,0	766,0	7,1	2,146	
YESA-1_123.FIN2	92,7	1,136	0,8270	0,01900	0,09910	0,0011	0,1398000	611,00	10,00	609,30	6,30	624,0	50,0	609,3	6,3	0,278	
YESA-1_124.FIN2	271,5	1,510	5,7170	0,04500	0,34300	0,0027	0,7294100	1933,10	6,90	1901,00	13,00	1979,0	13,0	1979,0	13,0	3,941	
YESA-1_125.FIN2	400,0	2,500	4,1040	0,03700	0,29330	0,0023	0,6927300	1654,10	7,40	1659,00	11,00	1665,0	13,0	1665,0	13,0	0,360	
YESA-1_126.FIN2	487,0	2,380	0,8180	0,01300	0,09760	0,0013	0,8052100	606,60	7,10	600,40	7,40	655,0	23,0	600,4	7,4	1,022	
YESA-1_127.FIN2	149,7	0,813	0,8010	0,01500	0,09480	0,0012	0,1723300	596,70	8,30	583,80	7,00	663,0	46,0	583,8	7,0	2,162	
YESA-1_128.FIN2	78,3	1,116	4,5770	0,06800	0,32060	0,0033	0,4143200	1745,00	13,00	1792,00	16,00	1697,0	28,0	1697,0	28,0	5,598	
YESA-1_129.FIN2	378,0	1,082	0,2544	0,00550	0,03686	0,0004	0,2027200	229,80	4,40	233,30	2,40	220,0	48,0	233,3	2,4	1,523	
YESA-1_130.FIN2	757,0	3,730	0,3340	0,01100	0,04230	0,0012	0,7082000	292,20	8,30	266,80	7,50	515,0	52,0	266,8	7,5	8,693	
YESA-2_1.FIN2	381,0	0,858	0,8590	0,01100	0,10332	0,0008	0,3209300	628,80	5,90	633,80	4,40	627,0	26,0	633,8	4,4	0,795	
YESA-2_2.FIN2	1225,0	10,300	0,4610	0,02300	0,06120	0,0030	0,7483900	384,00	16,00	383,00	18,00	407,0	78,0	383,0	18,0	0,260	Rim
YESA-2_2.FIN2	266,0	0,978	0,5980	0,01100	0,07619	0,0007	0,0828690	475,20	7,00	473,30	4,10	497,0	43,0	473,3	4,1	0,400	Core
YESA-2_3.FIN2	438,0	3,120	0,8720	0,01700	0,10550	0,0014	0,5624600	635,90	9,10	646,10	8,40	608,0	39,0	646,1	8,4	1,652	
YESA-2_4.FIN2	826,0	4,100	0,7918	0,00940	0,09656	0,0008	0,4321200	591,80	5,30	594,20	4,50	598,0	24,0	594,2	4,5	0,406	
YESA-2_5.FIN2	221,6	1,934	2,2490	0,02300	0,20370	0,0016	0,3319900	1197,40	6,90	1195,20	8,40	1214,0	21,0	1214,0	21,0	1,549	
YESA-2_6.FIN2	330,0	5,215	0,5829	0,00960	0,07397	0,0006	0,2961300	465,60	6,20	460,00	3,80	499,0	36,0	460,0	3,8	1,203	
YESA-2_7.FIN2	137,3	1,714	0,6190	0,01300	0,07870	0,0011	0,3410800	488,10	8,30	488,50	6,40	487,0	46,0	488,5	6,4	0,082	
YESA-2_8.FIN2	188,0	2,400	6,4820	0,07300	0,37450	0,0037	0,7462500	2041,60	9,90	2050,00	17,00	2042,0	17,0	2042,0	17,0	0,392	
YESA-2_9.FIN2	166,9	1,253	0,8030	0,01500	0,09780	0,0010	0,2364400	597,20	8,40	601,60	6,00	590,0	43,0	601,6	6,0	0,737	
YESA-2_10.FIN2	490,0	3,220	0,6054	0,00900	0,07594	0,0007	0,4660100	480,00	5,70	471,80	4,30	528,0	29,0	471,8	4,3	1,708	
YESA-2_11.FIN2	1213,0	2,790	0,3470	0,00530	0,04787	0,0006	0,4091900	302,30	4,00	301,40	3,60	316,0	35,0	301,4	3,6	0,298	
YESA-2_12.FIN2	328,0	3,080	0,7680	0,01200	0,09250	0,0010	0,5938800	577,50	7,10	570,10	6,10	618,0	30,0	570,1	6,1	1,281	
YESA-2_13.FIN2	205,0	3,680	0,6070	0,01600	0,07850	0,0010	0,3311600	481,00	10,00	487,30	6,30	454,0	63,0	487,3	6,3	1,310	Rim
YESA-2_13.FIN2	105,2	2,587	2,9900	0,17000	0,21750	0,0083	0,9259500	1395,00	41,00	1267,00	44,00	1604,0	45,0	1604,0	45,0	21,010	Core
YESA-2_14.FIN2	345,0	1,063	0,5532	0,00980	0,07196	0,0008	0,2277200	446,50	6,40	447,90	4,60	444,0	43,0	447,9	4,6	0,314	
YESA-2_15.FIN2	863,0	1,770	1,5340	0,06400	0,15460	0,0041	0,7623700	943,00	26,00	927,00	23,00	982,0	56,0	982,0	56,0	5,601	Rim
YESA-2_15.FIN2	618,0	2,051	3,3290	0,03700	0,25540	0,0027	0,7027600	1487,10	8,70	1466,00	14,00	1522,0	16,0	1522,0	16,0	3,679	Core
YESA-2_16.FIN2	164,0	2,280	1,0040	0,02000	0,11560	0,0015	0,5202900	704,00	10,00	705,10	8,50	700,0	37,0	705,1	8,5	0,156	
YESA-2_17.FIN2	353,0	2,420	0,9360	0,02800	0,10960	0,0025	0,4830500	670,00	14,00	670,00	15,00	666,0	59,0	670,0	15,0	0,000	Rim
YESA-2_17.FIN2	95,6	1,366	1,4080	0,03200	0,14400	0,0016	0,3881300	891,00	14,00	867,10	8,90	948,0	47,0	948,0	47,0	8,534	Core
YESA-2_18.FIN2	91,2	3,160	0,8650	0,03500	0,10120	0,0019	0,0800770	630,00	19,00	621,00	11,00	642,0	92,0	621,0	11,0	1,429	Rim
YESA-2_18.FIN2	98,7	2,320	4,6800	0,16000	0,29360	0,0084	0,8775700	1758,00	30,00	1658,00	42,00	1883,0	31,0	1883,0	31,0	11,949	Core
YESA-2_19.FIN2	2560,0	6,150	0,4040	0,01300	0,04930	0,0016	0,6419500	343,80	9,20	309,90	9,90	579,0	57,0	309,9	9,9	9,860	
YESA-2_20.FIN2	768,0	1,259	6,8500	0,16000	0,35180	0,0069	0,9377900	2087,00	22,00	1941,00	33,00	2241,0	15,0	2241,0	15,0	13,387	
YESA-2_21.FIN2	296,0	1,138	0,4059	0,00720	0,05447	0,0006	0,2529400	345,40	5,10	341,90	3,30	366,0	42,0	341,9	3,3	1,013	
YESA-2_22.FIN2	1709,0	27,200	0,4200	0,01700	0,05480	0,0018	0,6516800	356,00	12,00	344,00	11,00	423,0	75,0	344,0	11,0	3,371	Rim
YESA-2_22.FIN2	621,0	5,880	0,7750	0,01600	0,08830	0,0014	0,4494700	582,20	9,20	545,60	8,20	724,0	42,0	545,6	8,2	6,286	Core
YESA-2_23.FIN2	673,0	1,294	0,8650	0,01100	0,10149	0,0009	0,5517100	632,20	5,80	623,00	5,20	660,0	23,0	623,0	5,2	1,455	
YESA-2_24.FIN2	870,0	34,000	1,0620	0,06700	0,11200	0,0040	0,1390000	732,00	32,00	684,00	23,00	870,0	120,0	684,0	23,0	6,557	Rim
YESA-2_24.FIN2	225,0	1,093	3,5150	0,05800	0,24150	0,0035	0,7362700	1529,00	13,00	1394,00	18,00	1718,0	21,0	1718,0	21,0	18,859	Core
YESA-2_25.FIN2	1446,0	1,594	0,3681	0,00410	0,04991	0,0004	0,4744300	318,50	3,10	314,00	2,70	344,0	23,0	314,0	2,7	1,413	
YESA-2_26.FIN2	688,0	12,100	0,4450	0,01400	0,05960	0,0015	0,5558300	373,10	9,80	373,00	9,20	381,0	65,0	373,0	9,2	0,027	Rim

Sample Name:	[U]							207/235		206/238		207/206		Best age		Discordance	Rim/
Grain #	ppm	U/Th	207/235	2σ error	206/238	2σ error	RHO	Age Ma	2σ error	Age (Ma)	2σ error	Age (Ma)	2σ error	(Ma)	2σ error	%	Core
YESA-2_26.FIN2	333,7	0,840	0,8140	0,01700	0,09790	0,0011	0,3335000	604,20	9,50	602,20	6,60	601,0	43,0	602,2	6,6	0,331	Core
YESA-2_27.FIN2	308,0	0,506	0,9330	0,02000	0,10560	0,0012	0,1794800	670,20	9,80	647,30	7,10	740,0	44,0	647,3	7,1	3,417	
YESA-2_28.FIN2	871,0	1,312	6,2600	0,08400	0,27040	0,0036	0,8281200	2010,00	12,00	1542,00	19,00	2525,0	13,0	DISC	DISC	38,931	
YESA-2_29.FIN2	215,8	1,072	6,5770	0,09000	0,37310	0,0036	0,6702100	2054,00	12,00	2043,00	17,00	2059,0	18,0	2059,0	18,0	0,777	
YESA-2_30.FIN2	327,6	0,829	11,0210	0,09100	0,45890	0,0035	0,7008300	2523,80	7,70	2434,00	16,00	2592,0	10,0	2592,0	10,0	6,096	
YESA-2_31.FIN2	181,3	4,030	3,0200	0,08000	0,23370	0,0053	0,9059500	1406,00	22,00	1352,00	28,00	1497,0	27,0	1497,0	27,0	9,686	
YESA-2_32.FIN2	275,0	0,680	1,7990	0,02800	0,17330	0,0025	0,5930700	1044,00	10,00	1030,00	14,00	1067,0	27,0	1067,0	27,0	3,468	
YESA-2_33.FIN2	145,3	0,974	0,9670	0,01800	0,10970	0,0011	0,3995500	685,40	9,30	670,80	6,40	715,0	40,0	670,8	6,4	2,130	
YESA-2_34.FIN2	808,0	0,867	1,1740	0,01200	0,12570	0,0013	0,7937400	787,90	5,80	763,10	7,60	850,0	16,0	763,1	7,6	3,148	
YESA-2_35.FIN2	1796,0	5,420	0,6090	0,02400	0,07070	0,0032	0,8047500	481,00	15,00	440,00	19,00	696,0	56,0	440,0	19,0	8,524	
YESA-2_36.FIN2	340,0	4,550	0,5792	0,00970	0,07261	0,0007	0,2449000	463,20	6,20	451,80	4,30	491,0	39,0	451,8	4,3	2,461	
YESA-2_37.FIN2	290,0	3,219	2,2840	0,02500	0,20310	0,0018	0,6842900	1206,40	7,60	1191,60	9,50	1225,0	19,0	1225,0	19,0	2,727	
YESA-2_38.FIN2	1760,0	6,010	1,3000	0,05900	0,13150	0,0055	0,8043900	845,00	26,00	796,00	31,00	961,0	55,0	796,0	31,0	5,799	Rim
YESA-2_38.FIN2	501,0	0,948	2,2930	0,02100	0,20250	0,0014	0,5967900	1209,20	6,60	1188,40	7,70	1237,0	15,0	1237,0	15,0	3,929	Core
YESA-2_39.FIN2	366,0	1,251	0,9040	0,01300	0,10374	0,0010	0,3025000	653,00	6,80	636,20	5,70	695,0	31,0	636,2	5,7	2,573	
YESA-2_40.FIN2	564,0	6,940	0,5695	0,00740	0,07104	0,0009	0,5149300	457,30	4,80	442,30	5,10	503,0	25,0	442,3	5,1	3,280	
YESA-2_41.FIN2	418,0	6,020	0,6830	0,02900	0,08290	0,0025	0,5822300	527,00	17,00	513,00	15,00	569,0	78,0	513,0	15,0	2,657	Rim
YESA-2_41.FIN2	332,9	3,200	0,9670	0,01600	0,10890	0,0013	0,5229500	685,90	8,30	667,20	8,00	736,0	31,0	667,2	8,0	2,726	Core
YESA-2_42.FIN2	567,0	31,500	0,3940	0,01500	0,05240	0,0016	0,9253100	337,00	11,00	329,00	10,00	368,0	91,0	329,0	10,0	2,374	Rim
YESA-2_42.FIN2	985,0	5,410	0,6200	0,01200	0,07530	0,0010	0,6767700	489,50	7,90	467,90	6,00	573,0	33,0	467,9	6,0	4,413	Core
YESA-2_43.FIN2	347,0	1,069	0,8520	0,03000	0,09260	0,0031	0,7832000	624,00	17,00	570,00	18,00	813,0	51,0	570,0	18,0	8,654	
YESA-2_44.FIN2	279,0	0,980	1,2090	0,05800	0,12580	0,0045	0,1946000	803,00	27,00	764,00	26,00	890,0	120,0	764,0	26,0	4,857	Rim
YESA-2_44.FIN2	139,0	0,937	1,3040	0,02400	0,14070	0,0014	0,4038400	847,00	10,00	848,20	8,00	819,0	36,0	848,2	8,0	0,142	Core
YESA-2_45.FIN2	154,7	1,233	1,0370	0,02600	0,11820	0,0020	0,6826900	719,00	13,00	720,00	12,00	694,0	41,0	720,0	12,0	0,139	
YESA-2_46.FIN2	45,9	0,895	5,2730	0,08300	0,32150	0,0034	0,3727800	1863,00	14,00	1796,00	16,00	1922,0	28,0	1922,0	28,0	6,556	
YESA-2_47.FIN2	342,0	2,149	0,3575	0,00770	0,04916	0,0007	0,5069100	309,70	5,70	309,30	4,60	296,0	44,0	309,3	4,6	0,129	
YESA-2_48.FIN2	687,0	0,880	2,6880	0,06100	0,19520	0,0039	0,8768700	1321,00	17,00	1148,00	21,00	1605,0	21,0	1605,0	21,0	28,474	
YESA-2_49.FIN2	290,1	1,831	5,2810	0,04800	0,32590	0,0024	0,6791300	1864,70	7,80	1818,00	11,00	1908,0	12,0	1908,0	12,0	4,717	
YESA-2_50.FIN2	352,0	2,340	0,5499	0,00940	0,06955	0,0008	0,4863900	445,00	6,00	433,40	4,50	482,0	34,0	433,4	4,5	2,607	
YESA-2_51.FIN2	630,0	4,860	0,5360	0,02300	0,06700	0,0034	0,4785200	435,00	15,00	418,00	21,00	510,0	110,0	418,0	21,0	3,908	Rim
YESA-2_51.FIN2	228,9	1,192	0,7690	0,01600	0,09330	0,0010	0,6292200	578,20	9,10	575,20	6,10	574,0	35,0	575,2	6,1	0,519	Core
YESA-2_52.FIN2	225,1	4,000	0,5950	0,01800	0,07470	0,0015	0,3694300	473,00	11,00	464,40	8,80	491,0	64,0	464,4	8,8	1,818	Rim
YESA-2_52.FIN2	216,1	2,157	3,7310	0,09300	0,20010	0,0047	0,7796800	1579,00	19,00	1175,00	26,00	2159,0	26,0	DISC	DISC	45,577	Core
YESA-2_53.FIN2	960,0	10,600	0,3280	0,04200	0,04060	0,0040	0,8389500	286,00	32,00	257,00	25,00	500,0	150,0	257,0	25,0	10,140	Rim
YESA-2_53.FIN2	181,6	1,700	0,5480	0,01300	0,07030	0,0011	0,3950600	442,70	8,80	437,90	6,80	458,0	51,0	437,9	6,8	1,084	Core
YESA-2_54.FIN2	739,0	14,800	0,8615	0,00910	0,10209	0,0008	0,5252800	630,60	4,90	626,60	4,50	628,0	19,0	626,6	4,5	0,634	
YESA-2_55.FIN2	182,6	1,169	0,4410	0,01000	0,05831	0,0007	0,2906700	369,80	7,30	365,30	4,00	381,0	50,0	365,3	4,0	1,217	
YESA-2_56.FIN2	291,0	3,880	18,6300	0,24000	0,57880	0,0069	0,8652300	3021,00	12,00	2942,00	28,00	3070,0	13,0	3070,0	13,0	4,169	
YESA-2_57.FIN2	124,9	1,144	6,6640	0,06800	0,37560	0,0038	0,5915500	2068,60	9,40	2055,00	18,00	2076,0	16,0	2076,0	16,0	1,012	
YESA-2_58.FIN2	252,2	1,241	1,1050	0,01800	0,11770	0,0013	0,2702200	754,70	8,50	717,20	7,50	865,0	33,0	717,2	7,5	4,969	
YESA-2_59.FIN2	2620,0	1,346	0,2970	0,00510	0,03889	0,0007	0,8775500	263,70	4,00	245,90	4,40	422,0	19,0	245,9	4,4	6,750	
YESA-2_60.FIN2	252,0	2,250	0,8860	0,01500	0,10270	0,0012	0,3424700	643,90	8,00	630,00	7,20	685,0	38,0	630,0	7,2	2,159	
YESA-2_61.FIN2	450,0	5,900	0,4580	0,04000	0,06020	0,0028	0,6311300	382,00	27,00	377,00	17,00	400,0	150,0	377,0	17,0	1,309	Rim
YESA-2_61.FIN2	330,0	0,941	0,8360	0,01300	0,09924	0,0008	0,3974900	615,80	7,40	609,90	4,80	626,0	33,0	609,9	4,8	0,958	Core
YESA-2_62.FIN2	77,0	6,530	0,9950	0,03800	0,11230	0,0025	0,1633800	699,00	20,00	686,00	14,00	700,0	84,0	686,0	14,0	1,860	
YESA-2_63.FIN2	950,0	0,787	0,9070	0,02600	0,10190	0,0028	0,5764100	655,00	14,00	625,00	17,00	753,0	54,0	625,0	17,0	4,580	
YESA-2_64.FIN2	1531,0	1,330	0,9110	0,01500	0,09710	0,0015	0,8480200	656,70	8,10	597,40	8,90	856,0	22,0	597,4	8,9	9,030	

Sample Name:	[U]							207/235		206/238		207/206		Best age		Discordance	Rim/
Grain #	ppm	U/Th	207/235	2σ error	206/238	2σ error	RHO	Age Ma	2σ error	Age (Ma)	2σ error	Age (Ma)	2σ error	(Ma)	2σ error	%	Core
YESA-2_65.FIN2	131,8	0,865	3,9900	0,13000	0,28100	0,0082	0,2339700	1629,00	27,00	1595,00	41,00	1669,0	78,0	1669,0	78,0	4,434	Rim
YESA-2_65.FIN2	173,5	2,630	10,4000	0,25000	0,43200	0,0076	0,8830000	2465,00	22,00	2313,00	34,00	2596,0	22,0	2596,0	22,0	10,901	Core
YESA-2_66.FIN2	590,0	1,464	0,9580	0,01100	0,11170	0,0012	0,7293700	681,50	5,80	682,60	6,90	678,0	19,0	682,6	6,9	0,161	
YESA-2_67.FIN2	698,0	3,720	0,8980	0,09000	0,09980	0,0063	0,6149300	649,00	49,00	613,00	37,00	760,0	180,0	613,0	37,0	5,547	Rim
YESA-2_67.FIN2	130,7	0,551	1,8090	0,02900	0,17670	0,0019	0,4177200	1047,00	10,00	1049,00	10,00	1041,0	31,0	1041,0	31,0	0,768	Core
YESA-2_68.FIN2	1225,0	35,600	0,8615	0,00900	0,10110	0,0009	0,5775500	630,60	4,90	620,80	5,40	669,0	20,0	620,8	5,4	1,554	
YESA-2_69.FIN2	67,3	4,900	1,1650	0,02700	0,12730	0,0018	0,1859900	781,00	13,00	772,00	10,00	797,0	46,0	772,0	10,0	1,152	
YESA-2_70.FIN2	139,6	1,652	2,6410	0,04400	0,22620	0,0033	0,6979400	1310,00	13,00	1314,00	18,00	1309,0	24,0	1309,0	24,0	0,382	
YESA-2_71.FIN2	376,0	1,421	0,4090	0,00790	0,05340	0,0005	0,3346800	347,60	5,60	335,30	3,10	421,0	45,0	335,3	3,1	3,539	
YESA-2_72.FIN2	2310,0	1,253	0,5370	0,02200	0,06390	0,0029	0,5011300	436,00	15,00	399,00	17,00	634,0	81,0	399,0	17,0	8,486	Rim
YESA-2_72.FIN2	960,0	2,375	0,8220	0,00830	0,09778	0,0008	0,3901900	608,90	4,60	601,30	4,80	634,0	23,0	601,3	4,8	1,248	Core
YESA-2_73.FIN2	1292,0	30,200	0,4137	0,00470	0,05488	0,0005	0,4837600	351,70	3,40	344,40	2,80	399,0	23,0	344,4	2,8	2,076	
YESA-2_74.FIN2	626,0	121,000	0,8100	0,02700	0,09550	0,0023	0,2344600	602,00	15,00	588,00	13,00	652,0	83,0	588,0	13,0	2,326	Rim
YESA-2_74.FIN2	81,8	1,128	4,3900	0,15000	0,28410	0,0096	0,9378100	1698,00	29,00	1607,00	48,00	1836,0	22,0	1836,0	22,0	12,473	Core
YESA-2_75.FIN2	562,0	1,944	6,7200	0,20000	0,34770	0,0068	0,9454800	2065,00	25,00	1921,00	32,00	2217,0	22,0	2217,0	22,0	13,351	
YESA-2_76.FIN2	311,0	0,821	0,8130	0,01500	0,09760	0,0011	0,2849700	603,20	8,30	600,30	6,40	617,0	35,0	600,3	6,4	0,481	
YESA-2_77.FIN2	102,6	3,210	0,9290	0,02200	0,10890	0,0013	0,0179810	665,00	12,00	666,50	7,30	645,0	49,0	666,5	7,3	0,226	
YESA-2_78.FIN2	739,0	99,000	0,7950	0,03100	0,09580	0,0036	0,6088600	593,00	18,00	590,00	21,00	604,0	73,0	590,0	21,0	0,506	Rim
YESA-2_78.FIN2	57,9	0,744	1,6290	0,04800	0,15830	0,0029	0,4616700	979,00	18,00	947,00	16,00	1052,0	55,0	1052,0	55,0	9,981	Core
YESA-2_79.FIN2	790,0	6,820	0,9600	0,01100	0,11056	0,0010	0,5943300	682,70	5,50	675,90	5,50	703,0	20,0	675,9	5,5	0,996	
YESA-2_80.FIN2	183,7	1,235	0,5540	0,01100	0,07065	0,0006	0,2904500	447,40	7,60	440,00	3,80	479,0	45,0	440,0	3,8	1,654	
YESA-2_81.FIN2	370,0	3,750	0,6820	0,01100	0,08390	0,0011	0,6056000	527,10	6,90	519,50	6,50	560,0	29,0	519,5	6,5	1,442	
YESA-2_82.FIN2	764,0	2,355	0,8270	0,01100	0,09960	0,0010	0,6945800	611,10	6,00	611,90	5,90	609,0	23,0	611,9	5,9	0,131	
YESA-2_83.FIN2	410,0	14,600	12,1900	0,38000	0,45300	0,0130	0,9783800	2603,00	31,00	2401,00	58,00	2775,0	11,0	2775,0	11,0	13,477	
YESA-2_84.FIN2	2640,0	1,846	0,4100	0,01200	0,05060	0,0015	0,9144100	348,20	8,50	317,90	9,10	563,0	26,0	317,9	9,1	8,702	
YESA-2_85.FIN2	848,0	2,282	0,7831	0,00710	0,09543	0,0007	0,6515300	587,70	4,30	587,50	4,00	588,0	19,0	587,5	4,0	0,034	
YESA-2_86.FIN2	1430,0	1,459	0,4010	0,01500	0,04760	0,0015	0,7755900	342,00	11,00	300,00	9,50	635,0	52,0	300,0	9,5	12,281	Rim
YESA-2_86.FIN2	301,0	6,030	0,7260	0,02000	0,08840	0,0015	0,4356000	553,00	12,00	545,70	9,10	577,0	55,0	545,7	9,1	1,320	Core
YESA-2_87.FIN2	550,0	2,950	7,5000	0,10000	0,38200	0,0030	0,7103200	2169,00	13,00	2085,00	14,00	2251,0	18,0	2251,0	18,0	7,375	
YESA-2_88.FIN2	77,5	0,803	0,9500	0,02800	0,10280	0,0016	0,4686300	676,00	15,00	630,30	9,60	809,0	57,0	630,3	9,6	6,760	
YESA-2_89.FIN2	467,0	0,933	0,8510	0,01000	0,10150	0,0011	0,4932300	624,70	5,50	623,00	6,20	630,0	24,0	623,0	6,2	0,272	
YESA-2_90.FIN2	782,0	16,460	0,8490	0,01200	0,10133	0,0009	0,4760200	623,70	6,80	622,20	5,40	630,0	30,0	622,2	5,4	0,241	Rim
YESA-2_90.FIN2	279,5	1,869	1,1570	0,02100	0,12570	0,0015	0,3583900	779,80	9,70	763,10	8,80	825,0	40,0	763,1	8,8	2,142	Core
YESA-2_91.FIN2	166,0	0,801	1,6300	0,02300	0,16120	0,0020	0,4539000	980,60	9,00	963,00	11,00	1024,0	27,0	1024,0	27,0	5,957	
YESA-2_92.FIN2	253,0	3,270	1,4770	0,02200	0,15330	0,0017	0,6830200	920,90	9,00	919,30	9,70	928,0	23,0	928,0	23,0	0,938	
YESA-2_93.FIN2	395,0	1,270	0,8820	0,01200	0,10331	0,0008	0,3301100	641,10	6,50	633,70	4,50	668,0	29,0	633,7	4,5	1,154	
YESA-2_94.FIN2	679,0	1,373	0,4325	0,00540	0,05796	0,0005	0,4549300	364,70	3,80	363,20	2,70	364,0	26,0	363,2	2,7	0,411	
YESA-2_95.FIN2	459,0	0,431	0,8100	0,01100	0,09665	0,0009	0,4891200	602,70	6,00	594,60	5,50	630,0	28,0	594,6	5,5	1,344	
YESA-2_96.FIN2	378,0	1,198	0,8460	0,02300	0,10010	0,0021	0,6670900	628,00	13,00	615,00	12,00	656,0	52,0	615,0	12,0	2,070	
YESA-2_97.FIN2	244,6	2,980	0,5960	0,01300	0,07532	0,0009	0,4505300	473,40	8,00	468,10	5,60	489,0	42,0	468,1	5,6	1,120	
YESA-2_98.FIN2	194,0	1,152	1,8220	0,02800	0,18120	0,0019	0,5528300	1052,00	10,00	1073,00	10,00	1012,0	28,0	1012,0	28,0	6,028	
YESA-2_99.FIN2	649,0	1,736	0,7454	0,00800	0,09107	0,0007	0,3424900	565,10	4,70	561,80	4,10	581,0	24,0	561,8	4,1	0,584	
YESA-2_100.FIN2	272,0	2,162	0,3646	0,00840	0,04983	0,0005	0,4639000	314,90	6,20	313,40	3,20	312,0	46,0	313,4	3,2	0,476	
YESA-2_101.FIN2	1040,0	7,580	0,5630	0,02600	0,07200	0,0037	0,7974800	453,00	17,00	448,00	23,00	479,0	75,0	448,0	23,0	1,104	Rim
YESA-2_101.FIN2	880,0	11,040	0,8180	0,01100	0,09860	0,0010	0,6720900	607,30	6,10	606,20	6,10	609,0	21,0	606,2	6,1	0,181	Core
YESA-2_102.FIN2	623,0	1,608	0,3547	0,00520	0,04918	0,0004	0,0140980	307,90	3,90	309,50	2,70	291,0	34,0	309,5	2,7	0,520	
YESA-2_103.FIN2	92,0	10,000	1,0530	0,03600	0,12100	0,0025	0,2589800	730,00	18,00	736,00	14,00	712,0	72,0	736,0	14,0	0,822	

Sample Name:	[U]							207/235		206/238		207/206		Best age		Discordance	Rim/
Grain #	ppm	U/Th	207/235	2σ error	206/238	2σ error	RHO	Age Ma	2σ error	Age (Ma)	2σ error	Age (Ma)	2σ error	(Ma)	2σ error	%	Core
YESA-2_104.FIN2	690,0	2,170	5,6470	0,08100	0,32610	0,0043	0,9317200	1921,00	13,00	1818,00	21,00	2034,0	10,0	2034,0	10,0	10,619	
YESA-2_105.FIN2	130,5	2,386	0,7570	0,01700	0,09166	0,0009	0,1065500	570,80	9,60	565,30	5,40	575,0	51,0	565,3	5,4	0,964	
YESA-2_106.FIN2	438,0	1,072	1,8010	0,02900	0,17210	0,0035	0,7221000	1045,00	11,00	1023,00	19,00	1087,0	31,0	1087,0	31,0	5,888	
YESA-2_107.FIN2	348,0	2,100	0,3612	0,00790	0,04805	0,0007	0,3573800	312,50	5,90	302,50	4,20	373,0	47,0	302,5	4,2	3,200	
YESA-2_108.FIN2	154,4	0,896	0,8660	0,01900	0,10420	0,0012	0,3233400	632,00	10,00	638,70	6,90	598,0	45,0	638,7	6,9	1,060	
YESA-2_109.FIN2	432,0	2,310	0,6078	0,00930	0,07777	0,0009	0,4277300	482,30	5,70	482,80	5,10	478,0	33,0	482,8	5,1	0,104	
YESA-2_110.FIN2	406,3	0,559	0,8680	0,01100	0,10248	0,0008	0,4380400	633,60	6,00	628,80	4,90	643,0	26,0	628,8	4,9	0,758	
YESA-2_111.FIN2	153,6	0,526	0,8140	0,01500	0,09490	0,0011	0,2917000	603,10	8,60	584,30	6,60	662,0	40,0	584,3	6,6	3,117	
YESA-2_112.FIN2	271,5	0,730	5,1950	0,04600	0,32550	0,0027	0,6256700	1850,80	7,60	1816,00	13,00	1887,0	15,0	1887,0	15,0	3,763	
YESA-2_113.FIN2	2191,0	5,240	0,3545	0,00840	0,04665	0,0009	0,4795500	307,90	6,30	293,90	5,50	416,0	51,0	293,9	5,5	4,547	
YESA-2_114.FIN2	663,0	11,240	0,9520	0,01900	0,10920	0,0016	0,7987300	677,00	10,00	668,10	9,10	699,0	25,0	668,1	9,1	1,315	
YESA-2_115.FIN2	576,0	8,300	0,7530	0,05100	0,08880	0,0029	0,5585300	569,00	29,00	548,00	17,00	630,0	110,0	548,0	17,0	3,691	Rim
YESA-2_115.FIN2	799,0	1,109	1,0220	0,01000	0,11542	0,0008	0,5125600	714,60	5,00	704,10	4,40	740,0	18,0	704,1	4,4	1,469	Core
YESA-2_116.FIN2	206,8	1,853	1,0550	0,01600	0,11972	0,0010	0,4663800	730,10	7,90	729,60	5,70	719,0	30,0	729,6	5,7	0,068	
YESA-2_117.FIN2	558,0	4,410	0,5190	0,01300	0,06430	0,0012	0,5229500	423,80	8,50	401,70	7,60	536,0	48,0	401,7	7,6	5,215	
YESA-2_118.FIN2	95,9	1,414	1,1980	0,02300	0,13250	0,0015	0,2015700	799,00	11,00	801,70	8,70	778,0	43,0	801,7	8,7	0,338	
YESA-2_119.FIN2	127,9	2,839	3,0540	0,03500	0,24190	0,0023	0,4362500	1420,90	9,10	1396,00	12,00	1454,0	23,0	1454,0	23,0	3,989	
YESA-2_120.FIN2	375,0	1,600	0,5947	0,00940	0,07620	0,0008	0,4708500	473,20	6,00	473,30	4,80	464,0	33,0	473,3	4,8	0,021	
YESA-2_121.FIN2	919,0	18,100	0,8560	0,02300	0,10140	0,0023	0,5458200	627,00	13,00	623,00	13,00	633,0	51,0	623,0	13,0	0,638	
YESA-2_122.FIN2	698,6	18,000	0,8830	0,01200	0,10360	0,0009	0,5019000	642,30	6,30	635,40	5,20	659,0	25,0	635,4	5,2	1,074	
YESA-2_123.FIN2	164,0	1,156	1,2960	0,01900	0,13720	0,0013	0,2023000	842,70	8,30	828,90	7,30	866,0	33,0	828,9	7,3	1,638	
YESA-2_124.FIN2	114,4	0,727	1,8180	0,02800	0,17530	0,0018	0,3942600	1050,00	10,00	1041,00	10,00	1064,0	30,0	1064,0	30,0	2,162	
YESA-2_125.FIN2	265,0	7,000	9,7400	0,16000	0,40130	0,0065	0,9082200	2406,00	15,00	2173,00	30,00	2612,0	11,0	2612,0	11,0	16,807	
YESA-2_126.FIN2	304,1	0,872	1,3090	0,01500	0,14110	0,0012	0,5342500	848,70	6,60	850,50	7,00	839,0	21,0	839,0	7,0	0,212	
YESA-2_127.FIN2	654,0	1,420	4,6200	0,05600	0,29020	0,0034	0,5945500	1752,00	10,00	1642,00	17,00	1885,0	19,0	1885,0	19,0	12,891	
YESA-2_128.FIN2	410,0	3,840	0,6123	0,00950	0,07601	0,0008	0,4310900	484,40	6,00	472,20	4,80	544,0	31,0	472,2	4,8	2,519	
YESA-2_129.FIN2	87,6	12,700	1,6760	0,03100	0,16570	0,0018	0,2621800	997,00	12,00	988,30	9,90	1015,0	39,0	1015,0	39,0	2,631	
YESA-2_130.FIN2	93,2	1,231	1,0020	0,02300	0,11400	0,0016	0,3328500	704,00	12,00	696,00	9,20	726,0	52,0	696,0	9,2	1,136	
YESA-2_131.FIN2	80,0	1,352	1,6940	0,03200	0,16680	0,0014	0,2231300	1004,00	12,00	994,10	8,00	1021,0	38,0	1021,0	38,0	2,635	
YESA-3_1.FIN2	500,0	4,760	0,3516	0,00660	0,04840	0,0005	0,1763500	305,50	4,90	304,70	3,30	309,0	43,0	304,7	3,3	0,262	
YESA-3_2.FIN2	96,0	1,471	3,3460	0,04900	0,26150	0,0026	0,4325100	1489,00	12,00	1497,00	13,00	1487,0	25,0	1487,0	25,0	0,672	
YESA-3_3.FIN2	273,0	2,960	1,1830	0,02300	0,12930	0,0023	0,7102600	790,00	11,00	783,00	13,00	807,0	31,0	783,0	13,0	0,886	
YESA-3_4.FIN2	588,0	2,194	0,6290	0,01100	0,07949	0,0010	0,5594900	496,30	6,40	493,00	5,90	512,0	31,0	493,0	5,9	0,665	
YESA-3_5.FIN2	552,0	1,429	0,3514	0,00610	0,04857	0,0004	0,2277000	305,90	4,50	305,70	2,50	290,0	39,0	305,7	2,5	0,065	
YESA-3_6.FIN2	1670,0	149,000	0,4080	0,01600	0,05260	0,0022	0,6368900	349,00	12,00	331,00	13,00	477,0	77,0	331,0	13,0	5,158	
YESA-3_7.FIN2	578,0	92,000	0,7440	0,03200	0,09250	0,0043	0,7227600	563,00	19,00	570,00	25,00	539,0	71,0	570,0	25,0	1,243	Rim
YESA-3_7.FIN2	69,1	1,270	1,4970	0,05000	0,15520	0,0032	0,2881900	927,00	20,00	930,00	18,00	906,0	70,0	906,0	70,0	2,649	Core
YESA-3_8.FIN2	438,0	11,700	1,1040	0,03300	0,12280	0,0030	0,6530400	754,00	16,00	747,00	17,00	779,0	44,0	747,0	17,0	0,928	Rim
YESA-3_8.FIN2	110,5	1,384	1,6230	0,03200	0,16400	0,0022	0,5649700	977,00	12,00	979,00	12,00	957,0	40,0	957,0	40,0	2,299	Core
YESA-3_9.FIN2	519,0	27,200	0,8810	0,01100	0,10276	0,0010	0,5024500	640,60	6,00	630,40	5,70	669,0	25,0	630,4	5,7	1,592	
YESA-3_10.FIN2	800,0	2,030	0,5570	0,03100	0,05460	0,0033	0,6916800	449,00	20,00	342,00	20,00	1040,0	120,0	DISC	DISC	23,831	Rim
YESA-3_10.FIN2	78,9	1,627	1,6200	0,03400	0,16430	0,0016	0,4699600	977,00	14,00	980,50	9,00	964,0	44,0	964,0	44,0	1,712	Core
YESA-3_11.FIN2	247,5	1,986	0,7650	0,01200	0,09283	0,0009	0,2974100	576,20	6,70	572,20	5,30	587,0	34,0	572,2	5,3	0,694	
YESA-3_12.FIN2	4290,0	12,500	0,7090	0,02700	0,08100	0,0041	0,6119400	544,00	16,00	502,00	25,00	725,0	86,0	502,0	25,0	7,721	Rim
YESA-3_12.FIN2	1368,0	1,880	0,9290	0,01300	0,10690	0,0010	0,5520500	666,40	6,80	654,70	5,90	698,0	23,0	654,7	5,9	1,756	Core
YESA-3_13.FIN2	84,4	4,240	2,5990	0,05300	0,20910	0,0025	0,2762900	1297,00	15,00	1224,00	13,00	1410,0	40,0	1410,0	40,0	13,191	

Sample Name:	[U]							207/235		206/238		207/206		Best age		Discordance	Rim/
Grain #	ppm	U/Th	207/235	2σ error	206/238	2σ error	RHO	Age Ma	2σ error	Age (Ma)	2σ error	Age (Ma)	2σ error	(Ma)	2σ error	%	Core
YESA-3_14.FIN2	694,0	2,075	0,9130	0,01700	0,10430	0,0017	0,7203300	657,30	8,90	639,10	9,90	726,0	26,0	639,1	9,9	2,769	
YESA-3_15.FIN2	71,0	0,949	1,6910	0,04400	0,16760	0,0020	0,3273700	1001,90	17,00	999,00	11,00	990,0	51,0	990,0	51,0	0,909	
YESA-3_16.FIN2	195,0	1,980	0,5730	0,01200	0,07452	0,0008	0,2882300	459,20	7,60	463,20	4,70	421,0	44,0	463,2	4,7	0,871	
YESA-3_17.FIN2	774,0	1,270	0,7924	0,00880	0,09418	0,0009	0,6110700	592,00	5,00	580,10	5,40	626,0	20,0	580,1	5,4	2,010	
YESA-3_18.FIN2	689,0	1,770	0,3963	0,00620	0,05343	0,0006	0,5987100	338,60	4,50	336,00	3,80	346,0	30,0	336,0	3,8	0,768	
YESA-3_19.FIN2	82,7	1,163	0,8080	0,02200	0,09680	0,0013	0,1408900	598,00	12,00	595,50	7,80	582,0	61,0	595,5	7,8	0,418	
YESA-3_20.FIN2	262,4	1,146	0,8180	0,01100	0,09756	0,0010	0,2879200	606,20	6,40	600,00	5,80	631,0	35,0	600,0	5,8	1,023	
YESA-3_21.FIN2	686,0	22,200	0,7370	0,02600	0,09110	0,0030	0,7059300	562,00	16,00	562,00	18,00	559,0	60,0	562,0	18,0	0,000	Rim
YESA-3_21.FIN2	545,0	1,322	1,1090	0,01800	0,12090	0,0014	0,5583100	756,90	8,70	735,60	8,30	815,0	28,0	735,6	8,3	2,814	Core
YESA-3_22.FIN2	409,0	1,249	0,9420	0,01300	0,10940	0,0011	0,4461900	673,20	6,80	669,30	6,30	675,0	30,0	669,3	6,3	0,579	
YESA-3_23.FIN2	325,0	1,790	0,6660	0,01300	0,08226	0,0010	0,5662500	517,40	7,70	509,50	5,90	541,0	35,0	509,5	5,9	1,527	
YESA-3_24.FIN2	1705,0	1,134	0,7896	0,00970	0,09450	0,0011	0,6231300	590,60	5,50	582,20	6,20	613,0	23,0	582,2	6,2	1,422	
YESA-3_25.FIN2	514,0	2,340	0,5763	0,00810	0,07489	0,0009	0,3760400	462,90	5,50	465,40	5,30	432,0	34,0	465,4	5,3	0,540	
YESA-3_26.FIN2	1836,0	11,900	0,6780	0,02500	0,07660	0,0040	0,7275000	524,00	15,00	476,00	24,00	720,0	74,0	476,0	24,0	9,160	Rim
YESA-3_26.FIN2	563,0	2,300	0,9360	0,02300	0,10430	0,0017	0,7199400	670,00	12,00	639,20	9,70	751,0	36,0	639,2	9,7	4,597	Core
YESA-3_27.FIN2	219,0	7,570	0,8650	0,01300	0,10160	0,0012	0,3561100	632,00	7,10	623,90	6,90	647,0	33,0	623,9	6,9	1,282	
YESA-3_28.FIN2	764,0	9,100	0,5400	0,02900	0,06910	0,0026	0,6821100	436,00	19,00	430,00	16,00	431,0	82,0	430,0	16,0	1,376	Rim
YESA-3_28.FIN2	80,7	0,473	0,9080	0,03200	0,10930	0,0024	0,4384000	654,90	17,00	669,00	14,00	582,0	73,0	669,0	14,0	2,294	Core
YESA-3_29.FIN2	506,0	2,419	1,6920	0,01900	0,16550	0,0018	0,7228200	1005,50	7,40	987,00	10,00	1040,0	17,0	1040,0	17,0	5,096	
YESA-3_30.FIN2	831,0	2,442	0,3887	0,00660	0,05218	0,0006	0,4848300	333,00	4,80	327,80	3,80	349,0	36,0	327,8	3,8	1,562	
YESA-3_31.FIN2	60,5	0,536	1,6000	0,04600	0,15990	0,0029	0,5001900	968,00	19,00	956,00	16,00	985,0	53,0	985,0	53,0	2,944	
YESA-3_32.FIN2	1800,0	10,000	0,5160	0,03800	0,04620	0,0035	0,8133400	421,00	27,00	291,00	21,00	1210,0	100,0	DISC	DISC	30,879	Rim
YESA-3_32.FIN2	135,0	2,290	0,6240	0,02000	0,07870	0,0012	0,1588500	490,00	13,00	488,30	6,90	470,0	71,0	488,3	6,9	0,347	Core
YESA-3_33.FIN2	120,5	0,826	11,2300	0,16000	0,48120	0,0063	0,7191900	2541,00	14,00	2530,00	28,00	2541,0	18,0	2541,0	18,0	0,433	
YESA-3_34.FIN2	290,0	2,530	1,0950	0,01600	0,12000	0,0014	0,2333500	749,50	7,90	730,10	8,10	795,0	35,0	730,1	8,1	2,588	
YESA-3_35.FIN2	141,0	1,410	0,8500	0,02100	0,10220	0,0011	0,1568200	623,00	11,00	627,30	6,30	581,0	53,0	627,3	6,3	0,690	
YESA-3_36.FIN2	1219,0	0,831	4,0100	0,11000	0,24090	0,0054	0,9167700	1633,00	22,00	1390,00	28,00	1958,0	21,0	1958,0	21,0	29,009	
YESA-3_37.FIN2	114,4	24,500	0,4530	0,02800	0,05780	0,0024	0,3489100	377,00	19,00	362,00	15,00	430,0	120,0	362,0	15,0	3,979	Rim
YESA-3_37.FIN2	187,0	7,990	0,7270	0,02900	0,08990	0,0023	0,4547300	553,00	17,00	555,00	14,00	530,0	84,0	555,0	14,0	0,362	Core
YESA-3_38.FIN2	430,0	5,470	0,5865	0,00840	0,07521	0,0006	0,2590900	468,10	5,30	467,50	3,50	459,0	31,0	467,5	3,5	0,128	
YESA-3_39.FIN2	196,0	1,240	5,4000	0,18000	0,31830	0,0091	0,9445800	1885,00	29,00	1776,00	46,00	1995,0	22,0	1995,0	22,0	10,977	
YESA-3_40.FIN2	2010,0	1,290	0,3961	0,00510	0,05252	0,0007	0,7379600	338,60	3,70	329,90	4,40	387,0	24,0	329,9	4,4	2,569	
YESA-3_41.FIN2	182,0	1,055	1,6220	0,02300	0,16400	0,0014	0,2935500	977,40	9,00	978,80	7,50	969,0	29,0	969,0	29,0	1,011	
YESA-3_42.FIN2	85,8	1,197	0,9360	0,03600	0,09840	0,0031	0,1172200	668,00	19,00	605,00	18,00	860,0	100,0	605,0	18,0	9,431	Rim
YESA-3_42.FIN2	56,5	0,968	1,0890	0,05500	0,12260	0,0030	0,2864400	743,00	27,00	745,00	17,00	710,0	110,0	745,0	17,0	0,269	Core
YESA-3_43.FIN2	193,0	1,165	0,7890	0,02100	0,09460	0,0019	0,5711000	588,00	12,00	584,00	11,00	573,0	46,0	584,0	11,0	0,680	
YESA-3_44.FIN2	1350,0	6,750	0,3150	0,03400	0,03940	0,0050	0,8138400	277,00	26,00	249,00	31,00	540,0	170,0	DISC	DISC	10,108	Rim
YESA-3_44.FIN2	74,8	4,320	0,7670	0,02400	0,09360	0,0014	0,3698100	575,00	14,00	576,70	8,20	538,0	66,0	576,7	8,2	0,296	Core
YESA-3_45.FIN2	1051,0	15,400	0,7736	0,00950	0,09436	0,0010	0,4989000	581,30	5,40	581,20	5,70	568,0	26,0	581,2	5,7	0,017	
YESA-3_46.FIN2	194,5	0,879	1,7420	0,02600	0,17070	0,0017	0,4265800	1022,60	9,50	1015,60	9,40	1023,0	28,0	1023,0	28,0	0,723	
YESA-3_47.FIN2	425,0	1,489	1,0070	0,01200	0,11516	0,0009	0,4715400	706,40	6,10	702,60	5,30	711,0	23,0	702,6	5,3	0,538	
YESA-3_48.FIN2	805,0	6,720	1,4560	0,01600	0,14650	0,0015	0,5336900	911,60	6,60	881,20	8,30	981,0	20,0	981,0	20,0	10,173	
YESA-3_49.FIN2	384,0	0,919	9,9500	0,16000	0,42790	0,0059	0,8856800	2429,00	15,00	2295,00	26,00	2535,0	13,0	2535,0	13,0	9,467	
YESA-3_50.FIN2	1650,0	4,420	0,9010	0,01200	0,10430	0,0014	0,8042600	651,20	6,60	639,40	8,00	690,0	20,0	639,4	8,0	1,812	
YESA-3_51.FIN2	212,0	1,234	1,3610	0,02300	0,14090	0,0015	0,3725500	872,00	10,00	849,90	8,40	910,0	35,0	849,9	8,4	2,534	
YESA-3_52.FIN2	118,7	2,233	0,8480	0,01700	0,10030	0,0011	0,1129400	623,30	9,00	615,80	6,30	639,0	44,0	615,8	6,3	1,203	
YESA-3_53.FIN2	1151,0	1,982	0,3666	0,00560	0,04895	0,0007	0,6629300	316,80	4,10	308,00	4,40	377,0	26,0	308,0	4,4	2,778	

Sample Name:	[U]							207/235		206/238		207/206		Best age		Discordance	Rim/
Grain #	ppm	U/Th	207/235	2σ error	206/238	2σ error	RHO	Age Ma	2σ error	Age (Ma)	2σ error	Age (Ma)	2σ error	(Ma)	2σ error	%	Core
YESA-3_54.FIN2	5340,0	3,150	0,4770	0,02100	0,05830	0,0021	0,7874100	396,00	14,00	365,00	13,00	592,0	47,0	365,0	13,0	7,828	Rim
YESA-3_54.FIN2	488,0	2,328	0,7590	0,01200	0,09312	0,0009	0,2811600	572,50	6,60	573,90	5,20	558,0	33,0	573,9	5,2	0,245	Core
YESA-3_55.FIN2	356,0	0,986	0,8080	0,01300	0,09570	0,0012	0,3894100	600,20	7,20	589,20	7,10	638,0	34,0	589,2	7,1	1,833	
YESA-3_56.FIN2	166,0	0,893	5,5500	0,08600	0,33030	0,0045	0,7222400	1905,00	13,00	1838,00	22,00	1977,0	18,0	1977,0	18,0	7,031	
YESA-3_57.FIN2	159,2	1,134	1,0180	0,01500	0,11740	0,0011	0,1729700	712,60	7,80	715,30	6,40	696,0	36,0	715,3	6,4	0,379	
YESA-3_58.FIN2	127,0	1,016	4,8000	0,18000	0,27580	0,0084	0,8925100	1774,00	32,00	1567,00	42,00	2030,0	30,0	2030,0	30,0	22,808	
YESA-3_59.FIN2	446,0	14,000	0,8710	0,01900	0,10420	0,0019	0,4365000	635,00	10,00	641,00	11,00	624,0	50,0	641,0	11,0	0,945	Rim
YESA-3_59.FIN2	105,0	3,570	1,5920	0,05500	0,15980	0,0034	0,1235200	964,00	22,00	955,00	19,00	1006,0	69,0	1006,0	69,0	5,070	Core
YESA-3_60.FIN2	251,0	1,296	1,6520	0,02600	0,16590	0,0021	0,6091800	990,00	10,00	989,00	11,00	983,0	27,0	983,0	27,0	0,610	
YESA-3_61.FIN2	218,6	1,970	14,6300	0,20000	0,52980	0,0058	0,6564000	2789,00	13,00	2739,00	24,00	2820,0	17,0	2820,0	17,0	2,872	
YESA-3_62.FIN2	1568,0	3,900	4,2500	0,12000	0,25780	0,0069	0,9551100	1674,00	24,00	1475,00	36,00	1939,0	14,0	1939,0	14,0	23,930	
YESA-3_63.FIN2	1232,0	1,344	0,6022	0,00760	0,07459	0,0009	0,4744900	478,30	4,80	463,70	5,10	541,0	26,0	463,7	5,1	3,052	
YESA-3_64.FIN2	2913,0	10,810	0,8320	0,01700	0,09330	0,0022	0,6118000	613,80	9,50	575,00	13,00	738,0	37,0	575,0	13,0	6,321	Rim
YESA-3_64.FIN2	692,0	4,010	1,0900	0,02600	0,12240	0,0024	0,6024300	748,00	13,00	744,00	14,00	752,0	40,0	744,0	14,0	0,535	Core
YESA-3_65.FIN2	562,0	8,640	0,6620	0,03000	0,08130	0,0024	0,5553600	514,00	19,00	504,00	14,00	582,0	92,0	504,0	14,0	1,946	Rim
YESA-3_65.FIN2	190,3	2,390	0,9260	0,02300	0,10750	0,0014	0,3995400	664,00	12,00	658,00	8,10	663,0	51,0	658,0	8,1	0,904	Core
YESA-3_66.FIN2	1447,0	10,500	0,4230	0,00470	0,05593	0,0005	0,4613400	358,00	3,40	350,80	3,10	399,0	23,0	350,8	3,1	2,011	
YESA-3_67.FIN2	936,0	2,594	0,8450	0,02100	0,09760	0,0025	0,6485000	621,00	12,00	600,00	14,00	699,0	45,0	600,0	14,0	3,382	Rim
YESA-3_67.FIN2	209,0	1,659	1,1760	0,02000	0,12770	0,0014	0,4095000	788,70	9,40	774,90	8,30	819,0	34,0	774,9	8,3	1,750	Core
YESA-3_68.FIN2	630,0	5,890	0,9540	0,01300	0,10570	0,0012	0,6985700	679,60	6,70	647,50	7,20	789,0	22,0	647,5	7,2	4,723	
YESA-3_69.FIN2	813,0	7,910	0,7390	0,03300	0,08770	0,0035	0,7047000	561,00	19,00	542,00	21,00	640,0	70,0	542,0	21,0	3,387	Rim
YESA-3_69.FIN2	74,0	0,796	1,1290	0,03000	0,12790	0,0018	0,2401000	764,00	14,00	776,00	10,00	711,0	56,0	776,0	10,0	1,571	Core
YESA-3_70.FIN2	151,4	1,134	1,1540	0,02300	0,12710	0,0015	0,2926700	778,00	11,00	770,90	8,40	780,0	40,0	770,9	8,4	0,913	
YESA-3_71.FIN2	1460,0	16,200	0,3240	0,01800	0,04280	0,0016	0,5065100	285,00	14,00	270,00	10,00	390,0	110,0	270,0	10,0	5,263	Rim
YESA-3_71.FIN2	1008,0	3,167	0,7327	0,00740	0,08938	0,0008	0,5613600	557,90	4,30	551,80	4,60	581,0	22,0	551,8	4,6	1,093	Core
YESA-3_72.FIN2	707,0	8,800	0,8750	0,01100	0,10250	0,0010	0,6250600	638,50	6,20	628,70	6,00	667,0	22,0	628,7	6,0	1,535	
YESA-3_73.FIN2	322,6	0,575	1,2030	0,01700	0,13150	0,0014	0,4617800	801,80	7,80	796,50	7,70	811,0	26,0	796,5	7,7	0,661	
YESA-3_74.FIN2	415,0	2,273	0,9610	0,01300	0,11200	0,0011	0,6360900	682,80	6,70	684,30	6,20	677,0	26,0	684,3	6,2	0,220	
YESA-3_75.FIN2	637,0	1,388	0,8730	0,01200	0,10370	0,0011	0,5102300	636,40	6,40	636,20	6,40	638,0	26,0	636,2	6,4	0,031	
YESA-3_76.FIN2	536,0	2,006	0,9640	0,01100	0,11152	0,0010	0,4159600	684,80	5,90	681,50	5,70	690,0	25,0	681,5	5,7	0,482	
YESA-3_77.FIN2	67,6	0,930	5,3870	0,07800	0,34230	0,0043	0,4964900	1880,00	12,00	1897,00	21,00	1861,0	25,0	1861,0	25,0	1,934	
YESA-3_80.FIN2	190,6	1,383	13,2700	0,14000	0,52070	0,0049	0,5572000	2697,90	9,80	2704,00	20,00	2694,0	15,0	2694,0	15,0	0,371	
YESA-3_81.FIN2	457,0	10,040	0,8330	0,03200	0,09670	0,0026	0,1159000	615,00	18,00	595,00	15,00	690,0	94,0	595,0	15,0	3,252	Rim
YESA-3_81.FIN2	448,0	3,030	10,1700	0,37000	0,40900	0,0140	0,9715600	2431,90	38,00	2202,00	65,00	2648,0	15,0	2648,0	15,0	16,843	Core
YESA-3_82.FIN2	1026,0	4,410	0,4155	0,00660	0,05539	0,0007	0,5257300	352,50	4,70	347,50	4,00	383,0	31,0	347,5	4,0	1,418	
YESA-3_83.FIN2	1277,0	83,000	0,8520	0,03400	0,10280	0,0039	0,7872500	625,00	19,00	631,00	23,00	610,0	53,0	631,0	23,0	0,960	Rim
YESA-3_83.FIN2	241,0	3,750	5,4090	0,08300	0,33370	0,0041	0,7693100	1884,00	13,00	1856,00	20,00	1915,0	18,0	1915,0	18,0	3,081	Core
YESA-3_84.FIN2	333,0	0,975	0,8810	0,01200	0,10409	0,0009	0,3592300	641,40	6,50	638,30	5,40	648,0	29,0	638,3	5,4	0,483	
YESA-3_85.FIN2	303,0	1,246	0,8430	0,01200	0,10020	0,0010	0,2060800	620,10	6,80	615,70	5,90	628,0	35,0	615,7	5,9	0,710	
YESA-3_86.FIN2	819,0	8,530	0,5770	0,01000	0,07500	0,0013	0,6615800	462,40	6,60	467,10	7,80	452,0	33,0	467,1	7,8	1,016	
YESA-3_87.FIN2	311,0	1,470	0,8710	0,01800	0,10070	0,0013	0,3955100	635,10	9,90	618,30	7,80	701,0	44,0	618,3	7,8	2,645	
YESA-3_88.FIN2	134,7	2,061	5,6190	0,06600	0,33710	0,0035	0,5896400	1918,40	9,90	1872,00	17,00	1979,0	19,0	1979,0	19,0	5,407	
YESA-3_89.FIN2	698,0	7,800	0,5976	0,00940	0,07669	0,0009	0,5553100	475,20	5,90	476,30	5,60	462,0	30,0	476,3	5,6	0,231	
YESA-3_90.FIN2	305,7	1,065	1,4070	0,01800	0,14640	0,0014	0,3082500	890,80	7,70	880,30	7,90	917,0	27,0	917,0	27,0	4,002	
YESA-3_91.FIN2	262,0	0,907	0,8290	0,01900	0,09780	0,0017	0,4492400	612,00	11,00	601,30	9,80	650,0	46,0	601,3	9,8	1,748	
YESA-3_92.FIN2	232,0	0,949	1,6960	0,02800	0,16500	0,0022	0,5748500	1005,00	11,00	984,00	12,00	1051,0	28,0	1051,0	28,0	6,375	
YESA-3_93.FIN2	252,0	2,050	0,7460	0,01200	0,09037	0,0009	0,3187400	564,90	7,20	557,70	5,20	598,0	33,0	557,7	5,2	1,275	

Sample Name:	[U]							207/235		206/238		207/206		Best age		Discordance	Rim/
Grain #	ppm	U/Th	207/235	2σ error	206/238	2σ error	RHO	Age Ma	2σ error	Age (Ma)	2σ error	Age (Ma)	2σ error	(Ma)	2σ error	%	Core
YESA-3_94.FIN2	356,0	1,552	0,9270	0,01400	0,11000	0,0011	0,4298300	665,30	7,60	672,50	6,60	641,0	32,0	672,5	6,6	1,082	
YESA-3_95.FIN2	881,0	55,000	0,4215	0,00500	0,05677	0,0004	0,4184600	356,90	3,60	355,90	2,60	361,0	25,0	355,9	2,6	0,280	
YESA-3_96.FIN2	281,3	1,455	1,5740	0,02300	0,16200	0,0017	0,6456200	959,90	8,90	967,50	9,20	941,0	24,0	941,0	24,0	2,816	
YESA-3_97.FIN2	181,0	0,937	1,5210	0,02600	0,15350	0,0016	0,4531300	938,00	11,00	920,10	9,10	979,0	32,0	979,0	32,0	6,016	
YESA-3_98.FIN2	252,6	2,167	3,5490	0,04000	0,25710	0,0025	0,5408800	1537,30	8,90	1477,00	12,00	1630,0	19,0	1630,0	19,0	9,387	
YESA-3_99.FIN2	101,6	1,277	1,7710	0,03300	0,17250	0,0023	0,3154800	1032,00	12,00	1026,00	13,00	1046,0	39,0	1046,0	39,0	1,912	
YESA-3_101.FIN2	510,0	2,100	0,8790	0,01300	0,10430	0,0013	0,6390100	639,70	7,10	639,30	7,30	652,0	27,0	639,3	7,3	0,063	
YESA-3_102.FIN2	558,0	1,359	7,9990	0,08100	0,39740	0,0039	0,7683600	2229,60	9,20	2156,00	18,00	2299,0	12,0	2299,0	12,0	6,220	
YESA-3_103.FIN2	316,0	3,520	0,5620	0,00990	0,07260	0,0009	0,4738700	452,10	6,40	451,70	5,60	461,0	37,0	451,7	5,6	0,088	
YESA-3_104.FIN2	303,1	2,093	0,4147	0,00860	0,05679	0,0007	0,3962400	351,50	6,10	356,00	4,20	304,0	41,0	356,0	4,2	1,280	
YESA-3_105.FIN2	450,0	-5,000	0,9490	0,05100	0,10980	0,0036	0,6709600	676,00	26,00	672,00	21,00	690,0	86,0	672,0	21,0	0,592	Rim
YESA-3_105.FIN2	155,8	1,078	1,3620	0,02300	0,14220	0,0014	0,2949100	871,20	9,80	857,10	8,00	904,0	35,0	904,0	35,0	5,188	Core
YESA-3_106.FIN2	330,0	1,904	0,3487	0,00740	0,04810	0,0007	0,3833300	303,20	5,50	302,80	4,30	306,0	47,0	302,8	4,3	0,132	
YESA-3_107.FIN2	647,0	3,870	0,3620	0,01800	0,04880	0,0019	0,6084900	313,00	14,00	307,00	12,00	370,0	100,0	307,0	12,0	1,917	Rim
YESA-3_107.FIN2	422,6	2,375	0,7340	0,01400	0,08270	0,0013	0,3652600	558,30	8,30	512,40	7,60	749,0	43,0	512,4	7,6	8,221	Core
YESA-3_108.FIN2	327,0	1,259	0,3508	0,00820	0,04864	0,0005	0,3478600	304,60	6,20	306,10	3,10	296,0	48,0	306,1	3,1	0,492	
YESA-3_109.FIN2	660,0	35,000	0,4720	0,01700	0,06090	0,0023	0,4533200	392,00	11,00	381,00	14,00	464,0	85,0	381,0	14,0	2,806	
YESA-3_110.FIN2	60,1	1,289	1,6720	0,03800	0,16620	0,0022	0,2836000	996,00	15,00	991,00	12,00	999,0	49,0	999,0	49,0	0,801	
YESA-3_111.FIN2	1200,0	58,000	0,3620	0,01200	0,04780	0,0015	0,6645400	313,00	8,60	301,00	9,10	399,0	57,0	301,0	9,1	3,834	Rim
YESA-3_111.FIN2	603,0	1,831	0,6020	0,01200	0,07430	0,0013	0,5608200	478,10	7,60	462,20	8,00	548,0	41,0	462,2	8,0	3,326	Core
YESA-3_112.FIN2	2040,0	1,317	0,3570	0,00500	0,04759	0,0005	0,6010500	310,40	3,80	299,70	3,30	391,0	26,0	299,7	3,3	3,447	
YESA-3_113.FIN2	142,6	1,704	1,6190	0,02600	0,16420	0,0016	0,4578600	976,00	10,00	979,70	9,10	966,0	32,0	966,0	32,0	1,418	
YESA-3_114.FIN2	396,0	1,360	0,3780	0,00930	0,04894	0,0007	0,2520200	324,70	6,90	308,00	4,10	434,0	56,0	308,0	4,1	5,143	
YESA-3_115.FIN2	458,0	2,120	0,7880	0,01100	0,09510	0,0012	0,5413500	590,20	6,60	585,30	7,00	607,0	27,0	585,3	7,0	0,830	
YESA-3_116.FIN2	78,9	1,092	7,9100	0,23000	0,34600	0,0100	0,9351700	2220,00	25,00	1922,00	48,00	2510,0	20,0	2510,0	20,0	23,426	
YESA-3_117.FIN2	594,0	1,197	0,4183	0,00920	0,05533	0,0006	0,4485200	354,10	6,40	347,20	3,40	406,0	45,0	347,2	3,4	1,949	
YESA-3_118.FIN2	888,0	14,230	0,9420	0,01300	0,10790	0,0013	0,6923600	672,90	6,60	660,50	7,70	722,0	22,0	660,5	7,7	1,843	
YESA-3_119.FIN2	603,0	2,450	1,8070	0,02500	0,17470	0,0022	0,8113100	1046,60	9,30	1037,00	12,00	1070,0	19,0	1070,0	19,0	3,084	
YESA-3_120.FIN2	464,0	2,340	0,6400	0,01200	0,07950	0,0011	0,5794000	501,20	7,60	492,80	6,80	540,0	35,0	492,8	6,8	1,676	
YESA-3_121.FIN2	507,0	0,633	0,3743	0,00740	0,05109	0,0007	0,4637900	322,30	5,50	321,20	4,40	329,0	39,0	321,2	4,4	0,341	
YESA-3_122.FIN2	525,0	2,590	0,6130	0,00880	0,07761	0,0008	0,4836000	484,80	5,50	481,80	4,50	498,0	29,0	481,8	4,5	0,619	
YESA-3_123.FIN2	496,0	1,481	0,7980	0,01300	0,09590	0,0011	0,6463900	594,90	7,50	589,90	6,70	627,0	27,0	589,9	6,7	0,840	
YESA-3_124.FIN2	284,0	0,962	1,2000	0,01900	0,13280	0,0013	0,3051500	799,30	8,80	803,40	7,30	780,0	33,0	803,4	7,3	0,513	
YESA-3_125.FIN2	455,0	3,080	1,8250	0,02100	0,17210	0,0019	0,5967300	1053,50	7,60	1023,00	10,00	1119,0	21,0	1119,0	21,0	8,579	
YESA-3_126.FIN2	681,0	2,231	0,3627	0,00620	0,04900	0,0006	0,4388100	313,80	4,60	308,40	3,60	354,0	36,0	308,4	3,6	1,721	
YESA-3_127.FIN2	496,0	1,384	0,8020	0,01300	0,09720	0,0013	0,6683100	598,00	7,30	597,60	7,80	598,0	27,0	597,6	7,8	0,067	
YESA-3_128.FIN2	656,0	13,950	1,0230	0,02000	0,11590	0,0017	0,8166200	713,00	10,00	706,50	9,60	740,0	24,0	706,5	9,6	0,912	
YESA-3_129.FIN2	230,0	2,920	0,8920	0,01700	0,10450	0,0011	0,3622200	646,80	8,80	640,60	6,50	656,0	40,0	640,6	6,5	0,959	
YESA-3_130.FIN2	439,0	2,252	0,3693	0,00900	0,04710	0,0005	0,4213100	318,30	6,70	296,70	3,00	466,0	47,0	296,7	3,0	6,786	
YESA-3_131.FIN2	349,0	1,663	0,9340	0,01400	0,10940	0,0012	0,3335500	668,70	7,50	669,30	6,80	676,0	30,0	669,3	6,8	0,090	
YESA-5_1.FIN2	511,0	9,640	0,6010	0,01600	0,07632	0,0009	0,4417800	477,10	9,90	474,10	5,20	491,0	49,0	474,1	5,2	0,629	
YESA-5_2.FIN2	264,4	1,566	0,5510	0,01100	0,07020	0,0011	0,4364400	444,70	7,50	437,20	6,60	478,0	44,0	437,2	6,6	1,687	
YESA-5_3.FIN2	815,0	1,134	6,8700	0,18000	0,29320	0,0070	0,9072900	2086,00	22,00	1654,00	35,00	2550,0	17,0	DISC	DISC	35,137	
YESA-5_4.FIN2	145,4	0,850	1,6000	0,02400	0,16280	0,0018	0,3443300	968,60	9,50	971,80	9,90	953,0	32,0	953,0	32,0	1,973	
YESA-5_5.FIN2	258,0	2,880	6,2100	0,10000	0,35010	0,0036	0,7685400	2003,00	15,00	1934,00	17,00	2069,0	20,0	2069,0	20,0	6,525	
YESA-5_6.FIN2	125,1	1,470	0,9250	0,01800	0,10900	0,0011	0,0968750	663,20	9,40	666,70	6,30	637,0	46,0	666,7	6,3	0,528	

Sample Name:	[U]							207/235		206/238		207/206		Best age		Discordance	Rim/
Grain #	ppm	U/Th	207/235	2σ error	206/238	2σ error	RHO	Age Ma	2σ error	Age (Ma)	2σ error	Age (Ma)	2σ error	(Ma)	2σ error	%	Core
YESA-5_7.FIN2	344,0	1,480	0,5520	0,01000	0,07194	0,0009	0,4205700	446,30	6,80	447,70	5,20	424,0	40,0	447,7	5,2	0,314	
YESA-5_8.FIN2	171,3	6,120	0,9820	0,02500	0,11280	0,0026	0,6005500	692,00	13,00	688,00	15,00	697,0	48,0	688,0	15,0	0,578	
YESA-5_9.FIN2	483,0	12,800	0,6270	0,01000	0,07735	0,0008	0,2694400	493,80	6,50	480,20	4,50	544,0	37,0	480,2	4,5	2,754	
YESA-5_10.FIN2	972,0	1,861	0,6660	0,01400	0,07150	0,0013	0,5553400	518,20	8,60	445,10	7,90	847,0	39,0	445,1	7,9	14,107	
YESA-5_11.FIN2	376,0	0,922	1,7260	0,01900	0,16950	0,0016	0,4484800	1017,50	7,20	1009,30	8,90	1032,0	23,0	1032,0	23,0	2,200	
YESA-5_12.FIN2	56,7	1,287	1,6530	0,04100	0,16440	0,0024	0,3511400	986,00	16,00	980,00	13,00	988,0	49,0	988,0	49,0	0,810	
YESA-5_13.FIN2	39,9	4,830	0,9850	0,03400	0,11440	0,0019	0,1760600	690,00	18,00	698,00	11,00	638,0	75,0	698,0	11,0	1,159	
YESA-5_14.FIN2	182,0	16,700	0,8240	0,02100	0,09670	0,0013	0,1544000	609,00	11,00	595,00	7,50	647,0	50,0	595,0	7,5	2,299	
YESA-5_15.FIN2	345,0	2,050	0,7500	0,01100	0,09052	0,0008	0,3566600	567,40	6,10	558,60	4,70	587,0	30,0	558,6	4,7	1,551	
YESA-5_16.FIN2	149,3	0,662	0,8390	0,01800	0,09960	0,0012	0,3982700	618,00	10,00	612,10	6,90	621,0	44,0	612,1	6,9	0,955	
YESA-5_17.FIN2	549,0	1,128	0,3543	0,00590	0,04758	0,0004	0,4233600	307,60	4,40	299,60	2,60	349,0	34,0	299,6	2,6	2,601	
YESA-5_18.FIN2	265,0	1,059	5,0520	0,05900	0,32380	0,0038	0,8182000	1828,00	10,00	1809,00	19,00	1846,0	14,0	1846,0	14,0	2,004	
YESA-5_19.FIN2	392,0	0,669	0,8240	0,01600	0,09707	0,0009	0,3279900	608,80	8,80	597,10	5,50	632,0	37,0	597,1	5,5	1,922	
YESA-5_20.FIN2	2181,0	1,443	0,7079	0,00920	0,07043	0,0009	0,6387600	544,30	5,80	438,70	5,40	1004,0	23,0	DISC	DISC	19,401	Rim
YESA-5_20.FIN2	1020,0	3,460	0,9100	0,01600	0,10090	0,0015	0,8249500	656,40	8,60	619,70	8,70	780,0	24,0	619,7	8,7	5,591	Core
YESA-5_21.FIN2	33,7	1,343	6,5500	0,12000	0,35700	0,0050	0,5285100	2050,00	17,00	1966,00	24,00	2146,0	26,0	2146,0	26,0	8,388	
YESA-5_22.FIN2	409,0	0,952	0,7697	0,00970	0,09209	0,0010	0,4200200	579,80	5,70	567,80	5,80	624,0	29,0	567,8	5,8	2,070	
YESA-5_23.FIN2	677,0	2,150	0,8680	0,01100	0,09980	0,0010	0,2903100	633,90	6,10	612,90	6,00	697,0	31,0	612,9	6,0	3,313	
YESA-5_24.FIN2	149,0	7,300	0,8950	0,04700	0,10080	0,0048	0,3533900	646,00	25,00	619,00	28,00	730,0	110,0	619,0	28,0	4,180	
YESA-5_25.FIN2	354,7	2,037	0,8620	0,01200	0,09817	0,0009	0,4260400	630,60	6,80	603,60	5,20	720,0	28,0	603,6	5,2	4,282	
YESA-5_26.FIN2	48,5	0,361	1,4240	0,03700	0,14540	0,0022	0,3125100	897,00	16,00	875,00	13,00	936,0	56,0	936,0	56,0	6,517	
YESA-5_27.FIN2	236,2	0,913	1,0880	0,03200	0,09726	0,0010	0,1230300	743,00	16,00	598,20	5,70	1176,0	62,0	DISC	DISC	19,489	
YESA-5_28.FIN2	262,7	1,408	0,8690	0,01400	0,10110	0,0010	0,2685200	633,90	7,80	621,00	6,10	666,0	37,0	621,0	6,1	2,035	
YESA-5_29.FIN2	274,0	1,573	0,9070	0,01900	0,10480	0,0011	0,3009800	654,00	10,00	642,50	6,70	671,0	44,0	642,5	6,7	1,758	
YESA-5_30.FIN2	237,4	0,989	4,5050	0,06400	0,28100	0,0038	0,7927100	1731,00	12,00	1595,00	19,00	1889,0	17,0	1889,0	17,0	15,564	
YESA-5_31.FIN2	79,5	1,084	1,1120	0,02500	0,12270	0,0015	0,1700100	757,00	12,00	746,10	8,60	767,0	51,0	746,1	8,6	1,440	
YESA-5_32.FIN2	479,0	2,390	0,8880	0,01600	0,10340	0,0013	0,7689100	644,10	8,40	634,30	7,50	666,0	24,0	634,3	7,5	1,522	
YESA-5_33.FIN2	395,0	2,320	10,5700	0,11000	0,43890	0,0042	0,7796100	2484,50	9,60	2345,00	19,00	2592,0	11,0	2592,0	11,0	9,529	
YESA-5_34.FIN2	105,0	0,682	0,7060	0,02200	0,08830	0,0013	0,2557800	539,00	13,00	545,20	7,80	481,0	66,0	545,2	7,8	1,150	
YESA-5_35.FIN2	736,0	45,500	5,9330	0,05000	0,34410	0,0029	0,7008400	1965,20	7,30	1906,00	14,00	2017,0	12,0	2017,0	12,0	5,503	
YESA-5_36.FIN2	695,0	1,077	4,8140	0,07800	0,30020	0,0051	0,8793300	1784,00	14,00	1690,00	25,00	1885,0	14,0	1885,0	14,0	10,345	
YESA-5_37.FIN2	1510,0	5,490	0,3847	0,00860	0,04170	0,0016	0,3782600	330,40	6,30	263,50	9,60	819,0	74,0	DISC	DISC	20,248	Rim
YESA-5_37.FIN2	166,5	0,864	1,6080	0,02700	0,15780	0,0014	0,5414700	972,00	11,00	944,30	8,00	1018,0	31,0	1018,0	31,0	7,240	Core
YESA-5_38.FIN2	301,0	0,880	0,5270	0,01200	0,06840	0,0007	0,4381500	429,00	7,60	426,50	4,40	431,0	43,0	426,5	4,4	0,583	
YESA-5_39.FIN2	305,0	2,218	0,3456	0,00680	0,04652	0,0006	0,2167300	300,90	5,10	293,10	3,70	347,0	46,0	293,1	3,7	2,592	
YESA-5_40.FIN2	403,0	0,976	0,8210	0,04600	0,08620	0,0032	0,5451800	607,00	26,00	533,00	19,00	870,0	92,0	533,0	19,0	12,191	
YESA-5_41.FIN2	324,0	1,400	0,7210	0,01400	0,08460	0,0012	0,6034300	550,20	8,30	523,30	6,90	642,0	39,0	523,3	6,9	4,889	
YESA-5_42.FIN2	318,0	1,655	0,8550	0,01300	0,10160	0,0013	0,4188300	626,10	7,30	623,30	7,70	617,0	34,0	623,3	7,7	0,447	
YESA-5_43.FIN2	1412,0	1,418	0,4285	0,00710	0,05125	0,0006	0,5722000	362,40	4,90	322,10	3,50	607,0	29,0	322,1	3,5	11,120	
YESA-5_44.FIN2	348,0	3,000	0,8150	0,01700	0,09600	0,0016	0,5072200	603,60	9,50	590,60	9,50	608,0	42,0	590,6	9,5	2,154	
YESA-5_45.FIN2	495,0	4,040	0,5482	0,00800	0,07139	0,0007	0,5016200	444,00	5,40	444,50	4,10	424,0	29,0	444,5	4,1	0,113	
YESA-5_46.FIN2	211,6	3,110	0,6660	0,01400	0,08460	0,0012	0,4844000	517,20	8,40	523,40	7,00	472,0	41,0	523,4	7,0	1,199	
YESA-5_47.FIN2	316,8	0,861	0,3955	0,00870	0,05288	0,0006	0,2560400	337,70	6,30	332,10	3,80	359,0	50,0	332,1	3,8	1,658	
YESA-5_48.FIN2	1417,0	3,510	0,3453	0,00490	0,04739	0,0005	0,6038900	300,90	3,70	298,50	3,10	309,0	25,0	298,5	3,1	0,798	
YESA-5_49.FIN2	18,6	3,240	0,3340	0,02800	0,04420	0,0015	0,1733400	285,00	21,00	278,90	9,20	300,0	150,0	278,9	9,2	2,140	
YESA-5_50.FIN2	238,0	0,718	1,6710	0,02900	0,16460	0,0019	0,5961600	995,00	11,00	982,00	10,00	1013,0	28,0	1013,0	28,0	3,060	
YESA-5_51.FIN2	357,0	1,902	0,3730	0,00840	0,04679	0,0006	0,0795530	321,20	6,20	294,80	3,50	485,0	51,0	294,8	3,5	8,219	

Sample Name:	[U]							207/235		206/238		207/206		Best age		Discordance	Rim/
Grain #	ppm	U/Th	207/235	2σ error	206/238	2σ error	RHO	Age Ma	2σ error	Age (Ma)	2σ error	Age (Ma)	2σ error	(Ma)	2σ error	%	Core
YESA-5_52.FIN2	613,0	12,000	0,7980	0,01000	0,09510	0,0011	0,4613100	596,00	6,10	585,70	6,40	626,0	29,0	585,7	6,4	1,728	
YESA-5_53.FIN2	432,0	65,000	0,3770	0,01300	0,04935	0,0009	0,4968500	323,90	9,60	310,50	5,50	396,0	81,0	310,5	5,5	4,137	Rim
YESA-5_53.FIN2	873,0	10,200	6,5000	0,44000	0,32900	0,0180	0,9880200	2005,00	62,00	1821,00	86,00	2223,0	31,0	2223,0	31,0	18,084	Core
YESA-5_54.FIN2	363,0	1,620	5,2360	0,06000	0,32220	0,0037	0,6190200	1856,80	9,80	1800,00	18,00	1908,0	19,0	1908,0	19,0	5,660	
YESA-5_55.FIN2	421,0	0,669	0,7710	0,01300	0,09330	0,0012	0,5874900	579,60	7,30	575,00	7,10	594,0	36,0	575,0	7,1	0,794	
YESA-5_56.FIN2	468,0	0,660	0,7360	0,01200	0,09020	0,0010	0,4566500	561,80	7,20	556,80	6,20	569,0	35,0	556,8	6,2	0,890	
YESA-5_57.FIN2	475,0	6,260	0,5554	0,00830	0,07149	0,0007	0,3391700	447,90	5,40	445,60	4,10	450,0	33,0	445,6	4,1	0,514	
YESA-5_58.FIN2	879,0	3,070	0,6444	0,00810	0,08117	0,0007	0,5620200	504,60	5,00	503,00	4,20	508,0	23,0	503,0	4,2	0,317	
YESA-5_59.FIN2	99,1	1,972	2,1500	0,03600	0,19350	0,0023	0,5104200	1166,00	12,00	1140,00	12,00	1203,0	31,0	1203,0	31,0	5,237	
YESA-5_60.FIN2	2190,0	0,879	0,5961	0,00530	0,07539	0,0006	0,5679900	474,50	3,40	468,50	3,30	496,0	17,0	468,5	3,3	1,264	
YESA-5_61.FIN2	396,0	1,079	0,8010	0,01100	0,09550	0,0012	0,4160700	596,50	6,30	588,00	6,80	627,0	32,0	588,0	6,8	1,425	
YESA-5_62.FIN2	1850,0	8,400	0,7960	0,03600	0,07580	0,0049	0,8000200	594,00	20,00	471,00	29,00	1100,0	76,0	DISC	DISC	20,707	Rim
YESA-5_62.FIN2	1000,0	2,790	2,8300	0,13000	0,18090	0,0073	0,9120800	1359,00	36,00	1071,00	40,00	1850,0	39,0	DISC	DISC	42,108	Core
YESA-5_62.FIN2	154,2	1,295	6,3400	0,11000	0,35710	0,0052	0,7705600	2021,00	16,00	1968,00	25,00	2076,0	21,0	2076,0	21,0	5,202	Core
YESA-5_63.FIN2	378,0	0,321	0,8200	0,01500	0,09510	0,0013	0,6153100	607,00	8,70	585,20	7,70	686,0	37,0	585,2	7,7	3,591	
YESA-5_64.FIN2	141,7	1,680	0,8770	0,01600	0,10220	0,0010	0,2320500	637,90	8,90	627,00	6,00	673,0	43,0	627,0	6,0	1,709	
YESA-5_65.FIN2	569,0	2,248	0,3523	0,00880	0,04852	0,0009	0,5484300	305,90	6,60	305,40	5,20	307,0	47,0	305,4	5,2	0,163	
YESA-5_66.FIN2	96,3	2,073	0,9250	0,01900	0,10810	0,0013	0,2011800	664,00	10,00	661,60	7,70	668,0	47,0	661,6	7,7	0,361	
YESA-5_67.FIN2	528,0	2,493	0,3552	0,00610	0,04937	0,0005	0,3475800	308,30	4,50	310,60	3,10	288,0	36,0	310,6	3,1	0,746	
YESA-5_68.FIN2	537,0	4,980	0,9030	0,01100	0,10590	0,0010	0,4931900	652,80	6,00	648,60	5,90	671,0	24,0	648,6	5,9	0,643	
YESA-5_69.FIN2	310,0	0,727	1,6040	0,02000	0,16660	0,0014	0,4027600	1005,00	7,40	993,00	7,90	1033,0	23,0	1033,0	23,0	3,872	
YESA-5_70.FIN2	363,0	4,860	0,9140	0,03200	0,08020	0,0010	0,3488700	656,90	17,00	497,30	6,00	1222,0	64,0	DISC	DISC	24,192	
YESA-5_71.FIN2	470,0	0,730	0,8080	0,01000	0,09736	0,0007	0,3841400	601,70	5,90	598,90	4,40	612,0	27,0	598,9	4,4	0,465	
YESA-5_72.FIN2	371,0	1,002	6,1600	0,12000	0,31730	0,0049	0,8966000	1995,00	18,00	1775,00	24,00	2238,0	18,0	2238,0	18,0	20,688	
YESA-5_73.FIN2	521,0	4,860	0,4991	0,00870	0,06155	0,0006	0,2407100	410,50	5,90	385,00	3,60	553,0	37,0	385,0	3,6	6,212	
YESA-5_74.FIN2	243,0	1,380	1,2630	0,01900	0,13880	0,0013	0,3699900	828,10	8,60	837,60	7,60	814,0	29,0	837,6	7,6	1,147	
YESA-5_75.FIN2	1305,0	2,221	0,8483	0,00830	0,10133	0,0008	0,5311500	623,30	4,60	622,10	4,50	628,0	19,0	622,1	4,5	0,193	
YESA-5_76.FIN2	274,0	1,850	0,3460	0,00840	0,04685	0,0006	0,2579400	301,00	6,30	295,10	3,40	344,0	53,0	295,1	3,4	1,960	
YESA-5_77.FIN2	577,0	4,730	0,5460	0,01200	0,07200	0,0012	0,4338400	442,20	8,20	448,40	7,10	409,0	49,0	448,4	7,1	1,402	
YESA-5_78.FIN2	549,0	0,852	0,8480	0,01300	0,09960	0,0013	0,2971600	622,80	6,80	612,00	7,70	659,0	29,0	612,0	7,7	1,734	
YESA-5_79.FIN2	148,5	1,255	0,8910	0,02000	0,10210	0,0016	0,2627400	645,00	10,00	626,60	9,20	713,0	45,0	626,6	9,2	2,853	
YESA-5_80.FIN2	148,3	3,740	0,6100	0,01400	0,07810	0,0010	0,2477800	482,40	8,70	484,40	6,10	467,0	51,0	484,4	6,1	0,415	
YESA-5_81.FIN2	157,7	0,506	1,6260	0,02500	0,16250	0,0018	0,4567200	979,90	9,40	971,00	10,00	1003,0	30,0	1003,0	30,0	3,190	
YESA-5_82.FIN2	94,6	1,653	7,5300	0,16000	0,35680	0,0059	0,8220500	2173,00	19,00	1966,00	28,00	2380,0	25,0	2380,0	25,0	17,395	
YESA-5_83.FIN2	285,2	0,592	0,8430	0,01500	0,10040	0,0010	0,2029500	619,90	8,10	616,70	5,60	625,0	39,0	616,7	5,6	0,516	
YESA-5_84.FIN2	190,0	1,391	2,0850	0,02500	0,19450	0,0016	0,4103000	1144,10	8,50	1145,70	8,60	1143,0	23,0	1143,0	23,0	0,236	
YESA-5_85.FIN2	48,4	0,628	0,5030	0,01900	0,06640	0,0011	0,1072900	412,00	13,00	414,30	6,50	378,0	82,0	414,3	6,5	0,558	
YESA-5_86.FIN2	670,0	2,480	0,3653	0,00660	0,04581	0,0005	0,1768100	315,70	4,90	288,70	3,10	518,0	41,0	288,7	3,1	8,552	
YESA-5_87.FIN2	148,3	1,351	0,8090	0,01700	0,09630	0,0010	0,2178600	601,20	9,80	592,50	6,10	616,0	45,0	592,5	6,1	1,447	
YESA-5_88.FIN2	1108,0	2,060	0,7240	0,01600	0,07890	0,0023	0,3425800	552,50	9,70	489,00	14,00	823,0	64,0	489,0	14,0	11,493	
YESA-5_89.FIN2	556,0	1,496	10,4500	0,36000	0,40900	0,0150	0,9856900	2475,00	33,00	2215,00	67,00	2693,0	11,0	2693,0	11,0	17,750	
YESA-5_90.FIN2	615,0	0,864	9,8900	0,15000	0,41110	0,0056	0,9163000	2421,00	13,00	2218,00	25,00	2597,5	9,6	2597,5	9,6	14,610	
YESA-5_91.FIN2	211,0	6,700	0,8300	0,02100	0,10020	0,0012	0,2919700	611,00	12,00	615,60	7,20	576,0	55,0	615,6	7,2	0,753	
YESA-5_92.FIN2	111,2	0,711	4,0460	0,06000	0,28270	0,0032	0,5528800	1642,00	12,00	1605,00	16,00	1685,0	25,0	1685,0	25,0	4,748	
YESA-5_93.FIN2	995,0	12,360	6,2090	0,06200	0,34760	0,0034	0,7801200	2004,70	8,80	1923,00	16,00	2089,0	12,0	2089,0	12,0	7,946	
YESA-5_94.FIN2	294,0	4,690	0,5670	0,01100	0,07204	0,0008	0,2926900	454,90	7,20	448,40	4,90	476,0	43,0	448,4	4,9	1,429	
YESA-5_95.FIN2	116,1	0,465	0,7950	0,01900	0,09530	0,0010	0,1592500	592,00	11,00	586,90	6,20	590,0	54,0	586,9	6,2	0,861	

Sample Name:	[U]							207/235		206/238		207/206		Best age		Discordance	Rim/
Grain #	ppm	U/Th	207/235	2σ error	206/238	2σ error	RHO	Age Ma	2σ error	Age (Ma)	2σ error	Age (Ma)	2σ error	(Ma)	2σ error	%	Core
YESA-5_96.FIN2	467,0	1,342	0,3356	0,00620	0,04672	0,0005	0,2187400	293,40	4,70	294,30	2,80	276,0	42,0	294,3	2,8	0,307	
YESA-5_97.FIN2	496,0	0,889	1,2950	0,01500	0,13960	0,0013	0,4271900	843,00	6,70	842,40	7,60	840,0	24,0	842,4	7,6	0,071	
YESA-5_98.FIN2	295,0	1,589	1,3090	0,01700	0,13850	0,0014	0,4631600	849,50	7,60	835,80	7,90	883,0	24,0	835,8	7,9	1,613	
YESA-5_99.FIN2	2460,0	10,350	0,5390	0,03400	0,04520	0,0022	0,1350400	437,00	22,00	285,00	14,00	1330,0	140,0	DISC	DISC	34,783	Rim
YESA-5_99.FIN2	649,0	8,370	0,5920	0,01200	0,07150	0,0009	0,6579100	471,30	7,30	445,10	5,70	587,0	31,0	445,1	5,7	5,559	Core
YESA-5_100.FIN2	126,3	0,330	1,5700	0,02800	0,16050	0,0016	0,5093600	958,00	10,00	959,30	8,70	942,0	34,0	942,0	34,0	1,837	
YESA-5_101.FIN2	596,0	6,270	0,3817	0,00730	0,04738	0,0009	0,4845500	327,80	5,30	298,30	5,70	542,0	43,0	298,3	5,7	8,999	
YESA-5_102.FIN2	414,0	1,599	0,6270	0,01100	0,07872	0,0007	0,4999900	493,20	6,80	488,40	4,30	499,0	37,0	488,4	4,3	0,973	
YESA-5_103.FIN2	201,0	3,310	0,8910	0,01500	0,10490	0,0010	0,3648000	646,90	7,80	643,80	6,30	652,0	33,0	643,8	6,3	0,479	
YESA-5_104.FIN2	505,0	18,000	0,7490	0,01400	0,08900	0,0011	0,5437900	566,40	7,90	549,70	6,70	621,0	34,0	549,7	6,7	2,948	
YESA-5_105.FIN2	1000,0	4,170	0,9240	0,03600	0,10800	0,0045	0,7650700	664,00	19,00	661,00	26,00	665,0	59,0	661,0	26,0	0,452	Rim
YESA-5_105.FIN2	189,0	1,630	1,1840	0,02800	0,12920	0,0017	0,0273360	791,00	13,00	782,80	9,70	801,0	53,0	782,8	9,7	1,037	Core
YESA-5_106.FIN2	511,0	36,200	0,3736	0,00710	0,04987	0,0006	0,3797500	322,50	5,30	313,70	3,40	368,0	40,0	313,7	3,4	2,729	
YESA-5_107.FIN2	519,8	6,620	0,5903	0,00900	0,07618	0,0007	0,3750300	470,40	5,70	473,20	4,20	447,0	32,0	473,2	4,2	0,595	
YESA-5_108.FIN2	774,0	1,607	0,3566	0,00630	0,04758	0,0006	0,5156100	309,20	4,70	299,60	3,50	366,0	36,0	299,6	3,5	3,105	
YESA-5_109.FIN2	191,0	0,772	0,8310	0,01800	0,09920	0,0012	0,3258400	612,20	9,70	609,30	7,10	611,0	46,0	609,3	7,1	0,474	
YESA-5_110.FIN2	717,0	12,400	0,6640	0,01100	0,08210	0,0010	0,6027300	516,00	6,70	508,30	6,20	539,0	28,0	508,3	6,2	1,492	
YESA-5_111.FIN2	352,0	1,257	0,7770	0,01300	0,09351	0,0010	0,5351800	583,40	7,50	576,20	5,60	606,0	31,0	576,2	5,6	1,234	
YESA-5_112.FIN2	597,0	1,340	0,8020	0,01000	0,09718	0,0007	0,3983800	597,20	5,90	597,80	4,30	593,0	28,0	597,8	4,3	0,100	
YESA-5_113.FIN2	208,0	3,347	1,4530	0,02000	0,15090	0,0013	0,4155400	910,90	8,30	905,80	7,40	921,0	26,0	921,0	26,0	1,650	
YESA-5_114.FIN2	811,0	17,300	0,9180	0,01300	0,10750	0,0012	0,6670100	660,60	6,90	658,00	7,10	668,0	25,0	658,0	7,1	0,394	
YESA-5_115.FIN2	1420,0	4,800	0,5350	0,03000	0,05350	0,0019	0,8583900	434,00	20,00	336,00	11,00	980,0	63,0	DISC	DISC	22,581	Rim
YESA-5_115.FIN2	169,1	1,129	0,7620	0,02000	0,09070	0,0013	0,1646300	574,00	12,00	559,70	7,60	609,0	62,0	559,7	7,6	2,491	Core
YESA-5_116.FIN2	689,0	1,915	1,1750	0,02200	0,12830	0,0020	0,6950800	788,00	10,00	778,00	11,00	814,0	30,0	778,0	11,0	1,269	
YESA-5_117.FIN2	547,0	0,920	4,3030	0,04700	0,29070	0,0031	0,6617300	1692,60	9,20	1647,00	16,00	1749,0	16,0	1749,0	16,0	5,832	
YESA-5_118.FIN2	197,4	1,518	5,5390	0,06500	0,33670	0,0035	0,5414000	1905,00	10,00	1870,00	17,00	1942,0	20,0	1942,0	20,0	3,708	
YESA-5_120.FIN2	471,0	8,100	1,7000	0,01800	0,16840	0,0014	0,5536700	1007,70	6,80	1002,90	7,90	1020,0	19,0	1020,0	19,0	1,676	
YESA-5_121.FIN2	114,8	1,138	1,4670	0,03600	0,14800	0,0019	0,3202300	914,00	15,00	890,00	11,00	968,0	48,0	968,0	48,0	8,058	
YESA-5_122.FIN2	3770,0	2,620	0,7030	0,02000	0,06130	0,0021	0,6286000	540,00	12,00	383,00	13,00	1270,0	55,0	DISC	DISC	29,074	Rim
YESA-5_122.FIN2	221,0	1,230	0,8790	0,01800	0,10210	0,0014	0,2702400	639,10	9,80	626,40	8,10	674,0	46,0	626,4	8,1	1,987	Core
YESA-5_123.FIN2	136,2	1,302	1,5000	0,02700	0,15340	0,0020	0,3843000	928,00	11,00	920,00	11,00	945,0	37,0	945,0	37,0	2,646	
YESA-5_124.FIN2	217,3	3,806	0,8500	0,01500	0,10190	0,0011	0,3985400	625,60	8,50	625,30	6,50	610,0	37,0	625,3	6,5	0,048	
YESA-5_125.FIN2	448,0	1,876	0,7950	0,01400	0,09326	0,0010	0,5290200	593,70	8,20	574,70	5,70	662,0	33,0	574,7	5,7	3,200	
YESA-5_126.FIN2	284,0	5,800	1,0630	0,05400	0,11240	0,0041	0,4232900	734,00	27,00	687,00	24,00	870,0	110,0	687,0	24,0	6,403	Rim
YESA-5_126.FIN2	152,3	1,429	1,5160	0,02700	0,14970	0,0017	0,4552500	937,00	11,00	898,80	9,40	1019,0	33,0	1019,0	33,0	11,796	Core
YESA-5_127.FIN2	516,0	1,199	0,7250	0,01100	0,08791	0,0009	0,2324700	553,70	6,40	543,10	5,40	587,0	36,0	543,1	5,4	1,914	
YESA-5_128.FIN2	230,0	0,728	0,9660	0,02300	0,10780	0,0011	0,2295700	684,00	11,00	660,00	6,70	746,0	48,0	660,0	6,7	3,509	
YESA-5_129.FIN2	148,8	2,797	0,7190	0,01800	0,08790	0,0011	0,2714000	548,00	10,00	543,30	6,60	559,0	55,0	543,3	6,6	0,858	
YESA-5_130.FIN2	254,1	0,911	1,1340	0,01700	0,12440	0,0010	0,3703400	768,30	8,10	756,00	5,80	799,0	31,0	756,0	5,8	1,601	
YESA-5_131.FIN2	376,0	1,473	1,2770	0,01800	0,13700	0,0016	0,5680500	834,50	8,10	827,70	9,10	852,0	26,0	827,7	9,1	0,815	
YESA-5_132.FIN2	1670,0	6,300	0,4270	0,01600	0,04250	0,0015	0,2175500	360,00	11,00	268,30	9,50	994,0	97,0	DISC	DISC	25,472	Rim
YESA-5_132.FIN2	186,0	1,025	0,8260	0,02500	0,09490	0,0013	0,1788300	610,00	14,00	584,20	7,80	678,0	66,0	584,2	7,8	4,230	Core
YESA-5_133.FIN2	197,7	1,549	0,8100	0,01500	0,09745	0,0010	0,3289700	601,10	8,50	599,40	5,70	595,0	39,0	599,4	5,7	0,283	
YESA-5_134.FIN2	148,8	1,260	1,6580	0,03100	0,16370	0,0018	0,4345600	990,00	12,00	978,40	9,90	1009,0	34,0	1009,0	34,0	3,033	
EZK-2_1.FIN2	361,0	1,349	0,8640	0,01100	0,10358	0,0009	0,3160000	631,50	5,80	635,30	5,10	623,0	29,0	635,3	5,1	0,602	
EZK-2_2.FIN2	195,8	1,020	1,7180	0,02100	0,17030	0,0015	0,4097800	1015,10	7,90	1013,70	8,10	1021,0	24,0	1021,0	24,0	0,715	

Sample Name:	[U]							207/235		206/238		207/206		Best age		Discordance	Rim/
Grain #	ppm	U/Th	207/235	2σ error	206/238	2σ error	RHO	Age Ma	2σ error	Age (Ma)	2σ error	Age (Ma)	2σ error	(Ma)	2σ error	%	Core
EZK-2_3.FIN2	890,0	2,592	0,3309	0,00460	0,04609	0,0004	0,4213200	290,00	3,50	290,40	2,50	280,0	29,0	290,4	2,5	0,138	
EZK-2_4.FIN2	101,0	0,643	6,0780	0,09700	0,36020	0,0044	0,5677300	1985,00	14,00	1982,00	21,00	1981,0	28,0	1981,0	28,0	0,050	
EZK-2_5.FIN2	193,0	1,295	6,4870	0,07600	0,37220	0,0040	0,8942000	2042,00	10,00	2039,00	19,00	2037,0	16,0	2037,0	16,0	0,098	
EZK-2_6.FIN2	861,0	11,210	0,6194	0,00800	0,07823	0,0009	0,3663500	489,20	5,00	485,50	5,30	500,0	30,0	485,5	5,3	0,756	
EZK-2_7.FIN2	624,0	37,500	1,5230	0,02200	0,15720	0,0014	0,4828200	940,70	8,40	940,90	8,00	935,0	27,0	935,0	27,0	0,631	
EZK-2_8.FIN2	172,0	3,141	0,5960	0,01300	0,07607	0,0008	0,2212100	473,60	8,30	472,60	4,70	462,0	49,0	472,6	4,7	0,211	
EZK-2_9.FIN2	829,0	1,945	0,8830	0,01100	0,10590	0,0013	0,4845800	642,10	6,10	648,80	7,60	618,0	27,0	648,8	7,6	1,043	
EZK-2_10.FIN2	153,1	0,907	0,8040	0,01600	0,09680	0,0010	0,2229400	597,40	8,70	595,60	5,60	589,0	43,0	595,6	5,6	0,301	
EZK-2_11.FIN2	533,1	8,960	0,6098	0,00950	0,07745	0,0009	0,3144200	483,00	6,00	480,80	5,30	485,0	36,0	480,8	5,3	0,455	
EZK-2_12.FIN2	864,0	7,120	0,8470	0,01700	0,10140	0,0017	0,4564800	622,40	9,20	623,00	10,00	617,0	41,0	623,0	10,0	0,096	
EZK-2_13.FIN2	612,0	13,700	0,6366	0,00900	0,07964	0,0008	0,1059300	499,70	5,60	493,90	4,90	522,0	34,0	493,9	4,9	1,161	
EZK-2_14.FIN2	148,1	0,593	0,9050	0,01900	0,10116	0,0010	0,2116800	652,70	9,80	621,10	5,80	766,0	44,0	621,1	5,8	4,841	
EZK-2_15.FIN2	148,0	1,389	0,7360	0,01600	0,09236	0,0010	0,1790700	558,60	9,20	569,40	5,80	511,0	50,0	569,4	5,8	1,933	
EZK-2_16.FIN2	144,1	0,701	0,8410	0,01600	0,10120	0,0010	0,2790200	619,50	8,70	621,40	6,10	598,0	41,0	621,4	6,1	0,307	
EZK-2_17.FIN2	158,1	1,336	1,2950	0,02700	0,13900	0,0021	0,3491000	842,00	12,00	839,00	12,00	852,0	42,0	839,0	12,0	0,356	
EZK-2_18.FIN2	859,0	1,773	11,4100	0,11000	0,48380	0,0054	0,4889600	2557,20	8,70	2543,00	23,00	2562,0	14,0	2562,0	14,0	0,742	
EZK-2_19.FIN2	298,5	1,683	0,6080	0,01200	0,07740	0,0011	0,2567800	481,70	7,40	480,40	6,40	481,0	46,0	480,4	6,4	0,270	
EZK-2_20.FIN2	343,4	2,115	0,8740	0,02000	0,10420	0,0014	0,2005400	637,00	11,00	638,70	8,30	623,0	54,0	638,7	8,3	0,267	
EZK-2_21.FIN2	469,0	0,984	0,8030	0,01100	0,09574	0,0009	0,2948800	598,10	5,90	589,30	5,00	628,0	29,0	589,3	5,0	1,471	
EZK-2_22.FIN2	244,9	0,903	6,7560	0,07800	0,37690	0,0041	0,4932100	2079,00	10,00	2061,00	19,00	2101,0	20,0	2101,0	20,0	1,904	
EZK-2_23.FIN2	90,8	0,767	5,8900	0,10000	0,35410	0,0056	0,4489000	1958,00	15,00	1953,00	26,00	1964,0	32,0	1964,0	32,0	0,560	
EZK-2_24.FIN2	350,0	1,147	0,8550	0,01100	0,10082	0,0008	0,3542900	626,50	6,30	619,10	4,60	656,0	28,0	619,1	4,6	1,181	
EZK-2_25.FIN2	310,0	3,781	0,6100	0,01100	0,07728	0,0007	0,1222700	482,90	6,70	479,80	4,20	490,0	40,0	479,8	4,2	0,642	
EZK-2_26.FIN2	2240,0	33,500	0,3780	0,01500	0,05110	0,0017	0,2412700	325,00	11,00	321,00	11,00	360,0	100,0	321,0	11,0	1,231	Rim
EZK-2_26.FIN2	1345,0	2,473	0,6940	0,02100	0,08500	0,0025	0,5234000	535,00	12,00	526,00	15,00	573,0	71,0	526,0	15,0	1,682	Core
EZK-2_26.FIN2	251,0	1,366	0,8820	0,02400	0,10370	0,0014	0,3519800	641,00	13,00	635,70	8,20	651,0	53,0	635,7	8,2	0,827	Core
EZK-2_27.FIN2	439,0	2,382	0,3635	0,00740	0,04981	0,0006	0,3379700	314,30	5,50	313,30	3,80	323,0	44,0	313,3	3,8	0,318	
EZK-2_28.FIN2	850,0	1,237	1,7630	0,01700	0,17350	0,0012	0,1738000	1031,20	6,10	1031,40	6,30	1033,0	19,0	1033,0	19,0	0,155	
EZK-2_29.FIN2	380,0	69,000	0,8910	0,03300	0,10540	0,0039	0,6107500	646,00	18,00	646,00	22,00	652,0	71,0	646,0	22,0	0,000	Rim
EZK-2_29.FIN2	306,0	1,038	1,6180	0,02700	0,16270	0,0021	0,7832600	977,00	10,00	971,00	12,00	993,0	22,0	993,0	22,0	2,216	Core
EZK-2_30.FIN2	931,0	49,600	0,7431	0,00860	0,09178	0,0008	0,6090700	563,90	5,00	566,00	4,60	558,0	23,0	566,0	4,6	0,372	
EZK-2_31.FIN2	391,0	2,690	0,8200	0,01200	0,09750	0,0012	0,4086600	609,00	6,80	599,70	6,90	643,0	31,0	599,7	6,9	1,527	
EZK-2_32.FIN2	108,3	0,733	12,0800	0,17000	0,49600	0,0057	0,4617500	2609,00	13,00	2596,00	25,00	2628,0	23,0	2628,0	23,0	1,218	
EZK-2_34.FIN2	244,0	1,622	6,6850	0,08700	0,37690	0,0039	0,4469700	2070,00	12,00	2061,00	18,00	2082,0	23,0	2082,0	23,0	1,009	
EZK-2_36.FIN2	103,9	1,476	2,8890	0,06600	0,23770	0,0044	0,7209200	1378,00	18,00	1374,00	23,00	1379,0	45,0	1379,0	45,0	0,363	
EZK-2_37.FIN2	613,6	1,918	0,8176	0,00860	0,09765	0,0008	0,5565600	606,30	4,80	600,50	4,80	630,0	24,0	600,5	4,8	0,957	
EZK-2_38.FIN2	560,0	1,358	4,8910	0,04500	0,31140	0,0024	0,6844300	1800,90	7,50	1747,00	12,00	1862,0	13,0	1862,0	13,0	6,176	
EZK-2_39.FIN2	282,8	1,193	0,9290	0,01200	0,10844	0,0010	0,4323200	666,20	6,40	663,60	5,80	678,0	27,0	663,6	5,8	0,390	
EZK-2_40.FIN2	1097,0	65,000	0,4024	0,00950	0,05442	0,0009	0,4202800	343,10	6,80	341,60	5,60	351,0	52,0	341,6	5,6	0,437	Rim
EZK-2_40.FIN2	260,0	0,505	0,7520	0,02000	0,09320	0,0014	0,4012200	568,00	12,00	574,10	8,00	542,0	47,0	574,1	8,0	1,074	Core
EZK-2_41.FIN2	179,4	0,749	15,7300	0,13000	0,55560	0,0048	0,5398400	2859,00	8,10	2847,00	20,00	2868,0	14,0	2868,0	14,0	0,732	
EZK-2_42.FIN2	246,0	3,006	1,2850	0,01600	0,13910	0,0010	0,2654600	837,90	7,20	839,80	5,80	834,0	28,0	839,8	5,8	0,227	
EZK-2_43.FIN2	285,4	14,870	0,4617	0,00850	0,06141	0,0006	0,3429600	384,80	6,00	384,20	3,50	376,0	39,0	384,2	3,5	0,156	
EZK-2_44.FIN2	640,0	2,630	0,7950	0,00840	0,09546	0,0007	0,3303300	593,60	4,80	587,70	4,40	607,0	24,0	587,7	4,4	0,994	
EZK-2_45.FIN2	76,0	0,933	1,8130	0,03400	0,17630	0,0022	0,4651300	1047,00	13,00	1046,00	12,00	1040,0	36,0	1040,0	36,0	0,577	
EZK-2_46.FIN2	1440,0	40,000	0,4470	0,03300	0,06130	0,0043	0,1688100	374,00	23,00	383,00	26,00	320,0	200,0	383,0	26,0	2,406	Rim
EZK-2_46.FIN2	547,0	8,650	0,8840	0,02400	0,10630	0,0021	0,6479000	642,00	13,00	651,00	12,00	602,0	46,0	651,0	12,0	1,402	Core

Sample Name:	[U]							207/235		206/238		207/206		Best age		Discordance	Rim/
Grain #	ppm	U/Th	207/235	2σ error	206/238	2σ error	RHO	Age Ma	2σ error	Age (Ma)	2σ error	Age (Ma)	2σ error	(Ma)	2σ error	%	Core
EZK-2_46.FIN2	163,7	0,934	1,4940	0,03100	0,15360	0,0023	0,4008400	926,00	13,00	921,00	13,00	931,0	42,0	931,0	42,0	1,074	Core
EZK-2_47.FIN2	731,0	22,100	0,6180	0,01400	0,07740	0,0016	0,2093400	488,00	8,50	480,30	9,70	518,0	59,0	480,3	9,7	1,578	Rim
EZK-2_47.FIN2	478,0	2,780	0,7800	0,02000	0,09480	0,0018	0,2443200	585,00	12,00	584,00	11,00	582,0	63,0	584,0	11,0	0,171	Core
EZK-2_48.FIN2	722,0	2,726	0,3089	0,00690	0,04106	0,0005	0,1766000	273,00	5,30	259,40	2,90	384,0	49,0	259,4	2,9	4,982	
EZK-2_49.FIN2	121,9	0,620	5,8400	0,11000	0,34480	0,0060	0,6121600	1951,00	16,00	1909,00	28,00	1987,0	29,0	1987,0	29,0	3,926	
EZK-2_50.FIN2	164,3	1,769	1,4900	0,17000	0,12430	0,0031	0,4351700	923,00	68,00	755,00	18,00	1330,0	240,0	DISC	DISC	18,202	Rim
EZK-2_50.FIN2	141,2	1,096	1,7140	0,02900	0,16780	0,0015	0,2389700	1014,00	11,00	999,90	8,20	1037,0	37,0	1037,0	37,0	3,578	Core
EZK-2_51.FIN2	293,0	6,500	0,8180	0,02400	0,09740	0,0016	0,2754200	605,00	13,00	599,10	9,10	616,0	63,0	599,1	9,1	0,975	Rim
EZK-2_51.FIN2	110,0	0,924	1,2650	0,03700	0,13410	0,0022	0,2362700	831,00	17,00	811,00	12,00	864,0	65,0	811,0	12,0	2,407	Core
EZK-2_52.FIN2	30,4	0,357	0,7520	0,04100	0,09080	0,0025	0,2325300	563,00	24,00	560,00	15,00	550,0	110,0	560,0	15,0	0,533	
EZK-2_53.FIN2	95,4	1,890	0,8360	0,02700	0,09900	0,0016	0,6035500	614,00	15,00	608,40	9,20	637,0	58,0	608,4	9,2	0,912	
EZK-2_54.FIN2	71,9	0,882	1,6310	0,03600	0,16080	0,0022	0,0670080	980,00	14,00	961,00	12,00	1008,0	51,0	1008,0	51,0	4,663	
EZK-2_55.FIN2	101,5	0,889	1,8720	0,03200	0,17720	0,0016	0,1075200	1069,00	11,00	1051,40	9,00	1096,0	36,0	1096,0	36,0	4,069	
EZK-2_56.FIN2	543,0	0,517	0,8060	0,01400	0,09520	0,0011	0,2392900	599,70	7,80	586,30	6,70	631,0	42,0	586,3	6,7	2,234	
EZK-2_57.FIN2	369,0	0,799	0,8270	0,01400	0,09853	0,0010	0,0966370	611,20	7,40	605,70	5,60	617,0	38,0	605,7	5,6	0,900	
EZK-2_58.FIN2	226,0	1,305	5,1460	0,05800	0,31400	0,0039	0,4894300	1843,00	9,50	1760,00	19,00	1930,0	21,0	1930,0	21,0	8,808	
EZK-2_60.FIN2	1400,0	4,300	0,3450	0,02900	0,04040	0,0021	0,0482700	300,00	22,00	256,00	13,00	640,0	150,0	256,0	13,0	14,667	Rim
EZK-2_60.FIN2	130,4	1,008	0,7970	0,01700	0,09680	0,0012	0,1516700	595,00	9,80	595,40	6,90	570,0	51,0	595,4	6,9	0,067	Core
EZK-2_61.FIN2	670,0	1,125	0,4193	0,00980	0,05618	0,0006	0,7274800	356,50	6,70	352,30	3,70	396,0	38,0	352,3	3,7	1,178	
EZK-2_62.FIN2	663,0	6,400	0,8430	0,02000	0,09980	0,0014	0,3761200	620,00	11,00	613,40	8,00	635,0	48,0	613,4	8,0	1,065	Rim
EZK-2_62.FIN2	179,9	0,686	1,4000	0,03100	0,14650	0,0021	0,6939700	887,00	13,00	883,00	12,00	884,0	37,0	884,0	37,0	0,113	Core
EZK-2_63.FIN2	357,0	1,435	0,7030	0,01000	0,08720	0,0007	0,2067100	539,70	6,00	538,90	4,20	533,0	34,0	538,9	4,2	0,148	
EZK-2_64.FIN2	701,0	2,420	13,5600	0,21000	0,52300	0,0110	0,5732800	2717,00	14,00	2705,00	50,00	2729,0	32,0	2729,0	32,0	0,879	
EZK-2_65.FIN2	122,2	0,768	0,9240	0,01700	0,10750	0,0011	0,3073400	664,30	8,90	658,30	6,20	669,0	39,0	658,3	6,2	0,903	
EZK-2_66.FIN2	85,7	1,316	1,6150	0,03200	0,16180	0,0019	0,5039600	973,00	13,00	966,00	10,00	988,0	36,0	988,0	36,0	2,227	
EZK-2_67.FIN2	363,0	1,990	6,2100	0,23000	0,35000	0,0110	0,9333000	2001,00	34,00	1933,00	51,00	2054,0	26,0	2054,0	26,0	5,891	
EZK-2_68.FIN2	302,5	0,842	0,9420	0,01300	0,10918	0,0010	0,2687400	673,20	6,90	667,90	5,70	683,0	31,0	667,9	5,7	0,787	
EZK-2_69.FIN2	607,0	9,400	0,6180	0,01900	0,07740	0,0014	0,4453700	488,00	12,00	480,70	8,40	515,0	61,0	480,7	8,4	1,496	Rim
EZK-2_69.FIN2	138,8	1,153	0,7610	0,01900	0,09290	0,0013	0,3249700	574,00	11,00	572,30	7,40	569,0	57,0	572,3	7,4	0,296	Core
EZK-2_70.FIN2	502,9	1,106	1,1770	0,01700	0,12940	0,0013	0,7054400	790,00	8,00	784,00	7,30	814,0	22,0	784,0	7,3	0,759	
EZK-2_71.FIN2	145,3	3,000	0,4540	0,01100	0,06002	0,0006	0,1420400	379,20	7,60	375,70	3,50	384,0	55,0	375,7	3,5	0,923	
EZK-2_72.FIN2	249,0	1,148	1,6900	0,07300	0,16530	0,0062	0,6356300	1003,00	28,00	986,00	34,00	1036,0	79,0	1036,0	79,0	4,826	
EZK-2_73.FIN2	65,5	3,128	0,8860	0,02900	0,10070	0,0013	0,0499790	643,00	15,00	618,40	7,70	702,0	75,0	618,4	7,7	3,826	
EZK-2_74.FIN2	212,7	0,637	1,6910	0,02200	0,16790	0,0014	0,4845000	1003,90	8,30	1000,60	7,80	1005,0	24,0	1005,0	24,0	0,438	
EZK-2_75.FIN2	2730,0	10,100	0,4940	0,01200	0,05580	0,0015	0,8234100	407,20	8,20	350,10	9,30	744,0	33,0	350,1	9,3	14,023	Rim
EZK-2_75.FIN2	703,0	2,169	1,1840	0,01700	0,11860	0,0015	0,4853600	792,50	7,70	722,70	8,50	996,0	29,0	722,7	8,5	8,808	Core
EZK-2_76.FIN2	241,0	0,962	1,0990	0,02300	0,12330	0,0015	0,5069100	751,00	11,00	749,20	8,50	757,0	39,0	749,2	8,5	0,240	
EZK-2_77.FIN2	225,0	1,098	1,1380	0,01800	0,12650	0,0012	0,6765500	770,00	8,70	767,60	7,00	768,0	31,0	767,6	7,0	0,312	
EZK-2_79.FIN2	107,1	0,937	1,6030	0,02700	0,15520	0,0017	0,2673500	971,00	11,00	930,00	9,60	1054,0	36,0	1054,0	36,0	11,765	
EZK-2_80.FIN2	81,4	3,255	1,2530	0,02800	0,13470	0,0016	0,0567320	822,00	13,00	814,10	9,30	846,0	49,0	814,1	9,3	0,961	
EZK-2_81.FIN2	445,0	5,250	0,6090	0,01200	0,07645	0,0009	0,3178800	482,20	7,30	474,80	5,60	513,0	42,0	474,8	5,6	1,535	
EZK-2_82.FIN2	441,0	3,030	0,6970	0,01100	0,08585	0,0008	0,4491400	537,20	6,60	530,90	4,90	541,0	33,0	530,9	4,9	1,173	
EZK-2_83.FIN2	406,0	13,210	0,7246	0,00920	0,08863	0,0006	0,3416700	552,80	5,40	547,40	3,70	563,0	27,0	547,4	3,7	0,977	
EZK-2_84.FIN2	197,0	0,380	0,8720	0,01500	0,10350	0,0010	0,1860400	635,30	7,80	634,70	6,10	617,0	37,0	634,7	6,1	0,094	
EZK-2_85.FIN2	33,3	1,032	1,6080	0,06000	0,16070	0,0028	0,2814000	970,00	24,00	960,00	16,00	961,0	77,0	961,0	77,0	0,104	
EZK-2_86.FIN2	960,0	27,800	0,6390	0,04700	0,08080	0,0065	0,8909700	500,00	29,00	500,00	39,00	505,0	81,0	500,0	39,0	0,000	Rim
EZK-2_86.FIN2	121,1	1,387	4,7720	0,08700	0,30480	0,0038	0,4694100	1778,00	15,00	1715,00	19,00	1847,0	31,0	1847,0	31,0	7,147	Core

Sample Name:	[U]							207/235		206/238		207/206		Best age		Discordance	Rim/
Grain #	ppm	U/Th	207/235	2σ error	206/238	2σ error	RHO	Age Ma	2σ error	Age (Ma)	2σ error	Age (Ma)	2σ error	(Ma)	2σ error	%	Core
EZK-2_87.FIN2	107,4	0,438	1,6780	0,03600	0,16620	0,0021	0,2824100	999,00	13,00	991,00	12,00	1011,0	46,0	1011,0	46,0	1,978	
EZK-2_88.FIN2	299,0	2,390	9,9500	0,28000	0,41710	0,0067	0,7364700	2426,00	24,00	2247,00	30,00	2577,0	36,0	2577,0	36,0	12,806	
EZK-2_89.FIN2	86,9	0,700	1,6020	0,02800	0,15890	0,0016	0,3110700	969,00	11,00	950,40	8,60	1005,0	36,0	1005,0	36,0	5,433	
EZK-2_90.FIN2	53,5	0,771	10,3000	0,21000	0,46340	0,0079	0,6550800	2459,00	19,00	2453,00	35,00	2465,0	28,0	2465,0	28,0	0,487	
EZK-2_91.FIN2	148,5	2,750	0,6380	0,01700	0,07970	0,0011	0,0703780	500,00	10,00	494,10	6,80	507,0	64,0	494,1	6,8	1,180	
EZK-2_92.FIN2	246,2	1,654	1,5780	0,02000	0,15970	0,0016	0,2774500	960,70	7,80	954,80	8,60	967,0	29,0	967,0	29,0	1,262	
EZK-2_93.FIN2	113,5	0,414	6,5500	0,11000	0,35620	0,0045	0,4880300	2051,00	15,00	1964,00	22,00	2129,0	28,0	2129,0	28,0	7,750	
EZK-2_94.FIN2	163,0	20,000	0,4430	0,02100	0,06000	0,0014	0,0469710	372,00	15,00	375,70	8,60	340,0	120,0	375,7	8,6	0,995	Rim
EZK-2_94.FIN2	291,0	1,750	0,6660	0,01200	0,08313	0,0008	0,2184400	517,50	7,30	514,70	4,70	512,0	41,0	514,7	4,7	0,541	Core
EZK-2_95.FIN2	253,0	30,900	0,7490	0,03000	0,09280	0,0021	0,4432700	566,00	17,00	572,00	12,00	528,0	78,0	572,0	12,0	1,060	Rim
EZK-2_95.FIN2	214,9	1,410	0,9330	0,02300	0,10770	0,0014	0,2509900	668,00	12,00	659,30	8,20	693,0	52,0	659,3	8,2	1,302	Core
EZK-2_96.FIN2	1498,0	2,920	1,2710	0,03000	0,12320	0,0034	0,7922700	833,00	14,00	749,00	19,00	1059,0	33,0	749,0	19,0	10,084	Rim
EZK-2_96.FIN2	185,0	1,627	1,8000	0,02700	0,17950	0,0016	0,2354600	1043,90	9,80	1064,10	8,60	989,0	31,0	989,0	31,0	7,594	Core
EZK-2_97.FIN2	1634,0	4,870	0,3381	0,00550	0,04676	0,0007	0,5244900	295,50	4,10	294,50	4,10	292,0	34,0	294,5	4,1	0,338	
EZK-2_98.FIN2	409,0	1,647	1,5780	0,01500	0,15640	0,0011	0,3675700	960,80	5,90	936,40	6,10	1010,0	20,0	1010,0	20,0	7,287	
EZK-2_99.FIN2	444,0	0,751	0,7610	0,01000	0,09093	0,0008	0,4098900	574,10	5,90	561,00	4,70	616,0	27,0	561,0	4,7	2,282	
EZK-2_100.FIN2	405,0	7,750	0,5957	0,00990	0,07576	0,0008	0,4503800	474,50	6,40	470,70	4,90	489,0	35,0	470,7	4,9	0,801	
EZK-2_102.FIN2	542,0	0,812	8,0400	0,08000	0,41220	0,0038	0,6275900	2234,00	9,00	2224,00	17,00	2236,0	14,0	2236,0	14,0	0,537	
EZK-2_103.FIN2	694,0	24,200	0,3990	0,01600	0,05390	0,0014	0,2812100	341,00	12,00	338,40	8,80	345,0	95,0	338,4	8,8	0,762	Rim
EZK-2_103.FIN2	200,1	0,854	0,7820	0,01900	0,09450	0,0016	0,3297800	586,00	11,00	582,00	9,70	610,0	59,0	582,0	9,7	0,683	Core
EZK-2_104.FIN2	419,0	6,320	0,5590	0,00810	0,07189	0,0006	0,4018300	450,30	5,30	447,50	3,40	448,0	31,0	447,5	3,4	0,622	
EZK-2_105.FIN2	611,0	1,503	0,3929	0,00570	0,05295	0,0004	0,3232800	336,20	4,10	332,90	2,40	343,0	31,0	332,9	2,4	0,982	
EZK-2_106.FIN2	800,0	1,949	0,3689	0,00550	0,05058	0,0006	0,3293200	318,60	4,10	318,00	3,40	318,0	35,0	318,0	3,4	0,188	
EZK-2_107.FIN2	83,3	1,303	1,2150	0,03100	0,13310	0,0017	0,2337800	805,00	14,00	805,00	10,00	786,0	55,0	805,0	10,0	0,000	
EZK-2_108.FIN2	260,0	2,258	1,0730	0,02400	0,12060	0,0022	0,6941600	739,00	12,00	734,00	12,00	756,0	40,0	734,0	12,0	0,677	
EZK-2_109.FIN2	272,0	1,529	0,6910	0,01400	0,08484	0,0009	0,1727400	532,50	8,20	524,90	5,10	557,0	47,0	524,9	5,1	1,427	
EZK-2_110.FIN2	457,0	1,910	8,6300	0,32000	0,40400	0,0120	0,6698900	2297,00	34,00	2186,00	53,00	2394,0	47,0	2394,0	47,0	8,688	
EZK-2_111.FIN2	717,0	3,150	1,2830	0,02400	0,13800	0,0025	0,4944900	838,00	11,00	833,00	14,00	846,0	38,0	833,0	14,0	0,597	Rim
EZK-2_111.FIN2	201,0	2,449	1,3280	0,02200	0,14540	0,0014	0,3415400	856,80	9,80	874,90	7,60	804,0	33,0	804,0	7,6	2,113	Core
EZK-2_112.FIN2	378,0	1,393	4,4270	0,05400	0,30360	0,0029	0,6946400	1716,00	10,00	1709,00	14,00	1723,0	17,0	1723,0	17,0	0,813	
EZK-2_113.FIN2	233,0	1,530	0,8770	0,01700	0,10430	0,0014	0,4233400	637,60	9,40	639,20	8,00	613,0	41,0	639,2	8,0	0,251	
EZK-2_114.FIN2	264,0	1,231	0,6380	0,01100	0,08069	0,0007	0,5812400	500,00	6,90	500,20	4,30	496,0	37,0	500,2	4,3	0,040	
EZK-2_115.FIN2	407,0	2,900	0,7040	0,01000	0,08706	0,0008	0,3956100	540,50	6,00	538,10	4,60	540,0	29,0	538,1	4,6	0,444	
EZK-2_116.FIN2	1390,0	3,240	0,8400	0,14000	0,08480	0,0061	0,7975200	613,00	73,00	525,00	36,00	930,0	200,0	525,0	36,0	14,356	Rim
EZK-2_116.FIN2	521,0	2,018	2,4200	0,04600	0,19710	0,0035	0,4542900	1248,00	14,00	1160,00	19,00	1401,0	39,0	1401,0	39,0	17,202	Core
EZK-2_117.FIN2	203,0	2,147	1,5500	0,02500	0,15900	0,0017	0,4435600	951,00	10,00	951,20	9,30	947,0	32,0	947,0	32,0	0,444	
EZK-2_118.FIN2	169,0	26,000	0,4610	0,01100	0,06147	0,0007	0,1778100	383,80	7,90	384,50	3,90	370,0	54,0	384,5	3,9	0,182	
EZK-2_119.FIN2	3625,0	7,000	0,6348	0,00920	0,07410	0,0013	0,5103600	499,00	5,70	460,90	7,80	681,0	34,0	460,9	7,8	7,635	Rim
EZK-2_119.FIN2	884,0	6,510	1,3170	0,02200	0,14010	0,0018	0,7535300	852,10	9,60	845,00	10,00	876,0	23,0	845,0	10,0	0,833	Core
EZK-2_120.FIN2	227,9	1,137	1,7120	0,02800	0,16960	0,0022	0,4891900	1013,00	11,00	1009,00	12,00	1021,0	32,0	1021,0	32,0	1,175	
EZK-2_121.FIN2	229,0	7,700	0,6040	0,01200	0,07610	0,0008	0,3742500	478,70	7,20	472,80	4,60	510,0	43,0	472,8	4,6	1,233	
EZK-2_122.FIN2	586,1	8,000	0,8620	0,02500	0,10000	0,0014	0,1880200	630,00	13,00	614,20	8,40	687,0	53,0	614,2	8,4	2,508	Rim
EZK-2_122.FIN2	140,8	1,175	1,5840	0,03700	0,16230	0,0022	0,3965900	962,00	15,00	969,00	12,00	954,0	43,0	954,0	43,0	1,572	Core
EZK-2_123.FIN2	225,0	0,855	0,3300	0,01200	0,04550	0,0006	0,1535500	289,20	9,20	286,80	3,80	301,0	79,0	286,8	3,8	0,830	
EZK-2_124.FIN2	1188,0	3,537	0,8080	0,00770	0,10847	0,0009	0,5695700	650,80	4,10	663,80	5,00	607,0	17,0	663,8	5,0	1,998	
EZK-2_125.FIN2	540,0	13,530	0,6378	0,00870	0,08060	0,0007	0,6280000	500,40	5,40	499,70	4,40	509,0	28,0	499,7	4,4	0,140	
EZK-2_126.FIN2	312,0	3,360	0,8440	0,01200	0,10190	0,0008	0,2213200	620,80	6,70	625,50	4,90	605,0	33,0	625,5	4,9	0,757	

Sample Name:	[U]							207/235		206/238		207/206		Best age		Discordance	Rim/
Grain #	ppm	U/Th	207/235	2σ error	206/238	2σ error	RHO	Age Ma	2σ error	Age (Ma)	2σ error	Age (Ma)	2σ error	(Ma)	2σ error	%	Core
EZK-2_127.FIN2	299,0	0,997	0,8090	0,01300	0,09739	0,0010	0,6769800	601,00	7,40	599,00	5,70	609,0	37,0	599,0	5,7	0,333	
EZK-2_128.FIN2	339,0	11,800	0,7090	0,01100	0,08900	0,0010	0,3446500	543,20	6,40	549,60	5,90	517,0	34,0	549,6	5,9	1,178	
EZK-2_129.FIN2	1545,0	3,548	0,8980	0,01000	0,10644	0,0009	0,5173700	650,30	5,50	652,00	5,10	645,0	22,0	652,0	5,1	0,261	
EZK-2_130.FIN2	326,0	1,412	1,6610	0,01800	0,16790	0,0013	0,4498700	993,00	7,00	1000,60	7,20	978,0	21,0	978,0	21,0	2,311	
EZK-2_131.FIN2	382,0	1,311	6,7950	0,05600	0,37900	0,0030	0,5434900	2084,20	7,20	2071,00	14,00	2100,0	13,0	2100,0	13,0	1,381	
EZK-2_132.FIN2	422,6	0,680	0,8690	0,01100	0,10299	0,0008	0,2554500	634,40	6,00	631,80	4,90	644,0	29,0	631,8	4,9	0,410	
EZK-2_133.FIN2	687,0	0,876	0,7800	0,01100	0,09441	0,0008	0,4060500	584,80	6,10	581,50	4,50	607,0	29,0	581,5	4,5	0,564	
EZK-2_134.FIN2	3800,0	1,151	0,4650	0,06100	0,05550	0,0086	0,9080700	386,00	42,00	348,00	52,00	640,0	140,0	DISC	DISC	9,845	Rim
EZK-2_134.FIN2	216,0	1,107	0,7930	0,01300	0,09510	0,0010	0,2023700	592,60	7,50	585,80	6,10	626,0	37,0	585,8	6,1	1,147	Core
EZK-2_135.FIN2	102,5	1,475	7,5000	0,13000	0,39450	0,0072	0,9344400	2171,00	15,00	2143,00	33,00	2202,0	25,0	2202,0	25,0	2,679	
EZK-2_136.FIN2	219,0	6,220	0,7390	0,03700	0,08180	0,0013	0,0427680	558,00	20,00	506,50	7,50	780,0	110,0	506,5	7,5	9,229	
EZK-2_137.FIN2	458,0	2,560	0,3663	0,00850	0,05021	0,0005	0,1865600	316,40	6,30	315,80	3,10	306,0	53,0	315,8	3,1	0,190	
EZK-2_138.FIN2	79,9	1,043	1,8780	0,03400	0,18070	0,0018	0,2348200	1071,00	12,00	1070,30	9,80	1072,0	37,0	1072,0	37,0	0,159	
EZK-2_139.FIN2	1185,0	7,250	0,8000	0,01100	0,09690	0,0011	0,6476800	596,50	6,50	595,90	6,40	601,0	24,0	595,9	6,4	0,101	
EZK-2_140.FIN2	254,0	0,911	10,8800	0,11000	0,47150	0,0042	0,5154000	2512,20	9,00	2490,00	19,00	2533,0	16,0	2533,0	16,0	1,698	
EZK-2_141.FIN2	442,0	1,730	0,6490	0,01100	0,08085	0,0008	0,3360200	507,00	6,80	501,20	4,60	525,0	36,0	501,2	4,6	1,144	
EZK-2_142.FIN2	53,8	2,024	1,7540	0,04600	0,17310	0,0031	0,5715900	1027,00	18,00	1028,00	17,00	1027,0	50,0	1027,0	50,0	0,097	
EZK-2_143.FIN2	325,2	2,159	6,6130	0,04700	0,37690	0,0027	0,5231800	2060,40	6,30	2061,00	12,00	2062,0	12,0	2062,0	12,0	0,048	
EZK-2_144.FIN2	585,0	1,451	0,7100	0,01100	0,08878	0,0009	0,4482100	543,60	6,60	548,20	5,40	522,0	33,0	548,2	5,4	0,846	
IZA-1_1.FIN2	234,0	1,010	0,7850	0,01600	0,09540	0,0010	0,3889100	586,80	9,10	587,20	6,20	566,0	42,0	587,2	6,2	0,068	
IZA-1_2.FIN2	331,8	4,500	0,5580	0,01200	0,07190	0,0010	0,4364900	449,40	7,70	447,70	6,20	445,0	44,0	447,7	6,2	0,378	
IZA-1_3.FIN2	331,1	0,573	5,8870	0,07800	0,33730	0,0033	0,6406500	1957,00	11,00	1873,00	16,00	2038,0	18,0	2038,0	18,0	8,096	
IZA-1_4.FIN2	248,0	11,200	0,8540	0,04000	0,10080	0,0039	0,5316000	624,00	22,00	619,00	23,00	627,0	89,0	619,0	23,0	0,801	Rim
IZA-1_4.FIN2	121,6	1,866	1,1800	0,03900	0,12690	0,0022	0,0792760	788,00	18,00	770,00	12,00	818,0	76,0	770,0	12,0	2,284	Core
IZA-1_5.FIN2	347,5	8,000	0,7660	0,02400	0,09210	0,0029	0,4409400	576,00	14,00	568,00	17,00	598,0	74,0	568,0	17,0	1,389	Rim
IZA-1_5.FIN2	213,0	0,808	0,9760	0,02400	0,11430	0,0017	0,3705300	690,00	12,00	697,50	9,60	659,0	49,0	697,5	9,6	1,087	Core
IZA-1_6.FIN2	515,0	1,411	0,9760	0,01900	0,11190	0,0013	0,4157700	691,30	8,90	683,70	7,70	717,0	34,0	683,7	7,7	1,099	
IZA-1_7.FIN2	389,0	3,130	0,8710	0,01800	0,09990	0,0020	0,5080500	634,10	9,80	614,00	12,00	705,0	41,0	614,0	12,0	3,170	
IZA-1_8.FIN2	557,0	0,666	0,7150	0,01200	0,08760	0,0011	0,5303700	547,00	7,10	541,00	6,50	555,0	31,0	541,0	6,5	1,097	
IZA-1_9.FIN2	755,0	14,500	0,9840	0,03300	0,11270	0,0032	0,4953900	698,00	18,00	688,00	18,00	715,0	71,0	688,0	18,0	1,433	Rim
IZA-1_9.FIN2	414,0	0,714	1,3410	0,02700	0,13980	0,0022	0,6289700	864,00	11,00	843,00	12,00	901,0	33,0	843,0	12,0	2,431	Core
IZA-1_10.FIN2	1361,0	15,500	0,6690	0,04900	0,08230	0,0071	0,5788300	519,00	30,00	509,00	42,00	560,0	160,0	509,0	42,0	1,927	Rim
IZA-1_10.FIN2	732,0	4,370	2,1610	0,07900	0,14880	0,0042	0,4991100	1167,00	25,00	894,00	24,00	1710,0	65,0	DISC	DISC	47,719	Core
IZA-1_10.FIN2	393,0	2,250	2,9890	0,07400	0,19350	0,0050	0,8738800	1408,00	21,00	1139,00	27,00	1832,0	33,0	DISC	DISC	37,828	Core
IZA-1_11.FIN2	201,7	0,825	1,2100	0,03100	0,12080	0,0031	0,7985200	801,00	14,00	734,00	18,00	997,0	33,0	734,0	18,0	8,365	
IZA-1_12.FIN2	70,8	1,170	1,1600	0,03600	0,12230	0,0018	0,3095900	777,00	17,00	744,00	11,00	848,0	64,0	744,0	11,0	4,247	
IZA-1_13.FIN2	302,0	1,229	0,6890	0,03700	0,07360	0,0033	0,4588700	531,00	22,00	458,00	20,00	840,0	110,0	458,0	20,0	13,748	Rim
IZA-1_13.FIN2	179,6	1,263	0,9690	0,03400	0,09990	0,0015	0,3991800	685,00	17,00	613,70	8,90	916,0	65,0	613,7	8,9	10,409	Core
IZA-1_14.FIN2	502,0	1,177	0,7790	0,01200	0,09510	0,0011	0,4942200	583,90	6,90	585,40	6,60	567,0	31,0	585,4	6,6	0,257	
IZA-1_15.FIN2	128,4	0,354	1,6480	0,04300	0,16380	0,0033	0,5155800	986,00	17,00	977,00	18,00	997,0	45,0	997,0	45,0	2,006	
IZA-1_16.FIN2	256,0	4,560	0,9760	0,02700	0,11210	0,0022	0,6057800	688,00	14,00	684,00	13,00	687,0	47,0	684,0	13,0	0,581	
IZA-1_17.FIN2	428,0	2,090	2,3590	0,02600	0,20610	0,0019	0,5809200	1229,10	7,90	1208,00	10,00	1257,0	20,0	1257,0	20,0	3,898	
IZA-1_18.FIN2	188,0	2,340	1,0720	0,02500	0,11960	0,0014	0,3454400	737,00	12,00	727,90	8,10	740,0	47,0	727,9	8,1	1,235	
IZA-1_19.FIN2	280,0	1,710	0,8680	0,02000	0,10090	0,0015	0,5378000	633,00	11,00	619,20	9,00	653,0	41,0	619,2	9,0	2,180	
IZA-1_20.FIN2	321,4	7,440	0,5580	0,01000	0,07090	0,0008	0,2715100	449,60	6,80	441,50	4,60	485,0	43,0	441,5	4,6	1,802	
IZA-1_21.FIN2	556,7	3,460	0,8970	0,01300	0,10320	0,0014	0,5756300	650,30	7,20	634,10	8,50	699,0	32,0	634,1	8,5	2,491	

Sample Name:	[U]							207/235		206/238		207/206		Best age		Discordance	Rim/
Grain #	ppm	U/Th	207/235	2σ error	206/238	2σ error	RHO	Age Ma	2σ error	Age (Ma)	2σ error	Age (Ma)	2σ error	(Ma)	2σ error	%	Core
IZA-1_22.FIN2	44,6	1,637	0,7570	0,03000	0,09150	0,0018	0,2552500	566,00	17,00	564,00	11,00	544,0	83,0	564,0	11,0	0,353	
IZA-1_23.FIN2	217,0	1,372	1,7230	0,03200	0,16900	0,0019	0,2706500	1015,00	12,00	1007,00	11,00	1025,0	37,0	1025,0	37,0	1,756	
IZA-1_24.FIN2	174,0	0,979	0,9100	0,01900	0,10410	0,0013	0,3086600	656,00	10,00	638,00	7,70	702,0	46,0	638,0	7,7	2,744	
IZA-1_25.FIN2	164,0	1,029	1,6930	0,03700	0,16370	0,0019	0,3160500	1004,00	14,00	977,00	11,00	1055,0	42,0	1055,0	42,0	7,393	
IZA-1_26.FIN2	146,0	2,390	0,8820	0,02500	0,10560	0,0017	0,1589000	639,00	14,00	647,20	9,80	607,0	63,0	647,2	9,8	1,283	
IZA-1_27.FIN2	152,9	1,287	13,1800	0,19000	0,50520	0,0076	0,7625000	2690,00	14,00	2634,00	33,00	2732,0	17,0	2732,0	17,0	3,587	
IZA-1_28.FIN2	1080,0	1,640	0,6350	0,07100	0,05280	0,0054	0,8074600	493,00	43,00	331,00	33,00	1350,0	130,0	DISC	DISC	32,860	Rim
IZA-1_28.FIN2	367,0	1,065	0,7760	0,01400	0,09450	0,0014	0,4195900	584,50	8,30	581,80	8,00	583,0	38,0	581,8	8,0	0,462	Core
IZA-1_29.FIN2	601,0	5,990	9,8300	0,12000	0,41600	0,0055	0,7030400	2418,00	11,00	2244,00	24,00	2565,0	17,0	2565,0	17,0	12,515	
IZA-1_30.FIN2	612,0	2,021	1,3890	0,03700	0,13750	0,0034	0,8062900	880,00	15,00	829,00	19,00	1015,0	30,0	829,0	19,0	5,765	
IZA-1_31.FIN2	332,0	0,732	0,8010	0,01400	0,09630	0,0012	0,3892600	596,10	7,70	592,60	7,30	608,0	36,0	592,6	7,3	0,587	
IZA-1_32.FIN2	656,0	1,861	0,7540	0,01300	0,08820	0,0011	0,6666600	569,50	7,20	544,50	6,30	658,0	28,0	544,5	6,3	4,390	
IZA-1_34.FIN2	1085,0	40,100	0,4210	0,01300	0,05410	0,0015	0,5452600	356,20	9,60	339,90	9,30	460,0	64,0	339,9	9,3	4,576	Rim
IZA-1_34.FIN2	123,0	1,018	0,7940	0,03200	0,09140	0,0021	0,3395700	591,00	18,00	564,00	12,00	681,0	84,0	564,0	12,0	4,569	Core
IZA-1_35.FIN2	339,0	1,076	0,8040	0,01600	0,09760	0,0016	0,3397100	598,00	8,70	600,30	9,50	592,0	46,0	600,3	9,5	0,385	
IZA-1_36.FIN2	188,0	1,100	0,7800	0,01600	0,09570	0,0012	0,2150100	583,70	9,20	588,90	6,80	546,0	46,0	588,9	6,8	0,891	
IZA-1_37.FIN2	297,1	1,088	0,8070	0,01500	0,09650	0,0011	0,3327000	600,60	8,30	593,80	6,50	617,0	41,0	593,8	6,5	1,132	
IZA-1_38.FIN2	382,0	4,870	0,8740	0,02500	0,10060	0,0019	0,3340800	638,00	13,00	618,00	11,00	706,0	59,0	618,0	11,0	3,135	
IZA-1_39.FIN2	68,7	1,183	1,5000	0,04100	0,15050	0,0028	0,4200200	929,00	17,00	903,00	15,00	975,0	54,0	975,0	54,0	7,385	
IZA-1_40.FIN2	307,1	0,614	0,7520	0,01400	0,09060	0,0010	0,3504600	568,30	8,20	559,00	5,90	600,0	40,0	559,0	5,9	1,636	
IZA-1_41.FIN2	291,3	0,954	13,6200	0,16000	0,49520	0,0051	0,6706600	2722,00	11,00	2592,00	22,00	2822,0	14,0	2822,0	14,0	8,150	
IZA-1_42.FIN2	170,0	1,360	7,1730	0,09000	0,39520	0,0045	0,6256300	2131,00	11,00	2145,00	21,00	2116,0	18,0	2116,0	18,0	1,371	
IZA-1_43.FIN2	217,0	0,964	1,1340	0,01900	0,12650	0,0013	0,1967700	769,30	9,00	768,80	7,50	754,0	36,0	768,8	7,5	0,065	
IZA-1_44.FIN2	105,5	0,892	0,7930	0,02800	0,09440	0,0016	0,3231100	592,00	16,00	581,00	9,50	606,0	74,0	581,0	9,5	1,858	
IZA-1_45.FIN2	968,0	38,000	0,7500	0,06500	0,08690	0,0064	0,6720900	568,00	37,00	537,00	38,00	680,0	150,0	537,0	38,0	5,458	Rim
IZA-1_45.FIN2	251,0	1,123	4,3240	0,05900	0,29800	0,0034	0,6962800	1696,00	11,00	1683,00	17,00	1710,0	19,0	1710,0	19,0	1,579	Core
IZA-1_46.FIN2	858,0	4,800	0,8160	0,01900	0,08970	0,0018	0,4580900	608,00	12,00	554,00	10,00	797,0	46,0	554,0	10,0	8,882	
IZA-1_47.FIN2	140,7	0,716	1,0490	0,02800	0,11000	0,0014	0,0614890	725,00	14,00	672,70	8,30	870,0	62,0	672,7	8,3	7,214	
IZA-1_48.FIN2	558,0	6,490	0,3649	0,00770	0,05004	0,0007	0,4417900	315,20	5,70	314,70	4,20	322,0	45,0	314,7	4,2	0,159	
IZA-1_49.FIN2	922,0	5,250	0,3718	0,00720	0,04433	0,0007	0,4142400	320,50	5,30	279,60	4,60	616,0	41,0	279,6	4,6	12,761	
IZA-1_50.FIN2	109,5	2,090	0,6290	0,01800	0,07910	0,0011	0,2275300	493,00	11,00	490,70	6,60	482,0	63,0	490,7	6,6	0,467	
IZA-1_51.FIN2	282,0	3,340	0,8890	0,02600	0,10290	0,0020	0,3883700	644,00	14,00	631,00	12,00	688,0	58,0	631,0	12,0	2,019	
IZA-1_52.FIN2	516,0	0,832	1,6980	0,02800	0,16400	0,0025	0,7780300	1007,00	10,00	978,00	14,00	1062,0	22,0	1062,0	22,0	7,910	
IZA-1_53.FIN2	271,0	1,171	4,5800	0,35000	0,21100	0,0140	0,9855300	1671,00	63,00	1219,00	75,00	2379,0	23,0	DISC	DISC	48,760	
IZA-1_54.FIN2	95,0	1,110	6,0090	0,08300	0,36060	0,0044	0,4769800	1974,00	12,00	1984,00	21,00	1959,0	24,0	1959,0	24,0	1,276	
IZA-1_55.FIN2	317,2	2,700	1,1910	0,02100	0,12950	0,0017	0,4711300	794,50	9,90	785,00	9,90	810,0	33,0	785,0	9,9	1,196	
IZA-1_56.FIN2	188,8	1,805	0,8010	0,01500	0,09500	0,0011	0,4170600	596,10	8,80	585,10	6,70	617,0	40,0	585,1	6,7	1,845	
IZA-1_57.FIN2	173,0	0,941	0,9610	0,02200	0,10050	0,0013	0,4511500	682,00	11,00	617,20	7,40	882,0	41,0	617,2	7,4	9,501	
IZA-1_58.FIN2	353,9	0,886	4,6930	0,06400	0,30550	0,0040	0,6199700	1764,00	11,00	1718,00	19,00	1810,0	20,0	1810,0	20,0	5,083	
IZA-1_59.FIN2	363,0	0,427	1,1530	0,05500	0,11500	0,0032	0,4459500	776,00	26,00	702,00	19,00	962,0	94,0	702,0	19,0	9,536	Rim
IZA-1_59.FIN2	122,4	0,544	1,6920	0,03500	0,16030	0,0025	0,3848200	1007,00	13,00	1008,00	14,00	993,0	41,0	993,0	41,0	1,511	Core
IZA-1_60.FIN2	919,0	1,221	4,4940	0,06100	0,28040	0,0040	0,7594500	1728,00	11,00	1595,00	20,00	1892,0	18,0	1892,0	18,0	15,698	
IZA-1_61.FIN2	169,3	2,740	0,6600	0,02200	0,08210	0,0015	0,3832000	512,00	13,00	508,40	8,70	540,0	69,0	508,4	8,7	0,703	
IZA-1_62.FIN2	821,0	1,761	10,3500	0,49000	0,37100	0,0150	0,9661100	2431,00	43,00	2021,00	69,00	2821,0	21,0	2821,0	21,0	28,359	
IZA-1_63.FIN2	320,0	3,520	1,0400	0,03200	0,10540	0,0014	0,0279550	721,00	16,00	645,80	8,20	939,0	65,0	645,8	8,2	10,430	
IZA-1_64.FIN2	50,3	1,503	4,0070	0,09800	0,26770	0,0056	0,7452600	1629,00	20,00	1527,00	29,00	1765,0	30,0	1765,0	30,0	13,484	
IZA-1_65.FIN2	332,0	0,678	0,3774	0,00860	0,05083	0,0007	0,4173900	324,40	6,30	319,50	4,20	348,0	48,0	319,5	4,2	1,510	

Sample Name:	[U]							207/235		206/238		207/206		Best age		Discordance	Rim/
Grain #	ppm	U/Th	207/235	2σ error	206/238	2σ error	RHO	Age Ma	2σ error	Age (Ma)	2σ error	Age (Ma)	2σ error	(Ma)	2σ error	%	Core
IZA-1_66.FIN2	682,0	2,027	1,4080	0,02800	0,13370	0,0024	0,5526400	892,00	12,00	809,00	14,00	1077,0	35,0	809,0	14,0	9,305	
IZA-1_67.FIN2	246,0	0,662	0,8170	0,01800	0,09400	0,0013	0,4297800	604,00	10,00	578,90	7,90	689,0	43,0	578,9	7,9	4,156	
IZA-1_68.FIN2	61,9	0,464	1,7290	0,04600	0,17110	0,0025	0,3174000	1014,00	17,00	1018,00	14,00	999,0	52,0	999,0	52,0	1,902	
IZA-1_69.FIN2	206,9	3,072	1,7970	0,03100	0,17610	0,0020	0,5001300	1042,00	11,00	1047,00	11,00	1027,0	31,0	1027,0	31,0	1,947	
IZA-1_70.FIN2	187,3	2,020	8,1200	0,17000	0,40960	0,0070	0,6684100	2242,00	18,00	2214,00	33,00	2260,0	27,0	2260,0	27,0	2,035	
IZA-1_71.FIN2	204,0	1,410	0,6850	0,01500	0,08480	0,0011	0,5339700	528,20	9,00	524,60	6,80	540,0	42,0	524,6	6,8	0,682	
IZA-1_72.FIN2	514,0	1,022	0,6260	0,01000	0,07830	0,0009	0,3725800	492,70	6,20	485,90	5,40	509,0	34,0	485,9	5,4	1,380	
IZA-1_73.FIN2	350,0	1,683	0,7330	0,01100	0,08906	0,0010	0,4765200	557,60	6,70	549,90	5,90	574,0	33,0	549,9	5,9	1,381	
IZA-1_74.FIN2	126,1	2,004	1,3410	0,03400	0,14170	0,0021	0,4449500	861,00	15,00	854,00	12,00	870,0	53,0	870,0	53,0	1,839	
IZA-1_75.FIN2	438,1	56,700	5,7600	0,10000	0,34680	0,0052	0,8419100	1938,00	15,00	1918,00	25,00	1964,0	17,0	1964,0	17,0	2,342	
IZA-1_76.FIN2	280,0	1,744	0,3554	0,00880	0,04756	0,0008	0,4168300	308,00	6,60	299,50	4,70	368,0	51,0	299,5	4,7	2,760	
IZA-1_77.FIN2	181,0	2,250	0,7390	0,01600	0,09010	0,0011	0,4556800	561,10	9,10	555,90	6,50	569,0	42,0	555,9	6,5	0,927	
IZA-1_78.FIN2	205,2	0,930	0,5040	0,01200	0,06641	0,0009	0,4690600	413,30	7,80	414,40	5,10	393,0	46,0	414,4	5,1	0,266	
IZA-1_79.FIN2	63,0	1,300	0,7340	0,04200	0,08530	0,0022	0,1706100	558,00	23,00	528,00	13,00	640,0	120,0	528,0	13,0	5,376	
IZA-1_80.FIN2	538,0	0,941	1,2420	0,04100	0,12490	0,0040	0,9380300	814,00	18,00	757,00	23,00	989,0	23,0	757,0	23,0	7,002	
IZA-1_81.FIN2	231,2	1,288	6,9600	0,06800	0,38170	0,0036	0,5942200	2104,90	8,80	2083,00	17,00	2128,0	16,0	2128,0	16,0	2,115	
IZA-1_82.FIN2	137,0	0,680	0,8860	0,02100	0,10710	0,0012	0,2356600	643,00	11,00	655,60	7,00	587,0	52,0	655,6	7,0	1,960	
IZA-1_83.FIN2	263,6	3,449	4,0300	0,14000	0,25790	0,0075	0,9139900	1633,00	29,00	1477,00	38,00	1847,0	26,0	1847,0	26,0	20,032	
IZA-1_84.FIN2	262,0	6,440	0,7740	0,03400	0,09670	0,0031	0,3001600	580,00	19,00	595,00	18,00	520,0	100,0	595,0	18,0	2,586	Rim
IZA-1_84.FIN2	103,3	0,717	3,5660	0,09300	0,26400	0,0050	0,5014200	1538,00	21,00	1509,00	26,00	1591,0	37,0	1591,0	37,0	5,154	Core
IZA-1_85.FIN2	29,4	1,048	0,7800	0,03700	0,09490	0,0019	0,0881030	580,00	21,00	584,00	11,00	540,0	110,0	584,0	11,0	0,690	
IZA-1_86.FIN2	798,0	6,250	0,3561	0,00840	0,04817	0,0008	0,3894900	308,70	6,30	303,20	5,00	356,0	52,0	303,2	5,0	1,782	
IZA-1_87.FIN2	334,0	2,080	1,5810	0,02200	0,16140	0,0020	0,5420400	961,40	8,70	964,00	11,00	954,0	26,0	954,0	26,0	1,048	
IZA-1_88.FIN2	165,0	5,970	0,7050	0,06800	0,08070	0,0046	0,4923200	537,00	40,00	500,00	27,00	670,0	170,0	500,0	27,0	6,890	Rim
IZA-1_88.FIN2	43,5	1,132	1,6430	0,05700	0,16250	0,0028	0,1974800	984,00	22,00	970,00	15,00	1009,0	75,0	1009,0	75,0	3,865	Core
IZA-1_89.FIN2	551,0	3,950	0,9100	0,01200	0,10800	0,0012	0,5908100	656,90	6,50	660,80	7,00	646,0	25,0	660,8	7,0	0,594	
IZA-1_90.FIN2	460,0	3,670	0,5910	0,01100	0,07470	0,0012	0,5490300	470,40	6,80	464,10	7,00	503,0	37,0	464,1	7,0	1,339	
IZA-1_91.FIN2	76,7	1,123	1,6910	0,03800	0,16270	0,0028	0,4267100	1003,00	14,00	971,00	16,00	1067,0	46,0	1067,0	46,0	8,997	
IZA-1_92.FIN2	275,4	1,582	1,4210	0,02800	0,14710	0,0022	0,7132700	895,00	12,00	884,00	12,00	926,0	29,0	926,0	29,0	4,536	
IZA-1_93.FIN2	197,0	2,033	0,8160	0,01700	0,09650	0,0013	0,3639400	604,20	9,50	593,60	7,40	638,0	45,0	593,6	7,4	1,754	
IZA-1_94.FIN2	1440,0	34,500	0,3960	0,02000	0,04640	0,0021	0,5684600	338,00	15,00	292,00	13,00	661,0	97,0	292,0	13,0	13,609	Rim
IZA-1_94.FIN2	728,0	5,870	0,7080	0,01200	0,08930	0,0012	0,4329800	542,60	7,30	551,10	7,00	502,0	35,0	551,1	7,0	1,567	Core
IZA-1_95.FIN2	1307,0	5,110	0,4030	0,01000	0,04330	0,0010	0,5699600	343,10	7,30	273,50	6,30	848,0	48,0	DISC	DISC	20,286	
IZA-1_96.FIN2	116,0	1,053	1,6870	0,02900	0,16600	0,0019	0,3016100	1001,00	11,00	990,00	10,00	1032,0	35,0	1032,0	35,0	4,070	
IZA-1_97.FIN2	555,0	3,449	0,7350	0,01400	0,08550	0,0010	0,5989000	558,20	8,00	529,00	6,10	675,0	33,0	529,0	6,1	5,231	
IZA-1_98.FIN2	250,0	6,160	0,7050	0,01400	0,08713	0,0008	0,2642100	540,40	8,20	538,50	4,50	537,0	43,0	538,5	4,5	0,352	
IZA-1_99.FIN2	260,0	3,156	6,5850	0,08200	0,38690	0,0046	0,5701200	2056,00	11,00	2110,00	21,00	2010,0	20,0	2010,0	20,0	4,975	
IZA-1_100.FIN2	159,5	1,166	0,8310	0,01900	0,09760	0,0016	0,3464900	612,00	10,00	600,20	9,10	654,0	50,0	600,2	9,1	1,928	
IZA-1_102.FIN2	762,0	2,651	0,5931	0,00840	0,07495	0,0008	0,5222600	472,30	5,30	465,90	4,70	505,0	29,0	465,9	4,7	1,355	
IZA-1_103.FIN2	401,0	3,010	0,4171	0,00790	0,05533	0,0006	0,2658200	354,10	5,50	347,10	3,80	390,0	43,0	347,1	3,8	1,977	
IZA-1_104.FIN2	243,0	0,648	0,8940	0,01700	0,09515	0,0009	0,0285560	646,90	8,90	585,80	5,20	861,0	43,0	585,8	5,2	9,445	
IZA-1_105.FIN2	354,0	1,560	0,7600	0,02200	0,09030	0,0012	0,2645600	571,00	12,00	557,30	7,10	619,0	61,0	557,3	7,1	2,399	
IZA-1_106.FIN2	785,0	1,376	0,3561	0,00600	0,04876	0,0005	0,4997800	308,90	4,50	306,90	3,20	319,0	33,0	306,9	3,2	0,647	
IZA-1_107.FIN2	192,9	2,868	5,1020	0,05900	0,32740	0,0027	0,5488900	1836,20	9,90	1825,00	13,00	1847,0	19,0	1847,0	19,0	1,191	
IZA-1_109.FIN2	222,5	1,076	0,8920	0,01900	0,10280	0,0016	0,4912700	645,90	10,00	630,60	9,00	696,0	39,0	630,6	9,0	2,233	
IZA-1_110.FIN2	189,0	1,980	0,7500	0,01800	0,09150	0,0013	0,2826000	566,00	10,00	564,00	7,60	553,0	54,0	564,0	7,6	0,353	
IZA-1_111.FIN2	207,0	0,790	0,9390	0,02000	0,10270	0,0017	0,4891400	670,00	10,00	630,00	10,00	810,0	40,0	630,0	10,0	5,970	

Sample Name:	[U]							207/235		206/238		207/206		Best age		Discordance	Rim/
Grain #	ppm	U/Th	207/235	2σ error	206/238	2σ error	RHO	Age Ma	2σ error	Age (Ma)	2σ error	Age (Ma)	2σ error	(Ma)	2σ error	%	Core
IZA-1_112.FIN2	1288,0	12,150	0,6117	0,00790	0,07441	0,0010	0,5457400	484,20	5,00	462,60	5,90	586,0	27,0	462,6	5,9	4,461	
IZA-1_113.FIN2	155,2	1,171	1,5670	0,02600	0,16100	0,0017	0,3422900	956,00	10,00	961,80	9,30	939,0	34,0	939,0	34,0	2,428	
IZA-1_114.FIN2	207,0	1,710	4,8920	0,07300	0,30250	0,0035	0,6431700	1798,00	12,00	1703,00	17,00	1906,0	21,0	1906,0	21,0	10,651	
IZA-1_115.FIN2	129,0	1,582	10,0600	0,18000	0,45270	0,0068	0,7758900	2438,00	17,00	2406,00	30,00	2463,0	20,0	2463,0	20,0	2,314	
IZA-1_116.FIN2	89,1	1,820	0,6860	0,04000	0,08400	0,0018	0,2610500	526,00	24,00	520,00	10,00	510,0	120,0	520,0	10,0	1,141	Rim
IZA-1_116.FIN2	98,2	1,143	4,0600	0,23000	0,25300	0,0140	0,9124600	1632,00	47,00	1451,00	71,00	1889,0	42,0	1889,0	42,0	23,187	Core
IZA-1_117.FIN2	203,0	2,910	1,0270	0,05100	0,09670	0,0028	0,6679900	713,00	26,00	595,00	16,00	1109,0	76,0	DISC	DISC	16,550	
IZA-1_118.FIN2	338,0	1,689	0,3476	0,00870	0,04897	0,0007	0,3527600	302,10	6,50	308,20	4,10	249,0	50,0	308,2	4,1	2,019	
IZA-1_119.FIN2	237,0	1,230	3,8540	0,04800	0,27760	0,0030	0,5947200	1602,00	10,00	1579,00	15,00	1632,0	20,0	1632,0	20,0	3,248	
IZA-1_120.FIN2	198,3	4,400	0,6260	0,01500	0,07980	0,0010	0,2058400	492,20	9,10	494,60	6,20	462,0	53,0	494,6	6,2	0,488	
IZA-1_121.FIN2	189,5	1,026	0,8480	0,01900	0,09860	0,0014	0,5075000	621,00	10,00	607,20	8,60	673,0	41,0	607,2	8,6	2,222	
IZA-1_122.FIN2	321,0	1,204	0,8320	0,01600	0,10120	0,0011	0,4139400	613,00	9,10	621,30	6,40	586,0	40,0	621,3	6,4	1,354	
IZA-1_123.FIN2	812,0	0,716	0,8790	0,01300	0,10360	0,0011	0,5476900	640,40	7,00	635,20	6,50	657,0	28,0	635,2	6,5	0,812	
IZA-1_124.FIN2	378,0	2,428	0,3620	0,01100	0,04905	0,0009	0,1542900	313,50	8,50	308,70	5,30	335,0	73,0	308,7	5,3	1,531	
IZA-1_125.FIN2	250,0	0,476	1,7760	0,03500	0,16080	0,0022	0,2498700	1037,00	13,00	1011,00	12,00	1089,0	42,0	1089,0	42,0	7,163	
IZA-1_126.FIN2	354,0	1,560	0,7860	0,01700	0,09480	0,0015	0,4015900	587,10	9,70	583,60	8,80	579,0	44,0	583,6	8,8	0,596	
IZA-1_127.FIN2	827,0	2,590	10,4140	0,07600	0,45510	0,0031	0,6752100	2472,50	6,60	2417,00	14,00	2513,0	9,9	2513,0	9,9	3,820	
IZA-1_128.FIN2	258,2	1,990	0,5660	0,01300	0,07430	0,0011	0,3811600	455,90	8,70	461,90	6,30	411,0	50,0	461,9	6,3	1,316	
IZA-1_129.FIN2	269,3	2,592	7,1620	0,07900	0,38950	0,0042	0,6887900	2130,50	9,90	2123,00	19,00	2144,0	15,0	2144,0	15,0	0,979	
IZA-1_130.FIN2	301,0	12,700	0,6860	0,01200	0,08730	0,0011	0,3823400	529,40	7,30	539,40	6,40	480,0	38,0	539,4	6,4	1,889	
IZA-1_131.FIN2	460,0	5,570	0,3719	0,00750	0,04934	0,0007	0,3812400	320,50	5,50	310,40	4,20	398,0	45,0	310,4	4,2	3,151	
IZA-1_132.FIN2	75,2	1,134	0,7120	0,02200	0,08770	0,0012	0,2042300	543,00	13,00	542,00	7,00	524,0	68,0	542,0	7,0	0,184	
IZA-1_133.FIN2	781,0	8,880	0,7793	0,00950	0,09589	0,0009	0,5731400	584,60	5,40	590,20	5,10	557,0	22,0	590,2	5,1	0,958	
IZA-5_1.FIN2	247,2	0,568	0,3524	0,00510	0,04874	0,0005	0,5309800	491,00	13,00	471,10	6,00	575,0	66,0	471,1	6,0	4,053	
IZA-5_2.FIN2	486,0	7,220	1,3500	0,01800	0,14400	0,0015	0,5146900	481,50	9,30	481,10	5,80	477,0	57,0	481,1	5,8	0,083	
IZA-5_3.FIN2	248,6	0,963	1,6390	0,02400	0,16320	0,0022	0,7868600	759,00	11,00	762,40	8,80	744,0	46,0	762,4	8,8	0,448	
IZA-5_4.FIN2	599,0	0,986	0,7860	0,01100	0,09440	0,0012	0,5564200	582,90	6,80	567,90	6,20	637,0	34,0	567,9	6,2	2,573	
IZA-5_5.FIN2	750,0	0,922	1,6650	0,02200	0,16960	0,0018	0,5843000	368,70	3,90	368,60	2,70	364,0	28,0	368,6	2,7	0,027	
IZA-5_7.FIN2	88,9	0,654	0,6980	0,02200	0,08420	0,0019	0,5602700	1835,00	11,00	1823,00	16,00	1844,0	20,0	1844,0	20,0	1,139	
IZA-5_8.FIN2	618,0	1,460	0,9610	0,01400	0,10967	0,0010	0,4373700	329,60	3,80	328,80	2,80	332,0	33,0	328,8	2,8	0,243	
IZA-5_9.FIN2	576,0	2,214	0,5920	0,01500	0,07500	0,0012	0,6255500	319,80	4,30	315,70	2,80	336,0	35,0	315,7	2,8	1,282	
IZA-5_10.FIN2	648,0	1,374	1,1180	0,02300	0,12430	0,0024	0,7146400	329,90	4,00	327,80	2,60	338,0	33,0	327,8	2,6	0,637	
IZA-5_11.FIN2	117,3	2,134	1,8970	0,03700	0,18360	0,0028	0,6775600	498,00	11,00	493,70	6,10	498,0	62,0	493,7	6,1	0,863	
IZA-5_12.FIN2	147,2	1,491	9,7900	0,16000	0,41150	0,0054	0,8070800	652,00	12,00	644,50	6,40	671,0	53,0	644,5	6,4	1,150	
IZA-5_13.FIN2	265,0	1,018	0,8900	0,01700	0,10440	0,0017	0,5392300	490,70	8,10	485,40	4,80	499,0	45,0	485,4	4,8	1,080	
IZA-5_15.FIN2	84,4	0,730	0,9159	0,00940	0,10715	0,0010	0,5700000	656,00	12,00	641,50	7,80	694,0	53,0	641,5	7,8	2,210	
IZA-5_16.FIN2	1253,0	5,390	3,2750	0,05300	0,22720	0,0035	0,8470100	548,60	5,40	531,50	6,30	614,0	32,0	531,5	6,3	3,117	
IZA-5_18.FIN2	486,0	8,380	5,8970	0,09000	0,35020	0,0050	0,7037200	1206,00	13,00	1208,00	13,00	1203,0	29,0	1203,0	29,0	0,416	
IZA-5_19.FIN2	193,0	1,252	0,6730	0,01900	0,07780	0,0019	0,5773600	1623,00	16,00	1541,00	23,00	1722,0	24,0	1722,0	24,0	10,511	Rim
IZA-5_19.FIN2	174,2	8,140	1,3960	0,02800	0,13820	0,0018	0,5004000	495,00	12,00	504,70	5,70	441,0	62,0	504,7	5,7	1,960	Core
IZA-5_20.FIN2	506,0	1,265	1,9020	0,04100	0,17980	0,0025	0,3856000	349,80	6,00	339,00	3,30	416,0	41,0	339,0	3,3	3,087	
IZA-5_21.FIN2	401,0	0,976	0,7050	0,01700	0,08700	0,0010	0,1980900	353,10	9,30	347,10	5,20	378,0	69,0	347,1	5,2	1,699	
IZA-5_22.FIN2	141,0	1,384	6,2690	0,06500	0,34990	0,0037	0,7571200	393,00	12,00	382,80	5,60	448,0	79,0	382,8	5,6	2,595	
IZA-5_23.FIN2	466,0	4,810	9,8200	0,19000	0,38640	0,0074	0,7253500	305,50	5,50	304,40	2,60	301,0	43,0	304,4	2,6	0,360	
IZA-5_24.FIN2	318,0	4,500	0,5987	0,00840	0,07727	0,0008	0,3554900	482,40	6,10	484,10	4,20	462,0	36,0	484,1	4,2	0,352	
IZA-5_25.FIN2	1987,0	22,120	0,7610	0,04700	0,08870	0,0051	0,7227200	658,00	12,00	620,90	9,90	784,0	42,0	620,9	9,9	5,638	Rim

Sample Name:	[U]							207/235		206/238		207/206		Best age		Discordance	Rim/
Grain #	ppm	U/Th	207/235	2σ error	206/238	2σ error	RHO	Age Ma	2σ error	Age (Ma)	2σ error	Age (Ma)	2σ error	(Ma)	2σ error	%	Core
IZA-5_25.FIN2	357,0	1,500	7,3280	0,09300	0,38400	0,0047	0,8528400	2495,00	24,00	2465,00	36,00	2506,0	22,0	2506,0	22,0	1,636	Core
IZA-5_26.FIN2	450,0	47,000	1,1890	0,02200	0,13150	0,0015	0,3780600	575,00	23,00	569,00	18,00	590,0	110,0	569,0	18,0	1,043	
IZA-5_27.FIN2	220,0	1,860	0,5040	0,05200	0,05960	0,0044	0,5302700	1030,70	8,50	1029,50	8,50	1030,0	25,0	1030,0	25,0	0,049	Rim
IZA-5_27.FIN2	151,0	2,035	1,3280	0,02700	0,13580	0,0021	0,6293500	626,00	11,00	624,60	6,60	612,0	52,0	624,6	6,6	0,224	Core
IZA-5_28.FIN2	237,0	1,518	0,8720	0,01500	0,10350	0,0013	0,6582500	2692,80	6,50	2679,00	15,00	2702,0	11,0	2702,0	11,0	0,851	
IZA-5_29.FIN2	76,8	1,411	0,7630	0,02300	0,08910	0,0020	0,5048900	659,00	13,00	639,20	7,70	715,0	61,0	639,2	7,7	3,005	
IZA-5_30.FIN2	86,6	2,740	0,3375	0,00490	0,04664	0,0004	0,4260400	507,00	18,00	451,50	8,40	740,0	100,0	451,5	8,4	10,947	
IZA-5_31.FIN2	84,8	1,074	0,8080	0,01900	0,09690	0,0021	0,4670200	642,00	13,00	617,70	7,20	710,0	60,0	617,7	7,2	3,785	
IZA-5_32.FIN2	232,0	1,160	1,6510	0,02500	0,16760	0,0018	0,5486300	1958,90	8,40	1942,00	13,00	1977,0	15,0	1977,0	15,0	1,770	
IZA-5_33.FIN2	284,0	1,617	0,8820	0,01700	0,10240	0,0011	0,4476500	623,30	7,30	603,70	4,90	696,0	30,0	603,7	4,9	3,145	
IZA-5_34.FIN2	131,6	1,758	0,8820	0,01100	0,10320	0,0010	0,5965800	492,30	8,90	482,80	5,20	516,0	52,0	482,8	5,2	1,930	
IZA-5_35.FIN2	405,0	11,300	0,8960	0,01500	0,10460	0,0018	0,4444400	488,00	11,00	482,60	6,80	502,0	64,0	482,6	6,8	1,107	
IZA-5_36.FIN2	226,3	2,235	0,7400	0,01500	0,09050	0,0014	0,4856800	549,00	10,00	536,20	6,30	592,0	53,0	536,2	6,3	2,332	
IZA-5_37.FIN2	593,0	20,800	0,4088	0,00960	0,05100	0,0012	0,4807200	378,00	26,00	360,00	24,00	480,0	190,0	360,0	24,0	4,762	
IZA-5_38.FIN2	750,0	1,958	0,8000	0,01300	0,09630	0,0013	0,4895200	2068,60	7,60	1907,00	16,00	2230,0	12,0	2230,0	12,0	14,484	
IZA-5_39.FIN2	144,2	0,862	16,4500	0,23000	0,54090	0,0078	0,7390100	1046,00	14,00	1052,00	12,00	1019,0	40,0	1019,0	40,0	3,238	
IZA-5_40.FIN2	130,7	0,780	1,5880	0,01900	0,16090	0,0014	0,3301300	625,40	9,70	626,50	6,30	604,0	46,0	626,5	6,3	0,176	
IZA-5_41.FIN2	159,7	1,622	1,6490	0,08900	0,15500	0,0047	0,4406000	585,00	11,00	583,10	6,40	568,0	51,0	583,1	6,4	0,325	
IZA-5_42.FIN2	162,0	3,170	0,8080	0,01600	0,09700	0,0012	0,5100200	456,00	10,00	441,70	5,10	502,0	58,0	441,7	5,1	3,136	
IZA-5_43.FIN2	286,0	1,425	11,9200	0,17000	0,47110	0,0068	0,7348100	582,50	8,50	574,50	5,00	594,0	41,0	574,5	5,0	1,373	
IZA-5_44.FIN2	281,0	1,421	1,8560	0,02000	0,18130	0,0016	0,4344800	2569,00	14,00	2541,00	29,00	2588,0	16,0	2588,0	16,0	1,816	
IZA-5_45.FIN2	1786,0	2,310	1,7670	0,02000	0,17230	0,0016	0,7298300	325,50	3,40	312,50	3,20	412,0	22,0	312,5	3,2	3,994	
IZA-5_46.FIN2	157,0	1,763	1,3160	0,02000	0,13970	0,0014	0,6248500	562,00	21,00	542,00	13,00	630,0	120,0	542,0	13,0	3,559	
IZA-5_47.FIN2	413,0	1,311	1,6960	0,04000	0,16790	0,0026	0,4372900	374,00	6,80	370,00	4,00	377,0	43,0	370,0	4,0	1,070	
IZA-5_48.FIN2	500,0	2,602	0,8200	0,01500	0,09890	0,0012	0,3894400	604,00	12,00	610,00	11,00	569,0	51,0	610,0	11,0	0,993	
IZA-5_49.FIN2	222,0	1,471	1,5770	0,02500	0,15690	0,0015	0,4014200	304,90	7,50	301,40	4,50	315,0	57,0	301,4	4,5	1,148	
IZA-5_50.FIN2	113,7	1,657	4,6010	0,04700	0,30660	0,0027	0,6526300	303,20	8,70	308,90	4,50	246,0	71,0	308,9	4,5	1,880	
IZA-5_51.FIN2	317,0	1,970	5,4900	0,07500	0,34320	0,0035	0,8151600	310,70	5,90	308,40	3,30	304,0	49,0	308,4	3,3	0,740	
IZA-5_52.FIN2	208,9	0,840	0,7780	0,01500	0,09400	0,0010	0,3002700	654,60	7,50	654,70	5,70	649,0	32,0	654,7	5,7	0,015	
IZA-5_53.FIN2	557,0	0,732	4,9500	0,08100	0,29740	0,0045	0,6916600	580,90	8,40	585,00	8,50	554,0	40,0	585,0	8,5	0,706	
IZA-5_54.FIN2	126,9	1,182	1,6120	0,01900	0,15980	0,0015	0,4435500	302,80	8,80	302,10	3,50	295,0	71,0	302,1	3,5	0,231	
IZA-5_55.FIN2	511,0	4,680	0,6842	0,00930	0,08417	0,0009	0,6273800	636,30	7,00	628,10	5,60	652,0	31,0	628,1	5,6	1,289	
IZA-5_56.FIN2	1136,0	12,800	0,7630	0,03500	0,09150	0,0049	0,8522500	350,00	16,00	333,00	18,00	460,0	110,0	333,0	18,0	4,857	Rim
IZA-5_56.FIN2	308,0	1,984	1,6320	0,02500	0,16260	0,0018	0,6156100	657,00	10,00	672,70	9,30	602,0	50,0	672,7	9,3	2,390	Core
IZA-5_57.FIN2	1550,0	1,783	0,8850	0,03000	0,10500	0,0018	0,3734300	336,10	3,80	330,60	2,90	359,0	25,0	330,6	2,9	1,636	
IZA-5_58.FIN2	486,0	2,480	13,0000	0,15000	0,50850	0,0058	0,7568200	495,00	12,00	498,00	11,00	472,0	57,0	498,0	11,0	0,606	
IZA-5_59.FIN2	323,0	3,390	1,1330	0,01800	0,12530	0,0013	0,3132700	506,80	9,90	514,90	6,10	471,0	51,0	514,9	6,1	1,598	
IZA-5_60.FIN2	916,0	1,930	0,7807	0,00710	0,09412	0,0008	0,5313500	2527,00	11,00	2530,00	27,00	2523,0	14,0	2523,0	14,0	0,277	
IZA-5_61.FIN2	281,0	3,350	0,3620	0,00600	0,05004	0,0006	0,4118100	623,00	19,00	602,00	11,00	673,0	82,0	602,0	11,0	3,371	
IZA-5_62.FIN2	71,1	1,122	1,3340	0,03200	0,14080	0,0028	0,7229600	775,00	19,00	749,00	12,00	832,0	66,0	749,0	12,0	3,355	
IZA-5_63.FIN2	77,5	1,049	0,5490	0,02800	0,06780	0,0026	0,7881400	1643,00	17,00	1603,00	18,00	1692,0	32,0	1692,0	32,0	5,260	Rim
IZA-5_63.FIN2	295,0	0,806	1,1120	0,01500	0,12350	0,0015	0,4377700	644,40	9,60	658,60	6,30	590,0	42,0	658,6	6,3	2,204	Core
IZA-5_64.FIN2	40,4	0,559	0,8910	0,01400	0,10660	0,0015	0,5505200	967,00	18,00	979,00	12,00	925,0	65,0	925,0	65,0	5,838	
IZA-5_65.FIN2	150,5	1,386	1,1550	0,01300	0,12680	0,0014	0,6810700	540,20	9,90	534,40	6,20	551,0	54,0	534,4	6,2	1,074	
IZA-5_66.FIN2	1131,0	1,688	4,8860	0,07600	0,32400	0,0046	0,8825500	637,50	6,40	613,30	5,50	721,0	28,0	613,3	5,5	3,706	
IZA-5_67.FIN2	388,1	0,842	1,7960	0,02600	0,17380	0,0020	0,4074200	749,30	7,50	741,90	5,80	769,0	30,0	741,9	5,8	0,988	
IZA-5_69.FIN2	1498,0	2,940	0,5800	0,01600	0,07260	0,0016	0,6672700	306,40	9,10	300,00	5,40	351,0	74,0	300,0	5,4	2,089	Rim

Sample Name:	[U]							207/235		206/238		207/206		Best age		Discordance	Rim/
Grain #	ppm	U/Th	207/235	2σ error	206/238	2σ error	RHO	Age Ma	2σ error	Age (Ma)	2σ error	Age (Ma)	2σ error	(Ma)	2σ error	%	Core
IZA-5_69.FIN2	1853,0	6,970	1,2030	0,03900	0,13220	0,0030	0,2871200	327,40	4,40	315,40	4,60	419,0	45,0	315,4	4,6	3,665	Core
IZA-5_70.FIN2	67,8	0,818	1,6830	0,03000	0,16660	0,0026	0,7173500	598,00	14,00	583,90	8,00	634,0	73,0	583,9	8,0	2,358	
IZA-5_71.FIN2	1054,0	8,840	0,3609	0,00750	0,04970	0,0006	0,2925100	317,50	3,70	317,60	3,70	318,0	30,0	317,6	3,7	0,031	
IZA-5_72.FIN2	106,3	0,796	14,5000	1,90000	0,51700	0,0290	0,1045500	2331,00	12,00	2360,00	21,00	2305,0	25,0	2305,0	25,0	2,386	
IZA-5_73.FIN2	118,8	1,151	0,8070	0,01000	0,09690	0,0008	0,2795700	837,00	13,00	820,00	10,00	881,0	49,0	820,0	10,0	2,031	
IZA-5_74.FIN2	319,7	1,266	0,9040	0,01200	0,10630	0,0012	0,5973600	1963,50	8,70	1895,00	14,00	2034,0	16,0	2034,0	16,0	6,834	
IZA-5_75.FIN2	417,0	1,941	0,9680	0,02500	0,10790	0,0016	0,4899100	474,00	8,50	464,70	5,30	509,0	45,0	464,7	5,3	1,962	
IZA-5_77.FIN2	457,0	2,050	0,7760	0,01500	0,09300	0,0012	0,5144200	1018,70	9,90	1012,00	10,00	1041,0	25,0	1041,0	25,0	2,786	
IZA-5_78.FIN2	561,9	5,650	2,3350	0,02200	0,20360	0,0017	0,5980400	629,70	5,60	622,30	5,20	651,0	29,0	622,3	5,2	1,175	
IZA-5_79.FIN2	377,0	9,520	12,5700	0,20000	0,50820	0,0086	0,8755100	624,30	6,50	628,70	5,40	599,0	31,0	628,7	5,4	0,705	
IZA-5_80.FIN2	207,7	1,670	14,5300	0,17000	0,49180	0,0053	0,9141200	592,00	22,00	553,00	14,00	720,0	110,0	553,0	14,0	6,588	
IZA-5_81.FIN2	148,5	1,105	0,5952	0,00710	0,07700	0,0007	0,5038400	635,00	11,00	622,30	7,40	679,0	49,0	622,3	7,4	2,000	
IZA-5_82.FIN2	606,0	10,890	0,3769	0,00920	0,04851	0,0009	0,6177900	319,80	6,40	315,70	4,30	338,0	46,0	315,7	4,3	1,282	
IZA-5_83.FIN2	662,0	1,667	0,5618	0,00760	0,07161	0,0006	0,4723400	574,60	5,00	577,00	4,30	554,0	25,0	577,0	4,3	0,418	
IZA-5_84.FIN2	431,0	8,810	0,8850	0,01500	0,10167	0,0009	0,3370200	661,90	7,00	664,00	6,80	649,0	31,0	664,0	6,8	0,317	
IZA-5_85.FIN2	379,5	1,462	1,0150	0,01500	0,11610	0,0013	0,5659900	609,30	6,80	609,30	5,00	598,0	31,0	609,3	5,0	0,000	
IZA-5_86.FIN2	399,0	93,000	6,0380	0,07200	0,35250	0,0039	0,7243700	351,00	23,00	315,30	6,20	560,0	160,0	315,3	6,2	10,171	
IZA-5_87.FIN2	65,6	1,863	0,7690	0,01100	0,09169	0,0011	0,7006400	722,00	16,00	688,00	10,00	814,0	69,0	688,0	10,0	4,709	
IZA-5_88.FIN2	563,0	1,692	0,7039	0,00880	0,08704	0,0008	0,4476700	300,40	4,80	301,20	2,40	274,0	43,0	301,2	2,4	0,266	
IZA-5_89.FIN2	87,8	3,081	0,8105	0,00890	0,09755	0,0009	0,5939200	663,00	14,00	643,70	7,90	708,0	61,0	643,7	7,9	2,911	
IZA-5_90.FIN2	92,8	1,673	0,9820	0,02000	0,11260	0,0024	0,8187900	659,00	13,00	662,50	7,80	621,0	58,0	662,5	7,8	0,531	
IZA-5_91.FIN2	160,0	1,487	1,0060	0,01400	0,11417	0,0009	0,4425500	540,00	11,00	536,70	5,80	528,0	57,0	536,7	5,8	0,611	
IZA-5_92.FIN2	466,0	2,020	0,3506	0,00740	0,04885	0,0005	0,2212000	584,10	7,10	582,60	5,90	578,0	34,0	582,6	5,9	0,257	
IZA-5_93.FIN2	280,0	2,460	0,5814	0,00740	0,07466	0,0008	0,6795400	541,00	14,00	538,60	8,90	537,0	80,0	538,6	8,9	0,444	
IZA-5_94.FIN2	880,0	2,260	0,3270	0,00750	0,04582	0,0007	0,4580900	487,70	9,80	480,60	6,80	509,0	55,0	480,6	6,8	1,456	Rim
IZA-5_94.FIN2	111,9	0,701	0,7323	0,00950	0,09140	0,0010	0,5696700	612,00	17,00	616,00	13,00	585,0	89,0	616,0	13,0	0,654	Core
IZA-5_95.FIN2	256,0	0,588	1,5320	0,03200	0,15920	0,0025	0,7374400	1952,10	7,10	1951,00	12,00	1953,0	14,0	1953,0	14,0	0,102	
IZA-5_96.FIN2	0,0	0,000	4,9600	0,07700	0,31640	0,0042	0,7676500	0,00	0,00	0,00	0,00	0,0	0,0	#DIV/0!	#DIV/0!	#DIV/0!	
IZA-5_97.FIN2	353,0	1,132	1,1160	0,02200	0,11150	0,0021	0,7589400	472,00	6,30	473,80	4,20	463,0	40,0	473,8	4,2	0,381	
IZA-5_98.FIN2	216,1	0,774	0,7120	0,01200	0,08948	0,0009	0,3743300	1021,90	9,80	1008,20	7,70	1049,0	28,0	1049,0	28,0	3,889	
IZA-5_99.FIN2	66,1	2,670	9,1600	0,13000	0,40990	0,0051	0,8450700	677,00	14,00	663,70	9,00	704,0	64,0	663,7	9,0	1,965	
IZA-5_100.FIN2	962,0	28,700	1,8350	0,02500	0,17780	0,0021	0,5243400	658,20	8,70	654,10	8,00	673,0	35,0	654,1	8,0	0,623	
IZA-5_101.FIN2	460,0	0,547	0,4820	0,00710	0,06380	0,0006	0,5004300	1709,00	13,00	1625,00	15,00	1812,0	23,0	1812,0	23,0	10,320	
IZA-5_102.FIN2	741,0	1,514	1,6240	0,02200	0,16350	0,0022	0,5770000	702,00	5,90	693,80	5,50	740,0	22,0	693,8	5,5	1,168	
IZA-5_103.FIN2	80,0	1,489	0,8480	0,01200	0,10100	0,0010	0,5697700	573,00	15,00	562,50	8,00	611,0	77,0	562,5	8,0	1,832	
IZA-5_104.FIN2	207,1	1,155	1,8170	0,02600	0,17450	0,0018	0,4432100	1044,90	8,70	1031,40	8,10	1078,0	26,0	1078,0	26,0	4,323	
IZA-5_105.FIN2	619,0	0,694	0,8990	0,04500	0,10420	0,0039	0,0755240	327,50	4,60	321,80	2,80	362,0	36,0	321,8	2,8	1,740	Rim
IZA-5_105.FIN2	51,6	1,607	1,4440	0,01800	0,15000	0,0016	0,5393300	768,00	15,00	756,50	9,40	766,0	66,0	756,5	9,4	1,497	Core
IZA-5_106.FIN2	3,0	-0,380	0,8570	0,01400	0,10230	0,0013	0,7365200	147,00	62,00	75,00	13,00	-6700,0	4100,0	DISC	DISC	48,980	
IZA-5_107.FIN2	303,0	5,460	0,3515	0,00640	0,04857	0,0006	0,4271400	1066,50	7,30	1069,30	7,40	1059,0	22,0	1059,0	22,0	0,973	
IZA-5_108.FIN2	413,0	2,234	1,0010	0,01600	0,11680	0,0014	0,5885600	540,00	13,00	541,00	11,00	546,0	55,0	541,0	11,0	0,185	
IZA-5_109.FIN2	103,3	1,323	0,6020	0,00730	0,07460	0,0007	0,4003300	647,00	12,00	624,20	7,70	709,0	54,0	624,2	7,7	3,524	
IZA-5_110.FIN2	838,0	2,449	1,7070	0,01900	0,16970	0,0018	0,6589800	346,00	5,80	346,30	3,80	336,0	39,0	346,3	3,8	0,087	
IZA-5_111.FIN2	765,0	2,080	20,2800	0,16000	0,61060	0,0050	0,7854300	1870,30	8,90	1886,00	16,00	1847,0	16,0	1847,0	16,0	2,112	
IZA-5_112.FIN2	485,0	2,528	0,8110	0,02400	0,09030	0,0029	0,4226400	312,90	4,80	309,00	3,30	330,0	44,0	309,0	3,3	1,246	Rim
IZA-5_112.FIN2	318,0	1,287	1,1900	0,02000	0,13070	0,0017	0,4917000	305,70	6,30	303,50	2,80	310,0	53,0	303,5	2,8	0,720	Core
IZA-5_113.FIN2	424,0	1,914	0,3561	0,00630	0,04963	0,0006	0,4402900	570,40	5,80	566,20	4,20	579,0	28,0	566,2	4,2	0,736	

Sample Name:	[U]							207/235		206/238		207/206		Best age		Discordance	Rim/
Grain #	ppm	U/Th	207/235	2σ error	206/238	2σ error	RHO	Age Ma	2σ error	Age (Ma)	2σ error	Age (Ma)	2σ error	(Ma)	2σ error	%	Core
IZA-5_114.FIN2	70,3	2,220	0,8190	0,02000	0,09840	0,0016	0,5757700	797,00	20,00	787,00	12,00	802,0	76,0	787,0	12,0	1,255	
IZA-5_115.FIN2	401,8	0,660	1,5290	0,02600	0,15640	0,0019	0,5014900	645,20	6,90	636,90	5,30	660,0	31,0	636,9	5,3	1,286	
IZA-5_116.FIN2	164,2	0,942	0,8960	0,01100	0,10720	0,0010	0,6115500	2452,00	21,00	2196,00	34,00	2670,0	22,0	2670,0	22,0	17,753	
IZA-5_117.FIN2	568,0	6,650	0,6540	0,02600	0,08180	0,0020	0,3238100	481,00	11,00	467,40	5,00	548,0	48,0	467,4	5,0	2,827	Rim
IZA-5_117.FIN2	678,0	7,010	4,1400	0,12000	0,24810	0,0056	0,5646800	513,20	8,50	503,80	6,60	562,0	41,0	503,8	6,6	1,832	Core
IZA-5_118.FIN2	25,6	1,649	0,7530	0,01200	0,09220	0,0011	0,5000200	1994,00	20,00	1947,00	22,00	2035,0	39,0	2035,0	39,0	4,324	
IZA-5_119.FIN2	175,6	2,420	0,8020	0,01200	0,09790	0,0011	0,6940000	465,90	9,10	457,80	4,70	484,0	57,0	457,8	4,7	1,739	
IZA-5_120.FIN2	3780,0	0,418	1,1300	0,01800	0,12040	0,0016	0,7875700	310,00	5,70	300,40	6,30	379,0	38,0	300,4	6,3	3,097	
IZA-5_121.FIN2	304,0	0,903	0,8470	0,01600	0,10220	0,0012	0,2410200	605,80	8,10	602,20	5,60	604,0	39,0	602,2	5,6	0,594	
IZA-5_122.FIN2	604,0	4,560	13,7100	0,23000	0,50960	0,0089	0,8855400	587,80	5,60	582,00	4,90	604,0	25,0	582,0	4,9	0,987	
IZA-5_123.FIN2	183,0	1,246	1,3250	0,01600	0,13640	0,0014	0,6389500	573,10	8,20	571,10	5,40	567,0	42,0	571,1	5,4	0,349	
IZA-5_124.FIN2	1104,0	32,100	1,7870	0,02300	0,17340	0,0021	0,5188400	339,70	7,60	340,60	5,70	326,0	55,0	340,6	5,7	0,265	
IZA-5_125.FIN2	81,0	0,884	0,9310	0,01100	0,10870	0,0011	0,7353300	1984,00	24,00	1882,00	37,00	2072,0	56,0	2072,0	56,0	9,170	
IZA-5_126.FIN2	157,0	3,670	0,4910	0,01000	0,06510	0,0010	0,8468500	2708,00	11,00	2683,00	21,00	2731,0	17,0	2731,0	17,0	1,758	
IZA-5_127.FIN2	54,8	0,448	1,8820	0,05600	0,16850	0,0033	0,7059500	2585,00	12,00	2481,00	24,00	2667,0	20,0	2667,0	20,0	6,974	
IZA-5_128.FIN2	395,0	4,770	0,7030	0,01600	0,08780	0,0019	0,8338600	602,30	7,90	595,90	5,60	618,0	39,0	595,9	5,6	1,063	
IZA-5_129.FIN2	199,0	15,300	0,3680	0,00890	0,05007	0,0007	0,3749300	681,00	13,00	667,30	8,00	712,0	54,0	667,3	8,0	2,012	
IZA-5_131.FIN2	99,0	1,812	0,9990	0,01500	0,11500	0,0010	0,4604400	1406,00	11,00	1393,00	12,00	1438,0	29,0	1438,0	29,0	3,129	
IZA-5_132.FIN2	414,1	1,384	0,9499	0,00980	0,11150	0,0011	0,5581500	488,80	6,60	476,50	4,40	544,0	36,0	476,5	4,4	2,516	
IZA-5_133.FIN2	263,0	0,578	0,8050	0,01100	0,09805	0,0009	0,3408800	1869,10	8,00	1852,00	11,00	1890,0	17,0	1890,0	17,0	2,011	
IZA-5_134.FIN2	227,0	1,654	5,2260	0,04900	0,32000	0,0036	0,5911300	566,40	9,20	564,70	5,00	564,0	47,0	564,7	5,0	0,300	
IZA-5_135.FIN2	449,0	7,480	0,3521	0,00510	0,04774	0,0005	0,4440900	487,30	6,20	489,10	5,20	468,0	38,0	489,1	5,2	0,369	
IZA-5_136.FIN2	28,0	-2,000	0,7210	0,02100	0,08900	0,0011	0,1828200	695,00	70,00	742,00	41,00	530,0	280,0	742,0	41,0	6,763	
IZA-5_137.FIN2	167,0	10,130	1,6640	0,02000	0,16570	0,0016	0,4683700	657,90	8,40	601,40	7,10	908,0	25,0	601,4	7,1	8,588	
IZA-5_139.FIN2	146,0	1,780	5,6600	0,11000	0,33930	0,0058	0,8100800	1970,00	12,00	1961,00	17,00	1983,0	22,0	1983,0	22,0	1,109	
IZA-5_140.FIN2	1740,0	19,600	0,8720	0,04700	0,10130	0,0044	0,7104400	358,40	7,40	352,20	8,00	401,0	62,0	352,2	8,0	1,730	Rim
IZA-5_140.FIN2	118,0	1,272	3,2400	0,12000	0,21450	0,0063	0,8386500	634,00	14,00	628,50	8,30	653,0	70,0	628,5	8,3	0,868	Core
IZA-5_141.FIN2	304,0	2,000	0,1209	0,00600	0,00345	0,0002	0,2359100	326,90	7,20	325,10	4,10	335,0	62,0	325,1	4,1	0,551	Rim
IZA-5_141.FIN2	465,0	15,000	0,3480	0,00690	0,04854	0,0005	0,3587700	307,20	9,10	297,20	5,70	407,0	78,0	297,2	5,7	3,255	Core
IZA-5_142.FIN2	129,0	3,196	1,4180	0,02100	0,14190	0,0016	0,5451700	473,00	15,00	451,70	7,00	562,0	87,0	451,7	7,0	4,503	
IZA-5_143.FIN2	408,8	3,777	0,3725	0,00560	0,05126	0,0006	0,5065500	771,10	6,20	764,20	5,80	794,0	22,0	764,2	5,8	0,895	
IZA-5_144.FIN2	70,0	1,757	0,6630	0,01100	0,08251	0,0007	0,2751000	633,00	14,00	637,30	8,00	593,0	65,0	637,3	8,0	0,679	
IZA-5_145.FIN2	299,0	1,321	0,7790	0,01600	0,09454	0,0009	0,2936700	319,30	6,60	317,40	3,60	318,0	52,0	317,4	3,6	0,595	
IZA-5_146.FIN2	300,0	8,060	0,8840	0,03500	0,10430	0,0026	0,7469100	492,00	13,00	471,10	5,90	579,0	69,0	471,1	5,9	4,248	Rim
IZA-5_146.FIN2	289,0	1,594	1,3560	0,02600	0,14440	0,0019	0,4067600	301,10	5,80	300,20	3,50	310,0	52,0	300,2	3,5	0,299	Core
IZA-5_147.FIN2	187,1	0,775	0,7840	0,01300	0,09560	0,0010	0,4714600	997,30	8,80	994,40	9,10	1000,0	30,0	1000,0	30,0	0,560	
IZA-5_148.FIN2	8,8	-0,020	0,6400	0,01300	0,08005	0,0009	0,3499300	283,00	46,00	68,30	7,60	2200,0	2000,0	DISC	DISC	75,866	
IZA-5_149.FIN2	15500,0	1,180	1,5160	0,01800	0,14600	0,0018	0,7379600	280,00	16,00	69,40	7,00	2940,0	150,0	DISC	DISC	75,214	
IZA-5_150.FIN2	486,0	1,683	0,8410	0,05000	0,10120	0,0028	0,7822400	315,60	7,10	297,20	3,50	431,0	57,0	297,2	3,5	5,830	Rim
IZA-5_150.FIN2	81,0	2,630	10,5800	0,17000	0,43560	0,0055	0,6366800	811,00	14,00	785,90	8,00	860,0	53,0	785,9	8,0	3,095	Core
IZA-3_1.FIN2	206,0	1,440	0,8680	0,01400	0,10390	0,0011	0,4749000	633,60	7,50	636,90	6,30	635,0	31,0	636,9	6,3	0,521	
IZA-3_2.FIN2	177,1	2,028	1,6270	0,02500	0,16270	0,0020	0,4618900	979,50	9,60	972,00	11,00	1008,0	27,0	1008,0	27,0	3,571	
IZA-3_4.FIN2	359,0	1,258	0,3580	0,00710	0,04958	0,0006	0,4219600	311,60	5,60	311,90	3,50	318,0	42,0	311,9	3,5	0,096	
IZA-3_5.FIN2	245,8	1,300	1,0710	0,01500	0,11990	0,0011	0,3826300	738,00	7,10	730,10	6,20	768,0	27,0	730,1	6,2	1,070	
IZA-3_6.FIN2	96,3	1,270	0,7560	0,01600	0,09220	0,0010	0,1675500	570,30	9,20	568,40	6,10	575,0	49,0	568,4	6,1	0,333	
IZA-3_7.FIN2	197,7	0,874	6,7250	0,07600	0,37630	0,0037	0,6751300	2075,00	10,00	2058,00	17,00	2096,0	15,0	2096,0	15,0	1,813	

Sample Name:	[U]							207/235		206/238		207/206		Best age		Discordance	Rim/
Grain #	ppm	U/Th	207/235	2σ error	206/238	2σ error	RHO	Age Ma	2σ error	Age (Ma)	2σ error	Age (Ma)	2σ error	(Ma)	2σ error	%	Core
IZA-3_8.FIN2	249,0	3,590	1,0120	0,02100	0,11600	0,0016	0,4418300	709,00	10,00	707,20	9,10	727,0	42,0	707,2	9,1	0,254	
IZA-3_9.FIN2	482,0	0,639	7,7180	0,08400	0,40530	0,0046	0,8251900	2197,80	9,80	2193,00	21,00	2207,0	12,0	2207,0	12,0	0,634	
IZA-3_10.FIN2	165,0	2,150	0,7160	0,02600	0,08860	0,0023	0,5828300	547,00	16,00	547,00	14,00	554,0	67,0	547,0	14,0	0,000	
IZA-3_11.FIN2	111,0	1,347	10,3700	0,14000	0,44900	0,0054	0,6781000	2467,00	12,00	2389,00	24,00	2527,0	17,0	2527,0	17,0	5,461	
IZA-3_12.FIN2	120,6	1,311	1,2700	0,20000	0,11050	0,0031	0,5291200	810,00	71,00	675,00	18,00	1210,0	210,0	DISC	DISC	16,667	Rim
IZA-3_12.FIN2	135,5	1,459	1,5460	0,03400	0,15330	0,0019	0,3172300	947,00	14,00	919,00	11,00	1000,0	41,0	1000,0	41,0	8,100	Core
IZA-3_13.FIN2	1295,0	5,212	5,6970	0,07000	0,32560	0,0037	0,7732500	1932,50	9,80	1820,00	17,00	2059,0	15,0	2059,0	15,0	11,608	
IZA-3_14.FIN2	534,0	9,740	0,6077	0,00830	0,07606	0,0007	0,4564700	481,60	5,30	472,50	4,40	534,0	26,0	472,5	4,4	1,890	
IZA-3_15.FIN2	171,0	1,786	0,9720	0,01800	0,11280	0,0011	0,1902900	687,80	9,10	688,60	6,50	678,0	39,0	688,6	6,5	0,116	
IZA-3_16.FIN2	109,9	1,620	1,0060	0,01700	0,11420	0,0011	0,1502500	705,60	8,50	697,00	6,40	722,0	37,0	697,0	6,4	1,219	
IZA-3_17.FIN2	346,0	6,840	0,6195	0,00930	0,07876	0,0006	0,3741800	488,90	5,80	488,70	3,70	481,0	31,0	488,7	3,7	0,041	
IZA-3_18.FIN2	281,0	2,368	0,3557	0,00680	0,04922	0,0005	0,2912000	309,20	5,20	309,70	2,80	305,0	42,0	309,7	2,8	0,162	
IZA-3_19.FIN2	85,4	3,393	1,4930	0,03400	0,15290	0,0025	0,5171600	926,00	14,00	917,00	14,00	936,0	43,0	936,0	43,0	2,030	
IZA-3_20.FIN2	669,0	2,006	2,3690	0,06600	0,18890	0,0049	0,8590800	1232,00	20,00	1115,00	27,00	1443,0	28,0	1443,0	28,0	22,730	Rim
IZA-3_20.FIN2	285,4	1,326	3,6340	0,06400	0,26510	0,0043	0,7105300	1556,00	14,00	1515,00	22,00	1606,0	24,0	1606,0	24,0	5,666	Core
IZA-3_21.FIN2	69,7	0,904	0,8700	0,02200	0,10140	0,0012	0,2402700	633,00	12,00	622,30	6,80	651,0	54,0	622,3	6,8	1,690	
IZA-3_22.FIN2	1433,0	4,125	0,6400	0,01500	0,06680	0,0011	0,5587300	501,70	9,50	417,00	6,50	903,0	42,0	DISC	DISC	16,883	
IZA-3_23.FIN2	111,9	1,572	1,4400	0,02600	0,14640	0,0018	0,4448300	906,00	11,00	880,00	10,00	967,0	35,0	967,0	35,0	8,997	
IZA-3_24.FIN2	441,3	7,340	0,6800	0,11000	0,34810	0,0060	0,8219500	1987,00	16,00	1925,00	29,00	2049,0	19,0	2049,0	19,0	6,052	
IZA-3_25.FIN2	461,0	2,660	0,9740	0,01600	0,11410	0,0019	0,6185200	690,40	8,60	696,00	11,00	670,0	32,0	696,0	11,0	0,811	
IZA-3_26.FIN2	42,0	1,097	1,4540	0,05800	0,15050	0,0029	0,4175800	908,00	24,00	904,00	16,00	894,0	78,0	904,0	78,0	1,119	
IZA-3_27.FIN2	367,0	1,114	0,9420	0,01000	0,10882	0,0009	0,3913600	673,20	5,40	665,80	5,00	699,0	24,0	665,8	5,0	1,099	
IZA-3_28.FIN2	137,6	0,834	1,7040	0,02600	0,16640	0,0017	0,4225900	1008,60	9,90	992,30	9,50	1037,0	30,0	1037,0	30,0	4,311	
IZA-3_29.FIN2	1025,0	6,570	0,5120	0,02600	0,06100	0,0018	0,6695200	419,00	18,00	382,00	11,00	631,0	82,0	382,0	11,0	8,831	Rim
IZA-3_29.FIN2	352,0	0,900	0,8130	0,01400	0,09660	0,0012	0,6689900	603,10	7,90	594,40	7,00	625,0	28,0	594,4	7,0	1,443	Core
IZA-3_30.FIN2	288,3	4,290	0,5497	0,00990	0,07057	0,0007	0,3954300	444,40	6,50	439,60	4,40	461,0	38,0	439,6	4,4	1,080	
IZA-3_31.FIN2	259,0	0,847	10,0290	0,08800	0,45090	0,0043	0,7148500	2436,70	8,10	2399,00	19,00	2469,0	12,0	2469,0	12,0	2,835	
IZA-3_32.FIN2	445,3	1,440	0,6140	0,00850	0,07800	0,0007	0,4958000	485,50	5,40	484,10	4,40	490,0	28,0	484,1	4,4	0,288	
IZA-3_33.FIN2	771,0	2,140	0,3486	0,00520	0,04812	0,0005	0,4141500	303,40	3,90	302,90	3,20	314,0	33,0	302,9	3,2	0,165	
IZA-3_34.FIN2	342,0	1,582	0,8620	0,01300	0,09750	0,0013	0,6805200	631,60	7,50	599,60	7,40	740,0	26,0	599,6	7,4	5,066	
IZA-3_35.FIN2	222,8	5,600	0,5940	0,01000	0,07645	0,0007	0,3684800	472,40	6,30	474,80	4,30	463,0	35,0	474,8	4,3	0,508	
IZA-3_36.FIN2	188,9	3,694	3,8140	0,03700	0,28720	0,0021	0,5516300	1594,70	7,90	1627,00	11,00	1555,0	15,0	1555,0	15,0	4,630	
IZA-3_37.FIN2	96,2	0,298	0,7780	0,01600	0,09520	0,0010	0,0994910	584,30	8,90	586,30	5,90	566,0	50,0	586,3	5,9	0,342	
IZA-3_38.FIN2	709,0	1,459	0,3516	0,00470	0,04813	0,0004	0,4145100	305,70	3,50	303,00	2,20	323,0	28,0	303,0	2,2	0,883	
IZA-3_39.FIN2	165,0	1,910	0,6010	0,01400	0,07780	0,0010	0,4744000	477,60	9,00	482,90	6,00	438,0	46,0	482,9	6,0	1,110	
IZA-3_40.FIN2	11,3	-1,800	0,9900	0,13000	0,10770	0,0055	0,1294900	686,00	71,00	658,00	32,00	710,0	290,0	658,0	32,0	4,082	
IZA-3_41.FIN2	192,8	1,980	0,9700	0,01300	0,11191	0,0009	0,2461500	687,60	6,80	683,70	5,50	696,0	30,0	683,7	5,5	0,567	
IZA-3_42.FIN2	1053,0	2,183	1,2050	0,02200	0,11830	0,0018	0,6637300	805,00	11,00	721,00	10,00	1035,0	28,0	721,0	10,0	10,435	
IZA-3_43.FIN2	129,5	0,958	0,8690	0,01500	0,10263	0,0010	0,3376700	633,60	8,20	629,70	5,70	640,0	35,0	629,7	5,7	0,616	
IZA-3_44.FIN2	130,0	0,967	0,7620	0,01800	0,09210	0,0012	0,2861600	574,00	11,00	569,00	6,50	585,0	51,0	569,0	6,5	0,871	
IZA-3_45.FIN2	142,8	22,000	0,8190	0,04700	0,09470	0,0049	0,3312600	606,00	27,00	583,00	29,00	770,0	200,0	583,0	29,0	3,795	Rim
IZA-3_45.FIN2	191,8	0,804	1,6440	0,02800	0,16250	0,0017	0,4386300	986,00	11,00	970,30	9,60	1009,0	36,0	1009,0	36,0	3,835	Core
IZA-3_46.FIN2	225,0	1,180	1,8230	0,02200	0,17780	0,0018	0,6031400	1052,50	7,90	1054,60	9,80	1042,0	20,0	1042,0	20,0	1,209	
IZA-3_47.FIN2	161,1	0,915	0,8620	0,01900	0,10190	0,0013	0,6409900	630,00	10,00	625,60	7,50	633,0	41,0	625,6	7,5	0,698	
IZA-3_48.FIN2	161,0	1,914	1,7220	0,02900	0,16510	0,0021	0,4954500	1015,00	11,00	985,00	12,00	1069,0	32,0	1069,0	32,0	7,858	
IZA-3_49.FIN2	224,0	1,820	0,8130	0,02000	0,09820	0,0012	0,3454900	603,00	11,00	603,50	7,00	581,0	52,0	603,5	7,0	0,083	Rim
IZA-3_49.FIN2	138,0	1,448	1,7440	0,04300	0,16840	0,0030	0,6921200	1022,00	16,00	1003,00	16,00	1051,0	37,0	1051,0	37,0	4,567	Core

Sample Name:	[U]							207/235		206/238		207/206		Best age		Discordance	Rim/
Grain #	ppm	U/Th	207/235	2σ error	206/238	2σ error	RHO	Age Ma	2σ error	Age (Ma)	2σ error	Age (Ma)	2σ error	(Ma)	2σ error	%	Core
IZA-3_50.FIN2	199,8	0,544	0,8030	0,01400	0,09660	0,0011	0,5556500	597,30	7,70	594,40	6,70	598,0	33,0	594,4	6,7	0,486	
IZA-3_51.FIN2	180,2	1,828	6,4980	0,08000	0,35580	0,0042	0,7860100	2043,00	11,00	1961,00	20,00	2121,0	14,0	2121,0	14,0	7,544	
IZA-3_52.FIN2	294,0	5,810	6,1950	0,07700	0,34910	0,0040	0,7580400	2002,00	11,00	1929,00	19,00	2070,0	15,0	2070,0	15,0	6,812	
IZA-3_53.FIN2	133,1	0,725	6,6400	0,12000	0,36950	0,0059	0,7422100	2065,00	16,00	2026,00	28,00	2091,0	22,0	2091,0	22,0	3,109	
IZA-3_54.FIN2	386,0	2,810	0,7643	0,00910	0,09344	0,0008	0,3971600	575,90	5,20	575,80	4,80	565,0	25,0	575,8	4,8	0,017	
IZA-3_55.FIN2	370,9	0,975	2,8340	0,05200	0,21990	0,0041	0,4819200	1364,00	14,00	1281,00	22,00	1487,0	36,0	1487,0	36,0	13,853	
IZA-3_56.FIN2	366,0	1,005	0,8970	0,01100	0,10629	0,0010	0,4682800	649,50	6,10	651,10	5,60	634,0	26,0	651,1	5,6	0,246	
IZA-3_57.FIN2	376,0	7,110	0,6200	0,01000	0,07797	0,0007	0,6064200	489,20	6,30	483,90	4,30	501,0	36,0	483,9	4,3	1,083	
IZA-3_58.FIN2	112,4	1,180	0,8430	0,01800	0,10049	0,0010	0,3038900	620,00	10,00	617,20	5,60	615,0	45,0	617,2	5,6	0,452	
IZA-3_59.FIN2	295,7	3,810	0,9610	0,01300	0,11120	0,0013	0,4566000	683,30	6,90	679,60	7,70	691,0	28,0	679,6	7,7	0,541	
IZA-3_60.FIN2	255,8	0,632	2,0010	0,02200	0,18900	0,0016	0,4939400	1115,00	7,30	1115,90	8,40	1110,0	20,0	1110,0	20,0	0,532	
IZA-3_61.FIN2	301,0	2,352	3,8700	0,06600	0,25120	0,0040	0,6796700	1606,00	14,00	1445,00	21,00	1826,0	27,0	1826,0	27,0	20,865	
IZA-3_62.FIN2	123,6	1,311	0,8360	0,01500	0,09830	0,0010	0,2031900	615,90	8,50	604,50	5,90	649,0	42,0	604,5	5,9	1,851	
IZA-3_63.FIN2	166,5	1,130	0,8150	0,02100	0,09700	0,0013	0,4495800	605,00	12,00	596,80	7,60	627,0	50,0	596,8	7,6	1,355	
IZA-3_64.FIN2	61,6	0,578	0,8620	0,03100	0,09980	0,0017	0,2330600	628,00	17,00	613,00	10,00	660,0	78,0	613,0	10,0	2,389	
IZA-3_65.FIN2	3100,0	4,840	0,3350	0,01100	0,04420	0,0012	0,8991900	292,60	8,30	278,70	7,50	432,0	29,0	278,7	7,5	4,751	Rim
IZA-3_65.FIN2	1989,0	2,970	0,8060	0,01600	0,08840	0,0021	0,6661800	600,10	8,80	546,00	12,00	811,0	37,0	546,0	12,0	9,015	Core
IZA-3_66.FIN2	29,5	0,619	1,6860	0,04200	0,16240	0,0021	0,2974000	1000,00	15,00	970,00	12,00	1049,0	51,0	1049,0	51,0	7,531	
IZA-3_67.FIN2	119,0	0,454	0,7960	0,01700	0,09830	0,0011	0,2919200	594,10	9,60	604,40	6,40	550,0	47,0	604,4	6,4	1,734	
IZA-3_68.FIN2	261,4	3,374	0,7230	0,01300	0,08890	0,0011	0,4099800	551,50	7,80	549,10	6,50	568,0	40,0	549,1	6,5	0,435	
IZA-3_69.FIN2	472,0	1,565	0,8813	0,00960	0,10482	0,0008	0,4940800	641,20	5,20	642,50	4,70	638,0	21,0	642,5	4,7	0,203	
IZA-3_70.FIN2	126,4	1,614	0,9330	0,01800	0,10730	0,0011	0,4185200	667,70	9,60	657,00	6,50	693,0	39,0	657,0	6,5	1,603	
IZA-3_71.FIN2	554,0	2,184	0,6430	0,01000	0,08020	0,0009	0,4924600	503,70	6,20	497,30	5,60	533,0	32,0	497,3	5,6	1,271	
IZA-3_72.FIN2	697,0	3,760	0,3896	0,00500	0,05276	0,0005	0,4836800	333,80	3,60	331,40	3,00	341,0	26,0	331,4	3,0	0,719	
IZA-3_73.FIN2	860,0	147,000	0,3500	0,01800	0,04820	0,0010	0,4768100	305,00	14,00	303,70	6,40	306,0	99,0	303,7	6,4	0,426	Rim
IZA-3_73.FIN2	156,4	1,853	1,1070	0,03000	0,12140	0,0015	0,5133800	755,00	14,00	738,30	8,90	792,0	51,0	738,3	8,9	2,212	Core
IZA-3_74.FIN2	198,0	0,837	0,8400	0,01700	0,09880	0,0013	0,4396600	618,10	9,30	607,10	7,50	651,0	42,0	607,1	7,5	1,780	
IZA-3_75.FIN2	73,9	0,756	1,2400	0,03300	0,13440	0,0017	0,4075600	817,00	15,00	812,60	9,70	814,0	51,0	812,6	9,7	0,539	
IZA-3_76.FIN2	186,0	1,007	6,0200	0,13000	0,35810	0,0077	0,8709900	1978,00	20,00	1972,00	36,00	1974,0	20,0	1974,0	20,0	0,101	
IZA-3_77.FIN2	408,0	0,799	0,8980	0,01200	0,10470	0,0012	0,6058300	649,60	6,30	641,80	6,80	669,0	23,0	641,8	6,8	1,201	
IZA-3_78.FIN2	258,0	1,440	1,7610	0,03200	0,16800	0,0024	0,5984600	1030,00	12,00	1001,00	13,00	1082,0	30,0	1082,0	30,0	7,486	
IZA-3_79.FIN2	833,0	2,083	0,6016	0,00690	0,07513	0,0007	0,5492500	478,40	4,50	466,90	4,10	521,0	22,0	466,9	4,1	2,404	
IZA-3_80.FIN2	63,2	0,465	1,0860	0,02700	0,12200	0,0017	0,0548210	746,00	14,00	742,00	10,00	733,0	61,0	742,0	10,0	0,536	
IZA-3_81.FIN2	508,0	0,863	0,9130	0,01100	0,10538	0,0009	0,5197200	658,00	5,70	645,80	5,50	687,0	22,0	645,8	5,5	1,854	
IZA-3_82.FIN2	171,4	1,260	1,2900	0,02000	0,13880	0,0014	0,4852100	841,00	8,70	837,90	7,70	848,0	26,0	837,9	7,7	0,369	
IZA-3_83.FIN2	310,0	1,273	1,8400	0,03300	0,17900	0,0030	0,0816230	1060,00	12,00	1062,00	17,00	1050,0	47,0	1050,0	47,0	1,143	
IZA-3_84.FIN2	175,4	2,193	0,9210	0,01400	0,10540	0,0010	0,3900100	661,90	7,60	646,00	6,10	698,0	35,0	646,0	6,1	2,402	
IZA-3_85.FIN2	185,0	6,070	0,6030	0,01400	0,07626	0,0009	0,3231000	479,30	8,40	473,70	5,40	479,0	47,0	473,7	5,4	1,168	
IZA-3_86.FIN2	132,0	1,990	0,8820	0,04800	0,09700	0,0039	0,4100400	640,00	25,00	596,00	23,00	740,0	120,0	596,0	23,0	6,875	
IZA-3_88.FIN2	259,4	11,670	5,3770	0,09400	0,33490	0,0052	0,7245600	1880,00	15,00	1862,00	25,00	1896,0	22,0	1896,0	22,0	1,793	
IZA-3_89.FIN2	899,0	2,002	0,3668	0,00530	0,05005	0,0005	0,5977600	317,00	3,90	314,80	3,00	319,0	26,0	314,8	3,0	0,694	
IZA-3_90.FIN2	106,2	0,519	0,8540	0,02300	0,10150	0,0012	0,1489800	627,00	12,00	623,80	6,80	613,0	57,0	623,8	6,8	0,510	
IZA-3_91.FIN2	162,0	1,308	1,4860	0,03900	0,15190	0,0027	0,5043900	923,00	16,00	911,00	15,00	945,0	48,0	945,0	48,0	3,598	
IZA-3_92.FIN2	125,0	1,950	6,0300	0,17000	0,35950	0,0097	0,9160300	1975,00	25,00	1976,00	46,00	1982,0	21,0	1982,0	21,0	0,303	
IZA-3_93.FIN2	763,0	3,448	0,9410	0,01200	0,10480	0,0011	0,4253700	673,00	6,50	642,50	6,20	773,0	27,0	642,5	6,2	4,532	
IZA-3_94.FIN2	241,0	0,587	0,8130	0,01200	0,09767	0,0007	0,1580000	603,40	6,80	600,70	4,30	607,0	34,0	600,7	4,3	0,447	
IZA-3_95.FIN2	539,0	0,753	0,8571	0,00910	0,10056	0,0009	0,5062000	628,70	5,10	617,60	5,10	670,0	21,0	617,6	5,1	1,766	

Sample Name:	[U]							207/235		206/238		207/206		Best age		Discordance	Rim/
Grain #	ppm	U/Th	207/235	2σ error	206/238	2σ error	RHO	Age Ma	2σ error	Age (Ma)	2σ error	Age (Ma)	2σ error	(Ma)	2σ error	%	Core
IZA-3_96.FIN2	374,8	1,388	12,3400	0,11000	0,45150	0,0046	0,7766100	2629,60	8,70	2401,00	20,00	2808,0	11,0	2808,0	11,0	14,494	
IZA-3_97.FIN2	412,0	3,499	0,9250	0,01000	0,10959	0,0010	0,4973300	664,40	5,40	670,20	5,60	643,0	22,0	670,2	5,6	0,873	
IZA-3_98.FIN2	112,5	0,798	0,7530	0,01900	0,09230	0,0011	0,3047700	568,00	11,00	568,90	6,70	554,0	54,0	568,9	6,7	0,158	
IZA-3_99.FIN2	163,0	2,280	1,6400	0,02200	0,16590	0,0017	0,5101100	985,50	8,80	989,00	9,30	976,0	25,0	976,0	25,0	1,332	
IZA-3_100.FIN2	272,0	5,480	0,6450	0,01200	0,08220	0,0010	0,6488800	504,50	7,60	509,30	6,10	489,0	33,0	509,3	6,1	0,951	
IZA-3_101.FIN2	472,0	1,999	0,3564	0,00540	0,04888	0,0005	0,4635700	309,80	4,10	307,60	3,00	328,0	32,0	307,6	3,0	0,710	
IZA-3_102.FIN2	485,0	1,596	4,8280	0,04200	0,31600	0,0026	0,7536300	1790,00	7,50	1770,00	13,00	1816,0	11,0	1816,0	11,0	2,533	
IZA-3_103.FIN2	2661,0	45,000	0,8276	0,00650	0,09752	0,0006	0,6205500	612,00	3,60	599,80	3,60	660,0	13,0	599,8	3,6	1,993	
IZA-3_104.FIN2	967,0	7,630	0,8974	0,00970	0,10550	0,0011	0,6923100	649,90	5,20	646,70	6,20	667,0	18,0	646,7	6,2	0,492	
IZA-3_105.FIN2	379,0	1,810	0,5832	0,00810	0,07586	0,0007	0,4001200	466,00	5,20	471,30	3,90	435,0	29,0	471,3	3,9	1,137	
IZA-3_106.FIN2	168,0	1,166	0,8550	0,01400	0,10240	0,0011	0,3206000	626,50	7,90	628,60	6,70	617,0	39,0	628,6	6,7	0,335	
IZA-3_107.FIN2	35,5	4,200	15,0200	0,25000	0,54900	0,0080	0,7051000	2812,00	16,00	2818,00	33,00	2809,0	20,0	2809,0	20,0	0,320	
IZA-3_108.FIN2	252,0	5,710	0,6370	0,01100	0,08155	0,0010	0,5130100	499,50	6,90	505,30	5,80	466,0	34,0	505,3	5,8	1,161	
IZA-3_109.FIN2	196,6	1,163	15,4500	0,20000	0,56390	0,0063	0,8178400	2842,00	12,00	2882,00	26,00	2812,0	12,0	2812,0	12,0	2,489	
IZA-3_110.FIN2	318,4	0,414	1,3210	0,01700	0,13970	0,0012	0,2597100	854,40	7,40	843,10	7,00	877,0	28,0	843,1	7,0	1,323	
IZA-3_111.FIN2	374,0	2,113	1,1230	0,01800	0,12360	0,0016	0,6186100	763,20	8,70	751,20	9,40	794,0	28,0	751,2	9,4	1,572	
IZA-3_112.FIN2	164,0	1,366	0,9030	0,01400	0,10720	0,0011	0,3025200	653,30	7,80	656,60	6,30	632,0	35,0	656,6	6,3	0,505	
IZA-3_113.FIN2	333,0	1,399	0,7978	0,00860	0,09664	0,0009	0,4210300	595,20	4,90	594,60	5,20	595,0	24,0	594,6	5,2	0,101	
IZA-3_115.FIN2	288,0	6,630	0,6369	0,00990	0,07972	0,0006	0,3641600	499,60	6,20	494,40	3,60	512,0	33,0	494,4	3,6	1,041	
IZA-3_116.FIN2	104,0	2,000	0,7120	0,01700	0,08890	0,0012	0,3905200	544,20	9,80	549,10	6,90	512,0	49,0	549,1	6,9	0,900	
IZA-3_117.FIN2	110,9	0,753	4,9820	0,07100	0,32000	0,0042	0,5371500	1817,00	13,00	1789,00	21,00	1845,0	25,0	1845,0	25,0	3,035	
IZA-3_118.FIN2	302,0	4,430	0,7860	0,01200	0,09502	0,0009	0,4485300	588,70	7,10	585,10	5,40	589,0	31,0	585,1	5,4	0,612	
IZA-3_119.FIN2	764,0	8,480	0,7407	0,00750	0,08956	0,0009	0,5576700	563,00	4,40	552,90	5,30	595,0	21,0	552,9	5,3	1,794	
IZA-3_120.FIN2	6,0	-0,200	0,3800	0,07500	0,01450	0,0015	0,1000600	302,00	54,00	92,90	9,20	1980,0	490,0	DISC	DISC	69,238	
IZA-3_121.FIN2	314,0	3,390	0,6800	0,01200	0,08133	0,0008	0,4039600	525,60	7,40	504,00	5,00	600,0	36,0	504,0	5,0	4,110	
IZA-3_122.FIN2	703,0	2,976	0,3425	0,00550	0,04670	0,0004	0,3802800	298,80	4,20	294,20	2,70	314,0	35,0	294,2	2,7	1,539	
IZA-3_123.FIN2	247,1	1,054	0,7799	0,00930	0,09544	0,0008	0,3242800	585,60	5,40	587,60	4,70	561,0	27,0	587,6	4,7	0,342	
IZA-3_124.FIN2	96,6	1,458	1,3110	0,02300	0,14070	0,0015	0,2933700	850,00	10,00	848,60	8,50	835,0	37,0	848,6	8,5	0,165	
IZA-3_125.FIN2	38,4	0,442	1,8550	0,04200	0,18000	0,0023	0,2237100	1063,00	15,00	1066,00	13,00	1036,0	49,0	1036,0	49,0	2,896	
IZA-3_126.FIN2	496,5	1,501	0,7975	0,00880	0,09635	0,0008	0,4285300	595,00	5,00	592,90	4,90	587,0	23,0	592,9	4,9	0,353	
IZA-3_127.FIN2	242,5	0,763	0,8290	0,01200	0,09821	0,0010	0,3139500	613,30	6,50	603,80	5,60	624,0	32,0	603,8	5,6	1,549	
IZA-3_128.FIN2	233,0	2,770	1,4190	0,01700	0,14980	0,0013	0,5363700	896,90	7,40	899,80	7,30	874,0	23,0	874,0	23,0	2,952	
IZA-3_129.FIN2	359,0	1,213	0,8640	0,01200	0,10310	0,0011	0,6119700	632,20	6,80	632,30	6,50	618,0	25,0	632,3	6,5	0,016	
IZA-3_130.FIN2	723,0	1,790	0,8951	0,00900	0,10566	0,0008	0,5528800	648,60	4,80	647,40	4,80	643,0	18,0	647,4	4,8	0,185	
IZA-3_131.FIN2	172,0	0,926	0,8100	0,01500	0,09670	0,0011	0,4314900	600,90	8,60	595,00	6,20	611,0	36,0	595,0	6,2	0,982	
IZA-3_132.FIN2	255,0	1,996	2,7100	0,06800	0,21710	0,0047	0,8770800	1329,00	19,00	1266,00	25,00	1425,0	28,0	1425,0	28,0	11,158	
IZA-3_133.FIN2	598,0	1,317	1,7660	0,03100	0,17100	0,0031	0,5935100	1032,00	12,00	1017,00	17,00	1061,0	33,0	1061,0	33,0	4,147	
IZA-3_134.FIN2	1209,0	6,050	0,9440	0,02100	0,10830	0,0016	0,6411000	674,00	11,00	662,60	9,50	701,0	30,0	662,6	9,5	1,691	Rim
IZA-3_134.FIN2	247,1	2,272	2,2930	0,03200	0,18190	0,0022	0,6214400	1209,50	9,90	1077,00	12,00	1433,0	24,0	1433,0	24,0	24,843	Core
IZA-3_135.FIN2	174,3	1,048	1,7480	0,02400	0,16940	0,0022	0,6478300	1024,90	8,70	1008,00	12,00	1056,0	22,0	1056,0	22,0	4,545	
IZA-3_136.FIN2	395,0	6,190	0,6143	0,00860	0,07741	0,0008	0,5193500	485,70	5,40	480,60	4,90	513,0	29,0	480,6	4,9	1,050	
IZA-3_137.FIN2	194,5	5,850	0,6450	0,01100	0,08043	0,0008	0,2886100	504,30	6,50	498,60	4,50	519,0	36,0	498,6	4,5	1,130	
IZA-3_138.FIN2	343,5	1,503	1,0940	0,01300	0,12243	0,0010	0,3967600	749,90	6,40	744,50	5,50	764,0	23,0	744,5	5,5	0,720	
IZA-3_140.FIN2	187,0	42,000	0,4310	0,05100	0,04930	0,0040	0,4579600	362,00	36,00	310,00	25,00	690,0	230,0	310,0	25,0	14,365	Rim
IZA-3_140.FIN2	76,1	0,932	9,3800	0,14000	0,44150	0,0074	0,5372900	2378,00	12,00	2356,00	33,00	2389,0	24,0	2389,0	24,0	1,381	Core
IZA-3_141.FIN2	937,0	2,490	0,7252	0,00730	0,08813	0,0007	0,5635200	553,90	4,40	544,40	4,00	594,0	18,0	544,4	4,0	1,715	
IZA-3_142.FIN2	77,6	0,867	0,8550	0,02200	0,10240	0,0012	0,3076900	625,00	12,00	628,50	6,80	591,0	54,0	628,5	6,8	0,560	

Sample Name:	[U]							207/235		206/238		207/206		Best age		Discordance	Rim/
Grain #	ppm	U/Th	207/235	2σ error	206/238	2σ error	RHO	Age Ma	2σ error	Age (Ma)	2σ error	Age (Ma)	2σ error	(Ma)	2σ error	%	Core
IZA-3_143.FIN2	337,0	1,453	0,7880	0,01200	0,09580	0,0008	0,3928800	589,50	6,50	589,70	4,70	581,0	29,0	589,7	4,7	0,034	
IZA-3_144.FIN2	596,0	2,239	0,3574	0,00700	0,04725	0,0006	0,5228700	310,40	5,30	297,60	3,70	396,0	39,0	297,6	3,7	4,124	
IZA-3_145.FIN2	240,0	1,079	1,3670	0,02700	0,13390	0,0023	0,5302800	874,00	12,00	810,00	13,00	1040,0	37,0	810,0	13,0	7,323	
IZA-3_146.FIN2	114,5	1,051	0,7390	0,01700	0,08520	0,0011	0,2466300	560,00	10,00	526,80	6,50	689,0	54,0	526,8	6,5	5,929	
IZA-3_147.FIN2	463,0	6,530	0,9110	0,01200	0,10660	0,0010	0,4074200	657,10	6,30	652,90	5,80	673,0	29,0	652,9	5,8	0,639	
IZA-3_148.FIN2	515,0	0,896	1,7790	0,02500	0,16960	0,0017	0,4737000	1036,90	9,20	1009,60	9,40	1093,0	25,0	1093,0	25,0	7,630	
IZA-3_149.FIN2	567,0	3,330	3,1510	0,05100	0,22520	0,0028	0,7495300	1444,00	12,00	1309,00	15,00	1648,0	19,0	1648,0	19,0	20,570	
IZA-3_150.FIN2	478,0	45,800	0,6661	0,00830	0,08313	0,0007	0,4806200	517,80	5,10	514,70	4,20	524,0	24,0	514,7	4,2	0,599	
IZA-10_1.FIN2	1277,0	2,504	4,9890	0,06700	0,29900	0,0047	0,7234300	1816,00	11,00	1685,00	23,00	1939,0	18,0	1939,0	18,0	13,100	
IZA-10_2.FIN2	577,0	1,482	0,8750	0,01200	0,10190	0,0010	0,5085300	637,70	6,60	625,60	5,80	661,0	25,0	625,6	5,8	1,897	
IZA-10_3.FIN2	154,0	3,770	0,7630	0,01300	0,09177	0,0009	0,3782800	574,70	7,70	565,90	5,10	596,0	36,0	565,9	5,1	1,531	
IZA-10_4.FIN2	16,1	2,370	1,7580	0,06100	0,15870	0,0027	0,1843800	1026,00	24,00	949,00	15,00	1154,0	77,0	1154,0	77,0	17,764	
IZA-10_5.FIN2	414,0	1,374	3,4990	0,05700	0,23730	0,0040	0,7790000	1525,00	13,00	1377,00	21,00	1730,0	21,0	1730,0	21,0	20,405	
IZA-10_6.FIN2	150,9	1,150	12,0000	0,14000	0,48220	0,0057	0,7978000	2603,00	11,00	2536,00	25,00	2637,0	13,0	2637,0	13,0	3,830	
IZA-10_7.FIN2	69,3	1,030	1,6400	0,03900	0,15800	0,0018	0,2833700	982,00	15,00	945,20	9,80	1036,0	47,0	1036,0	47,0	8,764	
IZA-10_8.FIN2	585,0	3,540	9,8600	0,13000	0,42770	0,0066	0,6619200	2420,00	12,00	2294,00	30,00	2514,0	20,0	2514,0	20,0	8,751	
IZA-10_9.FIN2	114,4	1,421	1,5410	0,02400	0,15400	0,0018	0,4712600	945,10	9,60	923,10	9,80	981,0	31,0	981,0	31,0	5,902	
IZA-10_10.FIN2	644,0	11,900	0,6130	0,01300	0,07640	0,0012	0,4563500	484,80	8,30	474,70	7,30	514,0	39,0	474,7	7,3	2,083	Rim
IZA-10_10.FIN2	648,0	0,786	1,1990	0,02200	0,13370	0,0021	0,8206400	801,00	11,00	809,00	12,00	762,0	23,0	809,0	12,0	0,999	Core
IZA-10_11.FIN2	106,6	1,179	11,5200	0,13000	0,47200	0,0063	0,7158000	2564,00	11,00	2490,00	27,00	2615,0	16,0	2615,0	16,0	4,780	
IZA-10_12.FIN2	735,0	5,790	8,8400	0,14000	0,37600	0,0059	0,8249400	2319,00	15,00	2056,00	28,00	2528,0	16,0	2528,0	16,0	18,671	
IZA-10_13.FIN2	233,0	1,030	0,9280	0,01600	0,10580	0,0012	0,3624300	665,30	8,20	648,00	7,10	703,0	36,0	648,0	7,1	2,600	
IZA-10_14.FIN2	292,9	0,925	0,8900	0,01300	0,10090	0,0012	0,3135900	645,50	6,90	619,80	7,30	712,0	34,0	619,8	7,3	3,981	
IZA-10_15.FIN2	361,0	1,894	1,8980	0,02200	0,18350	0,0022	0,5498100	1079,30	7,60	1087,00	12,00	1059,0	22,0	1059,0	22,0	2,644	
IZA-10_16.FIN2	879,0	3,113	0,3626	0,00490	0,04925	0,0005	0,4308500	313,90	3,60	309,90	3,20	323,0	30,0	309,9	3,2	1,274	
IZA-10_17.FIN2	257,0	2,390	1,4980	0,02800	0,15600	0,0024	0,6681100	932,00	11,00	934,00	14,00	920,0	31,0	920,0	31,0	1,522	
IZA-10_18.FIN2	323,8	1,613	5,8710	0,06000	0,34250	0,0036	0,6635800	1955,50	8,80	1898,00	17,00	2008,0	16,0	2008,0	16,0	5,478	
IZA-10_19.FIN2	884,0	18,600	6,1250	0,09400	0,35100	0,0069	0,7411700	1992,00	14,00	1938,00	33,00	2030,0	19,0	2030,0	19,0	4,532	
IZA-10_20.FIN2	209,0	2,322	13,0400	0,16000	0,51410	0,0069	0,7533800	2680,00	12,00	2672,00	29,00	2677,0	17,0	2677,0	17,0	0,187	
IZA-10_21.FIN2	459,0	1,034	0,5870	0,01200	0,07510	0,0011	0,4694600	468,00	7,90	466,80	6,70	458,0	42,0	466,8	6,7	0,256	
IZA-10_22.FIN2	209,0	1,407	1,0660	0,01800	0,11940	0,0012	0,4060300	735,30	9,00	726,70	6,60	737,0	31,0	726,7	6,6	1,170	
IZA-10_23.FIN2	115,9	1,270	1,6050	0,02500	0,16330	0,0018	0,3362100	972,00	10,00	975,00	10,00	965,0	34,0	965,0	34,0	1,036	
IZA-10_24.FIN2	257,2	5,250	6,7070	0,07400	0,36890	0,0039	0,6606900	2072,50	9,80	2023,00	18,00	2119,0	16,0	2119,0	16,0	4,530	
IZA-10_25.FIN2	264,0	2,380	0,8780	0,01700	0,10430	0,0015	0,6393700	638,40	9,10	639,40	8,80	628,0	37,0	639,4	8,8	0,157	
IZA-10_26.FIN2	557,0	2,032	0,9840	0,02300	0,11200	0,0021	0,5504000	695,00	12,00	684,00	12,00	721,0	45,0	684,0	12,0	1,583	
IZA-10_27.FIN2	149,8	1,279	7,4240	0,08200	0,39400	0,0037	0,5107500	2162,00	10,00	2141,00	17,00	2185,0	17,0	2185,0	17,0	2,014	
IZA-10_28.FIN2	135,4	0,725	11,9600	0,15000	0,49310	0,0064	0,8128800	2599,00	12,00	2582,00	27,00	2611,0	13,0	2611,0	13,0	1,111	
IZA-10_29.FIN2	398,0	4,270	5,6800	0,23000	0,32300	0,0170	0,7805600	1924,00	34,00	1802,00	82,00	2067,0	58,0	2067,0	58,0	12,821	
IZA-10_30.FIN2	469,0	3,550	0,9620	0,01400	0,11140	0,0015	0,4856000	683,10	7,40	680,50	8,80	683,0	30,0	680,5	8,8	0,381	
IZA-10_31.FIN2	357,0	5,220	0,9140	0,01200	0,10770	0,0012	0,3615400	658,20	6,40	659,50	7,10	647,0	30,0	659,5	7,1	0,198	
IZA-10_32.FIN2	433,0	12,000	0,6310	0,01200	0,07880	0,0010	0,4792700	496,40	7,60	488,80	6,00	528,0	39,0	488,8	6,0	1,531	Rim
IZA-10_32.FIN2	464,5	0,960	0,9990	0,02400	0,11230	0,0020	0,5981300	703,00	12,00	686,00	11,00	752,0	44,0	686,0	11,0	2,418	Core
IZA-10_33.FIN2	1520,0	45,500	0,8040	0,04500	0,09490	0,0062	0,8781000	598,00	26,00	584,00	36,00	661,0	69,0	584,0	36,0	2,341	Rim
IZA-10_33.FIN2	249,0	1,667	1,7030	0,02600	0,16940	0,0023	0,6729400	1007,90	9,80	1009,00	12,00	1005,0	25,0	1005,0	25,0	0,308	Core
IZA-10_34.FIN2	54,0	0,962	6,0730	0,08400	0,35760	0,0044	0,6047000	1984,00	12,00	1970,00	21,00	1993,0	22,0	1993,0	22,0	1,154	
IZA-10_35.FIN2	107,0	3,000	0,6110	0,07200	0,07730	0,0091	0,6545500	481,00	46,00	479,00	55,00	500,0	210,0	DISC	DISC	0,416	Rim

Sample Name:	[U]							207/235		206/238		207/206		Best age		Discordance	Rim/
Grain #	ppm	U/Th	207/235	2σ error	206/238	2σ error	RHO	Age Ma	2σ error	Age (Ma)	2σ error	Age (Ma)	2σ error	(Ma)	2σ error	%	Core
IZA-10_35.FIN2	343,0	2,073	1,8530	0,02600	0,17510	0,0024	0,5874700	1065,50	9,80	1040,00	13,00	1154,0	26,0	1154,0	26,0	9,879	Core
IZA-10_36.FIN2	276,2	2,240	0,8770	0,01500	0,10140	0,0013	0,5663100	638,00	8,30	622,30	7,80	681,0	33,0	622,3	7,8	2,461	
IZA-10_37.FIN2	161,9	0,724	5,4310	0,07400	0,33970	0,0045	0,5650600	1888,00	12,00	1884,00	22,00	1881,0	22,0	1881,0	22,0	0,159	
IZA-10_38.FIN2	475,0	4,244	0,3651	0,00510	0,05008	0,0005	0,3192300	315,80	3,80	315,00	2,90	307,0	30,0	315,0	2,9	0,253	
IZA-10_39.FIN2	1230,0	7,700	0,8890	0,08400	0,09900	0,0100	0,9023500	641,00	47,00	608,00	59,00	780,0	100,0	608,0	59,0	5,148	Rim
IZA-10_39.FIN2	221,0	1,006	1,6170	0,02700	0,15990	0,0020	0,6632400	975,00	11,00	956,00	11,00	1007,0	28,0	1007,0	28,0	5,065	Core
IZA-10_40.FIN2	93,2	1,327	1,4100	0,03500	0,14700	0,0028	0,5560800	892,00	15,00	884,00	16,00	911,0	43,0	911,0	43,0	2,964	
IZA-10_41.FIN2	87,8	0,816	0,8590	0,02200	0,10170	0,0018	0,2333200	628,00	12,00	624,00	10,00	630,0	61,0	624,0	10,0	0,637	
IZA-10_42.FIN2	575,0	2,022	0,3515	0,00590	0,04867	0,0005	0,3454400	305,50	4,40	306,30	3,20	280,0	37,0	306,3	3,2	0,262	
IZA-10_44.FIN2	47,4	0,731	5,3640	0,09400	0,33730	0,0045	0,4860500	1878,00	16,00	1873,00	22,00	1878,0	30,0	1878,0	30,0	0,266	
IZA-10_45.FIN2	171,5	0,418	0,9030	0,01700	0,10490	0,0015	0,4271500	652,80	9,30	642,90	8,80	671,0	38,0	642,9	8,8	1,517	
IZA-10_46.FIN2	351,0	1,737	0,3538	0,00670	0,04832	0,0005	0,2792700	307,10	5,00	304,20	3,00	323,0	43,0	304,2	3,0	0,944	
IZA-10_47.FIN2	859,0	115,000	0,3602	0,00810	0,04910	0,0013	0,5176800	313,50	6,50	308,60	8,20	342,0	54,0	308,6	8,2	1,563	Rim
IZA-10_47.FIN2	284,0	5,430	0,6560	0,01800	0,08110	0,0017	0,3743400	513,00	11,00	502,80	9,90	549,0	59,0	502,8	9,9	1,988	Core
IZA-10_48.FIN2	249,0	4,460	0,7330	0,02200	0,08260	0,0017	0,7967300	557,00	13,00	511,00	10,00	755,0	56,0	511,0	10,0	8,259	Rim
IZA-10_48.FIN2	125,5	1,997	6,0100	0,10000	0,34050	0,0059	0,4867700	1981,00	17,00	1889,00	28,00	2078,0	32,0	2078,0	32,0	9,095	Core
IZA-10_49.FIN2	325,1	11,000	0,9310	0,01200	0,10640	0,0012	0,5687300	667,60	6,40	651,50	6,80	711,0	22,0	651,5	6,8	2,412	
IZA-10_50.FIN2	710,0	5,270	0,9350	0,03600	0,10330	0,0034	0,6105000	669,00	18,00	634,00	20,00	783,0	70,0	634,0	20,0	5,232	
IZA-10_51.FIN2	115,9	2,100	1,7300	0,04400	0,16910	0,0041	0,5272700	1018,00	16,00	1006,00	23,00	1048,0	51,0	1048,0	51,0	4,008	
IZA-10_52.FIN2	102,3	1,588	2,5400	0,04000	0,22010	0,0023	0,5165100	1282,00	11,00	1282,00	12,00	1281,0	27,0	1281,0	27,0	0,078	
IZA-10_53.FIN2	406,0	2,285	0,3400	0,01800	0,04620	0,0020	0,5243000	297,00	14,00	291,00	12,00	340,0	100,0	291,0	12,0	2,020	
IZA-10_54.FIN2	204,6	1,723	1,0590	0,01500	0,11980	0,0010	0,3355000	732,40	7,30	729,60	6,00	733,0	30,0	729,6	6,0	0,382	
IZA-10_55.FIN2	207,6	1,379	1,7530	0,02100	0,17130	0,0016	0,3675100	1027,20	7,70	1018,80	8,90	1041,0	25,0	1041,0	25,0	2,133	
IZA-10_56.FIN2	226,0	2,400	1,7110	0,02000	0,16830	0,0015	0,3852100	1011,70	7,50	1002,50	8,30	1031,0	23,0	1031,0	23,0	2,764	
IZA-10_57.FIN2	388,0	1,109	1,8600	0,02000	0,18010	0,0019	0,6534600	1066,10	7,20	1069,00	10,00	1057,0	17,0	1057,0	17,0	1,135	
IZA-10_58.FIN2	551,0	1,634	0,9040	0,01200	0,10620	0,0012	0,5577000	652,90	6,20	650,60	7,30	655,0	25,0	650,6	7,3	0,352	
IZA-10_59.FIN2	166,1	2,633	5,2240	0,07200	0,33030	0,0046	0,6902000	1854,00	12,00	1838,00	22,00	1874,0	21,0	1874,0	21,0	1,921	
IZA-10_60.FIN2	248,0	2,358	0,4080	0,01000	0,05452	0,0008	0,1083400	347,10	7,50	342,20	4,70	379,0	63,0	342,2	4,7	1,412	
IZA-10_61.FIN2	2140,0	4,980	0,3829	0,00770	0,05120	0,0010	0,3336400	328,80	5,60	321,90	6,40	370,0	45,0	321,9	6,4	2,099	
IZA-10_62.FIN2	370,2	1,783	0,7640	0,01000	0,09330	0,0009	0,4634100	575,80	5,90	575,00	5,40	581,0	28,0	575,0	5,4	0,139	
IZA-10_63.FIN2	181,1	1,272	1,4420	0,02300	0,14950	0,0021	0,3922700	904,90	9,60	898,00	12,00	918,0	36,0	918,0	36,0	2,179	
IZA-10_64.FIN2	318,0	73,500	0,9120	0,01300	0,10710	0,0012	0,6547800	658,30	7,20	656,40	6,70	664,0	25,0	656,4	6,7	0,289	
IZA-10_65.FIN2	705,0	1,917	0,9400	0,01500	0,09540	0,0013	0,4830200	672,00	7,60	587,20	7,70	974,0	29,0	587,2	7,7	12,619	
IZA-10_66.FIN2	521,0	79,000	0,4220	0,03600	0,05540	0,0029	0,7340900	355,00	25,00	347,00	18,00	390,0	120,0	347,0	18,0	2,254	Rim
IZA-10_66.FIN2	437,8	7,890	0,5660	0,01300	0,07330	0,0015	0,6534400	455,60	8,40	455,80	9,30	455,0	39,0	455,8	9,3	0,044	Core
IZA-10_67.FIN2	587,0	1,727	0,3319	0,00610	0,04558	0,0006	0,4516000	290,60	4,60	287,30	3,50	315,0	38,0	287,3	3,5	1,136	
IZA-10_68.FIN2	217,0	2,570	2,6910	0,03900	0,22840	0,0028	0,5962800	1324,00	11,00	1325,00	14,00	1325,0	24,0	1325,0	24,0	0,000	
IZA-10_69.FIN2	482,0	4,240	0,8680	0,01200	0,10360	0,0011	0,4757400	634,30	6,70	635,60	6,60	631,0	29,0	635,6	6,6	0,205	
IZA-10_70.FIN2	95,8	2,435	1,6940	0,03200	0,16730	0,0023	0,5484200	1004,00	12,00	996,00	13,00	1024,0	34,0	1024,0	34,0	2,734	
IZA-10_71.FIN2	74,7	2,020	3,6450	0,08800	0,25940	0,0059	0,4852300	1556,00	19,00	1484,00	30,00	1661,0	43,0	1661,0	43,0	10,656	
IZA-10_72.FIN2	581,0	1,419	6,5480	0,05800	0,36580	0,0035	0,7090700	2051,50	7,80	2009,00	17,00	2099,0	13,0	2099,0	13,0	4,288	
IZA-10_73.FIN2	266,0	0,735	1,6820	0,02100	0,16670	0,0015	0,4344700	1000,50	7,90	993,70	8,10	1019,0	24,0	1019,0	24,0	2,483	
IZA-10_74.FIN2	344,0	2,434	0,7300	0,01200	0,08620	0,0012	0,5395100	555,50	7,20	533,00	7,00	652,0	30,0	533,0	7,0	4,050	
IZA-10_75.FIN2	425,0	1,489	0,3661	0,00650	0,04935	0,0006	0,3266700	316,40	4,80	310,50	3,40	359,0	40,0	310,5	3,4	1,865	
IZA-10_76.FIN2	660,0	5,350	1,1900	0,08200	0,12800	0,0065	0,8612800	791,00	39,00	776,00	37,00	828,0	82,0	776,0	37,0	1,896	
IZA-10_77.FIN2	851,0	1,928	0,9220	0,02100	0,10120	0,0024	0,5492300	662,00	11,00	621,00	14,00	794,0	50,0	621,0	14,0	6,193	
IZA-10_78.FIN2	215,0	0,543	0,7960	0,01500	0,09860	0,0010	0,2805300	593,20	8,20	606,10	6,10	529,0	40,0	606,1	6,1	2,175	

Sample Name:	[U]							207/235		206/238		207/206		Best age		Discordance	Rim/
Grain #	ppm	U/Th	207/235	2σ error	206/238	2σ error	RHO	Age Ma	2σ error	Age (Ma)	2σ error	Age (Ma)	2σ error	(Ma)	2σ error	%	Core
IZA-10_79.FIN2	287,8	1,541	0,9680	0,01900	0,11030	0,0021	0,4671600	686,00	10,00	674,00	12,00	720,0	43,0	674,0	12,0	1,749	
IZA-10_80.FIN2	230,0	2,270	0,5817	0,00990	0,07409	0,0007	0,2626200	464,80	6,40	461,30	4,60	465,0	39,0	461,3	4,6	0,753	
IZA-10_81.FIN2	117,3	0,926	0,7750	0,01800	0,09090	0,0014	0,4450400	582,00	11,00	561,00	8,10	652,0	49,0	561,0	8,1	3,608	
IZA-10_82.FIN2	215,1	0,899	5,4560	0,08400	0,33130	0,0047	0,6940100	1891,00	13,00	1843,00	23,00	1941,0	21,0	1941,0	21,0	5,049	
IZA-10_83.FIN2	263,0	3,210	1,3970	0,03500	0,14630	0,0034	0,3066600	886,00	15,00	880,00	19,00	891,0	57,0	891,0	57,0	1,235	
IZA-10_84.FIN2	42,9	3,160	8,4800	0,43000	0,42300	0,0160	0,6676600	2278,00	47,00	2274,00	71,00	2274,0	65,0	2274,0	65,0	0,000	
IZA-10_85.FIN2	374,0	15,100	0,7430	0,02500	0,08780	0,0033	0,5576400	562,00	15,00	542,00	19,00	645,0	72,0	542,0	19,0	3,559	Rim
IZA-10_85.FIN2	137,3	1,707	1,8940	0,09300	0,17220	0,0041	0,1408000	1077,00	32,00	1024,00	23,00	1180,0	100,0	1180,0	100,0	13,220	Core
IZA-10_86.FIN2	838,0	192,000	0,3620	0,01100	0,04960	0,0012	0,7631900	312,90	8,10	311,70	7,10	304,0	45,0	311,7	7,1	0,384	Rim
IZA-10_86.FIN2	663,0	0,736	1,1540	0,04400	0,12680	0,0032	0,6703300	779,00	21,00	769,00	19,00	796,0	59,0	769,0	19,0	1,284	Core
IZA-10_87.FIN2	310,0	2,711	0,7350	0,01100	0,08490	0,0011	0,4644300	559,40	6,80	525,20	6,30	691,0	34,0	525,2	6,3	6,114	
IZA-10_88.FIN2	802,0	1,501	1,0270	0,01300	0,11540	0,0013	0,6636200	716,70	6,60	704,00	7,80	748,0	20,0	704,0	7,8	1,772	
IZA-10_89.FIN2	54,1	-1,000	0,8920	0,06500	0,10370	0,0037	0,2116900	642,00	35,00	636,00	21,00	630,0	160,0	636,0	21,0	0,935	Rim
IZA-10_89.FIN2	335,0	1,955	1,6030	0,02400	0,16100	0,0023	0,5183800	970,10	9,60	962,00	13,00	978,0	29,0	978,0	29,0	1,636	Core
IZA-10_90.FIN2	264,0	6,760	0,8940	0,01600	0,10310	0,0012	0,4897700	648,10	8,50	632,30	7,10	694,0	33,0	632,3	7,1	2,438	
IZA-10_91.FIN2	146,6	1,134	1,7800	0,02800	0,17650	0,0018	0,3036400	1036,00	10,00	1047,50	9,80	1005,0	33,0	1005,0	33,0	4,229	
IZA-10_92.FIN2	528,5	10,040	5,9170	0,06200	0,34240	0,0038	0,6440900	1963,30	8,90	1897,00	18,00	2026,0	16,0	2026,0	16,0	6,367	
IZA-10_93.FIN2	820,0	6,600	0,3730	0,01800	0,05030	0,0014	0,3010500	322,00	13,00	316,20	8,60	360,0	110,0	316,2	8,6	1,801	Rim
IZA-10_93.FIN2	561,0	2,480	0,7210	0,01200	0,08890	0,0011	0,5783700	550,60	6,80	549,00	6,70	538,0	28,0	549,0	6,7	0,291	Core
IZA-10_94.FIN2	478,0	1,952	0,3621	0,00590	0,04814	0,0004	0,3459600	313,40	4,40	303,10	2,70	380,0	37,0	303,1	2,7	3,287	
IZA-10_95.FIN2	107,2	4,360	0,9440	0,01800	0,10870	0,0013	0,1785800	674,50	9,40	665,20	7,40	685,0	45,0	665,2	7,4	1,379	
IZA-10_96.FIN2	243,0	0,880	0,8570	0,01300	0,10110	0,0011	0,4104400	627,40	7,00	620,80	6,40	638,0	32,0	620,8	6,4	1,052	
IZA-10_97.FIN2	59,7	0,684	5,1300	0,14000	0,32860	0,0065	0,5622800	1842,00	22,00	1831,00	32,00	1838,0	43,0	1838,0	43,0	0,381	
IZA-10_98.FIN2	142,2	1,390	5,0220	0,06500	0,32010	0,0038	0,6287300	1821,00	11,00	1789,00	18,00	1850,0	20,0	1850,0	20,0	3,297	
IZA-10_99.FIN2	544,0	2,030	0,3767	0,00680	0,04986	0,0005	0,4746400	324,10	5,00	313,60	2,90	383,0	36,0	313,6	2,9	3,240	
IZA-10_100.FIN2	498,0	128,000	0,3550	0,01000	0,04890	0,0011	0,7014900	308,60	7,50	307,90	6,90	310,0	53,0	307,9	6,9	0,227	Rim
IZA-10_100.FIN2	260,0	2,930	1,4350	0,02000	0,15130	0,0018	0,6264000	902,60	8,60	908,10	9,90	885,0	28,0	885,0	28,0	2,610	Core
IZA-10_101.FIN2	221,0	1,840	0,9020	0,03000	0,10210	0,0028	0,5847300	651,00	16,00	627,00	16,00	734,0	60,0	627,0	16,0	3,687	Rim
IZA-10_101.FIN2	123,0	1,382	1,1570	0,03000	0,12860	0,0020	0,5697500	778,00	14,00	780,00	11,00	762,0	45,0	780,0	11,0	0,257	Core
IZA-10_102.FIN2	130,6	1,199	0,6080	0,01300	0,07730	0,0010	0,2268500	481,10	8,50	479,90	6,00	474,0	50,0	479,9	6,0	0,249	
IZA-10_103.FIN2	368,0	4,360	0,3980	0,01800	0,04940	0,0018	0,4501600	339,00	13,00	311,00	11,00	532,0	94,0	311,0	11,0	8,260	Rim
IZA-10_103.FIN2	321,7	1,940	0,6630	0,01700	0,07340	0,0016	0,6421200	515,00	11,00	456,70	9,50	779,0	45,0	456,7	9,5	11,320	Core
IZA-10_104.FIN2	261,0	1,791	0,5970	0,01400	0,07330	0,0014	0,3032000	474,00	8,70	455,60	8,70	551,0	51,0	455,6	8,7	3,882	
IZA-10_105.FIN2	369,0	8,830	0,6163	0,00960	0,07747	0,0007	0,4020400	486,80	6,10	480,90	4,10	507,0	33,0	480,9	4,1	1,212	
IZA-10_106.FIN2	191,1	3,130	0,9240	0,02000	0,10170	0,0014	0,5110000	663,00	11,00	624,00	8,40	792,0	39,0	624,0	8,4	5,882	
IZA-10_107.FIN2	63,0	1,426	18,1100	0,22000	0,59330	0,0069	0,8148200	2995,00	11,00	3001,00	28,00	2988,0	13,0	2988,0	13,0	0,435	
IZA-10_108.FIN2	228,0	1,494	1,6690	0,02300	0,16520	0,0017	0,5327500	995,20	8,80	985,50	9,10	1018,0	24,0	1018,0	24,0	3,193	
IZA-10_109.FIN2	169,0	1,920	4,2140	0,06900	0,29770	0,0048	0,7073300	1674,00	14,00	1679,00	24,00	1674,0	24,0	1674,0	24,0	0,299	
IZA-10_110.FIN2	406,0	4,520	0,7860	0,01100	0,09517	0,0009	0,3837800	588,30	6,10	585,90	5,40	595,0	29,0	585,9	5,4	0,408	
IZA-10_111.FIN2	170,1	1,340	1,5530	0,03100	0,15750	0,0026	0,5127500	951,00	12,00	944,00	15,00	958,0	35,0	958,0	35,0	1,461	
IZA-10_113.FIN2	148,0	6,100	0,9330	0,03400	0,10470	0,0031	0,4651200	668,00	18,00	642,00	18,00	769,0	73,0	642,0	18,0	3,892	Rim
IZA-10_113.FIN2	49,0	1,777	1,7400	0,05300	0,17330	0,0037	0,6333800	1022,00	19,00	1029,00	20,00	987,0	50,0	987,0	50,0	4,255	Core
IZA-10_114.FIN2	501,0	11,400	0,9470	0,03900	0,10750	0,0069	0,7591600	676,00	21,00	658,00	40,00	748,0	84,0	658,0	40,0	2,663	Rim
IZA-10_114.FIN2	138,8	0,527	2,7300	0,08000	0,20650	0,0046	0,7124300	1334,00	22,00	1210,00	24,00	1544,0	39,0	1544,0	39,0	21,632	Core
IZA-10_115.FIN2	251,3	0,483	0,7850	0,01200	0,09520	0,0009	0,3805600	587,30	6,60	586,10	5,40	581,0	32,0	586,1	5,4	0,204	
IZA-10_116.FIN2	173,0	1,085	0,8800	0,02600	0,10410	0,0031	0,6094700	643,00	15,00	638,00	18,00	659,0	61,0	638,0	18,0	0,778	
IZA-10_117.FIN2	237,3	11,590	0,8760	0,01600	0,10460	0,0015	0,5093600	637,60	8,90	641,30	8,50	623,0	37,0	641,3	8,5	0,580	

Sample Name:	[U]							207/235		206/238		207/206		Best age		Discordance	Rim/
Grain #	ppm	U/Th	207/235	2σ error	206/238	2σ error	RHO	Age Ma	2σ error	Age (Ma)	2σ error	Age (Ma)	2σ error	(Ma)	2σ error	%	Core
IZA-10_118.FIN2	1490,0	42,800	1,0970	0,07300	0,11740	0,0074	0,4855000	748,00	35,00	715,00	43,00	850,0	130,0	715,0	43,0	4,412	Rim
IZA-10_118.FIN2	388,3	2,010	2,0110	0,03400	0,19050	0,0027	0,7780200	1119,00	12,00	1124,00	15,00	1111,0	23,0	1111,0	23,0	1,170	Core
IZA-10_120.FIN2	297,0	1,564	1,6770	0,06200	0,16630	0,0045	0,3092200	1005,00	17,00	991,00	25,00	1059,0	52,0	1059,0	52,0	6,421	
IZA-10_121.FIN2	389,0	5,150	1,0480	0,02600	0,11430	0,0024	0,8197000	726,00	13,00	697,00	14,00	811,0	40,0	697,0	14,0	3,964	
IZA-10_122.FIN2	664,0	3,060	0,5670	0,01200	0,07230	0,0015	0,4469900	455,30	8,10	450,20	8,90	477,0	50,0	450,2	8,9	1,120	
IZA-10_123.FIN2	107,4	1,840	0,9110	0,01900	0,10520	0,0012	0,3164600	656,00	10,00	644,80	6,80	679,0	43,0	644,8	6,8	1,707	
IZA-10_124.FIN2	770,0	26,300	0,5866	0,00740	0,07474	0,0007	0,5023500	468,20	4,80	464,60	4,30	479,0	26,0	464,6	4,3	0,769	
IZA-10_125.FIN2	376,0	1,658	6,6400	0,21000	0,29480	0,0084	0,9374100	2051,00	29,00	1661,00	42,00	2487,0	18,0	DISC	DISC	33,213	
IZA-10_126.FIN2	230,2	1,094	2,9120	0,04400	0,23680	0,0033	0,6678000	1384,00	11,00	1369,00	17,00	1407,0	23,0	1407,0	23,0	2,701	
IZA-10_127.FIN2	231,7	0,430	5,6850	0,06200	0,33950	0,0037	0,6614900	1927,60	9,50	1884,00	18,00	1975,0	16,0	1975,0	16,0	4,608	
IZA-10_128.FIN2	497,0	2,055	0,7760	0,01500	0,09430	0,0014	0,6025100	585,60	8,50	580,80	8,40	596,0	34,0	580,8	8,4	0,820	
IZA-10_129.FIN2	198,6	3,358	4,5740	0,05900	0,30850	0,0039	0,7703300	1743,00	11,00	1732,00	19,00	1755,0	18,0	1755,0	18,0	1,311	
IZA-10_130.FIN2	344,0	10,280	0,5310	0,02100	0,06910	0,0026	0,5301600	431,00	14,00	431,00	16,00	431,0	82,0	431,0	16,0	0,000	Rim
IZA-10_130.FIN2	87,1	2,310	0,8670	0,03600	0,10690	0,0034	0,3347300	632,00	20,00	654,00	20,00	583,0	79,0	654,0	20,0	3,481	Core
IZA-10_131.FIN2	243,0	0,900	1,6970	0,02300	0,16730	0,0018	0,6180200	1006,20	8,70	997,10	9,80	1023,0	22,0	1023,0	22,0	2,532	
IZA-10_132.FIN2	164,0	0,917	1,6300	0,02600	0,16350	0,0021	0,5023100	982,00	10,00	976,00	12,00	991,0	30,0	991,0	30,0	1,514	
IZA-10_133.FIN2	282,0	2,713	0,3525	0,00620	0,04779	0,0004	0,1837800	306,80	4,80	300,90	2,70	339,0	41,0	300,9	2,7	1,923	
IZA-10_134.FIN2	156,2	1,272	0,9100	0,02300	0,10080	0,0012	0,2857700	654,90	12,00	619,20	6,80	770,0	51,0	619,2	6,8	5,321	
IZA-10_135.FIN2	337,0	1,499	1,0030	0,01900	0,11210	0,0017	0,5783100	704,40	9,60	685,00	9,60	760,0	35,0	685,0	9,6	2,754	
IZA-10_136.FIN2	97,2	0,751	0,8310	0,01900	0,10000	0,0013	0,3961300	616,00	10,00	614,50	7,40	597,0	46,0	614,5	7,4	0,244	
IZA-10_137.FIN2	1763,0	4,930	0,3692	0,00460	0,04347	0,0006	0,6399900	318,80	3,40	274,20	4,00	660,0	27,0	274,2	4,0	13,990	
IZA-10_138.FIN2	216,4	0,963	0,7680	0,01200	0,09160	0,0009	0,3582700	577,70	7,10	564,90	5,50	626,0	34,0	564,9	5,5	2,216	
IZA-10_139.FIN2	348,0	93,000	0,8920	0,02500	0,10600	0,0020	0,5694500	649,00	14,00	649,00	12,00	641,0	52,0	649,0	12,0	0,000	Rim
IZA-10_139.FIN2	129,2	2,190	1,3960	0,03500	0,14310	0,0023	0,6927800	884,00	15,00	862,00	13,00	939,0	38,0	939,0	38,0	8,200	Core
IZA-10_140.FIN2	144,6	1,259	4,3350	0,04600	0,29890	0,0025	0,4725000	1698,60	8,70	1686,00	12,00	1716,0	18,0	1716,0	18,0	1,748	
IZA-10_141.FIN2	192,6	2,820	0,5890	0,01200	0,07460	0,0011	0,3430700	469,10	7,90	463,90	6,50	486,0	46,0	463,9	6,5	1,109	
IZA-10_142.FIN2	710,0	3,287	0,3768	0,00720	0,04765	0,0009	0,5543800	324,10	5,30	300,00	5,20	501,0	40,0	300,0	5,2	7,436	
IZA-10_143.FIN2	250,7	1,013	5,8540	0,06300	0,34360	0,0037	0,5601800	1952,80	9,40	1903,00	18,00	2014,0	18,0	2014,0	18,0	5,511	
IZA-10_144.FIN2	299,0	2,212	1,6740	0,03800	0,16730	0,0035	0,6821900	995,00	14,00	996,00	19,00	1000,0	36,0	1000,0	36,0	0,400	
IZA-10_145.FIN2	121,0	1,102	1,7010	0,02600	0,16760	0,0019	0,5106000	1007,90	9,80	1000,00	11,00	1022,0	28,0	1022,0	28,0	2,153	
IZA-10_146.FIN2	240,9	1,885	0,7610	0,01300	0,09170	0,0013	0,5884200	573,70	7,50	565,10	7,70	600,0	36,0	565,1	7,7	1,499	
IZA-10_147.FIN2	452,0	8,350	0,5910	0,01800	0,07350	0,0018	0,5202100	471,00	11,00	457,00	11,00	542,0	60,0	457,0	11,0	2,972	Rim
IZA-10_147.FIN2	312,0	5,120	1,1630	0,05400	0,11210	0,0044	0,6936700	781,00	26,00	685,00	25,00	1075,0	68,0	685,0	25,0	12,292	Core
IZA-10_148.FIN2	779,0	2,081	0,3520	0,00680	0,04765	0,0005	0,3509200	305,70	5,10	300,10	2,80	337,0	41,0	300,1	2,8	1,832	
IZA-10_149.FIN2	126,4	1,470	0,5050	0,01300	0,06730	0,0012	0,4065600	415,70	9,00	419,80	7,30	385,0	53,0	419,8	7,3	0,986	
IZA-10_150.FIN2	108,3	1,488	1,0770	0,03300	0,11680	0,0017	0,2630100	740,00	16,00	712,00	9,90	811,0	63,0	712,0	9,9	3,784	

Annex 5

Resultats d'(U-Th)/He en zircons detrítics

Sample	Age, Ma	err., Ma	U/Pb Age	U (ppm)	Th (ppm)	147Sm (ppm)	[U]e	Th/U	He (nmol/g)	mass (ug)	Ft	ESR
zBEMO-03-58	56,8	4,5	441,7	156,8932	61,3713	4,8738	171,0453	0,3912	45,1603	25,9900	0,8578	84,7000
zBEMO-03-47	57,7	4,6	482,8	83,8932	45,2854	1,6279	94,3260	0,5398	21,4860	3,5300	0,7278	42,6100
zBEMO-03-43	43,5	3,5	617,7	59,4347	37,7896	5,6273	68,1620	0,6358	12,4724	6,1300	0,7757	52,7700
zBEMO-03-57	52,4	4,2	583,1	133,4307	55,1627	4,5138	146,1517	0,4134	30,4027	3,8200	0,7325	43,1100
zBEMO-03-61	46,4	3,7	312,5	807,2200	268,3644	5,8848	869,0269	0,3325	178,8036	11,7300	0,8193	65,6000
zBEMO-03-95	47,9	3,8	317,6	734,3837	79,9862	5,7285	752,8251	0,1089	143,6743	3,0100	0,7372	43,0600
zBEMO-03-28	47,3	3,8	304,4	349,9532	80,7182	4,5257	368,5572	0,2307	70,7762	3,8100	0,7499	45,8900
zBEMO-03-59	54,4	4,3	574,5	144,9407	61,3084	2,7106	159,0675	0,4230	32,4695	2,1200	0,6932	37,0600
zBEMO-03-66	43,1	3,4	308,9	126,9920	61,4250	1,1268	141,1376	0,4837	25,3256	5,1000	0,7688	50,8000
zBEMO-03-71	63,2	5,1	302,1	76,1478	34,0565	0,9209	83,9922	0,4472	22,4195	6,2400	0,7786	53,0900
zBEMO-03-77	48,5	3,9	330,6	635,5332	297,5556	1,5918	704,0385	0,4682	136,9510	3,6100	0,7411	44,8400
zBEMO-03-94	81,4	6,5	583,9	25,8067	26,1513	3,1793	31,8427	1,0134	11,4632	10,8500	0,8119	64,5700
zBEMO-03-13	88,7	7,1	315,7	269,7807	125,1705	1,4811	298,6023	0,4640	106,9840	3,8800	0,7434	45,3000
zBEMO-03-11	73,7	5,9	1844,0	72,6443	16,0036	0,0000	76,3283	0,2203	22,9937	4,0000	0,7541	46,7400
zBEMO-03-83	108,8	8,7	2523,0	258,1997	73,6306	3,1063	275,1650	0,2852	111,7721	1,8500	0,6875	35,9800
zBEMO-03-103	277,2	22,2	622,3	428,3893	103,8008	2,1850	452,2951	0,2423	489,7084	2,6300	0,7110	39,2200
zBEMO-03-21	233,2	18,7	641,5	61,4353	45,5590	3,8314	71,9421	0,7416	66,6197	3,0000	0,7232	42,2500
zBEMO-12-9	42,2	3,4	321,8	332,9298	240,0214	3,3776	388,1996	0,7209	70,6624	8,5100	0,7948	58,5000
zBEMO-12-10	47,6	3,8	756,5	41,4842	19,3648	-0,9178	45,9374	0,4668	9,2266	6,2600	0,7787	53,2600
zBEMO-12-17	48,3	3,9	303,5	254,8549	129,4059	24,2898	284,7656	0,5078	55,9867	4,7400	0,7502	46,8000
zBEMO-12-30	44,1	3,5	2731,0	153,6282	55,6482	2,2448	166,4497	0,3622	27,8802	2,5600	0,7025	38,2300
zBEMO-12-76	38,0	3,0	330,9	201,9910	190,2264	6,0290	245,8113	0,9418	35,6720	2,8600	0,7040	39,4700
zBEMO-12-47	43,5	3,5	471,1	212,2702	72,2207	1,8658	228,9047	0,3402	38,8394	3,0800	0,7204	40,9200
zBEMO-12-123	46,2	3,7	603,4	359,1401	110,1752	5,9248	384,5320	0,3068	64,7697	1,9400	0,6738	34,3600
zBEMO-12-2	44,0	3,5	1049,0	373,2703	262,7792	72,1726	434,1230	0,7040	76,8114	4,1600	0,7414	45,4000
zBEMO-12-92	39,4	3,2	597,6	204,5000	90,5000	0,0000	225,3000	0,4400	31,8000	1,5800	0,6600	33,3400
zBEMO-12-41	44,0	3,5	325,1	529,3000	134,0000	0,0000	560,2000	0,2500	95,6000	3,0400	0,7200	40,0700
zBEMO-12-48	53,7	4,3	300,2	154,2000	51,5000	5,0000	166,1000	0,3300	36,7000	4,6200	0,7600	48,0200
zBEMO-12-67	52,2	4,2	300,1	187,4000	57,4000	0,0000	200,6000	0,3100	39,8000	2,3200	0,7000	38,0800
zBEMO-12-139	48,9	3,9	305,7	268,7000	83,4000	0,0000	287,9000	0,3100	56,9000	4,7800	0,7500	45,6400
zBEMO-12-121	41,8	3,4	606,5	56,5000	63,5000	0,0000	71,1000	1,1300	13,0000	9,1900	0,8000	62,4800

Sample	Age, Ma	err., Ma	U/Pb Age	U (ppm)	Th (ppm)	147Sm (ppm)	[U]e	Th/U	He (nmol/g)	mass (ug)	Ft	ESR
zBEMO-12-130	70,3	5,6	607,2	203,1000	131,2000	-5,5000	233,3000	0,6500	61,0000	2,0900	0,6900	36,5100
zBEMO-12-132	37,8	3,0	610,1	72,6000	21,1000	0,0000	77,4000	0,2900	12,4000	6,1200	0,7800	53,1700
zGAL-5-43	119,0	9,5	601,3	175,2182	121,8274	2,9534	203,2776	0,6953	110,5858	17,4200	0,8380	75,1800
zGAL-5-63	34,4	2,8	588,9	357,7601	78,4953	1,2391	375,8359	0,2194	53,3987	4,6100	0,7633	48,7300
zGAL-5-136	51,6	4,1	314,2	281,0550	74,1476	2,2287	298,1349	0,2638	68,4169	12,8200	0,8210	65,9700
zGAL-5-132	42,7	3,4	328,2	624,6108	498,0164	7,7133	739,2927	0,7973	133,5883	6,6700	0,7798	54,3100
zGAL-5-119	51,5	4,1	321,8	323,2469	221,7628	10,1100	374,3472	0,6860	85,2242	11,3200	0,8139	64,6100
zGAL-5-65	45,4	3,6	306,4	429,9737	156,2192	4,9036	465,9598	0,3633	78,6342	2,3300	0,6869	36,0700
zGAL-5-58	44,9	3,6	304,8	360,4229	65,3382	3,1817	375,4796	0,1813	72,2381	8,9800	0,7915	55,6200
zGAL-5-70	46,5	3,7	307,3	149,7332	29,6904	0,8172	156,5721	0,1983	31,2594	6,9900	0,7942	56,4600
zGAL-5-52	46,5	3,7	332,0	380,8472	107,5017	3,6106	405,6121	0,2823	80,1832	6,3300	0,7857	54,4600
zGAL-5-24	88,3	7,1	335,9	121,1589	64,0654	0,4772	135,9091	0,5288	53,3475	11,9700	0,8181	65,7800
zGAL-5-1	46,5	3,7	623,3	229,2573	96,6779	5,0710	251,5379	0,4217	46,5660	3,3800	0,7357	43,8200
zGAL-5-123	84,3	6,7	473,2	221,0278	73,7816	4,7142	238,0359	0,3338	87,5326	9,7000	0,8037	60,1900
zGAL-5-106	40,7	3,3	445,7	332,6478	63,1645	5,8815	347,2177	0,1899	58,3575	5,8300	0,7629	48,4300
zGAL-5-21	95,0	7,6	551,4	195,7117	132,4980	6,1181	226,2433	0,6770	87,2647	4,6700	0,7461	46,3400
zGAL-5-139	41,9	3,4	621,6	245,3902	97,8881	0,7989	267,9281	0,3989	47,9759	7,1500	0,7884	55,6100
zGAL-5-33	44,4	3,6	639,2	92,8688	69,5147	3,5123	108,8887	0,7485	20,0107	4,8800	0,7633	50,0600
zGAL-5-93	69,3	5,5	1074,0	60,1517	24,8939	0,0000	65,8822	0,4139	18,7342	4,1100	0,7561	47,7200
zGAL-5-129	41,2	3,3	294,7	594,4962	207,8754	6,9258	642,3837	0,3497	105,2029	3,3000	0,7345	43,3700
zGAL-5-137	267,4	21,4	1977,0	344,9654	183,1636	3,1918	387,1456	0,5310	439,7250	5,3700	0,7717	51,6600
zGAL-10-55	25,7	2,1	30,3	420,9864	381,8102	0,0000	508,8791	0,9069	47,4572	1,6400	0,6694	34,7800
zGAL-10b-66	27,7	2,2	31,3	379,0665	280,9152	-5,4203	443,7061	0,7411	41,7477	1,0600	0,6274	30,1400
zGAL-10-92	40,7	3,3	1047,0	381,8750	139,5201	0,0000	413,9926	0,3654	55,0585	0,8200	0,6048	27,6600
zGAL-10-111	44,3	3,5	2490,0	195,2483	134,2581	0,0000	226,1545	0,6876	33,6155	1,0400	0,6197	29,3700
zGAL-10-141	46,2	3,7	1854,0	524,1442	109,9429	0,0000	549,4530	0,2098	85,5369	1,1300	0,6229	28,8500
zGAL-10-70	67,5	5,4	301,1	360,9836	106,5015	-2,9018	385,4857	0,2950	95,9148	1,9800	0,6800	35,0400
zGAL-10-137	76,5	6,1	323,6	432,6763	149,2383	53,9138	467,3005	0,3449	116,4954	0,9600	0,6012	27,3200
zGAL-10-148	244,4	19,6	477,3	272,4061	67,4680	3,7559	287,9561	0,2477	252,2271	1,5300	0,6547	32,0400
zGAL-10-64	267,6	21,4	607,0	197,3912	159,1287	2,7364	234,0363	0,8062	234,0103	2,1000	0,6798	35,9900

Sample	Age, Ma	err., Ma	U/Pb Age	U (ppm)	Th (ppm)	147Sm (ppm)	[U]e	Th/U	He (nmol/g)	mass (ug)	Ft	ESR
zGAL-10-85	45,5	3,6	290,3	182,1000	72,6000	0,0000	198,8000	0,4000	32,0000	1,3500	0,6500	32,2500
zGAL-10-75	74,4	6,0	285,3	354,6000	112,9000	3,9000	380,6000	0,3200	116,6000	4,4500	0,7600	48,2000
zGAL-10-127	68,8	5,5	624,0	190,4000	16,5000	0,0000	194,2000	0,0900	54,3000	4,3200	0,7500	45,4900
zGAL-10-32	111,8	9,0	625,7	42,1000	23,5000	-4,6000	47,5000	0,5600	20,5000	2,5000	0,7100	39,9500
zGAL-10-74	39,1	3,1	644,1	270,2000	40,4000	-3,9000	279,5000	0,1500	39,5000	1,4800	0,6700	33,2700
zLUE-9-51	35,1	2,8	355,7	1025,7836	107,7079	7,6060	1050,6160	0,1050	152,6733	5,2600	0,7675	49,0900
zLUE-9-107	42,1	3,4	606,4	154,2552	110,0930	5,1245	179,6242	0,7137	30,9280	4,4600	0,7542	48,0900
zLUE-9-5	48,3	3,9	296,5	243,6353	58,0917	1,3633	257,0148	0,2384	50,1346	4,1900	0,7466	45,2300
zLUE-9-65	49,1	3,9	307,4	332,9243	114,9214	4,0016	359,3992	0,3452	74,4950	7,1400	0,7798	53,2200
zLUE-9-8	52,7	4,2	1966,0	33,4348	28,4244	0,8954	39,9825	0,8501	9,4126	12,7600	0,8223	68,2900
zLUE-9-110	54,3	4,3	633,7	263,6322	152,2688	59,3013	298,9810	0,5776	60,7439	2,2200	0,6899	36,9700
zLUE-9-1	58,4	4,7	540,6	196,9487	47,5777	1,0386	207,9063	0,2416	50,5374	5,5000	0,7681	49,9300
zLUE-9-24	65,4	5,2	1030,0	234,1763	43,0799	2,9965	244,1082	0,1840	65,7547	5,7200	0,7600	47,8000
zLUE-9-56	112,4	9,0	304,8	203,0000	97,6000	0,0000	225,5000	0,4800	107,2000	5,9000	0,7800	52,8200
zLUE-9-23	50,8	4,1	305,2	484,5000	76,2000	0,0000	502,0000	0,1600	102,4000	3,5900	0,7400	44,0500
zLUE-9-91	47,1	3,8	292,8	153,7000	51,9000	-0,7000	165,6000	0,3400	33,5000	8,3300	0,7900	56,8600
zLUE-9-26	46,8	3,8	600,3	484,4000	211,1000	0,0000	533,0000	0,4400	105,9000	6,8100	0,7800	54,3700
zLUE-9-13	37,0	3,0	593,0	53,0000	37,5000	2,7000	61,7000	0,7100	9,5000	6,3200	0,7700	51,8300
zLUE-2-95	33,1	2,6	587,5	178,2024	154,8309	11,2487	213,9007	0,8688	27,2957	2,5400	0,7111	40,4600
zLUE-2-67	33,8	2,7	325,1	519,5756	251,0326	38,7194	577,5569	0,4831	72,0252	1,9200	0,6809	35,5800
zLUE-2-101	34,0	2,7	2598,0	119,3553	81,2079	4,8413	138,0735	0,6804	17,5310	2,3600	0,6886	36,8900
zLUE-2-41	37,8	3,0	300,5	636,1758	256,8481	2,5847	695,3151	0,4037	99,1871	2,2100	0,6965	37,4800
zLUE-2-55	46,1	3,7	1946,0	298,6415	81,2159	0,0000	317,3374	0,2720	46,2784	0,7900	0,5846	25,8700
zLUE-2-13	52,3	4,2	310,8	412,6416	117,0616	6,8416	439,6234	0,2837	82,8566	1,6700	0,6660	33,4200
zLUE-2-94	58,6	4,7	307,7	369,7577	126,1487	2,8705	398,8115	0,3412	86,7936	1,9900	0,6854	35,8700
zLUE-2-117	59,6	4,8	719,8	124,0594	100,1786	5,6854	147,1489	0,8075	35,5344	4,0200	0,7459	46,4800
zLUE-2-65	61,4	4,9	459,6	147,2445	25,1000	4,4806	153,0449	0,1705	36,4452	2,5500	0,7165	39,7000
zLUE-2-23	257,2	20,6	318,4	430,3203	53,6164	15,6543	442,7410	0,1246	410,9333	1,4600	0,6589	32,1100
zLUE-2-35	356,3	28,5	305,6	137,6129	54,1347	7,7739	150,1135	0,3934	213,4598	2,9400	0,7215	41,2300
Sample	Age, Ma	err., Ma	U/Pb Age	U (ppm)	Th (ppm)	147Sm (ppm)	[U]e	Th/U	He (nmol/g)	mass (ug)	Ft	ESR

zLUE-2-84	294,2	23,5	668,1	343,9000	111,0000	7,1000	369,5000	0,3200	425,0000	2,4200	0,7100	39,2900
zLUE-2-71	33,0	2,6	302,2	474,3000	172,0000	3,2000	513,9000	0,3600	73,2000	9,0700	0,8000	58,2500
zLUE-2-10	74,7	6,0	576,6	87,4000	73,9000	1,2000	104,5000	0,8500	34,2000	9,3200	0,8100	62,3600
zEZK-2-1	280,4	22,4	653,3	190,4356	72,3827	3,3083	207,1146	0,3801	252,0118	6,9500	0,7877	55,4500
zEZK-2-5	239,1	19,1	2037,0	148,1692	66,5649	2,4145	163,5045	0,4492	151,0267	2,3800	0,7044	38,7400
zEZK-2-123	209,1	16,7	286,8	81,4787	45,7626	0,0000	92,0132	0,5617	74,5460	2,4600	0,7079	39,4100
zEZK-2-137	192,9	15,4	315,8	125,1894	26,8646	1,5123	131,3812	0,2146	103,8014	3,8000	0,7492	45,7300
zEZK-2-133	234,3	18,7	581,5	383,6866	241,2305	6,6319	439,2510	0,6287	396,6582	2,6000	0,7026	38,8100
zEZK-2-92	252,0	20,2	967,0	185,6812	84,8854	4,0763	205,2422	0,4572	209,0631	4,2300	0,7359	43,8500
zEZK-2-98	144,7	11,6	1010,0	129,7068	67,3386	0,0000	145,2081	0,5192	85,1021	3,7600	0,7428	45,3100
zEZK-2-85	101,0	8,1	961,0	39,1569	23,7832	3,6145	44,6499	0,6074	17,8697	3,1800	0,7280	42,8600
zIZA-5-113	61,4	4,9	566,2	807,8675	443,7831	28,7407	910,1700	0,5493	170,2280	0,8000	0,5617	24,6700
zIZA-5-8	96,5	7,7	328,8	112,0261	260,5840	0,0000	172,0125	2,3261	58,7964	1,4600	0,6478	33,2700
zIZA-5-55	187,4	15,0	628,1	216,7904	58,7380	-6,2786	230,2805	0,2709	158,5925	1,8300	0,6735	34,2200
zIZA-5-11	212,1	17,0	493,7	190,1614	122,9205	0,0000	218,4577	0,6464	179,3979	2,3700	0,7068	39,5100
zIZA-5-43	220,8	17,7	574,5	131,8126	15,3882	-2,6116	135,3419	0,1167	115,1448	2,2000	0,7047	37,8400
zIZA-5-98	243,3	19,5	1049,0	69,6451	60,0752	-4,2877	83,4529	0,8626	70,1360	1,3400	0,6299	30,5400
zIZA-5-104	252,9	20,2	1078,0	101,9434	85,1581	-8,4065	121,5048	0,8353	116,2678	2,0500	0,6890	37,2400
zIZA-5-44	383,5	30,7	2588,0	191,3229	148,4771	0,0000	225,5023	0,7761	318,0305	1,7400	0,6647	34,1000
zIZA-3-67	92,4	7,4	604,4	98,6238	95,0110	1,1094	120,5009	0,9634	46,5877	5,1800	0,7682	51,6500
zIZA-3-61	180,8	14,5	1826,0	306,6812	47,7353	0,0000	317,6699	0,1557	215,9831	1,8400	0,6896	35,9100
zIZA-3-13	200,7	16,1	2059,0	280,3044	52,0436	0,0000	292,2849	0,1857	241,8350	3,8400	0,7538	46,4700
zIZA-3-83	211,7	16,9	1050,0	141,6667	49,2909	0,0000	153,0135	0,3479	123,4299	2,3200	0,6965	37,3700
zIZA-3-97	238,3	19,1	670,2	273,9246	51,9372	0,0000	285,8806	0,1896	271,9070	3,1600	0,7284	41,8000
zIZA-3-38	254,2	20,3	303,0	228,7070	80,0919	0,0000	247,1442	0,3502	249,0632	2,7900	0,7222	41,1800
zIZA-3-122	295,8	23,7	294,2	457,8386	100,4393	1,7520	480,9685	0,2194	564,8712	3,2800	0,7214	40,6700
zIZA-3-121	322,4	25,8	504,0	136,6667	13,2566	0,0000	139,7183	0,0970	175,9703	2,4400	0,7092	38,3600
zIZA-10-60	59,0	4,7	342,2	482,5038	169,0946	-3,7552	521,4106	0,3505	108,6454	1,5300	0,6524	32,0100
zIZA-10-58	103,8	8,3	650,6	339,5591	135,4814	3,0245	370,7621	0,3990	143,2386	1,9000	0,6853	35,9600

Sample	Age, Ma	err., Ma	U/Pb Age	U (ppm)	Th (ppm)	147Sm (ppm)	[U]e	Th/U	He (nmol/g)	mass (ug)	Ft	ESR
zIZA-10-78	147,4	11,8	606,1	103,9857	86,9472	2,1205	124,0115	0,8361	71,5905	2,7100	0,7173	41,4300
zIZA-10-122	184,3	14,7	450,2	381,6166	132,7591	9,1232	412,2234	0,3479	282,4217	1,8900	0,6810	35,2900
zIZA-10-133	204,5	16,4	300,9	184,8343	30,8190	-3,5248	191,9112	0,1667	142,6512	1,6300	0,6659	33,0600
zIZA-10-63	249,6	20,0	918,0	95,0283	44,8071	0,0000	105,3429	0,4715	103,2097	2,7100	0,7151	40,3900